IAEA TECDOC SERIES

IAEA-TECDOC-1900

IAEA-TECDOC-1900

Understanding and Prediction of Thermohydraulic Phenomena Relevant to Supercritical Water Cooled Reactors (SCWRs)

Final Report of a Coordinated Research Project

IAEA
International Atomic Energy Agency

UNDERSTANDING AND PREDICTION OF THERMOHYDRAULIC PHENOMENA RELEVANT TO SUPERCRITICAL WATER COOLED REACTORS (SCWRs)

The following States are Members of the International Atomic Energy Agency:

AFGHANISTAN
ALBANIA
ALGERIA
ANGOLA
ANTIGUA AND BARBUDA
ARGENTINA
ARMENIA
AUSTRALIA
AUSTRIA
AZERBAIJAN
BAHAMAS
BAHRAIN
BANGLADESH
BARBADOS
BELARUS
BELGIUM
BELIZE
BENIN
BOLIVIA, PLURINATIONAL STATE OF
BOSNIA AND HERZEGOVINA
BOTSWANA
BRAZIL
BRUNEI DARUSSALAM
BULGARIA
BURKINA FASO
BURUNDI
CAMBODIA
CAMEROON
CANADA
CENTRAL AFRICAN REPUBLIC
CHAD
CHILE
CHINA
COLOMBIA
CONGO
COSTA RICA
CÔTE D'IVOIRE
CROATIA
CUBA
CYPRUS
CZECH REPUBLIC
DEMOCRATIC REPUBLIC OF THE CONGO
DENMARK
DJIBOUTI
DOMINICA
DOMINICAN REPUBLIC
ECUADOR
EGYPT
EL SALVADOR
ERITREA
ESTONIA
ESWATINI
ETHIOPIA
FIJI
FINLAND
FRANCE
GABON
GEORGIA
GERMANY
GHANA
GREECE
GRENADA
GUATEMALA
GUYANA
HAITI
HOLY SEE
HONDURAS
HUNGARY
ICELAND
INDIA
INDONESIA
IRAN, ISLAMIC REPUBLIC OF
IRAQ
IRELAND
ISRAEL
ITALY
JAMAICA
JAPAN
JORDAN
KAZAKHSTAN
KENYA
KOREA, REPUBLIC OF
KUWAIT
KYRGYZSTAN
LAO PEOPLE'S DEMOCRATIC REPUBLIC
LATVIA
LEBANON
LESOTHO
LIBERIA
LIBYA
LIECHTENSTEIN
LITHUANIA
LUXEMBOURG
MADAGASCAR
MALAWI
MALAYSIA
MALI
MALTA
MARSHALL ISLANDS
MAURITANIA
MAURITIUS
MEXICO
MONACO
MONGOLIA
MONTENEGRO
MOROCCO
MOZAMBIQUE
MYANMAR
NAMIBIA
NEPAL
NETHERLANDS
NEW ZEALAND
NICARAGUA
NIGER
NIGERIA
NORTH MACEDONIA
NORWAY
OMAN
PAKISTAN
PALAU
PANAMA
PAPUA NEW GUINEA
PARAGUAY
PERU
PHILIPPINES
POLAND
PORTUGAL
QATAR
REPUBLIC OF MOLDOVA
ROMANIA
RUSSIAN FEDERATION
RWANDA
SAINT LUCIA
SAINT VINCENT AND THE GRENADINES
SAN MARINO
SAUDI ARABIA
SENEGAL
SERBIA
SEYCHELLES
SIERRA LEONE
SINGAPORE
SLOVAKIA
SLOVENIA
SOUTH AFRICA
SPAIN
SRI LANKA
SUDAN
SWEDEN
SWITZERLAND
SYRIAN ARAB REPUBLIC
TAJIKISTAN
THAILAND
TOGO
TRINIDAD AND TOBAGO
TUNISIA
TURKEY
TURKMENISTAN
UGANDA
UKRAINE
UNITED ARAB EMIRATES
UNITED KINGDOM OF GREAT BRITAIN AND NORTHERN IRELAND
UNITED REPUBLIC OF TANZANIA
UNITED STATES OF AMERICA
URUGUAY
UZBEKISTAN
VANUATU
VENEZUELA, BOLIVARIAN REPUBLIC OF
VIET NAM
YEMEN
ZAMBIA
ZIMBABWE

The Agency's Statute was approved on 23 October 1956 by the Conference on the Statute of the IAEA held at United Nations Headquarters, New York; it entered into force on 29 July 1957. The Headquarters of the Agency are situated in Vienna. Its principal objective is "to accelerate and enlarge the contribution of atomic energy to peace, health and prosperity throughout the world''.

IAEA-TECDOC-1900

UNDERSTANDING AND PREDICTION OF THERMOHYDRAULIC PHENOMENA RELEVANT TO SUPERCRITICAL WATER COOLED REACTORS (SCWRs)

FINAL REPORT OF A COORDINATED RESEARCH PROJECT

INTERNATIONAL ATOMIC ENERGY AGENCY
VIENNA, 2020

COPYRIGHT NOTICE

For further information on this publication, please contact:

Nuclear Power Technology Development Section
International Atomic Energy Agency
Vienna International Centre
PO Box 100
1400 Vienna, Austria
Email: Official.Mail@iaea.org

Printed by the IAEA in Austria
February 2020

IAEA Library Cataloguing in Publication Data

Names: International Atomic Energy Agency.
Title: Understanding and prediction of thermohydraulic phenomena relevant to supercritical water cooled reactors (SWCRs) / International Atomic Energy Agency.
Description: Vienna : International Atomic Energy Agency, 2020. | Series: IAEA TECDOC series, ISSN 1011–4289 ; no. 1900 | Includes bibliographical references.
Identifiers: IAEAL 20-01298 | ISBN 978–92–0–102320–9 (paperback : alk. paper) | ISBN 978–92–0–102420–6 (pdf)
Subjects: LCSH: Water cooled reactors. | Nuclear reactors — Thermodynamics. | Thermal hydraulics.

FOREWORD

The supercritical water cooled reactor (SCWR) is an innovative concept that operates at a pressure higher than the thermodynamic critical point of water, allowing the core outlet coolant temperature to be much higher than that of the current generation of WCRs. The key technological advantages of the SCWR include its high thermal efficiency and simplified system configuration compared with conventional WCRs.

There has been a high level of interest in research and development of SCWRs in several Member States. In 2007, the IAEA started the coordinated research project (CRP) entitled Heat Transfer Behaviour and Thermo-hydraulics Code Testing for Super-critical Water Cooled Reactors (SCWRs), which promoted international collaboration among 16 institutes from 9 Member States and 2 international organizations. The CRP was successfully completed in September 2012. Information generated from that CRP was documented in numerous IAEA publications and reports. A database of thermohydraulic parameters of interest to SCWR development was compiled and is housed in the Nuclear Energy Agency's central server.

After the completion of the CRP, collaboration continued between several participating institutes. Most of these institutes expressed their strong interest in and support for a new CRP on thermohydraulics of SCWRs to continue the momentum of international collaboration. The overall objective of this second CRP, which started in 2014, was to improve the understanding of thermohydraulic phenomena and the prediction accuracy of thermohydraulic parameters related to SCWRs and to benchmark numerical toolsets for SCWR thermohydraulic analyses. Scientific investigators from participating institutes identified specific research objectives to improve the predictive capability of key technology areas (e.g. heat transfer and pressure drop for SCWR fuel related geometries, parallel channel stability boundary, natural circulation flow, critical heat flux at near critical pressures, critical flow, subchannel and plenum mixing). The predictive capability of subchannel codes and computational fluid dynamic tools was assessed through benchmarking exercises for heat transfer in tubes, annuli and bundles as well as pressure drops in annuli and bundles. In total, 12 institutes from 10 Member States and 2 international organizations were involved in this second CRP, which was completed with the planned outputs in 2019.

The present publication provides the background and objectives of the CRP; descriptions of a revised Canadian SCWR design concept and a new SCWR design concept being developed at the Nuclear Power Institute of China; updated information on key technology areas (e.g. heat transfer in simple geometries, stability and critical flow) obtained since the completion of the previous CRP; new experiments and data on supercritical heat transfer in bundles and on critical heat flux; and application of the direct numerical simulation approach for supercritical heat transfer. Results of three benchmarking exercises with subchannel codes and computational fluid dynamic tools are also presented, to demonstrate successes and show areas for further improvement. Experimental information and data were contributed by participating institutes through close collaboration.

This publication illustrates the state of the art of SCWR research and development. It is expected to be a key supporting publication for researchers and engineers pursuing the development of SCWRs or equipment/components operating at supercritical pressures.

The IAEA is grateful for the contributions of the chief scientific investigators of all participating institutes and of the CRP chairpersons, L. Leung (Canada) and W. Ambrosini (Italy). In particular, the efforts of L. Leung to collect and organize the contributions and to continuously encourage progress in the work are gratefully recognized. The IAEA officers responsible for this publication were T. Jevremovic and K. Yamada of the Division of Nuclear Power.

EDITORIAL NOTE

This publication has been prepared from the original material as submitted by the contributors and has not been edited by the editorial staff of the IAEA. The views expressed remain the responsibility of the contributors and do not necessarily represent the views of the IAEA or its Member States.

Neither the IAEA nor its Member States assume any responsibility for consequences which may arise from the use of this publication. This publication does not address questions of responsibility, legal or otherwise, for acts or omissions on the part of any person.

The use of particular designations of countries or territories does not imply any judgement by the publisher, the IAEA, as to the legal status of such countries or territories, of their authorities and institutions or of the delimitation of their boundaries.

The mention of names of specific companies or products (whether or not indicated as registered) does not imply any intention to infringe proprietary rights, nor should it be construed as an endorsement or recommendation on the part of the IAEA.

The authors are responsible for having obtained the necessary permission for the IAEA to reproduce, translate or use material from sources already protected by copyrights.

The IAEA has no responsibility for the persistence or accuracy of URLs for external or third party Internet web sites referred to in this publication and does not guarantee that any content on such web sites is, or will remain, accurate or appropriate.

CONTENTS

1. INTRODUCTION

The International Atomic Energy Agency (IAEA) fosters international cooperation on advanced designs of nuclear power plants (NPPs) for future deployments in minimizing the release of greenhouse gases as the primary cause of climate change. The Generation IV International Forum (GIF) was established in 2000 to support joint research and development (R&D) of these advanced nuclear systems [1.1]. Six advanced (referred to as the Generation IV) nuclear reactor systems were selected from over 1000 potential candidate designs. Among these six selected options, the Super Critical Water cooled Reactor (SCWR) is the only one that is directly evolved from the current NPPs designed and in operation for over 50 years.

The main goals of using supercritical water (SCW) in nuclear reactors are to increase the efficiency of NPPs, decrease capital and operational costs, and decrease electrical energy costs [1.2]. This would enhance the sustainability of nuclear power as the fuel consumption is reduced for generating the power and subsequently a reduction in spent fuel for disposal. Furthermore, the safety characteristics of SCWR are advanced from the introduction of passive safety systems. Depending on the concept configuration, the aspects of proliferation resistance and physical protection are improved.

Four countries (i.e., Canada, China, Japan and the Russian Federation) and the European Union are the signatories of the System Arrangement to participate in joint research and development (R&D) of the SCWR design concepts [1.3]. Most SCWR concepts are developed for large baseload power generations of over 1000 MWe, which are considered excessive for small remote communities, small mining operations and oil production[1.4]. With the modular configuration, SCWR concepts can be scaled down to meet the needs of local deployment. The development of small and very small SCWR concepts are as well initiated; Canada is developing a 300 MWe concept for replacing the fossil fired power plants and and a 15 MWe concept for installation at remote communities, while China, on the other hand, is developing a 150 MWe concept for demonstration plant [1.5].

The technology roadmap for developing SCWR concepts has been updated to identify key technology areas to be pursued [1.1]. Key technology areas remain focusing on materials, chemistry, thermal–hydraulics and safety. Strong collaboration among GIF participants in the SCWR system is well established [1.3]. Having said that, there is an interest in expanding the collaboration to advance these technology areas with research organizations in non GIF Member States of the International Atomic Energy Agency (IAEA).

1.1. OVERVIEW OF THE COORDINATED RESEARCH PROJECT

The IAEA has a mandate to “foster the exchange of scientific and technical information on peaceful uses of atomic energy” [1.6]. The organization has established Coordinated Research Projects (CRPs) in support of advancing R&D with international participants from Member States. This facilitates sharing of resources and expertise, as well as expediting the technology advancement [1.7].

There has been strong interest in SCWR R&D in a number of Member States. In 2008, the IAEA officially started the CRP on *Heat Transfer Behaviour and Thermo-hydraulics Code Testing for SCWRs*, which promoted international collaboration among 16 institutes from 9 Member States and 2 international organizations. The CRP was successfully completed in September 2012, and a technical document (TECDOC) synthesizing the results from the CRP was published in August 2014. A database of thermal–hydraulics parameters of interest to SCWR development was compiled and is hosted by the OECD/NEA.

Despite of the completion of the CRP, several collaborations continue between institutes participating in the CRP. Most of these institutes expressed their strong interest and support to initiate a new CRP on thermal–hydraulics of SCWRs to continue the momentum of international collaborations.

A new CRP on thermal–hydraulics of SCWRs was developed to improve the understanding of thermal–hydraulics phenomena relevant to SCWRs and the prediction accuracy of thermal–hydraulics parameters of interest to SCWR analyses. The identified scope of collaboration is considered as the applied R&D, as compared to the basis R&D in the former CRP.

1.2. OBJECTIVES OF THE COORDINATED RESEARCH PROJECT

The overall objective of this CRP was to improve the understanding of thermal–hydraulics phenomena and prediction accuracy of thermal–hydraulics parameters related to SCWRs and to benchmark numerical toolsets for SCWR thermal–hydraulics analyses. Scientific investigators from participating institutes identified specific research objectives to improve predictive capability of key technology areas (such as heat transfer and pressure drop for SCWR fuel related geometries, parallel channel stability boundary, natural circulation flow, critical heat flux at near critical pressures, critical flow, subchannel and plenum mixing). Predictive capability of subchannel codes and computational fluid dynamic tools were assessed through benchmarking exercises for heat transfer in tubes, annuli and bundles as well as pressure drops in annuli and bundles. In total, 12 institutes from ten Member States and two international organizations were involved in the CRP. The CRP was completed with the planned outputs in 2019..

1.3. ACTIVITIES OF THE COORDINATED RESEARCH PROJECT

Twelve activities (or tasks) were carried out collaboratively within the framework of the CRP as follows:

Activity 1: Concept update

Completed or proposed SCWR concepts at the time of the TECDOC publication for the CRP on *Heat Transfer Behaviour and Thermo-hydraulics Code Testing for SCWRs* were described [1.4]. Since then, the Canadian SCWR concept has been evolved with a revised core concept and an established plant concept [1.8] and a new reference Chinese SCWR concept has emerged [1.9]. These revised and new concepts are described in this TECDOC.

Activity 2: Heat transfer characteristics in non-bundle geometries

Heat transfer R&D with simple geometries (such as tubes and annuli) in water and surrogate fluids at supercritical pressures are continuing to enhance the understanding of the fundamental phenomena and provide validation data for computational fluid dynamics (CFD) tools. New studies are performed and compiled and their experimental data collected. Proposed fluid–to–fluid modelling approaches are presented to supplement the water database from surrogate fluid experiments.

Activity 3: Heat transfer characteristics in rod bundles

Many heat transfer experiments were focused on improving the understanding of the complexity of thermal–hydraulics in rod bundle geometries at supercritical pressures. Most of these experiments were performed using a 2×2 rod bundle configuration, which simulated partly the fuel rod arrangement in the pressure vessel type of SCWR assemblies. In addition, other bundle subassemblies with three or seven rods were also tested in water and surrogate fluids. These rod bundle experiments provided valuable data for validation of subchannel codes and CFD tools.

Activity 4: Pressure loss characteristics

Pressure loss characteristics have not been investigated closely in the CRP on *Heat Transfer Behaviour and Thermo-hydraulics Code Testing for SCWRs* due to a lack of relevant experimental data. While affecting mainly the pump design on a system (global) level, these characteristics have an impact in establishing the flow distribution within subchannels of a fuel assembly affecting the maximum cladding temperature prediction. Pressure loss experiments using simple geometries and rod bundles were examined. Experimental data were compiled and models for predicting frictional and form losses were identified.

Activity 5: Natural circulation and flow stability

The large density variation within the reactor core and use of passive cooling safety systems have led to concerns on natural circulation and related instability. Heat transfer during natural circulation and associated stability issues were described in detail in the TECDOC of the CRP on *Heat Transfer Behaviour and Thermo-hydraulics Code Testing for SCWRs* [1.4]. Improvement of the models is continuing to enhance the prediction capability. In addition, new experimental data on instability in tubes have been obtained for validation of analytical models, system codes and CFD tools. Despite of the strong interest, most experiments were performed using surrogate fluids rather than water (primarily due to the cost reduction and efficiency enhancement when performing the surrogate fluid experiments). Fluid–to–fluid modelling approaches to transform surrogate fluid data to water equivalent values have been established to extend the water database.

Activity 6: Critical flow

The focus on critical flow phenomenon arose from the design of the pressure relieve valve in the safety system and the analysis of large break loss of coolant accident scenarios. This phenomenon was covered in detail in the TECDOC of CRP on *Heat Transfer Behaviour and Thermo-hydraulics*

Code Testing for SCWRs. New experimental data on critical flow have been obtained with sharp edges nozzles of two opening sizes and a smooth convergent divergent nozzle. The main improvement in these new experiments is the fact that the back pressure was controlled (rather than blow down to atmospheric conditions), which had led to less scatter among the experimental data. In addition, new critical flow models have been derived from these new experimental data and are applicable for a wide range of flow conditions.

Activity 7: Critical heat flux near critical pressure

The coolant is considered a single phase fluid without phase change during normal operation of SCWRs. Therefore, the traditional safety criterion of critical heat flux for NPPs is no longer applicable. However, a reduction in pressure is encountered at large break loss of coolant accident scenarios and shut down of the SCWRs while an increase in pressure is associated with the start up process of the SCWRs. These pressure changes could lead to the occurrence of critical heat flux in the fuel assemblies leading to a sharp rise in cladding temperature that challenge the cladding integrity. An experimental database on critical heat flux with water and surrogate fluid flows has been compiled at near critical pressures (i.e., above 18 MPa). In addition, new experimental data have also been obtained with tubes and rod bundles. A compilation of new and previous data on critical heat flux has been assembled and compared. This new database was applied in assessing the prediction methods.

Activity 8: Subchannel model development

Subchannel codes are essential tools in supporting fuel assembly design and optimization for SCWRs. Their fundamental conservation equations are valid for supercritical pressure applications, but the constitutive equations are based mainly on experimental data obtained at subcritical pressures. Applicability of these equations to supercritical pressures need to be confirmed. If necessary, new equations need to be developed to improve the prediction accuracy and reduce the uncertainty of the SCWR core design. Several subchannel based phenomena have been identified including subchannel mixing, shape effect and spacing devices. Analytical findings and new data relevant to these phenomena were compiled to enhance the understanding.

Activity 9: Direct numerical simulations / large eddy simulations for SCWRs

The general thermal–hydraulics characteristics at supercritical pressures are understood in support of the conceptual design of SCWRs. However, specific in flow structure and the fundamental mechanism of some phenomena (such as the deteriorated heat transfer) remain elusive. Experiments were performed to improve the understanding but limited to the testing capability and instrumentation. Direct numerical and large eddy simulations have been applied to improve the fundamental understanding of thermal–hydraulics characteristics at supercritical pressures. Recent studies on these simulations have been summarized and a path forward is introduced.

Activity 10: Analysis code benchmarking exercises

Analytical tools, such as system codes, subchannel codes and CFD tools, are essential for design of SCWR cores, fuel assemblies and safety systems. SCWR designers applied mainly their own

analytical tools in the analyses. Although assessments were performed against selected experimental data, an improvement strategy has not been well defined due to the complexity of the phenomena and calculation. Benchmarking is an effective tool to assess the capability of the analytical tools. It identifies the limitation of these tools and provides improvement approaches based on the model comparison against other tools. Several benchmarking exercises have been identified in this CRP:

- Benchmarking of CFD tools against heat transfer tests performed with water flow in tubes and annuli at supercritical pressures;
- Benchmarking of subchannel codes and CFD tools against heat transfer tests performed with water flow through a 2×2 rod bundle at supercritical pressures;
- Benchmarking of CFD tools against pressure loss tests performed with water flow through an annuli and a 3-rod bundle at supercritical pressures.

Activity 11: Establishment of the database

New experimental data are compiled for sharing among the CRP participants through the OECD/NEA database system. Several databases have been established for the following thermal–hydraulics phenomena:

- Heat transfer in tubes, annuli and rod bundles with water and surrogate fluids;
- Pressure losses in tubes, annuli and rod bundles with water and surrogate fluids;
- Natural circulation and instability in single and parallel channels;
- Critical flow in orifices and nozzles;
- Critical heat flux in tubes and bundles.

These databases include the following:

- Openly available data including results of work conducted by institutes holding Research or Technical Contracts with the Agency; and data provided to the IAEA by institutes holding Research Agreements with the Agency for those cases where the Agreement holder indicates that the contributed data can be made openly available;
- Data provided by institutes holding Research Agreements with the Agency for those cases where the Agreement holder indicates that the data may be shared among the organizations participating within the CRP;
- Summary level information about experimental facilities and associated data that could be shared bilaterally under appropriate agreements between countries.

Activity 12: Information dissemination

The participating organizations are responsible to preparean IAEA TECDOC to disseminate the information compiled from the CRP in providing the state of the art of thermal–hydraulics development in support of the SCWR conceptual design and the description of available databases. The IAEA is responsible for the review, editing and issue of the publication to Member States. Organisations which have been granted Research Agreements / Contracts were expected to utilize the IAEA Guidance publication 50–C–Q/SG–8 *Quality Assurance in Research and Development*.

This ensures qualified data and calculations are disseminated for use in other applications (such as designs of the supercritical fossil fired power plants, Brayton cycle balance of plant with carbon dioxide flow, and carbon dioxide cooled reactors).

1.4. OUTPUTS FROM THE COORDINATED RESEARCH PROJECT

The CRP has generated the following deliverables collectively:

- Databases on thermal–hydraulics phenomena at supercritical pressures;
- IAEA TECDOC disseminating information compiled from the CRP;
- Joint papers by CRP participants presented at international conferences and published in technical journals.

Several new databases have been compiled from contribution of CRP participants at the OECD/NEA database system. These databases are shared among participants for facilitating expedition of the SCWR design and R&D. As mentioned above, these databases covered thermal–hydraulics phenomena such as heat transfer, pressure loss, stability, critical flow and critical heat flux at near critical pressures. This IAEA TECDOC is a deliverable of the CRP summarizing the results obtained through the collaboration among participating organizations. Many joint papers have been presented at international conferences and published in journals, and some others will be presented and published after the completion of the CRP.

1.5. RESEARCH COORDINATION MEETINGS

The first Research Coordination Meeting (RCM) of the CRP was held on 28–31 October 2014 at the IAEA Headquarters in Vienna, Austria. Each participant presented their completed, ongoing and future R&D activities on SCWR thermal–hydraulics relevant to the CRP at their institute. This has led to better understanding of the available information and coordination of the task plan for the CRP. All participants discussed and established tasks and subtasks to achieve the objective of the CRP considering R&D activities in each institute and common interests among institutes. A detailed work plan was established to identify partners, deliverables and leads for each task or subtask. Based on the work plan, an Integrated Research Plan (IRP) for the 1st year of the study was discussed and established. The participants elected Mr Leung of AECL, Canada, and Mr. Ambrosini of University of Pisa, Italy, as the Co-Chairs of the CRP.

The second RCM of the CRP was held on 23–27 November 2015 at Bhabha Atomic Research Centre in Mumbai, India. All participants presented the R&D activities performed during the 1st CRP period and planned for the 2nd period in their institute. The progress was discussed and the impact on the task plan was reviewed and adjusted accordingly. All participants established an Integrated Research Plan for the 2nd period. Several other topics related to the CRP, such as Technical Meeting on thermal–hydraulics of SCWRs and preparation of a TECDOC to synthesize the results of the CRP, were also discussed.

The third RCM was held on 26–29 June 2017 at University of Wisconsin, Madison in Madison, Wisconsin, of the United States of America. All participants presented the R&D activities performed during the 2nd CRP period and planned for the 3rd period in their institute. The progress

was discussed and its impact on the task plan was reviewed and adjusted accordingly. All participants agreed to propose a one year extension of the CRP allowing additional time for technical discussion on new experimental and analytical results and the incorporation of an additional task for the application of high performance computers in support of thermal–hydraulics relationship development for SCWRs. They discussed activities for future collaboration and suggested several topics to IAEA for initiating a new CRP. A proposal to start drafting the TECDOC was accepted.

The fourth RCM was held on 28–30 January 2019 at the IAEA Headquarters in Vienna, Austria. Technical Secretariat presented the structure of the Water Cooled Reactor Group under the Nuclear Energy Department at IAEA. She reiterated the focus of the meeting to identify the needs and schedule for completing the TECDOC. Each lead presented their draft section and discussed remaining submission and improvement. Leads of section preparation identified unique requirements for the TECDOC. Several documents for IAEA publication were provided to section leads for information. In view of the availability of most participants at the meeting, small group discussions were held to identify needs for finalizing the section. A schedule for completion has been established.

1.6. ORGANIZATION OF THE TECDOC

Section 2 provides an update on the SCWR concept development. It summarizes the revised core concept and the plant concept for the Canadian SCWR and the reference Chinese SCWR concept.

Section 3 summarizes the latest heat transfer experiments performed with tubes and annuli (i.e., nonbundle geometries) at supercritical pressures and their database. The proposed fluid–to–fluid modelling approaches are described. This Section is considered supplemental to information presented in the TECDOC of CRP on *Heat Transfer Behaviour and Thermo-hydraulics Code Testing for SCWRs* [1.4].

Section 4 focuses on the heat transfer experiments for rod bundles in water and surrogate fluids. Test facilities and test sections are described together with the covered flow conditions. Axial and circumferential cladding temperatures and corresponding heat transfer coefficients are shown for various rods. Assessments of several prediction methods against these experimental heat transfer coefficients are presented.

Section 5 summarizes the pressure loss experiments performed with annuli and rod bundles at supercritical pressures and their database. Analytical models for various pressure loss components are described.

Section 6 presents new experiments on natural circulation and stability performed in single and parallel channels. Experimental data on the stability boundaries at various channel configurations are compiled. The enhancement of the stability model is shown against experimental data.

Section 7 describes critical flow experiments performed with sharp edge nozzles with two opening sizes at supercritical upstream pressures. Critical flow behaviors are examined with flow

conditions and nozzle opening sizes. Critical flow models have been derived with these data for use in system code.

Section 8 presents the experimental characteristics of critical heat flux at near critical pressures. Historical experimental data were compared against those obtained recently. The CHF lookup table [1.10] has been assessed against the combined database. A new CHF correlation has been proposed.

Section 9 summarizes the examination of several subchannel phenomena, including mixing, spacing devices effect and subchannel shape effect. The impact of these phenomena on thermal–hydraulics predictions in subchannel codes was assessed.

Section 10 presents the results of three benchmarking exercises:

- Prediction accuracy of CFD tools on heat transfer in tubes and annuli with water flow at supercritical pressures;
- Prediction accuracy of subchannel codes and CFD tools on heat transfer in a 2×2 rod bundle with water flow at supercritical pressures;
- Prediction accuracy of CFD tools on pressure loss over an annuli and a 3-rod bundle with water flow at supercritical pressures.

Acronyms

CFD	Computational Fluid Dynamics
CRP	Coordinated Research Project
GIF	Generation IV International Forum
IAEA	International Atomic Energy Agency
IRP	Integrated Research Plan
NEA	Nuclear Energy Agency
NPP	Nuclear Power Plant
OECD	Organisation for Economic Cooperation and Development
R&D	Research and Development
RCM	Research Coordination Meetings
SCW	Supercritical Water
SCWR	Supercritical Water cooled Reactor
TECDOC	Technical Document

REFERENCES TO SECTION 1

[1.1] NUCLEAR ENERGY AGENCY, Technology Roadmap Update for Generation IV Nuclear Energy Systems, Organization for Economic Co-operation and Development, (2014).

[1.2] DUFFEY, R.B., LEUNG, L.K.H., Advanced Cycle Efficiency: Generating 40% More Power from the Nuclear Fuel, Proc. World Energy Congress (WEC), Montreal, 2010.

[1.3] NUCLEAR ENERGY AGENCY, 2017 Annual Report, Generation IV International Forum, (2018).

[1.4] INTERNATIONAL ATOMIC ENERGY AGENCY, Heat Transfer Behaviour and Thermohydraulics Code Testing for Supercritical Water Cooled Reactors (SCWRs), IAEA-TECDOC-1746, IAEA, Vienna (2014).
[1.5] YETISIR, M., PENCER, J., McDONALD, M., GAUDET, M., LICHT, J., DUFFEY, R., The Supersafe© Reactor: A Small Modular Pressure Tube SCWR, AECL Nuclear Review, **1, 2**, (2012), 13–18.
[1.6] INTERNATIONAL ATOMIC ENERGY AGENCY, The Statute of the IAEA, Article III.
[1.7] INTERNATIONAL ATOMIC ENERGY AGENCY, Coordinated Research Projects.
[1.8] SCHULENBERG, T., LEUNG, L., "Super-critical water-cooled reactors", Handbook of Generation IV Nuclear Reactors (PIORO, I.L., Ed.), Woodhead Publishing Series in Energy, (2016), 189–220.
[1.9] INTERNATIONAL ATOMIC ENERGY AGENCY, Status Report - Chinese Supercritical Water-Cooled Reactor (CSR1000), (2015).
[1.10] GROENEVELD, D.C., SHAN, J.Q., VASIĆ, A.Z., LEUNG, L.K.H., DURMAYAZ, A., YANG, J., CHENG, S.C., TANASE, A., The 2006 CHF Look-Up Table, Nuclear Engineering and Design, **237**, (2007), 1909–1922.

2. UPDATE OF SCWR DESIGN CONCEPTS

The SCWR is a high temperature, high pressure water cooled reactor that operates above the thermodynamic critical point of water (374 °C, 22.1 MPa) [2.1]. Two types of core configuration are being pursued: pressure vessel (PV) and pressure tube (PT). These core designs are based on thermal neutron, fast neutron, or mixed (thermal and fast) spectra.

The majority of SCWR plants are developed for power generation higher than 1000 MWe at operating pressures of about 25 MPa and reactor outlet temperatures from 500 to 625 °C. Under these conditions, the coolant does not change phase (boil) in the reactor. This facilitates the SCWR to adopt the direct cycle eliminating moisture separator reheaters and recirculation pumps as in the Boiling Water Reactors (BWRs), or steam generators as in the Pressurized Light Water and Heavy Water Reactors (PWRs and PHWRs). Without the major capital equipment, the sizes and footprints of the containment, building and plant of SCWRs are significantly reduced. This has led to reduction in capital cost of a SCWR plant compared to that of the Light Water Reactor (LWR) or Heavy Water Reactor (HWR) plants. The balance of plant configuration of the SCWR is the same as that of the fossil fired power plants, which has accumulated over 50 years of design and operation experience.

The main mission of the SCWR is to generate electricity efficiently, economically and safely. All SCWR designs could generate electricity with thermal efficiencies ranging from 43–48 %, which is better than 35 % for the current fleet of nuclear reactor systems. The high core outlet temperature of SCWRs facilitates cogeneration, such as hydrogen production, space heating and steam production [2.2].

SCWR concepts under development were described in [2.3]. Most organizations have been focusing on the R&D supporting the current design concepts. However, the Canadian SCWR concept has been updated and a new thermal spectrum SCWR concept has been proposed from the Nuclear Power Institute of China. Key parameters of all proposed SCWR concepts are listed in Table 2.1.

2.1. CANADIAN SCWR CONCEPT

The Canadian SCWR concept is a pressure tube type of concept [2.4]. It adopts the direct cycle, which includes a 2540 MW_{th} core that receives feed water at 315°C and 1176 kg/s and generates steam at 625°C and 25 MPa (supercritical pressure). As illustrated in Fig. 2.1, the Canadian SCWR core concept consists of a pressurized inlet plenum, a low pressure calandria vessel that contains heavy water moderator and 336 fuel channels that are attached to a common outlet header. A counter flow fuel channel is adopted to position the inlet and outlet piping above the reactor core so that a complete break of either an inlet pipe or an outlet pipe will not result in an immediate loss of coolant at the reactor core. A non fuel central flow channel is located at the centre of the fuel channel to increase neutron moderation close to the inner fuel rings.

The coolant flows into the inlet plenum, around the outside of the outlet header (blue arrows in Fig. 2.1) and then enters the pressure tube extension through a series of slots, into the fuel assembly

through a cross over piece (top right figure), down through a flow tube in the centre of the fuel assembly, back up through the fuel rods (bottom right figure) and then out through the outlet header.

TABLE 2.1. KEY PARAMETERS OF SCWR CONCEPTS

	CANADA	CHINA		EU	JAPAN		RUSSIAN FEDERATION
Type	PT	PV	PV	PV	PV	PV	PV
Spectrum	Thermal	Thermal	Mixed	Thermal	Thermal	Fast	Fast
Pressure (MPa)	25	25	25	25	25	25	24.5
Inlet Temp. (ºC)	350	280	280	280	290	280	290
Outlet Temp. (ºC)	625	500	510	500	510	501	540
Thermal Power (MW)	2540	2300	3800	2300	4039	2337	3830
Efficiency (%)	48	43	44	43.5	44	43	45
Active Core Height (m)	5	3	4.5	4.2	4.2	2.4	4.07
Fuel	Pu–Th (UO_2)	UO_2	UO_2/MOX	UO_2	UO_2	MOX	MOX
Moderator	D_2O	H_2O	H_2O/–	H_2O	H_2O	–/ZrH	–
# of Flow Passes	1	2	2	3	2	1	1/2

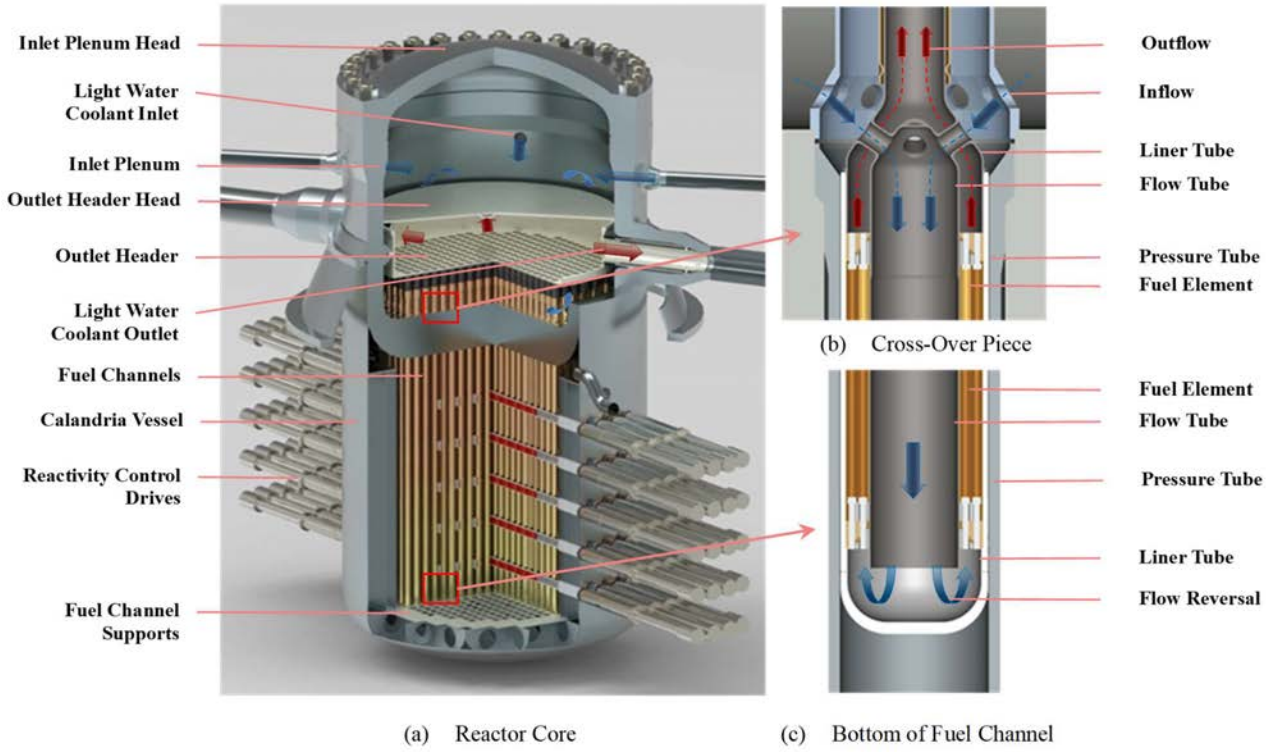

Fig. 2.1. Canadian SCWR core concept.

The fuel channel consists of the pressure tube extending into the moderator, and an extension connecting the pressure tube to the outlet header. All internals of the pressure tube are part of the fuel assembly. The pressure tube has an open end and a closed end (i.e., a test tube shape). A

pressure tube extension is connected to the pressure tube at the top of the tubesheet and incorporates several openings near the interface with the pressure tube to allow coolant entering into the fuel channel and subsequently to the fuel assembly. These openings act as orifices to control the amount of coolant flowing into each channel and to suppress instability. The size of these openings is determined through matching the channel power output to provide an outlet coolant temperature as close to 625°C as possible.

The calandria vessel is a low pressure vessel that contains the heavy water moderator, fuel channels, reactivity control mechanisms, and emergency shutdown devices. The reactivity control mechanisms located at the sides of the core are shielded, at a minimum, with a similar volume of moderator, with an increasing amount at the reactor centerline due to the curvature of the calandria vessel. The moderator operates at subcooled temperatures using a pumped recirculation system but in case of a station blackout, core decay heat is passively removed through the use a flashing driven natural circulation loop.

The fuel for the Canadian SCWR concept is similar to existing power reactor fuel in that a ceramic pellet produces heat which is transferred through the metallic cladding to the primary coolant. It is a mix of thorium (Th) and plutonium (Pu, which is extracted from the spent fuel of HWRs or LWRs). On average, the weight percentage of plutonium is 13 % in the fuel. With the high neutron economy of the heavy water moderator, other fuel mixes can also be accommodated. Studies have demonstrated the feasibility of using Low Enriched Uranium (LEU) of 7 %, a mix of LEU at 7.5 % with Th, a mix of transuranics (TRU) at 21 wt% with Th, or a mix of Pu at 8 %, Th and ^{233}U at 2 wt% (extracted from the SCWR fuel).

The fuel bundle concept consists of 64 fuel rods with 32 fuel rods in each ring (see Fig. 2.2 for the cross sectional view). The outer diameter of fuel rods is 9.5 mm in the inner ring and is 10 mm in the outer ring. Each fuel rod is 6.5 m long housing the fuel pellets, an inner filler tube in the plenum area to prevent collapse under external pressure, and a spring to hold the pellets in place but allow for pellet expansion. The active length of the fuel rod is 5 m. Each end of the fuel rod is closed with an end plug, which is welded to the cladding tube. Spacings between fuel rods, between inner ring rods and central flow tube, and between outer ring rods and the inner insulator liner are maintained by wires arranged in a spiral wrap around every fuel rod.

The reactor building configuration is shown in Fig. 2.3, which includes major systems and components. Its inner core structure is the primary containment building (simply referred to as the containment building from here on), which houses the reactor, high activity components and systems, the containment pool, all safety related pressure boundary components. The reactor is centrally located within the containment building. The containment building is enveloped by the shield building, which is equipped with means for the collection and filtration of leaks of fission products from the turbine and piping in the event of a beyond design basis accident. The shield building houses all lower radioactivity processes such as the containment pool filter system, drywell and steam tunnel cooling system, and fuel transfer pool cooling system.

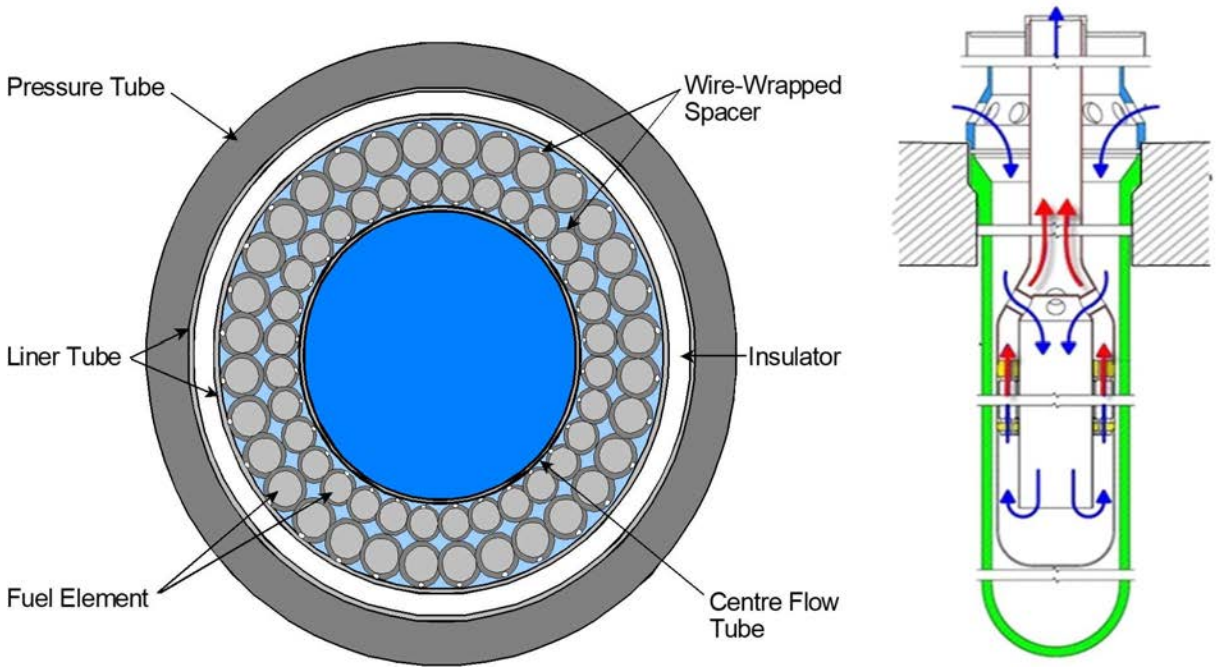

Fig. 2.2. Cross sectional view of the 64-rod fuel bundle concept inside the pressure tube.

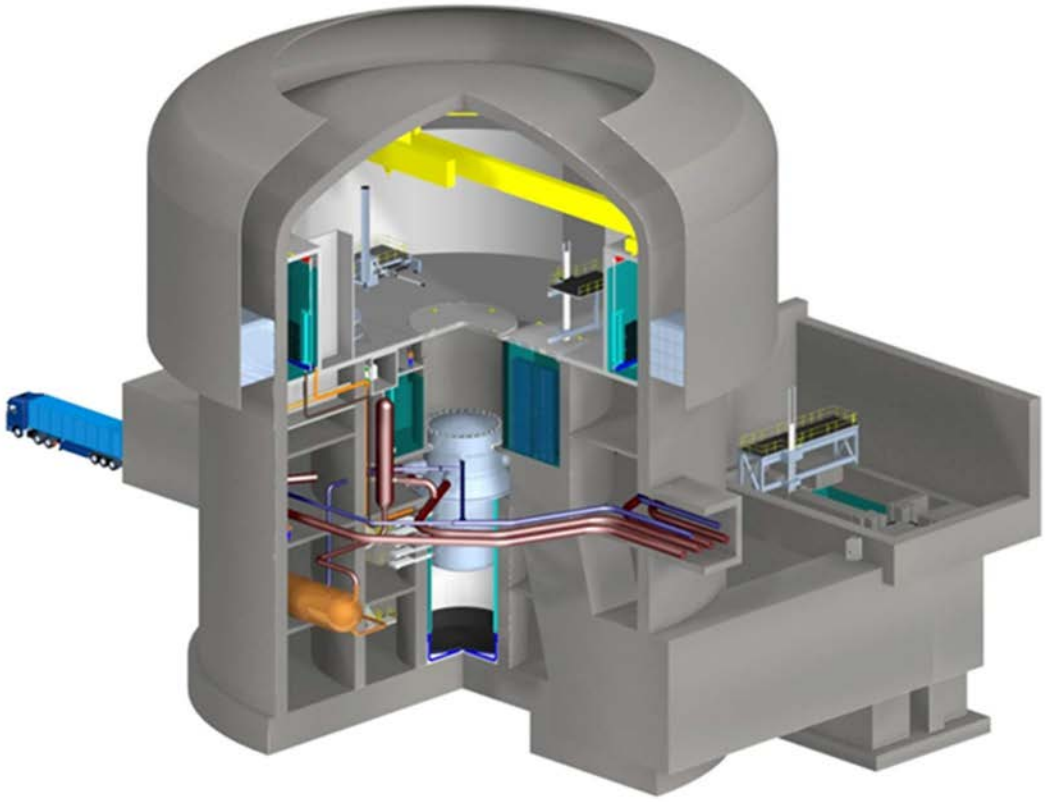

Fig. 2.3. Cutaway view of reactor building.

The envisioned layout of the turbine building is similar to that of the fossil fired power plant and is shown in Fig. 2.4. Live steam lines and high pressure turbine are enclosed in a containment. The steam and feed water piping within the shield building are enclosed in a piping tunnel connecting the shield building and the high pressure steam turbine containment. The portion of the steam tunnel within the shield building is an extension of the high pressure turbine containment rather than part of the shield building.

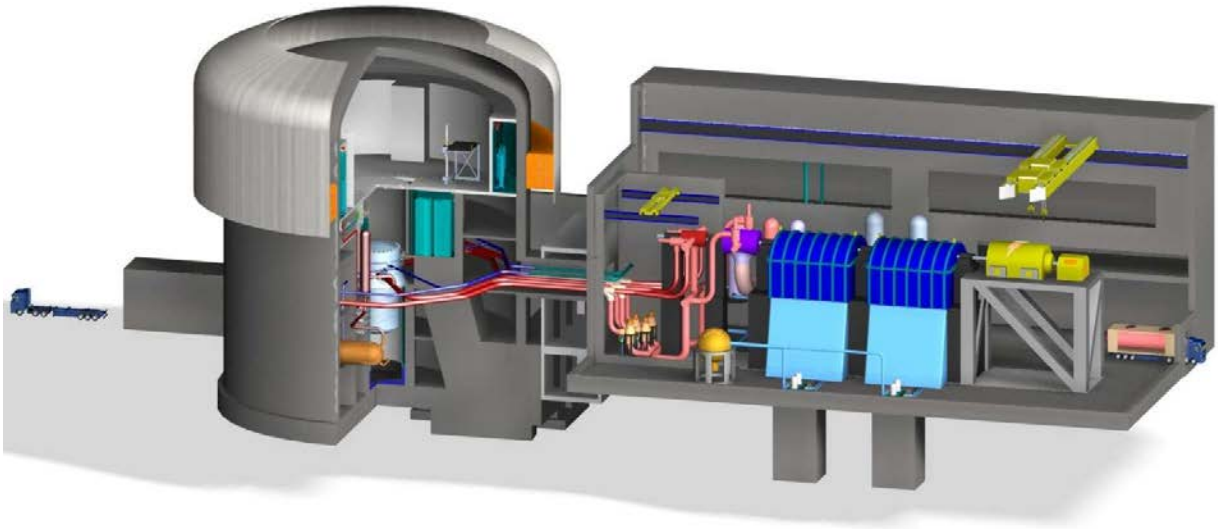

Fig. 2.4. Reactor buildings and the turbine building.

2.2. CHINESE SCWR CONCEPT

The first Chinese SCWR conceptual design was established at Nuclear Power Institute of China [2.5]. It is referred to as the CSR1000, which has the following characteristics:

- Its primary circuit is a direct cycle system consisting of a two pass, thermal neutron reactors cooled and moderated by light water in two primary loops connected with supercritical turbine and feedwater pumps. It is also interfaced with passive safety features.
- The core thermal power is 2300 MWt with electrical power of around 1000 MWe with system thermal efficiency of 43.5 %.
- Its primary circuit is operated at the pressure of 25 MPa, the coolant flow rate is 1189 kg/s, the feedwater temperature is 280°C and the average core outlet coolant temperature is about 500°C.

The CSR1000 core consists of 157 fuel assemblies, which are loaded in four batches, each affecting 1/4 symmetric core as shown in Fig. 2.5. Fig. 2.6 illustrates the fuel assembly arrangement within the core for two flow paths. The central region consists of 57 fuel assemblies (identified as I type) where the coolant travels downward from the top to the bottom of the core. The peripheral region consists of 100 fuel assemblies (identified as II type) where the coolant travels upward from the bottom to the top of the core.

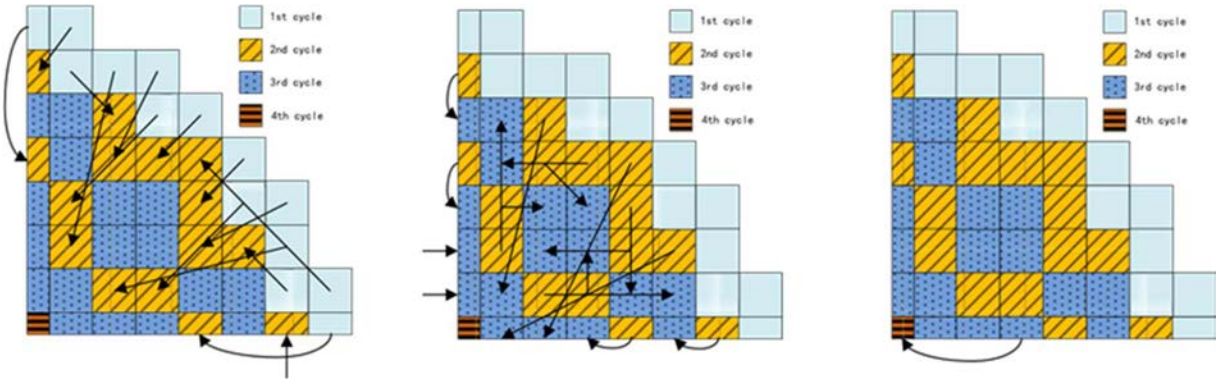

Fig. 2.5. Refuelling patterns of the Chinese SCWR concept (1/4 core shown).

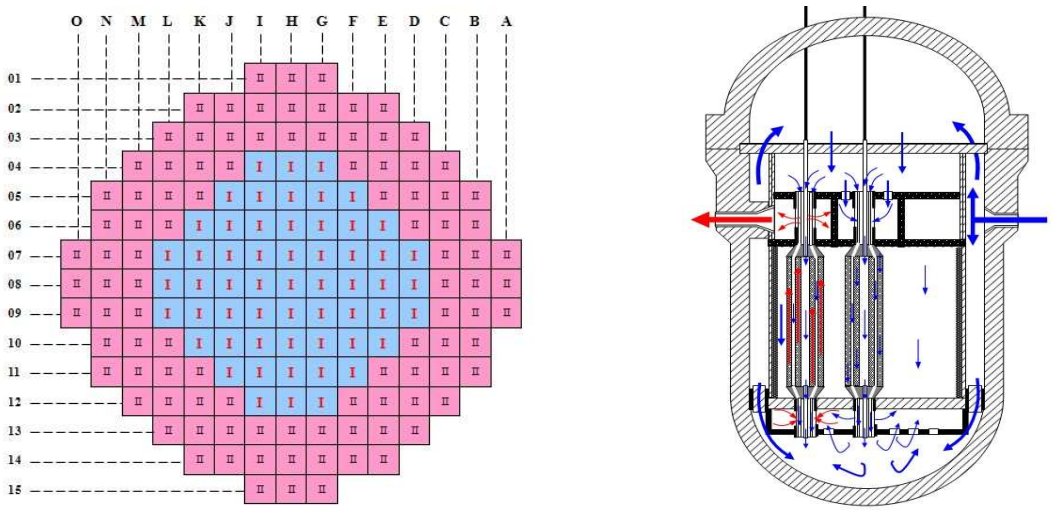

(a) *(b)*

Fig. 2.6. (a) Core configuration in the Chinese SCWR concept; (b) Flow paths in the Chinese SCWR concept.

The fuel rod consists of a modified stainless steel cladding of 9.5 mm in outer diameter and fuel meat of 5.6% enriched uranium, which facilitates reaching a discharge burnup of about 33,000 MWd/tU. Further optimization of the fuel indicated the possibility of reaching a discharge burnup of 45,000 MWd/tU with 6.2 % enrichment. The active fuel length is 4.2 m. Each fuel pellet consists of a hole in the centre to reduce the centre peak temperature and retain the fission gas (see Fig. 2.7). A dual wire is wrapped around the fuel rod to maintain spacing between fuel rods.

The standard fuel assembly cluster is composed of four subassemblies, each of which consists of 56 fuel rods and a square water (moderator) rod in the center surrounded by a square channel box (see Fig. 2.7). It has a total length of 5.9 m, including the top and bottom nozzles (see Fig. 2.8).

A cruciform control rod is inserted between the subassemblies from the top of the core. The low temperature coolant travels downward in the square water rod to enhance the moderation.

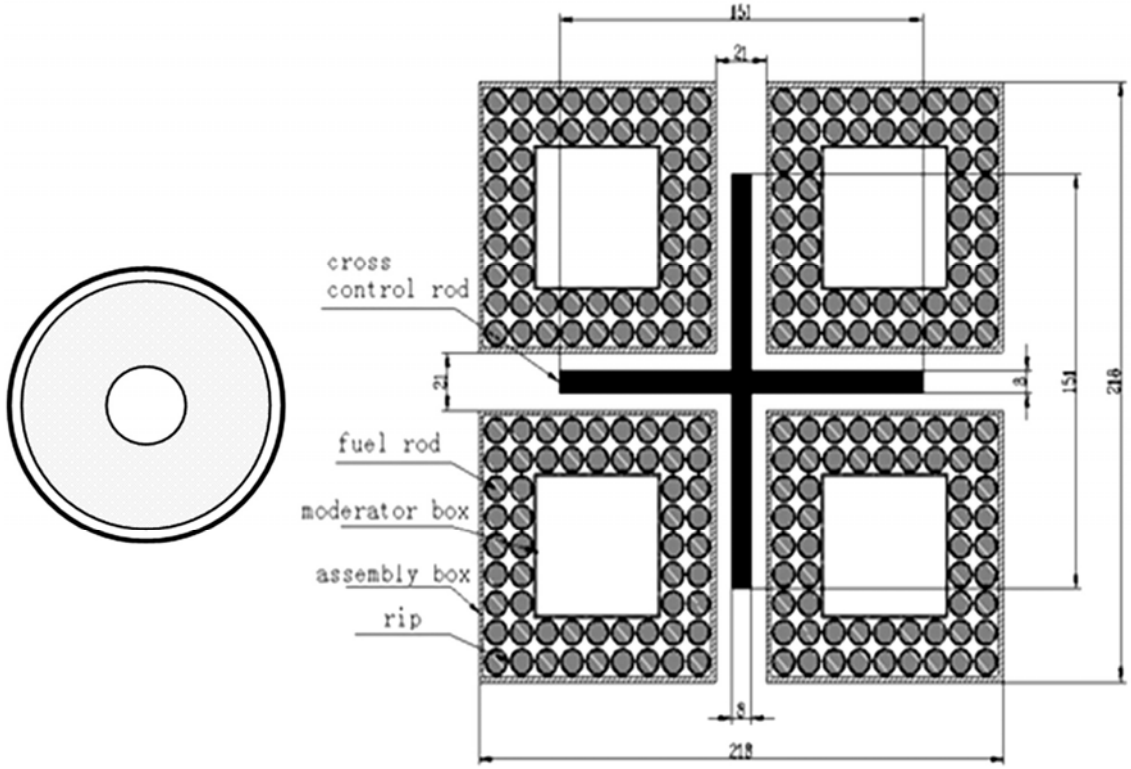

Fig. 2.7. Fuel rod and fuel assembly configurations for the Chinese SCWR concept.

The reactor system mainly includes reactor vessel, reactor internals, fuel assemblies and control rod drive mechanisms (see Fig. 2.9). Most water enters the upper plenum from the holes on the top of the core barrel and pressing barrel. It is distributed as the first pass coolant (38 %), moderator in assemblies (both the first and second pass assemblies, 6.5 % and 13.7 % respectively) and moderator between assemblies (35.8 %), then flows downward to the gathering structure in lower plenum. A small portion of water (6 %) flows downward from the ring cavity between the core barrel and the reactor vessel to the gathering structure. All the water collected in the gathering structure then flows upward, working as the second pass coolant, after mixing in the steam plenum, coolant leaves the reactor through the thermal sleeves in the outlets of the reactor vessel.

The reactor vessel mainly consists of upper head component, cylinder component, lower head component, outlet structures, fasteners and sealings. The upper head component is a hemispherical head, and the control rod drive mechanism nozzles and penetrations for instrumentation are disposed on it. The inlet and outlet nozzles are placed on the cylinder component with an axial height difference. The lower head component is also a half sphere head. The thermal sleeves are designed with the outlet structures to separate the high temperature coolant from the inner surface of the reactor vessel to avoid overheating the vessel material.

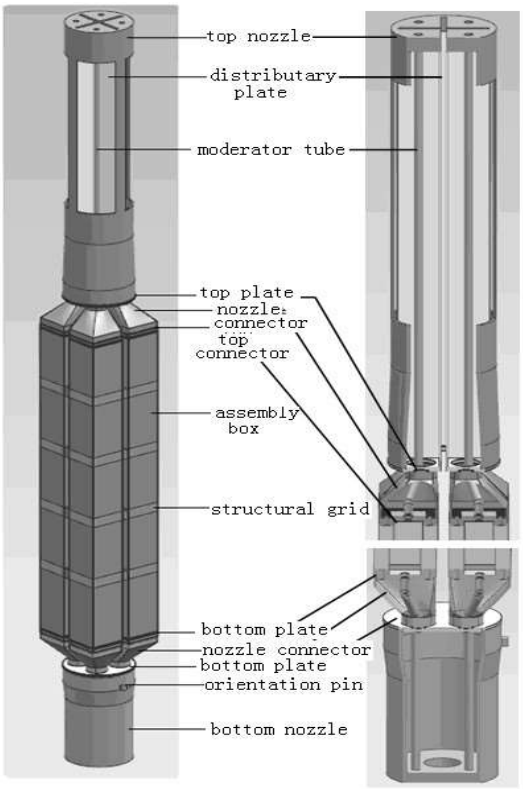

Fig. 2.8. Fuel assembly cluster of the Chinese SCWR concept.

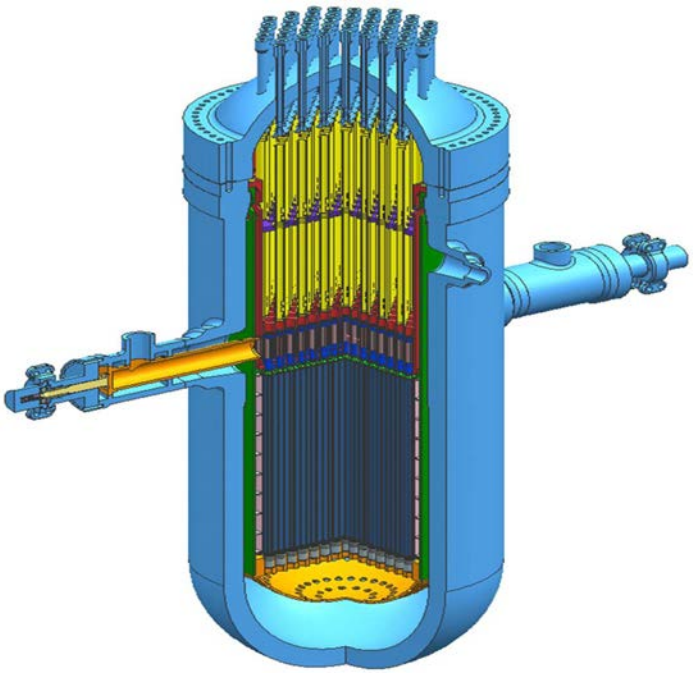

Fig. 2.9. Core concept of the Chinese SCWR.

The steam plenum is above the core of CSR1000 for separation of the first flow coolant, the second flow coolant and moderator. The steam plenum supplies a space for collection of outlet coolant, and a flow channel for coolant runoff. The structure is very simple and convenient for installation. The flow regulators are below the core of CSR1000 for flow distribution, located on internal of the lower core plate. These regulators adapt the core power distribution by transferring position or changing another one on refuelling shutdown condition. Fig. 2.10 illustrates the main coolant flow system of the CSR1000.

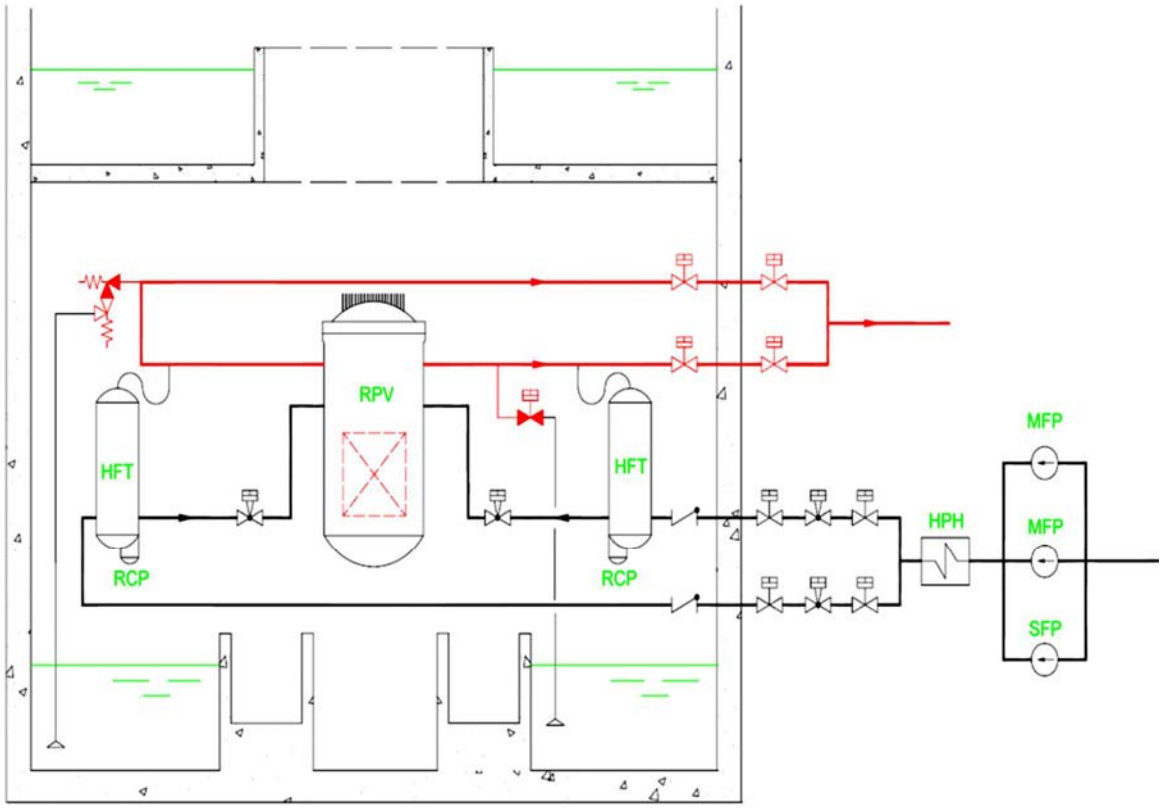

Fig. 2.10. Coolant flow system of the Chinese SCWR concept.

The thermal sleeves are installed between the barrel and the reactor vessel of CSR1000 to supply a channel for the outlet supercritical coolant to protect the vessel from large thermal stress. The structure is very simple and convenient to install and remove.

The safety system concept is based on inherent feature of water cooled reactor and well developed PWR safety technologies. The inherent feature includes negative void (density) and Doppler coefficients. The well developed PWR safety technologies mainly include reactivity control systems and emergency core cooling systems (ECCS). CSR1000 is once though cooling system, without water level monitoring in the reactor vessel, the ECCS design is needed to achieve the fundamental safety requirement, which is to ensure sufficient core coolant flow rate (coolant

supply from cold leg and coolant outlet at hot leg) after reactor shutdown for decay heat removal. Fig. 2.11 illustrates the safety system configuration of CSR1000.

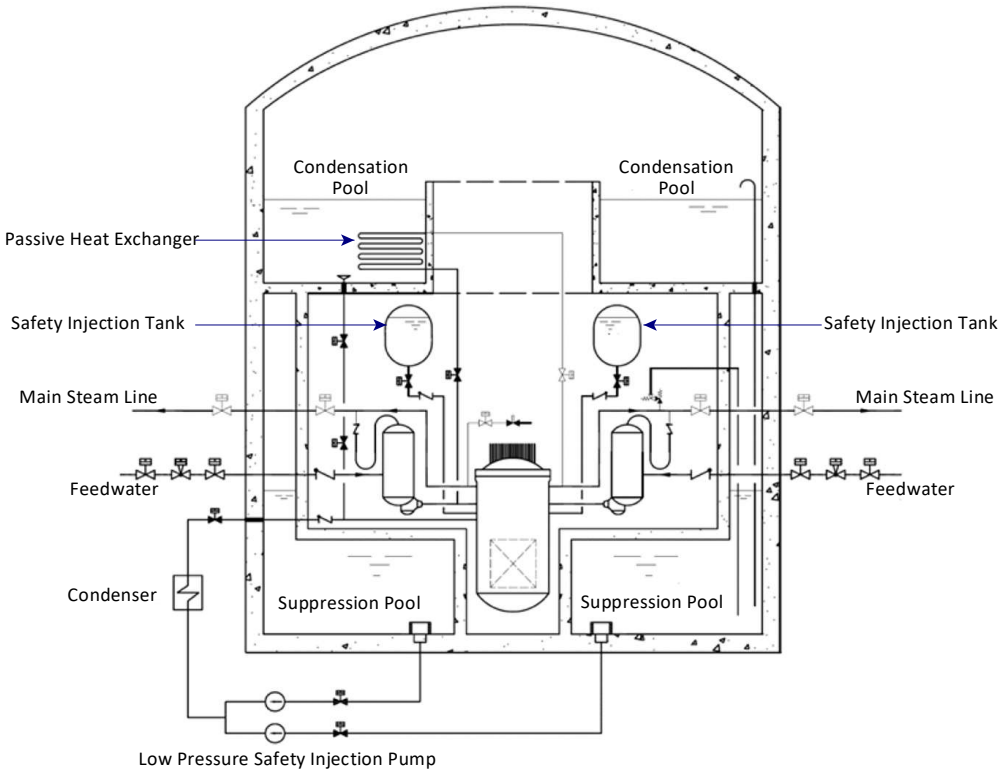

Fig. 2.11. Safety system of the Chinese SCWR concept.

The safety system concept of CSR1000 consists of the following systems: high pressure injection system, automatic depressurization system (ADS), passive core cooling system (PXS), pressure suppression type containment system, and reactor pit injection system (PIS). The high pressure injection system injects water from the high pressure feedwater tank (HFT) of the reactor coolant system (RCS) into the reactor vessel at the beginning of a loss of main feedwater (LOMF) event (as shown in Fig. 2.12).

The ADS is separated into two lines: ADS L1 and ADS L2. There is one isolation valve (normally closed) and one control valve (normally open) set on the ADS L1 line. The ADS L1 suction is connected to the main steam line and its downstream is in the condensation pool. When the RCS pressure reaches 27 MPa (abs), the ADS L1 isolation valve automatically open for discharging the high temperature steam to the condensation pool. There is an isolation valve (normally open) and one squib valve (normally closed) set on the ADS L2 line. The ADS L2 suction is connected to the main steam line and its downstream is directly to the atmosphere of the containment dry well. When the RCS pressure reaches 28 MPa (abs), the ADS L2 squib valve automatically open to discharge additional high temperature steam to the atmosphere.

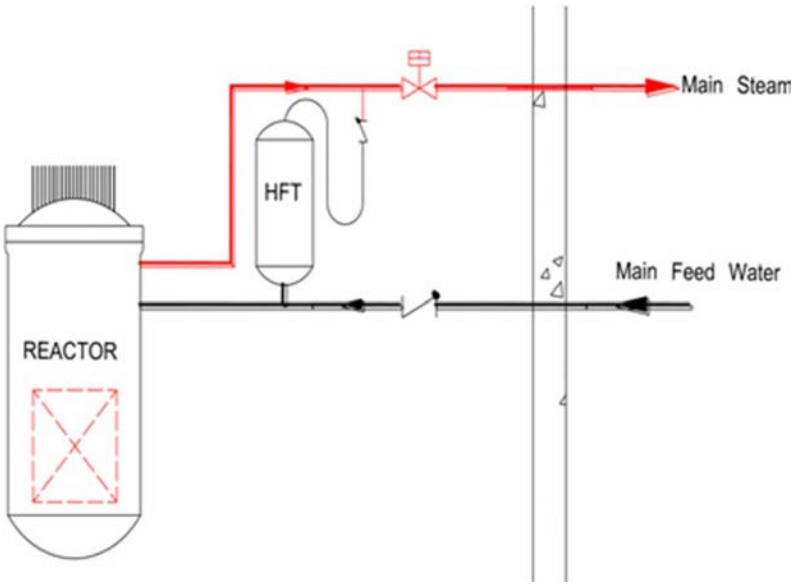

Fig. 2.12. High Pressure Injection System diagram.

The Passive Core Cooling System (PXS) is separated into the following subsystems: passive residual heat removal (PRHR) subsystem and passive reactor injection subsystem. The PRHR subsystem removes the residual decay heat from the reactor to the condensation pool through a passive heat exchanger (PRHR HX), which is connected to the RCS main steam line through an isolation valve (normally open) and the reactor with a high pressure injection line. When the normally closed isolation valve, which is set on the high pressure injection line, open, the PRHR HX can automatically operate for heat transfer from reactor core to the condensation pool. The passive reactor injection subsystem connects the condensation pool directly to the reactor with a passive reactor injection line. When the RCS depressurized to the atmospheric pressure during upset events, the two isolation valves automatically open to provide enough water for cooling the reactor when the main system is depressurized to the normal pressure and the active core cooling systems are unavailable.

The CSR1000 containment is pressure suppression type (see Fig. 2.13). The containment is divided into three areas: reactor pit, wet well and dry well. The reactor pit is used for containing the reactor vessel. The dry well is used for containing the RCS components and some safety system components. The wet well has a large condensation pool for suppressing the containment when the steam is discharged from the RCS to the containment.

There are a lot of pressure balance pipes set in the containment. When the dry well is pressurized by the steam which is discharged from the main system, the steam will be discharged to the condensation pool and condensed via the balance pipes. In this way, the containment can be suppressed after the ADS operation or a Loss Of Coolant Accident (LOCA).

The reactor pit is connected to the condensation pool by a balance line with a normally closed isolation valve. In case of a reactor core melt and the melted materials are dropped to the bottom

of the vessel, the PIS can inject enough water to the reactor pit to cool the bottom surface of the reactor vessel.

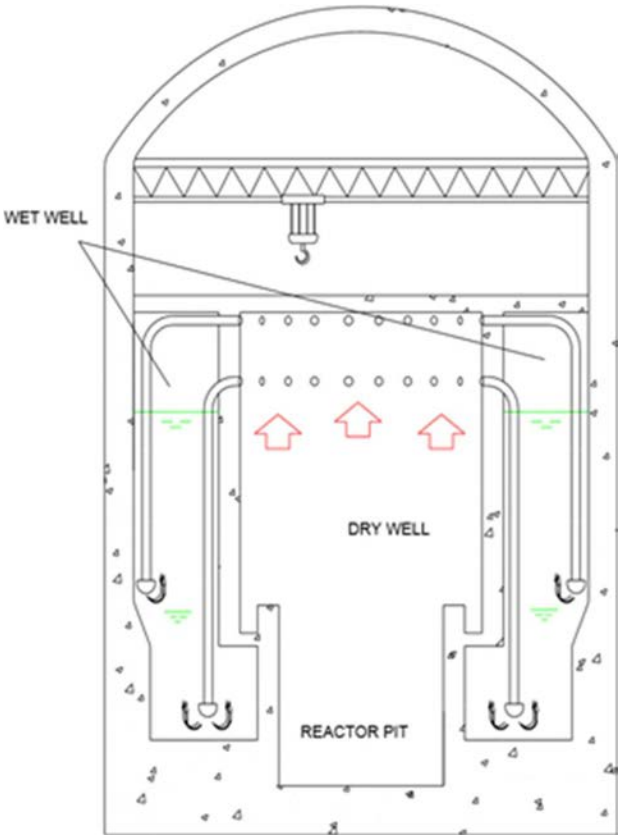

Fig. 2.13. CSR1000 Suppression Type Containment.

Acronyms

ADS	Automatic Depressurization System
D_2O	Heavy Water
ECCS	Emergency Core Cooling Systems
H_2O	Light Water
HFT	High pressure Feedwater Tank
HWR	Heavy Water Reactor
HX	Heat Exchanger
LEU	Low Enriched Uranium
LOCA	Loss Of Coolant Accident
LOMF	Loss Of Main Feedwater
LWR	Light Water Reactor
MOX	Mixed Oxide
PIS	Reactor Pit Injection System
PRHR	Passive Residual Heat Removal
PT	Pressure Tube

Pu	Plutonium
PV	Pressure Vessel
PWR	Pressurized Water cooled Reactor
PXS	Passive Core Cooling System
R&D	Research and Development
RCS	Reactor Coolant System
SCWR	Supercritical Water cooled Reactor
Temp.	Temperature
Th	Thorium
TRU	Transuranics
U	Uranium
UO_2	Uranium Oxide
ZrH	Zirconium Hydride

REFERENCES TO SECTION 2

[2.1] NUCLEAR ENERGY AGENCY, Technology Roadmap Update for Generation IV Nuclear Energy Systems, Organization for Economic Co-operation and Development, (2014).

[2.2] DUFFEY, R.B., LEUNG, L.K.H., Advanced Cycle Efficiency: Generating 40% More Power from the Nuclear Fuel, Proc. World Energy Congress (WEC), Montreal, 2010.

[2.3] INTERNATIONAL ATOMIC ENERGY AGENCY, Heat Transfer Behaviour and Thermohydraulics Code Testing for Supercritical Water Cooled Reactors (SCWRs), IAEA-TECDOC-1746, IAEA, Vienna (2014).

[2.4] SCHULENBERG, T., LEUNG, L., "Super-critical water-cooled reactors", Handbook of Generation IV Nuclear Reactors (PIORO, I.L., Ed.), Woodhead Publishing Series in Energy, (2016), 189–220.

[2.5] INTERNATIONAL ATOMIC ENERGY AGENCY, Status Report - Chinese Supercritical Water-Cooled Reactor (CSR1000), (2015).

3. THERMOPHYSICAL PROPERTIES AT CRITICAL AND SUPERCRITICAL PRESSURES

Thermophysical properties of all current and Generation IV nuclear power reactors within operating ranges and thermophysical properties of selected gases including helium and carbon dioxide at 0.1 MPa are shown in Handbook of Generation IV [3.1]. For better understanding of general trends, thermophysical properties of water, carbon dioxide and helium at critical and supercritical pressures are shown in Figs. 3.1–3.23 (these figures are based on data from [3.1]–[3.5]). Other properties of supercritical helium and properties of supercritical refrigerant R-134a are shown by [3.2]. Critical parameters of these selected fluids are listed in Table 3.1.

TABLE 3.1. CRITICAL PARAMETERS OF SELECTED FLUIDS [3.3].

Fluid	P_{cr} (MPa)	T_{cr} (ºC)	ρ_{cr} (kg/m^3)
Carbon dioxide (CO_2)	7.3773	30.98	467.6
Refrigerant R-134a (1,1,1,2 tetrafluoroethane, CH_2FCF_3)	4.0593	101.06	511.9
Helium (He)	0.2276	-267.95	72.567
Water (H_2O)	22.064	373.95	322.0

The NIST REFPROP software Version 9.1 [3.3] provides thermophysical properties for 121 pure fluids (including water, carbon dioxide, helium and refrigerants), five pseudo pure fluids (such as air), and mixtures with up to 20 components at different pressures and temperatures (including critical and supercritical regions).

3.1. THERMOPHYSICAL PROPERTIES OF WATER

Fig. 3.1a to Fig. 3.8a show variations in basic thermophysical properties of water at three subcritical pressures:

- 7 MPa nominal operating pressure of Boiling Water Reactors (BWRs) and many Rankine steam turbine cycles in Pressurized Water Reactors (PWRs), BWRs and Reaktor Bolshoy Moshchnosti Kanalnyy (RBMK) nuclear power plants;
- 11 MPa nominal inlet pressure for CANDU[1] reactors;
- 15 MPa nominal operating pressure for PWRs.

Fig. 3.1b to Fig. 3.8b show the properties at the critical (P_{cr} = 22.064 MPa) and four supercritical pressures (P = 25, 30, 35 and 40 MPa). This range of critical and supercritical pressures covers those in thermal power industry of supercritical pressure fossil fired power plants. Fig. 3.9 shows selected thermophysical properties near the pseudocritical point of water at 25 MPa.

[1] CANDU: Canada Deuterium Uranium, a registered trademark of Atomic Energy of Canada Limited.

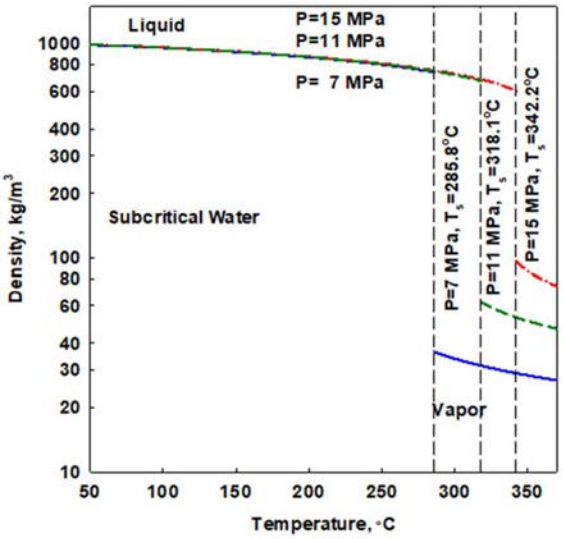

(a) Subcritical pressures

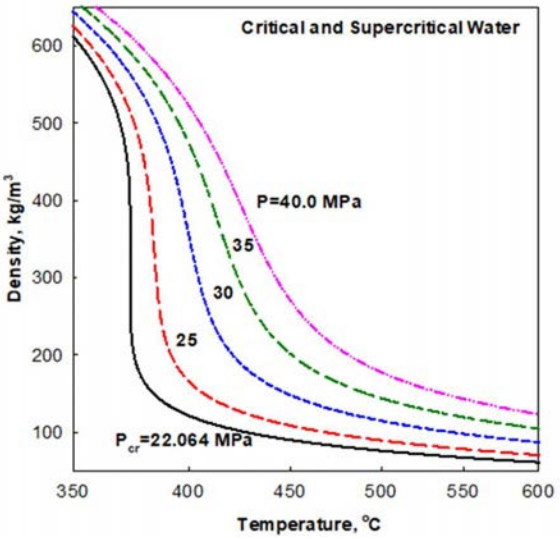

(b) Critical and supercritical pressures

Fig. 3.1. Variations of water density with temperature.

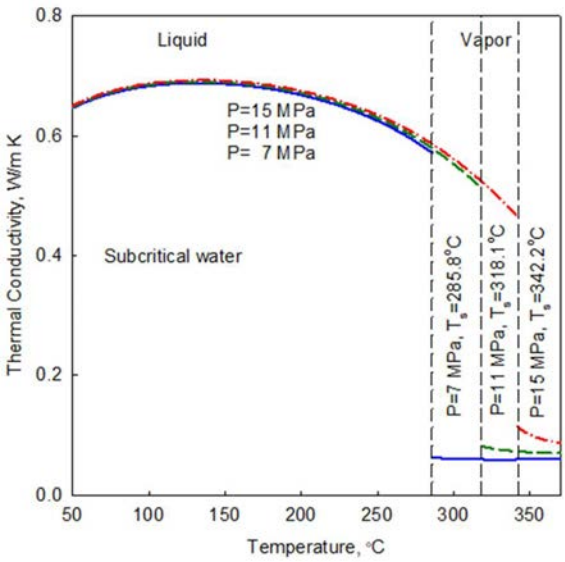

(a) Subcritical pressures

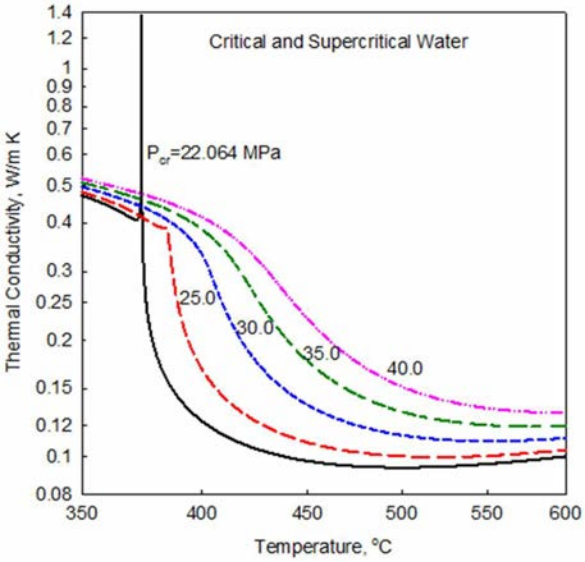

(b) Critical and supercritical pressures

Fig. 3.2. Variations of water thermal conductivity with temperature.

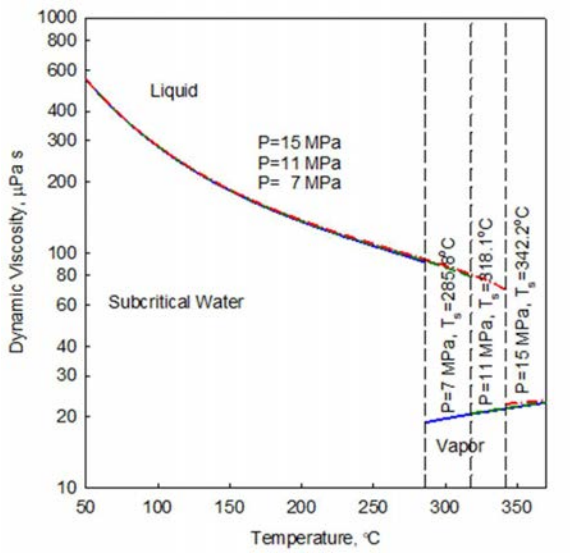

(a) Subcritical pressures

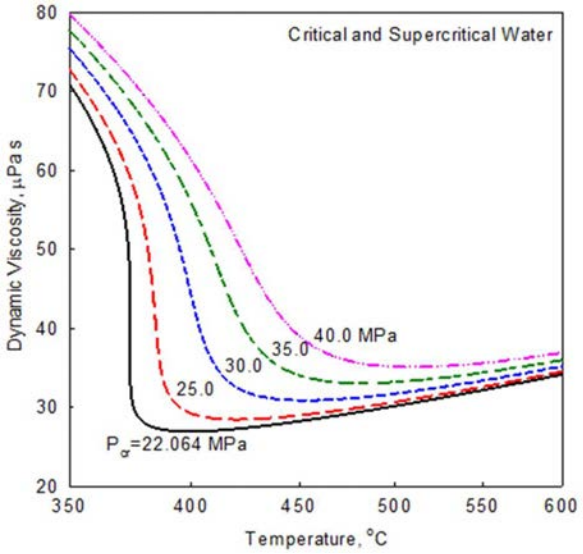

(b) Critical and supercritical pressures

Fig. 3.3. Variations of water dynamic viscosity with temperature.

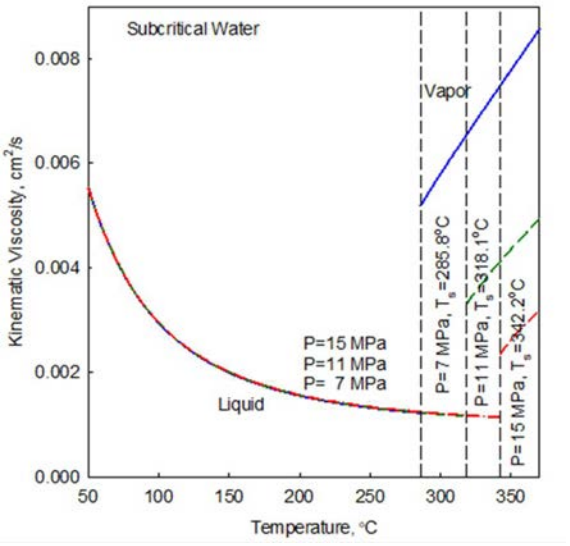

(a) Subcritical pressures

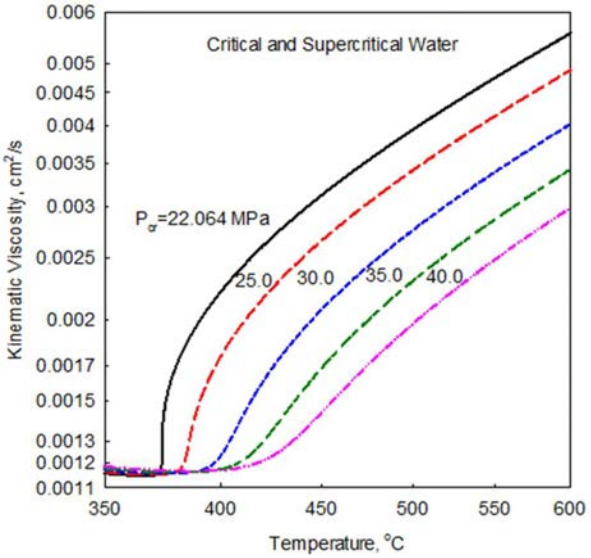

(b) Critical and supercritical pressures

Fig. 3.4. Variations of water kinematic viscosity with temperature.

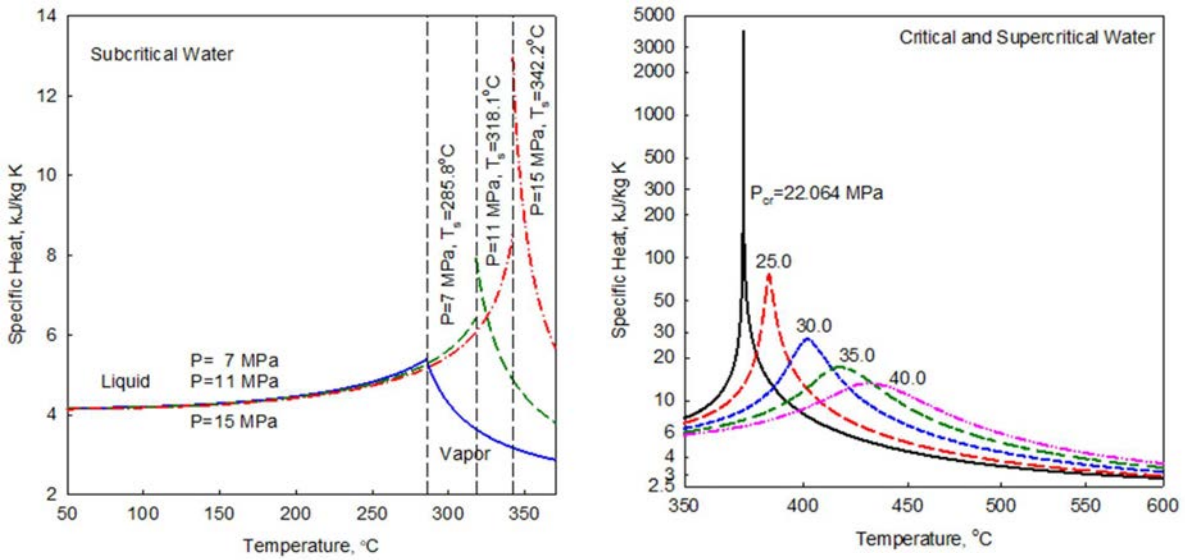

(a) Subcritical pressures *(b) Critical and supercritical pressures*

Fig. 3.5. Variations of water specific heat at constant pressure with temperature.

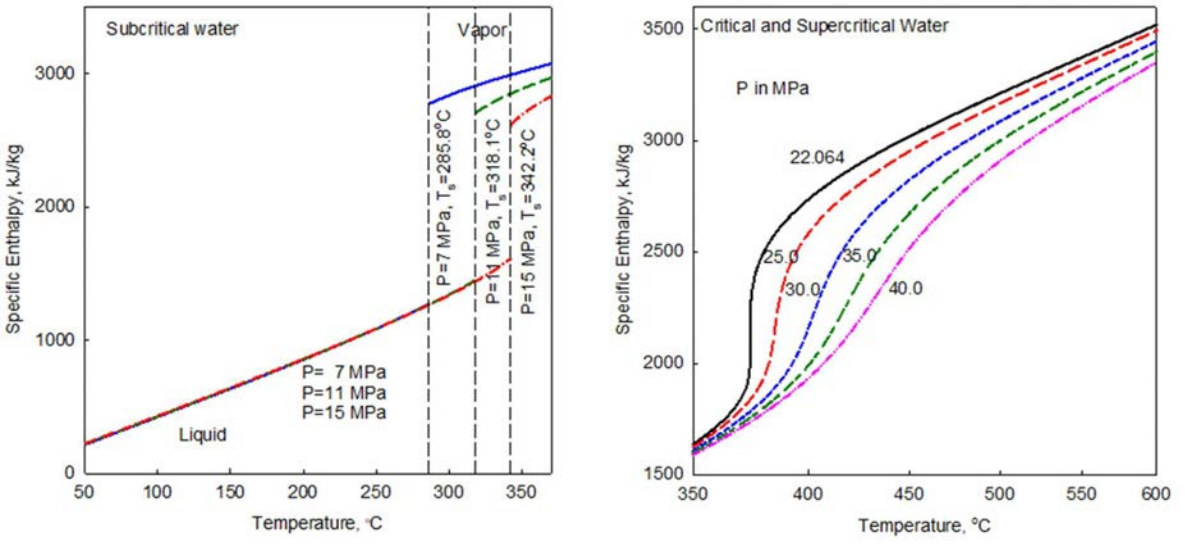

(a) Subcritical pressures *(b) Critical and supercritical pressures*

Fig. 3.6. Variations of water specific enthalpy with temperature.

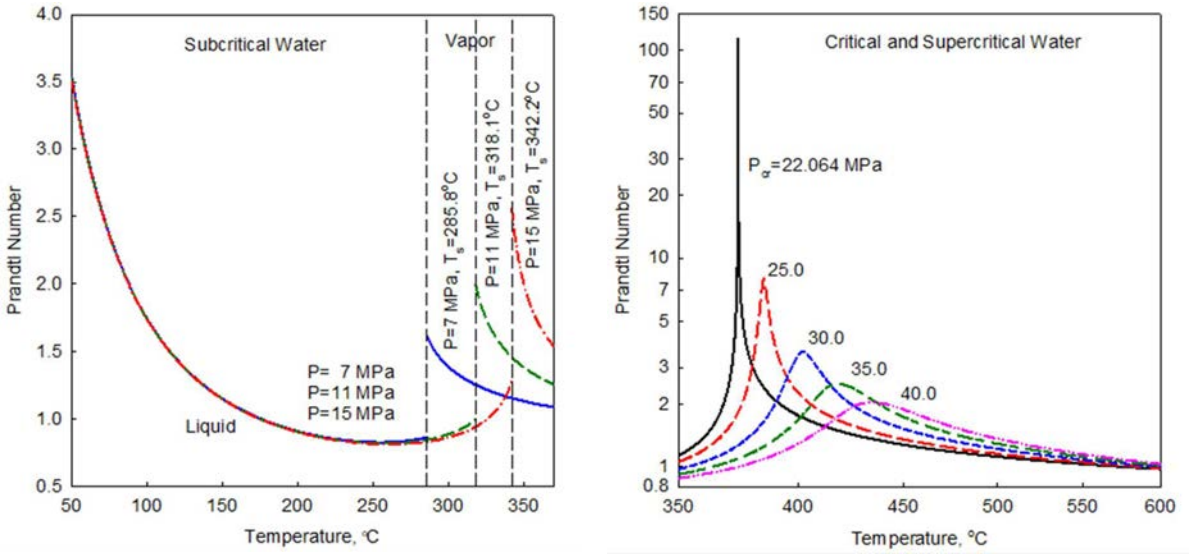

(a) Subcritical pressures *(b) Critical and supercritical pressures*

Fig. 3.7. Variations of water Prandtl number with temperature.

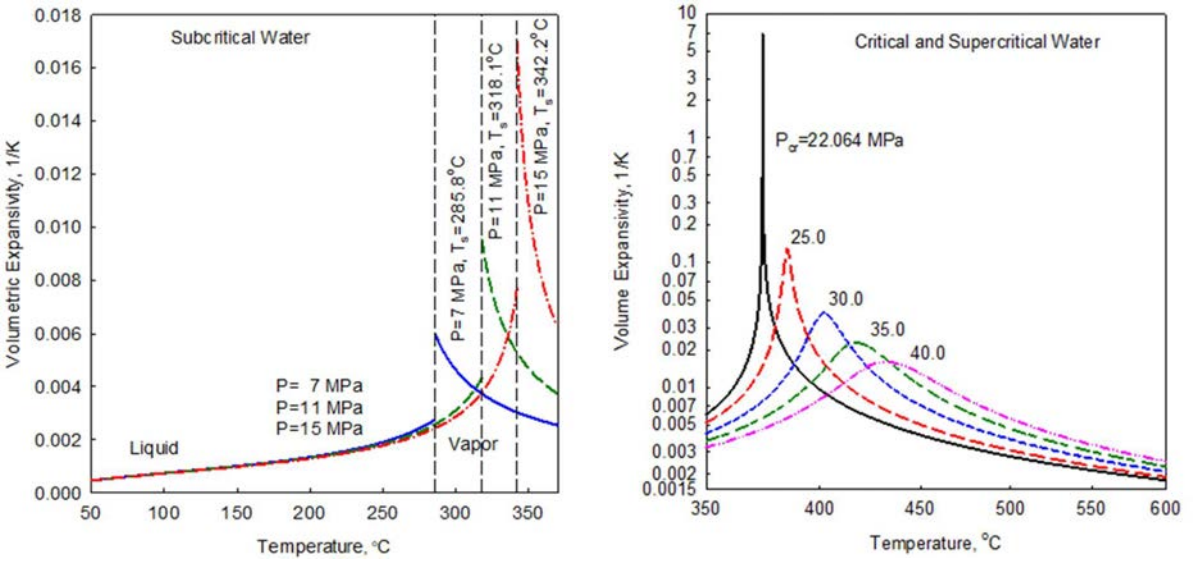

(a) Subcritical pressures *(b) Critical and supercritical pressures*

Fig. 3.8. Variations of water volumetric expansivity with temperature.

Analysis of profiles shown in Fig. 3.1 to Fig. 3.8 for water at subcritical pressures ((a) figures) and supercritical pressures ((b) figures) shows quite similar trends. There are generally two different values of any thermophysical property on the saturation line at subcritical pressures: one for liquid and one for vapor (steam). However, the difference is small for specific heat (e.g., specific heat of water is 5.4025 kJ/kg K and of steam is 5.3566 kJ/kg K at the pressure of 7 MPa, as shown in

Fig. 3.5a). Pressure has little effect on liquid properties, except close to the saturation point where a small pressure effect has been observed.

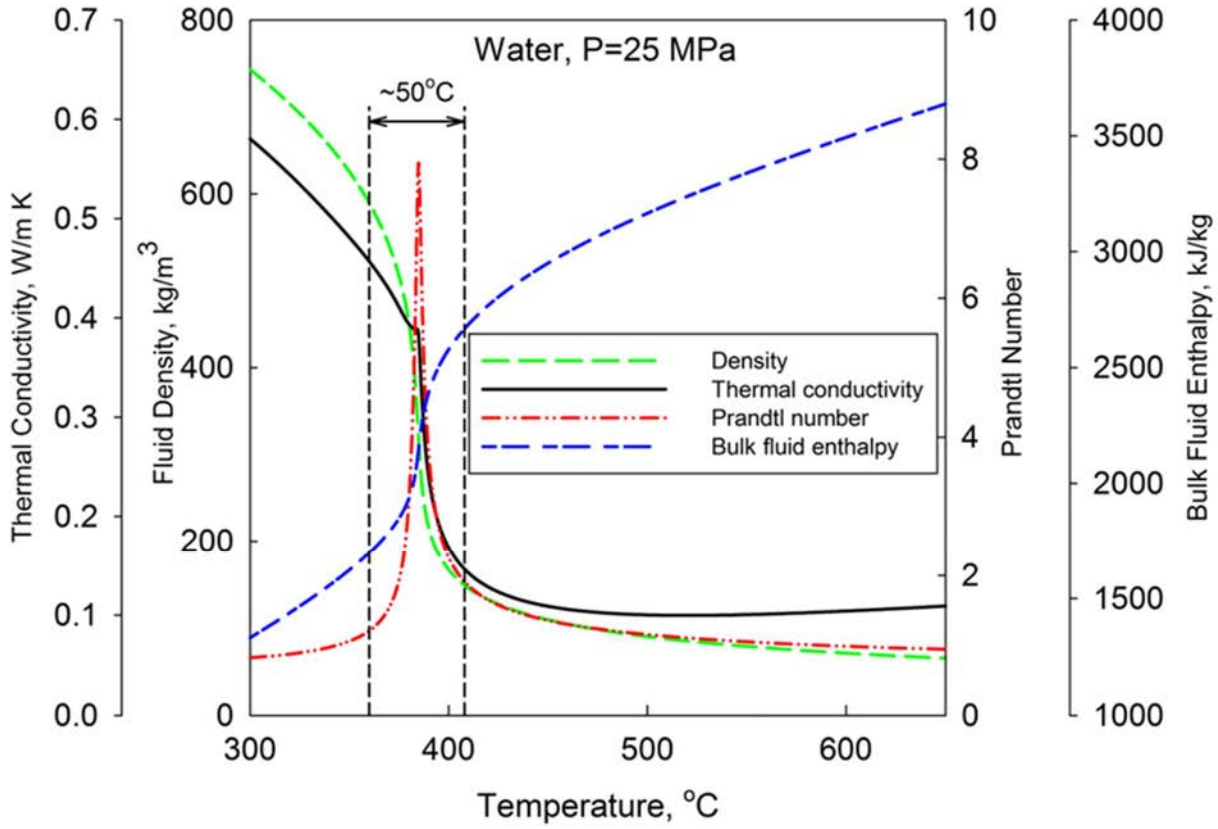

Fig. 3.9. Variations of selected thermophysical properties of water in pseudocritical region (around the pseudocritical point of 384.9°C).

3.2. THERMOPHYSICAL PROPERTIES OF CARBON DIOXIDE

Properties of carbon dioxide at equivalent pressures of water (the conversion is based on $\left(\frac{P}{P_{cr}}\right)_{H_2O} = \left(\frac{P}{P_{cr}}\right)_{CO_2}$) are shown in Fig. 3.10 to Fig. 3.17. Fig. 3.18 shows selected thermophysical properties near the pseudocritical point of carbon dioxide at 8.36 MPa, which is the equivalent pressure of 25 MPa in water.

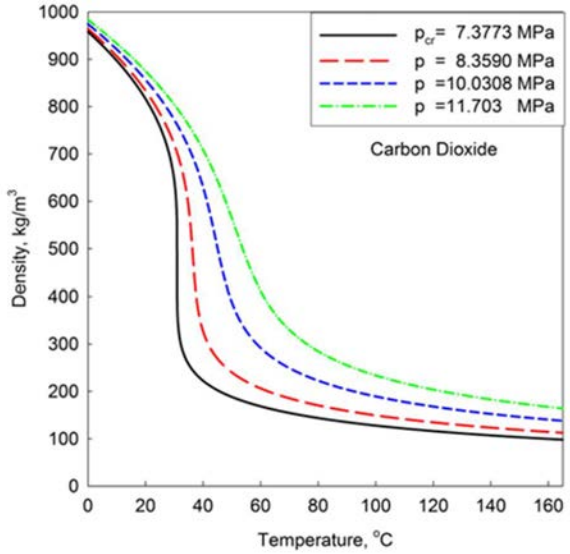

Fig. 3.10. Variations of carbon dioxide density with temperature.

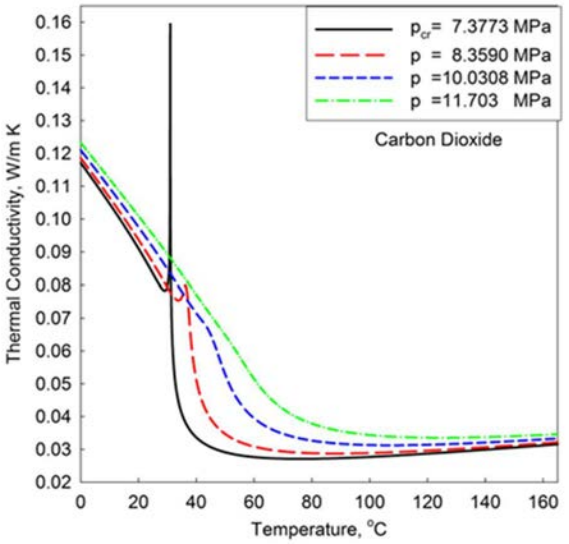

Fig. 3.11. Variations of carbon dioxide thermal conductivity with temperature.

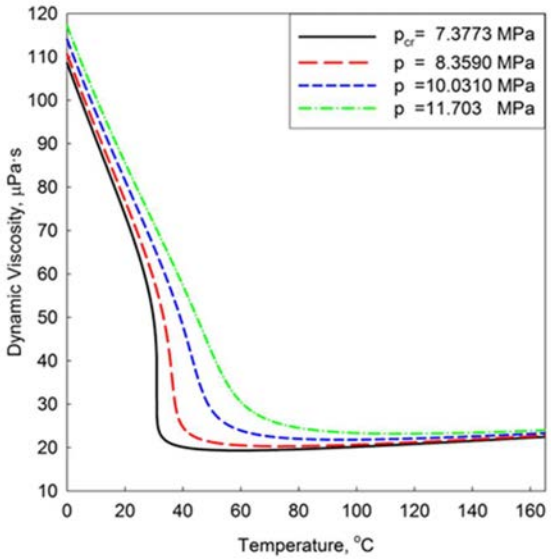

Fig. 3.12. Variations of carbon dioxide dynamic viscosity with temperature.

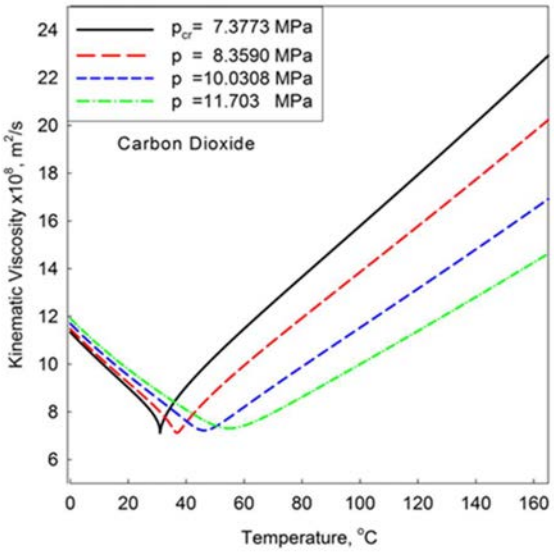

Fig. 3.13. Variations of carbon dioxide kinematic viscosity with temperature.

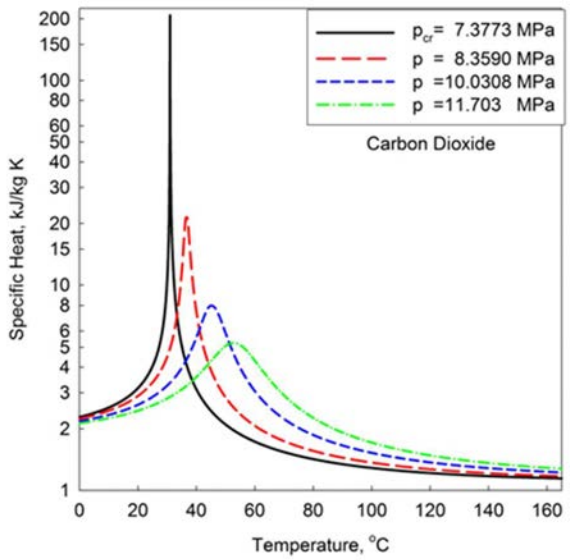

Fig. 3.14. Variations of carbon dioxide specific heat at constant pressure with temperature.

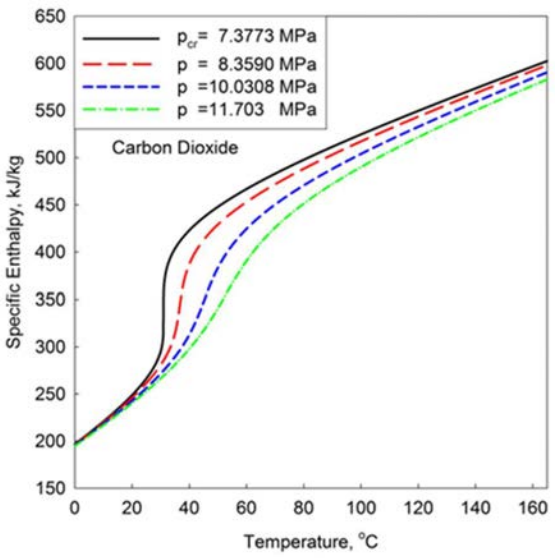

Fig. 3.15. Variations of carbon dioxide specific enthalpy with temperature.

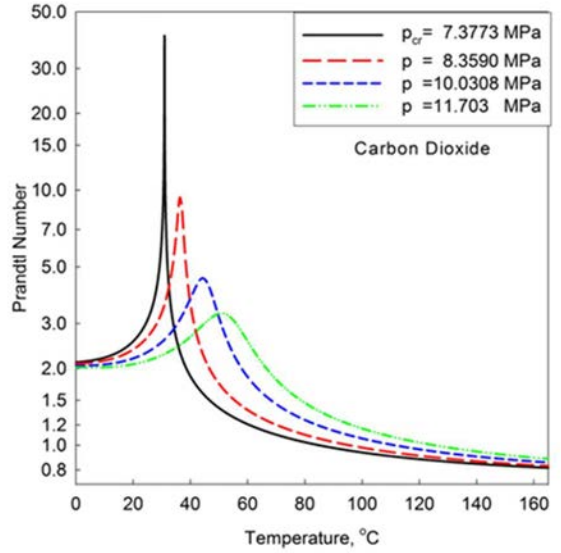

Fig. 3.16. Variations of carbon dioxide Prandtl number with temperature.

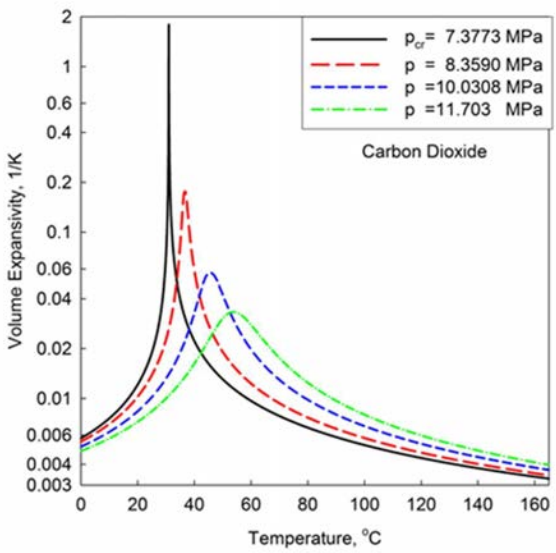

Fig. 3.17. Variations of carbon dioxide volume expansivity with temperature.

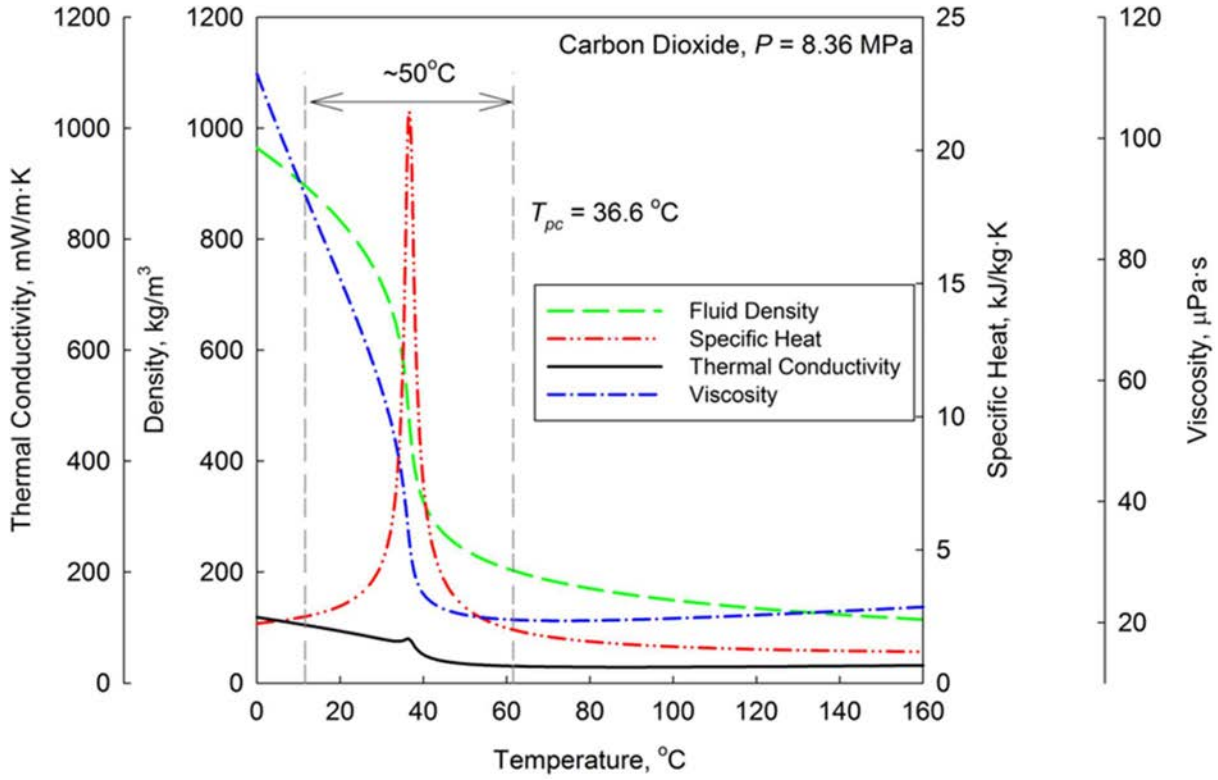

Fig. 3.18. Variations of selected carbon dioxide thermophysical properties in pseudocritical region.

3.3. SPECIFIC CHARACTERISTICS OF WATER AND CARBON DIOXIDE

"At critical and supercritical pressures, a fluid is considered to be a single phase substance, i.e., at any critical/supercritical pressure all properties have just a single value for any pressure–temperature combination, in spite of the fact that all thermophysical properties undergo significant changes within the critical and pseudocritical regions [3.4]. Near the critical point, these changes are dramatic (see Fig. 3.1b to Fig. 3.8b for water and Fig. 3.10 to Fig. 3.18 for carbon dioxide). At the vicinity of pseudocritical points, with an increase in pressure, these changes become less pronounced (see Fig. 3.1b to Fig. 3.8b for water and Fig. 3.10 to Fig. 3.18 for carbon dioxide)."

Density and dynamic viscosity undergo a significant drop (near the critical point this drop is almost vertical) within a very narrow temperature range (see Fig. 3.1b and Fig. 3.3b, respectively, for water and Fig. 3.10 and Fig. 3.12, respectively, for carbon dioxide). Kinematic viscosity and specific enthalpy undergo a sharp increase (see Fig. 3.4b and Fig. 3.6b, respectively, for water and Fig. 3.13 and Fig. 3.15, respectively, for carbon dioxide).

Thermal conductivity, specific heat, Prandtl number and volume expansivity exhibit local peaks near the critical and pseudocritical points (see Fig. 3.2b, Fig. 3.5b, Fig. 3.7b, and Fig. 3.8b, respectively, for water and Fig. 3.11, Fig. 3.14, Fig. 3.16, and Fig. 3.17, respectively, for carbon dioxide; also, see Fig. 3.19 for water and carbon dioxide). The magnitude of these local peaks decreases with an increase in pressure (see Fig. 3.20 for water and carbon dioxide). Thermal

conductivity, dynamic viscosity and kinematic viscosity undergo through their minimum right after the critical and pseudocritical points (see Fig. 3.2b, Fig. 3.3b, and Fig. 3.4b, respectively, for water and Fig. 3.11, Fig. 3.12, and Fig. 3.13, respectively, for carbon dioxide).

The specific heat of water (see Fig. 3.5b) (as well as of other fluids such as carbon dioxide and helium) has a maximum value at the critical poInt. The exact temperature that corresponds to the specific heat peak above the critical pressure is known as the pseudocritical temperature (see also Fig. 3.19 and Fig. 3.20, and Table 3.2 for water and carbon dioxide). For water at pressures approximately above 300 MPa and for carbon dioxide at pressures above 30 MPa (see Fig. 3.20), the peak (or the 'hump') in specific heat almost disappears. Therefore, the term such as the *pseudocritical point* no longer exists. The same applies to the *pseudocritical line*.

TABLE 3.2. PSEUDOCRITICAL TEMPERATURE AND CORRESPONDING PEAK VALUE OF SPECIFIC HEAT AT SUPERCRITICAL PRESSURES FOR WATER AND CARBON DIOXIDE [3.3].

Water			**Carbon Dioxide**		
Pressure (MPa)	**Pseudocritical temperature (ºC)**	**Peak value of specific heat (kJ/(kg·K))**	**Pressure (MPa)**	**Pseudocritical temperature (ºC)**	**Peak value of specific heat (kJ/(kg·K))**
23	377.5	284.3	7.5	31.7	228.1
24	381.2	121.9	8	34.7	35.3
25	384.9	76.4	8.5	37.4	18.7
26	388.5	55.7	9	40.0	12.8
27	392.0	43.9	9.5	42.6	9.9
28	395.4	36.3	10.0	45.0	8.1
29	398.7	30.9	10.5	47.4	6.9
30	401.9	27.0	11.0	49.7	6.1
31	405.0	24.1	11.5	51.8	5.5
32	408.1	21.7	12.0	53.9	5.0
33	411.0	19.9	12.5	55.9	4.6
34	413.9	18.4	13.0	57.8	4.3
35	416.7	17.2	13.5	59.5	4.1

In general, it is very difficult or actually impossible to define the exact pressure at which a maximum value of specific heat will disappear or cannot be defined. The major problem here is that the uncertainty of specific heat at high supercritical pressures is not easy to establish. If a maximum value of specific heat is within the uncertainty compared to those on a baseline, a pseudocritical point is assumed no present at this pressure. Peaks in thermal conductivity and volume expansivity may not correspond to the pseudocritical temperature, which is based on the maximum value of specific heat (see Table 3.3, Table 3.4 and Fig. 3.19). However, the differences are usually within a degree or so. The peak in thermal conductivity diminishes at about 25.5 MPa for water (see Fig. 3.2b and Table 3.3) and at about 8.4 MPa for carbon dioxide (see Fig. 3.11 and Table 3.4).

TABLE 3.3. PEAK VALUES OF WATER SPECIFIC HEAT, VOLUME EXPANSIVITY AND THERMAL CONDUCTIVITY AT CRITICAL AND SUPERCRITICAL PRESSURES [3.3].

Pressure (MPa)	**Pseudocritical temperature (ºC)**	**Temperature (ºC)**	**Specific heat (kJ/(kg·K))**	**Volume expansivity (1/K)**	**Thermal conductivity (W/(m·K))**
P_{cr}=22.064	T_{cr}=374.1	–	∞	∞	∞
22.5	375.6	–	690.6	1.252	0.711
23.0	–	377.4	–	–	0.538
	377.5	–	284.3	0.508	–
23.5	–	379.2	–	–	0.468
	–	379.3	–	0.304	–
	379.4	–	171.9	–	–
24.0	–	381.0	–	–	0.429
	381.2	–	121.9	0.212	–
24.5	–	382.6	–	–	0.405
	–	383.0	–	0.161	–
	383.1	–	93.98	–	–
25.0	–	384.0	–	–	0.389
	384.9	–	76.44	–	–
	–	385.0	–	0.128	–
25.5	386.7	–	64.44	0.107	no peak
26.0	388.5	-	55.73	0.090	0.355
27.0	392.0	-	43.93	0.069	0.340
28.0	395.4	-	36.29	0.056	0.329
29.0	398.7	-	30.95	0.046	0.321
30.0	401.9	-	27.03	0.039	0.316

"In general, crossing the pseudocritical line from left to right is quite similar to crossing the saturation line from liquid to vapour [3.5]. The major difference in crossing these two lines is that all changes (even drastic variations) in thermophysical properties at critical and supercritical pressures are continuous and gradual, and take place within a certain temperature range (see and Fig. 3.18). On the contrary, there are properties discontinuity at subcritical pressures on the saturation line: one value for liquid and another for vapour (see Fig. 3.1a to Fig. 3.8a for water). Therefore, critical and supercritical fluids behave as single phase substances. However, fluids behave as liquid like substances below the critical/pseudocritical temperature and gas or vapor like substances above the critical/pseudocritical temperatures (for details, see Fig. 3.1 for densities of subcritical and supercritical water)."

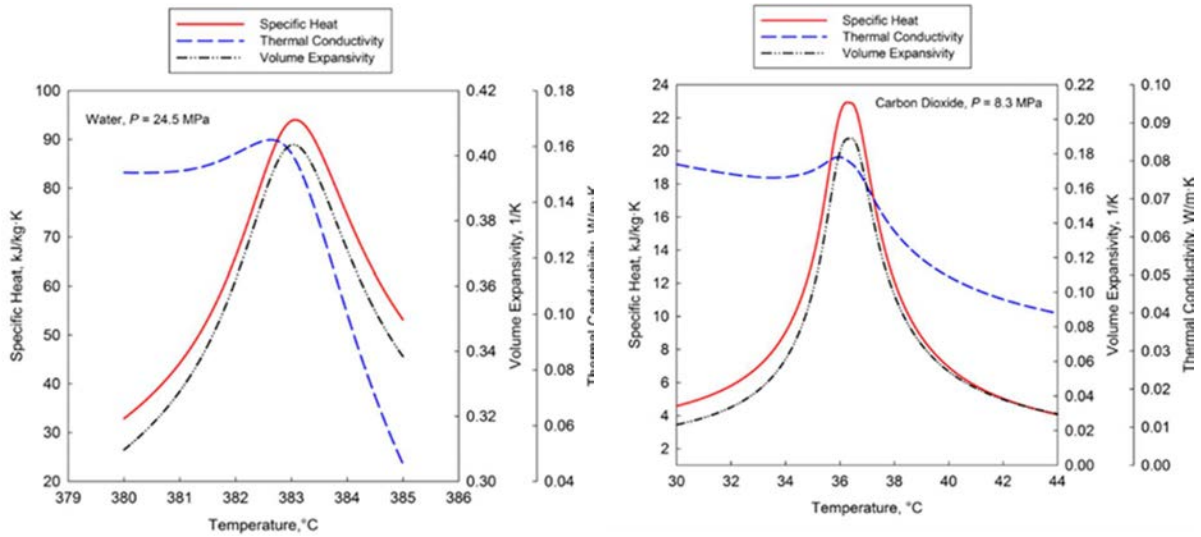

Fig. 3.19. Variations of specific heat, volume expansivity and thermal conductivity with temperature.

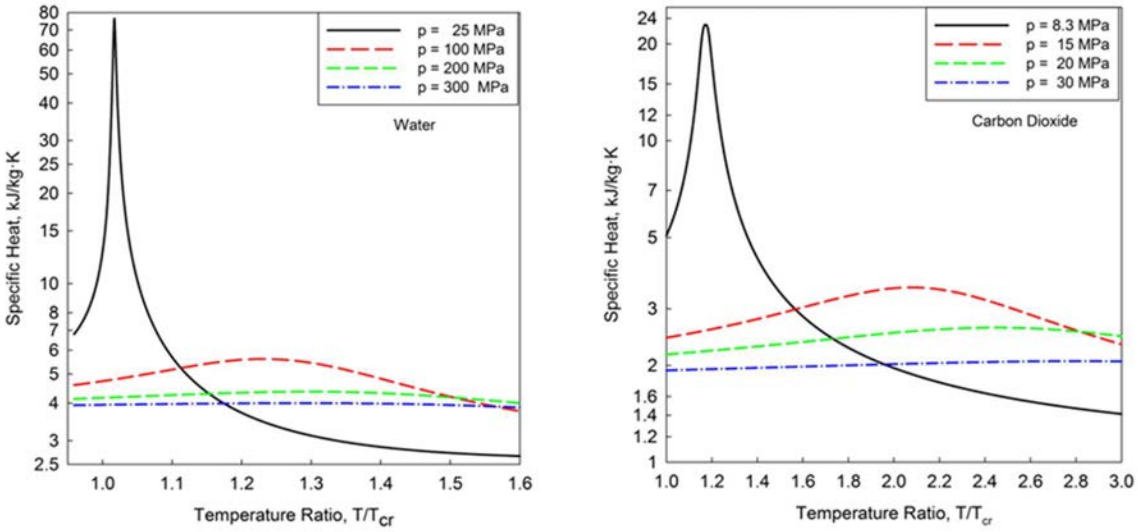

Fig. 3.20. Variations of specific heat with temperature ratio and pressure.

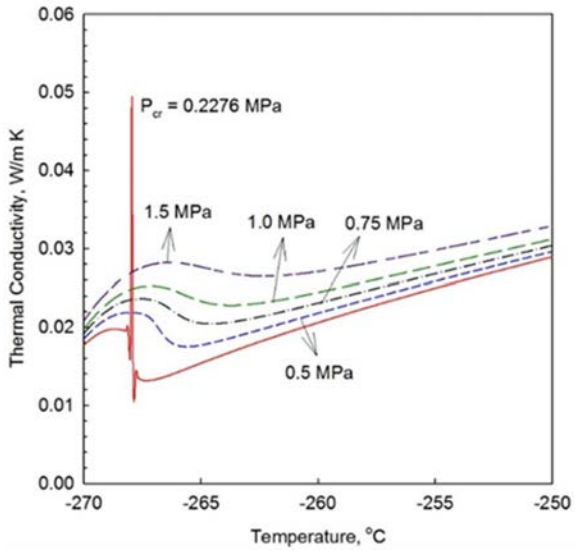

Fig. 3.21. Variations of helium thermal conductivity with temperature.

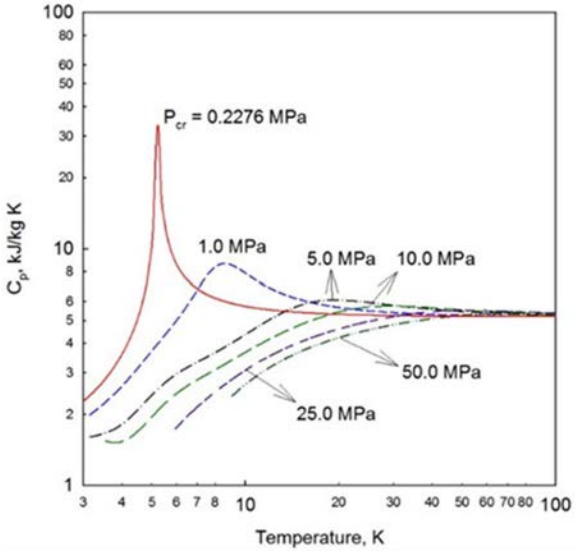

Fig. 3.22. Variations of helium specific heat with temperature.

Helium has also been selected as a reactor coolant, which operates mainly at supercritical pressures and above critical/pseudocritical temperatures. Therefore, it performs mainly as a compressed gas. Thermal conductivity, specific heat and thermal expansivity for helium are shown in Fig. 3.21 to Fig. 3.23, respectively.

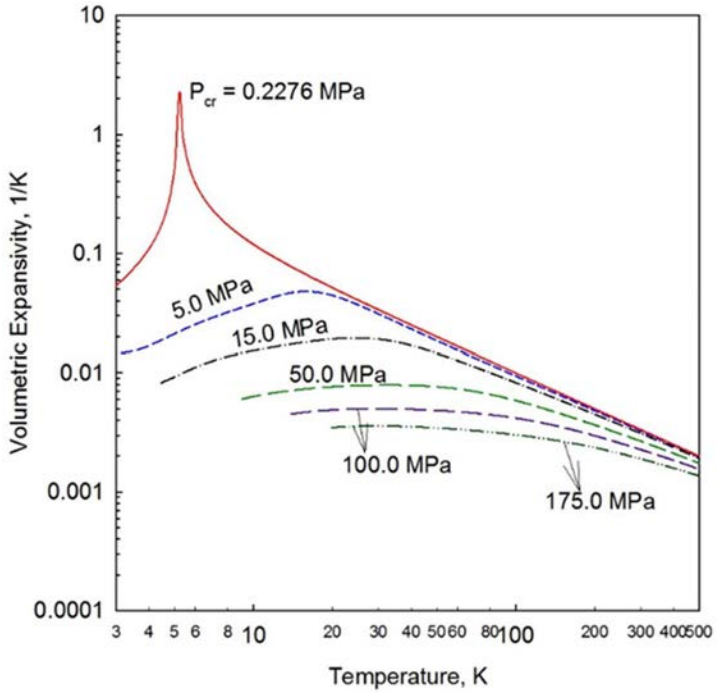

Fig. 3.23. Variations of helium volumetric expansivity with temperature.

TABLE 3.4. PEAK VALUES OF SPECIFIC HEAT, VOLUME EXPANSIVITY AND THERMAL CONDUCTIVITY AT CRITICAL AND SUPERCRITICAL PRESSURES FOR CARBON DIOXIDE.

Pressure (MPa)	**Pseudocritical temperature (ºC)**	**Temperature (ºC)**	**Specific heat (kJ/(kg·K))**	**Volume expansivity (1/K)**	**Thermal conductivity (W/(m·K))**
P_{cr}=7.3773	T_{cr}=30.978	–	∞	∞	∞
7.5	31.7	–	228.06	2.025	0.160
8.0	–	34.5	–	–	0.089
	34.7	–	35.27	0.300	–
8.5	–	36.9	–	–	0.078
	37.4	–	18.67	0.151	–
9.0	40.0	–	12.83	–	–
	–	40.1	–	0.0992	No peak
9.5	42.6	–	9.86	–	–
	–	42.8	–	0.0733	No peak
10.0	45.0	–	8.08	–	
	–	45.4	–	0.058	No peak
10.5	47.4	–	6.91	–	–
	–	480	–	0.048	No peak
11.0	49.7	–	6.07	–	–
	–	50.4	–	0.040	No peak
11.5	51.8	–	5.46	–	–
	–	52.8	–	0.035	No peak
12.0	53.9	–	4.99	–	–
	–	55.2	–	0.031	No peak
12.5	55.9	–	4.61	–	–
	–	57.4	–	0.028	No peak
13.0	57.8	–	4.30	–	–
	–	59.5	–	0.025	No peak
15.0	64.2	–	3.50	–	–
	–	67.5	–	0.018	No peak
20.0	75.8	–	2.62	–	–
	–	84.3	–	0.011	No peak
25.0	82.3	–	2.26	–	–
	–	97.4	–	0.008	No peak
30.0	86.4	–	2.06	–	–
	–	107.5	–	0.006	No peak

Nomenclature and Acronyms

C_p	Specific heat at constant pressure, J/(kg·K)
P, p	Pressure, Pa or MPa
T	Temperature, ºC
v	*S*pecific volume, m^3/kg

Greek Letters

ρ	Density, kg/m^3

Subscripts

cr	Critical
p	Pressure
pc	Pseudocritical

Acronyms

BWR	Boiling Water Reactor
CANDU	Canada Deuterium Uranium
CO_2	Carbon dioxide
H_2O	Light water
He	Helium
PWR	Pressurized Water cooled Reactor
RBMK	Reaktor Bolshoy Moshchnosti Kanalnyy

REFERENCES TO SECTION 3

[3.1] Handbook of Generation IV Nuclear Reactors, Editor: I.L. Pioro, Elsevier – Woodhead Publishing, Duxford, (2016).

[3.2] PIORO, I.L., DUFFEY, R.B., Heat Transfer and Hydraulic Resistance at Supercritical Pressures in Power Engineering Applications, ASME Press, (2007).

[3.3] NATIONAL INSTITUTE OF STANDARDS AND TECHNOLOGY, NIST Reference Fluid Thermodynamic and Transport Properties - REFPROP. NIST Standard Reference Database 23, Ver. 9.1, U.S. Department of Commerce, (2013).

[3.4] PIORO, I. L., "Specifics of thermophysical properties and heat transfer at supercritical pressures in power-engineering applications: a review", Proc. 12th Int. Symp. On Supercritical Fluids, Antibes Juan-Les-Pins, France (2018).

[3.5] PIORO, I. L., "Thermophysical properties at critical and supercritical pressures", Heat Transfer: Theoretical Analysis, Experimental Investigations and Industrial Systems (BELMILOUDI, A., Ed.) IntechOpen (2011).

4. HEAT TRANSFER CHARACTERISTICS IN NON-BUNDLE GEOMETRIES

Previous and recent investigations of supercritical water (SCW) heat transfer in straight tubes and annuli are presented. A concise review is shown about past research performed on SCW heat transfer characteristics in tubes prior to the initiation of the current coordinated research project (CRP). It is followed by the description of experimental tests and their database covered in both CRPs. Works done and lessons learnt in various fields (e.g., SCW correlations and scaling) during this CRP are presented.

4.1. OVERVIEW OF PAST EXPERIMENTAL WORKS ON HEAT TRANSFER OF SCW FLOW IN TUBES

Since the beginning of 1930s experimental work has been devoted to investigate thermal hydraulics phenomena (most of them focused on heat transfer issues) of supercritical fluids (SCFs, mainly SCW) in various types of channel. Most studies were performed with tube and annuli, and a few with rod bundles. During early experiments, glowing red hot spots on the outer surface of heated tube walls have been observed. This phenomenon can be explained by the appearance of wall temperature peak caused by local deterioration of heat transfer (DHT) reported for example by [4.1]. This glowing red hot spot was described as a 10 mm wide faintly glowing read halo. This halo appeared at the axial level of the seventh thermocouples where the heat flux was 300 kW/m^2. The heat load (q_w/G) was 0.938 kJ/kg in the case where the hot spot appeared first. The maximum wall temperature at the hot spot was 510°C. As the heat flux was increased to 337.21 kW/m^2 (it meant increased thermal load (q_w/G) as well to 1.054 kJ/kg), the glowing red hot spot moved to the axial level of the sixth thermocouples. The 'brilliance of the halo' was increased too, and the wall temperature raised to 555 °C. In the next step, the heat flux was increased further up to 386 kW/m^2 (q_w/G becomes 1.207 kJ/kg), the glowing red hot spot moved to the axial level of the fifth thermocouples, while the peak value of the wall temperature reached 600 °C. This DHT phenomenon was interpreted that the higher the heat flux the shorter the heated length for reaching the pseudocritical temperature at the heated wall. Shortly after the pseudocritical transition, DHT could occur under high enough (see the criteria for that in the following) thermal load conditions. In case of DHT, the higher the heat flux, the higher the wall temperature peak [4.2].

Based on the experimental investigation like [4.1], a consistent classification of heat transfer types for SCW was elaborated by the contributions of many researchers (e.g., [4.1], [4.3], [4.4], [4.5], [4.6], [4.7], [4.8] and [4.9]) based on their experiments [4.10]. The following experimental approach was generally used [4.10]: the geometry of investigated test sections was fixed and almost all parameters were kept constant (e.g., mass flow rate, power, pressure, inlet temperature, etc.) except one (it was the actual varying parameter). Then many steady state data were recorded within a well selected range of the varying parameter. At the evaluation stage, wall and bulk fluid temperatures were shown as a function of the bulk specific fluid enthalpy (h_b), which appears to be more appropriate than the axial position or the heated length in indicating the pseudocritical enthalpy, h_{pc}. Three different heat transfer types and a regeneration of heat transfer phenomenon (OHTR–onset of heat transfer regeneration) were identified from the experimental observations of flow in tubes [4.2]: the normal heat transfer (NHT), the enhanced heat transfer (EHT, in some early work it was also referred to as improved) and deteriorated heat transfer (DHT). These four

types of heat transfer are identified in Fig. 4.1 through the variations of heat transfer coefficient (HTC) and wall temperature (T_w) with bulk fluid enthalpy for upward flow of SCW in a straight smooth, bare vertically installed tube having an inner diameter of 9.4 mm [4.5]. An increase in imposed heat flux (here it is the varying parameter) had led to lowering of the HTC. At the heat flux of 630 kW/m^2, the difference between wall and bulk fluid temperatures decreases (Fig. 4.1b). It means enhancement in heat transfer (EHT) compared to the other cases. Within a narrow enthalpy range around the pseudocritical point (i.e., $h_b = h_{pc}$), heat transfer enhancement occurs (see Fig. 4.1a) for EHT case (e.g., at the heat flux of 630 kW/m^2). Constant temperature difference can be seen between wall and bulk fluid temperatures (Fig. 4.1b) in case of NHT (e.g., at heat fluxes of 787 and 945 kW/m^2). This leads to lower HTCs than those for the EHT case but HTC is still relatively high compared to the DHT case (see Fig. 4.1a). At the heat flux of 1260 kW/m^2, the heat transfer deteriorates before the pseudocritical point (i.e., h_{pc}). After a certain portion of the heated length, the heat transfer recovers and the OHTR occurs (Fig. 4.1b) [4.2].

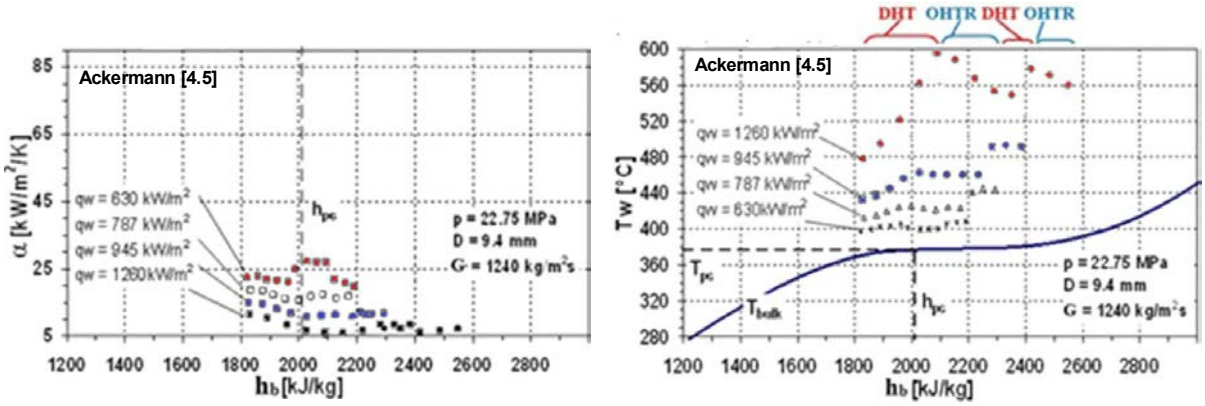

(a) HTC (α) versus h_b (b) T_w versus h_b

Fig. 4.1. Experimental results for different heat transfer regimes: EHT (630 kW/m^2), NHT (787 and 945 kW/m^2) and DHT & OHTR (1260 kW/m^2) [4.2], [4.5].

The presented high local HTC peaks in the EHT cases of the above example were reported slightly before the pseudocritical transition [4.6]. If heat flux increases, the value of the HTC peak descends and moves away from the position indicated by $h_b = h_{pc}$ towards lower h_b. Decades later, this characteristic feature was well confirmed by results of computational fluid dynamics (CFD) calculations [4.11], [4.12]. This EHT peak of HTC is probably caused by the peak of isobaric specific heat around the pseudocritical transition for cases with low thermal load [4.2], [4.10].

4.1.1. DEFINITION OF DHT AND CRITERION ON THE ONSET OF DHT

The second stage of experimental investigations focused on the setting up of a clear criterion for the onset of DHT, after the types of heat transfer were outlined with acceptable details and well confirmed experimentally. These investigations were performed without the elaboration of a clear definition of DHT, although some attempts have been done at the matter.

For example, the reference [4.6] proposed the following criterion for DHT [4.2]:

$$\alpha < 0.3\ \alpha_{NHT} \tag{4.1}$$

Here, α_{NHT} denotes the HTC value calculated with the Dittus–Boelter correlation [4.13]. This correlation is unable to capture DHT and thus predict NHT or EHT instead of DHT. Equation (4.1) means that, if HTC is smaller than 30 % of the $\alpha_{NHT,}$ DHT is assumed in the examined case. Equation (4.1) or other definitions of DHT have not been widely accepted in the literature [4.14]. Therefore, a generally used definition of DHT is adopted [4.2].

Many theoretical and experimental studies were devoted to the identification of conditions that lead to DHT [4.1], [4.4] and [4.6]. The theoretical assumption of these attempts was: the provided heat is conducted fully through the inner surface of the tube wall along the heated section (reflected by the left hand side of Eq. (4.2)) and the heat is fully absorbed in the coolant (reflected by the right hand side of Eq. (4.2)). The heat flux and mass flux as two global parameters are included in Eq. (4.2), but all other variables are geometric parameters or the overall warming up of the fluid ($h_{out} - h_{in}$) [4.2].

$$q_w(D\ \pi\ L_h) = G\ \left(\frac{D^2\pi}{4}\right)(h_{out} - h_{in}) \tag{4.2}$$

The following relation shows the reformulated form of Eq. (4.2) in order to set up the ratio of heat and mass flux (or in another words, the thermal load) [4.2]:

$$\frac{q_w}{G} = \left(\frac{D}{4\ L_h}\right)(h_{out} - h_{in}) = f(geom., warm - up) \tag{4.3}$$

Many experimental studies focused on investigating critical values of the thermal load for water under different conditions and ranges of parameters (i.e., the right hand side of Eq. (4.3)). These investigations have led to the elaboration of well accepted DHT criteria [4.10]. If the value of thermal load exceeds the critical value (Eq. (4.4)) then the heat transfer deteriorates which is reflected in a relatively low HTC locally (HTC minimum) and in the same time a generally global peak in wall temperature (Fig. 4.1) [4.2]. Ranges of critical values were proposed for thermal hydraulically stable and oscillatory flows [4.10]. The range of critical thermal load is around one for stable flow and is lower for oscillatory flow (see Eq. (4.4)). This signifies that DHT could be encountered at lower heat fluxes or higher mass fluxes in oscillating flow than those in stable flow [4.2].

$$\begin{aligned} \frac{q_w}{G} &\geq 0.95 - 1.05\ for\ stable\ flow \\ \frac{q_w}{G} &\geq 0.68 - 0.9\ for\ oscillating\ flow \end{aligned} \tag{4.4}$$

The HTC can be improved by devices enhancing turbulence [4.10], [4.15], [4.16]. Ribs and other spacer devices (such as wire wrapped spacers in the fuel assembly of the High Performance LWR or HPLWR [4.17]) were tested to identify the most effective method for improving the heat transfer

and to postpone or avoid DHT in SCWR fuel assemblies [4.10]. Based on these experimental works, it was concluded in general that turbulence enhancing spacers and other devices increase the HTC by several times compared to the bare tubes. The DHT type of heat transfer could be avoided or significantly postponed with these devices in circular shaped flow channels (like tubes or annuli). However, insufficient experimental data are available for SCWR rod bundles to confirm the improvement [4.18].

The physical mechanism has been only partially understood how the heat transfer types transform (e.g., from EHT to NHT, from NHT to DHT) and why the OHTR phenomena occurs directly after the DHT. DHT occurrences have been attributed to the rapid and steep variation of thermophysical properties [4.2], [4.10], [4.19], [4.20], [4.21], acceleration of SCW flow near the heated wall, [4.10], [4.19], [4.22], [4.23], buoyancy effect (strongest near the heated wall especially in upward SCW flow) [4.10], [4.19], and/or laminarization of SCW flow [4.24]. In the last two decades, detailed CFD models were used to examine the influence of buoyancy effect and variations of thermophysical properties on the type of heat transfer in SCW flows [4.2], [4.10], [4.19], [4.20], [4.21]. These CFD studies indicated a strong influence of buoyancy forces on the occurrence of DHT at low mass flow rates, which may not be relevant to current SCWR concepts with high nominal mass flow rates (i.e., ~1500 $kg/m^2/s$). On the other hand, at high mass flow rates, a weak heat conducting layer close to the heated solid wall could be created due to the variation of thermal conductivity. This rather heat insulator layer could act as a thermal barrier leading to the onset of DHT [4.19], [4.20], [4.21].

4.1.2. CRITERIA ON THE TYPE OF CONVECTION

Many independent researchers reported in the SCW literature (e.g., [4.6] and [4.18]) about identified and significant influence of buoyancy on heat transfer over a wide range of parameters in SCW flow. Three major types of convective heat transfer have been identified for subcritical flows: if the buoyance provides the circulation force of the flow then it fully governs the SCW flow in natural convection (NC); if the buoyance effect has an important impact on the heat transfer but basically a pump circulate the SCW flow then it is mixed convection (MC); if a pump provides the strong circulation of SCW flow in forced convection (FC) then the buoyance and its effects on heat transfer of SCW can be consider as negligible [4.2].

Regarding the direction of SCW flow (vertically upward or downward, horizontal or inclined), there is a significant difference in the way how the buoyance influences the heat transfer which has been foreseen and discussed in details in the past based on theoretical considerations and experiments [4.10]. The vertical case is the relevant one for the SCWRs due to the vertical orientation of the fuel assemblies in all SCWR concepts. The buoyance effect contradicts and slows down the SCW flow near the heated wall in downward flow because the main flow and the buoyance force have opposite directions. It is called as opposing (SCW) flow [4.10], [4.18]. It is on the contrary in upward flow because the buoyance adds and accelerates the SCW flow (mostly within the boundary layer) due to the directions of main flow and the buoyance force coincides. It is called adding (SCW) flow [4.10], [4.18]. Jackson et al. [4.25] introduced two dimensionless numbers to distinguish between the adding and opposing flows: a dimensionless buoyance number (Bo*) as independent variable; and a ratio of buoyance affected Nusselt number (Nu) and Nu in case of forced convection where buoyance neglected. The results of the application of these two

dimensionless numbers are shown in Fig. 4.2, which illustrates the effect of buoyance on convective heat transfer for fully developed flow in vertical tubes [4.2].

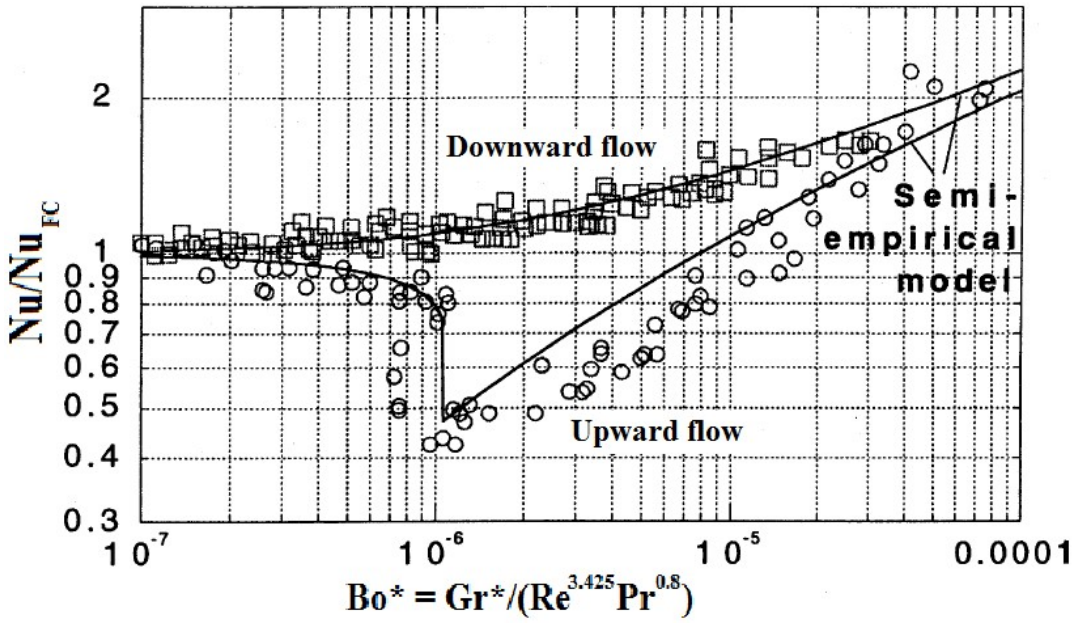

Fig. 4.2. Effect of buoyance on convective heat transfer for fully developed flow in vertical circular tubes [4.25], [4.26], [4.27].

The buoyance improves heat transfer in downward SCW flow (e.g., HTC is higher than or equal to that in the forced convection case). On the contrary, the buoyance decreases the HTC in upward SCW flow. For buoyance numbers (Bo*) larger than 10^{-6}, the influence of buoyance becomes strong and has to be considered. Jackson and Hall [4.28] proposed criteria based on the ratio of Grashof number (*Gr*) and Reynolds number (*Re*) to determine the convective heat transfer type [4.2], [4.28]:

$$FC: \frac{Gr}{Re^{2.7}} < 10^{-5}, MC: 10^{-5} \leq \frac{Gr}{Re^{2.7}} \leq 10^{-3}, NC: \frac{Gr}{Re^{2.7}} > 10^{-3}, \tag{4.5}$$

The *Gr* is defined as:

$$Gr = \frac{(\rho_b - \bar{\rho})D^3 g}{\rho_b \nu^2} \tag{4.6}$$

Where:

$$\bar{\rho} = \frac{1}{T_w - T_b}\int_{T_b}^{T_w} \rho dT \tag{4.7}$$

The *Re* is defined as:

$$Re = \frac{GD}{\mu} \tag{4.8}$$

4.1.3. SCW HEAT TRANSFER CORRELATIONS

As it was described above, the heat transfer in SCW flow is a rather complex phenomenon due to the steep, nonlinear variations of thermophysical properties of SCW in turbulent flows at different thermal load conditions and the issues related to the handling of these variations [4.2]. Its complexity was the main reason why fully adequate theoretical (analytical) approaches have not yet been applied. Semi-theoretical correlations based on experimental data have been derived to predict the Nusselt number (Nu, and in turn HTC) in SCW flow [4.18]. The first correlation was proposed by McAdams [4.29] for heat transfer in SCW flow and was based on the Dittus–Boelter correlation [4.13], i.e.,

$$Nu_b = 0.0243\, Re_b^{0.8}\, Pr_b^{0.4} \tag{4.9}$$

This correlation (i.e., Eq. (4.9)) worked with varying and thus contradictory performance in different ranges of the main flow parameters (e.g., mass flow rate, heat flux or pressure). It provides reasonable agreement with experimental data obtained with SCW flow in circular tubes at different pressures and low thermal loads [4.18], but estimated unrealistically the heat transfer in other ranges of main flow parameters (especially in case of DHT, near the critical and pseudocritical points). The issue was attributed to its strong sensitivity on the variation of thermophysical properties. Many correlations were proposed after the introduction of the McAdams correlation and were expressed in a general form as [4.10]:

$$Nu_{t,x} = C_1\, Re_{t,x}^{m_1}\, Pr_{t,x}^{m_2} \left(\frac{\rho_t}{\rho_t}\right)_x^{m_3} \left(\frac{\mu_t}{\mu_t}\right)_x^{m_4} \left(\frac{\lambda_t}{\lambda_t}\right)_x^{m_5} \left(\frac{\bar{c_p}}{c_{p,t}}\right)_x^{m_6} \left(1 + C_2 \frac{D_{hy}}{L_h}\right)^{m_7} \tag{4.10}$$

Many interesting details were reported related to the examinations of correlations for SCW flow, e.g., the application of averaged isobaric specific heat ($\bar{c_p}$) in these correlations gives better results, or the ratios of thermophysical properties improves the predictions, etc. On one hand, the extensive comparisons on these different correlations have revealed that most of them are able to provide usable preliminary estimations for heat transfer of SCW flow in tube and bundle geometries [4.10], [4.28], [4.30]. On the other hand, none of the published correlations is capable to predict accurately the DHT cases of SCW flow. Further studies are needed to improve the prediction accuracy of these correlations to support future R&D work for SCWRs.

4.2. SUMMARY ABOUT COLLECTED TESTS DATA IN NEA DATABASE

The need for an online database of experimental results on SCW thermal hydraulics performed in different types of channels emerged during the previous CRP. The NEA offered to host this database with access restricted to CRP participants. This Section gives a description about

experimental loops with tube and annular test section and introduces the database built based on these experiments. Related to experimental and numerical uncertainties, Appendix III is about experimental uncertainty analysis.

4.2.1. LOOP DESCRIPTIONS

Table 4.1 lists test loops of six research organizations: BARC, BME, CIAE, University of Ottawa, KIT and NTUU. Four of these test loops utilize water as the test fluid, two adopt carbon dioxide (CO_2) and the remaining one utilize R134a. Two of these loops cover only natural circulation experiments, three focus on forced circulation experiments and the remaining one loop is applicable for both natural and forced circulation experiments. The maximum heating power is 170 kW at the loop of CNL. The loops of NTUU and BARC deal with the highest temperatures (up to 600°C). The maximum pressure of the loops varies between 7 MPa (KIT) and 30 MPa (BARC). BME uses the smallest inner diameter in the test section (5 mm), CNL uses the biggest inner diameter (up to 22 mm).

TABLE 4.1. LOOP OVERVIEW

Institute	Fluid	Convection	Test section	Max. pressure (MPa)	Max. flow rate (kg/s)	Max. temperature (°C)	Heating power (kW)
BARC	CO_2/H_2O	Natural	Tube	30	0.13	600	10.5
BME	H_2O	Natural	Tube	27.5	0.0064	500	(4×1)
CIAE	H_2O	Natural or forced	Tube, annuli	25.9	0.389	400	160
University of Ottawa	CO_2	Forced	Tube, rod bundle	10	0.266	350	170
KIT	R134a	Forced	Tube, annuli, rod bundle	7	6	240	150
NTUU	H_2O	Forced	Tube, annuli, rod bundle	28	0.194	600	120

4.2.1.1.BHABHA ATOMIC RESEARCH CENTRE (BARC)

The test loop of Bhabha Atomic Research Centre (BARC) is called Supercritical Pressure Natural Circulation Loop (SPNCL). The schematic of the experimental loop is shown in Fig. 4.3, while its main data in Table 4.2. It works with a natural convection of CO_2 or water. The loop is made of stainless steel (SS-347) tubes with an inner diameter (ID) of 13.88 mm and an outer diameter (OD) of 21.34 mm. It contains two heater test sections and two cooler test sections, so it can be operated in four different orientations: Horizontal Heater Horizontal Cooler (HHHC), Horizontal Heater Vertical Cooler (HHVC), Vertical Heater Horizontal Cooler (VHHC) and Vertical Heater Vertical Cooler (VHVC). The cooler works with water as the secondary coolant. The annulus in the cooler has an ID of 77.9 mm and an OD of 88.9 mm. There is a pressurizer, which is installed to adjust the pressure of the loop. Furthermore, the loop is equipped with two rupture disks as a safety device.

The loop includes 44 thermocouples (K type) to measure the temperature of the primary fluid, secondary fluid and heater outside wall. For the measurement of the pressure there are two pressure transducers on the pressurizer and at the heater outlet. The heating power is measured by a wattmeter and the secondary flow rate is measured with three parallel flowmeters.

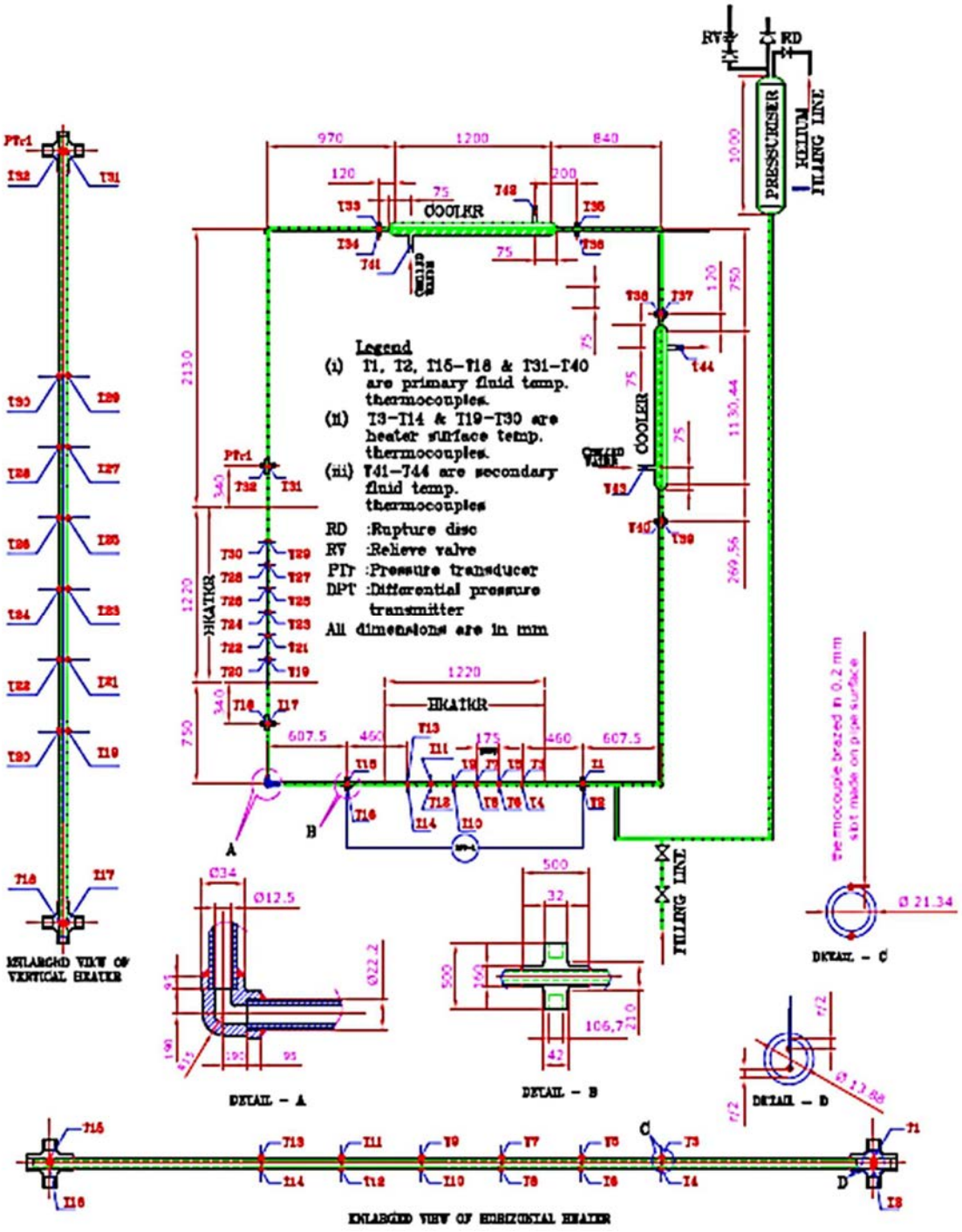

Fig. 4.3. BARC Test loop [4.31].

TABLE 4.2. BARC LOOP DATA

Fluid	Convection	Inner diameter (mm)	Outer diameter (mm)	Max. pressure (MPa)	Max. mass flow rate (kg/s)	Max. temperature (°C)	Heating power (kW)
CO_2, H_2O	Natural	13.88	21.34	30	0.13	600	10.5

4.2.1.2.BUDAPEST UNIVERSITY OF TECHNOLOGY & ECONOMICS (BME)

The MTA KFKI AEKI-BME NTI Budapest SuperCritical wAteR test fAcility (ANCARA) is a closed loop for natural circulation experiments with water as the coolant. It is schematically shown in Fig. 4.4 with its main loop data in Table 4.3.

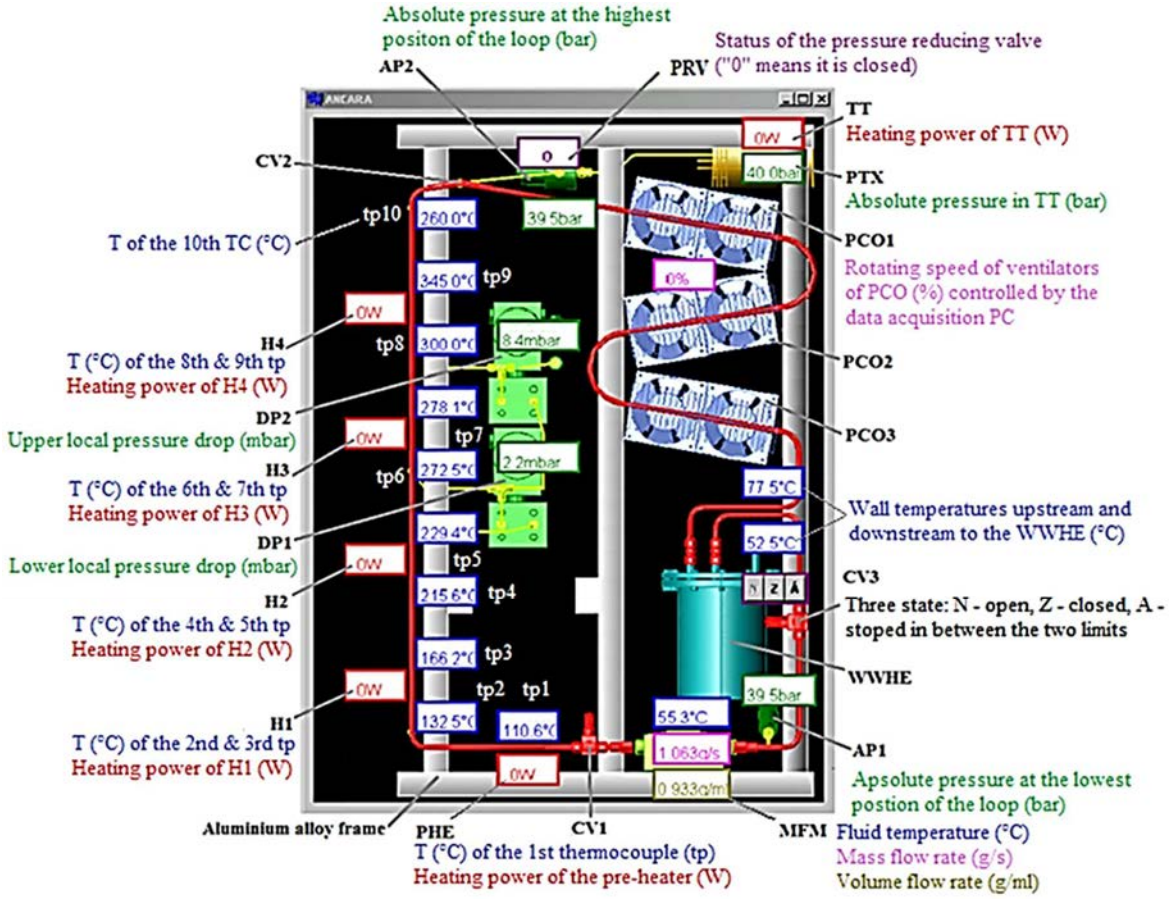

Fig. 4.4. BME Test loop [4.32], by courtesy of Elsevier.

TABLE 4.3. BME LOOP DATA.

Fluid	Convection	Inner diameter (mm)	Outer diameter (mm)	Max. pressure (MPa)	Max. mass flow rate (kg/s)	Max. temperature (°C)	Heating power (kW)
H_2O	Natural	5	8	27.5	0.0064	500	(4×1)

The main component is a stainless steel tube (ID of 5 mm and OD of 8 mm) with multiple bents. The ID of the loop (i.e., 5 mm) simulates the average equivalent diameter of four different types of subchannel in the HPLWR fuel assembly. The loop has a total length of 5.2 m and contains different tube parts which are welded or connected with Swagelok tube connectors. It has been designed for a maximum pressure of 27.5 MPa and temperatures between 50°C and 200°C. A preheater (PHE) with a power of 1 kW is installed before the test section to pre-heat the water. The test section has an approximate length of 1 m. Four identical heaters with a total power of 4 kW (4×1 kW) are attached to the test section. At the upper part of the cold leg there is a three-pass active air cooled precooler (PCO) to cool the coolant down. Downstream of the precooler, a cross current water–to–water heat exchanger is used to cool down the water. It is hosted in a stainless steel tank (WWHE). There are three identical valves (PB491021 type) installed downstream of the tank to control the mass flow rate (CV3) and for the vacuum and high purity water charge processes (CV1, CV2). The temperature on the outer wall is measured with nine thermocouples (K type). Two absolute pressure transducers (UNIK 5072–TD–A3–CC–H0–PE type) are installed to measure the absolute pressure in the loop and a mass flow meter (MFM) (SITRANS F C 300 type) to measure the mass flow rate as well as the density and temperature of the fluid and the volume flow rate. Two differential pressure transducers (SITRANS P DSIII 7MF4533–1DB32–2AA6–Z A01 type) are used to measure the local pressure drops over the test section.

4.2.1.3.CHINA INSTITUTE OF ATOMIC ENERGY (CIAE)

The test loop at the China Institute of Atomic Energy (CIAE) is shown schematically in Fig. 4.5 with its main loop data in Table 4.4. It consists of a pump, two heat exchangers, the test section (ID of 8.2 mm and OD of 11.5 mm), turbine flowmeters to measure the flow rate and a preheater with a heating power of 160 kW.

The loop is applicable for natural or forced circulation experiments with water as coolant. The test section is divided into two subsections with attached K type sheathed thermocouples to measure the temperature. A pressure transducer is installed to measure the outlet pressure. The loop has been used for heat transfer experiments at subcritical and supercritical pressures. Photocells are used to detect the onset of critical heat flux (CHF) at subcritical pressures.

TABLE 4.4. CIAE LOOP DATA.

Fluid	**Convection**	**Inner diameter (mm)**	**Outer diameter (mm)**	**Max. pressure (MPa)**	**Max. mass flow rate (kg/s)**	**Max. temperature (°C)**	**Heating power (kW)**
H_2O	Natural or forced	8.2	11.5	25.9	0.389	600	160

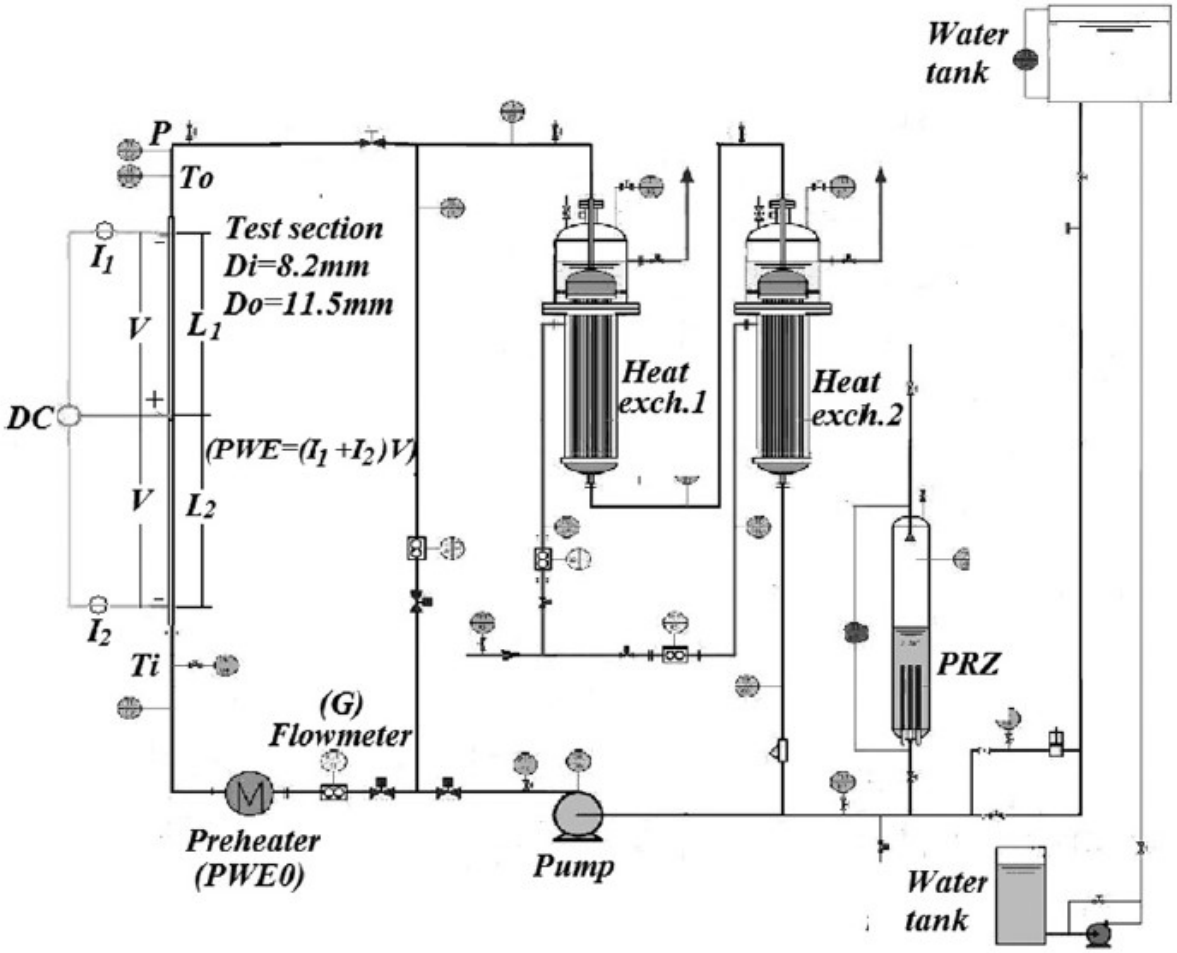

Fig. 4.5. CIAE test loop [4.33].

4.2.1.4.UNIVERSITY OF OTTAWA

The loop at the University of Ottawa is called Super Critical University of Ottawa Loop (SCUOL). It is schematically shown in Fig. 4.6 with its main loop parameter listed in Table 4.5. It is cooled with a forced convection of CO_2.

The loop consists of two parallel gear pumps and five accumulators for pressure adjustment (nitrogen is used as the secondary fluid). Discharging from pumps and accumulators, the CO_2 passes through a pre-heater and reaches the test section. Two test sections are installed in the experiments. One test section has an ID of 8 mm and an OD of 10 mm with a heated length of 1940 mm and an unheated developing length of 890 mm, and another has an ID of 22 mm and an OD of 25 mm with a heated length of 2000 mm and an unheated developing length of 728 mm. The test section is heated directly with an electrical power supply at a maximum voltage of 60 V (DC) and a maximum current of 2833 A. Two heat exchangers are installed downstream of the test section to cool the fluid with a centrally supplied chilled water and ethylene glycol.

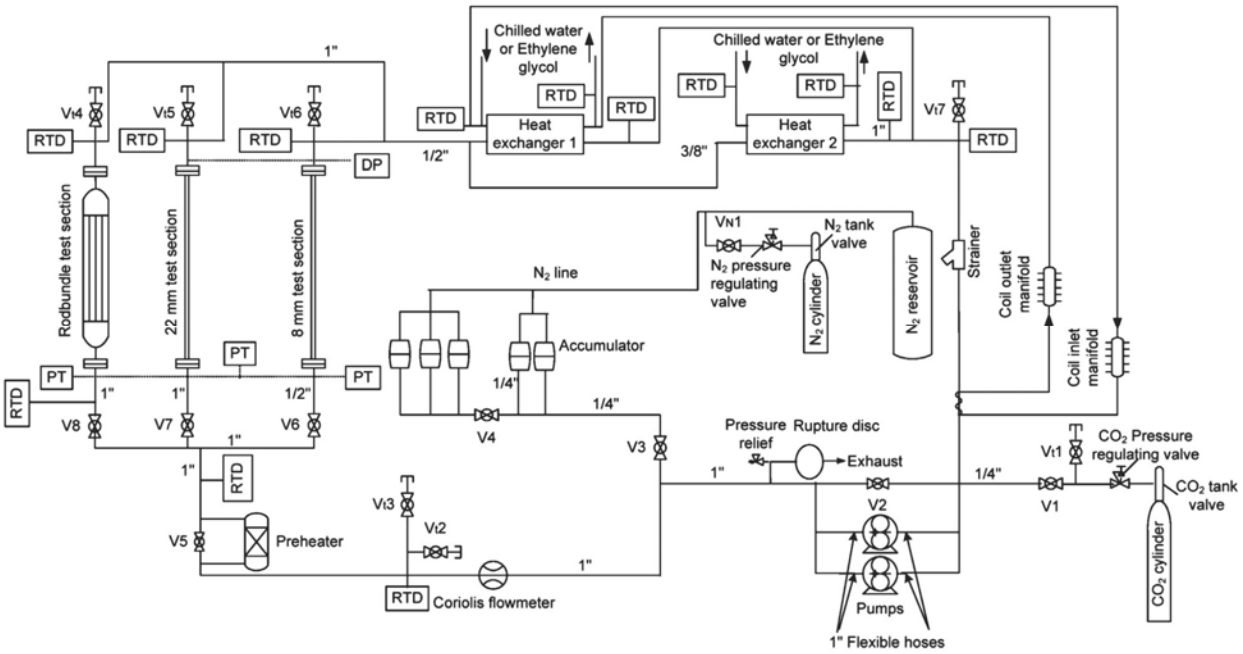

Fig. 4.6. Test loop at University of Ottawa [4.34].

TABLE 4.5. UNIVERSITY OF OTTAWA LOOP DATA.

Fluid	Convection	Inner diameter (mm)	Outer diameter (mm)	Max. pressure (MPa)	Max. mass flow rate (kg/s)	Max. temperature (°C)	Heating power (kW)
CO_2	Forced	8/22	10/25	10	0.266	350	170

The wall temperature distribution in the test section is measured with thermocouples (T type). At the inlet and outlet of the test section, ultraprecise immersion RTD sensors are used to measure the bulk fluid temperature. Pressure at the inlet of the test section is measured with two pressure transducers. A differential pressure transmitter is used to measure the pressure drop across the heated length of the test section. A coriolis flowmeter is used to measure the mass flow rate.

4.2.1.5.KARLSRUHE INSTITUTE OF TECHNOLOGY (KIT)

The KIT Modelfluid Facility (KIMOF) consists of a closed loop with a forced circulation of Regrigerant−134a (or R134a), as shown in Fig. 4.7 with its main loop parameter in Table 4.6.

TABLE 4.6. KIT LOOP DATA.

Fluid	Convection	Inner diameter (mm)	Outer diameter (mm)	Max. pressure (MPa)	Max. mass flow rate (kg/s)	Max. temperature (°C)	Heating power (kW)
R134	Forced	10	12	7	6	240	150

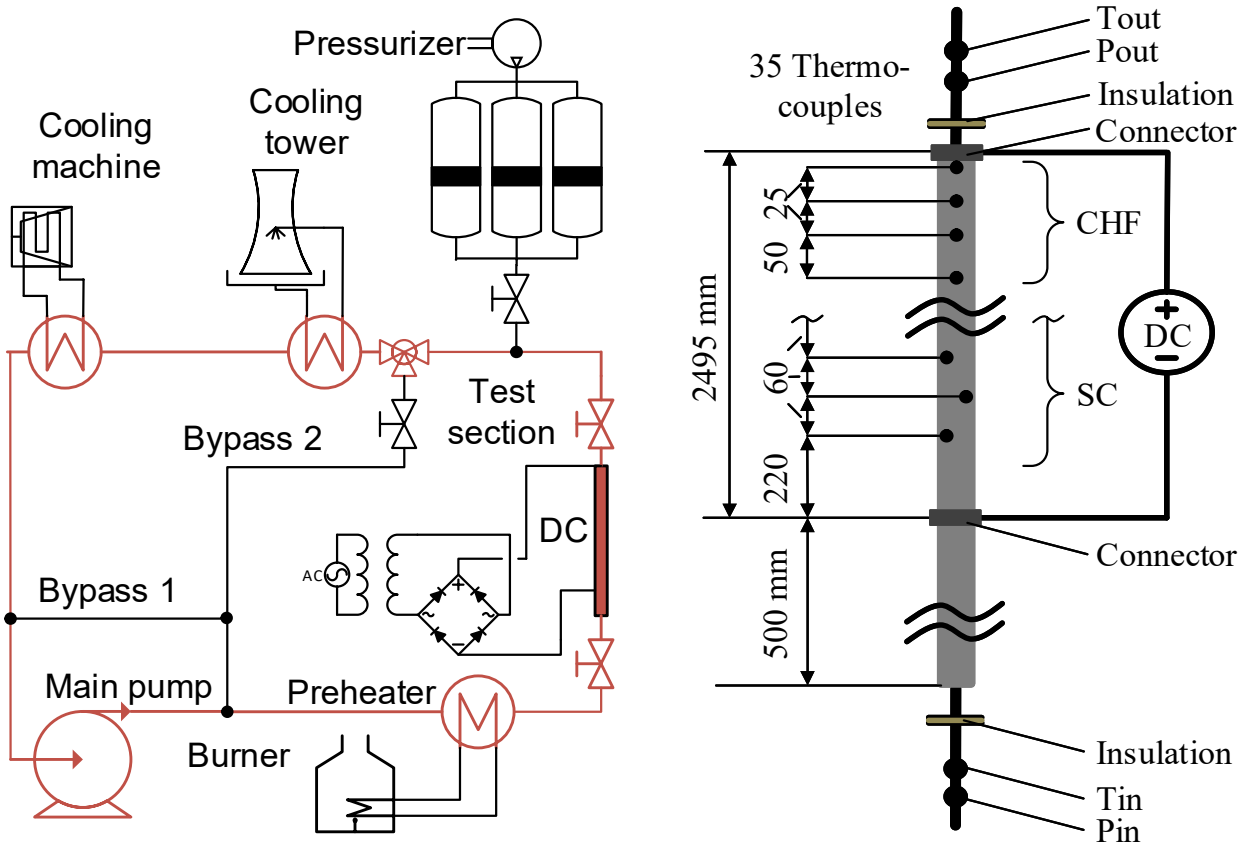

Fig. 4.7. KIT Test loop [4.35].

Prior to entering the test section, the Freon is preheated with a heat exchanger fed by a gas burner. It is cooled with two heat exchangers downstream of the test section before returning to the circulation pump. The heat is removed with a cooling tower and a cooling machine. A pressurizer, which consists of three piston accumulators, is connected to the loop for controlling the system pressure at the outlet of the test section. The mass flow through the test section is kept constant and adjusted with two bypasses. The data acquisition system consists of Wago programmable logic controllers and two 2640A data loggers connected to a PC with LABVIEW 2014.

The test section consists of a 3015 mm long stainless steel tube having inner and outer diameters of 10 and 12 mm, respectively. It is installed vertically and cooled with an upward flow of R134a. A transformer and rectifier are used to heat the test section with direct current. The heating length of the test section is 2495 mm and starts after 500 mm (i.e., 50 times the tube inner diameter) from the tube inlet to ensure full development of the turbulent flow. The test section is electrically insulated. Pressure and temperature sensors are placed at inlet and outlet of the tube. The tube outer wall temperature distribution is measured with 35 T type thermocouples. These thermocouples are attached in 60 mm intervals to the test section with only their tip touching the tube wall. To minimize heat loss, the test section is insulated with two layers of mineral wool with an overall thickness of 50 mm.

4.2.1.6. NATIONAL TECHNICAL UNIVERSITY OF UKRAINE KIEV POLYTECHNIC INSTITUTE (NTUU)

The loop of the National Technical University of Ukraine Kiev Polytechnic Institute (NTUU) is schematically shown in Fig. 4.8 with its main loop parameters in Table 4.7.

TABLE 4.7. NTUU LOOP DATA.

Fluid	**Convection**	**Inner diameter (mm)**	**Outer diameter (mm)**	**Max. pressure (MPa)**	**Max. mass flow rate (kg/s)**	**Max. temperature (°C)**	**Heating power (kW)**
H_2O	Forced	6.28, 9.5 (tube)	8.11, 12.28 (tube)	28	0.194	600	120

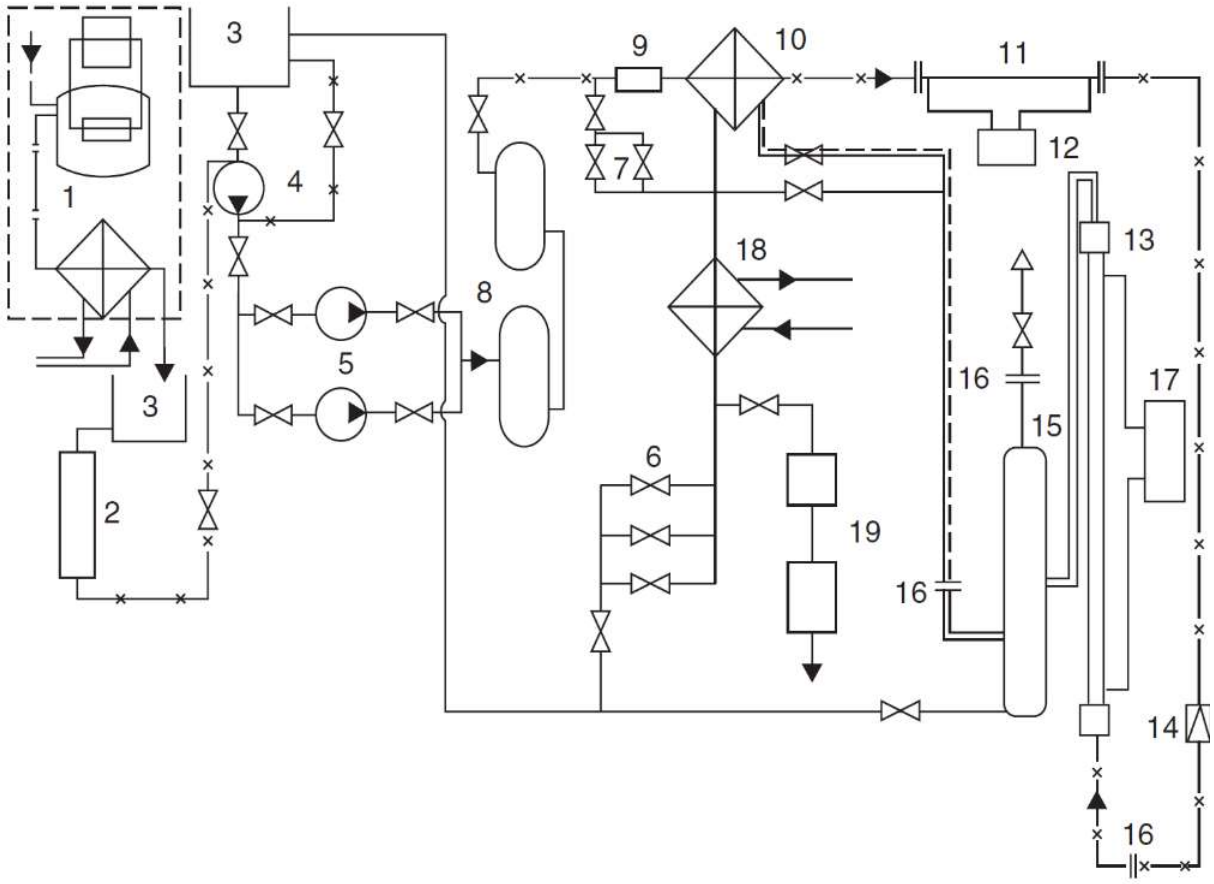

1 Electrodistiller;
2 Ion exchange filter;
3 Accumulator reservoirs;
4 Boosting pump;
5 Plunger pumps;
6, 7 Control valves;
8 Damping reservoirs;
9 Turbine flowmeter;
10 Heat exchanger;
11 Electrical preheater;
12 Dynamotor(s);
13 Test section;
14 Throttle valve;
15 Damping reservoir;
16 Electro isolating flanges;
17 Main power supply;
18 Cooler;
19 Throttling valves

Fig. 4.8. NTUU test loop [4.36].

It consists of a closed loop of stainless steel tubes with a forced circulation of water. The maxium design pressure of the loop is 28 MPa and the maximum temperature is 600°C. The loop is designed to investigate heat transfer and pressure drop characteristics in tubes, annuli, and 3 rod and 7 rod bundles at supercritical pressures. It consists of a boosting pump and two plunger pumps. Furthermore, there is a set of pressure regulating valves, a tube–in–tube pre-heater, a 75 kW electrical preheater, an AC power supply of 120 kW (60 V×2000 A) or a DC power supply of 90 kW (18/36 V×5000/2500 A). A turbine type flowmeter is used to measure the mass flow rate.

Axial dimensions of two test sections are shown in Fig. 4.9 with the locations of the pressure and voltage taps. Cross sectional configurations of the annular test section and the bundle simulators are shown in Fig. 4.10.

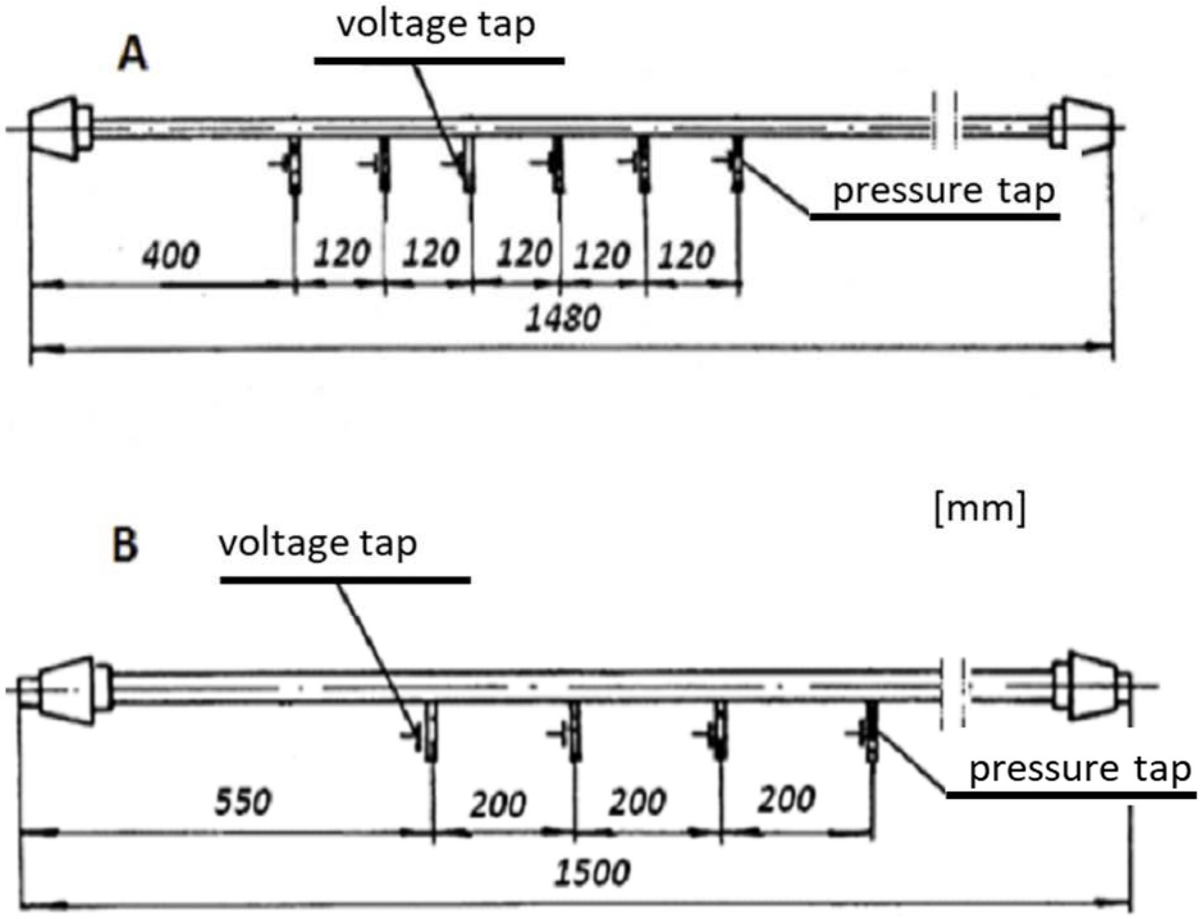

Fig. 4.9. Locations of pressure and voltage taps in test sections: A (D = 6.28 mm) and B (D = 9.50 mm) in NTUU tests.

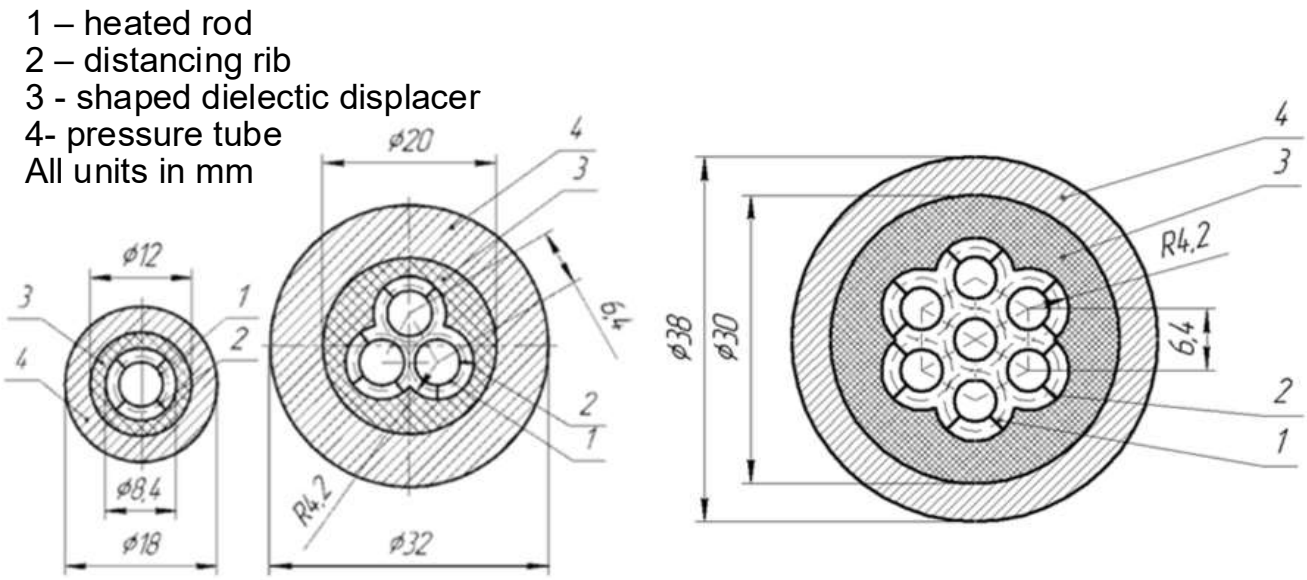

Fig. 4.10. Cross section of annular test section and bundle simulators.

4.2.2. DATA DESCRIPTIONS

Table 4.8 presents an overview of measurements obtained at different institutes. The maximum pressure was 27.5 MPa reached in the BME test loop. The highest mass flux was 2500 kg/m²s while the maximum heat flux was 3208.3 kW/m² achieved in the NTUU test loop. In total there are 22,559 measurements with the majority (10,966 points) contributed by the University of Ottawa.

TABLE 4.8. OVERVIEW OF PARAMETRIC RANGES COVERED IN ALL DATASETS.

Institute	Fluid	Geometry	Flow direction	Convection	ID (mm)	Pressure (MPa)	Mass flux (kg/(m²s))	Inlet temp. (°C)	Heat flux (kW/m²)	Data
KIT	R134a	tube	vertical, upward	forced	10	4.22–5.51	300–2000	50–80	10–200	947
BME	H_2O	tube	vertical, upward	natural	5	22.5–27.5	45–82	50–200	100–350	554
CIAE	H_2O	tube	vertical, upward	natural	4.62	22.6–25.1	614–1400	52–114	360–1930	176
CIAE	H_2O	tube	vertical, upward	natural	7.98	24.6– 25.8	495–1174	45–314	230–1160	441
CIAE	H_2O	tube	vertical, upward	forced	4.62	24.3–25.7	1137–2026	26–207	450–1780	160
CIAE	H_2O	tube	vertical, upward	forced	7.98	23.2–25.9	508–1107	24–105	230–1180	504
CIAE	H_2O	tube	vertical, upward	forced	10.89	23.5–25.4	797–1044	24–163	240–1530	469
UOttawa	CO_2	tube	vertical, upward	forced	8, 22	7.44–8.673	197–2027	7.1–13.8	5.1–436.4	10966
BARC	CO_2	tube	vertical, horizontal	natural	13.88	7.7–9.1	130–445	8–12	1–45	2945
BARC	H_2O	tube	vertical, horizontal	natural	13.88	22.4–24.2	136–575.7	75–405	13.1–111.4	3053
NTUU	H_2O	tube	upward, downward	forced	6.28–9.5	23.50	248–2193	160–395.5	103.4–2758	1588
NTUU	H_2O	annuli, rod bundles	upward	forced	2.56–2.67	22.6–27.5	800–2700	160–260	704.4–3289.1	756
									Total	22559

4.2.2.1.BUDAPEST UNIVERSITY OF TECHNOLOGY & ECONOMICS (BME)

The BME provided results of 20 different experiments (identified as E1 to E20) obtained with natural circulation of water in the ANCARA loop. An overview of parametric ranges covered in these experiments is listed in Table 4.9 and in each test case in Table 4.10. The inlet temperature was raised in steps of 50°C from 50 to 200°C (i.e., 50, 100, 150 and 200°C).

The minimal heating power was from 1420 W (E11, 50°C, 25 MPa) to 3280 W (E10, 200°C, 24.5 MPa), whereas the maximum heating power covered from 3450 (E10) to 4700 W (E8). The number of recorded steady state measurements was the highest in the E11 test (i.e., 18 points) and the lowest in the E9 test (i.e., 10 points).

TABLE 4.9. PARAMETRIC RANGES OF MEASUREMENTS OBTAINED AT BME.

Fluid	**Geometry**	**Flow direction**	**Convection**	**ID (mm)**	**Pressure (MPa)**	**Mass flux (kg/(m²s))**	**Inlet temp. (°C)**	**Heat flux (kW/m²)**	**Data**
H_2O	Tube	Vertical, upward	Natural	5	22.5–27.5	45–82	50–200	100–350	554

TABLE 4.10. RANGE OF PARAMETERS COVERED IN EACH TEST CASE AT BME TEST FACILITY.

Case	***P* (MPa) (absolute pressure)**	**P_R (-) (reduced pressure)**	**T_{in} (°C) (inlet temperature)**	**P_{min} (W) (minimal heating power)**	**P_{max} (W) (maximum heating power)**	**n_{point} (-) (number of steady state records)**
E1	22.5	1.02	50	1440	4050	14
E2	23.5	1.07	50	1630	4000	13
E3	24.0	1.09	50	1460	4050	14
E4	24.0	1.09	100	1650	4230	14
E5	24.0	1.09	150	1630	4450	15
E6	24.0	1.09	200	1880	4685	15
E7	24.5	1.11	50	1635	4000	13
E8	24.5	1.11	100	2770	4700	12
E9	24.5	1.11	150	3000	3900	10
E10	24.5	1.11	200	3280	3450	13
E11	25.0	1.14	50	1420	4000	18
E12	25.0	1.14	100	1570	4090	14
E13	25.0	1.14	150	1520	4270	15
E14	25.0	1.14	200	1700	4310	14
E15	25.5	1.16	50	1640	3900	13
E16	25.5	1.16	100	1600	4230	14
E17	25.5	1.16	150	1640	4450	15
E18	25.5	1.16	200	1860	4685	15
E19	26.5	1.2	50	1630	3920	13
E20	27.5	1.25	50	1470	4045	14

4.2.2.2. CHINA INSTITUTE OF ATOMIC ENERGY (CIAE)

The CIAE performed two types of experiments: forced convection and natural convection. Table 4.11 lists parametric ranges covered in each experiment. The forced convection experiment was performed with upward flow of water through three vertical tubes of different inner diameters (i.e., 4.62, 7.98 and 10.98 mm). Overall, the pressures varied from 23.2 to 25.9, mass fluxes from 508 to 2026 kg/(m²s), inlet temperatures from 24 to 207°C and heat fluxes from 0.23 to 1.78 MW/m^2 for 1133 data points. The natural convection experiment covered only two vertical tubes of 4.62 and 7.98 mm inner diameters. Overall, the pressure varied from 22.6 to 25.8, mass flux from 49 to 1400 kg/(m²s), inlet temperature from 45 to 314°C and heat flux from 0.23 to 1.93 MW/m^2 for 617 data points.

TABLE 4.11. PARAMETRIC RANGES OF MEASUREMENTS OBTAINED AT CIAE.

Fluid	Geometry	Flow direction	Convection	ID (mm)	Pressure (MPa)	Mass flux (kg/m²s)	Inlet temp. (°C)	Heat flux (MW/m²)	Data
H_2O	tube	vertical, upward	natural	4.62	22.6–25.1	614–1400	52–114	0.36–1.93	176
H_2O	tube	vertical, upward	natural	7.98	24.6–25.8	49–1174	45–314	0.23–1.16	441
H_2O	tube	vertical, upward	forced	4.62	24.3–25.7	1137–2026	26–207	0.45–1.78	160
H_2O	tube	vertical, upward	forced	7.98	23.2–25.9	508–1107	24–105	0.23–1.18	504
H_2O	tube	vertical, upward	forced	10.89	23.5–25.4	797–1044	24–163	0.24–1.53	469

4.2.2.3. UNIVERSITY OF OTTAWA

Experiments performed at the University of Ottawa used CO_2 as coolant in two tubes of 8 and 22 mm ID. Table 4.12 lists the parametric ranges covered in these experiments. In the experiments the mass flux was approximately set to the values: 400 kg/m^{2}s, 500 kg/m^{2}s, 700 kg/m^{2}s, 1000 kg/m^{2}s, 1500 kg/m^{2}s, 2000 kg/m^{2}s for ID 8 mm and to the values: 200 kg/m^{2}s, 500 kg/m^{2}s, 700 kg/m^{2}s for ID 22 mm. The maximum value of the bulk temperature was 82.5°C for an ID of 8 mm, a mass flux of 978 kg/m^{2}s and a heat flux of 274.3 kW/m^2. For ID 22 mm the bulk temperature reached a maximum of 39.6°C for a mass flux of 1002 kg/m^{2}s and a heat flux of 175.1 kW/m^2.

TABLE 4.12. PARAMETRIC RANGES OF MEASUREMENTS OBTAINED AT UNIVERSITY OF OTTAWA.

Fluid	Geometry	Flow direction	Convection	ID (mm)	Pressure (MPa)	Mass flux (kg/(m²s))	Inlet temp. (°C)	Heat flux (kW/m²)	Data
CO_2	tube	vertical, upward	forced	8	7.48–8.67	400–2027	7.1–13.8	19.6–436.4	10966
CO_2	tube	vertical, upward	forced	22	7.44–8.62	197–700	7.3–12.3	5.1–125	

4.2.2.4.BHABHA ATOMIC RESEARCH CENTRE (BARC)

Experiments at the SPNCL test loop in BARC were performed with both water and CO_2 as the working medium. Table 4.13 lists the parametric ranges of measurements in these experiments. The water experiments were performed in the horizontal heating, horizontal cooling configuration. The applied power varied from 1 to 8.5 kW and the mass flow rate from 7620 to 24413 l/min. The CO_2 experiments covered the horizontal heating, horizontal cooling; horizontal heating, vertical cooling; vertical heating, horizontal cooling; and vertical heating, vertical cooling configurations.

TABLE 4.13. PARAMETRIC RANGES OF MEASUREMENTS OBTAINED AT BARC.

Fluid	Geometry	Flow direction	Convection	ID (mm)	Pressure (MPa)	Mass flux (kg/m²s)	Inlet temp. (°C)	Heat flux (kW/m²)	Data
CO_2	tube	vertical, horizontal	natural	13.88	7.7–9.1	130–445	8–12	1–45	2945
H_2O	tube	vertical, horizontal	natural	13.88	21.7–24.1	136.8–575.7	75–405	13.1–111.4	3053

4.2.2.5.KARLSRUHE INSTITUTE OF TECHNOLOGY (KIT)

Experiments at KIT were performed with R134a as the coolant. Table 4.14 lists the parametric ranges of measurements in these experiments and Table 4.15 lists the test matrix. The maximum heat transfer coefficient (HTC) was 13.35 kW/m^{2}K and was reached for a pressure of 4.61 MPa, an inlet temperature of 79.9°C, a mass flux of 1993.9 kg/m²s and a heat flux 120.5 kW/m^2. The minimum of HTC was 0.489 kW/m^{2}K for a pressure of 4.807 MPa, an inlet temperature of 80.2°C, a mass flux of 511.1 kg/m²s and a heat flux 39.9 kW/m^2. The bulk temperature range covered from 54.6°C to 117.2°C. The wall temperature reached from 90.3°C to 203.1°C.

TABLE 4.14. PARAMETRIC RANGES OF MEASUREMENTS OBTAINED AT KIT.

Fluid	Geometry	Flow direction	Convection	ID (mm)	Pressure (MPa)	Mass flux (kg/m²s)	Inlet temp. (°C)	Heat flux (kW/m²)	Data
R134a	tube	vertical, upward	forced	10	4.22–5.51	300–2000	50–80	10–200	947

TABLE 4.15. TEST MATRIX OF EXPERIMENTS AT KIT.

Pressure (MPa)	Inlet temp. (°C)	Mass flux (kg/m²s)	Heat flux (kW/m²)
4.22	50	300	10, 20, 30, 40
4.59	60	500	20, 30, 40, 50
4.78	70	750	40, 50, 55, 60
5.15	80	1000	50, 60, 70, 80, 100, 110, 120
5.51	80	1500	80, 90, 100, 110, 120, 130, 140, 150, 160
5.51	80	2000	80, 90, 100, 110, 120, 130, 140, 150, 160, 170, 180, 190, 200

4.2.2.6. NATIONAL TECHNICAL UNIVERSITY OF UKRAINE KIEV POLYTECHNIC INSTITUTE (NTUU)

Experiments were performed at NTUU with water flow through the test section, which covered two tubes of 6.28 and 9.5 mm ID, an annular test section as well as 3-rod and 7-rod bundles. Hydraulics diameters were 2.67, 2.65 and 2.56 mm for the annulus, 3-rod bundle and 7-rod bundle, respectively. Both upward and downward flows of the coolant were tested in tube experiments covering three inlet enthalpies (i.e., 1400, 1600 and 1800 kJ/kg) and four heated lengths (i.e., 600, 480, 360 and 240 mm). Ranges of heat flux and mass flux have resulted in ratios from 0.288 to 1.215 kJ/kg. The maximum fluid temperature covered in the experiment was 420.5°C. A maximum heat flux was reached at 2758 kW/m² for tube A (see Fig. 4.9) with the heated length of 360 mm at the inlet enthalpy of 1400 kJ/kg and the ratio of heat flux to mass flux of 1.215 kJ/kg. Table 4.16 lists ranges of measurements in the NTUU experiment.

TABLE 4.16. PARAMETRIC RANGES OF MEASUREMENTS OBTAINED AT NTUU.

Fluid	Geometry	Flow direction	Convection	Hydraulics Diameter (mm)	Pressure (MPa)	Mass flux (kg/(m²s))	Inlet temp. (°C)	Heat flux (kW/m²)	Data
H_2O	Tubes	upward, downward	forced	6.28–9.5	23.5	248–2193	160 –395.5	103.4–2758	1588
H_2O	Annuli, rod bundles	upward	forced	2.56–2.67	22.6–27.5	800–2700	160–260	704.4–3289.1	756

The annulus and rod bundle experiments covered only the upward flow of coolant. The heated length of these channels was 485 mm. In the annulus tests, two mass fluxes at 2000 and 2500 kg/(m²s) were tested. The experiments achieved a maximum heat flux of 3208.3 kW/m^2 at the inlet temperature of 182°C and mass flux of 2500 kg/(m²s). Only a single mass flux at 1500 kg/(m²s) was covered in the 3-rod bundle experiments, while two mass fluxes at 800 kg/(m²s) and 1000 kg/(m²s) were performed for the 7-rod bundle experiments. The 3-rod bundle experiments achieved a maximum heat flux of 3289.1 kW/m^2 at the inlet temperature of 260°C and mass flux of 2700 kg/(m²s). On the other hand, the 7-rod bundle experiments achieved a maximum heat flux of 1326 kW/m^2 at the inlet temperature of 178°C and mass flux of 1000 kg/(m²s).

4.3. CONVENTIONAL INVESTIGATION OF HEAT TRANSFER IN TUBES AND ANNULAR CHANNELS

NTUU fulfilled a complex of experiments keeping in mind crucial position of DHT in the problem of SCWR operation safety. It is vital to clarify an impact of coolant free convection and of flow thermal acceleration that are the functions of density and dynamic viscosity, and, to a lesser extent, of thermal conductivity, beside that impact of friction resistance, as well as of thermoacoustic oscillation of pressure on the level of heat flux causing transition to DHT. As known, heat transfer and pressure drop are a resulting effect of molecular and turbulent forces in the flow of coolant, in their turn, depending upon its thermophysical properties, operating conditions (i.e., inlet temperature, heat flux, mass velocity, pressure, flow direction) and geometric parameters (i.e., heated diameter and length), including roughness and configuration of the heated surface. Interaction between these parameters becomes significantly complicated in the zone of

pseudocritical state with its extremely nonlinear variation of thermophysical properties (see Fig. 4.11). No wonder, that until now the attempts to describe this process either theoretically or empirically are not very successful and the difficulties could be overcome possessing only direct (velocity and temperature fields in channel cross sections that gradually will be more and more complemented by CFD modeling) or reliable indirect (friction and acceleration resistances) data on thermohydraulic structure of the flow.

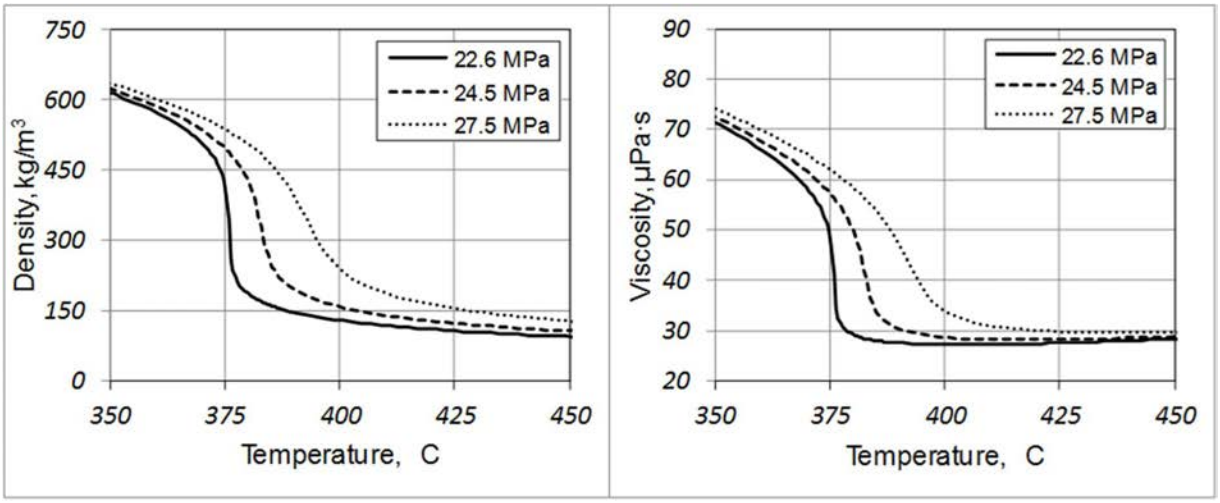

Fig. 4.11. Variations of density and viscosity of water at pressures covered in rod bundle experiments at NTUU [4.37].

For water at supercritical pressures, there is a strong correlation between heat transfer coefficient (HTC), α, and heat flux, q, when $T_w > T_m > T_b$. Namely, under low values of q the temperature head ($T_w - T_b$) is below one in a normal convective mode (enhanced heat transfer). Increasing q above a certain level results in deterioration of heat transfer, where T_w abruptly rises sometimes reaching maximum in one or more cross sections of the channel. In both cases, α could considerably differ from that at the normal convective mode.

DHT can be a significant issue, not so much because the high level of channel wall temperature, but because of its high dependence upon even negligible change in operating conditions. Inability to predict correctly DHT conditions and the scale of this deterioration are the main reasons of constant attention devoted to the phenomenon. Efforts to explain and evaluate DHT are perhaps known since its first description [4.38]. Until now for more than 60 years, neither of the methods to foresee and assess this deterioration (its location and level) with accuracy acceptable for practical application was proposed.

Results of experimental studies on heat transfer and hydraulic resistance of tubes and annular channel cooled with upward and downward flows of SCW at significant buoyancy, under impact of thermal acceleration and in a gas-like state of coolant are presented. A correlation for predicting heat transfer coefficient under fully developed turbulent flow of SCW has been derived. It was assessed with the experimental data and compared against prediction accuracies of other correlations.

Thermal hydraulic studies using annuli enhance the understanding of the complex phenomena. A sketch of the test section with such channel is shown in Fig. 4.12. It is important to exclude relative deviation of the surfaces forming the annular channel. Nevertheless, despite thorough performance of the distancing rods (Fig. 4.12, pos. 15 and 16) because of narrow gap between the walls circumferential difference in temperature was great enough (Fig. 4.13) and therefore in each cross section of measuring wall temperature four thermocouples over 90° each were mounted to get the mean value of T_w.

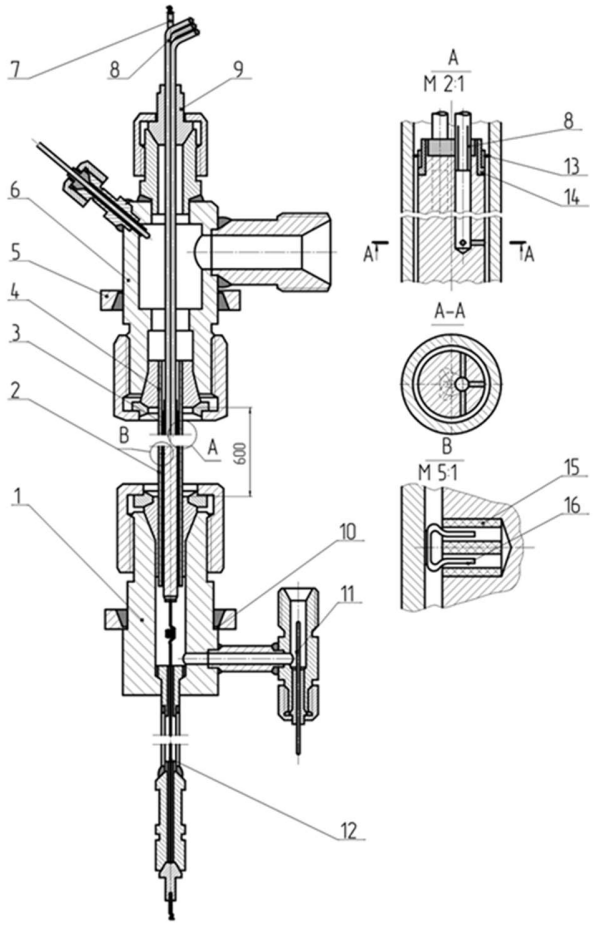

1, 6 Inlet and outlet chambers
2 External heated tube
3 Internal rod
4 Axial cone
5, 10 Current carrying steel buses
7, 8 Pressure impulse and thermocouple lines
9 Conical plug
11 Thermocouple cartridge
12 Current leakage control line
13 Ring with distancing ribs
14 Mica
15 Ceramic straw
16 Steel clip

Fig. 4.12. Test section with annular channel.

The conventional normal heat transfer occurs under linear change of flow parameters at moderate heat fluxes and follows the Reynolds analogy of thermal hydraulic processes interconnecting temperature head and pressure drop in coolant. At DHT these analogies are not application due to two main evident forces: buoyancy and thermal acceleration.

In annular channels even insignificant misalignment of its rod (3 to 5% of gap) at ratios of heat flux to mass flux (q/G) greater than 0.5 kJ/kg resulted in noticeable difference in temperature ($\Delta T = T_{av} - T$) around cross sections. Therefore, four thermocouples at 90° step were installed for establishing the average wall temperature at each cross sectional location (Fig. 4.13).

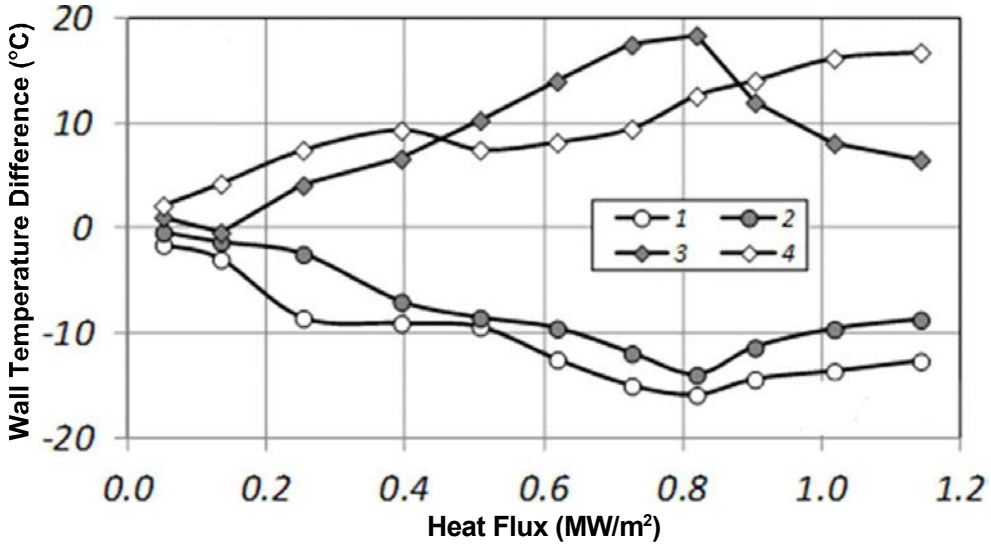

Fig. 4.13. Circumferential distribution of wall temperature in annular channel I (G = 1000 kg/(m²·s); 1, 2, 3 and 4: thermocouples in each cross section).

In some cases, the buoyancy and thermal acceleration forces change significantly radial temperature and velocity profiles of the flow. These profile changes could result in additional frictional and/or inertial pressure drop, as well as heat and mass transfer changes, causing heat transfer enhancement or deterioration (similar to boiling or crisis of heat transfer at subcritical pressures). An initial study to apply the Reynolds analogy in an explicit form for prediction of heat transfer in round tubes and annuli introduced the following correlation [4.39]:

$$Nu_0 = \frac{\left(\xi_0/8\right)\cdot \mathrm{Re}\cdot \mathrm{Pr}_b}{1+\frac{900}{\mathrm{Re}}+12.7\sqrt{\xi_0/8}\left(\mathrm{Pr}_b^{\,2/3}-1\right)}, \tag{4.11}$$

where the denominator could be considered as a coefficient of Reynolds analogy characterizing the sum of thermal resistances of viscous wall boundary layer and of turbulent core. The friction factor, ξ_0, corresponds to isothermal flow at mean temperature of coolant in the channel and is defined as [4.40]

$$\xi_0 = \left(1.82\cdot log_{10}\frac{Re_b}{8}\right)^{-2} \tag{4.12}$$

Equation (4.11) should be much more correct, had the friction resistance coefficient ξ_{fr} reflecting the real state of the coolant flow instead of ξ_0. The need of such substitution grows with approaching to the state, when $T_w > T_m > T_b$ (T_m is the temperature of SCW at its maximum isobaric specific heat capacity), and with increasing ratio of heat flux to mass flux (i.e., q/G). Under such thermal conditions the error in the estimation of the inertial hydraulic resistance could be high,

when flow thermal acceleration is determined by using conventional one dimensional model of flow profile based on the equation of motion. With uniform distributions of fluid velocity and temperature, if the change in their radial profiles is neglected, it is

$$\Delta P_{ac} = G^2(V_2 - V_1) \tag{4.13}$$

where V_2 and V_1 are specific volumes of coolant at outlet and inlet of the heated tube.

At the range of temperatures $T_w > T_m > T_b$, which corresponds to the zone of high specific thermal capacity ($c_p > 8$ kJ/(kg·K)) and the transition of SCW from the 'liquid' to the 'gaseous' state, this model could predict incorrectly both acceleration and frictional resistances. In turn, such relationship between ΔP_{ac} and ΔP_{fr} gives invalid interpretation of real thermohydraulic situation near the wall (the degree of flow profile laminarization) and, as a result, impacts on heat transfer.

At the temperatures within the zone of high c_p and under high ratios of heat flux to mass flux (i.e., q/G) the frictional pressure drop determined by subtracting the thermal acceleration resistance based on the one dimensional model from the measured pressure drop, as shown in Eq. (4.24), could exceed (sometimes by 15 to 30%) the value of isothermal friction factor, ξ_{fr0}. Since non-isothermal friction factor, ξ_{fr}, at the same bulk temperature is lower than the isothermal friction factor, ξ_{fr0}, (i.e., $\xi_{fr}/\xi_{fr0} < 1$), ΔP_{ac} is underestimated due to excluding the radial change of impulse (velocity) profile in applying the one dimensional flow model.

A correlation has been derived from data obtained from experiments of heat transfer and hydraulic resistance with water in bare tubes and annuli at supercritical pressure. Table 4.17 lists the test matrices of these experiments. Prediction accuracy of the correlation was compared against those of others correlations.

TABLE 4.17. PARAMETERS OF TEST SECTIONS AND RANGE OF OPERATING CONDITIONS FOR EXPERIMENTS WITH ONE DIMENSIONAL REDUCTION OF PRESSURE DROP DATA

Channel	L (mm)	D_2/D_1	D_{hydr} (mm)	L_{heat}/D_{hydr}	L_{hydr} (mm)	T_{in} (°C)	G (kg/(m²s))	q (MW/m²)	Flow direction
Annular I	650	10.02/8.04	1.98	300	25, 50	20–375	500–1500	0.5–1.5	upward
Annular II	360	6.1/4.2	1.99	150	20	100–420	1000	0.25–0.5	
Tubes	440	-	3.01	127	20, 40, 80	220–350	1000–2600	0.25–2.5	
	1480	-	6.28	31.8–95.5	200	20–415	250–750	0.06–2.5	up- and downward
	1500	-	9.50	21.0–63.2	200	20–377	250–2193		

The study focused on thermohydraulic regimes in smooth tubes under both (1) mixed turbulent convection in SCW and (2) $T_b > T_m$ (i.e., gas like region). Case (1) draws attention on the ambiguous impact of free convection on heat transfer and on the very limited information on heat transfer in inlet thermal section under various enthalpies of coolant, whereas case (2) was identified by the intention to design heat transfer systems for operation under the conditions of steady heat state at the highest possible temperature of coolant to increase thermal efficiency of the equipment.

Under the conditions of low coolant mass flow rate (e.g., when the power unit is partially loaded at rated temperature of coolant) the regime of mixed convection (viscous, gravitational flow mode)

takes place. It is known that in numerous experiments impact of mixed convection was noticed in a wide range of Gr/Re^2. Such regimes depend upon the thermal entrance section of a channel and it should be taken into consideration in the analysis of temperature profile of the channel. Two tubes of 6.28 and 9.50 mm diameter (Fig. 4.9**)** were chosen for the experiments that provided 1000 fold range of Gr/Re^2 from 0.001 to 1.0.

As a result, the regimes without and with impact of buoyancy were obtained. In the latter case, different effects were detected: (1) inlet thermal section (local deterioration of heat transfer) with extreme change in the outlet part of the channel and further movement of temperature peak to the entrance under heat flux growth (Fig. 4.14); (2) thermoacoustic oscillations of pressure (TOP); (3) instability of temperature regime; and (4) strong dependency of heat transfer upon flow direction. In some cases several effects could take place simultaneously.

4.3.1. HEAT TRANSFER IN TUBE ENTRANCE SECTION

In the experiments performed at NTUU to understand the nature of entrance peaks of wall temperature under low mass flow rates it was noticed that at a certain level of heat flux hardly seen local deterioration of heat transfer with weak increase in wall temperature starts in an outlet part of the channel with further movement to the entrance and its growth with increasing heat flux (Fig. 4.14a). Plots of the temperature profile vs. flow enthalpy (Fig. 4.14b) revealed that position of DHT temperature at all heat fluxes corresponds to the same flow enthalpy and the higher q, the higher 'peak'.

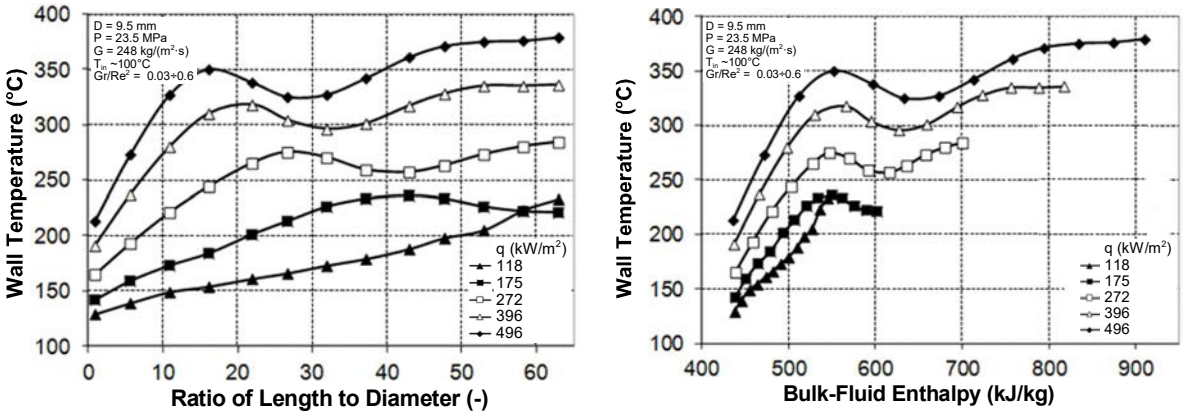

Fig. 4.14. Variations of wall temperature under upward flow of water.

A temperature 'peak' at mixed convection is located at an unique bulk enthalpy depending upon inlet enthalpy. This implies that, at any inlet enthalpies, the minimal Nusselt numbers occur at cross sectional locations with the same Reynolds number. Therefore, at the same thermohydraulic state of the flow, there is a certain Δh_{in} that should be contributed into coolant under any heat flux to reach the state of the temperature peak. That is why the higher heat flux q (at constant mass flow rate), the closer is the peak to the channel entrance. It means that the entrance thermal section length depends upon inlet enthalpy h_{in} and ratio of heat flux to mass flux (i.e., q/G).

The experimental results showed a linear decreasing trend of Δh_{in} with increasing h_{in}, as shown in Fig. 4.15 (i.e., $\Delta h_{in} = f(h_{in})$). For turbulent flow at $Gr/Re^2 \geq 0.06–0.08$, increments of the enthalpy at the wall temperature peak in tubes are correlated to

$$\Delta h_{in} = 195 - 0.07 \cdot h_{in} \qquad for\ Ø6.28\ \text{mm}$$
$$\Delta h_{in} = 155 - 0.06 \cdot h_{in} \qquad for\ Ø9.50\ \text{mm} \tag{4.14}$$

These correlations are applicable to establish the location of wall temperature peak once heat flux, mass flow rate and inlet enthalpy are known. Generalization of these correlation to take into the account of the channel diameter effect is feasible once additional experimental data for other tube ID are available. The experiments demonstrated that the length of the entrance section in a heated tube could be significant (it exceeded the whole heated length of 95·D in these cases). However, it is difficult to check at its beginning (far enough from the entrance), when heat flux is a rather low. At downward flow this phenomenon was not observed, since under very strong countercurrent of forced (by pump) and free (by buoyancy) convection, when $Gr/Re^2 = 0.6–0.8$, boundary layer should be ruined at the very entrance into the channel.

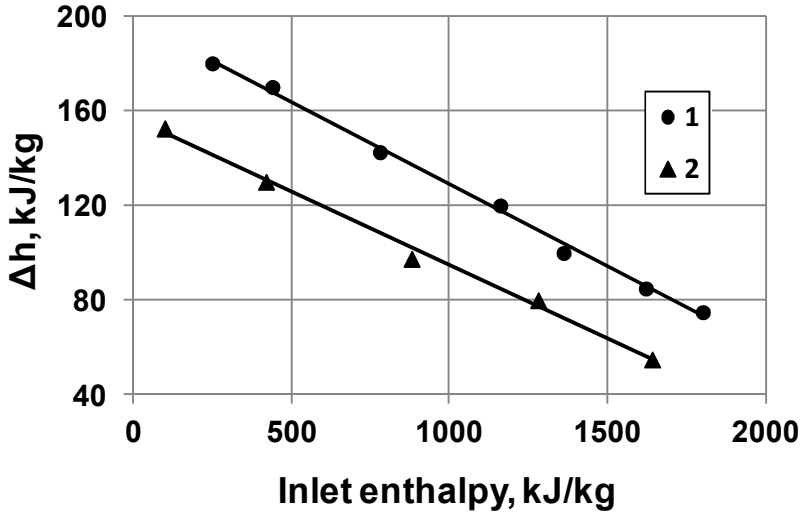

Fig. 4.15. Enthalpy increase at the section from entrance to the 'peak' of wall temperature in tubes as a function of h_{in} (inner diameter of the tubes: 1–6.28 mm; 2–9.50 mm).

With increasing flow turbulence (Reynolds number) free convection is degrading ($Gr/Re^2 \rightarrow 0.01–0.02$) and the entrance effect disappears. In the absence of free convection entrance heat transfer effect is expressed as [4.41]

$$A_x = 1 + 2.35 \cdot Re^{-0.15} \cdot Pr^{0.4} \cdot (x/d)^{-0.6} \cdot \exp(-0.39 \cdot Re^{-1} \cdot x/d) \tag{4.15}$$

Equation (4.15) is valid for Reynolds numbers from 1×10^4 to 5×10^5, Prandtl numbers from 0.7 to 100 and $x/d > 0.5$.

4.3.2. EFFECT OF FREE CONVECTION ON SUPERCRITICAL WATER HEAT TRANSFER IN TUBES

The phenomenon of DHT in descending flows was rarely investigated and reported, though it is developed by the same scenario of enhancing with further transition into deterioration but at much higher (by 1.5 to 3 times) heat flux rates. Fig. 4.16 demonstrates existance of enhanced and deteriorated heat transfer both in upward and downward flows of supercritical water in approximately the same range of Gr/Re^2 from 0.01 to 0.6 with the difference only in extent and even direction of heat transfer change. Here Gr/Re^2 varied from 0.03 to 0.09 for upward and to 0.07 for downward flow, while heat flux rate was q/G = 0.898 and 1.066 kJ/kg, respectively. However, the deteriorated heat transfer in both flow directions showed similar trend. The most significant effect of free convection is near Gr/Re^2 = 0.2 to 0.3 (Fig. 4.17). Usually, the deteriorated heat transfer started earlier in the upward flow compared to that in the downward one due to concurrent and countercurrent effects of free and forced convections in up and downward flows.

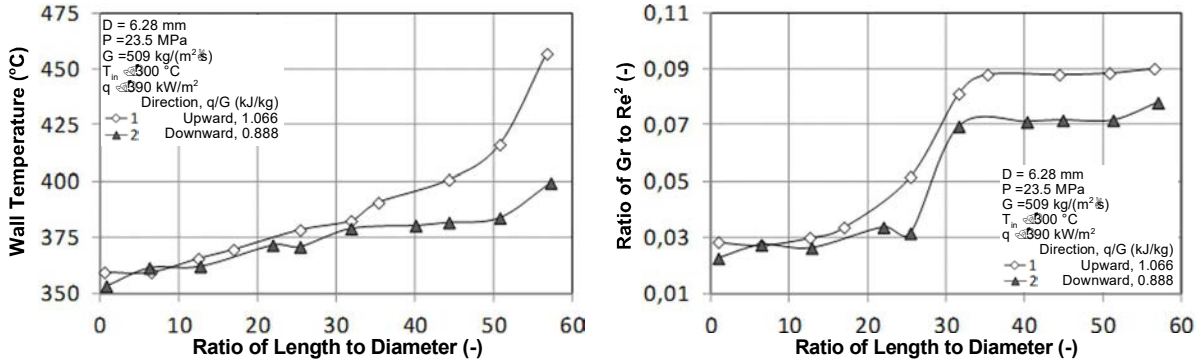

Fig. 4.16. Effect of mixed convection on wall temperature and ratio of Gr to Re^2.

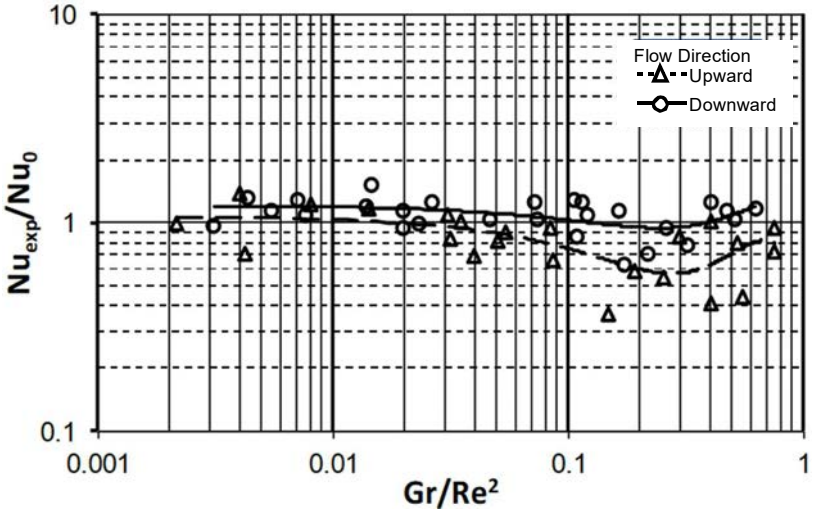

Fig. 4.17. Heat transfer as a function of Gr/Re^2 under impact of free convection in vertical tubes with ID of 6.28 and 9.5 mm.

4.3.3. FLOW FULL THERMAL ACCELERATION, METHOD OF TWO PRESSURE DROPS

Developed at the Institute of High Temperatures (IVTAN, Moscow) and tested for supercritical carbon dioxide the so-called method of two pressure drops [4.42] had made possible to define friction and acceleration hydraulic resistances of the channels under the conditions of significant thermal acceleration of SCW flow without probe measurements, indirectly determining the impulses of turbulent flow in the case of high heat flux rate and strong dependence of fluid density upon temperature. The basis of the method in brief consists in measurements of pressure drop both at heated section with accelerating flow and in a downstream adiabatic section with decelerating flow, whose minimal length l_{ad} should be enough to restore the developed isothermal turbulent flow under constant physical properties. Tentatively speaking, at the end of the heated section the flow reminds squeezed spring or, even better, a bow, whose form prior to shoot an arrow corresponds to the laminar (arc like) profile of the flow radial velocity, and at the end of the following adiabatic section the velocity profile is turbulent (almost flat), exactly as on shooting the bow returns to almost straight line form. So, unlike the traditional one dimensional model the two dimensional one, valid for axially symmetric flow, takes into account full kinetic energy (inertia resistance) absorbed during heated fluid acceleration and therefore the local resistance factor in adiabatic section is lower than isothermal one (Fig. 4.18). Table 4.18 lists the test matrix.

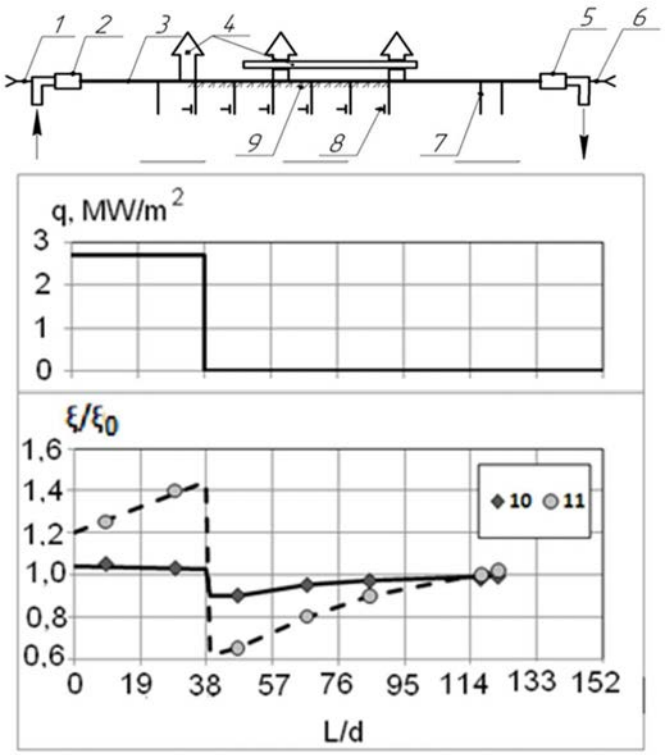

Fig. 4.18. Scheme of experimental section and the results of calibration measurements of adiabatic hydraulic resistance (1 - inlet thermocouples; 2, 5 - mixing chambers; 3 – channel; 4 - current buses; 6 – thermocouples; 7 - pressure taps; 8 - voltage taps; 9 - wall thermocouples; 10 hin: 1490 kJ/kg (Tin = 328.5°C); 11 hin: 1690 kJ/kg (Tin = 357.8°C).

TABLE 4.18. TEST MATRIX (COMBINATION OF OPERATING PARAMETERS AND HEATED LENGTH IN THE EXPERIMENTS WITH TWO PRESSURE DROPS)

q/G number	q/G, kJ/kg	h_{in}, kJ/kg		
		1400	1600	1800
		Number of heated sections of 120 mm length		
1	0.288	5	5	5
2	0.431	5	5	5
3	0.575	5	5	5
4	0.719	5	5	5
5	0.826	5	5	5
6	0.950	5	4	5
7	1.075	5	4	4
8	1.157	5	3	3
9	1.215	4	2	1
10	1.275	1	1	1
11	1.347	1	1	1
12	1.421	1	1	1
13	1.476	1	-	-

Two pressure drops allow considering of the system of two equations:

$$\left.\begin{aligned} \Delta P &= \Delta P_{fr} + \Delta P_{ac} + \Delta P_g \\ \Delta P_{ad} &= \Delta P_{fr.ad} + \Delta P_{ac.ad} + \Delta P_{g.ad} \end{aligned}\right\}, \tag{4.16}$$

where $\Delta P_{ac} = I_l - I_{in}$ and $\Delta P_{ac.ad} = I_{o.l} - I_{o.in}$ with I_l, $I_{o.in}$ and $I_{o.l}$ are flow impulses at the heated section outlet, adiabatic section inlet and outlet, respectively, $\Delta P_g = gd\int_0^{l/d} \rho d(l/d)$ and $\Delta P_{g.ad} = gd\rho(l/d)_{ad}$ are efficient hydrostatic heads in both sections. The flow impulse is defined as

$$(I = 2\int_0^1 \rho W^2 R dR = S(\rho W^2)/\rho; \tag{4.17}$$

The flow impulse at the heated section inlet after the section of hydrodynamic stabilization corresponds to the impulse of stabilized one dimensional turbulent flow of liquid with constant physical properties, i.e.,

$$I_{in} = S_0 \cdot G^2/\rho_{in}, \tag{4.18}$$

where $S_0 \approx$ const = 1.02 (at $Re > 5\cdot10^4$), which is an impulse factor of turbulent isothermal flow (Boussinesq ratio). In two dimensional model of heated flow, the real impulse factor, *S,* depends upon the degree of velocity profile population and increases from 1.02 to 1.3 as the latter decreases [4.43]. In the extreme case of laminar flow $S_l = 1.33$, where S_l is a laminar profile impulse factor. Thus, neglecting these aspects, the application of the one dimensional model is incorrect.

The frictional pressure drop (head) at the adiabatic section is expressed as [4.42]

$$\Delta P_{fr.ad} \approx \Delta P_{0.fr.ad}\left[1-\frac{a}{(l/d)_{ad}}\left(1-\frac{\xi_{fr.l}}{\xi_{o.fr.l}}\right)\right] \tag{4.19}$$

where a is a constant characterizing the restoration curve of the flow velocity isothermal radial profile that is analogous to ξ/ξ_0 curve in Fig. 4.18; $\Delta P_{0.fr.ad}$ is a friction resistance of the adiabatic section under isothermal flow, i.e., when $\xi_{fr.ad} = \xi_{0.fr.l}$; $\xi_{\text{fr.l}}$ and $\xi_{0.\text{fr.l}}$ are the friction factors at the last cross sections of the heating and adiabatic zones, respectively. Besides that, ratio ($\xi_{fr.l}/\xi_{0.fr.l}$) could be substituted by the following averaged value of the reduced friction factor at the heated section:

$$\frac{\xi_{fr.l}}{\xi_{fr.ad}} = \frac{\xi_{fr}}{\xi_0}\Big|_0^l = \Delta P_{fr}\left[\frac{G^2}{2}\int_0^l \frac{\xi_0}{\rho_b} d\left(\frac{l}{d}\right)\right]^{-1} \tag{4.20}$$

Finally, Eq. (4.16) is solved together with Eq. (4.19) and Eq. (4.20) resulted in

$$\Delta P_{fr} = \frac{\Delta P - I_{0.in} - I_{0.l} + \Delta P_{ad} - \xi_{0.l}\left(\frac{G}{2\rho_l}\right)\left(\frac{l}{d}-a\right)}{1+a\frac{\xi_{0.l}}{\rho_l}\left[\int_0^{l/d}\left(\frac{\xi_0}{\rho}\right)d\left(\frac{l}{d}\right)\right]^{-1}}, \tag{4.21}$$

where $\xi_{0.\text{l}} = \xi_{\text{ad}}$ is the friction coefficient at the outlet of the adiabatic section.

The series of ΔP_i and $\Delta P_{\text{i.ad}}$ measurements at different heated lengths ($0 < l_{\text{i}} < l$, where i = 1, 2, 3, 4 and 5) under the same operational conditions facilitates establishing a set of equations (4.17) for the distribution of full hydraulic resistance $\Delta P(l/d)$ and its components $\Delta P_{\text{fr}}(l/d)$ and $\Delta P_{\text{ac}}(l/d)$ along the channel. Local factors of hydraulic resistance are expressed as

$$\zeta_i = \frac{2\rho_i[d\Delta P(\tilde{l})/d\tilde{l}]_i}{G^2}; \xi_{fr_i} = \frac{2\rho_i[d\Delta P_{fr}(\tilde{l})/d\tilde{l}]_i}{G^2}; \xi_{ac_i} = \frac{2\rho_i[dI(\tilde{l})/d\tilde{l}]_i}{G^2} \tag{4.22}$$

These measurements resulted in the diagrams of the isothermal profile restoration, due to which constant a = 10 in Eq. (4.19) was obtained.

The values of the reduced (to isothermal conditions) local coefficients of hydraulic resistance, $\overline{\boldsymbol{\zeta}}, \overline{\boldsymbol{\xi}}_{\text{fr}}$ and $\overline{\xi}_{\text{ac}}$, as well as longitudinal temperature profiles, are shown in Fig. 6.5 (see Section 6 for the analysis). For obtaining the required sets of $\Delta P(l/d)$ and showing their local values under variable heated lengths using Eq. (4.21), sets of $T_w(l/d)$ have been obtained under similar operating parameters to minimize temperature differences and associated uncertainty. As noted in [4.42], flow effect on local heat transfer is not feasible under a significant impact of buoyancy. For buoyancy effect tests (Fig. 4.19a), the transition of regimes is shown with difference wall temperature profiles at G = 1400 kg/(m^2·s), where $Gr/Re^2 > 1.5\cdot10^{-2}$. As the mass flux increased, heat transfer changes to another temperature mode. For the tube of ID = 6.28 mm at the mass flux about 2000 kg/(m^2·s) ($Gr/Re^2 << 1\cdot10^{-2}$), influence of buoyancy or gravity (free convection) is

negligible. All experiments to confirm the method of two pressure drops were carried out at one mass velocity G = 2193 kg/(m^2·s), where $Gr/Re^2 < 2.5 \cdot 10^{-3}$. In this case (Fig. 4.19b), taking into account mismatching of operating conditions in different heated lengths, the wall temperature regimes were the parts of a common one and high enough pressure drops (about 500 Pa) were obtained. Table 4.19 lists the uncertainties of measurements and calculated parameters.

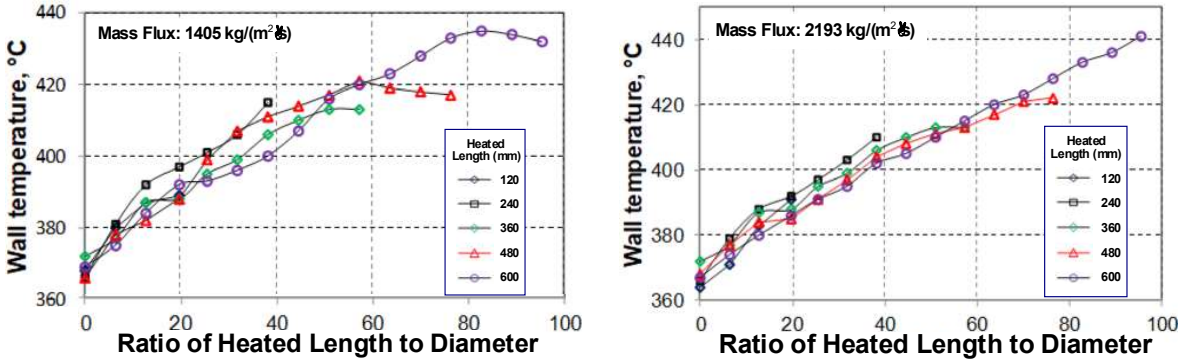

(a) (b)

Fig. 4.19. Variations of wall temperature distributions along the tubes (h_{in} = 1400 kJ/kg; q/G = 0.826 kJ/kg).

TABLE 4.19. MAXIMUM UNCERTAINTIES OF MEASURED AND CALCULATED PARAMETERS.

Parameter	Maximum uncertainty
Measured parameters	
Inlet pressure	±0.22%
Pressure drop	±0.4%
Bulk fluid temperatures	±3.4%
Wall temperature	±3.2%
Calculated parameters	
Mass flow rate	±2.3%
Heat flux	±3.5%
Heat transfer coefficient	±12.7%
Heat loss	≤3.4%

The criterion of thermal convection, as a factor impacting on heat transfer, has been proposed as [4.44]

$$Gr/Re_b^{2.7} > 1.2 \cdot 10^{-5} \tag{4.23}$$

or in another form as [4.45]

$$Gr/Re_b^2 > 0.01 \tag{4.24}$$

Due to high coolant mass velocity this critrion did not exceed 0.005. Therefore, heat transfer is affected by the thermal acceleration only.

4.3.4. ANALYSIS AND RESULTS

It is convenient to plot the diagrams for full hydraulic resistance and its frictional and accelerative components as ΔP, ΔP_{fr} and ΔP_{ac} versus q/G in all heated sections of the tube that reflect change in ΔP_{ac} and ΔP_{fr} obtained by using Eq. (4.16). As shown in Fig. 4.20, increasing q/G increases ΔP_{ac} and decreases ΔP_{fr} (dashed lines) of the total hydraulic resistance, ΔP (solid lines) until these pressure drops are equal at a certain boundary $(q/G)_b$. The shorter the section, the higher q/G of $\Delta P_{ac} = \Delta P_{fr}$. In further growth of q/G the resistance to thermal acceleration ΔP_{ac} exceeds friction resistance ΔP_{fr}.

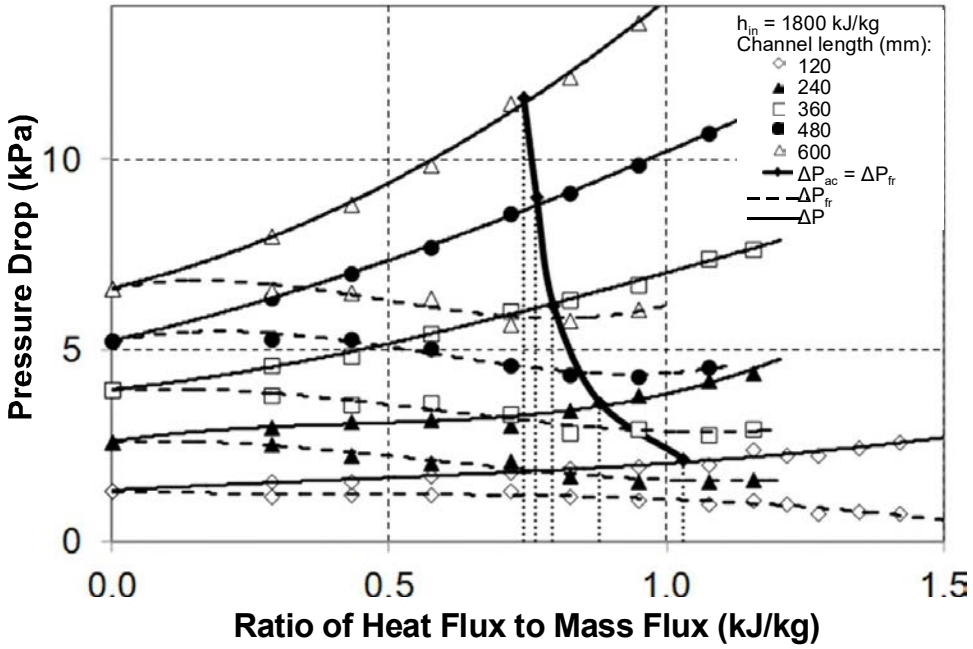

Fig. 4.20. Dependence of full hydraulic resistance and friction resistance upon heat flux rate.

ΔP_{fr} is monotonically changing and easy enough to foresee the trend of its growth (Fig. 4.21, curve 1). The analysis of temperature and pressure drop measurements shows that the values of $(q/G)_b$ corresponding to equality of friction and acceleration forces practically almost coincide with q/G of transition from normal to deteriorated heat transfer. It means that transition to flow with domination of acceleration force over friction one is a condition or index of the mentioned transition to DHT or, in other words, it takes place, if

$$\Delta P_{ac} > \Delta P_{fr} \text{ or } \xi_{ac}/\xi_{fr} > 1 \tag{4.25}$$

That is why inequality (4.19) could be considered as a hydrodynamic condition of DHT at developed turbulent flow in the tubes under weak influence of buoyancy.

The family of $l_b = f(q/G)_b$ (Fig. 4.20) was approximated with ±5% scattering by correlation

$$(q/G)_b = 0.04\,(l/d)^{-0.25}\cdot(h_m - h_{in})^{0.7}$$

(4.26)

where h_m and h_{in} are the enthalpies at the temperature of maximal specific isobaric thermal capacity c_{pm} and at water inlet temperature, respectively.

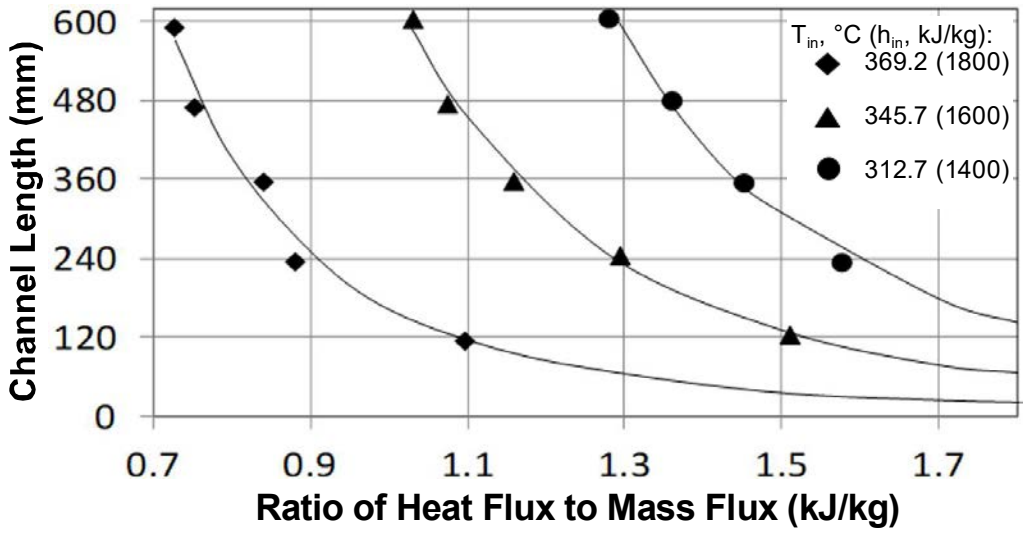

Fig. 4.21. Boundary heat flux rate vs. length of channel and inlet temperature (enthalpy).

The zones on the right side of the boundary lines in Fig. 4.21 correspond to the region of DHT. The heat flux rate for the initiation of DHT varies in a wide range of coolant average enthalpy (inlet enthalpy and relative heated length). For example, at the channel length of 600 mm ($L/D \approx 100$), $(q/G)_b$ changes from 0.7 to 1.3 kJ/kg, compared to $(q/G)_b \geq 0.6$ to 0.75 kJ/kg proposed in [4.46]. Similarly, the normal heat transfer regime is predicted at $q/G < 0.84$ kJ/kg with the correlation of Petuhkov et al. [4.47]

$$(q/G)_b \geq 3.4 \cdot 10^{-2} (c_p/\beta_p)_m \sqrt{\xi/8} \tag{4.27}$$

This correlation was proposed for water at P/P_c from 1.02 to 1.55, Re from 27000 to 380000, G from 400 to 1450 kg/(m^2·s), D from 6 to 20 mm and q from 0.29 to 1.75 MW. [4.47] assumed that DHT was attributed to decreasing turbulent exchange due to high density gradients. Yamagata et al. [4.6] proposed the correlation

$$(q/G)_b = 0.2 \cdot G_{av}^{0.2} \tag{4.28}$$

where G_{av} is the average mass flux the compiled database for SCW within the range from 310 to 1830 kg/(m^2·s) and pressures from 22.5 to 29.4 MPa. Gabarayev et al. [4.48] proposed the correlation for DHT limit as

$$(q/G)_b = 0.79(p/p_{cr})^{1.5} \tag{4.29}$$

which is valid for ranges of $(q/G)_b$ from 0.6 to 0.9 and from 0.81 to 1.21 kJ/kg, respectively. Based on the conditions of the NTUU experiments, the calculated boundary varied from 0.72 kJ/kg (h_{in} = 1800 kJ/kg, L/D = 95.6) to 1.57 kJ/kg (h_{in} = 1400 kJ/kg, L/D = 38.2). Grabyezhnaya and Kirillov

[4.49] recommended keeping this value even below 0.6 kJ/kg. Mokry et al. [4.50] proposed the correlation based on heat flux boundary

$$q_b = -58.97 + 0.745G \tag{4.30}$$

or $(q_b + 58.97)/G = 0.745$ kJ/kg.

Measurements of $\Delta P(l)$ by the method of two pressure drops allowed to get $\Delta P_{fr}(l)$, on the basis of which the coefficients of local full $\zeta(l)$, friction $\xi_{fr}(l)$ and acceleration $\xi_{ac}(l)$ resistances were predicted by Eq. (4.22) and are shown in Fig. 6.3.

Experiments and analytical studies (e.g., [4.51]) indicated that when h_b is near the enthalpy of the beginning of the zone of high specific isobaric heat capacity ($c_p > 8$ kJ/(kg·K); $1650 < h_b < 2750$ kJ/kg) and $T_w >> T_m$, correlation $\xi_{ac} >> \xi_{ac1}$ (ξ_{ac1} is ξ_{ac} corresponding to Eq. (4.22)) is of high probability, especially under the conditions of progressing DHT. At this stage in gas-like wall layer a significant portion of the input heat is detained. Due to great expansion work, this layer forces back flow solid core from the wall thus narrowing cross section for the main mass flow. This change results in a kind of gas nozzle that causes an abrupt acceleration of the solid core carrying the main share of flow momentum and quick growth of impulse factor, S_f, along the tube. That is followed by increasing both coefficient of inertia (acceleration) resistance, ξ_{ac}, and gradient $\partial P_{ac}/\partial(x/D)$ with corresponding consequences for turbulent transfer and heat transfer. Thus, the analysis of experimental data demonstrated that the deterioration of turbulent heat and mass transfer results from partial or complete 'laminarization' of flow in a tube caused by thermal expansion and acceleration of flow in the boundary area, deformation of velocity profiles and shear stresses in flow and finally by violation of turbulence generation.

Some studies (e.g., [4.6]) considered local heat transfer deterioration as the result of specific distribution of density and of other coolant properties in cross section due to location of T_m in the region of the boundary layer buffer zone ($T_b < T_m < T_w$). On the basis of this hypothesis even the recommendations, for example, in [4.52], on definition of the cross section, in which deterioration onsets, were proposed. However, verification of these recommendations by a wide array of experimental data did not confirm their efficiency and proved that occurrence of T_m in the buffer zone is necessary but absolutely insufficient for DHT, strongly depending upon heat flux rate q/G. Experimental data on deteriorated heat transfer showed that the main factor of turbulent heat transfer deterioration in tubes is not a certain specific distribution of thermophysical properties in flow cross section, but an effect of buoyancy and flow thermal acceleration [4.51].

The scattering of recommended values of $(q/G)_b$ is rather large. Undoubtedly, simple, unambiguous numerical correlation between boundary heat flux and mass flow rate could not exist in principal and a new, 'finer' method of $(q/G)_b$ prediction, taking into account long ago revealed flow laminarization under the impact of its thermal acceleration in the zone of pseudocritical state, should be developed. Equation (4.26) could be considered as the first attempt to involve the operating parameters and conditions, which determine coolant thermohydraulic state, in the prediction of DHT on the basis of the experimentally proved dependence of boundary heat flux rate $(q/G)_b$ upon inlet bulk enthalpy (temperature and pressure), heated length and diameter under developed turbulent upward flow and negligible effect of buoyancy in smooth round tubes and

annuli. Later on this equation has been modified into Eq. (5.12) to predict DHT onset in the 1-rod annular channel, 3 and 7 rod tight bundles.

DHT is not so dangerous by a high level of channel wall temperature, as by its strong dependence upon even negligible change in operating conditions that negatively impacts on reliability of heated surface, though usually in this case T_w is by a few hundred degrees below the temperature permissible by long term strength conditions, i.e., is far from the level of extreme temperatures that in some works resulted in wall burnout..

Wall temperatures along the channel as a function of heat flux rate are illustrated in Fig. 4.22 for h_{in} = 1800 kJ/kg (i.e., T_{in} = 368 ºC). High local wall temperatures, T_w, corresponding to the DHT regime were not observed. Temperature differences between wall and bulk fluid (i.e., $T_w - T_b$) are shown in Fig. 4.23 for all five heated lengths at h_{in} = 1400 kJ/kg (i.e., T_{in} = 313 ºC). These temperature differences at various locations did not exceed 10 to 15 K, which are acceptable at wall temperatures of 500 to 600 ºC, taking into account a real mismatch of operation conditions (h_{in} and q/G) under different heated lengths. At low heat fluxes and $T_w > T_m$ the temperature difference increases moderately. The $T(l)$ behavior is similar to that for boiling at subcritical pressures and corresponded to enhanced heat transfer, by 1.5 to 2 times exceeding the normal one. These figures demonstrate that at a certain high mass flow rate (G = 2193 kg/(m^2·s) and $Re > 1.5\times10^5$) the entrance section, where thermal boundary layer is formed, becomes short enough and does not impact on the temperature profile along the tube (i.e., at any point T_w does not depend upon the heated length of the tube).

Briefly summarizing the obtained data on heated channel friction and acceleration resistances it is proposed to apply a conditional division of the whole range of SCW thermal state into four zones of (*A*) viscous, (*B*) viscous inertial, (*C*) inertial viscous and (*D*) gas like flow with different behaviors of full pressure drop components. In particular, in Zone A of low enthalpies ($h_b \le 650$ kJ/kg) friction coefficient ξ_{fr} follows correlation reflecting strong dependence of viscosity upon coolant enthalpy [4.53].

In Zone B of viscous inertial flow with liquid phase ($650 \le h_b \le 1500$ kJ/kg) and in Zone *D* of the enthalpies of gaseous phase ($h_b \ge 2550$ kJ/kg) the data array for friction factors in tubes of D = 3÷10 mm at $q/G > 0.5$ kJ/kg was generalized with a scatter within ± 20% using Eq. (6.7).

In the intermediate Zone C of inertial viscous flow in transition from liquid to gaseous state (in the zone of high specific heat capacities ($c_p > 8$ kJ/(kg·K)), where thermal acceleration of flow plays a dominant role in hydraulic resistance and one dimensional model of thermal acceleration could cause substantial errors ($\xi_{fr}/\xi_0 > 1$), the best results in HTC prediction gives the following system of two interdependent iterative equations for ξ_{fr} and Nu:

$$\xi_{fr} = \xi_0 \cdot \left(\frac{\mu_w}{\mu_b}\right)^{0.15} \cdot \left(\frac{\rho_w}{\rho_b}\right)^{0.1} \tag{4.31}$$

and

$$Nu = 0.81 \cdot Nu_{fr} \cdot \left(\frac{\bar{c}_p}{c_{p_f}}\right)^{0.63} \tag{4.32}$$

where Nu_{fr} is Nu_0 from Eq. (4.11), in which ξ_0 from Eq. (4.12) is substituted by ξ_{fr} from Eq. (4.31).

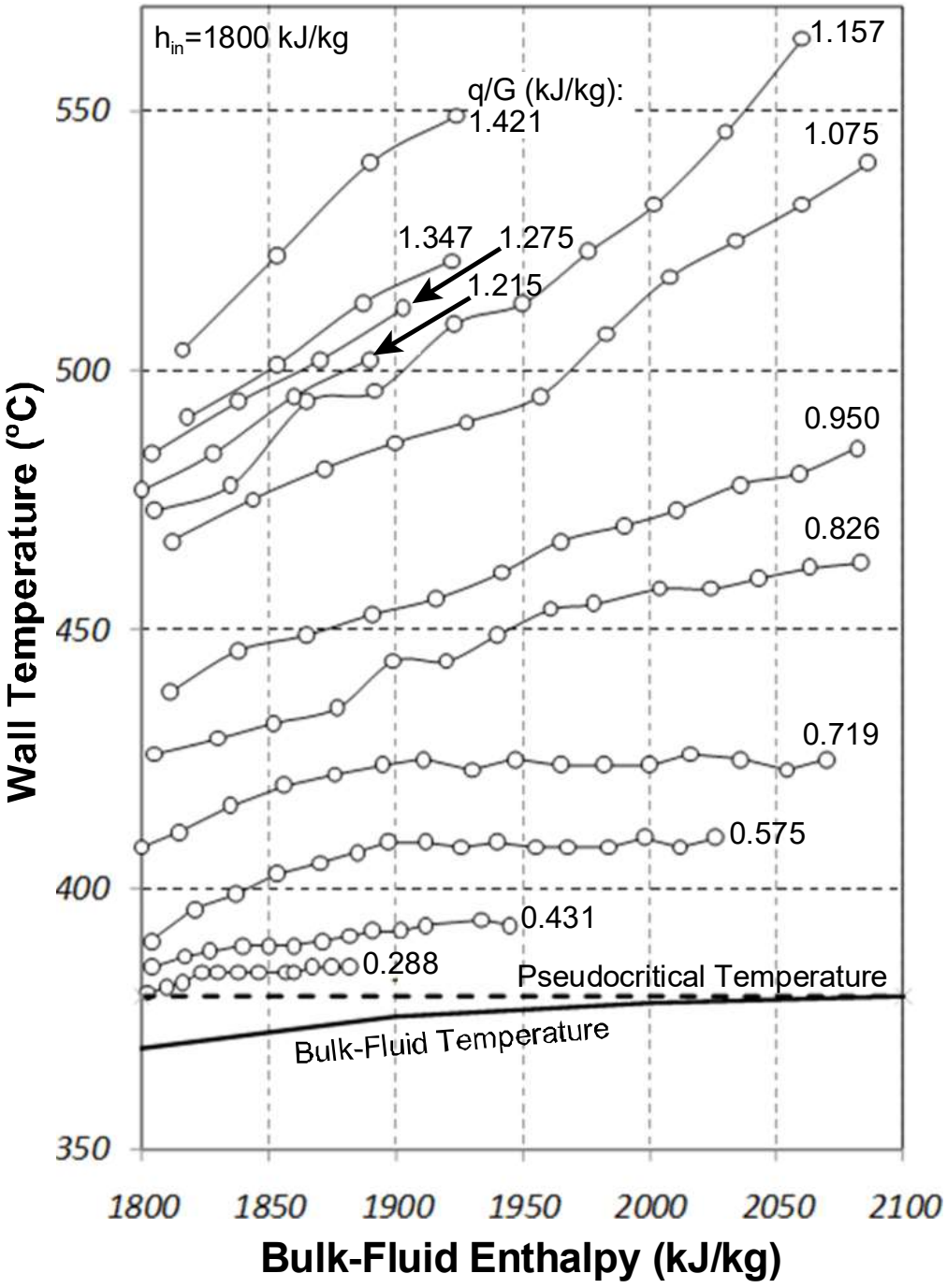

Fig. 4.22. Dependence of wall temperature upon heat flux rate.

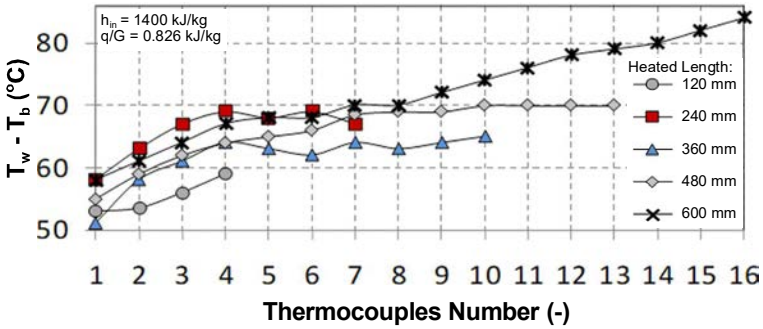

(a)

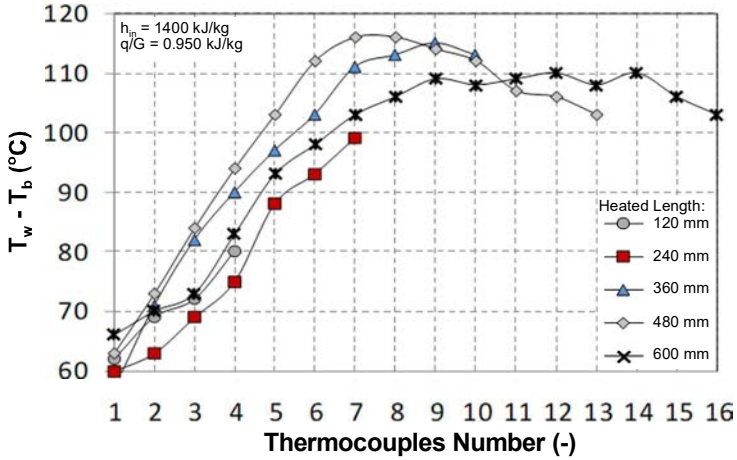

(b)

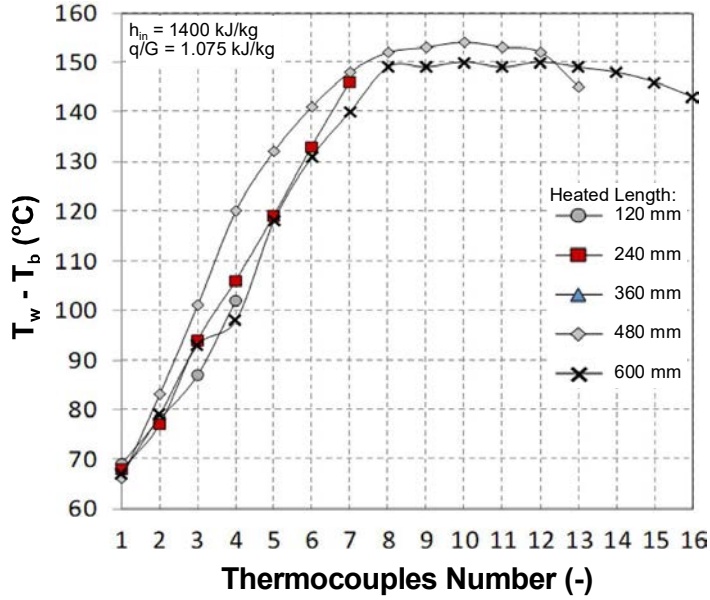

(c)

Fig. 4.23. Temperature head along the tube vs. heat flux rate.

The system of Eq. (4.31) and Eq. (4.32), derived with NTUU data for tubes, annular channels, and 3 and 7-rod bundles (see Section 5.6.5), has been verified against another set of data obtained with a 4 m long tube [4.54]. Its prediction accuracy has been compared against those of several correlations for SCW heat transfer (see Fig. 4.24). The NTUU system of two correlations agrees closely with the experimental data.

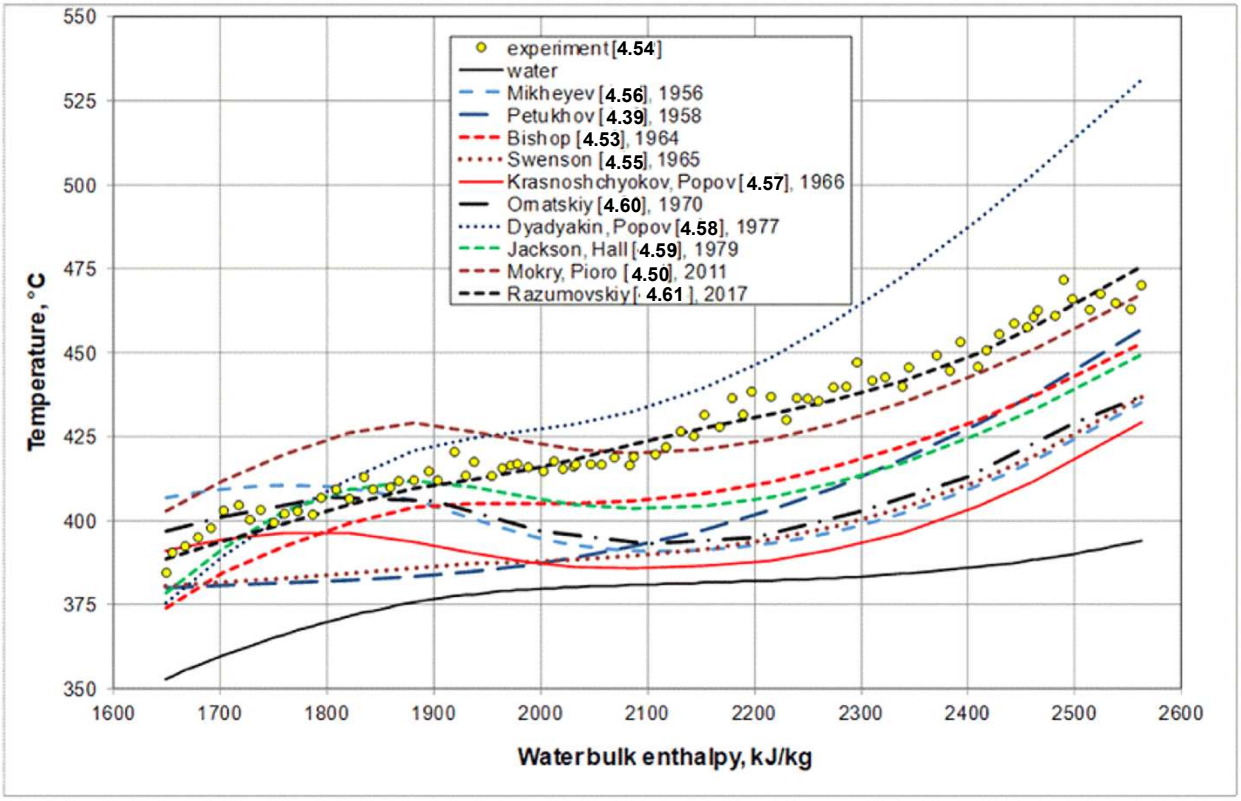

Fig. 4.24. Comparison of predictions of various correlations against experimental temperature profiles [4.54].

Table 4.20 lists mean prediction errors, δ, and standard (RMS) deviations, σ, of Nusselt numbers obtained with the 6.28 mm ID tube in upward and downward flows for various heat transfer correlations. The total number of data, n, applied in the calculation differs in each case, which is attributed to the non convergent in the iteration. The best prediction accuracy has been shown using correlations of Krasnoshchyokov–Protopopov [4.57], Razumovskiy [4.61] (i.e., Eq. (4.31) and Eq. (4.32)), and Dyadyakin–Popov [4.58].

Fig. 4.25 compares calculated and experimental Nusselt numbers for four correlations that have the best prediction accuracy. The correlation of Dyadyakin–Popov [4.58] predicts, on average, closely data for both upward and downward flow (i.e., with little bias). However, the scatter among predictions is quite large. Correlations of Krasnoshchyokov–Protopopov [4.57] and NTUU agree with the downward flow data (attributed as *T* (*DF*) Tube (Down Flow)). The correlation of Bishop et al. [4.53] predicts the upward flow data with little scatter but a bias of about +25 %. The Jackson–Hall correlation [4.59] well enough approximated the downflow data, however the

upflow heat transfer was overestimated with an unacceptable scattering sometimes exceeding even 100%. Correlations of Mikheyev [4.56], Swenson [4.55], Petukhov [4.39] and Ornatskiy [4.60] provide similar prediction accuracy to each other for the upward flow data (biases from about 60 to 200 %) and downward flow data (within ± 25 %). The correlation of Mokry et al. [4.50] underpredicts these data of 38 % but relatively little scatter.

TABLE 4.20. COMPARISON OF PREDICTION ACCURACY OF HEAT TRANSFER CORRELATIONS.

References	*n*	*δ*, %	*σ*, %	Percentage of data within error range				
				±10%	±20%	±30%	±40%	±50%
Krasnoshchyokov–Protopopov [4.57]	420	6.7	41.2	31.9	59.7	78.3	87.4	90.7
Razumovskiy [4.61]	402	6.7	24.5	30.3	59.0	74.1	86.3	95.8
Dyadyakin–Popov [4.58]	402	1.6	53.9	29.6	56.7	76.1	85.3	89.3
Ornatskiy [4.60]	420	59.2	126	21.9	37.6	51.2	61.4	68.1
Mikheyev [4.56]	392	73.2	199	16.2	32.6	46.9	58.2	67.9
Bishop [4.53]	402	27.0	33.9	20.6	43.8	60.9	78.4	86.3
Swenson [4.55]	365	200	242	17.0	30.4	39.4	42.5	44.7
Jackson–Hall [4.59]	359	31.7	47.5	20.6	41.5	53.5	66.8	75.8
Petukhov [4.39]	373	112	124	19.3	31.4	39.4	41.8	45.8
Mokry [4.50]	392	-38	25.0	13.8	25.8	38.5	49.2	62.2

4.3.5. HEAT TRANSFER TO SCW IN A GAS LIKE STATE

At the temperature higher than temperature of the minimal dynamic viscosity, T_{min}, which is about 409 ºC at the pressure of 23.5 MPa (see Fig. 4.26), the viscosity increases with temperature. This would lead to increase in both the boundary layer shear stress and the channel friction resistance. In turn, partial laminarization of the boundary layer would occur making it thicker and increasing the temperature head $\Delta T = T_w - T_b$. Fig. 4.26 shows internal wall temperature profiles along the heated section of the 6.28 mm ID tube with upward flow of supercritical water at such specific flow conditions.

It is known that the ratio Gr/Re^2 is used to estimate the effect of free convection. Usually, within a range of $Gr/Re^2 = 0.01 \div 0.6$ free convection decreases or increases the heat transfer coefficient (HTC) of upward or downward flow, respectively. In [4.59] heat transfer data were obtained at 23.5 MPa, two mass fluxes of 250 and 500 kg/(m^2·s), heat fluxes up to 515 kW/m^2 and inlet temperatures from 20 to 380 ºC, i.e., within the range of significant effect of mixed convection, where $Gr/Re^2 \approx 0.1 \div 0.5$ (the smallest value of this parameter corresponds to the lowest level of heat flux). Three modes of heat transfer have been observed: normal, improved and deteriorated. The latter entrance peaks, i.e. the deteriorated heat transfer regimes, are dangerous for heated surfaces, if a coolant flow rate is low, since within the peak vicinity the wall temperature could heavily fluctuate even at small variations of the operating parameters. At Gr/Re^2 value of about 0.5, the deteriorated heat transfer or peak (hump) in the wall temperature appeared along the outlet section of the channel. With heat flux increase these peaks moved towards the channel entrance.

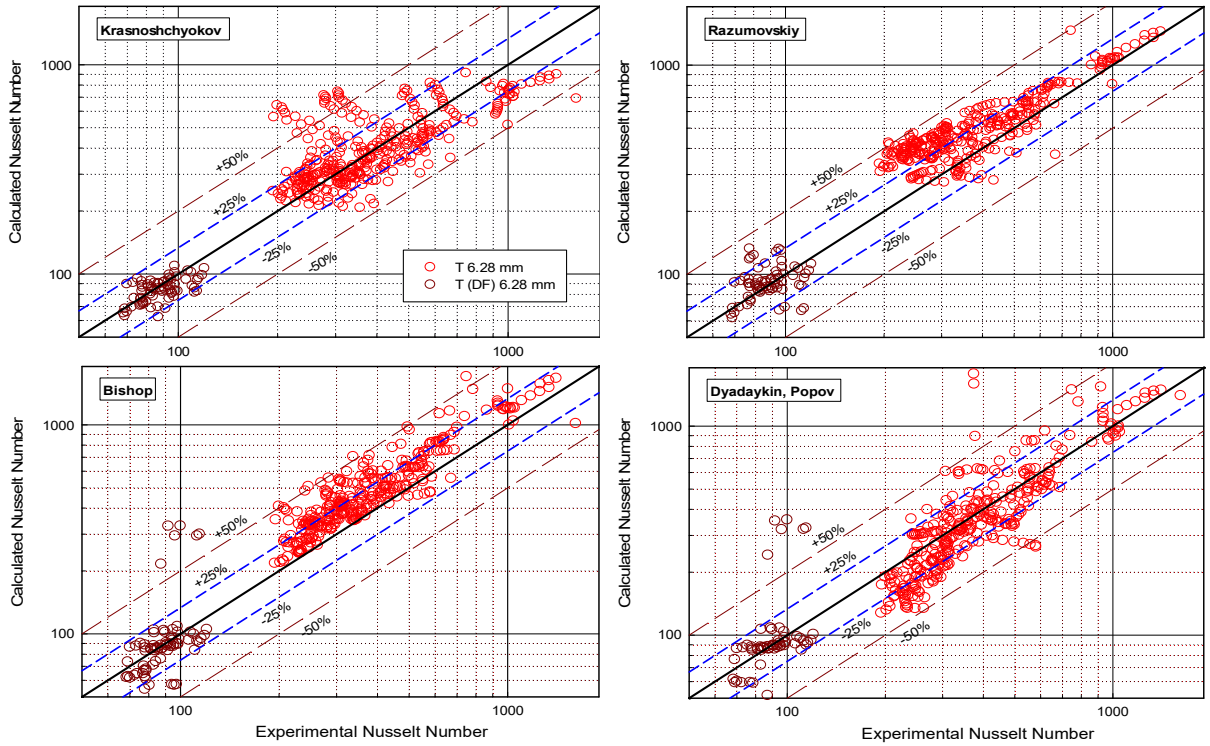

Fig. 4.25. Comparison of experimental and calculated Nusselt numbers for four correlations with the best prediction accuracy.

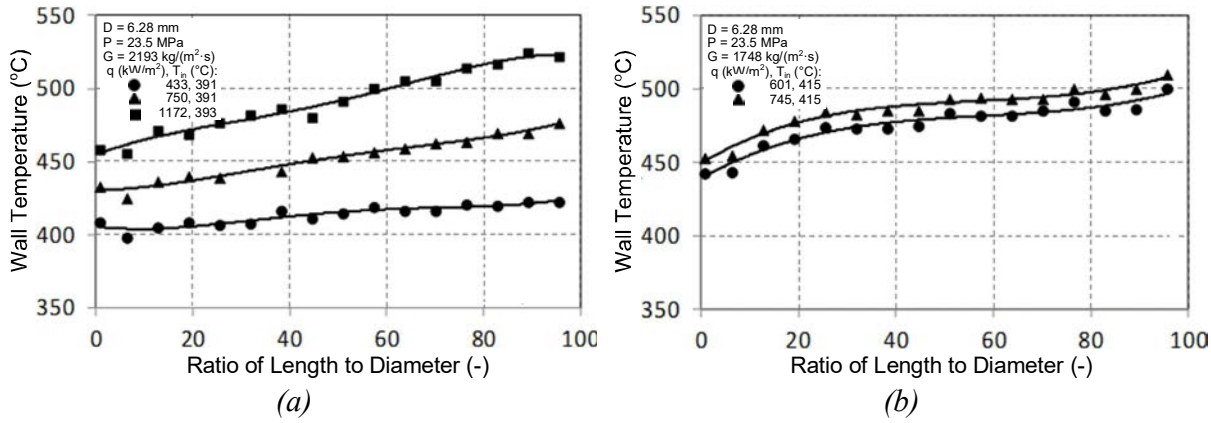

Fig. 4.26. Temperature profiles at supercritical water upward flow inside vertical tube heated beyond pseudocritical temperature.

4.3.6. COMPARISON OF THE CONDITIONS OF TOP AND DHT

Significant flow free convection and thermal acceleration resulting either in enhancement or deterioration of heat transfer under certain conditions, the most general of which is $T_w > T_m > T_b$, often coincide with onset of thermoacoustic instability (periodic oscillation with frequencies in acoustic range of up to 0.5 kHz) of pressure, temperatures of flow and wall. According to some

authors under the pressure of 24.5 MPa the amplitude of such oscillations could reach 2.5 MPa. Despite great importance of the problem of thermoacoustic oscillations of pressure (TOP) the phenomena is very weakly examined generally and in annular channels under supercritical pressure of water in particular. In previous works, e.g., [4.60], it was found that amplitude of the oscillations depends upon the ratio of input energy and its dissipation, while their frequency depends upon fluid elastic properties and channel geometry. The main objective of the study was to define the area of TOP existence in circular and annular cross section channels and the effect of inside and outside heating of vertical annular channel under upward flow of SCW and the following operating parameters on TOP occurrence: pressure P = 23.5 MPa and 27.5 MPa; mass velocity G = 500 to 3000 kg/(m^2·s); inlet temperature T_{in} = 20 to 379 ºC; heat flux $q \leq 4$ MW/m^2. The channels: (a) tubes of ID = 4.4 and 3.3 mm with heating length L_h = 960, 535 and 255 mm; (b) annular channel III (D_2/D_1 = 10 × 6 mm (2 mm annular gap) with L_h = 300 mm. The oscillations of 100 to 500 Hz took place. Their amplitude went through its maximum vs. heat flux and this maximum decreased, as T_{in} increased (Fig. 4.27a).

Side of heating (inner or outer) weakly affected the amplitude, but the area of TOP existence under heating inner side of the annular channel goes to higher heat fluxes. The experimental results convincingly demonstrate that lower frequency limit of TOP occurs at q/G significantly (by 2 to 3 times) below $(q/G)_b$. In the annular channel the upper frequency limit was not reached even at the maximal allowable wall temperature of 640 ºC. Due to the same reason at G > 1000 kg/(m^2·s) TOP was not generated either at outer or inner side of the channel at all. Dependence of the frequencies upon operating conditions was general for both tubes and annular channel: they decreased as heat flux or inlet temperature become higher that probably was connected with decreasing speed of acoustic wave propagation.

It was a methodological feature of the tests to reproduce their conditions (G, q, T_{in}) excluding possibility of the TOP due to connection of additional reservoirs (impulse tubes with differential manometer), which sharply changed acoustic characteristics of the channel without violation of coolant's hydrodynamics. Comparison of heat transfer regimes with and without TOPs shows that they induce local enhancement of heat transfer or do not change it depending upon the cross section coordinate along the channel. Sometimes thereby temperature profile $T_w(l)$ is strongly deformed creating visual similarity with the profile for deteriorated heat transfer.

Qualitative interconnection of TOP with thermohydraulic conditions in the channel is reflected in Fig. 4.27, where HTC and pressure drop (see Section 5, Fig. 5.5) between inlet and outlet chambers were compared with calculated α_c and ΔP_c. Averaged T_b and T_b were used. The α_c was predicted by Eq. (4.11) corrected by expression taking into account annular configuration of the channel:

$$Nu_2 = Nu_0\left[1 - \frac{0.45}{2.4 + Pr\left(\frac{d_1}{d_2}\right)^{0,6}}\right] \tag{4.33}$$

where indices '1' and '2' imply inside and outside surfaces of the annular channel, respectively. As seen, reduced HTC α/α_c grows with increasing amplitude of oscillations, while maximal value

of it does not exceed 50 to 60 % following increase in T_{in}. Reduced hydraulic resistance $\Delta P/\Delta P_c$ mostly is changed in an opposite side. Some regimes with modulated TOP, probably due to simultaneous oscillations at several neighboring frequencies, were observed. In this case, synchronously oscillated pressure drop with the amplitude shown in Fig. 6.5 (see Section 6) took place. It follows from the above that TOP is a multifactor, complicated and insufficiently studied phenomenon, until now very ambiguous in its quantitative and qualitative analysis.

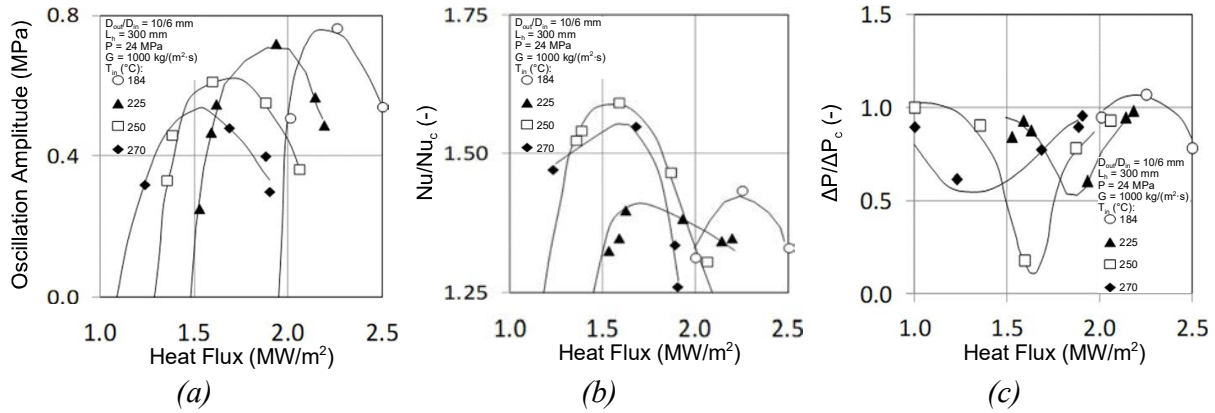

Fig. 4.27. Variations of (a) oscillation amplitude, (b) reduced heat transfer and (c) reduced hydraulic resistance with heat flux in an annular channel.

Considered in Section 4.3 problems of heat transfer in tubes and annular channels cooled by supercritical water at the conditions close to those in SCWR covered the items vital for understanding the variety of the phenomena that take place in the channels of simple geometry and could be encountered in fuel assemblies. In particular, mixed convection could play not the last role in heat transfer at downward flow of water in a probable SCWR with two way circulation scheme. Study of entrance effect can be useful as additional information on mechanism of formation and behavior of thermal boundary layer, sometimes causing high local thermal gradients. But the key problem of DHT draws the main attention and requires solving one day. It seems that at this stage a certain positive result in finding the way of solution has been achieved in both correct estimation of heat transfer and prediction of boundary heat flux rate. Analysis of the experimental data obtained in NTUU, based on them system of two iterative correlations for heat transfer and pressure drop effective under their joint solution gave the possibility to assess wide spectrum of existing empiric equations and recommendations for *Nu* and ΔP in order to propose the best of them for further application. Of course, still important is the problem of thermoacoustic oscillation of pressure even in tubes and annular channels and it deserves profound study.

4.3.7. WATER FLOW OVER ANNULI

An experiment was performed at the Xi'an Jiaotong University (XJTU) to obtain heat transfer data with water flowing in annuli at supercritical pressures [4.62]. It was carried out in the supercritical pressure test facility as shown in Fig. 4.28.

Two test sections were constructed, each consisted of an internal heated tube and an external unheated shroud, which acted as the pressure boundary. The internal heated tube was a stainless

steel (SS304) tube with an outer diameter of 8 mm and a wall thickness of 1.5 mm and was heated electrically over a length of 1400 mm. Two external unheated shrouds were constructed from stainless steel (SS304) tubes, one with an outer diameter of 20 mm and a wall thickness of 2 mm and the other with an outer diameter of 25 mm and a wall thickness of 2.5 mm. In another words, two gap sizes (4 mm and 6 mm, respectively) or hydraulic diameters (8 mm and 12 mm, respectively) were covered in the experiment. Fig. 4.29 shows the test section setup schematically. Details are provided in the [4.62].

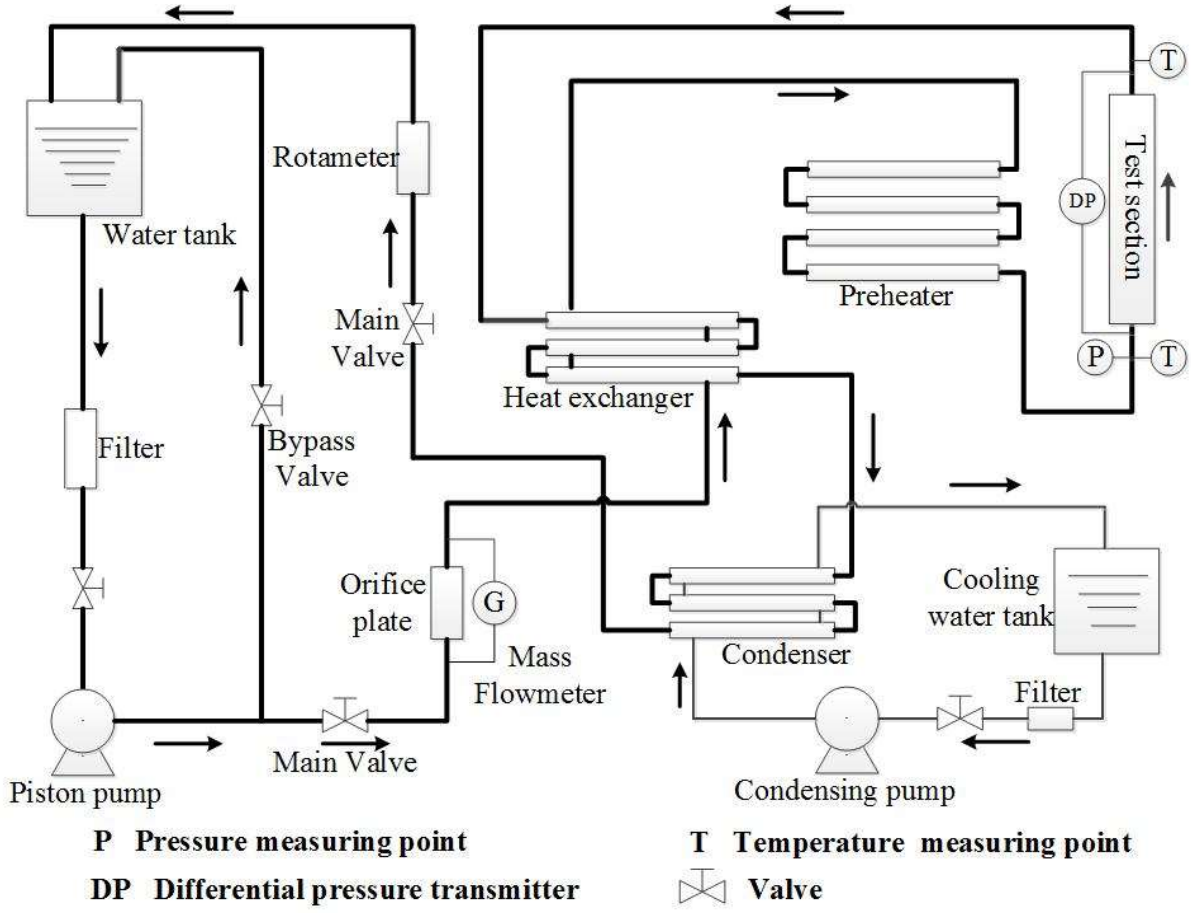

Fig. 4.28. Schematic diagram of the supercritical pressure water test facility.

Six spring loaded thermocouples were installed inside the heated central tube at locations shown in Fig. 4.30. Measurements on inlet pressure, pressure drop over the test section, fluid temperatures at the inlet and outlet of the test section, mass flow rate and power were obtained. Overall, the experiment covered ranges of pressures from 23 MPa to 28 MPa, mass fluxes from 350 to 1000 kg/(m^2.s) and heat fluxes up to 1.0 MW/m^2.

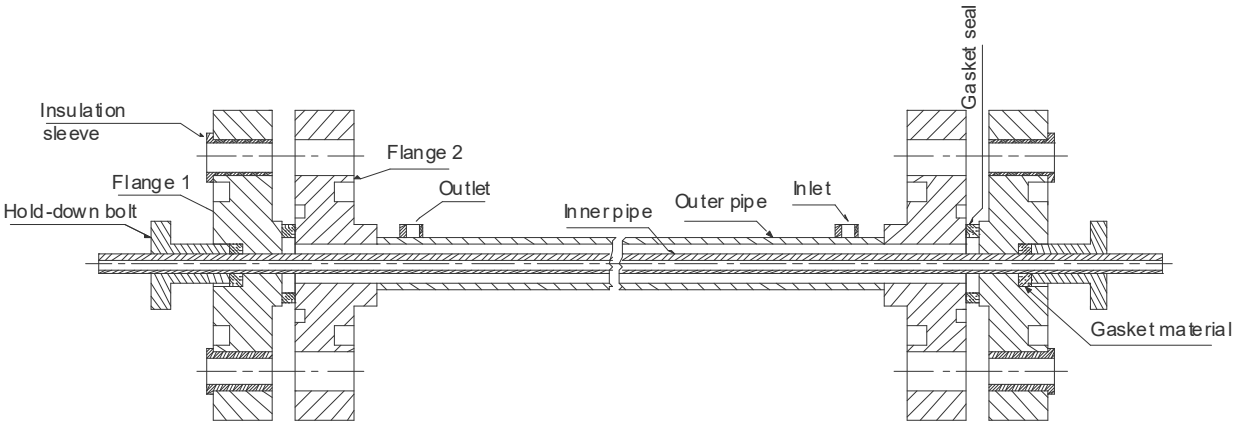

Fig. 4.29. Test Section Setup for supercritical heat transfer test.

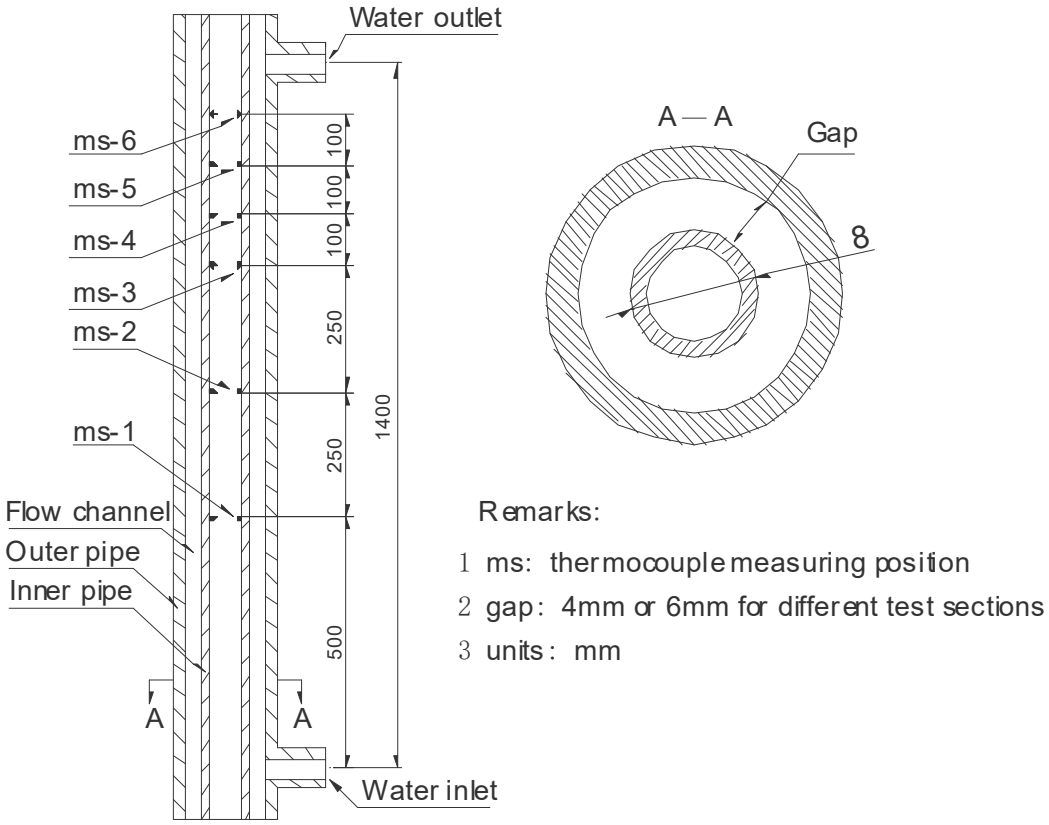

Fig. 4.30. Location of Thermocouples inside the central heated tube.

Fig. 4.31 illustrates the wall temperature variations along the heated length at subcooled (275 ºC), near pseudocritical (365 ºC) and supercritical (410 ºC) inlet fluid temperatures for the test section with a 4 mm gap. A gradual increase in wall temperature has been observed along the heated length; this represents the normal heat transfer mode.

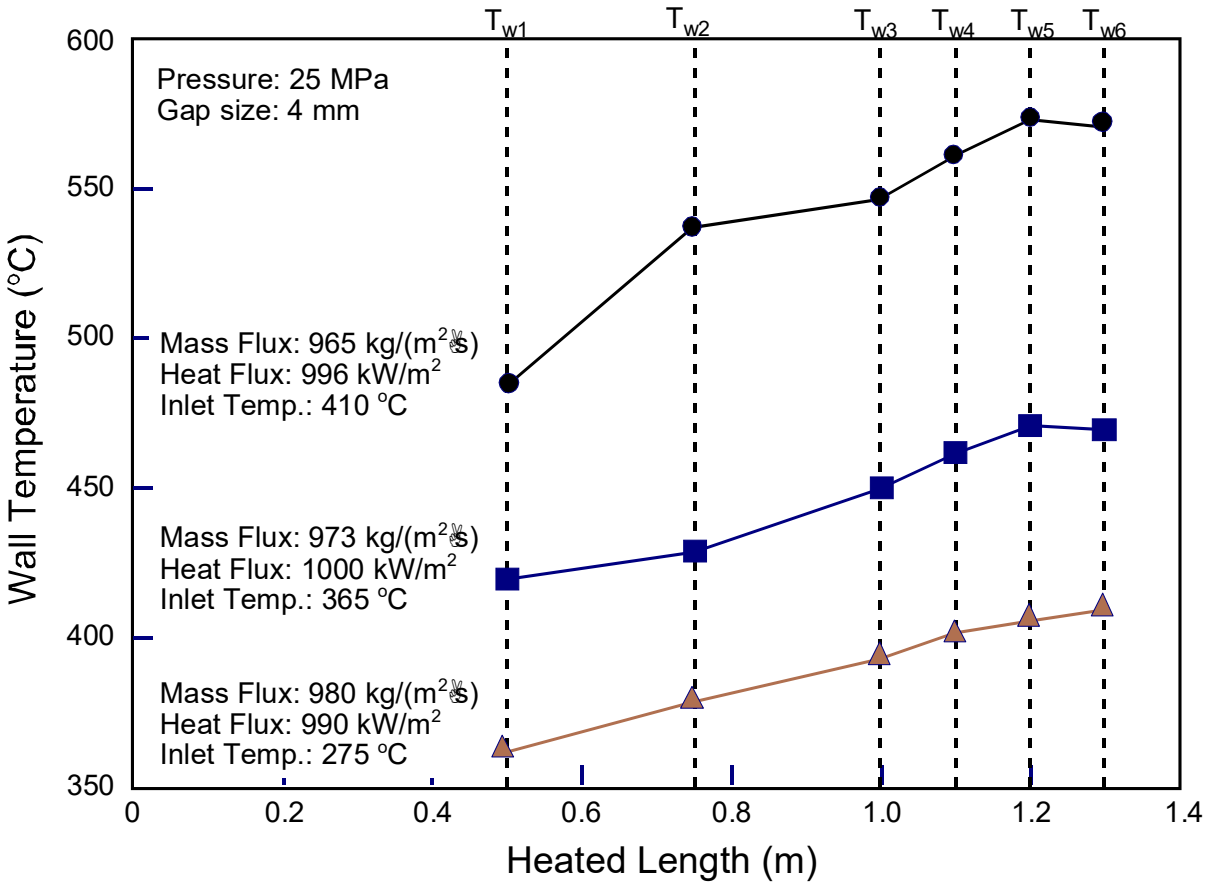

Fig. 4.31. Wall temperature distributions along heated length under normal heat transfer mode.

Fig. 4.32 illustrates cases for high heat fluxes and low mass fluxes for test sections with gap sizes of 6 and 4 mm. A sharp increase in wall temperature is shown at the second thermocouples location, followed by a sharp decrease at the downstream thermocouples. This corresponds to the deterioration heat transfer mode. Similar observations were made at other flow conditions for both test sections.

Fig. 4.33 illustrates variations of wall temperature and heat transfer coefficient with bulk fluid enthalpy and heat flux for the test section with a 4 mm gap. The wall temperature increases with increasing bulk fluid enthalpy and heat flux. This increasing trend levels off at the vicinity of the pseudocritical enthalpy, compared to other enthalpy ranges, at low heat fluxes but remains high at the heat flux of 1000 kW/m^2. Corresponding heat transfer coefficients are also shown with enthalpy and heat flux.

The heat transfer coefficient decreases with increasing heat flux. It increases before the pseudocritical enthalpy but decreases beyond the pseudocritical enthalpy with increasing enthalpy at low heat fluxes. At the heat flux of 1000 kW/m^2, however, there is no sharp variation in heat transfer coefficient but a gradual change with a local peak at the enthalpy well before the pseudocritical point.

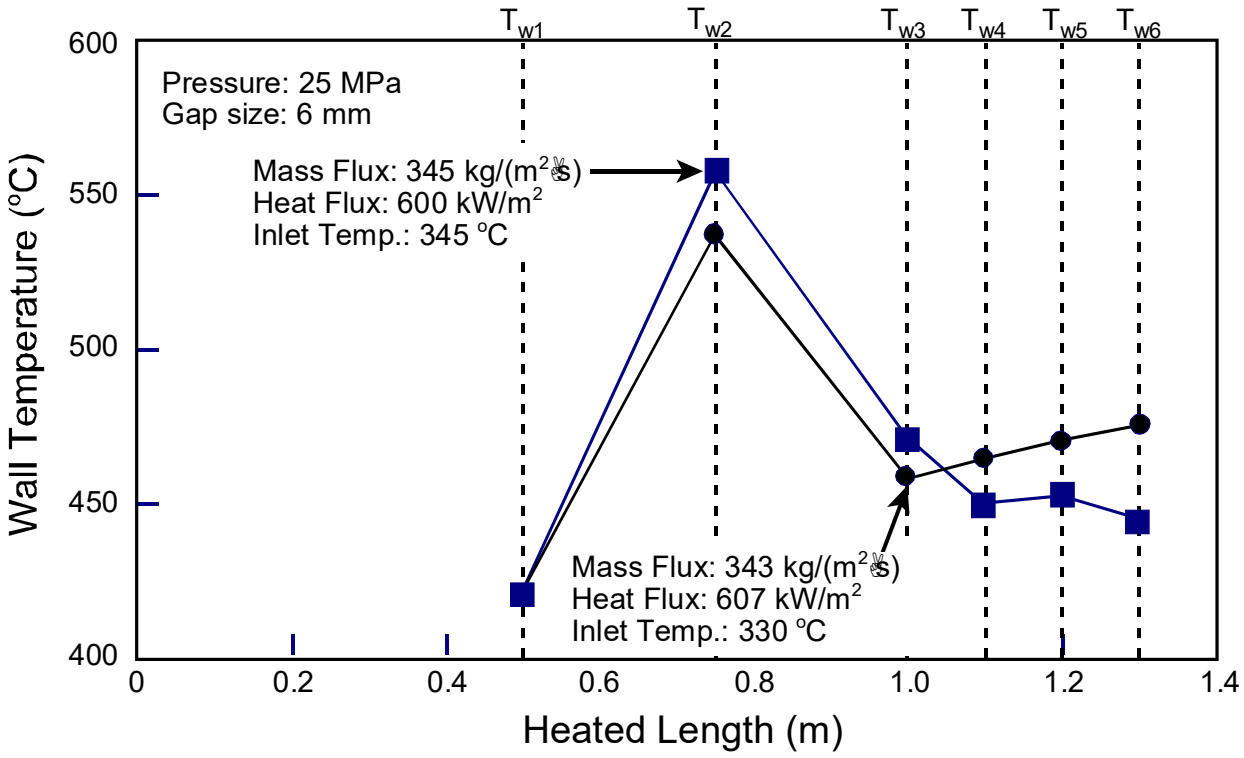

Fig. 4.32. Wall temperature distributions along heated length for deteriorated heat transfer mode.

Fig. 4.34 illustrates variations of wall temperature and heat transfer coefficient with bulk fluid enthalpy and mass flux for the test section with a 6 mm gap. The wall temperature increases with increasing bulk fluid enthalpy but decreases with increasing mass flux. This increasing trend levels off at the vicinity of the pseudocritical enthalpy, compared to other enthalpy ranges, at high mass fluxes but varies sharply at the mass flux of 350 kg/m^{2}s.

The wall temperature exhibits a peak when approaching the pseudocritical enthalpy and a local minimum after the pseudocritical enthalpy (about 2400 kJ/kg). Corresponding heat transfer coefficients are also shown with enthalpy and mass flux. The heat transfer coefficient increases with increasing mass flux. At the mass flux of 350 kg/m^{2}s, however, the heat transfer coefficient decreases with enthalpy when approaching the pseudocritical point and increases slightly after the pseudocritical poInt.

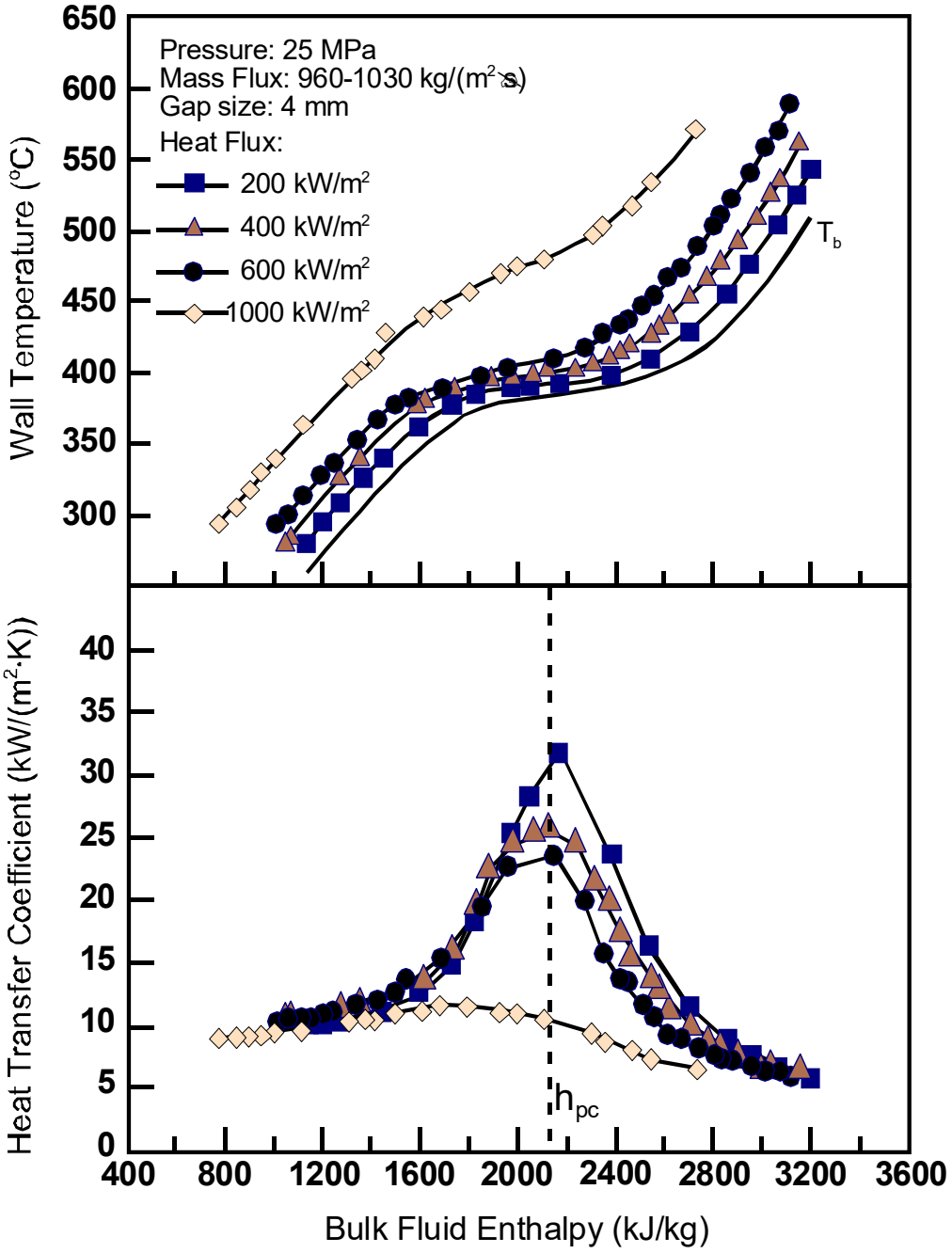

Fig. 4.33. Variations of wall temperatures and heat transfer coefficients with enthalpy and heat flux.

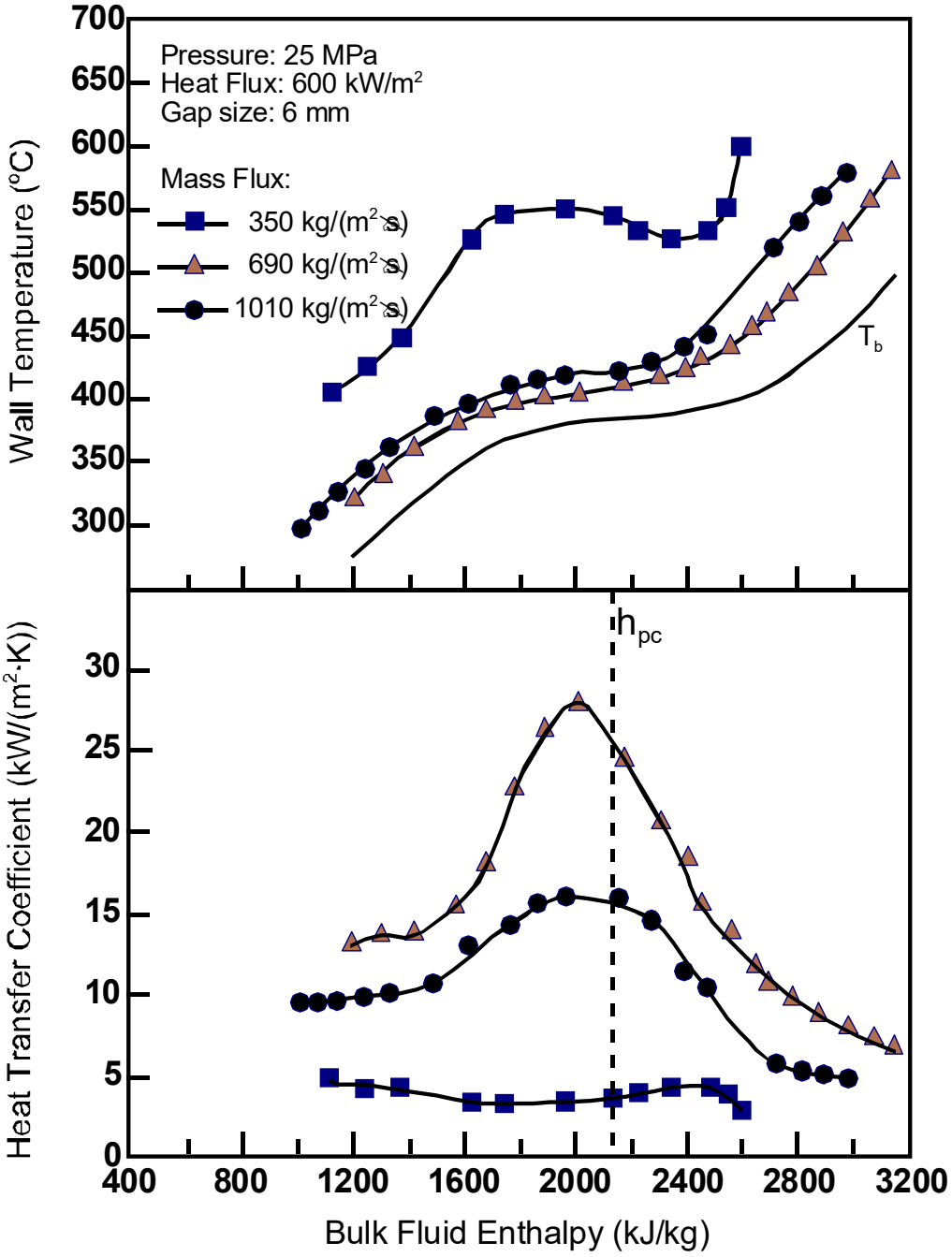

Fig. 4.34. Variations of wall temperatures and heat transfer coefficients with enthalpy and mass flux.

Fig. 4.35 compares heat transfer coefficients for test sections with 4 and 6 mm gaps at two different flow conditions. The heat transfer coefficient increases with increasing gap size at small ratios of heat flux to mass flux for normal heat transfer mode. Differences in heat transfer coefficient become small at large ratios of heat flux to mass flux but slightly higher heat transfer coefficient remains for the 6 mm gap then the 4 mm gap.

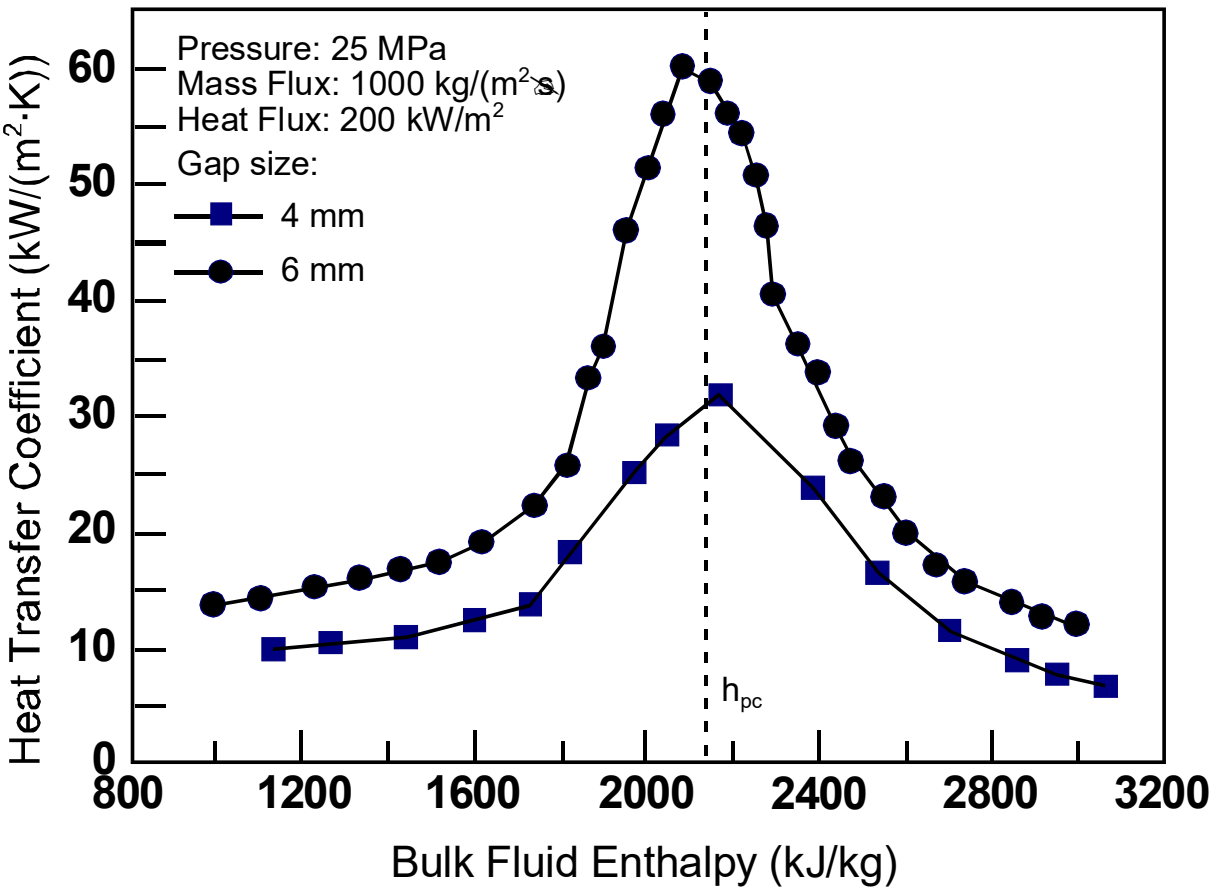

Fig. 4.35. Effect of gap size on heat transfer coefficient.

4.4. CORRELATION AND SCALING

4.4.1. FLUID–TO–FLUID MODELLING

In some cases, when modeling fluid (usually carbon dioxide, Freons, etc.) is used instead of a primary coolant (usually water) it is important to scale properly the equivalent conditions of the primary coolant to the equivalent conditions of the modeling fluid. Therefore, fluid-to-fluid modeling techniques or scaling laws should be used [4.10].

Jackson and Hall [4.59] proposed 12 nondimensional groups to satisfy the complete requirements for similarity between two systems, A and B, at supercritical pressures. However, they stated that it is unlikely all these similarities can be satisfied. Nevertheless, the basic similarities listed in Table 4.21 can be used for fluid-to-fluid modelling at supercritical conditions.

TABLE 4.21. BASIC SIMILARITIES FOR FLUID-TO-FLUID MODELING AT SUPERCRITICAL CONDITIONS BASED ON INLET CONDITIONS APPROACH.

Similarity criteria	**Equation**	
Geometric similarity	$D_A=D_B$ and (or) $(L_h)_A=(L_h)_B$	(1a)
Geometric similarity (optional)	$\left(\frac{x}{D}\right)_A = \left(\frac{x}{D}\right)_B$	(1b)
Pressure (based on reduced pressure (P_r) approach (thermodynamics scaling))	$\left(\frac{p}{p_{cr}}\right)_A = \left(\frac{p}{p_{cr}}\right)_B$	(2)
Bulk fluid temperature (all temperatures in K) (based on reduced temperature (T_r) approach (thermodynamics scaling))	$\left(\frac{T_b}{T_{cr}}\right)_A = \left(\frac{T_b}{T_{cr}}\right)_B$	(3a)
Bulk fluid temperature (all temperatures in K) (optional thermodynamics scaling) [4.63]	$\left(\frac{T_b}{T_{pc}}\right)_A = \left(\frac{T_b}{T_{pc}}\right)_B$	(3b)
Bulk fluid temperature (based on densities ratios) (optional scaling)	$\left(\frac{\rho_b}{\rho_{cr}}\right)_{at\ T_b\ A} = \left(\frac{\rho_b}{\rho_{cr}}\right)_{at\ T_b\ B}$	(3c)
Heat flux or wall superheat (all temperatures in K)	$\left(\frac{q\ D}{k_b\ T_b}\right)_A = \left(\frac{q\ D}{k_b\ T_b}\right)_B$ or $\left(\frac{T_w - T_b}{T_{cr}}\right)_A = \left(\frac{T_w - T_b}{T_{cr}}\right)_B$	(4) (5)
Mass flux (based on Reynolds number approach)	$Re_A=Re_B$ $\left(\frac{G\ D}{\mu_b}\right)_A = \left(\frac{G\ D}{\mu_b}\right)_B$	(6) (7)
HTC (based on Nusselt number approach)	$Nu_A = Nu_B$	(8)

Gorban et al. [4.64] developed a fluid-to-fluid modelling technique for supercritical pressures to scale water equivalent conditions into Freon–12 equivalent conditions and vice versa.

Fig. 4.36 to Fig. 4.41 compares selected thermophysical properties of water, carbon dioxide, and R-134a based on reduced temperatures.

Thermophysical properties profiles show similar trends for all three mentioned above fluids, which might coincide within certain ranges of reduced temperature (e.g., density and dynamic viscosity profiles for carbon dioxide and R-134 at $T_r > 1$; thermal conductivity, specific heat, and specific enthalpy profiles for carbon dioxide and R-134 at $T_r > 1.1$; Prandtl number for all three fluids at $T_r > 1.2$).

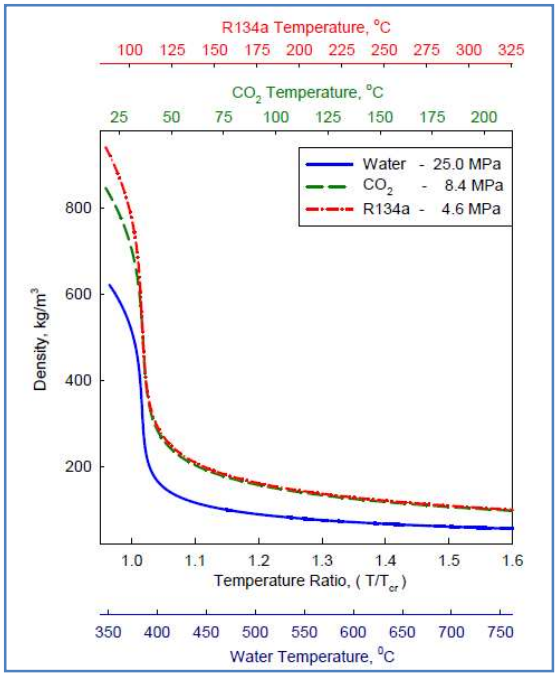

Fig. 4.36. Density vs. Temperature Ratio for water, CO_2 and R134a [4.65].

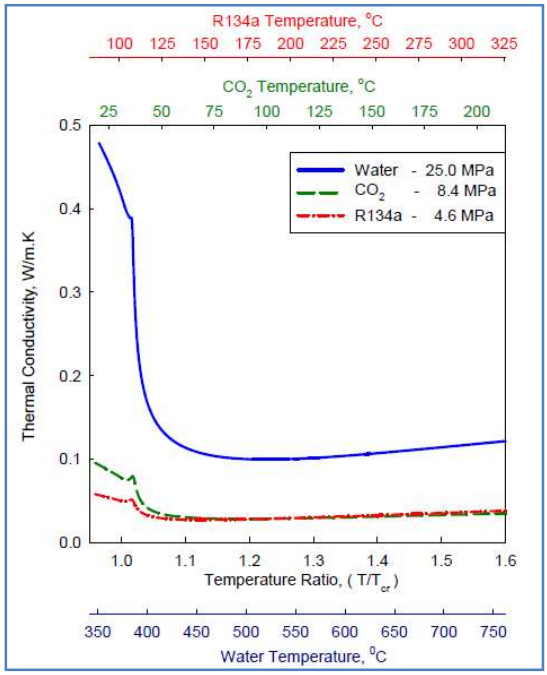

Fig. 4.37. Thermal Conductivity vs. Temperature Ratio for water, CO_2 and R134a [4.65].

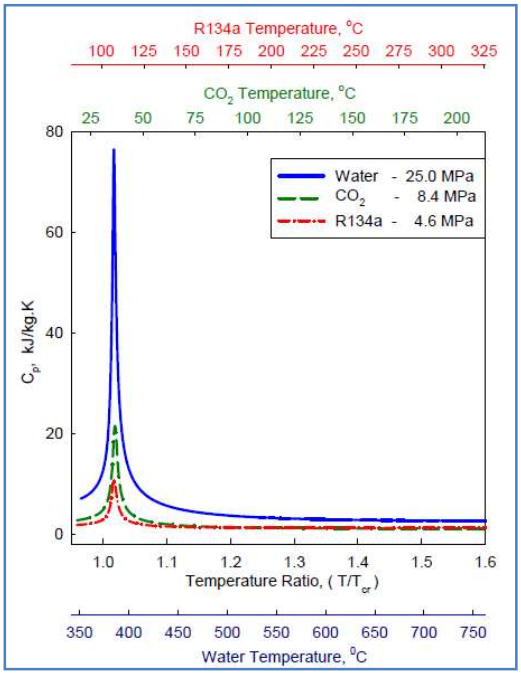

Fig. 4.38. Specific Heat vs. Temperature Ratio for water, CO_2 and R134a [4.65].

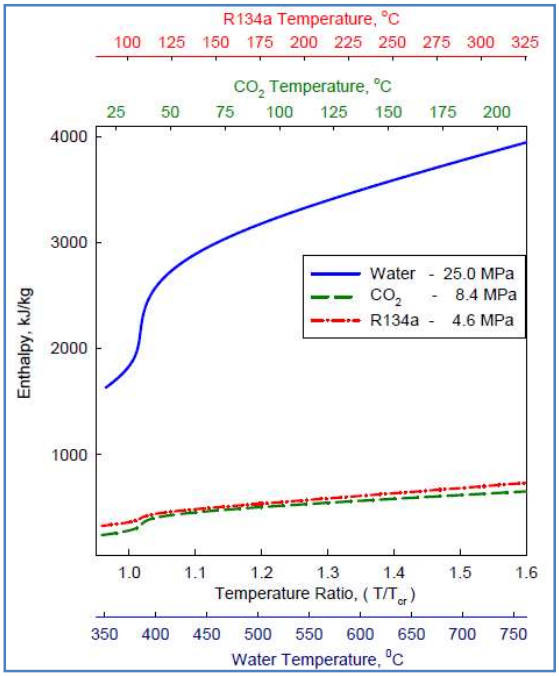

Fig. 4.39. Enthalpy vs. Temperature Ratio for water, CO_2 and R134a [4.65].

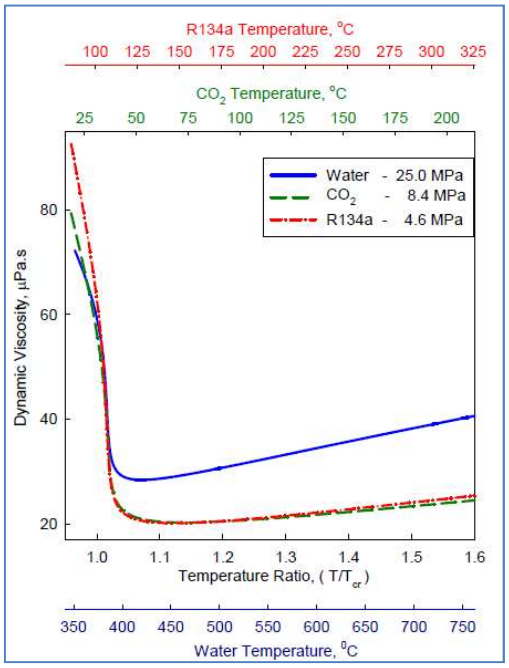

Fig. 4.40. Dynamic Viscosity vs. Temperature Ratio for water, CO_2 and R134a [4.65].

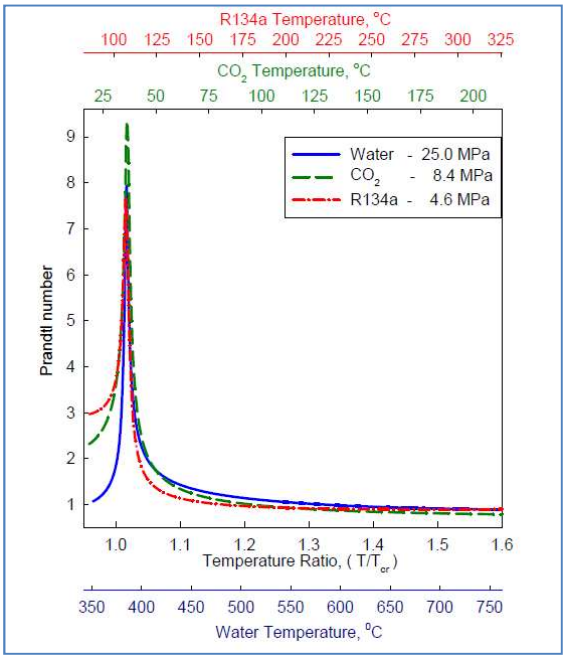

Fig. 4.41. Prandtl number vs. Temperature Ratio for water, CO_2 and R134a [4.65].

4.4.2. FLUID–TO–FLUID SCALING OF HEAT TRANSFER AT SUBCRITICAL AND SUPERCRITICAL PRESSURES

Zahlan et al. [4.66] examined the applicability of several sets of fluid–to–fluid scaling parameters (e.g., Jackson [4.67] and Cheng et al. [4.63]). They introduced a separate set based on those of Cheng et al. [4.63] for normal convective heat transfer in tubes at supercritical and high subcritical pressures. Their scaling parameters are based on local conditions and thermophysical properties. Zahlan et al. [4.66] applied their carbon dioxide and water databases to assess these scaling parameters, which are expressed as

$$D_{non-aqueous} = D_{water} \tag{4.34}$$

$$\left(\frac{P}{P_C}\right)_{non-aqueou} = \left(\frac{P}{P_C}\right)_{water} \tag{4.35}$$

$$\left(\frac{T_b}{T_{PC}}\right)_{non-aqueous} = \left(\frac{T_b}{T_{PC}}\right)_{water} \tag{4.36}$$

$$\left(\frac{q\ D}{k_b T_{PC}}\right)_{non-aqueou} = \left(\frac{q\ D}{k_b T_{PC}}\right)_{water} \tag{4.37}$$

$$\left(\frac{G\ D\ Pr_b^{\gamma}}{\mu_b}\right)_{non-aqueou} = \left(\frac{G\ D\ Pr_b^{\gamma}}{\mu_b}\right)_{water} \tag{4.38}$$

$$\left(\frac{h\ D}{k_b}\right)_{non-aqueou} = \left(\frac{h\ D}{k_b}\right)_{water} \tag{4.39}$$

where γ is the ratio of exponents in the generalized Dittus–Boelter type equation, defined as

$$Nu = C\ Re_b^{\alpha} Pr_b^{\beta} \tag{4.40}$$

$$\gamma = \frac{\beta}{\alpha} \tag{4.41}$$

Fig. 4.42 compares ratios of heat transfer coefficients between experiments and predictions using the transcritical look-up table [4.68] (i.e., h_{SC}/h_{LUT}). The experimental heat transfer coefficients were obtained with carbon dioxide in tubes and transformed into water-equivalent values using the four scaling methods (i.e., Jackson [4.67], Cheng et al. [4.63], the modified method of Cheng et al. [4.63] with optimized γ values of 0.82 for subcritical pressures and 0.63 for supercritical pressures, and the alternative method proposed by Zahlan et al. [4.66] with optimized γ values of 0.77 for subcritical pressures and 0.66 for supercritical pressures).

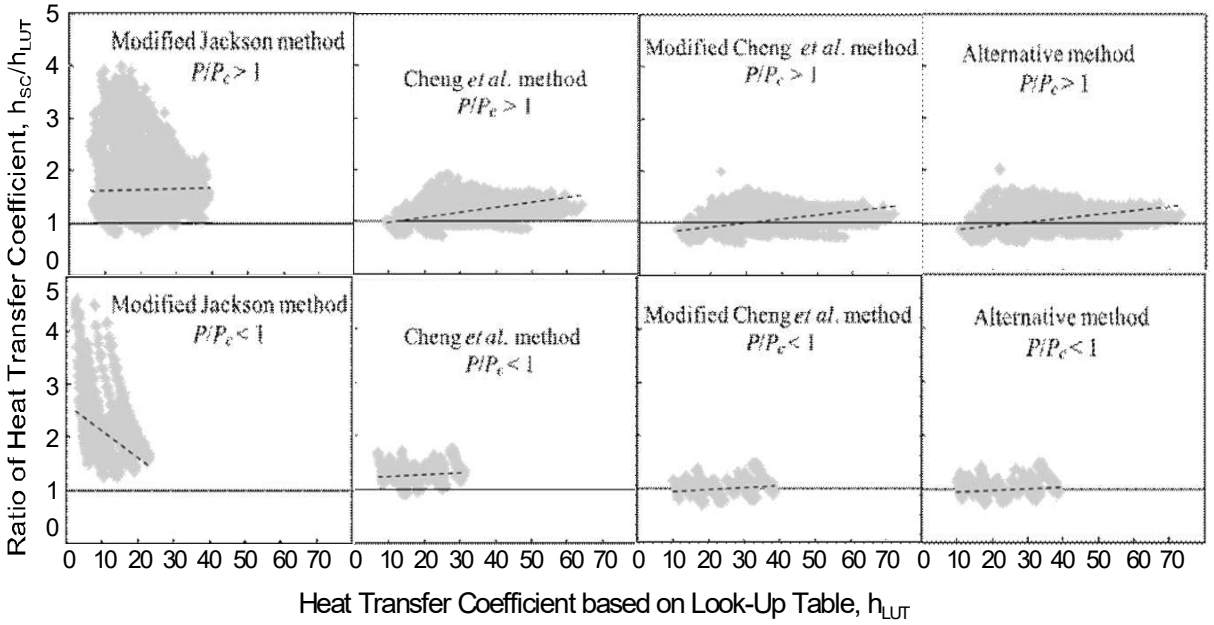

Fig. 4.42. Variations of the ratio of the water equivalent heat transfer coefficient for upward flow in an 8 mm ID tube, scaled from carbon dioxide data by four different methods, and the heat transfer coefficient predicted using the transcritical lookup table; the dashed lines are linear-least-squares fits through the HTC ratios [4.68].

The Jackson method [4.67] introduced large bias and scatter in the ratio of heat transfer coefficients. It may not be appropriate for use to transform the surrogate fluid data to water-equivalent values. The proposed method of Cheng et al. [4.63] appears to be reasonable for this set of data with relatively small scatter. However, a slight trend has been observed with increasing bias at large heat transfer coefficients. The increasing bias trend has been resolved to some extents after modifying the γ values in the method of Cheng et al. [4.63] (i.e., modified Cheng et al. method). Similar results are observed for the alternate method proposed by Zahlan et al. [4.66]. Both the modified Cheng [4.63] and Zahlan [4.66] methods are recommended for use as scaling parameters to transform heat transfer data of surrogate fluids into water equivalent values.

4.4.3. A SIMILARITY THEORY FOR HEAT TRANSFER IN TUBES WITH SUPERCRITICAL PRESSURE FLUIDS

4.4.3.1. THEORETICAL DEVELOPMENTS

The similarity theory recently developed at the University of Pisa is based on successful attempts obtained in the case of stability analysis for heated channels, which led to the proposal of new dimensionless numbers suitable for supercritical pressure fluids, in analogy with those adopted for boiling channels [4.69]. A key feature discovered in that work is that the relation between the dimensionless density and dimensionless enthalpy of a fluid can be considered a nearly unique invertible function, no matter the supercritical pressure (within a rather wide range of pressures) and, at a lower extent, irrespective of the considered fluid (in a sufficiently broad range).

This feature is clearly depicted in Fig. 4.43, where groups of curves for different fluids at different supercritical pressures show nearly exact coincidence in the gas like region, with limited deviations in the liquid like region. These results were obtained by the adoption of the following relations:

$$\rho^* = \frac{\rho}{\rho_{pc}};\ h^* = \frac{\beta_{pc}}{C_{p,pc}}\left(h - h_{pc}\right);\ w^* = \frac{w}{w_{in}};\ t^* = \frac{t w_{in}}{L} \tag{4.42}$$

$$z^* = \frac{z}{L};\ p^* = \frac{p}{\rho_{pc} w_{in}^2};\ G^* = \rho^* w^*;\ Fr = \frac{w_{in}^2}{gL};\ \Lambda = \frac{f\,L}{2\,D_h} \tag{4.43}$$

$$N'_{TPC} = \frac{q''_0 \Pi_h L}{\rho_{pc} w_{in} A}\frac{\beta_{pc}}{C_{p,pc}};\ N_{SPC} = \frac{\beta_{pc}}{C_{p,pc}}\left(h_{pc} - h_{in}\right);\ N_{TPC} = \frac{\dot{Q}_{chann}}{W_{channel}}\frac{\beta_{pc}}{C_{p,pc}} = \frac{N'_{TPC}}{\rho^*_{in}} \tag{4.44}$$

These definitions were found successful for stability analysis, since in the 1D treatment of flow with imposed heat flux at the heating wall balance equations do require only an equation of state relating density to enthalpy (operating pressure being established), which can be put conveniently in dimensionless form. The situation is instead quite different when dealing with fluid thermophysical properties (namely, dynamic viscosity and thermal conductivity) for which a unique dimensionless relation as a function of dimensionless specific enthalpy could not be achieved, thus introducing a dependence on operating pressure and on the specific fluid.

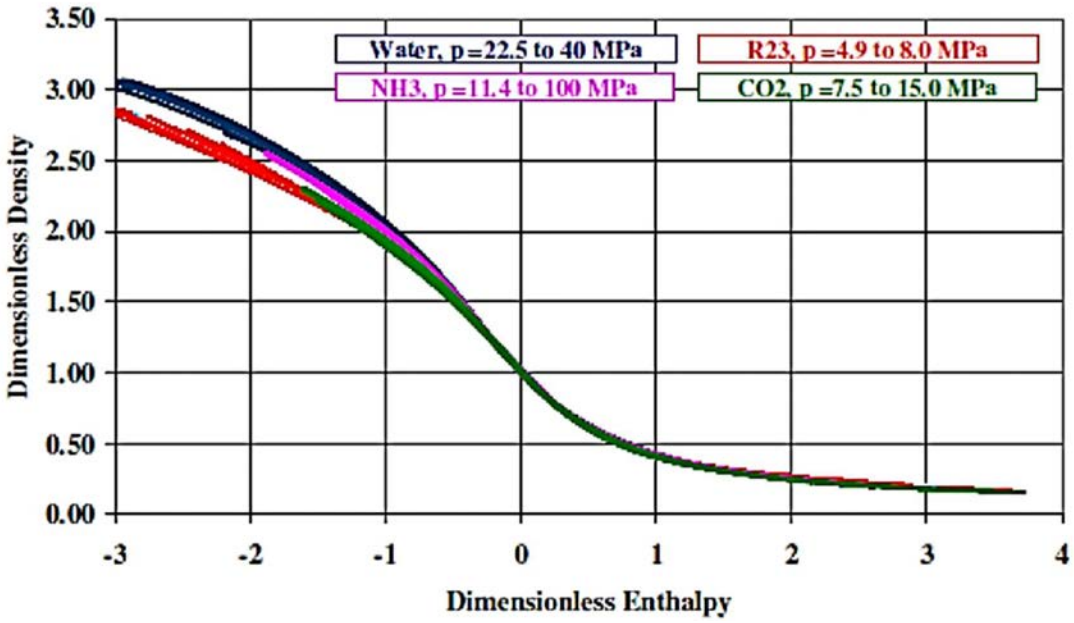

Fig. 4.43. Trend of dimensionless density as a function of dimensionless enthalpy for various fluids at supercritical pressure.

First attempts in regard [4.70], [4.71] clearly highlighted this difficulty, which definitely complicates the issue of considering similarity for heat transfer phenomena, partly as a consequence of the changing value of the molecular Prandtl number as a function of supercritical pressure, an effect that rules out any possibility to establish a strict similarity at different pressures. However, these first works on the subject already defined the basic approach to similarity developed later on, stemming from the above mentioned functional dependence of the dimensionless density vs. dimensionless enthalpy for supercritical pressure fluids. In particular, the following considerations were firstly introduced:

- Zero value of the dimensionless specific enthalpy identifies the pseudocritical threshold, i.e. the status of the fluid ideally separating the two regions of liquid like and gas like behaviour; in addition, the dimensionless specific enthalpy, owing to its unique link to dimensionless density, is able to quantitatively represent expansion (i.e., fluid acceleration) and buoyancy effects;
- As a consequence of the above, the inlet dimensionless enthalpy (represented by N_{SPC}), together with the dimensionless power-to-flow ratio, N_{TPC}, fully specify how much liquid like or gas like fluid will be found along the pipe, thus determining its potential to expand along the duct axis;
- On the other hand, since the specific enthalpy is depending uniquely on temperature, once specified the operating pressure, also the distribution of density in the radial direction, having so great importance for the heat transfer regimes, will depend on dimensionless specific enthalpy;

— Finally to note that both enhanced and deteriorated heat transfer occur around the pseudocritical threshold: e.g., enhancement is due to the high value of the specific heat at the pseudocritical temperature, while deteriorated heat transfer is often observed when the wall temperature is above the pseudocritical threshold and the bulk value is below it.

These considerations suggest an important role of the dimensionless specific enthalpy in governing the whole behaviour of the fluid and its heat transfer phenomena along the pipe, so that it is quite meaningful to define 'similar' as any pair of operating conditions with different fluids if the trends of dimensionless specific enthalpy match closely everywhere in the duct. In fact, by virtue of the above considerations, they will have quite similar distributions of dimensionless density everywhere (implying also similar acceleration and buoyancy) suggesting that they could exhibit similar conditions of enhancement or deterioration of heat transfer.

While the above reasoning is very suggestive, the inability to find a unique dependence of thermophysical properties (in some dimensionless form) as a function of dimensionless enthalpy introduces an unpleasant complication. In fact, since the Prandtl number of two fluids may be considerably different at a same dimensionless specific enthalpy, the occurrence of deterioration, for instance, may be anticipated or delayed in one case with respect to the other. This, combined with the great sensitivity of the addressed heat transfer phenomena, represents a tough obstacle to the development of a coherent fluid-to-fluid similarity theory.

A step forward in achieving a sufficiently satisfactory theory was performed in [4.72], where the heat transfer phenomena were represented as a function of the dimensionless bulk specific enthalpy, in place of the dimensionless coordinate in terms of inner diameter units. The latter representation, in fact, was dictated by the attempt to preserve in the similarity also the geometrical aspect ratio of the pipe, i.e., the length over diameter ratio. It is in fact usual for dynamic similarity theories to request as a prerequisite also a geometrical similarity. However, evidence obtained by making use of a RANS model to perform comparisons between different fluids and operating conditions suggested the usefulness to abandon this sort of prejudice. On the other hand, more than a real dynamic similarity here it is searched for a reasonable correspondence between steady state conditions, somehow restricting the request of applicability of the similarity theory.

The developed theory is based on the considerations described below [4.72]. The mass, energy and momentum balance equations in dimensionless form can be written as

$$\frac{\partial \rho^*}{\partial t^*} + \frac{\partial \rho^* w^*}{\partial z^*} = 0 \tag{4.45}$$

$$\frac{\partial \rho^* w^*}{\partial t^*} + \frac{\partial \rho^* w^{*2}}{\partial z^*} + \frac{\partial p^*}{\partial z^*} = -\frac{\rho^*}{Fr} - \left[\Lambda + \frac{1}{2} K_{in} \delta_d^*(z^*) + \frac{1}{2} K_{out} \delta_d^*(z^* - 1)\right] \rho^* w^{*2} \tag{4.46}$$

$$\frac{\partial \rho^* h^*}{\partial t^*} + \frac{\partial \rho^* w^* h^*}{\partial z^*} = N'_{TPC} f_q^*(z^*) \tag{4.47}$$

Hence, the steady state mass balance equation is

$$\frac{d}{dz^*}(\rho^* w^*) = \frac{dG^*}{dz^*} = 0 \tag{4.48}$$

where it is also

$$G^* = G^*_{in} = \rho^*_{in} \tag{4.49}$$

since $w^*_{in} = 1$, by definition. The steady state energy balance equation becomes

$$G^*_{in}\frac{dh^*}{dz^*} = N'_{TPC} f^*_q(z^*) \;\Rightarrow\; \frac{dh^*}{dz^*} = \frac{N'_{TPC}}{\rho^*_{in}} f^*_q(z^*) = N_{TPC} f^*_q(z^*) \tag{4.50}$$

suggesting that the increase rate of dimensionless specific enthalpy along the duct in case of uniform heat flux ($f^*_q(z^*) = 1$) is given by N_{TPC}. By the way, assuming uniform heat flux, N_{TPC} is related to the heat flux to mass flux ratio, which is often considered as a parameter influencing heat transfer deterioration; in fact:

$$N_{TPC} = \frac{q''_0 \Pi_h L}{\rho_{in} w_{in} A}\frac{\beta_{pc}}{C_{p,pc}} = \frac{q''_0}{G_{in}}\frac{\beta_{pc}}{C_{p,pc}}\frac{\Pi_h L}{A} = \frac{q''_0}{G_{in}}\frac{\beta_{pc}}{C_{p,pc}}\frac{4L}{D} \tag{4.51}$$

Considering the convection heat transfer law, it is

$$q''_0 = H(T_w - T) \tag{4.52}$$

and then:

$$N_{TPC} = \frac{H(T_w - T)}{G_{in}}\frac{\beta_{pc}}{C_{p,pc}}\frac{4L}{D} = \frac{H(h_w - h)}{\bar{C}_p G_{in}}\frac{\beta_{pc}}{C_{p,pc}}\frac{4L}{D} = \frac{H}{\bar{C}_p G_{in}}(h^*_w - h^*)\frac{4L}{D} \tag{4.53}$$

This expression has particular interest because, having introduced the mean specific heat at constant pressure between bulk and wall temperature, we relate N_{TPC} to the corresponding dimensionless enthalpy difference through a Stanton number and a geometrical parameter:

$$\overline{St} = \frac{H}{\bar{C}_p G_{in}};\; N_{TPC} = \overline{St}(h^*_w - h^*)\frac{4L}{D} \tag{4.54}$$

An ideal similarity could be obtained for different fluids with the same local values of $h^*_w - h^*$ and the same value of N_{TPC} only if the local values of the product $\overline{St}\frac{4L}{D}$ are the same. Noting that the Stanton number is a function of fluid properties and will certainly vary with the particular considered fluid, a possible way of achieving this result is changing the length over diameter ratio of the pipe in order to obtain the following approximate equalities:

$$N_{TPC} \approx \overline{St}_{fluid} \quad \left[\frac{4L}{D}\right]_{fluid-1}[h^*_w - h^*]_{fluid} \quad \approx \overline{St}_{fluid} \quad \left[\frac{4L}{D}\right]_{fluid} \quad [h^*_w - h^*]_{fluid-1} \approx \cdots \tag{4.55}$$

On the other hand, changing the length over diameter ratio at constant N_{TPC} implies that

$$N_{TPC} = \left[\frac{q_0''}{G_{in}}\frac{\beta_{pc}}{C_{p,pc}}\right]_{fluid-1}\left[\frac{4L}{D}\right]_{fluid} = \left[\frac{q_0''}{G_{in}}\frac{\beta_{pc}}{C_{p,pc}}\right]_{fluid-2}\left[\frac{4L}{D}\right]_{fluid-2} = \cdots \tag{4.56}$$

which can be obtained by changing $\frac{q_0''}{G_{in}}$ as necessary.

In order to impose the other suitable boundary conditions, it is then chosen to preserve the Froude number at the inlet of the heated section. It can be shown, in fact, that preserving the Froude number at the inlet, its value is preserved all along the pipe, following the trend of the dimensionless specific enthalpy, which in turn determines the dimensionless density:

$$Fr_D = \frac{w^2}{gD} = \frac{w_{in}^2}{gD}\frac{w^2}{w_{in}^2} = \frac{w_{in}^2}{gD}w^{*2} = \frac{w_{in}^2}{gD}\frac{G^{*2}}{\rho^{*2}} = \frac{w_{in}^2}{gD}\frac{\rho_{in}^{*\,2}}{\rho^{*2}} = Fr_{D,in}\frac{\rho_{in}^{*\,2}}{\rho^{*2}} \tag{4.57}$$

A useful consequence of this finding and of assuming a same dimensionless trend of specific enthalpy in bulk and at the wall is that the Richardson number is also preserved (see [4.72] for details):

$$Ri_D = \frac{\rho^* - \rho_w^*}{\rho^*}\frac{1}{Fr_D} = \frac{\rho^* - \rho_w^*}{\rho^*}\frac{1}{Fr_{D,in}}\frac{\rho^{*2}}{\rho_{in}^{*\,2}} = \frac{\rho^*(\rho^* - \rho_w^*)}{\rho_{in}^{*\,2}}\frac{1}{Fr_{D,in}} \tag{4.58}$$

By preserving N_{TPC}, N_{SPC} (to have similar inlet conditions) and the inlet Froude number, the heat flux in the heated pipe can be changed in order to achieve approximately the condition (Equation (4-27)) while maintaining a similar ratio between buoyancy and inertia, as represented by the Richardson number. A mention should be made in relation to the selection of corresponding operating pressures, which should be selected considering the minimum deviations of the ratio of Stanton numbers computed for the two fluids (see [4.72] for details).

4.4.3.2.SAMPLE RESULTS

While it is quite difficult to find similar cases, as above specified, in available experimental databases, especially when comparing water with CO_2, the availability of a CFD code [4.73] with reasonably accurate models allowed achieving a preliminary validation of the above described rationale. Among the different examples reported by [4.72], the one in Fig. 4.44 refers to experimental data by [4.74], obtained with supercritical water, which could be predicted with a relatively good accuracy by a RANS model. Basing on this result, this case was considered again, in view of checking the similarity theory, using CO_2 with boundary conditions scaled according to the above rationale. As it can be noted in Fig. 4.44, the heat flux was progressively adjusted at constant N_{TPC}, searching for an adequate correspondence of the dimensionless specific enthalpy at the wall obtained with CO_2 with the one predicted for water. In the case of water, the operating pressure was 23.5 MPa, while for CO_2 it was selected to be 7.584 MPa on the basis of a reasonably limited variation of the Stanton numbers.

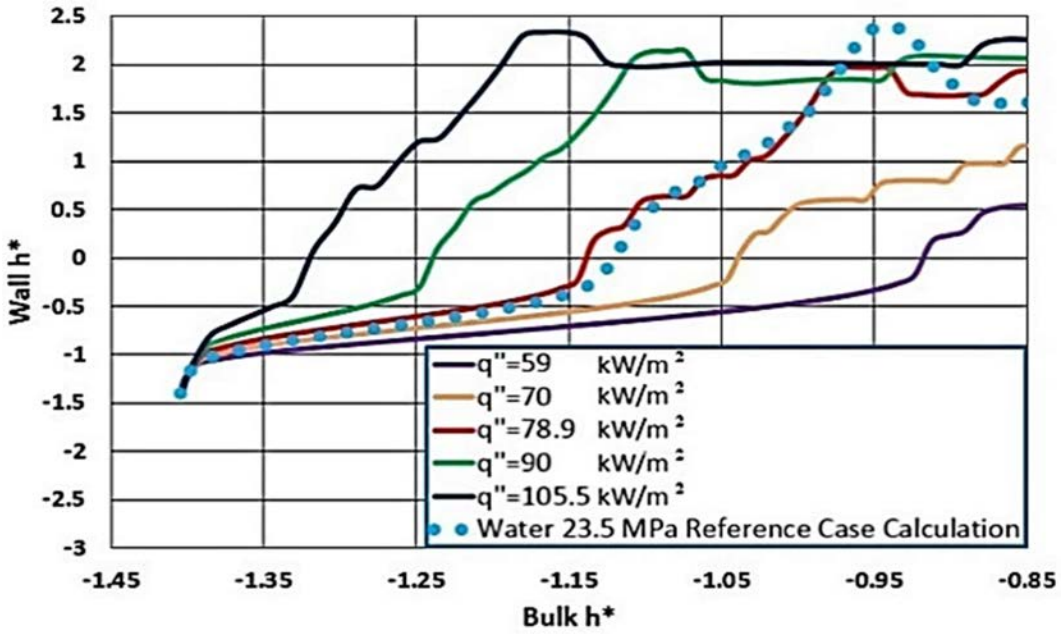

Fig. 4.44. Dimensionless enthalpy trends at different values of heat flux for the supercritical water experiment of [4.74] addressed in similarity with CO_2 (P=7.584 MPa, T_{pc} = 32.21°C, 6.28 mm ID T_{in} = –8.272°C, G = 688.46 kg/(m²s), [4.72]).

It should be noted that the addressed case involved heat transfer deterioration that, as previously mentioned, represents a relatively tough phenomenon to be predicted. So, the fact that the two trends of wall dimensionless enthalpy could be matched testified for the prediction of similar phenomena for the two fluids in correspondingly similar conditions. It needs to be stressed the point that the comparison was made as a function of dimensionless bulk specific enthalpy, implying that the length of the heated section in the two cases was different.

In this regard, Fig. 4.45 and Fig. 4.46 add additional interesting information, showing the comparison of the radial trends of the dimensionless axial velocity and of the dimensionless specific enthalpy; it should be remarked that the radial distributions were compared at cross sections where the same value of dimensionless bulk specific enthalpy was obtained; so the equivalent values of *x/D* reported in the legend for CO_2 need to be intended as axial locations at which the dimensionless specific enthalpy was the same as in the case with water. The figures clearly show that the dimensionless distributions obtained for water and CO_2 match very closely, showing that the similarity is not limited to the wall specific enthalpy distribution along the pipe, being extended also to the radial distributions of the flow and the temperature fields. This result, as well as those obtained for other cases and fluids, revealed the described approach as very promising.

The similarity theory described in the previous pages is based on the assumption to consider similar those phenomena that produce nearly the same trends of the adopted dimensionless parameters as a function of dimensionless bulk specific enthalpy. In the above description, in particular, it was mentioned that an experimental validation of the theory is difficult to achieve with the presently available data sets, especially for water and CO_2. This occurs because in available experiments

the subcooling of CO_2 with respect to pseudocritical conditions is much lower than in water experiments, making very difficult a direct comparison. The best way to produce data amenable to a direct comparison would be to collect experimental data obtained with one fluid and purposely searching for the similar conditions in terms of dimensionless parameters with another, thus requiring a specifically designed experimental campaign. Hopefully, the interesting results obtained by simply using RANS models may suggest performing such an experimental campaign in order to assess the promising features and the limitations of the proposed approach.

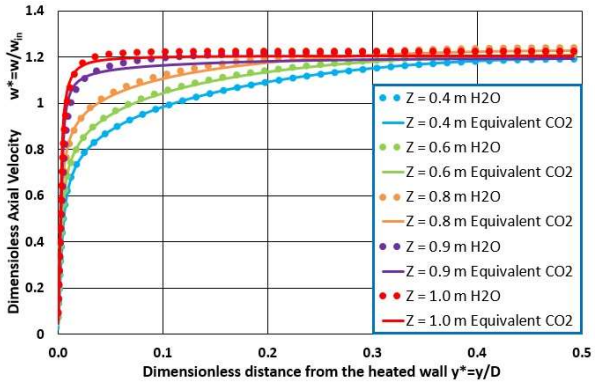

Fig. 4.45. Radial trend of the dimensionless axial velocity for some selected positions for water and CO_2 [4.72].

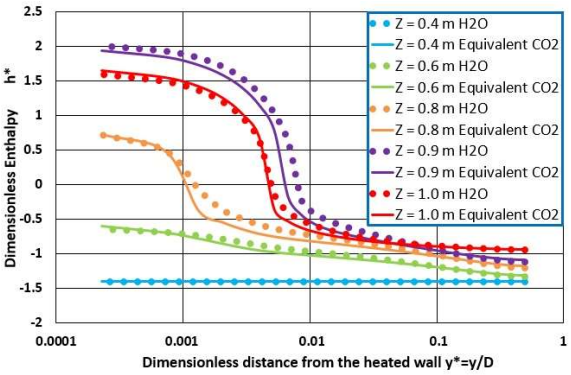

Fig. 4.46. Radial trend of the dimensionless enthalpy for some selected positions for water and CO_2 [4.72].

4.5. ANALYSIS OF FLUENT CFD CODE CAPABILITIES FOR SUPERCRITICAL WATER HEAT TRANSFER APPLICATIONS IN VERTICAL BARE TUBES

This Section (4.5) is based on or directly reproduced from [4.75] and published with permission from the American Society of Mechanical Engineers (ASME).

The main empirical correlations and models developed to predict SCW heat transfer behavior to date only capture 1D effects. Performing experiments to accurately capture 3 D effects are costly. The CFD studies have been performed in this area in attempts to determine various 3D effects of heat and mass transfer within subchannels of fuel assemblies [4.10]. [4.75] simulated experimental data obtained in a bundle geometry and overestimated the temperatures with an inconsistent prediction of the DHT phenomenon. Most modeling experts in the nuclear industry support the approach of using CFD codes such as FLUENT to analyze 3D effects [4.75], [4.76], [4.77]. However, the accuracy of CFD codes for SCW is not well known at this time [4.78]. A study on well known experimental datasets is needed to verify the accuracy of CFD codes versus empirical correlations.

The CFD code needs to be rigorously tested before it may be deemed accurate enough to be applied to fuel channel heat transfer simulations. CFD codes are routinely used in the industry in attempts to quantify flow effects at normal operating and accident scenarios [4.79], but none have been validated for use at supercritical conditions.

The CFD code, FLUENT was used to predict wall temperature profiles inside vertical bare tubes with SCW as the cooling medium, to assess the capabilities of FLUENT for SCW heat transfer applications. Numerical results are compared with experimental data and current 1D models represented by existing heat transfer empirical correlations.

Wall temperatures and heat transfer coefficients were analyzed to select the best model to describe the fluid flow before, at and after the pseudocritical region. The k–ε and k–ω turbulent models were evaluated in the process, with variations in the submodel parameters such as viscous heating, thermal effects, and low Reynolds number correction.

Results of the analysis show a fit of ± 10 % for wall temperatures using the SST k–ω model within the deteriorated heat transfer regime and less than ± % within the normal heat transfer regime. The accuracy of the model is higher than any empirical correlation tested in the mentioned regimes, and provides additional information about the multidimensional effects between the bulk fluid and wall temperatures.

This study will provide guidance to identify the next set of experiments that will be needed to validate CFD codes for supercritical nuclear designs.

In this section, assessment of the capability of the CFD code FLUENT to capture heat transfer phenomena of SCW flowing through a vertical bare tube is performed as a preliminary analysis with the specific objective to determine limitations and capabilities near the pseudocritical region.

4.5.1. EMPIRICAL 1D CORRELATIONS

The issue arising from the dramatic changes in water properties is the difficulty in predicting the heat transfer phenomena occurring within the pseudocritical region, and the phenomenon known as the DHT.

In the case of nuclear power plants, the ability to predict correctly HTCs along a fuel bundle string is essential for the reactor design. There is, however, a lack of experimental data and correspondingly empirical correlations for heat transfer in fuel bundles. Only one correlation is known for a helically finned, 7-rod bundle by Dyadyakin and Popov, developed in 1977 [4.80].

This test bundle was designed for applications in small reactors, and not for large power reactors. Moreover, heat transfer correlations for bundles are usually very sensitive to a particular bundle design, which makes such a correlation inadequate for other bundle geometries.

To overcome this problem, attempts at developing wide range heat transfer correlations based on bare tube data have been conducted to serve as a conservative approach. The conservative approach is based on the fact that traditionally, in subcritical conditions, HTCs are generally lower in bare tubes than in bundle geometries, where the heat transfer is enhanced with appendages such as endplates, bearing pads, spacers, etc. [4.81]. The assumption here is that the same principles apply for supercritical conditions.

A new empirical correlation was proposed by Mokry et al. in 2011 [4.82] based on the same approach as the Bishop et al. correlation [4.83].

$$Nu_b = 0.0061\, Re_b^{0.904}\, \overline{Pr}_b^{0.684} \left(\frac{\rho_w}{\rho_b}\right)_x^{0.564} \tag{4.59}$$

The correlation is based on experimental data collected at supercritical conditions similar to those of the proposed SCWR concepts. The uncertainty analysis conducted by Mokry et al. [4.82] showed a deviation of roughly ± 15 % from experimental data in the Normal Heat Transfer (NHT) regime only. Data for DHT, entrance region, and outliers have been removed from the analysis.

4.5.2. DETERIORATED HEAT TRANSFER

DHT is a phenomenon resulting in an observed increase in the wall temperature likely resulting from an inferred reduction in the HTC at a heated wall [4.50], [4.58]. In this regard, it is similar to the Critical Heat Flux (CHF) phenomenon. The most contributing factors to DHT occurrence are the heat flux, mass flux, and the geometry. In general, many authors attribute the ratio of heat to mass fluxes to be a major factor for the onset of DHT [4.19], [4.53], [4.58].

What is agreed among researchers is that DHT is caused by local changes in thermophysical properties of water near the heated wall. [4.84] argues two means of DHT occurrence. One occurrence is when the mass flux is higher than a certain value, while keeping the heat flux constant, the HTC decreases consistently.

The second occurrence is when the mass flux is kept constant at lower than this certain value while increasing the heat flux, the HTC decreases abruptly at certain heat flux values and gradually increases thereafter. [4.84] claims this is due to the effects of buoyancy forces; when the heat flux increases the buoyancy force becomes stronger near the heated wall which leads to a flattening of the velocity profile radially. As the generation of turbulent energy is proportional to the gradient of the mean velocity, turbulence is then suppressed. Consequently, this results in the reduction of the HTC. Once the heat transfer is increased, the buoyancy force undergoes further enhancement, which causes a velocity peak near the heated wall. This in turn results in higher turbulence, because of the newly generated gradient, and the heat transfer is improved again. This means the HTC will be enhanced with mixing; that is when the fluid near the wall mixes with the bulk fluid. There have been some empirical correlations proposed for heat flux calculations at which the deteriorated heat transfer regime appears (onset of DHT). One such correlation used to highlight the onset of DHT heat flux for a specific mass flux value is suggested by Gabaraev et al. [4.85]:

$$q_{dht} = 7.9 \cdot 10^{-4}\, G \left(\frac{P}{P_{cr}}\right)^{1.5}, MW/m^2 \tag{4.60}$$

4.5.3. METHODOLOGY

The proposed methodology is to benchmark CFD models against a set of experimental data. For the same dataset, different numerical options can be chosen. The ability to predict the wall temperatures will form the base of the analysis.

4.5.4. EXPERIMENTAL SETUP

A large experimental dataset was made available by the Institute for Physics and Power Engineering (Obninsk, Russia), with conditions similar to those of the pressure tube type SCWR concepts currently proposed in Canada. This dataset includes 80 test configurations of heat and mass flux. The experiments were conducted by [4.86] for SCW conditions. The data is used to benchmark the ability of the FLUENT code to solve heat- and mass-transfer problems in the supercritical region.

The test section of the experimental loop consists of a 4 m long vertically oriented tube of inner and outer diameters of 10 mm and 14 mm respectively. The diameter of the tube is close to the hydraulic equivalent diameters of the proposed SCWR bundles. The test section follows an unheated entrance region (the length is not specified in the publication by [4.86]). The tube wall material is stainless steel (close to SS–304), with an average surface roughness height of 0.63 to 0.8 μm. The experiments encompass a wide range of operating conditions at a pressure of 24 MPa with inlet temperatures ranging from 320°C to 350°C. Mass fluxes range from 200 to 1500 kg/m^{2}s while heat fluxes up to 1250 kW/m^2 were used for several combinations of wall and bulk fluid temperatures that were at, below, or just above the pseudocritical temperature. Table 4.22 lists the range of operating conditions for the experiments from [4.86]. The highlighted regions are the ones closely related to the proposed conditions for SCWR's. Table 4.23 lists the uncertainties in the measured and calculated parameters for the experimental setup. The temperature at the inlet of the heated section is measured, and the bulk fluid temperature profile is then calculated based on the uniform constant heat flux using energy balance calculations. The enthalpy rise determines the bulk fluid temperature along the length of the tube, and the calculated outlet temperature is compared to the experimentally measured value for confirmation.

Wall temperatures were measured using thermocouples located on the outside wall. Inner wall temperatures were then calculated as described in [4.86]. Heat transfer coefficients are calculated based on the bulk fluid and calculated inner wall temperatures. The inner wall temperature behaviors are used for comparison with the CFD FLUENT code predictions.=

TABLE 4.22. DATASET TEST MATRIX OF [4.86]

Mass Flux (kg/(m^{2}s))	Inlet Pressure (MPa)	Bulk Fluid Inlet Temperature (°C)	Heat Flux (kW/m^2)
200	24.0 – 24.2	320 – 450	73 – 214
500	24.0 – 24.2	325 – 450	141 – 454
1000*	23.9 – 24.1	325 – 425	392 – 826
1500*	24.0 – 24.1	320 – 425	489 – 1256

*Highlighted section represents most relevant conditions to SCWR operations

TABLE 4.23. UNCERTAINTIES OF PRIMARY PARAMETERS [4.86]

Parameter	Maximum Uncertainty
Test section power	±1.0%
Inlet pressure	±0.25%
Wall temperatures	±3.0°C
Mass flow rate	±1.5%
Heat loss	≤3%

4.5.5. COMPUTATIONAL DOMAIN

The vertical bare tube geometry was meshed in Gambit, for analysis in the FLUENT solver. The mesh tested in this work is a 2D axisymmetric 5 mm radius tube of 2 m and 4 m lengths. This mesh was used to test heat transfer regimes of the tube while minimizing the effects of other regimes on the computational domain. The mesh size was chosen based on a mesh convergence (independence) study to check whether the mesh satisfactorily balances accuracy and computational resources [4.87]. The final mesh consists of 5000 axial nodes and 120 radial total nodes, including a 21 μm boundary layer. The boundary layer consists of a 1 μ first node and a growth ratio of 1.1, resulting in a Y+ value of roughly 1.

The mesh size and density are determined as the result of a mesh independence study, in which the mesh size for the geometry is varied, and the results are compared (the convergence criteria and the parameters of interest) until the changes are negligible (i.e. same convergence is reached, difference in temperature values are less than 0.3 ºC, etc.).

A 20 cm unheated entrance region was added to stabilize and develop the hydraulic boundary layer of the flow before entering the heated section of the tube. The use of an unheated entrance length also reduces turbulence effects at the entrance, and better represents the experimental setup.

The mesh representation is shown in Fig. 4.47(a). The heat flux is constant at the wall, and heat is transferred to the bulk fluid. Fig. 4.47(b) shows the axisymmetric mesh in 3D space.

4.5.6. GOVERNING EQUATIONS AND TURBULENCE MODELS

As the flow is considered 2D axisymmetric, the governing equations for the continuity, momentum, and enthalpy for such a flow in the cylindrical coordinate system are as follows:

Continuity:

$$\frac{1}{r}\left\{\frac{\partial}{\partial x}(r\rho u)+\frac{\partial}{\partial r}(r\rho v)\right\}=0 \tag{4.61}$$

U momentum:

$$\frac{1}{r}\left\{\frac{\partial}{\partial x}(r\rho u^2)+\frac{\partial}{\partial r}(r\rho vu)\right\}=-\frac{\partial p}{\partial x}+\rho g+\frac{1}{r}\left\{2\frac{\partial}{\partial x}\left[r\mu_e\left(\frac{\partial u}{\partial x}\right)\right]+\frac{\partial}{\partial r}\left[r\mu_e\left(\frac{\partial u}{\partial r}+\frac{\partial v}{\partial x}\right)\right]\right\} \tag{4.62}$$

V momentum:

$$\frac{1}{r}\left\{\frac{\partial}{\partial x}(r\rho uv)+\frac{\partial}{\partial r}(r\rho v^2)\right\}=-\frac{\partial p}{\partial x}+\frac{1}{r}\left\{\frac{\partial}{\partial x}\left[r\mu_e\left(\frac{\partial v}{\partial x}+\frac{\partial u}{\partial r}\right)\right]+2\frac{\partial}{\partial r}\left[r\mu_e\left(\frac{\partial v}{\partial r}\right)\right]\right\}-2\frac{\mu_e v}{r^2} \tag{4.63}$$

The term $\mu_e$is the effective viscosity defined as $\mu_e=\mu+\mu_t$, where μ is the molecular (dynamic) viscosity and the turbulent viscosity is defined as:

$$\mu_t=\rho C_\mu f_\mu\left(\frac{k^2}{\epsilon}\right) \tag{4.64}$$

where: f_μ is a dampening function to account for the near wall effects (which varies with each type of viscous model), and C_μ is an empirical constant built in the models based on experimental data fitting.

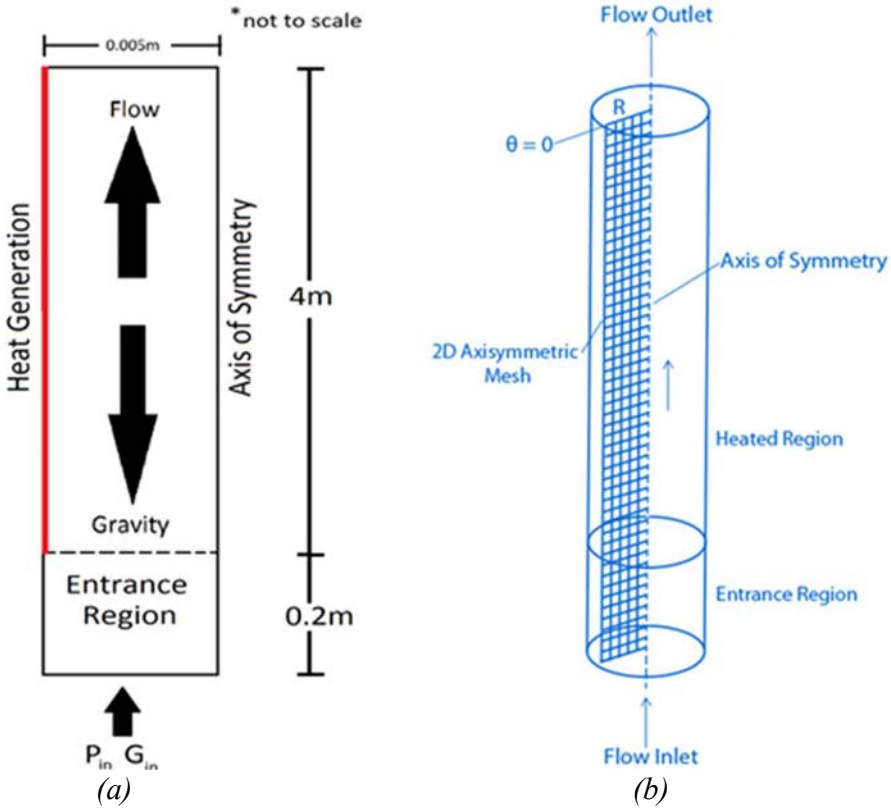

Fig. 4.47 (a) Graphical representation of computational domain; (b) Graphical representation of the 2D mesh in the 3D space.

Energy:

$$\frac{1}{r}\left\{\frac{\partial}{\partial x}(r\rho uh)+\frac{\partial}{\partial r}(r\rho vh)\right\}=\frac{1}{r}\left\{\frac{\partial}{\partial x}\left[r\left(\frac{\mu}{\boldsymbol{Pr}}+\frac{\mu_T}{\sigma_T}\right)\left(\frac{\partial h}{\partial x}\right)\right]+\frac{\partial}{\partial r}\left[r\left(\frac{\mu}{\boldsymbol{Pr}}+\frac{\mu_T}{\sigma_T}\right)\left(\frac{\partial h}{\partial r}\right)\right]\right\} \tag{4.65}$$

where: ***Pr*** is the molecular Prandtl number and σ_T is the turbulent Prandtl number, which is usually used as a constant of 0.9 for general subcritical flows [4.88].

The turbulent models evaluated in the study are derived from the Navier–Stokes equations, in an approach named Reynolds averaged Navier–Stokes [4.54]. This approach is based on the Reynolds decomposition of flow parameters, into mean (time averaged) and fluctuating components. The two models considered in this study are the realizable *k–ε* model (RKE) and the *k–ω* shear stress transport (SST) model. These models conserve the turbulent kinetic energy (*k*), its dissipation rate (*ε*), and specific dissipation rate (*ω*). A collection of models were studied for initial results in a previous analysis, and these two models showed the best approximation of the experimental data while capturing the expected trends.

The general form of the models can be expressed as follows:

$$\left\{\frac{\partial}{\partial x}(\rho u k)+\frac{1}{r}\frac{\partial}{\partial r}(r\rho v k)\right\} = \left\{\frac{\partial}{\partial x}\left[\left(\mu+\frac{\mu_T}{\sigma_k}\right)\left(\frac{\partial k}{\partial x}\right)\right]+\frac{1}{r}\frac{\partial}{\partial r}\left[r\left(\mu+\frac{\mu_T}{\sigma_k}\right)\left(\frac{\partial k}{\partial r}\right)\right]\right\}+P_k+G_k-\rho(\epsilon-D) \tag{4.66}$$

where: P_k is the production term due to the mean velocity gradient:

$$P_k=\mu_t\left[2\left\{\left(\frac{\partial u}{\partial x}\right)^2+\left(\frac{\partial v}{\partial r}\right)^2+\left(\frac{v}{r}\right)^2\right\}+\left(\frac{\partial u}{\partial r}+\frac{\partial v}{\partial x}\right)^2\right] \tag{4.67}$$

The gravitational production term is computed by the equation

$$G_k=\overline{\rho' u'}g_x=c_\theta\beta\rho g x\frac{k}{\epsilon}\left[\mu_T\left(\frac{\partial u}{\partial r}+\frac{\partial v}{\partial x}\right)\left(\frac{\partial T}{\partial r}\right)+\left(2\mu_T\frac{\partial u}{\partial x}-\frac{2}{3}\rho k\right)\left(\frac{\partial T}{\partial x}\right)\right] \tag{4.68}$$

where: $g_x=-g$ for upward flow, $g_x=g$ for downward flow and $c_\theta=0.3$.
The conservation of turbulent dissipation rate (*ε*) is represented as

$$\left\{\frac{\partial}{\partial x}(\rho u\epsilon)+\frac{1}{r}\frac{\partial}{\partial r}(r\rho v\epsilon)\right\} = \frac{\partial}{\partial x}\left[\left(\mu+\frac{\mu_t}{\sigma_\epsilon}\right)\left(\frac{\partial\epsilon}{\partial x}\right)\right]+\frac{1}{r}\frac{\partial}{\partial r}\left[r\left(\mu+\frac{\mu_t}{\sigma_\epsilon}\right)\left(\frac{\partial\epsilon}{\partial r}\right)\right]+C_{\epsilon1}f_1\left(\frac{1}{T_t}\right)(P_k+G_k) - C_{\epsilon2}f_2\left(\frac{\rho\epsilon}{T_t}\right)+\rho E \tag{4.69}$$

The empirical constants $C_{\epsilon1} and\ C_{\epsilon1}$ and the functions $f_1 and\ f_2$ are model specific. In a similar manner, the conservation of specific dissipation rate (*ω*) is

$$\left\{\frac{\partial}{\partial x}(\rho u\omega)+\frac{1}{r}\frac{\partial}{\partial r}(r\rho v\omega)\right\} = \frac{\partial}{\partial x}\left[\left(\mu+\frac{\mu_t}{\sigma_\omega}\right)\left(\frac{\partial\omega}{\partial x}\right)\right]\ +\ \frac{1}{r}\frac{\partial}{\partial r}\left[r\left(\mu+\frac{\mu_t}{\sigma_\omega}\right)\left(\frac{\partial\omega}{\partial r}\right)\right]+G_\omega-Y_\omega+S_\omega+D_\omega \tag{4.70}$$

where G_ω is the generation of ω, Y_ω is the dissipation of ω, S_ω is a user defined source term, and D_ω is a cross diffusion term.

4.5.7. INITIAL RESULTS

A reference case model was developed based upon FLUENT model options expected to predict heat transfer at supercritical conditions. The initial simulations for the 4 m mesh showed a good fit for the normal heat transfer regime as shown in Fig. 4.48. Both models display a fit of about ±5 % for the experimental wall temperatures, with a slight over prediction.

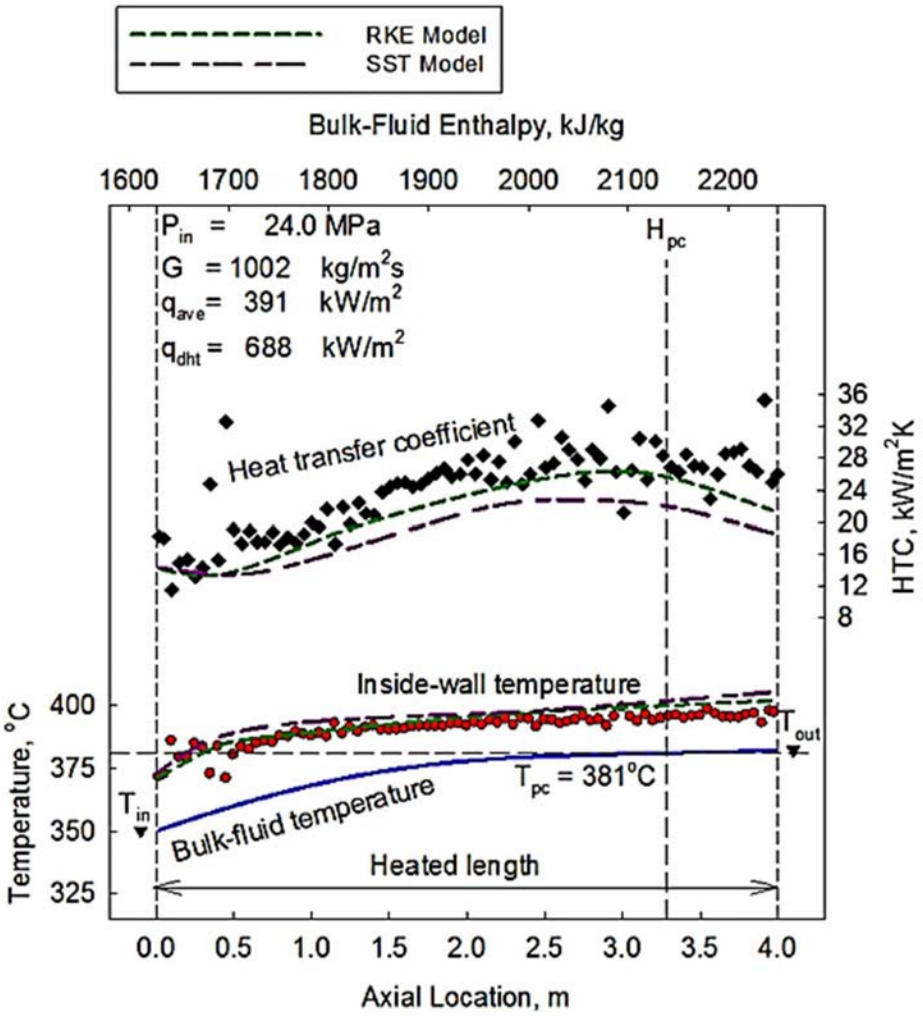

Fig. 4.48 Initial experimental, calculated and simulated results for low range mass and heat fluxes, in 4 m mesh.

However, within the DHT regime, the results showed a discontinuity in the wall temperature predictions for both turbulent models, as shown in Fig. 4.49. Near the entrance region, the SST

model experiences some discontinuities, and does not capture the DHT phenomenon but the temperature rather increases steadily until the exit. This is due to problems with convergence.

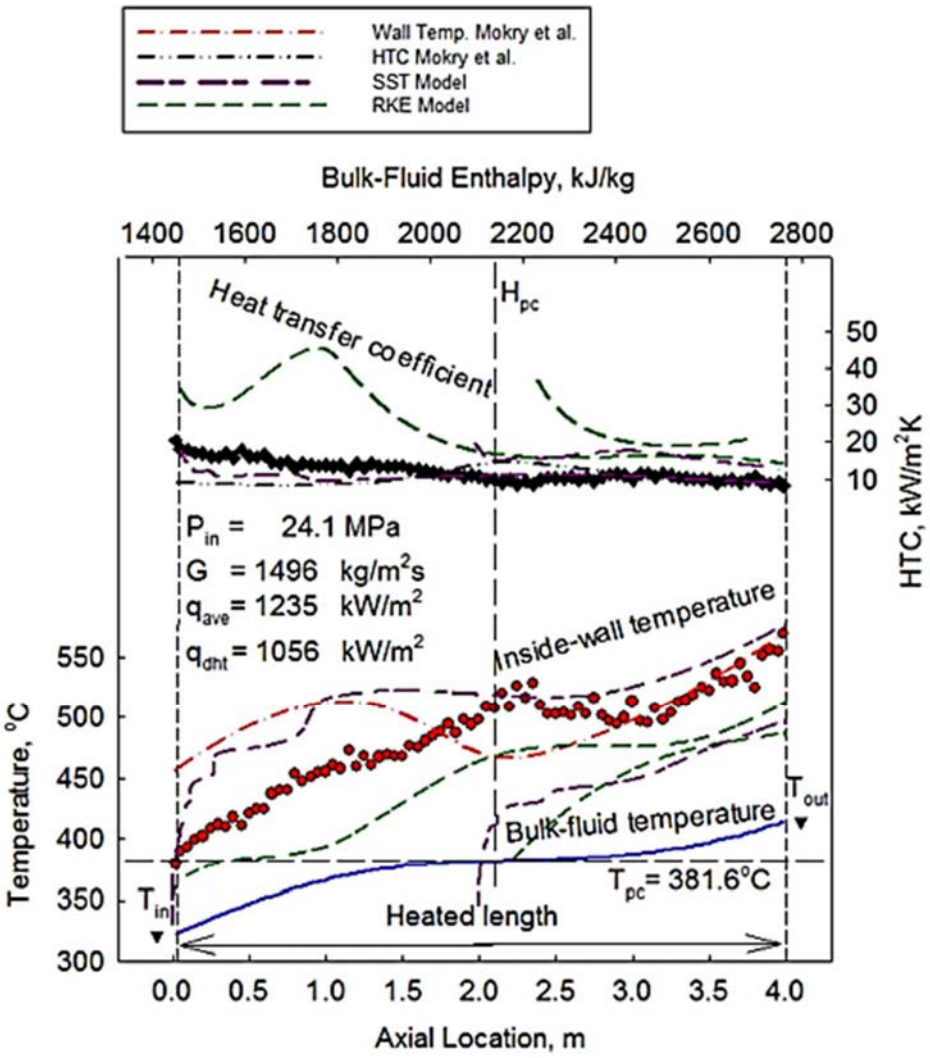

Fig. 4.49 Initial experimental, calculated and simulated results for mid range mass and heat fluxes, in 2 and 4 m meshes.

To remedy the issue in DHT predictions, the 2 m mesh was used to minimize the effect of the rest of the tube on the region in study. Computationally, smaller sections provide better convergence and are better able to capture various phenomena within the normal, deteriorated and enhanced heat transfer regimes without resorting to large computational power. The effects of each regime on the computational domain would then be minimized, and only the phenomenon occurring in the shortened region is studied. According to this method, the middle two meters, and last 2 m of the tube are to be simulated using various viscous models to determine which viscous models best describe the different heat transfer phenomena along the tube.

The simulations in a shortened length in the tube also means the boundary conditions have to be modified accordingly. As such the boundary conditions are adjusted to the studied length, based on the experimental data provided by [4.86] to match the conditions studied at the specified length of the tube.

The simulation results show a deviation from the experimental results for both 2 m and 4 m meshes in the DHT regime as shown in Fig. 4.49. The SST model shows a discontinuity in the prediction near the entrance region, while the RKE model largely underpredicts the results yet mostly as a bias to the experimental results. The same behavior applies for both mesh lengths, which suggests the viscous model options or the solution method needs to be altered to better predict the temperature profiles in the DHT regime.

4.5.8. PARAMETRIC TRENDS AND SENSITIVITY ANALYSIS

To study the SCW conditions in FLUENT, it was apparent that modifications had to be made to the solver options, and possibly the computational mesh. To reduce the computational time needed to complete the simulations, a sensitivity analysis was conducted to assess the operational ranges where FLUENT resolves the solutions without discontinuities, and accuracy of different convergence criteria from the experimental results. In order to clearly see the effects of various operating parameters on the temperature distributions, a control case is selected where FLUENT predicts the experimental values accurately as shown in Fig. 4.50 and then the parameters are varied individually. The parametric trends are shown for pressure and heat flux.

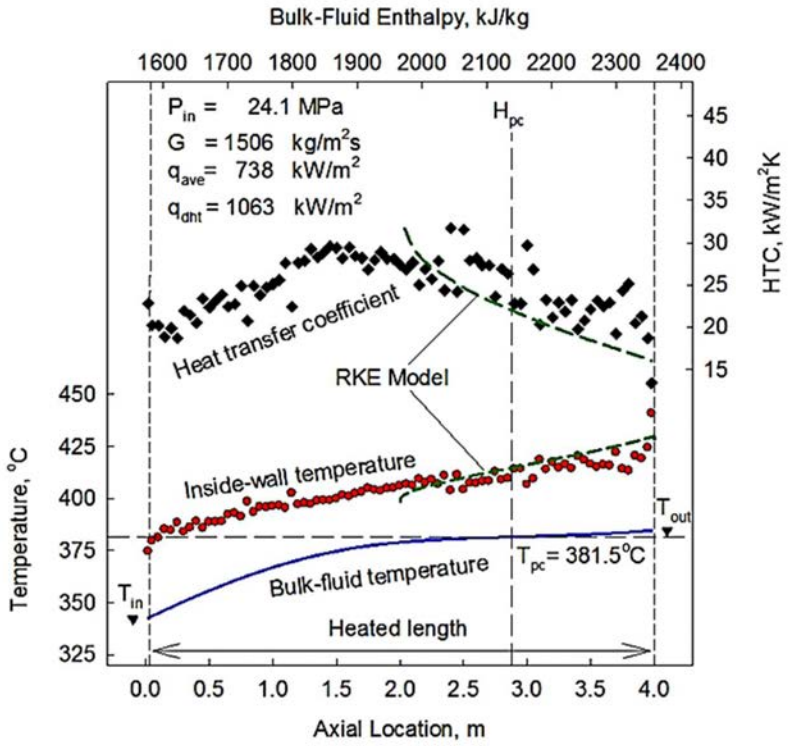

Fig. 4.50 Control case for sensitivity analysis.

4.5.9. PRESSURE PARAMETRIC TREND

Pressure change in the supercritical region has an effect on the thermophysical properties profiles, and thus it is useful to know the effect it has on FLUENT's calculations. The pressure was varied from 22 to 25 MPa for the analysis, in increments of 1 MPa to find out the trends in temperatures as a result of this change.

The temperature distributions along the wall as well as the centerline temperature were plotted for each case. Fig. 4.51 shows the reduction in wall temperatures as the pressure is increased well beyond the critical poInt. This is due to the fact that the 22 and 23 MPa cases involved water which has already developed past the pseudocritical point and into the dense gas-like region. As a result, the water in these regions has considerably low thermal conductivity which effectively insulates the inner surface of the tube, raising the temperatures dramatically.

An interesting effect observed is that once the pressure reaches 24 MPa, changes in the wall temperature distribution for subsequent pressures becomes minimal. This is due to the fact that changes in the properties of the water in the region past the critical point but before the pseudocritical point are much less pronounced. This effect can be seen in specific heat trends as shown in Fig. 4.52.

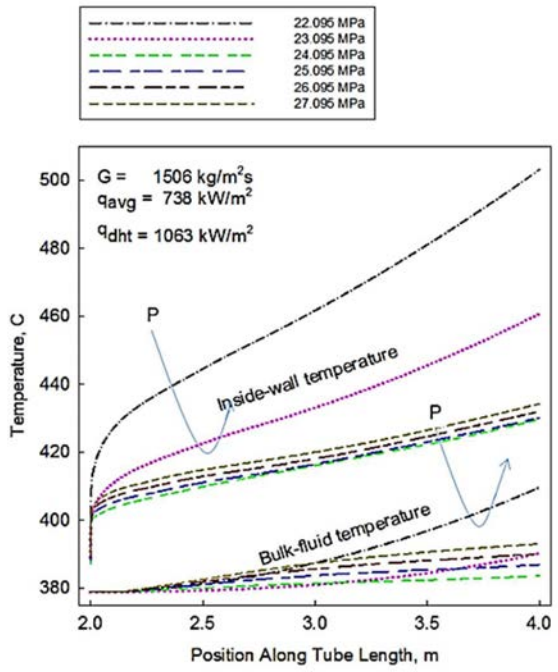

Fig. 4.51 Pressure variation effect on bulk fluid and wall temperature distributions.

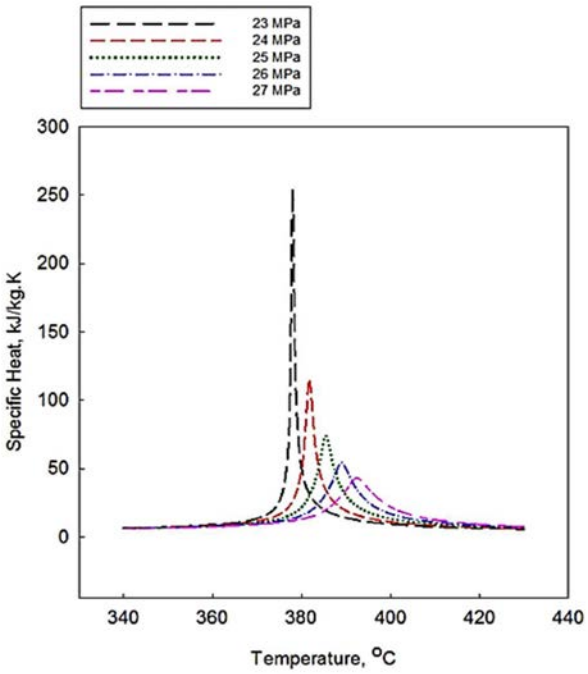

Fig. 4.52 Specific heat trends with pressure variation.

While the wall temperature distributions simulated by FLUENT produced similar temperature profiles for all cases, the centerline temperature distributions were observed to be much different than one would expect. Fig. 4.51 shows a steadily increasing temperature along the length of the tube for the 22 and 23 MPa cases, but much flatter distributions for higher pressures. This is

unexpected as the very high wall temperatures for these cases would indicate that much of the heat was not transferred to the bulk fluid, even with the lower specific heat values at increased pressures as shown in Fig. 4.52. Furthermore, the centerline temperature for the 24 and 25 MPa cases initially increase but flatten three quarters of the way through the tube. One possible explanation of the results obtained is FLUENT's interpretation of the property changes, specifically the spike in specific heat, which occurs at the pseudocritical poInt. To test this hypothesis NIST REFPROP [4.89] was used to determine the corresponding pseudocritical point temperatures for each pressure used. The data obtained can be found in Table 4.24.

TABLE 4.24. PSEUDOCRITICAL TEMPERATURES AT VARIOUS PRESSURES

Inlet Pressure, MPa	Pseudocritical Temperature, ^{o}C
22.095	374.1
23.095	377.8
24.095	381.7
25.095	385.4
26.095	388.9
27.095	392.4

From the data in the table we can see that the fluid observed in the 22 and 23 MPa cases were past the pseudocritical point throughout the entire length. Because a very large spike in the specific heat of the fluid occurs at the pseudocritical point, very little temperature change can be seen in the bulk fluid for this case. This can also be observed in the 24 and 25 MPa cases in the form of a plateau in centerline temperature as they approach their respective pseudocritical points. This indicates that the large, although brief, spike in specific heat of the fluid has a very dramatic effect on the calculations in the turbulent models.

Another point of interest is the increase in wall temperatures at pressures greater than 24 MPa. This phenomenon occurs because as the pressure increases, the specific heat becomes higher after the pseudocritical point than its counterpart at a lower pressure for the same temperature. The result of this trend (shown in Fig. 4.52) is an increase in the wall temperatures due to the corresponding increase in specific heat.

4.5.10. HEAT FLUX PARAMETRIC TREND

The effect of varying heat flux was studied next, while keeping the other parameters constant, as shown in Fig. 4.53 and Fig. 4.54. A well defined drop in wall temperature was observed at heat fluxes well above where it was expected to occur based on empirical correlations. An upper limit on heat flux for this set of operating conditions was reached when the fluid temperature at the wall exceeded the limit of the fluid properties the program used, around 1600 kW/m^2. No lower limit was found, since the solver can predict down to adiabatic conditions.

The centerline temperatures show a more interesting phenomenon around 1200 kW/m^2 where the temperatures being to decrease below the expected values half way through the heated length, before rising again at the end. The dip in temperatures corresponds to the increase in the wall temperature at the same location, indicating the existence of DHT at these heat fluxes.

This result can be used to give an idea of how the turbulent models predicts DHT phenomenon for different heat fluxes. The onset for DHT is around 1000 kW/m^2 as predicted by the empirical correlation. The tests included a range from 638 to 1438 kW/m^2 to demonstrate NHT, DHT, and possibly Improved Heat Transfer (IHT) conditions.

At lower heat fluxes, the temperature profiles tend to be linear for wall temperatures, as expected and visualized in NHT regimes (an example is depicted in the control case). This occurs up to around 1000 kW/m^2, after which a peak begins to emerge in the wall temperatures as the heat flux continues to rise

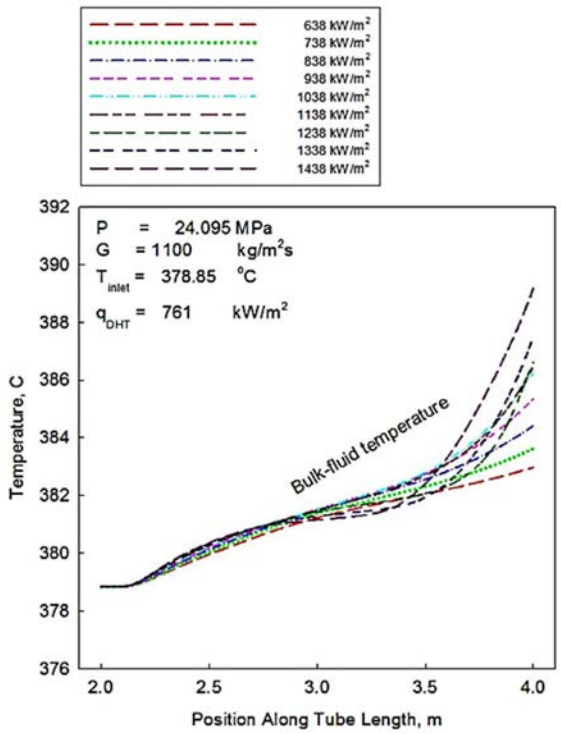

Fig. 4.53 Heat flux variation effect on bulk fluid temperature distributions.

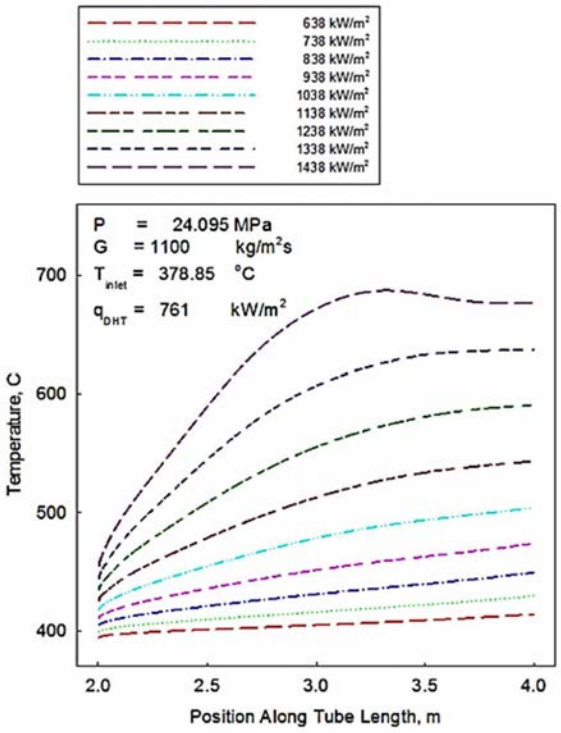

Fig. 4.54 Heat flux variation effect on wall temperature distributions.

At the current operating conditions (of the inlet temperature, pressure, and mass flux) in Fig. 4.54, DHT can be seen in the 1438 kW/m^2 simulation as a peak in wall temperatures where turbulence is suppressed and then a drop to lower temperatures can be seen at the end of the heated length.

4.5.11. BEST FIT MODEL

After studying the effects of the individual parameters on the prediction of the viscous models, it was concluded that they should function well within the operating conditions of interest. The trends show the expected global behavior in the normal and deteriorated heat transfer regimes. The extent of the prediction's accuracy however is still to be judged based on the dataset from [4.86] and empirical correlation comparison.

Based on all the information collected thus far, the 2 m mesh is deemed the best option to use in the simulations due to the lack of discontinuities displayed in 4 m mesh simulations and the proximity of the predictions to the experimental data. The RKE and SST models are used with the sub-models options varied to test their effect on the temperature and HTC profiles.

The cases studied are in the normal and in deteriorated heat transfer regime. In all of the cases, the temperatures plots and heat transfer coefficients are studied for lengths of 1–3 m and 2–4 m.

The corresponding turbulent kinetic energy profiles are plotted for the centerline flow, for both RKE and SST models. These plots are used to observe the behavior of the models in predicting the turbulence production in the fluid, and to help choose the best fit model.

4.5.12. TEMPERATURE, HTC, AND TURBULENT ENERGY — NORMAL HEAT TRANSFER REGIME

At the normal heat transfer regimes, FLUENT demonstrated reasonable accuracy in capturing the basic heat transfer phenomena correctly, by predicting the wall temperatures and the heat transfer coefficients. The following is an analysis of the way FLUENT behaves under these conditions, by studying the turbulent kinetic energy in addition to the wall and bulk fluid temperatures.

All the simulations were done in a 2 m heated length computational domain, between 1–3 m and 2–4 m in the test section. Fig. 4.55 shows good agreement between the experimental and simulated results for both RKE and SST models, where the SST model overestimates the wall temperature slightly more than the RKE model (by less than 5°C), and this results in a lower heat transfer coefficient prediction as well. The prediction by Mokry et al. correlation [4.82] is more accurate over the tested range of 1–4 m heated length, however this is due to the fact that the correlation was developed based on this dataset and a slightly better approximation is to be expected. The good heat transfer and low wall temperatures mean, according to the DHT theory presented in an earlier section, that there should be enough turbulence in the bulk fluid to remove the heat efficiently. The difference between the turbulence kinetic energy (k) at the wall and the bulk fluid should be ample to enhance the heat transfer.

Fig. 4.56 shows the turbulent kinetic energy calculated by FLUENT in both RKE and SST models. The first 0.5 m (1–1.5 m) show the distance it takes for the solution to stabilize, and thus local prediction in this region is not representative of the experimental data. The cause for this is the large sudden addition of heat flux at the inlet after 20 cm of unheated development length, which causes the properties to be perturbed in the numerical solution before stabilizing.

The figures show a consistent rise in the turbulent energy at the center of the flow throughout the heated length, which remains higher than the fluid at the wall, as it is limited in turbulence to almost nil, due to the no-slip conditions in the solver.

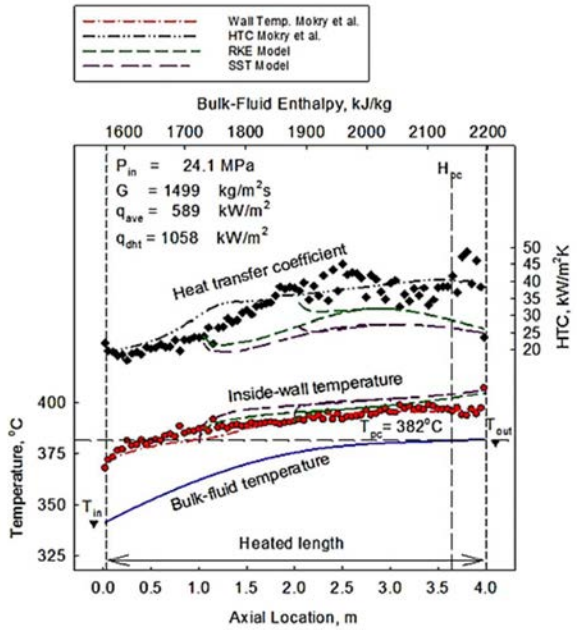

Fig. 4.55 Experimental, calculated and CFD simulated results for NHT in 2 m computational domains.

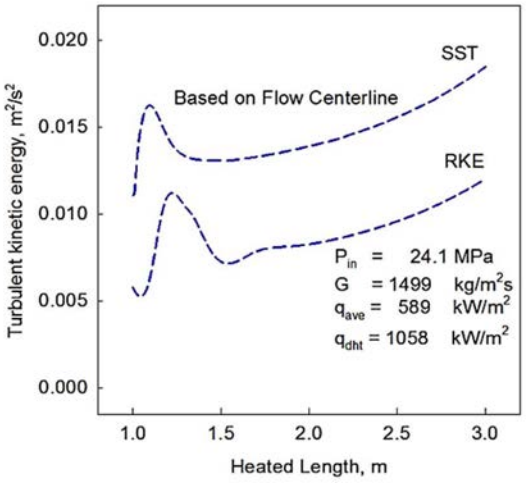

Fig. 4.56 Turbulent kinetic energy based on flow centerline for the RKE and SST models, 1–3 m.

4.5.13. TEMPERATURE, HTC, AND TURBULENT ENERGY – DETERIORATED HEAT TRANSFER REGIME

The DHT regime is then studied for heat fluxes well beyond the predicted onset of DHT (200 kW/m^2) to evaluate FLUENT's predictions in that regime. Fig. 4.57 shows a clear depiction of DHT near $x = 2$ m, where in the length of 1 m the temperature reaches a maximum before dropping slightly at which point the heat transfer is restored and a steady increase occurs after that until the outlet of the test section.

As far as the first half of the heated length is concerned, the rise in both bulk fluid and wall temperatures match that of the NHT regime, after that, the bulk fluid temperature flattens. This could be either due to passing through the pseudocritical point, the DHT phenomenon, or more likely, a combination of both occurring.

For the bulk fluid, passing through the pseudocritical point would reduce the density of the bulk fluid, causing an acceleration effect accompanied by the simultaneous reduction in thermal conductivity and corresponding spike in heat capacity means the fluid will not have a significant increase in temperature until passing through the pseudocritical region. These combined effects of the pseudocritical point mean a flattened temperature profile, seen through about a meter of heated length from 1.5–2.5 m. The DHT effect in the same time means lower heat transfer to the fluid from the wall, which raises the wall temperature and consequently lowers the rate of bulk fluid temperature increase.

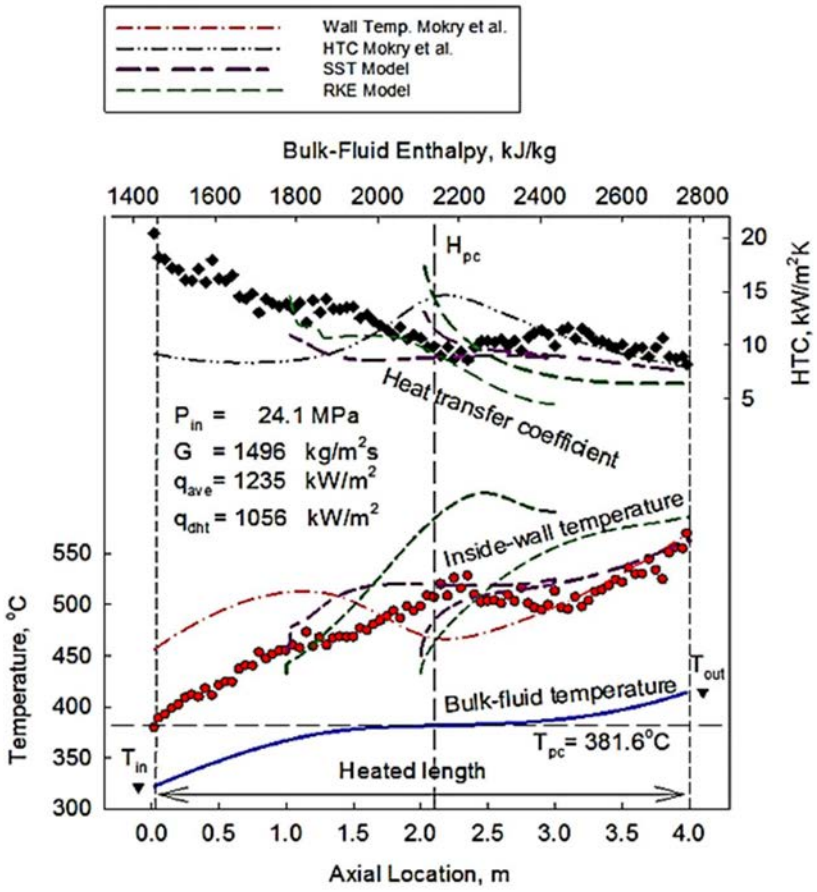

Fig. 4.57 Experimental, calculated and simulated results for DHT in 2 m computational domains.

The fluid at the wall on the other hand, at the inlet of the heated section is at a temperature just over the pseudocritical point, after which there's a similar drop in the density, viscosity, and thermal conductivity, as well as the heat capacity which reaches its peak at the inlet. The combination of these effects leads to the large overestimation of wall temperatures as seen by the Mokry et al. correlation [4.82], which continues for the next 1.25 m. A similar effect can be observed in the initial results of the turbulent models in Fig. 4.49; where the correlation shows the same behavior, as well as the RKE and SST models in the 4 m mesh, which appear to be affected by the same phenomenon.

After the first 2 m, the temperature at the wall reaches its maximum, where the constant addition of heat to the fluid reduces the density, viscosity and thermal conductivity further, causing the DHT phenomenon to occur. According to the hypothesis mentioned in the DHT section, this is due to the acceleration of the fluid near the wall, until the velocity profile flattens radially and the turbulence is suppressed. By suppressing turbulence, the heat transfer is deteriorated and the wall temperatures increase as the bulk fluid temperature does not.

After the region of deteriorated heat transfer, the velocity is expected to keep increasing at the wall, by the addition of more heat, surpassing the velocity of the bulk, which leads to an enhancement of heat transfer until the outlet of the test section.

From the temperature and HTC plots in Fig. 4.57, the RKE model seems to capture the DHT phenomenon in the 1–3 m length where it reaches the expected maximum and the following decrease with a deviation of about a 100 ºC above the experimental data. The 2–4 m test, however, shows less deviation (about 50 ºC) but without following the experimental data trend, and without showing continuity in the prediction between the 1–3 and 2–4 m range. This is a clue to possible fluid history effects, whereby the behavior of the fluid prior to the test section affects the prediction in subsequent sections. This may be particularly apparent near the pseudocritical region.

The SST model on the other hand, shows a very similar behavior to the case of the onset of DHT, where the increase in temperature is less pronounced than the RKE model and the continuity between the 1–3 and 2–4 m is preserved. The outlet temperatures are also well resolved for both cases and match the experimental values.

By examining these results from the turbulence kinetic energy point of view, the difference between the center and the wall should be decreased as the DHT occurs to suppress the turbulence in the fluid. This is shown in Fig. 4.58 where the RKE model captures that effect by suppressing the turbulence in the fluid at the maximum wall temperature location. The velocity at the wall does not surpass the bulk fluid because of the imposed no-slip conditions, which limits the velocity to almost nil for the entire heated length (at the first node from the wall). This suppression of the turbulence explains the overprediction of temperature seen in the RKE model throughout the DHT region and requires further investigation.

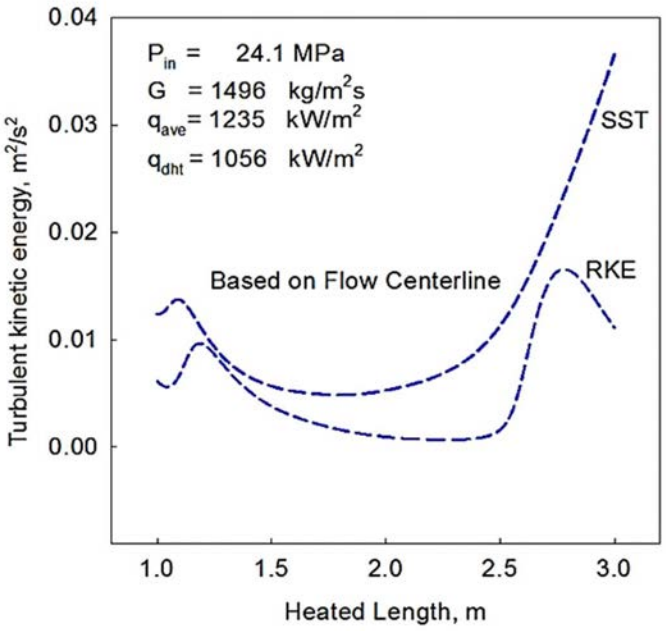

Fig. 4.58 kinetic energy based on flow centerline for the RKE and SST models, 1–3 m.

This suppression in turbulence is also shown in Fig. 4.58 when the turbulent kinetic energy lines are suppressed. It is, however, less pronounced in the case of SST model prediction, where it is about an order of magnitude lower than that predicted by RKE for the 1–3 m test. This leads to a lower wall temperature from the SST model as it does not suppress turbulence as much and thus the heat transfer capabilities are not lost.

Comparing these results to the DHT phenomenon explanation proposed by [4.84], it is apparent that the suppression of turbulence does in fact factor in the creation of DHT. What is not clear yet however, is the mechanism by which it happens, as the turbulent kinetic energy at the center of the flow drops to meet values at the wall, which are consistently low. As the driving force for turbulence is the velocity differential, this could mean the velocity at a layer near the wall increases enough to match that of the bulk fluid. Further analysis using 3D plots of the properties in the axial and radial directions is needed to visualize and understand the behavior of the fluid under DHT conditions.

4.5.14. ERROR ANALYSIS

To determine the extent of FLUENT's accuracy in predicting SCW flow and heat transfer phenomena, the CFD simulated data using RKE and SST models is compared to the experimental data and results obtained using 1D correlation for wall temperatures and heat transfer coefficients at the wall and for bulk fluid.

The Mokry et al. correlation [4.82] is used to represent 1D correlations for comparison since it was developed using this dataset. The errors associated with the correlation when predicting the cases studied in this publication are shown in Fig. 4.59 and Fig. 4.60. The deviation from experimental data reaches 20 % for cases showing DHT phenomena.

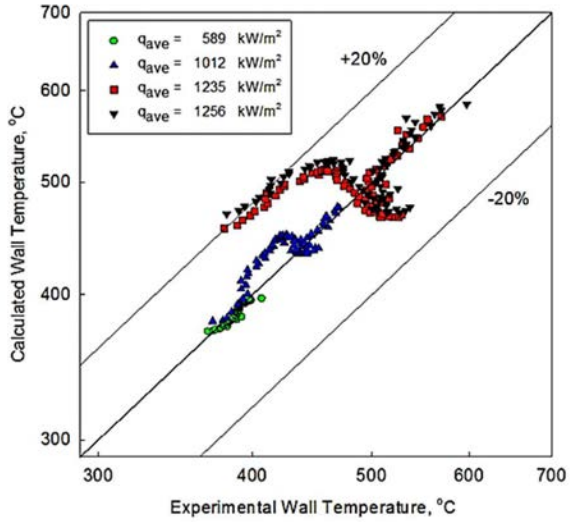

Fig. 4.59 Uncertainty in wall temperatures for correlation of Mokry et al. [4.82].

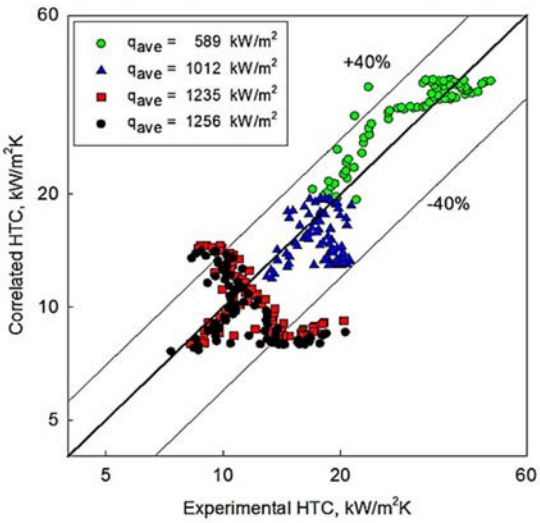

Fig. 4.60 Uncertainty in HTCs for correlation of Mokry et al. [4.82].

For the RKE and SST models in the NHT regime, the wall temperatures were resolved accurately where the maximum deviation was less than 5 % in both cases, as shown in Fig. 4.61 and Fig. 4.62. When compared to the experimental error in the dataset of 3 % (refer to Table 4.23), the combined uncertainty can be calculated as [4.90]:

$$u_T = \sqrt{(u_{Texp}^2 + u_{Tbias}^2)} = \sqrt{(3^2 + 5^2)} = 5.8\% \tag{4.71}$$

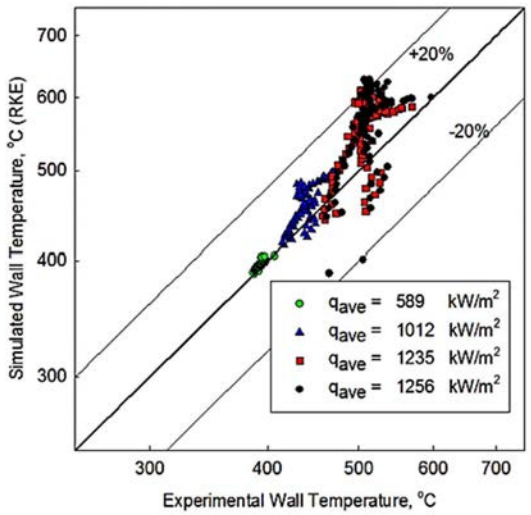

Fig. 4.61 Uncertainty in wall temperatures for RKE model.

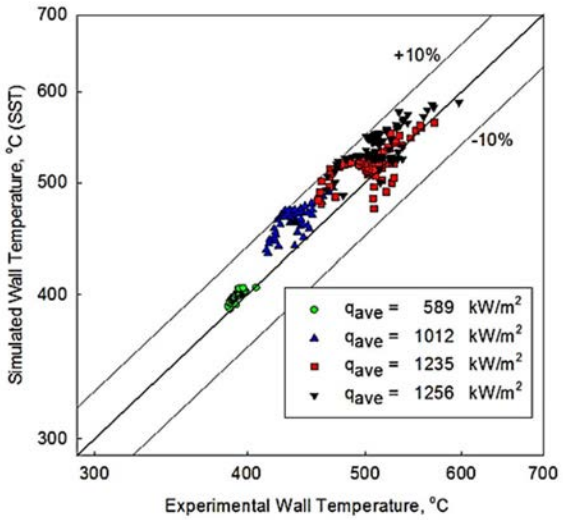

Fig. 4.62 Uncertainty in wall temperatures for SST model.

The error in temperatures for the DHT region, on the other hand, is ±20 % for the RKE model and ±10 % for the SST model. Both models tend to overestimate the temperatures in these regions, representing a conservative estimation; however, the RKE model deviates more from the experimental data for the DHT region.

In the correlation development, DHT points were eliminated from the study, along with the entrance region and outlier points. The purpose was to predict only the NHT regime. In this regime, the RKE and SST models achieve less than 5 %, and in the DHT region the SST model achieves a 10 % deviation, while the correlation reaches up to 20 %.

As for the HTC errors shown in Fig. 4.63 and Fig. 4.64, the RKE and SST models deviate by about 40 % from the experimental data for both NHT and DHT regimes. The SST model however, does underestimate the HTC values more than RKE for the DHT regime. The Mokry et al. correlation [4.82] deviates similarly at 40 % for NHT, however it does not predict the trend correctly for DHT and deviates by more than 40 %.

The results suggest that the normal and enhanced heat transfer are resolved reasonably well with the correlation, while the uncertainty increases with higher heat fluxes, where heat transfer to the

fluid begins to decrease. In the case of deteriorated heat transfer, the uncertainties will be higher than 40 %.

Overall, the SST model provides a better fit than the Mokry et al. correlation [4.82] for prediction of wall temperatures, while maintaining a more conservative approach in predicting higher wall temperatures than the experimental values in the DHT regime.

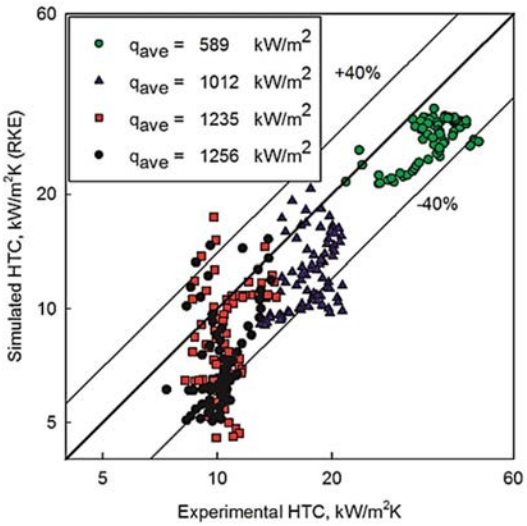

Fig. 4.63 Uncertainty in HTC values for RKE model.

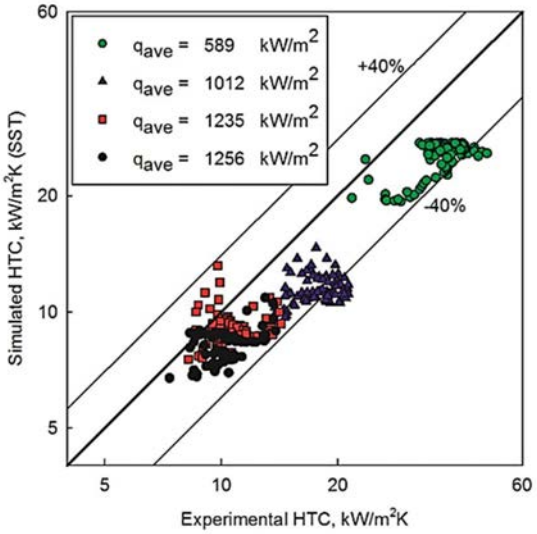

Fig. 4.64 Uncertainty in HTC values for SST model.

By studying the trends using the correlation prediction in the DHT regime (such as in Fig. 4.57), the errors in the DHT region for the correlation are explained. Due to the iterative nature of the correlation prediction, the temperatures are overestimated in the first section of the tube (NHT), and underestimated in the DHT region, and only match the experimental data in the last IHT section. This means the correlation can only be applied for cases where only NHT is present. This also leads to the error graphs showing no trends in the prediction, whilst the SST model shows a valid trend, following the temperature profiles.

Nomenclature and Acronyms

A	area, m^2
c_p	specific heat, J/kg · K
C_1	empirical constant, -
D	diameter, m
D_{hy}	hydraulic equivalent diameter, m $\left(\frac{4\,A_{fl}}{p_h}\right)$
dx	step axial length change, m
g	Gravitational acceleration, m/s^2
G	mass flux, kg/m^{2}s $\left(\frac{\dot{m}}{A_{fl}}\right)$
HTC	Heat Transfer Coefficient, W/m^{2}K

h	specific enthalpy, $\mathrm{J/kg}$
i	axial step position
k	thermal conductivity, $\mathrm{W/m \cdot K}$
L	length, m
$\dot{m}$	mass flow rate, $\mathrm{kg/s}$
P	pressure, Pa
p	perimeter, m
q	heat flux, $\mathrm{W/m^2}$
T	temperature,°C
x	axial position, m

Greek Letters

α	heat transfer coefficient, $\mathrm{W/m^2/K}$
μ	dynamic viscosity, $\mathrm{Pa \cdot s}$
ν	kinematic viscosity, $\mathrm{m/s^2}$
ρ	density, $\mathrm{kg/m^3}$

Non-dimensional Numbers

Bo*	dimensionless buoyance number, -
Gr	Grashof number, -
Nu	Nusselt number $\left(\frac{HTC \cdot D_{hy}}{k}\right)$, -
Pr	Prandtl number $\left(\frac{\mu \cdot c_p}{k}\right)$, -
Re	Reynolds number $\left(\frac{GD_{hy}}{\mu_b}\right)$, -

Subscripts

b	Bulk fluid
calc	calculated
cr	critical point
dht	deteriorated heat transfer
eqv	equivalent
Exp	Experimental
in	inlet
fl	flow
h	heated
out	outlet
pc	pseudocritical point
w	wall
wet	wetted

Abbreviations and Acronyms

AC	Alternating Current
DHT	Deteriorated Heat Transfer
EHT	Enhanced Heat Transfer

HT	Heat Transfer
HTC	Heat Transfer Coefficient
ID	Inner Diameter
KPI	Kiev Polytechnic Institute
MAX	Maximum
NHT	Normal Heat Transfer
NPP	Nuclear Power Plant
NTUU	National Technical University of Ukraine "Igor Sikorsky Kiev Polytechnic Institute" (Kiev, Ukraine)
OD	Outer Diameter
SCF	SuperCritical Fluid
SCP	SuperCritical Pressure
SCW	SuperCritical Water
SCWR	SuperCritical Water cooled Reactor
SMR	Small Modular Reactor
UOIT	University of Ontario Institute of Technology (Oshawa, Ontario, Canada)

REFERENCES TO SECTION 4

[4.1] SHITSMAN, M.E., Impairment of the heat transmission at supercritical pressures, J High Temp., **1** 2 (1963), 237–244.

[4.2] KISS, A., Thermal Hydraulic Investigations of the Coolant Flow in Supercritical Water-cooled Reactor Relevant Geometries, Budapest University of Technology & Economics, Ph.D. Dissertation, (2018).

[4.3] HENDRICKS, R.C., SIMONEAU, R.J., SMITH, R.V., Survey of Heat Transfer to Near-Critical Fluids, Report No. NASA TN-D-5886, Lewis Research Center (Report No. E-5084), NASA, Cleveland, (1970).

[4.4] ORNATSKIY, A.P., GLUSHCHENKO, L.F., KALACHEV, S.I., Heat transfer with rising and falling flows of water in tubes of small diameter at supercritical pressures, Therm Eng, **18** 5 (1971), 137–141.

[4.5] ACKERMAN, J.W., Pseudo-boiling heat transfer to supercritical pressure water in smooth and ribbed tubes, J Heat Transfer, Trans. ASME, **92** 3 (1970), 490–498.

[4.6] YAMAGATA K., NISHIKAWA K., HASEGAWA S., FUJI T., YOSHIDA S., Forced convective heat transfer to supercritical water flowing in tubes, J Heat Mass Transfer, **15** 12 (1972), 2575–2593.

[4.7] JACKSON, J.D., FEWSTER, J., Forced Convection Data for Supercritical Pressure Fluids, HTFS 1975, Paper No. 21540, 1975.

[4.8] MCADAMS, W.H., KENNEL, W.H., ADDOMS, J.N., Heat Transfer to Superheated Steam at High Pressure, Trans. ASME, **72** 4 (1950) 421–428.

[4.9] HALL, W.B., "Heat transfer near the critical point", Advances in Heat Transfer (IRVINE, T.F, HARTNETT, J.P., Eds.), Academic Press, New York, **7** (1971), 1–86.

[4.10] PIORO, I.L., DUFFEY, R.B., Heat Transfer and Hydraulic Resistance at Supercritical Pressures in Power Engineering Applications, ASME Press (2007).

[4.11] KISS, A., ASZÓDI, A., Summary for Three Different Validation Cases of Coolant Flow in Supercritical Water Test Sections with the CFD Code ANSYS CFX 11.0, Nuclear Technology, **170** 1 (2010), 40–53.

[4.12] KAO,, M.-T., LEE, M., FERNG, Y.-M., CHIENG, C.-C., Heat Transfer Deterioration in a Supercritical Water Channel, Nucl. Eng. Des., **240, 10**, (2010), 3321–3328.
[4.13] MIHEJEV, M.A., Fundamentals of the Practical Calculations of Heat Transfer, 6th Hungarian Edition. Tankönyvkiadó, Budapest, (1987).
[4.14] MA, D., ZHOU, T., LI, B., MUHAMMAD, A.S., HUANG, Y., An Improved Correlation on the Onset of Heat Transfer Deterioration in Supercritical Water, Nucl. Eng. Des., **326**, (2018), 290–300.
[4.15] KISS, A., MERVAY, B., Numerical Analysis on the Effect of Wrapped Wire Spacers on Thermal Hydraulics in a Four Rod Fuel Bundle, Proc. 26th Symposium of AER on VVER Reactor Physics and Reactor Safety, Helsinki, 2016.
[4.16] KISS, A., MERVAY, B., Numerical Analysis on the Thermal Hydraulic Effect of Wrapped Wire Spacer in a Four-Rod Fuel Bundle, Nucl. Eng. Des., **342**, (2019), 276–307.
[4.17] SCHULENBERG, T., STARFLINGER, J., High Performance Light Water Reactor - Design and Analyses, KIT Scientific Publishing, Karlsruhe (2012).
[4.18] PIORO, I.L., DUFFEY, R.B., Experimental Heat Transfer in Supercritical Water Flowing inside Channels (Survey), Nucl. Eng. Des., **235, 22**, (2005), 2407–2430.
[4.19] PALKO, D., ANGLART, H., Investigation of the Onset of Heat Transfer Deterioration to Supercritical Water, Proc. 4th International Symposium on SCWRs, Heidelberg, 2009.
[4.20] KISS, A., ASZÓDI, A., Sensitivity Studies on CFD Analysis for Heat Transfer of Supercritical Water Flowing in Vertical Tubes, Proc. Experimental Validation and Application of CFD and CMFD Codes in Nuclear Reactor Technology (CFD4NRS-4 conference), Daejeon, 2012.
[4.21] KISS, A., ASZÓDI, Numerical Investigation on the Physical Background of Deteriorated Heat Transfer Mode in Supercritical Pressure Water, Proc. 6th International Symposium on Supercritical Water-Cooled Reactors (ISSCWR-6), Shenzhen, 2013.
[4.22] MIKIELEWICZ, D.P., SHEHATA, A.M., JACKSON, J.D., MCELIGOT, D.M., Temperature, Velocity and Mean Turbulence Structure in Strongly Heated Internal Gas Flows: Comparison of Numerical Predictions with Data, J. Heat Mass Transf., **45**, (2002), 4333–4352.
[4.23] BANKSTON, C.A., MCELIGOT, D.M., Turbulent and Laminar Heat Transfer to Gases with Varying Properties in the Entry Region of Circular Ducts, Int J. Heat Mass Transf., **13**, (1970), 319–344.
[4.24] MCELIGOT, D.M., COON, C.W., PERKINS, H.C., Relaminarization in Tubes, Int J. Heat Mass Transf., **9**, (1970), 1151–1152.
[4.25] MCELIGOT, D.M., JACKSON, J.D., Deterioration' Criteria for Convective Heat Transfer in Gas Flow through Non-Circular Ducts, Nucl. Eng. Des., **232, 3**, (2004), 327–333.
[4.26] JACKSON, J.D., COTTON, M.A., AXCELL, B.P., Studies of Mixed Convection in Vertical Tubes, Int. J. Heat Fluid Flow, **10, 1**, (1989), 2–15.
[4.27] LI, J.K., Studies of Buoyancy-Influenced Convective Heat Transfer to Air in a vertical Tube, Ph.D. thesis, University of Manchester, 1994.
[4.28] JACKSON, J.D., HALL, W.B., Influence of Buoyancy on Heat Transfer to Fluids Flowing in Vertical Tubes under Turbulent Conditions, Hemisphere Publishing Company, Turbulent Forced Convection in Channels and Bundles, **2**, (1979), 613–640.
[4.29] MCADAMS, W.H., Heat Transmission, 2nd edition, McGraw-Hill, New York, (1942).

[4.30] JACKSON, J.D., Consideration of the Heat Transfer Properties of Supercritical Pressure Water in Connection with the Cooling of Advanced Nuclear Reactors, Proc. 13th Pacific Basin Nuclear Conference, Shenzhen, 2002.
[4.31] VIJAYAN, P.K., SHARMA, M., PILKHWAL, D.S., Steady State and Stability Characteristics of a Supercritical Pressure Natural Circulation Loop (SPNCL) with CO_2, BARC--2013/E/003, India, 2013.
[4.32] KISS, A., BALASKÓ, M., HORVÁTH, L., KIS, Z., ASZÓDI, A., Experimental Investigation of the Thermal Hydraulics of Supercritical Water under Natural Circulation in a Closed Loop, Annals of Nuclear Energy, **100, 2**, (2017), 178–203.
[4.33] CHEN, Y., ZHAO, M., BI, K., YANG, B., ZHANG, D., DU, K., Critical Heat Flux of Flowing Water in Tube for Pressure Up to Near Critical Point—Experiment and Prediction, J Nuclear Engineering and Radiation Science, 4, 1, (2018), 011006-1.
[4.34] ZAHLAN, H., GROENEVELD, D., TAVOULARIS, S., Measurements of Convective Heat Transfer to Vertical Upward flows of CO_2 in Circular Tubes at Near-Critical and Supercritical Pressures, Nuclear Engineering and Design, **249**, (2015), 92–107.
[4.35] FEUERSTEIN, F., COELHO SILVA, A., KLINGEL, D., CHENG, X., Large-Scale Heat Transfer Experiments with Supercritical R134a Flowing Upward in a Circular Tube, Proc. 47th Annual Meeting on Nuclear Technology (AMNT-16), Hamburg, 2016.
[4.36] PIS'MENNY, E.N., RAZUMOVSKIY, V.G., MAEVSKIY, E.M., KOLOSKOV, A.E., PIORO, I.L., "Heat transfer to supercritical water in gaseous state or affected by mixed convection in vertical tubes", in Proc. 14th Int. Conf. On Nuclear Engineering (ICONE-14), Miami, 2006, ASME, New York (2006).
[4.37] WaterSteamPro software.
[4.38] STYRIKOVICH, V.A., SHITSMAN, M.YE., MIROPOL'SKIY, Z.L., Some Data on Temperature Regimes of Vertical Boiling Tube under Near-Critical Pressures., Heat Power Engineering (Tyeploenergyetika), **12**, (1955), 32–36, (In Russian).
[4.39] PETUKHOV, B.S., KIRILLOV, V.V., On Heat Exchange under Turbulent Flow of Liquid in Tubes, Heat Power Engineering (Tyeploenergyetika), **4**, (1958), 63–68 (In Russian).
[4.40] FILONENKO, G.K., Hydraulic Resistance of Pipelines, Thermal Engineering (Tyeploenergyetika), **4**, (1954), 40–44 (In Russian).
[4.41] PETUKHOV, B.S., GRYGOR'YEV, V.S., POLYAKOV, A.F., et al., Experimental Research of Heat Exchange in Tubes under Variable Heat Flux through Their Walls, Heat Transfer Exchange-V, Minsk, **1, 1**, (1976), (In Russian).
[4.42] ANKUDINOV, V.B., Experimental Study of Friction Resistance and Heat Exchange under Turbulent Flow of Supercritical Fluid in Tubes, Cand. of Sc. Thesis, IVTAN, Moscow, 1982 (In Russian).
[4.43] PETUKHOV, B.S., MEDVYEDSKAYA, N.V., Turbulent Flow and Heat Transfer in Vertical Tubes under Strong Effect of Buoyancy, Thermophysics of High Temperatures (Tyeplofizika Vysokikh Tyempyeratur), **16, 4**, (1978), 778–786 (In Russian).
[4.44] HALL, W.B., JACKSON, J.D., Heat Transfer near the Critical Point, Proc. 6th Int. Heat Transfer Conf., **6**, (1979), 377–392.
[4.45] SHIRALKAR, B.S., GRIFFITH P., Deterioration in Heat Transfer to Fluids near Critical Point Flowing in Circular Tube, J. Heat Transfer, 91, 1, (1969), 27–36.
[4.46] VIKHREV YU., V. et al., Temperature Profiles on Steam-Generating Channels under Supercritical Pressures, The 4th All-Union Conference on Heat Transfer and Hydraulic

Resistance to Two-Phase Flow in the Components of Electrical Machines and Apparatuses, Part 1, 1971 (In Russian).
[4.47] PETUKHOV, B.S., PROTOPOPOV, V.S., SILIN, V.A., Experimental Investigation of the Modes of Deteriorated Heat Exchange under Turbulent Flow of Carbon Dioxide at Supercritical Pressure, Thermophysics of High Temperatures, **10, 2**, (1972), 347, (In Russian).
[4.48] GABARAYEV, B.A., SMOLIN, V.N., SOLOV'YOV, S.L., Promising Trend in Development of NPP Water-Cooled Reactors in 21st Century: Implementation of Coolant Supercritical Parameters, Thermal Engineering (Tyeplotyekhnika), **9**, (2006), 33, (In Russian).
[4.49] GRABYEZHNAYA, V.A., KIRILLOV, P.L., Heat Exchange under Supercritical Pressures and Boundaries of Heat Exchange Deterioration, Thermal Engineering, **4**, (2006), 46–51, (In Russian).
[4.50] MOKRY, S., PIORO, I.L., FARAH, A., KING, K., GUPTA, S., PEIMAN, W., KIRILLOV, P.L., Development of Supercritical Water Heat-Transfer Correlation for Vertical Bare Tubes, Nuclear Engineering and Design, 241, (2011), 1126–1136.
[4.51] KURGANOV, V.A., ZEIGARNIK, Y.A., YAN'KOV, G.G., MASLAKOVA, I.V., Heat Exchange and Resistance in Tubes under Supercritical Pressures of Coolant: Resume of Scientific Research and Practical Recommendations, Shans Publ. House, 2018 (In Russian).
[4.52] POLYAKOV, A.F., On Mechanism and Boundaries of Onset of the Regimes with Deteriorated Heat Transfer at Supercritical Pressure of Coolant, Thermophysics of High Temperatures, **13, 6**, (1975), 1210–1219, (In Russian).
[4.53] BISHOP, A.A., SANDBERG, L.O., TONG, L.S., Forced Convection Heat Transfer to Water at Near-Critical Temperature and Supercritical Pressures, Westinghouse Electric Corporation Report (WCAP-2056), Pittsburg, 1964.
[4.54] KIRILLOV, P.L., POMET'KO, R., SMIRNOV, A., GRABEZHNAIA, V., PIORO, I., DUFFEY R., KHARTABIL, H., Experimental Study on Heat Transfer to Supercritical Water Flowing in 1- and 4-m Long Vertical Tubes, Proc. GLOBAL 2005, Tsukuba, 2005.
[4.55] SWENSON, H.S., CARVER, J.R., KAKARALA, C.R., Heat transfer to Supercritical Water in Smooth-Bore Tubes, J Heat Transfer, **87**, **4**, (1965), 477–484.
[4.56] MIKHEYEV, M.A., Principals of Heat Transfer, 3rd Edition, Gosenergoizdat Publ. House, 1956.
[4.57] KRASNOSHCHYOKOV, E,A., PROTOPOPOV, V.S., Experimental Investigation of Carbon Dioxide Heat Exchange in Supercritical Region under High Temperature Head, Tyeplofizika Vysokikh Tyempyeratur, **4, 3**, (1966), 389–398.
[4.58] DYADYAKIN, B.V., POPOV, A.S., Heat Transfer and Thermal Resistance of Tight Seven-Rod Bundle Cooled with Water Flow at Supercritical Pressures, Transactions of VTI, **11**, (1977), 244–253, (In Russian).
[4.59] JACKSON, J.D., HALL, W.B., Forced Convection Heat Transfer to Fluids at Supercritical Pressure, Turbulent Forced Convection in Channels and Bundles, Editors: S. Kakaç and D.B. Spalding, Hemisphere Publishing Corp., New York, **2**, (1979), 563–612.
[4.60] ORNATSKY, A.P., GLUSHCHENKO, L.P., SIOMIN, E.T., KALACHYOV, S.I., The Research of Temperature Conditions of Small Diameter Parallel Tubes Cooled by Water

under Supercritical Pressures, Proc. 4th International Heat Transfer Conference, Paris-Versailles, 1970.
[4.61] FILONOV, V.V., FILONOVA, YU.S,, RAZUMOVSKIY, V.G., PIS'MENNYI E.N., On Experimental and Computational Investigation of Heat Transfer Deterioration and Hydraulic Resistance in Annular Channel and SCWR 3-Rod Bundle, Proc. 26th International Conference on Nuclear Engineering (ICONE-26), London, 2018.
[4.62] WU, G., BI, Q., YANG, Z., WANG, H., ZHU, X., HAO, H., LEUNG, L.K.H., Experimental Investigation of Heat Transfer for Supercritical Pressure Water Flowing in Vertical Annular Channels, Nuclear Engineering Design, **241, 9**, (2011) 4045–4054.
[4.63] CHENG, X., LIU, X.J., GU, H.Y., Fluid-To-Fluid Scaling of Heat Transfer in Circular Tubes Cooled with Supercritical Fluids, Nuclear Engineering and Design, 241, (2011), 498–508.
[4.64] GORBAN', L.M., POMET'KO, R.S., KHRYASCHEV, O.A., Modeling of Water Heat Transfer with Freon of Supercritical Pressure, FEI-1766, Institute of Physics and Power Engineering, Obninsk, Russia, 1990 (in Russian).
[4.65] GUPTA, S., SALTANOV, EU., MOKRY, S.J., PIORO, I., TREVANI, L., MCGILLIVRAY, D., Developing Empirical Heat-Transfer Correlations for Supercritical CO_2 Flowing in Vertical Bare Tubes, Nuclear Engineering and Design, **261**, (2013), 116–131.
[4.66] ZAHLAN, H., GROENEVELD, D.C., TAVOULARIS, Fluid-to-Fluid Scaling for Convective Heat Transfer in Tubes at Supercritical and High Subcritical Pressures, Int. J. of Heat and Mass Transfer, **73**, (2014), 274–283.
[4.67] JACKSON, J.D., A Semi-Empirical Model of Turbulent Convective Heat Transfer to Fluids at Supercritical Pressure, Proc. 16th Int. Conf. on Nuclear Engineering, Orlando, 2008.
[4.68] ZAHLAN, H., GROENEVELD, D.C., TAVOULARIS, S., A Look-Up Table for Trans-Critical Heat Transfer for Water Cooled Tubes, Proc. 3rd China-Canada Joint Workshop on Supercritical Water-cooled Reactors (CCSC-2012), Xi'an, 2012.
[4.69] AMBROSINI, W., SHARABI, M., Dimensionless Parameters in Stability Analysis of Heated Channels with Fluids at Supercritical Pressures, Nucl. Eng. Des., **238**, (2008), 1917–1929.
[4.70] AMBROSINI, W., Discussion of Similarity Principles for fluid-To-fluid Scaling of Heat Transfer Behaviour at Supercritical Pressures, Nuclear Engineering and Design, **241**, (2011), 5149–5173.
[4.71] AMBROSINI, W., DE ROSA, M., Application of Similarity Principles for Heat Transfer and Fluid-Dynamics to Different Fluids at Supercritical Pressure, Proc. 5th Int. Sym. SCWR (ISSCWR-5), Vancouver, 2011.
[4.72] PUCCIARELLI, A., AMBROSINI, W., Fluid-to-Fluid Scaling of Heat Transfer Phenomena with Supercritical Pressure Fluids: Results from RANS Analyses, Annals of Nuclear Energy, **92**, (2016), 21–35.
[4.73] CD-Adapco, 2012. USER GUIDE STAR-CCM+ Version 7.04.006.
[4.74] PIS'MENNYY, E.N., RAZUMOVSKIY, V.G., MAEVSKIY, E.M. KOLOSKOV, A.E., PIORO, I.L., DUFFEY, R.B., "Experimental study on temperature regimes to supercritical water flowing in vertical tubes at low mass fluxes", in Proc. Int. Conference GLOBAL-2005, Tsukuba, 2005, Atomic Energy Society of Japan, Tokyo (2005).

[4.75] FARAH, A., HARVEL, G., PIORO, I., Analysis of computational fluid dynamics code FLUENT capabilities for supercritical water heat-transfer applications in vertical bare tubes, ASME Journal of Nuclear Engineering and Radiation Science 2 (2016).
[4.76] SHARABI, M., AMBROSINI, W., FORGIONE, N., HE, S., "SCWR rod bundle thermal analysis by a CFD Code", in Proc. International Conference on Nuclear Engineering (ICONE-16), Orlando, 2008, Atomic Energy Society of Japan (2008).
[4.77] Handbook of Generation IV Nuclear Reactors, Editor: I.L. Pioro, Elsevier – Woodhead Publishing, Duxford, (2016).
[4.78] HOLLOWAY, M.V., BEASLEY D.E., Investigation of Swirling Flow in Rod Bundle Subchannels Using CFD, Proc. International Conference on Nuclear Engineering (ICONE-14), Miami, 2006.
[4.79] MUHANA, A., NOVOG, D.R., Validation of FLUENT for Prediction of Flow Distribution and Pressure Gradients in a Multi-Branch Header Under Low Flow Conditions, Proc. International Conference on Nuclear Engineering (ICONE-16), Orlando, 2008.
[4.80] PIETRALIK, J., SMITH, B.A., CFD Application to FAC in Feeder Bends, Proc. International Conference on Nuclear Engineering (ICONE-14), Miami, 2006..
[4.81] VANYUKOVA, G.V., KUZNETSOV, Yu.N., LONINOV, A.Ya., PAPANDIN, M.V., SMIRNOV, V.P., PIORO, I.L., "Application of CFD-code to calculations of heat transfer in a fuel bundle of SCW pressure-channel reactor", in Proc. 4th International Symposium on Supercritical Water-Cooled Reactors (ISSCWR-4), Heidelberg (2009).
[4.82] INTERNATIONAL ATOMIC ENERGY AGENCY, Heat Transfer Behaviour and Thermohydraulics Code Testing for Supercritical Water Cooled Reactors (SCWRs), IAEATECDOC-1746, IAEA, Vienna (2014).
[4.83] NATIONAL INSTITUTE OF STANDARDS AND TECHNOLOGY, NIST Reference Fluid Thermodynamic and Transport Properties - REFPROP, Standard Reference Database 23, Ver. 9.1, Department of Commerce, Boulder, CO, USA, 2013.
[4.84] AMBROSINI, W., FORGIONE, N., BADIALI, S., JACKSON, J.D., SHARABI, M., Capabilities of Two-Equation Low-Reynolds Number Turbulence Models in Predicting Heat Transfer to Fluids at Supercritical Pressure, Proc. 15th International Topical Meeting on Nuclear Reactor Thermalhydraulics (NURETH-15), Pisa, 2013.
[4.85] SHIRALKAR, B.S., GRIFFITH P., The Deterioration in Heat Transfer to Fluids at Supercritical Pressure and High Heat Fluxes, Report No. DSR 70332-55, Department of Mechanical Engineering, Massachusetts Institute of Technology, Cambridge, MA, USA, 1968.
[4.86] KOSHIZUKA, S., TAKANO, N., OKA, Y., Numerical Analysis of Deterioration Phenomena in Heat Transfer to Supercritical Water, Int. J. Heat Mass Transfer, **38, 16**, (1995), 3077–3084, 1995.
[4.87] CHENG, X., SCHULENBERG, T., KOSHIZUKA, S., OKA, Y., SOUYRI, A., Thermal-Hydraulic Analysis of Supercritical Pressures Light Water Reactors, Proc. International Congress on Advances in Nuclear Power Plants (ICAPP), Hollywood, 2002.
[4.88] GABARAEV, B.A., KUZNETSOV, Yu.N., PIORO, I.L., DUFFEY, R.B., "Experimental study on heat transfer to supercritical water flowing in 6-m long vertical tubes", in Proc. 15th International Conference on Nuclear Engineering (ICONE-15), Nagoya, 2007.

[4.89] WITHAG, J., SALLEVELT, J., BRILMAN, BRAMER, D.E., BREM, G., Heat Transfer Characteristics of Supercritical Water in a Tube: Application for 2D and an Experimental Validation, Journal of Supercritical Fluids, **70**, (2012), 156–170.
[4.90] MALHOTRA, A., KANG, S.S., Turbulent Prandtl number in circular pipes, International Journal of Heat and Mass Transfer, **27, 11**, (1984), 2158–2161.

5. HEAT TRANSFER CHARACTERISTICS IN ROD BUNDLES

Previous experimental studies on heat transfer at supercritical pressures were performed using simple channels such as tubes and annuli [5.1], [5.2]. Experimental data obtained from these studies were applied in improving the understanding of the phenomena and developing correlations (e.g., Jackson [5.3]) for subchannel-code applications in support of design and optimization of SCWR fuel assemblies. These data or studies, however, are not applicable for examining the complex heat transfer characteristics in bundles, such as flow and enthalpy imbalances, spacing devices, axial and radial power distributions, gap size and others. In addition, the occurrence of the deteriorated heat transfer phenomena at one side of the fuel rod could lead to a non-uniform circumferential cladding temperature distribution causing the fuel rod to bow, which reduces the gap size and adversely impacting the cladding temperature further. Current prediction methods (such as applying correlations of Dittus–Boelter [5.4] and of Jackson [5.3]) have to be revised to account for various separate effects on heat transfer at supercritical pressures.

The present section summarizes the latest experimental studies on heat transfer at supercritical pressures with bundle subassemblies. It serves as a review of the complex heat-transfer characteristics in bundles and as a supplement to previous study [5.5].

Heat transfer experiments performed with bundle subassemblies at supercritical pressures are summarized in following subsections. The compilation focused on those experiments with water as the working fluid and includes 2x2 rod bundles (such as [5.6]), 3-rod and 7-rod bundles. In addition, supplemental information from experiments using surrogate fluids is included to enhance the understanding of the complex phenomena. A series of heat transfer experiments were performed with refrigerant and carbon dioxide flow through 3-rod and 7-rod bundles at supercritical pressures [5.7], [5.8]. These experiments provided data for developing prediction methods and validating subchannel codes as well as computational fluid dynamics tools.

5.1. HEAT TRANSFER IN 4-ROD BUNDLE COOLED WITH WATER

[5.9] performed heat-transfer experiments with water flowing through a 2×2 rod bundle at supercritical pressures. As illustrated in Fig. 5.1, the test section in the heated region consisted of an outer unheated stainless steel tube, which served as the pressure boundary, and a square insulator (20.32×20.32 mm^2) for electrical isolation of the heated bundle from the outer tube. Fibre-glass insulation was installed outside of the outer tube to minimize heat loss.

The rod bundle was constructed with four stainless steel (SS–304) tubes of 8 mm in outer diameter and 1.5 mm in wall thickness. Gaps between two heated rods and between the heated rod and the ceramic insulator were maintained at 1.44 mm. The bundle was equipped with two grid spacers at locations just outside of the heated section. These spacers maintained the gap size between the heated rod and the ceramic insulator. Spacings between heated rods within the heated section were maintained with welds at two locations (as shown in Fig. 5.2).

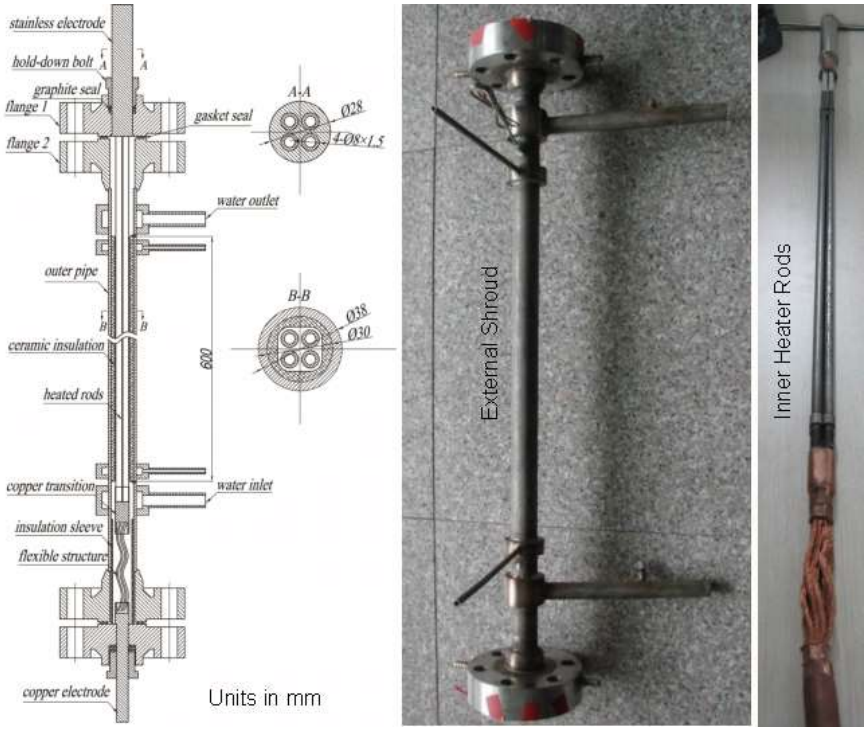

Fig. 5.1. Setup of the 4-rod bundle test section.

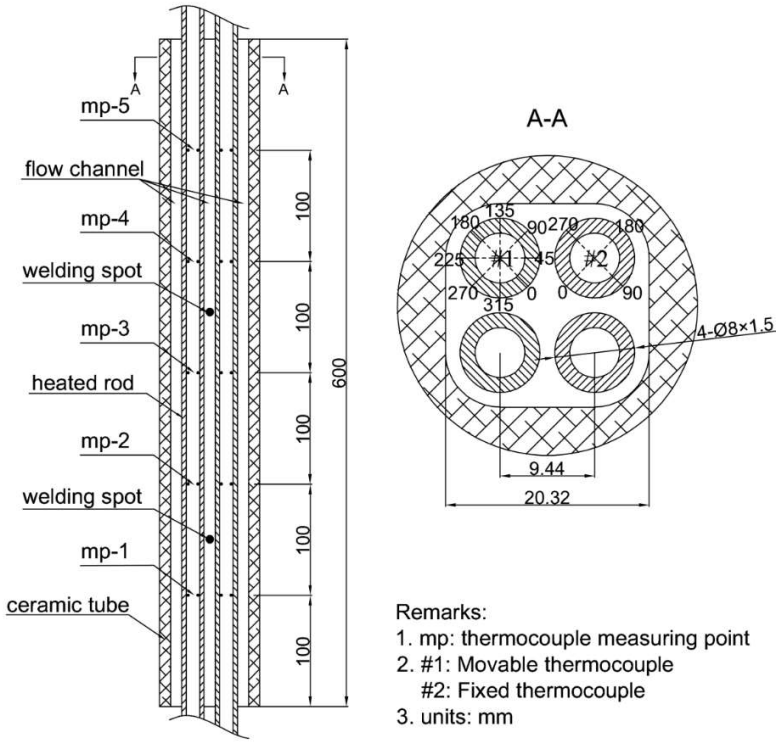

Fig. 5.2. Thermocouple measuring points and the cross section of the flow channel.

The rod was heated with electric current (joule heating). A silver coating was plated at both ends of each rod to minmize electrical resistance and power generation. This has resulted in an overalll heated length of 600 mm. The top end of rods was fixed while the bottom end was connected to copper wire ribbons, which was subsequently connected to the copper electrode, allowing thermal expansion.

Two of the four rods in the bundle were equipped with thermocouples to measure inner surface temperature (as shown in Fig. 5.2). Rod #1 contained a set of moveable thermocouples, which was attached to a transversable mechanism, as showin in Fig. 5.3. These thermocouples were rotated four times at an interval of 22.5° around the rod circumference at five locations identified as "mp-1" to "mp-5" in Fig. 5.2. Rod #2 contained four sets of fixed thermocouples installed at a location 100 mm upstream of the end of the heated length (which was the same as the "mp-5" location in Rod #1). These thermocouples measured inner surface temperatures of the rod at angles 0°, 90°, 180° and 270° (where 0° angle was located at the central subchannel of the bundle).

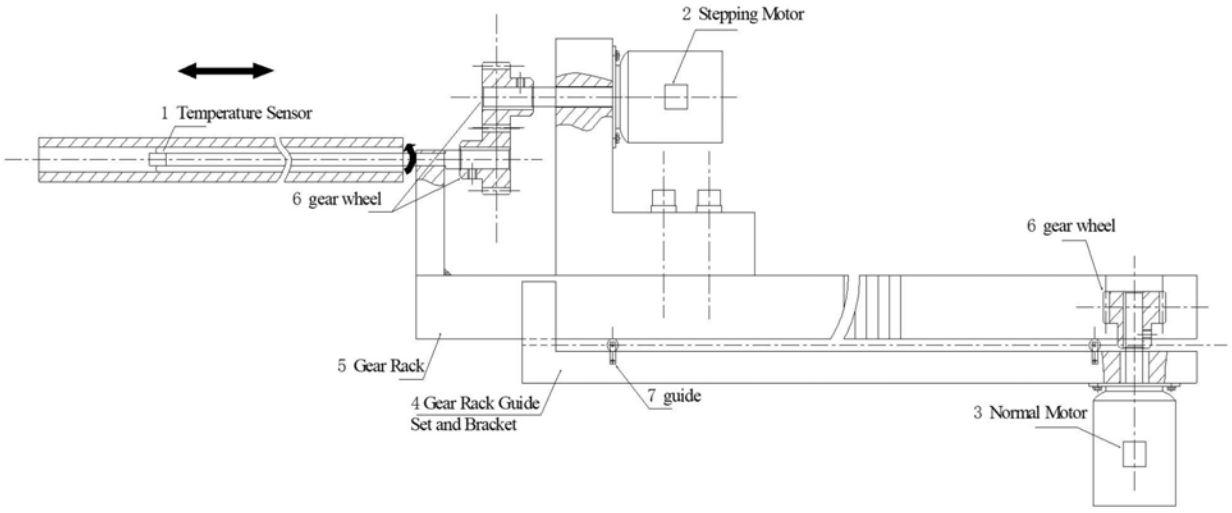

Fig. 5.3. Schematic diagram of the moveable thermocouple drive assembly unit.

[5.9] performed steady-state experiments at inlet pressures varying from 23 to 28 MPa, mass flow rates from 0.065 to 0.186 kg/s, powers from 12.1 to 60.5 kW and inlet fluid temperatures from 200 to 450 °C. They observed variations in surface temperature around the heated rods with the lowest surface temperature observed at the subchannel and the highest at the narrow gap between the heated rod and the ceramic insulator (i.e., 180° angle). Comparisons of results between moveable and fixed thermocouples in Rod #1 and Rod #2, respectively, showed good agreement in measured surface temperatures at the location 100 mm upstream of the end of the heated length. This confirmed the adequacy in using the moveable thermocouples to measure the surface temperatures at other locations.

Fig. 5.4 illustrates the change in circumferential outer wall temperature distributions with increasing inlet fluid temperature at the fifth thermocouple measuring point (mp-5) at the pressure of 25 MPa, mass flux of 1000 kg/m^{2}s and surface heat flux of 600 kW/m^2. Wall temperatures are significantly higher at angles of 135°, 180° and 225° than those of other angles, demonstrating the

relatively poor heat transfer at the corner region. Heat transfer is more efficient at the surface facing the central subchannel (i.e., angles of 0° or 45°) with corresponding low wall temperatures.

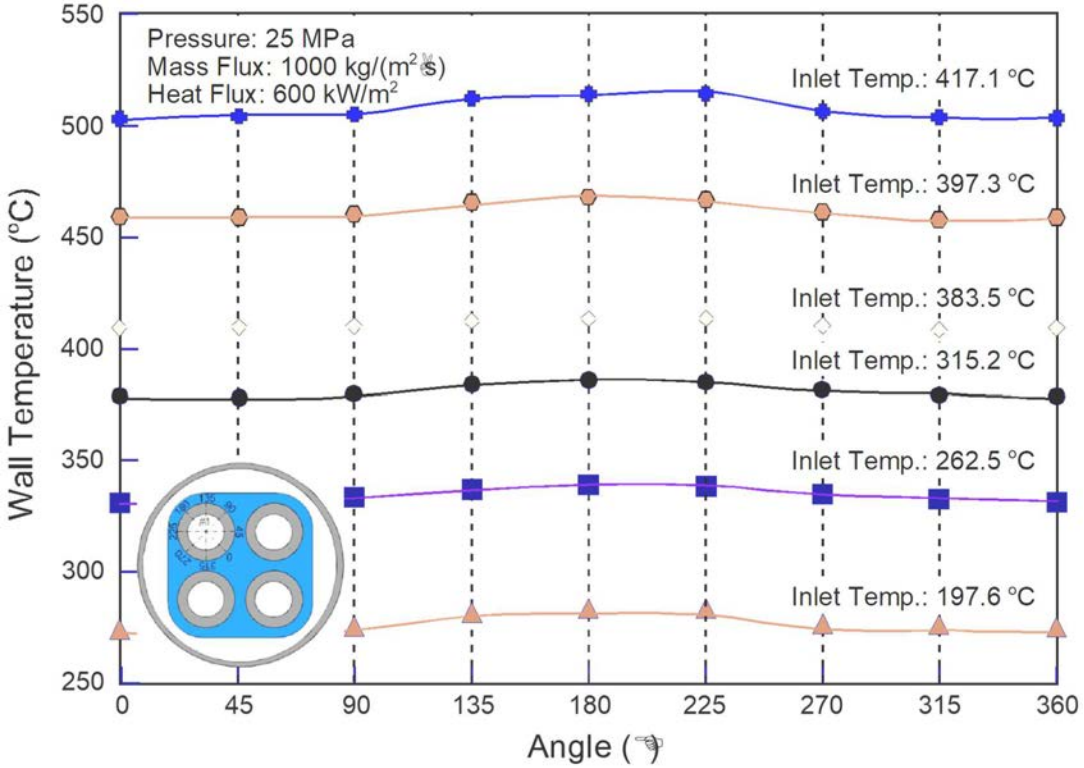

Fig. 5.4. Circumferential wall temperature distributions with inlet fluid temperature.

Reference [5.9] examined the circumferential temperature gradient (i.e., the difference between the maximum and minimum wall temperatures) around the heated rod at each measuring point. Fig. 5.5 illustrates variations of circumferential temperature gradient with cross sectional average bulk fluid enthalpy. The circumferential temperature gradient decreases with increasing enthalpy at the liquid-like region, reaching a minimum at the pseudocritical point, and increases at the vapour-like region. This signifies that the liquid-like fluid in the narrow gap region approaches the pseudocritical point much more rapidly than those in other regions. Surface temperature of the vapour-like fluid also increases more rapidly in the narrow gap region. Overall, the circumferential temperature gradient is relatively small over the test conditions.

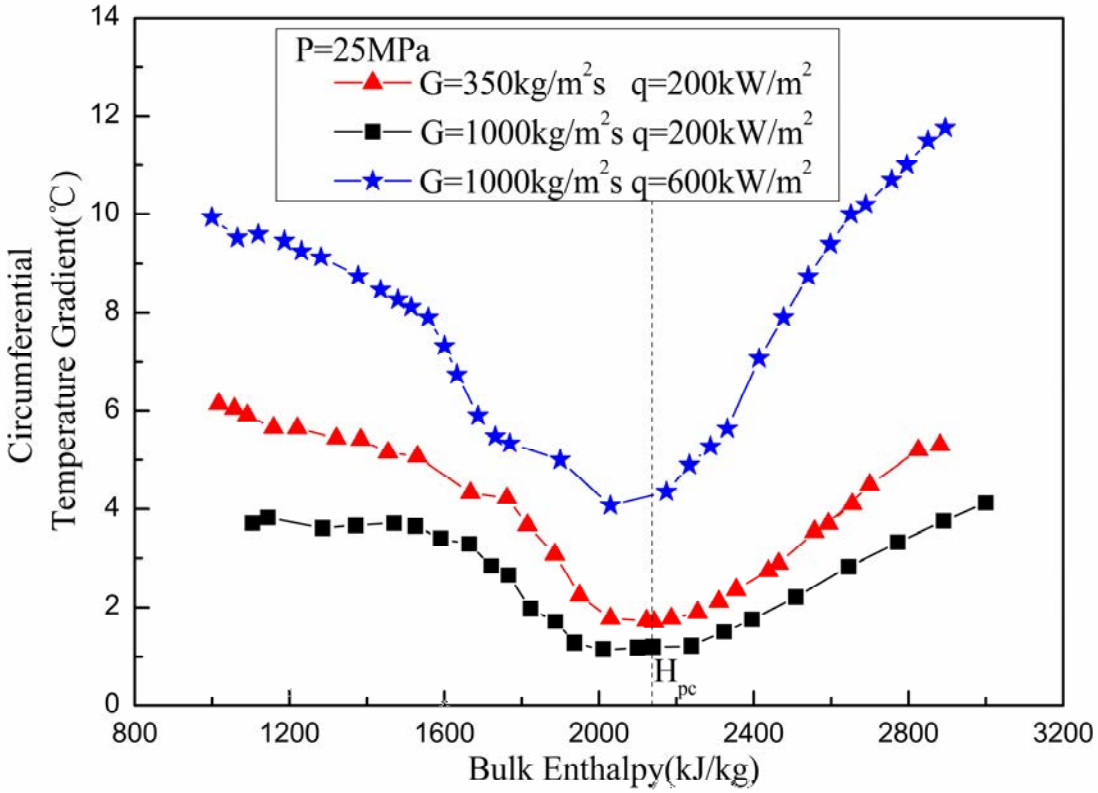

Fig. 5.5. Variations of circumferential temperature gradient with bulk fluid enthalpy.

Maximum wall temperature measurement and the minimum heat transfer coefficients at various measuring locations were examined in Fig. 5.6.

The wall temperature measurements at various locations are consistent at the same local flow conditions. No significant differences have been observed irrespective of the measuring location. The minimum heat transfer coefficients, however, vary slightly at the low and high enthalpy regions, and relatively large at the vicinity of the pseudocritical point at "mp-1" and "mp-2" locations. Differences in minimum heat transfer coefficient are small at "mp-3", "mp-4" and "mp-5" locations. Reference [5.9] focused on measurements obtained at the "mp-5" location, where the maximum wall temperature has been observed, in their analysis.

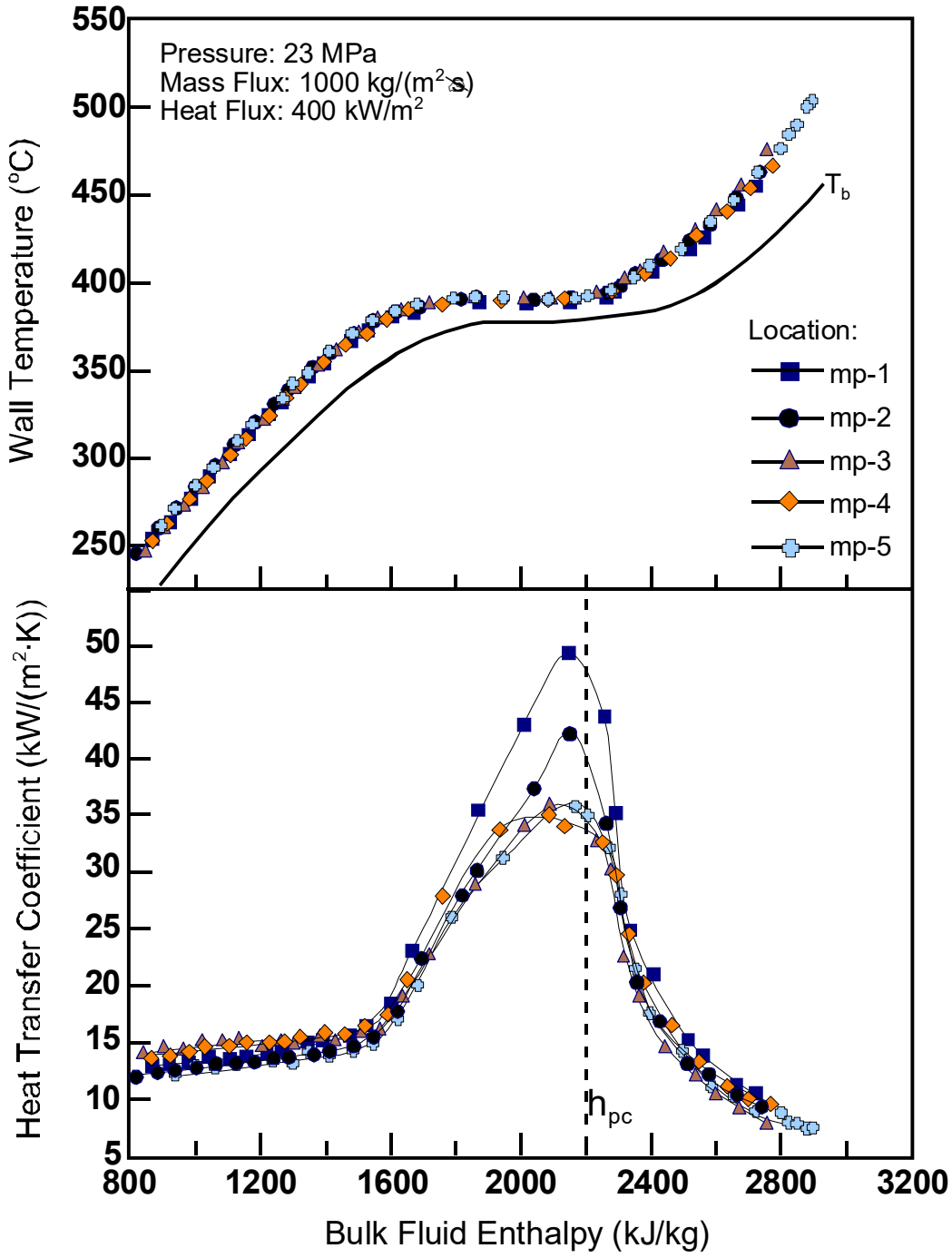

Fig. 5.6. Variations of maximum wall temperature and minimum heat-transfer coefficient with bulk fluid enthalpy at various measuring points.

Fig. 5.7 illustrates variations of maximum wall temperature and minimum heat transfer coefficient with bulk enthalpy and heat flux. The experimental results follow the same observed trends as those in tubes where the maximum wall temperature increases with increasing bulk fluid enthalpy and the minimum heat transfer coefficient increases gradually at low enthalpies, sharply as the

enthalpy approaches the pseudocritical point, reaching a maximum and decreases sharply at high enthalpies. The maximum wall temperautre increases with increasing heat flux while the minimum heat-transfer coefficient decreases. Over the current range of test conditions, deteriorated heat transfer has not been observed although the peak heat transfer coefficient shifts to low bulk fluid enthalpy with increasing heat flux.

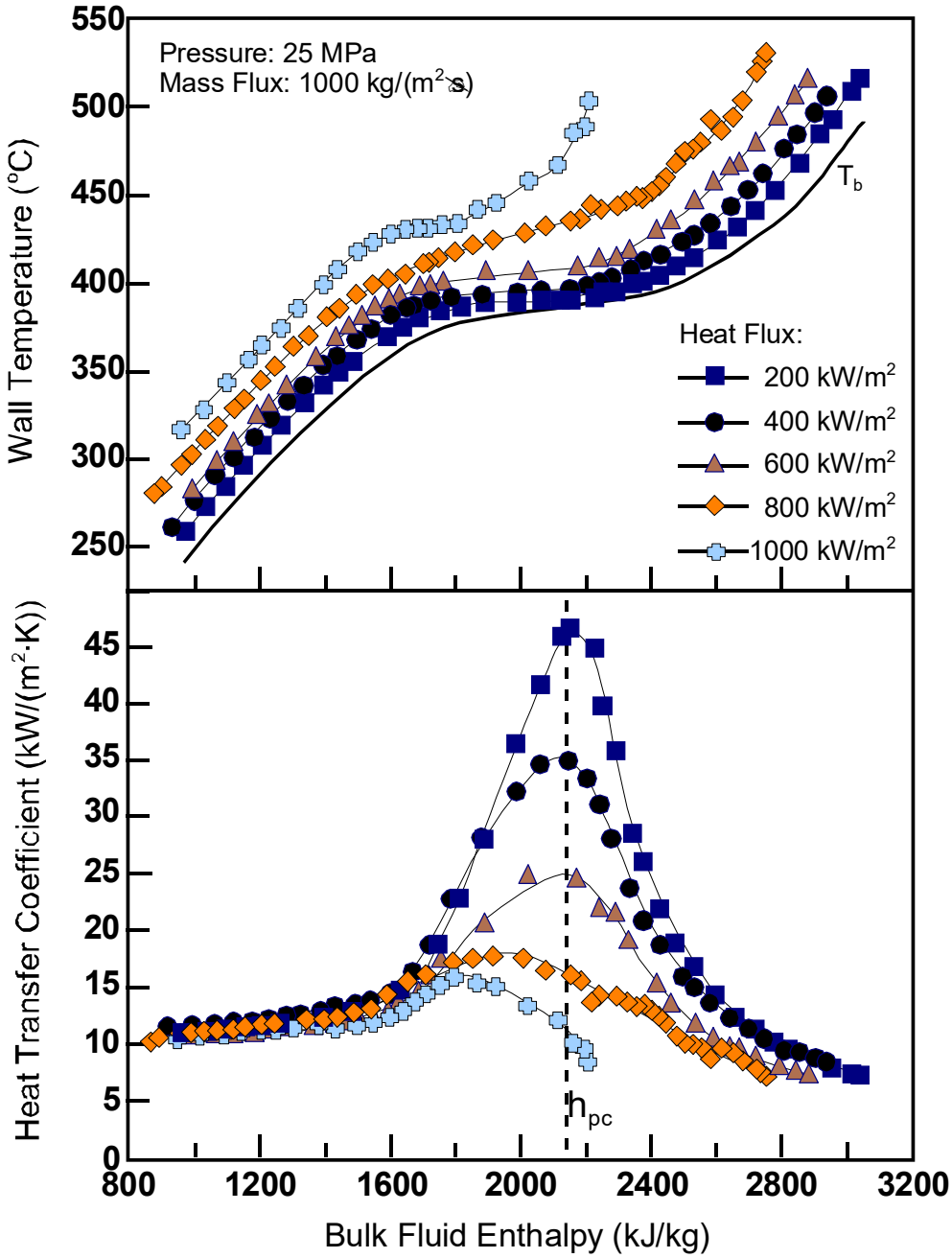

Fig. 5.7. Variations of maximum wall temperature and minimum heat-transfer coefficient with bulk fluid enthalpy and heat flux.

Fig. 5.8 illustrates variations of the maximum wall temperature and minimum heat-transfer coefficient with bulk fluid enthalpy and mass flux. The experimental trends are similar to those observed in previous figure. The maximum wall temperature increases with decreasing masss flux while the minimum heat-transfer coefficient decreases.

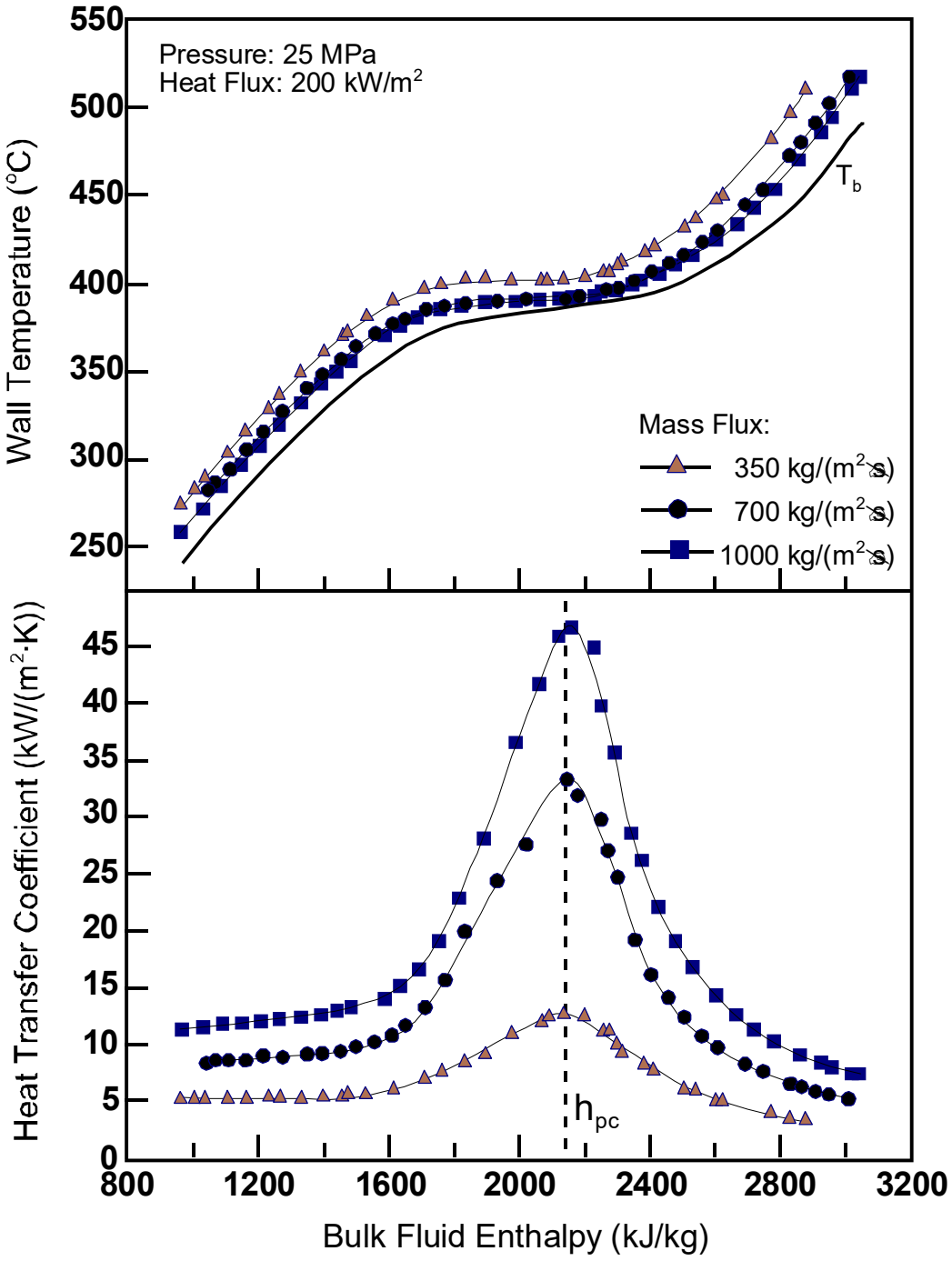

Fig. 5.8. Variations of maximum wall temperature with bulk fluid enthalpy and mass flux.

Fig. 5.8 illustrates variations of maximum wall temperature and minimum heat-transfer coefficient with bulk fluid enthalpy and pressure. Little differences in maximum wall temperature and minimum heat-transfer coefficient have been observed at low enthalpies (i.e., the liquid-like region) for various pressures. The differences increase as the enthalpy approaches the pseudocritical point. Overall, the maximum wall temperature increases with increasing pressure while the minimum heat transfer coefficient decreases.

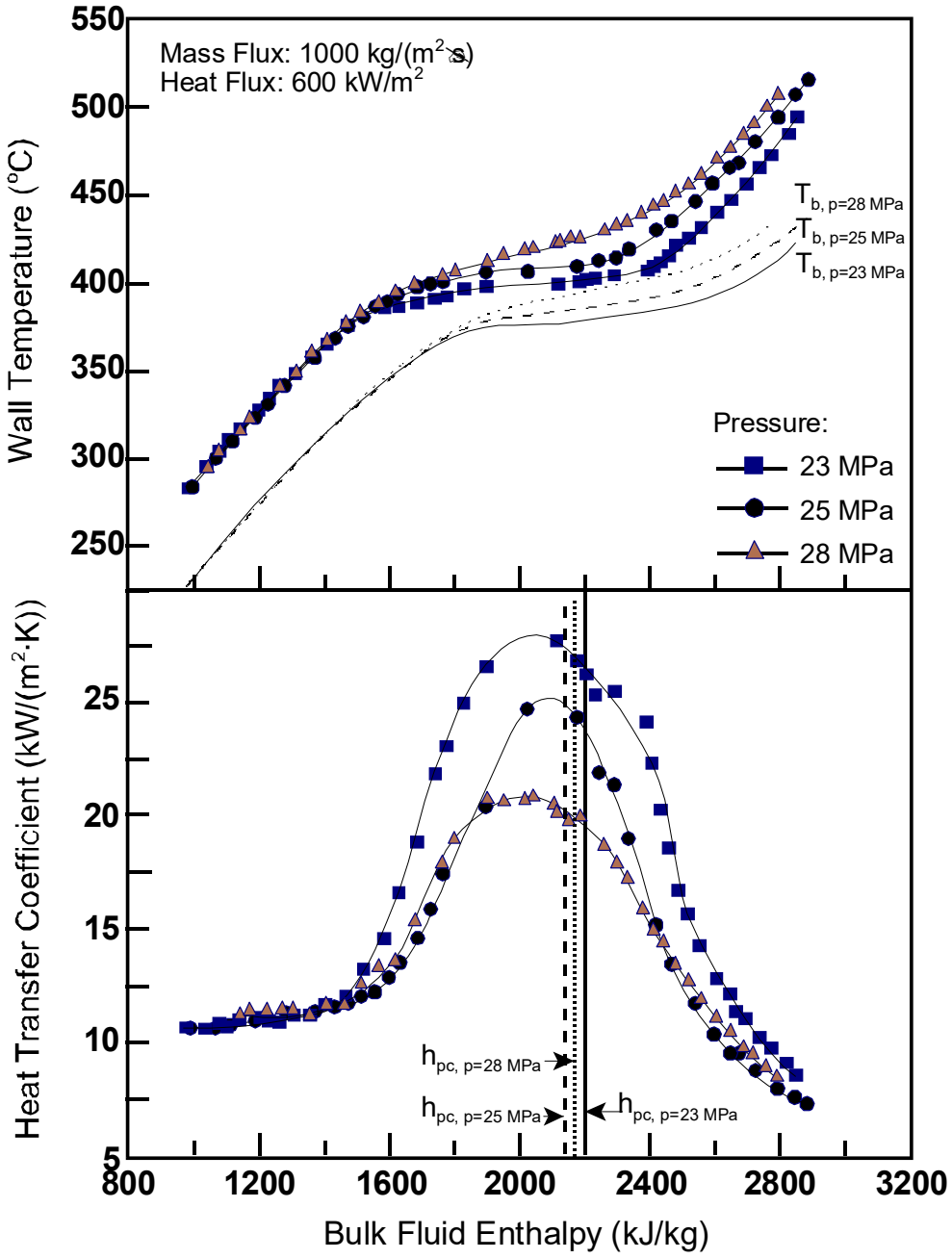

Fig. 5.9. Variations of maximum wall temperature and minimum heat-transfer coefficient with bulk fluid enthalpy and pressure.

5.2. HEAT TRANSFER IN 3-ROD BUNDLE COOLED WITH CARBON DIOXIDE

An experiment was performed at the University of Ottawa to obtain heat transfer data with carbon dioxide flow through a 3-rod bundle at supercritical pressures [5.10]. The test section consisted of a steel shroud acting as the pressure boundary, a ceramic insert acting as the insulator between the shroud and the bundle, and a 3-rod bundle. It was mounted vertically in the test loop, which is illustrated schematically in Fig. 5.10. The external surface of the test section was insulated to minimize the heat loss. Each rod in the bundle was constructed with an Inconel-600 tube of 10 mm in outer diameter. It had an overall length of 2500 mm but was heated with electricity over a length of 1500 mm. Fig. 5.11 shows various components and the cross sectional geometry of the rod bundle. Three unheated filler segments were installed at the outer subchannels to reduce those subchannel areas and minimize the maldistribution of flow in the bundle. Moveable thermocouples were installed inside each rod to measure the inner wall temperature.

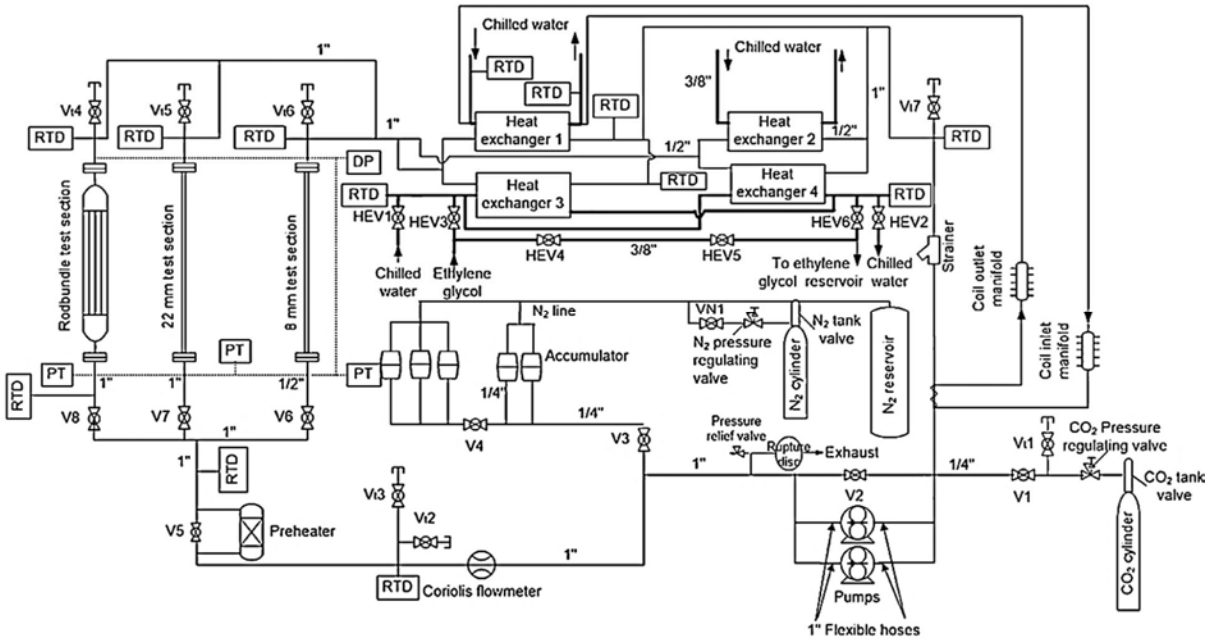

Fig. 5.10. Schematic diagram of carbon dioxide test facility at the University of Ottawa [5.10].

Two types of spacing devices were tested: grid and wire wrapped spacers. Fig. 5.12 illustrates the configurations and locations of these spacing devices. Four grid spacers (GSs) were placed along the heat length with the first one at the start and the other located 500 mm apart. Each spacer was constructed with three stainless steel shims of 0.102 mm in thickness and 4 mm in width, which were welded to a central stainless steel (SS304) tubing of 2.9 mm in outer diameter, 0.25 mm in wall thickness and 12 mm in length. The spacing between the unheated filler segment and the heated tubes was maintained with another piece of shim of 76 mm in length (same width and thickness as the other shims). The calculated blockage area ratio of each spacer was 5.3%.

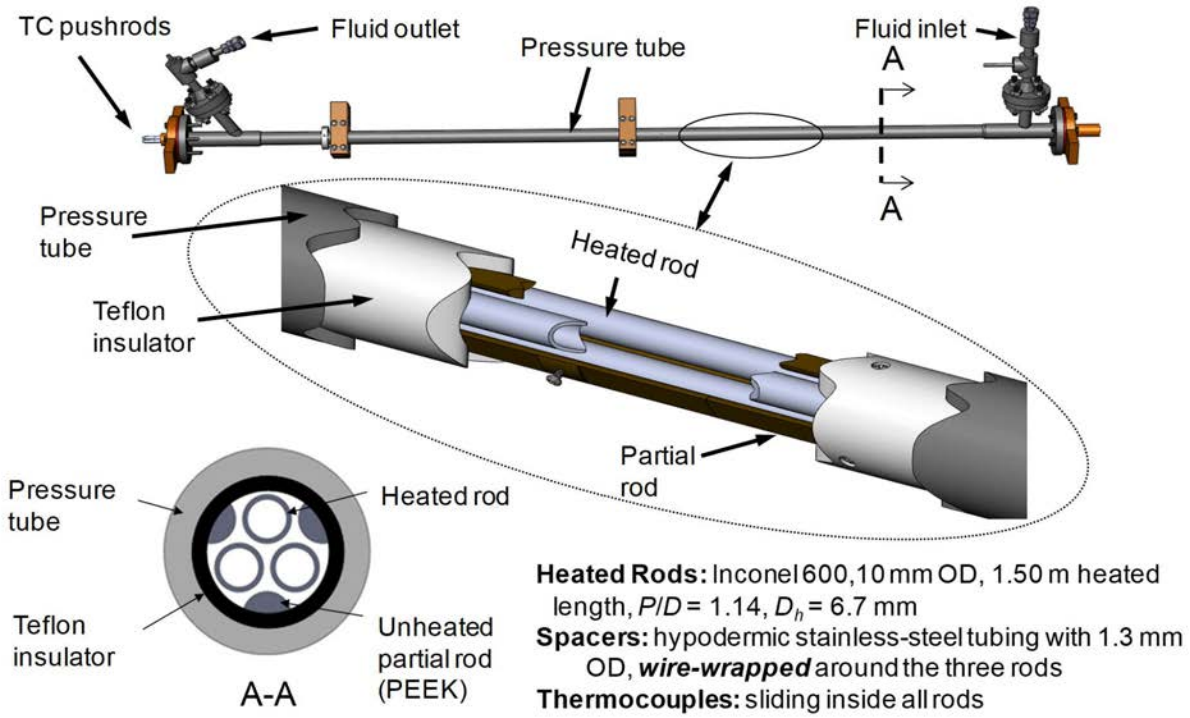

Fig. 5.11. Description of components in the 3-rod bundle.

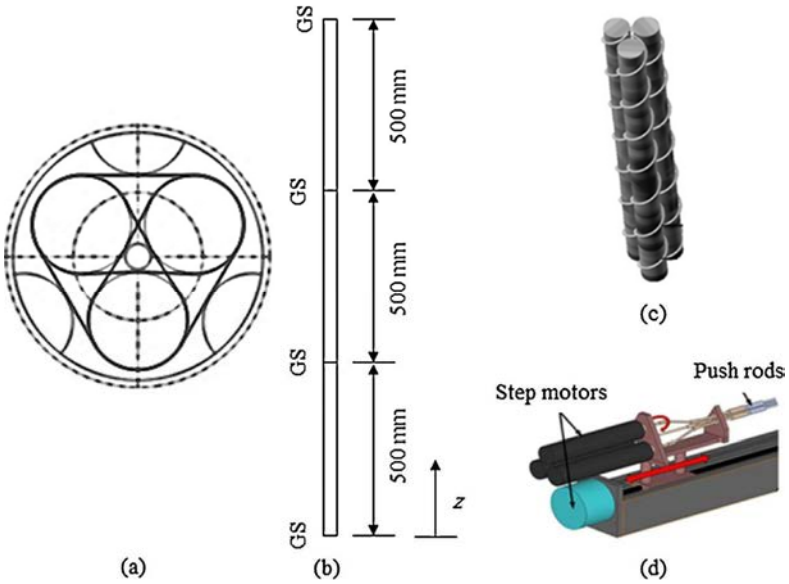

Fig. 5.12. Configurations and locations of the grid and wire wrapped spacers in the 3-rod bundle [5.10].

After completing the grid spacer tests, the grid spacers were removed and a small stainless steel (SS304) tubing of 1.3 mm in outer diameter was installed wrapping around each heated tube. Despite of the tubing configuration, it is referred as wire hereafter. The wire was welded at the

start of the heated length and wrapped in a 100 mm pitch over a 200 mm length in the heated section and 200 mm pitch thereafter. It has a resistance of 1.82 Ohm/m compared to 0.036 Ohm/m of the heated tube. Having said that, a negligible amount of power could be generated at the wire through joule heating. The total blockage area area of three wires was 32 % at each cross section of the bundle.

Surface temperature along the heated tube was measured with five moveable (J Type) thermocouples. These thermocouples were installed at three carriers, which were attached to a push rod 480 mm apart. Each set of thermocouples was spring loaded in contact with the inner surface of the heated tube. The push rod was traversed axially and rotated circumferentially to facilitate these thermocouples measuring the inner surface temperature profile. A thermocouples-traversing mechanism, which consisted of three potentiometers to identify the axial and angular positions of the thermocouples, was connected to one end of the bundle to drive the push rods.

Measurements obtained from these experiments included inlet pressure, inlet and outlet fluid temperatures, mass flow rate, power, axial and angular positions, and inner surface temperatures.

The three rods were identified as Rod A, Rod B and Rod C. Angular coordinate systems for temperature measurements around each rod are shown while viewing from downstream. The central subchannel was identified as 'CSC', the intermediate subchannel as SC, and the outer subchannel as OSC. Fig. 5.13 illustrates the circumferential temperature distribution at the outer wall surface of each rod with the wire wrapped spacer. The temperature was converted from the inner wall temperature measurement taken into the account of conduction heat transfer over the wall. The scan of Rod C was incomplete due to malfunction of the thermocouples. Overall, peak temperatures have been observed at surfaces facing the intermediate subchannels.

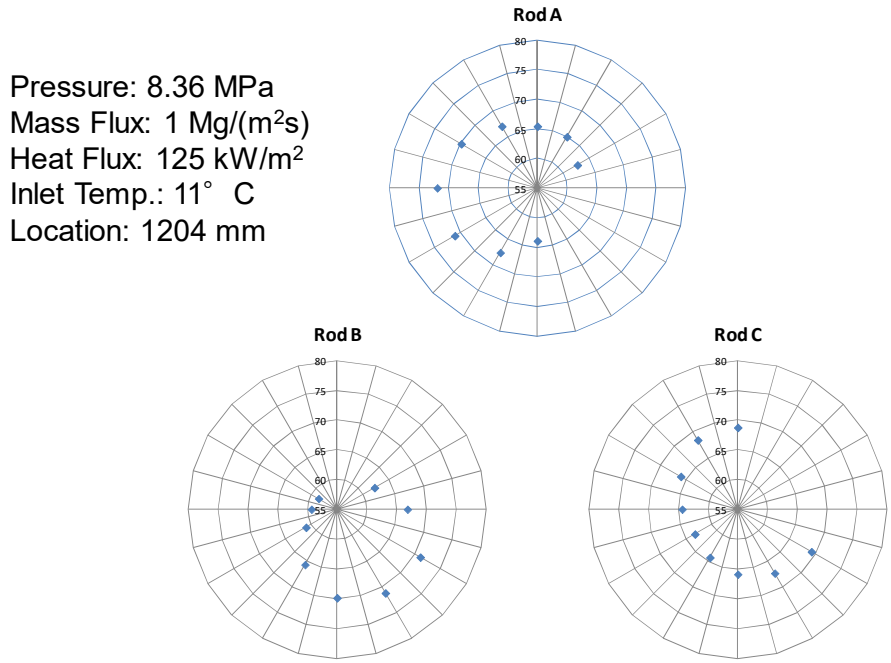

Fig. 5.13. Circumferential wall temperature distributions in the 3-rod bundle with sc co_2 flow.

Fig. 5.14 illustrates the axial temperature distribution at the peak temperature angle of each rod. As shown in Fig. 5.13, peak temperatures were observed at the angle of 240° in Rod A and Rod B, but 0° in Rod C (due to incomplete scanning). Wall temperatures in Rod A and Rod B increase generally with increasing distance but appear levelling off at locations beyond 1.2 m. The zig zag profiles correspond to the location of the wire wrapped spacer. Wall temperatures in Rod C behave differently and might be attributed to the thermocouple malfunction.

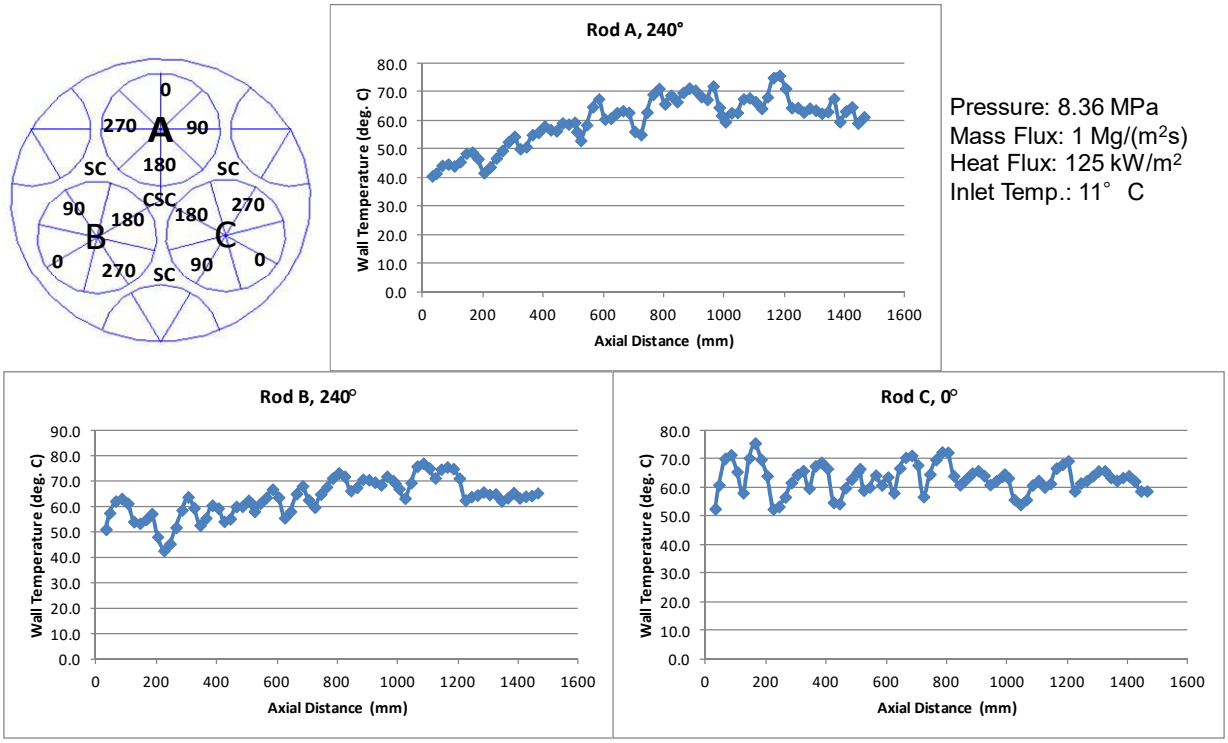

Fig. 5.14. Axial wall temperature distributions in the 3-rod bundle with SC CO_2 flow.

Fig. 5.15 shows variations of circumferential surface temperature and heat transfer coefficient for Rod B in bundles with grid and wire wrapped spacers as a function of fluid enthalpy at a relatively low mass flux and high heat flux. In general, the surface temperature decreases with increasing enthalpy at the inlet end when approaching the pseudocritical point (the dashed line). A localized minimum was observed at the enthalpy lower than the pseudocritical point for the bundle with wire wrapped spacers but close to the pseudocritical point for the bundle with grid spacers. Slight variations in surface temperature have been observed at various azimuthal positions. Minor fluctuation in surface temperature are shown with enthalpy for the bundle with wire wrapped spacers. That was attributed to the small spacers effect on heat transfer. On the other hand, distinct drop and rise in surface temperature are shown at the grid spacer locations of the bundle (solid lines). The enhancement effect on heat transfer of grid spacer appears to be small and within a short downstream distance.

The scatter in heat transfer coefficient increases with various azimuthal positions, particularly for the region of vapour like fluid at enthalpies higher than the pseudocritical poInt. Heat transfer coefficient increases at enthalpies lower than the pseudocritical poInt. Localized peaks in heat

transfer coefficient are shown around the pseudocritical poInt. Heat transfer coefficient decreases at enthalpies higher than the pseudocritical point but only up to the enthalpy around 440 kJ/kg, beyond which the heat transfer coefficient generally increases with enthalpy. There was little localized effect of wire wrapped spacers on heat transfer coefficient. However, the heat transfer enhancement effect of the grid spacer has been observed. As indicated above, the affected region is relatively small.

Reference [5.10] compared the surface temperature profiles for these bundles against those for an 8 mm tube. Overall, similar surface temperature variations were observed for these 3-rod bundles and the tube. The installation of the grid spacers had led to increased scatter in surface temperature for the bundle.

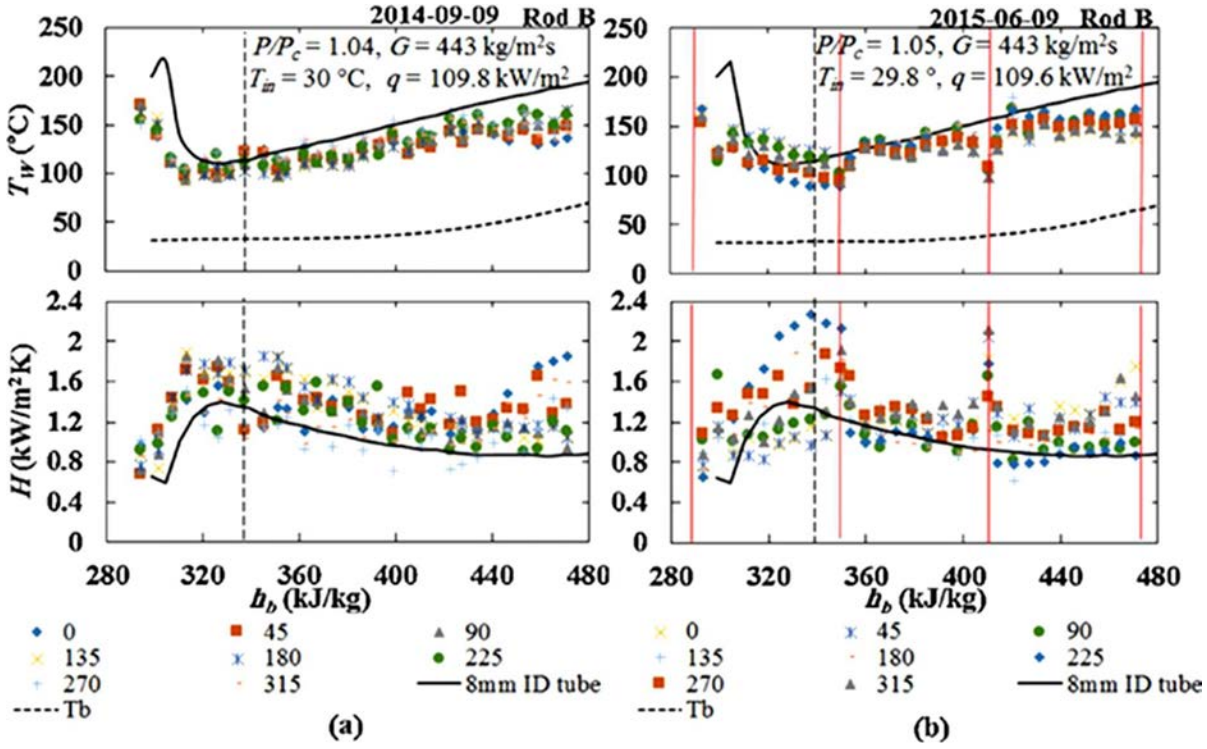

Fig. 5.15. Wall temperature and heat transfer coefficient at various circumferential positions along rod B of the rod bundle equipped with (a) wire wraps and (b) grid spacers [5.10].

Fig. 5.16 shows variations of circumferential surface temperature and heat transfer coefficient for Rod B in bundles with grid and wire wrapped spacers as a function of fluid enthalpy at a relatively high mass flux and low heat flux. The range of fluid enthalpy covered in the test corresponds to the liquid-like region below the pseudocritical poInt. In general, the surface temperature increases with increasing enthalpy for the rod with the wire wrapped spacers. A scatter in surface temperature has been observed at the inlet end of the heated length and could be attributed to the entrance effect due to the installation of the wire wrapped spacer. The scatter of the surface temperature profiles for the bundle with grid spacers is larger than that for the bundle with wire wrapped spacer. It was attributed to the enhancement effect of the grid spacer on heat transfer at the location (solid lines).

The scatter in heat transfer coefficient increases with various azimuthal positions, especially for the bundle with the grid spacers. Overall, the heat transfer coefficient increases with enthalpy, in particular at high enthalpies approaching the pseudocritical poInt. There was little localized effect of wire wrapped spacers on heat transfer coefficient. However, the heat transfer enhancement effect of the grid spacer has been observed and increases the scatter among the heat transfer coefficient.

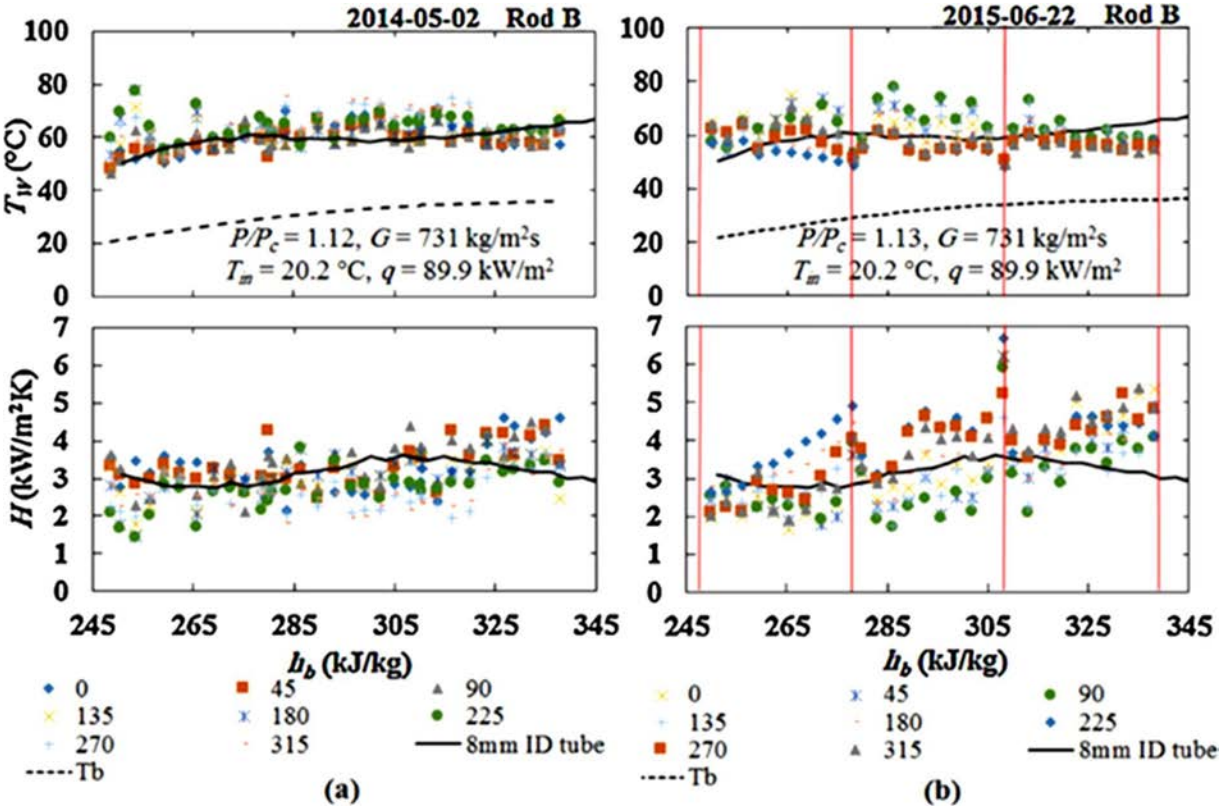

Fig. 5.16. Wall temperature and heat transfer coefficient vs. bulk enthalpy at different circumferential positions along Rod B of the rod bundle equipped with (a) wire wraps and (b) grid spacers [5.10].

In view of the variation in surface temperature azimuthally for different rods, [5.10] focused their analysis on the maximum surface temperature (and correspondingly the minimum heat transfer coefficient) within a cross section of the bundle. Fig. 5.17 compares the maximum surface temperature and minimum heat transfer coefficients at two different heat fluxes and two separate pressures for the bundle with the wire wrapped spacers. Overall, the maximum surface temperature increases with increasing heat flux but the effect of heat flux appears to be minor on the minimum heat transfer coefficient (albeit the increased scatter). As the enthalpy approaches the pseudocritical point, the minimum heat transfer coefficient becomes higher for low than high heat fluxes.

Fig. 5.18 compares the maximum surface temperature and minimum heat transfer coefficients at four different mass fluxes for the bundle with the wire wrapped spacers [5.10]. The maximum

surface temperature decreases but the minimum heat transfer coefficient increases with increasing mass flux.

Reference [5.10] examined effects of pressure and inlet temperature on the maximum surface temperature and minimum heat transfer coefficients. Both the pressure and inlet temperature have little effects on these parameters.

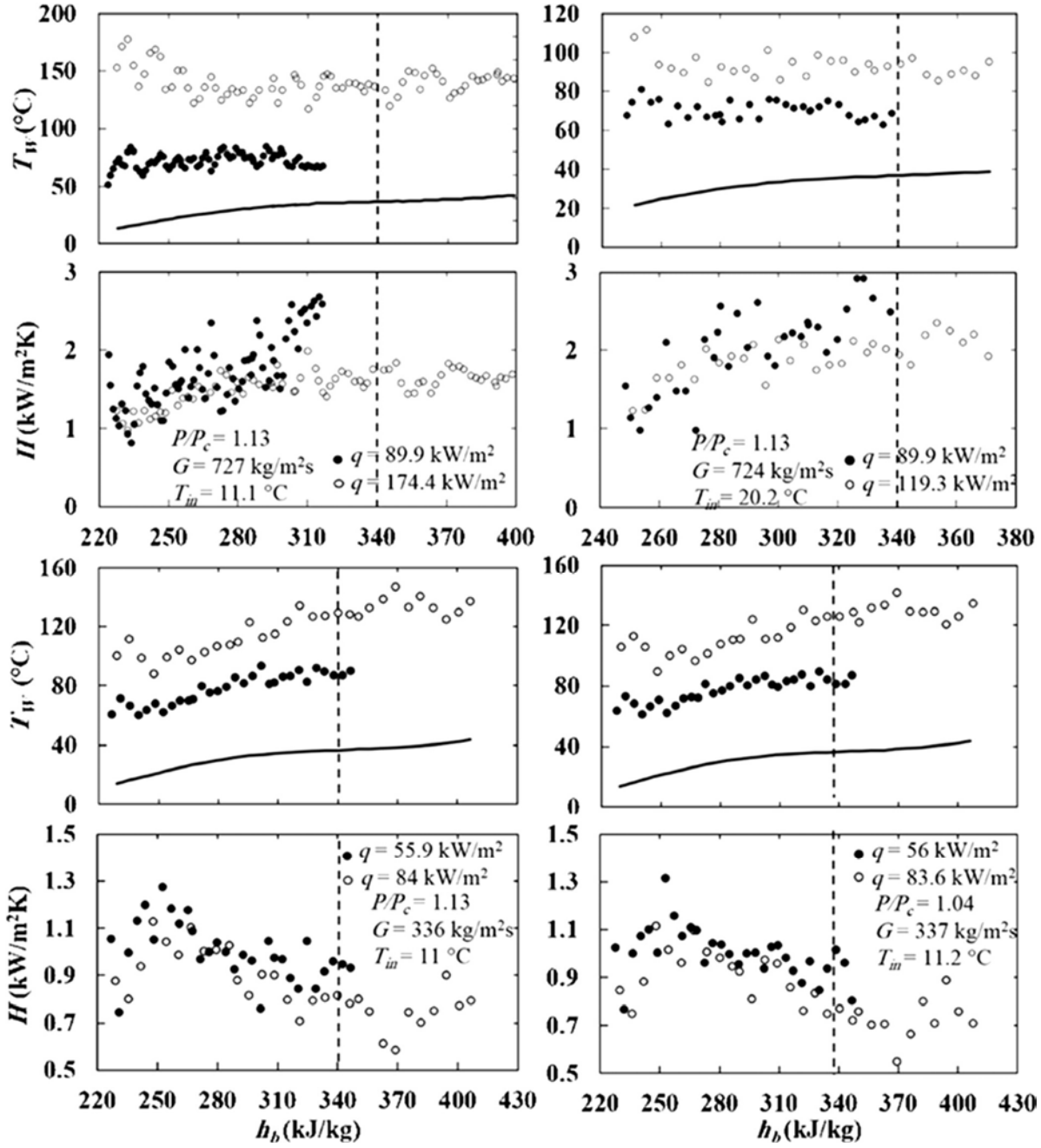

Fig. 5.17. Effect of heat flux on the maximum wall temperature and the minimum heat transfer coefficient for the wire wrapped rod bundle [5.10].

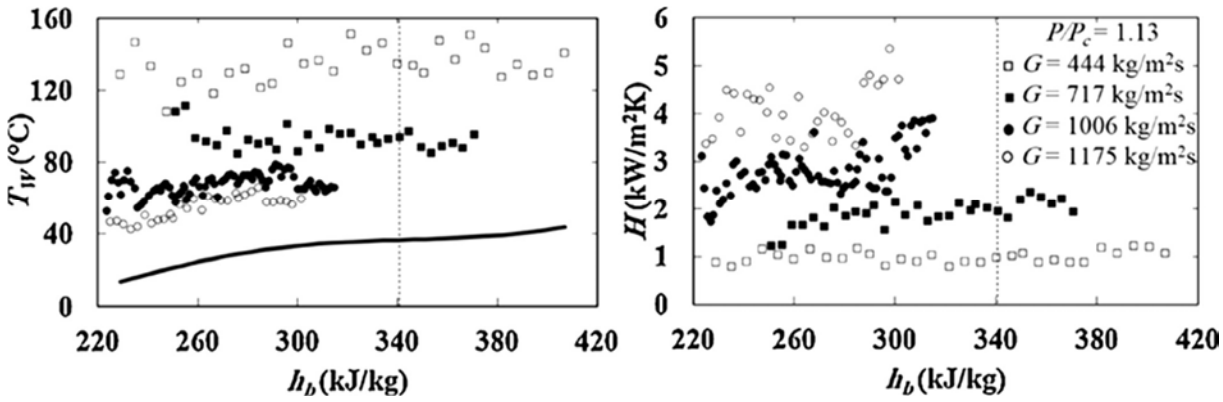

Fig. 5.18. Effect of mass flux on the maximum wall temperature and the minimum heat transfer coefficient for the wire wrapped rod bundle [5.10].

5.3. HEAT TRANSFER IN 7-ROD BUNDLE COOLED WITH REFRIGERANT-134A

Reference [5.11] performed heat transfer experiments with vertical upward Refrigerant-134a (or R-134a) flow through a 7-rod bundle at supercritical pressures. Fig. 5.19 illustrates the configuration of the refrigerant test facility. The bundle consisted of seven heated rods, each was constructed from an Inconel 625 tube of 7.4 mm in outer diameter and 1.2 mm in wall thickness with a length of 2482 mm (see Fig. 5.20). Each rod was equipped with a wire wrapped spacer, which was constructed from a PTFE tubing of 0.91 mm in outer diameter. The pitch of the spacer was 74 mm, which provided a pitch-to-diameter ratio of 10. The bundle was inserted inside an Inconel 625 tube of 27.9 mm in inner diameter and 10.2 mm in wall thickness with a length of 2153 mm, which was unheated and acted as the pressure boundary.

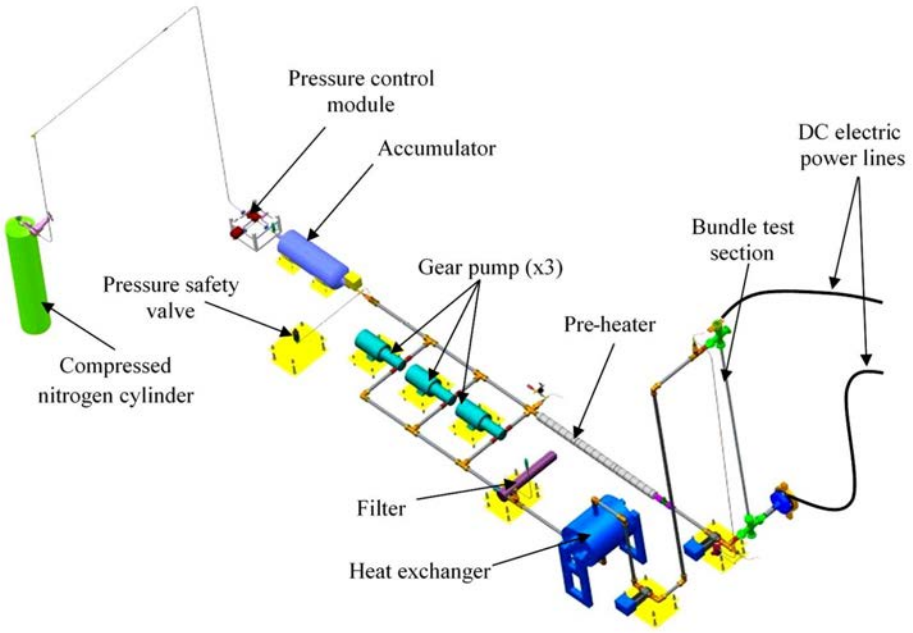

Fig. 5.19. Schematic of the CR134a loop showing primary components.

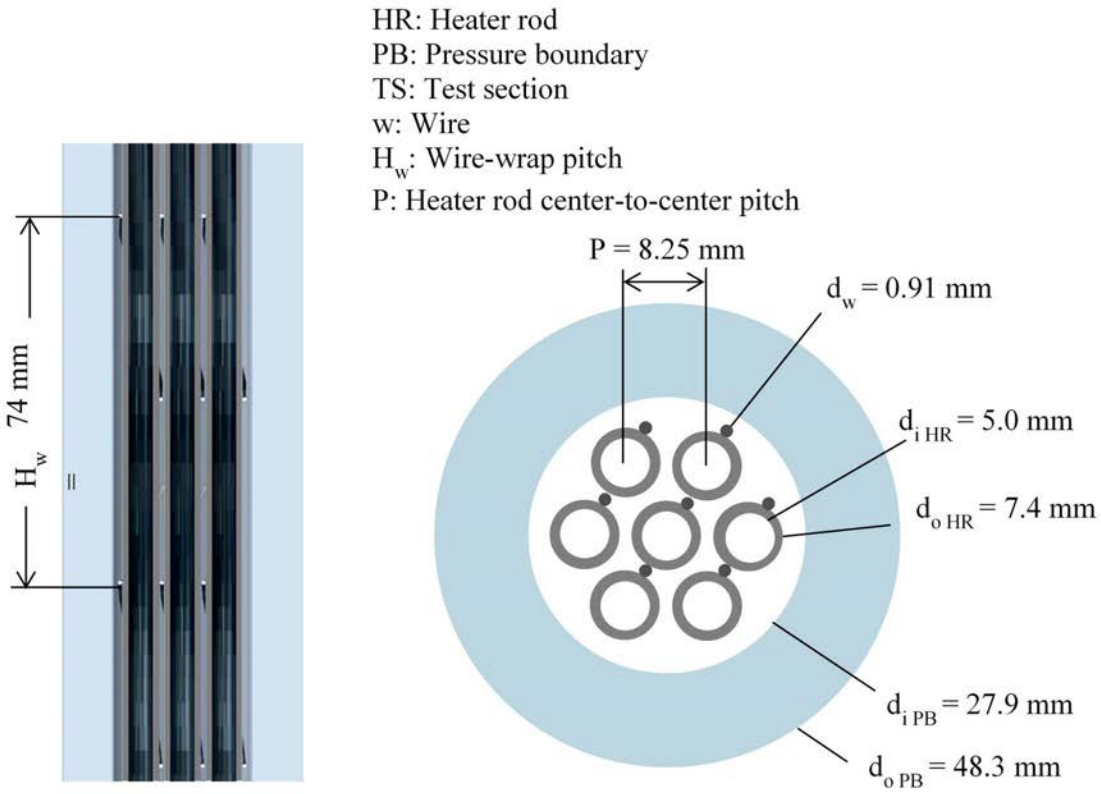

Fig. 5.20. 7-rod bundle configuration in the Refrigerant-134a heat transfer test.

Three moveable (K type) thermocouples were installed 120° apart in a probe inside each heated rod to obtain the inner surface temperature. Circumferential and axial locations of the probe were controlled with a stepper motor driven pulley system. Measurements included outlet pressure, pressure drop, mass flow rate, inlet and outlet fluid temperatures, current and voltage. The steady state experiment covered the pressure of 4.88 MPa (i.e., P/P_c = 1.06), mass flux of 297 kg/(m^{2}s), inlet fluid temperature of 21.9°C and heat flux range from 20–35 kW/m^2.

The experiment was performed continuously with a stepwise increase in power while maintaining steady flow conditions (within the uncertainty). Fig. 5.21 illustrates the surface temperature profiles for the seven heated rods in the bundle with increasing power (reflected in the bulk fluid temperature variation). The surface temperature increases with increasing power in a relatively linear trend. At the time of 4600 s, however, two of these rods (TC6 and TC7) exhibited a sharp increase in surface temperature. As the flow conditions have not reached the pseudocritical point (maximum ratio of bulk fluid to critical temperature reaches 0.95 only), [5.11] attributed that to an instability issue within the system.

Variations in Nusselt number are shown in Fig. 5.22. There appears to be an improvement in heat transfer starting at about 1000 s. The improvement continued until 1800 s and started to diminish. At 4600 s, a sharp decrease in Nusselt number is shown for the two rods (as mentioned above).

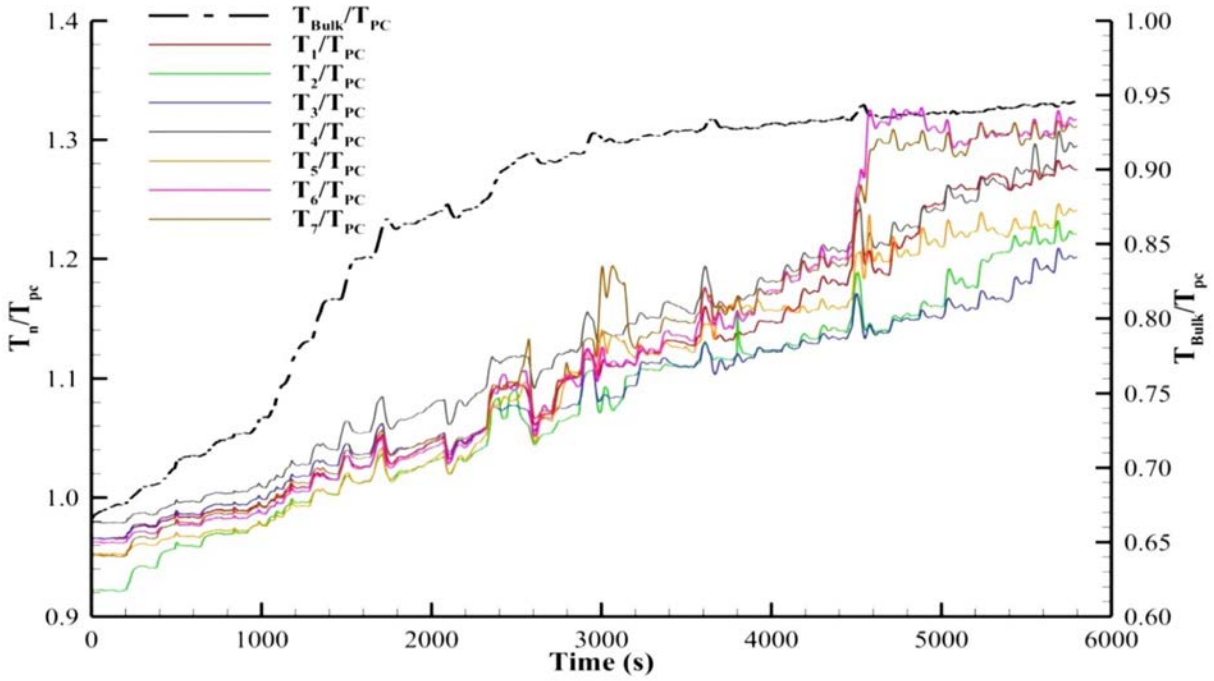

Fig. 5.21. Temperature profiles observed from the 7-rod bundle refrigerant flow experiment.

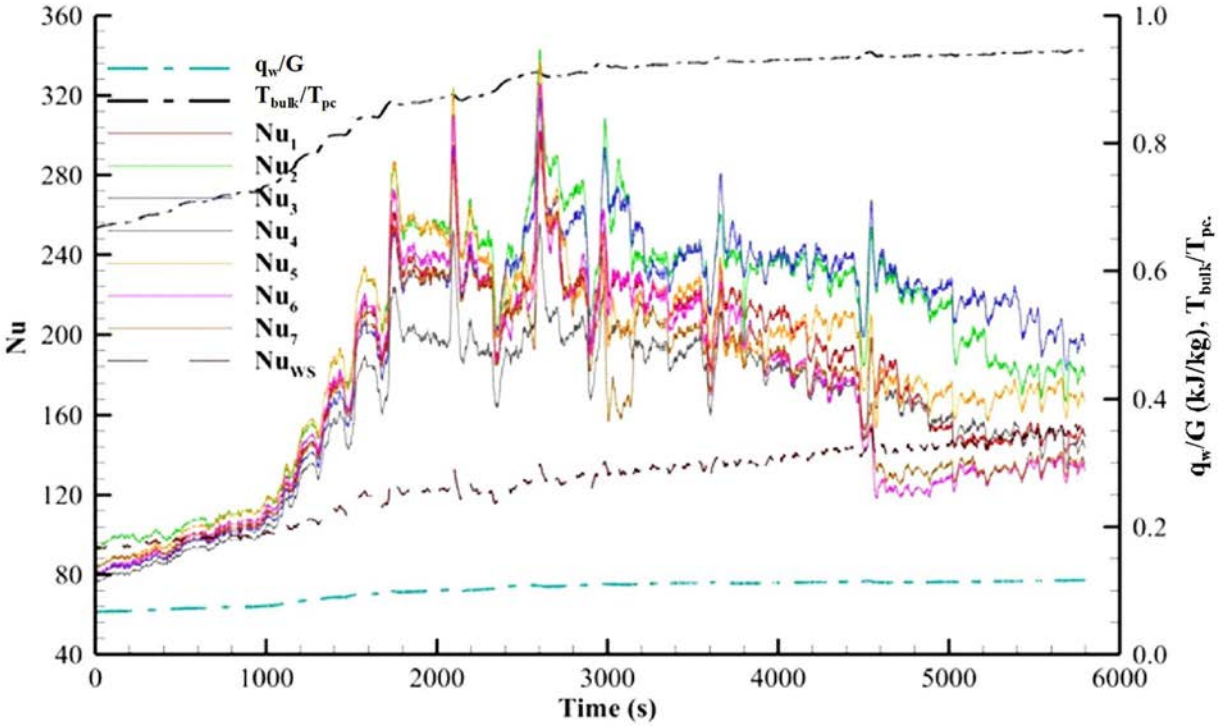

Fig. 5.22. Nusselt number profiles for the 7-rod bundle refrigerant flow experiment.

5.4. HEAT TRANSFER EXPERIMENTS IN VERTICAL BARE 7-ROD BUNDLE COOLED WITH SUPERCRITICAL FREON R-12

This Section (5.4) is mainly based on or directly reproduced from [4.75] and [5.12] and is published with permission from the American Society of Mechanical Engineers (ASME).

Experiments in SCW are technically quite complicated and very costly due to high pressures and temperatures. However, SCW operating conditions can be modeled with lower critical pressure and temperature fluids such as Freons as a preliminary approach to complement our knowledge of supercritical fluids' behaviour. Freon R−12 was widely used in industry some time ago as a refrigerant for air conditioning systems. Therefore, its thermophysical properties are well known within a wide range of conditions including the critical and SC pressure region. Using SC R−12 as a fluid with lower critical parameters instead of SCW will lower costs of experimental setup and tests, and reduce risks associated with operation at a high pressure, temperature, and heat flux SCW test facility.

The critical parameters of Freon R−12 are as the following: Pressure of 4.1361 MPa and temperature of 111.97 ºC (details on thermophysical properties of critical and SC R−12 are provided in Appendix I), which are significantly lower compared to those of SCW (critical pressure of 22.064 MPa and critical temperature of 373.95 ºC) [5.13].

5.4.1. SUPERCRITICAL REFRIGERANT TEST FACILITY

All experimental data were obtained at the State Scientific Center of Russian Federation, Institute for Physics and Power Engineering Supercritical Test Facility in Obninsk, Russian Federation [5.14]. The dataset was obtained using Freon R−12 working fluid at similar parameters as the proposed conditions of Canadian SCWR (using scaling laws; see Table 5.1 and Table 5.2). The SC Pressure Test Facility (SCPTF) is designed to gain further knowledge of Heat Transfer (HT) to SCW in bundles by using a modelling (surrogate) fluid, Freon R−12, within a wide range of operating conditions.

TABLE 5.1. MAJOR SCALING PARAMETERS FOR FLUID–TO–FLUID MODELING AT SUPERCRITICAL CONDITIONS BASED ON INLET CONDITIONS APPROACH [5.15].

No.	Parameter	Equation
1	Pressure	$\left(\frac{p}{p_{cr}}\right)_w = \left(\frac{p}{p_{cr}}\right)_f$
2	Bulk Fluid Temperature	$\left(\frac{T}{T_{cr}}\right)_w = \left(\frac{T}{T_{cr}}\right)_f$
3	Heat Flux	$\left(\frac{q\,D}{k_b}\right)_w = \left(\frac{q\,D}{k_b}\right)_f$
4	Mass Flux	$\left(\frac{G\,D}{\mu_b}\right)_w = \left(\frac{G\,D}{\mu_b}\right)_f$

Schematic of the SCPTF, Freon R-12 test loop, is shown in Fig. 5.23. The loop consists of a number of basic components including: Two circulating pumps (5); preheater (6); two Test Sections (TSs) (1); heat exchangers (2, 4); recuperator (3); deaerator (7); level indicator (8); two Freon R-12 storage tanks (9); and filters (10). All components and piping in the test facility were made of stainless steel with an internal diameter of 50 mm (where applicable). Also, the unit is designed to operate up to pressure of 5.0 MPa.

TABLE 5.2. SCALING FACTORS FOR FREON R-12 TO WATER AT SUPERCRITICAL CONDITIONS.

No.	Parameter	Equation
1	Pressure	$\frac{p_W}{p_F} = 5.37$
2	Temperature	$\frac{T_w}{T_F} = 3.3$
3	Heat Flux	$\frac{q_W}{q_F} = 20$
4	Temperature difference	$\frac{\Delta T_W}{\Delta T_F} = 15.4\left(\frac{k_W}{k_F}\right)^{0.66}$

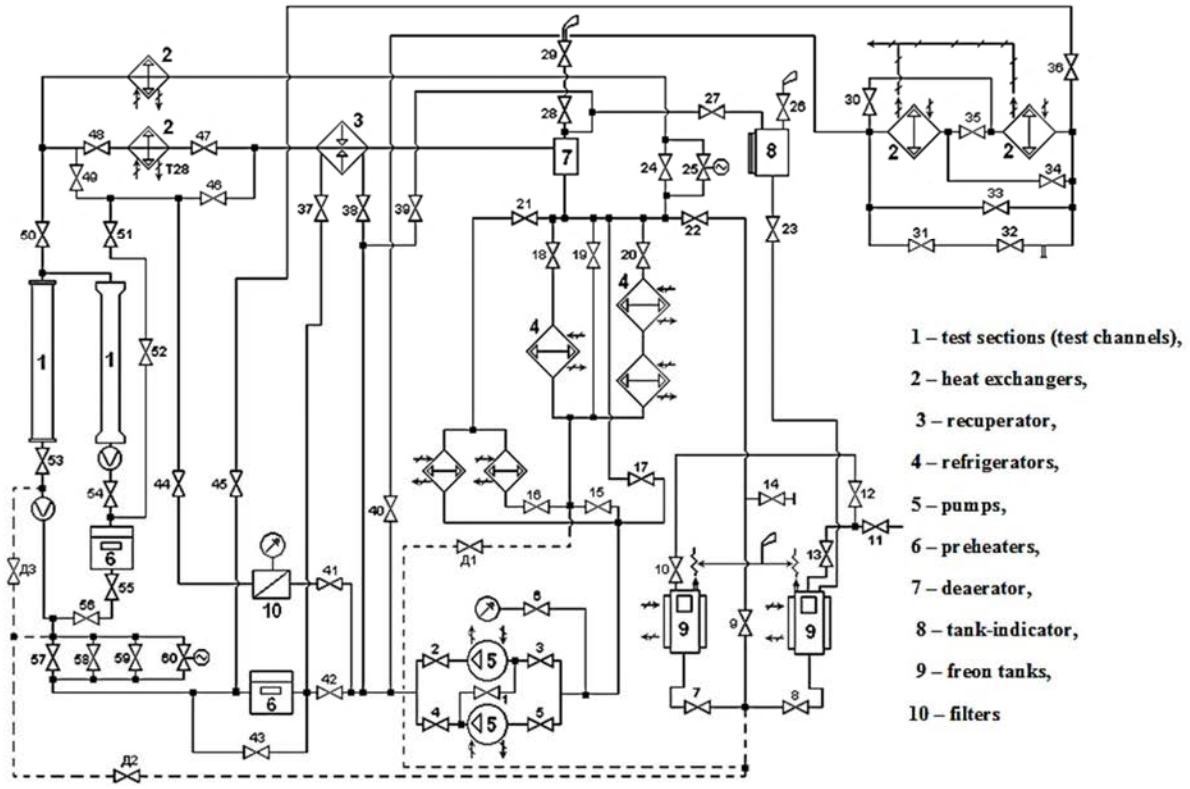

Fig. 5.23. Schematic of SCPTF – Freon R–12 test loop.

The circulating pumps (5) are able to operate in series, parallel or independently of one from another. Each pump has a capacity of 20 m^3/h and a pressure of 1.0 MPa. The preheater (6) is manufactured as an electrically heated tube. Electrical power of 160 kW can be applied with the preheater, however, if this is insufficient for any reason, heat exchangers (2) can be used for additional preheating of the coolant. The heat exchangers are supplied with either hot or cold water in a secondary loop not shown in Fig. 5.23.

There are two different TSs (1) used in the SCPTF. In most cases a single channel is used for testing, while the other is being prepared for different experiments. In cases, where higher power is needed, the leftmost channel is used with the heat exchangers to remove excess heat. The Freon tanks (9) are placed below the level of the test loop and are also used as pressurizers during experiments with the testing loop. Additionally, there are electrical heaters in the Freon tanks to serve as a first stage preheater as well as to provide pressure control in the system. Each tank has a total volume of 0.25 m^3.

The TS was heated with an AC current from a power supply. The maximum power input to the TS was up to 200 kW. However, a DC power supply can provide with 540 kW, which is equivalent to 8 MW in water. The main parameters of the SCPTF test facility are listed in Table 5.3.

TABLE 5.3. MAIN EXPERIMENTAL SETUP PARAMETERS FOR FREON R-12 HEAT TRANSFER EXPERIMENTS.

No.	Parameter	Value(s)
1	Pressure	Up to 5.0 MPa
2	Temperature of Freon R-12	Up to 120°C (400°C heating rods)
3	Maximum mass flow rate	20 + 20 m^3/h
4	Maximum pump pressure	1.0 + 1.0 MPa
5	Experimental test section power	up to 1 MW
6	Experimental test section height	up to 8 m
7	Data Acquisition System (DAS)	up to 256 channels

5.4.2. TEST SECTION

The experimental TS (Fig. 5.24) consists of a pressure tube and a seven-rod bundle. The pressure tube is a round pipe (Ø40×4 mm) with welded flanges. The flow tube is placed inside the pressure tube creating a hexagonal coolant flow channel with a side length of 18.3 mm. The flow tube is manufactured from aluminum dioxide with high temperature treatment, and, also, is provided electric insulation between the electrically heated rods (fuel rod simulators) and the pressure tube.

The heated rods – fuel rod simulators are stainless steel tubes of Ø9.5×0.6 mm. They are arranged in a 6 + 1 rod bundle inside the hexagonal flow tube (channel) as shown in Fig. 5.25 as well as rod numbering, thermocouple layout and channel dimensions. The seven rods are kept in their positions through the use of three spacer grids as shown in Fig. 5.26 and Fig. 5.27. Parameters of the 7-rod bundle are listed in Table 5.4

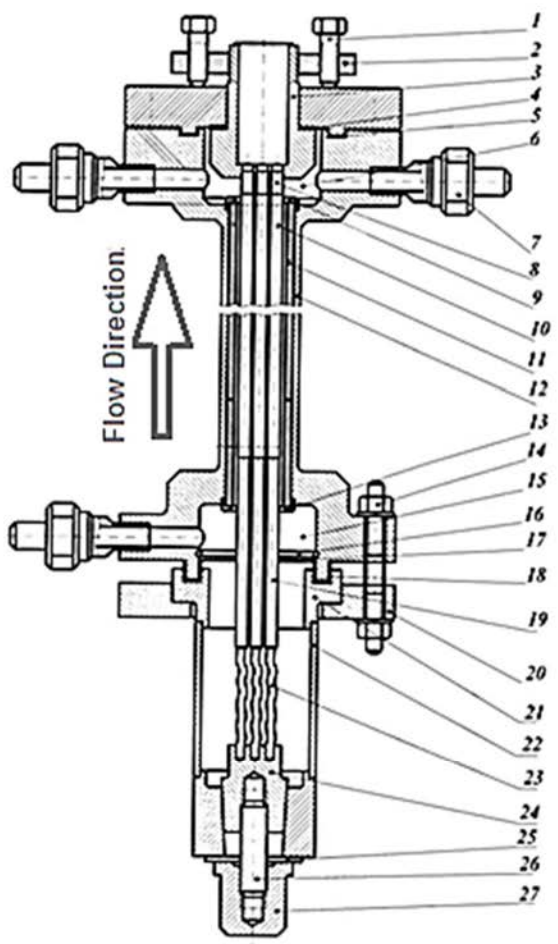

1 – holding-down bolts;
2 – holding-down plate;
3 – upper current terminal;
4 – copper gasket;
5, 18 – insulators;
6 – upper chamber;
7 – union;
8 – copper-tube insert;
9, 13 – clamp rings;
10 – heated elements;
11 – ceramic sleeves;
12 – shell (flow tube);
14 – pin;
15 – lower chamber;
16 – check ring;
17 – Teflon spacer;
19 – copper rods;
20 – lower flange;
21 – adapter;
22 – can;
23 – flexible current leads;
24 – cone;
25 – gasket;
26 – pin;
27 – nut.

Fig. 5.24. Experimental test section design.

The DAS used in the SCPTF facility is equipped with more than 100 measuring channels. The system includes a control panel, high speed multiplexers, AD converter, and sensors for the measurement of temperature, pressure, flow rate, current, and voltage. The data is sampled with a frequency of 300 Hz and subsequently averaged.

Wall temperature in the central rod was measured with two movable probes with three chromel-copel thermocouples installed at 120 º with respect to each other. The design of the movable probe is shown in Fig. 5.28. Two chromel-copel thermocouples were placed in both the inlet and outlet chambers of the TS. Coolant temperature at the outlet was also measured with chromel-copel thermocouples at the centers of subchannels 5, 7, 8, 12, and 17. Each individual thermocouple was calibrated providing an accuracy of ± 0.3–0.5 ºC for temperatures between 0 ºC and 300 ºC.

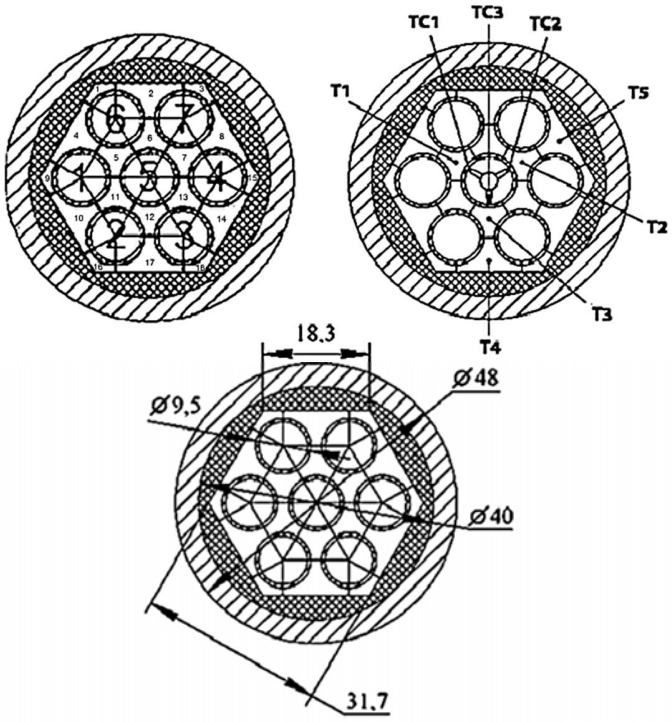

Fig. 5.25. Test section cross section with rod / subchannel numbering, thermocouple layout: T – bulk fluid temperature and TS – wall temperature (all dimensions are in mm).

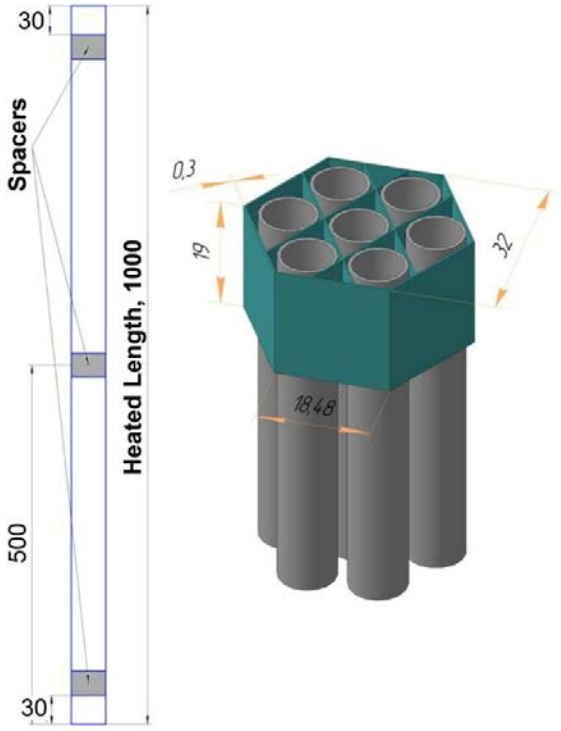

Fig. 5.26. Spacer grid locations (all dimensions are in mm).

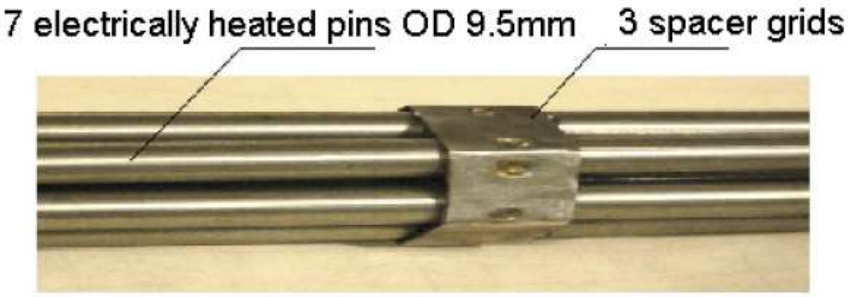

Fig. 5.27. Photo of central part of 7-rod bundle with spacer grid.

TABLE 5.4. 7-rod BUNDLE PARAMETERS.

Flow area, A_{fl}, mm²			**Geometry of 7-rod bundle**	
No. of subchannel	**Value**	**Total**		
1	9.45	374.1	Outside diameter of rod, *D*, mm	9.5
2	33.1		Wall thickness, δ, mm	0.6
3	9.45		Spacer grid pitch, *S*, mm	11.29
4	33.1		Relative pitch of spacer grid, *S/D*	1.19
5	19.8		Heated Length, *L*, m	1.0
6	19.8		**Rated currents and resistances (at T = 150 °C)**	
7	19.8		Material of heater rod tubes	1X18H10T
8	33.1			
9	9.45		Electrical resistivity, Ohm·m	$8.25 \cdot 10^{-3}$
10	33.1			
11	19.8		Conductivity of one heater rod tube, 1/Ohm	20.33
12	19.8			
13	19.8		Resistance of one heater rod tube, Ohm	0.049
14	33.1			
15	9.45		Resistance of rod bundle, Ohm	$7.0 \cdot 10^{-3}$
16	9.45			
17	33.1		Current (A), at bundle power 50 kW	2668
18	9.45			

The three movable thermocouples were in contact with the inner wall surface of the central heated rod. External wall temperature was calculated using the following equation:

$$T_w^{ext} = T_w^{int} - \frac{q_v d_{ext}}{2\,k}\left(\frac{1}{2} - \frac{d_{int}^2}{d_{ext}^2 - d_{int}^2}\right) ln\left(\frac{d_{ext}}{d_{int}}\right) \tag{5.1}$$

Pressure was measured in the TS inlet and outlet using Sapfir-22DI transducers with an accuracy of ± 0.25 %. Each transducer was individually calibrated with an accuracy up to ± 0.5–1 %.

Pressure drop in the test channel was calculated using Sapfir-22DD transducers and confirmed using the difference between the transducers at the inlet and outlet.

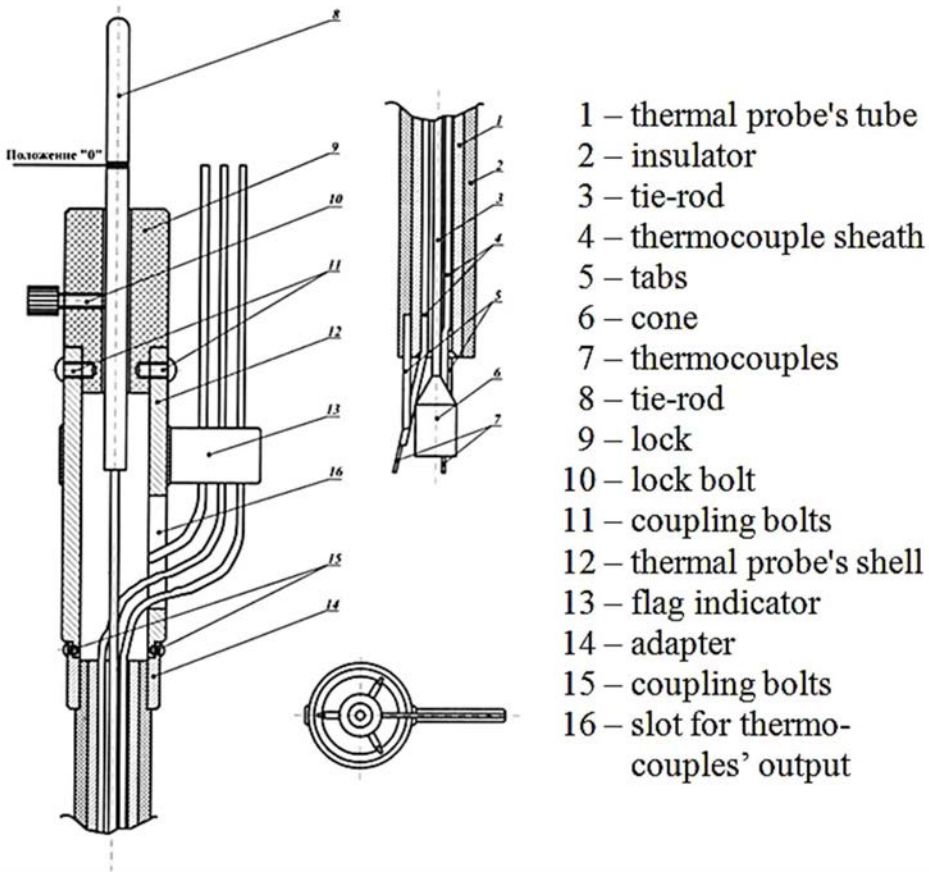

Fig. 5.28. Design of movable thermocouple probe temperature measuring inside central rod.

Coolant flow rate was measured using orifice flow meters and a Sapfir-22DD pressure difference transducer. The flow meter was calibrated in water with the volume time method certified by State Standard Service of Russian Federation with a measurement accuracy of ± 0.11 %. The approximate relative relationship for flow rate has a relative error of ± 0.4 %.

Electrical current for the heated rods was measured using calibrated shunts with an accuracy of ± 0.5 %. Voltages were measured using dividers with an accuracy of ± 0.1 %. The electrical power of the heated rods was calculated using the current and power measurements with a relative error of no more than ± 2 %.

Supercritical Freon R-12 was used as the coolant in the TS in all cases. The coolant flowed upward, entering the heated region at the bottom of the channel.

5.4.3. EXPERIMENTAL RESULTS

A total of 12 runs were performed using the experimental setup. However, this dataset can be broken down into three major cases:

1) Below pseudocritical point: Freon R−12 bulk fluid temperature was below the pseudocritical temperature along the whole heated length of the bundle;
2) Crossing the pseudocritical point: Freon R−12 bulk fluid temperature was below the pseudocritical temperature at the inlet but reached the pseudocritical temperature before the outlet of the bundle;
3) Above pseudocritical point: Freon R−12 bulk fluid temperature was above the pseudocritical temperature along the entire heated length of the bundle.

The three major cases can be further divided into subcases based on a range of mass flux. These subcases are:

1) Low mass flux: 440–520 kg/m^{2}s;
2) Moderate mass flux: 990–1030 kg/m^{2}s;
3) High mass flux: 1190–1320 kg/m2s

Text matrix is listed in Table 5.5, and variations of bulk fluid and wall temperature, and HTC profiles are shown in Fig. 5.29 to Fig. 5.40.

TABLE 5.5. TEST MATRIX (PRESSURE AT 4.65 MPA IN R−12 CORRESPONDS TO 25 MPA PRESSURE IN WATER).

Run No.	***Q*, kW**	***G*, kg/m^{2}s**	***P*$_{in}$, MPa**	***P*$_{out}$, MPa**	***T*$_{in}$, °C**
1	2.05	441.3	4.64	4.64	86.1
2	9.98	447.1	4.63	4.63	89.9
3	4.05	508.4	4.65	4.65	74.4
4	11.0	510.8	4.67	4.67	77.5
5	14.0	516.9	4.64	4.64	73.8
6	17.0	515.6	4.63	4.63	73.4
7	6.98	517.2	4.64	4.63	111.8
8	6.99	516.5	4.63	4.63	119.0
9	9.09	515.6	4.65	4.64	119.3
11	16.9	1020.2	4.63	4.61	80.0
12	25.0	1019.4	4.64	4.63	80.1
14	20.1	1002.6	4.64	4.63	100.4
Bulk fluid temperature is **BELOW** pseudocritical temperature		Bulk fluid temperature is **CROSSING** pseudocritical temperature		Bulk fluid temperature is **ABOVE** pseudocritical temperature	

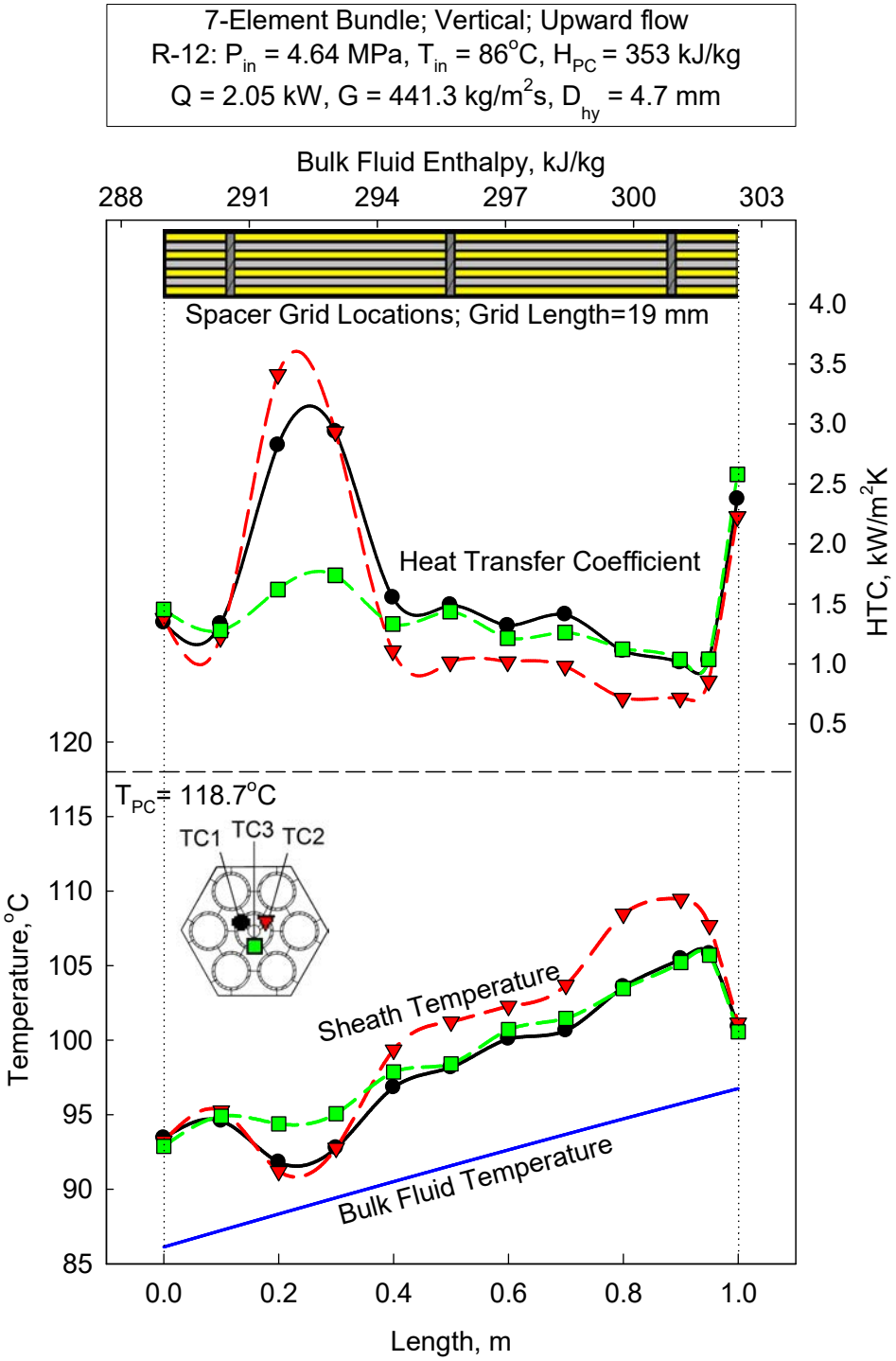

Fig. 5.29. Bulk fluid and wall temperatures, and HTC profiles along the heated length of vertical bare 7-rod bundle cooled with upward flow of SC R–12 for Run 1.

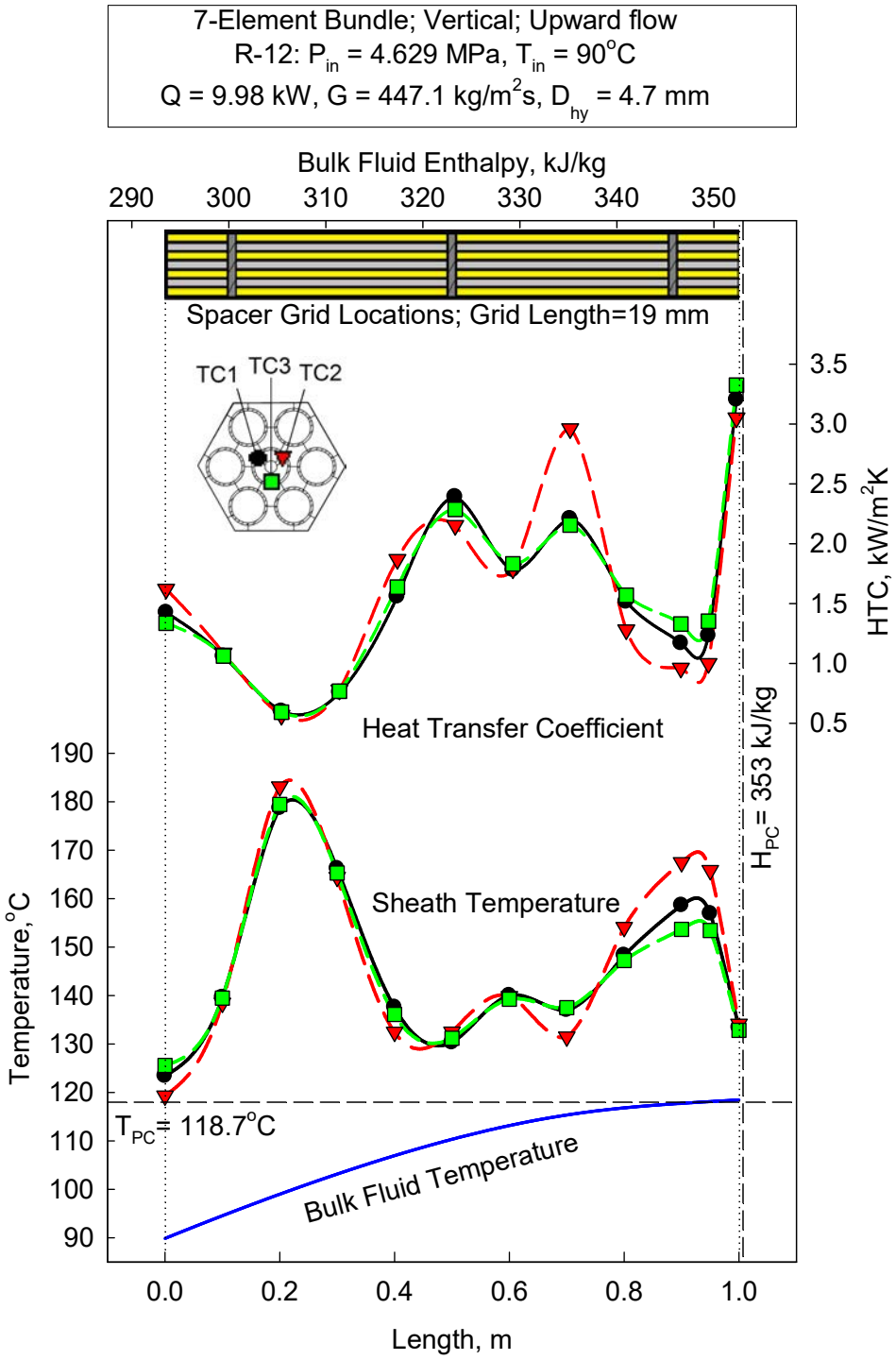

Fig. 5.30. Bulk fluid and wall temperatures, and HTC profiles along the heated length of vertical bare 7rod bundle cooled with upward flow of SC R–12 for Run 2.

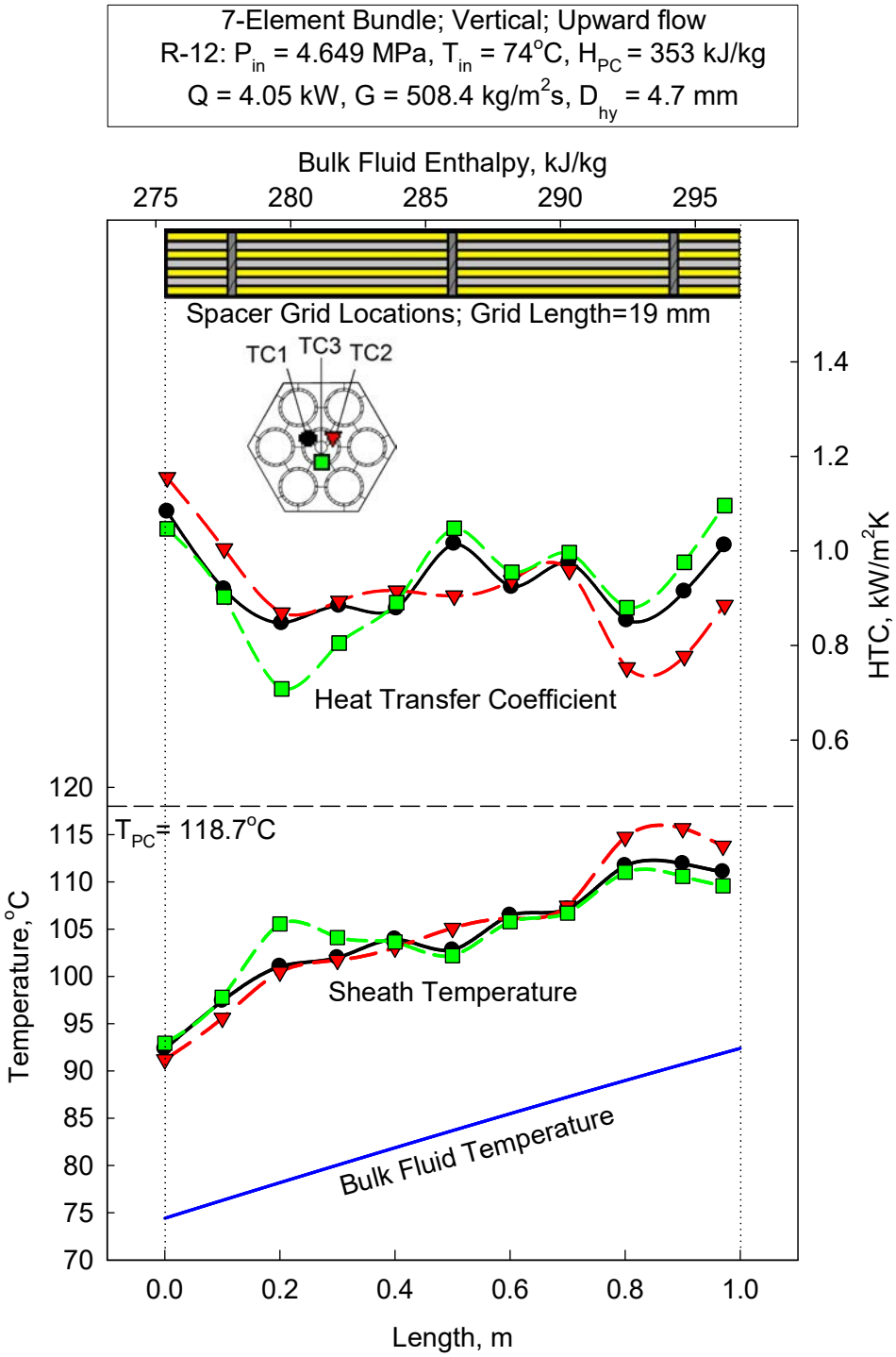

Fig. 5.31. Bulk fluid and wall temperatures, and HTC profiles along the heated length of vertical bare 7-rod bundle cooled with upward flow of SC R–12 for Run 3.

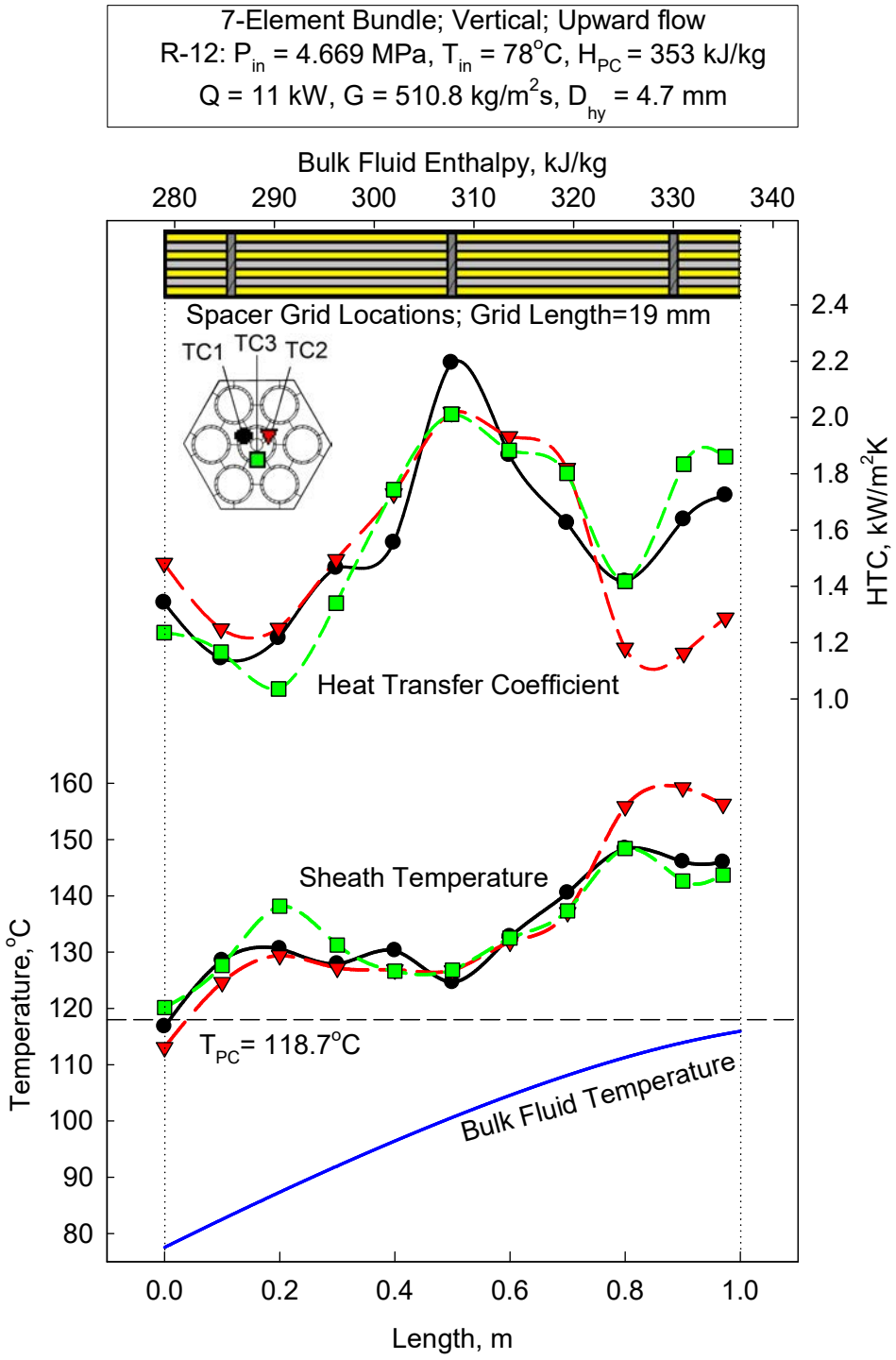

Fig. 5.32. Bulk fluid and wall temperatures, and HTC profiles along the heated length of vertical bare 7-rod bundle cooled with upward flow of SC R–12 for Run 4.

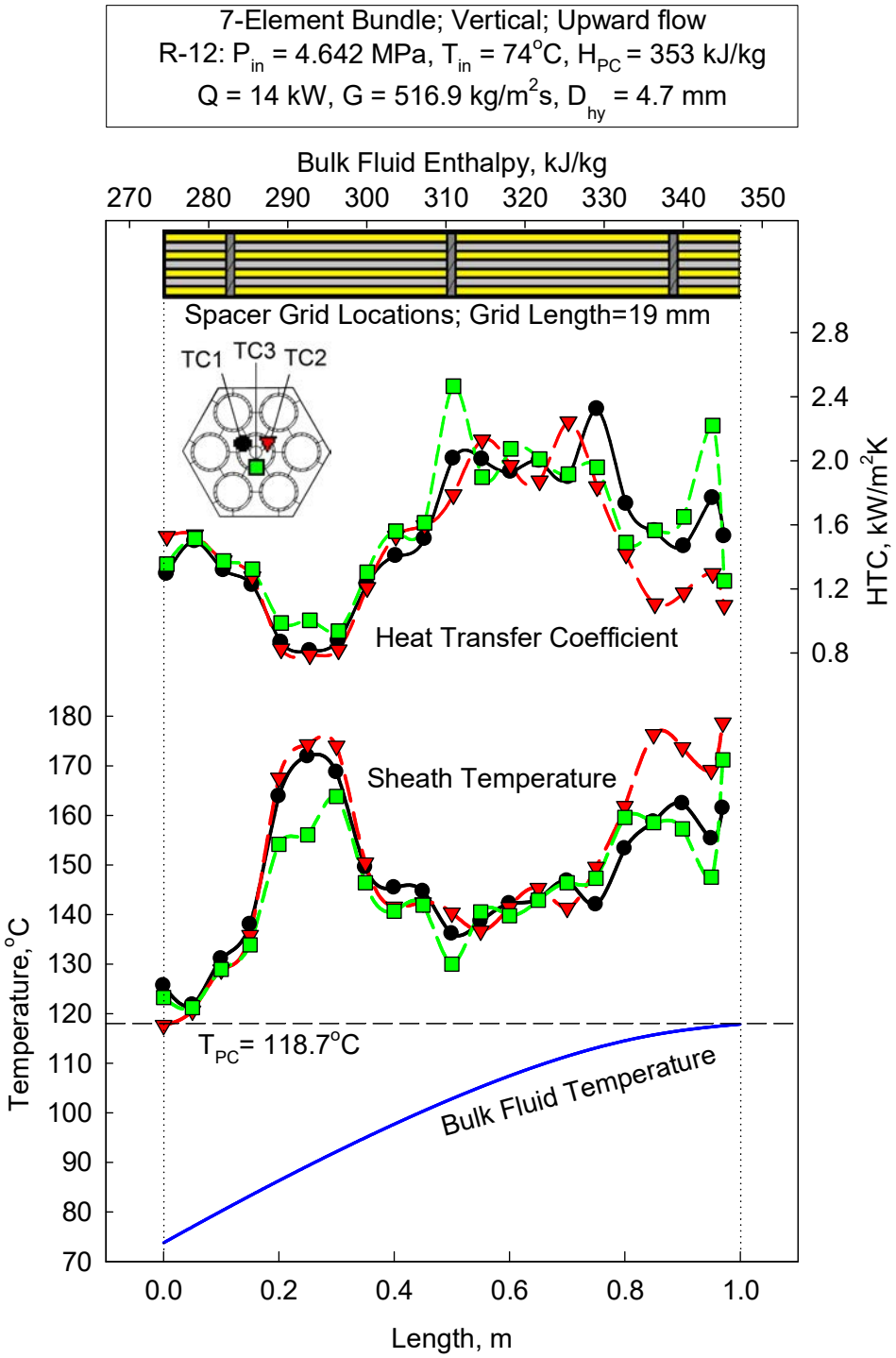

Fig. 5.33. Bulk fluid and wall temperatures, and HTC profiles along the heated length of vertical bare 7-rod bundle cooled with upward flow of SC R–12 for Run 5.

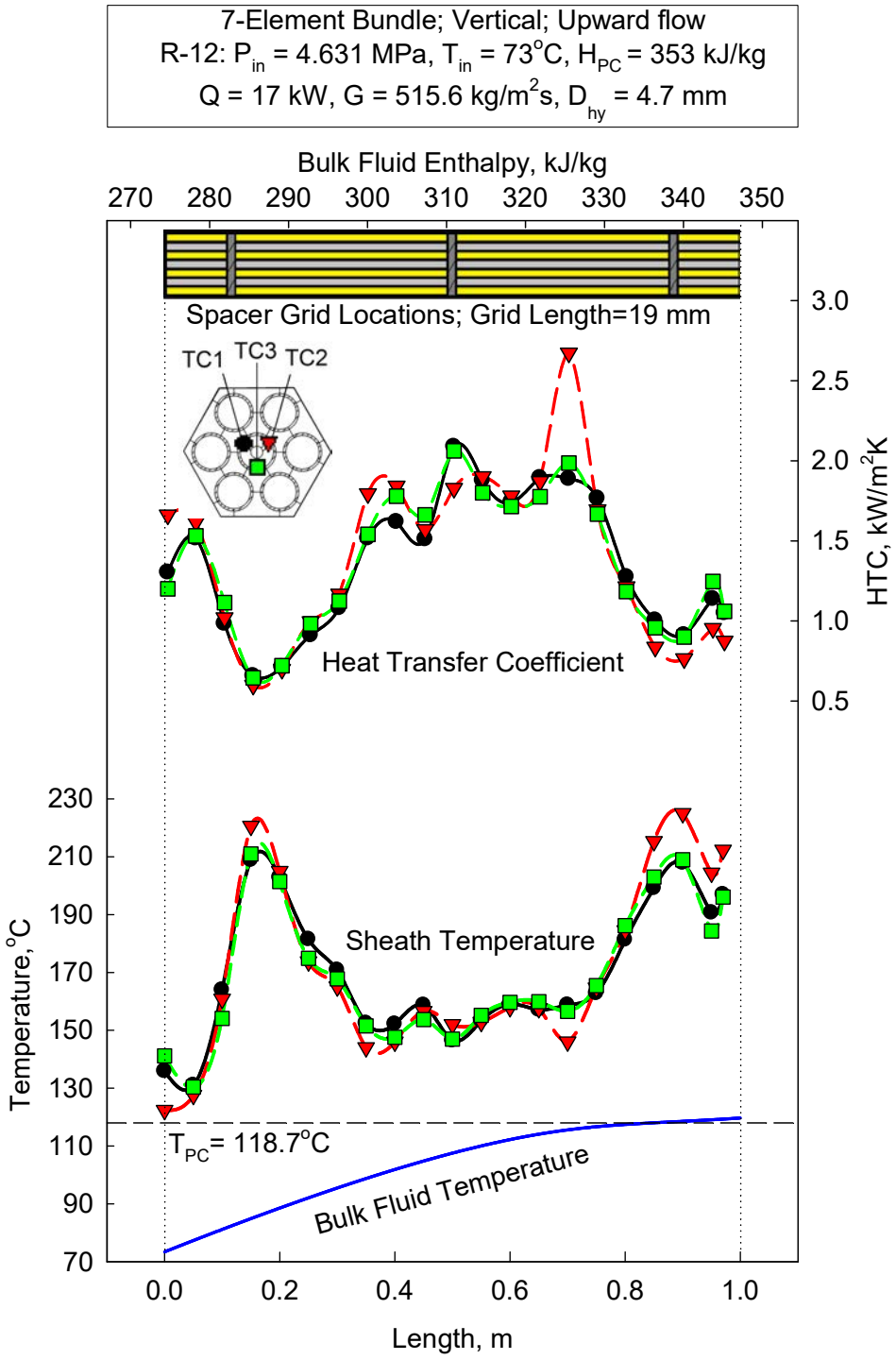

Fig. 5.34. Bulk fluid and wall temperatures, and HTC profiles along the heated length of vertical bare 7-rod bundle cooled with upward flow of SC R–12 for Run 6.

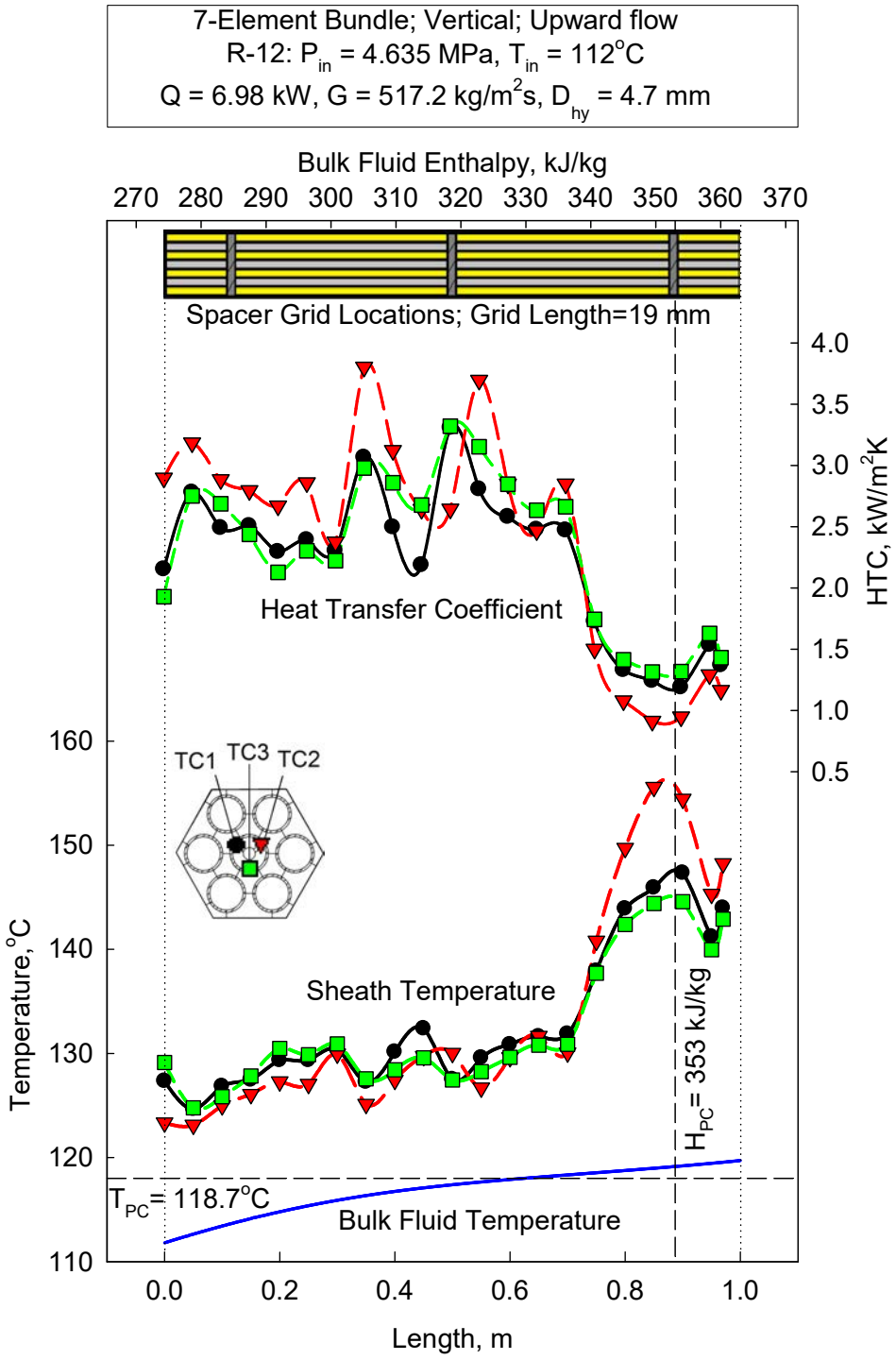

Fig. 5.35. Bulk fluid and wall temperatures, and HTC profiles along the heated length of vertical bare 7-rod bundle cooled with upward flow of SC R–12 for Run 7.

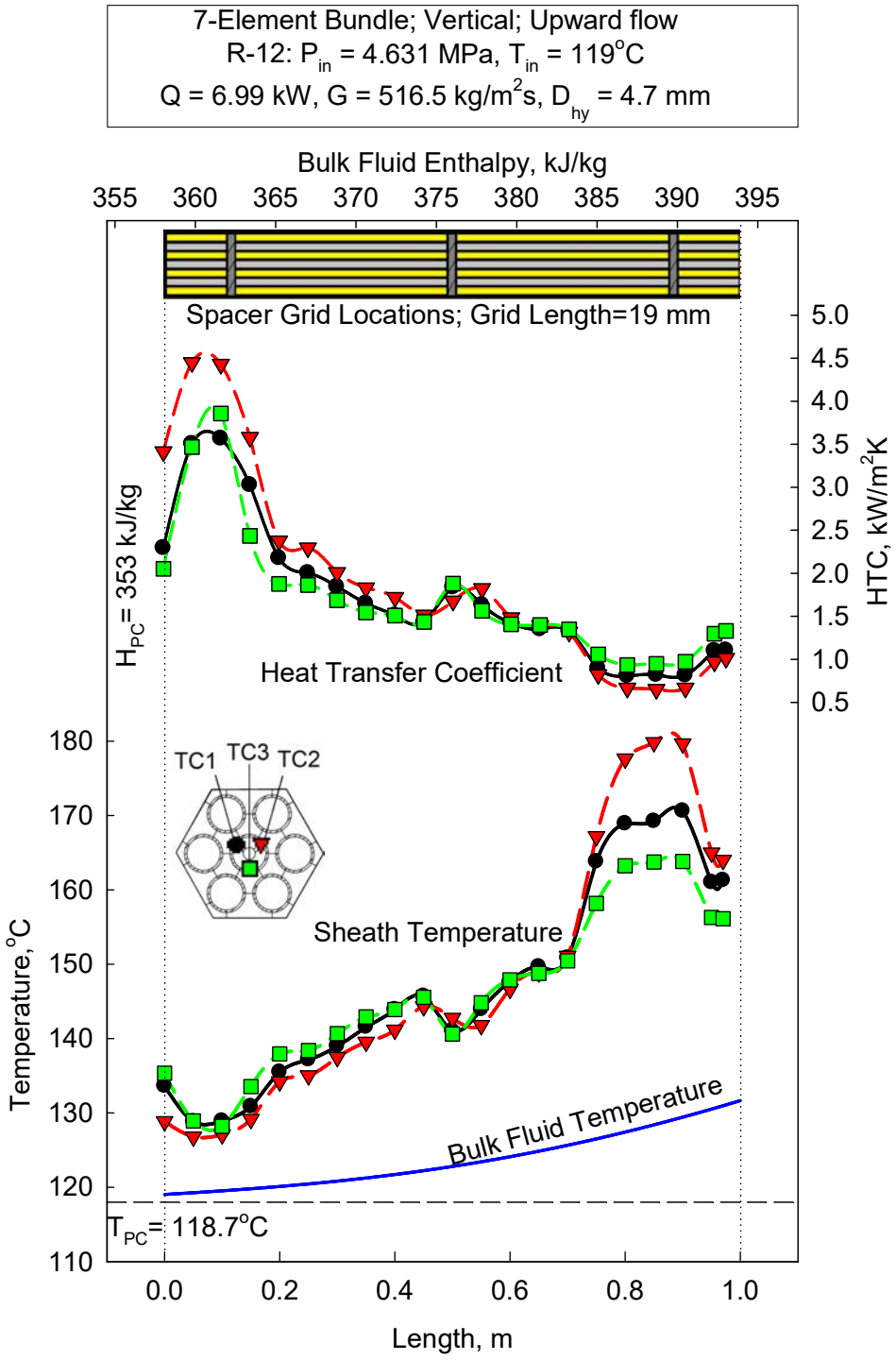

Fig. 5.36. Bulk fluid and wall temperatures, and HTC profiles along the heated length of vertical bare 7-rod bundle cooled with upward flow of SC R–12 for Run 8.

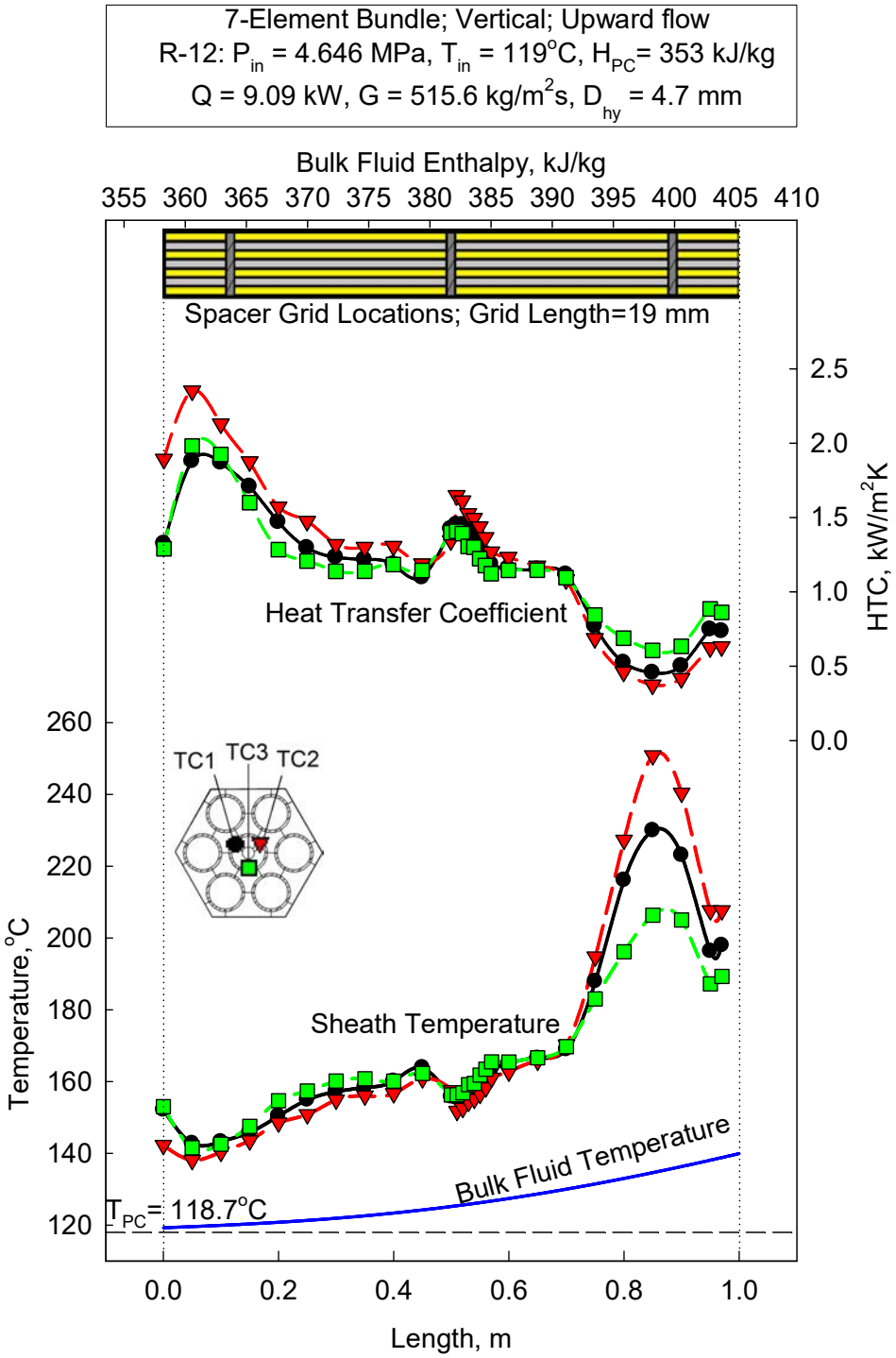

Fig. 5.37. Bulk fluid and wall temperatures, and HTC profiles along the heated length of vertical bare 7-rod bundle cooled with upward flow of SC R–12 for Run 9.

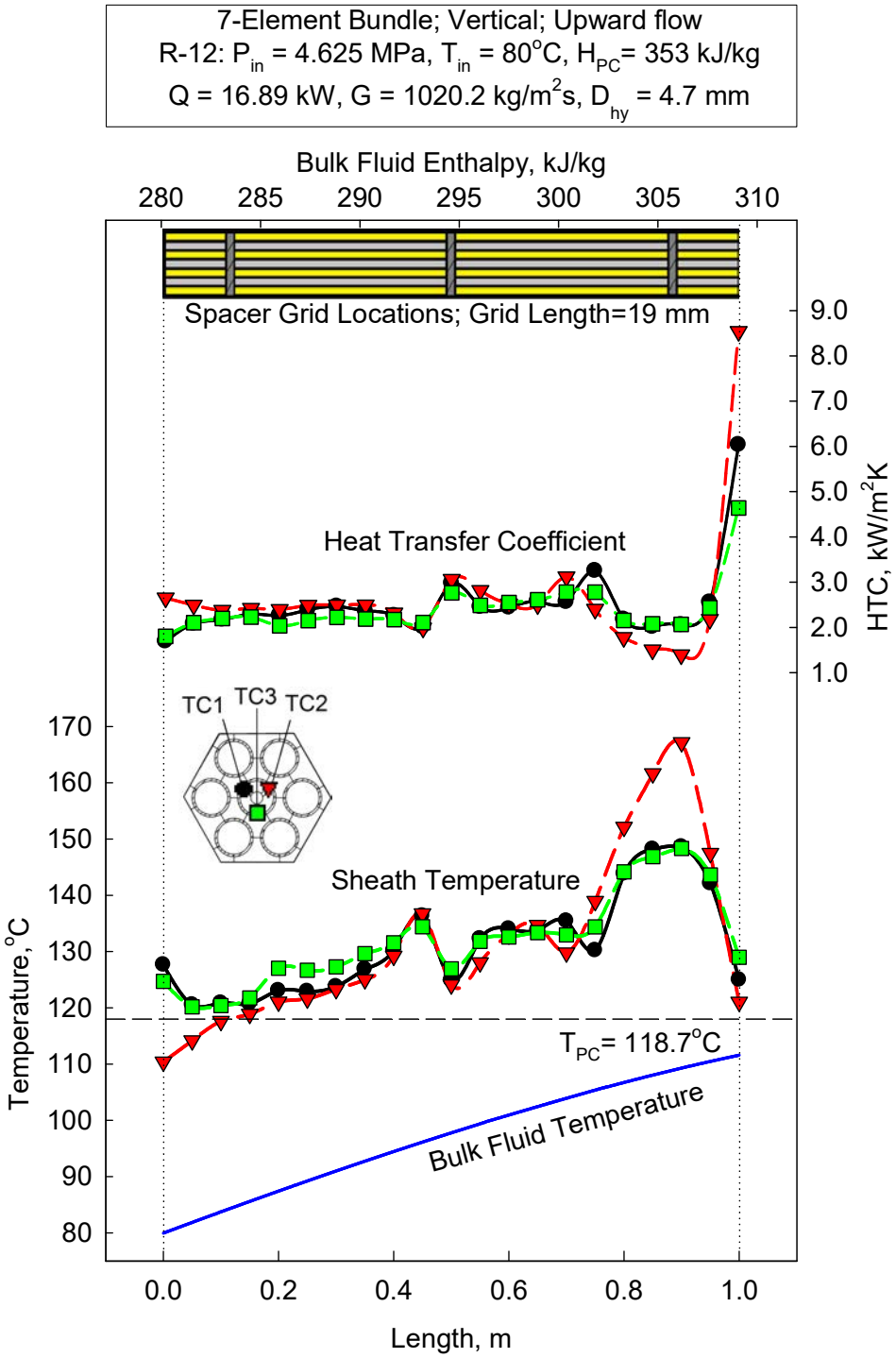

Fig. 5.38. Bulk fluid and wall temperatures, and HTC profiles along the heated length of vertical bare 7-rod bundle cooled with upward flow of SC R–12 for Run 11.

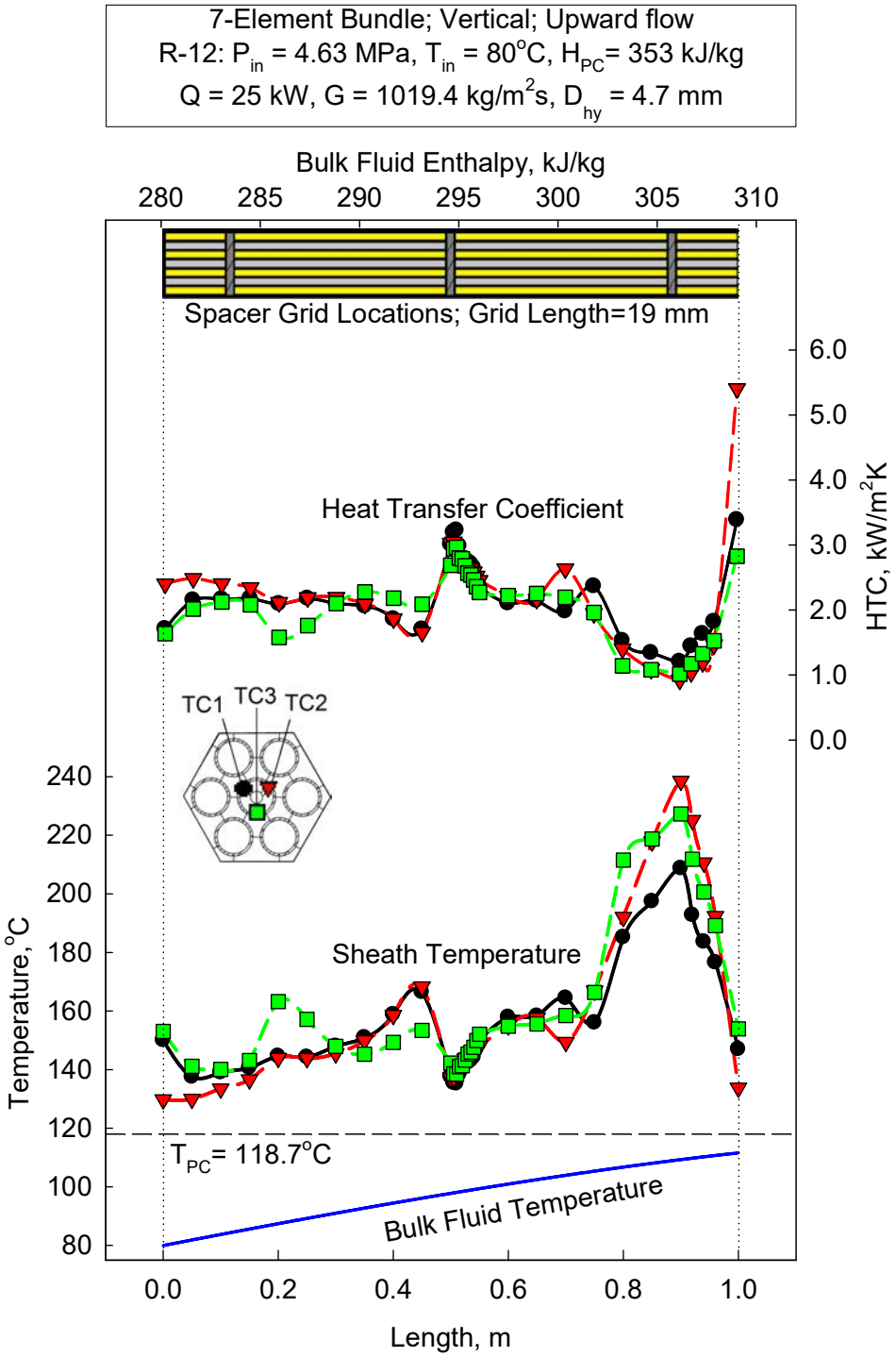

Fig. 5.39. Bulk fluid and wall temperatures, and HTC profiles along the heated length of vertical bare 7-rod bundle cooled with upward flow of SC R–12 for Run 12.

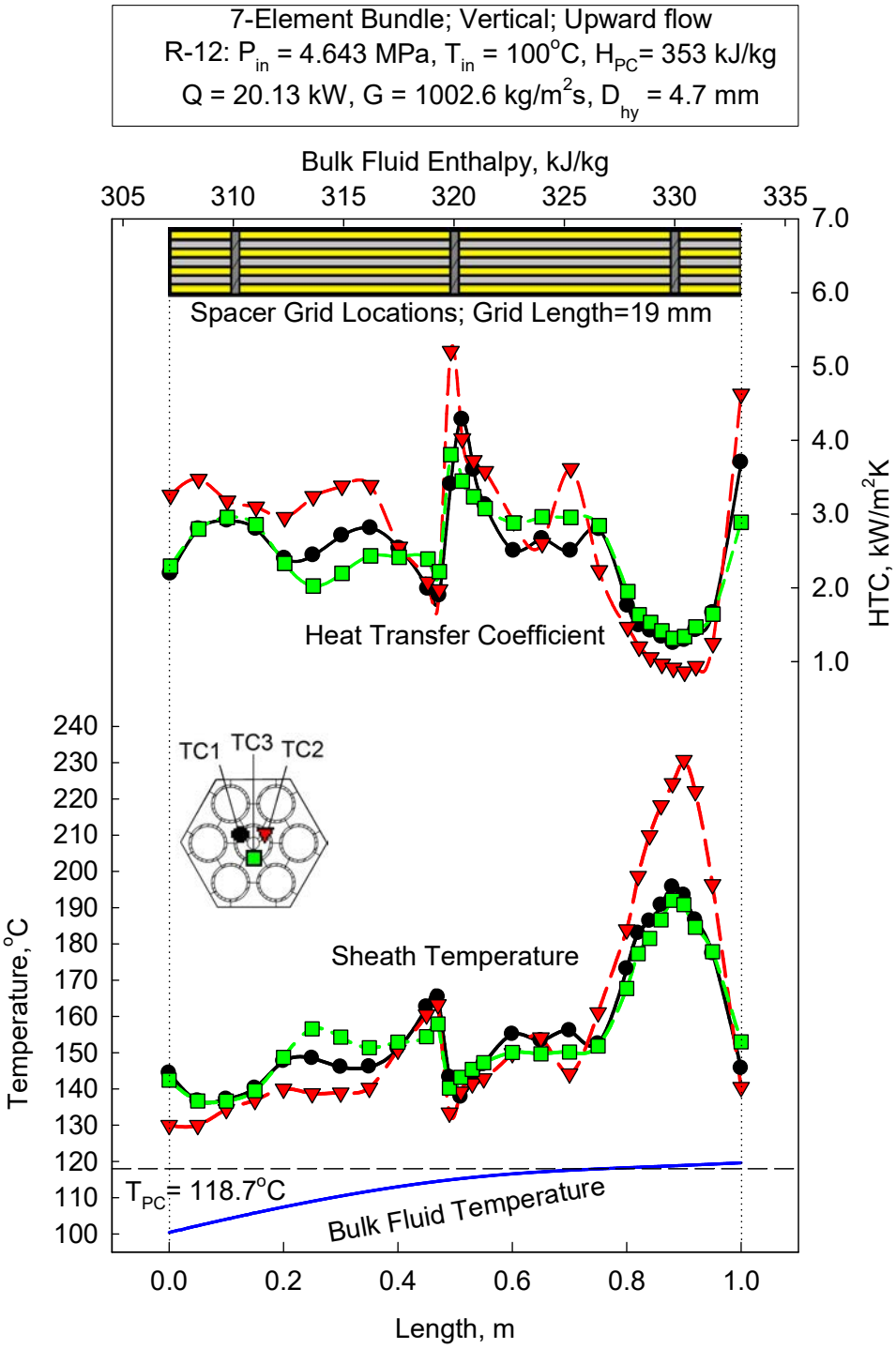

Fig. 5.40. Bulk fluid and wall temperatures, and HTC profiles along the heated length of vertical bare 7-rod bundle cooled with upward flow of SC R–12 for Run 14.

Analyzing data presented in Fig. 5.29, Fig. 5.40 shows the phenomena as summarised in the following items:

— The 7-rod vertical bare bundle cooled with upward flow of SC R−12 is experienced the same three HT modes or regimes as vertical bare tubes [5.5], [5.16], [5.17], [5.18], [5.19], annular channels and bundles [5.5], [5.20] cooled with upward flow of SC water, CO_2 or other SC fluids, i.e.: 1) NHT; 2) IHT; and 3) DHT.
— However, HTC and wall temperature circumferential distribution over the central heated rod (rod) can be significantly non-uniform, i.e., HTCs can vary up to 2.5 times and wall temperatures can vary up to 40 °C. This finding differs from that known in vertical bare tubes and is obviously dependent on the more complex geometrical features.
— Moreover, HTCs and wall temperatures can vary considerably in the axial direction, i.e., HTCs up to 7 times and wall temperatures up to 130 °C.
— There is a possibility that wall temperatures measured with the first downstream thermocouples at the axial location of 0 m and the last upstream one at the axial location of 1 metre might be affected with current terminals attached to the heated rods (rods), because temperatures measured with these thermocouples can be significantly lower than those measured with the rest of thermocouples. Therefore, these measurements should be regarded with caution.
— In some runs, all three HT regimes or modes can be noticed; e.g., in Run 8: IHT in the last part of the TS, where the bulk fluid temperature is slightly above the pseudocritical temperature; NHT within the central part of TS; and NHT within the upstream part of the TS; in Run 14: NHT regime within downstream half of the TS, then IHT within a quite short heated length (~50 mm), then NHT again and, within the upstream part of the TS (from 0.8 m to 1.0 m) DHT regime.
— DHT regime can appear at certain ratio of heat flux to mass flux and its location can be: (a) within the downstream part of the TS, when the wall temperature crossed the pseudocritical one; (b) within the upstream part of the TS, when the bulk fluid temperature is approaching or crossing the pseudocritical one; but (c) it can appear also quite unexpectedly within the upstream part of the TS, when wall and bulk fluid temperatures are above the pseudocritical one, i.e., at the 'gas-like' fluid cooling, which is unusual for bare tube data.

5.5. SJTU TESTS AND DATA

Experiments of supercritical water heat transfer for upward flow in 2×2 rod bundles have been performed in SJTU, with system pressure ranging from 23 to 26 MPa, mass flux between 450 and 1500 kg/m^{2}s, and heat flux from 0.4 to 1.5 MW/m^2 [5.38].

5.5.1. SJTU TEST FACILITY

The Supercritical WAter MUltiPurpose loop (SWAMUP) test facility in SJTU is shown in Fig. 5.41. It mainly contains a main test loop, a cooling water loop, a water purification loop and I&C system. The main test loop is made up of a circulating pump, pre-heater, mixing chamber, two heat exchangers, accumulator and test sections. As summarized in Table 5.6, the test facility is designed with pressure up to 30 MPa, maximum temperature up to 550°C, mass flow rate up to 1.3 kg/s, and electrical power up to 1.2 MW.

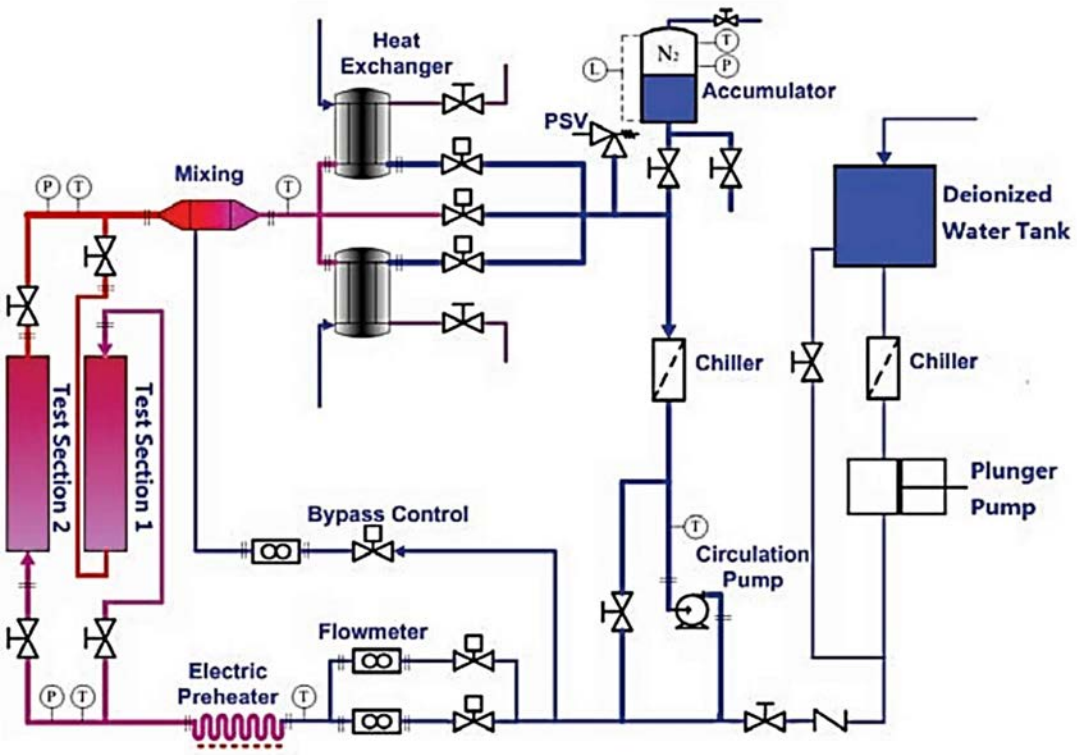

Fig. 5.41. Scheme of the SWAMUP test facility.

TABLE 5.6. TECHNICAL SPECIFICATION OF THE SWAMUP TEST FACILITY

Parameters	**Values**	**Units**
Design pressure	30	MPa
Design temperature	550	°C
DC power for test section	0.9	MW
Heating power for pre-heater	0.3	MW
Heat exchanger capacity	1.2	MW
Max. flow rate	5.0	t/h
Pump head at maximum flow rate	80	m

5.5.2. BUNDLE GEOMETRY

More details of the test section are shown in Fig. 5.42. It contains four heating tubes (Inconel 718, 8 mm OD and 1.5 mm thickness) and a ceramic square tube (20.32×20.32 mm and 23.2×23.2 mm thickness) with hydraulic diameters of 4.6 mm and 7.3 mm, respectively. The length of each rod bundle is 1328 mm and the bundles are supported by 5 or 6 spacer grids at different elevations. To

measure the inner wall temperature of the heated tubes, a sliding thermal couple is installed inside of the heating tube. During experiments, four sliding thermocouples for four heating tubes were used with the circumferential position shown in Fig. 5.43. Sliding thermocouples were moved axially and circumferentially. Meanwhile, the square tube is not heated and is insulated from the environment by fiberglass.

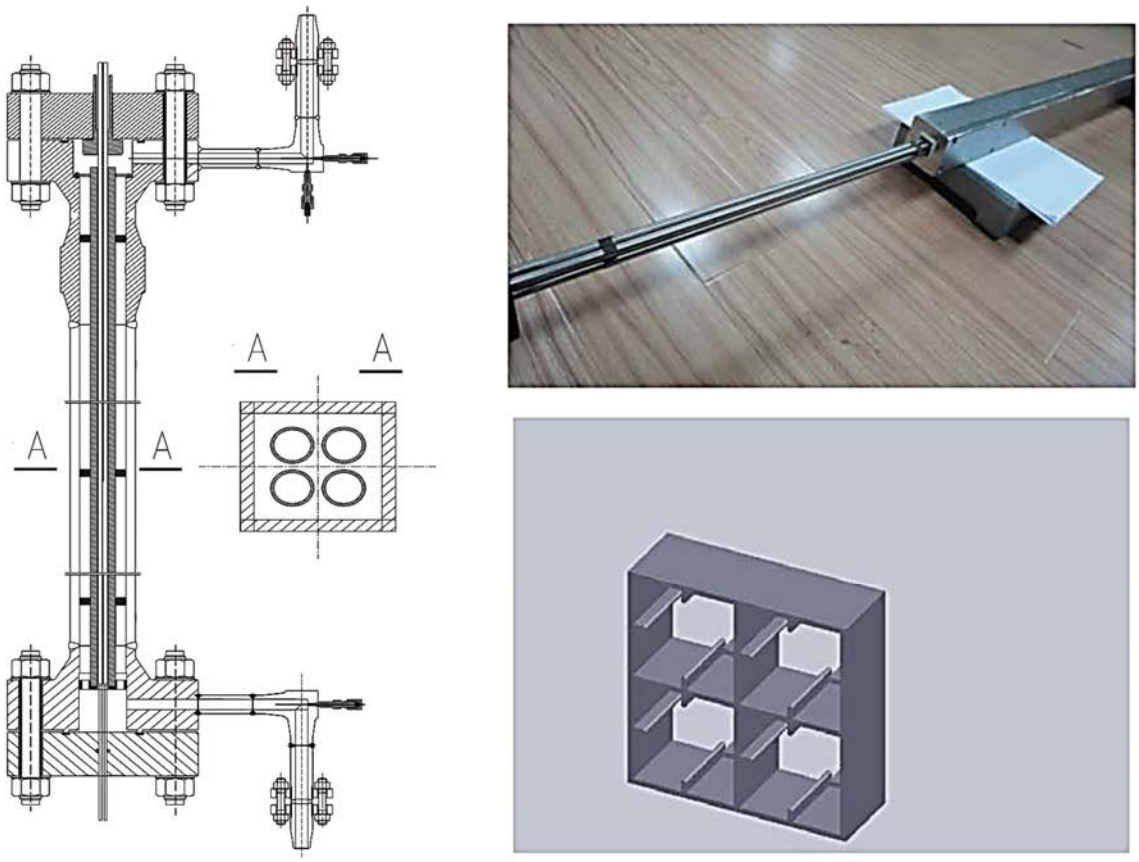

Fig. 5.42. Schematic diagram of test section and space grid.

5.5.3. TEST MATRIX AND EXPERIMENTAL PROCEDURE

Ahead of main experiments, a heat balance test under single phase flow condition was conducted to assess the heat loss from the test section and to guarantee the performance of the test instrumentations. In these previous heat balance tests, after comparing the enthalpy rise of working fluids through the test section with the total power supplied to the test section under certain inlet pressure, inlet temperature and mass flux, the heat loss was concluded much less than +5 %.

The pressure in the test loop is controlled by the pressure regulator valve at the outlet of the loop while the pump is operating. The mass flow velocity is adjusted by the control valves in the bypass loop. The power to the test section is increased in steps until the expected value is reached. Experiments are performed by holding the pressure, heating power and mass flow velocity at constant values for each run. The fluid temperature at the inlet of the test section is increased

gradually by controlling the power of the preheater. The experimental data including pressure at the inlet of the test section, pressure drop of the test section, mass flow velocity and power to the test section, inlet and outlet fluid temperature, and the wall temperature are recorded continuously during each run. The test is terminated when the wall temperature at any location exceeds 580 °C or when the outlet fluid temperature is over 500 °C.

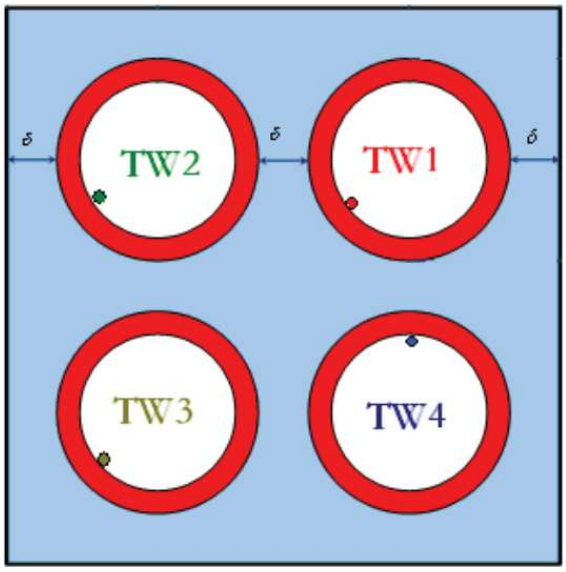

Fig. 5.43. Circumferential Position of Sliding Thermocouples.

During the experiments, an abrupt increase in the recorded wall temperature is treated as the onset of heat transfer deterioration (HTD). Significant HTD occurs when the local wall temperature rises by more than 10 % in a short time.

5.5.4. EXPERIMENTAL DATA REDUCTION

The experimental parameter ranges are shown in Table 5.7 More than 500 measurement points were recorded. The heating tube was uniformly heated. By neglecting the axial heat conduction and assuming a one-dimensional heat conduction equation, the outside surface temperature of the heating tube could be derived from the measured inner surface temperature. The effect of temperature on thermal conductivity of the heating tube is also taken into consideration in the calculation. Table 5.8 provides the uncertainty of test parameters.

The heat flux of the heating tube is described as follows:

$$q_s = \frac{U \cdot I}{\pi D_0 L} \eta \tag{5.2}$$

where q_s stands for the heat flux on the outside surface of the heating tubes, U the measured DC voltage, I the current, η the thermal efficiency, D_0 outside diameter of the heating tube, and L heating length.

TABLE 5.7. RANGES OF TEST PARAMETERS

Parameters	**Values**	**Units**
Pressure	23, 25, 26	MPa
Mass flow rate	500 –1500	kg/(m^{2}s)
Heat flux	0.40 –1.50	MW/m^2
Bulk temperature	310 –390	°C

TABLE 5.8. UNCERTAINTIES OF PRIMARY PARAMETERS

Parameters	**Maximum uncertainty**
Pressure	0.2%
Mass flow rate	0.4%
Fluid temperature	1.5°C
DC current	1.0%
DC voltage	1.0%
Heated tube diameter	0.04 mm
Heated tube thickness	0.02 mm

The enthalpy at each measurement point can be calculated with the energy conservation equation as follows:

$$H(z) = H_{in} + \frac{4zq_s}{GA_{flow-channel}} \tag{5.3}$$

in which H_{in} stands for enthalpy at the inlet of the test section, z represents the distance from a certain measurement point to the inlet, G is mass flux, and $A_{flow-channel}$ is the area of the flow channel.

The outside wall temperature of the heating tube can be calculated by the following equation:

$$T_{wo} = T_{wi} + \frac{q_v}{4k_w}\left[\left(\frac{D_0}{2}\right)^2 - \left(\frac{D_i}{2}\right)^2\right] - \frac{q_v}{2k_w}\left(\frac{D_0}{2}\right)^2 ln\frac{D_i}{D_0} \tag{5.4}$$

where T_{wo} describes the outer wall temperature, D_i and D_0 are the inner and outside heating tube diameter and k_w represents the thermal conductivity of the heating tube.

Assuming the heating power density is uniform in the heating tube, the heat flux q_v is calculated:

$$q_v = \frac{4U \cdot I}{\pi\left({D_0}^2 - {D_i}^2\right)L}\ ^{\eta} \tag{5.5}$$

Finally, the local bundle average heat transfer coefficient can be calculated with:

$$HTC_{ave} = \frac{q_s}{T_{wo}(z) - T_{b-ave}(z)} \tag{5.6}$$

where $T_{b-ave}(z)$ is the bulk fluid temperature. To get the bulk fluid temperature, two different methods are used. The first method uses the measured bundle average fluid temperature. As for the second one, CFD simulation is used to get the subchannel average fluid temperature. Therefore, the subchannel based heat transfer coefficient is caluculated with:

$$HTC_{sub} = \frac{q_s}{T_{wo}(z) - T_{b-CFD}(z)} \tag{5.7}$$

in which HTC_{sub} is the heat transfer coefficient of a certain subchannel, $T_{b-CFD}(z)$ stands for the average fluid temperature calculated by CFD method in this subchannel.

5.5.5. HEAT TRANSFER CHARACTERISTICS

The relationship between the measured wall temperature and the distance from the inlet of the test section in three kinds of subchannels and rod gap are displayed in Fig. 5.44 for test condition: P = 23 MPa, G = 900 kg/(m^{2}s) and q = 1.2 MW/m^2. There is a clear trend of decreasing of the wall temperature in the downstream of the spacer grids, where the heat transfer is enhanced. This trend can be observed by the wall temperature measured by 4 thermocouples in different subchannels. Overall, the center subchannel corresponds to the lowest wall temperature and the corner subchannel is the highest.

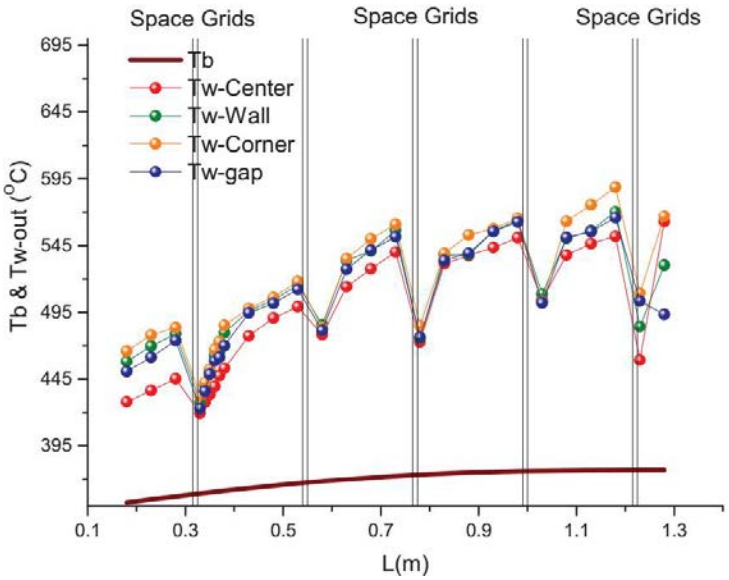

Fig. 5.44. Wall and Average Fluid Temperatures vs Axial Position (P = 23 MPa, G = 900 kg/(m²s) and q = 1.2 MW/m²).

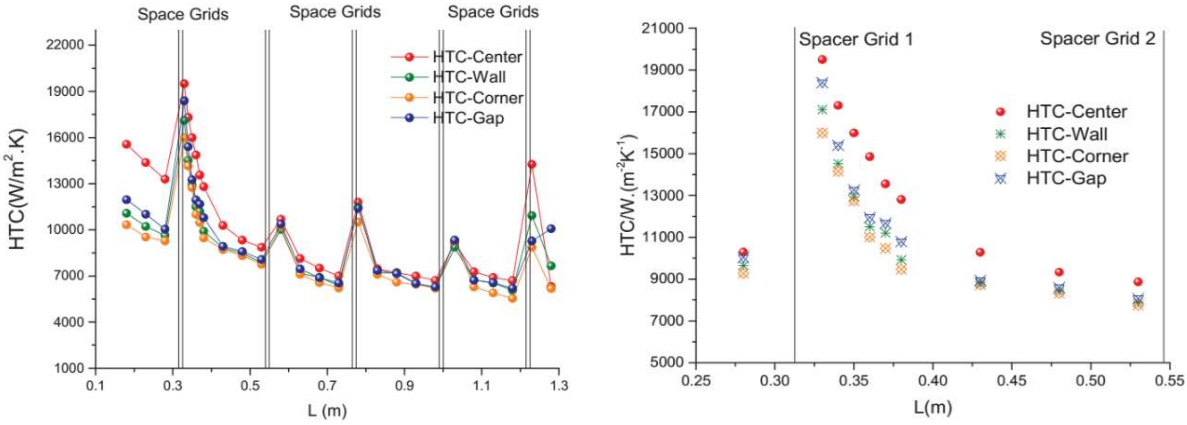

(a) Total heated length

(b) Between two spacers

Fig. 5.45. Average Heat Transfer Coefficient vs Axial Position (P/D = 1.3, P = 23 MPa, G = 900 kg/(m²s) and q = 1.2 MW/m²).

In addition, with the same experimental condition in Fig. 5.44, the bundle average heat transfer coefficients at different distance from the inlet of the test section are shown in Fig. 5.45. the distribution of the heat transfer coefficient over the entire heating length and between two spacer grids are displayed in Fig. 5.45(a) and Fig. 5.45(b) respectively. As illustrated, there is an apparent increase of heat tranfer coefficient in the downstream of the spacer grid. With the increase in the downstream distance from the spacers, the heat transfer coefficient first drops sharply and then falls steadily. For positions far from the upstream spacers(e.g., 40 times the hydraulic diameter), the heat transfer coefficient tends to be constant. It can be concluded that at a distance greater than 40 times the hydraulic diameter, the effect of the spacer grid on the heat transfer coefficient is negligible. This conclusion is valid for all test cases.

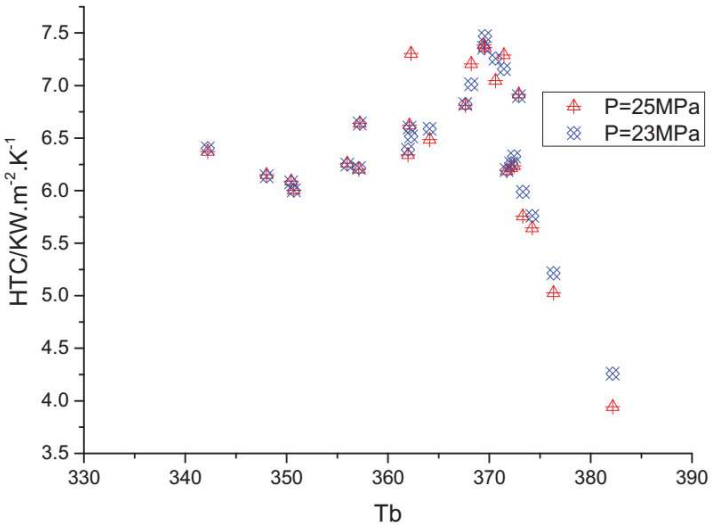

Fig. 5.46. Effect of pressure on HTC (P/D = 1.3, G = 800 kg/(m²s), q = 0.8 MW/m²).

Fig. 5.46, Fig. 5.46 and Fig. 5.46 provide subchannel averaged HTCs in center subchannel versus bulk temperature under different conditions. Therefore, the effect of pressure, heat flux and mass flux on the heat transfer coefficient can be analyzed respectively. In order to eliminate the influence of spacer grids, data points with the distance from the upstream spacer grid larger than 40 times the hydraulic diameter are selected. As shown in Fig. 5.46, strong heat transfer reduction occurs while subchannel temperature near to the pseudocritical values. It can be seen from Fig. 5.47 that the effect of the heat flux on the heat transfer coefficient is not obvious. As for the effect of mass flux which is shown in Fig. 5.46, the higher mass flux leads to higher heat transfer coefficients.

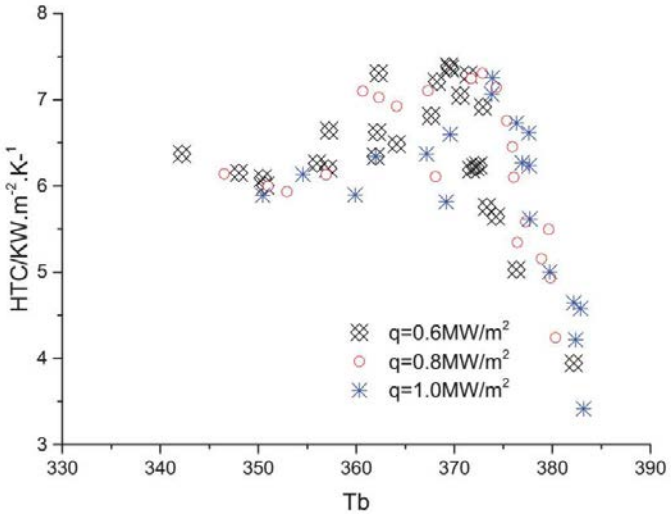

Fig. 5.47. Effect of heat flux on HTC (P/D = 1.3, P = 25 MPa, G = 800 kg/(m²s))

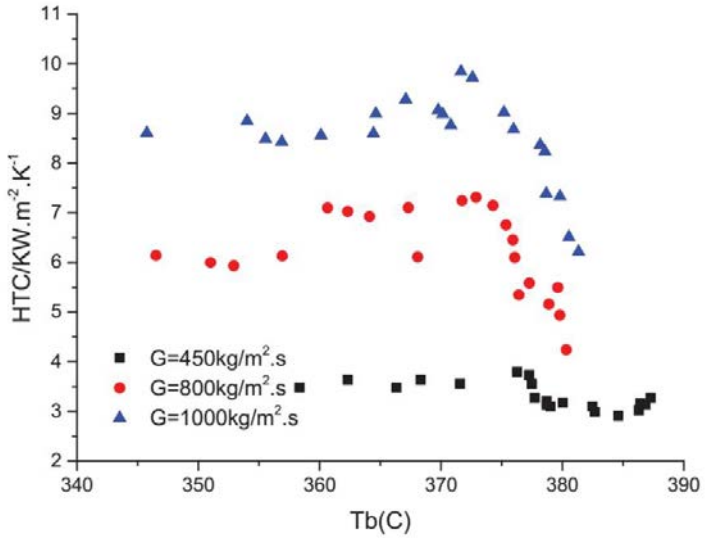

Fig. 5.48. Effect of mass flux on HTC (P/D = 1.3, P = 25 MPa, q = 0.8 MW/m^2).

5.6. EXPERIMENTAL HEAT TRANSFER IN A 3-ROD BUNDLE COOLED WITH UPWARD FLOW OF SUPERCRITICAL WATER AT HIGH HEAT FLUXES

The National Technical University of Ukraine 'Igor Sikorsky Kyiv Polytechnic Institute' has recently completed a study started several decades ago. The study included experiments on heat transfer and pressure drop of supercritical water in round tubes with upward and downward flows, and in annuli with heating of either outer or inner wall. The test rig consisted in a system of parallel tubes; checks were systematically performed for low frequency fluctuations of flow rate in some of them or the thermoacoustic oscillations of pressure, if any, caused by a certain impact of coolant physical and operating parameters on elasticity in the vicinity of pseudocritical thermal state (e.g., [5.13], [5.21]–[5.25]). The accumulated data and experience served as a basis for further development of the experiments related to the investigation of the frictional and inertial components in the hydraulic resistance for a fluid with sharply changing viscosity and density; these changes can crucially affect wall boundary layer heat transfer conditions. In particular, the method of 'two pressure drops', devised and set up at the Institute of High Temperatures of the Academy of Sciences of the USSR (IVTAN) and tested on supercritical carbon dioxide, was adapted to the conditions of supercritical water and applied at the NTUU enabling estimation of real two dimensional pattern of flow acceleration [5.24]. This was obtained without the measurement of the radial velocity profile by means of anemometric probes inserted into the channel of around 6 to 8 mm in diameter, something that until now is practically impossible.

For a long time, the need of taking into account non-isothermal but real frictional factors of the hydraulic resistance of heated channel was ignored by the majority of the researchers who tried to compensate this lack by composing very sophisticated correlations with numerous dimensionless groups included even in the expressions for the correlation's exponents.

The system of two iterative equations for Nu and ζ_{fr} (frictional resistance factor) in terms of Re, Pr, and q/G occurred to be currently one of the best among the ones investigated by NTUU for the channels including 1-rod annular channel, 3 and 7-rod bundles.

5.6.1. NTUU TEST FACILITY

A schematic diagram of the high temperature and high pressure water test loop at NTUU is shown in Fig. 5.49. The supercritical water facility is an open stainless steel loop operating at pressures up to 28 MPa and at temperatures up to 600 °C. Chemically desalinated water (pH = 7.2 and average hardness of 0.2 μg-eqv./kg) was used as a coolant.

From a reservoir, the fluid passes through the pumps, one boosting and two parallel main plunger pumps capable to achieve a pressure up to 70 MPa under the total output of 1400 l/h. Then, the fluid is routed to sets of pressure regulating valves, turbine type flow meter, tube–in–tube preheater, 75 kW electrical preheater, test section, tube-in-tube cooler, and then returns to the reservoir through a set of the throttling valves. The reservoir is open to the atmosphere. The test section is installed vertically for upward or downward flow of water and heated by 120 kW (60 V × 2000 A, AC) and 90 kW (18/36 V × 5000/2500 A, DC) dynamotors or 1 MW thyristor rectifier (100 V × 10,000 A, DC).

The following test section parameters were measured or calculated during the experiments:

- Test section current, based on readings from a measuring transformer in case of AC or on voltage readings from a calibrated shunt for DC, and voltage; these parameters were used to calculate the heat flux;
- Pressure at the test section outlet and pressure drop at the heated length;
- Temperatures at the test section inlet and outlet; these temperatures were measured using Chromel–Alumel sheathed thermocouples of 0.2 mm diameter (wire) inserted into the fluid stream inside the mixing chambers; the latter were used to minimize non-uniformity in the cross sectional temperature distribution and to decrease pressure pulsations within the test section; the thermocouples were calibrated within the temperature range of 20 to 500 ºC.

The temperature trip of the electric power supply was set at 650°C for the internal wall. All wall thermocouples were calibrated within the range of 20 to 700 ºC.

The instrumentation used to measure the loop parameters was thoroughly checked and calibrated. Uncertainties of primary parameters are summarized later in Table 5.9.

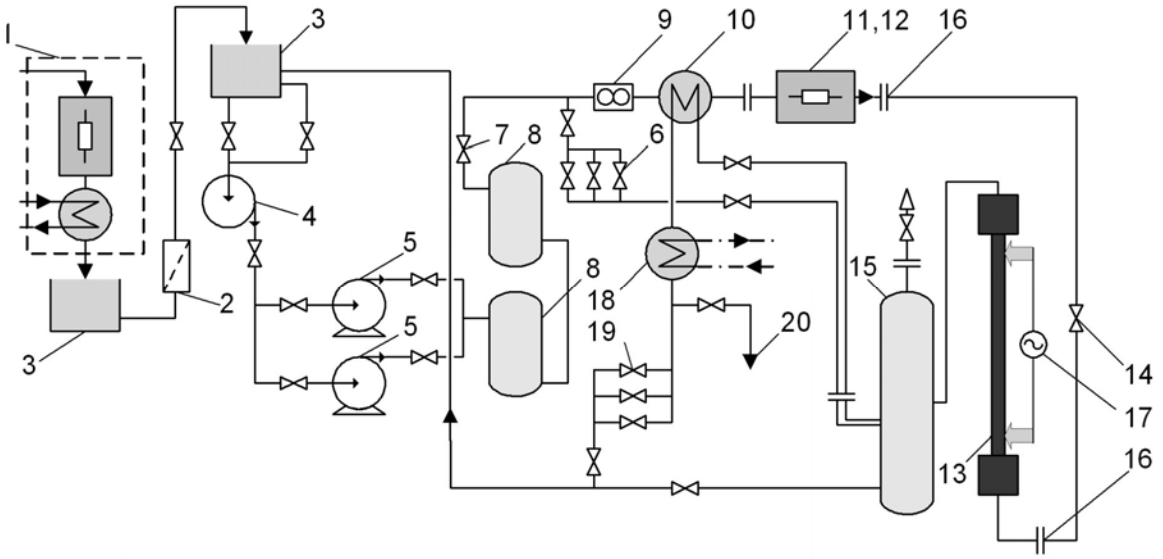

1 – electrodistiller
2 – ion exchange filter
3 – accumulator reservoirs
4 – boosting pump
5 – plunger pumps
6, 7 – control valves
8 – damping reservoirs
9 – turbine flowmeter
10 – heat exchanger
11– electrical preheater
12 – dynamotor(s)
13 – test section
14 – throttle valve
15 – damping reservoir
16 – electro-isolating flanges
17 – main power supply
18 – cooler
19 – throttling valves

Fig. 5.49. General schematic diagram of SCW experimental loop.

TABLE 5.9 UNCERTAINTIES OF MEASURED AND CALCULATED PARAMETERS.

Measured Parameter	**Uncertainty**
Inlet pressure	±0.9%
Current	±0.5%
Voltage	±0.2%
Pressure drop	±2.0%
Mass flow rate	±2.3%
Water inlet/outlet temperature	±2.34%
Wall temperature	±3.21%
Calculated parameters	**Uncertainty**
Heat flux	±3.5%
Heat transfer coefficient	±12.7%
Heat loss	≤2.4%

5.6.2. TEST SECTIONS AND 1 ROD ANNULAR CHANNEL AND 3, 7-ROD BUNDLE SIMULATOR GEOMETRY

Until now there is no information on experimental studies on heat transfer in the core, except for the case concerning a tight and short bundle (H/D = 1.23, $L/D \approx 100$) [5.26]. As many authors revealed [5.27], [5.28], it is sufficient to investigate heat transfer in relatively short channels (25–30 < L/D < 100–120), since beyond this length heat transfer is definitely stabilized and, in general,

the longer is the channel the more is stable the thermal hydraulic situation. Therefore, it is important to investigate supercritical heat transfer in flow geometries, which could simulate short fuel bundle subchannels of relatively small hydraulically equivalent diameters.

The experiments were performed in a vertical 1 rod annular channel and in 3- and 7-rod bundle simulators. The rod was constructed with a cold drawn tube of 485 mm heated length, 5.2 mm OD and 4.5 mm ID. Four helical ribs of 0.6 mm height and 1 mm width were formed along the tube in a 400 mm pitch. The rods were arranged in a triangular array with the rib maintaining the 1 mm gap size (see Fig. 5.50 *b* and *c*). A shaped heat resistant dielectric displacer was installed with calibrated stainless steel fins of 0.1 mm thickness welded to the cylindrical surface of the rods at seven axial locations (i.e., 125, 185, 245, 305, 365, 425, and 485 mm) from the start of the heated length. With reference to Fig. 5.51, the heated rod (1) is inserted into the dielectric displacer (2) composed by shaped dielectric cartridges to provide the flow area of annuli cross section. The displacer is inserted into a stainless steel pressure tube (14) of 18 mm OD and 12 mm ID. After the outlet chamber (12), water enters into the damping reservoir (11) partially filled with nitrogen. The reservoir and the inlet throttle valve (pos.14 in Fig. 5.51) stabilize pressure in the channel resulting in flow rate stabilization. In order to prevent mechanical destruction of the rods by an external pressure of water, they are charged inside by nitrogen from spherical hydraulic accumulator under the initial pressure of 6 MPa, then automatically following operating outside pressure.

All fuel rods were accurately selected to have the same electric resistance. In designing 3 and 7rod bundles essential attention was drawn to the modeling of the multi rod systems. It was taken into account that the hydraulic diameter, D_{hydr}, of the channel with limited number of rods significantly depends upon dimensions and configuration of a bundle shell. Under such conditions and the same design of a real bundle and of its simulator their hydraulic diameters could be strongly different. Therefore, for 3 and 7-rod simulators (Fig. 5.50 *b, c*) configuration and dimensions of the displacers were chosen, on the one hand, to get their hydraulic diameters as close as possible to hydraulic diameter of a bundle with unlimited number of rods and, on the other hand, to have the all three simulators of approximately equal hydraulic diameters.

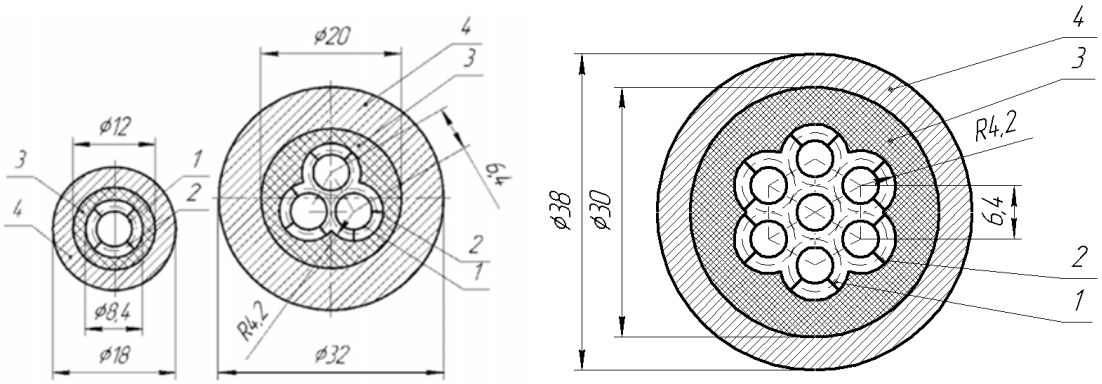

Fig. 5.50. Cross section of test sections: 1 – heated rod (rod); 2 – distancing rib; 3 – shaped dielectric displacer; 4– pressure tube.

The three test sections differed only by the heated rods (1 rod channel and 3, 7-rod bundle simulators), while inlet and outlet mixing chambers were the same. As an example, in Fig. 5.51, the 1 rod channel is shown. Table 5.10 lists the geometric dimensions of the bundles.

TABLE 5.10 MAIN GEOMETRIC CHARACTERISTICS OF BUNDLES

Crosssectional Flow area, S, mm^2	Heated Surface Area, F, mm^2	Wetted Perimeter, Π, mm	Hydraulic Diameter, D_{hydr}, mm	S/F
1 rod annular channel				
31.77	10286	47.59	2.67	0.00309
3-rod bundle				
74.16	30855	111.8	2.65	0.00240
7-rod bundle				
140,09	71995	218,46	2,56	0,00194

Wall temperatures in the test sections were measured by a thermoprobe containing 7 thermocouples mounted on a ceramic tube of 3 mm diameter and tightly pressed to the rod wall. The thermocouples are entered into the rod (a), or in one of them in the 3-rod bundle (b), or in the central one in the 7-rod bundle (c) and positioned at the distances of 95, 195, 255, 315, 375, 415, and 475 mm from the entrance into the heated section. The first location is far beyond the entrance section ((l/d) > 25), where a boundary layer is forming. In each of the two or six other rods for 3 or 7-rod bundle, respectively, a control thermocouple was located in the cross section corresponding to the 7th thermocouple in the test rod. In several tests, the 7-rod bundle was equipped also by one additional thermoprobe with 6 thermocouples in one of the peripheral rods.

Thermocouple terminals were welded to the assembly (7) of 14 (2 per 1 thermocouple) electrically isolated from each other steel rings clamped between the flanges. The material of the rods is stainless steel 12Kh18N10T (Kh – Cr; N – Ni; T – Ti). Table 5.11 list the conductivity and resistance of the material. Basing on the dependence of the electrical resistance of the steel upon its temperature, local values of heat flux q were calculated. They varied by about 5 % along the rods.

TABLE 5.11. HEAT CONDUCTIVITY AND SPECIFIC ELECTRIC RESISTANCE OF STAINLESS STEEL 12KH18N10T STEEL VS. TEMPERATURE.

T, °C	20	100	200	300	400	500	600	700	800
λ, W/(m·K)	15	16	18	19	21	23	25	27	26
$R\cdot10^9$, Ohm·m	725	792	861	920	976	1028	1075	1115	–

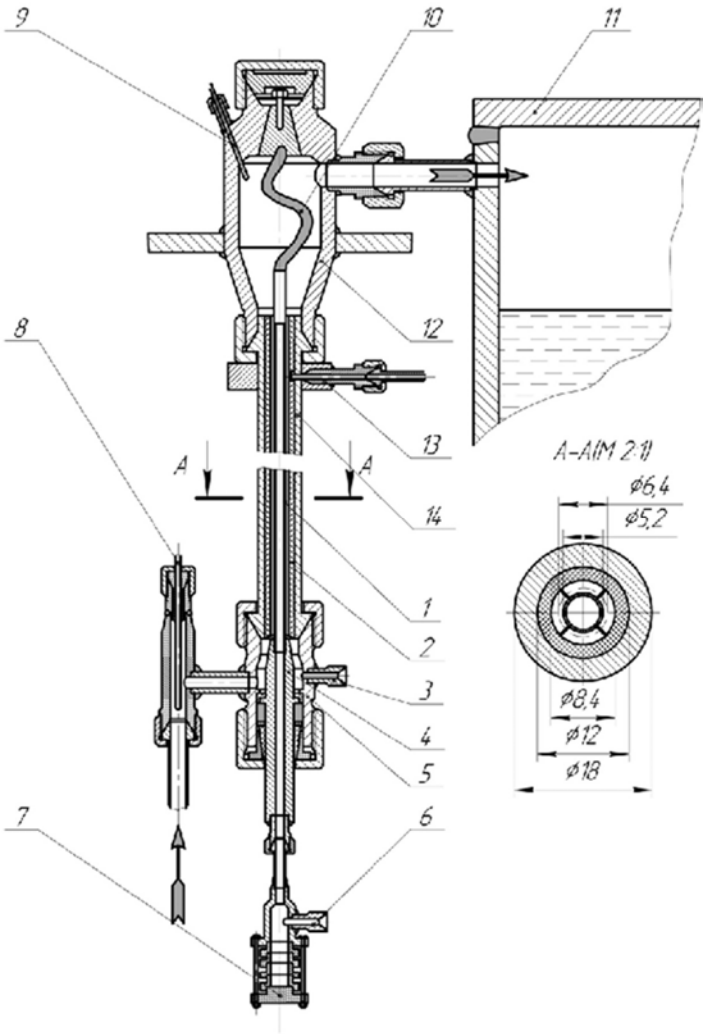

1 – heated rod
2 – dielectric displacer
3, 13 – pressure taps
4 – lower current carrying copper electrode
5, 12 – inlet and outlet chambers
6 – pressurized nitrogen tap
7 – assembly of thermocouple terminals
8, 9 – thermocouple cartridges
10 – flexible copper feeder
11 – damping reservoir
14 – pressure tube (Ø18 x 3 mm)

Fig. 5.51. Test section with annular channel.

5.6.3. TEST MATRIX AND EXPERIMENTAL PROCEDURE

The experimental data were recorded by a data acquisition system when the desired flow conditions and power level were reached and stabilized. After that, a new power level or/and new set of flow conditions were established. Increase in power was limited to the tolerated values either electric current/voltage of power supply or the maximum wall temperature of 650°C.

The experiments aimed both to get a data base of heat transfer with 'accompanying' hydraulic resistance under normal steady conditions and to detect boundary heat fluxes threshold values exceeding which results in onset of a dangerous heat transfer deterioration. The latter could be reached by gradual heat load increasing. As a criterion for identifying this phenomenon, the detection of a considerably non linear wall temperature trend along the channels was used. In many cases, the tests were repeated and reproducibility of the results proved their statistical regularity. Upon satisfaction of these conditions, they were included in the data base.

To simplify the test matrix listed in Table 5.12 and the analysis of the results, three operating pressures were selected including 22.6 MPa (the closest to the critical point where physical properties of water vary drastically with temperature), 24.5 and 27.5 MPa (relevant to operations and analyzes of SCWRs). Mass fluxes covering the range from 700 to 3000 kg/(m^{2}s) and a series of entrance temperatures were selected for all tests.

TABLE 5.12 TEST MATRIX.

P, MPa	T_{in}, ºC	T_{out}, ºC	G, kg/(m^{2}s)	q, MW/m^2	q/G, kJ/kg
1-rod annular channel					
22.6, 24.5	125–352	206–366	800–3000	1.03–3.45	<2.4
3-rod bundle					
22.6, 24.5, 27.5	125–337	216–372	1000–2700	1.25–4.58	<2.5
7-rod bundle					
22.6, 24.5, 27.5	125–325	290–379	700–1500	0.50–1.60	<1.5

The experiments were conducted by increasing the thermal load at preset mass flow rate and inlet temperature of water.

5.6.4. EXPERIMENTAL DATA REDUCTION

The experiments covered a wide range of the operating parameters. The internal wall temperatures, inlet and outlet fluid bulk temperatures, mass flow rate, pressure drop, electric current and voltage were used as the basis for calculations of local parameters. These local parameters include thermal and electrical conductivity of the wall material, power, heat flux, volumetric heat flux, external wall temperature, heat loss, and fluid bulk temperature.

In all test runs, the thermal balance between supplied electric power and the transferred heat was verified. The imbalance usually did not exceed 5 % taking into account preliminary evaluated heat loss; otherwise, the test was repeated.

All calculations were standard and targeted to obtain values of the local heat transfer coefficient and, in the majority of runs, also the total friction resistance factor of the experimental section. Despite only 0.35 mm in thickness of the rod wall, it was important to determine its external temperature with high accuracy, particularly at high heat fluxes and high mass flow rates, when the cross sectional temperature difference in the wall was relatively high, while in water flow it was low. This combination of the parameters could cause a significant error in the estimation of the Nusselt number.

Thermophysical properties of SCW were calculated using the WaterSteamPro software, which is equivalent to the NIST REFPROP software.

External wall temperature was determined following the well known equation from [5.29] as in case of thermal sources uniformly distributed in the wall, for a temperature difference in wall cross section:

$$\Delta t_w = \frac{q_v \cdot R_2}{4 \cdot \lambda}\left[2\,ln\frac{R_1}{R_2} + \left(\frac{R_2}{R_1}\right)^2 - 1\right] \tag{5.8}$$

where R_1 and R_2 are inner and outer radiuses of rod's cylindrical surfaces in metres, respectively; $q_v = q_2 \frac{2R_2}{R_2^2 - R_1^2}$ — wall volumetric heat flux in W/m^3; q_2 — heat flux from wall to water in W/m^2. Thus, $T_w = T_2 = T_1 - \Delta T_w$ and

$$Nu\frac{q \cdot D_{hydr}}{(T_w - T_b) \cdot \lambda_{exp}} \tag{5.9}$$

The desired expression for total friction resistance factor is:

$$\xi_{fr} = \Delta p_{fr} \cdot \frac{2D_{hydr}}{l \cdot G^2 \cdot \overline{v}} \tag{5.10}$$

where $\Delta P_{fr} = \Delta P_{exp} - \Delta P_g - \Delta P_{ac}$, ΔP_{exp}, ΔP_g and ΔP_{ac} are frictional, full experimental (directly measured by a gauge), gravitational and accelerative (inertial) hydraulic resistances of the channel section, respectively, and $\overline{v}$ is the mean specific volume of coolant in the section.

5.6.5. HEAT TRANSFER CHARACTERISTICS

Altogether 137 regimes in the 1 rod annular channel, 156 regimes in 3-rod bundle and until now 47 in 7-rod bundle were investigated and over 2,750 data on wall temperature were obtained.

Fig. 5.52 shows external wall temperature variations with heat flux increase in the annular channel.

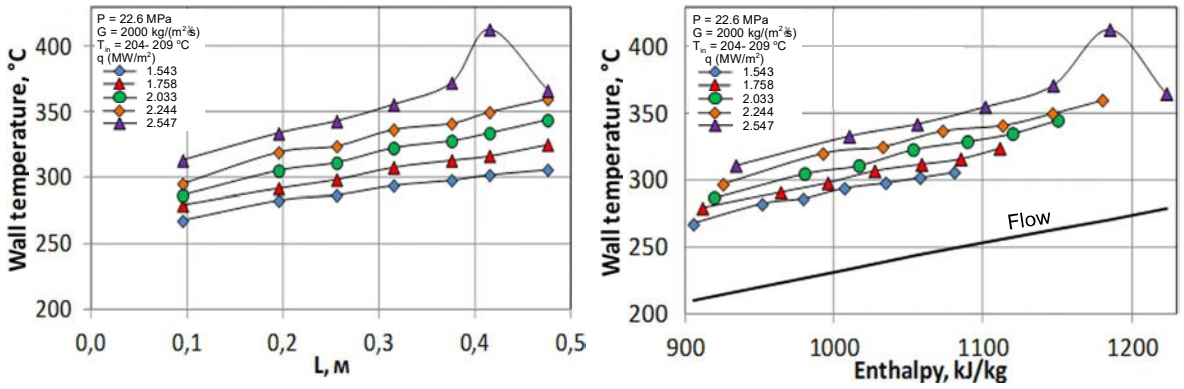

Fig. 5.52. Effect of heat flux on wall temperature profile in 1-rod annular channel.

Temperature profiles were stable, close to linear and easily reproducible within a wide range of mass and heat fluxes. The readings of 2 control thermocouples and of the 7th one in the rod usually did not differ from each other by more than 3−5 ºC in regular regimes, proving the uniformity of heating and cooling conditions in all the rods. It is seen that at a certain heat flux the regular heat

transfer changed into the deteriorated one at the end of the rod. As the heat flux increased the place of an abrupt temperature increase moved to the beginning of the rod.

The same trend in the wall temperature profile took place in the 3-rod and 7-rod bundles. Such regimes were not observed in a previous study [5.26], despite heat flux rate *q/G* reached the level corresponding to the deterioration obtained in the present experiments. In the mentioned above experimental work the authors obtained a good enough correlation, not demonstrated by them but validated and fairly estimated in [5.29], for 7-rod bundle of the same geometry:

$$Nu = 0.021 \cdot Re_b^{0.8} \cdot \overline{Pr_b}^{0.7} \left(\frac{\rho_w}{\rho_b}\right)^{0.45} \left(\frac{\mu_b}{\mu_{in}}\right)^{0.2} \left(\frac{\rho_b}{\rho_{in}}\right)^{0.1} \left(1 + \frac{2.5}{x/d_{hydr}}\right) \tag{5.11}$$

where $\overline{Pr_b} = \frac{h_w - h_b}{t_w - t_b} \cdot \frac{\mu_b}{\lambda_b}$; μ_{in} and ρ_{in} take into account the upstream history of the flow.

Contrary to the mentioned study, no oscillation of the pressure even in the regimes of deteriorated heat transfer was detected. The above mentioned low frequency oscillations prevented increasing the heat load in those experiments or caused burnout of the bundle. One of the reasons of the oscillations could be an insufficient volume of the mixing chambers that should play the role of a screen reflecting pressure pulsations of the outside part of the circuit loop.

A comparison of the wall temperature of the test (1) and reference (2) rods in the 3-rod bundle is illustrated in Fig. 5.53. The wall temperature in the rod 2 sometimes (in the case of an evident DHT) was measured. It testifies for a very good mixing of flow even under developed DHT.

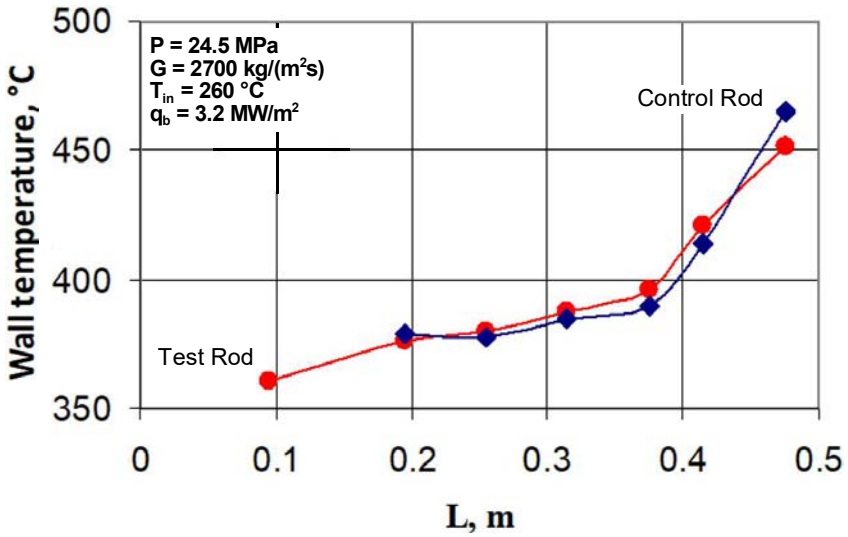

Fig. 5.53. Wall temperature profiles at deteriorated heat transfer regime in test and control rods of 3-rod bundle.

In Fig. 5.54 two patterns of temperature profiles of neighboring enhanced (1) and deteriorated (2) heat transfer conditions obtained by just increasing the water inlet temperature in 3-rod bundle are

presented. Such sequence of temperature profiles from normal one through enhanced to deteriorated not always could be checked due to, as a rule, its short distance. The increasing of heat flux caused similar changes in heat transfer conditions. It was found that cooling of the vertical rods by supercritical water under steady operating conditions both at normal and deteriorated heat transfer regimes took place with a stable temperature profile along the heated length.

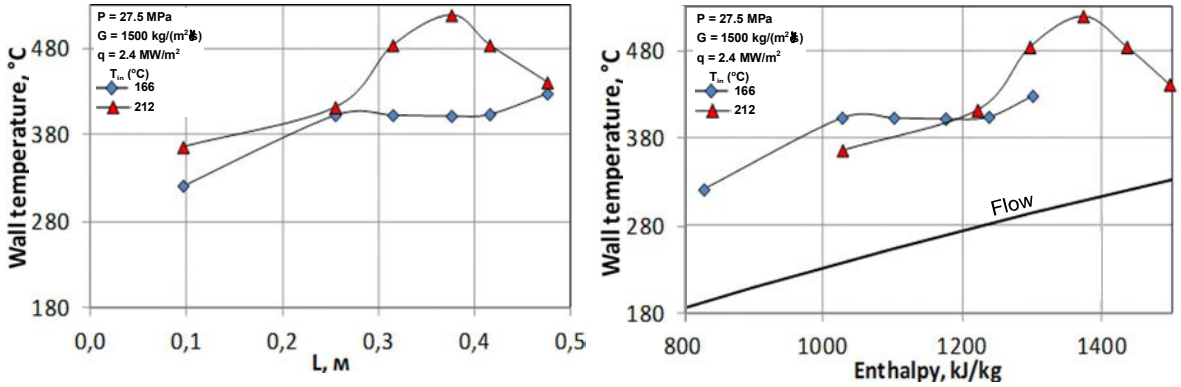

Fig. 5.54. Effect of inlet temperature on wall temperature profile in 1-rod annular channel.

Pressure of SCW did not play any significant role as a parameter determining the level and place of DHT in all bundle geometries. As shown in Fig. 5.55, the maximal variation in pressure by 5 MPa resulted in a difference in extreme temperature within the range of measurement accuracy at exactly the same channel coordinate with a slight increase in t_{DHT} as pressure is growing from 22.6 MPa to 27.5 MPa even under a high degree of deterioration.

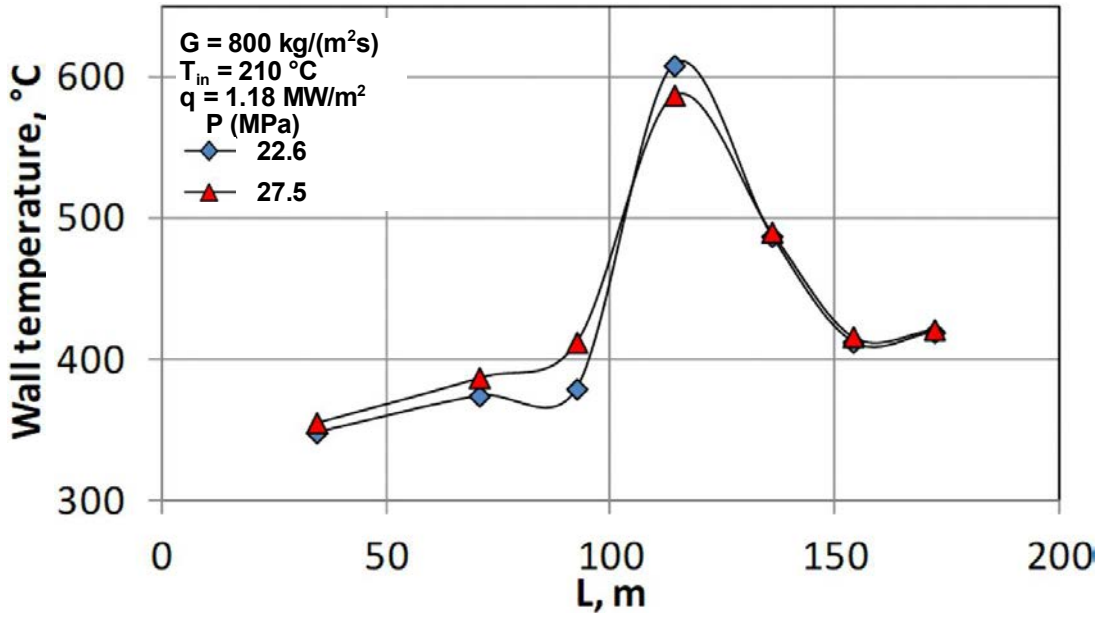

Fig. 5.55. Dependence of deteriorated temperature profile upon water pressure in 7-rod bundle (P, MPa: 1 – 22.6; 2 – 27.5; G = 800 kg/(m²s); T_{in} = 210 °C; q = 1.18 MW/m²).

The temperature regime could be evidently different in central (1) and peripheral (2) rods of the 7-rod bundle under high heat flux rates (see Fig. 5.56 where $q/G = 1.288$ kJ/kg). As listed in Table 5.13, relation of $S/F = (q/G)/\Delta h$ for the central subchannel to that for the peripheral one is 1.18×10^{-3} to 2.57×10^{-3}, which suggests a higher Δh in the central subchannel than peripheral subchannel assuming a uniform heat flux rate, q/G, across the bundle. On the other hand, it clearly indicates good enough mixing in the bundle under so different heat removal efficiency of the subchannels. To compare heat transfer in the subchannels in several experiments, as mentioned before, one of the peripheral rods was provided with an additional thermoprobe with six thermocouples.

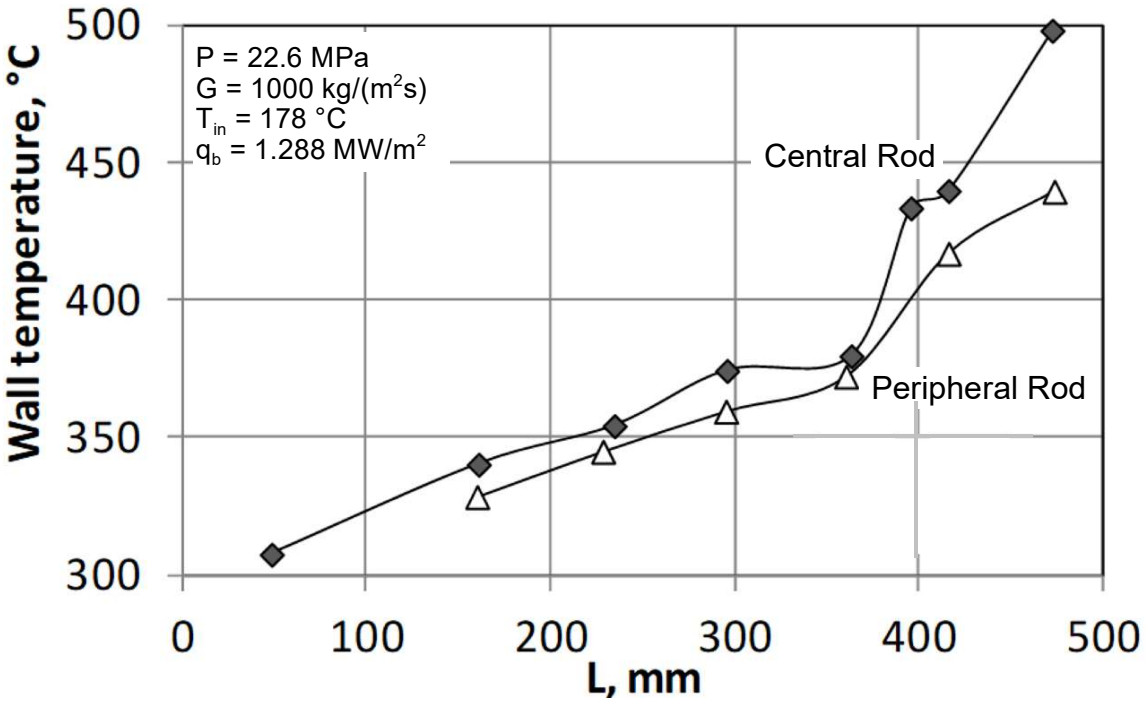

Fig. 5.56. Comparison of wall temperature profiles in central and peripheral rods of 7-rod bundle.

TABLE 5.13 MAIN GEOMETRIC PARAMETERS OF THE 3- AND 7-ROD BUNDLE SUBCHANNELS.

Subchannel	S, mm^2	F, mm^2	S/F
3-rod bundle			
Central	12.517	10051	1.25E-3
Peripheral	61.414	20204	3.04E-3
7-rod bundle			
Central	35.817	30235	1.18E-3
Peripheral	103.91	40452	2.57E-3

5.6.6. COMPARATIVE ANALYSIS OF HEAT TRANSFER DETERIORATION IN THE BUNDLES

The effect of the number of rods in fuel assembly on the conditions of DHT is of great interest, since it should prove the validity of experimental data application for full scaled assemblies. Availability of the data on DHT in the 1- rod annular channel, 3- and 7-rod bundles of identical geometry under the same operating conditions could help to propose conclusions in regard.

Comparative analysis of the results reveals that wall temperature along the whole length of 1-rod channel is higher than in the case of 3-rod and that deterioration is located closer to the channel entrance (Fig. 5.57).

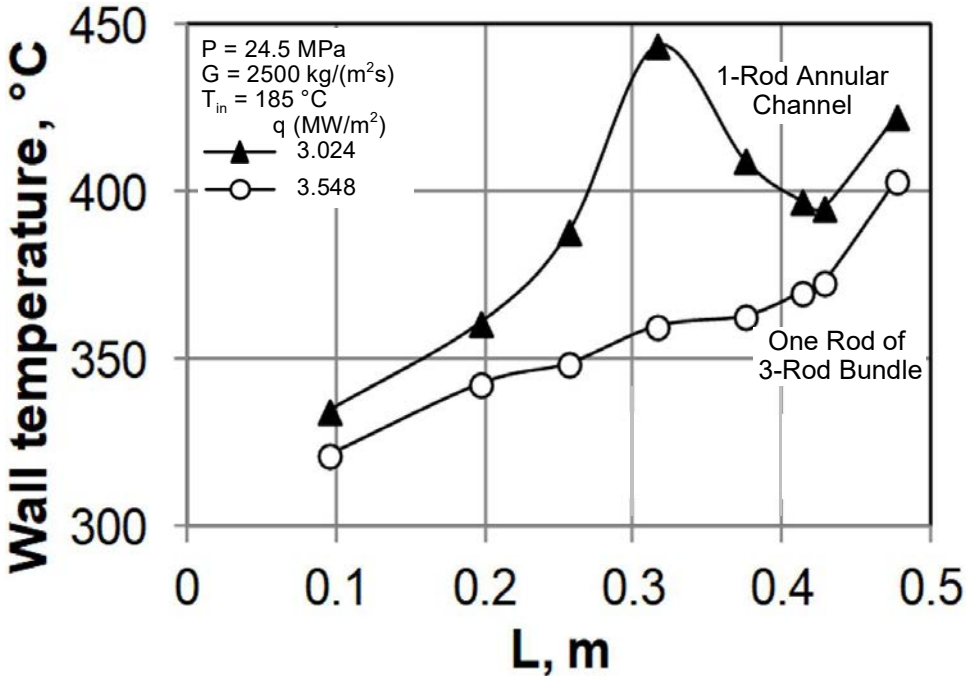

Fig. 5.57. Comparison of wall temperature profiles between 1 rod annular channel and 3-rod bundle.

This could be explained by several reasons. The unheated perimeter length per rod in the 3-rod bundle is about 16 mm against about 26 mm in the annular channel. It means that the share of coolant contacting with unheated surface of the channel is higher in the 1-rod channel: therefore, under equal averaged enthalpy in a given cross section the coolant temperature near the rod should be higher than in the bundle. On the other hand, under such ratio of the unheated perimeters and keeping equal all the other conditions, heating of 1-rod is lower and, as follows from the comparison between the flow cross section and the heated surface S/F (see Table 5.10) of the channels ($3.09\times10^{-3}/2.40\times10^{-3}$), $\Delta h = (q/G)/(S/F)$ is higher in 3-rod bundle, because heat flux rate q/G = idem. However, wall temperature is higher in the annular channel. Probably, it is caused by the following reasons:

— Flow swirling should be stronger in annular channel and provide entrainment of high density and high thermal conductivity medium in the direction of unheated displacer; such separation should worsen rod cooling;
— Intensifying effects of neighboring rods in 3-rod bundle that enhances heat removal particularly in the central subchannel.

As follows from the difference in S/F, according to the adopted (conditional) configuration of the subchannels (Fig. 5.58), the total share of the peripheral subchannels in general *S/F* of the 3-rod bundle that characterizes its heat removal capability is by 12 % higher than the mentioned share of the 7-rod bundle (TABLE 5.13).

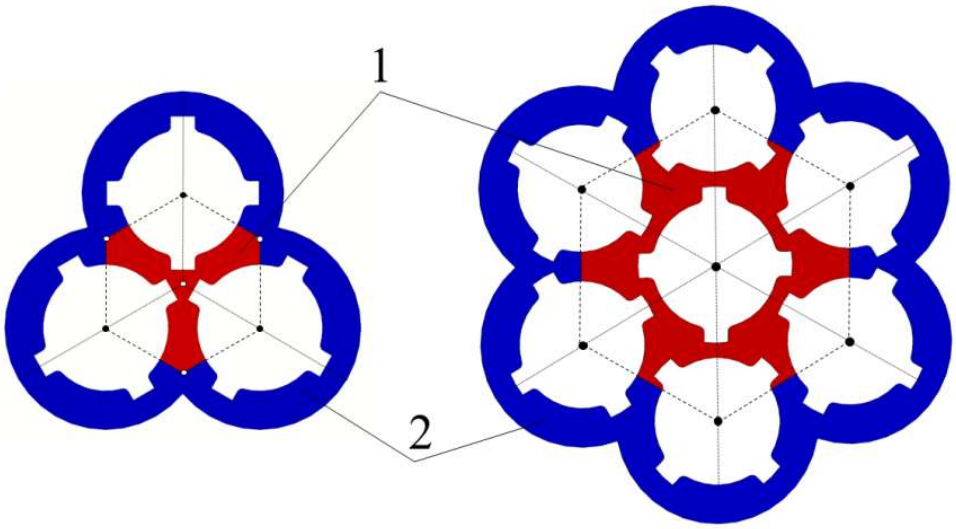

Fig. 5.58. Versions of the 3 and 7-rod bundle flow area division into central (1) and peripheral (2) subchannels.

Far from the entrance ($L > 250$ mm, $L/D > 100$) cooling of the central (hot) rod is slightly worsened versus cooling in 3-rod bundle, where all the rods are under the same conditions, more favorable to heat removal. Then until the onset of DHT, appearing earlier in the central rod of 7-rod bundle, in both of them heat transfer gradually transits from NHT through slightly enhanced heat transfer on a very short section of the bundle to DHT.

Taking into account the described features of heat transfer in the bundles there are good reasons to assume that in fuel assemblies with much greater number of the rods the heat transfer would resemble the case considered above only in the peripheral rows. For instance, in 61 rod bundle (1+6+12+18+24 rods in the 1+2+3+4+5 rows, respectively) only in 24 outer rods the heat transfer would be close to that shown in Fig. 5.59 by the peripheral rod of 7-rod bundle, while the rest of the rows would mostly be under heat transfer conditions similar to the ones of the (hot) rod of the 7-rod bundle. This reasoning holds of course only if the heat flux is uniform all over the assembly cross section. An important deduction can be made that 7-rod simulator of fuel assembly is an optimal one for the investigation on full-scale hydrodynamic features at its triangle or honeycomb

configuration. Similar conclusion were reached already in 1963 by the authors of [5.30], who obtained a good agreement between critical heat fluxes in 7- and 19-rod bundles.

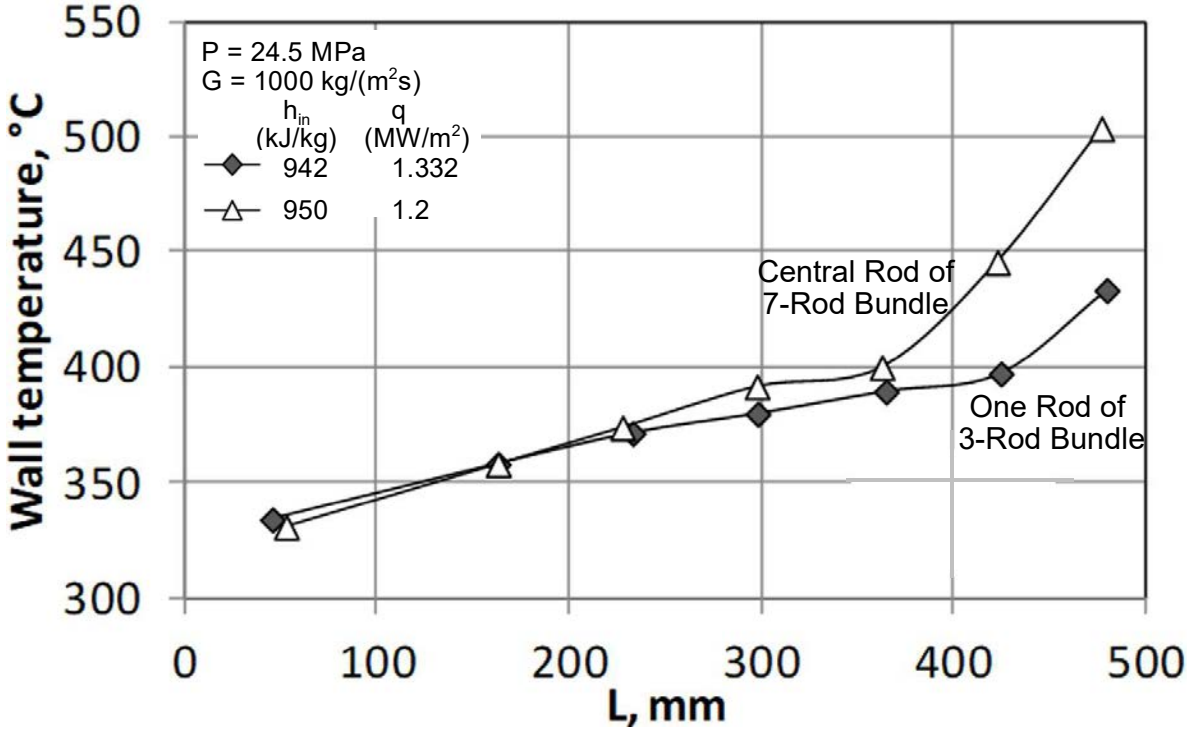

Fig. 5.59. Comparison of wall temperature profiles in one rod of the 3-rod and 7-rod bundles.

5.6.7. STATISTICAL ANALYSIS OF THE CORRELATIONS APPLIED FOR BUNDLE HEAT TRANSFER PREDICTION

The data were compared with the calculations by commonly used correlations. The correlation by Dyadyakin and Popov [5.26], derived for 7-rod bundle, as well as correlations by Krasnoshchyokov and Protopopov [5.31] and by Bishop et al. [5.32] proved to be the closest among them. Contrary to expectation, Eq. (4.1) gave wider scattering than the equations derived by the above-mentioned other authors. As to the system of two jointly iterative equations Eq. (4.31) and Eq. (4.32), they occurred to be the best not only for tubes under upward and downward flow, but for annular channel, 3- and 7-rod bundles as well. The most successful approximation was achieved for 3-rod bundle (Fig. 5.60).

Statistical features of the correlations used for the comparison were estimated basing on the results of *Nu* values predicted by them for the annular channel, 3- and 7-rod bundles obtained in NTUU (Table 5.14). In the following, n is the number of processed data (in some cases, as in Table 4.20 computational problems occurred in the application of the correlation, so the number of reported cases is lower than available), δ is the arithmetical mean error and σ is the standard deviation. As seen, the best accuracy has been provided by Razumovskiy [5.33] (jointly solved Eq. (4.30) and Eq. (4.31)), Krasnoshchyokov and Protopopov [5.31], Bishop et al. [5.32] and Dyadyakin and Popov [5.26]. Despite the result of Mikheyev et al. [5.34] looks the best, it was put down in Table

4.20 due to very high share of nonconvergence in iteration required by joint solution of Eq. (4.31) and Eq. (4.32).

Processing the whole array of DHT data (tubes, annular channels, 3- and 7-rod bundles) correlation (4.20) for the onset of DHT was updated to the following correlation:

$$(q/G)_b = 0.035 \cdot n^{0.069} \cdot (l/d)^{-0.25} \cdot (h_m - h_{in})^{0.636} \tag{5.12}$$

where n is the number of rods in the bundle. Predictions of the correlation are compared against experimental results in Fig. 5.61.

Good agreement has been observed for results of the 3-rod bundle. At the same time, the values of boundary heat flux rate for 1 rod annular channel and 7-rod bundle are predicted with a rather wide scatter. The experimental values of $(q/G)_b$ in many cases are much higher than predicted, since Eq. (5.12) does not take into account additional turbulence of flow in bundle geometries.

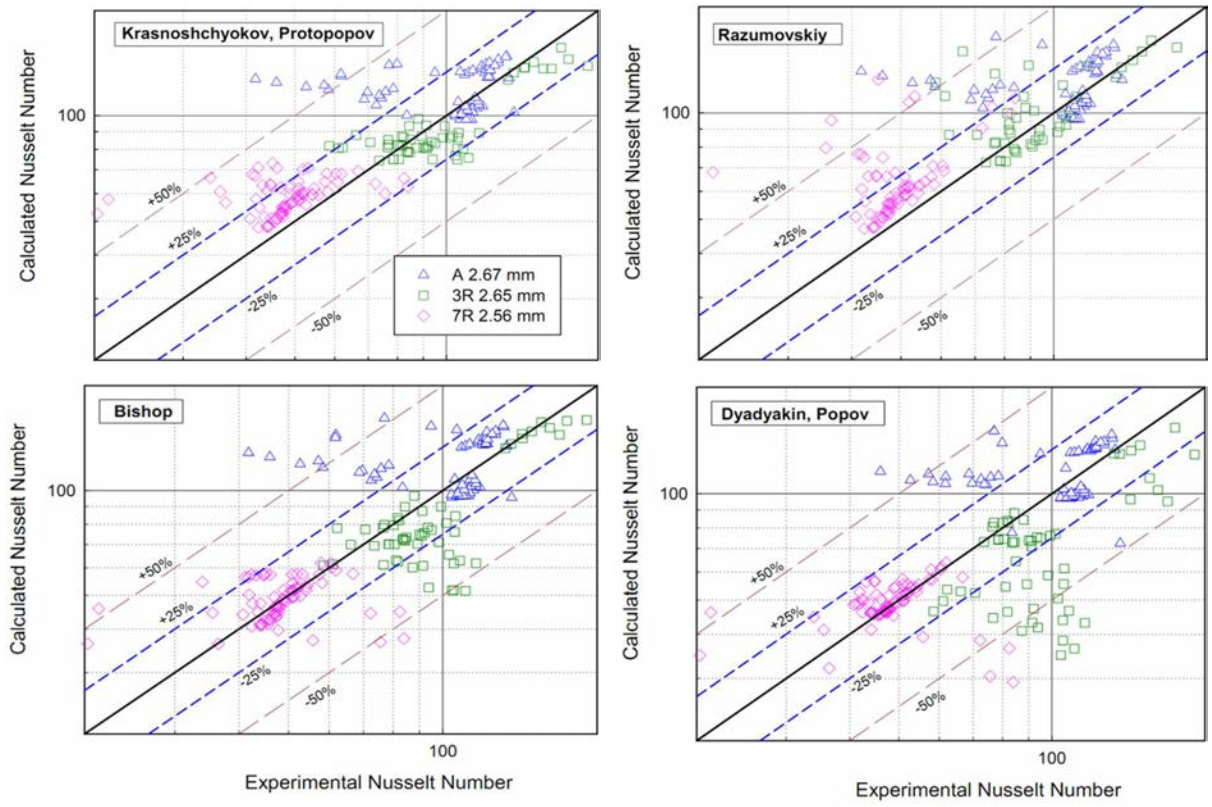

Fig. 5.60. The best four approximations of NTUU data on HT in annular channel (A), 3- and 7-rod bundles (3R and 7R, respectively).

TABLE 5.14. ASSESSMENT OF PREDICTION ACCURACY OF NUSSELT NUMBER FOR CORRELATIONS AGAINST NTUU EXPERIMENTAL RESULTS

Authors	n	δ, %	σ, %	Share of data within error ranges				
				±10%	±20%	±30%	±40%	±50%
Bishop et al. [5.32]	209	4.4	36.0	45.5	69.8	79.9	85.1	89.5
Krasnoshchyokov & Protopopov [5.31]	210	14.7	35.9	34.2	70.0	79.5	85.7	88.1
Razumovskiy [5.33]	210	8.1	43.4	35.7	56.6	84.7	87.1	87.6
Dyadyakin and Popov [5.26]	209	-1.7	32.4	41.1	68.9	75.6	79.4	86.1
Petukhov et al. [5.35]	198	28.6	45.0	33.3	60.6	74.7	78.3	82.3
Swenson et al. [5.36]	210	37.0	57.0	33.8	53.8	66.1	72.4	76.7
Ornatskiy et al. [5.21]	210	34.0	44.3	26.7	44.7	69.5	78.6	80.9
Jackson and Hall [5.37]	180	39.5	44.9	15.0	35.6	51.7	72.8	81.1
Mikheyev et al. [5.34]	178	9.1	32.7	48.9	72.5	82.6	87.1	88.2
Mokry et al. [5.19]	170	-39	28.6	10.0	27.0	51.2	55.3	57.1

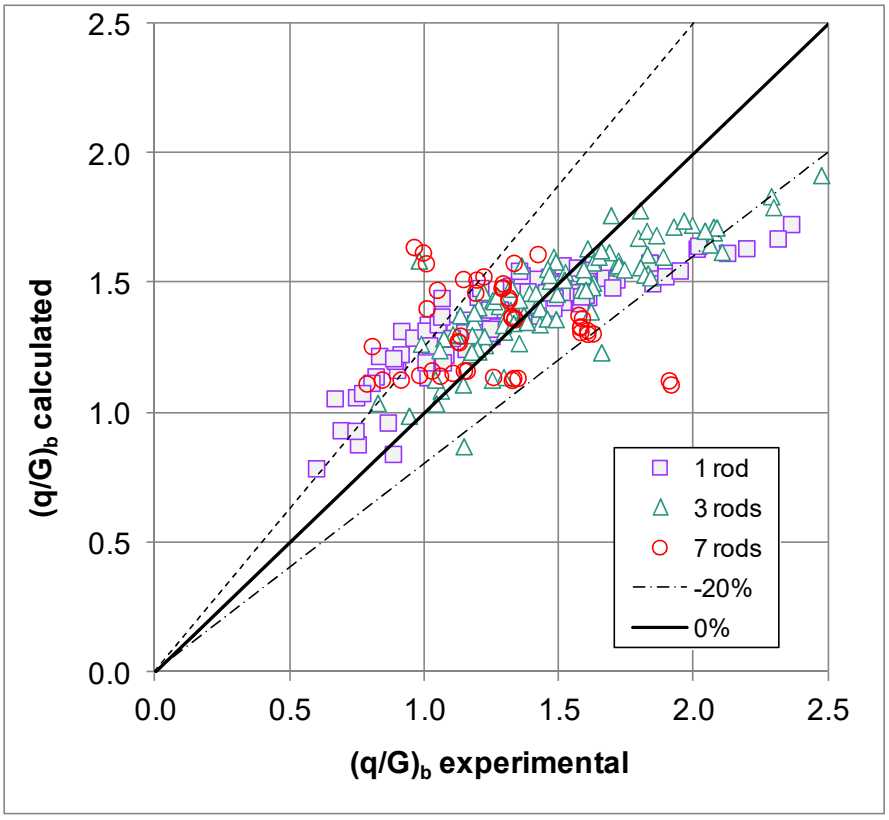

Fig. 5.61. Predicted boundary values of deteriorated heat flux rate in 1 rod annular channel, 3 and 7-rod bundles vs. experimental data.

Nomenclature and Acronyms

A_{fl}	flow area, m^2
D, d	diameter, mm
G	mass flux, kg/m^2s; $\left(\frac{m}{A_{fl}}\right)$
H	specific enthalpy, J/kg
k	thermal conductivity, W/m K
m	mass flow rate, kg/s; (ρV)
P, p	pressure, Pa
q	heat flux, W/m^2
q_v	volumetric heat flux, W/m^3
Q	heat transfer rate, W
T	temperature, K
V	velocity, m/s

Greek Letters

Δ	difference
μ	dynamic viscosity, Pa s
ρ	density, kg/m^3

Subscripts or Superscripts

b	bulk
cr	critical
ext	external
F, f	Freon
hy	hydraulic
int	internal
pc	pseudocritical
v	volumetric
W, w	Water

Abbreviations and Acronyms

AC	Alternating Current
AD	Analog to Digital
ASME	American Society of Mechanical Engineers
CA	California
CO	Colorado
DAS	Data Acquisition System
DC	Direct Current
DHT	Deteriorated Heat Transfer

El. Element
HT Heat Transfer
HTC Heat Transfer Coefficient
IAEA International Atomic Energy Agency
ICONE International Conference On Nuclear Engineering
IPPE Institute of Physics and Power Engineering (Obninsk, Russian Federation)
IHT Improved Heat Transfer
M.A.Sc. Master of Applied Science
NHT Normal Heat Transfer
NIST National Institute of Standards and Technology
NY New York
OD Outside Diameter
R Refrigerant
SC SuperCritical
SCW SuperCritical Water
SCWR SuperCritical Water cooled Reactor
SCPTF SuperCritical Pressure Test Facility
TC ThermoCouple
TS Test Section
UOIT University of Ontario Institute of Technology

REFERENCES TO SECTION 5

[5.1] LICHT, J., ANDERSON, M., CORRADINI, M., Heat Transfer to Water at Supercritical Pressures in A Circular and Square Annular Flow Geometry, Int. J. Heat Fluid Flow, **29**, (2008), 156–166.

[5.2] WU, G., BI, Q., YANG, Z., WANG, H., ZHU, X., HAO, H., LEUNG, L.K.H., Experimental Investigation of Heat Transfer for Supercritical Pressure Water Flowing in Vertical Annular Channels, Nuclear Engineering Design, **241, 9**, (2011) 4045–4054.

[5.3] JACKSON, J.D., Consideration of the Heat Transfer Properties of Supercritical Pressure Water in Connection with the Cooling of Advanced Nuclear Reactors, Proc. 13th Pacific Basin Nuclear Conference, Shenzhen, 2002.

[5.4] DITTUS, F.W., BOELTER, L.M.K., Heat Transfer in Automobile Radiators of the Tubular Type, University of California, Berkeley, Publications on Engineering, **2, 13**, (1930), 443–461.

[5.5] INTERNATIONAL ATOMIC ENERGY AGENCY, Heat Transfer Behaviour and Thermohydraulics Code Testing for Supercritical Water Cooled Reactors (SCWRs), IAEA-TECDOC-1746, IAEA, Vienna (2014).

[5.6] ZHAO, M., LI, H., YANG, J., GU, H., CHENG, X., Experimental Study on Heat Transfer to Supercritical Water Flowing through Circular Tubes and 2×2 Rod Bundles, Proc. 6th International Symposium on Supercritical Water-cooled Reactors, Shenzhen, 2013.

[5.7] MORI, H., KAIDA, T., OHNO, M., YOSHIDA, S., HAMAMOTO, Y., Heat Transfer to A Supercritical Pressure Fluid Flowing in Sub-Bundle Channels, Journal of Nuclear Science and Technology, **49**, (2012), 373–383.

[5.8] RICHARDS, G., HARVEL, G.D., PIORO, I.L., SHELEGOV, A.S., KIRILLOV, P.L., Heat Transfer Profiles of A Vertical, Bare, 7-Element Bundle Cooled with Supercritical Freon R-12, Nucl. Eng. Des., **264**, (2013), 246–256.

[5.9] WANG, H., BI, Q., WANG, L., LV, H., LEUNG, L.K.H., Experimental Investigation of Heat Transfer from a 2×2 Rod Bundle to Supercritical Pressure Water, Nuclear Engineering Design, **275**, (2014), 205–218.

[5.10] ETER, A., GROENEVELD, D., TAVOULARIS, S., An Experimental Investigation of Supercritical Heat Transfer in A Three-Rod Bundle Equipped with Wire wrap and Grid Spacers and Cooled by Carbon Dioxide, J. Nuclear Engineering and Design, **303**, (2016), 173–191.

[5.11] YARAS, M.I., Steady and Unsteady Forced-Convection Heat Transfer Measurements in Upward Flow of R134a at Supercritical Thermodynamic States in a Heated Bundle Test Section with a Wire wrap Spacer, Carleton University Report submitted to Canadian Nuclear Laboratories, Report CU-M&A-2014-03, 2015.

[5.12] RICHARDS, G., SAMUEL, J., SHELEGOV, A.S., KIRILLOV, P.L., PIORO, I.L., HARVEL, G., "Experimental study on heat transfer in a 7-element bundle cooled with supercritical freon-12", in Proc. 20th International Conference On Nuclear Engineering (ICONE-20) – ASME 2012 POWER Conference, Anaheim, 2012.

[5.13] NATIONAL INSTITUTE OF STANDARDS AND TECHNOLOGY, NIST Reference Fluid Thermodynamic and Transport Properties - REFPROP, Standard Reference Database 23, Ver. 7.0, Department of Commerce, Boulder (2002).

[5.14] KIRILLOV, P.L., OPANASENKO, A.N., POMETKO, R., SHELEGOV, A., Experimental Study of Heat Transfer on Rod Bundle at Supercritical Parameters of Freon-12, IPPE Preprint, Obninsk, Russia, 2006.

[5.15] CHENG, X., LIU, X.J., GU, H.Y., Fluid-To-Fluid Scaling of Heat Transfer in Circular Tubes Cooled with Supercritical Fluids, Nuclear Engineering and Design, 241, (2011), 498-508.

[5.16] ZVORYKIN, A., MAHDI, M., POPOV, R., BARATI FAR, K., PIORO, I., "Heat transfer to supercritical water (liquid-like state) flowing in a short vertical bare tube with upward flow", in Proc. 26th International Conference On Nuclear Engineering (ICONE-26), London, 2018.

[5.17] PIORO, I.L., "Heat transfer and pressure drop in forced convection to fluids at supercritical pressures", in Appendix A4 of Handbook of Generation IV Nuclear Reactors (PIORO, I.L., Ed.), Elsevier – Woodhead Publishing (WP), Duxford, UK, (2016) 795–823.

[5.18] GUPTA, S., SALTANOV, EU., MOKRY, S.J., PIORO, I., TREVANI, L., MCGILLIVRAY, D., Developing Empirical Heat-Transfer Correlations for Supercritical CO_2 Flowing in Vertical Bare Tubes, Nuclear Engineering and Design, **261**, (2013), 116–131.

[5.19] MOKRY, S., PIORO, I.L., FARAH, A., KING, K., GUPTA, S., PEIMAN, W., KIRILLOV, P.L., Development of Supercritical Water Heat-Transfer Correlation for Vertical Bare Tubes, Nuclear Engineering and Design, 241, (2011), 1126–1136.

[5.20] RAZUMOVSKIY, V.G., PIS'MENNYI, EU.N., SIDAWI, K., PIORO, I.L., KOLOSKOV, A.EU., Experimental Heat Transfer in an Annular Channel and 3-Rod Bundle Cooled with Upward Flow of Supercritical Water, ASME Journal of Nuclear Engineering and Radiation Science, **2, 1**, (2016).

[5.21] ORNATSKY, A.P., GLUSHCHENKO, L.P., SIOMIN, E.T., KALACHYOV, S.I., The Research of Temperature Conditions of Small Diameter Parallel Tubes Cooled by Water under Supercritical Pressures, Proc. 4th International Heat Transfer Conference, Paris-Versailles, 1970.
[5.22] ORNATSKY, A.P., GLUSHCHENKO, L.F., GANDZYUK, O.F., An Experimental Study of Heat Transfer in Externally-Heated Annuli at Supercritical Pressures, Heat Transfer – Soviet Research, **4, 6**, (1972), 25–29.
[5.23] VETROV, V.I., GERLIGA, V.A., RAZUMOVSKIY, V.G., Experimental Research of Thermoacoustic Oscillations in Heated Channels under Supercritical Pressures of Water, Problems of Nuclear Science and Technology (Voprosy atomnoy nauki i tekhniki), 2, 12, (1977), 51–57 (In Russian).
[5.24] RAZUMOVSKIY, V.G., ORNATSKIY, A.P., MAYEVSKIY, E.M., Hydraulic Resistance and Heat Transfer in Smooth Channels under Turbulent Flow of Water at Supercritical Pressure, Heat Engineering (Tyeploenergetika), **2**, (1984), 69–72, (In Russian).
[5.25] PIS'MENNYY, E.N., RAZUMOVSKIY, V.G., MAEVSKIY, E.M., KOLOSKOV, A.E., PIORO, I.L. AND DUFFEY, R.B., "Experimental study on temperature regimes to supercritical water flowing in vertical tubes at low mass fluxes", in Proc. International Conference GLOBAL-2005, Tsukuba, 2005, Atomic Energy Society of Japan, Tokyo (2005).
[5.26] DYADYAKIN, B.V., POPOV, A.S., Heat Transfer and Thermal Resistance of Tight Seven-Rod Bundle Cooled with Water Flow at Supercritical Pressures, Transactions of VTI, **11**, (1977), 244–253, (In Russian).
[5.27] PETUKHOV, B.S., GENIN, L.G., KOVALYOV, S.A., Heat Exchange in Nuclear Power Units, Atomizdat Publ. House, 1974 (In Russian).
[5.28] KIRILLOV, P., POMET'KO, R., SMIRNOV, A., GRABEZHNAIA, V., PIORO, I., DUFFEY R., KHARTABIL, H., "Experimental study on heat transfer to supercritical water flowing in 1- and 4-m long vertical tubes", in Proc. GLOBAL-2005 Tsukuba, 2005, Atomic Energy Society of Japan, Tokyo (2005).
[5.29] RAZUMOVSKIY, V.G., PIS'MENNYY, E.N., KOLOSKOV, A.E., PIORO, I.L., "Heat transfer to supercritical water in vertical 7-rod bundle", in Proc. 16th International Conference on Nuclear Engineering (ICONE-16), Orlando, 2008, Atomic Energy Society of Japan (2008).
[5.30] MATZNER et al. US AEC DP-857, 1963.
[5.31] KRASNOSHCHYOKOV, E,A., PROTOPOPOV, V.S., Experimental Investigation of Carbon Dioxide Heat Exchange in Supercritical Region under High Temperature Head, Tyeplofizika Vysokikh Tyempyeratur, **4, 3**, (1966), 389–398.
[5.32] BISHOP, A.A., SANDBERG, L.O., TONG, L.S., Forced Convection Heat Transfer to Water at Near-Critical Temperature and Supercritical Pressures, Westinghouse Electric Corporation Report (WCAP-2056), Pittsburg, 1964.
[5.33] FILONOV, V.V., FILONOVA, YU.S,, RAZUMOVSKIY, V.G., PIS'MENNYI E.N., On Experimental and Computational Investigation of Heat Transfer Deterioration and Hydraulic Resistance in Annular Channel and SCWR 3-Rod Bundle, Proc. 26th International Conference on Nuclear Engineering (ICONE-26), London, 2018.
[5.34] MIKHEYEV, M.A., Principals of Heat Transfer, 3rd Edition, Gosenergoizdat Publ. House, 1956.

[5.35] PETUKHOV, B.S., KIRILLOV, V.V., On Heat Exchange under Turbulent Flow of Liquid in Tubes, Heat Power Engineering (Tyeploenergyetika), 4, (1958), 63, 68 (In Russian).
[5.36] SWENSON, H.S., CARVER, J.R., KAKARALA, C.R., Heat transfer to Supercritical Water in Smooth-Bore Tubes, J Heat Transfer, **87**, **4**, (1965), 477–484.
[5.37] JACKSON, J.D., HALL, W.B., Forced Convection Heat Transfer to Fluids at Supercritical Pressure, Turbulent Forced Convection in Channels and Bundles, Editors: S. Kakaç and D.B. Spalding, Hemisphere Publishing Corp., New York, **2**, (1979), 563–612.
[5.38] ZHAO, M., GU, H. Y., CHENG, X., "Experimental and Numerical Study on Heat Transfer of Supercritical Water Flowing Upward in 2x2 Bundles", Proc. 16th Int. Topical Mtg on Nucl. Reactor Thermal Hydraulics (NURETH-16), Chicago (2015).

6. PRESSURE LOSS CHARACTERISTICS AND PRESSURE DROP MODELS

At the beginning of the 1930s, it was experimentally proved that under coolant non-isothermal flow in channels the pressure loss due to friction, ΔP_{fr}, is affected by the physical state of fluid near the wall and in the flow core. [6.1] proposed to correct ΔP_{fr} with the factor $(\mu_w/\mu_b)^{0.25}$. Since then, little studies were focused on hydraulic resistance in annular channels and tubes cooled by water at supercritical pressure. Table 6.1 summarizes the available studies, based partly on information of [6.2], since 1984. The references [6.3] and [6.4] were the only studies focusing on hydraulics resistances at normal and deteriorated heat transfer.

TABLE 6.1. PARAMETERS OF TEST SECTIONS AND BOUNDARY CONDITIONS FOR EXPERIMENTS WITH WATER

Reference	Pressure (MPa)	Temperature (°C)	Heat flux (MW/m^2)	Mass flux (kg/(m^2·s))	Flow direction	Channel (D, mm; l, m)
Tarasova and Leont'yev [6.3]	22.6–26.5	200–430	0.58–2.32	2000; 5000	upward and downward	tubes (8.03, 3.43; 0.6, 0.136)
Kondrat'yev [6.4]	22.6–29.4	25–135	0.12–1.16	Re<10^5	horizontal	10.47; 0.525
Krasyakova et al. [6.5]	23; 25	195–388	0.2 – 0.9	500–5000	horizontal, upward and downward	tubes (20; 2.2, 4.2, 7.7)
Ishigai et al. [6.6]	25, 30, 40	185–430	1.63	500–1500	horizontal upward and downward	4.44, 3.92; 0.831, 0.627
Dyadyakin and Popov [6.7]	24.5	90–567	4.7	500–4000	upward	7-rod bundle (D_{hydr}=2.15–2.77; 0.485)
Razumovskiy et al. [6.8]	23.5	20–420	0.5–2.5	250–3000	upward and downward	tubes (3.0; 0.44; 6.28; 0.12, 0.24, 0.36, 0.48, 0.60); annular channels (D_{out}/D_{inn} = 10/8; 0.65; 6/4; 0.36); 1, 3 and 7-rod bundles (D_{hydr}=2.67, 2.65, 2.56; 0.485)

The reference [6.3] shows the measured hydraulic resistance at supercritical pressure under pseudophase transition of water and proposed a general friction factor correction as

$$\xi_{fr}/\xi_{fro} = (\mu_w/\mu_b)^{0.22} \tag{6.1}$$

where ξ_{fro} is the friction factor for isothermal fluid flowing inside a tube. The references [6.4] and [6.5] show an anomalous and substantial decrease (down to about 60 %) in friction factor ξ_{fro} within the range of water enthalpies corresponding to the region of pseudophase transition both in vertical (up or downward) and horizontal flows. They assumed that this phenomenon was caused by decreasing turbulent viscosity and close to zero diffusion rate of medium in the region. NTUU [6.9] measured frictional pressure drops, ΔP_{fr}, over a tube (ID = 3.01 mm and L = 0.4 m) and an annular channel (D_{out}/D_{inn} = 10.02/8.04 mm and L = 0.6 m) at G = 500–2000 kg/(m^2·s) and T_b = 360–415 °C. These measurements confirmed the friction factor expression of [6.10]:

$$\xi_{fro} = (1.82\,\log(Re/8))^{-2} \tag{6.2}$$

The observed anomalous decrease in friction factor ξ_{fro} was attributed to the issue in calculation and measurement uncertainty. This observation was affirmed by [6.11] in experiments with carbon dioxide flow.

Pressure loss data with water flow in tubes and annular channels were obtained mainly from two sources: [6.6] and [6.8]. [6.7] performed unique for that time measurements of heat transfer and pressure drop in 7-rod tight bundles (see Table 6.1 and short comments in Section 5.6.5 with highly reliable, as next validation confirmed, empiric correlation (5.11) for Nu). As a result, the following equation for pressure drop assessment appeared:

$$\xi_{fr} = \left[\frac{0.55}{lg\frac{Re_b}{8}}\right]^2 \cdot \left(\frac{\rho_w}{\rho_b}\right)^{0.2} \cdot \left(\frac{\mu_w}{\mu_{in}}\right)^{0.2} \cdot \left(\frac{\rho_b}{\rho_{in}}\right)^{0.1} \tag{6.3}$$

where μ_{in} and ρ_{in} take into account the upstream history effect.

In [6.8] it was experimentally found that in thermal state of SCW corresponding to $c_p > 8$ kJ/(kg·K) at $q/G > 0.5$ kJ/kg one dimensional definition of accelerative hydraulic resistance ξ_{ac} could result in calculated $\xi_{fr} > \xi_{fro}$ that is invalid (Fig. 6.1), since in heated channel friction is always lower than under isothermal flow at the same bulk temperature.

The way out was in application of the experimental method developed at the Institute of High Temperatures (IVTAN, Moscow) and tested for supercritical carbon dioxide (the so called method of two pressure drops) [6.12]. The adaptation of the method to SCW and the results were described in Section 4.3.3. Besides, four zones of water enthalpies (A, B, C and D) determining effect of viscosity and friction on flow pattern in the wall vicinity were considered.

The main part of the experimental data for friction factor at $q/G > 0.5$ kJ/kg in tubes of $ID = 3 \div 10$ mm and in annular channels (D_{out}/D_{inn} = 10/8 and 6/4 mm) both of zone B (viscous inertial flow of 'liquid' phase, where $650 \le h_b \le 1500$ kJ/kg) and of zone D (gaseous phase, where $h_b \ge 2550$ kJ/kg) the data array was approximated with a scatter within ± 20 % by correlation

$$\xi_{fr} = \xi_{fro}\left(\frac{\mu_w}{\mu_b}\cdot\frac{\rho_w}{\rho_b}\right)^{0.18}. \tag{6.4}$$

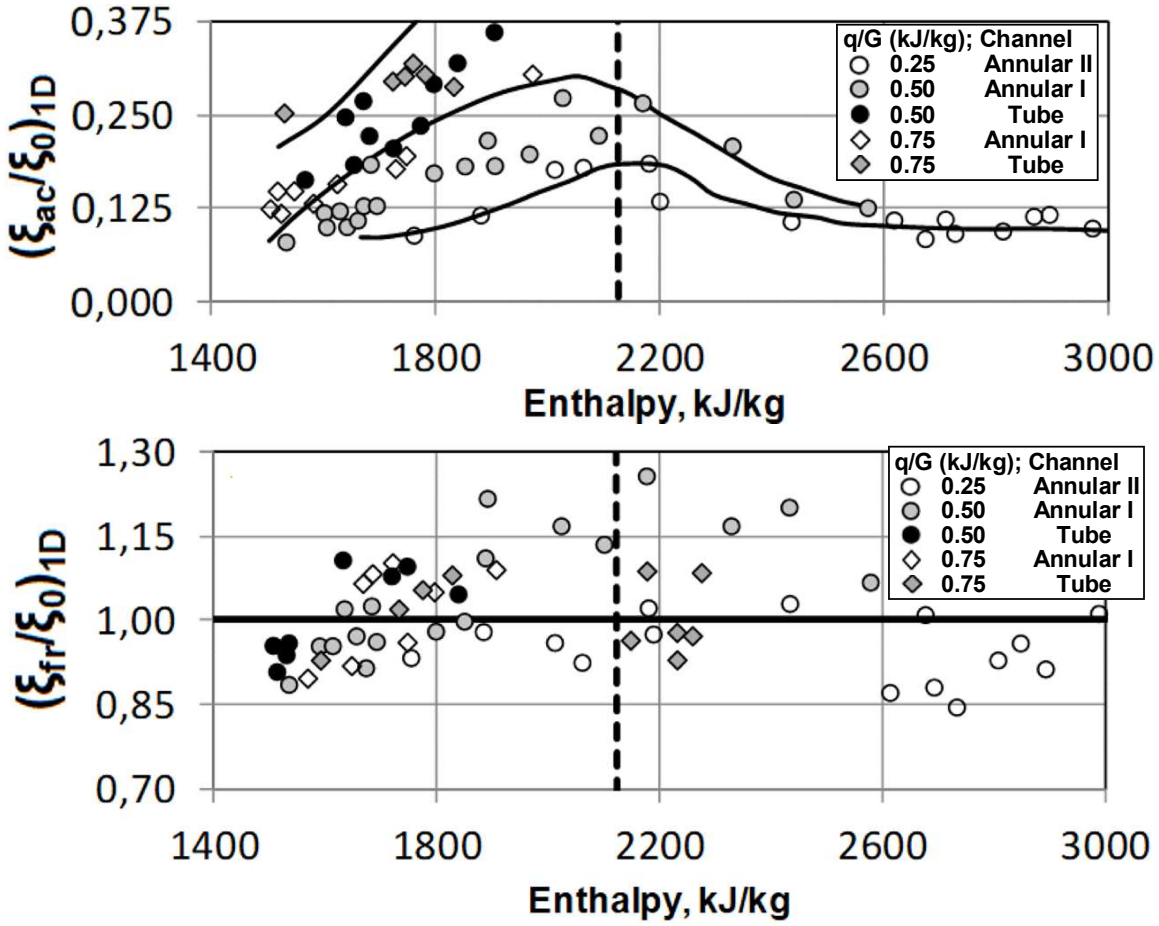

Fig. 6.1. Reduced factors of frictional and inertial (accelerative) hydraulic resistance of channels based on one dimensional model (Annular channel II: D_{out}/D_{inn} = 6/4 mm; Annular channel I: D_{out}/D_{inn} = 10/8 mm; Tube: D = 3.01 mm).

The experiments revealed that in zone C it is just acceleration factor ξ_{ac} that significantly affects full hydraulic resistance to flow. From Eq. (4.22), it follows that

$$\xi_{ac} = \int_0^{l/D} \frac{dI}{d(l/D)} \cdot \frac{2\rho}{G^2} \tag{6.5}$$

where $\frac{dI}{d(l/D)}$ is a longitudinal change in flow impulse characterizing connection between turbulent exchange and the field of averaged velocities, i.e., acceleration factor is a function of $(\partial v/\partial h)_p$. In its turn, a response of ξ_{ac} to the change in thermal state of the flowing medium is $(\partial \xi_{ac}/\partial h)_p = f(\partial^2 v/\partial h^2)_p = f(v'')_p$. It is indicative that the reduced one dimensional acceleration factor $(\xi_{ac}/\xi_0)_{1D}$ (Fig. 6.1) and 'two dimensional' acceleration factor $(\xi_{ac}/\xi_0)_{2D}$ (see Fig. 6.6 below) qualitatively repeat (the second of them more evidently, as it is much closer to the real behaviour of ξ_{ac}) the trend of function $v'' = f(h)$ plotted in Fig. 6.2 by using [6.12]. Thus, the second derivative of the specific volume v'' could be considered as a parameter of the velocity head sensibility (response) to averaged bulk enthalpy at the heated section of a channel.

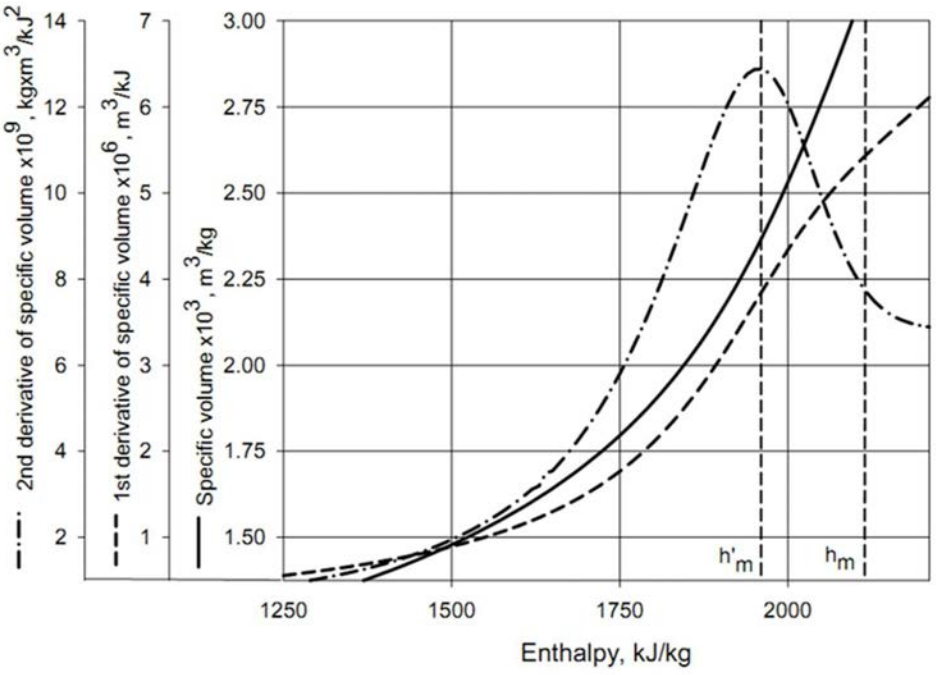

Fig. 6.2. Specific volume of SCW, its first and second derivatives as the functions of the enthalpy at P = 23.5 MPa.

Analysis of the parameters defining the experimental value of full hydraulic resistance factor ζ (the sum of ξ_{fr} and ξ_{ac}) has shown that the product $p \cdot v'' \cdot (q/G)$ (kg·m/kJ) expresses dependence of the expansion work performed by the coolant mass unit upon its enthalpy at a given heat flux rate. In other words, this product (referred to as *Se*) represents sensitivity of the specific work of volumetric expansion to change in mean volumetric thermal state of the flow. It is expressed in a dimensionless form as

$$\overline{Se} = \frac{Se}{Se_m} = \frac{v''(q/G)}{v''_m(q/G)_{lim}} \tag{6.6}$$

where v''_m is a maximal value of v'' at a given pressure (e.g., for water at P = 23.5 MPa $v''_m \approx 1.18 \cdot 10^{-8}$ kg·m^3/kJ^2 and corresponding to it enthalpy $h \approx 1980$ kJ/kg).

Eq. (6.6) indicates how much *Se* differs from Se_m at the given parameters of thermal state under the conditions of maximal rate of change in velocity (dynamic) head, if the value of heat flux rate q/G is limiting the conditions of normal heat transfer. Design correlation for $(q/G)_b$ that could be considered as the boundary between normal and deteriorated heat transfer at distance l from inlet of water with enthalpy $h_{in} \leq 2000$ kJ/kg into the channel was derived in [6.8] and then updated to Eq. (5.11) (see Section 5.6.5). In its turn, being a generalizing parameter of both thermal state and operating conditions $\overline{Se}$ itself is a strong parameter in the following correlation that without iteration determines the value of full hydraulic resistance factor of smooth tube in zones B and C:

$$\xi = \xi_{fr} + \xi_a = \xi_{fro}\left[1 + \left(\frac{\overline{\Delta h}}{\overline{D}}\right)^{0.5} \overline{Se}^{0.7}\overline{C}_{pm}^{-1}\right], \tag{6.7}$$

where ξ_{fro} is the friction factor in isothermal flow; $\overline{\Delta h} = (h_{out} - h_{in})/h_m$; $\overline{D} = D_h/D_{ref}$ (D_h is heated diameter; D_{ref} = 8 mm as mostly used (referred to) diameter in the studies of the kind); $\overline{C}_{pm} = C_{pm}/C^*_{pm}$ ($C^*_{pm} \approx 160$ kJ/(kg·K) and C_{pm} are pseudocritical heat capacity corresponding to h_m of water at 23.5 MPa and at a given pressure, respectively).

Equation (6.7) approximated the whole data array from [6.8] and [6.11] with scattering not exceeding ±15 % and somewhat worse (within ±20 %) the data from [6.13] (Fig. 6.3). To analyze the latter data the first (v') and the second (v'') derivatives of CO_2 specific volume versus enthalpy at P = 7.7 MPa were plotted by numerical differentiation of the data from [6.14] (Fig. 6.4). For CO_2 at this pressure $h''_m \approx 633$ kJ/kg.

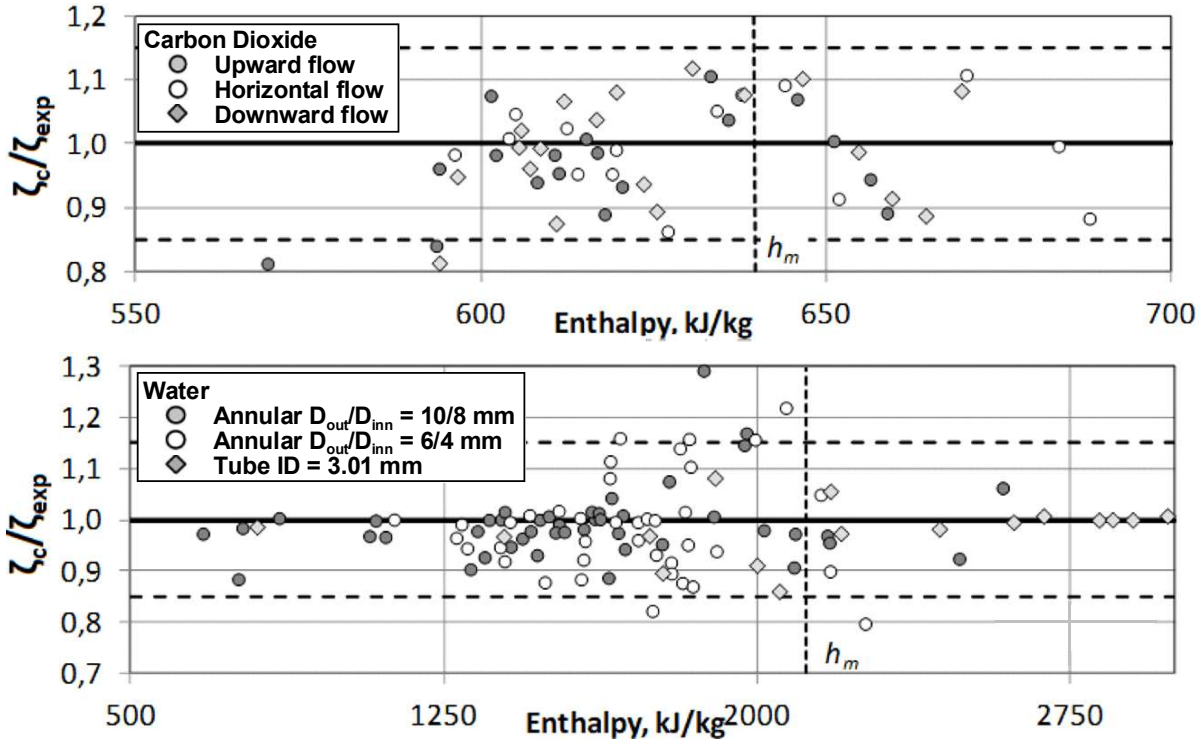

Fig. 6.3. Approximation of full resistance factor (ζ_c calculated using Eq. (6.7)).

It is worth to note that parameter $\overline{Se}$ for carbon dioxide is more than 20 times higher than that for water, i.e., thermal and inertial properties of these fluids are quite different. It is significant that accuracy of the correlation did not decrease in the region of pseudocritical state of the fluids, where all thermal and physical properties of fluid abruptly and even extremely vary, and at deterioration of heat transfer by 2 to 3 times for water and by 2 to 7 times for carbon dioxide.

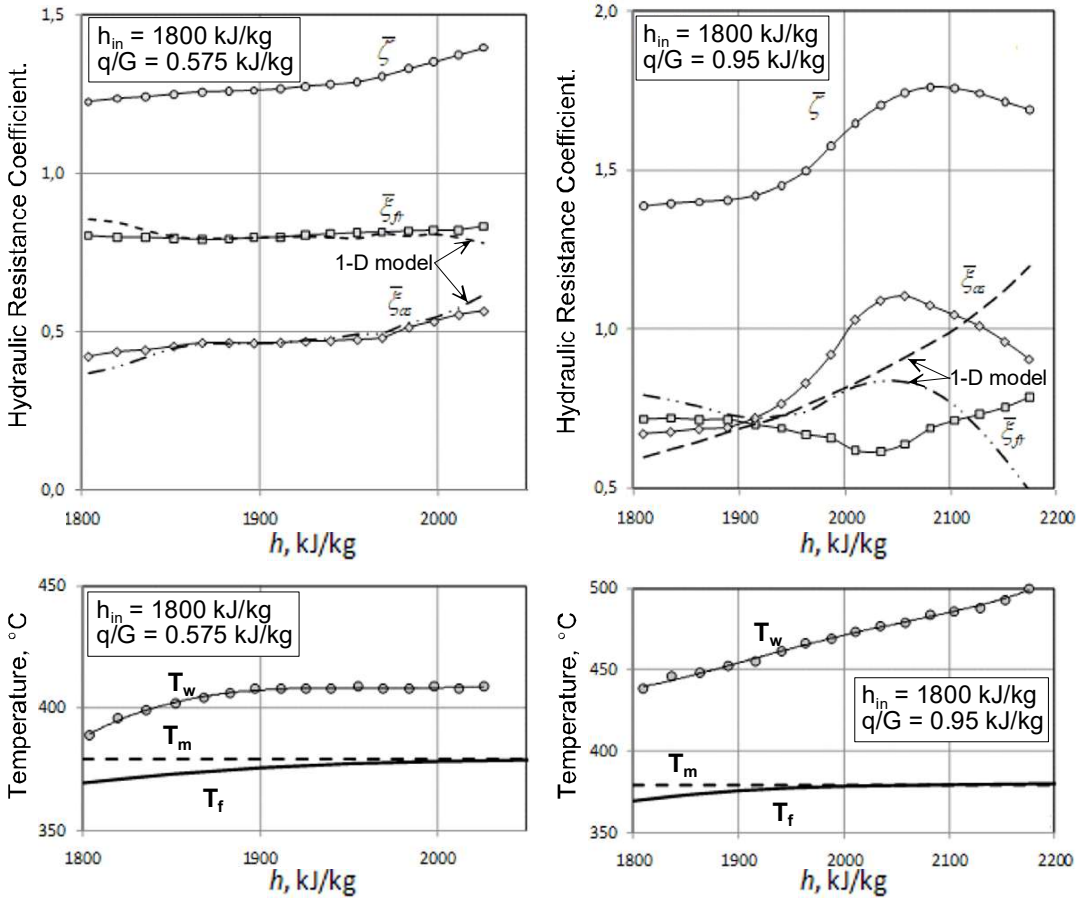

Fig. 6.4. Hydraulic resistance coefficients and axial temperature profiles.

In Fig. 6.1 to Fig. 6.4 [6.15] experimental values of pressure losses were compared with those calculated by using correlations derived by Blasius and by Colebrook and White (C–W) [6.16]. The Blasius friction factor equation, analogous to Eq. (6.2) and based on the assumption of fully developed turbulent flow in a smooth tube, is

$$\xi_{Bl} = \frac{0.3164}{Re_b^{0.25}}. \tag{6.8}$$

It is applicable for $Re_b < 10^5$. The C–W friction factor equation is applicable for turbulent flow and takes into the account surface roughness ε [6.16]:

$$\frac{1}{\xi_{C-W}^{0.5}} = -2\,log\left(\frac{\varepsilon/D}{3.7} + \frac{2.51}{Re_b\sqrt{\xi_{C-W}}}\right). \tag{6.9}$$

Strictly speaking, these equations are applicable for isothermal (adiabatic) flow only. The intensive heating (cooling) would increase the pressure losses. At the zone of low enthalpies (h_b

≤ 650 kJ/kg), where friction coefficient ξ_{fr} follows correlation reflecting strong dependence of viscosity upon coolant enthalpy [6.17]:

$$\xi_{fr}/\xi_0 = 1 - 0.5\cdot(1+X)\cdot B\cdot log(1+X), \tag{6.10}$$

where $X = (\mu_b/\mu_w - 1)(\mu_b/\mu_w)^{0.17}$; $B = 0.17 - 2\cdot10^{-6}\cdot Re + 1800/Re$. In this zone of practically zero flow acceleration the ratio ξ_{fr}/ξ_0 is a function of not only μ_b/μ_w but of *Re* as well (the lesser *Re* the stronger function). If $Re > 10^5$, $\xi_{fr}/\xi_0 = f(Re) \rightarrow 1$.

The method of two pressure drops enabled to get corrected values of local friction and acceleration factors of hydraulic resistance in Zone C (Fig. 6.4). It resulted in the correlation:

$$\xi_{fr} = \xi_0 \cdot \left(\frac{\mu_w}{\mu_b}\right)^{0.15} \cdot \left(\frac{\rho_w}{\rho_b}\right)^{0.1} \tag{6.11}$$

which was applied jointly with Eq. (4.32) to predict by iteration of them the levels both of heat transfer efficiency (*Nu*) and of hydraulic resistance (ξ_{fr}).

Not numerous series of the measurements (29) of $\Delta P(l_{heated})$ in 1 rod annular channel, 3 and 7-rod bundles (see Section 5.6.5) included in OECD-NEA database proved that Eq. (6.11) is in a good enough agreement (within ±25 % for the regimes of normal heat transfer) with the experiments.

Fig. 6.4 demonstrates that local inertial (accelerative) and frictional factors in zone C, determined by:

$$\zeta_i = \frac{2\rho_i[D\Delta P(\tilde{l})/d\tilde{l}]_i}{G^2}; \xi_{fr_i} = \frac{2\rho_i[D\Delta_{fr}(\tilde{l})/d\tilde{l}]_i}{G^2}; \xi_{ac_i} = \frac{2\rho_i[dI(\tilde{l})/d\tilde{l}]_i}{G^2} \tag{6.12}$$

are closer to real ones than predicted by 1D model.

The method of two drops gave the possibility to estimate the level of the maximum error $\delta_{fr.1D}$ in definition of friction resistance caused by conventional one dimensional model of flow thermal acceleration. With scattering natural for experimental measurements of pressure drop in short channels (l/D < 100) impulse factor *S* of turbulent flow, which can vary from S_0 = 1.02 in isothermal turbulent flow (see Eq. (4.18)) to S_l = 1.33 in laminar flow with parabolic radial profile of velocity, in NTUU experiments reached the values up to 1.07–1.09 at the longest heated section. Keeping in mind that

$$S = 1.02 + \frac{\Delta P_{ac} - \Delta P_{ac1D}}{G^2} \cdot \rho_{out} \tag{6.13}$$

it is not difficult to define the maximum error $\delta_{fr.1D}$:

$$\delta_{fr.1D} = \frac{\Delta P_{fr.1D} - \Delta P_{fr}}{\Delta P_{fr}} \cdot 100 = \frac{(S - 1.02) \cdot G^2}{\Delta P_{fr} \cdot \rho_{out}} \cdot 100 \tag{6.14}$$

According to Eq. (6.12) maximum error in traditional prediction of ξ_{fr} under the conditions of NTUU experiment and equally correct measurements by both methods could not exceed 35 %. Under normal heat transfer was below 15 % ($S \leq 1.05$). It means that in absence of DHT in the whole range of water enthalpy up to h_m with accuracy practically sufficient for definition of channel hydraulic resistance the one dimensional model could be used.

This conclusion agrees with the results of the first work on carbon dioxide [6.17], which $\delta_{fr.1D}$ reached 80 %. Its so high value is explained by significantly stronger variation of thermo inertial properties of CO_2. Unlike the results of the mentioned work, in NTUU experiments extreme wall temperatures did not take place.

It is seen that at low heat flux rates function $\xi_{fr}(l)$ negligibly varies, i.e., friction resistance weakly depends upon thermal state of the flow. It means that for estimation of reduced friction resistance ξ_{fr}/ξ_0 in a channel cooled by SCW flow at heat flux rate $q/G < 0.5$ kJ/kg simple formula (6.1) can be used. Comparison of predicted friction factor versus experimental data is plotted in Fig. 6.5. As seen, the results obtained by Eq. (6.1) are evidently overestimated by 30–60 % (Fig. 6.5a). As it was underlined in Section 4.3.3, just the opposite result (Fig. 6.5b) is obtained by the following expression [6.18]:

$$\xi_{fr}/\xi_0 = (\rho_w/\rho_b)^{0.4} \tag{6.15}$$

probably due to much higher (by several times) acceleration effect in carbon dioxide, which lefts too small share of full pressure loss in case of SCW for predicted frictional resistance. So, in the case of hydraulic resistance an idea of fluid-to-fluid scaling until now occurs to be not properly adequate. Unexpectedly, correlation $\xi_{fr}/\xi_0 = (\mu_w/\mu_b)^{0.2} \cdot (\rho_w/\rho_b)^{0.33}$, proposed by [6.15] on the basis of numerical computation of SC helium friction resistance, was better than (6.1) and (6.9) at normal heat transfer (Fig. 6.5c).

In Fig. 4.27 (see Section 4.3.6) amplitude of thermoacoustic oscillations of SCW pressure (a) and reduced heat transfer (b) in annular channel vs. heat flux were plotted. It was detected that in most regimes increasing heat flux was followed by an extreme change in the amplitude of the oscillations that decreased with increasing T_{in} and decreasing heat flux. At the same time, as q and T_{in} were increasing the frequency of these oscillations was lowering, probably due to decreasing velocity of sound propagation. Impact of the amplitude and heat flux upon hydraulic resistance of annular channel is shown in Fig. 6.6. At the time, when reduced HTC increases as the amplitude grows, reduced hydraulic resistance mostly changed in an opposite side. It could be explained by decreasing friction resistance that means violation of Reynolds analogy.

There it was yet mentioned that under certain operating conditions some regimes with modulated TOP, probably due to simultaneous oscillations at several neighboring frequencies, were observed.

In this case, synchronously oscillated pressure drop with the amplitude about 25 % of stabilized (without TOP) pressure ΔP_{st} at frequency about 0.3 Hz, shown in Fig. 6.7, took place.

In Fig. 6.1 to Fig. 6.3 [6.15] experimental values of pressure loss were compared with those calculated by using the correlations derived by Blasius and by Colebrook and White (C–W) [6.16].

The Blasius friction factor equation, analogous to Eq. (6.2) and based on the assumption of fully developed turbulent flow in a smooth tube. It is applicable for $Re_b = 4\times10^3–10^5$. The C–W friction factor equation is applicable for turbulent flow and takes into the account of surface roughness ε:

$$\frac{1}{\xi_{C-W}^{0.5}} = -2\,log\left(\frac{\varepsilon/D}{3.7} + \frac{2.51}{Re_b\sqrt{\xi_{C-W}}}\right). \tag{6.16}$$

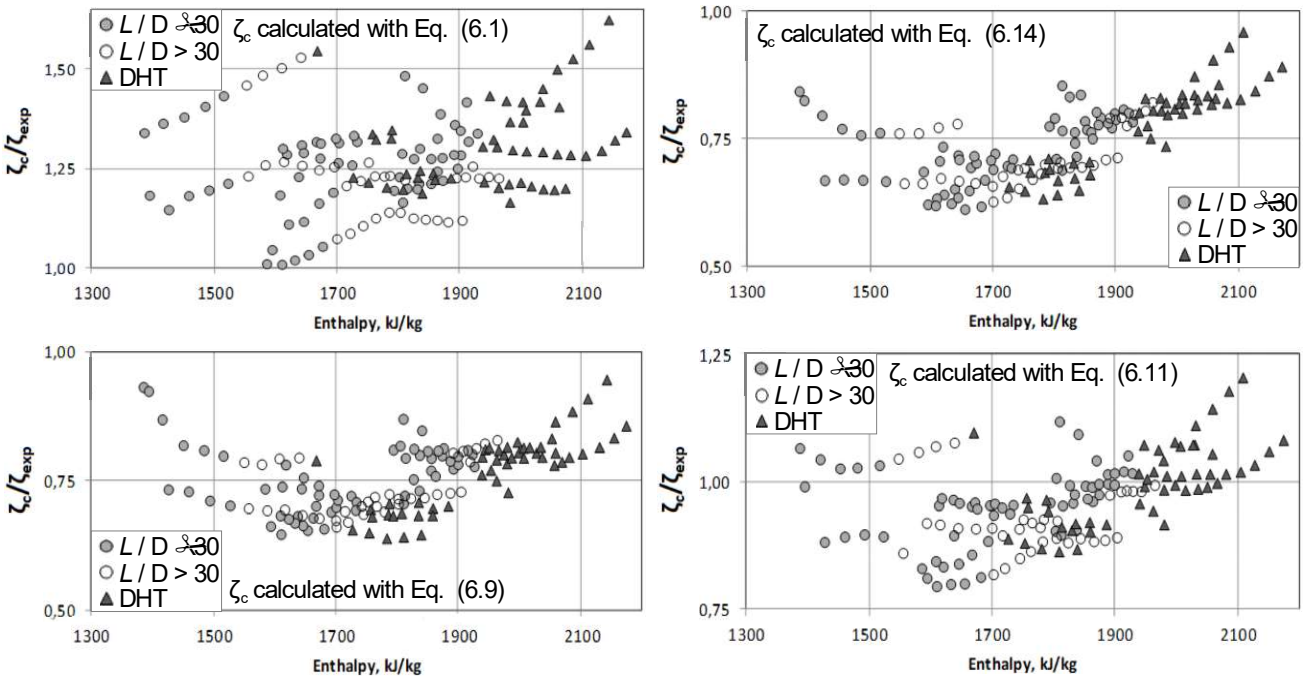

Fig. 6.5. Predictions of full hydraulic resistance factor using various correlations.

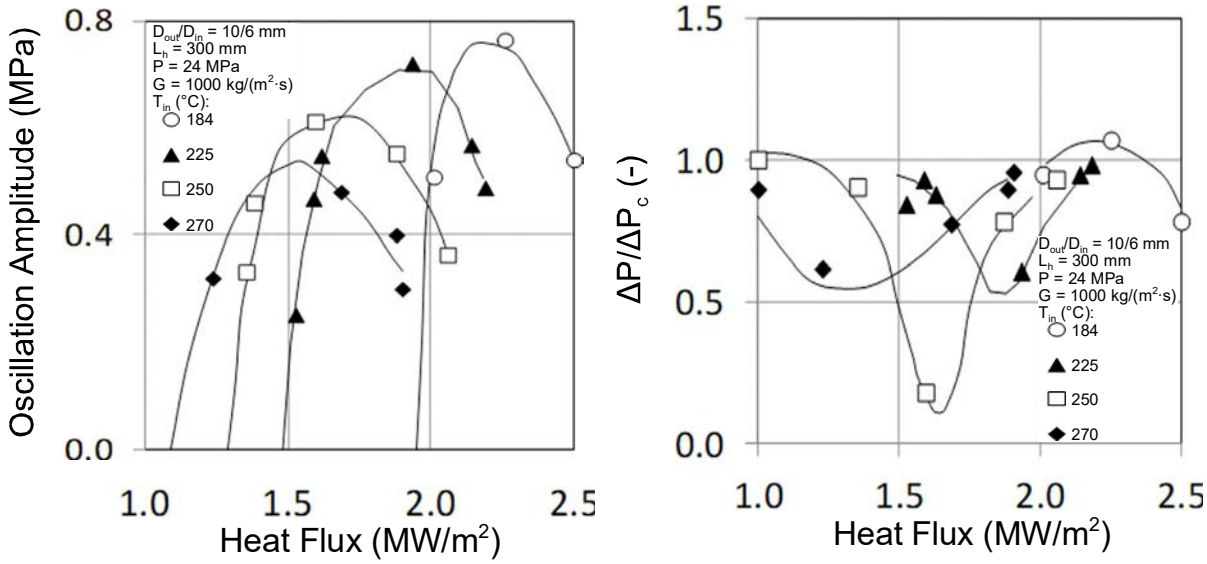

Fig. 6.6. Variation of oscillation amplitude and reduced pressure drop with heat flux in an annular channel.

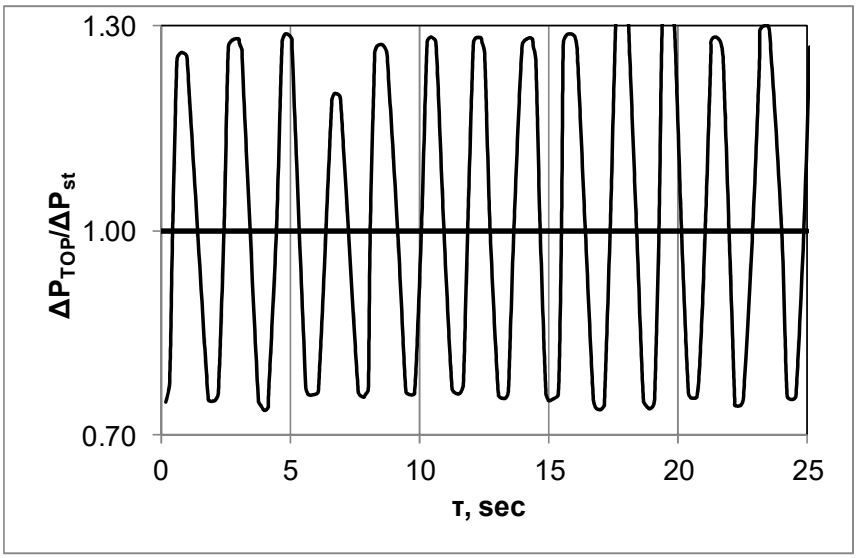

P = 24 MPa
G = 1000 kg/(m^2·s)
T_{in} =230°C
q = 2.3 MW/m^2
$2A$ = 1.4 MPa
T_w = 510 – 460°C
D = 3.3 mm
L_{heated} =255 mm

Fig. 6.7. Low frequency pulsation of pressure caused by TOP.

Strictly speaking, it is not correct to compare pressure loss in heated channel with one estimated by Eq. (6.12) and Eq. (6.13), since they are applicable for isothermal (adiabatic) flow only. So, the more intensive heating takes place, the higher are pressure losses in comparison with those calculated in such a way.

The performed analysis of the works devoted to hydraulic resistance to SCW flow in non-bundle and bundle geometries shows that allows to state that friction resistance is rather conservative component of full hydraulic resistance and in zone of viscous inertial flow of liquid phase (650 ≤

$h_b \leq 1500$ kJ/kg) and in zone of the enthalpies of gaseous phase ($h_b \geq 2550$ kJ/kg) the friction factor in tubes of d = 3÷10 mm at $q/G > 0.5$ kJ/kg could be estimated (with a scatter within ± 20 %) by Eq. (6.4). In intermediate zone of inertial viscous flow in transition from liquid to gaseous state (in the zone of high specific heat capacities ($c_p > 8$ kJ/(kg·K)), where thermal acceleration of flow plays dominant role in hydraulic resistance the best results in ΔP prediction gives Eq. (6.11).

Nomenclature and Acronyms

A	Amplitude (MPa)
c_p	Specific heat at constant pressure (kJ/(kg·K))
D	Diameter (mm)
G	Mass flux (kg/(m^2·s))
h	Enthalpy (kJ/kg)
I	Flow impulse
l	Length (m)
Nu	Nusselt number (-)
P	Pressure (MPa)
q	Heat flux (kW/m^2)
Re	Reynolds number (-)
S	Impulse factor (-)
T	Time (sec)
t	Temperature (°C)
ε	Roughness height (mm)
ξ	Friction factor (-)
μ	Dynamic viscosity (kg/(m·s))
ρ	Density (kg/m^3)

Subscripts

ac	Acceleration
b	Bulk fluid
c	Calculated
C–W	Colebrook–White
exp	Experimental
f	Fluid
fr	Friction
fro	Friction for isothermal liquid
hydr	Hydraulics equivalent
in	Inlet
inn	Inner
out	Outer, outlet
w	Wall

Acronyms

CO_2	Carbon Dioxide
DHT	Deteriorated Heat Transfer
HTC	Heat Transfer Coefficient
ID	Inner diameter

IVTAN	Institute of High Temperatures
NEA	Nuclear Energy Agency
NTUU	National Technical University of Ukraine
OECD	Organization for Economics Cooperation and Development
SCW	Super Critical Water

REFERENCES TO SECTION 6

[6.1] ALLEN, ECKERT, Measurement of Friction Factors and Heat Transfer under Turbulent Flow of Water in Tubes (Pr = 7 and 8) at Constant Heat Flux on the Wall, J. Heat Transfer, Ser. C, **3**, (1964), 3–9.

[6.2] KURGANOV, V.A., ZEIGARNIK, Y.A., YAN'KOV, G.G., MASLAKOVA, I.V., Heat Exchange and Resistance in Tubes under Supercritical Pressures of Coolant: Resume of Scientific Research and Practical Recommendations, Shans Publ. House, 2018 (In Russian).

[6.3] TARASOVA, N.V., LEONT'YEV, A.I., Hydraulic Resistance at Flow of Water in Heated Tubes under Supercritical Pressures, Tyeplofysika Vysokikh Tyemperatur (Thermal Physics of High Temperatures), **6, 4**, (1968), 755–756, (In Russian).

[6.4] KONDRAT'YEV, N.S., Heat Transfer and Hydraulic Resistance under Flow of Supercritical Water in Tubes, Thermal Engineering (Теплоэнергетика), **8**, (1969), 49–51, (In Russian).

[6.5] KRASYAKOVA, L.YU., BELYAKOV, I.I., FEFELOVA, N.D., Hydraulic Resistance under Isothermal and Non-isothermal Flow of Medium at Supercritical Pressure, Thermal Engineering (Теплоэнергетика), **4**, (1973), 31–35, (In Russian).

[6.6] ISHIGAI, S., KAJI, M., NAKAMOTO, M., Heat Transfer and Friction for Water Flow in Tubes at Supercritical Pressures, Teplomassoobmen (Heat-Mass-Transfer)-V, Proc. of 5th All-Union Conf. on Heat Mass Transfer, Minsk, Belarus, **1, 1**, (1976), 261–269, (In Russian).

[6.7] DYADYAKIN, B.V., POPOV, A.S., Heat Transfer and Thermal Resistance of Tight Seven-Rod Bundle Cooled with Water Flow at Supercritical Pressures, Transactions of VTI, **11**, (1977), 244–253, (In Russian).

[6.8] RAZUMOVSKIY, V.G., ORNATSKIY, A.P., MAYEVSKIY, E.M., Hydraulic Resistance and Heat Transfer in Smooth Channels under Turbulent Flow of Water at Supercritical Pressure, Heat Engineering (Tyeploenergetika), **2**, (1984), 69–72, (In Russian).

[6.9] MAYEVSKIY, E.M., RAZUMOVSKIY, V.G., Experimental Investigation of Hydraulic Resistance of Channel at Isothermal Flow of Water under Supercritical Pressure, Information in Abstracts on R&Ds Completed at the Universities of the UkSSR, Energetika, **XI**, (1977), 36–37, 1977 (In Russian).

[6.10] FILONENKO, G.K., Hydraulic Resistance of Pipelines, Heat Power Engineering (Tyeploenergyetika), **4**, (1954), 40, 44 (In Russian).

[6.11] PETUKHOV, B.S., KURGANOV, B.A., ANKUDINOV, V.B., GRYGOR'YEV, V.S., Experimental Investigation of Resistance and Heat Transfer in Tubes under Turbulent Flow of Liquid at Supercritical Pressure, Tyeplofysika Vysokikh Tyemperatur (Thermal Physics of High Temperatures), **18, 1**, (1980), 100–111, (In Russian).

[6.12] RIVKIN, S.L., ALEXANDROVA, A.A., KREMENEVSKAYA, E.A., Thermodynamic derivatives for water and water steam, Energiya Publ. House, 1977, (In Russian).

[6.13] POPOV, V.N., Theoretical Design of Heat Transfer and Friction Resistance in Tubes under Flow of Incompressible Fluid with Variable Physical Properties, Abstract of candidate thesis, MEI, 1964, (In Russian).
[6.14] ALTUNIN, V.V., Thermophysical Properties of Carbon Dioxide, Standarty Publ. House, 1975, (In Russian).
[6.15] BYELYAEV, V.M., Investigation of Heat Transfer and Turbulent Flow of Fluid with Variable Physical Properties (One-Phase Near-Critical Region, Gases, Dropping Liquid), Abstract of candidate thesis, MEI, 1980, (In Russian).
[6.16] COLEBROOK, C.F., Turbulent Flow in Pipes, with Particular Reference to Transition Region between Smooth and Rough Pipe Laws, Institution of Civil Engineers of London, **12, 4**, (1939), 393–422.
[6.17] LAFAY, J., Mesure du Coefficient de Frottment avec Transfert de Chaleur en Convection Forcée dans un Canal Circulaire, Rep. Centre d'Études Nucléaires de Grenoble, CEA-R-3896, 1970.
[6.18] PETUKHOV, B.S., KURGANOV, B.A., ANKUDINOV, V.B., New Experimental Data on Resistance and Heat Transfer in Round Tube under Heating of Carbon Dioxide at Near-Critical State Parameters, Convective Heat Exchange, Methods and Results of the Investigations, IVTAN, (1982), 29–67 (In Russian).

7. NATURAL CIRCULATION AND FLOW STABILITY

Several SCWR designs with forced circulation of primary coolant have been proposed in the past ([7.1], [7.2]; [7.3] and [7.4]).

Cooling a reactor at full power with natural instead of forced circulation is generally considered as enhancement of passive safety. Natural circulation (NC) can also be used for passive decay heat removal after reactor shutdown. The NC loops based on supercritical water generate equivalent density gradients in comparison to NC loops based on two-phase water. Therefore, in SCWR the NC can be considered as a possible way of heat removal ([7.5]; [7.6]). Natural circulation can also be used for passive decay heat removal after reactor shutdown. Cooling a reactor at full power with natural instead of forced circulation is generally considered as enhancement of passive safety. But the occurance of instabilities in the operation of these reactors may lead to power oscillations which is undesirable. This can also lead to failure of control systems due to mechanical vibration of components.

As the supercritical fluids experience a steep change in their thermodynamic and transport properties (e.g., density, viscosity, specific heat, etc.) in the pseudocritical region, the SCWR could undergo density wave instability. Further, the heat transfer behaviour in the pseudocritical region is quite different then the heat transfer in subcritical region. The drastic change in the density in the pseudocritical region has strong effects in the buoyany and acceleration which causes the flow and heat transfer behaviour to change. Hence the Dittus-Boelter type of heat tranfer correlations may not be valid for supercritical conditions.

In view of the above, design of SCWRs pose many challenges with respect to certain thermal hydraulic characteristics for which a confidence level has been developed for the presently operating fleet of reactors which make use of fluids at subcritical pressures either in single phase (for e.g. Pressurized Heavy Water Reactor (PHWR)) or in two phase (e.g. Boiling Water Reactor (BWR)) conditions. Thus, having detailed knowledge of flow and heat transfer behaviour of supercritical fluids is necessary for progressing in the technology. To achieve this, more and more experimental efforts can be undertaken to boost the confidence level in understanding the basic thermal hydraulic phenomena of flow, heat transfer and stability in case of natural circulation.

Experimental efforts in the form of a broad database can be used as a part of development of set of reliable analytical tools which can be utilized for design and safety analysis of the SCWRs with reasonable accuracy. However, the development of such a tool can be completed successfully if it can be benchmarked against varied range of experimental data. It can be understood that due to unavailability of sufficient experimental database, having more and more experimental efforts on the generation of flow, stability and heat transfer data for supercritical fluids under natural / forced is of prime importance to help design, safety analysis and ultimately, the regulatory clearances of SCWRs.

The present section is devoted to investigations related to flow characteristics in single and twin parallel channels under natural circulation condition with different dimensions / geometries. The contributions made in this section regarding experimental wok comprise test data generated in the following test facilities:

— An experimental facility to address natural circulation in a rectangular single channel loop at Bhabha Atomic Reserch Center (BARC), India;
— An experimental facility at China Institute of Atomic Energy (CIAE), China to address stability under two parallel channels;
— An experimental test facility at Canadian Nuclear Laboratories (CNL), Canada to address stability;
— An experimental test facility to address natural circulation at Budapest University of Technology & Economics (BME).

7.1. REVIEW OF PREVIOUS WORK

The literature reported only very few experimental studies on natural circulation with supercritical fluids. However, recently the field has attracted interest of many researchers across the world and hence few more experimental investigations are available.

Studies with Freon near critical region have been conducted by [7.7] and reported high and low frequency oscillations near the pseudocritical temeprature of the bulk fluid. The studies of heat transfer by [7.8] in a 4 m high loop with CO_2 also observed pressure oscillations around pseudocritical point. The reported experiments with carbon dioxide by [7.9] in a 2 m high natural circulation loop at supercritical pressure. A steady state characteristic of the loop was generated but no flow instabilities were observed in these tests as the fluid was heated through thermodynamic pseudocritical point. [7.10] has studied the steady state performance of a natural circulation system operating with supercritical CO_2.

Reference [7.11] conducted steady state and stability experiments with artificial neutronic feedback in scaled natural circulation driven HPLWR (High Performance Light Water Reactor) facility named Delight maintaining the inlet temperature constant (i.e. with open loop boundary conditions). They used Freon R23 at 5.7 MPa as the scaling fluid. The decay ratios and frequencies of the riser inlet temperature oscillations were measured. They found that for a single inlet temperature the system undergoes two transitions as the power is increased. At low power the system is stable and becomes unstable as the power is increased, but on further increasing the power the system stabilizes.

Experiments have been carried out for parallel channel flow instability with supercritical water by [7.12] in the pressure range of 23-25 MPa and inlet temperature range of 180-260 ^{O}C. They obtained the parameters for the onset of flow stability and its boundary.

A 3D numerical investigation by [7.13], in two heated parallel channels reported out of phase flow instability and compared the results with experimental data. [7.14] conducted experimental investigations for the flow and stability features of the SC–CO2 under natural circulation. NC flow characteristics are greatly influenced by the charging pressure at fixed initial temperature. Also no instability is found to occur for the supercritical flow.

Reference [7.15] conducted experimental investigations for studying effect of buoyancy and flow acceleration on heat transfer behaviour of SC–CO_2 under natural circulation in a loop. Experimental parameters included 7.45–10.19 MPa pressure, mass flux from 235–480 kg/(m^2.s),

bulk fluid temperature between 21–205 deg C and 10.5–96 kW/m^2 of heat flux. Noticeable heat transfer deterioration was reported and it was found that point of deterioration moved towards inlet of test section with the increase of power, the effect of buoyancy was found to be more pronounced than that of acceleration effect. Heat transfer deterioration was found to occur with the maximum value of buoyancy parameter, whereas when buoyancy parameter gets below 2×10^{-5}, and heat transfer deterioration occurred. [7.16] in another study conducted both experimental and theoretical investigations for studying flow instability in a natural circulation loop using SC–CO_2. Flow oscillations were attributed to the transition of heat transfer mode from deteriorated heat transfer to normal heat transfer which might results in pressure fluctuations which in turn could get amplified with appropriate non-dimensional pressure drop subsequently resulting in flow oscillations. System stability was found to be enhanced with an increase in system pressure and local resistance coefficient in cold section and decrease in the local resistance coefficient in the hot section.

References [7.17], [7.18] studied natural circulation behaviour of natural circulation loop based on SC–CO_2 with air as the cooling medium. In their study, both steady and transient modes of operations were discussed. Based on steady state results, a regression equation that relates Reynolds number with Grashof number was obtained. Under transient conditions, the start up and shutdown processes were analyzed with different heater powers. Local condensation of CO_2 was observed at the heat sink outlet during shutdown, leading to heating due to latent heat of condensation. For complete power failure study, results show the rise in pressure and temperature for a short duration followed by a slow cooling through natural convection heat loss to the ambient.

Theoretical investigations on stability in NC loops with supercritical water have been carried out by various researchers. Reference [7.19] predicted steady state and non-linear stability with supercritical water in rectangular loop with uniform area with a heater (horizontal) and a cooler (vertical). They have observed the threshold of stability as the steady state peak mass flow rate in the power curve. Reference [7.20] obsereved that the instability behaviour is not strictly related to steady state peak flow rate in the NC loops with supercritical water. [7.21] have developed stability parameter in non-dimensional form for supercritical fluid similar to two-phase system. These parameters are independent of working fluid and system pressure.

A few investigations were also conducted with supercritical CO_2 (which can be considered good simulant fluid for water) using one dimensional nonlinear stability codes ([7.22], [7.23]). [7.24] conducted experiments in a closed Supercritical Pressure Natural Circulation Loop (SPNCL) operating with supercritical CO_2 at lower pressures i.e. 8.0–9.0 MPa and compared the experimental steady state data with NOLSTA code predictions. NOLSTA code predicted the steady state natural circulation mass flow rates of SPNCL operating with supercritical carbon dioxide appreciably well ($\pm$ 15 %).

Reference [7.25] numerically studied the effect of heat transfer on stability and transition temperature of supercritical CO_2 in a rectangular natural circulation loop using a two dimensional model. They identified a transition average fluid temperature around 375 K for supercritical CO_2 below which the flow shows repetitive flow reversals and beyond which flow changes to stable single direction flow. Reference [7.26] also numerically studied the natural convection of SC–CO_2 in a uniform diameter rectangular loop. In their study the effects of loop inclination angle,

sink temperature and temperature difference on convection motion and heat transfer performance was presented. It was observed that with an increase in inclination angle, there was a deceleration in the convective flow and so in heat transfer performance due to decrease in buoyancy. The flow rate and heat transfer are found to firstly increase, attain a maximum and the gradual decrease with the increase in temperature difference. Similarly, heat sink temperature found to have a great effect on flow and heat transfer performance.

Reference [7.27] has developed a one dimensional numerical model to predict the transient behaviour (flow initiation, power step up and power step back) of a rectangular natural circulation loop. In all the cases studied, no instability has been observed and steady behaviour was obtained for vertical heater and vertical cooler orientation for SC–CO_2 as working fluid. In another study, [7.28] numerically studied flow behaviour of supercritical CO_2 natural circulation loop with the help of in-house developed 1D and 2D axi symmetric codes. It was found that 2D axisymmetric formulation prediction are more accurate than the 1D formulation. Predictions cover all three heat transfer regimes viz. Normal, enhanced and deteriorated heat transfer.

Reference [7.29] carried out dynamic analysis of a open natural circulation loop working on supercritical water using 1 dimensional conservation equations. Nonlinear analysis revealed instability as the power step was given to the system. Within stability boundary also, with step rise in power, system was found to take more time to reach a steady state. The investigations were carried out with horizontal heater and horizontal cooler orientation.

Reference [7.30] carried out numerical studies to compare thermal hydraulic aspects of SC–CO_2 and subcritical water based natural circulation loop operating under identical set of conditions with the help of a three dimensional model. Presence of large asymmetry in velocity and temperature profiles was observed in a single cross section due to local buoyancy effect which is more prominent for supercritical fluids. However, bulk fluid temperature level across the loop was found higher for water compared to the SC–CO_2.

Reference [7.31] applied modified SIMPLE algorithm to get rid of convergence problem presented by conventional SIMPLE algorithm while applying it for numerical analysis of a two dimensional unsteady natural convection flow in a rectangular cavity. Modified algorithm updates the density at each time step based on its value at the previous time step to satisfy the mass conversation. With the modified algorithm the continuous and physically consistent velocity profile was obtained compared to the discontinuous velocity profile.

Reference [7.32] studied the flow characteristics of SC–water under different heating power distribution conditions using ANSYS–CFX. It was concluded that different power distribution had a great influence on the natural circulation flow when the total power of heating is constant. Peak flow was observed for monotonically decreasing heating power distribution. [7.33] developed a model to predict dynamic behaviour of flow oscillations at supercritical pressures for both single and twin parallel channel systems. Validation of model was carried out against the experimental data available in the open literature [7.12] and [7.34]. It was concluded that for single channel system higher pressure drop across the channel significantly increase the flow and stabilize the system. Increase in the system pressure and higher loss coefficient at inlet and lower one at the outlet were also found to stabilize the system. In parallel channels, the effects of throttling

were found similar to those in single channel system. Moreover, adiabatic sections at inlet and outlet too have similar effects as those of inlet and outlet throttling respectively. Flow is found to be most stable in the case of vertical upward condition and worst stable in vertical downward flows which include flow excursion behavor too. However, authors emphasized to have more of experimental data for further benchmarking of the code.

The forced convective heat transfer have been experimentally studied by several researchers for SCW ([7.35]; [7.36]) and SC-CO_2 ([7.37]; [7.38]). [7.39]; [7.40] have done exhaustive literature survey confirming three modes of heat transfer (normal, improved and deteriorated) for supercritical fluids. The expected HTC in the normal heat transfer regime is that calculated by Dittus–Boelter correlation. Improved heat transfer is observed at low heat fluxes and deteriorated heat transfer is observed at higher heat fluxes and lower mass fluxes.

In literature, there is still no unique definition for the onset of heat transfer deterioration because reduction in heat transfer coefficient is gradual as compared to sharp increase in wall temperature (or sharp reduction in heat transfer coefficient) associated with boiling crisis at subcritical pressure conditions. For the steady state natural circulation experiments conducted with supercritical carbon dioxide in SPNCL ([7.41]) an exhaustive comparison of experimental heat transfer coefficients for heater was made with various empirical heat transfer correlations available in literature for supercritical fluids. They found Jackson [7.42] and Shitsman [7.43] correlations are predicting well in the subcritical, pseudocritical and supercritical region of loop operation. However, it was indirectly concluded for loop specific conditions that Bringer Smith [7.44] and Swenson [7.36] correlations predicts well for cooler heat transfer coefficient ([7.45]). The difference of heating and cooling heat transfer coefficient has also been studied theoretically by [7.46] for laminar flow of supercritical carbon dioxide in miniature tubes.

Recently, [7.47] carried out experimental investigations, although under forced circulation, on flow instabilities for water under ultrasupercritical conditions in parallel channels for the pressures ranging from 23–30 MPa and flow rates between 0.05–0.2 kg/s with inlet temperature between 200–390 ^{o}C. Inlet pressure drop coefficient was varied from 0–5.5 and heat flux was ranging between 0–500 kW/m^2. During the flow instability, variation of mass fluxes and pressure in the parallel channels were recorded along with oscillations in the wall temperature. Pressure and mass flow rate were found to have a reverse phase pulsation during oscillations. With the increase in heat flux, three regions of oscillations were appeared categorized as region 1, region 2 and region 3. Region 1 and region 2 oscillations observed for the first time in ultrasupercritical pressure are system oscillations and have long periods and large amplitudes whereas those in region 3 belong to density wave oscillation (DWO) having short period and small amplitude. Increase in system pressure, mass flow rate, inlet pressure drop coefficient or decreasing the inlet water temperature are found to stabilize the system.

In view of the availability of numerous studies on theoretical investigations which makes use of several considerations for accurate prediction of phenomena related to natural circulation and stability behaviour of the supercritical fluids, there is a need to focus more on the experimental efforts to generate more and more data for benchmarking of theoretical tools. Vast knowledge set acquired for fluids at subcritical pressures is the basis of the present set of theoretical prediction

made for supercritical fluids. These tools are though an extension of previous knowledge set but still need further improvements.

The gap area in the field of heat regimes (normal, deteriorated and improved heat transfer), use of heat transfer correlation for design purpose, stability and flow under natural circulation can only reliably be addressed by consistent experimental efforts. The very purpose of the present exercise is to improve the content of literature to provide more experimental information for furthering the understanding of phenomena.

Finally, it can be said that as the theoretical treatment of two phase mixtures started firstly considering them as homogeneous mixture which was based on the knowledge set available at that time with the background of single phase fluids and with time the understanding in two phase flow characteristics improved with the help of state of the art experimental techniques bringing out the multidimensional aspects of the fluid flow and thus bringing in to development of new theoretical/CFD models for reliable predictions of phenomena. In the similar way, treatment of supercritical fluid (which is considered as a homogeneous fluid) is based on the skill set available for two phase fluid. Due to presence of sudden property variations near pseudocritical region, there are possibilities to explore more of insights which are either missing or documented in very limited manner in the literature. Gaining more experimental information will definitely help to bring out hidden characteristics of supercritical fluids.

7.2. SUPERCRITICAL PRESSURE NATURAL CIRCULATION TEST AT BHABHA ATOMIC RESEARCH CENTRE, INDIA

7.2.1. TEST FACILITIES

A closed Supercritical Pressure Natural Circulation Loop (SPNCL) has been set up and operated in Bhabha Atomic Research Centre (BARC), India to generate data on flow and heat transfer behavior for supercritical fluids (i.e. water & carbon dioxide) under natural circulation conditions. Currently, the experiments were conducted in SPNCL with water at supercritical pressures between 22.3–24.5 MPa and carbon dioxide at higher supercritical pressures (i.e. 10 to 12 MPa). Carbon dioxide can be considered as good modelling fluid for water at supercritical conditions because of analogous change of properties particularly density and viscosity across the pseudocritical point as shown in Fig. 7.1.

A computer code NOLSTA ([7.45]), developed for steady state and stability analysis of thermosiphon with supercritical fluids has been used to carry out steady state analysis of closed SPNCL. Besides, the steady state experimental heat transfer coefficients have been compared with predictions of various heat transfer correlations available in literature for supercritical fluids.

The test facility (SPNCL) as shown in Fig. 7.2, is a rectangular geometry made up of uniform diameter Inconel-625 pipes of size DN15 Sch. 80 (OD: 21.34 mm; thickness: 3.73 mm) interconnected with SS-347 fittings. Design pressure of the SPNCL is 30 MPa and a design temperature of 450 ^{o}C whereas, heater pipe sections are designed for 600 ^{o}C. The loop has two heaters (a vertical and a horizontal) directly heated through resistance heating and two coolers (a vertical and a horizontal) which are basically tube-in-tube heat exchangers with outer tube ID as 38.1 mm. The coolant (air or chilled water) flows in the annualr space between outer tube and

inner tube (main loop). A power supply of 200 kW capacity (25 V; 8000 A) has been connected to the heater section with flexible bus-bars. A pressurizer with safety devices (rupture discs), is connected at the bottom of the loop to accommodate swell and shrinkage in the loop. The pressurizer also accommodate the cover gas (nirogen or helium). Six layers (1 inch each) of ceramic mat having thermal conductivity of 0.06 W/m.K, has been used for loop insulation. SPNCL enables to conduct experiments with one of four different combinations of heater and cooler orientations: Horizontal Heater Horizontal Cooler (HHHC); Horizontal Heater Vertical Cooler (HHVC); Vertical Heater Horizontal Cooler (VHHC); or Vertical Heater Vertical Cooler (VHVC).

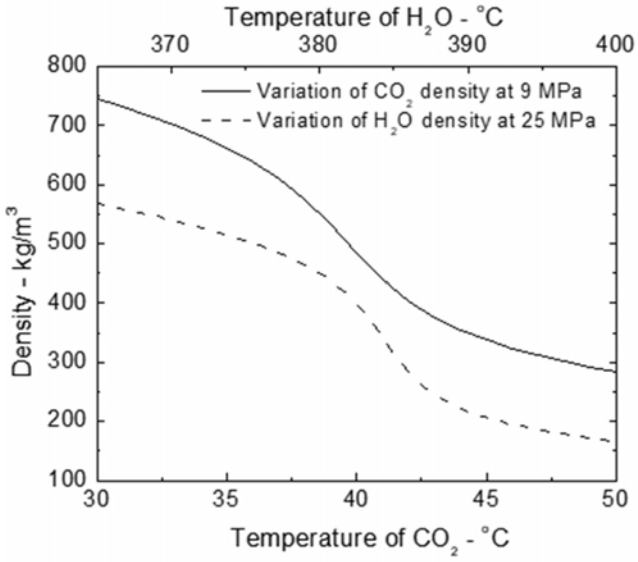

(a)

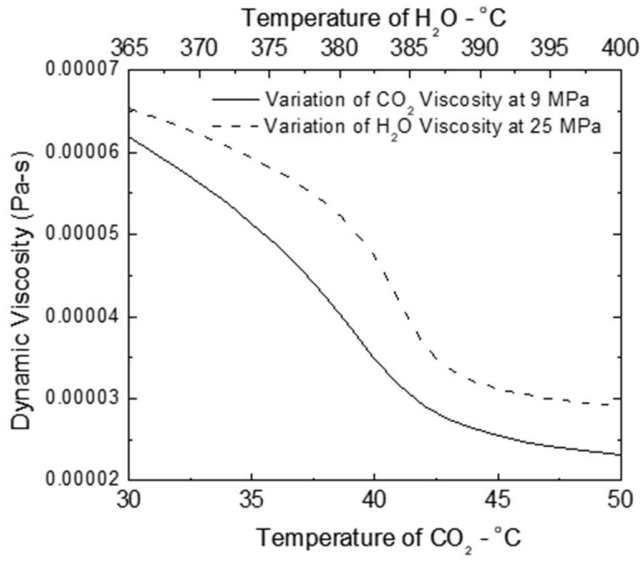

(b)

Fig. 7.1. Comparison of water and CO_2 (a) density and (b) dynamic viscosity at supercritical conditions.

K-type thermocouples are installed for temperature measurements on primary (main loop) and secondary (coolant) sides. Primary side fluid temperatures are taken as average measured readings of two thermocouples, which are installed at *r*/2 distance from pipe center in opposite directions across the cross-sections. Seondary side coolant temperature is measured at inlet and outlet of the cooler section. Heater surface temperatures are measured by the thermocouples brazed on the heater surfaces as typically shown in Fig. 7.3. Kellar make transducers are used to measure the loop pressure. Differential pressure transmitter (DPT) is used to measure the pressure drop across the heater section. A turbine flow meter (0–100 lpm) is used for secondary side flow measurement. Accuracy for different measurements is as given: ±0.5 ºC for thermocouples; ±0.3 MPa for pressure; ±0.18 mm for DPT; ±0.5 % for secondary flow; and ±0.5 % for power.

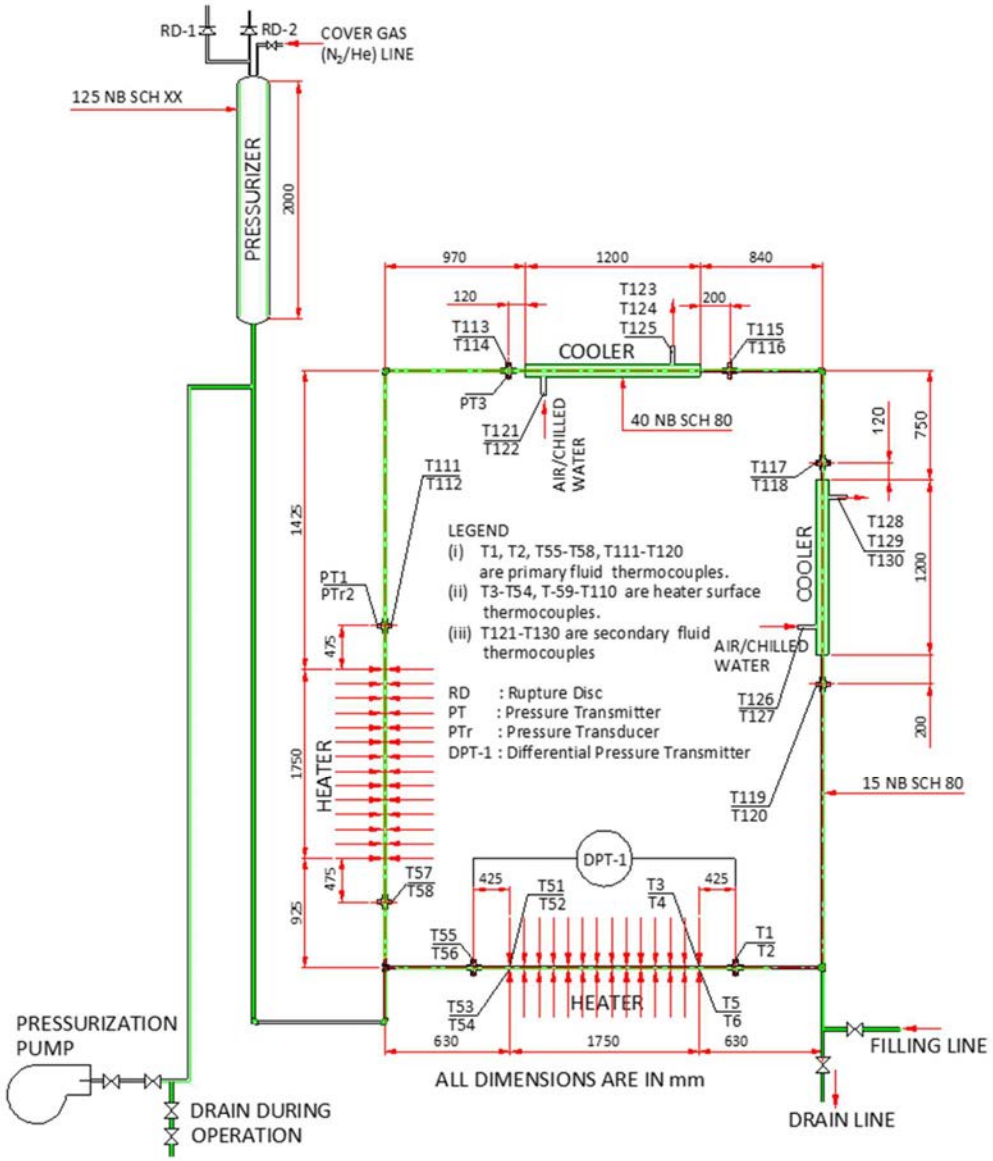

Fig. 7.2. Schematic of SPNCL test facility [7.48].

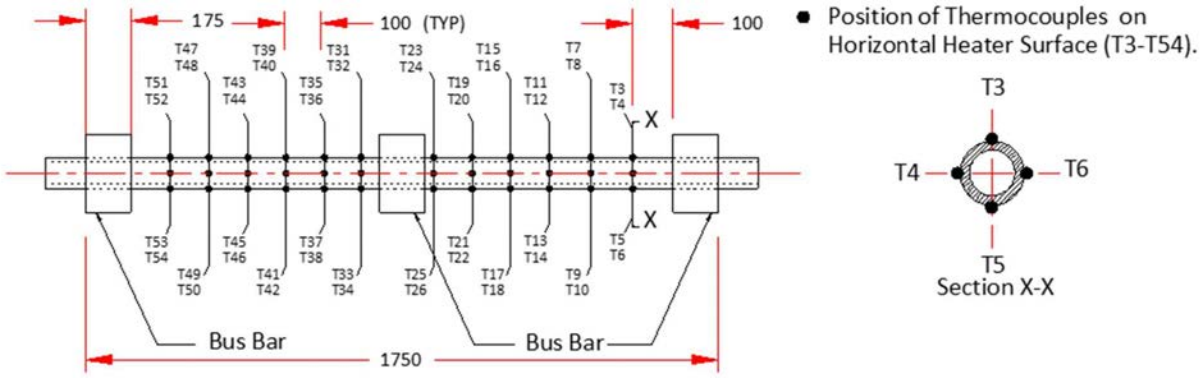

Fig. 7.3. Thermocouple locations in heater section [7.48].

7.2.2. EXPERIMENTAL PROCEDURE FOR SC–WATER

The loop is filled up to the required level in the pressurizer with water and pressurized externally up to 11 MPa by connecting pressurized Nitrogen cylinder. Haskel pump is used to further pressurize the loop to 22 MPa by adding more water in the liquid volume of the pressurizer. Further, loop pressurization is achieved through thermal expansion of the fluid initaited due to switching ON the power in the heater section. This pressurizes the loop upto the desired system pressure beyond critical pressure. The pressure is maintained at the desired pressure as water inventory is either added or drained from the pressurizer. The power was then further raised to different levels in steps to conduct the experiment.

7.2.3. STEADY STATE EXPERIMENTS WITH SUPERCRITICAL WATER

The steady state experiments were carried out for HHHC, VHHC and VHVC orientation only for different heater powers (5.0–9.3 kW) and loop pressures (22.3–24.5 MPa). The steady state mass flow rate for experimental conditions has been obtained by energy balance across heater test section which can be expressed as

$$W_{ss} = \text{Heater Power} / (h_{out} - h_{in}) \tag{7.1}$$

Enthalpy at heater outlet (h_{out}) can be calculated from heater outlet temperature and operating pressure measured experimentally and enthalpy at heater inlet (h_{in}) can be calculated from heater inlet temperature and operating pressure measured experimentally. The experimental steady state mass flow rate, heater inlet and outlet temperatures versus power for HHHC orientation with constant secondary side air flow rate are shown in Fig. 7.4a & Fig. 7.4b respectively. The temperature difference between heater inlet and outlet is reducing as we are approaching the pseudocritical temperature because of the increase in the specific heat (Fig. 7.5a, pseudocritical temperature is the temperature corresponding to maximum specific heat at a given pressure) of the fluid. After pseudocritical point, the specific heat starts decreasing with increase in temperature, which causes the temperature difference to increase. Thus, the flow rate at steady state increases up to the pseudocritical temperature value attained at the heater inlet, corresponding to 8.5 kW power. On raising the power above 8.5 kW the flow rate suddenly decreases due to increase in frictional resistance since the fluid condition in both the legs (hot and cold) become supercritical.

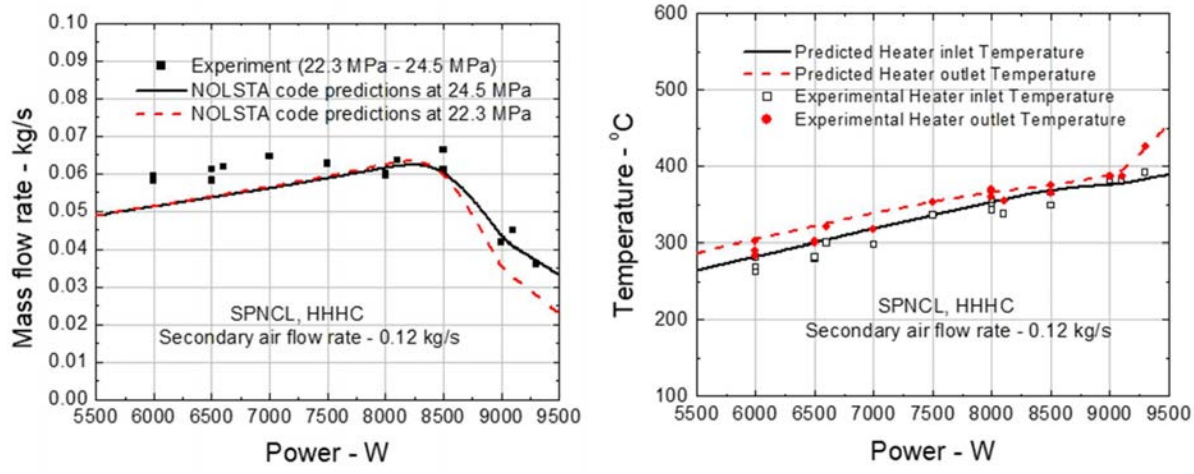

(a) Mass flow rate (b) Heater Inlet and outlet temperature

Fig. 7.4. Measured and predicted steady state performance with supercritical water for HHHC orientation.

For analysis of experimental results, NOLSTA code steady state solution procedure for closed loop boundary conditions has been used [7.45]. For steady state calculations, Bringer–Smith correlation [7.44] is used for calculating primary side heat transfer coefficient of cooler, as was concluded in [7.45], whereas no heat transfer correlation is used in heater test section (i.e. the heat flux is directly imposed on flowing fluid). The predicted mass flow rate does not change much with pressure at subcritical temperatures as thermophysical properties (especially density and viscosity) do not change much with pressure at subcritical temperatures. However, near pseudocritical temperatures, the thermo physical properties change dramatically with pressure (as shown in Fig. 7.5b & Fig. 7.5c) resulting in large variation of steady state mass flow rate with pressure (Fig. 7.4a).

The experimental steady state mass flow rates for VHHC and VHVC orientation with constant secondary side air flow rate are shown in Fig. 7.6 & Fig. 7.7 respectively. Similar to HHHC orientation, the steady state mass flow rate increases till the heater inlet temperature reaches pseudocritical temperature and beyond the pseudocritical temperature the mass flow rate starts reducing. The experimental data have been compared with NOLSTA code predictions which again shows a large variation in mass flow rate with pressure near pseudocritical temperature conditions, however at subcritical conditions the variation is much less. The highest mass flow rate is observed for HHHC orientation (Fig. 7.4a) due to the largest buoyancy head available owing to maximum elevation difference between heater and cooler. VHVC orientation has the minimum elevation difference between heater and cooler thereby exhibiting lowest flow rates (Fig. 7.7). The intermediate flow rates are observed for VHHC orientation (Fig. 7.6). The predicted mass flow rates for all orientations show a maximum deviation of $\pm$ 30 % from experimental values.

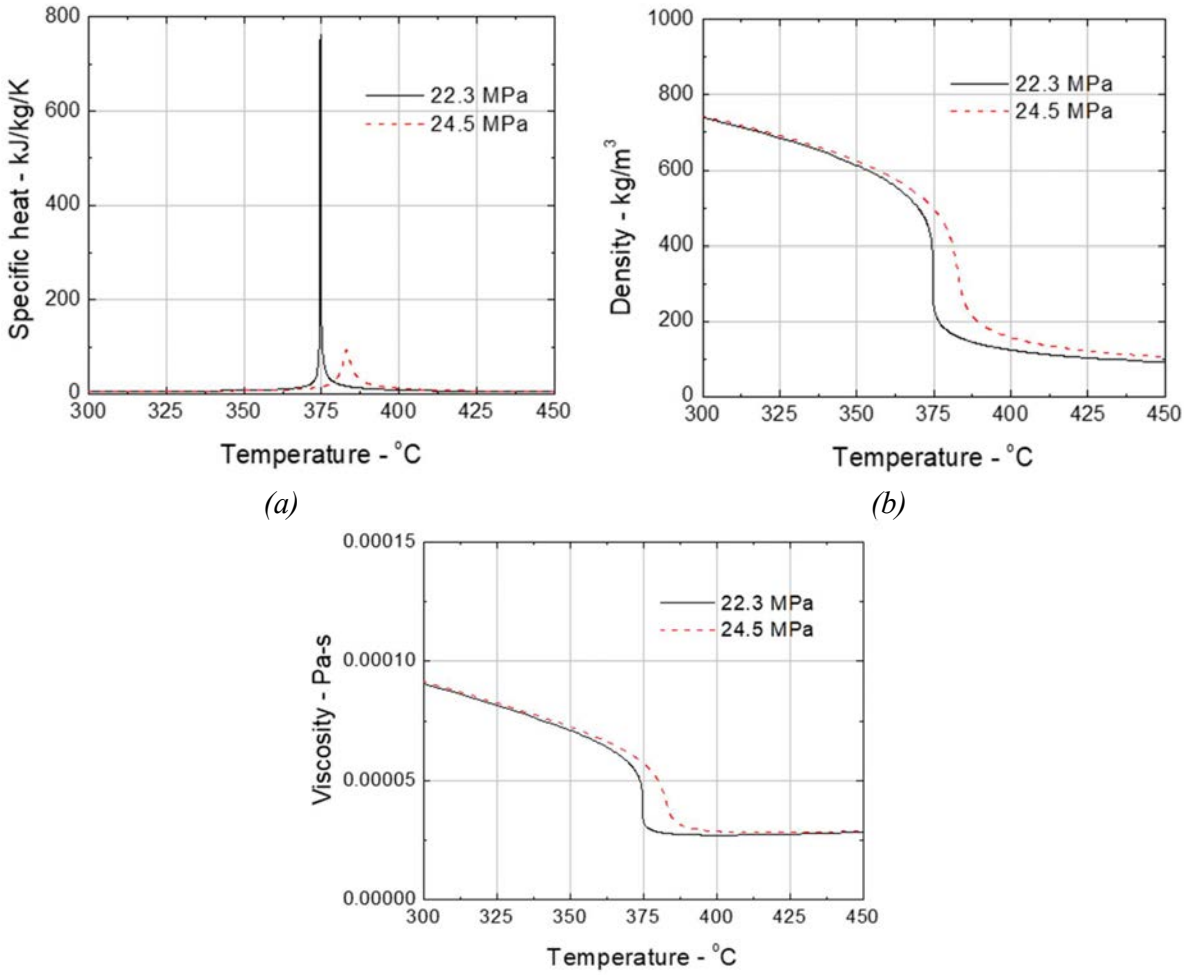

Fig. 7.5. Variation of thermo physical properties of supercritical water with temperature and pressure.

Reference [7.21] found that if dimensionless density (ρ^*) is plotted as a function of dimensionless enthalpy (h*) for various supercritical fluids, then they collapse into a unique curve. Swapnalee et al. [7.49] has proposed a generalized correlation to estimate the steady state flow in supercritical natural circulation loops based on a relationship between dimensionless density and dimensionless enthalpy. They estimated the relationship between ρ^* and h* by three straight lines which divides the curve in to three regions i.e. subcritical, pseudocritical and supercritical. The steady state Reynolds number can be simply expressed in terms of modified Grashof number as:

$$Re_{ss} = C\left[\frac{Gr_m}{N_G}\right]^{0.364} Re_{SS} = C\left(\frac{Gr_m}{N_G}\right)^{0.36} \tag{7.2}$$

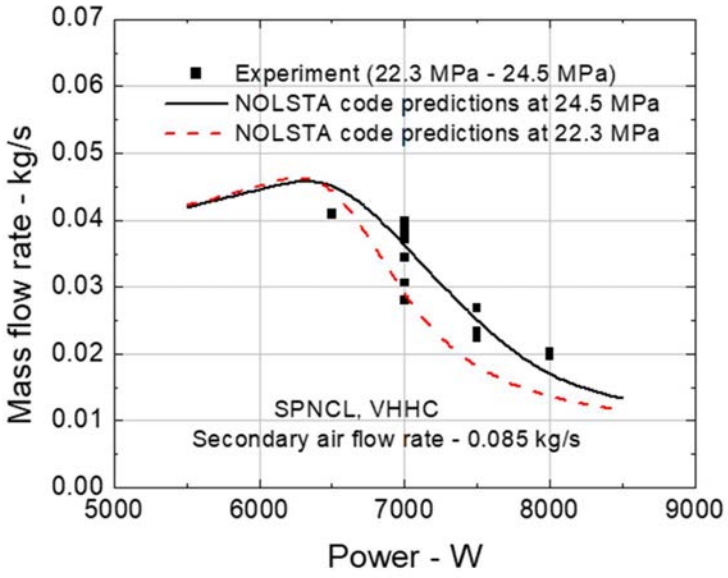

Fig. 7.6. Measured and predicted steady state mass flow rate with supercritical water for VHHC orientation.

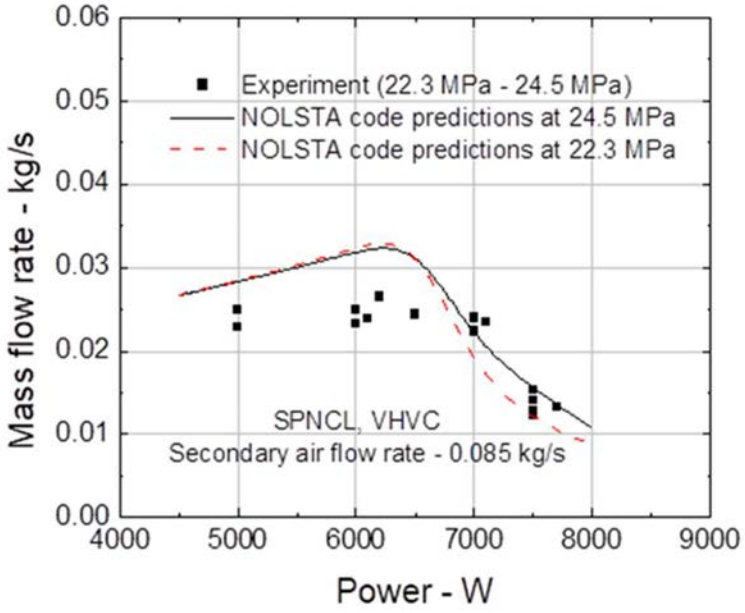

Fig. 7.7. Measured and predicted steady state mass flow rate with supercritical water for VHVC orientation.

The experimental data for supercritical water (HHHC, VHHC & VHVC orientations) has been compared with Swapnalee's correlation [7.49] as shown in Fig. 7.8.

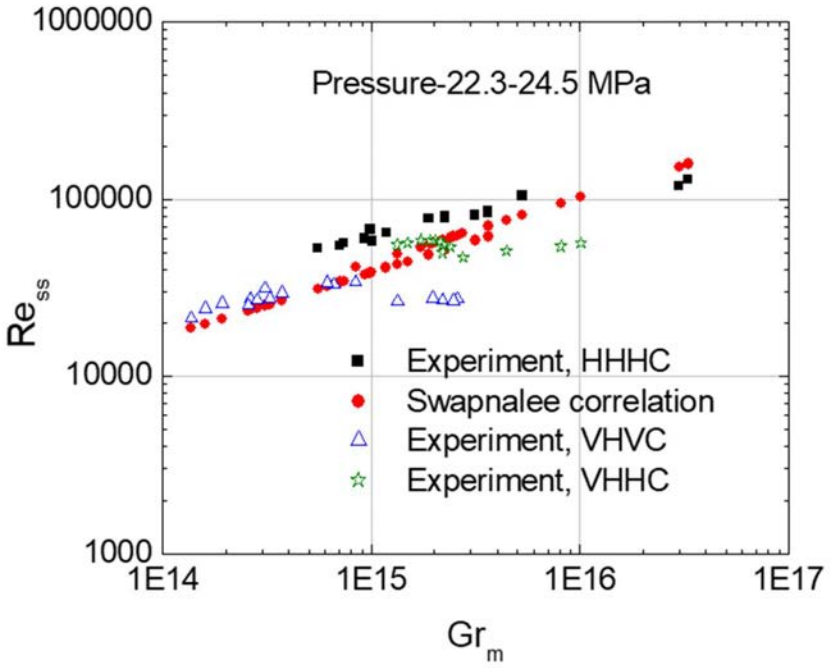

Fig. 7.8. Comparison of experimental data with Swapnalee's correlation [7.49].

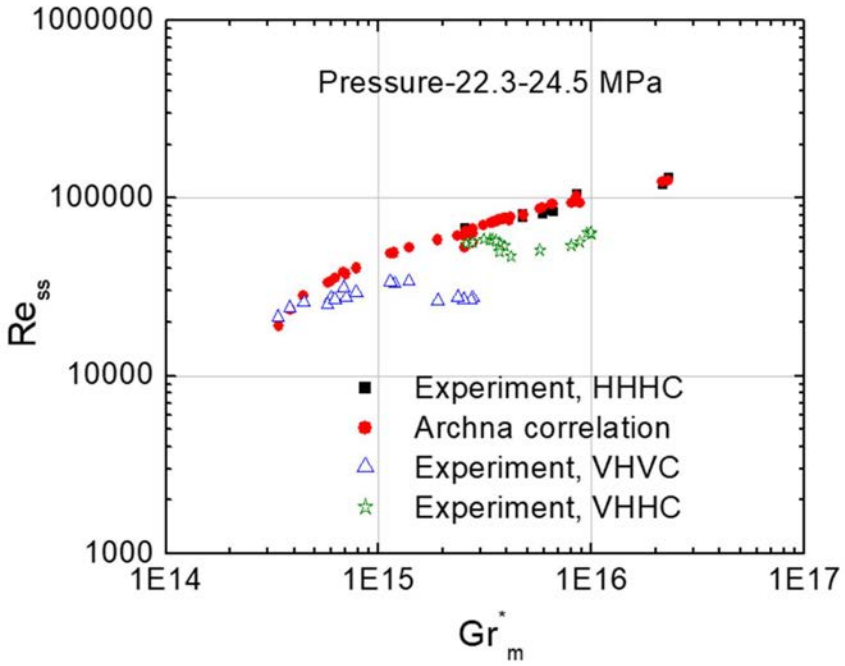

Fig. 7.9. Comparison of experimental data with Archana's correlation.

Archana [7.50] also derived a generalized correlation to estimate the steady state flow in supercritical natural circulation loops based on a single polynomial curve fit between

dimensionless density and dimensionless enthalpy. The steady state Reynolds number can be calculated by Eq. (7.2) with a different definition of modified Grashof number (Gr_m^*). The experimental data for supercritical water (HHHC, VHHC & VHVC orientations) has been compared with Archana's correlation as shown in Fig. 7.9.

The experimental data is deviating from generalized correlations for VHVC and VHHC orientations at higher values of modified Grashof number ($Gr_{m,}/ Gr^*_m$).

7.2.4. STEADY STATE HEAT TRANSFER

The outside heater surface temperature is estimated as avaerage of four thermocouple readings at each of the locations (shown in Fig. 7.3). The measured value of outside surface temperatures (T3 through T54) of heater are used to estimate the inner wall temperature of the heater as per following conduction equation.

$$T_{wi} = T_{wo} - \frac{q'''}{2k}\left[r_o^2 \, ln\frac{r_o}{r_i} + \frac{r_i^2 - r_o^2}{2}\right] \tag{7.3}$$

The fluid temperatures at heater inlet (T_{in}) and outlet (T_{out}) are estimated as average of two thermocouples provided at each of these locations. The fluid enthalpies at these locations are read from the property table and these enthalpies are used to interpolate the enthalpy values at the locations along the heater length corresponding to the temperature measuremnet locations as per following equation.

$$h_b = h_{in} + \frac{x(h_{out} - h_{in})}{L} \tag{7.4}$$

Bulk fluid temperature at different axial locations of the heater section are again read from the property tables corresponding to the enthlapies calculated above. With the help of available values of local bulk fluid and wall temperatures, the heat transfer coefficient (htc) is calculated as per equation given below:

$$htc = \frac{q'''\,(r_o^2 - r_i^2)}{2r_i(T_{wi} - T_b)} \tag{7.5}$$

Volumetric heat generation is estimated as the ratio of the total experimental power and heater section volume and is assumed to be uniform across the heater wall. Variation of HTC with bulk fluid temperature along the heater length is shown in the Fig. 7.10a, Fig. 7.10b and Fig. 7.10c for different operational regimes. It may be observed that at a single operating power in SPNCL, the temperature range covering all regions (i.e. subcritical to supercritical) is not available and thus, there is no significant variation in the fluid properties from heater inlet to heater outlet. It is due to this that the HTC values do not vary significantly with the hesater length.

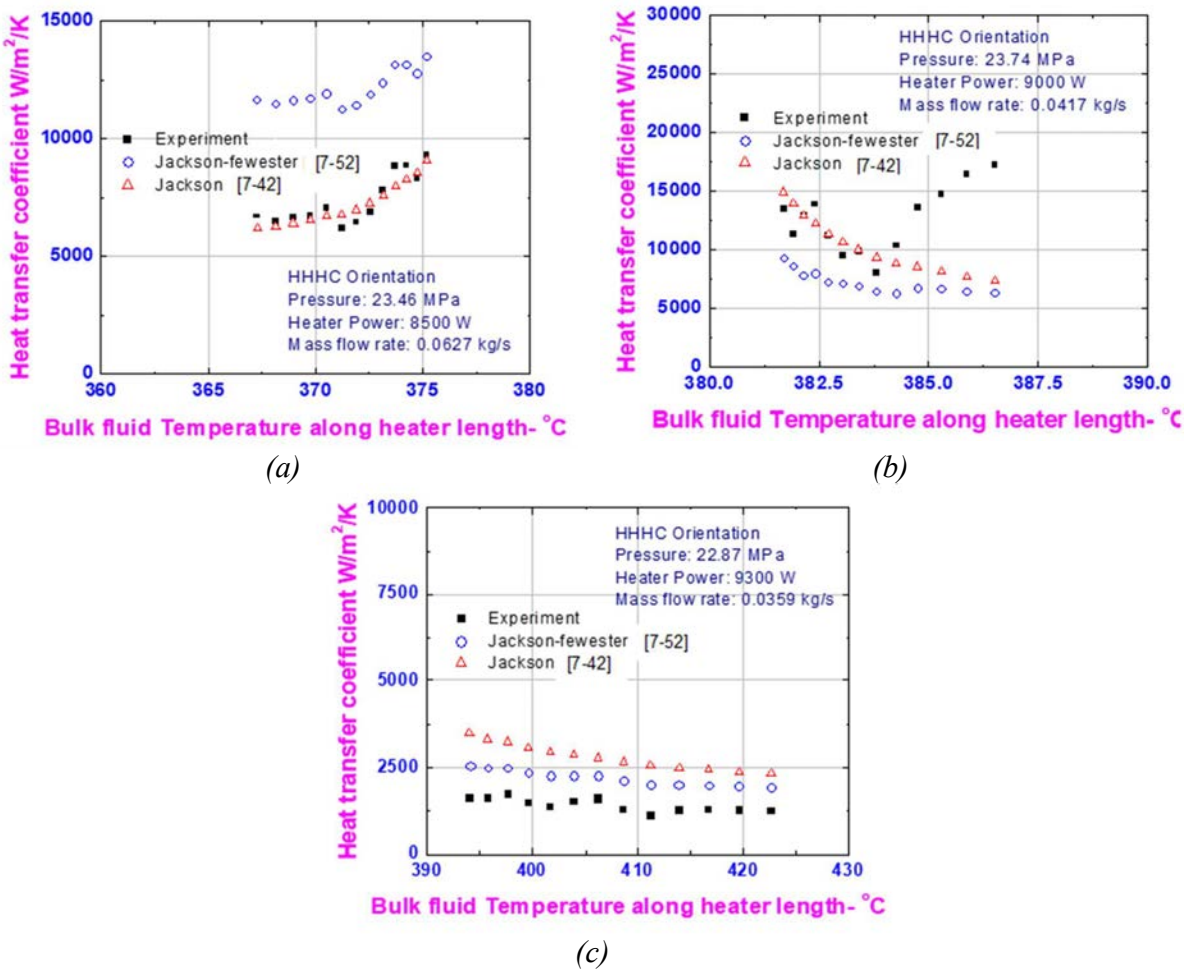

Fig. 7.10. Variation of local experimental heat transfer coefficients along heater length for HHHC orientation.

No deterioration in heat transfer has been observed for the current range of operation of SPNCL for all the orientations as the heat flux encountered is very low i.e. 81–436 kW/m^2. Hence, it is worthwhile to plot the average heat transfer coefficient versus the average bulk fluid temperature across the heater section corresponding to various operating powers. The measured average heat transfer coefficients for HHHC orientation were compared with various heat transfer correlations (see Appendix IV) available in literature for supercritical fluids (see Fig. 7.11). The predictions by the heat transfer correlations are at the same values of pressures as in the tests. The peak heat transfer coefficient is observed near the pseudocritical temperature. Jackson [7.42] and McAdams [7.51] correlations are in good agreement with experimental data.

The measured average heat transfer coefficients for VHHC and VHVC orientation were compared with various heat transfer correlations available in literature for supercritical fluids as shown in Fig. 7.12 and Fig. 7.13 respectively. Again, the peak heat transfer coefficient is observed near the pseudocritical temperature. For vertical heater orientation, Jackson [7.42] correlation is in good agreement with experimental data. The highest heat transfer coefficients are observed for HHHC

orientation due to highest mass flow rates observed and lowest heat transfer coefficients are observed for VHVC orientation due to minimum mass flow rates observed. VHHC exhibits intermediate heat transfer coefficients owing to intermediate mass flow rates. The predicted heat transfer coefficients using Jackson [7.42] correlation show a maximum deviation of $\pm$ 30 % from experimental values for all the orientations.

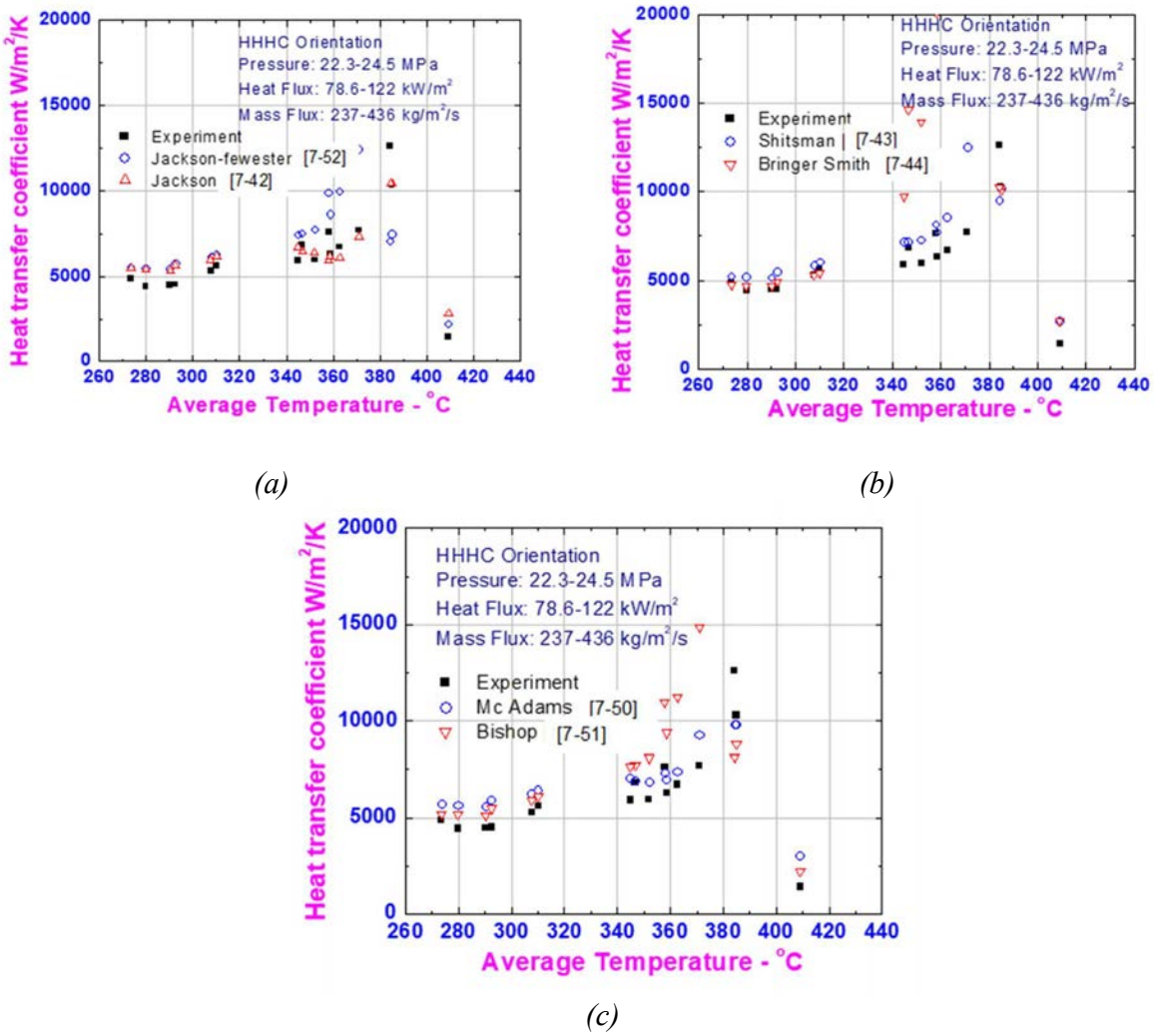

Fig. 7.11. Comparison of experimental heat transfer coefficient data with various correlations for HHHC orientation.

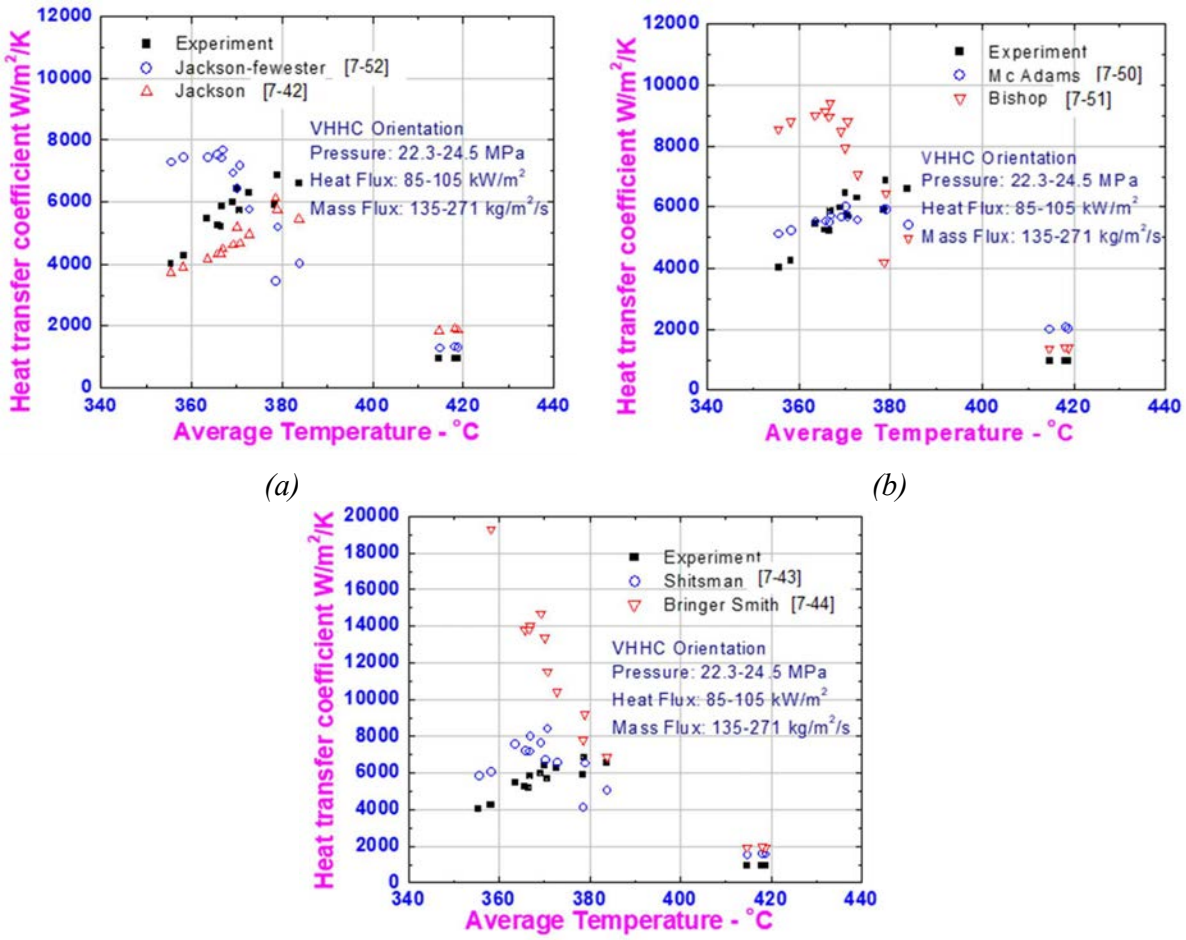

Fig. 7.12. Comparison of experimental heat transfer coefficient data with various correlations for VHHC orientation.

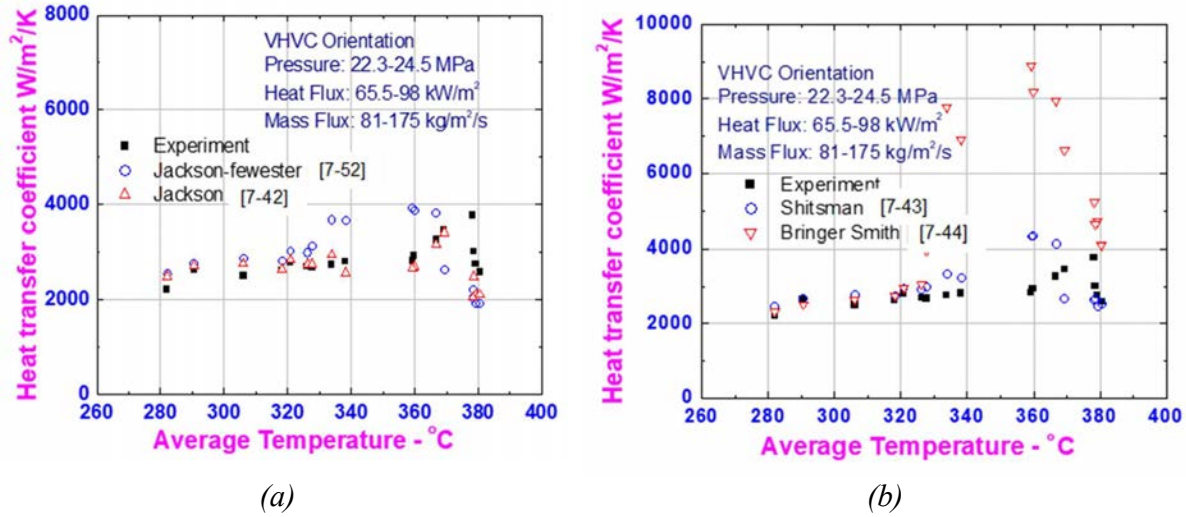

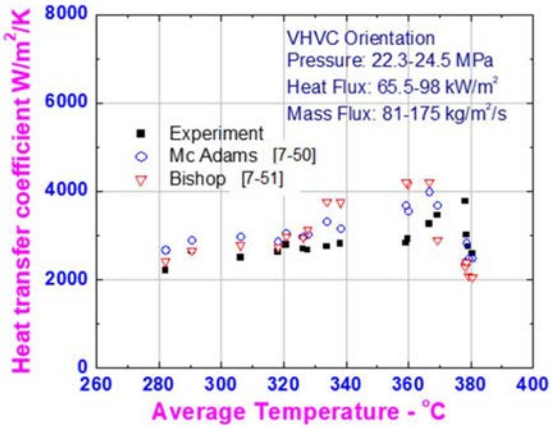

(c)

Fig. 7.13. Comparison of experimental heat transfer coefficient data with various correlations for VHVC orientation.

7.2.5. EXPERIMENTAL PROCEDURE FOR SC–CO_2

Before the loop operation with SC-CO_2, the loop is firstly filled, vented and flushed repeatedly with CO_2 through the main loop, drain and impulse lines. Then the loop is filled and pressurized with the CO_2 at the maximum possible pressure (5.5 MPa) using pressurized CO_2 cylinder. The CO_2 in the gaseous form in the loop is then liquefied by cooling the loop using chilled water in both the coolers. This results in fall in the loop pressure thus again CO_2 is injected from cylinder. The process is repeated several times till no further fall in the loop pressure is observed. In order to bring CO_2 pressure at the desired operating value above its critical point value, cover gas i.e. Helium is inserted in the pressurizer from the top. As Helium is much lighter than CO_2, both are expected to get mixed and thus a level shall be formed in the pressurizer. Helium cylinder is isolated after pressurizing the loop at desired value. Experiment was started by switching ON the heater power and the power was raised further to the next step after allowing the loop to achieve steady state at each of the power level. Pressure was maintained using feed and bleed technique.

7.2.6. STEADY STATE EXPERIMENTS WITH SUPERCRITICAL CO_2

The steady state experiments were carried out for vertical heater orientation i.e. (VHHC and VHVC orientation) with heater power varying from 0.4–8.8 kW and horizontal heater orientation i.e. (HHHC and HHVC orientation) with heater power varying from 0.5 to 9.8 kW. Two type of experiments were carried out

- Increasing power with controlled pressure at 12.0 $\pm$ 0.2 MPa;
- Increasing power with uncontrolled pressure at with initial pressure at 8.0 MPa or 12.0 MPa.

The experimental steady state mass flow rate and heat transfer coefficients for SC–CO_2 was obtained in the similar way as was obtained for the SC–water as explained earlier.

It may be observed that at a single operating power in SPNCL, the temperature range covering all regions (i.e. subcritical to supercritical) is not available and thus, there is no significant variation in the fluid properties from heater inlet to heater outlet. It is due to this that the HTC values do not vary significantly with the hater length. Due to low range of operating heat flux (6–160 kW/m^2) heat transfer deterioration was also not observed. Thus, average values of bulk fluid temperature at each power level are utilized to plot the variation of heat transfer coefficient. Experimentally obtained values of heat transfer coeffcients are compared with various correlations for SC fluids as lisetd in Appendix IV.

7.2.7. ANALYSIS OF STEADY STATE FLOW AND HEAT TRANSFER CHARACTERISTICS OF SPNCL

The experimental steady state mass flow rate, heater inlet and outlet temperatures versus power for VHHC orientation at controlled pressure of 12.0 MPa with constant secondary side chilled water flow rate are shown in Fig. 7.14(a) and Fig. 7.14(b) respectively. The temperature difference between heater inlet and outlet is reducing as we are approaching the pseudocritical temperature (54°C at 12.0 MPa) because as one approaches the pseudocritical temperature the specific heat (c_p) of fluid increases and is maximum at pseudocritical temperature but as the fluid temperature is increased beyond pseudocritical point the c_p value again starts reducing (see Fig. 7.15) resulting in increased temperature difference. The steady state mass flow rate increases till the heater outlet temperature reaches pseudocritical temperature at 3000 W. As the power is increased beyond 3500 W, both hot and cold leg becomes supercritical and there is a reduction in experimental flow due to increased frictional resistance.

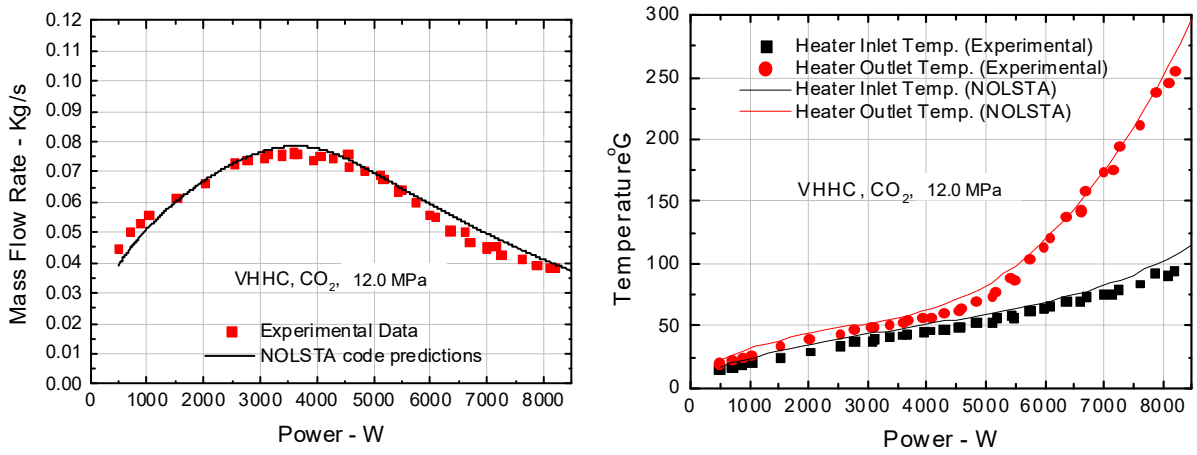

(a) Mass flow rate *(b) Heater inlet and outlet temperatures*

Fig. 7.14. Measured and predicted steady state performance with supercritical carbon dioxide for VHHC orientation.

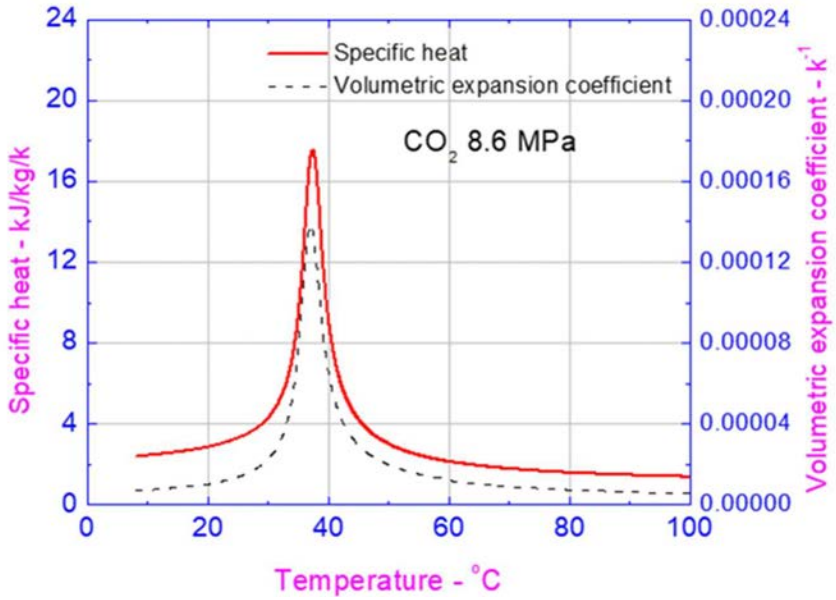

Fig. 7.15. Variation of specific heat of CO_2 with temperature at 8.6 MPa pressure.

For analysis of experimental results, the NOLSTA code steady state solution procedure for closed loop boundary conditions has been used [7.45]. For steady state calculations, Swenson correlation [7.36] is used for calculating primary side heat transfer coefficient of cooler, whereas no heat transfer correlation is used in heater test section (i.e. the heat flux is directly imposed on flowing fluid). The code is predicting the experimental mass flow rates very closely.

The heat transfer characteristics for the VHHC orientation at controlled pressure of 12.0 MPa are shown in Fig. 7.16(a), Fig. 7.16(b) and Fig. 7.16(c). The heat transfer coefficient keeps increasing with average bulk fluid temperature and reaches a maximum near the pseudocritical temperature i.e. approx. 2000 $W/m^2/K$ at 50 ^OC. Pseudocritical temperature is the temperature at which specific heat (c_p) of a supercritical fluid reaches a maximum value at a given pressure (i.e., 54°C is the pseudocritical temperature for SC–CO_2 at 12.0 MPa). With further increase of average bulk fluid temperature of loop above the pseudocritical temperature the specific heat of fluid reduces which is also accompanied with reduction of natural circulation flow resulting in fast reduction of heat transfer coefficient. The experimental heat transfer coefficients are compared with predicted values using various correlations available from literature. Jackson [7.42] and Swenson [7.36] correlations are most close to experimental data. Both correlations are exhibiting peak near the pseudocritical temperature, however, the magnitude is slightly over predicted. However, prediction of heat transfer coefficients by Swenson correlation [7.36] are very accurate beyond the pseudocritical temperature.

A similar characteristic for mass flow rate (Fig. 7.17(*a*) & Fig. 7.17(b)) and heat transfer (Fig. 7.18 (*a*), (*b*) & (*c*)) middle is obtained at uncontrolled pressure experiment with starting pressure of 12.0 MPa. As power is increased the loop average temperature increases resulting in pressure rise due to thermal expansion of supercritical fluid with maximum pressure of 13.1 MPa achieved at 8.8 kW. However, the properties do not change significantly with pressure rise from 12.0 to 13.1 MPa resulting in almost same steady state characteristics.

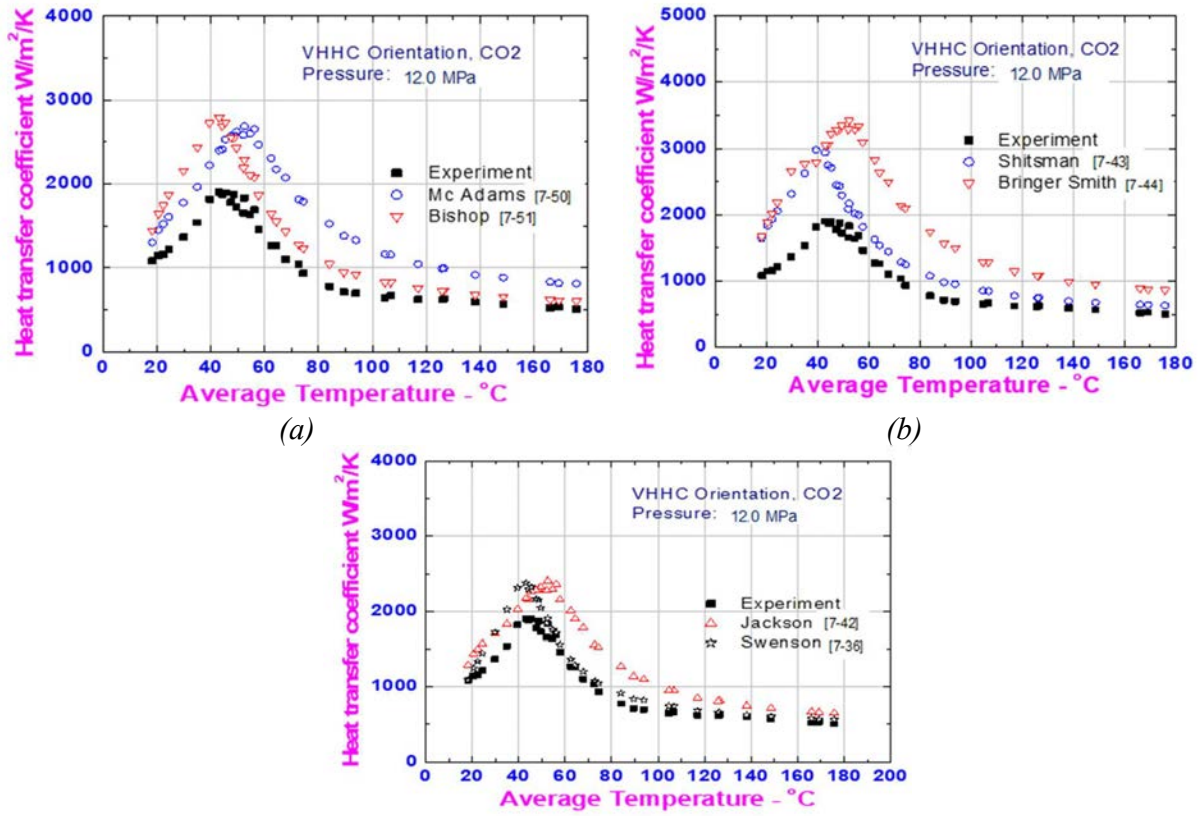

Fig. 7.16. Comparison of experimental heat transfer coefficient data with various correlations for VHHC orientation at controlled pressure of 12.0 MPa.

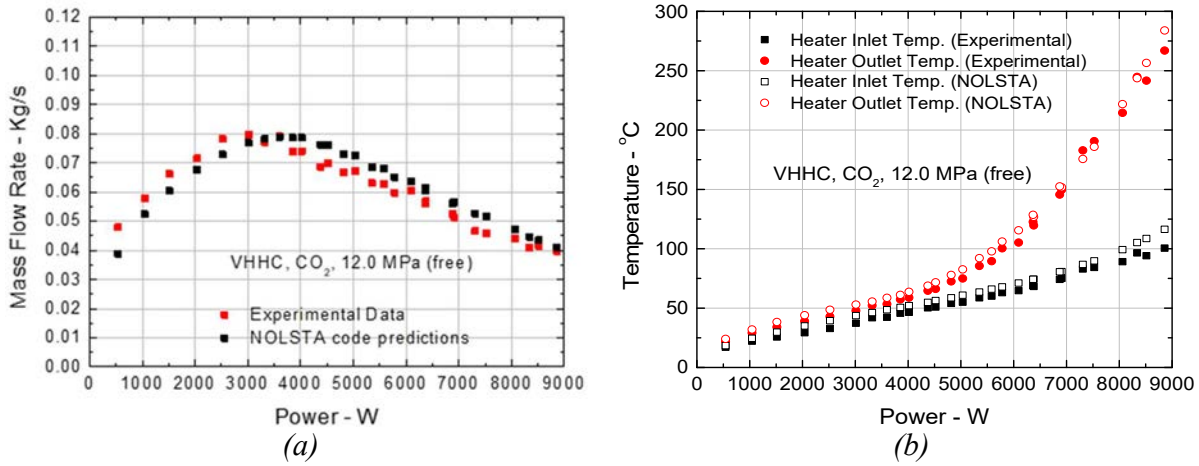

Fig. 7.17. Steady state characteristics of SPNCL for VHHC orientation at uncontrolled pressure with initial pressure of 12.0 MPa.

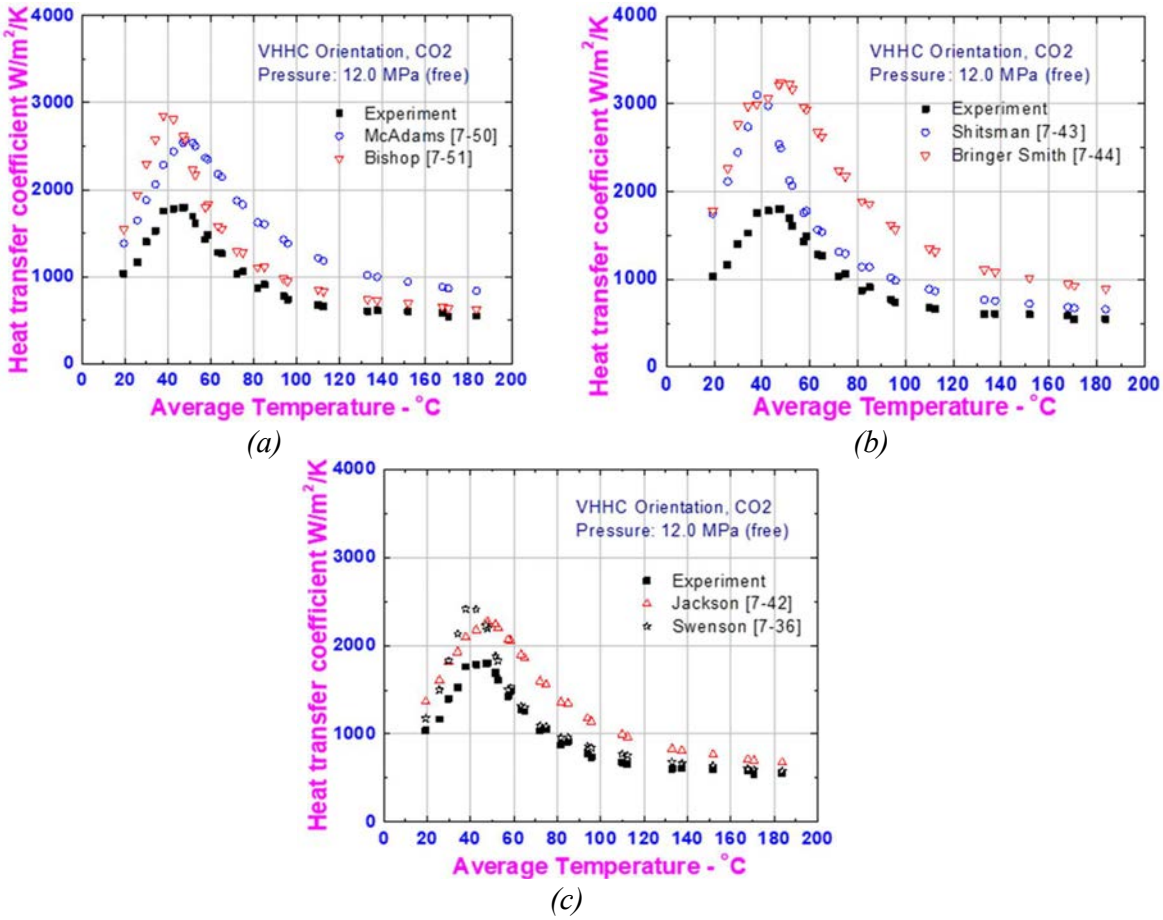

Fig. 7.18. Comparison of experimental heat transfer coefficient data with various correlations for VHHC orientation at uncontrolled pressure with initial pressure of 12.0 MPa.

The steady state mass flow and heater inlet/outlet temperature characteristics for uncontrolled pressure experiment with starting pressure of 8.0 MPa are shown in Fig. 7.19(a) and Fig. 7.19(b) respectively. The mass flow rate first increases with power due to increase in buoyancy force and, beyond the pseudocritical temperature of 37 ºC at 8.5 MPa obtained at 3.5 kW, the mass flow rate starts reducing due to increased frictional resistance. However, the reduction in flow rate is sharper as compared to smoother reduction of flow at controlled/ uncontrolled pressure experiments at 12.0 MPa. The sharper reduction of flow is also associated with steeper rise in heater outlet temperature reaching 250 ºC at 7.25 kW for uncontrolled 8.0 MPa experiment; however, the same heater outlet temperature is achieved at 8.5 kW for uncontrolled 12.0 MPa experiment. The sharp reduction of flow is due to larger decrease of density across the pseudocritical temperature at lower pressures causing higher frictional resistance. NOLSTA code predicts the mass flow rates and heater inlet/outlet appreciably well. The peak heat transfer coefficient for uncontrolled 8.0 MPa experiment is higher 3000 W/m^2/K and the same is obtained at lower average bulk fluid temperature of 35 ºC (Fig. 7.20). The higher value of peak heat transfer coefficient is due to higher value of specific heat corresponding to pseudocritical temperature at lower pressures. However, the pseudocritical temperature value reduces with reduction of pressure due to which peak heat

transfer coefficient is obtained at lower bulk fluid temperatures lower uncontrolled pressure experiment i.e. 8.0 MPa.

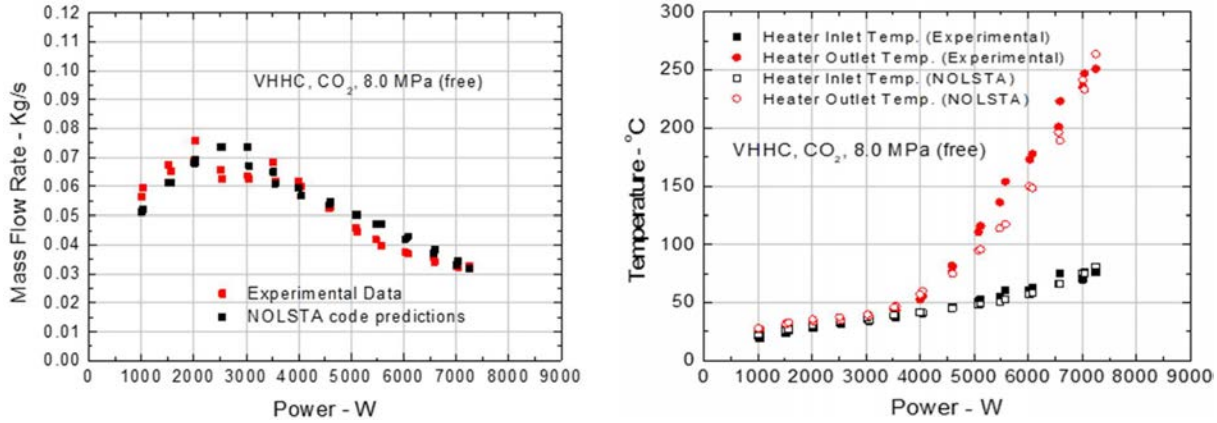

Fig. 7.19. Steady state characteristics of SPNCL for VHHC orientation at uncontrolled pressure with initial pressure of 8.0 MPa.

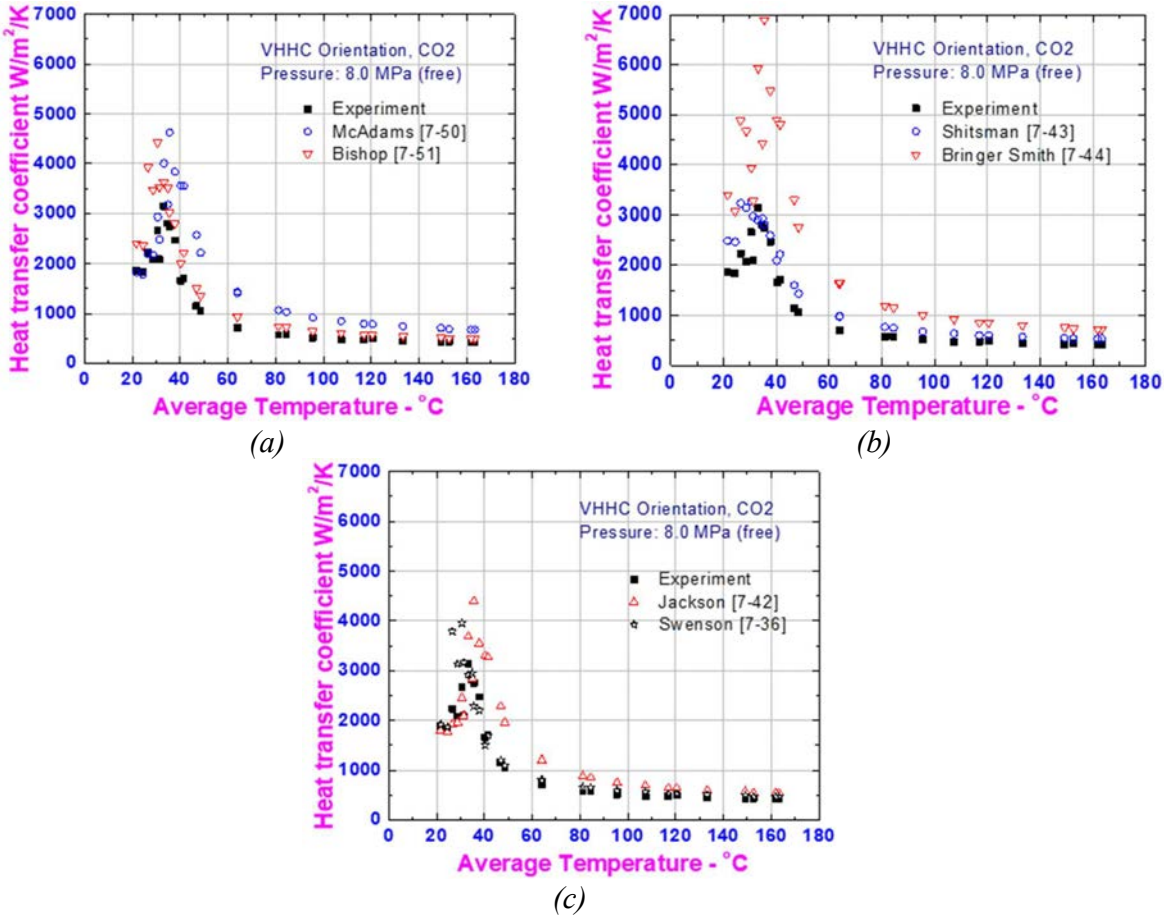

Fig. 7.20. Comparison of experimental heat transfer coefficient data with various correlations for VHHC orientation at uncontrolled pressure with initial pressure of 8.0 MPa.

The steady state heat transfer characteristics for VHVC orientation at controlled pressure experiments at 12.0 MPa are shown in Fig. 7.21(a) and Fig. 7.21(b). The flow first increases and then reduces smoothly beyond pseudocritical temperature. However, the peak mass flow rate (0.05 kg/s) is lower than for VHHC orientation (0.08 kg/s) due to lower buoyancy head available due to lower elevation difference between centre line of heater and cooler for VHVC orientation. The corresponding heat transfer results show peak heat transfer coefficient of 1500 W/m^2.K at average bulk fluid temperature of 50 ^{o}C (Fig. 7.22(a), Fig. 7.22(b) & Fig. 7.22(c)). Due to lower flow rate the peak value of heat transfer coefficient is also less in VHVC orientation as compared to that in VHHC orientation.

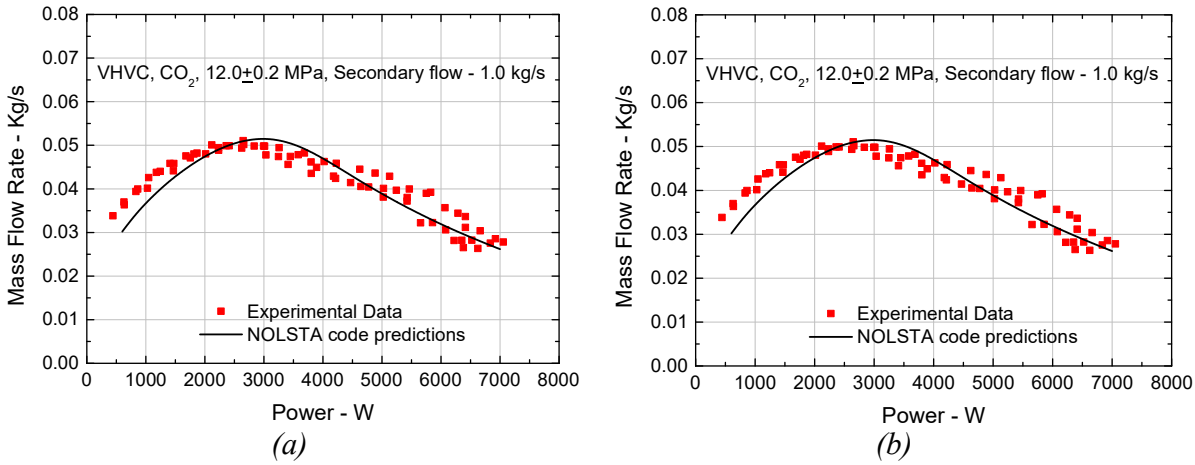

Fig. 7.21. Steady state characteristics of SPNCL for VHVC orientation at controlled pressure of 12.0 MPa.

The uncontrolled pressure experiment with initial pressure of 8.0 MPa again shows sharper reduction in flow rate beyond pseudocritical temperature as shown in Fig. 7.23(*a*) and Fig. 7.23(*b*). NOLSTA code predicts the mass flow rates and heater inlet/outlet appreciably well.

Again peak heat transfer coefficient increases (2000 W/m^2.K) at lower pressure experiment due to increase of peak specific heat at pseudocritical temperature with decrease of pressure and the peak heat transfer coefficient is also obtained at lower average temperature of 35°C (Fig. 7.24(*a*), Fig. 7.24(*b*) and Fig. 7.24(*c*)). Jackson [7.42] and Swenson et al. [7.36] correlations are the closest to experimental data. Both correlations are exhibiting peak near the pseudocritical temperature, however, the magnitude is slightly over predicted. However, prediction of heat transfer coefficients by Swenson et al. [7.36] correlation are very accurate beyond the pseudocritical temperature.

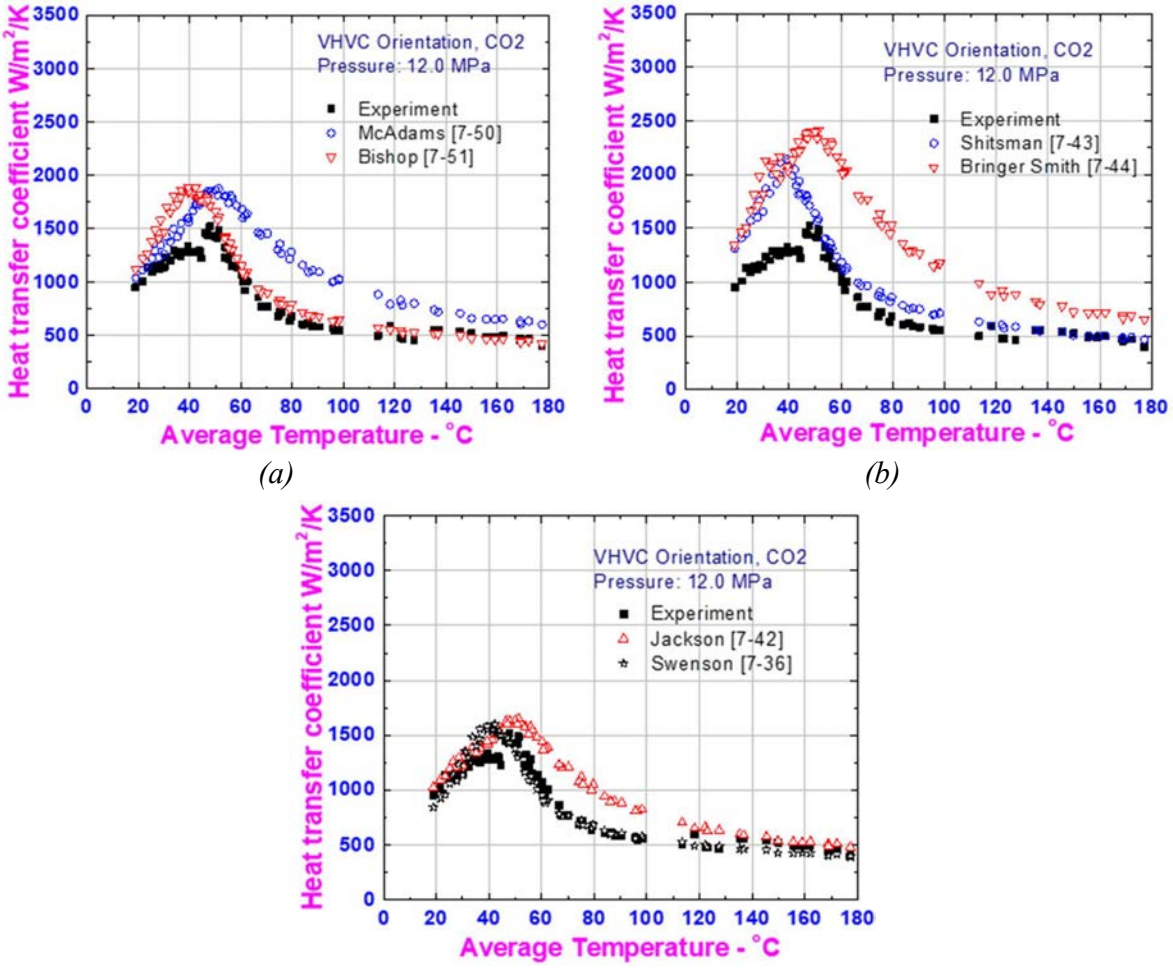

Fig. 7.22. Comparison of experimental heat transfer coefficient data with various correlations for VHVC orientation at controlled pressure of 12.0 MPa.

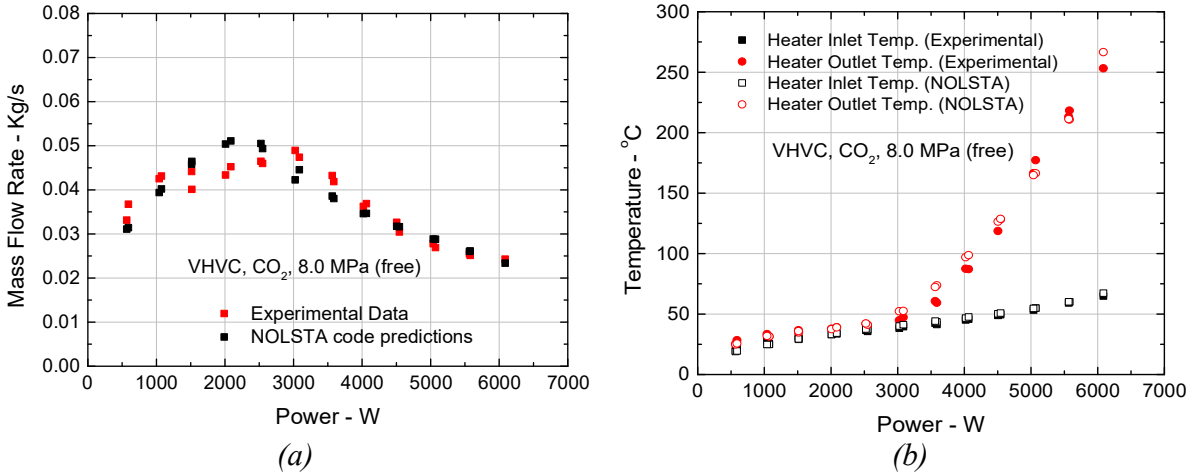

Fig. 7.23. Steady state characteristics of SPNCL for VHVC orientation at uncontrolled pressure with initial pressure of 8.0 MPa.

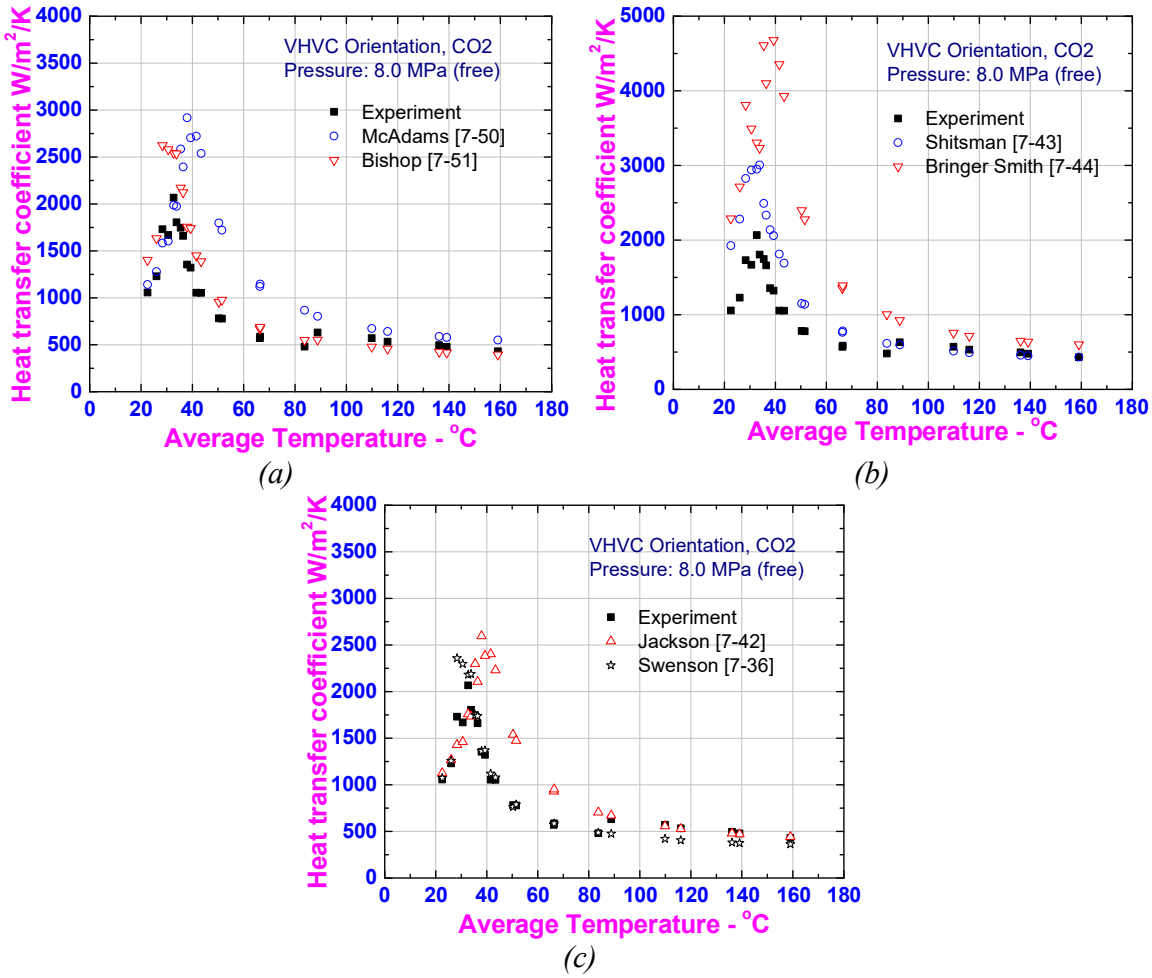

Fig. 7.24. Comparison of experimental heat transfer coefficient data with various correlations for VHVC orientation at uncontrolled pressure with initial pressure of 8.0 MPa.

The steady sate flow and heater inlet/outlet temperature characteristics of HHHC at a controlled pressure of 12.0 MPa are shown in Fig. 7.25(a) and Fig. 7.25(b). The mass flow rate first increases and then reduces smoothly beyond the pseudocritical temperature. The experimental mass flow rates match well with NOLSTA predictions both above and below the pseudocritical temperature. The heater inlet/outlet temperatures are also matching well.

The predicted heat transfer coefficient estimated on the basis of experimental mass flow rates are shown in Fig. 7.26(a), Fig. 7.26(b) and Fig. 7.26(c). The experimental heat transfer coefficient shows a peak of 2800 W/m^2.K at 45 ^{O}C. The peak heat transfer coefficient is the highest among all orientations due to maximum value of flow rates due to maximum elevation difference between heater and cooler. Jackson [7.42] and Swenson et al. [7.36] correlations predict the heat transfer coefficients closer than others.

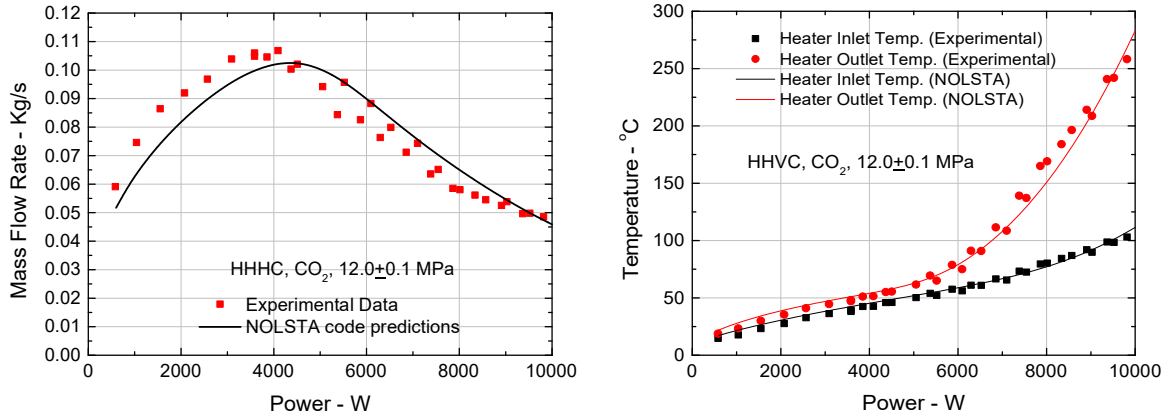

(a) *(b)*

Fig. 7.25. Steady state characteristics of SPNCL for HHHC orientation at controlled pressure of 12.0 MPa

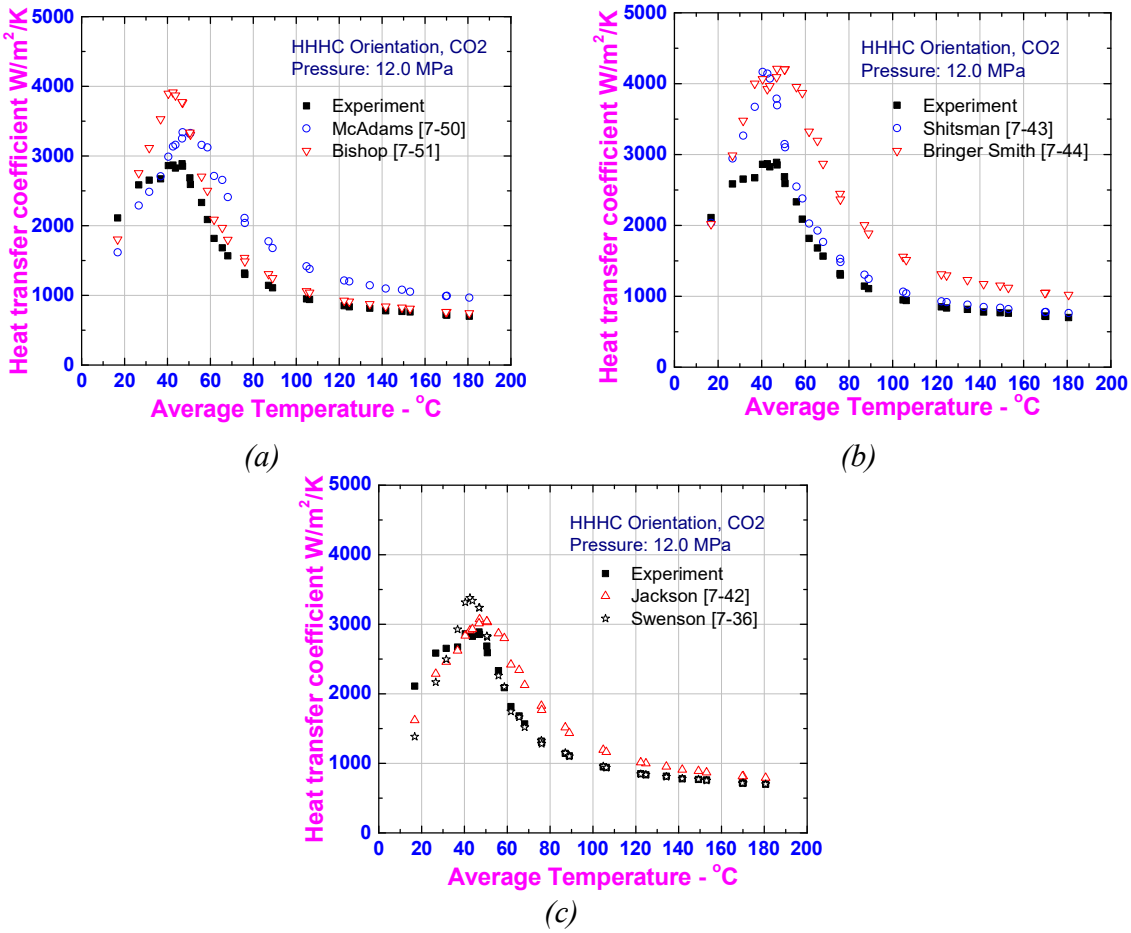

(a) *(b)*

(c)

Fig. 7.26. Comparison of experimental heat transfer coefficient data with various correlations for HHHC orientation at controlled pressure of 12.0 MPa.

7.2.8. ASSESSMENT OF HEAT TRANSFER CORRELATIONS

Assessment of the 53 HTC correlations against the experimental data has been carried out. The experimental data considered in the assessment work is generated in the SPNCL, BARC with SC–CO_2 for both, horizontal and vertical, orientations of heater. The data have been presented earlier in this section and do not include degraded heat transfer. The correlations considered in the present work include both, legacy as well as new correlations. Both types of correlations were developed during 1930–2016. Correlations considered here are a mix of those developed for different fluids, heater orientation, pressures, mass fluxes and heat fluxes. The Dittus–Boelter correlation [7.52] is also assessed since it has been considered as a reference for single phase heat transfer. Description about these correlations is given in Appendix IV. For one set of steady state data at a given power, there are a maximum of 12 surface temperature readings depending on the availability of working thermocouples during a particular steady state. Thus, there will be 12 experimental HTC values available locally and a same number of HTC values available for each correlation. In the present study there are 44 steady state data available for horizontal orientation of heater whereas for vertical heater orientation, 163 steady state data are available. The following procedure has been adapted for the assessment of correlations:

- Evaluation of experimental HTC from the available data at each (say, *y*) of the 12 thermocouple locations for a given steady state (say, *x*) i.e. power level;
- Evaluation of HTC using each of the correlations for the same experimental conditions at each of the 12 locations;
- Evaluation of the average of 12 values of HTCs for steady state data — experimental and those using correlations, as given by Eq. 7.6 and 7.7 respectively;

$$HTC_{Exp_x} = \frac{\sum_{y=1}^{J} HTC_{Exp_{xy}}}{J} \tag{7.6}$$

$$HTC_{Corr_x} = \frac{\sum_{y=1}^{J} HTC_{Corr_{xy}}}{J} \tag{7.7}$$

- Evaluation of relative percentage error for a steady state between average value of experimental HTC and those using each of the correlations, as per Eq. 7.8:

$$E_{P_x} = \frac{\left(HTC_{Corr_x} - HTC_{Exp_x}\right)}{HTC_{Exp_x}} \times 100\% \tag{7.8}$$

After performing calculations at each of the steady state as per procedure given above, different statistical parameters are evaluated as defined in following equations:

Mean relative error

$$E_{P_m} = \frac{\sum_{x=1}^{N} E_{P_x}}{N} \tag{7.9}$$

Mean absolute relative error,

$$E_{P_{m-abs}} = \frac{\sum_{x=1}^{N} \left| E_{P_x} \right|}{N} \tag{7.10}$$

RMS relative error,

$$E_{P,rms} = \sqrt{\frac{\sum_{x=1}^{N} (E_{P_x})^2}{N}} \tag{7.11}$$

Standard deviation of errors,

$$SD_{E_{Corr}} = \sqrt{\frac{\sum_{x=1}^{N} (E_{P_m} - E_{P_x})^2}{N-1}} \tag{7.12}$$

Extensive assessment is carried out as per procedure outlined above. All the properties used in the correlations are taken from NIST database [7.53]. Linear interpolation has been carried out for evaluating value of properties which are directly not available in tabular form. Thermal conductivity of the Inconel-625 (loop pipe material) is taken as 19.0 W/m-K.

Results for assessment of different correlations are given in Appendix IV for horizontal flow and vertical flow cases. Detailed inferences can be drawn from the tables as values of the statistical parameters defined in the previous section are given in these tables.

For horizontal flow, it can be noted from mean relative errors that 23 correlations underpredict the experimental heat transfer coefficients, whereas remaining correlations overpredict the experimental HTC. Maximum and minimum underpredictions correspond to Zhao et al. [7.54] and Bae & Kim [7.55] respectively. Whereas, Yamagata et al. [7.35] and Swenson [7.36] correlations give the maximum and minimum overpredictions respectively. This might be due to the fact that the correlation was developed for a different fluid, namely supercritical water (SCW).

It can be noted from the mean relative error that Swenson [7.36] and Bae & Kim [7.55] correlations are found to be closest to the experimental data. The earlier one negligibly overpredicts (0.06%) the data whereas the latter slightly underpredicts the data (–1.31%). On the other hand, Zhao et al. [7.54] and Yamagata et al. [7.35] correlational gives maximum underprediction (–29.97%) and overpredictions (217.29%) respectively among the correlations developed for heating conditions. Correlations which have mean relative errors in the range ±10% are summarized in Table 7.1.

Besides, having mean relative error less than ±10%, Swenson et al. [7.36], Jackson and Fewster [7.67], Jackson and Hall [7.70], Watts and Chou [7.62], Petukhov et al. [7.58], Jackson [7.42] and Yu et al. [7.69] correlations have RMS errors also less than 10%. Also, standard deviation of the errors associated with these correlations at each steady state from mean errors is less than 10%.

Similarly for flow in a vertical heater tube the interpretations can be drawn from Appendix IV. Observing at mean relative error, Preda et al. [7.65] and Krasnoshchekov et al. [7.71] are found to

be closest to the experimental data with error as 0.03 % and −1.48 % respectively. With 502.75 % and −33.40 % errors Yamagata et al. [7.35] and Bae & Kim [7.55] are found to give most deviated predictions. Table 7.2 summarizes the correlations with predictions in the range of ±10 % for flow in vertical tube.

TABLE 7.1. CORRELATIONS WITH PREDICTIONS UNDER ±10% RANGE FOR HORIZONTAL TUBE

Correlations	**Underprediction (%)**	**Correlations**	**Overprediction (%)**
Bae & Kim [7.55]	-1.31	Swenson et al. [7.36]	0.06
Wang and Li [7.56]	-2.17	Ornatsky et al. [7.57]	1.07
Petukhov et al. [7.58]	-3.07	Bae et al. [7.59]	4.04
Liu et al. [7.60]	-5.26	Petukhov et al. [7.61]	4.05
Watts & Chou [7.62]	-5.65	Kim & Kim [7.63]	4.45
Mokry et al. [7.64]	-6.83	Preda et al. [7.65]	4.75
Gupta et al. [7.66]	-7.59	Jackson and Fewster [7.67]	5.20
Razumovskiy et al. [7.68]	-7.72	Yu et al. [7.69]	6.29
		Jackson and Hall [7.70]	6.42
Krasnoshchekov et al. [7.71]	-8.58	Jackson [7.42]	6.42
		Chen and Fang [7.72]	9.40

TABLE 7.2. CORRELATIONS WITH PREDICTIONS UNDER ±10% RANGE FOR VERTICAL TUBE

Correlations	**Underprediction (%)**	**Correlations**	**Overprediction (%)**
Krasnoshchekov et al. [7.71]	-1.48	Preda et al. [7.65]	0.03
Gupta et al. [7.66]	-2.65	Razumovskiy et al. [7.68]	0.16
Mokry et al. [7.64]	-3.03		
Saltanov et al. [7.73]	-3.49	Wang and Li [7.56]	1.56
Gupta et al. [7.74]	-5.57	Watts & Chou [7.62]	3.64
Kim & Kim [7.75]	-5.58	Bae et al. [7.59]	5.07
Liu et al. [7.60]	-6.25	Petukhov et al. [7.58]	5.39
Mokry & Pioro [7.76]	-6.84		
Gupta et al. [7.77] — Based on Bulk Fluid Temp	-8.26	Swenson et al. [7.36]	6.37
Gorban et al. [7.78]	-9.57	Ornatsky et al. [7.57]	7.40

It is to be noted that the best prediction HTC correlations are a mix of both legacy and recent correlations as well. Saltanov et al. [7.73] and Liu et al. [7.60] are the latest correlations considered which predicts the HTCs very close to the experimental values. These correlations were originally developed for SC–CO_2 as the working fluid under heating condition.

From Appendix IV it is also evident that none of the correlation is having RMS error within 10 % range. However, the minimum RMS percentage error for both, horizontal and vertical tube flows, is obtained for Petukhov et al. [7.58] whereas maximum is observed for Yamagata et al. [7.35].

Standard deviation between errors from its mean value is found to be least for Jackson and Fewster [7.67] with 5.83 % for horizontal tube and Chen and Fang [7.72] with 7.18 % for vertical tube. Maximum standard deviation is obtained for Yamagata et al. [7.35] for both horizontal and vertical tubes with values as 226.82 % and 918.25 % respectively.

Swenson et al. [7.36] is found to best suit HTC correlation for the natural circulation experimental data with horizontal tube for SC–CO_2. Even though the correlation is basically developed for SC–H_2O, it still predicts HTC for SC–CO_2 very well. However, for the same reason, Yamagata et al. [7.35] predictions are found to be largely deviated from the experimental data of SC–CO_2.

For vertical upward flow data, Preda et al. [7.65] has been found to be best correlation which has mean relative error practically zero compared to the experimental data. However, it has both, RMS error and standard deviation of errors at around ~24 %. Preda et al. [7.65] was originally developed for the SC–CO_2 based on the multiple databases. As found for horizontal orientation too, Yamagata et al. [7.35] is found to give most erroneous predictions.

7.2.9. NATURAL CIRCULATION EXPERIMENTS AT CHINA INSTITUTE OF ATOMIC ENERGY (CIAE)

7.2.9.1.LOOP DESCRIPTION

The experimental facility is a vertical rectangular loop of with 3.62 m in length and 2.76 m in height [7.79]. The design pressure is 30 MPa and the maximum water outlet temperature exceeds 650 ℃. An annular heat exchanger is at the top side with the hot water flowed in the tube and the cooling water in the annulus. The inner diameter of primary system is 16 mm, including all the junctions and branches, except parallel channels. At the secondary side of the annulus the diameters are 25×20 mm. The schematic of the test loop is shown in Fig. 7.27.

The test section consists of vertical parallel channels with inner diameters of 7.98 mm, outer diameters of 9.6 mm and heated lengths of 1.3 m. The total lengths are 2.1 m. The test section is heated by a DC supply with capacity of 70 V×6750 A. The test section is insulated by silicon fibre, in which an electrical heating wire is wrapped to compensate the heat loss.

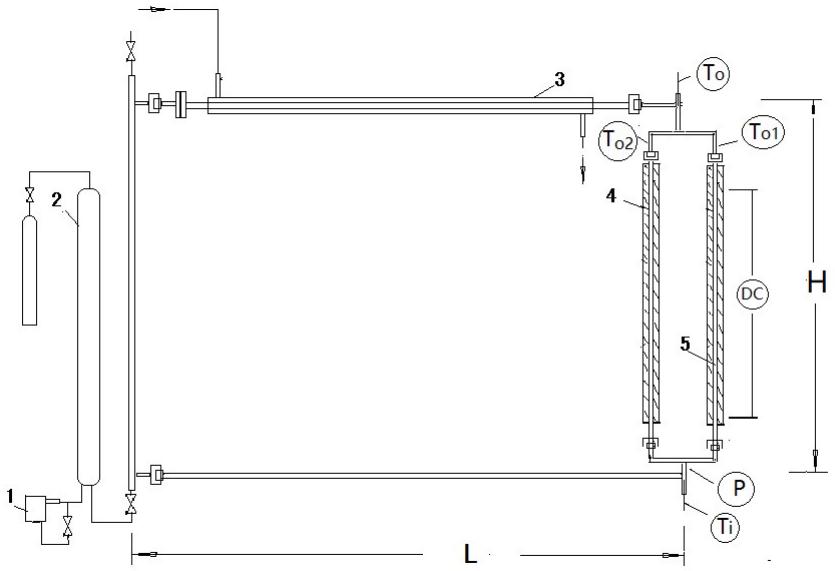

1. piston pump
2. pressurizer
3. heat exchanger
4. thermal insulation
5. heated test section

Fig. 7.27. The Schematic diagram of CIAE natural circulation loop [7.79].

7.2.9.2.MEASUREMENTS

The most important measurement parameters include the inlet and outlet water temperatures and the outer surface temperatures by K type thermocouples, the inlet pressure by a pressure transducer (DCY1151), the current and voltage across the test section [7.79]. The outer surface temperatures at locations of 0.7, 0.9 and 1.1 m from the beginning of heating are measured by sheathed thermocouple. At each location two or three thermocouples are installed.

The flow rate at each channel is determined by the heat balance of test section. At the oscillation condition this method tends to give an average flow rate basically, except for very strong instability.

At the secondary side the inlet and outlet water temperatures are measured by thermocouples and the flow rate by a turbine flowmeter. All these parameters are recorded by a data acquisition system throughout the experiment with frequency of one second.

7.2.9.3.TEST PROCEDURE

During the experiment the primary side pressure and the flow rate at the secondary side of heat exchanger were kep constant. The test started with 0 kW and proceeded with increased power of small step by step. At each step the power was kept constant for enough time to reach a stable condition.

7.2.9.4.EXPERIMENTAL RESULTS

Fig. 7.28 shows the variation of inlet temperature (T_i) and outlet water temperatures (T_{O1} and T_{O2}) of heated tube with heat flux. Initially, the water temperature increases gradually with increasing

heat flux. When the heat flux reaches 1.12 MW/m^2 the outlet water temperature jumps from about 325 ℃ to 360 ℃, and the dynamic instability occurs. When the heat flux exceeds 1.38 MW/m^2, in one channel the outlet water temperature increases to nearly the pseudocritical point, while in another one it decreases. They exhibit a strong oscillation, accompanying with a sound. When the heat flux exceeds about 1.6 MW/m^2 the outlet water temperatures of two channels reach to the pseudocritical point.

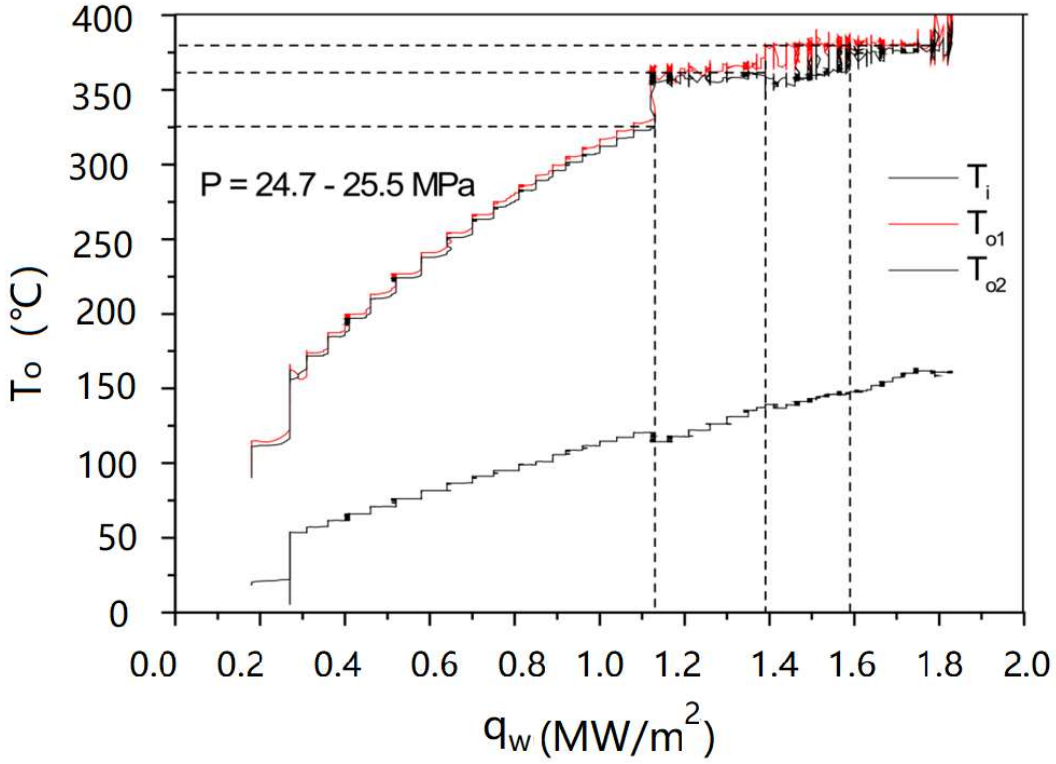

Fig. 7.28. Variations of the inlet and outlet water temperature with heat flux [7.79].

The variation of flow flux with heat flux is shown in Fig. 7.29. For lower heat flux the mass flux increases as heat flux increasing. At heat flux of 1.12 MW/m^2 the mass flux jumps from 750 to 625 kg/(m^2·s). The sharp decrease in mass flux is caused by the increase in flow resistance by the branches and elbows as the water temperature exceeds 300 ℃.Then it increases faster with heat flux increasing further. For heat fluxes greater than 1.38 MW/m^2 the flow rate increases in one channel and decreases in another one. At heat fluxes of about 1.6 MW/m^2 and the outlet water temperatures of pseudocritical point the flow rates in both channels reach to nearly the same value.

The inner wall temperatures (T_{Wi}) in two channels exhibit the same behaviour. The results for the location Z=0.9 m and location Z=1.1 m at different channels are shown in Fig. 7.30(*a*) and Fig. 7.30(*b*), respectively.

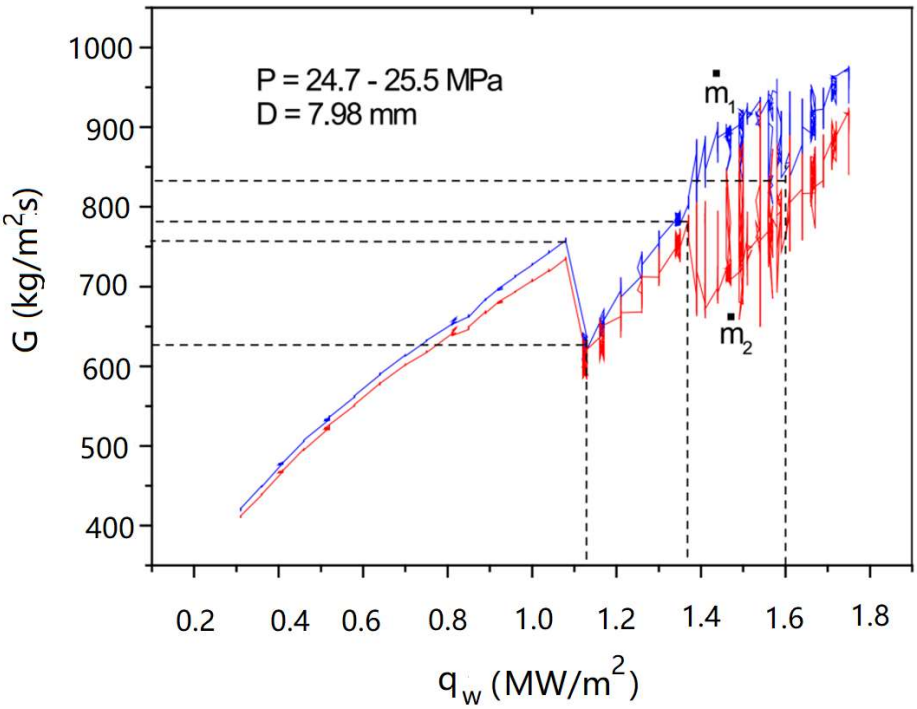

Fig. 7.29. Variations of the mass flux with heat flux in parallel channels [7.79].

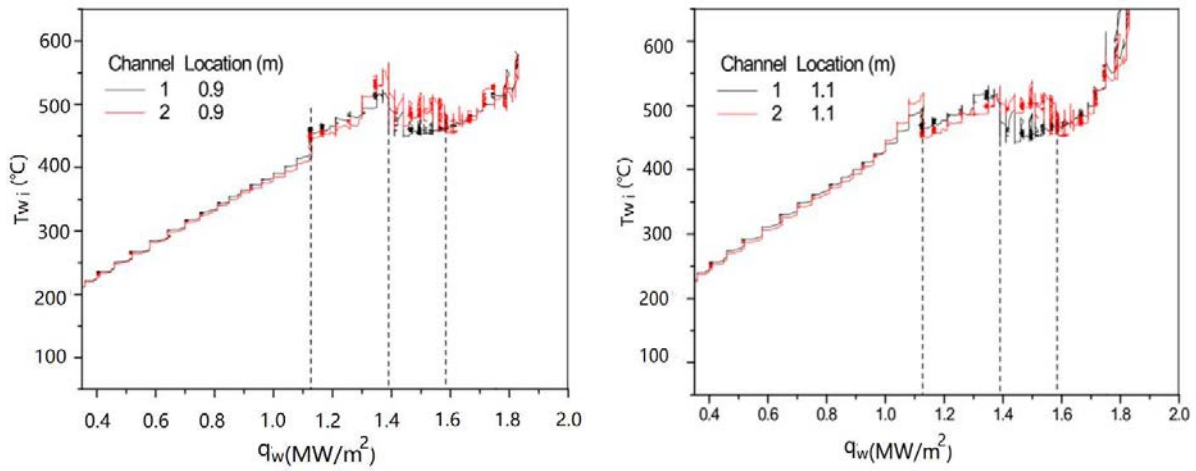

(a) (b)

Fig. 7.30. Variations of wall temperature with heat flux in two channels [7.79].

In Channel 1, the variation of inner wall temperature, which is calculated with heat conduction equation, at different heat fluxes is shown in Fig. 7.31(a) and the corresponding variation of heat transfer coefficient is shown in Fig. 7.31(b). The wall temperature increases from locations of 0.7, 0.9 and 1.1 m, and the heat transfer coefficients increase with increasing heat flux. At heat fluxes of about 0.9 MW/m^2, the inner wall temperature at 1.1 m reaches the pseudocritical point, then it increases rapidly to about 500 °C, associated with a decrease in heat transfer coefficient. This is

apparently caused by the gas-like film created on the surface. For heat fluxes higher than 1.12 MW/m^2 the heat transfer coefficient increases, indicating the transition of gas film from laminar to turbulent state. After heat flux exceeding 1.38 MW/m^2 the heat transfer coefficient increases substantially. Until heat fluxes of about 1.6 MW/m^2 the outlet water temperatures in both channels reach the pseudocritical point.

A natural circulation experiment of supercritical water is performed with parallel heated channels to study the flow and heat transfer behaviour. At present conditions the following conclusions are achieved.

At parallel heated channels, when the outlet water temperature increases to 325 °C, a dynamic instability occurs, and the heat transfer coefficient increases noticeably. When the outlet water temperature reaches to around 360 °C, the flow exhibits a strong dynamic instability with an accompanying sound. As power increases further, in one channel the flow rate increases and in another one it decreases. When the outlet water temperature reaches the pseudocritical point the flow rate reaches nearly the same value in the two parallel pipes.

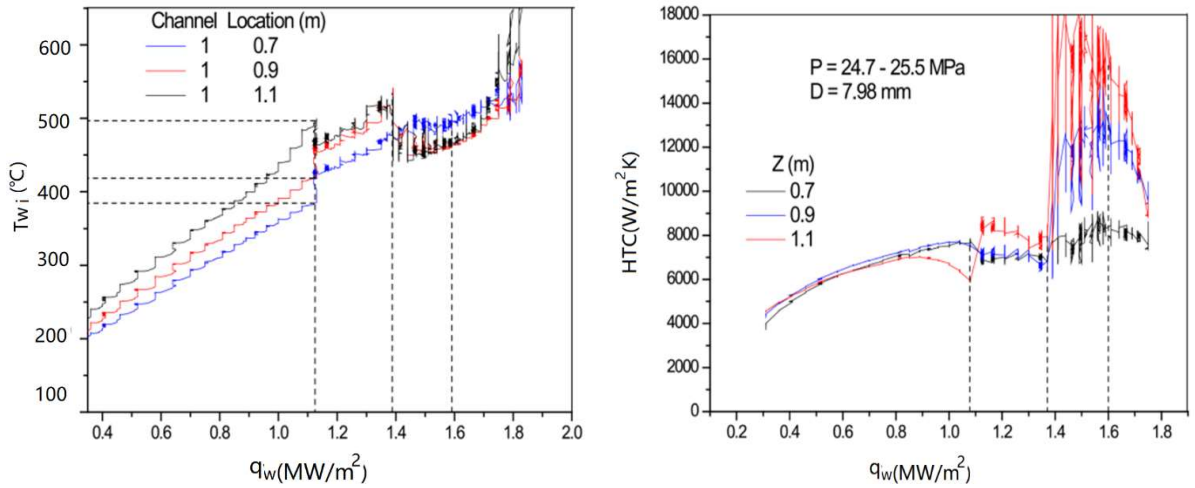

Fig. 7.31. Variations of the inner wall temperature and heat transfer coefficient with heat fluxes for different locations for channel 1 [7.79].

7.2.10. NATURAL CIRCULATION TESTS AT UNIVERSITY OF MANITOBA

[7.80] performed natural circulation experiments with carbon dioxide flow through a horizontal channel at supercritical pressures. A schematic diagram of the test facility is shown in Fig. 7.32. The heated channel was constructed with a 2.6 m long Inconel 625 tube of 12.95 mm in inner diameter and 3.05 mm in wall thickness. Electro–Pneumatic valves were installed at inlet and outlet of the test section for adjusting hydraulic resistance. Power was applied to the heated section through joule heating at about 15 kW. Measurements from these experiments included system pressure, pressure drops, mass flow rate, secondary side coolant flow rate, channel inlet and outlet fluid temperatures, heat exchanger inlet and outlet coolant temperature, test section wall temperatures, voltage drop across test section, voltage drop across shunt resistor located at the

back part of rectifier and electric current. These measurements covered ranges of pressure from 7.6–8.6 MPa, inlet fluid temperature from 18 to 26°C, and local loss coefficient of the outlet valve from 0 to 30. Twelve (K type) thermocouples were spot welded at equal intervals on the top and bottom surfaces of the heated section to measure surface temperatures.

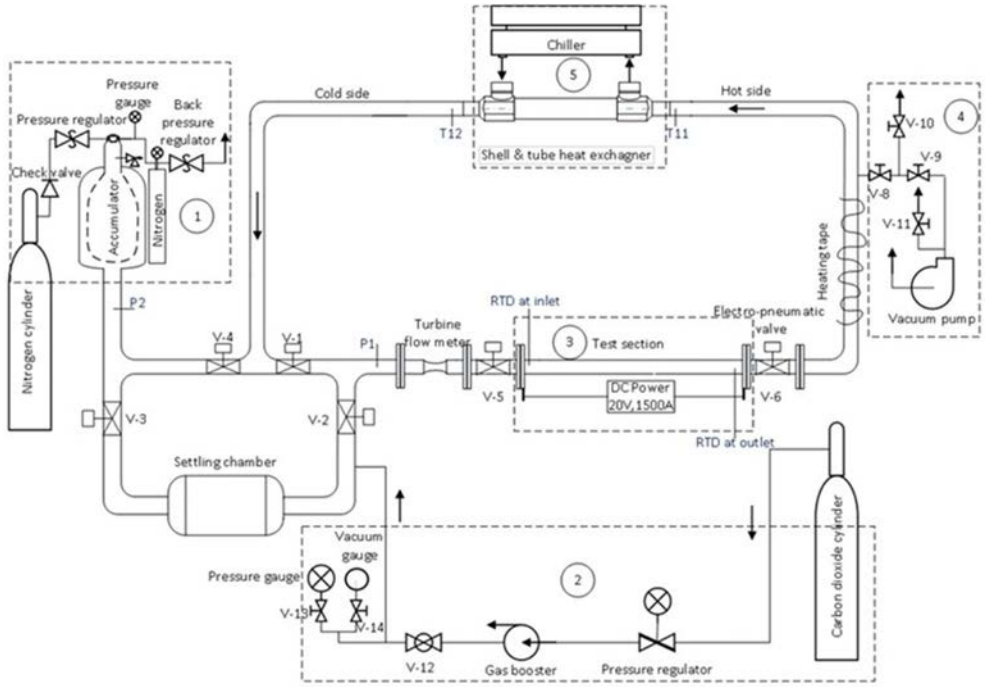

Fig. 7.32. Schematic diagram of natural circulation loop with carbon dioxide flow through horizontal channels.

A flow–power map is illustrated in Fig. 7.33. The mass flow rate increases with increasing power reaching a peak at around 7 kW. Reference [7.80] attributed that to the increase in buoyancy force from the density difference. Beyond the peak, the mass flow rate decreases with increasing power due to increase in frictional forces. It appears that the peak coincides closely with the pseudocritical point of the fluid at the outlet. The solid red symbol indicates the instability boundary poInt. [7.80] noted that flow oscillation occurs at powers beyond the peak (or temperature beyond the pseudocritical point) for all their cases.

Reference [7.80] examined parametric effects on instability boundary points. They observed a shift in the peak of the mass flow rate to high powers with increasing system pressure. This was attributed to the increase in pseudocritical temperature. While the effect of inlet fluid temperature is small, a reduction in inlet fluid temperature has also led to a shift in the peak of the mass flow rate to high powers. This was attributed to the increase in density difference between hot and cold legs. The outlet hydraulics resistance has a strong impact on the stability of the system. A reduction in the hydraulic resistance (or loss coefficient) at the outlet has led to increase in mass flow rate and a shift in the peak of the mass flux rate to high powers.

A flow–power map is illustrated in Fig. 7.33. The mass flow rate increases with increasing power reaching a peak at around 7 kW. Reference [7.80] attributed that to the increase in buoyancy force from the density difference. Beyond the peak, the mass flow rate decreases with increasing power due to increase in frictional forces. It appears that the peak coincides closely with the pseudocritical point of the fluid at the outlet. The solid red symbol signifies the instability boundary point. [7.80] noted that flow oscillation occurs at powers beyond the peak (or temperature beyond the pseudocritical point) for all their cases.

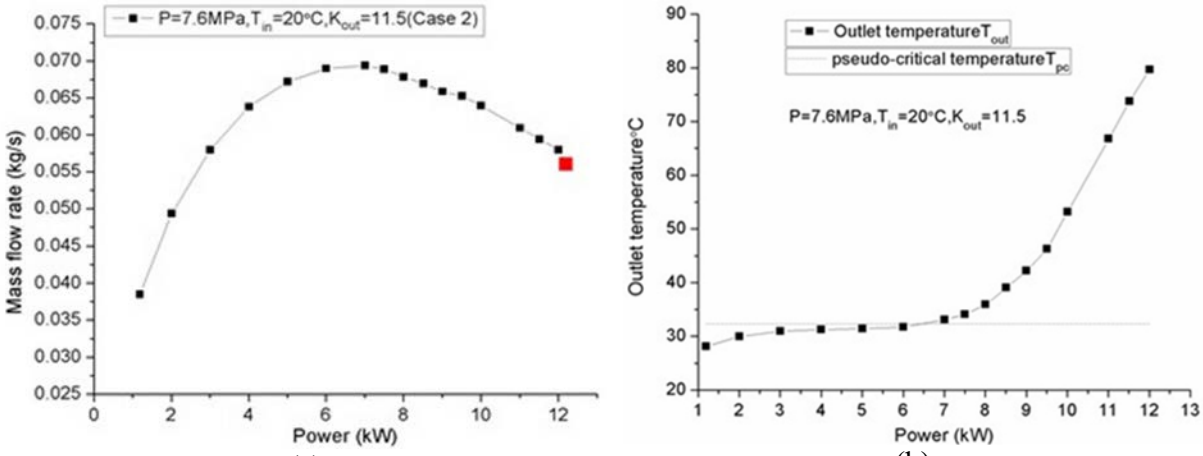

(a) (b)

Fig. 7.33. Variations of mass flow rate and outlet temperature with power.

Reference [7.80] examined parametric effects on instability boundary points. They observed a shift in the peak of the mass flow rate to high powers with increasing system pressure. This was attributed to the increase in pseudocritical temperature. While the effect of inlet fluid temperature is small, a reduction in inlet fluid temperature has also led to a shift in the peak of the mass flow rate to high powers. This was attributed to the increase in density difference between hot and cold legs. The outlet hydraulics resistance has a strong impact on the stability of the system. A reduction in the hydraulic resistance (or loss coefficient) at the outlet has led to increase in mass flow rate and a shift in the peak of the mass flux rate to high powers.

The flow instability behaviours are illustrated in Fig. 7.34 for Case 8 with the pressure at 8 MPa, inlet fluid temperature at 18°C and outlet loss coefficient at 18.8. The mass flow rate decreases slightly with increasing power. It started to oscillate when the power was increased from 11 to 11.5 kW. Both the system pressure and outlet fluid temperature also become unstable. The boundary mass flow rate was established at 0.0509 kg/s with the heating power at 11.31 kW.

Reference [7.80] noticed a strong effect of the accumulator on the system stability. Fig. 7.35 illustrates two cases where the accumulator was valved in and out of the system. The system is more stable with the accumulator valved out than in. [7.80] attributed that to the compressibility of the fluid and the interaction between the accumulator and the hot leg of the loop.

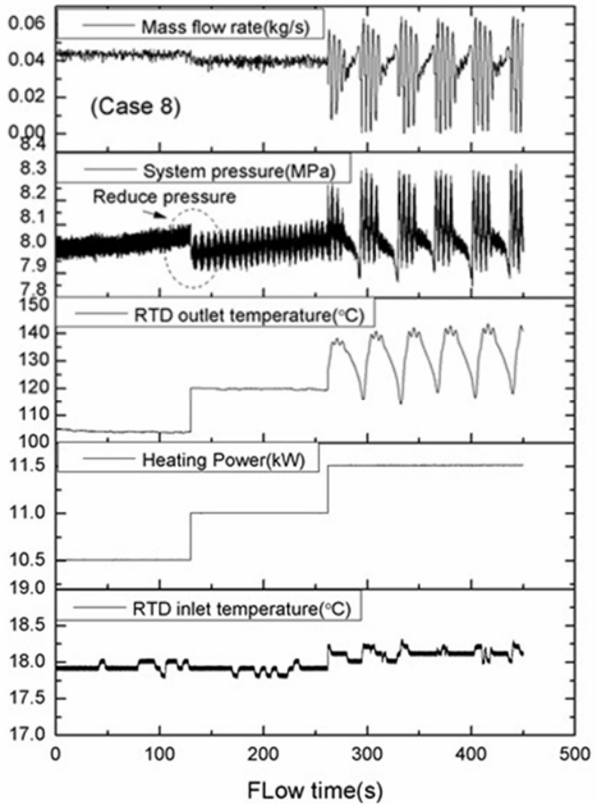

Fig. 7.34. Illustrations of flow instability behaviours.

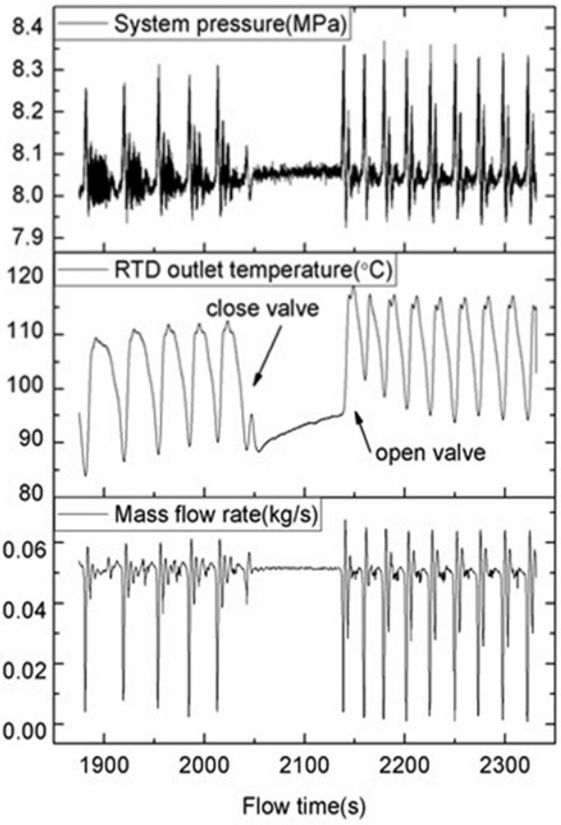

Fig. 7.35. Impact of accumulator on system stability.

7.2.11. EXPERIMENTAL STUDY ON NATURAL CIRCULATION AT BUDAPEST UNIVERSITY OF TECHNOLOGY & ECONOMICS (BME), HUNGARY

The objective of the ANCARA loop was to investigate heat transfer and pressure drop in supercritical water under natural circulation condition in a closed pipe system by conventional measurement tools (absolute and differential pressure transducers, thermocouples, mass flow mater) and to visualize the flow by neutron radiography (not fully reached goal) [7.81], [7.82], [7.83], [7.84], [7.85].

7.2.11.1. DESCRIPTION OF THE ANCARA LOOP

The investigated loop is essentially a multiply bent closed tube with many different measurement equipment mounted on an aluminium alloy frame (Fig. 7.36).

The tube was made of stainless steel with the inner (ID) and outer diameter (OD) of 5 mm and 8 mm, respectively. The loop has been designed to represent the current European SCWR concept, the High Performance Light Water Reactor (HPLWR). That is the reason why the ID of the loop equals to the average equivalent diameter of the four different type subchannels of the HPLWR fuel assembly [7.84], [7.85].

The loop consists of more tube parts with a total length of 5.2 m, but the heated length is 0.948 m long (Fig. 7.37). Each tube part has been welded to the neighbouring one or connected with a Swagelok type tube connector. The total volume of the closed loop is 102.1 cm^3 at room temperature. The maximal change of this volume due to thermal expansion is negligible (less than 0.5% of the total volume) in case of the considered highest total heating power (5 kW) [7.84], [7.85].

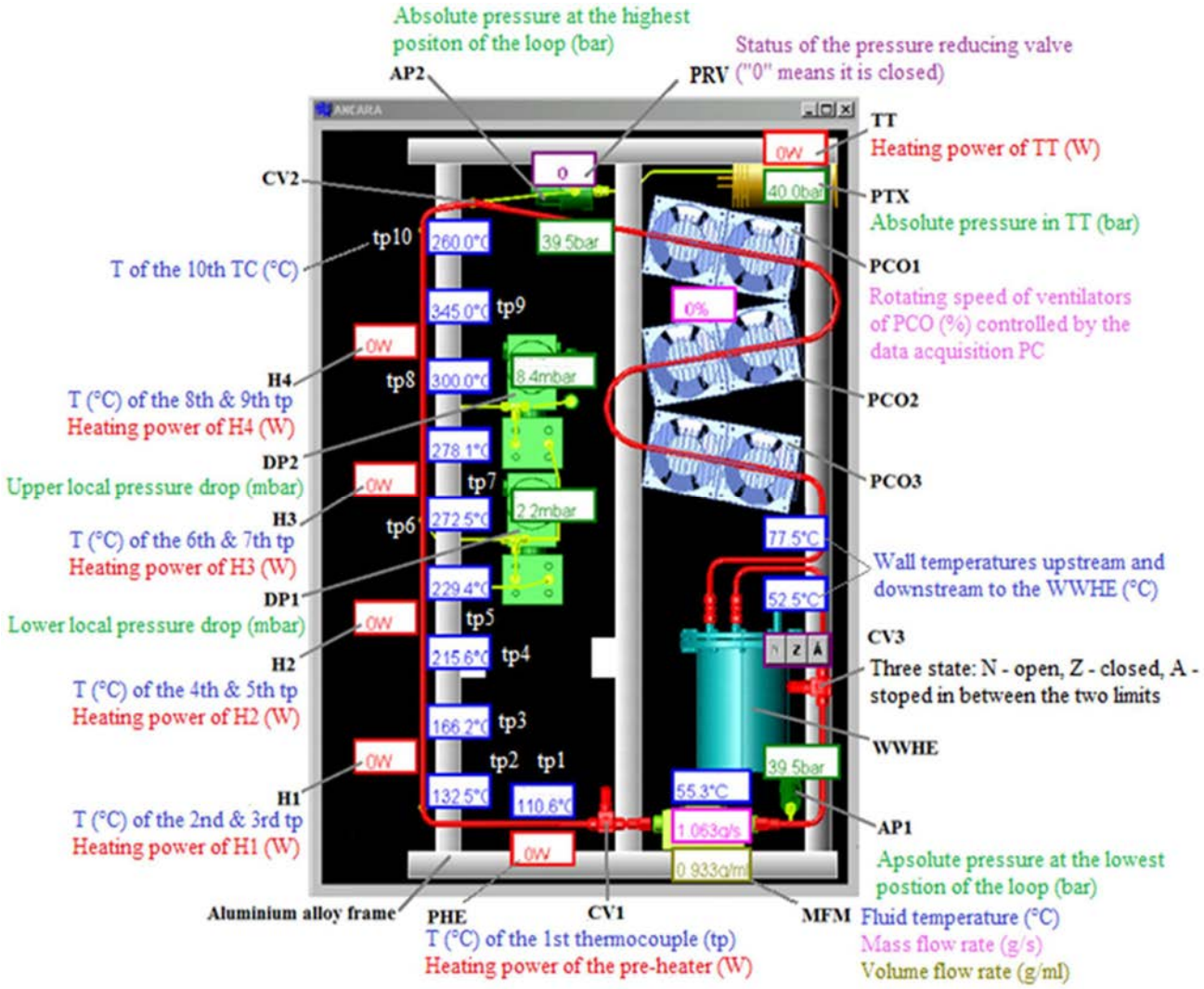

Fig. 7.36. Schematic of the ANCARA loop: abbreviations are explained in the following text below (1 bar = 0.1 MPa, 1 mbar = 100 Pa) [7.84], [7.85].

The description of the measurement tools (meters) of the loop are presented in the following starting from the AP1 (absolute pressure 1) element located at the lower right corner of the loop (Fig. 7.36). The direction of this description is clockwise which coincides with the flow direction in the loop (Fig. 7.38) [7.84], [7.85].

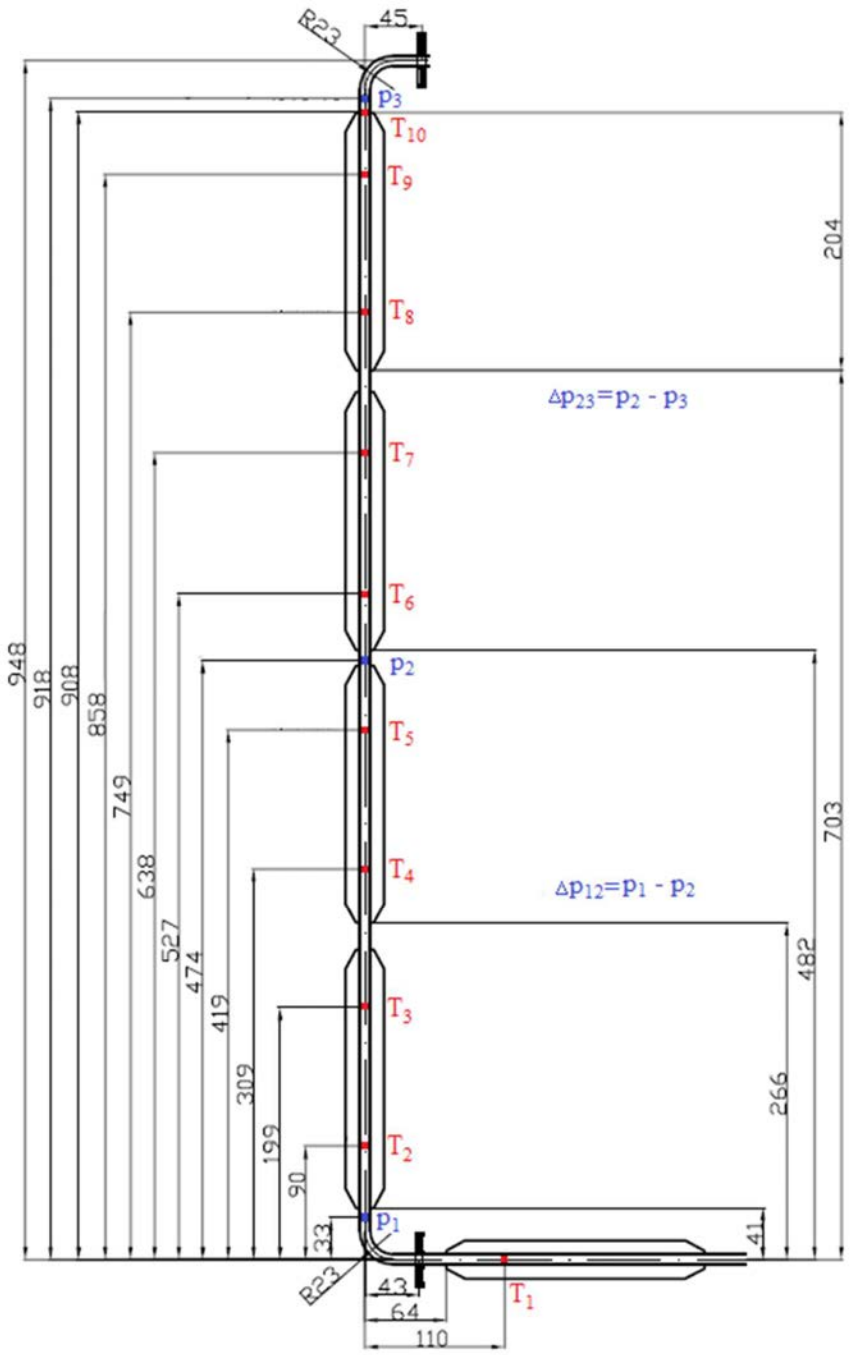

Fig. 7.37. The geometry and dimensions of the heated section of ANCARA loop: T – thermocouples, p – absolute pressure (MPa), Δp – pressure difference (MPa) [7.84], [7.85].

Two absolute pressure transducers (type: UNIK 5072–TD–A3–CC–H0–PE) measure the absolute pressure in the loop. One of them (AP1 in Fig. 7.36) is located at the lowest elevation in the cooled leg at the bottom right corner and another at the top elevation in the hot leg at the upper left corner [7.84], [7.85].

Left to the AP1 there is a SITRANS F C 300 type mass flow meter (MFM) made by SIEMENS (Fig. 7.36). This mass flow meter measures simultaneously the density and temperature of the fluid, the volume flow rate and the mass flow rate (flow error ≤ 0.1% of rate) working by the Coriolis theory. The MFM enables the option to record the so-called steady state characteristics (Fig. 7.39) [7.84], [7.85].

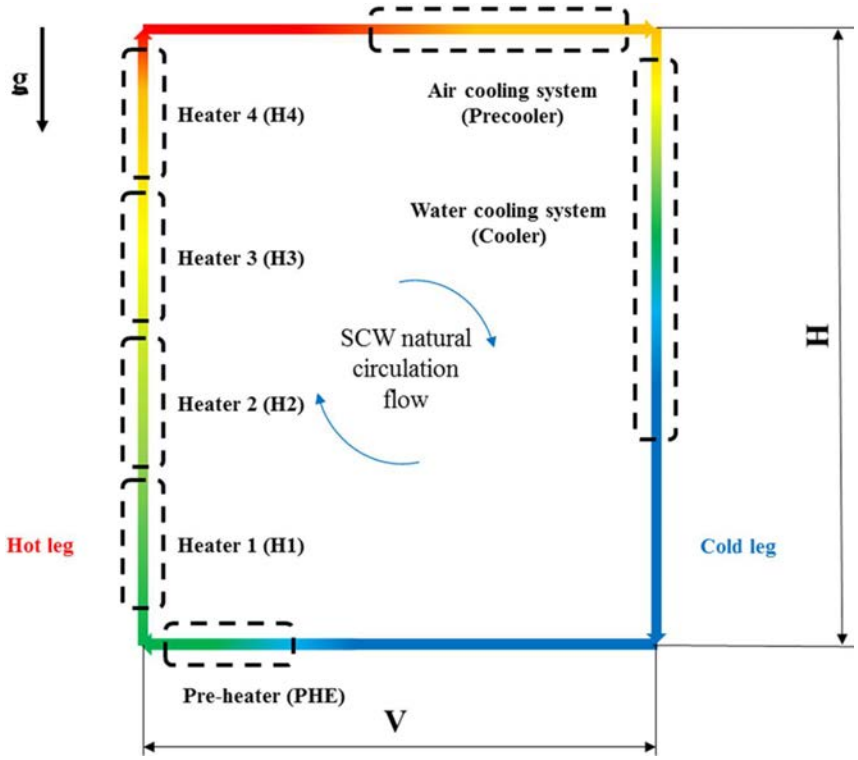

Fig. 7.38. Overview of the operation of the ANCARA loop: V – width (m), H – height (m), g – gravitational acceleration (m/s^2) [7.84], [7.85].

The last equipment in the lower horizontal part is the preheater (PHE in Fig. 7.36). This is a uniquely manufactured heater which is identical with the four heaters located in the vertical hot leg (denoted by H_1–H_4 in Fig. 7.36 and Fig. 7.38). The preheater is an indirect type heater element which consists of a multiply bent heating coil placed in the milled grooves of the two halves bodies of the PHE. The type of the heating coil is 1NcI20 and has been made by Thermocoax. The total heating power of the preheater and the heater elements is 1 kW per unit [7.84], [7.85].

The hot leg heated by the above mentioned four heaters with a total heating power of 4 kW (e.g. 4 × 1 kW). The temperature distribution on the outer wall of the hot leg can be measured by nine 'K' type thermocouples. The distance between two thermocouples is 110 mm (Fig. 7.37). The heaters (next to the dimensions of the loop) have been designed in order to represent the suitable conditions of HPLWR. The natural circulation can occur in the HPLWR during shutdown process or accidents. Because the shutdown process is more often, thus it was the basis of the design for the thermal power of the heaters. That is the reason why the heaters have been scaled in order to cover the range from 50% of HPLWR nominal power (50% of 2300 MW_{th}, which corresponds to

4875.5 W/m linear heating power for one subchannel) to the range of remnant heat (its linear power range is from 0 to 700 W/m for one subchannel). The total heating power of the hot leg (as an important parameter) can be varied between 0 and 4000 W. It is from 0 to 4615 W/m linear power in case of the ANCARA loop. It means that the heaters approximately fully cover the power range of natural circulation which could occur during the shutdown process or after that when the only heat source is the remnant heat during the switched off state of a HPLWR [7.84], [7.85].

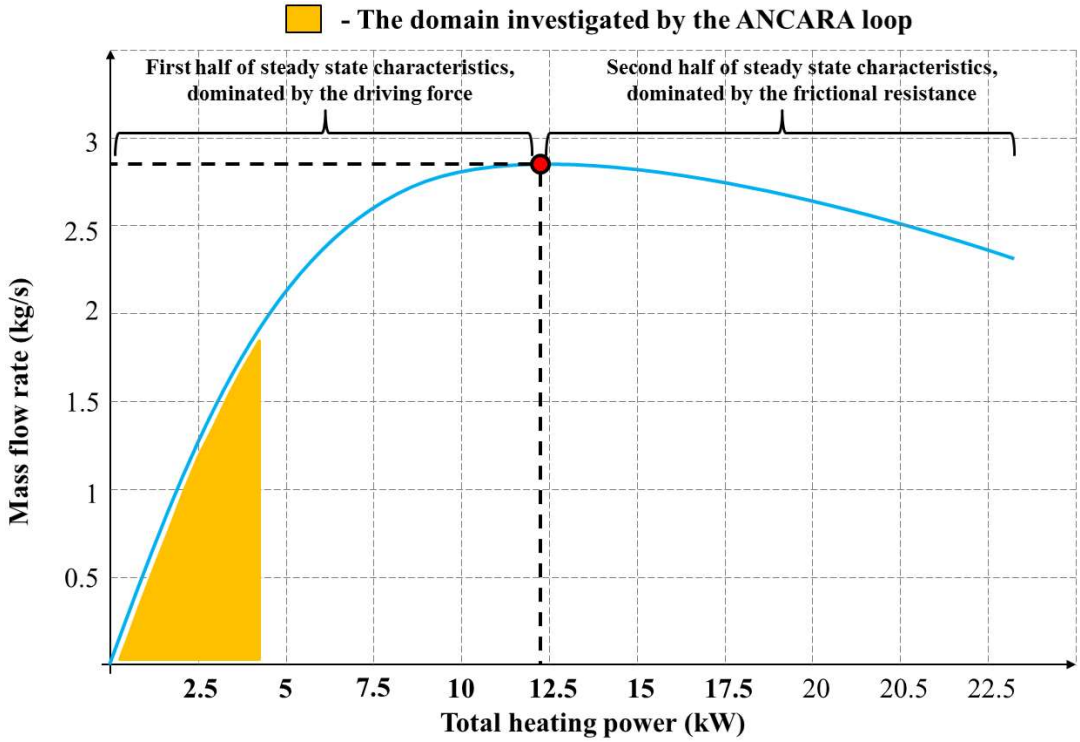

Fig. 7.39. Schematics of the steady state characteristics and the measured portion (orange range) recorded in the ANCARA loop [7.84], [7.85].

The length of the hot leg is approximately 1 m where the local pressure drops are measured by two SITRANS P DSIII 7MF4533-1DB32-2AA6-Z A01 type differential pressure transducers made by SIEMENS. The differential pressure transducer 1 (DP1 in Fig. 7.36) measures the pressure drop between the starting and middle point of the hot leg ((lower local pressure drop – Δp_{12}) while the differential pressure transducer 2 (DP2 in Fig. 7.36) measures the pressure drop between the middle and end point of the hot leg (upper local pressure drop – Δp_{23}). The measured local pressure drop error is less than 1 % (~0.82 %) [7.84], [7.85].

In order to reach the SCW state the high purity water was heated from room temperature to around or above the critical temperature. In the meantime, the fluid expanded and thus the pressure of SCW increased. If sometimes the pressure could not be controlled fast enough by changing the heating power (generally the pressure gets higher than needed) then a fast cooling possibility was needed. To realize this option one rough (by the blowing down system) and one soft (by the active air cooling system) pressure control option was implemented in the loop. This is the way how the pressure was controlled [7.84], [7.85].

An electrically controlled blow down or pressure reducing valve (PRV in Fig. 7.36) has been installed at the beginning of the upper horizontal part. The PRV '0' means that the valve is fully closed (Fig. 7.36). This valve is a 30-041-A024 type magnet valve. Its shortest opening time is 0.1 s which normally causes 2.5–3.0 MPa fall in the system pressure. The water which leave the loop through this valve can be collected in a tiny tank (TT in Fig. 7.36). The total volume of the TT is 55 cm^3. This tank has its own heating capability which enables water feed back to the loop after its pressure and temperature properly adjusted. The pressure in this tank can be measured by a PTX 1400 type absolute pressure transducer (PTX in Fig. 7.36) [7.84], [7.85].

In order to use the soft pressure control function due to cooling the loop down there is a three pass active air cooled pre-cooler (PCO1, PCO2 and PCO3 in Fig. 7.36, PCO in Fig. 7.40) at the upper part of the cold leg. This pre-cooler consists of cooling ribs (which are mounted around the tube of the loop) actively cooled by two ventilators per each pass (it means totally 6 ventilators). This configuration is from commercial PC technique. The rotation speed of the ventilators can be controlled by data acquisition and process management PC between 0–100% [7.84], [7.85].

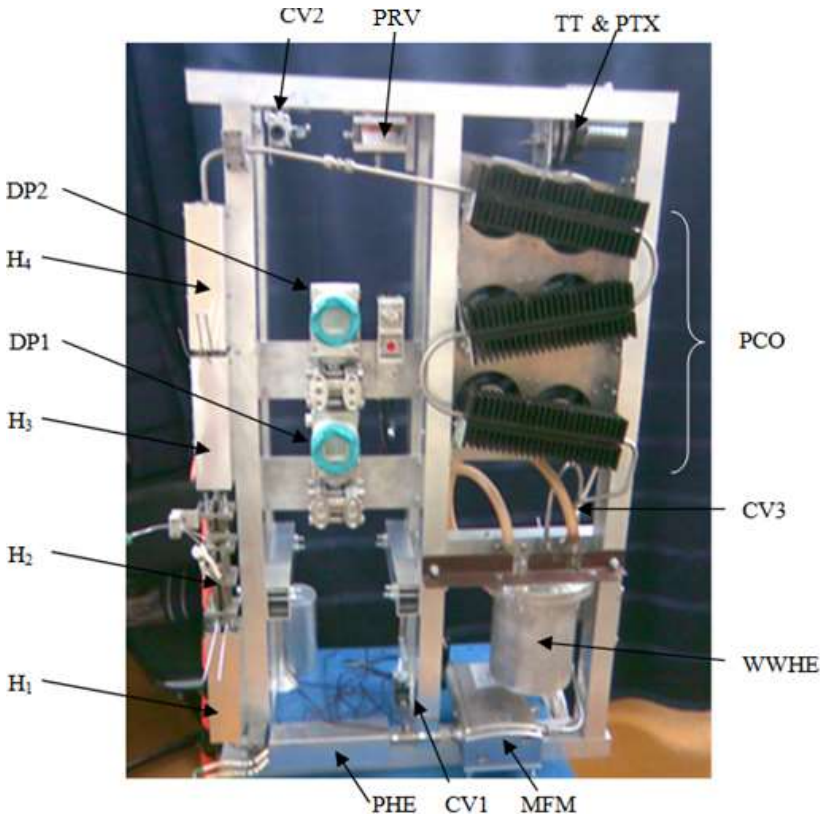

Fig. 7.40. Semifinal configuration of the ANCARA loop before final mounting [7.84], [7.85].

Downstream to the pre-coolers there is a crosscurrent water–water heat exchanger hosted in a stainless steel tank (WWHE in Fig. 7.36) [7.84], [7.85].

Downstream from the WWHE there is a PB491021 type valve (CV3 in Fig. 7.36 and Fig. 7.40). Its function is controlling the mass flow rate. This valve is controlled by the PC through an

electrical motor. The valve can be controlled by three buttons through manipulation of the online loop scheme. Pressing the button 'N' the electrical motor opens the valve. Pressing the button Z the motor closes the valve while pressing the button 'Á' the motor stops the valve in its instantaneous position. By these buttons the operator of the loop can open or close this valve or stop it in between the two limits in order to maintain the mass flow rate [7.84], [7.85].

For the necessary vacuum and high purity water charge processes two PB491021 type valves (CV1 and CV2 in Fig. 7.36 and Fig. 7.40) have been installed at the bottom and upper horizontal parts. CV1 connects to the lowest while CV2 connects to the highest level of the loop [7.84], [7.85].

Finally, two safety thermocouples (Fig. 7.36) have been mounted onto the outer surface of the closed tube upstream and downstream to the water–water heat exchanger (WWHE). These thermocouples provide important information about the effectiveness of the pre-cooler and the heat exchanger in order to prevent the overheating of mass flow meter which is directly downstream to the heat exchanger [7.84], [7.85].

7.2.11.2. DESCRIPTION OF THE CONDUCTED EXPERIMENTS

A series of experiment on the pressure drop in the vertical test section of ANCARA loop (tube with 5 mm inner and 8 mm outer diameters and a heating length of 0.948 m) cooled by supercritical pressure water was performed in a relatively wide set of parameters. The operating pressure values were 22.5, 23.5, 24, 24.5, 25, 25.5, 26.5 and 27.5 MPa. The inlet temperatures were 50, 100, 150 and 200°C. The heating power of the pre-heater and four heater elements varied from 1420 to 4700 W. The number of recorded steady state mesurements was in the range of 3–24. The absolute pressure and inlet temperature were set and held constant. When all parameters (outlet wall temperatures) were steady, the heating power was increased slowly by steps with a maximum of 200 W until either the tenth thermocouple (TC-10) showed 500°C or the heaters reached their maximum heating power (1 kW/heater). A more detailed description about the experimental procedure applied and about the results achieved can be found in the relevant publications [7.84], [7.85].

7.3. NUMERICAL ANALYSIS

[7.80] assessed the capability of their in-house nonlinear analytical tool (i.e., the SPORTS code [7.86] and the system code 'CATHENA' [7.87] for predicting the instability boundary. Fig. 7.41 compares predicted flow–power relationship using the SPORTS code against the experiment for Case 2 with the pressure at 7.6 MPa, inlet fluid temperature at 20 °C and outlet loss coefficient at 11.5. The code captures the relationship quite well. It agrees closely with the experiments at low powers but the peak of mass flow rate is predicted at a higher power than observed at the experiment. With this shift, the predicted mass flow rate is higher than the experimental value. Having said that, the differences are within the measurement uncertainty.

[7.80] noted that the CATHENA code is not applicable for carbon dioxide flow. They applied the non-dimensional parameters proposed by [7.21] for the comparison. Fig. 7.42 compares predicted Froude numbers, *Fr*, using the SPORTS and the CATHENA codes and the experimental values against the transpseudocritical number, N_{tpc}, for Case 2. The Froude number is defined as

$$Fr = \frac{w_{in}}{\sqrt{g \cdot L}} \tag{7.13}$$

The transpseudocritical number is defined as

$$N_{tpc} = \frac{Q_{channel}}{M_{channel}} \frac{\beta_{pc}}{C_{p,pc}} \tag{7.14}$$

Good agreement has been shown between predictions and experimental values. In particular, the CATHENA code predicts closely the trend and magnitude of the Froude number over the range of power (albeit the mass flow rate was slightly underpredicted at the vicinity of the pea).

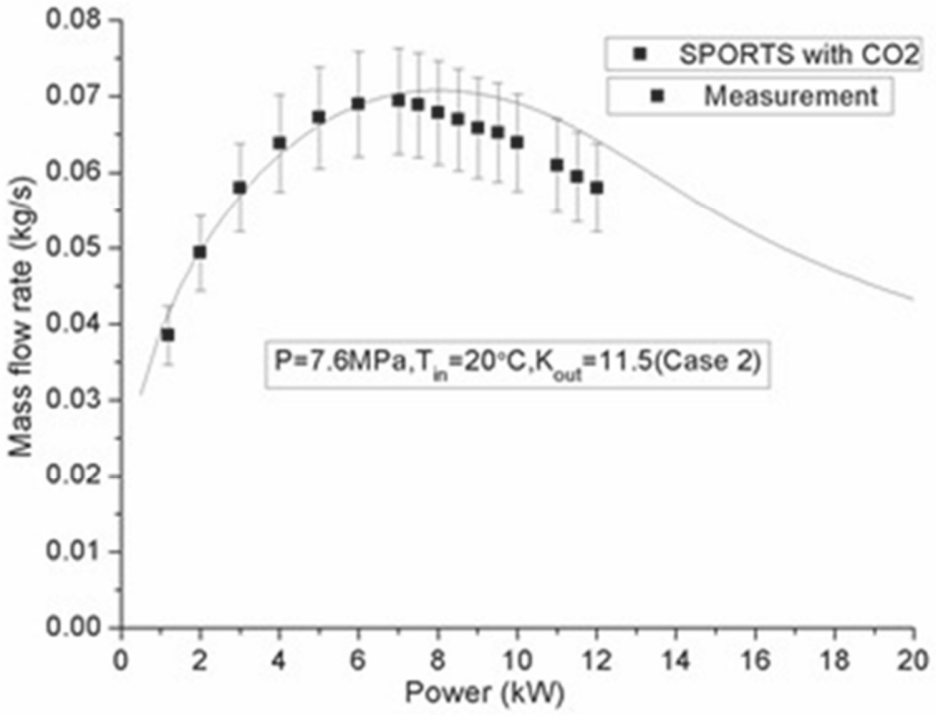

Fig. 7.41. Comparison of SPORTS code calculation and experimental result (Case 2).

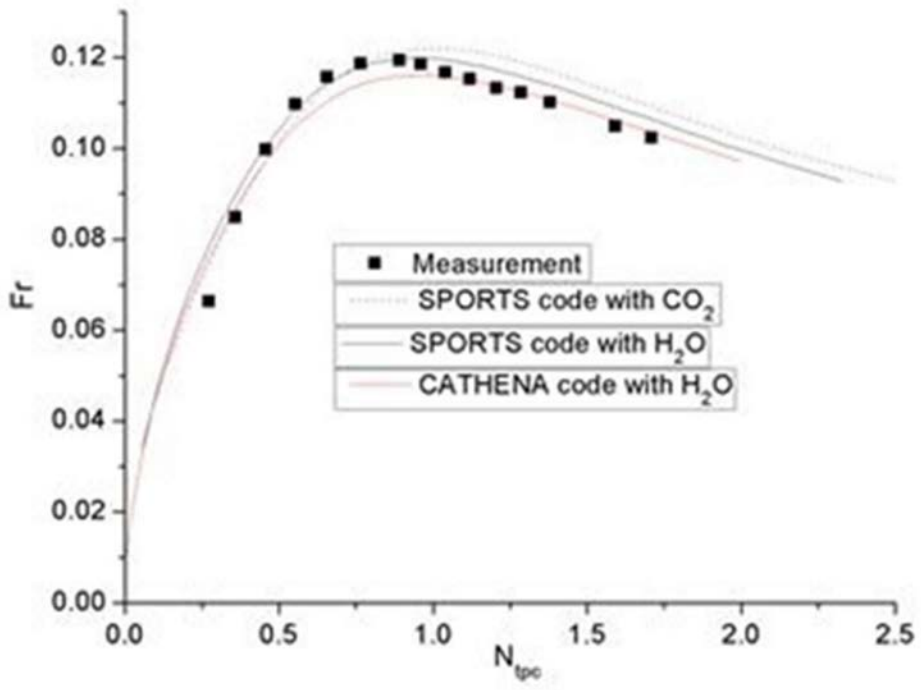

Fig. 7.42. Comparison of non-dimensional code predictions against experimental results (Case 2).

7.4. SCALING: A SIMILARITY THEORY OF NATURAL CIRCULATION STABILITY WITH SUPERCRITICAL PRESSURE FLUIDS

7.4.1. THEORETICAL DEVELOPMENTS

The present treatment, firstly published in [7.88], represents an extension of the one developed for the stability of heated pipes containing supercritical pressure fluids that was proposed at the ICONE–14 conference held in Miami in 2006, USA, and then selected for journal publication [7.21]. The theory, in the form presented herein, is quite simplified and applicable to a number of geometrically similar loops having somehow idealised boundary conditions, e.g., uniform diameter, imposed heat flux at both heating and cooling sections, adiabatic legs between the heater and the cooler.

As duly highlighted in the following discussion, some of these assumptions may considerably affect the predicted stability behaviour; consequently, the present theory is meant only to highlight the main parameters having an effect on stability. A generalisation of this approach is possible, though at the price of greater complexity, making the dimensionless treatment somehow limiting. Modelling of the pipe wall structures, demonstrated to considerably affect stability also in recent work [7.89], is one of the aspects that is necessary to include in detailed analyses. This is the reason why, after developing the presently discussed theory, it was devoted attention to the

development of models for setting up stability maps in dimensional form for natural circulation loops containing fluids at supercritical pressure [7.90].

The loops addressed in the present treatment have anyway enough general layout to encompass a range of real devices, addressed within the above mentioned limitations. Fig. 7.43 reports a sketch of such loops, implying that the orientation and location of the different pipes and of the heated and cooled sections may be arbitrary. As usual in similarity theories, loops to be considered dynamically similar should have similar geometrical features in terms of pipe layout, orientation and distribution of heating and cooling sections. For the present discussion, we will assume that a single heater and a single cooler are present in the system, though the similarity could be extended further.

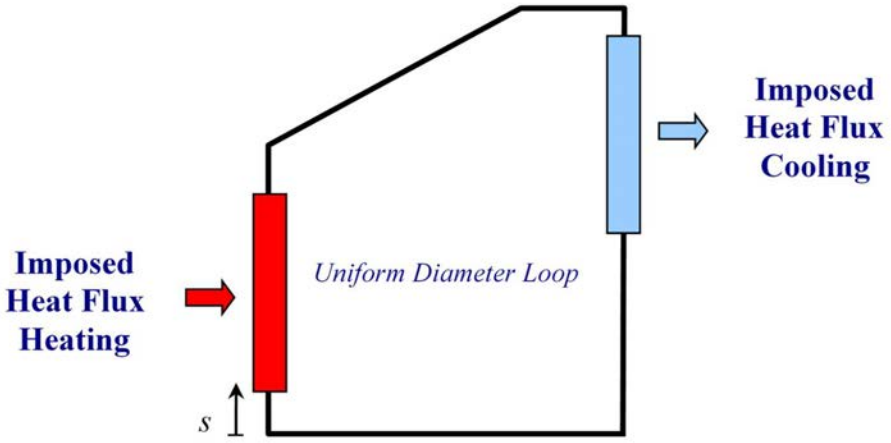

Fig. 7.43. Sketch of the general loop geometry: the location of heaters and coolers is arbitrary.

It is necessary to acknowledge that the occasion for discussing the proposed similarity theory in front of numerical code predictions came from the cooperation between the University of Pisa and the China Institute of Atomic Energy (CIAE) in the analysis of flow stability in natural circulation loops with supercritical water. The cooperation led to a couple of joint papers ([7.88] and [7.90]) where the similarity theory was presented and further steps in modelling stability were made.

The dimensionless parameters adopted in the treatment are defined in analogy with those adopted for the single heated channel by [7.21]:

$$\rho^* = \frac{\rho}{\rho_{pc}} \tag{7.15}$$

$$h^* = \frac{1}{v_{pc}}\left(\frac{\partial v}{\partial h}\right)_{p,pc}\left(h - h_{pc}\right) = \frac{\beta_{pc}}{C_{p,pc}}\left(h - h_{pc}\right) \tag{7.16}$$

$$p^* = \frac{p}{\rho_{pc} w_0^2} \tag{7.17}$$

$$N'_{TPC} = \frac{q''_h \Pi_h L_{heater}}{\rho_{pc} w_0 A} \frac{\beta_{pc}}{C_{p,pc}} \tag{7.18}$$

$$N_{SPC} = \frac{\beta_{pc}}{C_{p,pc}} (h_{pc} - h_0) \tag{7.19}$$

$$N_{TPC} = \frac{N'_{TPC}}{\rho_0^*} = \frac{q''_h \Pi_h L_{heate}}{\rho_0 w_0 A} \frac{\beta_{pc}}{C_{p,pc}} = \frac{\dot{Q}}{W} \frac{\beta_{pc}}{C_{p,pc}} \tag{7.20}$$

In these relationships, the length adopted for defining the transpseudocritical number, N_{TPC}, is the one of the heater, something matching closely the choice adopted for the single heated channels. Since the dimensionless coordinate along the loop is now defined with reference to the total length of the loop, L, it will be therefore necessary to make appearing the ratio between the loop length and the heater length, as it can be observed in the following balance equations:

$$\frac{\partial \rho^*}{\partial t^*} + \frac{\partial G^*}{\partial s^*} = 0 \tag{7.21}$$

$$\frac{\partial G^*}{\partial t^*} + \frac{\partial}{\partial s^*}\left(\frac{G^{*2}}{\rho^*}\right) + \frac{\partial p^*}{\partial s^*} = -f_g^*(s^*)\frac{\rho^*}{Fr} - \left[\Lambda + \frac{1}{2}\sum_{k=1}^{N_K} K_k\, \delta^*(s^* - s_k^*)\right]\frac{G^{*2}}{\rho^*} \tag{7.22}$$

$$\frac{\partial \rho^* h^*}{\partial t^*} + \frac{\partial G^* h^*}{\partial s^*} = \frac{L}{L_{heate}} N'_{TPC} f_q^*(s^*) \tag{7.23}$$

where, it is assumed

$$w^* = \frac{w}{w_0} \tag{7.24}$$

$$t^* = \frac{t w_0}{L} \tag{7.25}$$

$$s^* = \frac{s}{L} \tag{7.26}$$

$$G^* = \rho^* w^*$$

(7.27)

$$\Lambda = \frac{f\,L}{2\,D_h}$$

(7.28)

$$Fr = \frac{w_0^2}{gL}$$

(7.29)

In the above formulations, w_0, is the velocity at the heater inlet and, ρ_0, the density at the same location. It is evident from the above that the inlet conditions at the heater will play a role in both the static and the dynamic behaviour of the loop and will need a steady state calculation for properly defining the specific working poInt. The functions $f_q^*(s^*)$ and $f_g^*(s^*)$ represent heating/cooling and gravity distributions along the loop; their values need to be bound to the constraints:

$$\int_0^1 f_q^*(s^*)\,ds^* = 0$$

(7.30)

$$\int_0^1 f_g^*(s^*)\,ds^* = 0$$

(7.31)

These relationships are a consequence of the fact that total heating and cooling powers should be equal and opposite in sign, despite of the specific location of the heater and the cooler, and that the loop is closed, giving rise to no unbalance in the distribution of the component of the gravity acceleration along the loop itself. These two functions need to satisfy additional constraints:

— First one is needed to specify that the overall energy balance is preserved and that the heater power is conveniently normalised in order to make N_{TPC} represent the actual dimensionless power-to-flow ratio:

$$\int_{heater} f_q^*(s^*)\,ds^* = -\int_{cool} f_q^*(s^*)\,ds^* = \frac{L_{heater}}{L}$$

(7.32)

— Further (somehow obvious) constraint is obtained by considering that the component of gravity along the loop cannot be larger than the gravity magnitude:

$$\left|f_g^*(s^*)\right| \leq 1$$

(7.33)

In the partial differential equations, Eq. (7.32) to (7.33), friction parameters appear, both distributed and localised, being respectively Λ and the singular pressure drop coefficients that,

unlike in the older treatment by [7.21], are defined to satisfy the relation $\Delta p_{singular,k} = \frac{K_k \rho w^2}{2}$, thus being different by a factor 2 with respect to the ones adopted in the mentioned paper.

The fact that the loop is closed has a consequence also on the boundary conditions imposed in steady state and transient analyses. In particular, in steady state we need to assume the following:

— Temperature or the specific enthalpy at some location in the loop has to be specified in order to define the otherwise arbitrary thermal working point; in fact, imposing heat flux heating and cooling leaves undetermined the level of temperature that in real life apparatuses is specified by a finite heat conductance of the cooler and by the temperature of the secondary fluid; in the present case, we need therefore to specify, for instance, the heater inlet dimensionless enthalpy that can be assigned as follows:

$$h^*\ (0) = h_0^* = -N_{SPC}$$

(7.34)

— Since the loop is closed, the mass flux at the section $s^* = 0$ has to be equal to the one at $s^* = 1$; since by definition $w^*(0) = 1$, this leads to:

$$G^*\ (0^+) = G^*\ (1^-) = \rho^*\ (h_0^*) w^*(0) = \rho^*\ (h_0^*)$$

(7.35)

this condition, holding in steady state, is simplified to

$$G^*\ (0^+) = G^*\ (1^-)$$

(7.36)

in transient conditions, thus allowing the flow rate to fluctuate according to the predicted behaviour;

— Pressure is also imposed to be continuous along the loop

$$p^*\ (0^+) = p^*\ (1^-)$$

(7.37)

It should be here recalled that the present similarity theory is basing on the well assessed observation that it is possible to assume a single trend of dimensionless density as a function of dimensionless enthalpy; this finding, which was one of the most important observations highlighted by [7.21], holds with good approximation for a range supercritical pressures and several fluids; its consequence is that the dimensionless density is

independent from the dimensionless pressure to a large extent, being only a function of dimensionless enthalpy:

$$\rho^* = \rho^*(h^*) \tag{7.38}$$

Therefore, since the pressure level is immaterial, it is useful to define it equal to zero both in steady state and in transient conditions, leading to:

$$p^*\ (0^+) = p^*\ (1^-) = 0 \tag{7.39}$$

It needs to be explicitly noted that in steady state conditions imposing the value of the dimensionless mass flux and of the dimensionless specific enthalpy at a given location in the loop means actually specifying the dimensionless enthalpy everywhere, according to the heating and cooling sections distribution. This may seem at first glance somehow arbitrary, since in a natural circulation loop the steady flow rate should be a consequence of buoyancy, determined by the enthalpy distribution, and friction. Actually, despite of the apparent redundant specification of boundary conditions, the value of the velocity w_0 is not specified unless the momentum equation is used together with mass and energy balances in order to identify the value of the key governing dimensionless number containing this parameter, being the Froude number. Therefore, *Fr* is determined in steady state conditions by identifying the value which satisfies the condition $p^*\ (0^+) = p^*\ (1^-)$. Stability maps can be thus set up, for a given geometry and assigned friction parameters, in terms of N_{SPC} and N_{TPC} only, leading to the value of the Froude number as a dependent variable. This, in fact, is the dimensionless counterpart of the usual procedure of evaluating the actual flow rate in a given natural circulation loop as a function of the heating power.

As anticipated, the boundary conditions for transient analysis are similar to the ones mentioned above for steady state, resulting in the equality of the dimensionless mass fluxes at $s^* = 0$ and $s^* = 1$ (though the common value is left free to evolve in time) and in the equality of dimensionless pressure and specific enthalpy at the same locations.

7.4.2. STABILITY ANALYSIS METHODOLOGY AND APPLICATION TO A SAMPLE LOOP

As in previous similar works, also in [7.88], the methodology adopted for transient stability analysis is based on the numerical discretisation of the balance equations, the linearization by perturbation of the obtained algebraic equations and the calculation of the eigenvalues of the resulting matrix embedding the linear dynamics of the system. The reader is referred to [7.88] for the details of the algebraic developments; however, it is here recalled that:

— The adopted numerical discretization scheme is a semi-implicit one, allowing for pressure–velocity coupling by a staggered mesh scheme, involving ‘control nodes’ and ‘junctions’;

— The variables defining the state of a system at any time are the nodal values of dimensionless pressure and specific enthalpy, together with the dimensionless junction mass fluxes;
— Given the loop geometry and the pressure drop parameters, the steady state conditions are evaluated on the basis of N_{SPC} and N_{TPC}, also determining the corresponding values of the Froude number.

The eigenvalues of the matrix relating the old time step system variables to the new ones are considered for evaluating stability, with main reference to the spectral radius, whose value allows for discriminating between stable and unstable cases. In fact, perturbations grow or are damped in time according to the fact that the spectral radius is greater or lower than unity. Usual information to be extracted from the spectral radius and the eigenvalue corresponding to it are an amplification exponent and the pulsation of the fastest growing or least damped perturbations. These quantities are defined as:

$$z_R = \frac{1}{\Delta t^*} ln\big(\rho(\boldsymbol{A})\big)\,;\; z_I = \frac{1}{\Delta t^*} arccos\left(\frac{Re\left(\lambda_{i_\rho}\right)}{\rho(\boldsymbol{A})}\right) \tag{7.40}$$

As in previous work, the former quantity is used to set up contour plots highlighting the degree of stability or instability of the loop, by virtue of the fact that leading perturbations are depending on time as $exp(z_R t)\,[cos(z_I t) + i\, sin(z_I t)]$. Therefore, a variety of linearly stable or unstable behaviours can be identified for a given steady state condition on the basis of knowledge of z_R and z_I.

The loop considered for a sample application of the methodology is an idealised one, roughly based on the configuration of a real loop installed and operated at CIAE [7.91] and also considered in [7.88] for performing stability analyses. The layout of the idealised loop is rectangular, having a width of 2.4 m, a height of 1.8 m, a vertical heater length of 1.4 m and a horizontal cooler length of 1.7 m. The inner diameter is assumed uniform and equal to 4.62 mm. Using equal nodes of 0.05 m each, an overall number of 168 nodes is obtained; these nodes are evenly distributed along the total length of 8.4 m. In a few calculation cases, the mesh size was halved [7.88], in order to observe the effect of a decreased truncation error. Singular pressure drop coefficients equal to unity are adopted in the 90° bends and the value of the friction factor is estimated on the basis of the flow rate.

Stability of the loop was assessed by two different programmes:

— The RELAP5/MOD3 code (SCIENTECH [7.92]), applied to the physical loop as described in the previous paragraph;
— An inhouse discretised model, solving the above reported dimensionless balance equations for a loop which in terms of dimensionless space units has the configuration illustrated in Fig. 7.44; this loop is the dimensionless counterpart of the loop adopted for RELAP5 analyses in dimensional form.

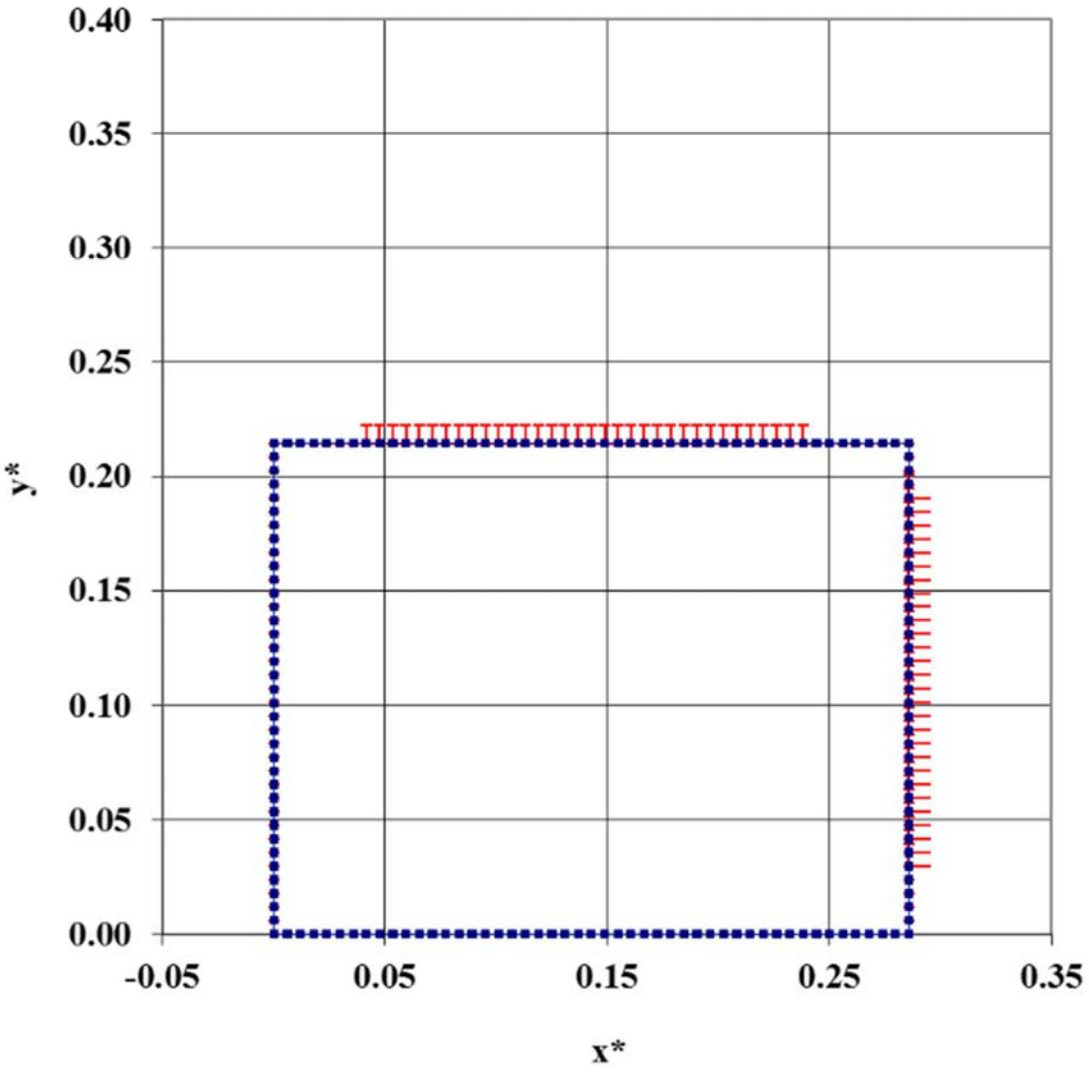

Fig. 7.44. Geometrical representation of the CIAE loop in dimensionless space units.

In RELAP5 calculations, the heating and cooling structures in which power was respectively injected and extracted were initially assumed very thin and highly conductive, in order to avoid any influence of their heat capacity on stability, thus keeping coherence with the simplified model adopted in the in-house code. In further analyses, they were instead introduced with their real physical properties, in order to assess their influence on stability.

The in-house code was used to generate the mentioned stability maps in the form of the contour plots of z_R, as the one shown in Fig. 7.45 and Fig. 7.46; the corresponding values of the Froude number resulting for steady state conditions are shown in Detail of *oscillations*

Fig. 7.47.

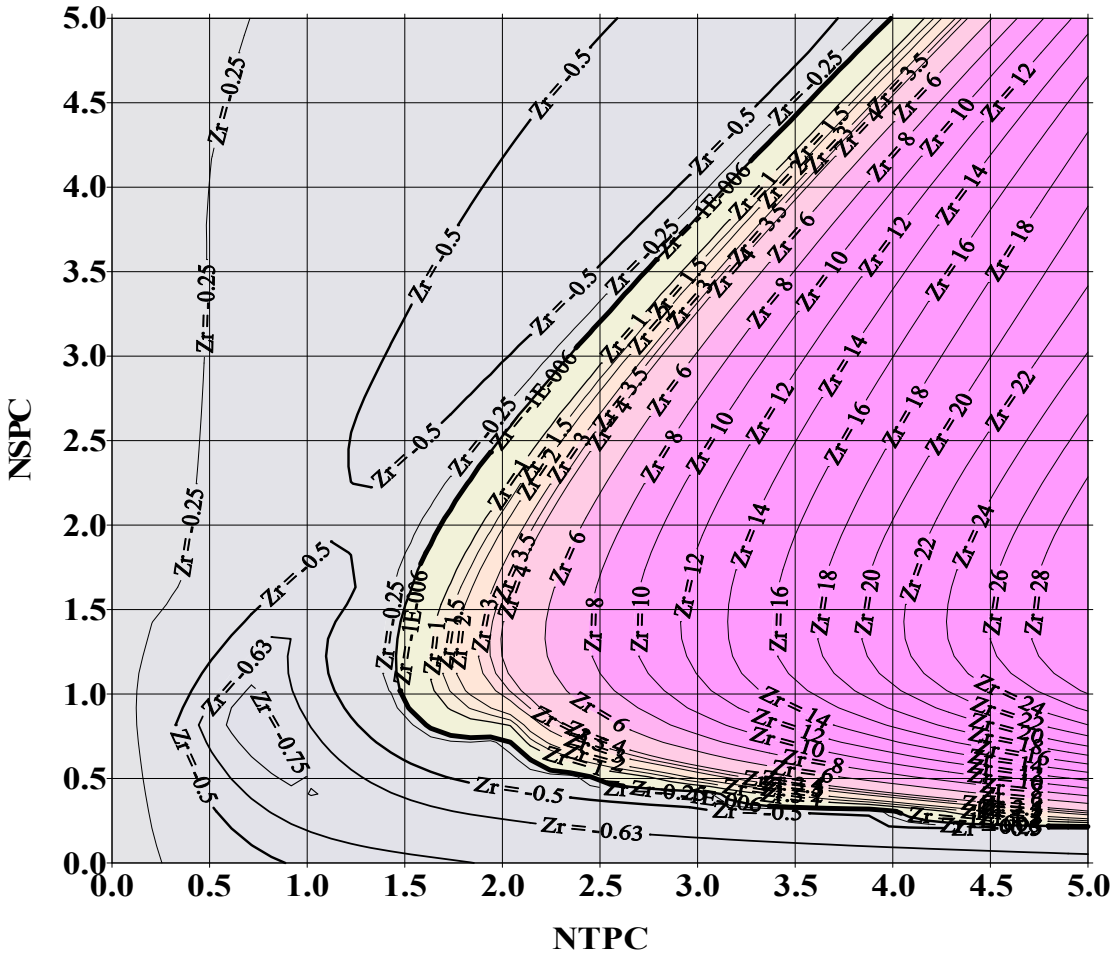

Fig. 7.45. Stability map obtained as a contour plot of z_R for Λ=36 and 168 nodes: the stable region is the grey one outside the thick stability boundary, where $z_R < 0$.

The corresponding calculations performed by RELAP5 with the idealised loop were run for water at pressures around 25 MPa, as in the real CIAE loop, and for ranges of power from a few kilowatts up to 10 kW, as required to reach unstable behaviour. In particular, the methodology adopted for identifying the stability threshold involved adopting values of power slowly increasing with time in the heater and in the cooler, up the point in which oscillations started to be detected. Detail of oscillations

Fig. 7.47 shows a typical trend of loop flow rate during power increase, showing out-of-phase oscillations at the inlet and the outlet of the heater.

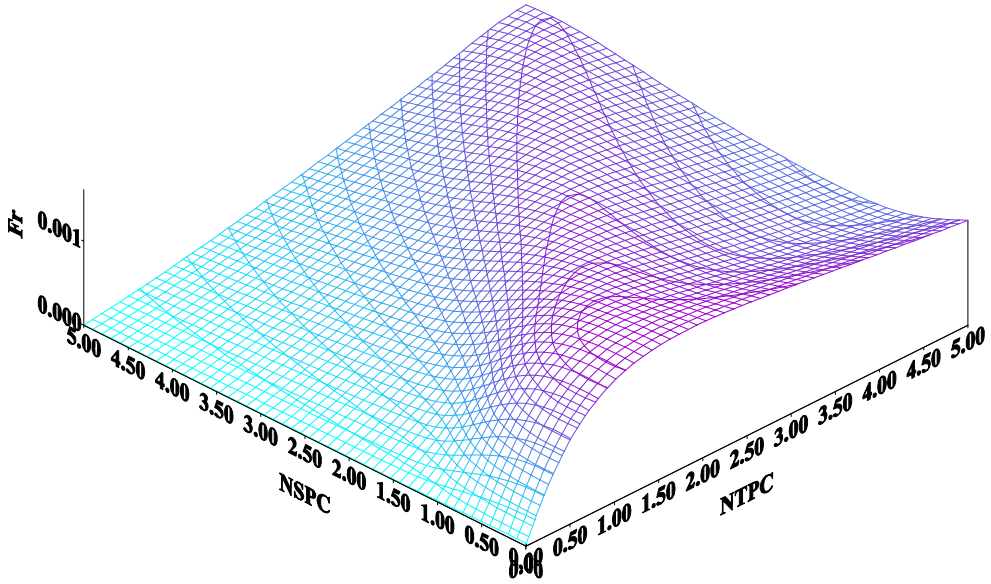

Fig. 7.46. Distribution of the Froude number for Λ=36 and 168 nodes.

The results obtained in dimensional form by the RELAP5 code were then reported in terms of threshold values of the dimensionless N_{TPC} and N_{SPC} numbers, to be compared with the marginal stability boundary in the contour plots obtained by the inhouse code. This is shown by the markers appearing in Fig. 7.48 to Fig. 7.50; these data show that:

— The calculations performed with RELAP5 and very thin heating and cooling structures, match quite closely with the marginal stability boundary obtained by the in-house code assuming imposed heat flux heating and cooling (see Fig. 7.48);
— The use of different values for pipe roughness (25 μm and 50 μm) does not determine any relevant difference in RELAP5 predictions, except at low N_{SPC}, where the boundary has a very little slope (see Fig. 7.48); this finding was confirmed by sensitivity analyses made with the in-house code by varying the friction parameter in a corresponding range from 27 to 45;
— When the heating structures are simulated with a thickness as in the actual CIAE loop, a different behaviour is noted whether they are introduced in the heater or in the cooler; in the former case, in fact, the value of N_{TPC} at the onset of stability is shifted at higher values, while in the latter the introduction of the actual thickness in the cooler seems definitely less relevant (see Fig. 7.49);
— Noting that the convective heat transfer coefficient measured in CIAE experiments showed a high degree of deterioration with respect to the Dittus–Boelter correlation adopted in RELAP5, with values decreased even by a factor 0.3 with respect to the correlation, calculations were performed making use of a similar ‘fouling’ factor, showing that the presence of heating structures affects much less stability in the case of heat transfer deterioration (see Fig. 7.50).

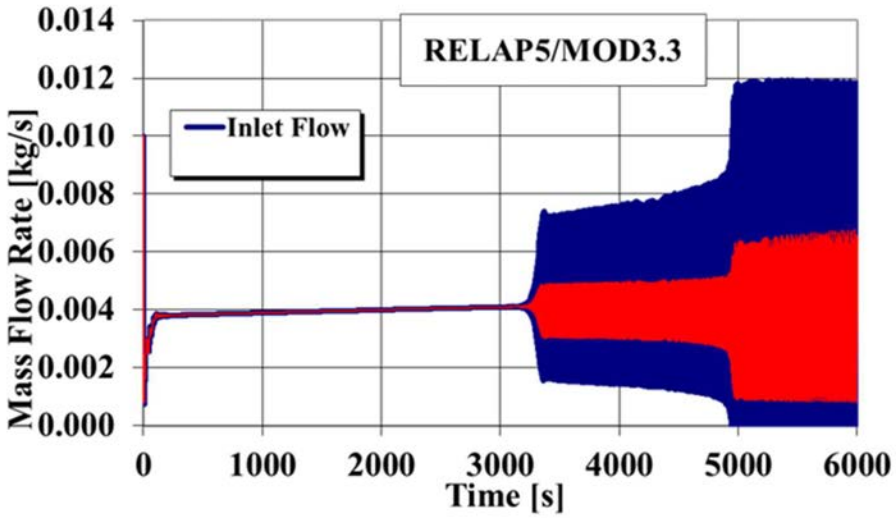

(a) Overall trend

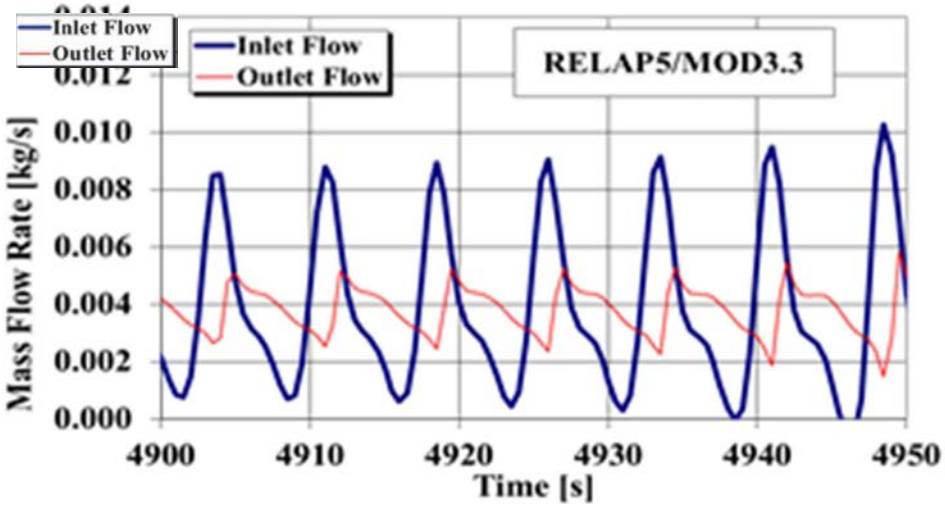

(b) Detail of oscillations

Fig. 7.47. Idealised loop analysed by RELAP5: sample trend of flow rate during an increasing power transient.

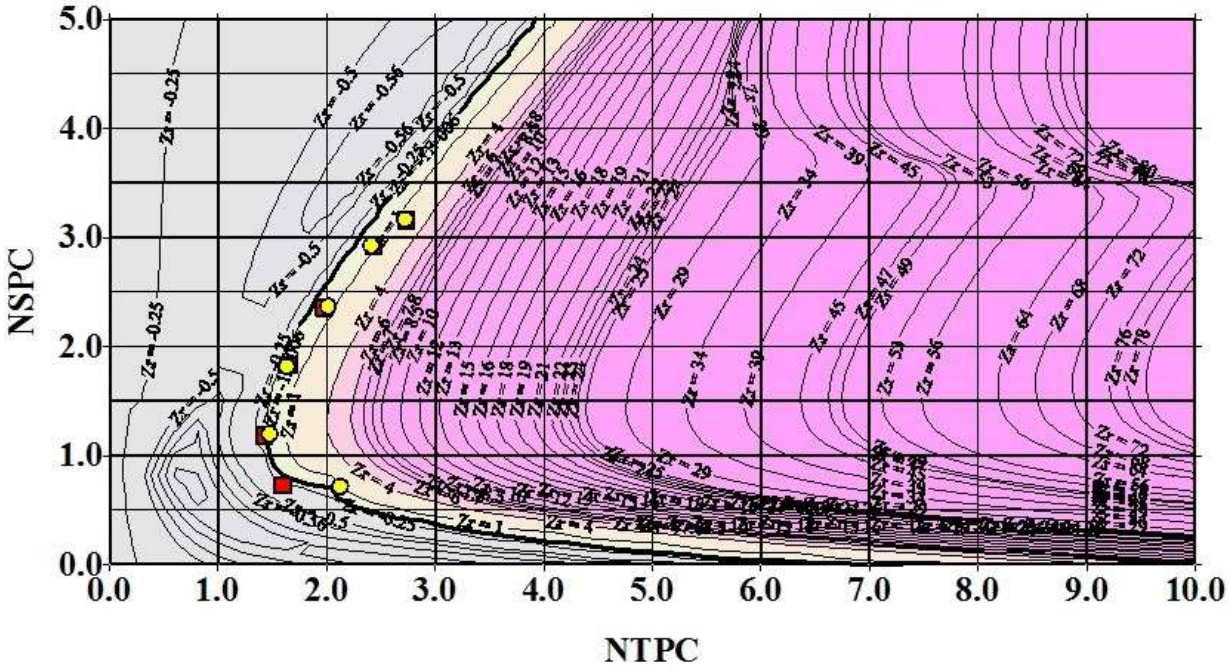

Fig. 7.48. Idealised loop: comparison of the stability boundaries obtained by RELAP5 for different roughness parameters (yellow circles: 25 μm; red squares: 50 μm) with the map obtained in dimensionless form.

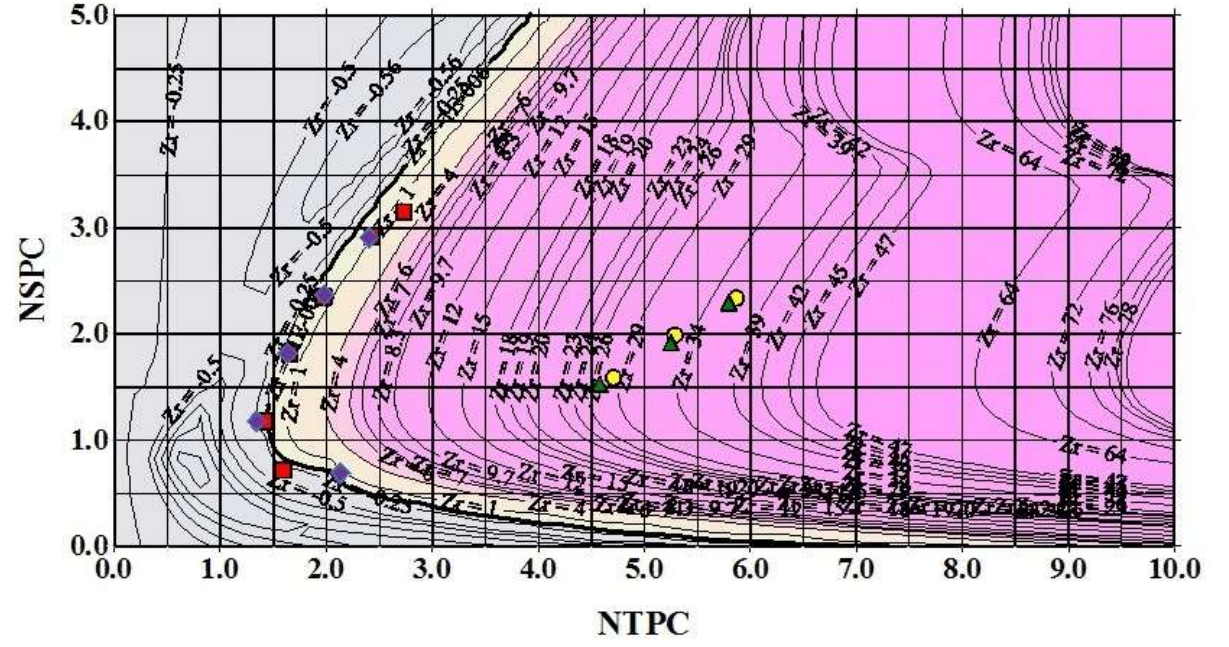

Fig. 7.49. Idealised loop: stability map showing the effect of heating structures in RELAP5 calculations (red squares: no heating structures; blue diamonds: only cooler structure; yellow circles: only heater structure; green triangles: with both heater and cooler structures).

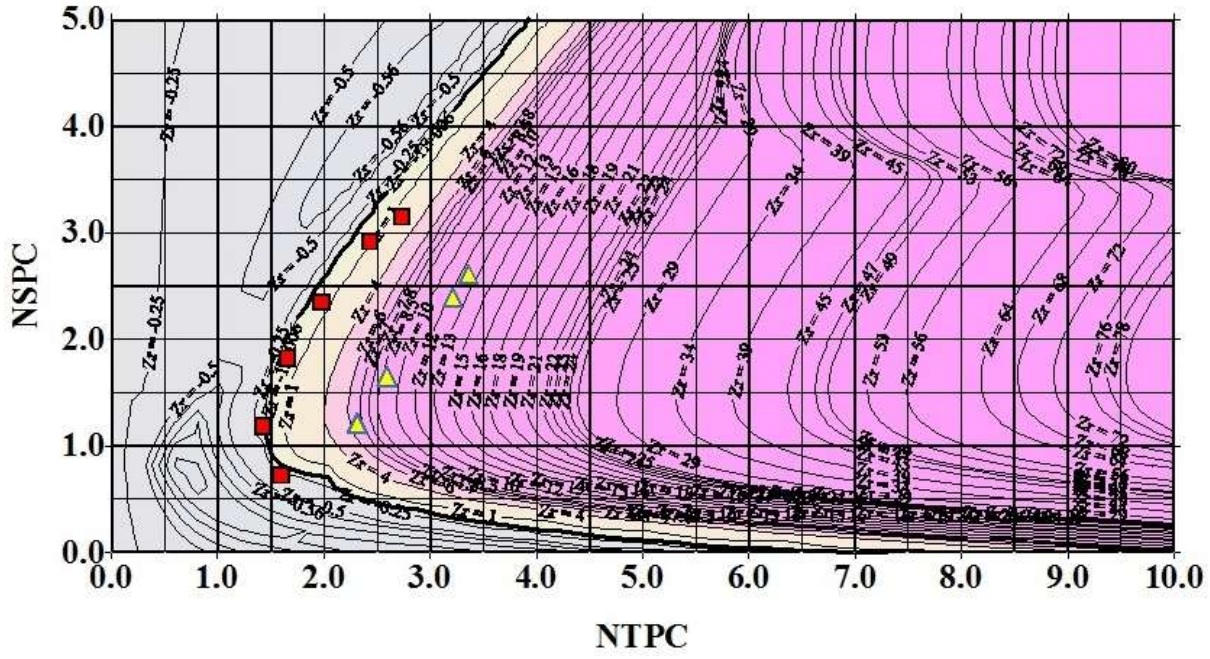

Fig. 7.50. Idealised loop: stability map showing the effect of the use of fouling factors (red squares: no heating structures; yellow triangles: heater and cooler structures with 0.3 fouling).

7.4.3. LESSON LEARNED

The simplified similarity theory presented above highlights the role of the dimensionless power-to-flow ratio (N_{TPC}) and of the dimensionless subcooling with respect to the pseudocritical temperature (N_{SPC}) in determining unstable natural circulation. In particular, it is noted that increasing the power-to-flow ratio leads to instability, with a threshold value that depends on the pseudo subcooling in a way similar to the case of density wave oscillations in single heated channels. While the effect of distributed friction was found minor in the explored range for the considered loop, it should be recalled that friction actually determines the flow rate as a function of power, thus directly affecting the power-to-flow ratio.

The stability boundary obtained by the simplified theory is strongly affected by the presence of the pipe wall structures, having the effect to damp perturbations which favours stability. This observation should be considered in the light of the sensitivity analysis performed with RELAP5 by introducing a fouling factor, which suggests that deteriorated heat transfer may reduce the stabilising effect of heating structures, since it decreases the thermal coupling between the fluid and the metallic mass of the walls.

The latter observation justifies the difficulties encountered in predicting stability in actual natural circulation loops, as the CIAE one, when adopting heat transfer correlations not suitable for deteriorated heat transfer prediction. In fact, on one hand the presence of heating structures tends

certainly to stabilise the dynamics, though on the other hand this effect is quantitatively uncertain owing to the present uncertainties in evaluating heat transfer coefficients.

Nomenclature and Acronyms

A	cross section area (m^2)
C_p	specific heat (J/(kg.K))
C	Constant
$\boldsymbol{D_h}$	hydraulic diameter (m)
f	friction factor
f_q	normalized distribution of heat flux
f_g	normalized distribution of gravity
Fr	Froude number
g	gravity (m/s^2)
G	mass flux ($kg/m^2/s$)
HTC	heat transfer coefficient (W/m^2. K)
h	enthalpy (J/kg)
k	thermal conductivity (W/(m.K))
K_k	k-th localized pressure drop coefficient
$\boldsymbol{L}$	length of a section or channel (m)
n	exponent
N_{SPC}	sub-pseudocritical number
N'_{TPC}, N_{TPC}	apparent and true transpseudocritical numbers
Nu	Nusselt number (hd/k)
P	pressure, Pa
Pr	Prandtl No. ($\mu c_p/k$)
Q	power (W)
q or q''	heat flux (W/m^2)
$\boldsymbol{q}'''$	heat applied/unit volume of coolant (W/m^3)
r	radius (m)
Re	Reynolds number (GD/μ)
s	axial coordinate (m)
t	time (s)
T	temperature (°C or K)
W	mass flow rate (kg/s)
w	velocity (m/s)
$\boldsymbol{x}$	axial distance (m)
z	elevation (m)
z_R	amplification parameter
z_I	angular oscillation frequency

$$\text{Bu} = \text{Simplified Buoyancy Parameter} = \frac{\overline{\text{Gr}_b}}{\text{Re}_b^{2.7}}$$

$$\text{Bu}^* = \text{Modified buoyancy parameter} = \frac{\overline{\text{Gr}_b}}{\text{Re}_b^{2.7}\overline{\text{Pr}_b}^{0.5}}$$

C_p = Specific heat

$\overline{C_p}$= Average specific heat = $\left(\frac{H_w\text{-}\mathrm{H}_b}{T_w\text{-}\mathrm{T}_b}\right)$

D = Diameter

E = Error

G = Mass flux

Gr = Grashof no.= $\left(\frac{\rho_b(\rho_b\text{-}\rho_w)D^3g}{\mu^2}\right)$

$\overline{\mathrm{Gr}}$=Avg. Gr. no.= $\left(\frac{\rho_b(\rho_b-\overline{\rho})D^3g}{\mu^2}\right)$

Gr*= Grashof no. based on heat flux

$=\frac{\mathrm{g}\beta_b(T_w\text{-}\mathrm{T}_b)D_{\mathrm{hyd}}^3}{\nu_b^2}\times\frac{\alpha\mathrm{D}_{\mathrm{hyd}}}{k_b}=\frac{\mathrm{gq}\beta_b D_{\mathrm{hyd}}^4}{k_b\nu_b^2}$

H = Enthalpy

HTC = Heat Transfer coefficient

k = Thermal conductivity

L = Length

m = Mass flow rate

N= No. of steady state data

Nu = Nusselt no.

P = Pressure

Pr = Prandtl no.

$\overline{\mathrm{Pr}}$=Modified Pr no.= $\left(\frac{H_w\text{-}\mathrm{H}_b}{T_w\text{-}\mathrm{T}_b}\right)\frac{\mu}{k}$

q = Heat flux

q^*= Non-dimensional heat flux = $\frac{\mathrm{q}\beta}{G\overline{\mathrm{Cp}}}$

Re = Reynolds no.

RMS = Root mean square

SD = Standard deviation

t = Temperature

Abbreviations

BARC	Bhabha Atomic Research Centre
HHHC	Horizontal Heater Horizontal Cooler
HHVC	Horizontal Heater Vertical Cooler
NOLSTA	NOn-Linear STAbility
SCW	Supercritical Water
SPNCL	Supercritical Pressure Natural Circulation Loop
VHHC	Vertical Heater Horizontal Cooler
VHVC	Vertical Heater Vertical Cooler

Greek Symbols

β	isobaric thermal expansion coefficient (K^{-1})
δ^*	dimensionless Dirac delta function

Λ	friction dimensionless group (Euler number)
λ	eigen value
Π_h	heated perimeter (m)
$\boldsymbol{\rho}$	density (kg/m^3) or spectral radius
μ	dynamic viscosity of fluid (Pa-s)

ρ = Density
μ = Dynamic Viscosity
ν = Kinematic viscosity

π_B = Non-dimensional parameter for buoyancy effect = $\frac{q\beta_b D}{k_b}$

Subscripts

0	reference value
b	bulk fluid
h	Heated
heater	Heater
i	Inside
in	Inlet
min	Minimum
o	Outside
osc	Oscillation
out	Outlet
pc	Pseudocritical
ss	steady state
w	Wall

b = Bulk fluid
Corr = Correlation
Exp = Experimental
J = No. of thermocouple locations
m = Mean
min = Minimum
P = Percentage error
pc = Pseudocritical
rms = root mean square
t = Temperature
w = Wall
x = Steady state no.
y = Thermocouple location no.

REFERENCES TO SECTION 7

[7.1] OKA, Y., KOSHIZUKA, S., Concept and Design of a Supercritical-Pressure, Direct-Cycle Light Water Cooled Reactor, Nuclear Technology, **103**, (1993), 295–302.

[7.2] OKA, Y., KOSHIZUKA, S., Design Concept of Once-Through Cycle Supercritical Light Water Cooled Reactors, Proc. International Symposium on Supercritical Reactor (SCR-2000), Tokyo, 2000.

[7.3] HEUSENER, G., MULLER, U., SCHULENBERG, T., SQUARER, D., A European Development Program for A High Performance Light Water Reactor (HPLWR), Proc. International Symposium on Supercritical Reactor (SCR-2000), Tokyo, 2000.
[7.4] ZHAO, J., SAHA P., KAZIMI, M.S., Stability of Supercritical Water-Cooled Reactor during Steady-State and Sliding Pressure Start-Up, Proc. 11th Int. Topical Meeting on Nuclear Thermal–hydraulics (NURETH-11), Avignon, 2005.
[7.5] SILIN, V.A., VOZNESENSKY, V.A., AFROV, A.M., The Light Water Integral Reactor with Natural Circulation of the Coolant at Supercritical Pressure (B:500 SKDI), Nuclear Engineering and Design, **144**, (1993), 327–336.
[7.6] BUSHBY, S.J., DIMMICK, G.R., DUFFEY, R.B., SPINKS, N.J., BURRILL, K.A., CHAN, P.S.W., Conceptual Designs for Advanced, High-Temperature CANDU Reactors, Proc. International Symposium on Supercritical Reactor (SCR-2000), Tokyo, 2000.
[7.7] HARDEN, D., BOGGS, J., Transient Flow Characteristics of a Natural Circulation Loop Operated in the Critical Region, Proc. Heat Transfer Fluid Mech. Inst., **38**, 1964.
[7.8] ADELT, M., MIKIELEWICZ, J., Heat Transfer in a Channel at Supercritical Pressure, International Journal of Heat and Mass Transfer, **44**, (1981), 1667–1674.
[7.9] LOMPERSKI, S., CHO, D., JAIN, R., CORRADINI, M.L., Stability of a Natural Circulation Loop with a Fluid Heated through the Thermodynamic Pseudo-Critical Point, Proc. 4th International Congress on Advances in Nuclear Power Plants (ICAPP'04), Pittsburgh, 2004.
[7.10] YOSHIKAWA, S., SMITH, R.L. JR., INOMATA, H., MATSUMURA, Y., ARAI, K., Performance of a Natural Circulation System for Supercritical Fluids, Journal of Supercritical Fluids, **36**, (2005), 70–80.
[7.11] T'JOEN, C., ROHDE, M., Experimental Study of the Coupled Thermo-Hydraulic–Neutronic Stability of a Natural Circulation HPLWR, Nuclear Engineering and Design, **242**, (2012), 221– 232.
[7.12] XIONG, T., YAN, X., XIAO, Z., LI, Y., HUANG Y., YU, J., Experimental Study on Flow Instability in Parallel Channels with Supercritical Water, Annals of Nuclear Energy, **48**, (2012), 60–67.
[7.13] XI, X., XIAO, Z., YAN, X., XIONG T., HUANG, Y., Numerical Simulation of the Flow Instability between Two Heated Parallel Channels with Supercritical Water, Annals of Nuclear Energy, **64**, (2014), 57–66.
[7.14] CHEN, L., DENG, B.L., ZHANG, R.X., Experimental Study of Trans-Critical and Supercritical CO_2 Natural Circulation Flow in a Closed Loop, Applied Thermal Engineering, **59**, (2013), 1–13.
[7.15] LIU, G., HUANG, Y., WANG, J., LV, F., Effect of Buoyancy and Flow Acceleration on Heat Transfer of Supercritical CO_2 in Natural Circulation Loop, International Journal of Heat and Mass Transfer, **91**, (2015), 640–646.
[7.16] LIU, G., HUANG, Y., WANG, J., LV, F., LIU, S., Experimental Research and Theoretical Analysis of Flow Instability in Supercritical Carbon Dioxide Natural Circulation Loop, Applied Energy, **205**, (2017), 813–821.
[7.17] SADHU, S., RAMGOPAL, M., BHATTACHARYYA, S., Experimental Studies on an Air-Cooled Natural Circulation Loop based on Supercritical Carbon Dioxide – Part A: Steady State Operation, Applied Thermal Engineering, **133**, (2018), 809–818.

[7.18] SADHU, S., RAMGOPAL, M., BHATTACHARYYA, S., Experimental Studies on an Air-Cooled Natural Circulation Loop based on Supercritical Carbon Dioxide – Part B: Transient Operation, Applied Thermal Engineering, **133**, (2018), 819–827.
[7.19] CHATOORGOON, V., Stability of Supercritical Fluid Flow in a Single-Channel Natural-Convection Loop, International Journal of Heat and Mass Transfer, **44**, (2001), 1963–1972.
[7.20] JAIN, R., CORRANDINI, M.L., A Linear Stability Analysis for Natural-Circulation Loops under Supercritical Conditions, Nuclear Technology, **155**, (2006), 312–323.
[7.21] AMBROSINI, W., SHARABI, M., Dimensionless Parameters in Stability Analysis of Heated Channels with Fluids at Supercritical Pressures, Nucl. Eng. Des., **238**, (2008), 1917–1929.
[7.22] CHATOORGOON, V., VOODI, A., UPADHYE, P., The Stability Boundary for Supercritical Flow in Natural-Convection Loops Part II: CO_2 and H_2, Nuclear Engineering and Design, **235**, (2005), 2581–2593.
[7.23] JAIN, P.K., RIZWAN-UDDIN, Numerical Analysis of Supercritical Flow Instabilities in a Natural Circulation Loop, Nuclear Engineering and Design, **238**, (2008), 1947–1957.
[7.24] SHARMA, M., PILKHWAL, D.S., VIJAYAN, P.K., SAHA, D., SINHA, R.K., Steady State Behaviour of Natural Circulation Loops Operating with Supercritical Fluids for Open and Closed Loop Boundary Conditions, Heat Transfer Engineering Journal, **33, 9**, (2012), 1–12.
[7.25] CHEN, L., ZHANG, X.R., YAMAGUCHI, H., LIU, Z.S., Effect of Heat Transfer on Instabilities and Transitions of Supercritical CO_2 Flow in a Natural Circulation Loop, International Journal of Heat and Mass Transfer, **53**, (2010), 4101–4111.
[7.26] CAO, Y., ZHANG, X.-R., Flow and Heat Transfer Characteristics of Supercritical CO_2 in a Natural Circulation Loop, International Journal of Thermal Sciences, **58**, (2012), 52–60.
[7.27] ARCHANA, V., VAIDYA, A.M., VIJAYAN, P.K., Flow Transients in Supercritical CO_2 Natural Circulation Loop, (2015).
[7.28] ARCHANA, V., VAIDYA, A.M., VIJAYAN, P.K., Numerical Modelling of Supercritical CO_2 Natural Circulation Loop, Nuclear Engineering and Design, **293**, (2015), 330–345.
[7.29] TILAK, A.K., BASU, D.N., Computational Investigation of the Dynamic Response of a Supercritical Natural Circulation Loop to Aperiodic and Periodic Excitations, Nuclear Engineering and Design, **284**, (2015), 252–263.
[7.30] KRISHNA, M., SARKAR, S., BASU, D.N., Numerical Comparison of Thermalhydraulic Aspects of Supercritical Carbon Dioxide and Subcritical Water Based Natural Circulation Loop, Nuclear Engineering and Technology, **49**, (2017), 503–512.
[7.31] ASAKO, Y., SHARMA, M., Modification of SIMPLE Algorithm to Handle Supercritical Natural Circulation in a Loop, International Journal of Heat and Mass Transfer, **126**, (2018), 425–431.
[7.32] MA, D., ZHOU, T., FENG, X., HUANG, Y., Research on Flow Characteristics in Supercritical Water Natural Circulation: Influence of Heating Power Distribution, Nuclear Engineering and Technology, **50**, (2018), 1079–1087.
[7.33] CHEN, J., GU, H., XIONG, Z., Development of One-Dimensional Transient Model for Predicting Flow Instability at Supercritical Pressures, Progress in Nuclear Energy, **112**, (2019), 162–170.

[7.34] INTERNATIONAL ATOMIC ENERGY AGENCY, Heat Transfer Behaviour and Thermohydraulics Code Testing for Supercritical Water Cooled Reactors (SCWRs), IAEA-TECDOC-1746, IAEA, Vienna (2014).
[7.35] YAMAGATA K., NISHIKAWA K., HASEGAWA S., FUJI T., YOSHIDA S., Forced Convective Heat Transfer to Supercritical Water Flowing in Tubes, J Heat Mass Transfer, **15, 12**, (1972), 2575, 2593.
[7.36] SWENSON, H.S., CARVER, J.R., KAKARALA, C.R., Heat transfer to Supercritical Water in Smooth-Bore Tubes, J Heat Transfer, **87**, **4**, (1965), 477–484.
[7.37] JACKSON, J.D., LUTTERODT, K.E., WEINBERG, R., Experimental Studies of Buoyancy-Influenced Convective Heat Transfer in Heated Vertical Tubes at Pressures Just Above and Just Below the Thermodynamic Critical Value, Proc. GENES4/ANP, Kyoto, 2003.
[7.38] FEWSTER, J., JACKSON, J.D., Experiments on Supercritical Pressure Convective Heat Transfer Having Relevance to SCWR, Proc. 4th International Congress on Advances in Nuclear Power Plants (ICAPP'04), Pittsburgh, 2004.
[7.39] PIORO, I.L., DUFFEY, R.B., Experimental Heat Transfer in Supercritical Water Flowing inside Channels (Survey), Nucl. Eng. Des., **235, 22**, (2005), 2407, 2430.
[7.40] DUFFEY, R.B., PIORO, I.L., Experimental Heat Transfer in Supercritical Carbon Dioxide Flowing inside Channels (Survey), Nucl. Eng. Des., **235, 8**, (2005), 913, 924.
[7.41] SHARMA, M., PILKHWAL, D.S., VIJAYAN, P.K., SAHA, D., Heat Transfer Studies for Supercritical Fluids under Natural Circulation Conditions,Proc. of 5th Int. Sym. SCWR (ISSCWR-5), Vancouver, 2011.
[7.42] JACKSON, J.D., Consideration of the Heat Transfer Properties of Supercritical Pressure Water in Connection with the Cooling of Advanced Nuclear Reactors, Proc. 13th Pacific Basin Nuclear Conference, Shenzhen, 2002.
[7.43] SHITSMAN, M.W., Heat Transfer to Supercritical Helium, Carbon-Dioxide, and Water: Analysis of Thermodynamic and Transport Properties and Experimental Data, Cryogenics, **14, 2**, (1974), 77–83.
[7.44] BRINGER, R.P., SMITH, J.M., Heat Transfer in the Critical Region, AIChE J., **3, 1**, (1957), 49–55.
[7.45] SHARMA, M., VIJAYAN, P.K., PILKHWAL, D.S., ASAKO, Y., Steady State and Stability Characteristics of Natural Circulation Loops Operating with Carbon Dioxide at Supercritical Pressures for Open and Closed Loop Boundary Conditions, Nuclear Engineering and Design, **265**, (2013), 737–754.
[7.46] DANG, C., HIHARA, E., Numerical Study on In-Tube Laminar Heat Transfer of Supercritical Fluids, Applied Thermal Engineering, **30**, (2010), 1567–1573.
[7.47] WANG, W., YANG, D., LIANG, Z., QU, M., OUYANG, S., Experimental Investigations on Flow Instabilities of Ultra-Supercritical Water in Parallel Channels, Applied Thermal Engineering, **147**, (2019), 819–828.
[7.48] SHARMA, M., VIJAYAN, P. K., PILKHWAL, D. S., ASAKO, Y., Natural convective flow and heat transfer studies for supercritical water in a rectangular circulation loop, Nucl. Eng. Des. **273** (2014) 304–320.
[7.49] SWAPNALEE, B.T., VIJAYAN, P.K., SHARMA, M., PILKHWAL, D.S., Steady State Flow and Static Instability of Supercritical Natural Circulation Loops, Nuclear Engineering and Design, **245**, (2012), 99–112.

[7.50] ARCHANA V., Steady State and Transient Characteristics of Supercritical Pressure Natural Circulation Loop, Ph.D. Thesis, Homi Bhabha National Institute, Mumbai, 2017.
[7.51] MCADAMS, W.H., Heat Transmission, 2nd edition, McGraw-Hill, New York, (1942).
[7.52] DITTUS, F.W., BOELTER, L.M.K., Heat Transfer in Automobile Radiators of the Tubular Type, University of California, Berkeley, Publications on Engineering, **2, 13**, (1930), 443–461.
[7.53] NATIONAL INSTITUTE OF STANDARDS AND TECHNOLOGY, NIST Reference Fluid Thermodynamic and Transport Properties - REFPROP, Standard Reference Database 23, Ver. 9.1, Department of Commerce, Boulder, CO, USA, 2013.
[7.54] ZHAO, M., GU, H.Y., CHENG, X., Experimental Study on Heat Transfer of Supercritical Water Flowing Downward in Circular Tubes, Annals of Nuclear Energy, **63**, (2014), 339–349.
[7.55] BAE, Y.Y., KIM, H.Y., Convective Heat Transfer to CO_2 at a Supercritical Pressure Flowing Vertically in Tubes and an Annular Channel, Experimental Thermal and Fluid Science, **33**, (2009), 329–339.
[7.56] WANG, C., LI, H., Evaluation of the Heat Transfer Correlations for Supercritical Pressure Water in Vertical Tubes, Heat Transfer Eng., **35, 6–8**, (2014), 685–692.
[7.57] ORNATSKY, A.P., GLUSHCHENKO, L.P., SIOMIN, E.T., KALACHYOV, S.I., The Research of Temperature Conditions of Small Diameter Parallel Tubes Cooled by Water under Supercritical Pressures, Proc. 4th International Heat Transfer Conference, Paris-Versailles, 1970.
[7.58] PETUKHOV, B.S., KURGANOV, V.A., ANKUDINOV, V.B., Heat Transfer and Flow Resistance in the Turbulent Pipe Flow of a Fluid with Near-Critical State Parameters, High Temp. Sci., **21**, (1983), 81–89.
[7.59] BAE, Y.Y., KIM, H.Y., KANG, D.J., Forced and Mixed Convection Heat Transfer to Supercritical CO_2 Vertically Flowing in a Uniformly-Heated Circular Tube, Experimental Thermal and Fluid Science, **34**, (2010), 1295–1308.
[7.60] LIU, G., HUANG, Y., WANG J., LEUNG, L.H.K., Heat Transfer of Supercritical Carbon Dioxide Flowing in a Rectangular Circulation Loop, Applied Thermal Engineering, **98**, (2016), 39–48.
[7.61] PETUKHOV, B.S., KRASNOSHCHEKOV, E.A., PROTOPOPOV, V.S., An Investigation of Heat Transfer to Fluids Flowing in Pipes under Supercritical Conditions, Proc. 1961 International Heat Transfer Conference, Boulder, (1961), 569–578.
[7.62] WATTS, M.J., CHOU, C.T., Mixed Convection Heat Transfer to Supercritical Pressure Water, Proc. 7th Int. Heat Transfer Conference (IHTC-7), Munich, (1982), 495–500.
[7.63] KIM, D.E., KIM, M.H., Experimental Investigation of Heat Transfer in Vertical Upward and Downward Supercritical CO_2 Flow in a Circular Tube, International Journal of Heat and Fluid Flow, **32**, (2011), 176–191.
[7.64] MOKRY, S., PIORO, I.L., FARAH, A., KING, K., GUPTA, S., PEIMAN, W., KIRILLOV, P.L., Development of Supercritical Water Heat-Transfer Correlation for Vertical Bare Tubes, Nuclear Engineering and Design, **241**, (2011), 1126–1136.
[7.65] PREDA, T., SALTANOV, EU., PIORO, I., GABRIEL, K., Development of a Heat Transfer Correlation for Supercritical CO_2 based on Multiple Data Sets, Proc. 20th International Conference On Nuclear Engineering (ICONE-20), Anaheim, (2012), 211–217.

[7.66] GUPTA, S., MOKRY, S., PIORO, I., Developing a Heat-Transfer Correlation for Supercritical-Water Flowing in Vertical Tubes and Its Application in SCWR, Proc. 19th Int. Conf. On Nuclear Engineering (ICONE-19), Makuhari, 2011.
[7.67] JACKSON, J.D., FEWSTER, J., Forced Convection Data for Supercritical Pressure Fluids, HTFS 1975, Paper No. 21540, (1975).
[7.68] RAZUMOVSKIY, V.G., ORNATSKIY, A.P., MAYEVSKIY, Y.M., Local Heat Transfer and Hydraulic Behavior in Turbulent Channel Flow of Water at Supercritical Pressure, Heat Transfer-Soviet Res., **22, 1**, (1990), 91–102.
[7.69] YU, J., JIA, B., WU, D., WANG, D., Optimization of Heat Transfer Coefficient Correlation at Supercritical Pressure Using Genetic Algorithms, Heat Mass Transfer, **45**, (2009), 757–766.
[7.70] JACKSON, J.D., HALL, W.B., Forced Convection Heat Transfer to Fluids at Supercritical Pressure, Turbulent Forced Convection in Channels and Bundles, Editors: S. Kakaç and D.B. Spalding, Hemisphere Publishing Corp., New York, **2**, (1979), 563–612.
[7.71] KRASNOSHCHEKOV, E.A., PROTOPOPOV, V.S., VAN, F., KURAEVA, I.V., Experimental Investigation of Heat Transfer for Carbon Dioxide in the Supercritical Region, Gazley, Jr., C., Hartnett, J.P., Ecker, E.R.C. (Eds.), Proc. 2nd All-Soviet Union Conference on Heat and Mass Transfer, Minsk, 1964 (Published as Rand Report R-451-PR, **1**, (1967), 26–35).
[7.72] CHEN, W., FANG, X., A New Heat Transfer Correlation for Supercritical Water Flowing in Vertical Tube, International Journal of Heat and Mass Transfer, **78**, (2014), 156–160.
[7.73] SALTANOV, E., PIORO, I., MANN, D., GUPTA, S., MOKRY, S., HARVEL, G., Study on Specifics of Forced-Convective Heat Transfer in Supercritical Carbon Dioxide, J. Nucl. Eng. Radiat. Sci., **1**, (2015), 1–8.
[7.74] GUPTA, S., FARAH, A., KING, K., MOKRY, S., PIORO, I., Developing New Heat-Transfer Correlation for Supercritical-Water Flow in Vertical Bare Tubes, Proc. 18th International Conference on Nuclear Engineering (ICONE–18), Xi'an, 2009.
[7.75] KIM, D.E., KIM, M.H., Experimental Study of the Effects of Flow Acceleration and Buoyancy on Heat Transfer in a Supercritical Fluid Flow in a Circular Tube, Nucl. Eng. Des., **240**, (2010), 3336–3349.
[7.76] MOKRY, S., PIORO, I., Heat Transfer Correlation for Supercritical Carbon Dioxide Flowing Upward in a Vertical Bare Tube, Proc. Supercritical CO_2 Power Cycle Symposium, Boulder, 2011.
[7.77] GUPTA, S., SALTANOV, E., MOKRY, S.J., PIORO, I., TREVANI, L., MCGILLIVRAY, D., Developing Empirical Heat-Transfer Correlations for Supercritical CO_2 Flowing in Vertical Bare Tubes, Nuclear Engineering and Design, **261**, (2013), 116–131.
[7.78] GORBAN', L.M., POMET'KO, R.S., KHRYASCHEV, O.A., Modeling of Water Heat Transfer with Freon of Supercritical Pressure, FEI-1766, Institute of Physics and Power Engineering, Obninsk, Russia, 1990 (in Russian).
[7.79] CHEN, Y., YANG, C., ZHAO, M., BI, K., DU, K., An Experiment of Natural Circulation Flow and Heat Transfer with Supercritical Water in Parallel Channels, Journal of Nuclear Engineering and Radiation Science, **2**, (2016), 011006-1 - 011006-8.

[7.80] ZHANG, L., CHATOORGOON, V., DERKSEN, R., Experimental Flow Instability Study of a Natural Circulation Loop with Supercritical CO_2, Proc. 2016 Pacific Basin Nuclear Conference, Beijing, 2016.
[7.81] BALASKÓ, M., HORVÁTH, L., HORVÁTH, Á., KISS, A., ASZÓDI, A., Study on the Properties of Supercritical Water Flowing in a Closed Loop Using Dynamic Neutron Radiography, Proc. 7th International Topical Meeting on Neutron Radiography, Kingston, 2012.
[7.82] BALASKÓ, M., HORVÁTH, L., HORVÁTH, Á., KISS, A., ASZÓDI, A., Study on the Properties of Supercritical Water Flowing in a Closed Loop Using Dynamic Neutron Radiography, Physics Procedia, **43**, (2013), 254–263.
[7.83] BALASKÓ, M., HORVÁTH, L., HORVÁTH, Á., KISS, A., ASZÓDI, A., Study on the Heat Transfer of Supercritical Pressure Water Flowing in a Closed Loop using Dynamic Neutron Radiography, Proc. 6th International Symposium on Supercritical Water-Cooled Reactors (ISSCWR-6), Shenzhen, 2013.
[7.84] KISS, A., BALASKÓ, M., HORVÁTH, L., KIS, Z., ASZÓDI, A., Experimental Investigation of the Thermal Hydraulics of Supercritical Water under Natural Circulation in a Closed Loop, Annals of Nuclear Energy, **100, 2**, (2017), 178–203.
[7.85] KISS, A., BALASKÓ, M., HORVÁTH, L., KIS, Z., BARTOS, J., ASZÓDI, A., Study on the Thermal Hydraulics of Supercritical Water under Natural Circulation Flowing in a Closed Loop, Proc. 8th International Symposium on Supercritical Water-Cooled Reactors (ISSCWR-8), Chengdu, 2017.
[7.86] CHATOORGOON, V., SPORTS - A Simple Non-Linear Thermalhydraulic Stability Code, Nuclear Engineering and Design, **93, 1**, (1986), 51–67.
[7.87] HANNA, B.N., CATHENA: A Thermalhydraulic Code for CANDU Analysis, Nuclear Engineering and Design, **180, 2**, (1998), 113–131.
[7.88] DEBRAH, S.K., AMBROSINI, W., CHEN, Y., Discussion on the Stability of Natural Circulation Loops with Supercritical Pressure Fluids, Annals of Nuclear Energy, **54**, (2013), 47–57.
[7.89] AMBROSINI, W., On Some Relevant Effects in the Simulation of Flow Stability with Fluids at Supercritical Pressure, Journal of Nuclear Engineering and Radiation Science, **2**, (2016).
[7.90] DEBRAH, S.K., AMBROSINI, W., CHEN, Y., Assessment of a New Model for the Linear And Nonlinear Stability Analysis of Natural Circulation Loops with Supercritical Fluids, Annals of Nuclear Energy, **58**, (2013), 272–285.
[7.91] CHEN, Y., ZHAO, M., YANG, C., BI, K., DU, K., An Experiment on Flow and Heat Transfer Characteristics in Natural Circulation of Supercritical Water, Proc. 3rd China–Canada Joint Workshop on Supercritical-Water-Cooled Reactors (CCSC-2012), Xi'an, 2012.
[7.92] SCIENTECH INC., RELAP5/Mod3 Code Manual. Volume I: Code Structure, System Models and Solution Methods, The Thermal Hydraulics Group, Idaho, 1999.

8. CRITICAL FLOW

An accurate prediction of the amount of coolant discharging from an opening is essential in the design of the pressure relieve valve and the confirmation of the effectiveness of the safety system in SCWRs. The high system pressure could lead to the choking flow phenomenon at the opening affecting the discharge flow rate. This is referred to as the 'critical flow'.

For SCWRs with a low pressure emergency core cooing system, the pressure relieve valve in the automatice depressurization system is activated to depressurize the system and facilitate the injection of cooling water in case of accidents. An adequate design of the valve would ensure proper opening for pressure relieve.

During a postulated large break loss of coolant accident (LBLOCA) event, coolant in the core is discharged from the break location and could lead to choking at supercritical pressures. The amount of coolant discharged from the break has a significant implication on the reactor safety due to the low coolant inventory in SCWRs compared to LWRs.

Publications on critical flow available prior to 2013 have been reviewed and summarized [8.1]. While a relatively large amount of experiment data were collected at subcritical pressures, data obtained at restrictions with supercritical upstream pressures are scarce. Furthermore, large scatter has been observed among data obtained at supercritical pressures, particularly at the vicinity of the pseudocritical poInt.

Prediction methods for critical flow at subcritical pressures (such as the homogeneous model [8.2], the Moody model [8.3] and the Henry–Fauske non-equilibrium model [8.4]) were assessed against the limited database. The Henry–Fauske model generally underpredicts the discharge flow rate while the homogeneous model overpredicts. Improvement to these models would enhance the prediction accuracy and strengthen the analytical results of the LBLOCA event.

Experiments and databases obtained prior to 2013 have been summarized in the IAEA publication [8.1] and are not repeated. The latest experiments are summarized below.

8.1. WATER FLOW THROUGH NOZZLES

[8.5] performed critical flow experiments with water flow through a nozzle at supercritical upstream pressures. A schematic diagram of the test facility is shown in Fig. 8.1. The test facility consists of two loops: the supercritical water loop and the medium pressure water loop. Water was heated up to the desired pressure at the supercritical water loop and discharged through the nozzle to the medium pressure water loop, where the discharge pressure were controllable separately up to 4.0 MPa.

Two nozzles with a sharp-edge opening were manufactured from solid Hastelloy C-276 cylinders. Fig. 8.2 illustrates the configuration and dimensions of the nozzle. The opening sizes covered in the experiment were 1.0 and 1.395 mm over a distance of 3.175 mm. Three and five pressure taps were allocated at the upstream and downstream sections, respectively, of the small opening. These pressure taps facilitated establishing the pressure profile along the nozzle. Measurements were

obtained at ranges of upstream pressure from 22.1 to 32.1 MPa, upstream temperature from 52 to 502°C and discharge pressure from 0.1 to 3.6 MPa.

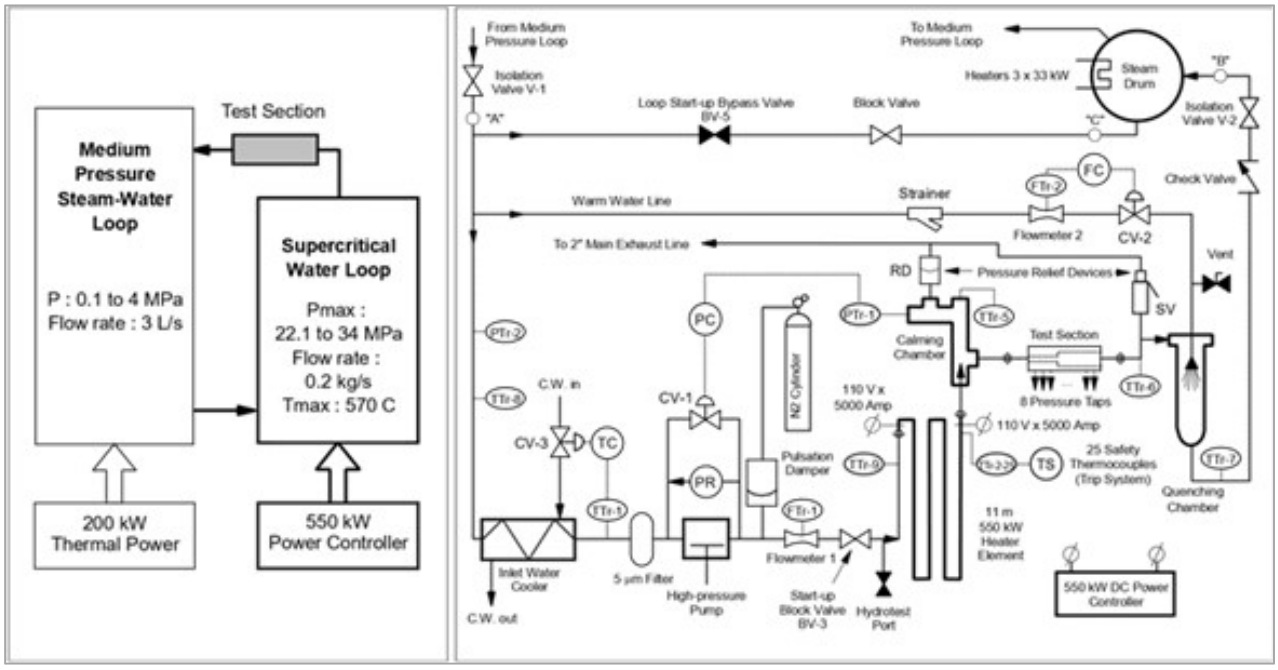

(a) Parallel hydraulic arrangement *(b) Flow diagram of the supercritical water system*

Fig. 8.1. Schematic diagram of critical flow test facility.

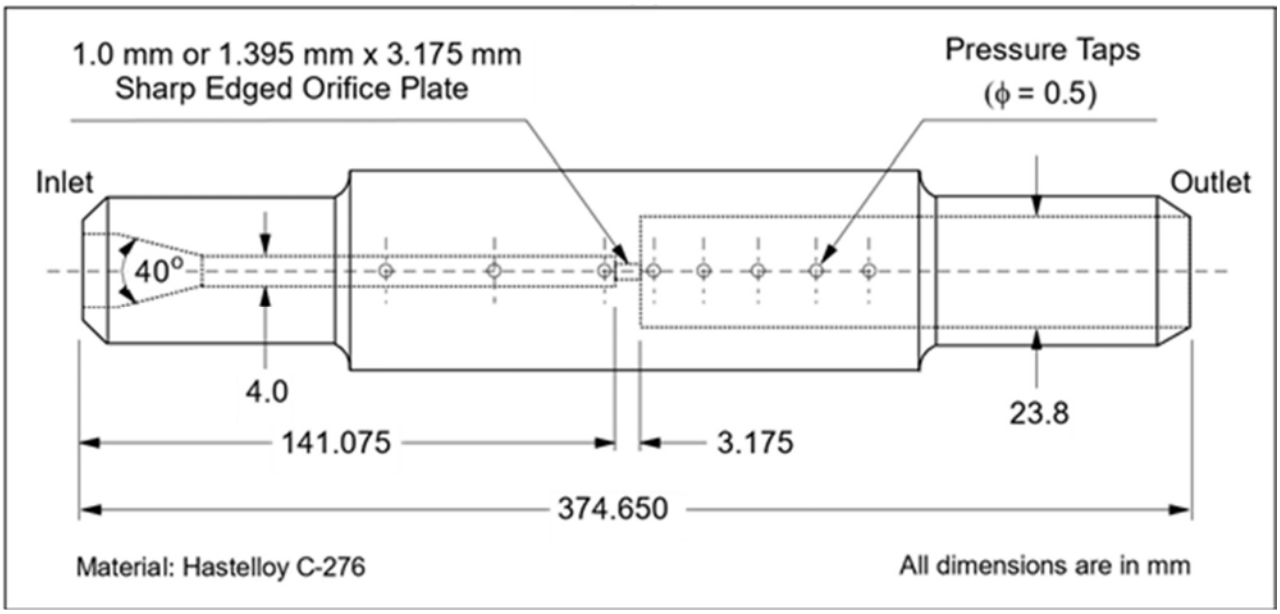

Fig. 8.2. Schematic diagram of nozzle with a sharp edge opening.

Fig. 8.3 presents the critical mass flux with flow through the two nozzles at supercritical upstream pressures. The critical mass flux decreases monotonically with increasing fluid temperature (or decreasing ΔT_{pc}). It is higher for the nozzle with 1 mm opening than that with 1.395 mm opening at ΔT_{pc} greater than 50°C. There are little differences in critical mass flux between the two nozzles at ΔT_{pc} less than 50°C. [8.5] compared their experimental results against those of [8.6]. They observed significant differences in critical mass flux at the high ΔT_{pc} region, but similarity between these two experiments at ΔT_{pc} less than 50°C. The scatter among experimental results of [8.6] for one size of orifice opening (i.e., 1.41 mm) is much larger than those of [8.5].

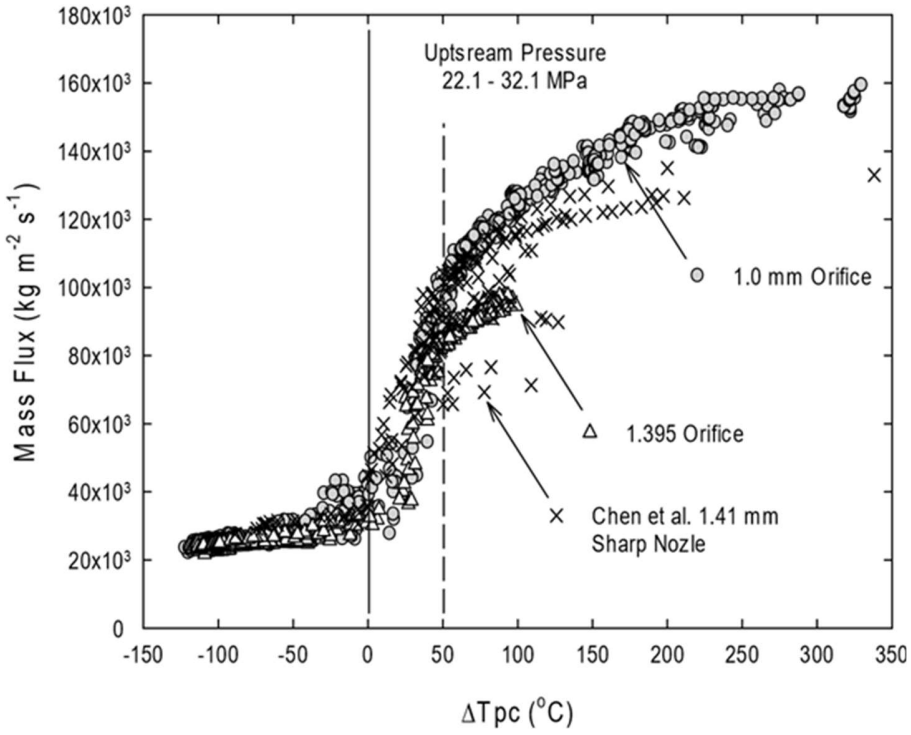

Fig. 8.3. Critical mass flux with flow through two nozzles at supercritical upstream pressures.

8.2. CRITICAL FLOW CORRELATION

[8.6] introduced a modified homogeneous equation to represent their critical mass flux measurement. The modified homogeneous equation is expressed as

$$G_{cr} = \left(\frac{2\left(h_o - (1-x_E)h_{lE} - x_E h_{gE}\right)}{\frac{C}{\rho^2} + \left((1-x_E)v_{lE} + x_E v_{gE}\right)^2} \right)^{1/2} \tag{8.1}$$

Reference [8.6] recommended a coefficient 'C' of 0.6 based on their experimental results of critical mass flux. Reference [8.5] correlated their critical mass flux values using the same equation but noted different coefficients for the two nozzles. A value of 0.8 was appropriate for the nozzle with

an 1 mm opening, but 1.6 for the nozzle with an 1.395 mm opening (see Fig. 8.4 for the comparison between predictions and experimental critical mass fluxes). [8.5] commented on the complex nature of critical flow and the use of the modified homogeneous equation represented an interim approach until a better understanding of the phenomena is advanced.

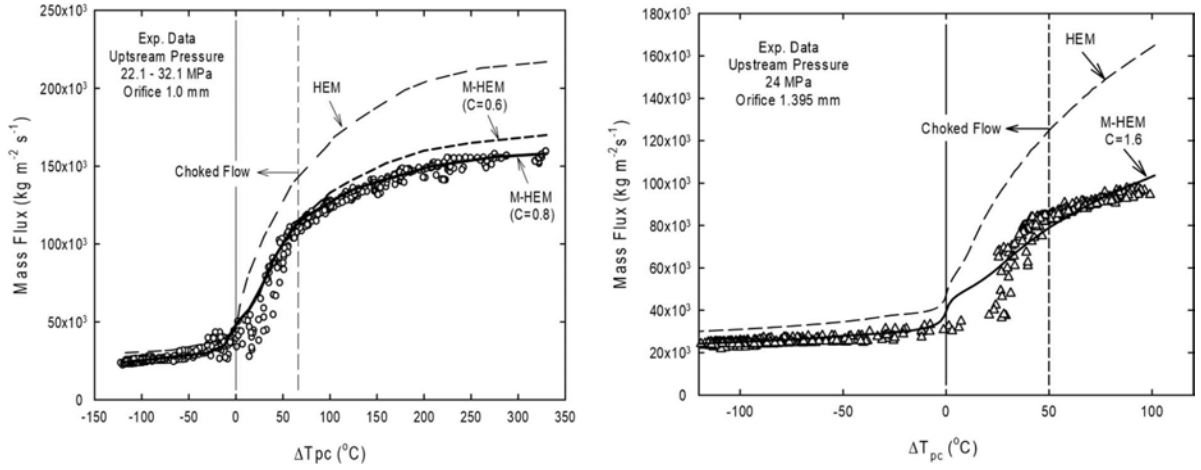

(a) *(b)*

Fig. 8.4. Comparison of predictions obtained with the HEM and M-HEM with data: a) 1.0 mm orifice; b) 1.395 mm orifice.

Reference [8.7] developed a critical flow model based on isentropic flow and thermal equilibrium assumptions, then considering the influence of friction and local resistance, the final model is expressed as following:

$$G = C\rho(P_e, s_0)\sqrt{2(h_0 - h(P_e, s_0))} \tag{8.2}$$

where C is resistance factor, h_o is the specific enthalpy at the nozzle inlet, s_o is the specific entropy at the nozzle outlet, P_e is the nozzle outlet pressure. A method of using the CFD software to calculate resistance factor C is proposed. The actual nozzle geometry is modelled and meshed, then for room temperature water flowing in nozzle condition, the mass flux can be calculated by CFD. Because the flow would not achieve critical flow for room temperature water, the resistance factor C can be calculated by the following expression:

$$C = \frac{G}{\sqrt{2\rho(p_0 - p_e)}} \tag{8.3}$$

where G is the mass flux calculated by CFD, ρ is fluid density, p_o is initial pressure, p_e is the atmosphere pressure. The comparisons of the present model with the data from [8.6] and the data from [8.8] are shown in Fig. 8.5 and Fig. 8.6, the corresponding resistance factor C is 0.8 and 0.9, respectively.

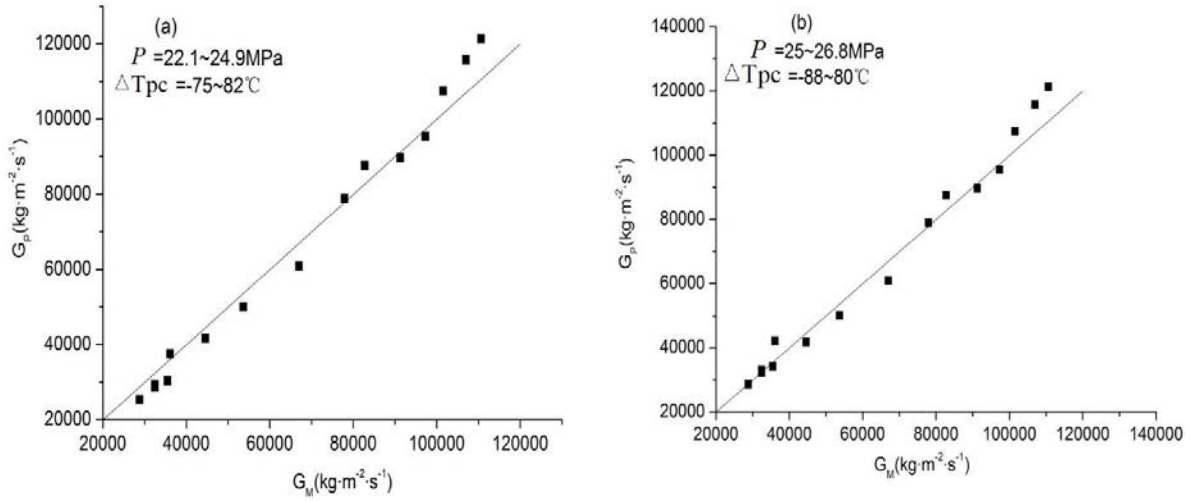

(a) *(b)*

Fig. 8.5. Comparison to the result of [8.6] (nozzle A with round edge, L/D=3, D=1.41mm) [8.7].

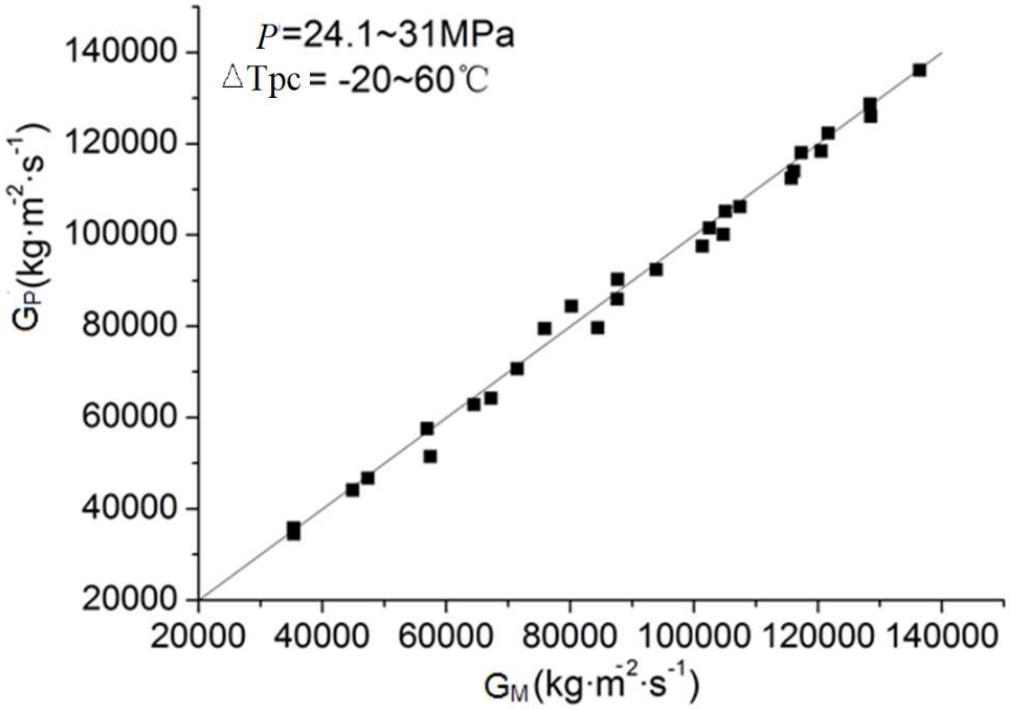

Fig. 8.6. Comparison to the result of [8.8] (Nozzle B, D=1.78mm, L/D=3) [8.7].

Nomenclature and Acronyms

C	*R*esistance factor (-)
D	Nozzle diameter (mm)
G	Mass flux (kg/(m^{2}s))
h	*S*pecific enthalpy (kJ/kg)
L	Nozzle length (mm)
P	Pressure (MPa)
s	Specific entropy (kJ/(kg·K))
T	Temperature (°C)
x	Quality (-)
ΔT_{pc}	Temperature difference between pseudo critical point and bulk fluid (°C)
ρ	Fluid density (kg/m^3)
ϕ	Hole diameter (mm)
υ	Specific volume (m^3/kg)

Subscripts

cr	critical
E, e	Nozzle exit
gE	Gas phase at exit
lE	Liquid phase at exit
M	Measure
max	Maximum
o	Stagnation condition
P	Predict
pc	*P*seudo-critical

Acronyms

HEM	Homogeneous equilibrium model
IAEA	International Atomic Energy Agency
LBLOCA	Large Break Loss Of Coolant Accident
LWR	Light Water Reactor
M-HEM	Modified homogeneous equilibrium model
SCWR	Super Critical Water cooled Reactor

REFERENCES TO SECTION 8

[8.1] INTERNATIONAL ATOMIC ENERGY AGENCY, Heat Transfer Behaviour and Thermohydraulics Code Testing for Supercritical Water Cooled Reactors (SCWRs), IAEATECDOC-1746, IAEA, Vienna (2014).

[8.2] STARKMAN E.S., S., V.E., NEUSEN, K.F. et al., Expansion of a Very Low Quality Two-Phase Fluid through A Convergent-Divergent Nozzle, J. Basic Engineering, **82, 2**, (1964), 247–256.

[8.3] MOODY, F.J., Maximum Flow Rate of a Single Component, Two-Phase Mixture, ASME Trans C, J. Heat Transfer, **87, 1**, (1965), 134–142.

[8.4] HENRY, R.E., FAUSKE, H.K., The Two-Phase Critical Flow of One-Component Mixtures in Nozzles, Orifices, and Short Tubes, Transactions of the ASME, Series C, Journal of Heat Transfer, **93**, (1971), 179–187.

[8.5] TEYSSEDOU, A., MUFTUOGLU, A., HIDOUCHE, A., Experimental Study of Choking Water Flow across Sharp Edged Orifices at Supercritical Pressures, Proc. 7th International Symposium on Supercritical Water-Cooled Reactors (ISSCWR-7), Helsinki, 2015.

[8.6] CHEN, Y., ZHAO, M., YANG, C., BI, K., DU, K., ZHANG, S., Research on Critical Flow of Water under Supercritical Pressures in Nozzles, Journal of Energy and Power Eng., (2012), 201–208.

[8.7] LV, Y., ZHAO, M., DU, K., A Critical Flow Model for Supercritical Pressures, Proc. 9th International Symposium on SCWRs (ISSCWR-9), Vancouver, 2019.

[8.8] LEE, D.H., SWINNERTON, D., Evaluation of Critical Flow for Supercritical Steam-Water, NP-3086, 1983.

9. CRITICAL HEAT FLUX NEAR CRITICAL PRESSURE

Phase change is not encountered at supercritical pressures during normal operating conditions. Therefore, the traditional safety criteria based on the critical heat flux (CHF) is no longer applicable. Instead, the cladding and fuel temperatures have been considered as the safety criterion for SCWRs. Having said that, information on CHF is still required for analyses of large break loss of coolant accidents, where the pressure decreases rapidly from supercritical to subcritical value, and for analyses of startup and shutdown operations, where the pressure changes gradually from subcritical to supercritical value and vice versa, respectively. The analysis of startup process focused on bringing the reactor to operating conditions without CHF occurrences.

9.1. TESTS AND DATABASE FOR TUBES

Many CHF studies were performed in support of the design and operations of the current fleet of nuclear reactors. This has led to an enormous amount of CHF data covering a wide range of flow conditions. However, most CHF data were obtained at pressures up to 18 MPa (covering the accident scenarios of LWRs). The following sections focus on CHF data obtained near the critical pressure (i.e., beyond 18 MPa), which is of interest to the SCWR safety analyses.

9.1.1. CHF DATABASES FOR WATER FLOW IN TUBES AT PRESSURES HIGHER THAN 18 MPA

A previously compiled CHF database (a result of collaboration work between AECL and University of Ottawa) for water flowing vertically upward in a circular tube [9.1] was added into the present water database to assess a CHF look-up table. The previously compiled CHF database covered the near critical pressure conditions. This database included 1163 CHF data points at different pressures, mass fluxes, and inlet temperatures.

TABLE 9.1. EXPERIMENTAL CONDITIONS COVERED IN CHF DATABASE AT HIGH PRESSURES

Reference	*D* (mm)	L_h (m)	*P* (MPa)	*G* (kg/(m²·s))	T_{in} (°C)	x_e (-)	q_c (MW/m²)
Alekseev et al. [9.2]	10	1–5	19.6	368–7304	94–350	-0.3–0.8	0.13–3.13
Bailey and Lee [9.3]	9.3	3.05	18.2	1028–4242	276–347	0.18–0.44	0.34–1.90
Becker et al. [9.4]	10	1–5	18–20	179–6977	94–357	-0.3–0.9	0.14–3.46
Kirillov et al. [9.5]	8	6	18	998–1002	43–310	0.3–0.52	0.25–0.59
Smolin et al. [9.6]	10.5	3–3.8	19.6	498–3496	152–343	0–0.445	0.23–1.72
Soderquist [9.7]	8–8.1	1–6	18–20	248–6025	255–355	-0.04–0.97	0.05–3.2
Yin et al. [9.8]	13.4	3.66	18–20	2018–2065	290–357	0.23–0.39	0.65–1.20
Zenkevich et al. [9.9]	5.8–15.1	0.25–6	19.6	499–5082	34–362	-0.49–0.62	0.14–4.75
Zenkevich et al. [9.10]	5.9–10.8	1–5.34	19.6	497–4500	131–357	-0.18–0.45	0.23–2.78

A comparison between different datasets ensures reliability and reproducibility of data. To obtain a second dataset that matches specific experimental conditions of interest, in most cases, one has to perform an experiment to reproduce the data. Besides the scarcity of the CHF data near the critical point, as discussed earlier, finding a second CHF dataset that very closely matches all flow conditions of a particular dataset turned out to be unattainable. For the present study, a comparison between old and recent data was performed to show agreement between old and recent data or provide an idea about the old and recent data trends. The CHF data presented in Fig. 9.1 were obtained at comparable pressures and mass fluxes. The [9.7] data, and the [9.3] data agree very well, though they were collected at very different times. The critical quality for the [9.11] data does not, however, overlap with the rest of the data.

9.1.2. RECENT CHF DATA OBTAINED WITH TUBES IN WATER FLOW AT PRESSURES HIGHER THAN 18 MPA

It is generally recognized that the mechnism governing low quality and subcooled CHF (referred to as departure from nucleate boiling, DNB) differs substantially from that governing CHF at high local quality (dryout). Over the past 8 years, CHF experiments under subcooled boiling condition [9.11] [9.12] and saturated boiling condition [9.13] with water flowing vertically upward in a circular tube at near critical pressures are performed by Chen in CIAE.

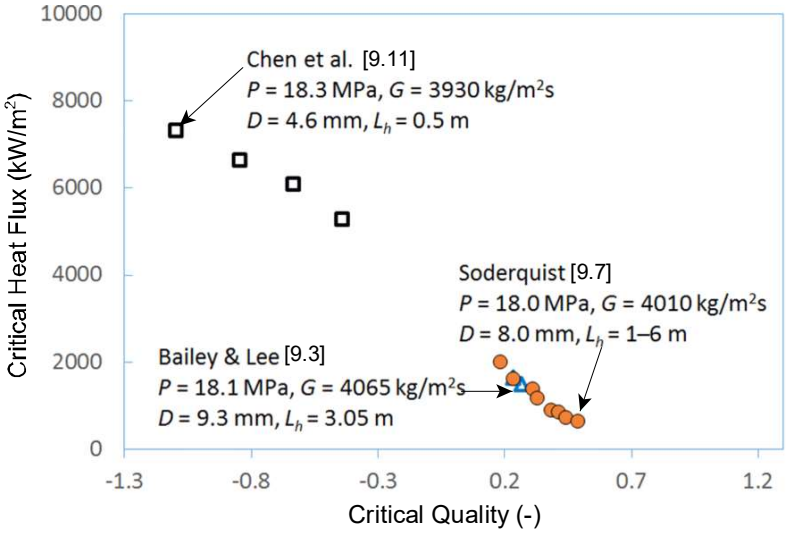

Fig. 9.1. CHF data comparison.

For the subcooled boiling CHF experiments, three Inconel-625 tubes were used: i) 4.62 mm ID, 6.5 mm OD and 0.5 m in heated length, ii) 7.98 mm ID, 9.6 mm OD and 0.8 m in heated length, iii) 10.89 mm ID, 12.7 mm OD and 1.1 m in heated length; and for the saturated boiling CHF tests, one tube of 8.2 mm ID, 11.5 mm OD and 2.4 m in heated length were adopted. The test section was heated by a DC supply with capacity of 7,000 A×65 V.

During the experiment, the pressure and the flow rate were kept constant, and the CHF is approached by increasing slowly the water temperature or the power to test section. When the CHF occurs and the wall temperature exceeds about 500°C, the photocell produces an output,

which switches off the power supply to test section. This technique was applied to detect CHF in tubes and annuli for all experiments [9.11]. Table 9.2 lists the experimental conditions covered in the exxperiments.

TABLE 9.2. EXPERIMENTAL CONDITIONS FOR DIFFERENT DIAMETERS OF TUBES

D (mm)	L_h (m)	P_{max} (MPa)	G (kg m^{-2}s^{-1})	T_{sat}-T_{in} (K)	To-T_s (K)	q_c (MWm^{-2})
4.62	0.5	20.6	556– 4055	110–354	1–169	0.77–9.3
7.98	0.8	20.4	476–1653	53–361	3–158	0.26–4.95
10.89	1.1	20.0	454–1144	169–345	4–141	0.92–3.3
8.20	2.4	21.0	1454–4500	169–345	20–0, (x=0.6)	0.2–5.6

The effect of inlet subcooling (T_{sat}–T_{in}) on the CHF with different diameters of tubes is shown in Fig. 9.2. Under all conditions, the CHF increases with an increase in inlet subcooling (T_{sat}–T_{in}) and decreases with a pressure increase. Reference [9.12] also supported the finding of [9.14] that the effect of heating length on CHF vanishes at axial distances greater than 200 mm, and CHF at subcooled conditions would only depend on local flow conditions.

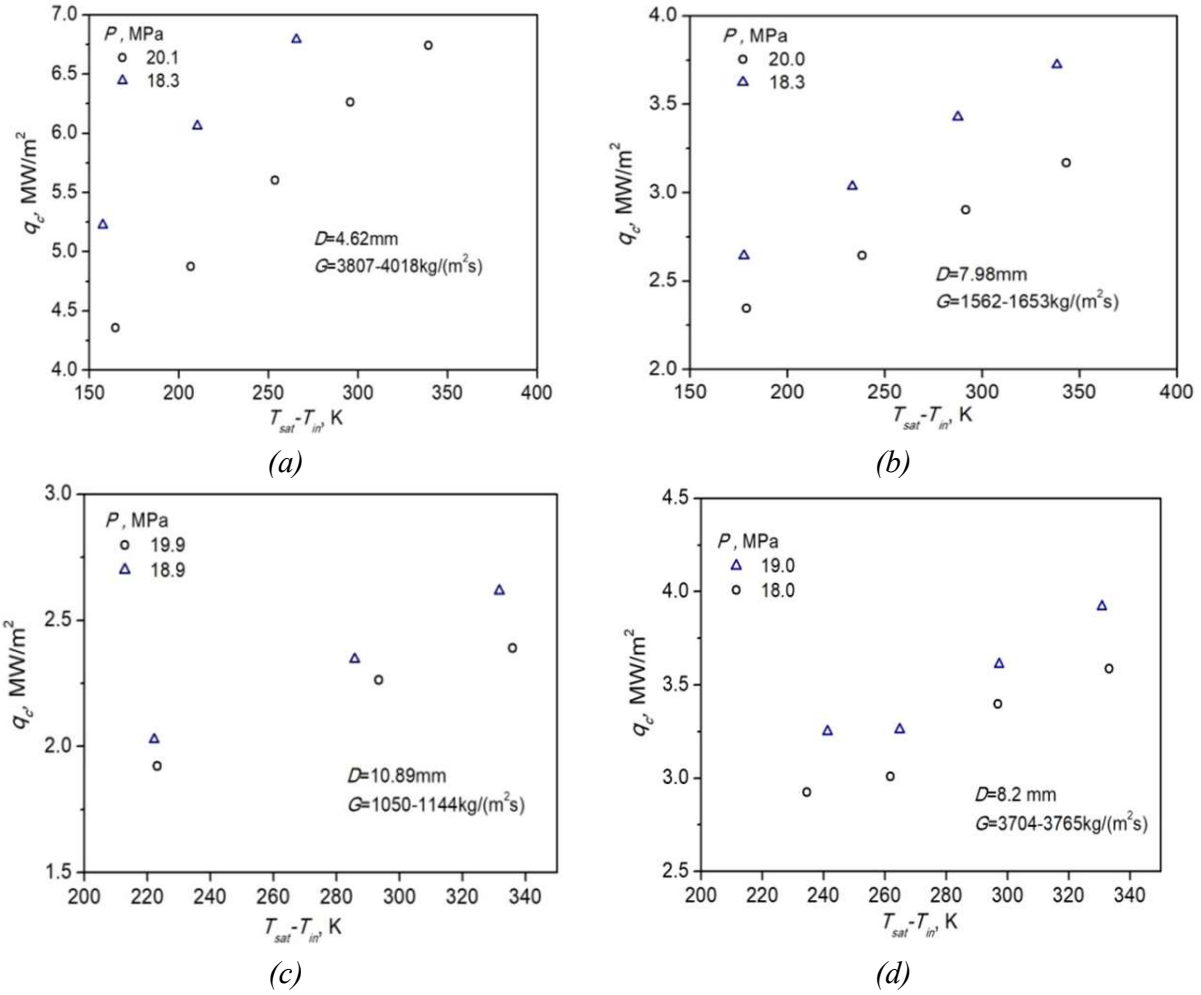

Fig. 9.2. Variations of CHF with inlet subcooling for different tubes (based on [9.11]).

The effect of mass flux on CHF is shown in Fig. 9.3, indicating the CHF *i*ncreases with increasing mass flux for the same pressure. At low mass fluxes, the CHF increases gradually withincreasing subcooling. The increasing trend is more distinct at high mass fluxes.

Reference [9.12] discussed the effect of pressure on CHF for low-to-medium flows (Fig. 9.4). As can be observed, at lower pressure the slope is relatively larger than that at higher pressure, which suggests when the pressure closes to the near critical point, the trend of CHF with inlet subcooling is not so strong as lower pressure. This is because at higher pressure the latent heat of evaporation decreases remarkably.

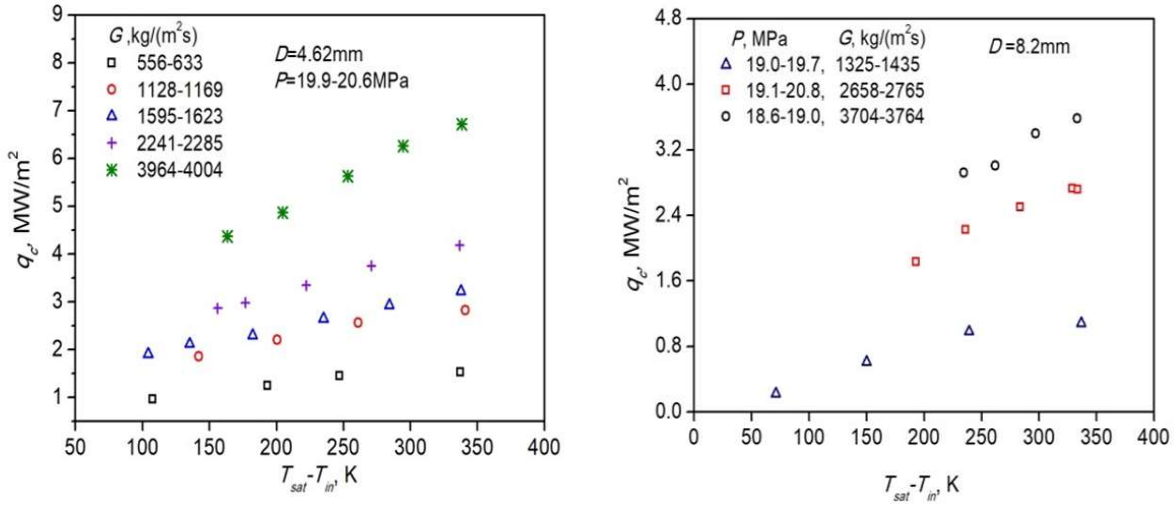

(a) *(b)*

Fig. 9.3. Variation of CHF with mass flux for (based on [9.12] [9.13]).

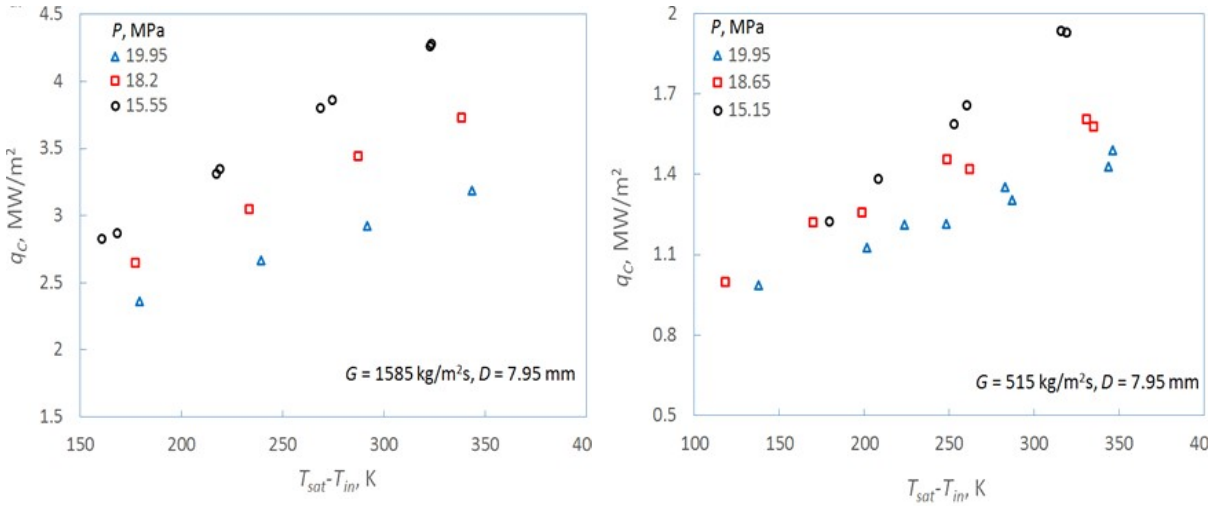

(a) *(b)*

Fig. 9.4. Variations of CHF with pressure [9.12].

The effect of tube diameter on CHF is shown in Fig. 9.5. As can be seen, For the same pressure, mass flux with $-0.3>x>-1.5$, higher CHF is obtained in smaller tube. This result was also observed by the authors and other investigators at lower pressure, though the extent of this effect was different greatly for different conditions. The diameter effect was accounted by a factor $(D/8)^n$ with the n ranged from –0.1 to –0.5 [9.15].

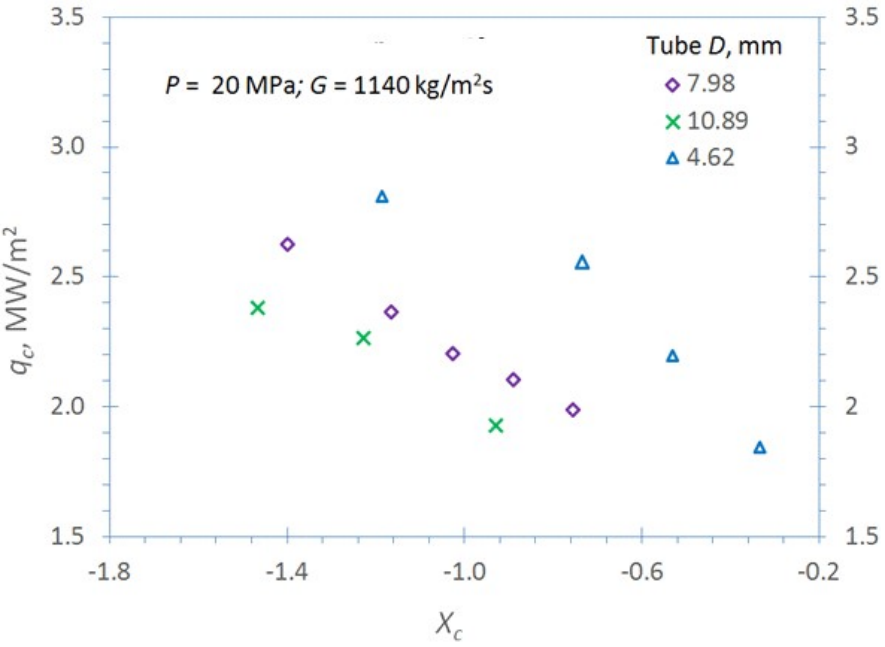

Fig. 9.5. Variations of CHF with tube diameter [9.12].

9.1.3. CHF DATABASES FOR CARBON DIOXIDE FLOW IN TUBES AT NEAR CRITICAL PRESSURES

[9.16] performed forced convective boiling heat transfer experiments with CO_2 flowing vertically upward in an 8 mm ID tube to measure CHF and film boiling heat transfer near the critical point of CO_2. Heat transfer measurements were collected at the University of Ottawa Supercritical Test Facility. Using the same test facility, [9.17] also investigated convective heat transfer to CO_2 flowing vertically upward in a circular 8 mm diameter tube. CHF data were obtained for a non-obstructed (bare) and an obstructed flow. Spacing between obstacles was 250, 500, and 1000 mm. Table 9.3 shows the ranges of the compiled CHF data from the two studies [9.16] [9.17].

TABLE 9.3. RANGES AND NUMBERS OF THE COMPILED CHF DATA, COLLECTED AT UNIVERSITY OF OTTAWA

Reference	TS Flow	q_c (kW·m^{-2})	P/P$_c$ (-)	G (kg·m^{-2}s^{-1})	x_c	Number of Points
Zahlan et al. [9.16] and Eter et al. [9.17]	Unobstructed	48–225	0.84–0.96	494–2041	-0.77– 0.31	32
Eter et al. [9.17]	Obstructed	60–122	0.89–0.95	526–1019	-0.89–0.46	22

9.1.4. CHF DATABASES FOR REFRIGERANT-134A FLOW IN TUBES AT NEAR CRITICAL PRESSURES

[9.18] conducted CHF experiments with R-134a flowing vertically upward. The TS was a tube made of SS-304 with an inner diameter of 12.7 mm and a uniformly heated length of 3.0 m. They maintained constant inlet subcooling by 3 K for all performed CHF tests. CHF was not enforced to occur at the exit of the heated section. In fact, it occurred at different locations along the heated length, and was calculated as a fraction of the imposed heat flux (q_{imposed}) at the location of detection. For example, assume CHF occurred at an arbitrary position z, along the heated section; CHF was calculated as $q_c = \frac{z}{L_h}\, q_{\text{imposed}}$. Table 9.4 shows the range of the compiled CHF data for a circular tube geometry. Sixty-six data points were extracted from tables.

TABLE 9.4. RANGES OF THE COMPILED CHF DATA FOR A CIRCULAR TUBE GEOMETRY

Reference	q_c (kW·m^{-2})	P/P$_c$ (-)	G (kg·m^{-2}·s^{-1})	x_c	Number of Points
Vijayarangan et al. [9.18]	2.8–48.5	0.75–0.95	200–2000	0.12– 0.71	66

Additional CHF experiments were performed at the KIT Modelfluid Facility (KIMOF), using R-134a as a fluid [9.19]. All CHF experiments were conducted in steady state meaning that for every measurement the inlet temperature, the pressure, the mass flux as well as the heat flux were kept steady. After each measurement the heat flux was increased in defined steps of 200 W/m^2 while all the other parameters were maintained. This procedure was repeated until the boiling crisis was detected at the top of the heated length.

Table 9.5 lists the overall range of measurements obtained at KIT. The nominal pressure was set to 2.8 MPa, 3.3 MPa, 3.8 MPa and 4 MPa and the nominal mass fluxes at 500, 1000, 2000, 3000 and 4000 kg/(m^{2}s). The nominal inlet temperature varied from 23°C–73°C in steps of 10 °C at the pressure of 2.8 MPa, from 31°C–81°C at the pressure of 3.3 MPa, from 38 to 78°C in steps of 10 °C at the pressure of 3.8 MPa, and from 30°C–70°C in steps of 10°C at the pressure of 4 MPa. Those inlet temperatures correspond to an inlet subcooling of 10°C up to a maximum of 60°C.

TABLE 9.5. CHF MEASUREMENT DATA OBTAINED AT KIT

Fluid	Geometry	Flow direction	Convection	ID (mm)	Pressure (MPa)	Mass flux (Mg/m²s)	Inlet temp. (°C)	CHF (kW/m²)	Data
R134a	tube	vertical, upward	forced	10	2.8–4	0.5–4	23–81	25–245	96

The maximum CHF was 243.24 kW/m^2 at the pressure of 3.81 MPa, mass flux of 4024.93 kg/(m^{2}s) and inlet temperature of 58.07°C. The minimum CHF was 30.3 kW/m^2 at the pressure of 4 MPa, mass flux of 506.20 kg/(m^{2}s) and inlet temperature of 80.27°C. The maximum critical vapor quality was 0.63 at the pressure of 2.81 MPa, mass flux of 490.62 kg/(m^{2}s) and inlet temperature of 72.82°C, and the minimum was -2.56 at the pressure of 4.01 MPa, mass flux of 2985.30 kg/(m^{2}s) and inlet temperature of 40.69°C.

Fig. 9.6 shows variations of critical heat flux with mass flux and pressure at the inlet subcooling of 30°C. The critical heat flux increases with increasing mass flux due to higher turbulences in the flow and therefore better heat transfer. Increasing pressure generally reduces the CHF.

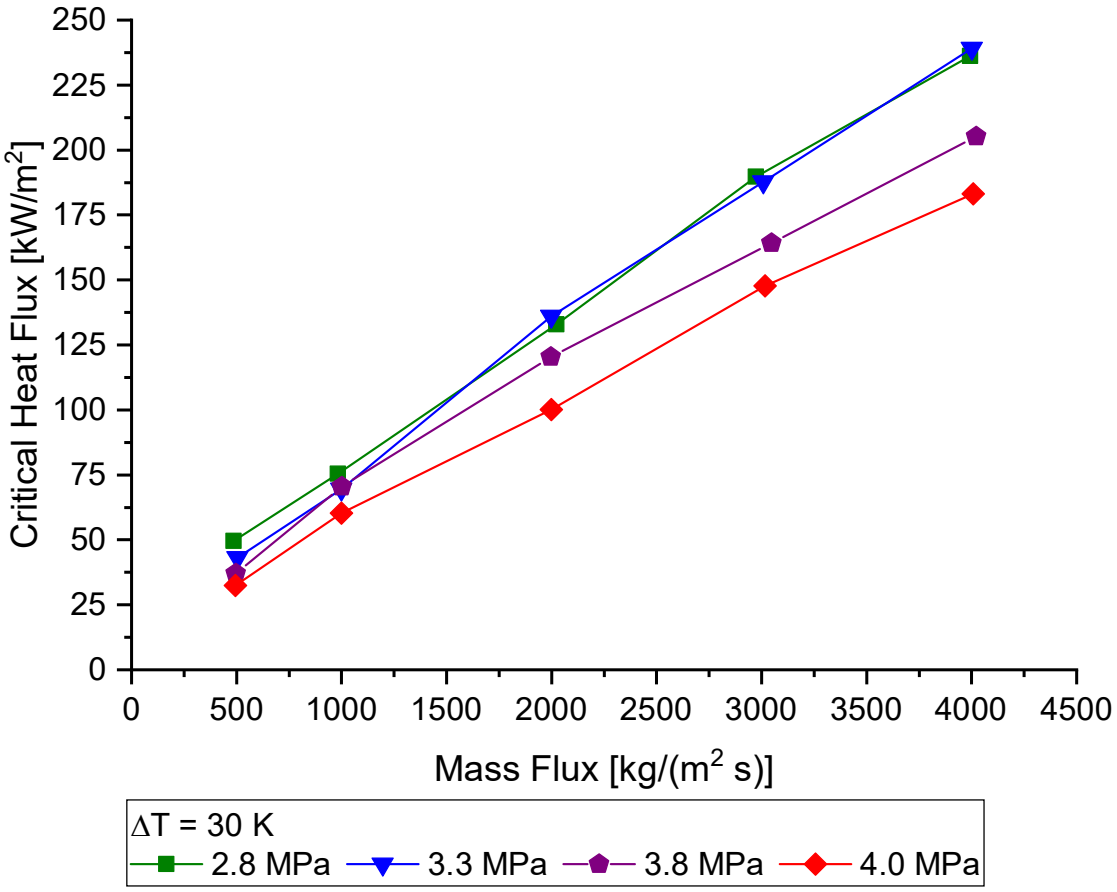

Fig. 9.6. Influence of the mass flux on CHF for a subcooling of 30 K [9.19].

Fig. 9.7 shows variations of CHF with inlet subcooling for all data. CHF increases with increasing subcooling. The increasing trend is almost linear especially at high mass fluxes. It is gradual at low mass fluxes but becomes steep with increasing mass flux.

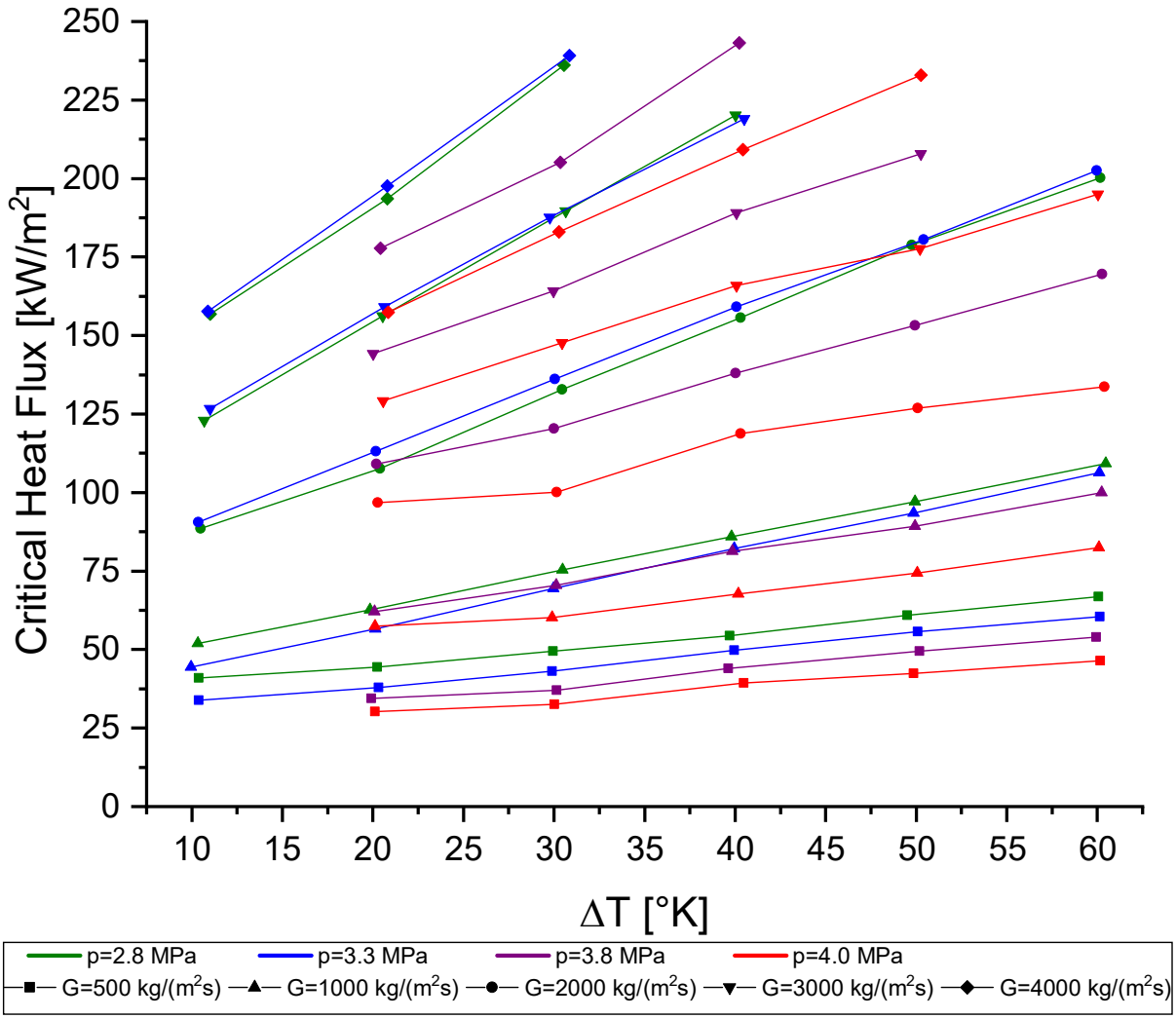

Fig. 9.7. Influence of subcooling on CHF for different pressures and mass fluxes [9.19].

Fig. 9.8 shows variations of CHF with pressure for all data. At the mass flux of 500 kg/(m^{2}s), a linear reduction in CHF is observed with increasing pressure. At high mass fluxes (i.e., above 1000 kg/(m^{2}s)), CHF appears to be constant or even increases slightly at pressures up to 3.3 MPa beyond which the CHF decreases with increasing pressure. The decrease is more significant at high mass fluxes. This agrees well with the phenomena previously observed in [9.20].

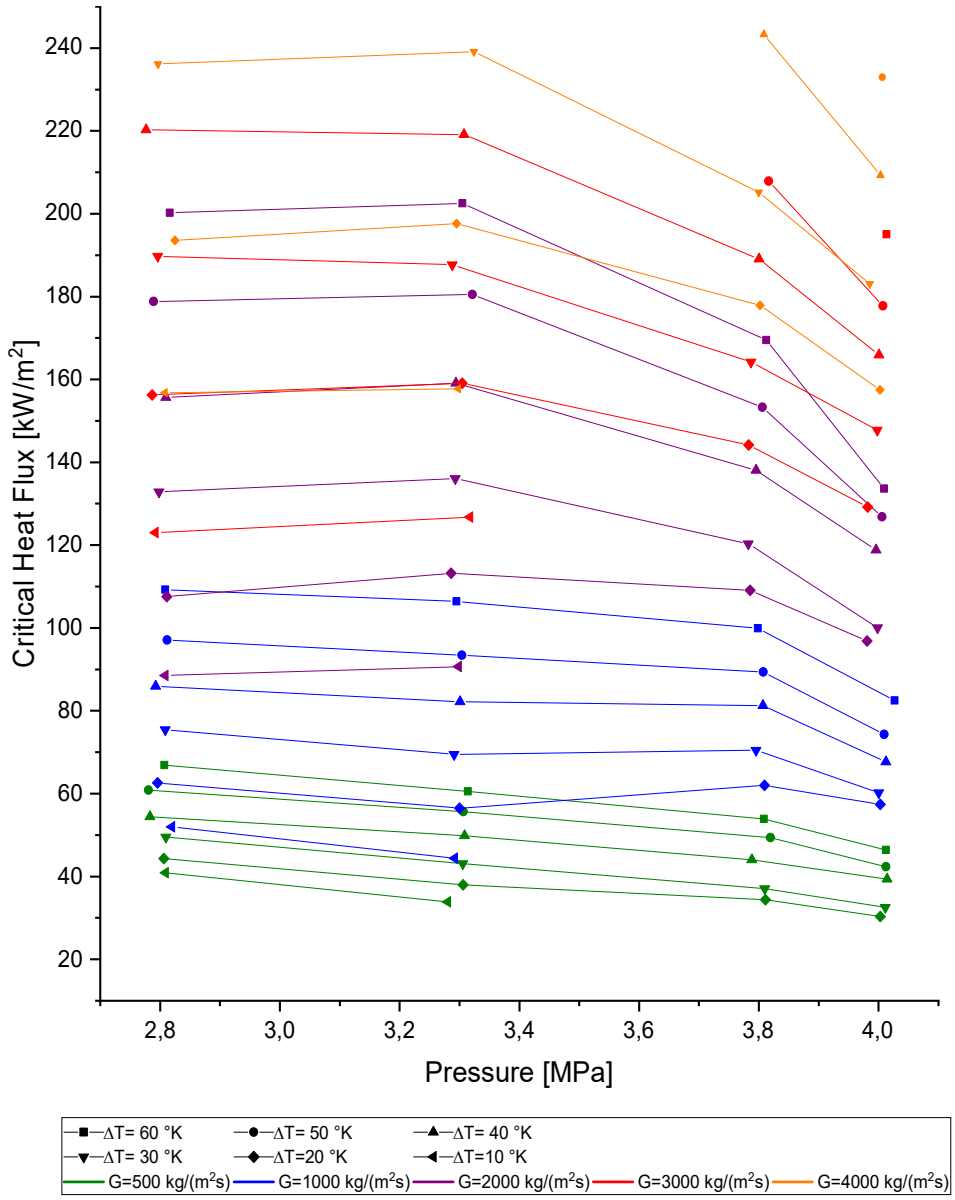

Fig. 9.8. Influence of the pressure on CHF for different subcoolings and mass fluxes [9.19].

Fig. 9.9 shows variations of critical heat flux with critical vapor quality for all data at different stages of subcooling marked by the single measurement points for given pressure and mass flux. CHF increases generally with decreasing vapor quality. Furthermore, the critical vapor quality increases with decreasing subcooling. At vapor qualities above 0, CHF increases significantly with increasing subcooling. This trend is valid for all mass fluxes. For all mass fluxes, CHF occurs at lower critical vapor qualities as the pressure increases.

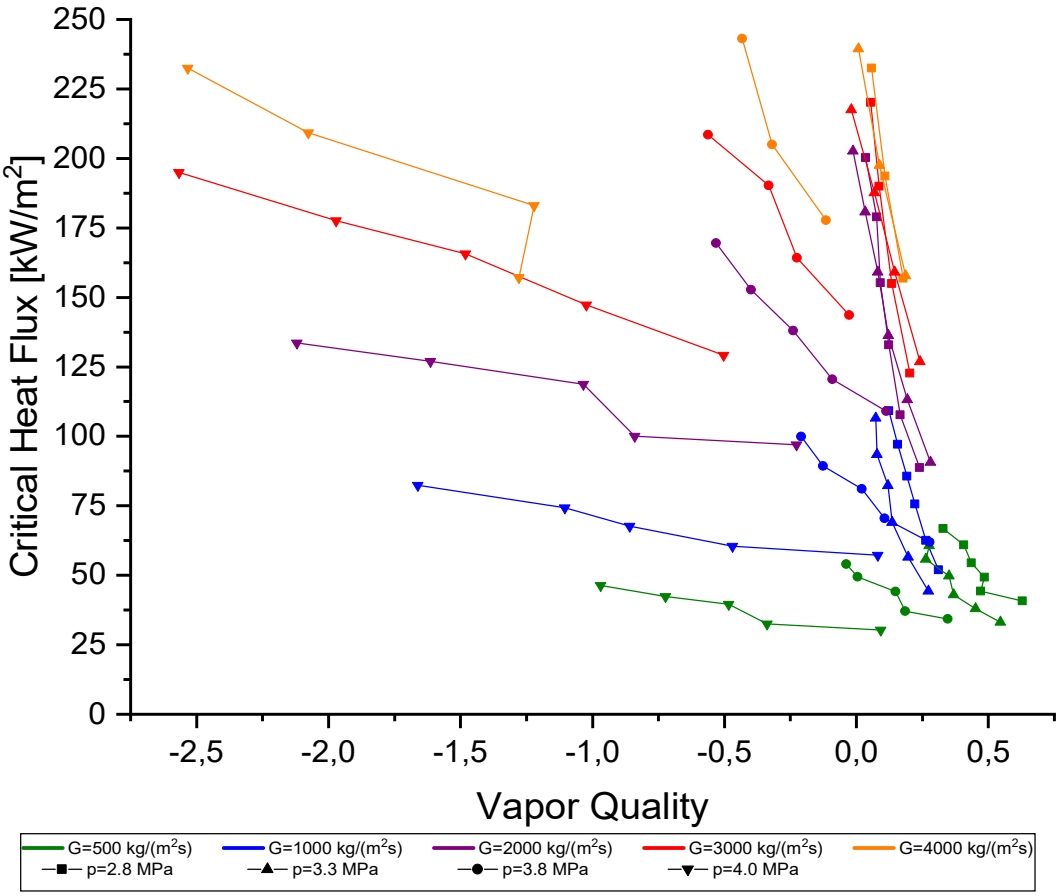

Fig. 9.9. Influence of the vapor quality on CHF for different pressures and mass fluxes [9.19].

9.1.5. CHF UNDER NATURAL CONVECTION IN TUBES WITH CARBON DIOXIDE FLOW AT HIGH PRESSURES

9.1.5.1.NATURAL CONVECTION TEST FACILITY

CHF experiments were conducted in the existing test facility viz. Supercritical Pressure Natural Circulation Loop (SPNCL) installed at BARC. Schematic of the loop is shown in Fig. 9.10 The test facility is a rectangular natural circulation (NC) based loop having uniform diameter. It consists of two heaters sections (a vertical and a horizontal) and two cooler sections (a vertical and a horizontal) interconnected with Inconel pipes of DN 15 Sch. 80 size (ID: 13.88 mm; OD: 21.3 mm). This facilitates the SPNCL to conduct experiments with four different combinations of heater and cooler orientations viz. Horizontal Heater Horizontal Cooler (HHHC), Horizontal Heater Vertical Cooler (HHVC), Vertical Heater Horizontal Cooler (VHHC) and Vertical Heater Vertical Cooler (VHVC). The heater sections are directly heated with electrical bus-bars whereas the coolers are pipe-in-pipe type configuration with outer pipe made-up with DN 40 Sch. 80 pipe (ID: 38.14 mm; OD: 48.3 mm). Chilled water is employed as coolant in the annular space of the cooler. The loop is equipped with a pressurizer connected to the bottom portion of the loop. This

pressurizer facilitates loop pressurization with the cover gas and also absorbs shrinks and swells in the loop.

SPNCL is extensively instrumented to measure pressure and temperatures at different locations. Temperature measurements include surface and bulk fluid temperatures. The horizontal heater section is equipped with surface thermocouples at fourteen locations across the length at uniform distances. Four thermocouples each are provided at twelve locations. These thermocouples are provided at a cross section installed at 90° phase difference thus covering the entire cross section. At the remaining two locations (at either ends), two thermocouples each are provided. In this manner, a total of 52 thermocouples are installed for surface temperature measurements in the horizontal heater section. Similarly, in the vertical heater section, surface thermocouples are provided at 13 locations along the length at uniform distances. At twelve locations, four thermocouples each are installed at the cross section at 90° phase difference whereas, two thermocouples are provided towards the outlet of the vertical heater section. In this manner, a total of 50 thermocouples are provided for surface temperature measurements at different locations in the vertical heater section. For bulk fluid temperatures, thermocouples are installed at different locations across the loop as shown in Fig. 9.10. Accuracy associated with different measurements are summarized in Table 9.6.

TABLE 9.6. ACCURACY OF MEASUREMENTS.

Sr. No.	Measurement	Accuracy
1.	Pressure	± 0.03 MPa
2.	Temperature	± 1.5 °C
3.	Power	± 0.5%

9.1.5.2.NATURAL CONVECTION CHF TEST MATRIX

Extensive experiments have been conducted to generate CHF data near the critical pressure of CO_2. The operating pressures varied from 6.6 to 7.2 MPa which is close to the critical pressure of CO_2 at 7.39 MPa. Tests have been conducted for all possible combinations of heater and cooler orientations viz. HHHC, HHVC, VHHC and VHVC. For HHHC, HHVC and VHHC orientations, the pressure was increased in steps of 0.2 MPa, thus resulting in four experimental sets. Whereas for VHVC orientation, only three sets of experiments were carried out at pressures between 6.8 – 7.2 MPa in steps of 0.2 MPa. The test matrix is summarized in Table 9.7.

9.1.5.3.EXPERIMENTAL RESULTS

In general, CHF experiments are conducted with constant mass flux at the inlet of the test section and then power is raised till the occurrence of CHF (i.e., the conditions with flow, sub-cooling, power and pressure can be controlled independently as the fluid flows under forced circulation). Quality during CHF occurrence can be calculated conveniently. In the present case as the experiments are conducted under natural circulation, the flow rate at each of the power step during the course of reaching up to the CHF power, changes with each step. Also, the sub-cooling at the heater inlet changes with the flow which in turn changes with power. Also, as the flow circulates naturally and changes with each power step, the flow rate at the power level just below the CHF

occurrence differs from that at CHF. Thus, the flow rate at the CHF condition is difficult to predict under NC condition as CHF is a transient phenomenon.

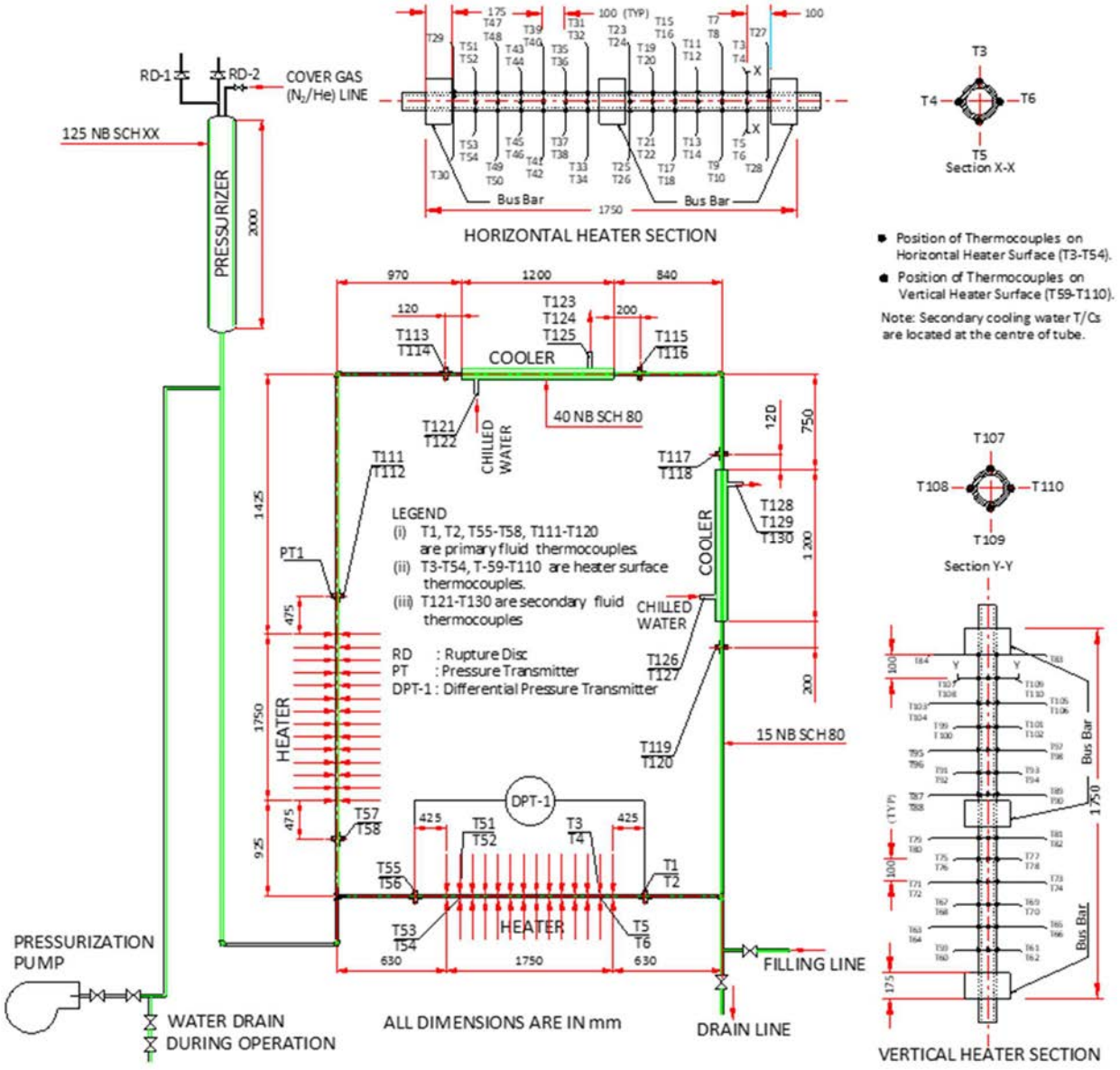

Fig. 9.10. Schematic of Supercritical Pressure Natural Circulation Loop (SPNCL).

TABLE 9.7. TEST MATRIX FOR CHF EXPERIMENTS.

Sr. No.	Orientation	Pressure range, MPa	No. of data	Pressure (g), MPa
1.	HHHC	6.6 – 7.2	4	6.6, 6.8, 7.0, 7.2
2.	HHVC	6.6 – 7.2	4	6.6, 6.8, 7.0, 7.2
3.	VHHC	6.6 – 7.2	4	6.6, 6.8, 7.0, 7.2
4.	VHVC	6.8 – 7.2	3	6.8, 7.0, 7.2

Fig. 9.11 shows that CHF occurred at the power of 2.08 kW at multiple locations of the HHHC configuration. However, it was captured firstly by the thermocouple TT-47 which is located towards the heater outlet. Among four locations with installed thermocouples at the circumferential positions, the CHF occurred at the thermocouple which is located at the top surface of the horizontal tube due to stratification. In addition, the CHF occurred at multiple locations at the same power level. These locations are towards the inlet of the heater section. Thermocouples tags viz. TT-43, TT-39, TT-35 and TT-31 were the subsequent thermocouple locations where CHF occurred sequentially after first occurrence at TT-47. Thus, the CHF locations travelled towards the inlet of the heater section at the same power level. All thermocouples detecting CHF were installed at the top surface of the heater tube. CHF occurrence took place at other locations with increasing power. At these powers the new locations include TT-50, TT-48, TT-49, TT-23, TT-19 sequentially and many more. It is interesting to note that TT-50, TT-48 and TT-49 are located at the same cross section to that of TT-47, where the CHF occurred firstly. Whereas TT-23, and TT-19 are again the ones installed towards the heater inlet and at the top of the heater surface.

Fig. 9.12 shows that at 7.0 MPa pressure, the CHF occurrence took place almost at all the locations at the same power level (i.e., 2.265 kW). Temperature trends at these power levels show a dip simultaneously which is due to fluctuation in the power and can be ignored presently as CHF had occurred earlier than the power fluctuation happened. CHF occurred firstly at the TT-30 which is located the top surface of the heater section at the heater outlet, followed by TT- 51, TT-47, TT-43, TT-39 in sequential manner and at other location. The mentioned thermocouples are all located the top surfaces of the heater.

Similar observations can be made from the trends for temperatures at 6.8 MPa shown in Fig. 9.13. CHF occurred firstly at locations TT-30 followed by TT-51, TT-47, TT-43 in sequential manner. All thermocouples are installed at top of the surface. With increase in power, CHF occurred at the remaining locations. Trends for CHF at 6.6 MPa show the similar findings where CHF occurrence first observed at TT-51 followed by TT-30, TT-47, TT-39 and TT-35 sequentially followed by other locations (see Fig. 9.14).

Surface temperature trends (including bulk fluid at heater inlet and outlet) are shown in Fig. 9.15–Fig. 9.18 at various pressures for the HHVC configuration. At 7.2 MPa pressure, CHF occurred at 1.801 kW almost simultaneously at TT-51 and TT-30 locations at the heater outlet top surface. Most locations encountered CHF occurrence at the same power. However, CHF spread to locations towards the inlet of the heater section with increasing power. Similarly, at other pressures (i.e., 7.0 MPa, 6.8 MPa and 6.6 MPa), CHF occurred simultaneously at TT-51 and TT-30 locations and sequentially occurred at locations (TT-47, TT-43, TT-39, TT-35 etc.) propagating towards the inlet of the heater section.

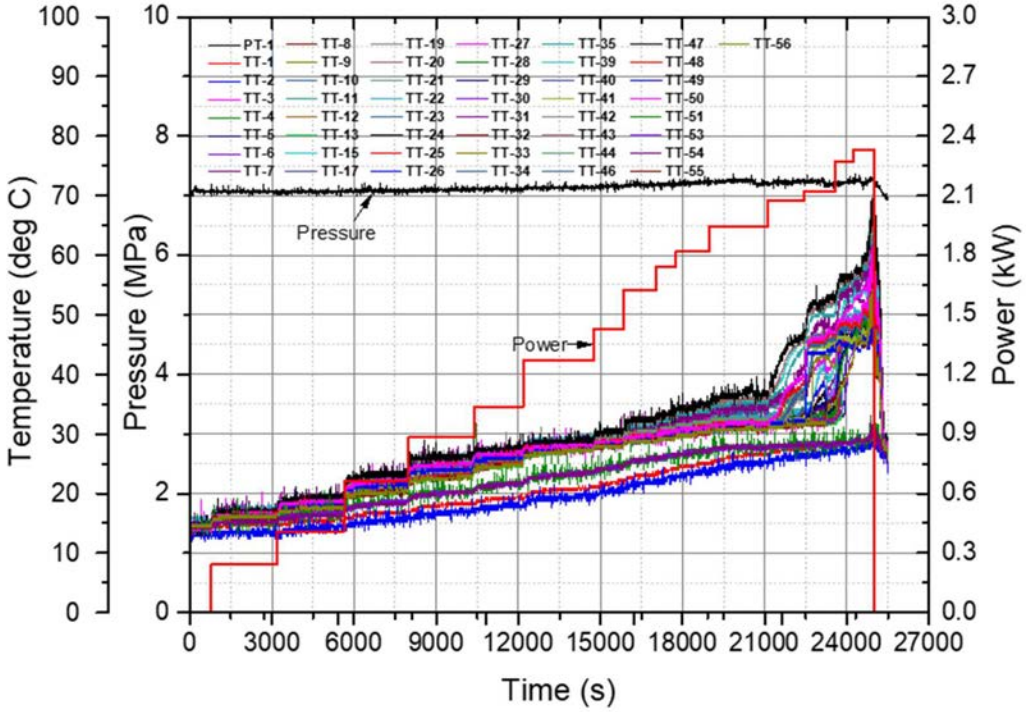

Fig. 9.11. Temperature trends for CHF experiments at 7.2 MPa in HHHC orientation.

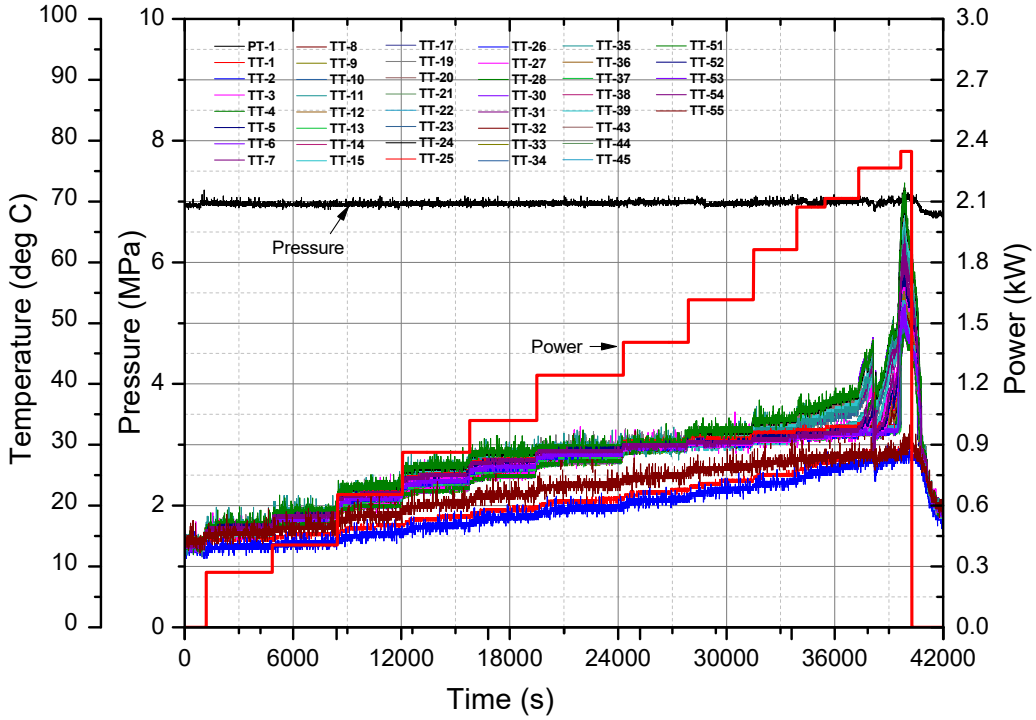

Fig. 9.12. Temperature trends for CHF experiments at 7.0 MPa in HHHC orientation.

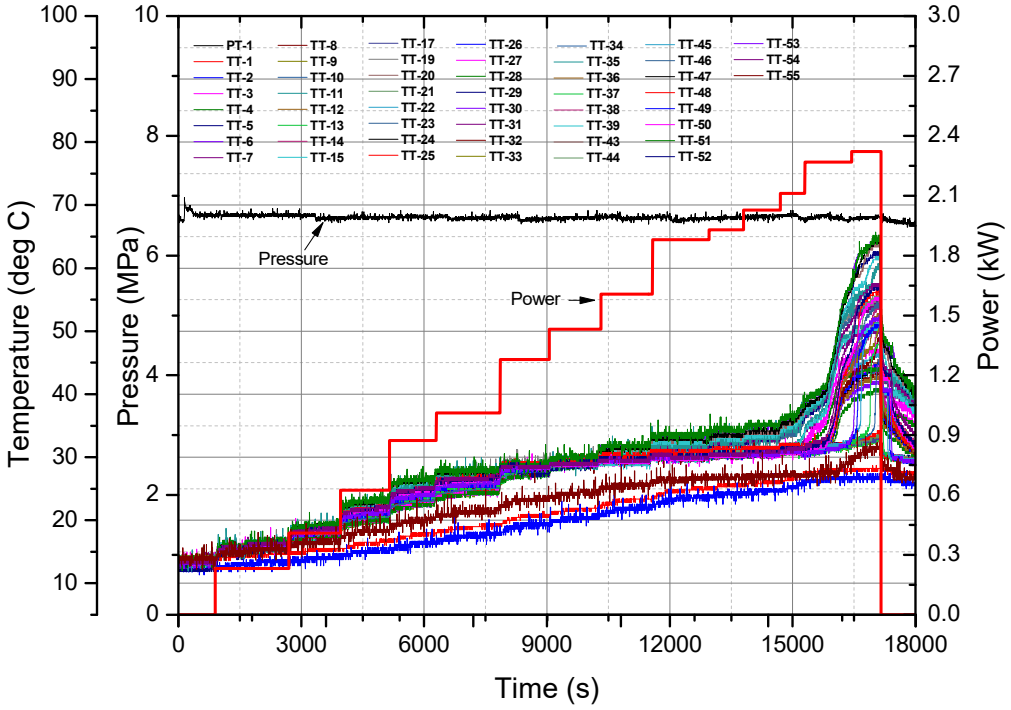

Fig. 9.13. Temperature trends for CHF experiments at 6.8 MPa in HHHC orientation.

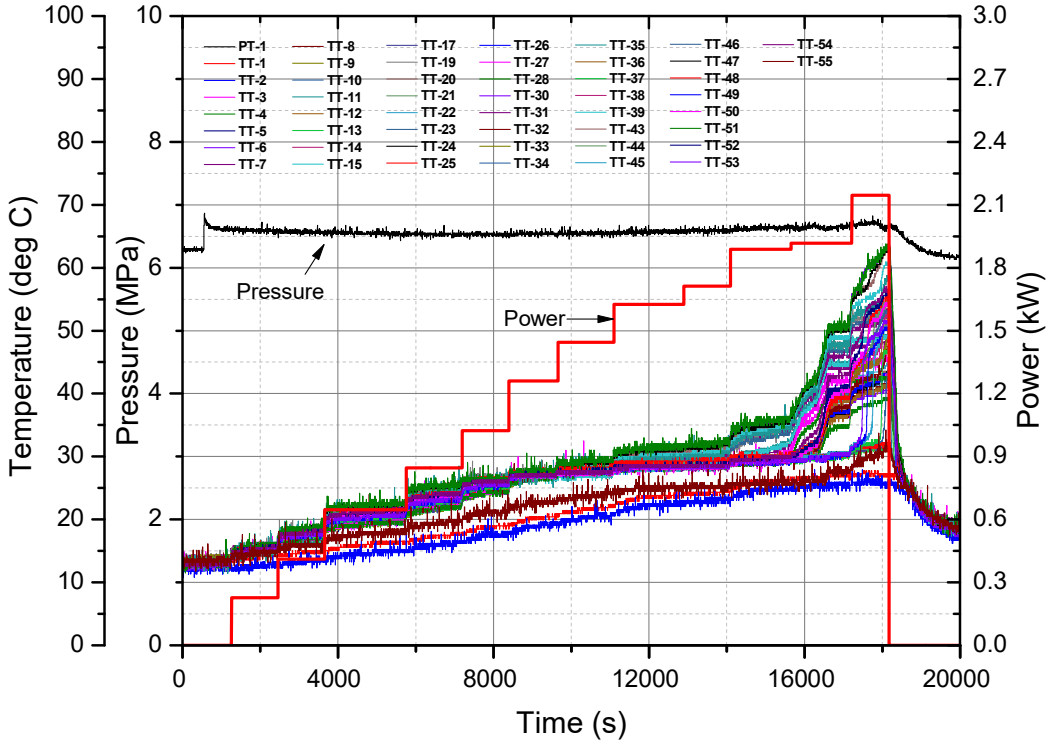

Fig. 9.14. Temperature trends for CHF experiments at 6.6 MPa in HHHC orientation.

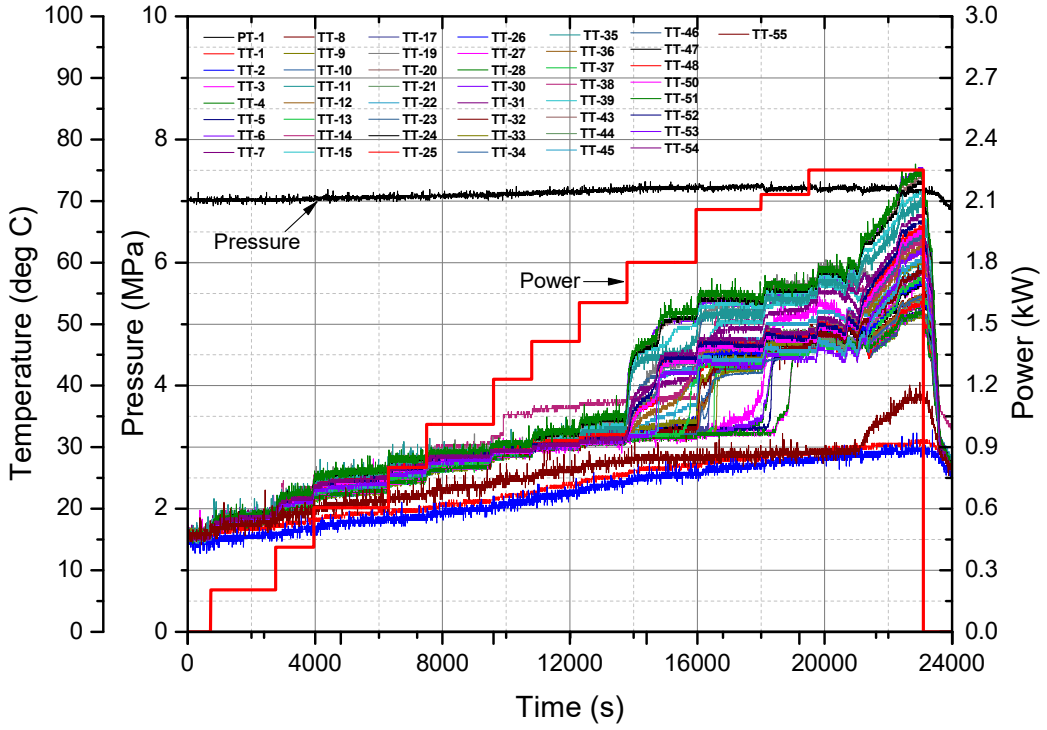

Fig. 9.15. Temperature trends for CHF experiments at 7.2 MPa in HHVC orientation.

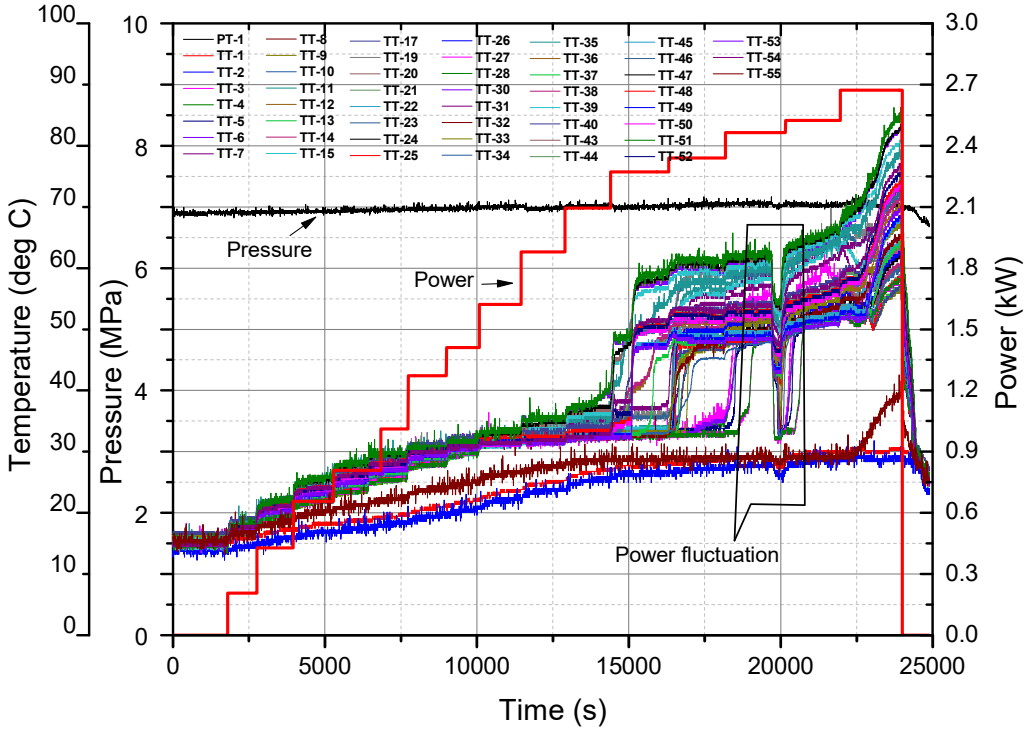

Fig. 9.16. Temperature trends for CHF experiments at 7.0 MPa in HHVC orientation.

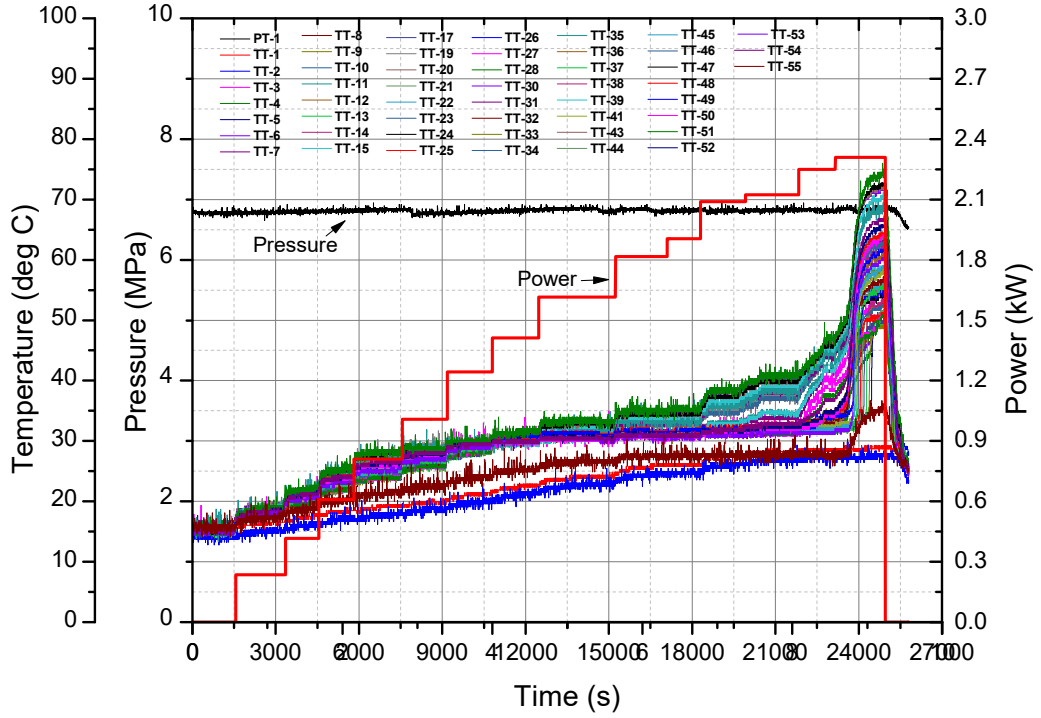

Fig. 9.17. Temperature trends for CHF experiments at 6.8 MPa in HHVC orientation.

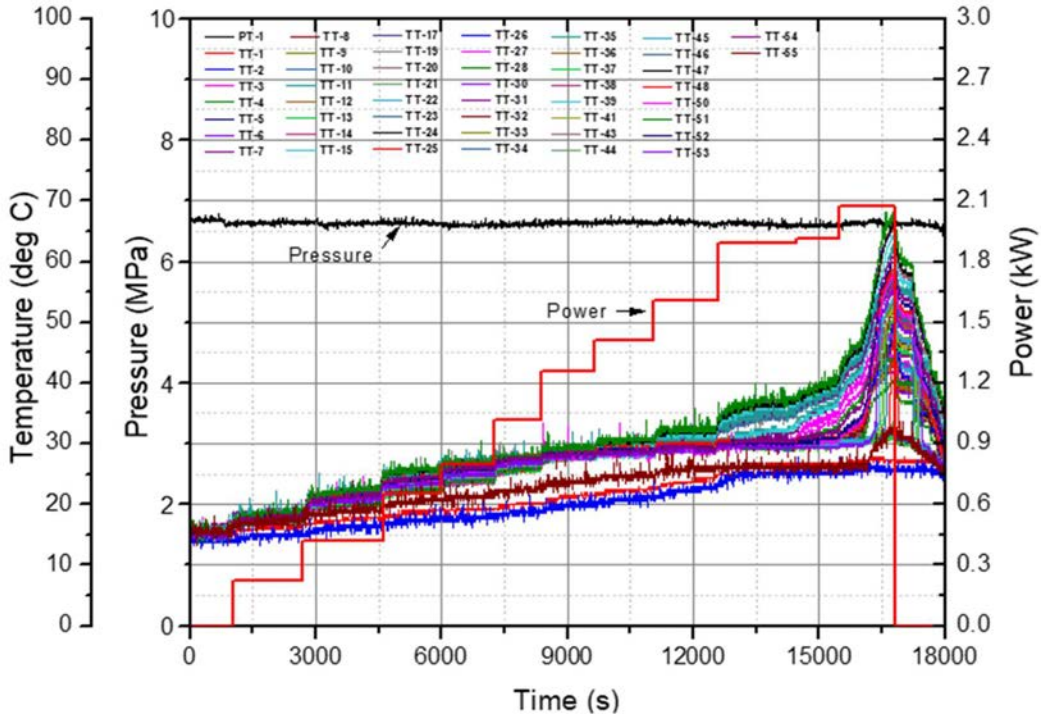

Fig. 9.18. Temperature trends for CHF experiments at 6.6 MPa in HHVC orientation.

Experimental trends for VHHC orientations are illustrated from Fig. 9.19–Fig. 9.22. It is evident for the cases with VHHC orientation that the CHF occurred firstly at the location TT-88 (located just above the middle of the heater section) and then the CHF occurrence propagated in the upward direction towards the outlet of heater section at same power. On further increasing the power, the CHF occurred at the locations towards heater inlet too. Further it can be noted that the CHF for the experiments at 7.2 MPa and 7.0 MPa occurred in the highly sub-cooled conditions as the bulk fluid temperature at the outlet of heater section was lesser than the saturation temperature of the fluid.

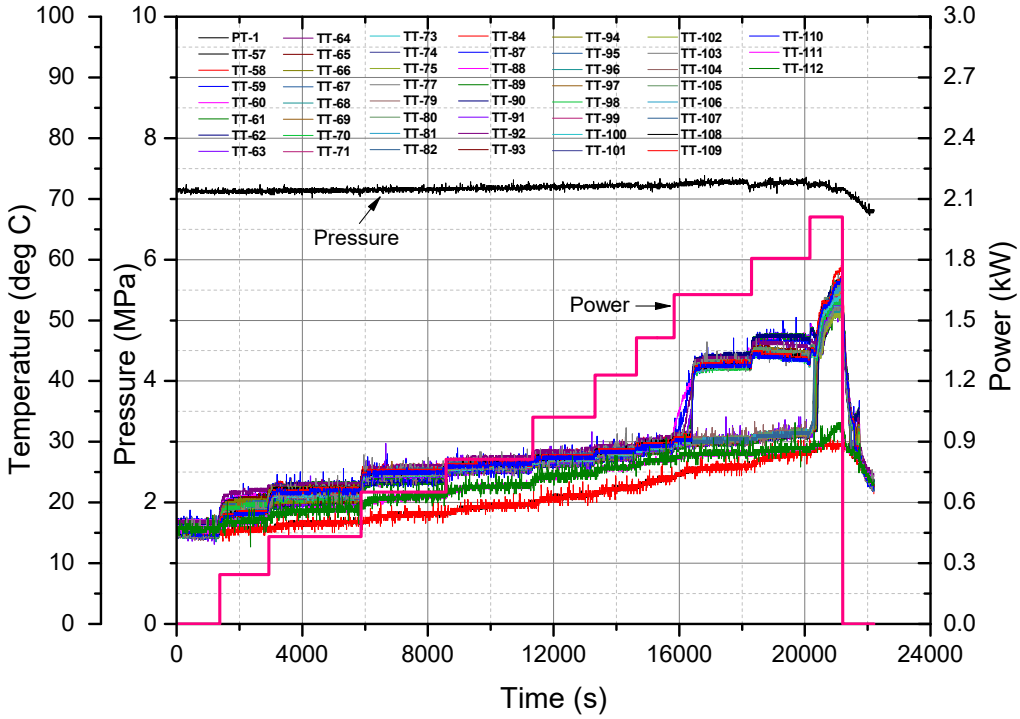

Fig. 9.19. Temperature trends for CHF experiments at 7.2 MPa in VHHC orientation.

Experimental results for VHVC orientation case are depicted in Fig. 9.23–Fig. 9.25. It can be seen that the CHF occurrence takes place at the locations which are situated at less than mid-length of the heater section. That is the CHF location changed to a lower elevation towards the heater inlet. This can be attributed to the fact that the flow rate in the case of VHVC is lesser than VHHC orientation thus causing the CHF to occur at lesser power. However, as the power is increased the CHF occurs at other locations too and the difference between inlet and outlet bulk fluid temperature keep on decreasing. At a point, the inlet bulk fluid temperature becomes almost equal to that at the outlet and then the fluid converts into vapours and the bulk fluid temperature increases rapidly. From Fig. 9.24 it is observed that the CHF occurs at a power of 1.3091 kW at the locations TT-79, TT-81 and TT-82. It is also to be noted that a sharp increase in temperature is observed at locations TT-95 and TT-101 at 1.14125 kW. However, as the increase in temperature is less than 5°C, this has not been considered as CHF.

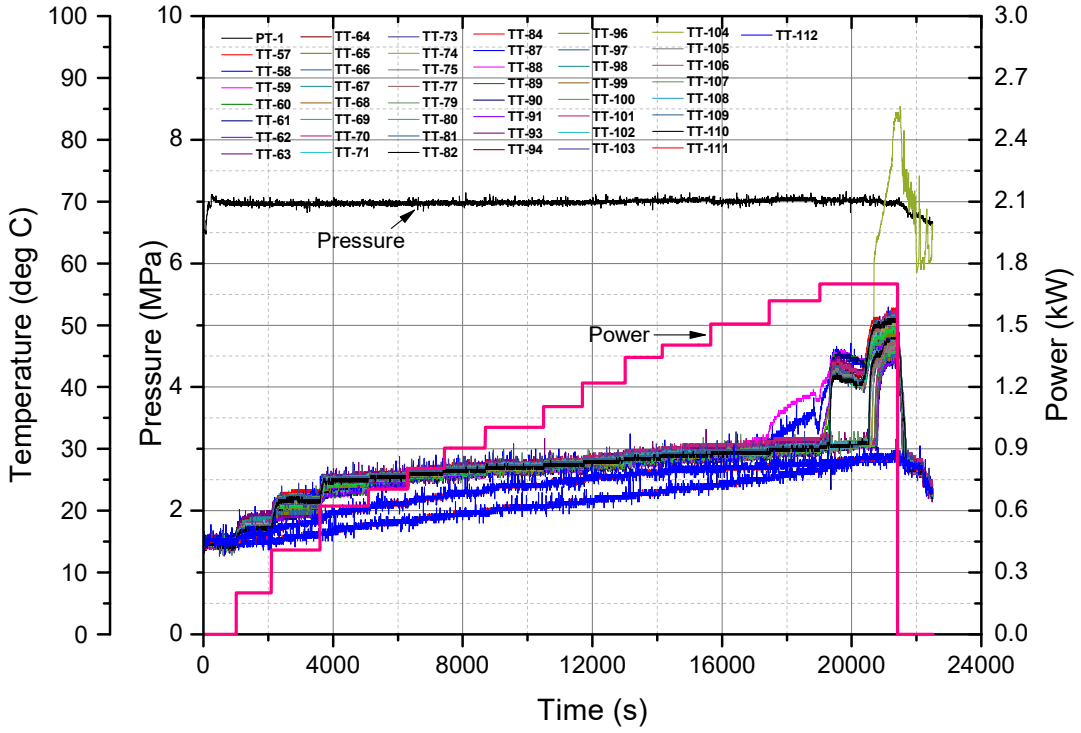

Fig. 9.20. Temperature trends for CHF experiments at 7.0 MPa in VHHC orientation.

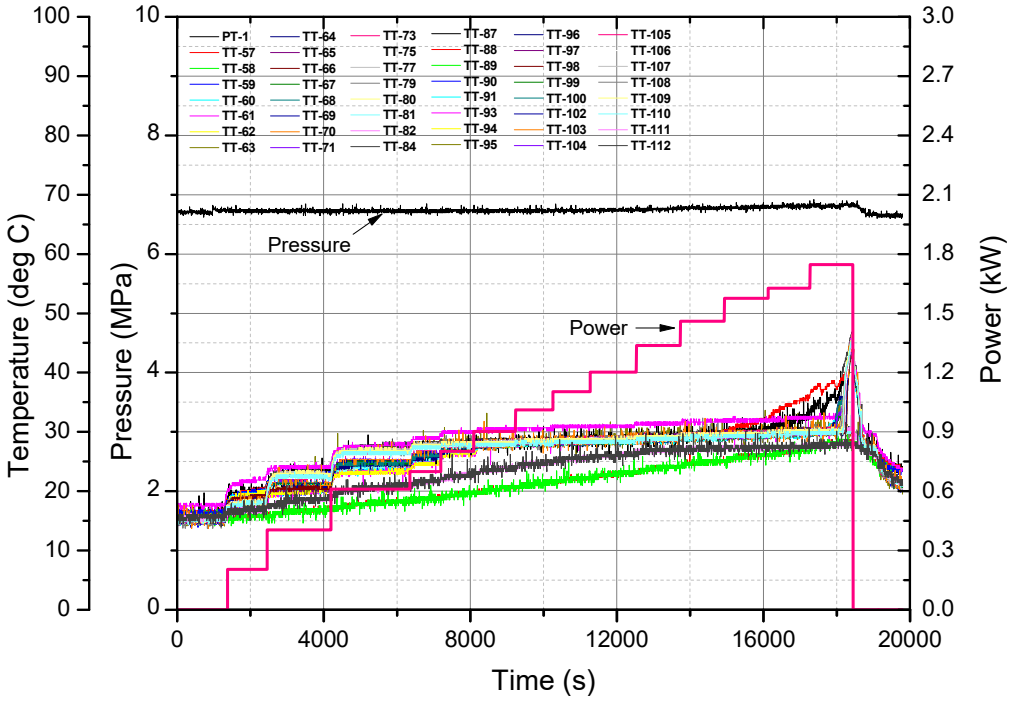

Fig. 9.21. Temperature trends for CHF experiments at 6.8 MPa in VHHC orientation.

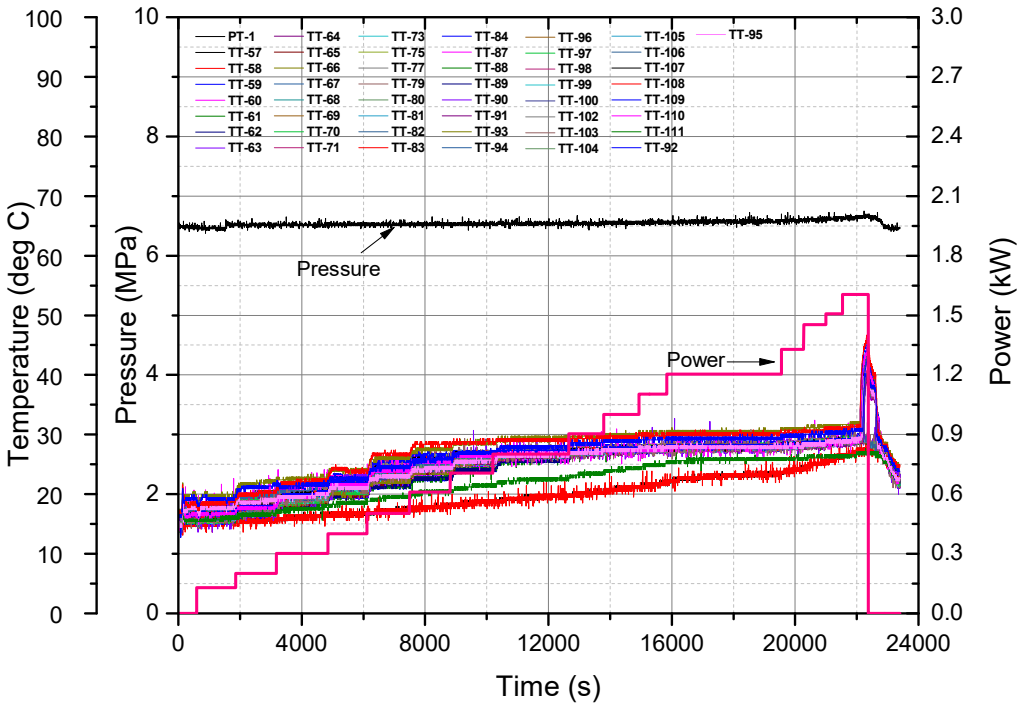

Fig. 9.22. Temperature trends for CHF experiments at 6.6 MPa in VHHC orientation.

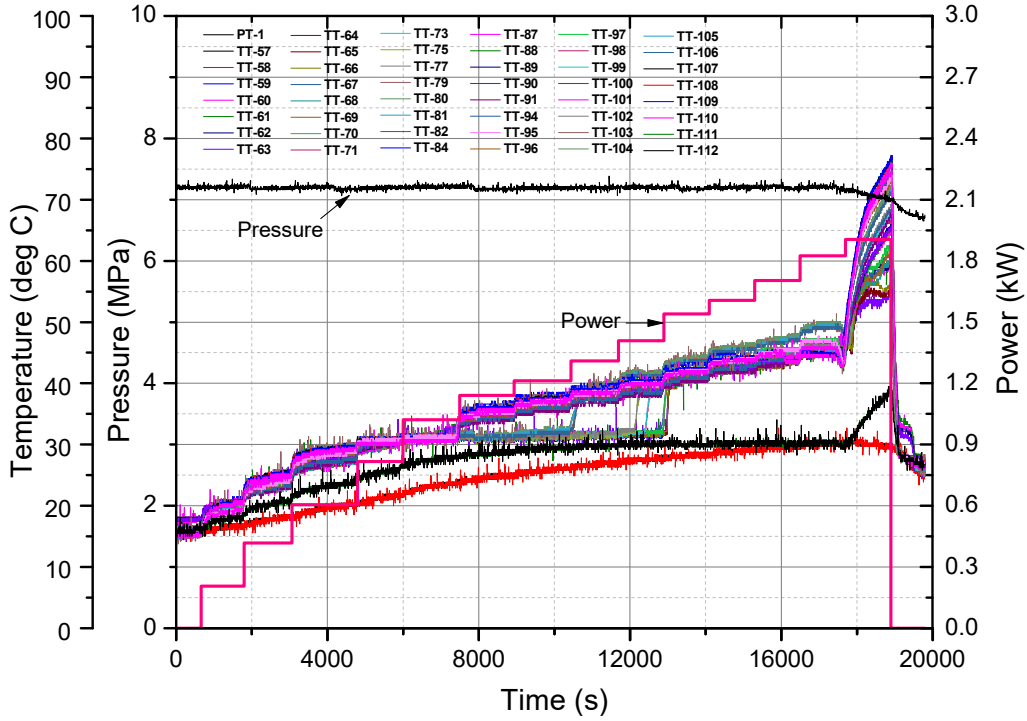

Fig. 9.23. Temperature trends for CHF experiments at 7.2 MPa in VHVC orientation.

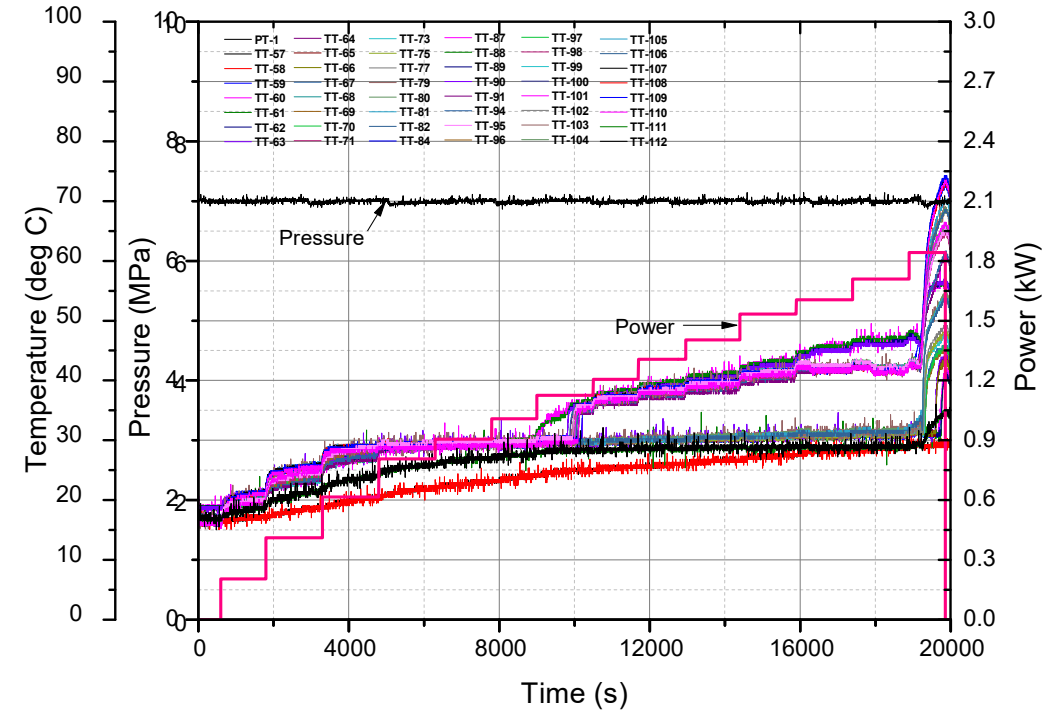

Fig. 9.24. Temperature trends for CHF experiments at 7.0 MPa in VHVC orientation.

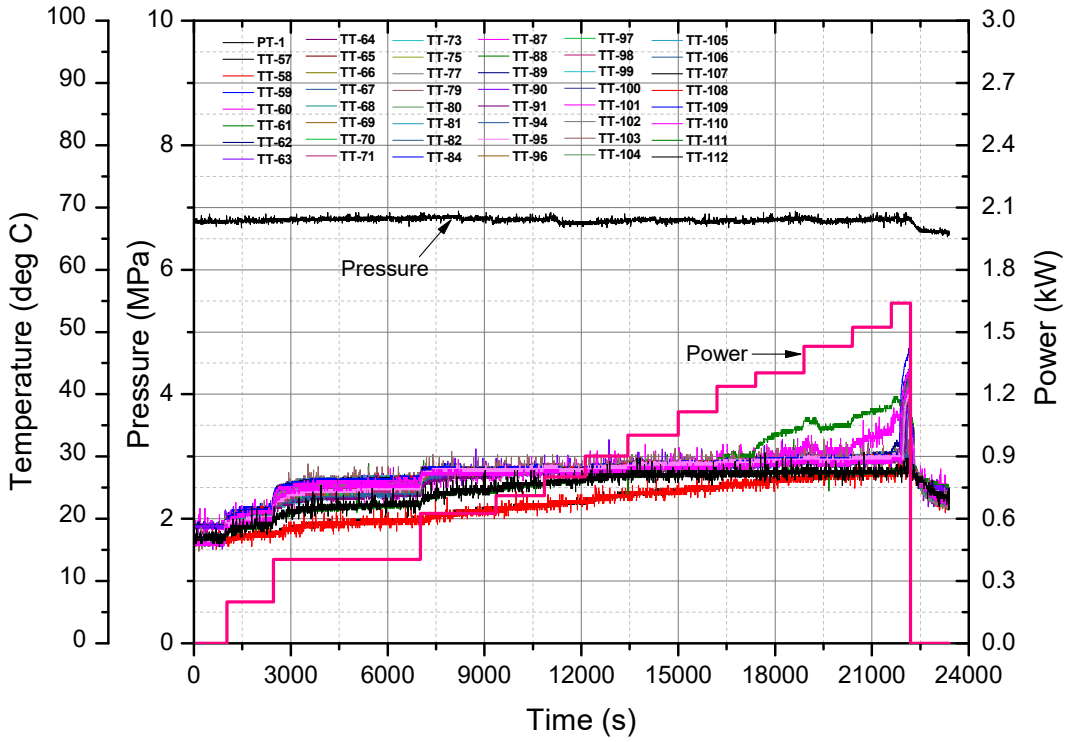

Fig. 9.25. Temperature trends for CHF experiments at 6.8 MPa in VHVC orientation.

Results for various CHF experiments with different orientations are summarized in Table 9.8 and Table 9.9 respectively for horizontal and vertical heater tubes. As mentioned earlier also, it is difficult to predict flow during CHF in natural circulation condition, therefore, flow rate has been evaluated at the power step at which flow conditions were single phase (based on the heater outlet temperature) and which is previous to that at which CHF occurred. Flow rates, and correspondingly mass fluxes, are evaluated from heat balance across the heater section. Similarly, the inlet temperatures in Table 9.8 and Table 9.9 correspond to those at the power level where flow rates are evaluated. Subsequently, quality was also predicted using the enthalpy balance method at the heater outlet. The calculations were made using the subcritical CO_2 properties from the NIST database.

TABLE 9.8. CHF FOR FLOW UNDER HORIZONTAL HEATER TUBE

Sr. No.	Pressure (g) (MPa)	Flow rate (kg/s)	Mass Flux (kg/(m^{2}s))	Inlet Temp. (°C)	Quality (-)	Power at CHF (kW)	CHF (kW/m^2)	Orientation
1.	6.63	0.576	3804.24	25.58	-0.061	1.9166	25.12	HHHC
2.	6.84	0.205	1353.21	25.71	-0.092	2.268	29.72	
3.	6.99	0.285	1884.30	26.86	-0.181	2.2650	29.68	
4.	7.22	0.054	359.34	24.15	-0.396	2.0779	27.23	
5.	6.61	0.128	843.99	23.54	-0.061	2.0735	27.17	HHVC
6.	6.82	0.369	2444.08	26.62	-0.078	2.25	29.49	
7.	7.02	0.145	962.62	26.18	-0.160	2.2716	29.77	
8.	7.17	0.127	840.36	24.82	-0.587	1.8009	23.60	

TABLE 9.9. CHF FOR FLOW UNDER VERTICAL HEATER TUBE

Sr. No.	Pressure (g) (MPa)	Flow rate (kg/s)	Mass Flux (kg/(m^{2}s))	Inlet Temp. (°C)	Quality (-)	Power at CHF (kW)	CHF (kW/m^2)	Orientation
1.	6.63	0.79	5275.99	26.31	-0.032	1.6044	21.03	VHHC
2.	6.81	0.177	1172.47	26.10	-0.067	1.6268	21.32	
3.	7.02	0.151	998.27	25.09	-0.296	1.6184	21.21	
4.	7.22	0.105	693.58	23.97	-0.879	1.6268	21.32	
5.	6.78	0.128	843.69	25.58	-0.073	1.3026	17.07	VHVC
6.	6.98	0.057	374.45	24.07	-0.205	1.12625	14.76	
7.	7.19	0.059	391.49	25.96	-0.408	1.3091	17.15	

It can be inferred from Table 9.8 and Table 9.9 that the present set of experiments covered mass fluxes ranging from 359.34–3804.24 kg/(m^{2}s) with CHF values ranging between 23.60–29.72 kW/m^2 for experiments with horizontal heater tube whereas for vertical heater tube, the mass flux and CHF values are ranging between 374.45–5275.99 kg/(m^{2}s) and 14.76–21.32 kW/m^2, respectively. CHF phenomena occurred at lesser power for vertical heater cases compared to that of horizontal heater.

9.2. TESTS AND DATABASE FOR ROD BUNDLES

9.2.1. CHF IN AN AXIALLY NON-UNIFORMLY HEATED 2X2 ROD BUNDLE AT HIGH WATER PRESSURES

[9.21] performed CHF experiments with an upward flowing water through a 2x2 rod bundle having a cosine axial power profile. A schematic diagram of the test facility is shown in Fig. 9.26. Water is moved through the test section or through an unheated recirculation branch fitted with an orifice plate. The flow recombines after the test section and a portion of this flow is cooled by travelling through the heat exchanger. The remaining flow bypasses the heat exchanger. The amount of flow through the heat exchanger is controlled by the heat exchanger bypass valve. The flow from the heat exchanger recombines with any bypass flow and re-enters the pump. An accumulator tank located behind the flow loop accommodates any thermal expansion of the fluid and a cylinder of argon gas is connected to pressurize the system. The system can reach 25 MPa and 400°C with a maximum achievable mass flux of 1500 kg/m^{2}s.

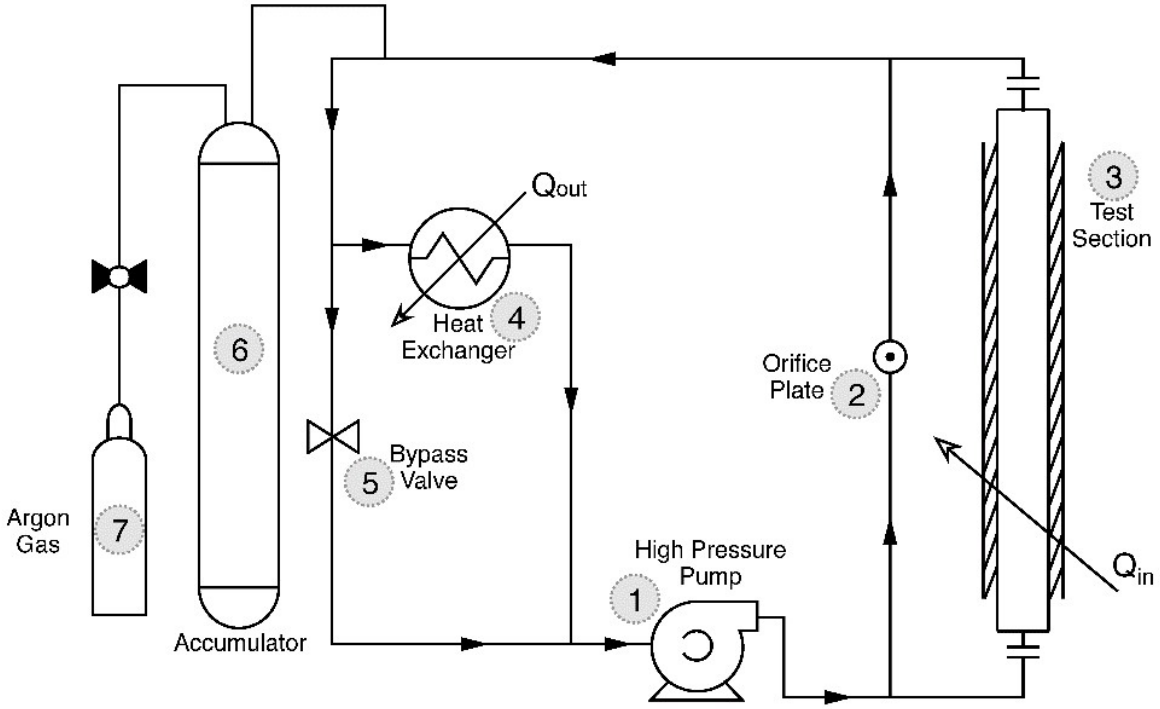

Fig. 9.26. Schematic diagram of high pressure water-test facility at University of Wisconsin-Madison.

9.2.1.1. TEST SECTION DESIGN

The test section has a square cross section and encloses a 2x2 bundle of heater rods, each capable of providing 100 kW. Each rod contains an electrically heated Inconel 718 filament. Grade AX05 boron nitride provides insulation for the filament and a sheath of Monel K500 encloses the filament and insulation. Grooves cut into this sheath allow for embedded thermocouples. Finally, a

cladding of Monel K500 is swaged onto the entire assembly to ensure good thermal conductivity. The dimensions of the channel and heater rods are shown in Fig. 9.27. In this experimental setup, the pitch to diameter ratio is 1.33 and the flow area is 4.32 cm^2. The walls of the square channel were fabricated from 316 stainless steel and the inner corners were milled to limit the corner inner radius of the square to 0.3 mm or less. The square flow channel fits snugly inside a two-inch schedule 160 SS316 pipe which provides the pressure boundary for the system. Five grid spacers were installed to provide alignment for the heater rods. Each grid spacer was welded to a small piece of the square flow section. The nominal reduction in flow area of these spacers is calculated to be 17%.

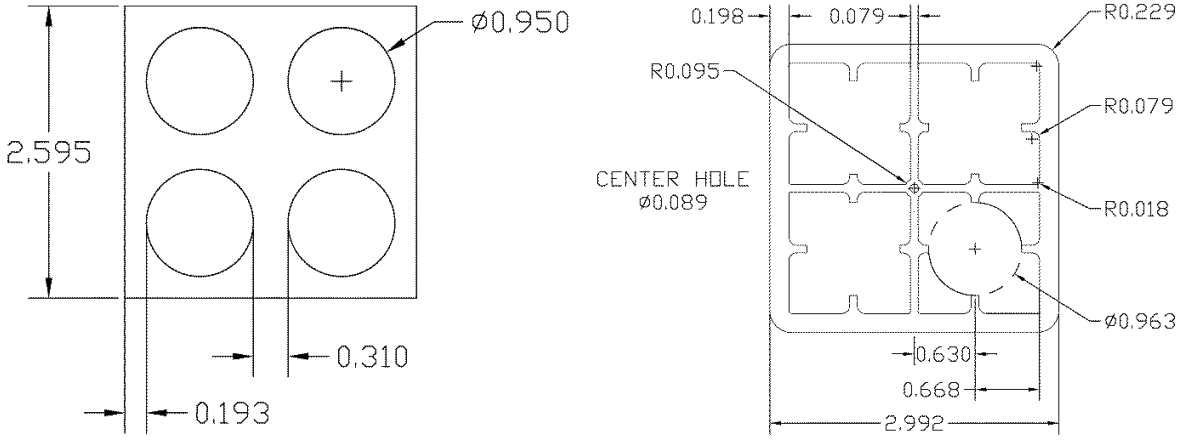

Fig. 9.27. Schematic diagram of the 2×2 rod bundle and grid spacer configuration.

Each rod in the test section provides a cosine axial power to simulate the heat flux distribution created during fission within a fuel rod. A helical cut through fully annealed seamless Inconel tubing enables the filament inside the rod to produce the power profile, which is shown graphically in Fig. 9.28 and is expressed as

$$\frac{q(z)}{q_{average}} = 0.8187458177 + 0.6812541823\ cos\left\{22.436354311\left[\frac{z}{L_{HL}} - 0.5\right]\right\} \tag{9.1}$$

where z is the axial distance in metres and L_{HL} is the total heated length (i.e., 2 m).

Each heater rod has ten imbedded Type K thermocouples located at various angular and axial positions. The angular distribution of the thermocouples varies between two types. The angular position and the heater orientation in the square channel are listed in Table 9.10.

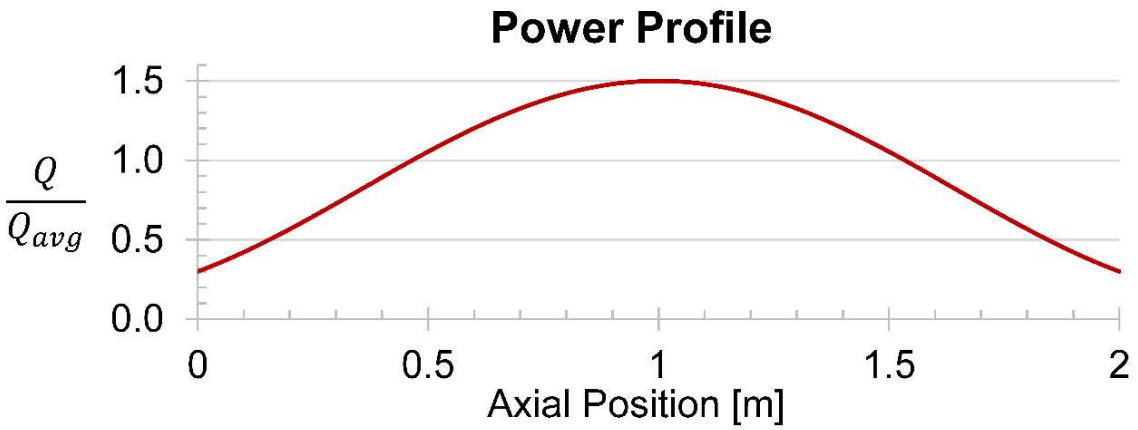

Fig. 9.28. Axial power profile for the 2x2 rod bundle test at University of Wisconsin, Madison.

TABLE 9.10. INTERNAL THERMOCOUPLE ANGULAR AND AXIAL LOCATIONS INSIDE THE 2X2 ROD BUNDLE.

T/C #	1	2	3	4	5	6	7	8	9	10
Angular Location Rods 1/2	0°	60°	330°	225°	300°	180°	30°	270°	90°	135°
Angular Location Rods 3/4	330°	225°	270°	90°	180°	0°	60°	300°	135°	30°
Axial location (mm)	961.9	1038.1	1333.5	1333.5	1462.0	1462.0	1538.2	1778.0	1778.0	1974.6

Bulk fluid temperatures at six different axial locations were measured with thermocouples inserted into the subchannels through the pressure boundary. Locations of these thermocouples are listed in Table 9.11. The last axial location was monitored with three thermocouples, each 90° apart. The inlet and outlet temperature are measured by thermocouples located before and after the test section respectively.

TABLE 9.11. AXIAL LOCATIONS OF THERMOCOUPLES MEASURING BULK FLUID TEMPERATURE INSIDE THE 2X2 ROD BUNDLE.

T/C #	1	2	3	4	5	6, 7 and 8
Axial Location (mm from start of heated section)	579	1038	1333	1462	1538	1778

The experiment covered pressures of 16.5 and 18 MPa at two mass fluxes and three inlet subcoolings.

9.2.1.2.EXPERIMENTAL RESULTS

Generally, CHF occurred predominantly in outer subchannels and between the rods at the axial location towards the second half of the test section. Fig. 9.29 illustrates the variation of local CHF based on the measured locations with local quality, which is calculated from

$$x(z) = \frac{h(z) - h_f}{h_g - h_f} \tag{9.2}$$

where h_f and h_g are enthalpies for saturated liquid and vapour, respectively, in kJ/kg. The local enthalpy, h(z), is defined as

$$h(z) = h_0 + \frac{1}{\dot{m}} \int_0^z Q(z)\, dz \tag{9.3}$$

The significant uncertainty displayed in the figure was attributed to the limited number of fixed thermocouples along the axial length. Having said that, the general trend of decreasing local CHF is shown with increasing local quality.

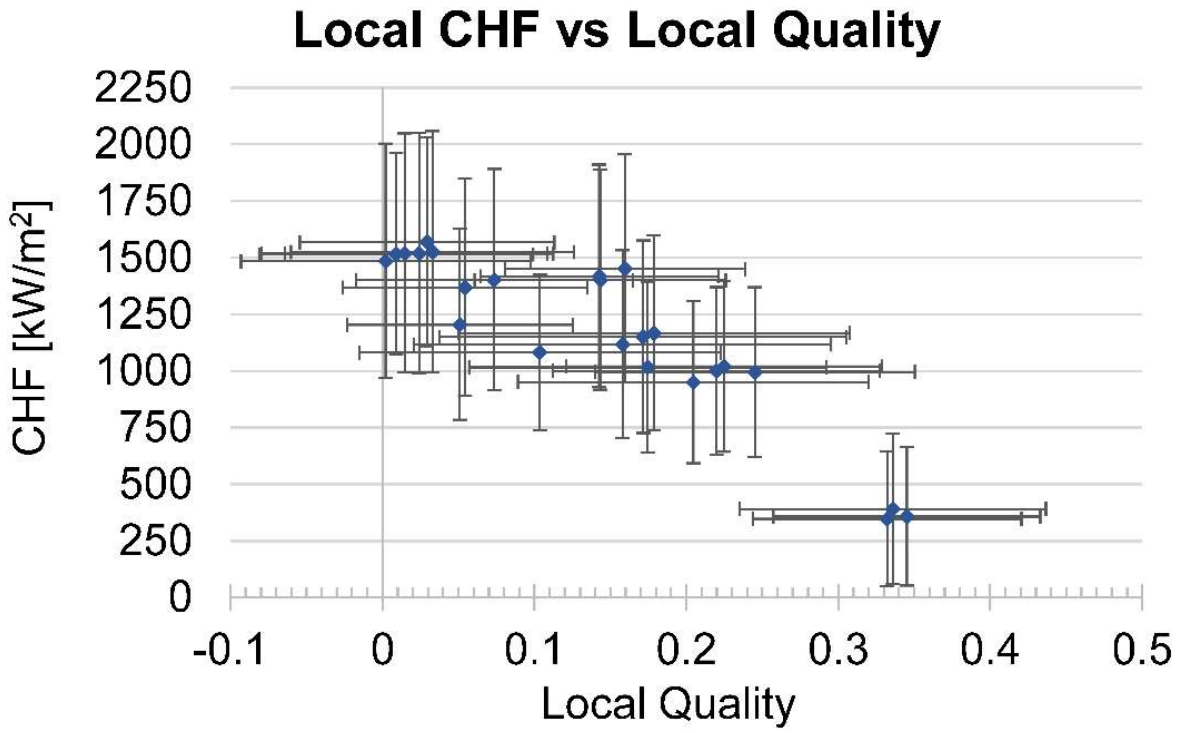

Fig. 9.29. Variation of local CHF with local quality.

In view of the significant uncertainty, [9.21] analyzed the average CHF value, q_c, which is defined as

$$q_C = \frac{Q_C}{\pi DL} \tag{9.4}$$

where Q_C is the critical power and D and L are the diameter and length, respectively, of the heated rod. Fig. 9.30 illustrates variations of average CHF values with pressure, mass flux and inlet subcooling.

The average CHF value decreases with increasing pressure but increases with increasing mass flux and inlet subcooling. [9.21] assessed the Biasi correlation [9.22], the W3 correlation [9.23], the EPRI correlation [9.24] and the 2006 CHF look-up table [9.25] against their average CHF values. They indicated that only the 2006 CHF look-up table is applicable over the range of their database and extrapolations were applied for the other correlations. Most experimental average CHF values were underpredicted, but within ±20 %, using these prediction methods. Predicted average CHF values are compared against experimental values in Fig. 9.31.

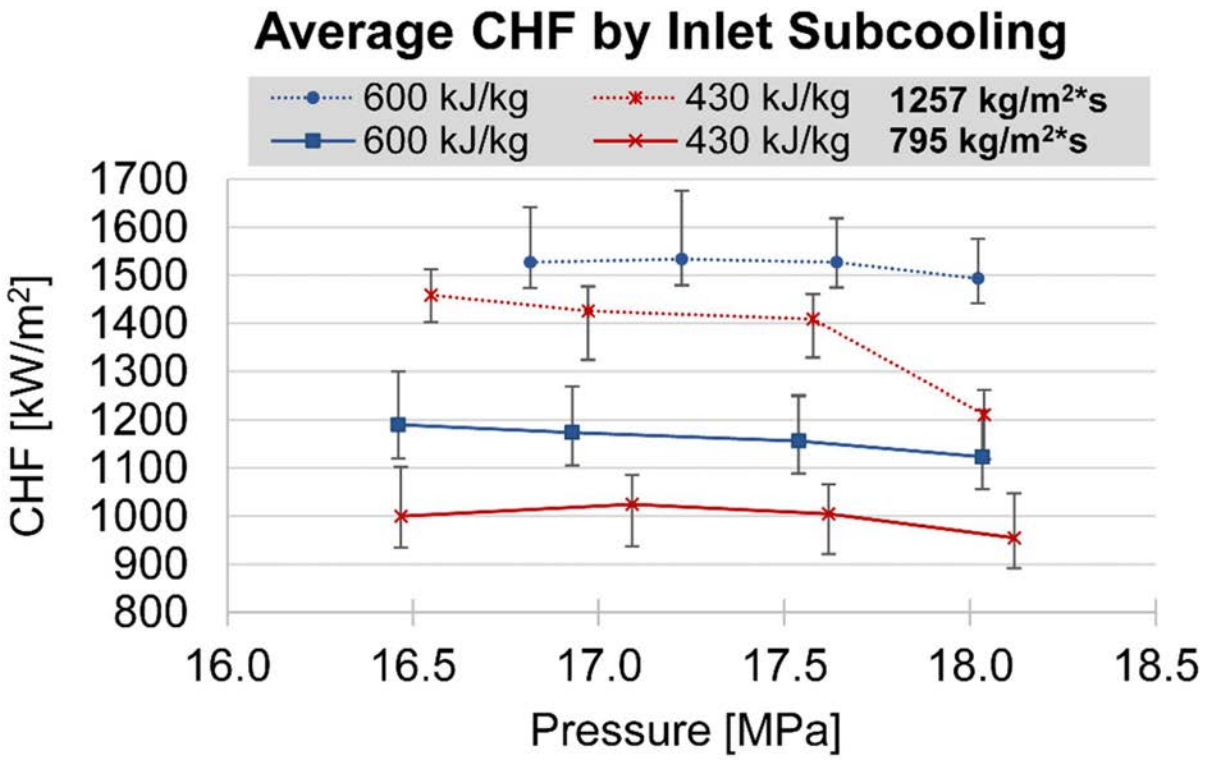

Fig. 9.30. Variations of average CHF with pressure and inlet subcoolings.

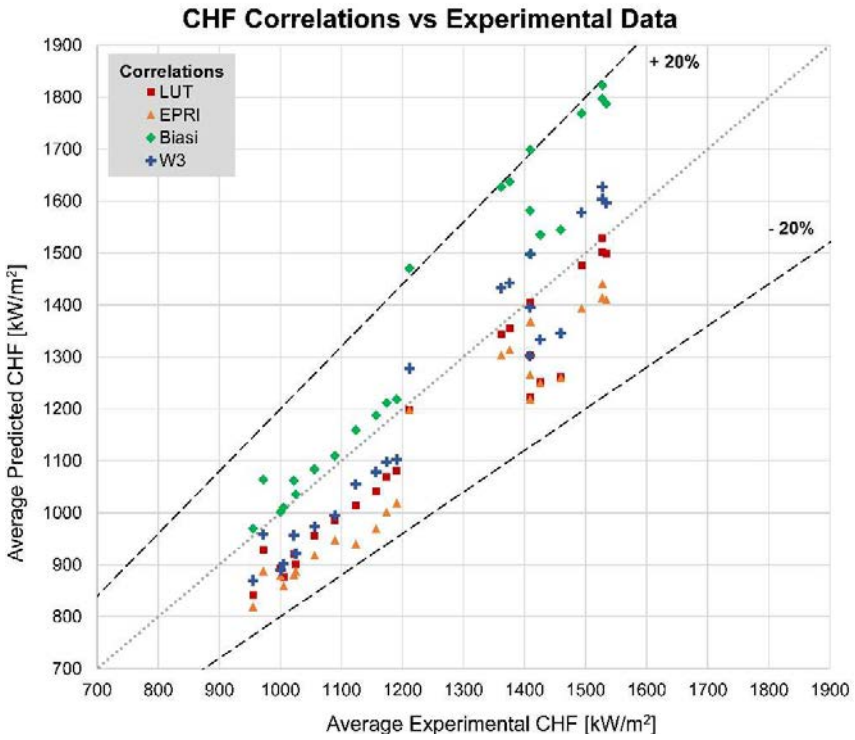

Fig. 9.31. Assessment of CHF prediction methods against average CHF values.

9.2.2. CHF IN AXIALLY HEATED 5X5 ROD BUNDLE AT HIGH REFRIGERANT PRESSURES

[9.26] performed CHF experiments at high subcritical pressures. The TS was a 5×5 square array rod bundle cooled by R-134a, flowing vertically upward. The rods were made of Alloy 601 tubing with an outer diameter of 9.5 mm and a heated length of 2.0 m. The 5×5 rod bundle was inserted into a square flow housing, which measured 66.9 mm × 66.9 mm. The rods were spaced at a pitch of 12.85 mm and heated by a DC power supply. The axial power profile was uniform, and the radial power distribution was non-uniform. The power of the nine central rods was around 20% higher than that of the surrounding 16 rods. The rod bundle was supported by simple grid spacers without mixing vanes; the vertical spacer pitch was 564 mm. 68 K type TCs were mounted 10 mm upstream from the top end of the heated section of the rods on the inner surface. CHF occurred mostly at the higher power rods (central rods). It is known that spacers improve turbulence mixing and affect CHF. Since the axial power profile is uniform, it was expected that CHF would tend to occur towards the exit of the heated length. The distance between the exit of the heated length and the most upstream spacer was 511 mm; [9.26] reported that this spacing did not affect CHF. Fig. 9.32 shows the effect of inlet subcooling and reduced pressure on the critical power (Q) of the rod bundle at two different mass fluxes. Fig. 9.33 shows the variation of critical power with reduced pressure and mass flux. The comparison was performed at a fixed inlet fluid enthalpy of 70 kJ/kg. Table 9.12 presents the compiled CHF data range for the 5×5 square array rod bundle cooled by R−134a. The hydraulic diameter (D_{hy}) of the rod bundle was 10.67 mm.

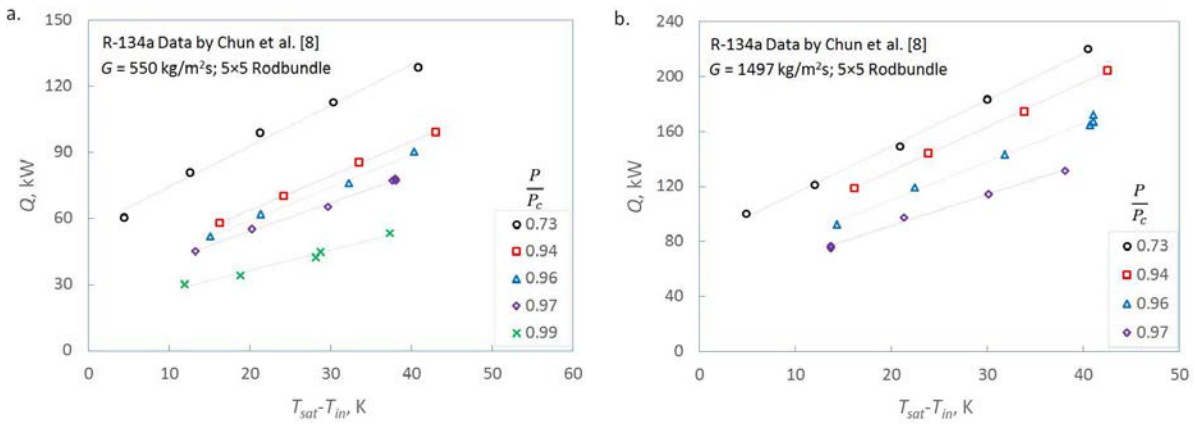

(a) *(b)*

Fig. 9.32. Variation of critical power (Q) vs. inlet subcooling at different reduced pressures, for (a) G = 550 kg/m2s and (b) G = 1497 kg/m²s. R–134a flow in a 5×5 rod bundle [9.26].

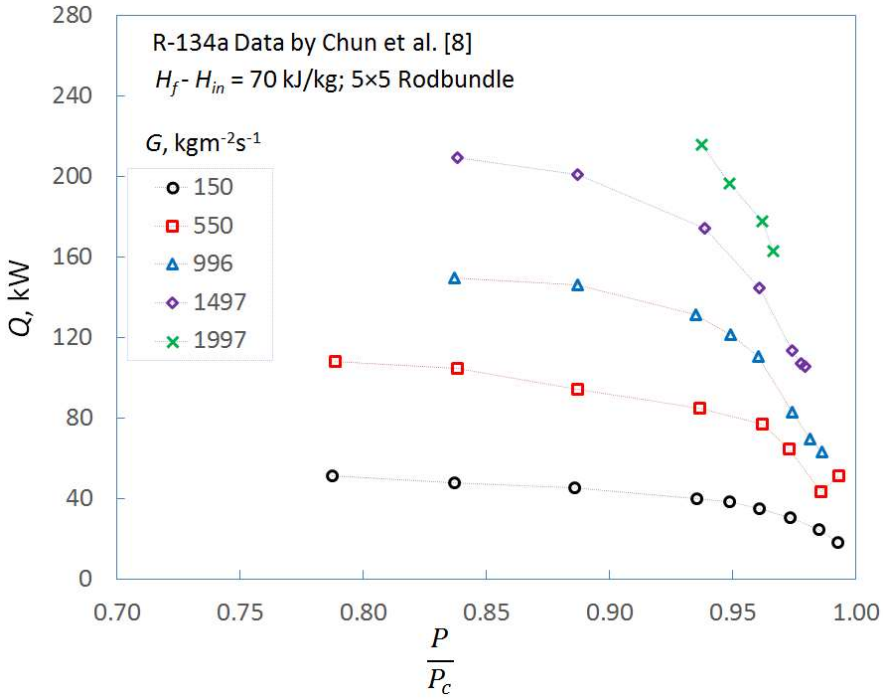

Fig. 9.33. Critical power variation with reduced pressure near the critical point for different mass fluxes at a fixed inlet fluid enthalpy of 70 kJ/kg [9.26].

TABLE 9.12. RANGES OF THE COMPILED CHF DATA FOR A 5×5 ARRAY ROD BUNDLE COOLED WITH R-134A

Reference	D_{hy} **(mm)**	Q **(kW)**	**P/P$_c$ (-)**	G **(kg·m^{-2}·s^{-1})**	x_{in}	**Number of Points**
Chun et al. [9.26]	10.67	7.36–314.7	0.60–0.99	49–2495	–3.07 to –0.102	315

9.3. ANALYSIS & CORRELATION

9.3.1. CHF PREDICTION METHODS AT HIGH PRESSURES

The predicted CHF by [9.25] was compared with the corresponding experimental value. Generally speaking, results showed that the look-up table overpredicted the CHF data at the high subcritical pressure range 18–22 MPa. Concerning the data of [9.11], they were overestimated significantly; a main reason for this overprediction is the distant extrapolation of the LUT CHF outside of the table applicable range for the quality. It's worth reporting that [9.11] applied the 1995-CHF-Table by [9.25] to their data. Most of the data from [9.11] were obtained at high subcooling; as a result, the application of the 1995-CHF-Table to these data was substantially beyond the limits of the table. This extrapolation caused large deviation in the 1995 CHF Table prediction. It is worth noting that the 1995-CHF-Table used by [9.11] is not only older than the 2005-version, but also narrower in the range of applicability.

Within the applicable range, the 2005-CHF-Table represented 1190 data points with an average and an rms errors of 1.7% and 26%, respectively. Outside the applicable range, however, the table overpredicted the data (25 data points) with an average and an rms errors of 63% and 66%, respectively. Fig. 9.34 shows a comparison between the predicted CHF by [9.25] and the experimental data by [9.11]. Fig. 9.34a shows an overprediction of the experimental CHF and Fig. 9.34b shows the variation of the error for the same data. As can be seen, the prediction accuracy is worse when extrapolating the table beyond its limits, as expected.

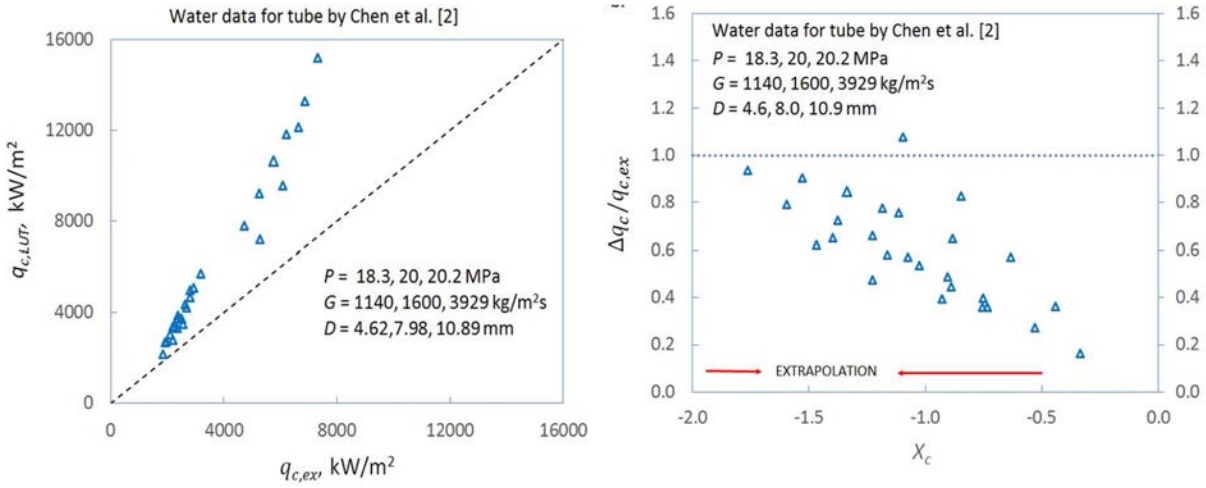

(a) *(b)*

Fig. 9.34. A comparison of predicted CHF by [9.25] and experimental data by [9.11].

9.3.2. CHF PREDICTION METHODS AT HIGH PRESSURES

9.3.2.1.EMPIRICAL CORRELATION

A CHF correlation has been proposed for tubes of different diameters under subcooled boiling conditions and is expressed as [9.12]:

$$q_c = c_{sub} q_{sat} \tag{9.5}$$

$$q_{sat} = \frac{(h_f - h_{in})GD}{L} \tag{9.6}$$

$$c_{sub} = Min\left(2350(1 - 0.0307\,P)\left(G\left(h_f - h_{in}\right)\right)^{-0.35}\left(\frac{D}{0.008}\right)^{-0.32}, 1.0\right) \tag{9.7}$$

where q_c is the critical heat flux in W/m^2, q_{sat} is the heat flux in W/m^2 for reaching the saturation temperature at the tube outlet, G is the mass flux in kg/(m^{2}s), h_f is the saturated liquid enthalpy in J/kg, h_{in} is the inlet enthalpy in J/kg, D and L are the inner diameter and heated length, respectively, in metres.

The prediction accuracy of this correlation was assessed against the experimental results. Fig. 9.35 shows variations of prediction error with pressure and mass flux. The prediction error is defined as

$$\text{Prediction error} = (q_{c,p} - q_{c,m})/q_{c,m} \tag{9.8}$$

where $q_{c,p}$ and $q_{c,m}$ are predicted and experimental CHF values, respectively. Overall, the average errors, AVG, are -0.8%, 2.1% and 2%, with standard errors of 5.5 %, 8.5 % and 5.9 % for tubes with diameter of 4.62, 7.98 and 10.89 mm, respectively. More than 90 % of these data points are predicted with less than $\pm$10 % errors.

Another correlation has been derived with experimental CHF results at saturated boiling conditions and is expressed as [9.13]

$$q_c = c_{sat} q_0 \tag{9.9}$$

$$q_0 = \frac{(1-x_0)GD_{fg}}{4L} \tag{9.10}$$

$$c_{sat} = 1 - 0.00216(Gh_{fg})^{0.25} \tag{9.11}$$

where h_{fg} is the latent heat of evaporation in J/kg and x_o is the critical quality.

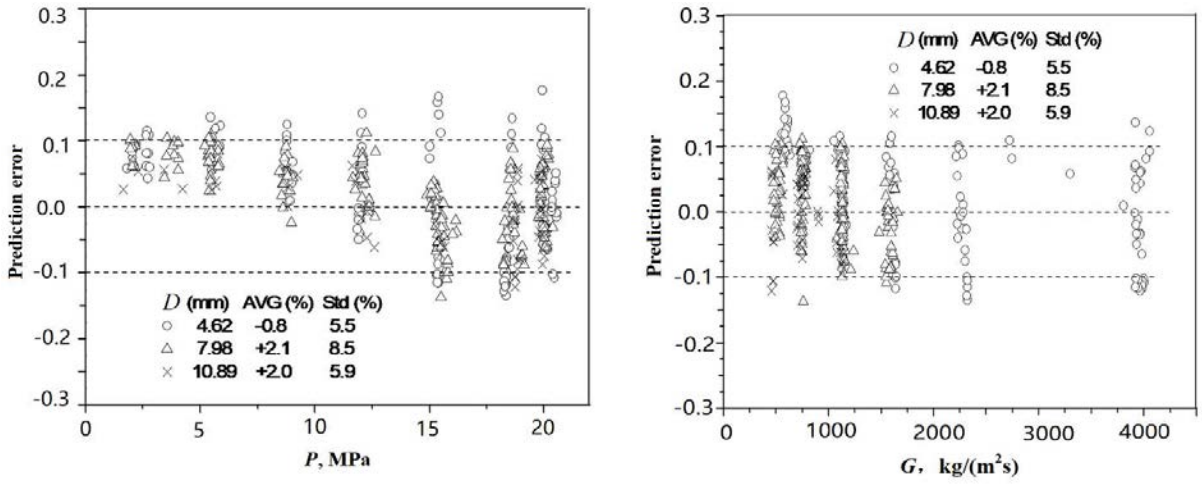

Fig. 9.35. Variations of prediction error of subcooled CHF correlations with pressure and mass flux [9.11].

Fig. 9.36 shows variations of prediction error with pressure, mass flux and inlet quality, x_i. For more than 95% data points the deviations are less than 15%. Overall, the average error and standard deviation are 0.03% and 7.3%, respectively. Almost all experimental CHF values are predicted within $\pm$15% errors.

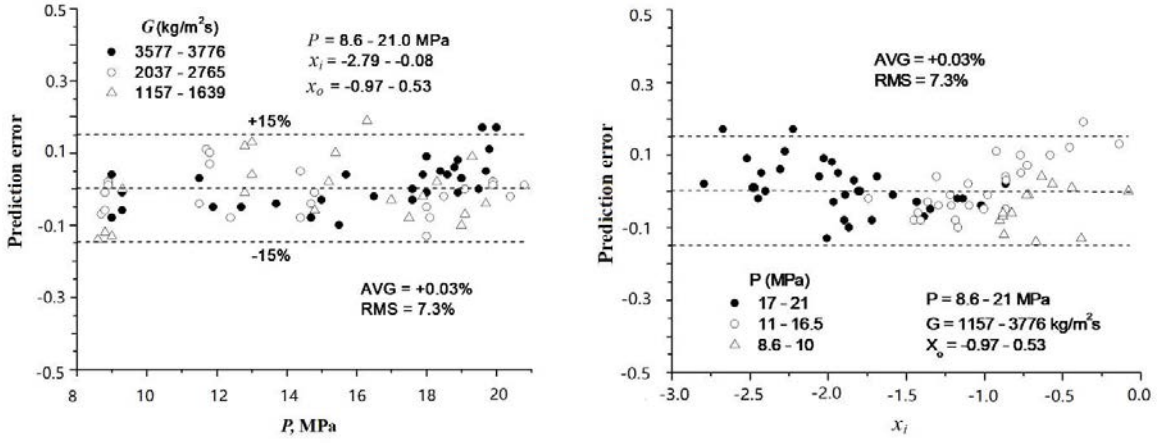

Fig. 9.36. Variations of prediction error of saturated CHF correlations with pressure, mass flux and inlet quality [9.12].

9.3.2.2.PHYSICAL MODEL FOR TUBES

[9.27] modified the thickness of bubbly layer calculation in the liquid sublayer dryout model for the high and low subcooling regions. The model calculates the thickness of bubbly layer, the velocity distribution, temperature distribution, total flow rate, the vapor and liquid flow rate in the bubbly layer, average temperature from the edge of bubbly layer. CHF is evaluated through iterations by comparing the local enthalpy using the mixture enthalpy equation and that through a

heat balance. Predictions of CHF using the model were compared against the experimental results in Fig. 9.37. The average prediction errors are —0.8 %, 0.3 % and 1.9 % with standard deviation of 5.4 % 5 % and 7.3 % for tubes of 4.62, 7.98 and 10.89 mm in diameter, respectively.

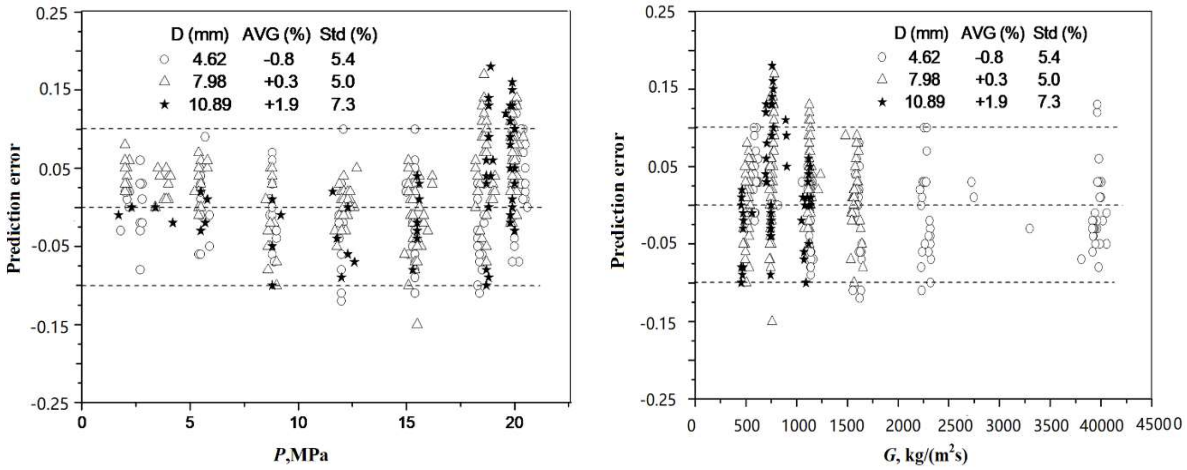

Fig. 9.37. Variations of prediction error of the model against experimental CHF results [9.11].

Nomenclatures and Acronyms

AVG	Average error (%)
CHF	Critical Heat Flux (kW/m^2)
D	Diameter (m)
G	Mass flux (kg/(m^2·s))
h	Enthalpy (kJ/kg)
L	Length (m)
$\dot{m}$	Mass flow rate (kg/s)
P	Pressure (MPa)
Q	Power (MW)
q	Heat flux (MW/m^2)
RMS	Root-mean-square error (%)
Std	Standard deviation (%)
T	Temperature (°C)
x	Quality (-)
ΔT	Temperature difference (K)
z	Axial Location (m)

Subscripts

avg	Average
c	Critical
ex	Experiment
f	Liquid
fg	Difference between vapour and liquid
g	Vapour

HL	Heated
h	Heated
hy	Hydraulics equivalent
in	Inlet, Input
m	measured
max	Maximum
o	Outlet
out	Output
p	Predicted
sat	Saturated

Acronyms

AECL	Atomic Energy of Canada Limited
CO_2	Carbon Dioxide
DNB	Departure from Nucleate Boiling
EPRI	Electric Power Research Institute
ID	Inner Diameter
HHHC	Horizontal Heater Horizontal Cooler
HHVC	Horizontal Heater Vertical Cooler
KIMOF	KIT Modelfluid Facility
KIT	Karlsruhe Institute of Technology
LUT	Look-Up Table
LWR	Light Water Reactor
NC	Natural Circulation
OD	Outer Diameter
R-134a	Refrigerant-134a
SCWR	Super-Critical Water-cooled Reactor
SPNCL	Supercritical Pressure Natural Circulation Loop
SS	Stainless Steel
T/C	Thermocouples
TT	Thermocouples location
TS	Test Section
VHHC	Vertical Heater Horizontal Cooler
VHVC	Vertical Heater Vertical Cooler
W3	Westinghouse-3

REFERENCES TO SECTION 9

[9.1] GROENEVELD, D.C., IRELAND, A., KAIZER, J., VASIC, A., An Overview of Measurements, Data Compilations and Prediction Methods for the Critical Heat Flux in Water-Cooled Tubes, Nuclear Engineering and Design, **331**, (2018), 211-221.

[9.2] ALEKSEEV, G.V., ZENKEVICH, B.A., PESKOV, O.L., SERGEEV, N.D., SUBBOTIN, V.I., Burnout Heat fluxes under Forced Water Flow, Proc. 3rd U.N. International Conference on the Peaceful Uses of Atomic Energy, International Atomic Energy Agency, Vienna, 1964, 295-304.

[9.3] BAILEY, N.A., LEE, D.H., An Experimental and Analytical Study of Boiling Water at 2000 to 2600 psi. Part I. Dryout and Post-Dryout Heat Transfer, AEEW-R 659, 1969.

[9.4] BECKER, K.M., HERNBORG, O, BODE, M. ERIKSSON, O., Burnout Data for Flow of Boiling Water in Vertical Round Ducts, Annuli and Rod Clusters, Aktiebolaget Atomenergi, Stockholm, Sweden, Report AE-177, 1965.

[9.5] KIRILLOV, P.L., PESKOV, O.L., SERDUN, N.P., Control Experiment on Critical Heat Transfer during Water Flow in Pipes, Heat Transfer-Soviet Research, (1985), 858-860 (translation from original article by Kirillov et al. in Atomnaya Energiya, **57, 6**, (1984), 422- 423).

[9.6] SMOLIN, V.N., POLYAKOV, V.K., ESIKOV, V.I., On the Heat Transfer Crisis in SteamGenerating Pipes, Soviet Journal of Atomic Energy, **13**, (1962), 968–972, (translation from Atomnaya Energiya, **13, 4**, 360–364).

[9.7] SODERQUIST, B., Department of Nuclear Reactor Engineering, Royal Institute of Technology, Stockholm, Sweden. Swedish CHF Data received via personal communication with D.C. Groeneveld in March 1994.

[9.8] YIN, S.T. et al., Proc. 25th Nat. Heat Transfer Conf., Houston, 1988.

[9.9] ZENKEVICH, B.A., PESKOV, O.L., PETRISHCHEVA, N., SERGEEV, N., SUBBOTIN, B.I., An Analysis and Correlation of the Experimental Data on Burnout in the Case of Forced Flow of Boiling Water in Pipes, Physico-Energy Institute, Automizdat, Moscow (HTFS translation 12022), 1969.

[9.10] ZENKEVICH, A., Analysis and Generalization of Experimental Data on Heat Transfer Crisis Associated with Forced Convection of Cooling Water in Tubes, Atomic Energy of Canada Report (AECL-Tr-Misc304), 1974.

[9.11] CHEN, Y., BI, K., ZHAO, M., YANG, C., DU, K., Critical Heat Flux with Subcooled Flowing Water in Tubes for Pressures from Atmosphere to Near-Critical Point, J. Energy and Power Engineering, **10**, (2016), 211–222.

[9.12] CHEN, Y., BI, K., ZHAO, M., YANG, C., DU, K., Critical Heat Flux with Flowing Water in Tubes for Pressures of up to Near-Critical Point, Proc. 16th International Topical Meeting on Nuclear Reactor Thermal Hydraulics (NURETH-16), Chicago, 2015.

[9.13] CHEN, Y., ZHAO, M., BI, K., YANG, B., ZHANG, D., DU, K., Critical Heat Flux of Flowing Water in Tube for Pressure Up to Near Critical Point—Experiment and Prediction, J Nuclear Engineering and Radiation Science, 4, 1, (2018), 011006-1.

[9.14] BERGLES, A.E., Burnout in Boiling Heat Transfer, Part II: Subcooled and Low-Quality Forced-Convection System, Nuclear Safety, **18, 2**, (1977), 154 – 167.

[9.15] YANG, B., ZHAO, M., CHEN, Y., BI, K., ZHANG, D., DU, K., Experimental Investigation on CHF of Water Flowing in Upward Tube, Proc. 8th Korea-China Workshop on Nuclear Reactor Thermal–hydraulics (WORTH-8), Yeosu, 2017.

[9.16] ZAHLAN, H., JIANG, K., TAVOULARIS, S., GROENEVELD, D.C., Measurements of Heat Transfer Coefficient, CHF and Heat Transfer Deterioration in Flows of CO_2 at Near-Critical and Supercritical Pressures, Proc. 6th Int. Symposium on Supercritical Water-Cooled Reactors (ISSCWR-6), Shenzhen, 2013.

[9.17] ETER, A., GROENEVELD, D., TAVOULARIS, S., Convective Heat Transfer at High Subcritical Pressures in Tubes with and without Flow Obstacles, Nucl. Eng. Des., **318**, (2017), 1-23.

[9.18] VIJAYARANGAN, B.R., JAYANTI, S., BALAKRISHAN, A.R., Studies on Critical Heat Flux in Flow Boiling at Near Critical Pressures, Int. J. Heat Mass Transfer, **49, 1-2**, (2006), 259-68.

[9.19] FEUERSTEIN, F., SCHINDLER, P., KLINGEL, D., CHENG, X., Experimental Study on Critical Heat Flux (CHF) in a R134a Cooled Vertical Tube at High Pressures, Proc. 11th International Topical Meeting on Nuclear Reactor Thermal Hydraulics, Operation and Safety (NUTHOS-11), Gyeongju, 2016.
[9.20] CHENG, X., MUELLER, U., Review on Critical Heat Flux in Water Cooled Reactors, Wissenschaftliche Berichte FZKA 6825, Forschungszentrum Karlsruhe, 2003
[9.21] LYONS, K., ANDERSON, M., Critical Heat Flux in Rod Bundles at High Pressure, private communication, 2019.
[9.22] BIASI, L., CLERICI, G.C., GARRIBA, S., SALA, R., TOZZI, A., A New Correlation for Round Duct and Uniform Heating - Comparison with World Data, EURAEC Report No. 1874), EURATOM/US Agreement for Cooperation, ARS, SpA, Societa Applicazioni Ricerche Scientifiche, 1967.
[9.23] TONG, L.S., Prediction of Departure from Nucleate Boiling for an Axially Non-Uniform Heat Flux Distribution, Journal of Nuclear Energy, **21**, (1967), 241–248.
[9.24] REDDY, D.G., FIGHETTI, C.F., Parametric Study of CHF Data. Volume 2: A Generalized Subchannel CHF Correlation for PWR and BWR Fuel Assemblies, Project Report No. NP-2609, Electric Power Research Institute, New York, New York, 1983.
[9.25] GROENEVELD, D.C., SHAN, J.Q., VASIĆ, A.Z., LEUNG, L.K.H., DURMAYAZ, A., YANG, J., CHENG, S.C., TANASE, A., The 2006 CHF Look-Up Table, Nuclear Engineering and Design, **237**, (2007), 1909–1922.
[9.26] CHUN, S.Y., HONG, S.D., KIKURA, H., ARITOMI, M., Critical Heat Flux in A Heater Rod Bundle Cooled by R-134a Fluid Near Critical Pressure, J Nucl Sci Technol, **44, 9**, (2007), 1189-1198.
[9.27] CHEN, Y., YANG, C., ZHAO, M., BI, K., DU, K., ZHANG, S., Subcooled Boiling Critical Heat Flux of Water Flowing Upward in a Tube for Lower Flow and Pressure up to 20 MPa, Proc. 14th Int. Topical Meeting on Nuclear Reactor Thermal Hydraulics (NURETH-14), Toronto, 2011.

10. SUBCHANNEL MODEL IMPROVEMENT

Subchannel codes have been applied in support of design and optimization of SCWR cores and fuel assemblies. These codes were developed with fundamental models but applied constitutive equations derived from data obtained from subcritical pressure experiments. In view of a lack of experimental data at supercritical pressures, this approach is applicable during the conceptual design phase. Nevertheless, improved subchannel models would enhance the confidence on the design of the SCWR cores and fuel assemblies. Primary parameters in constitutive equations of subchannel codes include heat transfer and hydraulics resistance, which have been covered in previous sections. This section focuses on secondary parameters, which would still have implication to the subchannel-code prediction.

10.1. INTER SUBCHANNEL MIXING

The mixing of mass, energy and momentum between subchannels in single phase flow consists of forced and natural mixing. The forced mixing is attributed to the presence of spacers (i.e., grids or wrapped wires). It depends on the geometry and location of the fixture and is generally established through relevant experimental data. The natural mixing includes the diversion flow and the turbulent mixing. The diversion-flow mixing is mainly caused by the net convective transport (diversion crossflow) of energy from one subchannel to another. This type of mixing would result from flow redistribution due to the pressure gradient between the subchannels. Mixing of this type can be computed with reasonable accuracy from the momentum and energy equations.

The turbulent mixing is attributed to the eddy motion of the fluid across the gap between adjacent subchannels, enhances the exchange of the momentum and the energy through the gap with no net transport of the mass. It has been considered as a component superimposed upon the diversion mixing. The effect of turbulent mixing is considered in the axial momentum equation and the energy conservation equation in subchannel codes. It is often predicted using a turbulent mixing model, which determines the turbulent mixing flow rate from subchannel i to j per unit length as

$$w'_{ij} = \rho_i v_{ef} \; s_{ij} \tag{10.1}$$

where v_{eff} is the effective mean fluctuating velocity. The sharp variation of thermophysical properties in the vicinity of the pseudo-critical temperature brings large non-uniformity of properties and buoyancy forces over the cross section of channels for fluids at supercritical pressures. This has significant impact on the hydraulics and heat transfer characteristics of the coolant.

[10.1] applies the second order closure turbulence model with enhanced wall treatment in the CFD code Fluent 6.1 to examine the turbulence mixing behaviours in subchannels under supercritical pressures. Two types of subchannel lattices in a bare bundle (i.e., without any spacing devices) have been studied in the calculation: triangular to triangular and square to square (see Fig. 10.1).

Inter-subchannel mixing in the shaded area is considered as the computational domain in the CFD analysis, which represents 1/6 of the triangular lattice and 1/8 of the square lattice. Table 10.1 lists

subchannel parameters for various case studies in the analysis, where p is the pitch in mm, *D* is the rod diameter in mm (which is assumed as 11.526 mm) and s is the gap between rods in mm.

(a) Triangular array *(b) Square array*

Fig. 10.1. Schematic diagram of rod bundle and flow channels.

TABLE 10.1. PARAMETERS FOR TRIANGULAR ARRAY AND SQUARE ARRAY

p/D	*p* (mm)	*s* (mm)
1.1	12.6786	1.1526
1.15	13.2549	1.7289
1.2	13.8312	2.3052
1.25	14.4075	2.8815
1.3	14.9838	3.4578
1.173521	13.526	2
1.347041	15.526	4

The reference [10.1] studied two cases for turbulent mixing: adiabatic and heated conditions. The mixing coefficient under adiabatic conditions is expressed as

$$\beta_{adi} = \frac{|\bar{v}|}{W} = 0.11 \cdot Re^{-0.125} \tag{10.2}$$

for the triangular array in rod configuration and

$$\beta_{adi} = \frac{|\bar{v}|}{W} = 0.1391 \cdot \left(\frac{s}{D}\right)^{0.1679} \cdot Re^{-0.125} \tag{10.3}$$

for the square array in rod configuration. They estimated the mixing coefficients of 0.026 and 0.025, respectively, for these configurations at a Reynolds number of 10^6 and a *p/D* of 1.2. The turbulent mixing coefficient under heated conditions is expressed as

$$\beta_{heat} = \beta_{adi}\left(\frac{\rho_W}{\rho_b}\right)^{0.2} \tag{10.4}$$

10.2. SPACER/WIRE EFFECTS ON HT

Spacing devices are required in fuel assemblies to maintain spacing between fuel rods and minimize vibration. These devices are often located along the flow path and interfere with the fluid hence increasing the hydraulics resistance and pressure loss. On the other hand, the devices enhance the turbulence and mixing between subchannels leading to improved heat transfer. Two types of spacing devices (i.e., grid and wrapped wires) have been proposed for fuel assemblies of SCWRs. Experimental and analytical studies have been performed to investigate the enhancement effect of these spacing devices on heat transfer.

10.2.1. EFFECT OF WIRE WRAPPED SPACERS ON HEAT TRANSFER IN ANNULI

[10.2] installed a string of miniature ceramic tubes of 3 mm in outer diameter as the spacing device (referred as wire wrapped spacer hereafter) in the annular test section to maintain the position of the central heated rod. Section 4.3 describes the experiments and some of the test results. Fig. 10.2 illustrates the spacer configuration and the location in the annuli. The wounding pitch of the spacer is 50 mm at an angle of 45^o over a length of 100 mm. The spacer was located only at the first thermocouple location (i.e., no other location was equipped with spacer).

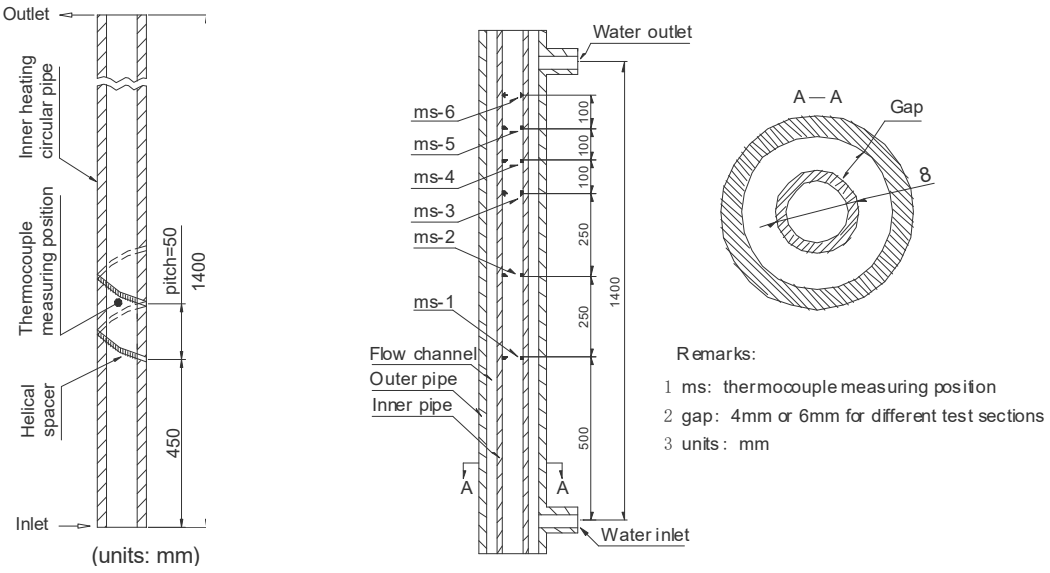

Fig. 10.2. Schematic diagram of the wire wrapped spacer and its location in the annuli [10.2].

Surface temperature and heat-transfer coefficient between bare (i.e., no spacer) and spacer-equipped annuli (see Fig. 10.3). The surface temperature is systematically lower while the heat transfer coefficient is higher for the spacer equipped than the bare annuli. This clearly demonstrates the enhancement effect of spacer on heat transfer at supercritical pressures.

The heat-transfer-enhancement effect decays with increasing distance downstream of the spacer. Fig. 10.4 compares heat transfer coefficients at various axial locations of thermocouples for two sets of flow conditions (see Fig. 10.2 for the thermocouples locations). At the mass flux of 965 kg/(m^{2}s), the heat-transfer coefficient is higher at locations close to than away of the spacer (e.g.,

comparing thermocouples at the ms-1 location where the spacer was located to those at the ms-6 location close to the outlet). It reduces with increasing distance from the spacer and there are little differences at ms-5 and ms-6 locations. At the mass flux of 350 kg/(m^{2}s), on the other hand, the decay in heat-transfer enhancement is very rapid as high heat-transfer coefficients are shown only at the ms-1 location while little differences in heat transfer coefficient are noticed at other thermocouples locations.

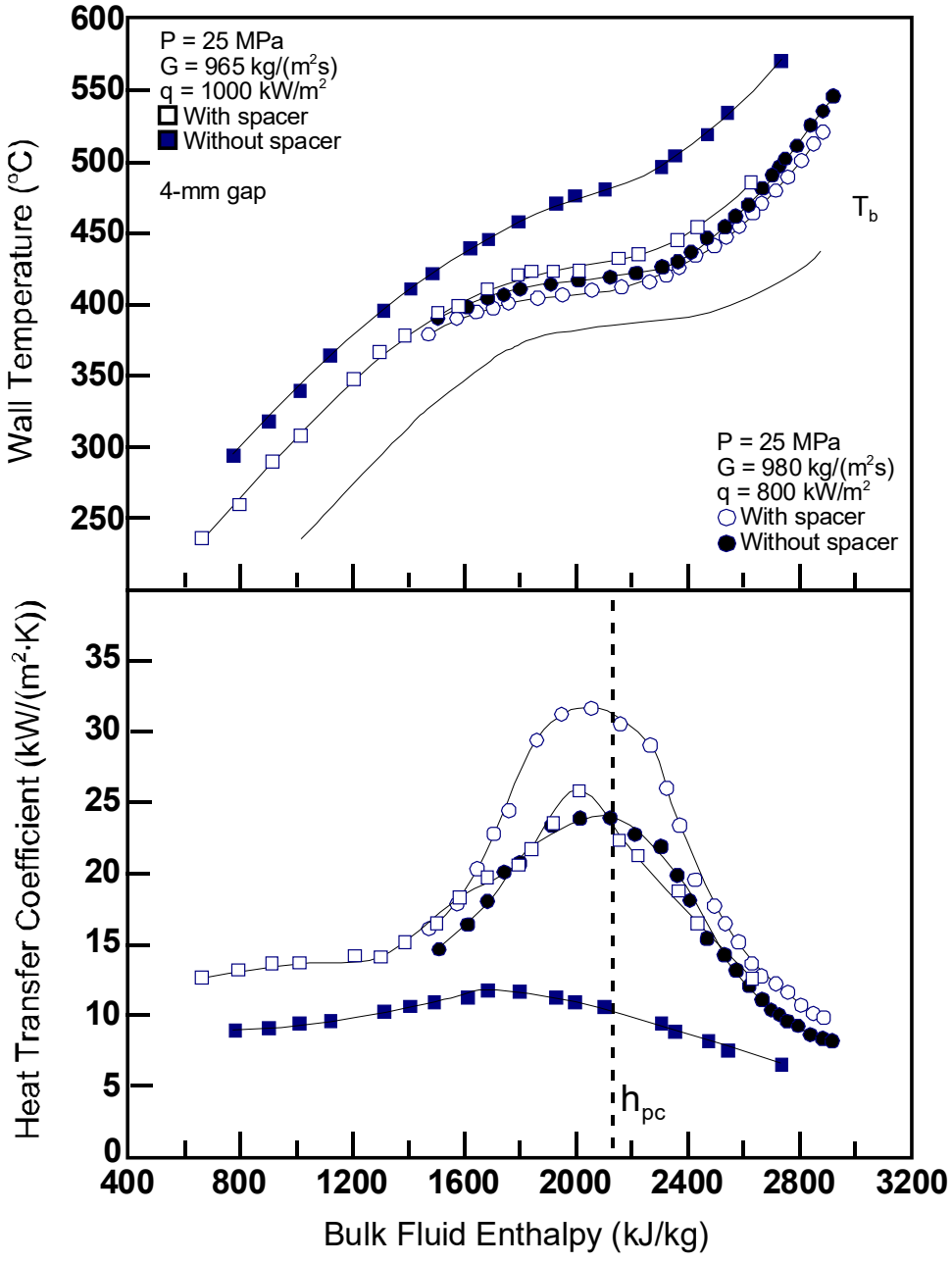

Fig. 10.3 Comparisons of wall temperature and heat transfer coefficients in annuli with and without spacers.

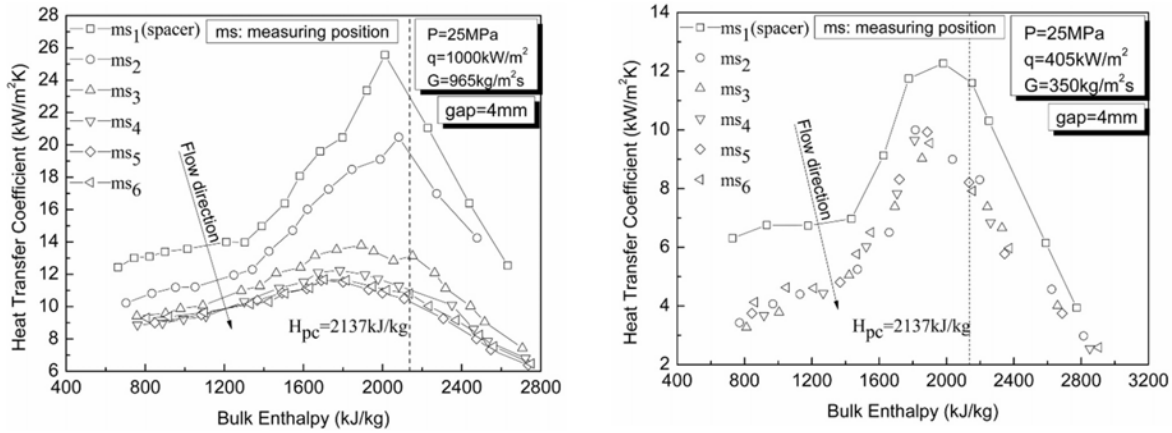

(a) High mass fluxes *(b) Low mass fluxes*

Fig. 10.4. Comparison of heat transfer coefficients at all six measuring positions.

10.2.2. EFFECT OF WIRE WRAPPED SPACERS ON HEAT TRANSFER IN A 4-ROD BUNDLE

[10.3] installed a wire wrapped spacer on each rod of the 4-rod bundle after completing the bare bundle test (see Section 5.1). The spacer was manufactured from a stainless-steel wire of 1.2 mm in outer diameter and was wounded around the rod with an axial pitch of 200 mm. It maintained the spacing of 1.44 mm (with a tolerance of 0.24 mm) between heated rods and between the heated rod and the ceramic insulator. The electric resistance of the wrapped wire was much higher than the rod. Nevertheless, a small power increase was anticipated at the wire location due to joule heating. The increase was localized at the wire location onlyFig. 10.5 shows the test section setup for the wire-wrapped bundle and the wire configurations at each measuring location. The experiments covered ranges of pressure at the inlet of the test section from 23 to 28 MPa, mass flow rates from 0.075 to 0.186 kg/s, heating powers on the test section from 12.1 to 60.5 kW, and inlet fluid temperatures from 200 to 450°C depending on the heated power and mass flow rate.

[10.3] examined the circumferential surface temperature distributions around the rods for various inlet fluid temperatures at the pressure of 25 MPa, mass flux of 1000 kg/(m^2·s) and heat flux of 600 kW/m^2. The wall temperature reaches a maximum at the narrow gap region between the heated rod and the ceramic liner and a minimum at the central subchannel between the heated rods. In general, a slight reduction in surface temperature has been observed for the wire-wrapped bundle. However, a small increase in wall temperature (bout 2°C) is shown at the wire locations and was attributed to the slight increase in power at the wire from joule heating.

To further understand the impact of the wire-wrapped spacer on the heat-transfer characteristic, wall-temperature measurements were obtained at measuring points 25 mm below the original planned locations at the pressure of 25 MPa and mass flux of 1000 kg/(m^2·s) but with the heat flux at 600 kW/m^2 (instead of 400 kW/m2). The change in measuring points shifted the spacer location by 45° in the clockwise direction. Spacers of Rod #1 and Rod #3 located at gaps with Rod #4 and Rod #2, respectively, while those of Rod #4 and Rod #2 located at gaps with the flow tube at

measuring points 25 mm lower than “mp-5” and “mp-3”, and vice versa at measuring points 25 mm lower than “mp-4” and “mp-2”.

Fig. 10.6 shows the circumferential wall temperature distributions at the inlet fluid temperature of 190.7 °C. With the spacer located away from the fixed thermocouples locations (i.e., 0°, 90°, 180° and 270°) at the measuring point “mp-5”, the wall-temperature distributions for Rod #3 and Rod #4 are relatively symmetrical at both sides of the narrow gap in each rod. The peak temperature is observed at the narrow-gap location (i.e., 180°) of each rod. Wall temperature distributions for Rod #1 and Rod #2 are a bit more complicated. Two peak wall temperatures are observed in Rod #1 corresponding to the spacer location at 45° and the narrow gap location at 180°. The wall temperature at the central subchannel remains low. A small wall temperature rise is also observed at the gap between Rod #1 and Rod #3 (i.e., 315°), which is located between the spacer of Rod #1 (located at 50-mm upstream) and the spacer of Rod #3 (located at 50-mm downstream). High temperatures at both spacer locations might have led to the wall-temperature increase. In Rod #2, only two peak wall temperatures are observed at the 45° and 225°, both correspond to the spacer locations. The first peak was attributed to the spacer of Rod #3 while the second peak to the spacer of Rod #2. In this case, the wall temperature at the narrow gap is not as high as that at the neighbouring location of 225° angle, where the spacer is located. The coupling effect of spacer and narrow gap has worsen the heat transfer and led to higher wall-temperature rise than each individual effect. The small increase in wall temperature observed at the angle of 315° in Rod #1 is not observed in Rod #2, probably attributed to the high temperature at the neighbouring location of 270°.

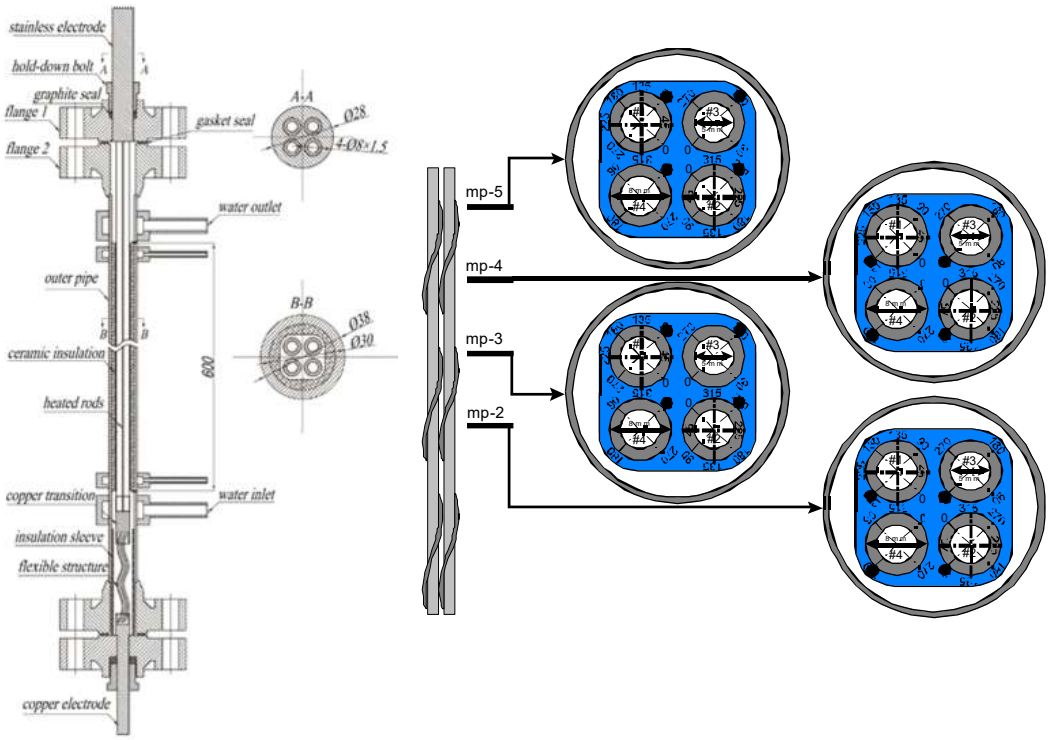

Fig. 10.5. Schematic geometry of the wire-wrapped bundle test section and wire configurations at each measuring location.

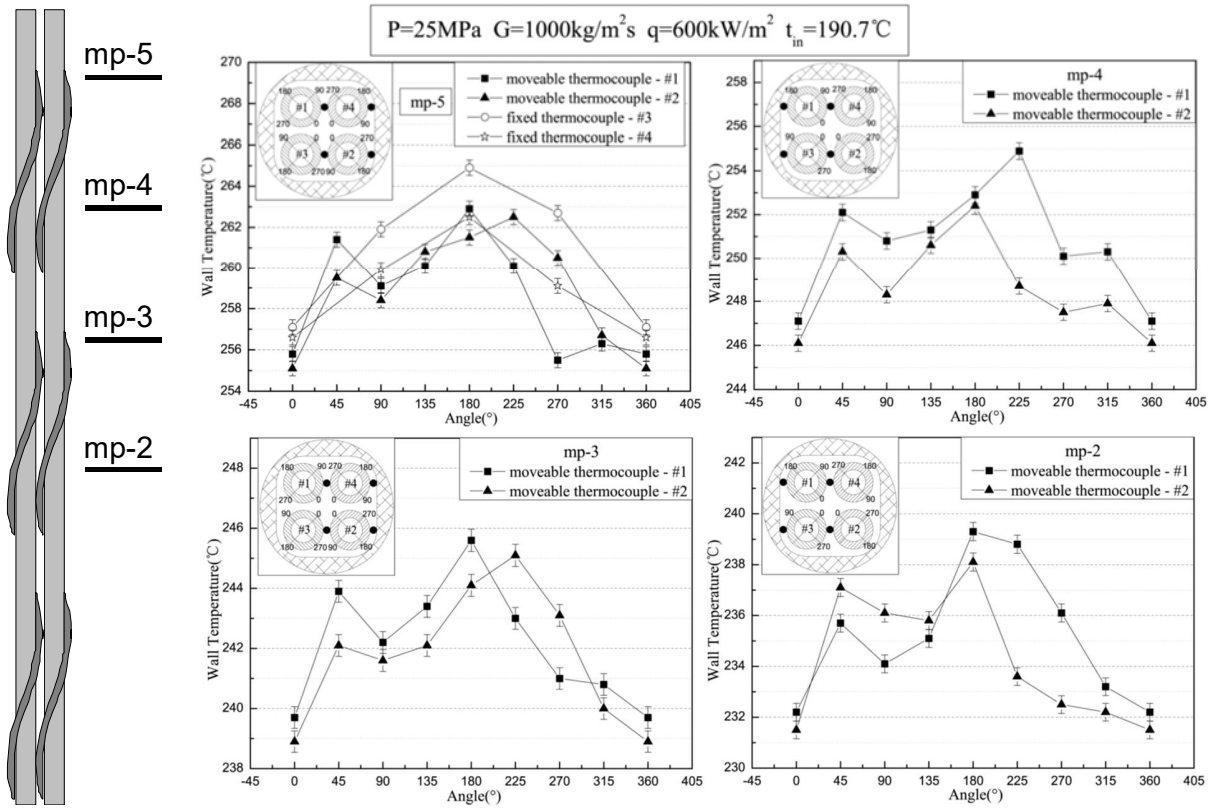

Fig. 10.6. Circumferential wall temperature distributions at subcritical inlet fluid temperature.

Variations of circumferential wall temperature gradient are shown in Fig. 10.7 with cross-sectional average bulk-fluid enthalpy and mass flux. The peak circumferential wall-temperature gradient is about 13 °C at the mass flux of 400 kg/(m^2·s) and bulk-fluid enthalpy of 2600 kJ/kg. The circumferential wall temperature gradient decreases with increasing mass flux. It is more drastic at low mass fluxes than high mass fluxes. The decrease is about 2 °C at the sub-critical enthalpy region and 3 °C at the super-critical enthalpy region when increasing the mass flux from 700 to 1000 kg/m^2s. On the other hand, the decrease is about 3.5 °C at the subcritical enthalpy region and 4 °C at the supercritical enthalpy region when increasing the mass flux from 400 to 700 kg/m^2s. However, the decrease is smaller at the pseudo-critical region.

Fig. 10.8 compares the circumferential wall temperature gradients between the bare and spacer equipped bundles. In general, the circumferential wall temperature gradients for the bare rod bundle are larger than those for the bundle with the wire wrapped spacers. The differences are larger at high than low heat fluxes.

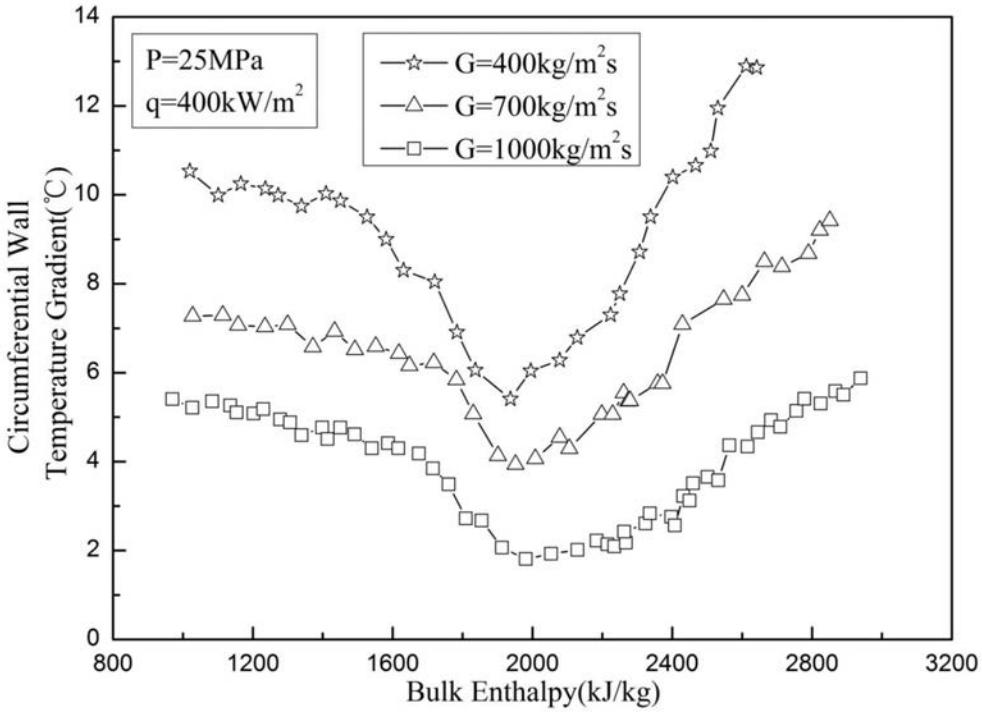

Fig. 10.7. Variations of circumferential wall temperature gradient with bulk enthalpy and mass flux.

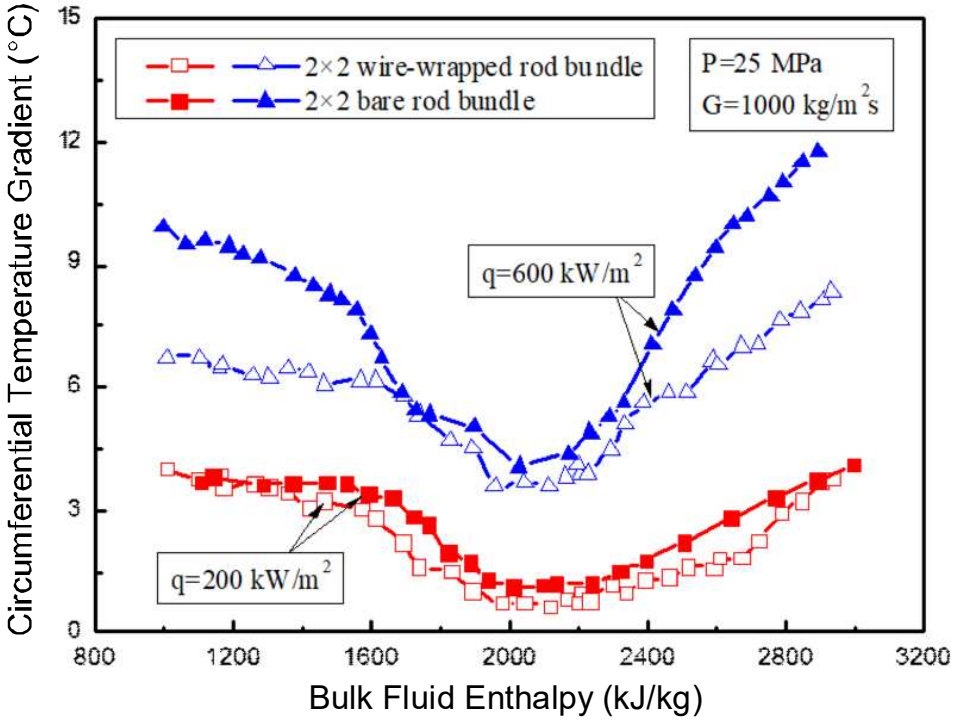

Fig. 10.8. Circumferential wall temperature gradient around the heated rod with and without the wire wrapped spacer

Fig. 10.9 compares wall temperatures and heat transfer coefficients between 2x2 rod bundles with and without wire-wrapped spacers. Wall temperatures of the wire-wrapped bundle are lower than those of the bare (i.e., without the wire-wrapped spacers) bundle. Heat-transfer coefficients of the wire-wrapped bundle are higher than those of the bare bundle.

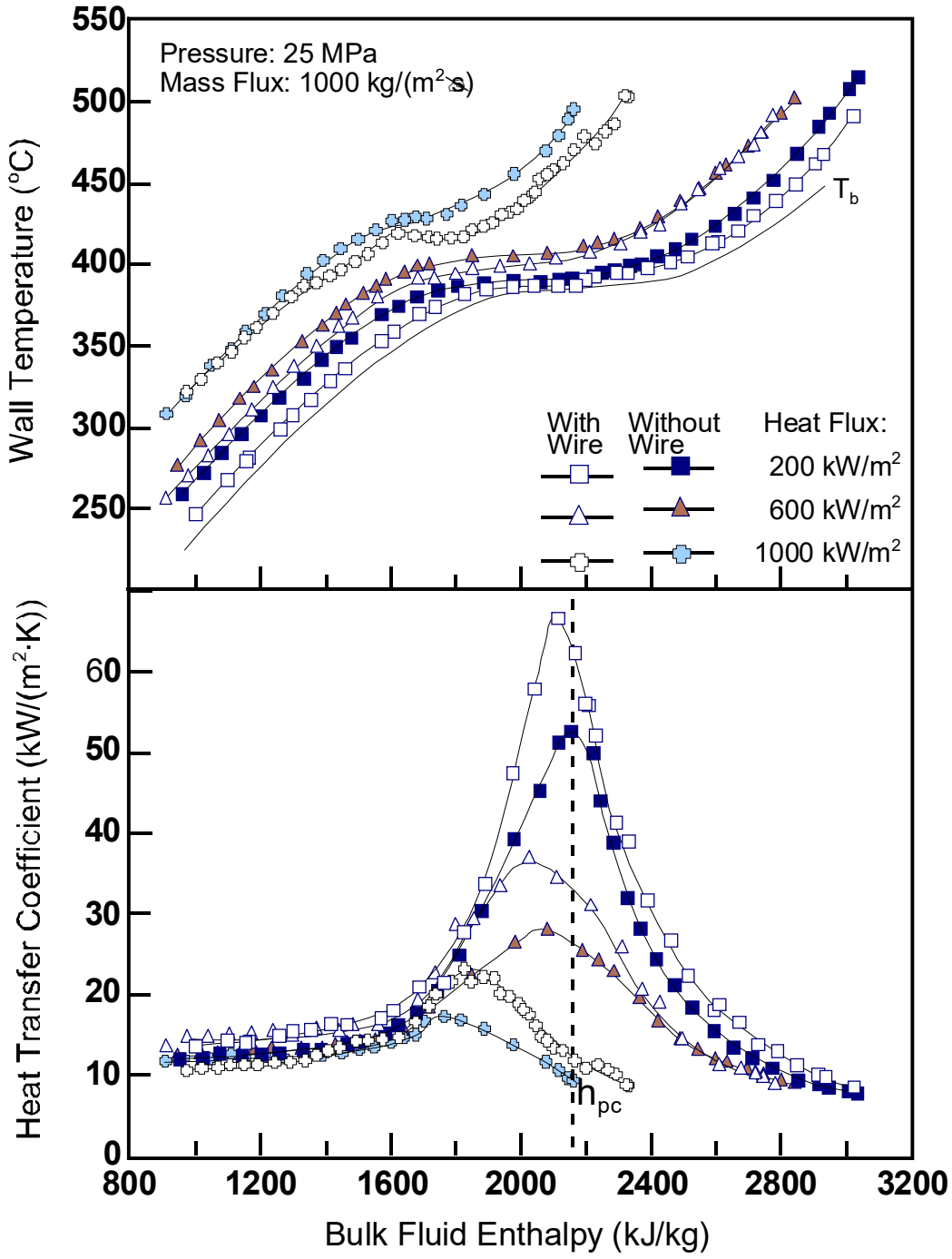

Fig. 10.9. Comparisons of average wall temperature and heat transfer coefficient between bundles with and without wire-wrapped spacers.

10.2.3. EFFECT OF SPACERS ON HEAT TRANSFER IN A 3-ROD BUNDLE

The effect of spacing devices on heat transfer was examined in [10.4]. Two different types of spacers (i.e., grid and wrapped wires) were tested in a 3-rod bundle. Section 5.2 describes the test facility and results. Fig. 10.10 compares distributions of surface temperature and heat-transfer coefficient at two different angles along a rod with grid spacers (their locations are illustrated in vertical solid lines). The surface temperature and heat-transfer coefficient are about the same at these two angles. However, sharp variations in surface temperature and heat transfer coefficient are shown at the vicinity of the grid spacer. Low surface temperature and corresponding high heat transfer coefficient are exhibited at the grid spacer location, and higher surface temperatures beyond that poInt. The decay length of the heat-transfer enhancement is relatively short in view of the small blockage area ratio of the grid spacer.

Fig. 10.11 compares the surface temperature and heat-transfer coefficient between grid and wire wrapped spacers at one angle of the same rod. The fluctuation in surface temperature is more severe for the rod with the wire wrapped spacers than that for the rod with the grid spacers. This is attributed to the continuous heat transfer enhancement of the wire along the heated length. Overall, the surface temperature is lower and corresponding the heat-transfer coefficient is higher for the wire wrapped spacers than the grid spacers.

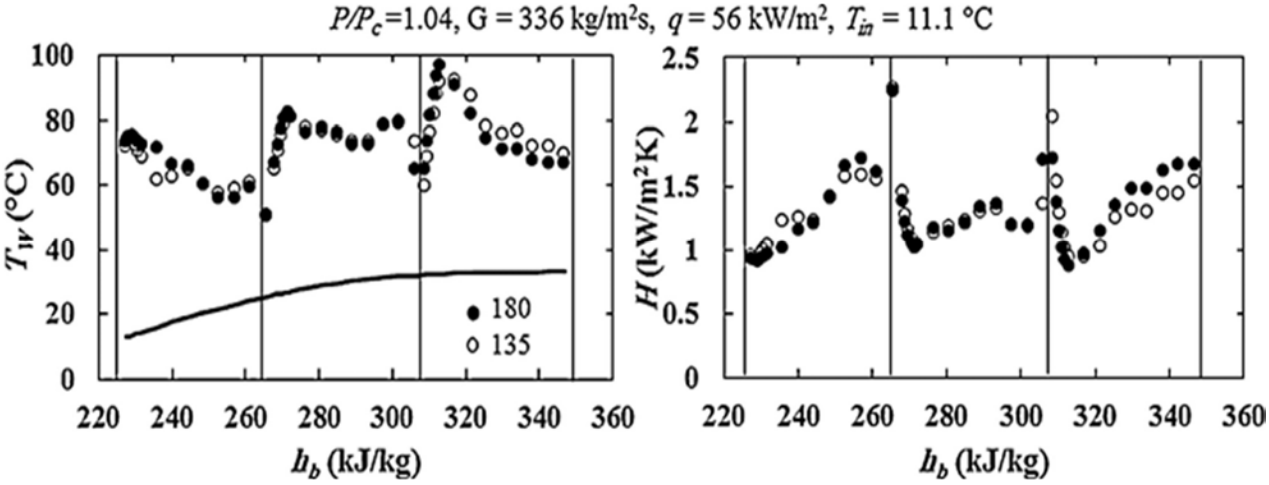

Fig. 10.10. Axial variations of wall temperature and local heat transfer coefficient along a rod at circumferential locations facing the axis of the rod-bundle subassembly (180◦ angle) and a gap between two heated rods (135◦ angle) [10.4].

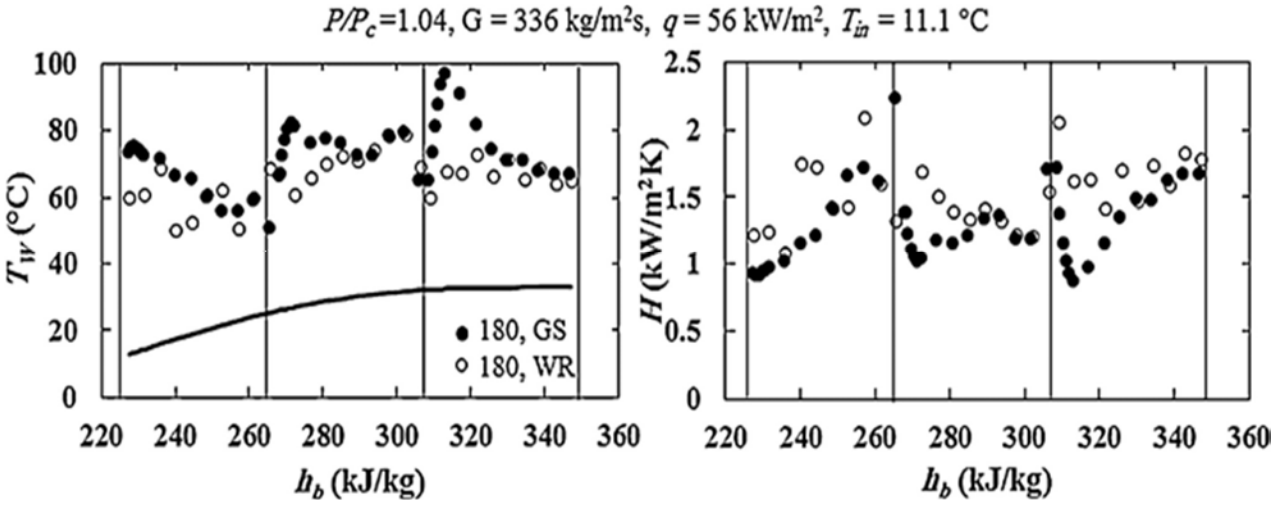

Fig. 10.11. Comparison between wire wrap and grid spacer effects on wall temperature and HTC at circumferential locations facing the axis of the rod-bundle subassembly (angle of 180◦) [10.4].

10.3. SUBCHANNEL SHAPE AND THE EFFECT ON HEAT TRANSFER

Tube-data-based correlations have been applied in subchannel codes for predicting wall temperature in subchannels of fuel assemblies, even though none of these subchannels resemble the shape of a tube. The applicability of the tube-data-based correlations for non-circular shaped subchannels needs to be demonstrated.

Other than the fuel assemblies for the Canadian and the fast-spectrum SCWRs, fuel rods are positioned in a square lattice configuration. [10.5] performed an experiment with water through a subchannel shaped channel at supercritical pressures. The test section was constructed from a stainless steel (SS-321) rod, which was cut to the subchannel-shaped channel, simulating the central subchannel of the 2×2 rod bundle (see Section 5.1). Its length was 680 mm and wall thickness was 2.5 mm. Outer surface temperatures were measured at four axial locations along the channel, each with eight thermocouples.

Fig. 10.12 shows the geometry of the subchannel-shaped channel and the thermocouples locations at each plane. Measurements of inlet pressure, inlet fluid temperature, pressure loss and power were obtained. These experiments covered ranges of pressures at the inlet of the test section from 23 to 28 MPa, mass fluxes from 700 to 1300 kg/(m^{2}s), heat fluxes on the inner wall of the test section from 200 to 1000 kW/m^2 and inlet fluid temperatures from 200 to 500°C depending on the power and mass flow rate.

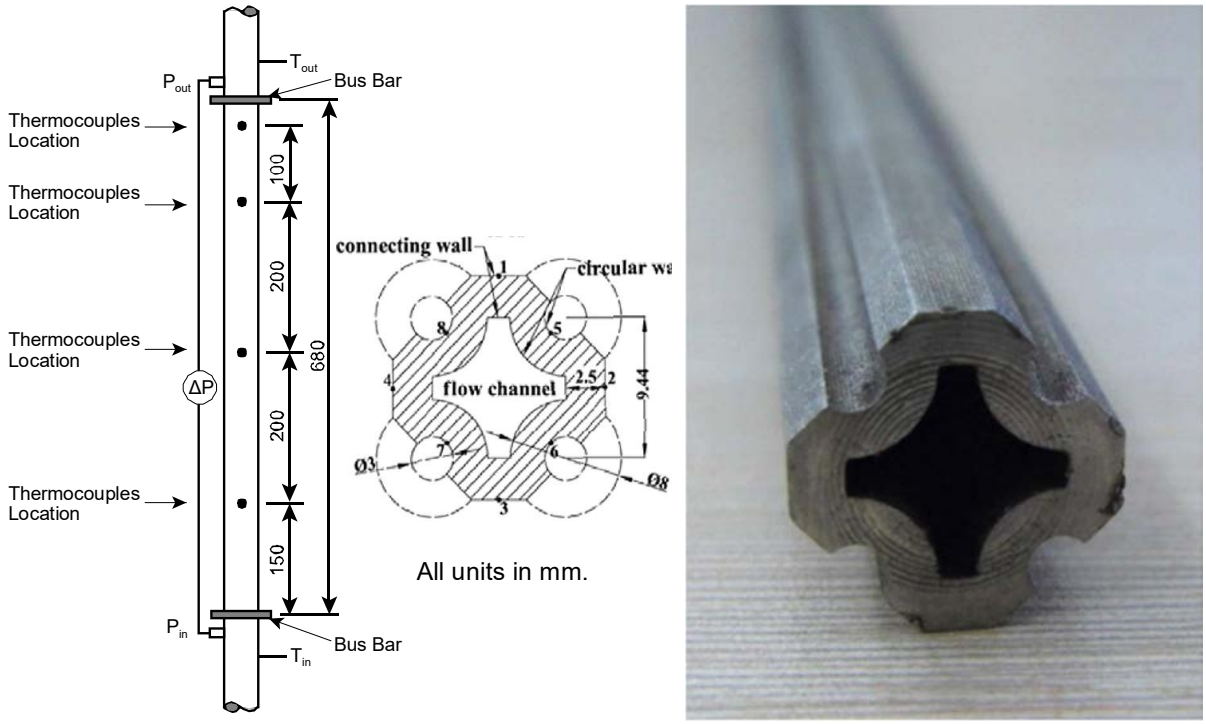

Fig. 10.12. Subchannel-shaped test section and thermocouples locations [10.5].

The reference [10.5] observed higher surface temperature and correspondingly lower heat-transfer coefficient at the connecting wall than the circular wall (see Fig. 10.12 for definitions). Fig. 10.13 illustrates the variations of surface temperatures and heat transfer coefficients at these two positions at one plane. The reference [10.5] attributed the differences to the reduction in flow velocity near the connecting wall. Their analysis focused only on the measurements at the circular wall region.

The parametric trends of surface temperature and heat-transfer coefficient for the subchannel-shaped channel are similar to those for tubes or annuli. Fig. 10.14 illustrates effects of heat flux and enthalpy on surface temperature and heat transfer coefficient for the subchannel shaped channel. The surface temperature generally increases with increasing enthalpy and heat flux. However, there is a levelling off trend in surface temperature near the pseudo-critical point at low heat fluxes. The trend gradually diminishes with increasing heat flux.

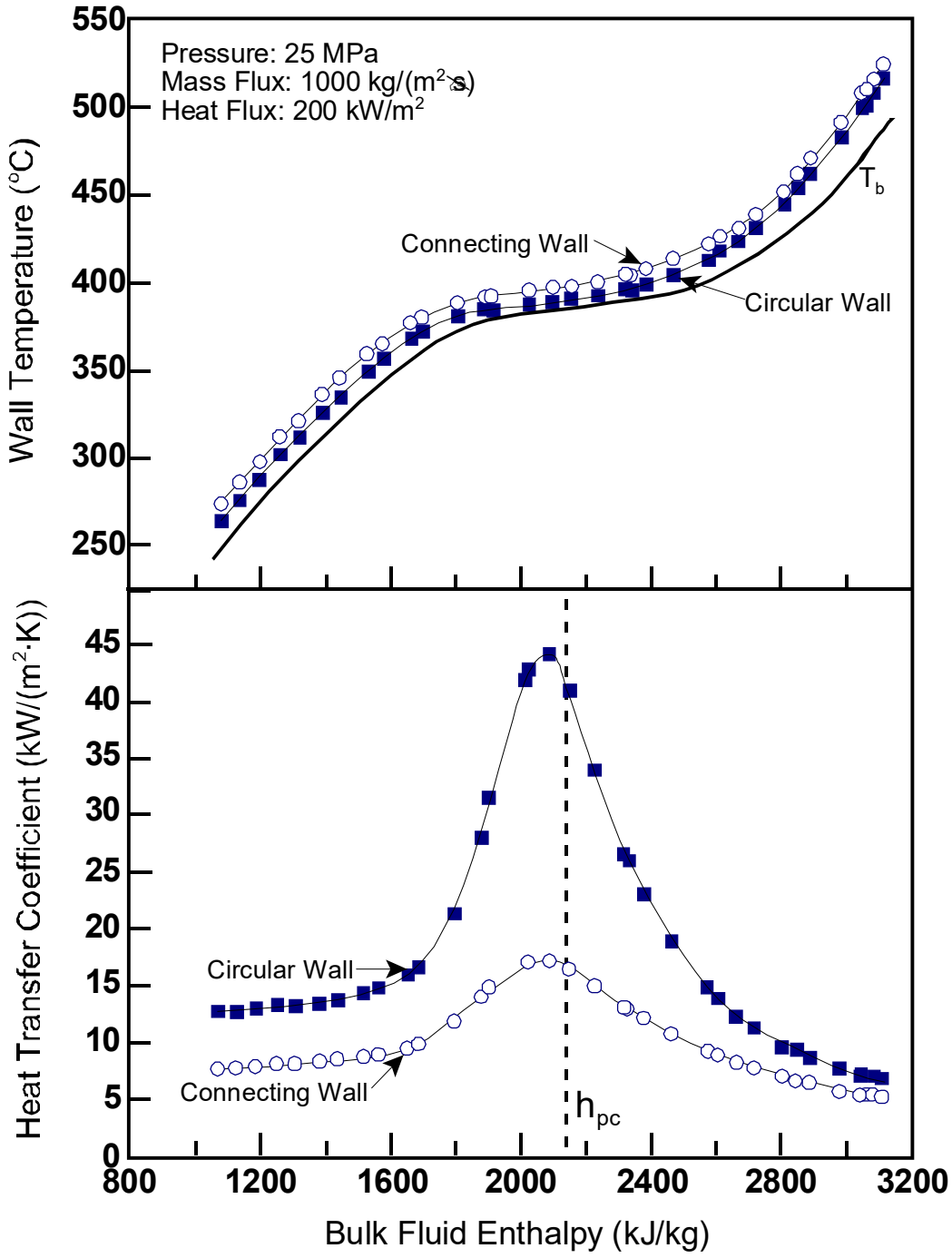

Fig. 10.13. Wall temperature and heat transfer coefficient at circular wall and connecting wall of subchannel shaped test section.

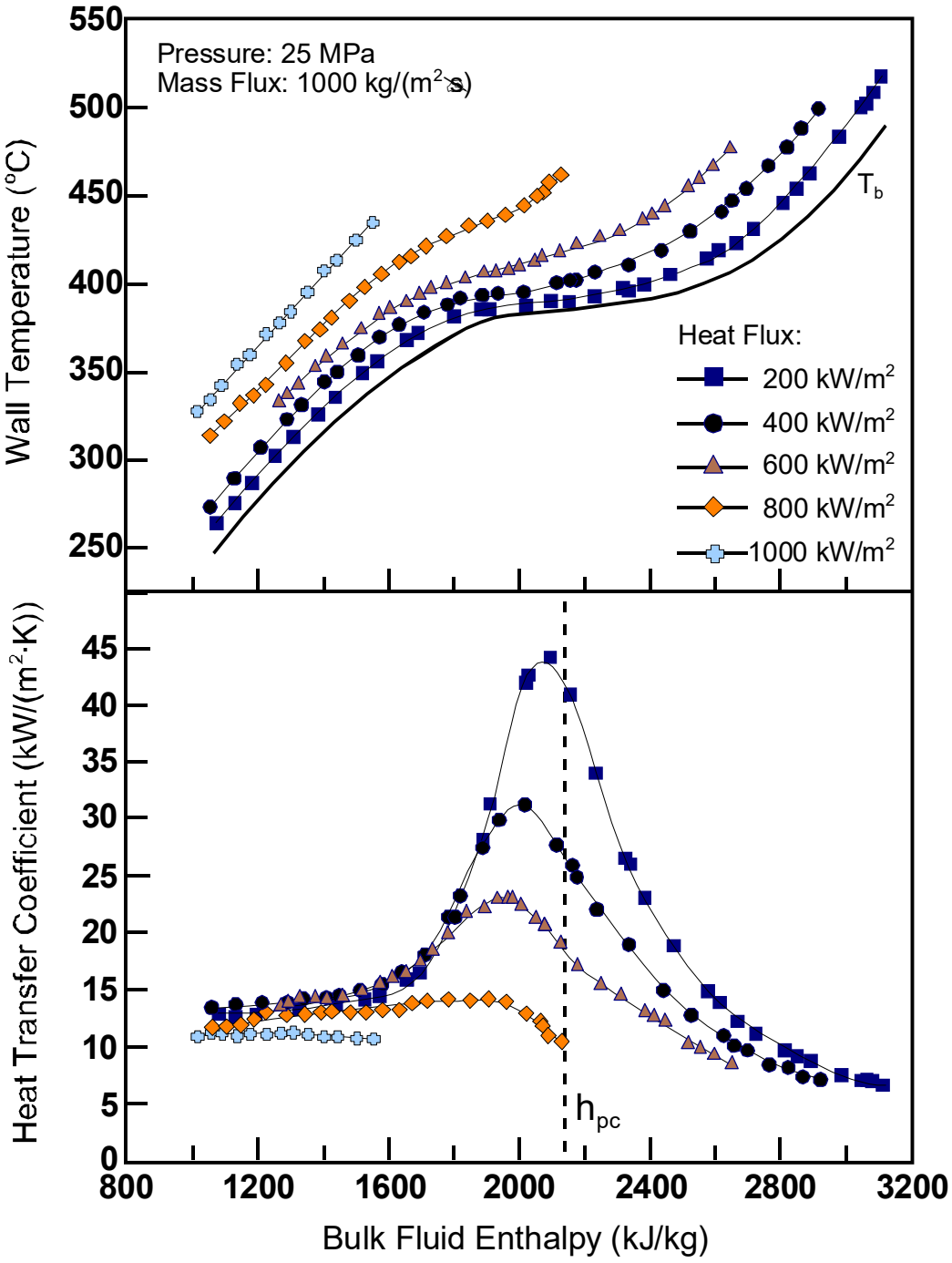

Fig. 10.14. Variations of wall temperature and heat transfer coefficient with heat flux in the subchannel-shaped channel.

Fig. 10.15 illustrates effects of mass flux and enthalpy on surface temperature and heat transfer coefficient in the subchannel-shaped channel. Similar to those observed in tubes and annuli, surface temperature decreases and heat-transfer coefficient increases with increasing mass flux. The levelling trend in surface temperature becomes more pronounced at high than low mass fluxes.

In addition, the peak of heat-transfer coefficient appears shifting slightly toward lower enthalpies, away from the pseudo-critical point, with decreasing mass flux. Similar trends were observed in tubes and annuli.

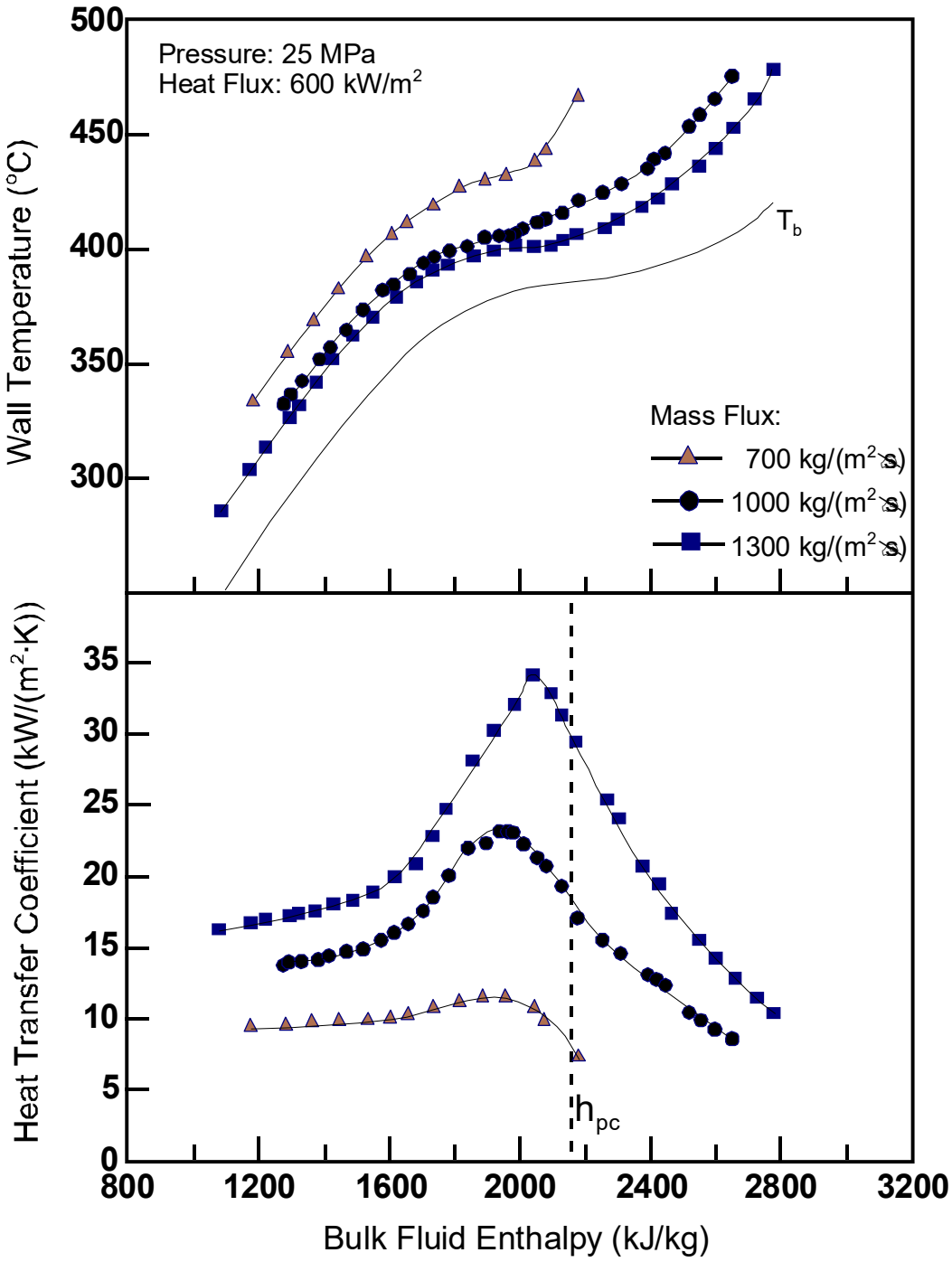

Fig. 10.15. Variations of wall temperature and heat transfer coefficient with mass flux in the subchannel shaped channel.

[10.5] did not compare directly their results of the subchannel shaped channel to those of a tube. However, they assessed various tube-based correlations against heat transfer coefficient obtained in the experiment. The correlation proposed by [10.6] agreed closely with their results.

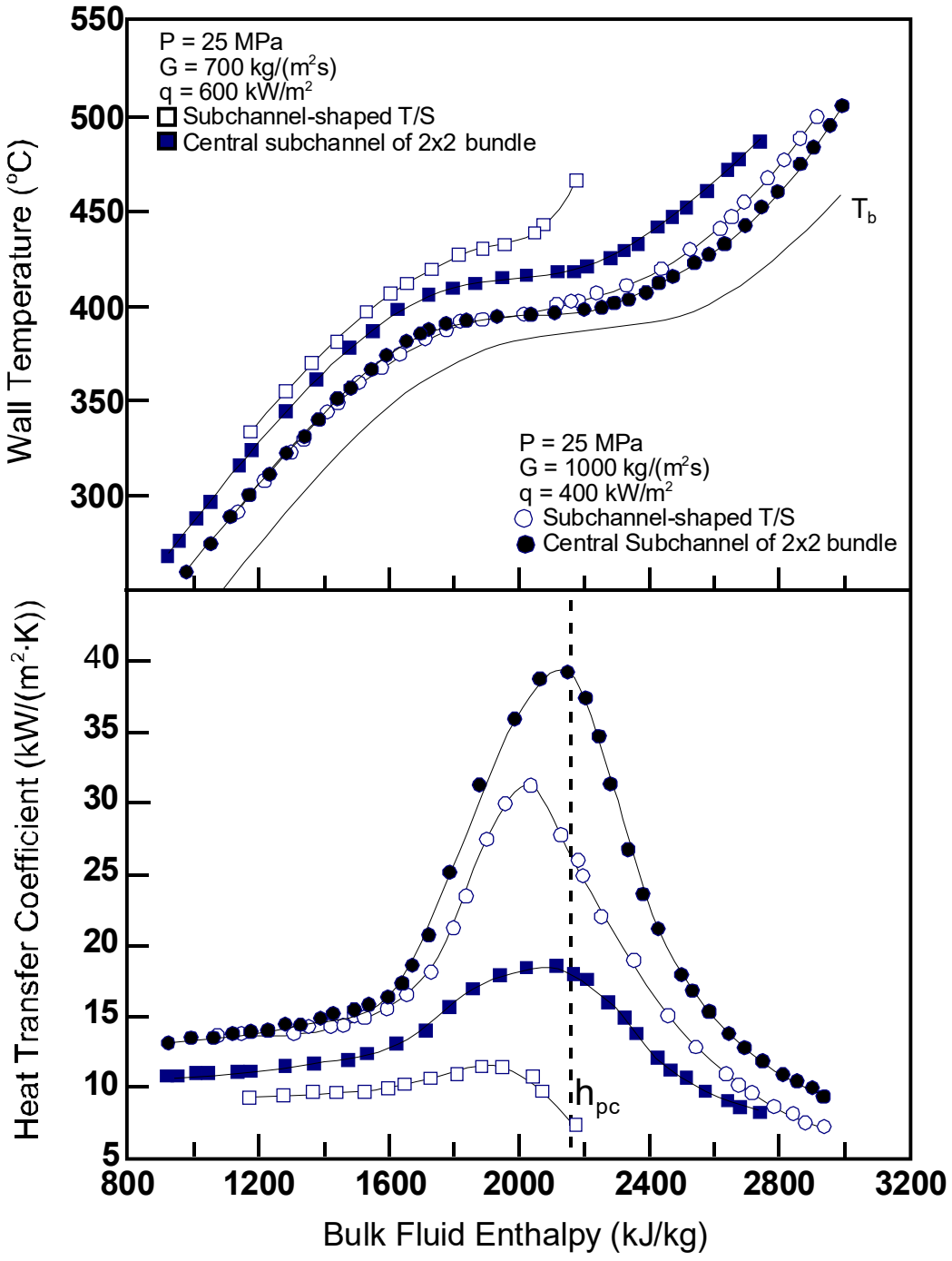

Fig. 10.16. Comparisons of heat transfer characteristics in subchannel-shaped test section (T/S) and central subchannel of a 2x2 bundle.

As mentioned above, the subchannel-shaped channel represented the central subchannel of a 2×2 rod bundle, which were used in another heat-transfer test (see Section 5.1). Fig. 10.16 compares the surface temperature and heat transfer coefficient obtained in that subchannel of the 2×2 rod bundle (without spacers) against those in the subchannel-shaped channel for two sets of flow conditions [10.5]. Information on the local flow conditions at the central subchannel of the 2×2 rod bundle is unavailable. The cross sectional average flow conditions are applied in the comparison. Surface temperature in the subchannel shaped channel is systematically higher than those in the central subchannel of the 2×2 rod bundle. Correspondingly, the heat transfer coefficient is lower. The reference [10.5] attributed the differences to the strong circumferential flow and mixing in the rod bundle. In view of the lack of local flow conditions at the central subchannel of the 2×2 rod bundle, the comparison is qualitative.

Nomenclatures and Acronyms

D	Diameter (mm)
G	Mass flux (kg/(m^{2}s))
H, h	Enthalpy (kJ/kg)
P	Pressure (MPa)
p	Rod pitch (mm)
q	Heat flux (kW/m^2)
Re	Reynolds number (-)
s	Gap size (mm)
T, t	Temperature (°C)
W	Mass flow rate (kg/s)
w'	Turbulent mixing flow rate (kg/s)
β	Mixing coefficient (-)
ρ	Density (kg/m^3)
v	Mean fluctuating velocity (m/s)

Subscripts

adi	Adiabatic conditions
b	Bulk fluid
c	Critical
eff	Effective
heat	Heated conditions
in	Inlet
ij	From subchannel i to j
pc	Pseudocritical point
w	Wall

Acronyms

CFD	Computational Fluid Dynamics
ms	Measurement position
SCWR	Super-Critical Water-cooled Reactor
SS	Stainless Steel

REFERENCES TO SECTION 10

[10.1] ZHANG, B., SHAN, J., JIANG, J., Turbulent Mixing Model Applicable to Supercritical Condition, Proc. 5th Int. Sym. SCWR (ISSCWR-5), Vancouver, 2011.

[10.2] WU, G., BI, Q., YANG, Z., WANG, H., ZHU, X., HAO, H., LEUNG, L.K.H., Experimental Investigation of Heat Transfer for Supercritical Pressure Water Flowing in Vertical Annular Channels, Nuclear Engineering Design, **241, 9**, (2011) 4045-4054.

[10.3] WANG, H., BI, Q., LEUNG, L.K.H., Heat Transfer from a 2×2 Wire wrapped Rod Bundle to Supercritical Pressure Water, Int. J. of Heat and Mass Transfer, **97**, (2016), 486–501.

[10.4] ETER, A., GROENEVELD, D., TAVOULARIS, S., An Experimental Investigation of Supercritical Heat Transfer in A Three-Rod Bundle Equipped with Wire wrap and Grid Spacers and Cooled by Carbon Dioxide, J. Nuclear Engineering and Design, **303**, (2016), 173-191.

[10.5] WANG, H., WANG, W., BI, Q., WANG, L., Experimental Study of Heat Transfer and Flow Resistance of Supercritical Pressure Water in a SCWR Sub-Channel, J. Supercritical Fluids, **100**, (2015), 15-25.

[10.6] MOKRY, S., PIORO, I.L., FARAH, A., KING, K., GUPTA, S., PEIMAN, W., KIRILLOV, P.L., Development of Supercritical Water Heat-Transfer Correlation for Vertical Bare Tubes, Nuclear Engineering and Design, 241, (2011), 1126-1136.

11. HEAT TRANSFER CHARACTERISATION USING DNS AND LES CALCULATIONS

Direct numerical simulation (DNS) offers a good opportunity to complement experiments by providing detailed information on flow and thermal fields and hence improving our understanding of the physics even though simulations are currently limited to low Reynolds numbers. Bae et al. [11.1], [11.2] reported detailed statistics of turbulence produced through DNS of heat transfer to CO_2 at supercritical pressure in a vertical tube and annulus respectively. Buoyancy production was found to be significant when the flow is close to laminarisation and the shear production is at its minimum; such effect appears to facilitate turbulence recovery further downstream (also see [11.3]). Streaky structures close to the wall disappear when the wall temperature is peaking and turbulence is severely suppressed. Data of [11.1], [11.2] have been widely used for validation or assessment of the performance of turbulence models. [11.4] compared simulations with boundary conditions allowing and dis-allowing temperature fluctuations on the wall in forced convection and found that wall temperature fluctuations contribute up to 7% of the heat transfer to the wall.

[11.5], [11.6] performed DNS of flow in an annulus of a heated inner wall and cooled outer wall with equal heat flows on them. By analysing the transport equation of the coherent streak flank strength, the authors found that the thermophysical property fluctuations influence streak evolution significantly and are responsible for the increase and decrease of turbulence motions on the hot and cold walls, respectively. In their second paper, the influences of varying thermal properties, including specific heat, thermal diffusivity, Prandtl number, independently have been investigated to gain a better understanding of the direct influences of each property on heat transfer enhancement and deterioration.

[11.7] used the open source finite volume OpenFOAM to carry out DNS of flow and heat transfer of CO_2 reproducing the work of [11.1]. Their results compared very well with the results of [11.1] This methodology was used in the following studies on a horizontal flow [11.8] and for a flow of fluid at supercritical pressure under cooling conditions [11.9], [11.10]. The latter study found that as expected, buoyancy has an effect opposite to the flows in a heated flow.

The purpose of this section is to describe some recent research carried out at Universities of Sheffield, Pisa and Tsinghua in the study of supercritical fluid using DNS and large eddy simulation (LES). In particular, the topics include (i) Heat transfer deterioration mechanisms: is the flow lamiarised or not? (ii) Vertical flow in parallel plates with a cold and a hot wall on either side; (iii) fluid to fluid similarity and scaling; (iv) flow instability in a trapezoidal annular passage and (v) effect of conjugate heat transfer.

11.1. METHODOLOGY

The physical properties of fluids at supercritical pressure often exhibit large variations though the flow of such fluids under consideration is still in the low Mach number regime. The conventional approach in solving the Navier-Stokes equations in a fully compressible form is inefficient because of the numerical stiffness associated with acoustic wave propagation [11.11]. Instead, the low-Mach number approximation is more appropriate and has been widely adopted in the solution of problems of this kind (e.g., [11.12]; [11.1]; [11.13]; [11.3]). In such a method, the interactions

between acoustic and thermal waves are neglected. Under the condition of the low Mach number limit, pressure is decomposed into a thermodynamic pressure p_0 and a hydrodynamic pressure p. The hydrodynamic pressure p is negligibly small compared to the thermodynamic pressure p_0. Thus, the thermodynamic variables can be safely assumed to be independent of the hydrodynamic pressure p at a given thermodynamic pressure p_0. In the energy equation, heat generation due to viscous force and work done by hydrodynamic pressure and gravity are much smaller than heat transfer rate via convection and conduction. Therefore, these terms are also neglected. With the above assumptions, the governing equations in dimensionless form, including the mass conservation equation, the momentum conservation equation and the energy conservation equation, are written as:

$$\frac{\partial \rho}{\partial t} + \frac{\partial (\rho u_k)}{\partial x_k} = 0 \tag{11.1}$$

$$\frac{\partial (\rho u_k)}{\partial t} + \frac{\partial (\rho u_i u_k)}{\partial x_k} = -\frac{\partial p}{\partial x_i} + \frac{1}{Re_0}\frac{\partial \tau_{ik}}{\partial x_k} + \frac{\rho}{Fr_0^2} \tag{11.2}$$

$$\frac{\partial (\rho h)}{\partial t} + \frac{\partial (\rho h u_k)}{\partial x_k} = \frac{1}{Re_0 Pr_0}\frac{\partial}{\partial x_k}\left(\lambda \frac{\partial T}{\partial x_k}\right) \tag{11.3}$$

where Einstein summation notation is used. The symbol x_k is the spatial Cartesian coordinates (k = 1, 2, 3 for x, y, z directions, representing the streamwise, wall-normal and spanwise directions respectively) and u_k denotes the velocity field (k = 1, 2, 3 for velocity in x, y, z directions, also denoted as u, v, w). The symbols t, p, ρ, T, λ and h are time, pressure, density, temperature, thermal conductivity and enthalpy, respectively. The symbol τ_{ij} represents stress tensor. In Stokes's hypothesis, the stress tensor τ_{ij} is expressed as

$$\tau_{ij} = \mu 2 S_{ij}, where\ S_{ij} = \frac{1}{2}\left(\frac{\partial u_i}{\partial x_j} + \frac{\partial u_j}{\partial x_i}\right) - \frac{1}{3}\frac{\partial u_k}{\partial x_k}\delta_{ij} \tag{11.4}$$

where δ_{ij} is the Kronecker delta. Other symbols in the above equations are, the Reynolds number (Re), the Prandtl number (Pr) and the Froude number (Fr), which are defined as:

$$Re_0 = \frac{\rho_0 u_0 \delta}{\mu_0}, Pr_0 = \frac{c_{p0}\mu_0}{\lambda_0}, \frac{1}{Fr_0^2} = \frac{\delta g_i}{u_0^2} \tag{11.5}$$

where the subscript 0 stands for the reference state. The symbol δ is the half channel height. μ is the dynamic viscosity. c_p is the specific heat capacity at constant pressure, and g_i is gravity acceleration in x_i direction. For forced convection with body force neglected, g_i equals 0, whereas g_i is +/- in downward/upward mixed convection flows.

The dimensionless variables in the above governing equations are defined by normalizing the dimensional quantities (with the superscript $\hat{}$) with the corresponding values at the reference state (with the subscript 0),

$$t = \frac{\hat{t}}{\hat{\delta}/\hat{u}_0}, x_k = \frac{\hat{x}_k}{\hat{\delta}}, u_k = \frac{\widehat{u_k}}{\hat{u}_0}, p = \frac{\hat{p}}{\hat{\rho}_0 \hat{u}_0^2} \tag{11.6}$$

$$h = \frac{\hat{h}}{\widehat{c_p}_0 \hat{T}_0}, \phi = \frac{\hat{\phi}}{\hat{\phi}}, where\ \phi = \rho, T, \mu, \lambda, c_p \tag{11.7}$$

An in-house direct numerical simulation (DNS) code CHAPSim, originally developed for an incompressible flow [11.14], [11.15], has been re-developed to solve the above governing equation for flow of fluids at supercritical pressure [11.16], [11.17]. The flow fields are solved in a staggered grid with a spatially second order finite difference method. The Poisson equation for the pressure-correction in the fractional step method is implemented to enforce the continuity equation [11.18]. For the temporal discretization, a third order explicit Runge-Kutta scheme is used for the nonlinear terms in the momentum equations, and a second order implicit Crank-Nicholson scheme for the linear terms. Details on the spatial discretization schemes for the momentum and continuity equations are provided in [11.14] and [11.15]. The enthalpy-based energy equation is numerically solved using an explicit Runge-Kutta method. The process to solve the coupled governing equations in each Runge-Kutta stage is as follows: Firstly, the energy equation is solved based on flow field solved in the previous step to obtain a conservative provisional enthalpy ρh. Then, temperature, density, viscosity and thermal conductivity are updated based on this provisional enthalpy by searching a physical property table generated with the NIST 9.1 database [11.19]. Next, a new enthalpy is searched based on the updated temperature, and variable properties are updated again based on this new enthalpy. After that, the momentum equations are solved with updated density and viscosity in place. Finally, the continuity equation is ensured with a predictor-corrector method by solving the Poisson equation. This solving procedure is similar to [11.11]. Uniquely in the current DNS code, a limiter on the conservative enthalpy ρh is applied to protect it from exceeding its maximum value in the distribution of ρh based on the temperature in the studied fluids at supercritical pressure.

11.2. HEAT TRANSFER DETERIORATION MECHANISMS: IS THE FLOW LAMINARISED?

Strong variations of thermal properties of fluids at a supercritical pressure bring about significant challenges to the understanding and prediction of the heat transfer in the reactor core of SCWRs. An important phenomenon is the effect of the buoyancy on turbulence and heat transfer. A similar phenomenon also exists in the heat transfer system at subcritical pressure, but buoyancy is generally speaking much strong in a system of fluid at supercritical pressure.

The general trend of the buoyancy on heat transfer is well known. In an upwards heated flow, buoyancy aids the flow accelerating the fluid close to the wall causing the formation of a fuller velocity profile. This hampers turbulence production, causing a partial flow re-laminarisation and

hence a reduction in heat transfer. When the buoyancy is sufficiently strong, the flow many be fully laminarised resulting the so-called heat transfer deterioration. As the buoyancy is further increased, the mean velocity profile is inverted into the so-called M-shape, leading to the generation of new turbulence and hence recovery of heat transfer effectiveness. In a downwards heated flow, the buoyancy is against the flow causing the velocity to distort in a fashion that turbulence production is enhanced, and consequently heat transfer is improved. The overall behaviour of the influence of buoyancy is well demonstrated in Fig. 11.1 [11.20].

Despite the understanding of the general picture described above, the understanding of the heat transfer deterioration mechanisms and prediction of this phenomenon are far from satisfactory. A major barrier is related to the fact that flow physics is rather complex in supercritical fluid flow and the buoyancy effect is nonlinearly coupled with influences such as flow acceleration and strong variations of thermal properties such as specific heat capacity and thermal conductivity.

The aim of the research described in this section is to study the effect of buoyancy in isolation from other effects using high fidelity numerical simulation, that is, direct numerical simulation (DNS) so as to develop a better understanding of the laminarisation (and heat transfer deterioration) mechanisms, and also to produce high quality data for use for turbulence model validation or refinement. The 'buoyancy' force is prescribed in either a linear form or a step change shape and no thermal field is considered. Much of the results discussed here originate from [11.21], [11.22].

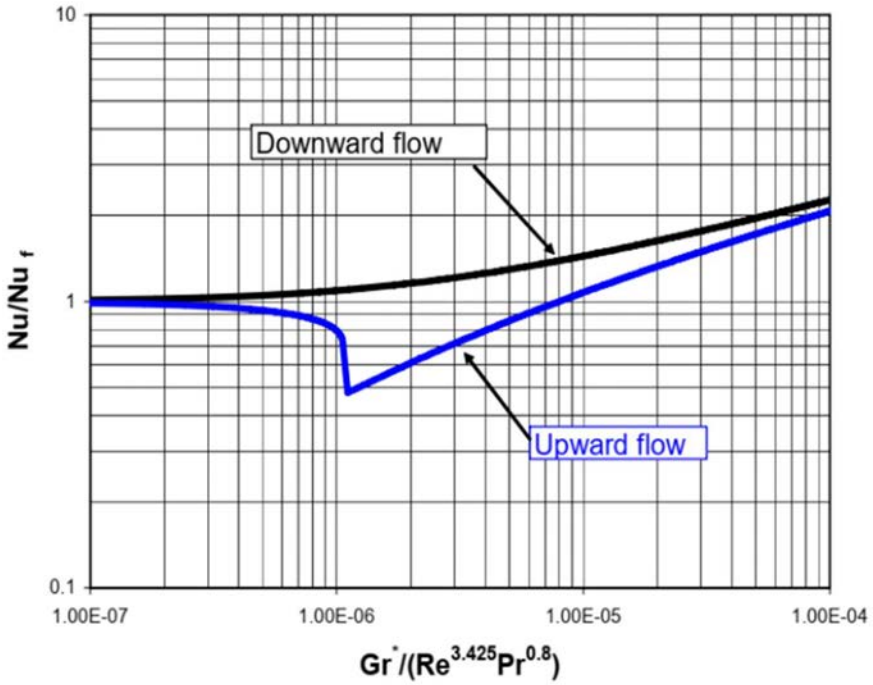

Fig. 11.1. Effect of buoyancy on heat transfer (reprinted from [11.20] with permission from Begell House, Inc).

11.2.1. METHODOLOGY AND CASES SETUP

The DNS reported herein have been carried out using a constant property version of the CHAPSim [11.14], [11.15], while the buoyancy in the momentum equation is prescribed using a body force (see below) and the energy equation is not solved.

Fig. 11.2 shows the variations of the radial distributions of density at several axial locations in a heated upward flow of air at atmospheric conditions and those of CO_2 a supercritical pressure. The region where the density varies strongly corresponds to the extent of the thermal boundary layer. It can be seen that the variation of the density in the air flow is largely linear and the thickness of the thermal boundary layer increases with distance reaching about y^+=25 towards the last station shown. Interestingly, the density profile of the CO_2 appears to show a step change at most stations. This is an indication of the location of the pseudo critical temperature, across which a rapid density variation occurs. This point is not necessarily directly related to the edge of the thermal boundary layer. In fact, it appears that the thermal boundary is likely to extend beyond this poInt. It should be said that the density profiles shown in this figure are two examples, and the detailed density profiles in different flows will vary significantly. It is however true that the linear profile and step change are representative of distributions of density in mixed convection in a vertical pipe.

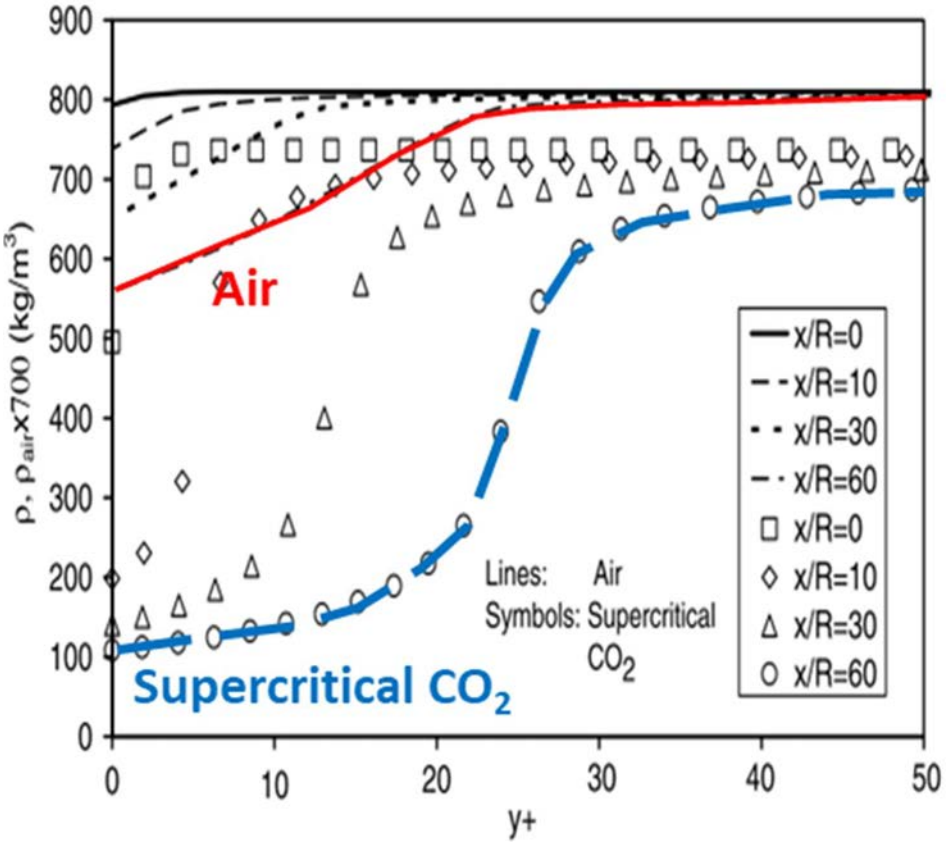

Fig. 11.2. Density distribution in a flow of air and a flow of CO2 at a supercritical pressure (reproduced from [11.23]).

Idealised buoyancy force profiles have been studied which include linear profiles and step-change profiles inspired by the observations in Fig. 11.2. Two groups of tests are carried out for each type of profiles, one with a fixed amplitude but different ranges of coverage and one with the same spatial coverage but different amplitude of the body force. Hence a total of four groups have been studied referred to as Groups A to D, as shown in Fig. ***11.3***.

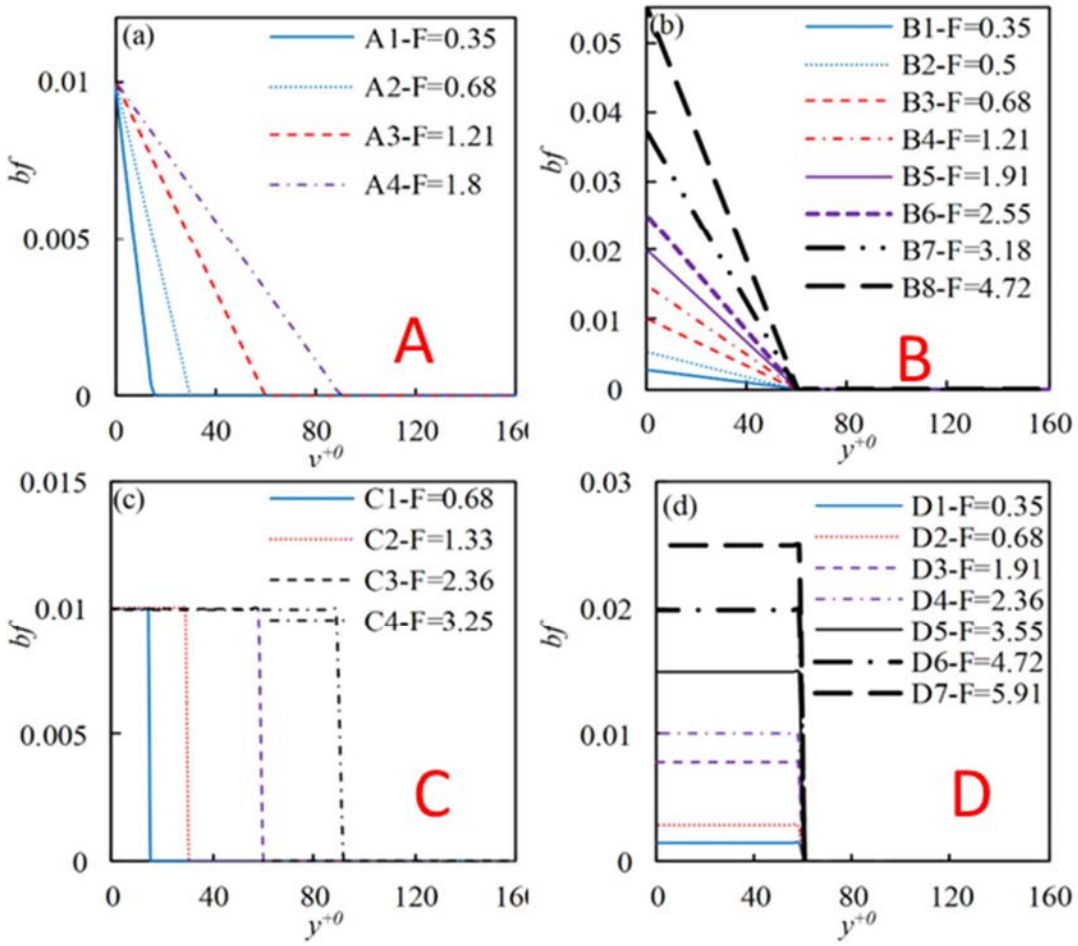

Fig. 11.3. Profiles of nonuniformly distributed body force used in the simulations.

Mathematically, the body force distribution is described as follows:

— Linear variation:

$$f = \begin{cases} a(r - r_0)/(1 - r_0) & r \geq r_0 \\ 0 & r < r_0 \end{cases} \tag{11.8}$$

— Step variation:

$$f = \begin{cases} a & r \geq r_0 \\ 0 & r < r_0 \end{cases} \tag{11.9}$$

where a and r_0 are constants.

11.2.2. RESULTS AND DISCUSSION

11.2.2.1. GENERAL PICTURE OF THE INFLUENCE OF BODY FORCE FLOW LAMINARISATION AND RECOVERY

Fig. 11.4(a) shows the velocity profiles ($\bar{u}_z$) in all simulations carried out in the four groups. The general trends are the same in each of the groups, regardless of the linear or step change profiles or the way the body force is altered, namely by changing the coverage or amplitude. The effect of the buoyancy observed in 'real' flows are reproduced in each of the cases. Considering Group B for example, with the increase of the body force, the velocity first becomes flattened (B1, B2 and B3), and further increasing the body force causes the velocity profile to flip to the so-called M-shape (B4), in which the peak of the velocity moves to a region close to the wall and a trough results in the centre of the pipe. The stronger the body force is, the larger the differences between the peak and the trough.

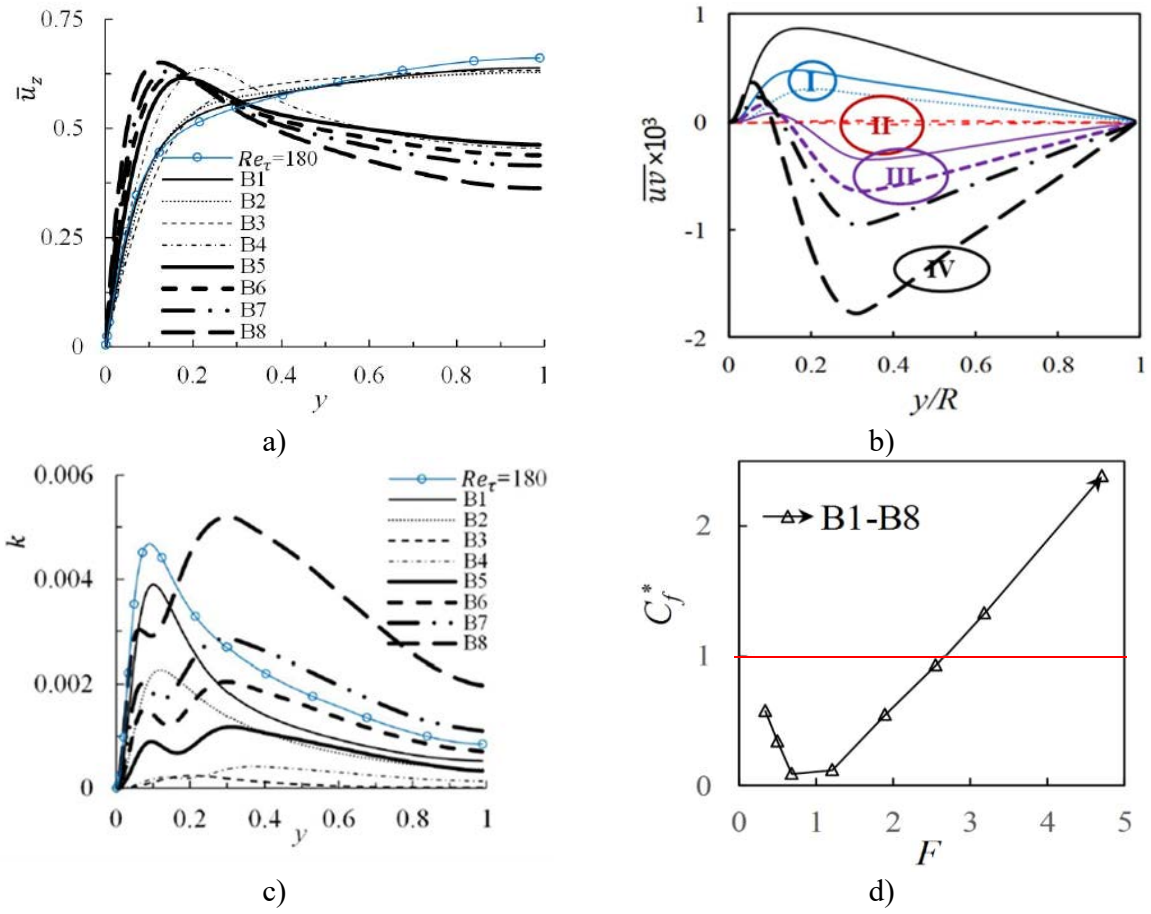

Fig. 11.4. Radial distribution of the mean velocity and turbulent shear stress and kinetic energy in Group B test cases.

Accompanying the changes in velocity profile, turbulence first reduces and then recovers as the body force increases as exhibit in Fig. 11.4(b) and (c) where the turbulent shear stress, $\overline{uv}$ and kinetic energy, k are shown. According to the above results, the flow can be classified into three regimes, i.e., the laminarising regime, the fully laminarised regime and the recovery regime. In the ***laminarising regime***, the velocity profile is flattened and turbulence production is suppressed and both $\overline{uv}$ and k reduces (B1 & B2). In this regime, heat transfer will also be reduced. In the ***fully laminarised regime***, the velocity may be strongly flattened or just flipped to an M shape (B3 & B4), and both the $\overline{uv}$ and k are at the minimum, and the worst deterioration of heat transfer would have occurred in these cases. In the ***recovery regime***, turbulence is produced both near the wall and in the core region. The latter occurs due to the new shear in the middle of the M-profile, where the strain rate has changed its sign and the $\overline{uv}$ is consequently negative. Meanwhile, the turbulent kinetic energy exhibits two peaks one with each regions of turbulence production.

The above classification of flow regimes can be clearly seen from Fig. 10.4(d) which shows the correlations of modified friction coefficient, C_f^* with the strength of the body forces, $F = \int_0^1 2rfdr$ for group B. The former is defined as $C_f^* \equiv \frac{\pi DL\tau_w - F}{\pi DL\tau_{w0}}$, where τ_w and τ_{w0} are wall shear stress for the body-force influenced and zero-body force cases. The turning region around F=1is where fully laminarisation occurs. Recovery occurs when F>1.

11.2.2.2.NEW PERSPECTIVE OF FLOW LAMINARISATION

A new perspective regarding flow laminarisation caused by buoyancy or other types of body forces have been proposed in [11.21] which is illustrated in this section. Essentially it has been proposed that, for a turbulent shear flow, the addition of a body force, such as the buoyancy in a mixed convection, does not change the key turbulence characteristics, including the mixing that it causes as represented by the eddy viscosity, when the pressure gradient is maintained unchanged while the body force is imposed. The frictional Reynolds number based on this pressure gradient can be viewed as the apparent Reynolds number of this flow. The implication of this proposition is that the so-called flow laminarisation due to buoyancy that is commonly known is a conclusion drawn when the buoyancy influenced flow is compared with a reference flow of the same Reynolds number. The key turbulence characteristics are not altered if the buoyancy influenced flow is compared with a new reference flow which has the same pressure force.

Fig. 11.5(a) shows the total shear distribution in the body-force influenced flow (B2) and in the equal flow rate (EFR) reference flow commonly used in previous studies and the new reference flow based on equal pressure gradient (EPG). The wall shear of the EPG (τ_{wp}) can be used to define a friction velocity (which is referred to as the apparent friction velocity), which can in turn be used to define a Reynolds number referred to as the apparent Reynolds number ($Re_{\tau p}$) of the body-force influenced flow.

Fig. 11.5(b) shows the comparison of the turbulent shear stresses in the various laminarising cases compared with predictions based on the new theory described above (refer to [11.21] for details). The new theory suggests that the body force influenced flow is a sum of the EPG reference flow plus a perturbation flow due to the imposed body force. The latter is readily calculated using the

eddy viscosity of the EPG flow and the body force. Consequently, the turbulent shear stress comprises contributions from the EPG reference and one due to the perturbation flow:

$$\overline{u'v'} \approx (\overline{u'v'})_p + (\overline{u'v'})_b^e \tag{11.10}$$

where $\left(\overline{u'v'}\right)_p$ is the contribution from EPG and $\left(\overline{u'v'}\right)_b^e$ is an estimate of the contribution of the perturbation flow. The latter can be calculated as $\left(\overline{u'v'}\right)_b^e = -\frac{\nu_{t1}}{Re}\frac{\partial(U)_b^e}{\partial r}$, where ν_{t1} the eddy viscosity of the EGP flow. The reader is referred to [11.21] for further discussion. The figure shows that the predictions agree very well with the results calculated from the DNS for all cases, and the discrepancies are mostly small.

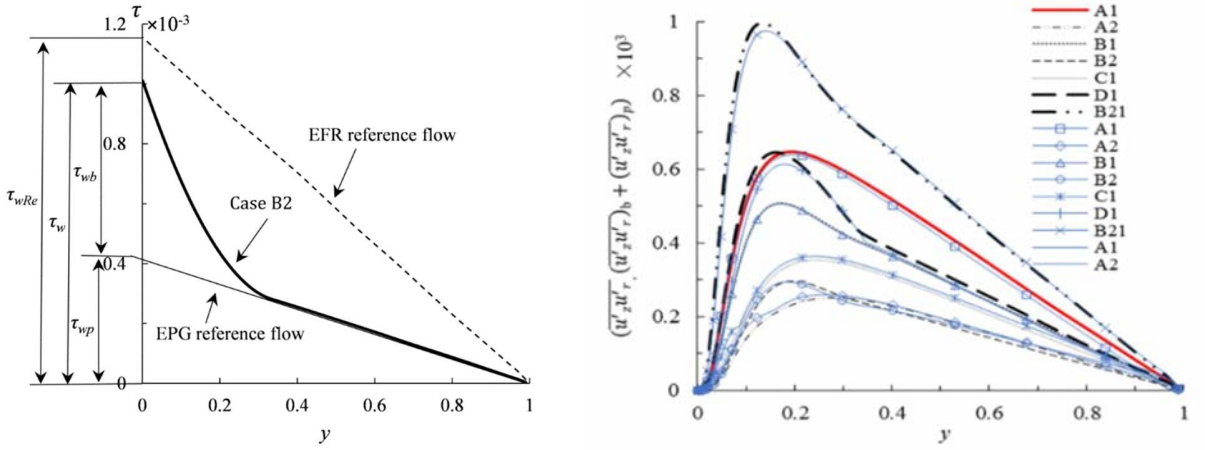

(a) (b)

Fig. 11.5. Total wall shear stress in Case B (a) and Turbulent shear stresses in partially laminarising flow cases (b), with reference of (a) conventional friction velocity and (b) apparent friction velocity (reprinted with permission [11.21]).

Fig. 11.6 shows the normalised eddy viscosity in all laminarising cases of all of the four groups. It is clear that the eddy viscosity reduces significantly as expected in some of the laminarising cases in Fig. 11.6(a) where it is shown against y^+. In Fig. 11.6(b) where the eddy viscosity is plotted against y^{+1} based on the apparent friction velocity, it assumes a value that is very similar in each case. In fact, the spread between the values of the various cases is due to the change in the apparent Reynolds number. The values of ν_t for corresponding reference cases are also shown in the figure for comparison. The ν_t in the body force influenced cases and their corresponding reference cases are very similar in each case. This result confirms that the imposition of a body force on the flow does not alter the eddy viscosity when compared with the EPG reference flow implying no significant change in the key turbulence characteristics.

Similarly, the radial and circumferential rms turbulent velocities normalised by τ_{wp} agree well with those in their respective reference flows (Fig. 11.7). The steamwise rms velocity however is

significantly higher than the corresponding reference flow. This is due to the fact that stronger streaks are generated as the result of the imposition of the body force even though the turbulent vertical structures are not significant increased.

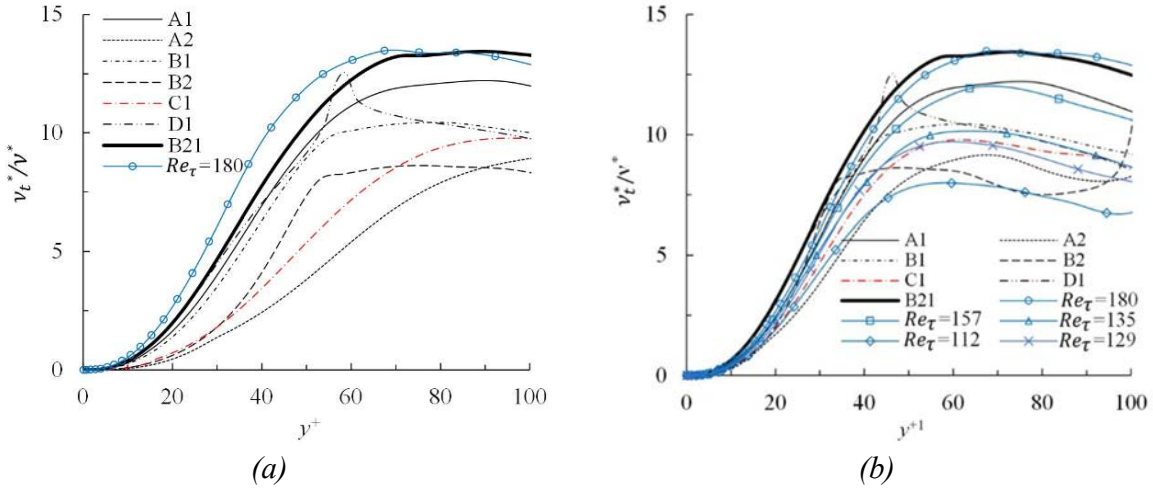

Fig. 11.6. Eddy viscosity in laminarising flow cases (reprinted with permission [11.21]).

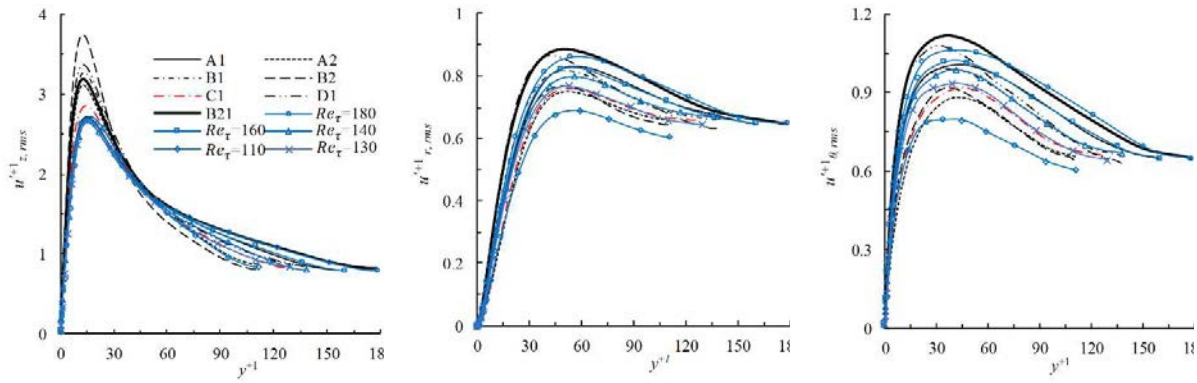

Fig. 11.7. Distribution of rms turbulent velocities normalised by the apparent friction velocity.

Fig. 11.8 shows the friction factors for the various laminarising flow cases. Three values are shown in each case, i.e., those obtained directly from DNS, those estimated using the so-called FIK formulation based on turbulent shear stress from the DNS [11.24] and finally those (denoted as Prediction in the figure) obtained using the FIK formulation but the turbulent shear stress employed is that predicted with the new theory the undisturbed EPG reference flow and the body force distribution. It is clear that all results obtained in the three different approaches are very similar in each test case, further demonstrating the soundness of the new theory.

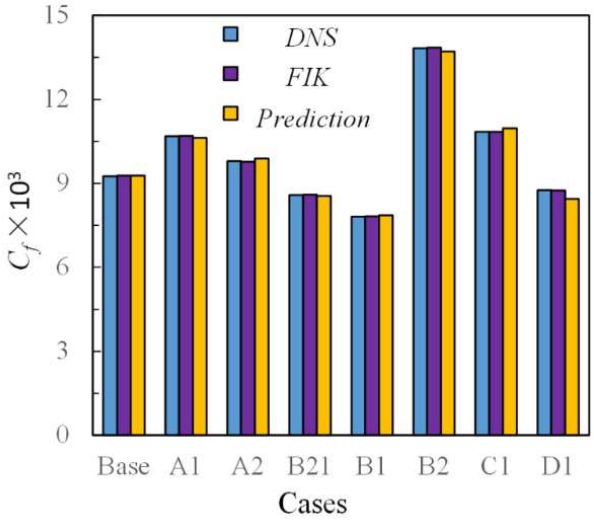

Fig. 11.8. Friction factor in laminarising flow cases.

11.3. VERTICAL FLOW IN PARALLEL PLATES WITH A COLD AND A HOT WALL ON EITHER SIDE

Due to the strong and nonlinear dependence on temperature of thermal properties of fluids at supercritical pressure, the flow and heat transfer in a channel or pipe or a subchannel often develops continuously along its length never reaching the so-called fully developed stage. Engineering calculations need to address this problem. However, in order to develop fundamental understanding of heat transfer phenomena in flow at supercritical pressure, it would be useful to create some situations where the flow and heat transfer behaviour may reach a fully developed stage where they do not vary in the flow direction. Test cases of this kind are also valuable for turbulence model development and validation.

The purpose of the research described in this section is to produce benchmark data using direct numerical simulation (DNS) for a condition where the flow is fully developed streamwise, and hence the bulk temperature, velocity and temperature profiles together with other flow parameters remain unchanged in the flow direction. The problem solved is a vertical flow of water at a supercritical pressure through a passage between parallel plates with a cold and a hot wall on either side. The temperature of the cold wall was fixed at a value below the pseudo critical temperature in all cases, whereas the hot wall temperature just below and just above this value in two groups of test cases, respectively. In each case, a forced convection scenario (i.e., neglecting the buoyant term in the momentum equation), together with an isothermal case were also carried out for comparison.

The data generated in this study can be used for turbulence model validation as well as for developing a better understanding of effect of variable thermal properties and buoyancy on turbulence and heat transfer. Some of the results described here are from [11.17].

11.3.1. METHODOLOGY AND MODEL SETUP

The in-house DNS code CHAPSim described in §11.2 has been used for all simulations. The computational domain for the twodimensional channel flow (or flow between parallel plates) is $16\delta \times 4\delta \times 2\delta$ for streamwise × spanwise × wall-normal directions as shown in Fig. 11.9, and this is represented by a mesh 512 × 160 × 160. Periodical boundary conditions are used in the spanwise direction to represent an infinitive large spread in that direction. Such boundary conditions are also used in the flow direction to describe a fully developed scenario.

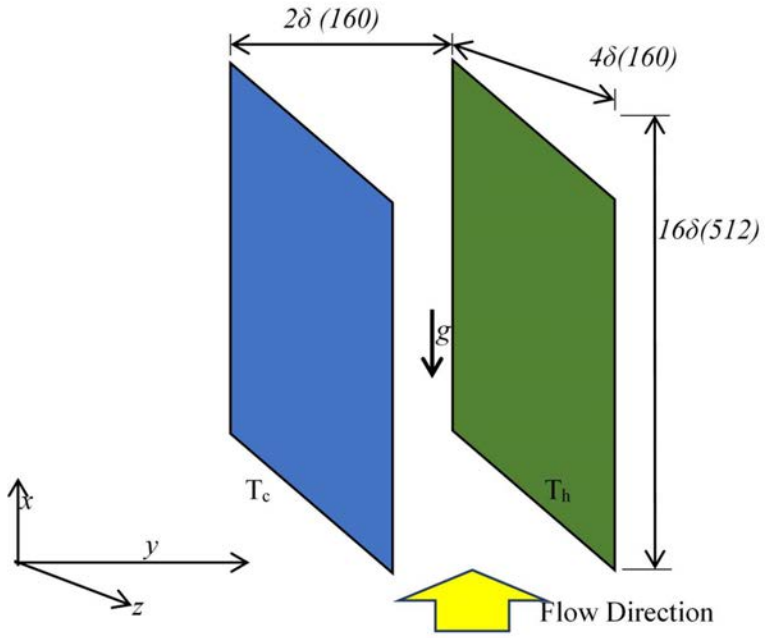

Fig. 11.9. Sketch of the computational domain.

The thermodynamic critical point of water occurs at 647 K and 22.1 MPa. In this study, the system pressure is chosen to the 23.5 MPa, slightly above the critical value and the cold wall has been maintained at 640.15 K for all test cases. Two group of cases have been carried out with the hot wall temperature just below the pseudocritical temperature at 650.15 K (Group 1) and just above it at 653.15 K (Group 2). In each group, a forced convection with the gravity switched off is also simulated. Also simulated is the isothermal test case. The mass flux has been fixed to the same value of 108.6 $kgm^{-2}s^{-1}$ in all cases. For the reference flow, this gives a Reynolds number based on the channel height and the bulk velocity of $Re_0 = 5600$, and a corresponding friction Reynolds number of $Re_\tau \approx 178$. Since the bulk temperature for each case is necessarily slightly different, thus the bulk Reynolds number in the various cases are also different, ranging from 5670 to 5829. The friction Reynolds number on each wall of each test case varies strongly corresponding to the turbulence and flow conditions. A summary of the flow conditions, mesh parameters and some derived parameters for the five cases are shown in Table 11.1 and Table 11.2.

Statistics based both the Reynolds average and Favre average have been produced and a small selection of data are presented in the next section.

TABLE 11.1. WALL TEMPERATURES AND MESH PARAMETERS.

		Group 1				**Group 2**			
Cases	Isothermal (**Isot**)	Forced 1 (**frc1**)		Mixed Convection Upward 1 (**upd1**)		Forced 2 (**frc2**)		Mixed Convection Upward 2 (**upd2**)	
Tw(cold)	-	640.15K		640.15K		640.15K		640.15K	
Tw(hot)	-	**650.15K**		**650.15K**		**653.15K**		**653.15K**	
mesh		hot	cold	hot	cold	hot	cold	hot	cold
Δx+	5.5	6.6	5.1	7.9	4.7	9.5	4.1	11.6	4.3
Δz+	4.4	5.3	4.1	6.3	3.7	7.6	3.3	9.3	3.5
Δy+	0.4~4.4	0.5~5.2	0.4~4.0	0.6~6.2	0.3~3.7	0.7~7.5	0.3~3.2	0.8~9.1	0.3~3.4

TABLE 11.2. BULK PARAMETERS.

Case	isothermal	forced-1	upward-1	forced-2	upward-2
$\boldsymbol{q_w\ (kWm^{-2})}$		17.2	21.2	16.8	41.4
$\boldsymbol{h_b\ (kJkg^{-1})}$		1856	1847	1988	1916
$\boldsymbol{T_b\ (K)}$		646.4	645.8	651.2	649.3
$\boldsymbol{\rho_b\ (kgm^{-3})}$		493.1	498.6	403.9	453
$\boldsymbol{l_c}$	1.00	0.83	0.60	0.45	0.33
$\boldsymbol{l_h}$	1.00	1.17	1.40	1.55	1.67
$\boldsymbol{Re_b}$	5600	5730	5670	6829	6192
$\boldsymbol{Re_{bc}}$	2800	2217	1287	987	549
$\boldsymbol{Re_{bh}}$	2800	3529	4377	5903	5629
$\boldsymbol{Pr_b}$		2.24	2.14	6.31	3.43
$\boldsymbol{Pr_{bc}}$		2.10	1.99	2.84	2.54
$\boldsymbol{Pr_{bh}}$		2.36	2.19	7.46	3.56
$\boldsymbol{\tau_{wc} \times 10^3}$	4.00	3.60	3.10	2.40	2.50
$\boldsymbol{\tau_{wh} \times 10^3}$	4.00	5.00	7.10	8.10	12.70
$\boldsymbol{Re_{\tau c}}$	178	134	90	59	45
$\boldsymbol{Re_{\tau h}}$	178	247	351	465	634
$\boldsymbol{Nu_{bc}}$		9.54	9.67	3.42	6.82
$\boldsymbol{Nu_{bh}}$		22.40	26.21	53.80	68.10

Note: Most of the notions are conventional and self-explanatory, though a few need clarifications. The label $l_c$and $l_h$are the distance of the peak mean velocity to the cold and hot wall respectively. These are used as the length scales in $Re_{bc}, Re_{bh}, Re_{\tau c}, Re_{\tau h}, Nu_{bc}, Nu_{bh}$.

11.3.2. DESCRIPTION OF RESULTS, DATA & DISCUSSION

Fig. 11.10 shows the profiles of the enthalpy, temperature, density and specific heat to demonstrate the overall thermal field and properties to facilitate the discussion and understanding of the flow in this section. The wall temperature on the right/hot side is kept slightly above the pseudocritical temperature. It can be seen that the thermal boundary layer on the hot-side appears to be much

thinner than that on the cold side. The temperature and thermal properties are relatively uniform across the core in all cases except in the case labelled as 'frc2', where there is a continuous change of temperature/properties indicating a rather laminar-like core flow. The h, c_p and ρ all reduce sharply and in a greater magnitude on the hot-side than on the cold side. This is not surprising considering that wall temperature of the hot wall is close to the pseudo-critical temperature.

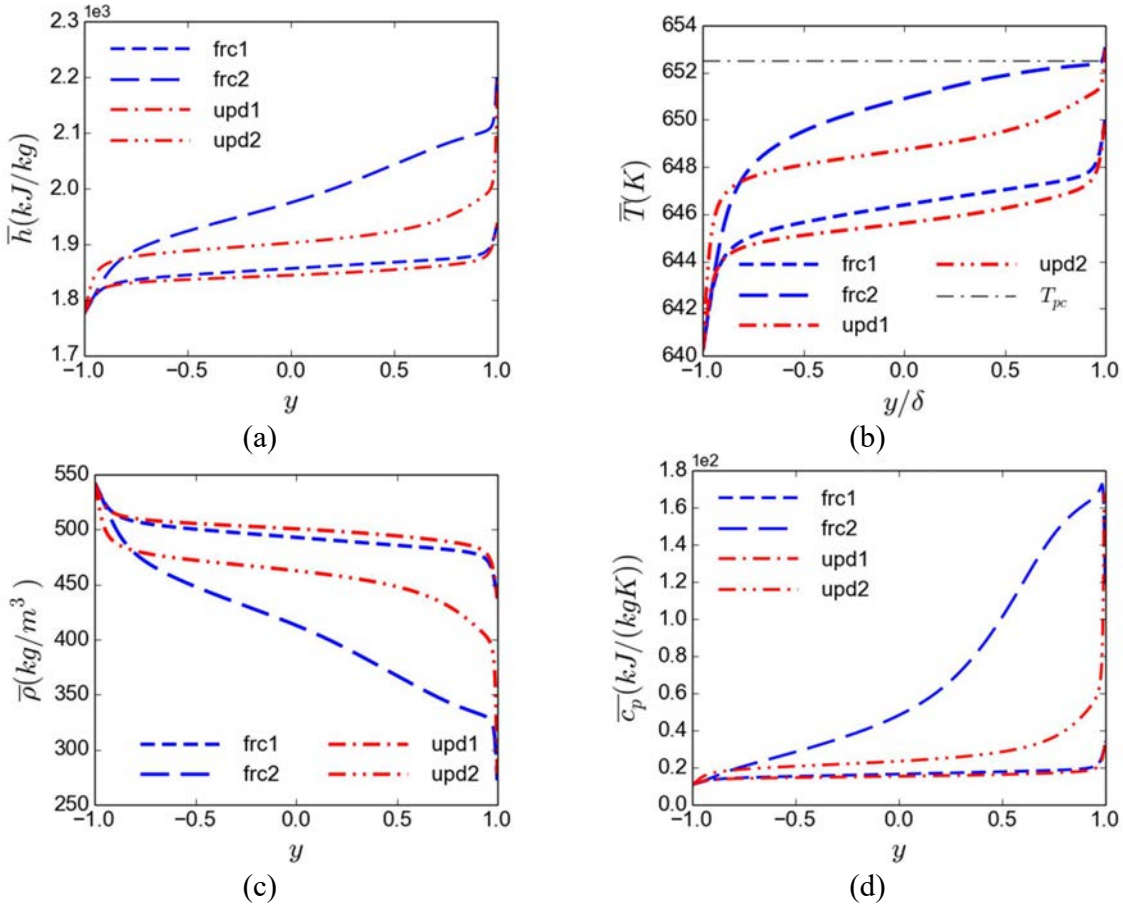

Fig. 11.10. Distribution of enthalpy, temperature and thermal properties.

Another interesting quantity, which also provide information useful in understanding the flow behaviour is the force balance. The total shear stress across the channel width together with those of the turbulent and viscous shear stress and buoyant force are shown in Fig. 11.11. The first thing to note in Fig. 11.11(d) is that the total shear stress distribution in the forced convection cases is shifted downwards indicating that the wall shear stress is increased on the hot side and reduced on the cold side. The distribution is however still linear as there is no non-uniform body forces. In the mixed convection flows, the wall shear stresses are also higher on the hot side than on the cold side, and in addition, the total shear distribution is now strongly nonlinear. This is reflected by the additional buoyant force in Fig 11.11(c). In the forced convection cases, the turbulent shear stress is much higher on the hot side than on the cold side, which is likely to be responsible for the increase of wall shear stress on the hot side. In the mixed convection cases, turbulence is

significantly increased on the cold side, especially in upd2, and it is reduced slightly on the hot slide.

Fig. 11.12 shows the mass flux and Favre averaged streamwise velocity. In all cases, the velocity is increased on the hot side and reduced somewhat on the cold side. This is understandable for buoyancy influenced cases, where the flow is buoyancy aided on the hot side and buoyancy opposed on the cold side. The distortion in the velocity profile in the forced convection cases maybe due to a number of reasons, but the reduction in the density on this side is likely to be the main contributing factor to this trend, noting that the distortion on the mass flux is much less in this case. At this stage, it is of interest to note that in some cases, such as 'frc2', the location of the zero velocity-gradient and the location of the zero turbulent shear stress do not correspond to each other. This often occurs in asymmetric flow or heating condition. Under such conditions, eddy viscosity turbulence models will fail to predict suitable heat transfer.

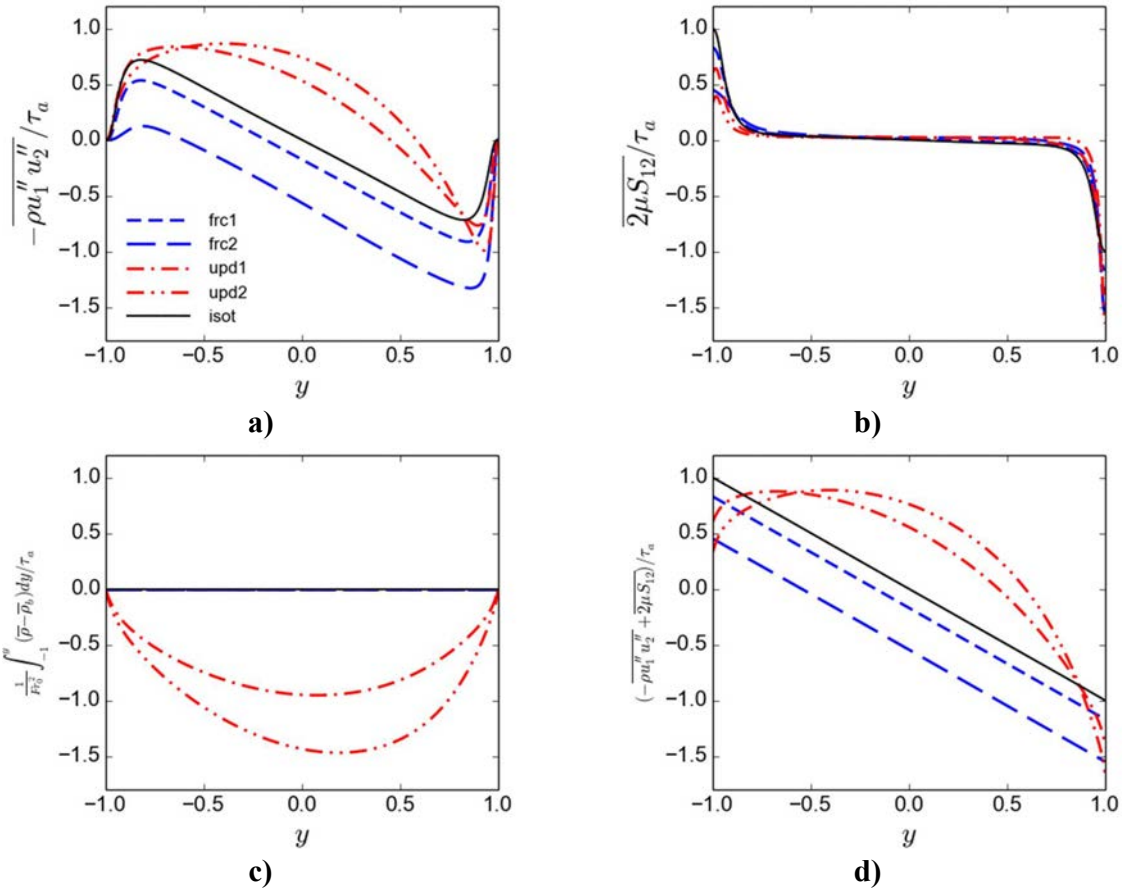

Fig. 11.11. Normalised turbulent shear stress, viscous shear stresses, buoyancy force and total shear stress.

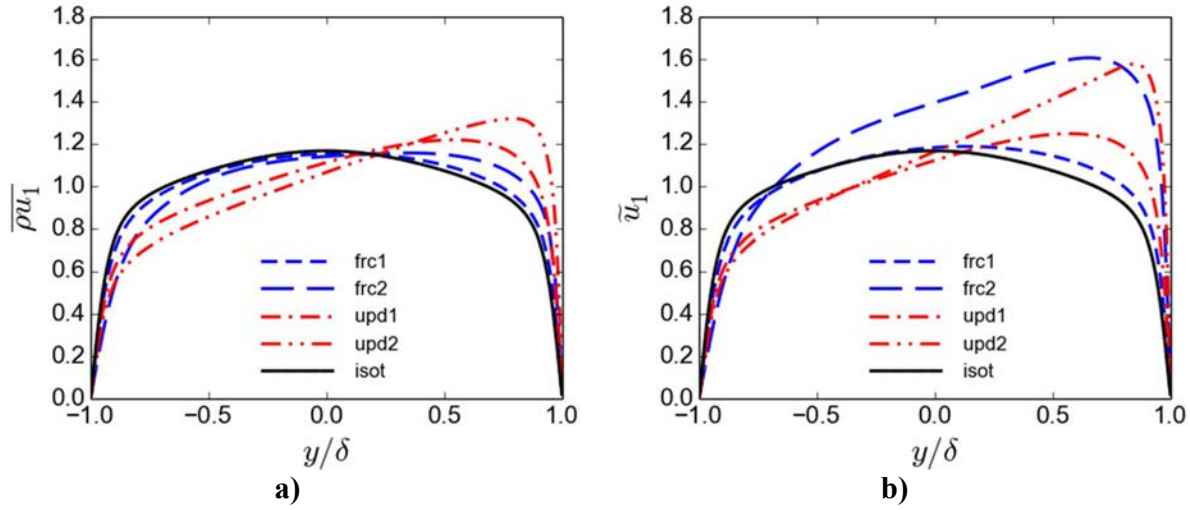

Fig. 11.12. (a) Reynolds averaged streamwise mass and (b) Farve averaged streamwise velocity.

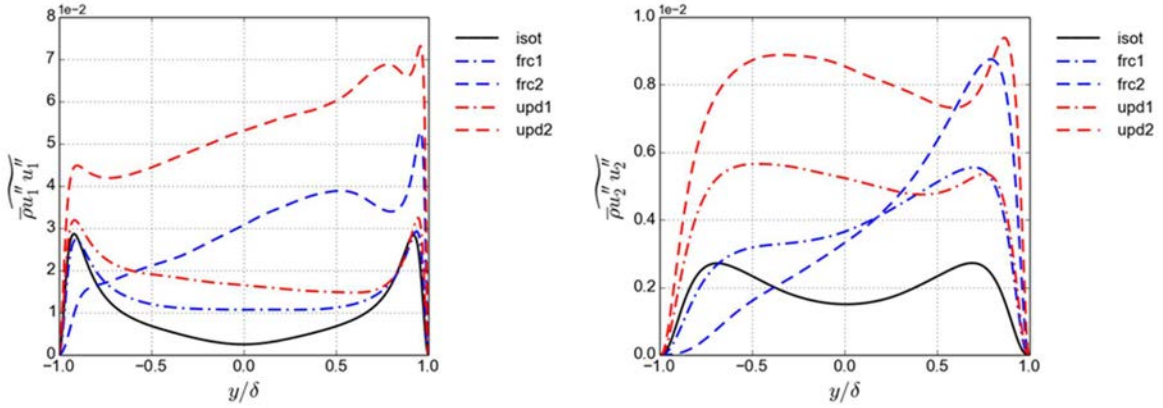

Fig. 11.13. Streamwise and wall normal Reynolds stresses (reproduced from [11.17]).

Fig. 11.13 shows the streamwise and wall normal Reynolds stresses. In frc1, the streamwise component remains largely unchanged from that in the forced convection whereas the wall normal component is increased significantly on the hot side. Both components are significantly increased on the hot side in frc2. The wall normal component is completely suppressed near the cold wall, and streamwise component is also significantly reduced.

Fig. 11.14 shows the streamwise and wall normal turbulent heat flux, which are valuable information for turbulence model validation.

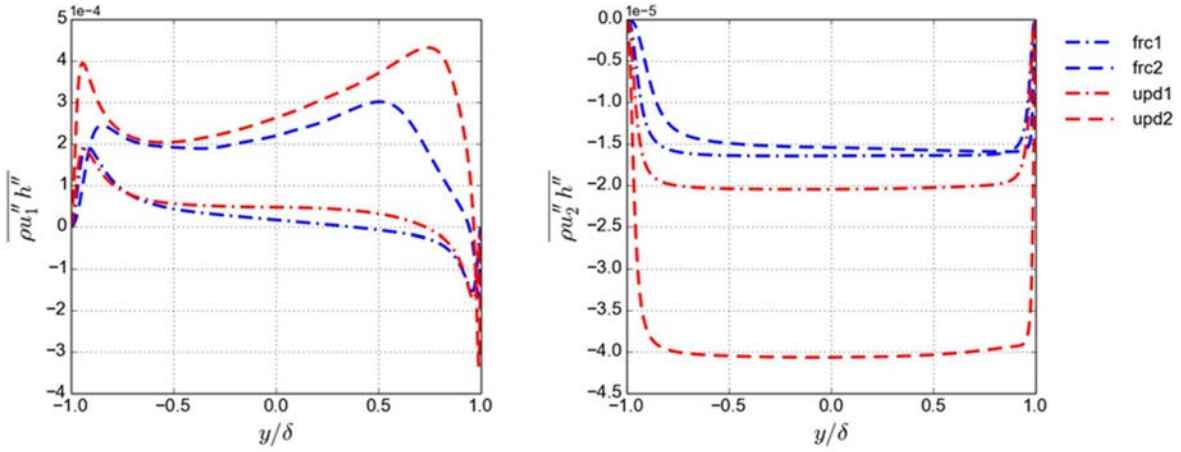

Fig. 11.14. Streamwise and wall normal turbulent heat flux (reproduced from [11.17]).

DNS has been carried out for the flow of water at supercritical pressure in a channel with a cold and hot wall at fixed temperature, and hence resulting in a fully developed condition, for an upwards mixed and associated forced conditions. Reynolds and Favre averaged statistics are available for model validation. The results show that under the conditions studied, the variable density has a strong influence on the flow under both forced and mixed conditions whereas the variation of the viscosity has little influence. Further information may be gained from [11.17] and some of the figures used in the section are taken from a technical paper under development, which will report more detailed data and discussion.

11.4. FLUID TO FLUID SIMILARITY AND SCALING

The general understanding of the flow and heat transfer behaviour is transferable between flows of different fluids. The useful theory of buoyancy-induced flow laminarisation and enhancement and heat transfer deterioration e.g. [11.20], [11.25] is generic for all fluids and has been widely used in the research on a variety of fluids and for applications in different fields beyond nuclear engineering. However, due to the strong and nonlinear variations of thermal properties of fluids at supercritical pressure, strictly speaking, the detailed correlations developed for one fluid is often only applicable to flows of that fluid. There are large discrepancies between the correlations developed from different fluids using conventional non-dimensional parameters.

Recently, a number of studies have been carried out on the fluid to fluid scaling or fluid similarity, which are aimed at unifying the predictions of heat transfer of different fluids. Examples include [11.26]-[11.28].

In particular, [11.27] proposed a set of non-dimensional parameters to specify flow conditions. Their theory predicts the flows and heat transfer behaviour will be the same along the pipe regardless of the working fluids if these parameters match each other.

The purpose of the research described in this section is to demonstrate the validity of the theory of [11.27] by performing DNS of flows of four different fluids under conditions calculated using the

criterion specified in [11.27] to achieve similarity. The work will create a benchmark database for testing other fluid-to-fluid scaling theories as well. Some of the results reported here are originally described in [11.27].

11.4.1. METHODOLOGY AND MODEL SETUP

DNS of an upward flow of fluids at supercritical pressure have been carried out using the in-house code CHAPSim described in §11.2. Four different fluids, namely, water (H_2O), Carbon dioxide (CO_2), ammonia (NH_3) and fluoroform (R23), have been considered to study fluid-to-fluid scaling. The aim of fluid similarity is to achieve similar behaviours in different flows under certain dimensionless form by choosing the dimensions of the flow domains and the inlet and boundary conditions of the various cases. The operation pressure is an additional parameter, which by choosing suitably can improve similarity despite this is not theoretically required (see [11.27] for further discussion).

In the study reported here, following [11.27], the pressures are chosen to be 8.67 MPa, 25 MPa, 12.63 MPa and 5.7 MPa for CO_2, H_2O, NH_3 and R23, respectively. The flow of CO_2 is the base case, the condition of which is chosen arbitrarily and the values of the key parameters are shown in

TABLE 11.3. Also shown in the table are parameters for the flows of other fluids chosen to match the non-dimensional parameters of N_{TPC}, N_{SPC}, Fr_0 and Re_0 of the base case. In addition, L/D=30 is used for all cases.

Here, the N_{TPC} and N_{SPC} are transpseudocritical number and sub-pseudocritical number, respectively, which are effectively power-to-flow ratio and the dimensional inlet enthalpy (with a negative sign) [11.27]. These are defined as:

$$N_{TPC} = \frac{\dot{Q}}{\dot{m}}\frac{\beta_{pc}}{c_{p,pc}} = 4\frac{q''\beta_{pc}L}{G_{in}c_{p,pc}D}, N_{SPC} = \left(h_{pc} - h_{in}\right)\frac{\beta_{pc}}{c_{p,pc}} = -h_{in}^{**} \tag{11.11}$$

where Q and q are the rate of heat input and heat flux, and m and G_{in} are the mass flow rate and mass flux, and $h^{**} = \left(h - h_{pc}\right)\frac{\beta_{pc}}{c_{p,pc}}$. The subscript '$pc$' refers to properties at pseudo-critical condition.

TABLE 11.3. CONFIGURATIONS OF THE SIMULATIONS

Case	q (W/m^2)	G_{in} (kg/m^{2}s)	h_{in} (J/kg)	D (m)	L (m)	N_{TPC}	N_{SPC}	Fr	Re_0	Pe_0
CO_2	30870	166.62	2.712x10^5	0.002	0.06	0.1783	0.5669	0.08249	5234.02	14954
H_2O	113739.32	128.68	1.815x10^6	0.0025	0.074	0.1783	0.5669	0.08249	5234.02	8806
NH_3	54050.83	94.01	1.064x10^6	0.0026	0.078	0.1783	0.5669	0.08249	5234.02	11390
R23	20884.68	179.76	2.439x10^5	0.0028	0.055	0.1783	0.5669	0.08249	5234.02	10954

11.4.2. DESCRIPTION OF RESULTS, DATA & DISCUSSION

11.4.2.1. GENERAL FLOW HEAT TRANSFER BEHAVIOUR

The general development of the flow and heat transfer along the flow direction for the case of CO_2 is shown in Fig. 11.15, which clearly exhibits a number of stages of development. Following the initial condition (Stage 1 – initial flow), the flow undergoes a partial laminarisation with turbulence structures progressively reducing (Stage 2 – partial laminarisation), reaching a full laminarisation at around x/D=17 (Stage 3 – full laminarisation), after which turbulence structures are generated, becoming stronger downstream (Stage 4 – recovery). Alongside the changes in the flow and turbulence, the Nusselt number reduces during stage 2 (partially due to the thermal boundary development and partially due to reduction of turbulence), reaching a minimal at x/D=18, after which it begins increasing. The Reynolds number increases in the flow direction and the laminarisation is therefore not due to a reduced Re, but due to the effect of buoyancy. Typical radial distributions of the mean velocity, turbulent shear stress and the rms of the streamwise fluctuating velocity at the various stages of flow development are shown in Fig. 11.16. These results support the established understanding of the flow and heat transfer under such conditions but with detailed information which can be used for model validation.

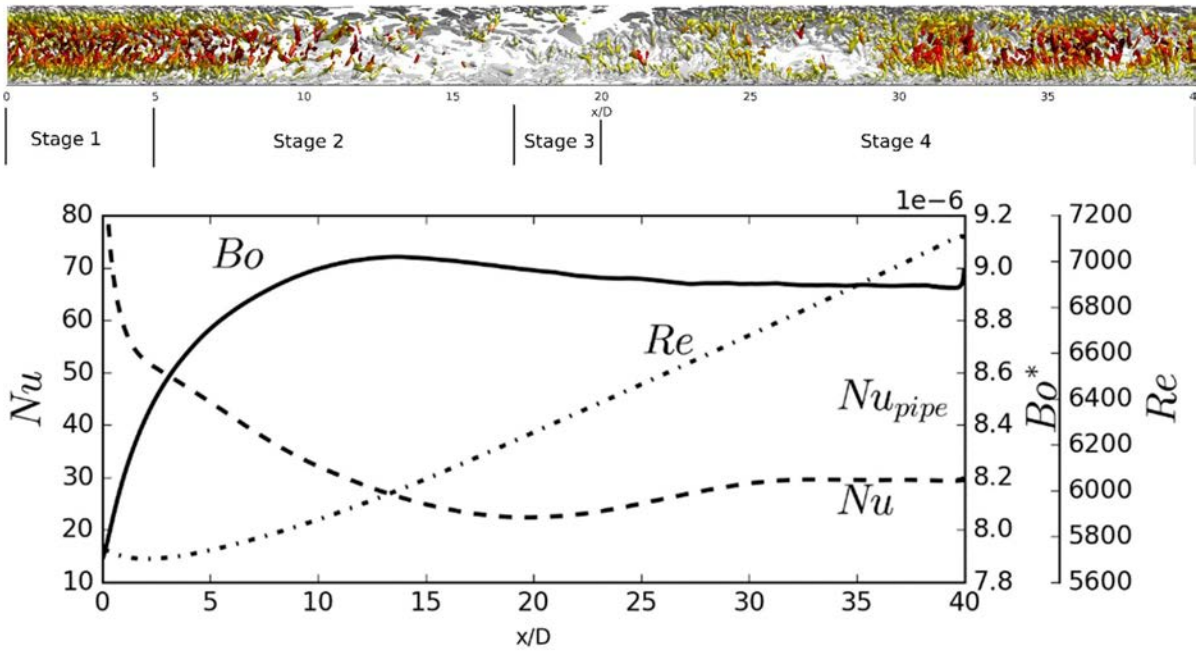

Fig. 11.15. Overall flow development. (a) Vortical flow structures and (b) Development of Reynolds and Nusselt numbers and buoyancy parameter along the pipe.

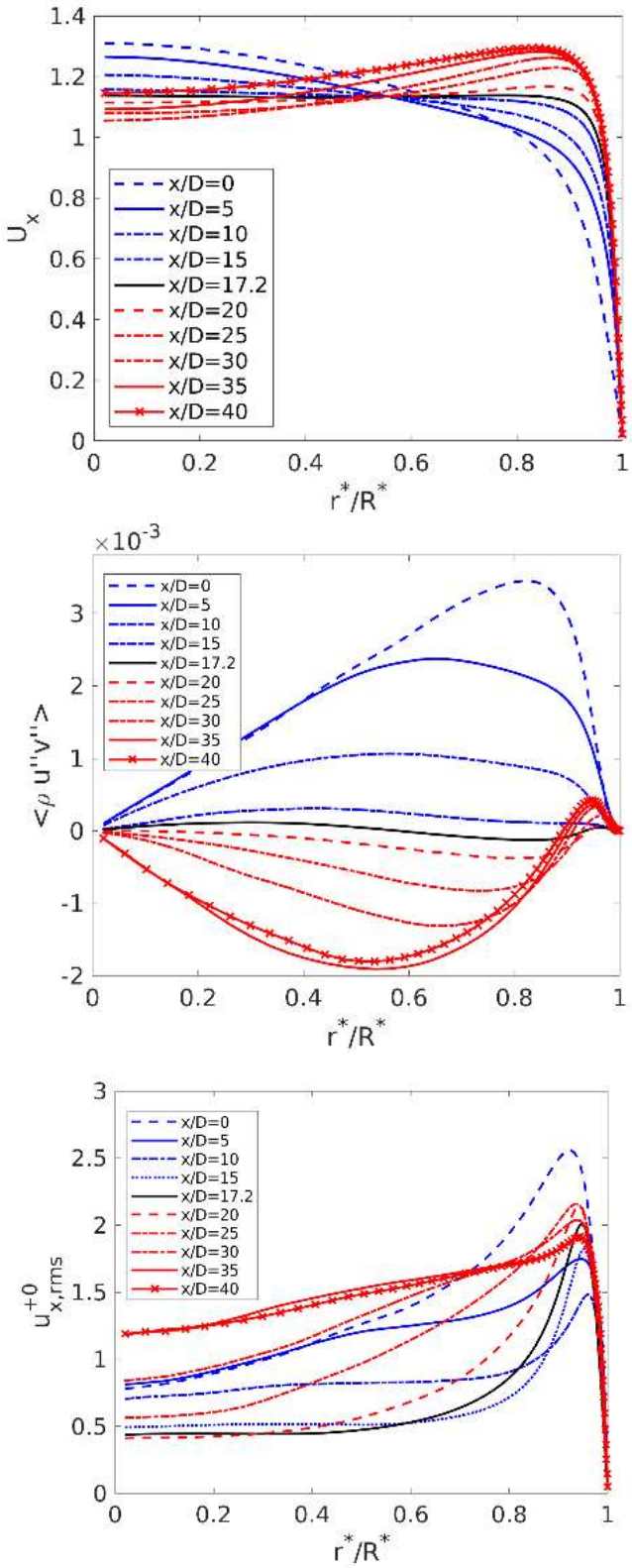

Fig. 11.16. Flow and turbulence statistics at the various stages of development.

11.4.2.2.FLUID SIMILARITY

Fig. 11.17 shows the streamwise development of a number of flow and heat transfer parameters. The most interesting observation is that the peak wall temperature occurs at exactly the same location in the flows of different fluids, at which location the Nusselt number reaches its minimum.

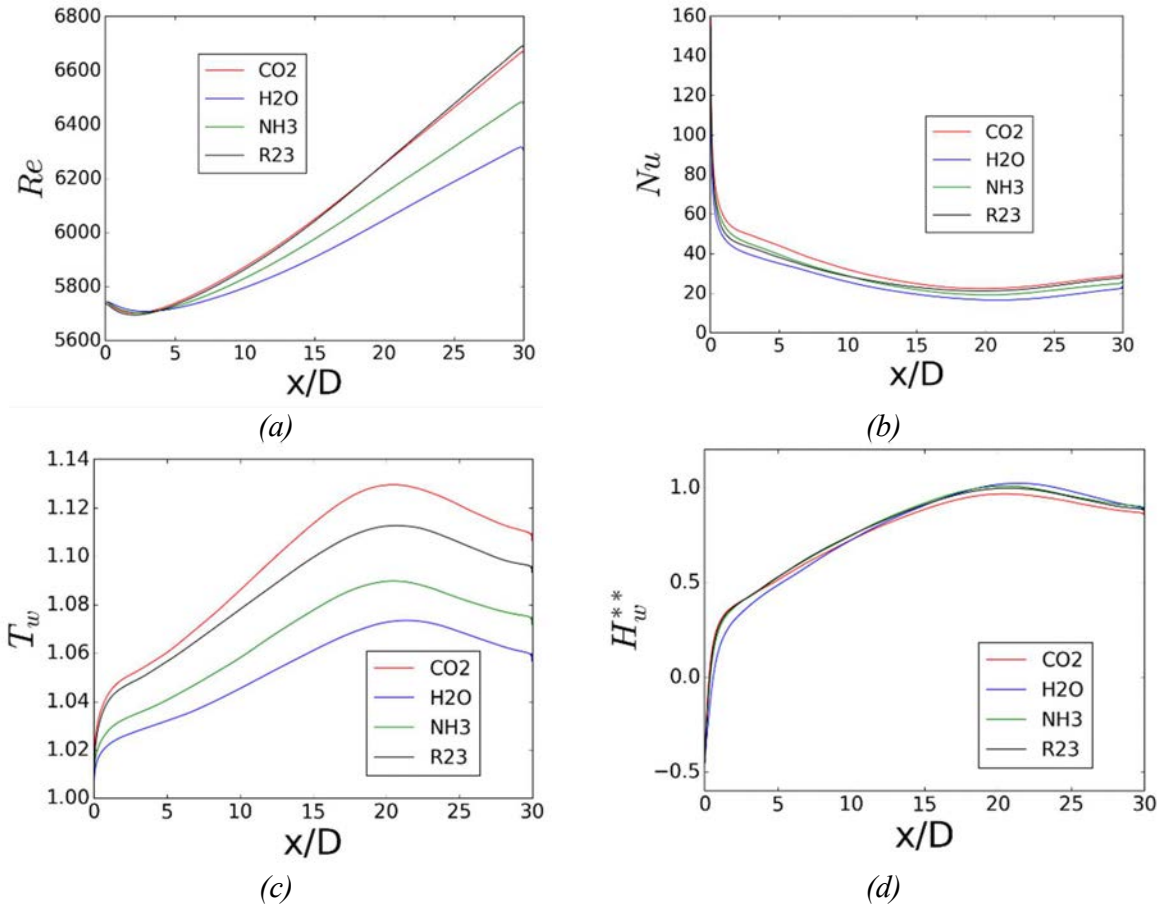

Fig. 11.17. Comparison of axial development of a number of parameters in the flows of different fluids (reprinted from [11.29] with permission from Begell House, Inc.).

This confirms that by matching the flow operation and inlet conditions proposed by [11.27], the flow and heat transfer behaviour including laminarisation and heat transfer deterioration occur at the same positions regardless of the fluids. Additionally, the values of h_w^{**} match very well in the cases of different fluids as predicted by [11.27]. Fig. 11.18 to Fig. 11.20 further show that the mean velocity, the turbulent kinetic energy and the turbulent shear stress in different fluids undergo exactly the same development along the streamwise direction, demonstrating that the effects of buoyancy and other thermal properties in different fluids are the same throughout the length when the flow conditions are specified using the criterion proposed by [11.27]. This is significant since it suggests a new framework of data correction to unify data/calculation for different fluids which has to date proven challenging.

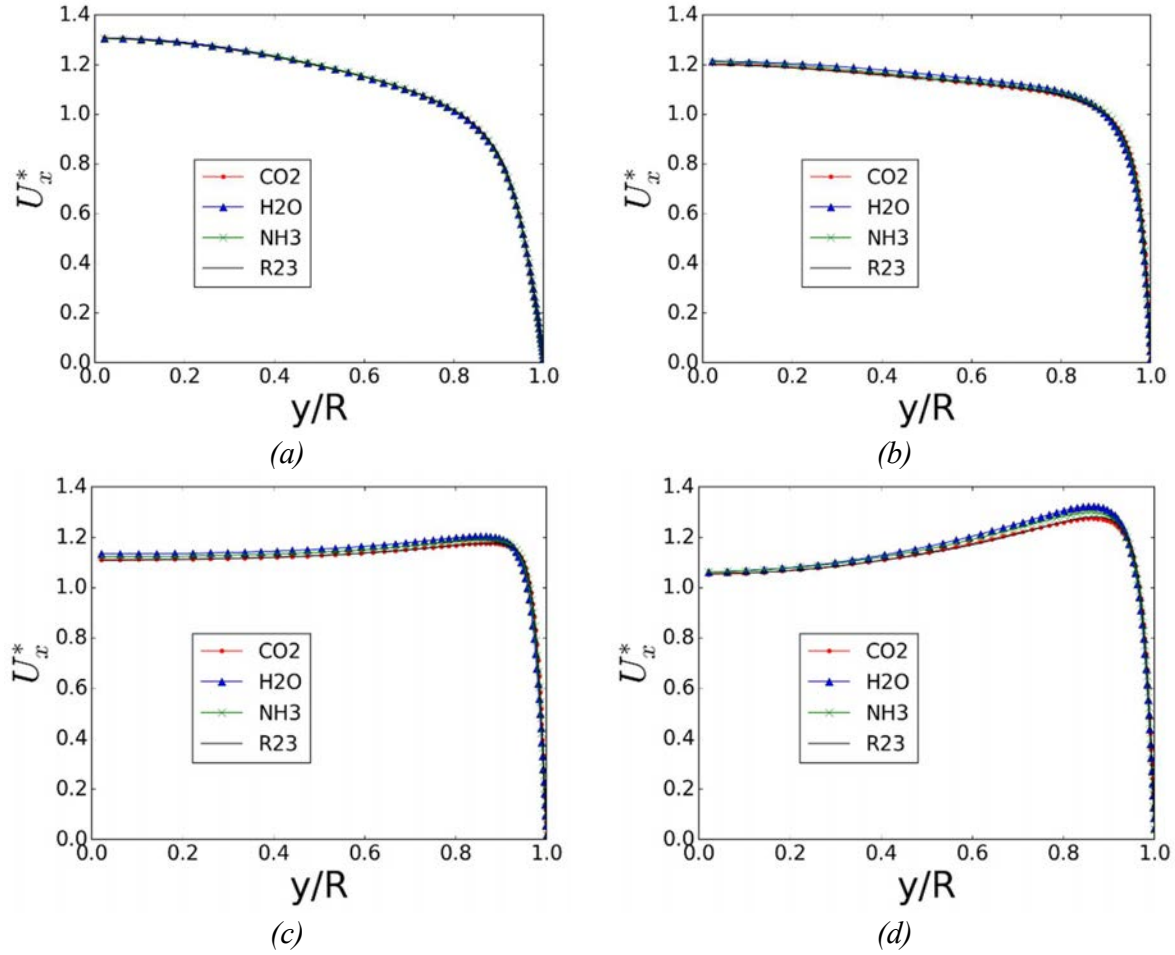

Fig. 11.18. Velocity profiles at several stages of the flow (a) x/D=5, (b) x/D=15, (c) x/D=20 and (d) x/D=30 (reprinted from [11.29] with permission from Begell House, Inc.).

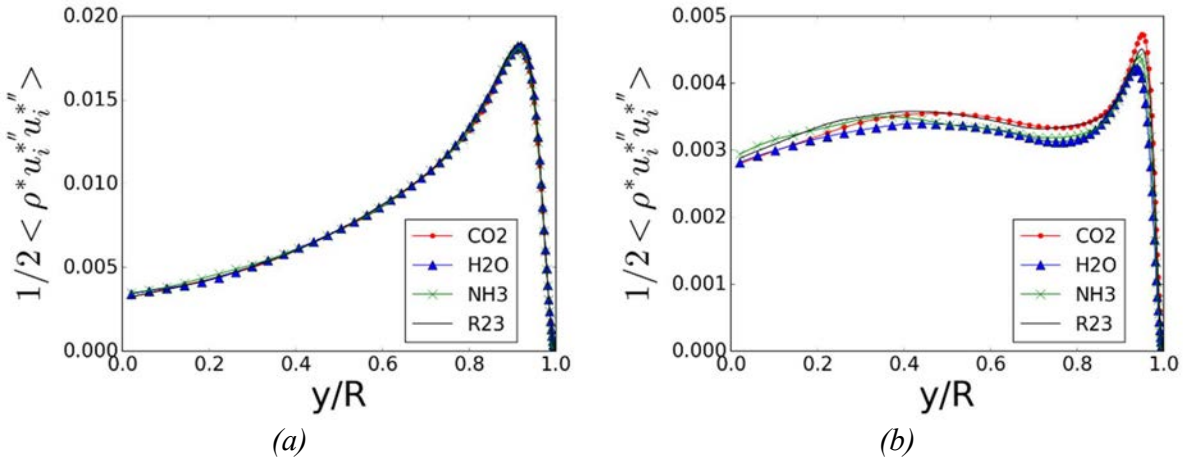

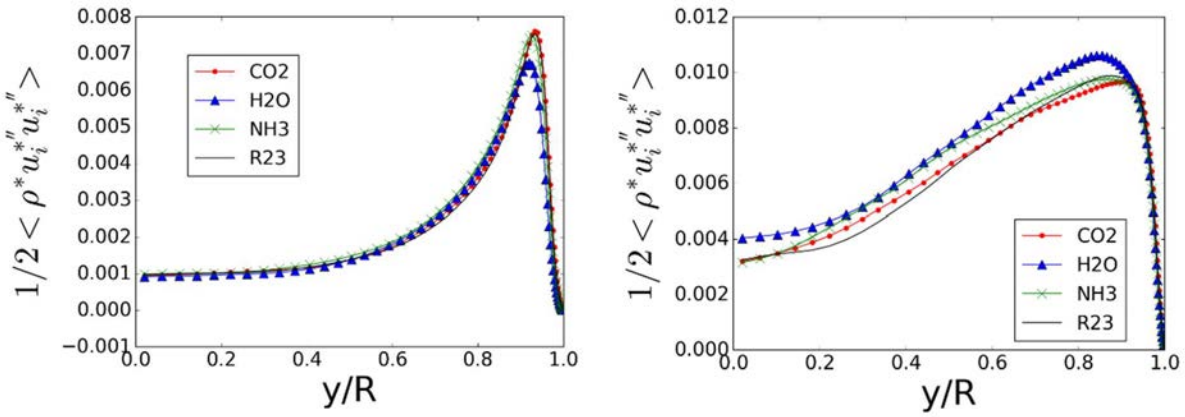

(c) *(d)*

Fig. 11.19. Profiles of turbulent kinetic energy at several flow stages (a) x/D=5, (b) x/D=15, (c) x/D=20 and (d) x/D=30 (reprinted from [11.29] with permission from Begell House, Inc.).

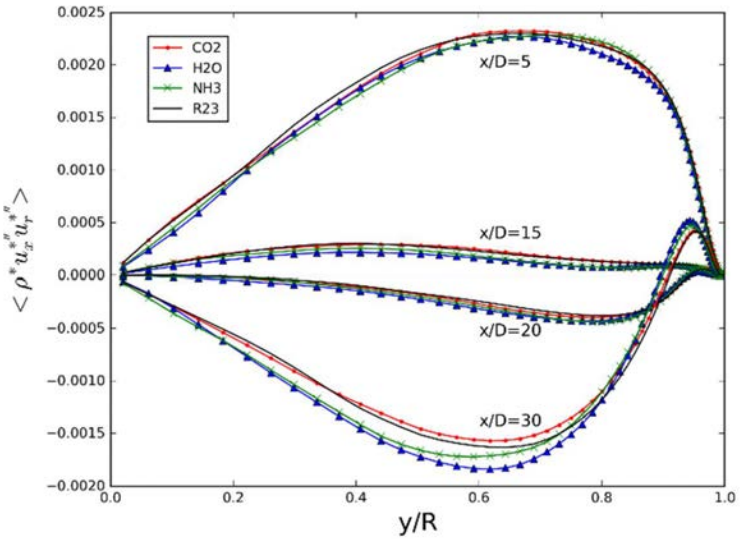

Fig. 11.20. Comparison of the turbulent shear stress development in flows of different fluids (reprinted from [11.29] with permission from Begell House, Inc.).

DNS of vertical upflow of four different working fluids at supercritical pressure have been carried out to study fluid-to-fluid similarity. The inlet and other conditions of each case have been chosen according to the non-dimensional parameters proposed by [11.27]. It has been shown that the flow and heat transfer behaviours are indeed very similar in the various cases, especially the worst heat transfer deterioration occur at the same *x/D* location, hence demonstrating the validity of the analysis of [11.27]. In addition, the data can be used as a benchmark for validation of other similarity work and model development or assessment.

11.5. FLOW INSTABILITY IN A TRAPEZOIDAL ANNULAR PASSAGE

It has been known for some time that flow in a tightly packed rod bundle or through a channel of a non-uniform cross sectional area involving small gaps may find strong flow oscillation/instabilities occurring in the gapping area [11.30]–[11.36]. These are characterised by large unsteady flow structures with a strong horizontal velocity. Such flow instabilities are not due to secondary flow caused by the anisotropic Reynolds stresses, but may be related Kelvin-Helmholtz instability.

A number of studies have been carried out to study the above phenomena using experimental or numerical simulations, mostly using unsteady RANS but also LES in some cases. All of these studies are however concerned with isothermal flow except a recent study by [11.37], [11.38], which studied effect of buoyancy.

The purpose of the research described in this section is to carry out large eddy simulations (LES) of flow in a triangular annular passage formed with a circular rod placed in a trapezoidal enclosure. Water at supercritical temperature is used as the fluid. This geometry has been used by a number of researchers in their studies [11.35]-[11.38]. The open-source Code_Saturne package is used in the study. Some of the results report here are from [11.39], [11.40].

11.5.1. METHODOLOGY AND MODEL SETUP

The trapezoidal flow passage used in the simulations is shown in Fig. 11.21. The rod is placed off centre resulting in a narrow gap (NG) and a wider gap (BG). The overall passage can be seen as made of two –subchannels. The dimensions are shown in the figure, but it is useful to note that the hydraulic diameter (D_h) of the flow passage is 0.0314 m, and the pitch-diameter ratio, (Rod Diameter + gap size)/Rod Diameter, is 1.079 and 1.22 for the narrow and wider gaps respectively. According to previous studies, there are likely large-scale unsteady flows result in narrow gap region, whereas these are less likely to occur in the wider gap region. Table 11.4 lists conditions for various cases.

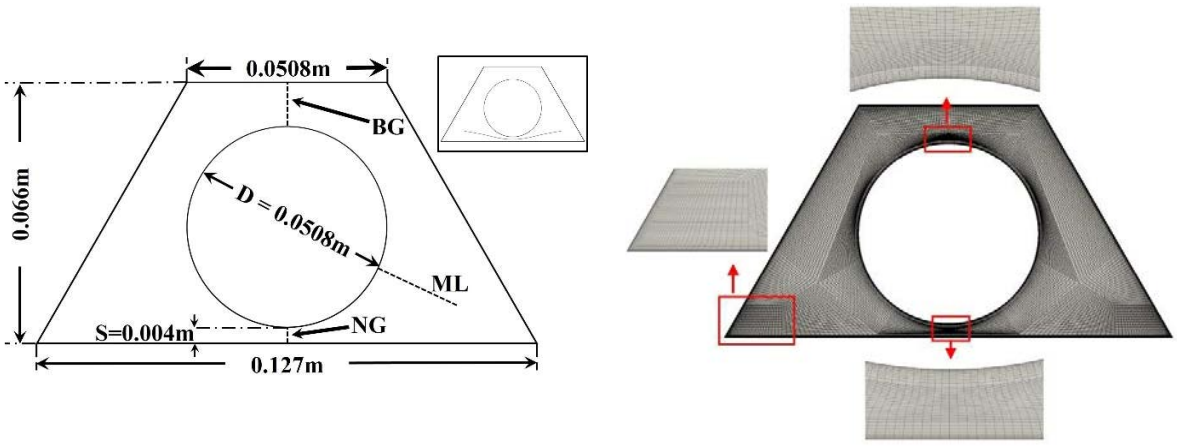

Fig. 11.21. Sketch of the cross section of the trapezoidal flow passage by Mohd Amin M. licensed under CC BY-NC-ND 2.0 [11.39].

TABLE 11.4. SUMMARY OF FLOW AND HEATING CONDITIONS AT RE=10540, T_O=633K (FC=FORCED CONVECTION; MC=MIXED CONVECTION). ADAPTED FROM [11.39].

Case	Type	Q^+	q (kW/m^2)	D_h (mm)	U_b (m/s)	L_t/D_h	Bo^*
FC_L1	FC	1.07	10	31.4	0.0388	30	–
FC_L3	FC	8.01	75	31.4	0.0388	30	–
MC_L3	MC	0.01	0.13	31.4	0.0388	50	2×10^{-5}
MC_S2	MC	1.73	161.5	3.14	0.388	50	2.5×10^{-6}
MC_S3	MC	6.90	646	3.14	0.388	50	1×10^{-5}

The total length of the computational domain is divided into two parts, the inflow generator of $10D_h$ and the heated length of 30 D_h or 50 D_h long. The inflow generator is isothermal with a periodic buoyancy condition streamwise to produce a fully developed flow for the heated length. The inner rod is heated with a constant heat flux of 10 and 75 kW/m^2 for forced convection simulations namely FC_L1 and FC_L3. Meanwhile for mixed convection simulations, three cases were considered with two different dimensions where the heat flux was varied to achieve different level of Bo^*. The value of Bo^* for the large dimension case (similar to forced convection cases) of MC_L1 is set at 2×10^{-5}, while MC_S2 and MC_S3 which have a smaller dimension (1/10th of the large dimension) having values of 2.5×10^{-6} and 1×10^{-5} respectively. In all cases specified, the initial targeted Reynolds number is 10540. The pressure and fluid temperature at inlet are 25 MPa and 633 K respectively.

Large eddy simulation (LES) have been carried out using the open-source CFD solver of Code_Saturne developed by EDF and the wall adapting local eddy viscosity (WALE) subgrid scale model was used. NIST property database was used for fluid properties. The computational domain was meshed using a structured mesh containing 33 million elments with finer mesh flower to the walls (see Fig. 11.21). The nodes of the first mesh next to the wall are in the range of $5 \leq \Delta x+ \leq 17$, $0.13 \leq y+ \leq 0.2$ and $\Delta z+ \approx 23$. There are about 13 cells located within $y+ \leq 20$ with ~9 cells located in the range $0 \leq y+ \leq 10$. The nondimensional time step is $t^* = \frac{\Delta t U_b}{D_h} = 0.0012$ for all cases, which gives a CFL number below 0.5. The velocity and pressure coupling is obtained using SIMPLEC algorithm and a second order central difference scheme is used for spatial discretisation.

11.5.2. DESCRIPTION OF RESULTS, DATA & DISCUSSION

Fig. 11.22 and Fig. 11.23 show the instantaneous streamwise velocity and temperature in the narrow gap. It is clear that flow oscillations occur in all test cases though the oscillations vary strongly and differently in the flow direction in different cases. In forced convection FC_L1 when the heat flux is low, the flow oscillations are maintained at the same level throughout the flow domain. In the strongly heated forced convection FC_L3, the flow oscillations are suppressed downstream along the flow. This is likely due to the strong variations of thermal properties. In the weakly buoyancy influenced case (MC_S1), the flow oscillations are maintained downstream but with reduced intensity. For the strongly buoyancy-influenced cases (MC_L3 and MC_S3), the flow oscillations appear to reduce to minimal around x/D=30, after which some oscillations start appearing again. The temperature contours show similar picture but it should be noted that no

oscillations can be seen at the upstream of the flow since the fluid is not been heated yet. In addition, the contours are light in FC_L1 due to low heating in that case, but the oscillations are however strong.

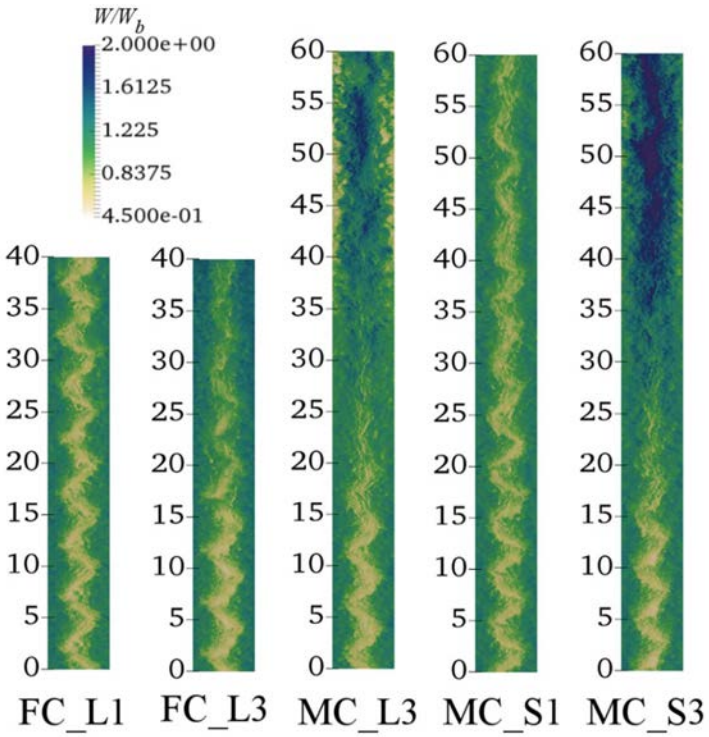

Fig. 11.22. Instantaneous streamwise velocity at equidistant planes in the narrow gap by Mohd Amin M. licensed under CC BY-NC-ND 2.0 [11.39].

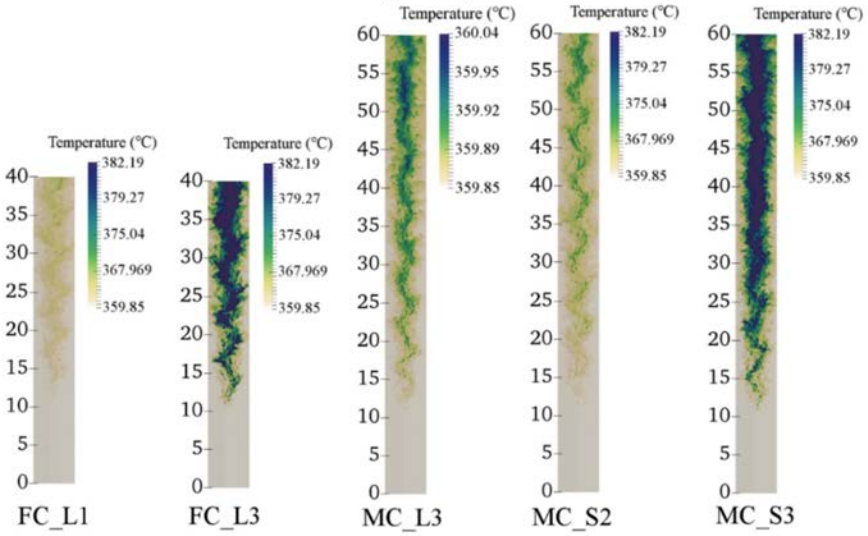

Fig. 11.23. Instantaneous temperature at equidistant planes in the narrow gap by Mohd Amin M. licensed under CC BY-NC-ND 2.0 [11.39].

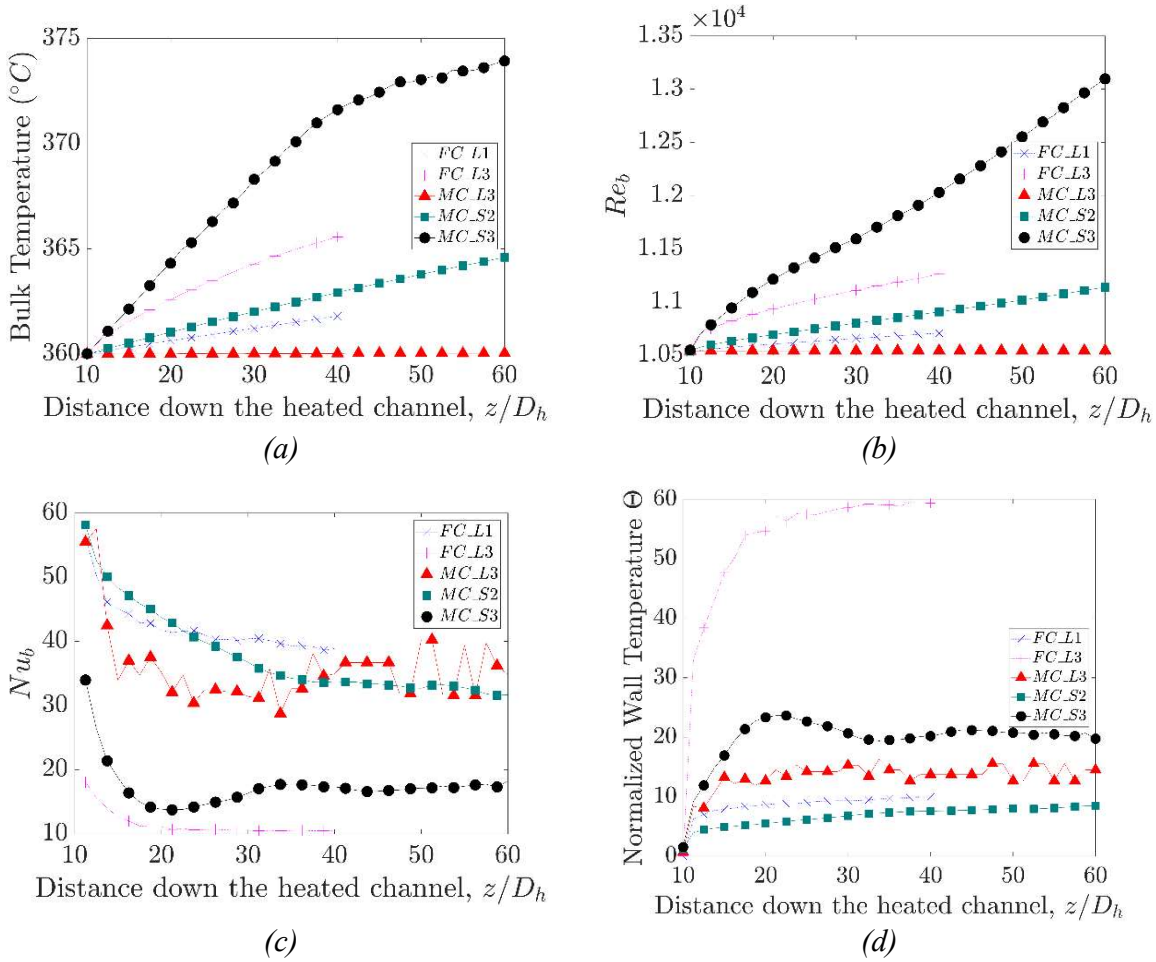

Fig. 11.24. Development of some key flow parameters in the various flow cases by Mohd Amin M. licensed under CC BY-NC-ND 2.0 [11.39].

Fig. 11.24 shows the streamwise developed of the cross sectional averaged bulk temperature, *Re*, *Nu* and Wall temperature. It is clear that the *Nu* reduces to a very low level in FC_L3, demonstrating a strong influence of thermal properties. In the case of MC_S3, *Nu* reduces to a minimal at about *x/D*=20, after which the *Nu* recovers. This is typical of a strong buoyancy influenced flow in a pipe, which also occurs in a subchannel type of flow passage. The wall temperature reaches its peak at corresponding location showing effect of heat transfer deterioration.

Fig. 11.25 and Fig. 11.26 show profiles of the velocity and turbulent kinetic energy across the narrow gap and the wide gap and along line ML (see Fig. 11.21). They show how the mean velocity values are influenced by the thermal properties in case FC_L3, and how they are influenced by the buoyancy in MC_L3 and MC_S3. The influences are clearly different in the narrow and the wider gaps. Similarly, the turbulence shows different characteristics in the various flow cases and in the narrow and wider gaps. These are consistent with observations shown in the integral parameters in Fig. 11.24.

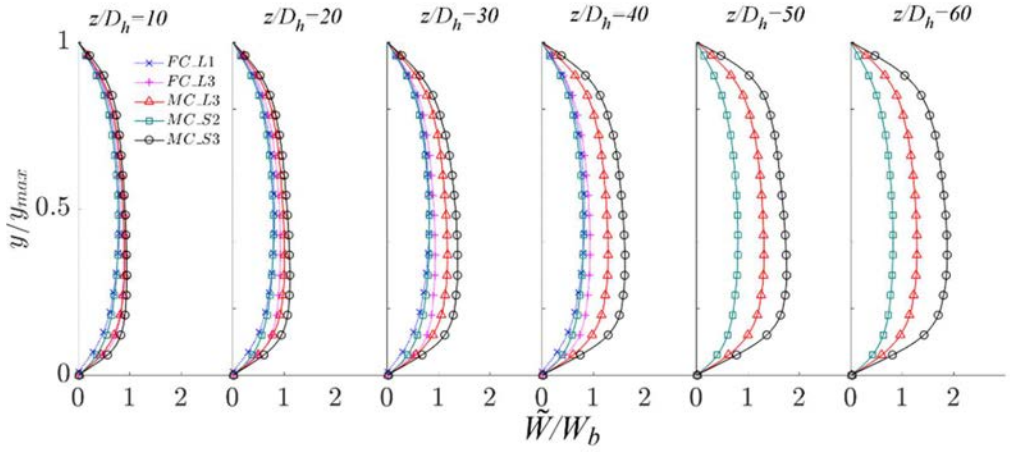

(a)

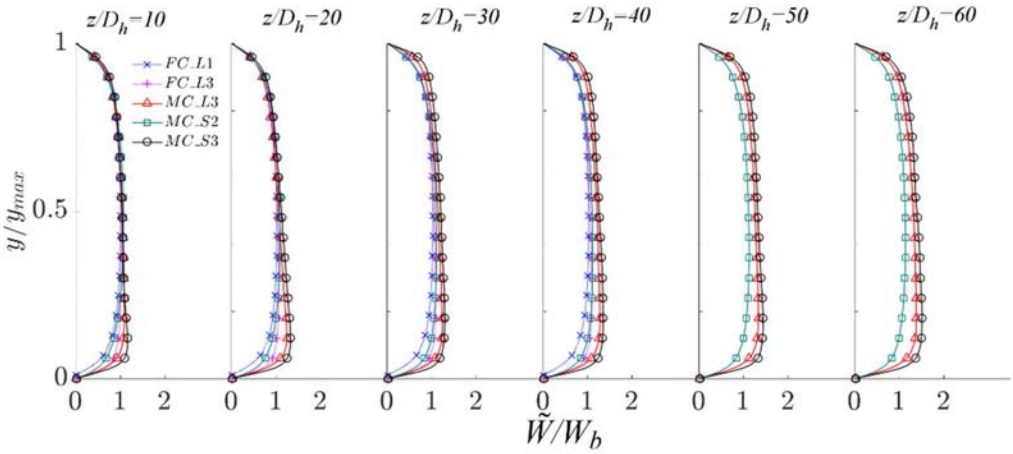

(b)

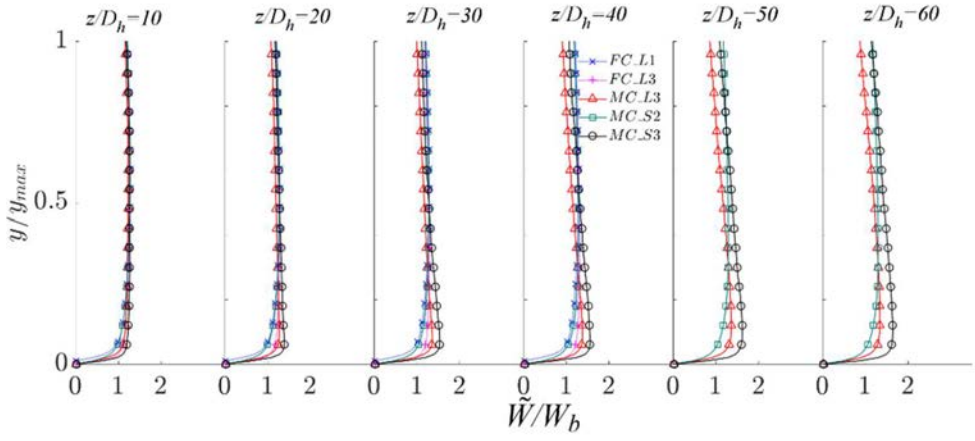

(c)

Fig. 11.25. Velocity profiles along a) the narrow, b) wider gaps and c) the line ML by Mohd Amin M. licensed under CC BY-NC-ND 2.0 [11.39].

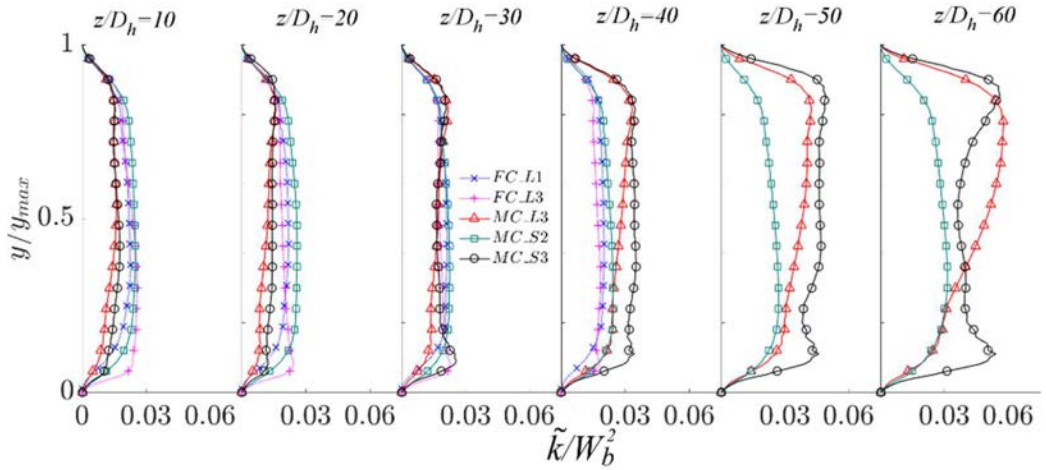

(a)

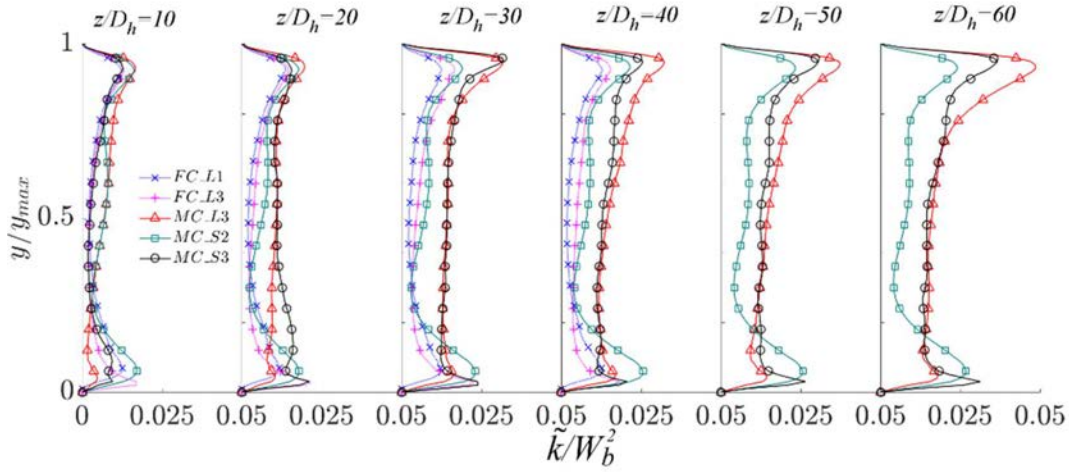

(b)

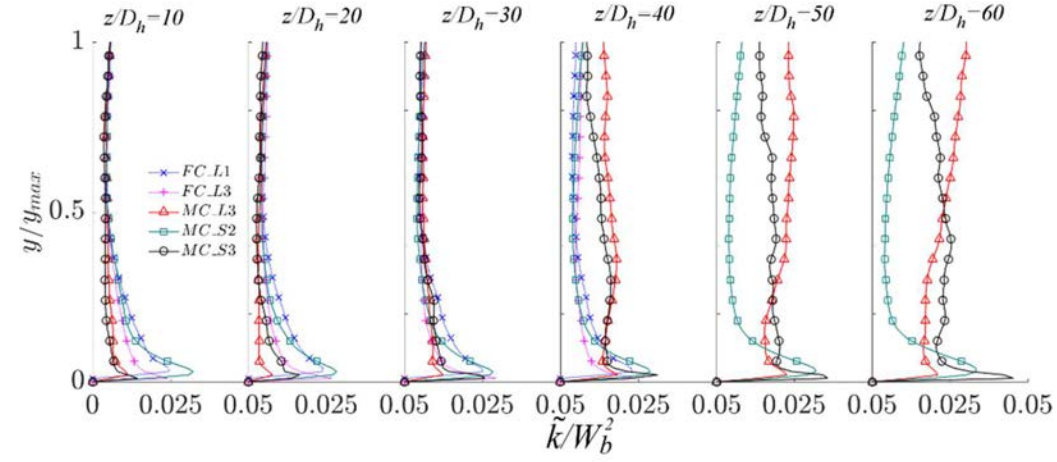

(c)

Fig. 11.26. Profiles of turbulent kinetic energy in a) the narrow, b) wider gaps and c) along line ML by Mohd Amin M. licensed under CC BY-NC-ND 2.0 [11.39].

Finally, it is interesting to study the mixing coefficient Y down the heated channel at the narrow gap. This is defined as

$$Y = \frac{u_{eff}\delta_{ij}}{\bar{\epsilon}} \tag{11.12}$$

where u_{eff} is the effective mixing velocity, $\delta_{ij}$is the distance between the subchannels and $\bar{\epsilon}$ is the reference eddy viscosity. The effective velocity is defined as:

$$u_{eff} = \sqrt{\int_{f-f_p/4}^{f+f_p/4} E_{uu}(f)df} \tag{11.13}$$

where f_p is the peak frequency and $E_{uu}(f)$ the power spectrum density function. Further information can be found in [11.41].

It is interesting to note that the variation of *Y* does not always vary monotonically in the flow direction (see Fig. 11.27). Additionally, the reduction of *Y* does not always correspond to the variation of the *Nu* shown in Fig. 11.24. This is not surprising considering that channel is highly non-uniform circumferentially and the mixing at the narrow gap is only one of many contributing factors to the changes in heat transfer across the channel. For example, the *Nu* in MC_S3 is minimal at *x/D*=20 (Fig. 11.23), but the mixing coefficient reaches the minimal at *x/D*=40 in this flow.

It has been shown that the strong variations of thermal properties of fluid at supercritical pressure have effects similar to those of buoyancy. Both have the effect of reducing the large-scale flow structures in and around a narrow gap. The unsteady flow structures appear to re-occur downstream when the buoyancy is very strong. A mixing coefficient has been calculated for the narrow gap for the various cases, indicating the complex behaviour in this region.

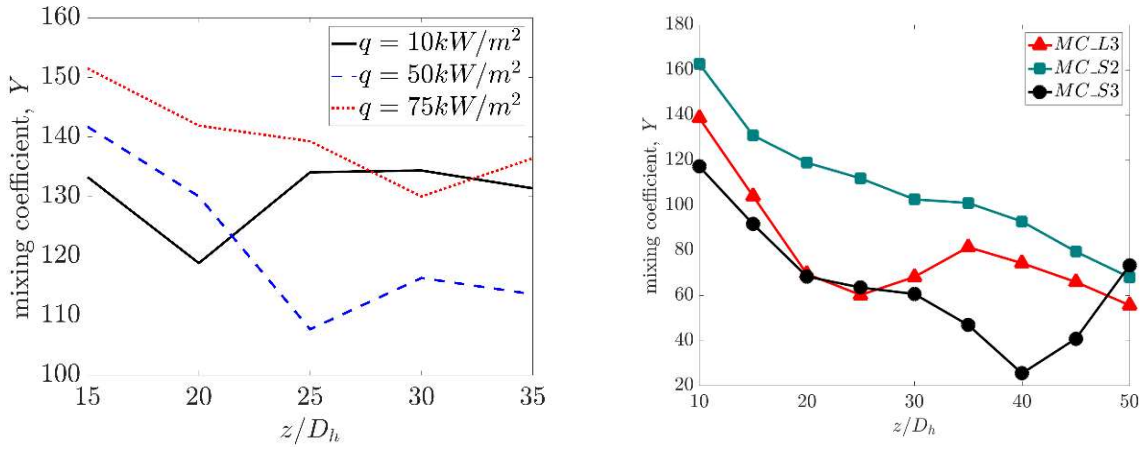

Fig. 11.27. Mixing coefficient (Y) down the heated channel at NG by Mohd Amin M. licensed under CC BY-NC-ND 2.0 [11.39].

11.6. CONJUGATE HEAT TRANSFER EFFECTS ON RESOLVED CALCULATIONS

As it is shown in several examples in this section, analysing supercritical pressure fluid behaviour by resolved computational fluid dynamic techniques (e.g., DNS and LES) is an important means to get information about the subtleties of turbulence governing the complex phenomena of heat transfer enhancement and deterioration. In this regard, the boundary conditions to be imposed in performing these very time and resource consuming calculations should be carefully considered because, when abandoning the time averaged approach, their role may become different than in usual conditions. While this is quite clear for fluid entrance conditions at the duct inlet, this may be less evident for thermal boundary conditions applies at the wall.

However, looking at the time evolution of temperature at the wall obtained e.g. by LES by imposing a constant heat flux owing to turbulence (see the Fig. 11.28), it is clearly understood that the large fluctuations of temperature possible in that case will be strongly damped by the presence of a wall. Indeed, the high frequency fluctuations of temperature induced by imposing heat flux would be filtered out by the presence of a wall with heat conduction and volumetric capacity values characteristic of metallic tubes. So, while imposing a constant heat flux and ignoring the presence of a conductive wall may be absolutely correct for calculations with Reynolds Averaged Navier Stokes (RANS) models, this should be looked at with some suspicion of being an undue simplification for LES and DNS.

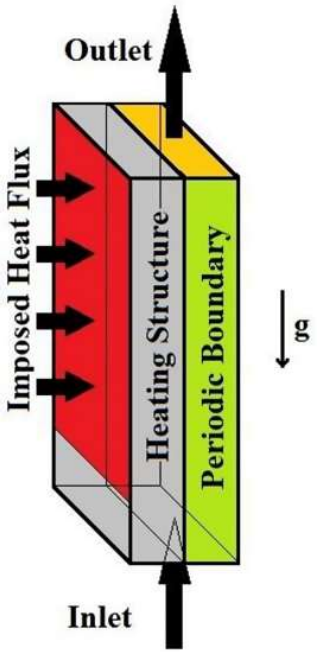

Fig. 11.28. Considered computational domain.

Previous studies on this aspect devoted to single phase fluids with nearly constant properties reported only limited effects on the turbulent structures induced by the different boundary conditions [11.42]-[11.44]. However, considering that supercritical pressure fluids experience so large changes in properties close to the pseudo-critical temperature, in particular in relation to

density, it can be feared that such changes can modify also the structure of turbulence in a way that it may actually change heat transfer behaviour.

It was this very suspect that drove a specific study [11.45], whose conclusions are summarised in the following sections.

11.6.1. METHODOLOGY AND MODEL SETUP

Large Eddy Simulation (LES) calculations were performed for water at supercritical pressure considering the computational domain reported in Fig. 11.28 [11.45]. The STAR-CCM+ code [11.46] was used in this purpose, considering the following conditions: the operating pressure was 25 MPa, the inlet fluid temperature was 645.45 K, the inlet mass flux was 117.1 kg/(m^2s), the heat flux was 130 kW/m^2, while the channel height and width were respectively 1 and 2 mm. The length of the channel was assumed to be 7 cm; periodic boundary conditions were imposed on the lateral faces in order to simulate the presence of an infinitely broad flow, while a symmetry condition was instead imposed on the surface of the domain parallel to the heated one and far enough from it. Whereas it is customary to impose a recirculation boundary conditions at the entrance of the duct, in order to stabilise the fluid to an asymptotical flow distribution before entering the heated section, in this case it was preferred to assign specified turbulent conditions at the inlet of a 1 cm long unheated section of the duct. This was done in consideration of the low entrance value of the Reynolds number (equal to 3868) that would have made the flow turbulence to die out or develop at an insufficient degree.

Calculations were made both with and without a 1 mm stainless steel wall, making use of a fluid mesh having 1400, 61 and 40 cells in the axial, normal to the wall and spanwise directions. In the presence of the solid wall, conjugated heat transfer calculations were performed in order to calculate the wall surface temperature accounting for the heat conduction and heat capacity of the wall.

11.6.2. DESCRIPTION OF RESULTS

Fig. 11.29 and Fig. 11.30 show instantaneous profiles of wall temperature along the wall in the two mentioned calculation cases. As it can be noted, while in the case with imposed heat flux ample oscillations are observed, being quite unrealistic, in the case with the wall, the interfacial temperature is much more stable.

As noted in introducing the problem, this may lead to different averaged flow fields, and heat transfer capabilities. Fig. 11.31 to Fig. 11.33 report relevant data in regard.

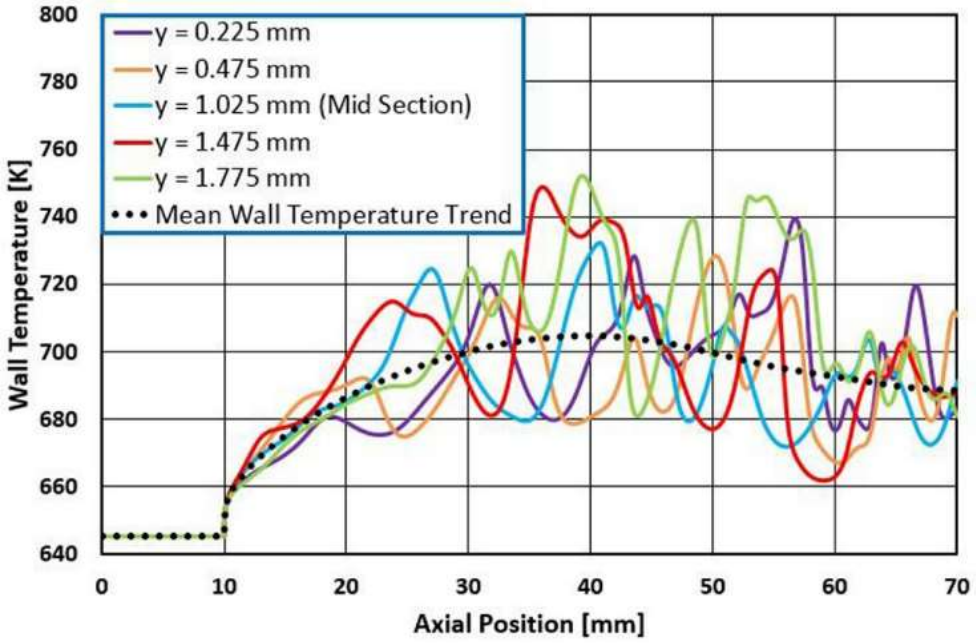

Fig. 11.29. Instantaneous fluctuations at different spanwise locations along the channel: case with imposed wall heat flux.

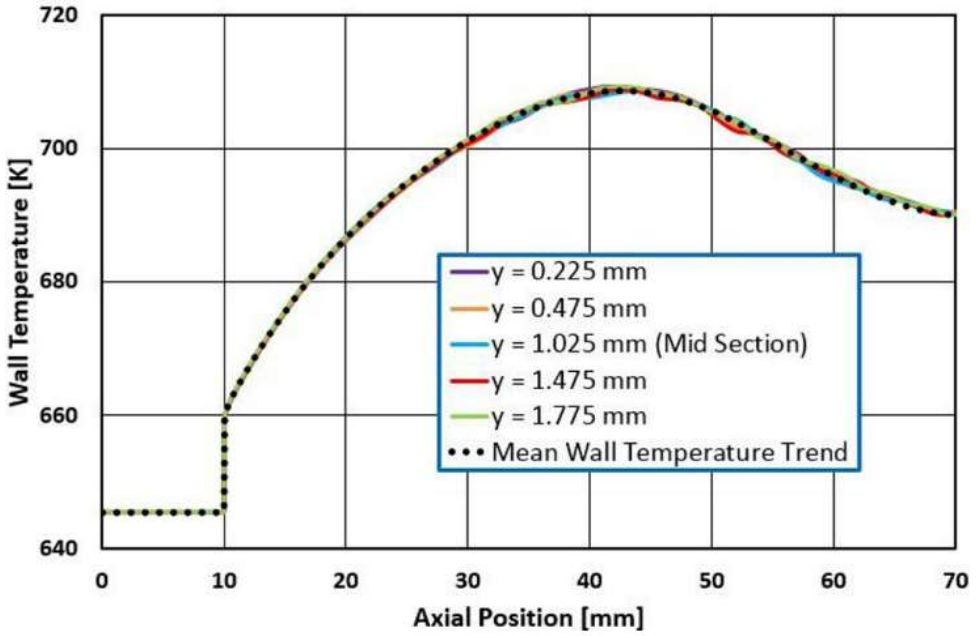

Fig. 11.30. Instantaneous fluctuations at different spanwise locations along the channel: case with a 1 mm thick.

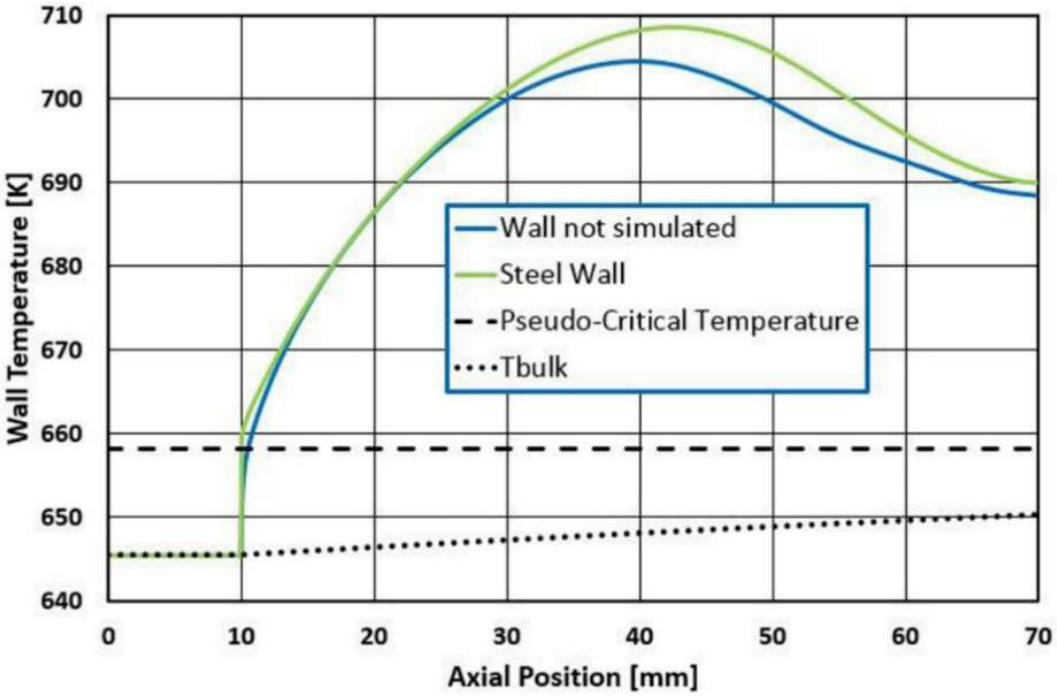

Fig. 11.31. Averaged wall temperature in the two cases.

As it can be noted, the greater fluctuations in temperature occurring at the wall while neglecting the wall thickness result in a higher turbulent kinetic energy with respect to the case in the presence of conjugated heat transfer with the wall. In fact, as it could be expected, the higher turbulence kinetic energy generated in the former case leads to a higher turbulent heat flux, as a consequence of the corresponding change in the flow field. This effect could be fully anticipated by the observation of the different levels of temperature fluctuations experienced in the two cases and is now quantitatively evaluated for a sample case.

The above described results show that neglecting the thickness of the wall in resolved turbulence calculations (DNS or LES) may lead in general to obtain a possibly unrealistic characterisation of the turbulence in the near wall region. These results, though preliminary, constitute therefore a warning in relation to the use of DNS data obtained without accounting for wall heat conduction and heat capacitance, since they may overestimate in some cases turbulence intensity.

It is anyway clear that the inclusion of walls with conjugated heat transfer in DNS and LES calculations increases the computational burden involved in these already heavy calculations. This results not only because of the inclusion of additional meshes in the calculation domain, but also because the time needed to achieve a good statistics in view of the evaluation of turbulence parameters may considerably increase owing to the inertia of the wall. These findings therefore, unfortunately, represent a new challenge to be faced in the development of RANS turbulence models for heat transfer to supercritical pressure fluids on the basis of data from resolved CFD techniques.

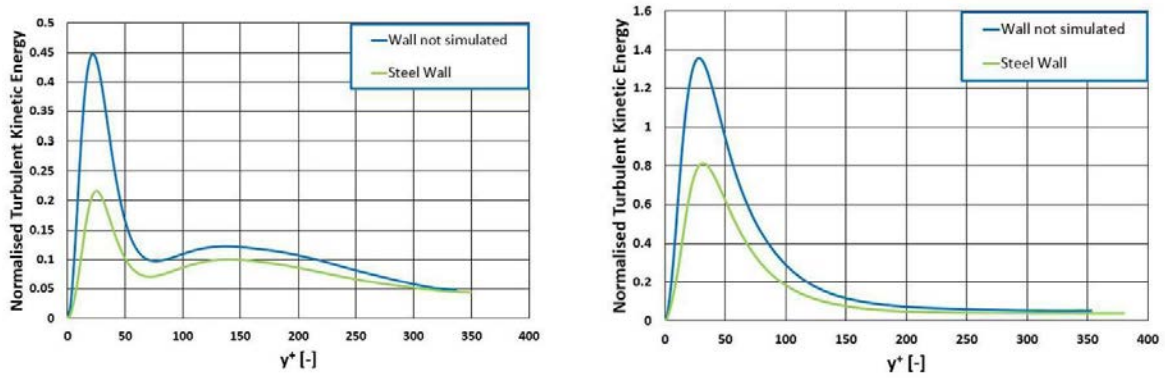

(a) 30 mm *(b) 45 mm*

Fig. 11.32. Normalised turbulent kinetic energy at two axial locations along the channel.

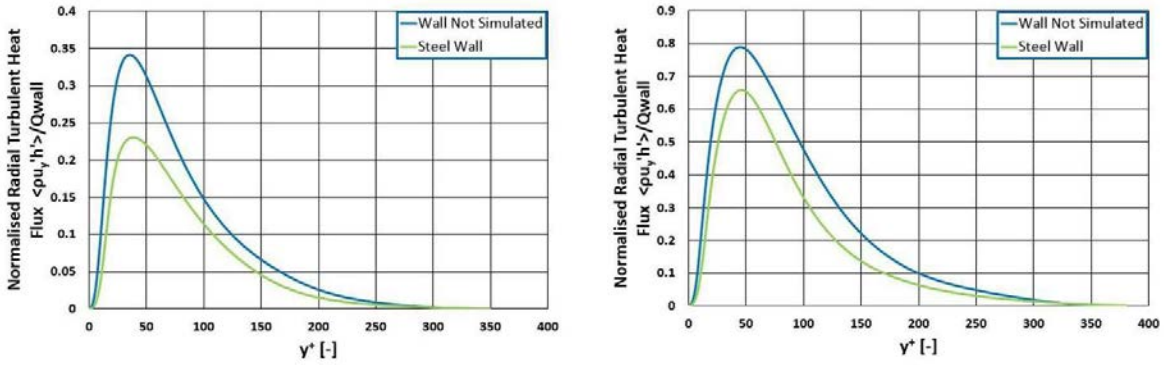

(a) 30 mm *(b) 45 mm*

Fig. 11.33. Normalised turbulent heat flux at two axial locations along the channel.

Nomenclatures and Acronyms

C	Coefficient (-)
c_p	Specific heat at constant pressure (J/(kg·K))
D	Diameter (m)
F	Body force
f	frequency (Hz)
Fr	Froude number (-)
Gr	Grashof number (-)
g	Gravity acceleration (m/s^2)
h	Specific enthalpy (J/kg)
k	Kinetic Energy
L	Length (m)
Nu	Nusselt number (-)
Pr	Prandtl number (-)
p	Hydrodynamic pressure (Pa)
p_0	Thermodynamic pressure (Pa)

q Heat flux (kW/m^2)
Re Reynolds number (-)
r Radius (m)
T Temperature (K)
t Time (s)
u Velocity (m/s)
x Axial distance (m)
Y Mixing coefficient (-)
y Distance from the wall (m)
δ Half channel height (mm)
δ_{ij} Kronecker delta (-)
λ Thermal conductivity (W/(m·K))
μ Dynamic viscosity (kg/(m·s))
ρ Density (kg/m^3)
τ Shear stress (kg/(m·s^2))

Subscripts

0 Reference state
b Bulk fluid
f Friction
i, j, k Directional symbols
p peak
w Wall
w_0 Wall wih zero body force

Acronyms

CO_2	Carbon Dioxide
DNS	Direct Numerical Simulation
EFR	Equal Flow Rate
EPG	Equal Pressure Gradient
LES	Large Eddy Simulation

REFERENCES TO SECTION 11

[11.1] BAE, J.H., YOO, J.Y., CHOI, H., Direct Numerical Simulation of Turbulent Supercritical Flows with Heat Transfer, J. Phys. Fluids, **17, 10**, (2005), 1–24.

[11.2] BAE, J.H., YOO, J.Y., MCELIGOT, D.M.,Direct Numerical Simulation of Heated CO_2 Flows at Supercritical Pressure in a Vertical Annulus at Re=8900, Phys. Fluids, **20, 5**, (2008), 1, 20.

[11.3] NEMATI, H., PATEL, A., BOERSMA, B.J., PECNIK, R., Mean Statistics of A Heated Turbulent Pipe Flow at Supercritical Pressure, Int. J. Heat Mass Transf., **83**, (2015), 741–752.

[11.4] NEMATI, H., PATEL, A., BOERSMA, B.J., PECNIK, R., The Effect of Thermal Boundary Conditions on Forced Convection Heat Transfer to Fluids at Supercritical Pressure, J. Fluid Mech., **800**, (2016), 531–556.

[11.5] PEETERS, J.W.R., PECNIK, R., ROHDE, M., VAN DER HAGEN, T.H.J.J., BOERSMA, B.J., Turbulence Attenuation in Simultaneously Heated and Cooled Annular Flows at Supercritical Pressure, J. Fluid Mech., **799**, (2016), 505–540.

[11.6] PEETERS, J.W.R., PECNIK, R., ROHDE, M., VAN DER HAGEN, T.H.J.J., BOERSMA, B.J., Characteristics of Turbulent Heat Transfer in An Annulus at Supercritical Pressure, J. Phys. Rev. Fluids, **2, 2**, (2017) ,1–24.
[11.7] CHU, X., LAURIEN, E., Direct Numerical Simulation of Heated Turbulent Pipe Flow at Supercritical Pressure, J. Nucl. Eng. Radiat. Sci., **2, 3**, (2016), 31011–31019.
[11.8] CHU, X., LAURIEN, E., Flow Stratification of Supercritical CO_2 in A Heated Horizontal Pipe, J. Supercrit. Fluids, **116**, (2016), 172–189.
[11.9] PANDEY, S., CHU, X., LAURIEN, E., Investigation of In-Tube Cooling of Carbon Dioxide at Supercritical Pressure by Means of Direct Numerical Simulation, Int. J. Heat Mass Transf., **114**, (2017), 944–957.
[11.10] PANDEY, S., CHU, X., LAURIEN, E., WEIGAND, B., Buoyancy Induced Turbulence Modulation in Pipe Flow at Supercritical Pressure under Cooling Conditions, J. Phys. Fluids, **30, 6**, (2018), 65105.
[11.11] WALL, C., PIERCE, C.D., MOIN, P., A Semi-Implicit Method for Resolution of Acoustic Waves in Low Mach Number Flows, J. Comput. Phys., **181, 2**, (2002), 545–563.
[11.12] NICOUD, F.C., Numerical Study of a Channel Flow with Variable Properties, CTR Annual Research Briefs, Center for Turbulence Research, (1998), 289–310.
[11.13] ZAINALI, A., LESSANI, B., Large-Eddy Simulation of Unstably Stratified Turbulent Channel Flow with High Temperature Differences, Int. J. Heat Mass Transf., **53, 21–22**, (2010), 4865–4875.
[11.14] SEDDIGHI-MOORMANI, M., Study of Turbulence and Wall Shear Stress in Unsteady Flow over Smooth and Rough Wall Surfaces, University of Aberdeen, (2011).
[11.15] HE, S., SEDDIGHI, M., Turbulence in Transient Channel Flow, J. Fluid Mech., **715**, (2013), 60–102.
[11.16] WANG, W., HE, S., Mechanisms of Buoyancy Effect on Heat Transfer in Horizontal Channel Flow, Proc. 7th International Symposium on Supercritical Water-Cooled Reactors (ISSCWR-7), Helsinki, (2015).
[11.17] WANG, W., HE, S., Direct Numerical Simulation of Fluid Flow at Supercritical Pressure in a Vertical Channel, Proc. 16th International Topical Meeting on Nuclear Reactor Thermal Hydraulics (NURETH-16), **3**, (2015), 2334–2347.
[11.18] KIM, J., MOIN, P., Application of a Fractional-Step Method to Incompressible Navier-Stokes Equations, J. Comput. Phys., **59, 2**, (1985), 308–323.
[11.19] NATIONAL INSTITUTE OF STANDARDS AND TECHNOLOGY, NIST Reference Fluid Thermodynamic and Transport Properties - REFPROP, Standard Reference Database 23, Ver. 9.1, Department of Commerce, Boulder, CO, USA, 2013.
[11.20] JACKSON, J.D., Studies of Buoyancy-Influenced Turbulent Flow and Heat Transfer in Vertical Passages, Proc. 13th International Heat Transfer Conference (IHTC13), Sydney, (2006).
[11.21] HE, S., HE, K., SEDDIGHI, M., Laminarisation of Flow at Low Reynolds Number due to Streamwise Body Force, J. Fluid Mech., **809**, (2016), 31–71.
[11.22] HE, K., Effect of Body Force on Turbulent Pipe Flow, The University of Sheffield, (2015).
[11.23] HE, S., KIM, W.S., BAE, J.H., Assessment of Performance of Turbulence Models in Predicting Supercritical Pressure Heat Transfer in A Vertical Tube, Int. J. Heat Mass Transf., **51, 19–20**, (2008), 4659–4675.

[11.24] FUKAGATA, K., IWAMOTO, K., KASAGI, N., Contribution of Reynolds Stress Distribution to the Skin Friction in Wall-Bounded Flows, J. Phys. Fluids, **14, 11**, (2002), L73–L76.
[11.25] JACKSON, J.D., COTTON, M.A., AXCELL, B.P., Studies of Mixed Convection in Vertical Tubes, Int. J. Heat Fluid Flow, **10, 1**, (1989), 2, 15.
[11.26] AMBROSINI, W., DE ROSA, M., Application of Similarity Principles for Heat Transfer and Fluid-Dynamics to Different Fluids at Supercritical Pressure, Proc. 5th Int. Sym. SCWR (ISSCWR-5), Vancouver, 2011.
[11.27] AMBROSINI, W., Discussion of Similarity Principles for fluid-to-fluid Scaling of Heat Transfer Behaviour at Supercritical Pressures, Nuclear Engineering and Design, **241**, (2011), 5149–5173.
[11.28] PUCCIARELLI, A., AMBROSINI, W., Fluid-to-Fluid Scaling of Heat Transfer Phenomena with Supercritical Pressure Fluids: Results from RANS Analyses, Annals of Nuclear Energy, **92**, (2016), 21–35.
[11.29] HE, J., YAN, J., WANG, W., HE, S., Direct Numerical Simulation for Fluid-to-Fluid Scaling for Fluids at Supercritical Pressure, Proc. 16th International Heat Transfer Conference (IHTC-16), Beijing, (2018).
[11.30] CHANG, D., TAVOULARIS, S., Simulations of Turbulence, Heat Transfer and Mixing across Narrow Gaps between Rod-Bundle Subchannels, Nucl. Eng. Des., **238, 1**, (2008), 109–123.
[11.31] CHANG, D., TAVOULARIS, S., Unsteady Numerical Simulations of Turbulence and Coherent Structures in Axial Flow Near a Narrow Gap, J. Fluids Eng., **127, 3**, (2005), 458–466.
[11.32] GUELLOUZ, M.S., TAVOULARIS, S., The Structure of Turbulent Flow in A Rectangular Channel Containing A Cylindrical Rod - Part 2: Phase-Averaged Measurements, J. Exp. Therm. Fluid Sci., **23, 1–2**, (2000), 75–91.
[11.33] MEYER, L., REHME, K., Large-Scale Turbulence Phenomena in Compound Rectangular Channels, J. Exp. Therm. Fluid Sci., **8, 4**, (1994), 286–304.
[11.34] GUELLOUZ, M.., TAVOULARIS, S., The Structure of Turbulent Flow in A Rectangular Channel Containing A Cylindrical Rod – Part 1: Reynolds-Averaged Measurements, J. Exp. Therm. Fluid Sci., **23, 1–2**, (2000), 59–73.
[11.35] WU, X., TRUPP, A.C., Experimental Study on the Unusual Turbulence Intensity Distributions in Rod-to-Wall Gap Regions, J. Exp. Therm. Fluid Sci., **6, 4**, (1993), 360–370.
[11.36] WU, X., TRUPP, A.C., Spectral Measurements and Mixing Correlation in Simulated Rod Bundle Subchannels, Int. J. Heat Mass Transf., **37, 8**, (1994), 1277–1281.
[11.37] DUAN, Y., HE, S., Large Eddy Simulation of A Buoyancy-Aided Flow in A Non-Uniform Channel – Buoyancy Effects on Large Flow Structures, Nucl. Eng. Des., **312**, (2017), 191–204.
[11.38] DUAN, Y., HE, S., Heat Transfer of A Buoyancy-Aided Turbulent Flow in A Trapezoidal Annulus, Int. J. Heat Mass Transf., **114**, (2017), 211–224.
[11.39] MOHD AMIN, M., Instability and Mixing of Flow of Supercritical Water between Subchannels, The University of Sheffield, (2018).
[11.40] AMIN, M.M., DUAN, Y., HE, S., Large Eddy Simulation Study on Forced Convection Heat Transfer to Water at Supercritical Pressure in a Trapezoid Annulus, J. Nucl. Eng. Radiat. Sci., **4, 1**, (2017), 11007–11014.

[11.41] REHME, K., The Structure of Turbulence in Rod Bundles and the Implications on Natural Mixing between The Subchannels, Int. J. Heat Mass Transf., 35, 2, (1992), 567–581.
[11.42] TISELJ, I., CIZELJ, L., DNS of Turbulent Channel Flow with Conjugate Heat Transfer at Prandtl Number 0.01, Nucl. Eng. Des., **253**, (2012), 153–160.
[11.43] TISELJ, I., POGREBNYAK, E., LI, C., MOSYAK, A., HETSRONI, G., Effect of Wall Boundary Condition on Scalar Transfer in A Fully Developed Turbulent Flume, J. Phys. Fluids, **13, 4**, (2001), 1028–1039.
[11.44] TISELJ, I., ODER, J., CIZELJ, L., Double-Sided Cooling of Heated Slab: Conjugate Heat Transfer DNS, Int. J. Heat Mass Transf., **66**, (2013), 781–790.
[11.45] PUCCIARELLI, A., AMBROSINI, W., On the Effect of Conjugate Heat Transfer on Turbulence in Supercritical Fluids: Results from a LES Application, Ann. Nucl. Energy, **111**, (2018), 340–346.
[11.46] CD-adapco, User Guide STAR-CCM+, Version 10.06.010 (2015).

12. ANALYSIS CODE BENCHMARK EXERCISES

Heat transfer to water at supercritical pressures is complex even for simple channels, such as a straight vertically installed smooth bore tube ([12.1], [12.2], [12.3] and [12.4]). This is attributed to three different heat transfer regimes that can be encountered: Normal- (NHT), Enhanced- (EHT), Deteriorated Heat Transfer (DHT) regimes. Among these regimes, the deteriorated heat transfer regime is of the most concern because the heated solid surface could exceed its temperature limit (it is maximum 620°C for the most advanced nuclear grade materials such as Inconel alloy). Most heat-transfer correlations were developed for normal and enhanced heat transfer regimes and are not applicable for capturing heat-transfer deterioration [12.1], [12.4]. Advanced computational fluid dynamics (CFD) analytical tools have been applied to enhance the understanding of the deteriorated heat transfer phenomena [12.3], [12.5]. At this point, accurate predictions of deteriorated heat transfer remains challenging and there is no consensus on the choice of models to be used for modelling [12.3], [12.4].

As the temperature of the supercritical water (SCW) increases, its thermophysical properties (such as density, dynamic viscosity, isobar specific heat, thermal conductivity, etc.) change nonlinearly and drastically over the pseudocritical poInt. This causes significant changes in the flow pattern, wall temperature and turbulent fields. Under distinct conditions, the heat transfer deteriorates and undesirably high wall temperatures (hot spots) could occur on the heated wall of structural materials [12.1], [12.6]. Therefore, the accurate simulation capability of supercritical water is essential for the detailed design of SCWRs [12.1], [12.2], [12.3], [12.4].

Heat-transfer correlations have been applied in predicting cladding temperatures in fuel design and safety analysis of SCWRs. These correlations were developed from experimental results of local wall and bulk temperature measurements [12.7], [12.8], [12.9]. The formulations of these correlations are relatively simple and hence can be easily implemented into analytical tools (such as subchannel and system codes). However, these correlations have been developed for specific channel geometries (mainly circular tubes) over a limited range of conditions and are limited to normal and enhanced heat transfer regimes only. In case of such correlations, the extrapolation is not recommended as these correlations mimic the experimental data but do not cover the complex heat transfer mechanism of supercritical water [12.4]. A more fundamental approach is needed to understand the phenomena and extend the prediction capability beyond the current experimental database in support of the SCWR development.

A more fundamental approach in predicting heat transfer at supercritical pressure is applied using the Reynolds Averaged Navier-Stokes approach of the CFD tools. CFD simulations adopt different turbulence models, built in tables of material properties and other models to simulate the thermal hydraulics of supercritical water [12.3], [12.4], [12.5], [12.10], [12.11]. The development process for a turbulence model is time consuming and requires validation against experimental results. Existing turbulence models are general in nature and not specifically developed for supercritical water. Their applicability for heat transfer to supercritical water needs to be investigated.

12.1. TWO CFD BENCHMARKS FOR TUBE AND ANNULUS GEOMETRIES

This Section (12.1) is mainly based on or directly reproduced from [12.12] and published with permission from the American Society of Mechanical Engineers (ASME).

This benchmark has been initiated and performed in the framework of Coordinated Research Project (CRP) Understanding and Prediction of Thermal–hydraulics Phenomena Relevant to SCWRs under the umbrella of the International Atomic Energy Agency (IAEA). This activity was aimed at the assessment of computational fluid dynamics (CFD) models and methods by results comparisons of many independently performed CFD analysis against heat transfer data obtained in experiment on the geometries of one tube and two different annular channels. The relevant experimental results were not released in advance to participants of the benchmark. It was done at the end of the so-called 'blind stage' only. The experimental data consisted of wall temperature distributions along the axial position on heated wall of tube or annular channel geometries. After the so-called 'blind stage', the follow-up calculation stage was performed consisting of two different parts: Part A, which repeated CFD calculations applying improved boundary conditions, and Part B, which performed sensitivity analyses on mesh resolution and the parameter of global boundary conditions in order to quantify their effect on CFD results.

The aim of this section is to provide an overview on the performed blind benchmarks. It describes the investigated geometries, the boundary conditions applied in the CFD models, the used CFD settings, comparisons between CFD predictions versus experimental results, and summarizes the lessons learned during the sensitivity analyses. At first, the two benchmark specifications (in the original form) are introduced with detailed information about the experimental setup and boundary conditions of the benchmark cases. The CFD models and numerical approaches developed by the benchmark participants are described together with the results submitted during the blind benchmark phase. Two participants (BME and KIT) have repeated the calculations after the blind phase (after the experimental results were released). Their CFD results of the follow-up calculation phase are also presented. Finally, a detailed sensitivity analysis (the effect of numerical mesh and boundary conditions on the numerical results were investigated) is presented. Its findings and the lessons learned are described afterward.

12.1.1. THE SPECIFICATIONS OF BLIND BENCHMARKS

The specification of the first benchmark was based on the experimental setup with an upward flow of supercritical water flowing in a vertically installed tube. This experiment has been performed at China Institute of Atomic Energy (CIAE) [12.13]. Two experimental cases were selected and analysed during this first benchmark

Experiments on supercritical water flowing upward in two different geometries of annular channel were performed at University of Wisconsin-Madison (UW). UW has provided these experimental results for the second blind benchmark [12.14], [12.15]. The geometries of the channels consist of one inner heated tube and 14 thermocouples enabling wall temperature measurement on the outer surface of the heated tube. The first channel has a circular while the second has a square shroud wall surronding the heated tube. Four (two for each channel geometry) cases were investigated during the second benchmark.

BME coordinated the above mentioned two benchmarks with major assistance of the two originators of the experimental results. The coordination covered the following tasks: preparation of benchmark specifications to ensure identical boundary conditions applied at different benchmark participants, compilation of CFD results data sheet, release and distribution of CFD results data sheet, collection of the results from participants, and analysation of submitted benchmark results data.

12.1.1.1.BLIND BENCHMARK SPECIFICATION OF CIAE

Five CRP partners (GIDROPRESS, BME, BARC, KIT, UPisa) participated in the first CFD benchmark which was against the tube heat transfer data provided by CIAE. This benchmark was intended to improve the understanding of the participants on the CFD modelling of SCW flow in simple tube geometries. An experiment was performed with upward SCW flow inside a straight, smooth bore, vertically installed tube (see Fig. 12.1). The geometrical parameters are as follows: the inner (D_i) and outer (D_o) diameters are 7.98 and 9.6 mm respectively, and the heated length (L_h) is 2.85 m. The outer wall temperatures were measured at nine positions: 0.4, 0.7, 1.0, 1.3, 1.6, 1.9, 2.2, 2.5 and 2.75 m from the beginning of the heated length (see Fig. 12.1). A direct current power supply was connected to the test section, as shown in the Fig. 12.1. The tube was made from INCONEL alloy 625. The thermal hydraulic parameters of the two experimental cases provided by CIAE are listed in Table 12.1. The outer surface of the tube was assumed to be adiabatic due to sufficient thermal insulation applied at the experiment.

Both investigated experimental cases can be assumed to be deteriorated heat transfer (DHT) cases (see Table 12.1) based on the following criterion [12.1]. DHT occurs in stable flows if:

$$q_w/G > 950 - 1050\ J/kg \tag{12.1}$$

DHT occurs in oscillatory flows if:

$$qw/G > 680 - 900\ J/kg \tag{12.2}$$

In order to determine the degree of buoyance influence on the heat transfer, the widely accepted Jackson criterion was used [12.7], [12.8]. The flow is forced convection if:

$$Gr/Re^{2.7} < 10^{-5} \tag{12.3}$$

or the flow is mixed convection if:

$$Gr/Re^{2.7} > 10^{-5} \tag{12.4}$$

Applying the above mentioned buoyance influence criterion, Case 1 can be classified as mixed convection case, while Case 2 as forced convection case (see (3), (4) and Table 12.1).

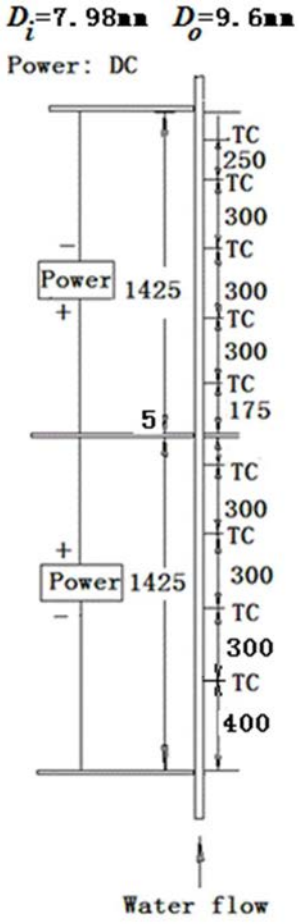

Fig. 12.1. The geometrical parameters of the test section of CIAE tube experiment, by courtesy of ASME.

TABLE 12.1. THERMAL HYDRAULIC PARAMETER OF THE TWO CIAE EXPERIMENTAL CASES, BY COURTESY OF ASME.

	p_{ref} (MPa)	q_w[1] (kW/m^2)	G (kg/m^2/s)	T_{pc} (°C)	T_{in} (°C)	T_{out} (°C)	q_w/G (J/kg)	Gr/Re$^{2.7}$ (-)
Case 1:	25.25	623	587.6	385.8	34.4	356	1060	$8\cdot10^{-5}$
Case 2:	24.5	1181	1102	383.05	37	358.5	1072	$9\cdot10^{-13}$

12.1.1.2.BLIND BENCHMARK SPECIFICATION OF UW

Two similar geometries have been investigated in the second benchmark. Here, four CRP partners (namely BME, BARC, CNL, UPisa) participated. This benchmark was against the heat transfer

[1] The heat flux defined at the inner surface of the tube.

data of two different shaped annular channels. The UW experiments were performed in a SCW test loop [12.14], [12.15].

As it was mentioned previously, in this second benchmark two different test sections were modelled (see Fig. 12.2). The geometrical parameters of the two test sections are (see Fig. 12.2):

- The outer diameter of the heater rod is 10.7 mm;
- The inner and outer diameters of the outer piping are 42.9 and 60.33 mm, respectively;
- The heated length is 1.01 m;
- The entrance and discharge lengths upstream and downstream of the test section are 760 mm;
- The square annular test section geometry is a 10.7 mm diameter heater rod within a 28.8 mm wide flow channel (see Fig. 12.2/b).

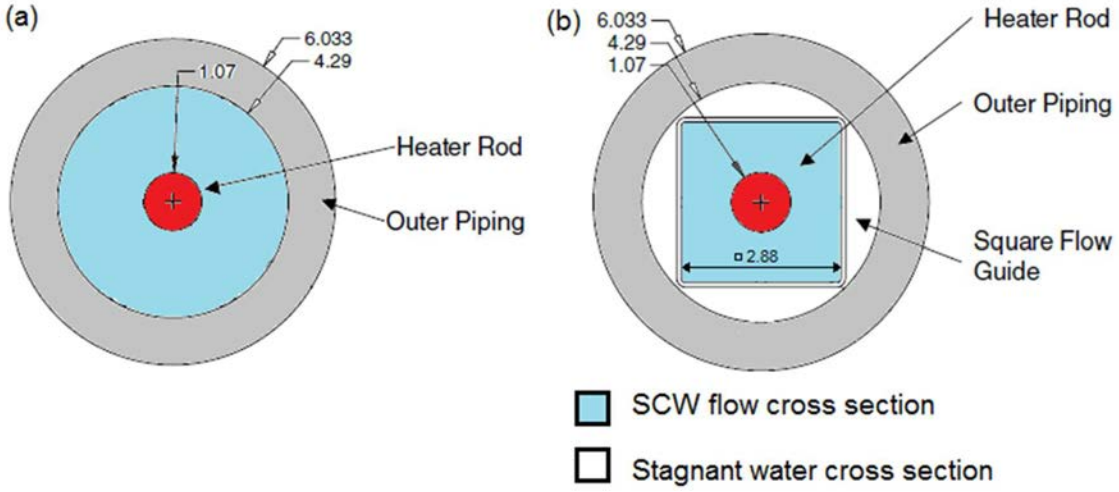

Fig. 12.2. The annular cross sections of the two different test sections of UW: a., the circular and b., the square test section (dimensions are in cm) [12.14], [12.15], by courtesy of ASME.

The inner wall temperature of the heater rod was measured at the positions listed in Table 12.2 (z (mm) means the axial position starts from the beginning of heating) [12.14], [12.15].

TABLE 12.2. AXIAL POSITIONS OF THE THERMOCOUPLES (TCS) AT UW EXPERIMENTS, BY COURTESY OF ASME.

TC#:	1	2	3	4	5	6	7	8	9	10	11	12	13	14
z (m):	67.3	134.7	202	269.3	336.7	404	471.3	538.7	606	673.3	740.6	808	875.3	942.6

Two test cases have been selected for each of the circular and the square test section. Thermal hydraulic parameters of these two experimental cases for the circular and square test sections are listed in Table 12.3 and Table 12.4 respectively [12.14], [12.15]. Only Case B can be classified

as DHT case, the rest are normal or enhanced heat transfer cases. Case A and C are forced-, while Case B and D are mixed convection cases.

The outer surface of the outer piping tube (see Fig. 12.2) is nearly adiabatic due to proper heat insulation applied [12.14], [12.15]. The tube was made from INCONEL Alloy 625.

TABLE 12.3. THERMAL HYDRAULIC PARAMETERS OF TWO UW EXPERIMENTS FOR CIRCULAR TEST SECTION, BY COURTESY OF ASME

	p_{ref} (MPa)	q_w[2] (kW/m^2)	G (kg/m^2/s)	T_{pc} (°C)	T_{in} (°C)	T_{out} (°C)	q_w/G (J/kg)	Gr/Re$^{2.7}$ (-)
Case A:	25	1000	1160	384.9	370	-	860	$2.4\cdot10^{-6}$
Case B:	25	500	400	384.9	350	-	1250	$5\cdot10^{-5}$

TABLE 12.4. THERMAL HYDRAULIC PARAMETERS OF TWO UW EXPERIMENTS FOR SQUARE TEST SECTION, BY COURTESY OF ASME.

	p_{ref} (MPa)	q_w[3] (kW/m^2)	G (kg/m^2/s)	T_{pc} (°C)	T_{in} (°C)	T_{out} (°C)	q_w/G (J/kg)	Gr/Re$^{2.7}$ (-)
Case C:	25	0	308	384.9	175	-	0	$1.2\cdot10^{-8}$
Case D:	25	220	308	384.9	175	-	714	$3\cdot10^{-5}$

12.1.2. NUMERICAL APPROACHES

This section describes numerical approaches applied by the participants in their RANS CFD analysis for the benchmarks. Each participant independently selected the code (commercial or in-house), the configuration of modelling domains and their dimensions, the turbulence models, the mesh configuration and density, the inclusion (or not) of conjugated heat transfer (CHT) and the method (database) for the water properties. Table 12.5 summarizes selected numerical approaches of participants.

Only one participant (BARC) used in-house CFD code which is called as 'NAFA'. The other five institutions applied commercial multipurpose CFD packages (Star-CCM+ or ANSYS CFX). All participants performed RANS simulations.

All participants have been implemented two equations turbulence models into their CFD models. Most of them used built-in models like: standard k–ε, RSM Linear Pressure Strain Two-Layer, LIEN k-ε Low Re or SST/SST k–ω model. One participant, UPisa implemented special turbulence model with some self tuning: AHFM for turbulent heat fluxes calculation for Case 1 and Case 2.

[2] The heat flux defined at the outer surface of the heater rod.

[3] The heat flux defined at the outer surface of the heater rod.

As it is well known, the boundary layer has to be fully resolved in case of heat transfer in SCW [12.3], [12.5], [12.11]. That is the reason for the 'near wall' modelling indicated in Table 12.5 among the most important circumstances of CFD modelling and settings. BARC and KIT used (standard) wall function. It is widely known that using (standard) wall functions is rather a bed choice due to wall functions have been derived assuming constant material properties of the fluid. This assumption is invalid for heat transfer of SCW [12.1], [12.4] and [12.5].

TABLE 12.5. NUMERICAL APPROACHES SELECTED BY PARTICIPANTS, BY COURTESY OF ASME.

	BARC	BME	CNL	GIDROPRESS	KIT	UPisa
CFD package	NAFA	ANSYS CFX	STAR-CCM+	STAR-CCM+	ANSYS CFX	STAR-CCM+
Description	in house	commercial, multipurpose	commercial, multipurpose	commercial, multipurpose	commercial, multipurpose	commercial, multipurpose
Turbulence modelling	standard k-ε	k-ε and SST	spec.[4]	k-ω-SST	k-ε	spec.[5]
Near wall modelling	Standard Wall Function	yes	spec.[6]	yes	Standard Wall Function	yes
Grid size[7]	- (uniform)	2.6, 3.5, 3.6 M	-	-	3.4 M	-
Computational domain	2D axisymmetric	10°/45° sector for 1st/2nd benchmark	45° sector for the 2nd benchmark	2D axisymmetric	Full 3D pipe	2D axisymmetric
CHT	no	yes	yes	yes	no	no
Fluid properties	NIST	IAPWS-IF97	NIST	IAPWS-95	IAPWS-IF97	REFRPROP 7.0

The participants applied different size of numerical grids and modelled different extent of the experimental geometries (Table 12.5).

Half of the participants (BME, CNL and GIDROPRESS) modelled the cases considering conjugate heat transfer (CHT) while the other half developed CFD models without heat conducting solid domain (Table 12.5).

The fluid properties of water were evaluated with the NIST, IAPWS-95, IAPWS-IF97 or REFRPROP 7.0 tools [12.4].

[4] For Case A: standard k-ε model two layers. For Case B: SST k-ω. For Case C: RSM Linear Pressure Strain Two-Layer. For Case D: SST k-ω.

[5] LIEN k-ε Low Re and in-house implementation of AHFM for turbulent heat fluxes calculation for Case 1, standard k- ε two layers model for Case 2.

[6] For Case A and C: All y^+ wall treatment. For Case B and D: Low y^+ wall treatment.

[7] It means the number of elements of the numerical grid for Case 1+2, A+B, C+D (M - million).

12.1.3. RESULTS OF THE BLIND CALCULATIONS, COMPARISONS

Distributions of axial wall temperature and radial velocity were compared between the experimental and CFD results for both benchmarks.

12.1.3.1. COMPARISONS FOR THE 1ST BENCHMARK

Fig. 12.3 shows the comparison between the measured and calculated results for Case 1. As it can be seen the measured values increases monotonically along the axial height. Two of the submitted CFD results (from BARC and KIT) show good qualitative and quantitative agreement with the experimental distribution. The remaining three (from BME, GIDROPRESS and UPisa) predicted heat transfer deterioration (it was forecasted by the q_w/G ratio) at the end of the heated length after the calculated wall temperature exceeded the pseudocritical temperature. It is worth to note that UPisa reported three deteriorations in its CFD results which appeared within two wall temperature measurement points while the CFD results of BME and GIDROPRESS show only a single deterioration at the position of the eighth thermocouple. It is theoretically possible that between two thermocouples (note that the distance between two thermocouples is 300 mm) deterioration (wall temperature peak) occurred while the two nearest thermocouples measure normal wall temperature value.

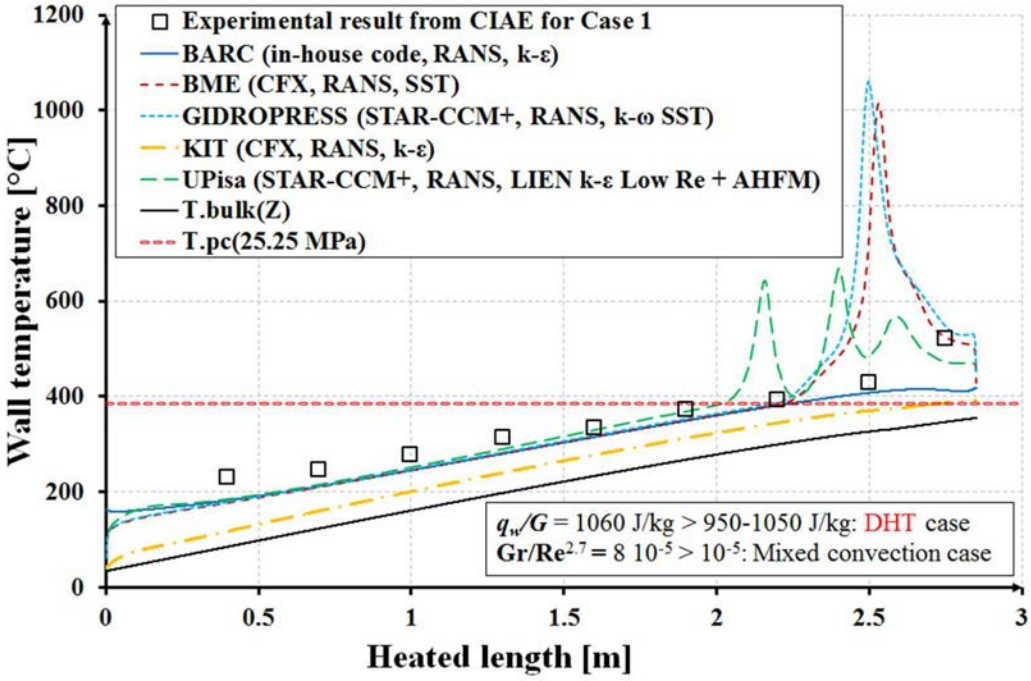

Fig. 12.3. Comparison of wall temperature between experimental and CFD results for Case 1 (p_{ref} = 25.25 MPa, q_w = 623 kW/m^2, G = 587.6 kg/m^2/s, T_{pc} = 385.8°C, T_{in} = 34.4°C), by courtesy of ASME.

Fig. 12.4 shows the comparison between the measured and calculated results for Case 2 of CIAE. The measured distribution of wall temperature increases monotonically along the heated length as

well as at Case 1. The majority of the CFD analyses show a deviation from the measured wall temperature after the sixth measured wall temperature value (~1.9 m). It is worth to mention that the calculated wall temperatures exceed here the pseudocritical value just like at Case 1. The results of BME, GIDROPRESS, UPisa overestimate the subsequent 3 wall temperature vales after the sixth thermocouple while the results from BARC and KIT underestimate them with a monotonically increasing trend (see Fig. 12.4). There is an important difference between the two groups of CFD results: the CFD model of BARC and KIT consists of the k-ε turbulence model and wall function while the others uses low-Re-SST or special k-ε turbulence model (UPisa) with enhanced wall treatment. It was reported in past analyses that the standard k-ε turbulence model cannot predict the DHT, but the SST model with enhanced near wall treatment at most of the cases can do that [12.3], [12.4], [12.5].

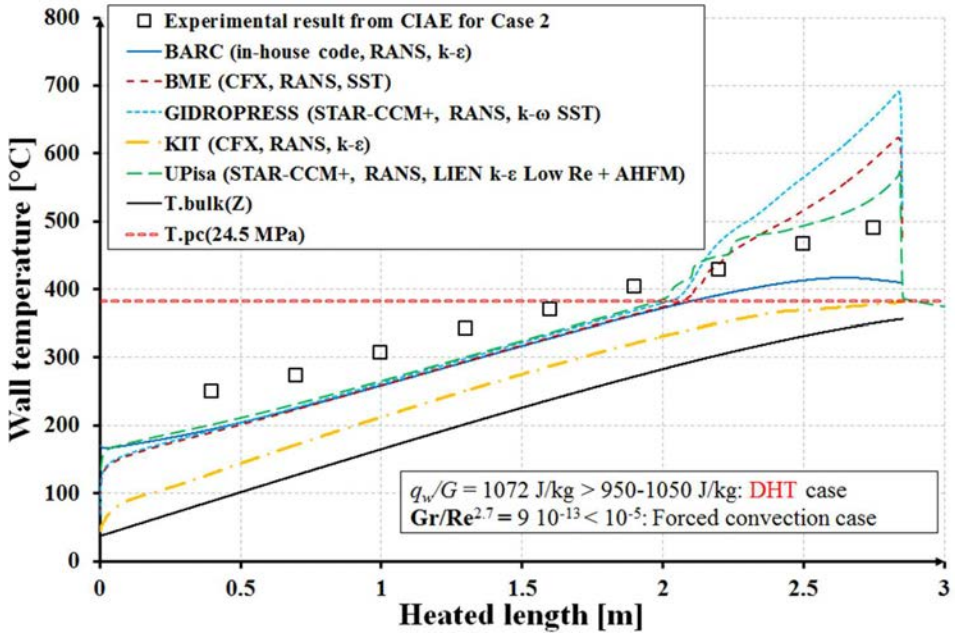

Fig. 12.4. Comparison of wall temperature between experimental and CFD results for Case 2 (p_{ref} = 24.5 MPa, q_w = 1181 kW/m^2, G = 1102 kg/m^2/s, T_{pc} = 383.05°C, T_{in} = 37°C), by courtesy of ASME.

12.1.3.2. COMPARISONS FOR THE 2ND BENCHMARK

Fig. 12.5 shows the comparison between measured and calculated distributions of wall temperature for Case A. Best prediction has been given by the model of CNL in qualitative and quantitative terms. The results of BARC and BME are good in qualitative terms although under- and overestimate the measured distribution. The CFD result of UPisa seriously over predicted the measured distribution with a DHT like wall temperature trend.

Fig. 12.6 illustrates the results for Case B of UW. The measured distribution consists of a small peak around the third measurement position of wall temperature. The CFD result of BARC gives back the measured distribution best. The results of CNL and UPisa show deterioration effect along

the first one-third of the heated length witch is disagree with the experimental result. The result of BME shows good match in qualitative terms but underestimates the measured wall temperatures.

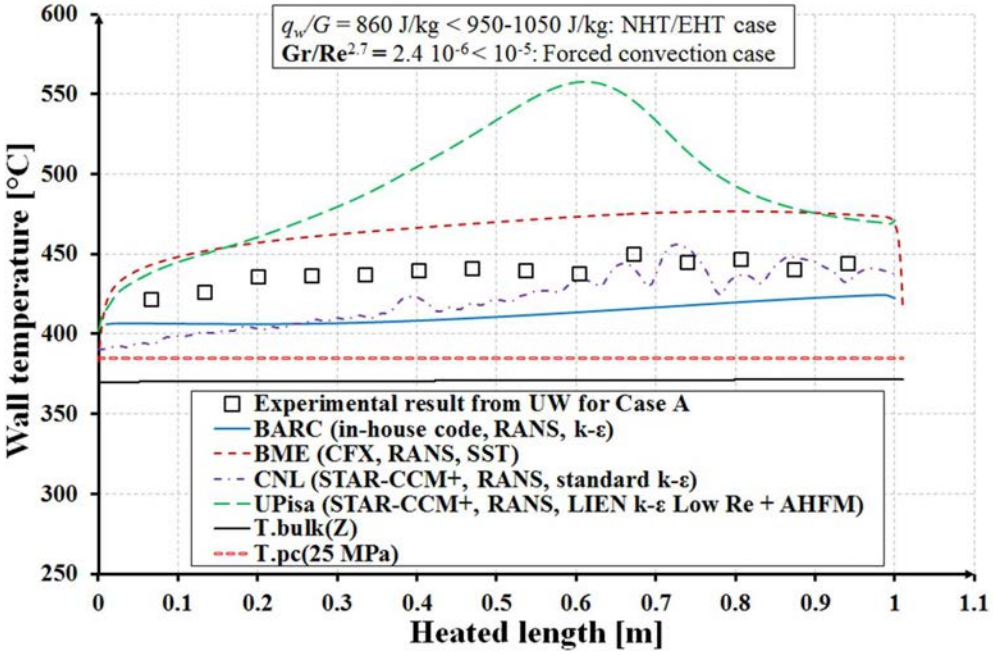

Fig. 12.5. Comparison of wall temperature between experimental and CFD results for Case A (p_{ref} = 25 MPa, q_w = 1000 kW/m^2, G = 1160 kg/m^2/s, T_{pc} = 384.9°C, T_{in} = 370°C), by courtesy of ASME.

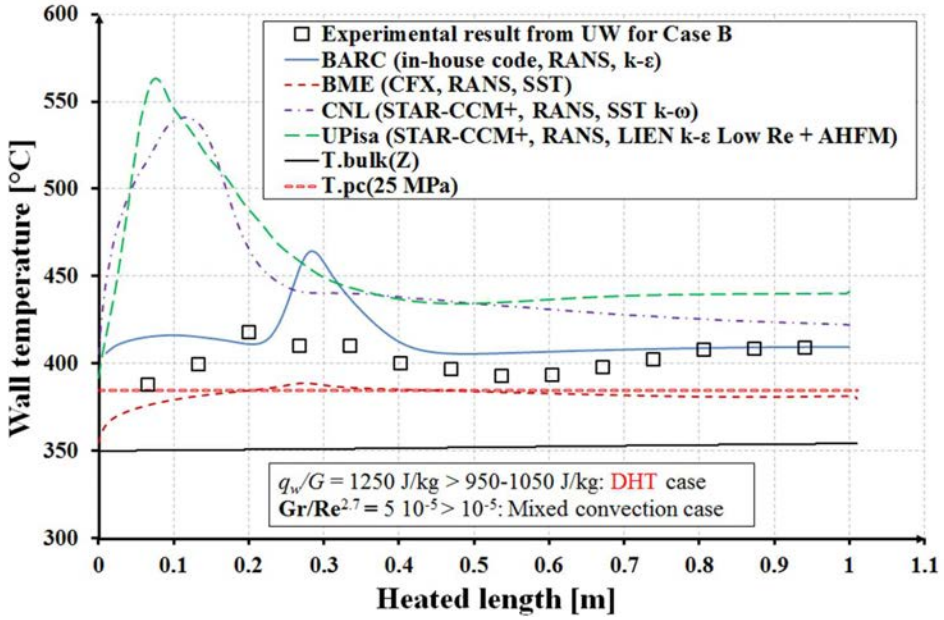

Fig. 12.6. Comparison of wall temperature between experimental and CFD results for Case B (p_{ref} = 25 MPa, q_w = 500 kW/m^2, G = 400 kg/m^2/s, T_{pc} = 384.9°C, T_{in} = 350°C), by courtesy of ASME.

The wall temperature of Case C is not discussed here due to Case C is an isothermal case and the distribution of wall temperature remains unchanged. The radial velocity field was compared instead (see Fig. 12.7) at the middle of the heated section (0.5 m downstream to the beginning of heating). As it can be seen that the distributions calculated by BME and UPisa agree well with the experimental data: the peak velocity value (~0.4 m/s) and its radial position (~3.6 mm) have been well predicted (see Fig. 12.7). The CFD results of CNL significantly differ from the measured velocity distribution: its peak value is at 7 mm instead of 3.6 mm, the shape of the whole calculated distribution is different, only the peak value (0.413 m/s) agrees approximately well.

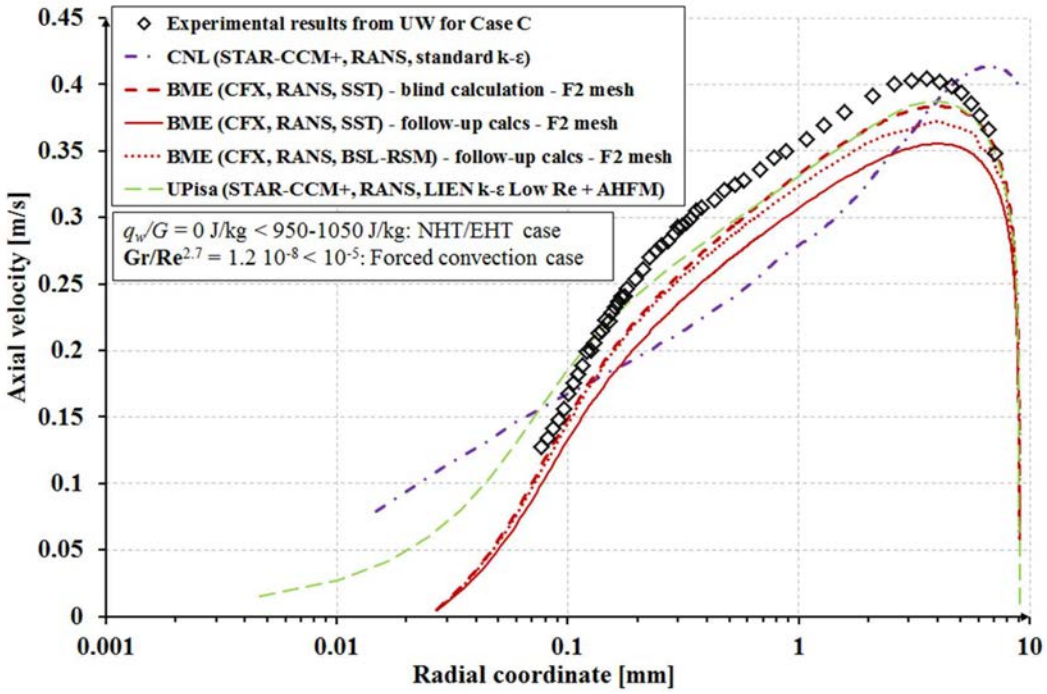

Fig. 12.7. Comparison of axial velocity along radial direction between experimental and CFD results for Case C (z = 0.5 m from BoHL, p_{ref} = 25 MPa, q_w = 0 kW/m^2, G = 308 kg/m^2/s, T_{pc} = 384.9°C, T_{in} = 175°C), by courtesy of ASME.

Fig. 12.8 shows the comparison between measured data and CFD results for Case D of UW. Based on the shape of the measured wall temperature distribution and the boundary conditions (Table 12.4) this case can be determined as normal or enhanced heat transfer case. The result of UPisa predicts best qualitatively the measured distribution even if there are some discrepancies in the quantitative terms. The CFD predictions of BME and CNL under estimated the measured wall temperatures.

The measured velocity distribution can be seen in Fig. 12.9. All the three CFD results show good agreement with the experimental data especially the prediction of UPisa.

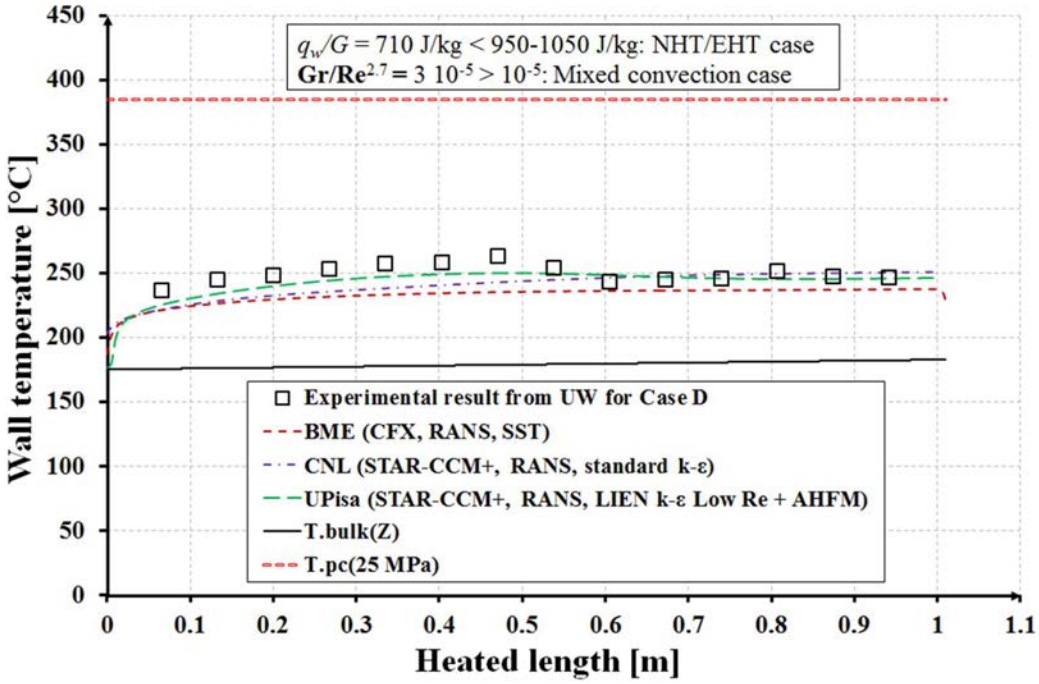

Fig. 12.8. Comparison of wall temperature between experimental and CFD results for Case D (p_{ref} = 25 MPa, q_w = 220 kW/m^2, G = 308 kg/m^2/s, T_{pc} = 384.9°C, T_{in} = 175°C), by courtesy of ASME.

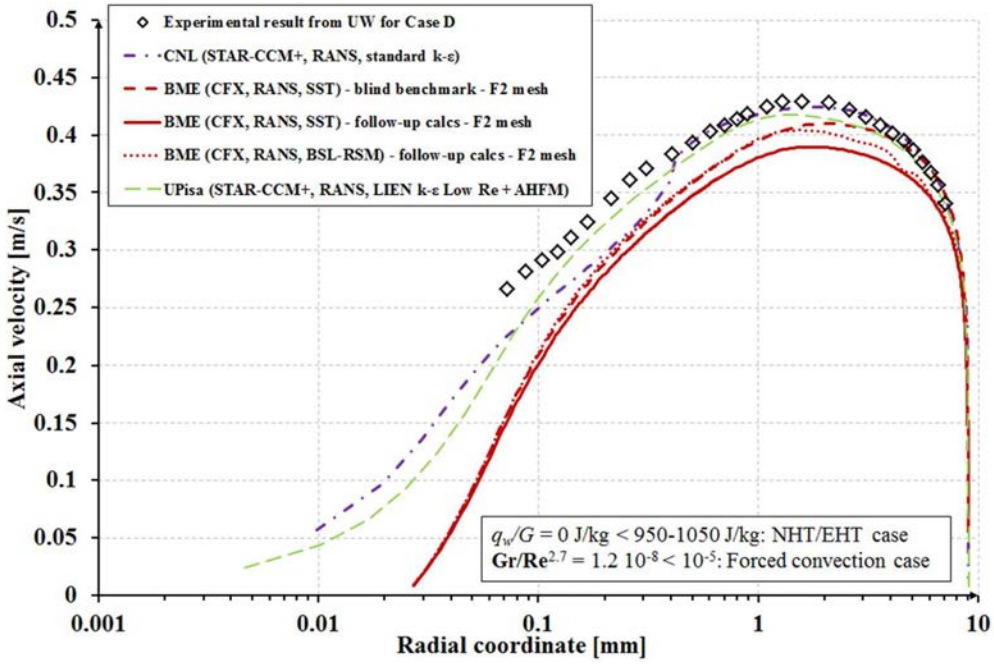

Fig. 12.9. Comparison of axial velocity in radial direction between experimental and CFD results for Case D (z = 0.5 m from BoHL, p_{ref} = 25 MPa, q_w = 220 kW/m^2, G = 308 kg/m^2/s, T_{pc} = 384.9°C, T_{in} = 175°C), by courtesy of ASME.

12.1.4. THE FOLLOW-UP CALCULATIONS

After the blind phase of the benchmarks, some discrepancies turned out regarding the boundary conditions specified in the specification of the benchmarks and some details of the CFD modelling. That is the reason why a follow-up calculation phase has been conducted.

In case of the first benchmark, if any the solid domain was modelled its material was set as stainless steel instead of INCONEL Alloy 625 (as it was in the reality). That was the reason the temperature dependent material properties of the INCONEL Alloy 625 [12.16] have been specified to the partners in order to model the tube material in their follow-up CFD calculations.

At the second benchmark, it turned out that besides the issue regarding the modelling of solid domain, the boundary conditions were not specified accurately enough. Table 12.6 and Table 12.7 show the slightly modified (the modifications are marked by red) boundary conditions set for the follow-up calculations. The material of the heater rod, outer piping and the square flow guide (see Fig. 12.2) is INCONEL Alloy 625 as well as at the first benchmark.

TABLE 12.6. THE MODIFIED TH PARAMETERS FOR TWO EXPERIMENTAL CASES OF CIRCULAR TEST SECTION, BY COURTESY OF ASME

	p_{ref} (MPa)	q_w[8] (kW/m^2)	G (kg/m^2/s)	T_{pc} (°C)	T_{in} (°C)	T_{out} (°C)	q_w/G (J/kg)	$Gr/Re^{2.7}$ (-)
Case A2:	25	989.4	1191	384.9	367.7	-	831	$2.4\ 10^{-6}$
Case B2:	25	496	398	384.9	303	-	1246	$5\ 10^{-5}$

TABLE 12.7. THE MODIFIED TH PARAMETERS FOR TWO EXPERIMENTAL CASES OF SQUARE TEST SECTION, BY COURTESY OF ASME

	p_{ref} (MPa)	q_w[9] (kW/m^2)	G (kg/m^2/s)	T_{pc} (°C)	T_{in} (°C)	T_{out} (°C)	q_w/G (J/kg)	$Gr/Re^{2.7}$ (-)
Case C2:	25.15	0	285.6	384.9	174.3	-	0	$1.2\ 10^{-8}$
Case D2:	25.2	218.5	286.9	384.9	177.6	-	762	$3\ 10^{-5}$

12.1.5. RESULTS OF THE FOLLOW-UP CALCULATIONS AND MESH SENSITIVITY STUDY

A mesh sensitivity study (MSS) has been performed together with the follow-up calculations. Thus the results of the follow-up calculations and the MSS were presented together in this section.

[8] The heat flux defined at the outer surface of the heater rod.

[9] The heat flux defined at the outer surface of the heater rod.

12.1.5.1.RESULTS FOR CASE 1 AND 2 OF CIAE

Fig. 12.10a shows the comparison between the blind and the follow-up CFD results of BME and KIT for Case 1 of CIAE. As it can be seen practically there is no difference between the blind and follow-up CFD results. It means that the modelling the INCONEL alloy 625 instead of Stainless steel makes no difference in the heat transfer of SCW.

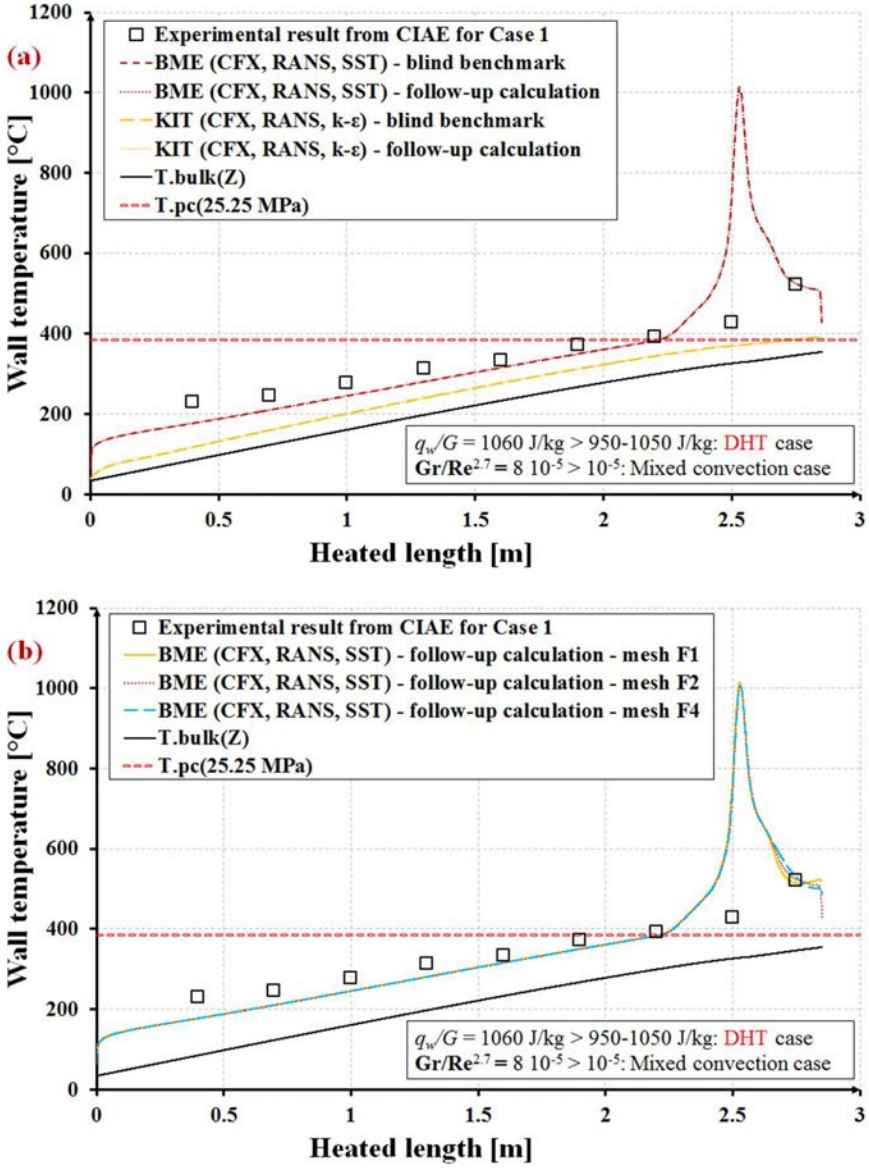

Fig. 12.10. Comparison of wall temperature: a., between blind and follow-up calculations, b., mesh sensitivity study for Case 1 (p_{ref} = 25.25 MPa, q_w = 623 kW/m^2, G = 587.6 kg/m^2/s, T_{pc} = 385.8°C, T_{in} = 34.4°C), by courtesy of ASME.

Two additional numerical grids (a coarser (F1) and a finer (F4)) have been created for the geometry of the first benchmark. The number of elements has been decreased by 50% at F1 (1.247 M) compared to the original grid, F2 (2.6 M). The F4 mesh has 5.628 M elements, so twice as many as F2 have. The mesh sensitivity study was performed for Case 1 (see Fig. 12.10b). As it can be seen in Fig. 12.10b**,** there is no significant difference between the CFD results of the three meshes. A small discrepancy can be seen only at the position of the temperature peak (see Fig. 12.10b).

Fig. 12.11 shows further details about the results of the MSS for Case 1. Four of the selected target variables can be seen in Fig. 12.11**:** the maximum- and average wall temperatures over the whole heated wall, the total pressure drop and the average velocity over the total fluid domain [12.17]. All of these comparisons show that the size of the grid influences only marginally the target variables in the investigated mesh size range. The difference between the values of F4-F2 is generally smaller than the difference between the values of F2-F1. The F2 mesh represents a good compromise between the viewpoint of resolution and numerical cost.

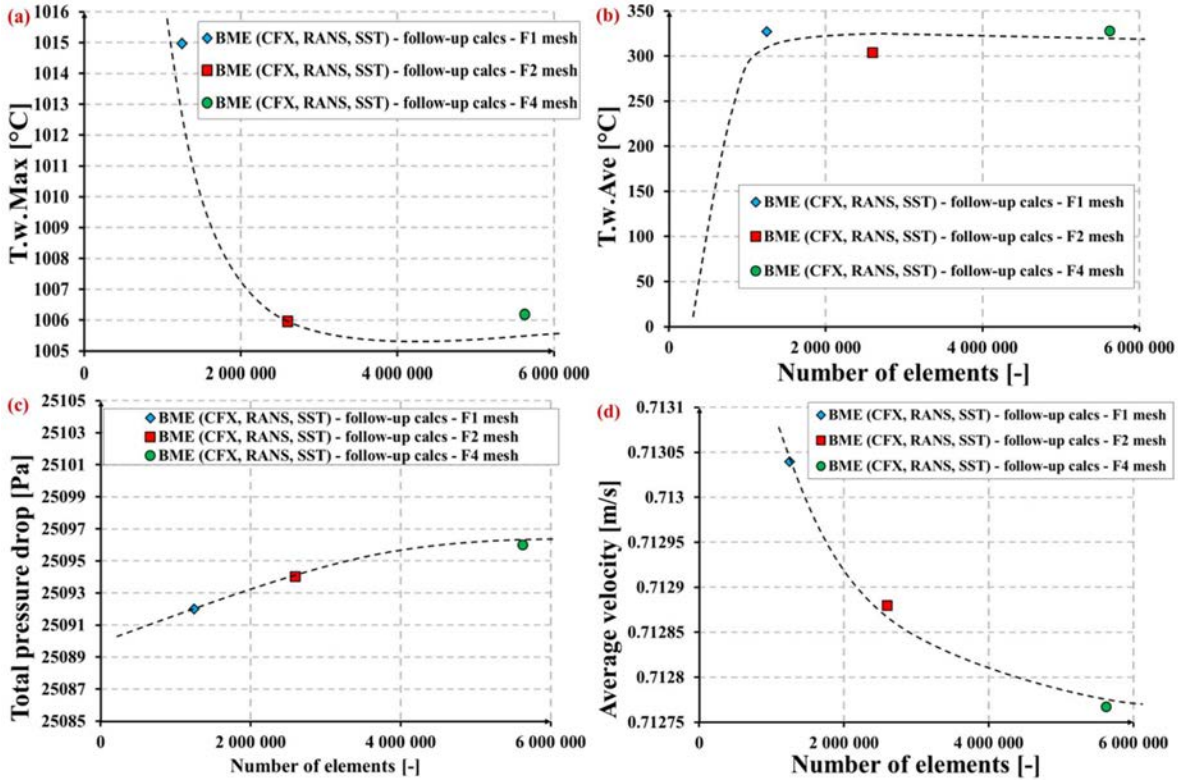

Fig. 12.11. Further results of mesh sensitivity study for Case 1 (p_{ref} = 25.25 MPa, q_w = 623 kW/m^2, G = 587.6 kg/m^2/s, T_{pc} = 385.8°C, T_{in} = 34.4°C), comparison of: a., maximum-, b., average wall temperatures, c., total pressure drops, d., average velocities, by courtesy of ASME.

Fig. 12.12 depicts the comparison between the CFD results of the blind and the follow-up calculations performed by BME for Case 2. As it can be seen there is no difference between the results of the two CFD calculations, which led to identical conclusion than in case of Case 1: the modelling the INCONEL alloy 625 instead of Stainless steel does not change the CFD results for the heat transfer of SCW.

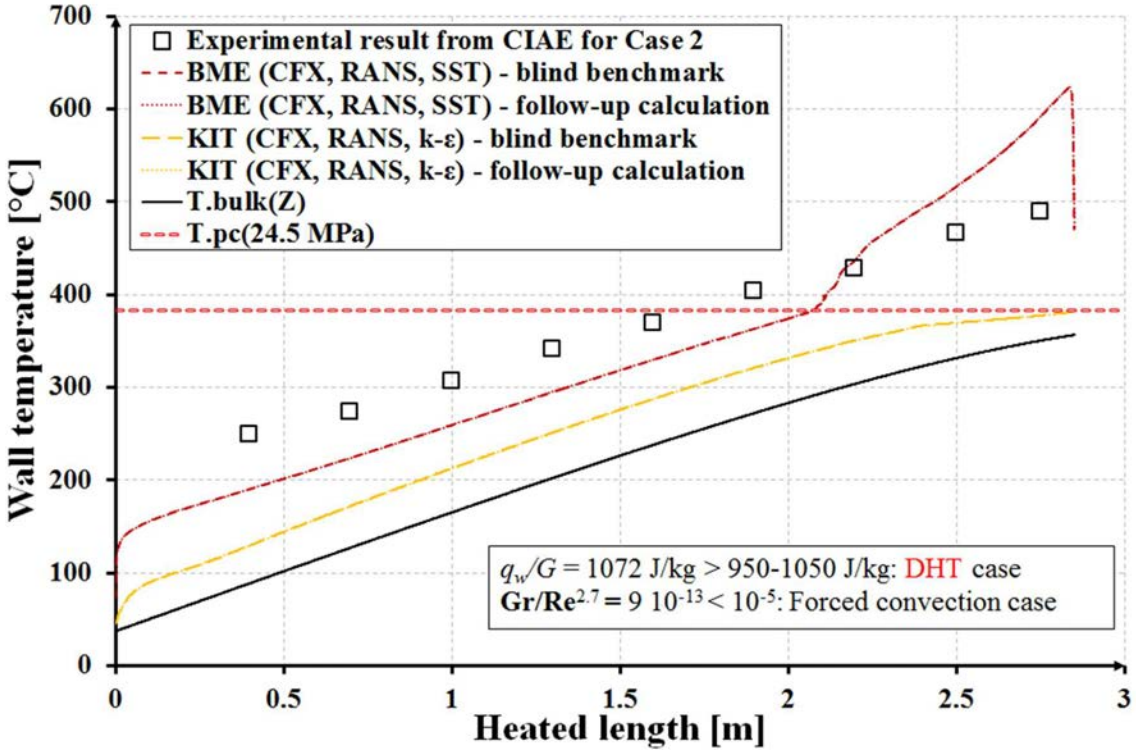

Fig. 12.12. Comparison of wall temperature between blind and follow-up results for Case 2 (p_{ref} = 24.5 MPa, q_w = 1181 kW/m^2, G = 1102 kg/m^2/s, T_{pc} = 383.05°C, T_{in} = 37°C), by courtesy of ASME.

12.1.5.2.RESULTS FOR CASE A AND B OF UW

Fig. 12.13a shows the comparison between the CFD results of the blind and follow-up calculations for Case A. As it can be seen, the wall temperature values obtained with the modified boundary conditions are closer to the measured values than the result of blind calculation.

Fig. 12.13b depicts the results of the mesh sensitivity study for Case B. It can be seen that the wall temperature values of the blind calculation fall closer to the measured values than the predictions of the follow-up calculations. It should be noted that all of the three distributions of MSS (F1 – 1.66 M, F2 – 3.522 M and F4 – 7.454 M elements) overlap each other (see Fig. 12.13b).

Fig. 12.14 shows further results of mesh sensitivity study for Case B. Identical conclusion can be pointed out here as at Case 1: all of these comparisons show that the size of the grid influences marginally the selected target variables.

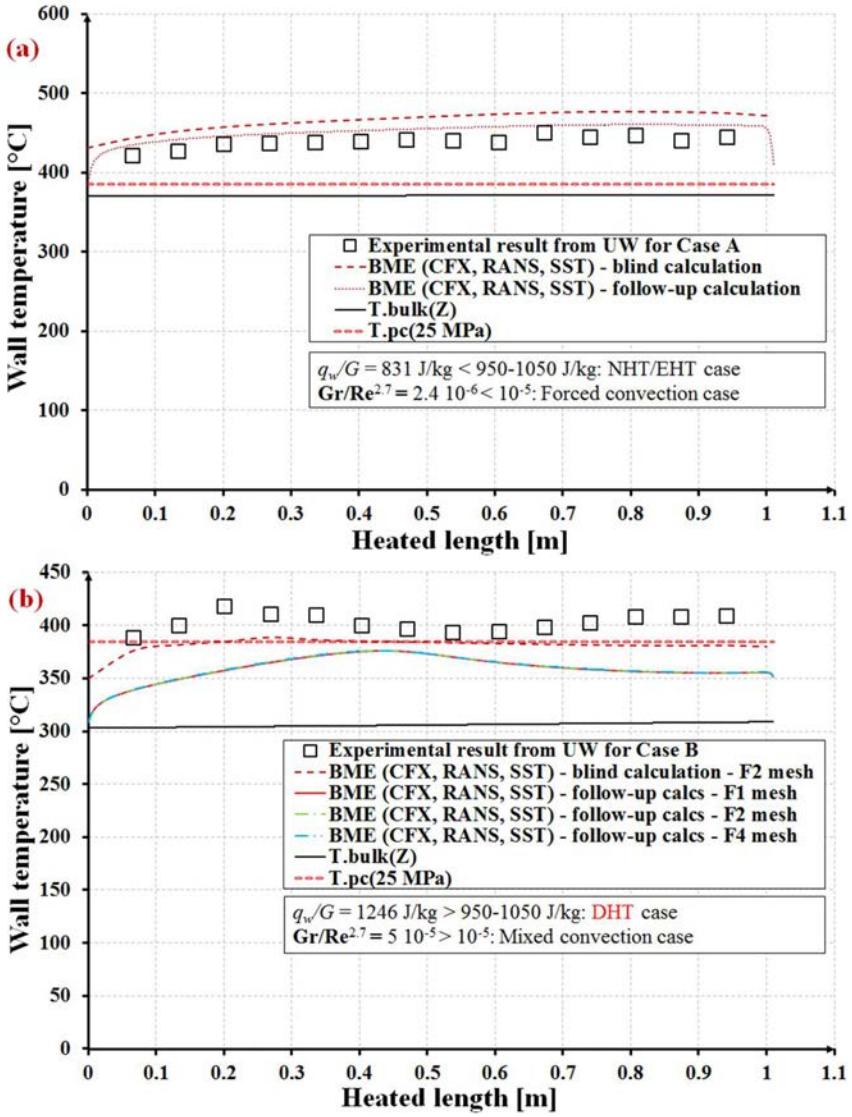

Fig. 12.13. Comparison of wall temperature: a., between blind and follow-up calculations for Case A and A.2 (p_{ref} = 25 MPa, q_w = 989.4 kW/m^2, G = 1191 kg/m^2/s, T_{pc} = 384.9°C, T_{in} = 367.7°C), b., mesh sensitivity study for Case B and B2 (p_{ref} = 25 MPa, q_w = 496 kW/m^2, G = 398 kg/m^2/s, T_{pc} = 384.9°C, T_{in} = 303°C), by courtesy of ASME.

12.1.5.3.RESULTS FOR CASE C AND D OF UW

Fig. 12.7 and Fig. 12.9 show the radial velocity distributions for the follow-up and the blind calculations of Case C and D. Based on the comparison between the blind and follow-up CFD results of BME it can be concluded that the blind SST result falls closer to the experimental data than the follow-up SST result for both Case C and D. The application of BSL Reynolds Stress turbulence model (BSL-RSM) improves the CFD prediction (see Fig. 12.7 and Fig. 12.9).

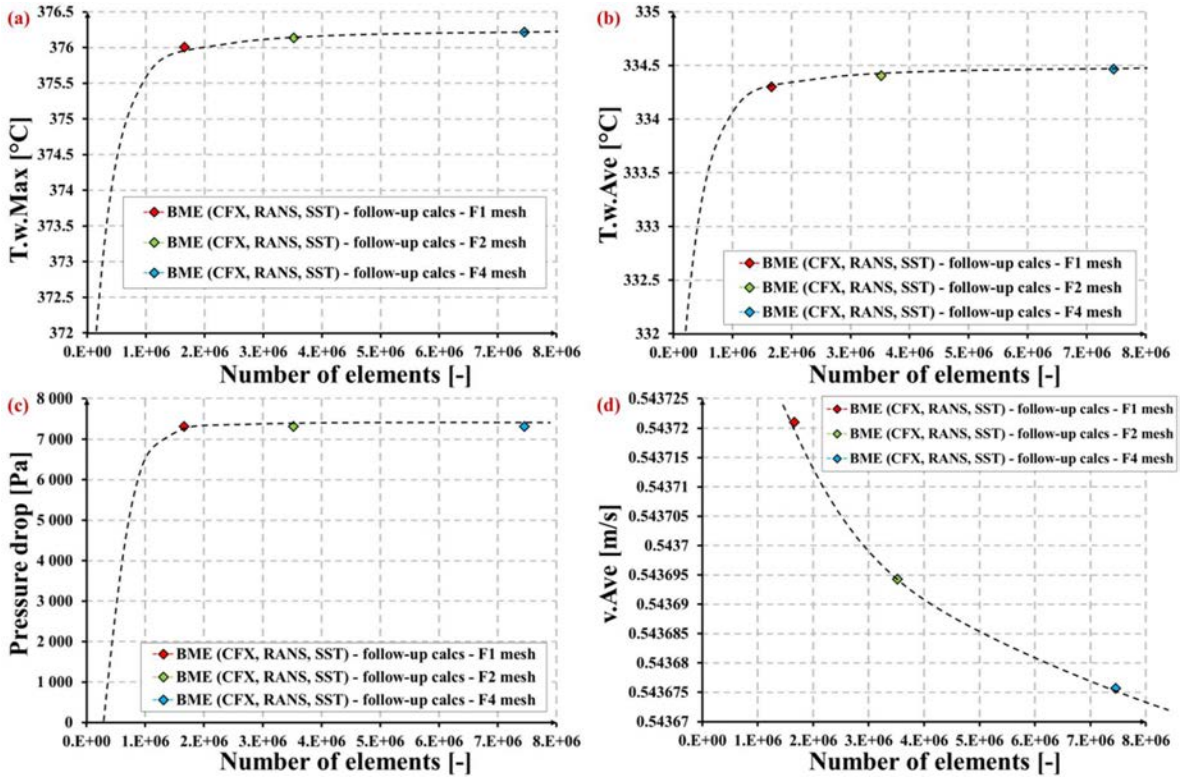

Fig. 12.14. Further results of mesh sensitivity study for Case B.2 (p_{ref} = 25 MPa, q_w = 496 kW/m^2, G = 398 kg/m^2/s, T_{pc} = 384.9°C, T_{in} = 303°C), comparison of: a., maximum-, b., average wall temperatures, c., total pressure drops, d., and average velocities, by courtesy of ASME.

Fig. 12.15 depicts the comparison between the blind-, the follow-up calculations and the MSS for Case D. As it can be seen the wall temperature values of the follow-up calculations fall closer to the measured values, but neither the blind calculation nor the follow-up calculations predicted qualitatively acceptable the distribution of the measured values.

Fig. 12.16 shows additional results of MSS for Case D: all of these comparisons show that the size of the grid influences marginally the selected target variables.

12.1.6. SENSITIVITY ANALYSIS AND RESULTS

It is widely accepted that the local thermal hydraulic fields strongly depend on the global boundary conditions in supercritical water [12.1], [12.3], [12.11], [12.18]. In order to investigate this phenomena a detailed boundary condition sensitivity study (BCSS) has been performed after the MSS. The sensitivity of the CFD result has been investigated regarding the mass flow rate, the reference pressure, the heat flux, the inlet bulk fluid temperature and the inlet turbulence intensity.

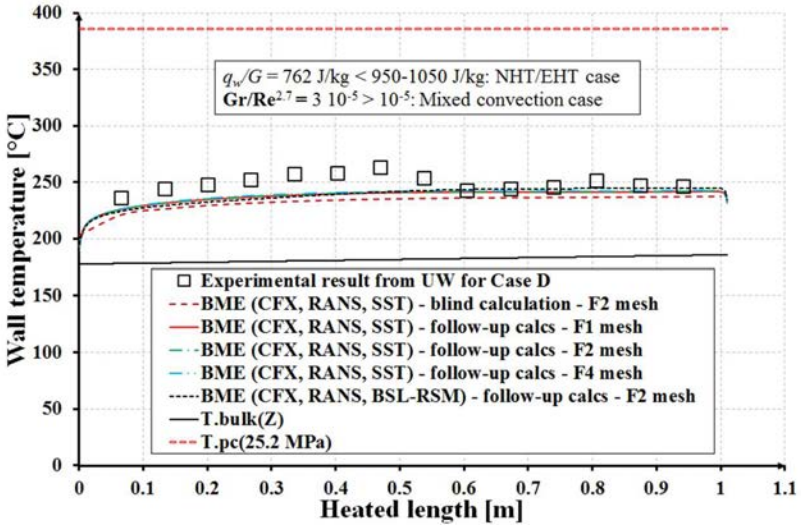

Fig. 12.15. Comparison of wall temperature between blind-, follow-up calculations and the mesh sensitivity study for Case D and D.2 (p_{ref} = 25.2 MPa, q_w = 218.5 kW/m^2, G = 286.9 kg/m^2/s, T_{pc} = 385.7°C, T_{in} = 177.6°C), by courtesy of ASME.

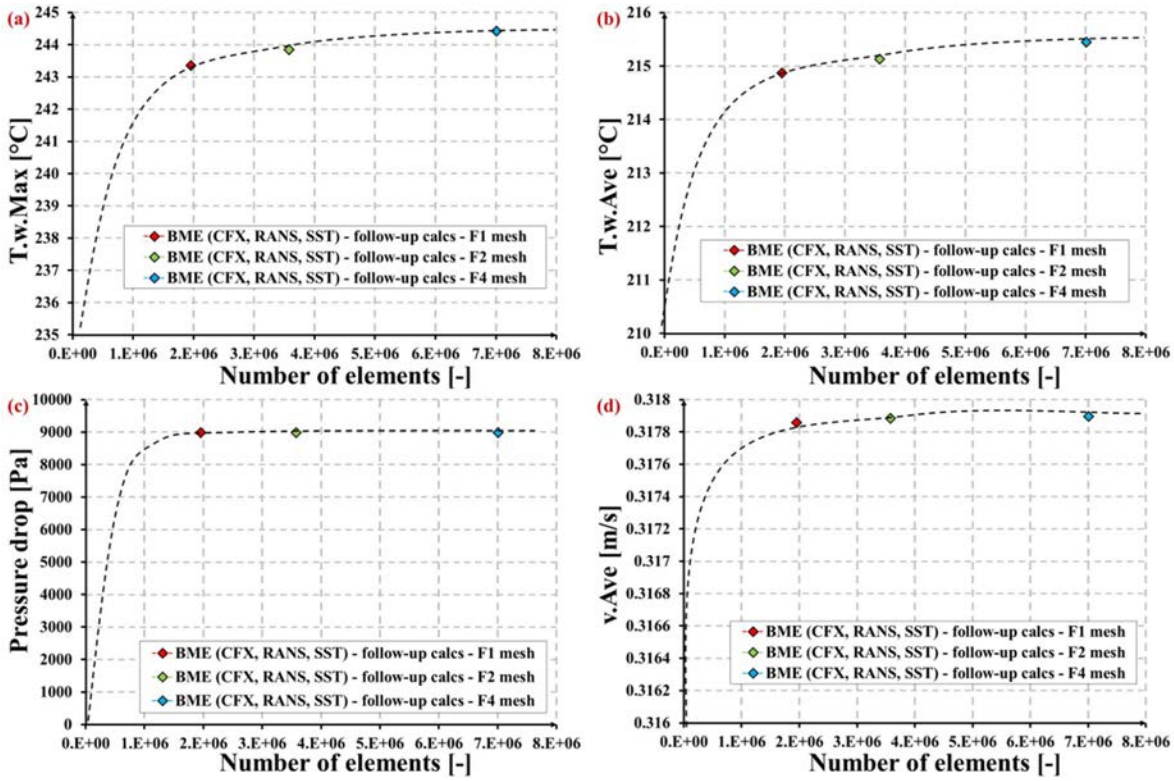

Fig. 12.16. Further results of mesh sensitivity study for Case D.2 (p_{ref} = 25.2 MPa, q_w = 218.5 kW/m^2, G = 286.9 kg/m^2/s, T_{pc} = 385.7°C, T_{in} = 177.6°C), comparison of: a., maximum-, b., average wall temperatures, c., total pressure drops, d., and average velocities, by courtesy of ASME.

12.1.6.1.SENSITIVITY ANALYSIS ON THE MASS FLOW RATE

Fig. 12.17 depicts the sensitivity of CFD results of BME on the mass flow rate (MFR). MFR has been found to be the only global boundary condition which influences not only the values but the shape of wall temperature distribution as well (Fig. 12.17a): the CFD results with 80% MFR coincides almost perfectly with the experimental data. The lower the MFR the higher the wall temperature (see Fig. 12.17a). As previously expected, if MFR increases the maximum and average wall temperature decreases as the heat transfer strengthening (Fig. 12.17b and c). That is also obvious that the average velocity over the computational domain increases linearly with increasing MFR (Fig. 12.17d). Furthermore, if the velocity increases over the whole computational domain by the increasing MFR then the pressure drop due to strengthening friction intensifies and thus the total pressure drop consequently increases proportional to the square of the velocity as well (Fig. 12.17e).

12.1.6.2.SENSITIVITY ANALYSIS ON THE REFERENCE PRESSURE

Fig. 12.18 shows the sensitivity of CFD results on the set reference pressure (p_{ref}). p_{ref} doesn't influences the distribution of wall temperature (Fig. 12.18a), but slightly increases the maximum and average wall temperatures (Fig. 12.18b and c) as well as the pressure drop (Fig. 12.18d). The average velocity slightly decreases as the reference pressure increases (Fig. 12.18e).

12.1.6.3.SENSITIVITY ANALYSIS ON THE HEAT FLUX

The heat flux is among the three boundary conditions (beside the MFR and inlet temperature of SCW) which are expected to have significant influence on the heat transfer in case of the investigated cases. Fig. 12.19 depicts the sensitivity of CFD results of BME to the specified heat flux. The whole distribution of wall temperature increases as the heat flux become higher and higher (+10% each step, see Fig. 12.19a), but its shape did not get closer to the measured one: remains monotonically increasing instead. Obviously, the maximum and average wall temperatures get higher and higher values (Fig. 12.19b and c) as the heat flux increases. The pressure drop shows opposite trend (see Fig. 12.19d) than the wall temperature. The average velocity of the whole fluid domain increases as well with the increasing heat flux (Fig. 12.19e) due to the flow acceleration effect [12.1].

12.1.6.4.SENSITIVITY ANALYSIS ON THE INLET TEMPERATURE

This is the third boundary conditions which are expected to have a significant influence on the heat transfer in the examined cases. Fig. 12.20 shows the result of the performed sensitivity analyses on the value of set inlet temperature of SCW. The overall pattern is identical to that what was presented at the sensitivity analyses of heat flux: the higher the inlet temperature the higher the whole distribution of wall temperature, maximum- and average wall temperature (see Fig. 12.20a, b and c). The average velocity in the whole computational domain slightly increases ((Fig. 12.20e)) while the total pressure drop moderately decreases due to the effect of the decreasing (strongly temperature dependent) dynamic viscosity (Fig. 12.20d).

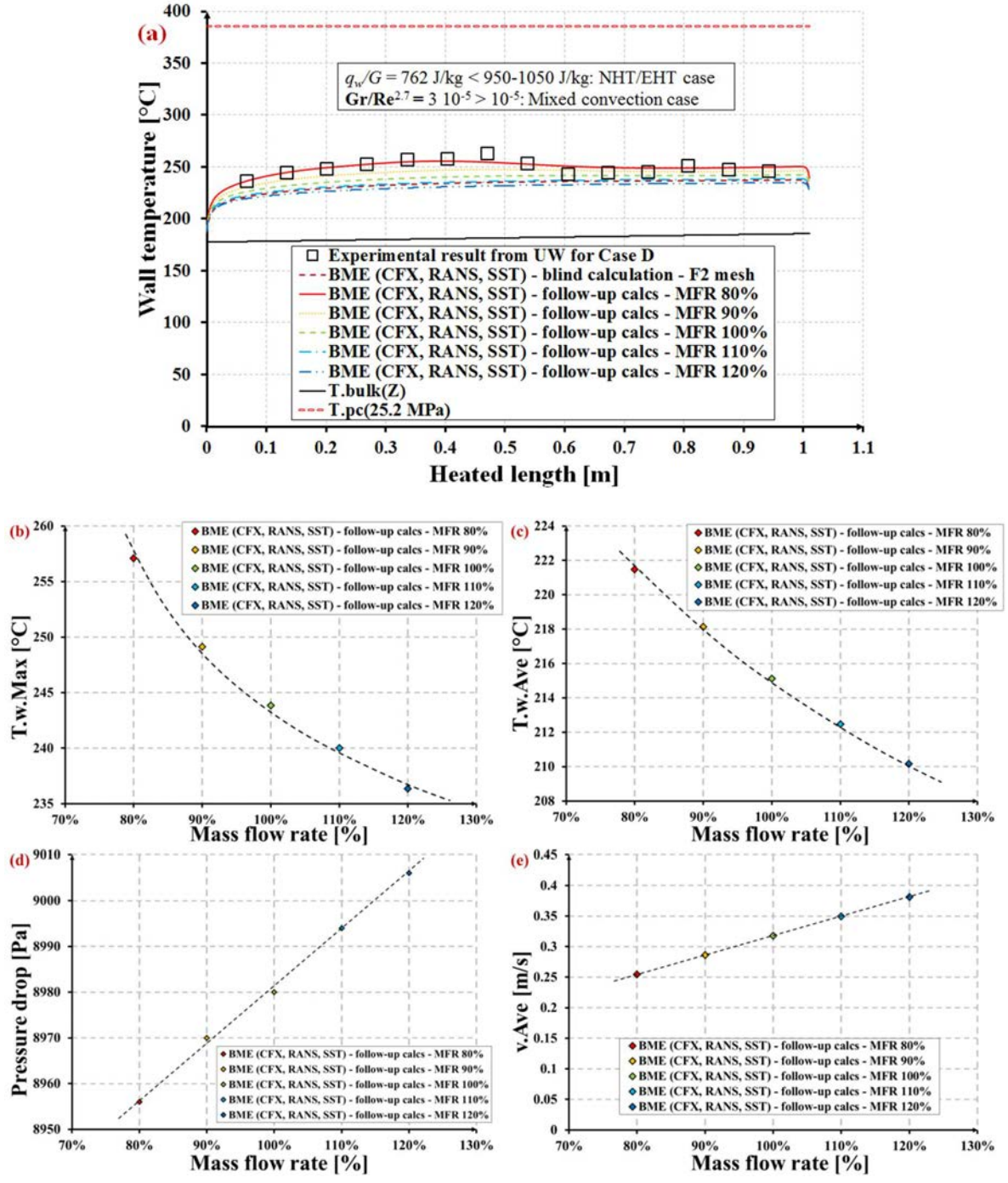

Fig. 12.17. Results of boundary condition sensitivity study on mass flow rate for Case D and D.2 (p_{ref} = 25.2 MPa, q_w = 218.5 kW/m^2, G = 286.9 kg/m^2/s, T_{pc} = 385.7°C, T_{in} = 177.6°C), comparison of: a., distribution-, b., maximum-, c., average of wall temperatures, d., total pressure drops and e., average velocities, by courtesy of ASME.

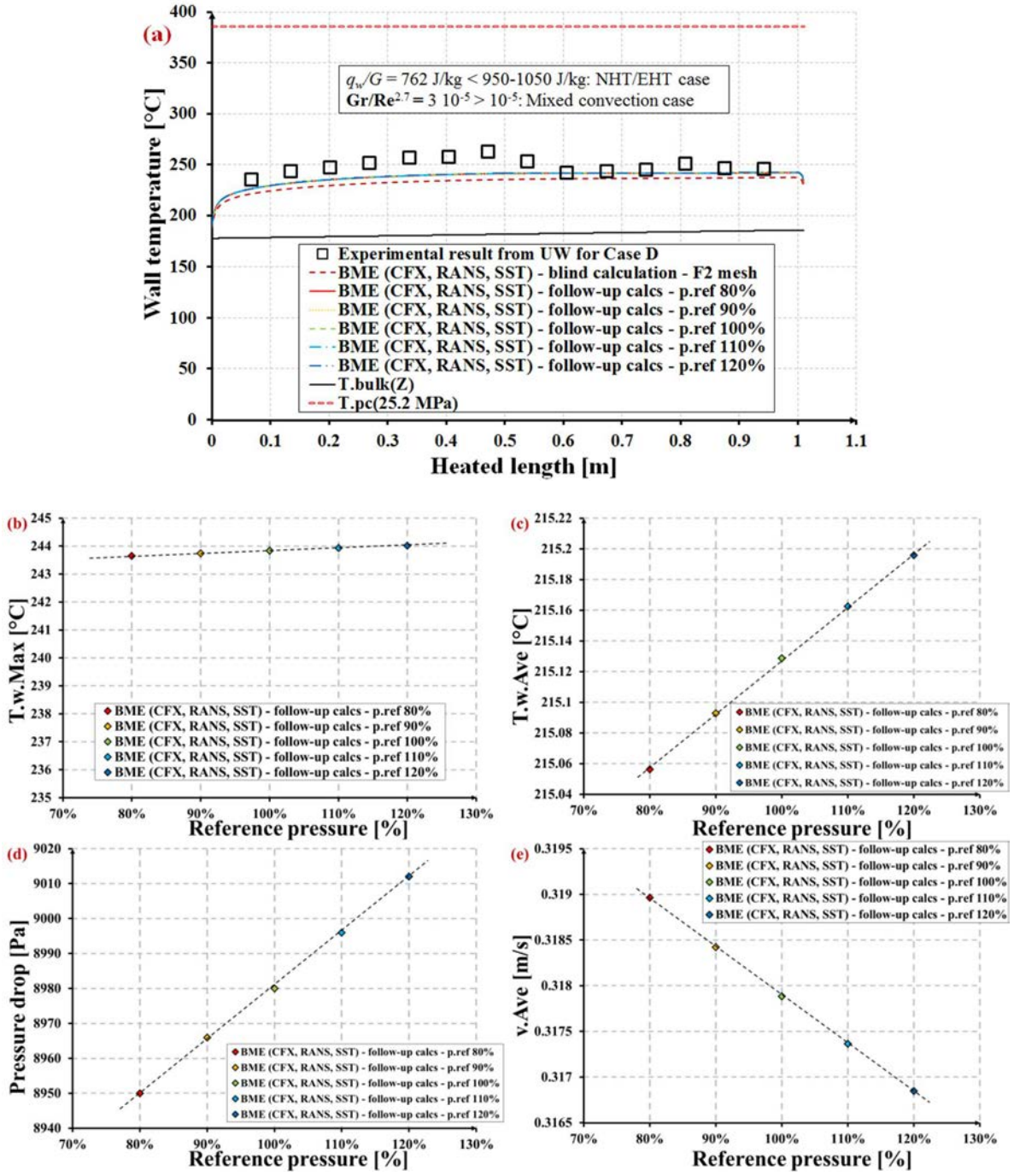

Fig. 12.18. Results of boundary condition sensitivity study on reference pressure for Case D.2 (p_{ref} = 25.2 MPa, q_w = 218.5 kW/m^2, G = 286.9 kg/m^2/s, T_{pc} = 385.7°C, T_{in} = 177.6°C), comparison of: a., distribution-, b., maximum-, c., average of wall temperatures, d., total pressure drops and e., average velocities, by courtesy of ASME.

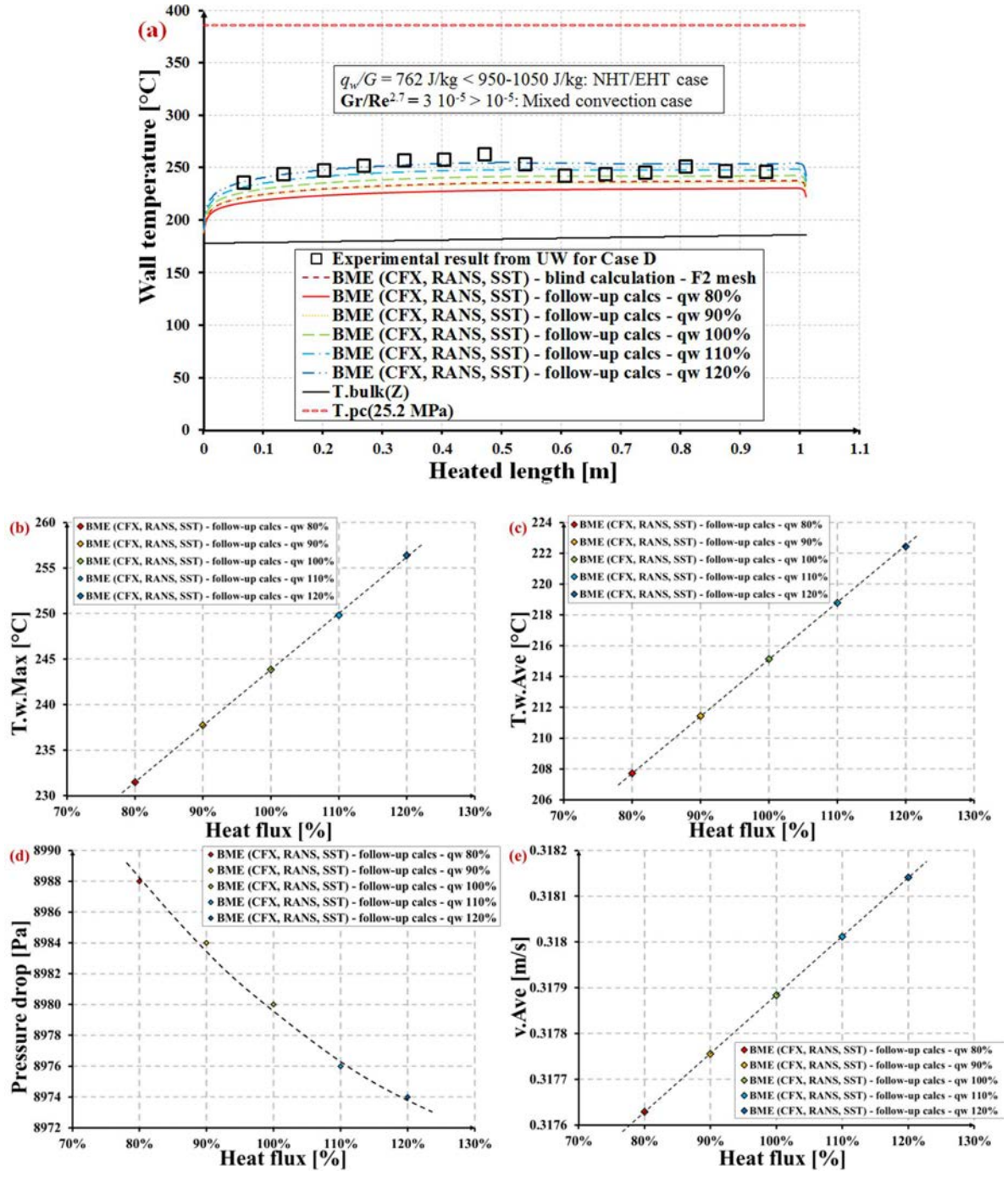

Fig. 12.19. Results of boundary condition sensitivity study on heat flux for Case D.2 (p_{ref} = 25.2 MPa, q_w = 218.5 kW/m^2, G = 286.9 kg/m^2/s, T_{pc} = 385.7°C, T_{in} = 177.6°C), comparison of: a., distribution-, b., maximum-, c., average of wall temperatures, d., total pressure drops and e., average velocities, by courtesy of ASME.

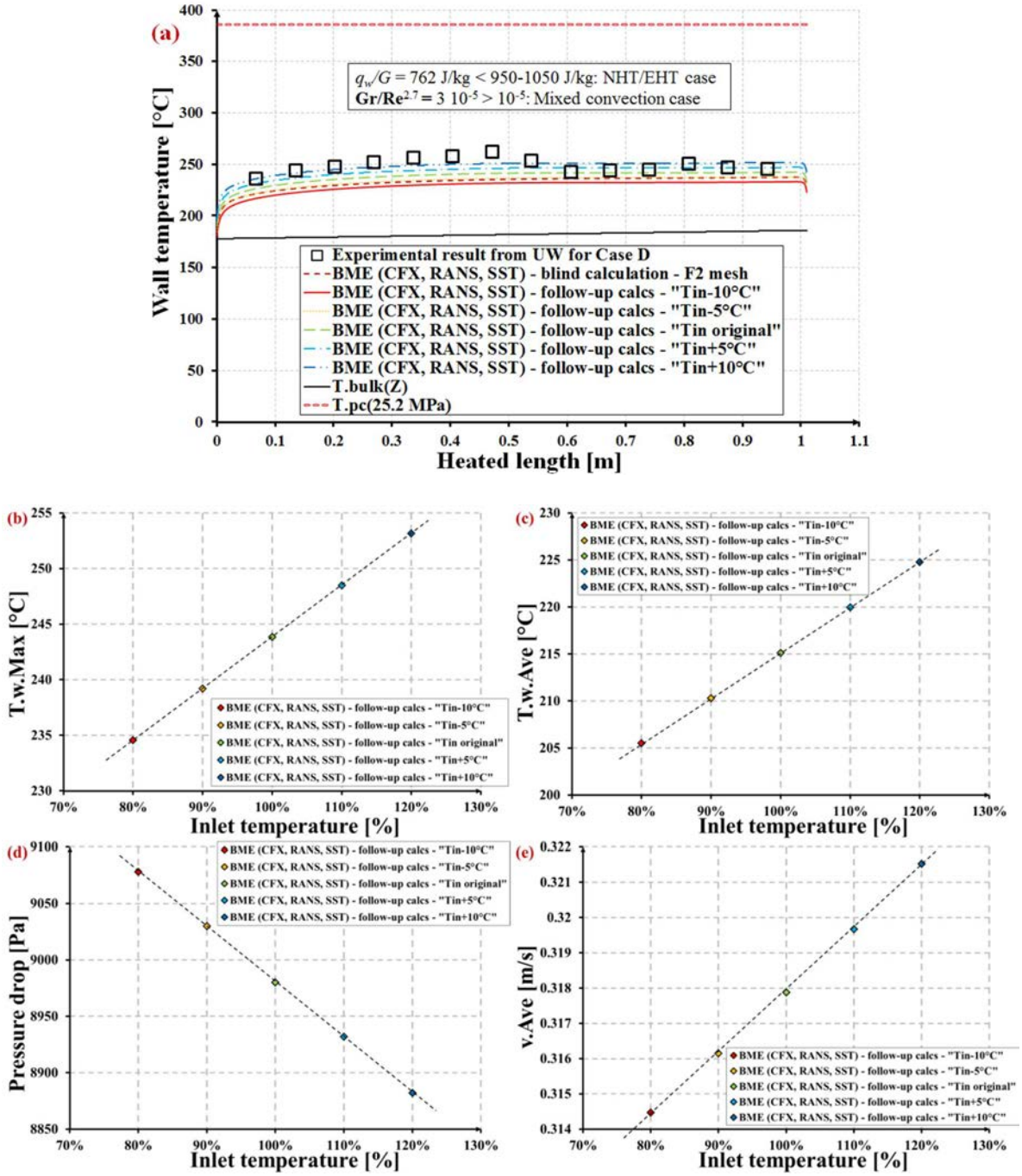

Fig. 12.20. Results of boundary condition sensitivity study on inlet temperature for Case D.2 (p_{ref} = 25.2 MPa, q_w = 218.5 kW/m^2, G = 286.9 kg/m^2/s, T_{pc} = 385.7°C, T_{in} = 177.6°C), comparison of: a., distribution-, b., maximum-, c., average of wall temperatures, d., total pressure drops and e., and average velocities, by courtesy of ASME.

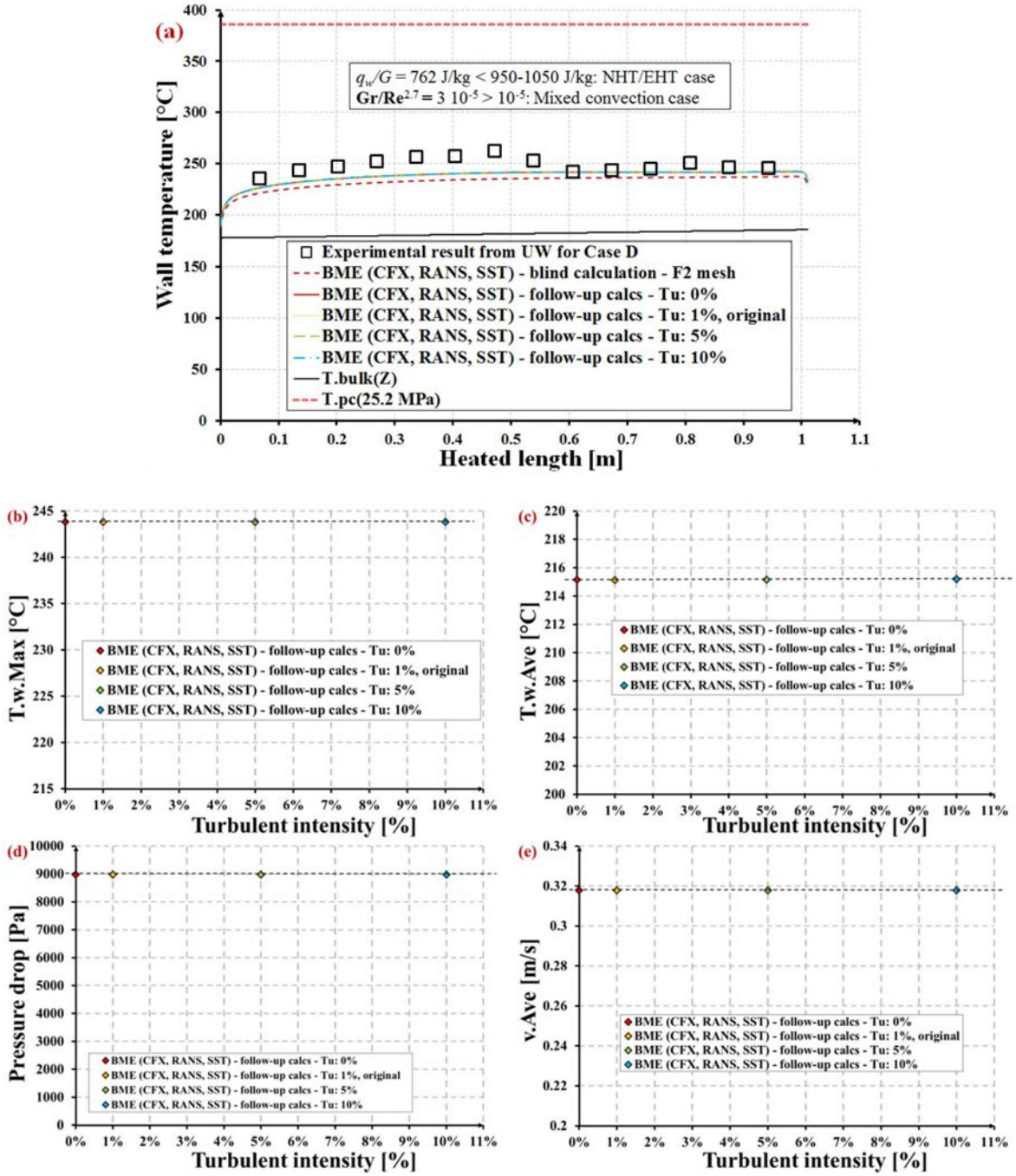

Fig. 12.21. Results of boundary condition sensitivity study on inlet turbulence intensity for Case D.2 (p_{ref} = 25.2 MPa, q_w = 218.5 kW/m^2, G = 286.9 kg/m^2/s, T_{pc} = 385.7°C, T_{in} = 177.6°C), comparison of: a., distribution-, b., maximum-, c., average of wall temperatures, d., total pressure drops and e., average velocities, by courtesy of ASME.

12.1.6.5.SENSITIVITY ANALYSIS ON THE INLET TURBULENCE INTENSITY

The possible effect of the spacer device upstream to the inlet of the test section [12.14], [12.15] was tested by the sensitivity analysis on the inlet turbulence intensity. Fig. 12.21 depicts the sensitivity of CFD results on the specified inlet turbulence intensity. As it can be seen, the whole distribution of wall temperature (Fig. 12.21a), its maximum and average values (Fig. 12.21b and c), just like the pressure drop (Fig. 12.21d) and average velocity (Fig. 12.21e) are independent (at least in the investigated range) of the turbulence intensity. This observation indicates that the spacer device upstream to the inlet very likely does not have significant effect on the thermal hydraulics occurring in the downstream direction in the test section.

12.1.6.6.TURBULENCE MODEL SENSITIVITY ANALYSIS

The effect of the applied turbulence model on the CFD result has been investigated by BME in the framework of a detailed turbulence model sensitivity study (TMSS). Fig. 12.22 shows the results of TMSS for Case 1 which was performed in the follow-up calculation phase. As it can be seen the models of *k–ε* family (*k–ε*, *k–ε* EARSM, RNG *k–ε*) give significantly different distributions of wall temperature compared to the *k–ω* type models (BSL, BSL EARSM, *k–ω*, SST). While the k-ω type models predict deterioration of heat transfer at the end of the heated section (directly after the height where the wall temperature exceeds the pseudocritical value, see Fig. 12.22) the *k–ε* type models do not. The *k–ε* type models seem to be not capable to predict heat transfer deterioration, while the low Re *k–ω* type models can predict DHT. Thus, obviously, the applied turbulence model strongly influences the CFD results as it was reported by previous studies [12.1], [12.3], [12.4], [12.10], [12.11], [12.18].

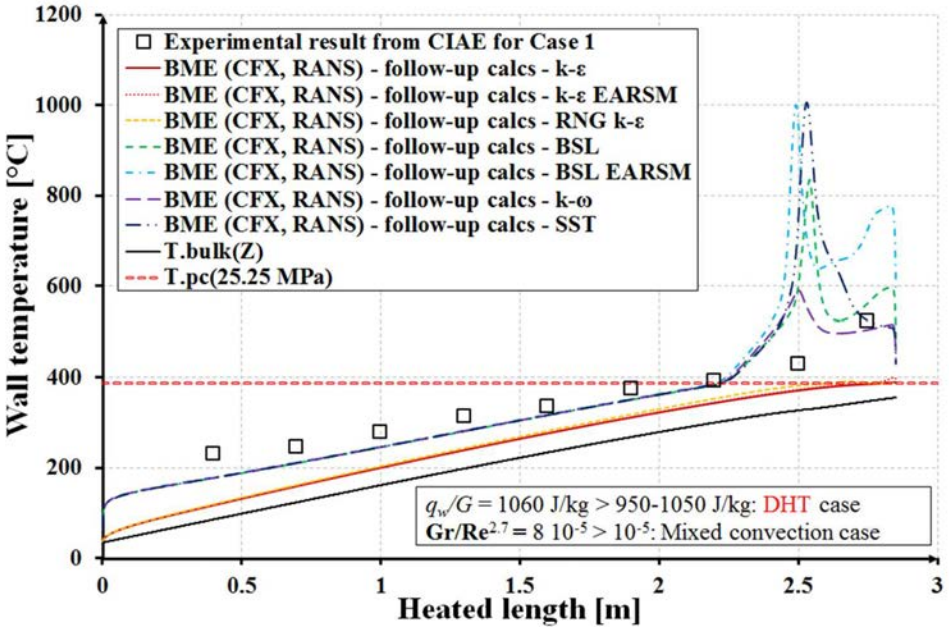

Fig. 12.22. Results of turbulence model sensitivity study for Case 1 (p_{ref} = 25.25 MPa, q_w = 623 kW/m^2, G = 587.6 kg/m^2/s, T_{pc} = 385.8°C, T_{in} = 34.4°C): the axial distribution of wall temperature, by courtesy of ASME.

12.2. BENCHMARKING AGAINST SJTU 4-ROD BUNDLE TEST

The majority of the CRP partners (Gidropress, KIT, BME, UOIT, BARC, CNL, CIAE) have participated in benchmarking of CFD tool and subchannel codes against the 4-rod bundle heat-transfer data offered by Shanghai Jiao Tong University (SJTU).

12.2.1. SPECIFICATIONS FOR THE BENCHMARK EXERCISE BASED ON THE SJTU SWAMUP EXPERIMENT

The SJTU has performed many experiments on its SWAMUP test loop. In this benchmark one test section has been modelled and shown in Fig. 12.23.

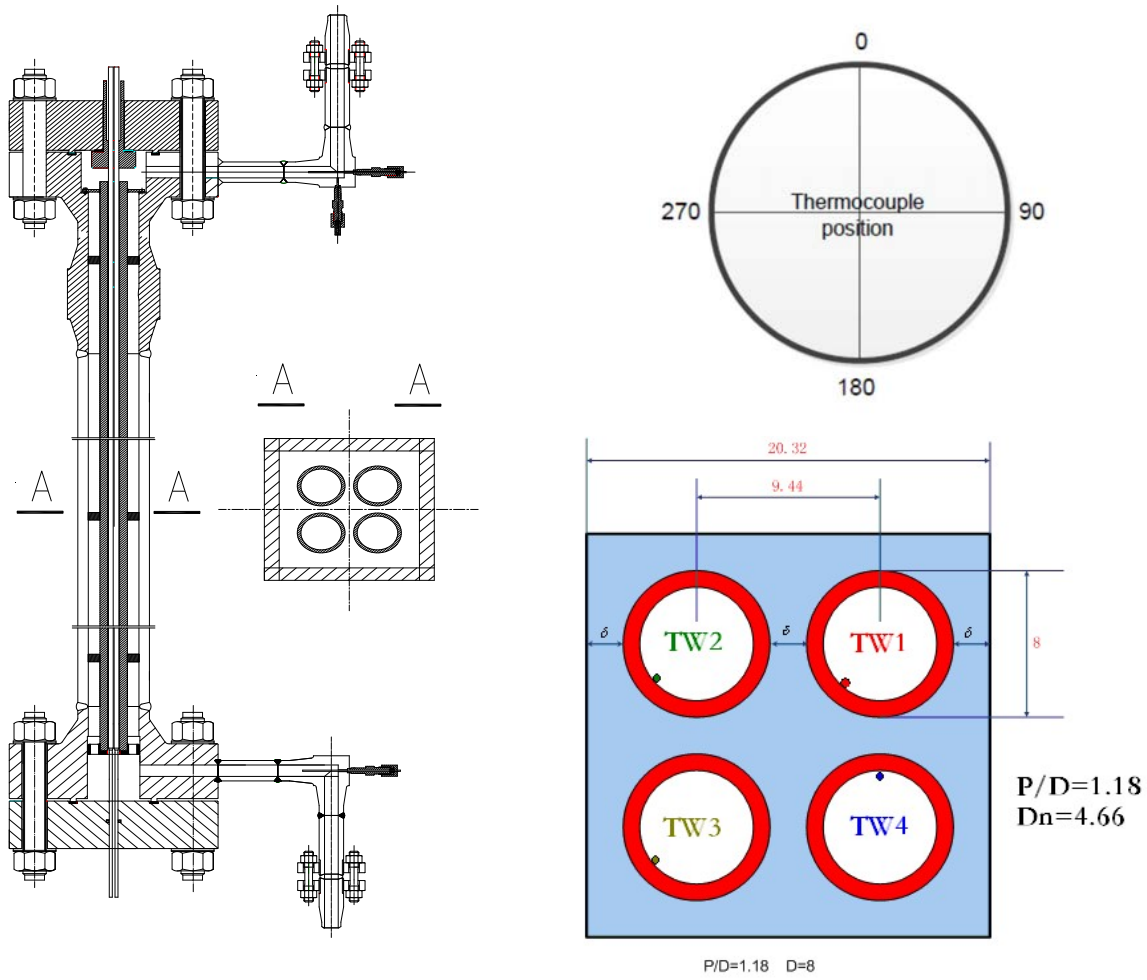

Fig. 12.23. The Cross Sections of the Test Sections (dimensions are in mm).

The geometrical parameters are as follows (see Fig. 12.23):

— The outer diameter of the heater tube (Inconel-718) is 8.0 mm, pitch is 9.44 mm, duct δ is 1.44 mm;

— The inner diameter of the heater tube is 4.66 mm;
— The heated length is: L_{heated} = 1.328 m;
— The test section geometry is 20.32 mm wide flow channel.

There are six grid spacers (SS-304) uniformly arranged along the axial direction with the spacer span of 225 mm. Detailed information about the grid spacer (starting and ending point from the bottom of the bundle) are listed in Table 12.8. The cross section of the grid spacer is shown in Fig. 12.24.

TABLE 12.8. LOCATION OF THE GRID SPACERS (SPACER HEIGHT 8 MM)

Space Grid	Location (mm)	Start	End
SP1	91-99	90	100
SP2	316-324	315	325
SP3	541-549	540	550
SP4	766-774	765	775
SP5	991-999	990	1000
SP6	1216-1224	1215	1225

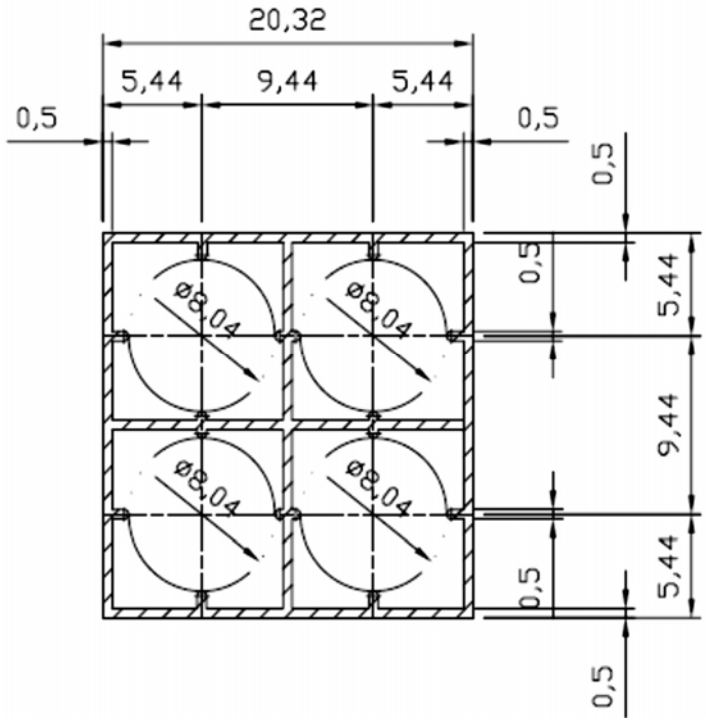

Fig. 12.24. Detailed geometry of the crosscsection of the grid spacer.

The spacer grids are fixed on four heated tubes by several raised points (very small) on the surface of heated tube to prevent them from moving up or down . As shown in Table 12.8, the location distance is slightly smaller than 'START' and 'END'.

The inner wall temperature of the heater rod was measured at positions listed in Table 12.9. The circumferential position of the fixed thermocouples for each rod is shown in Fig. 12.23 (Rod 1, 2 and 3 at 225°; Rod 4 at 0°).

TABLE 12.9. AXIAL POSITIONS OF THERMOCOUPLES (TCS) FROM THE START OF HEATED LENGTH

TC#	*z* (m)
1	0.145
2	0.195
3	0.245
4	0.295
5	0.345
6	0.395
7	0.445
8	0.495
9	0.545
10	0.595
11	0.645
12	0.695
13	0.745
14	0.795
15	0.845
16	0.895
17	0.945
18	0.995
19	1.045
20	1.095
21	1.145
22	1.195
23	1.245

Two cases have been selected from the 4-rod bundle tests. Thermalhydraulic parameters of these cases are listed below.

Case A:

- Inlet pressure: 25.09 MPa;
- Heat flux at the surface of heater rod: q_w = 800.2 kW/m^2;
- Mass flux: 844.52 kg/(m^{2}s);
- Inlet water temperature of heated section: T_{in} =346.4°C;
- The outer surface of the pressure boundary was insulated (i.e., adiabatic surface).

Case B:

- Inlet pressure: 25 MPa;
- Heat flux at surface of heater rod: q_w = 551.6 kW/m^2;
- Mass flux: 451.2 kg/(m^{2}s);
- Inlet water temperature of heated section: T_{in} = 340.1°C;
- The outer surface of the pressure boundary was insulated (i.e., adiabatic surface).

12.2.2. CFD TOOLS BENCHMARK

For the CFD model description, the information shown below was collected from each participant (see Table 12.10):

- Code;
- Models (applied approach (e.g., RANS, LES, DNS), turbulence modeling, wall treatment, simplified or CHT model, etc.);
- Model settings (steady state or transient simulation, numerical schemes, bulk and near-wall mesh sizes, buoyancy, etc.);
- Properties of coolant (values at 175 and 400°C, source of the properties);
- Properties of solid (values at 175 and 600°C, source of the properties);
- Modeled computational domain and applied boundary conditions; and
- Convergence statistics and imbalances of conservation equations.

The following calculated results were contributed by the participants:

- Average and maximum wall temperatures on the heater rod with the predicted peak temperature location;
- Axial profiles (along the heated section) of:
    - Absolute pressure;
    - Circumferential average of heat flux on the heater rod surface;
    - Coolant bulk temperature and the circumferential average of wall temperature on the heater rod surface;
    - Circumferential average of heat transfer coefficient;
    - Cross section averaged velocity;
    - Average y^+ value along the outer surface of the heater rod.
- Radial profiles (at the position of each thermocouple) of:
    - Velocity;
    - Temperature;
    - Turbulent kinetic energy;
    - Production of turbulent kinetic energy;
    - Turbulent viscosity, diffusivity and shear stress;
    - Thermophysical properties (density, specific heat, dynamic viscosity and thermal conductivity).
- The predicted temperature at the locations of thermocouples (23 TCs per rod).

All compiled results are shown in Fig. 12.25 to Fig. 12.28.

TABLE 12.10. CFD MODEL DESCRIPTION

Participants	For short	Code	Turbulence Model	Near wall treatment	Mesh size at the bulk fluid region (approx.) (mm):	Mesh size at the near-wall region (approx.) (mm):
Karlsruhe Institute of Technology	KIT	ANSYS CFX	SSG Reynolds Stress	Standard Wall Function	N/A	N/A
University of Pisa	Pisa1	STAR-CCM+ 10.06.06	AKN, Low-Re	Low y^+	0.1	0.001
University of Pisa	Pisa2	STAR-CCM+ 10.06.06	Standard κ-ε, Two Layers	All y^+	0.1	0.001
Canadian Nuclear Laboratories	CNL	STAR-CCM+ 9.02.007	K-Omega turbulence model for CASE A and v2f model for CASE B	All y^+	1.2	0.003
OKB GIDROPRESS	OKB	CFX 14.5	RSM SSG	Low Reynolds	0.175	0.005
University of Wisconsin-Madison	UWM	Fluent 17.1	SST	Enhanced Wall Function	0.068	0.025
Budapest University of Technology and Economics	BUTE	ANSYS CFX 17.0	Baseline Reynolds Stress (BSL RSM)	N/A	0.1	0.00066

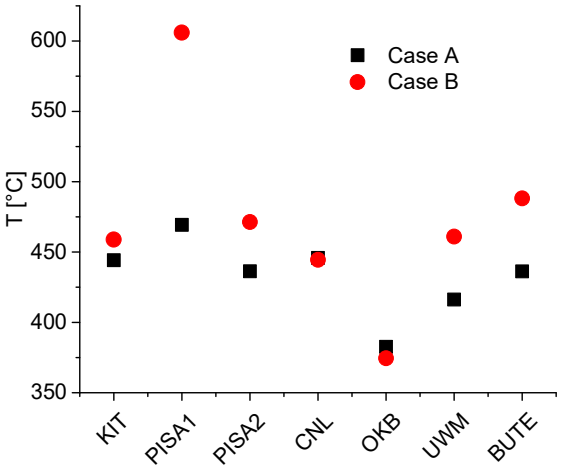

(a) Averaged temperature of rods

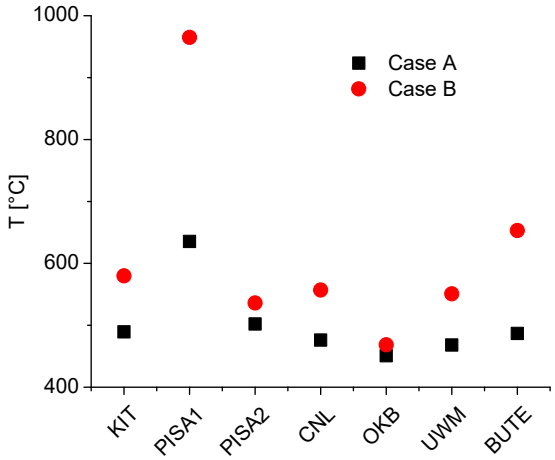

(b) Maximum temperature of rods

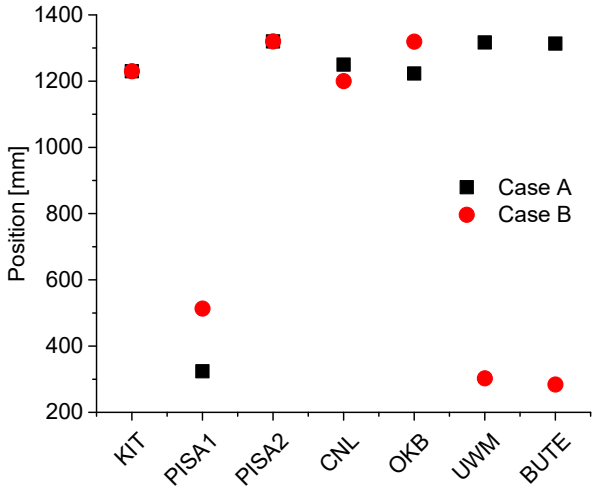

(c) Maximum temperature position of rods

Fig. 12.25. General results of rods.

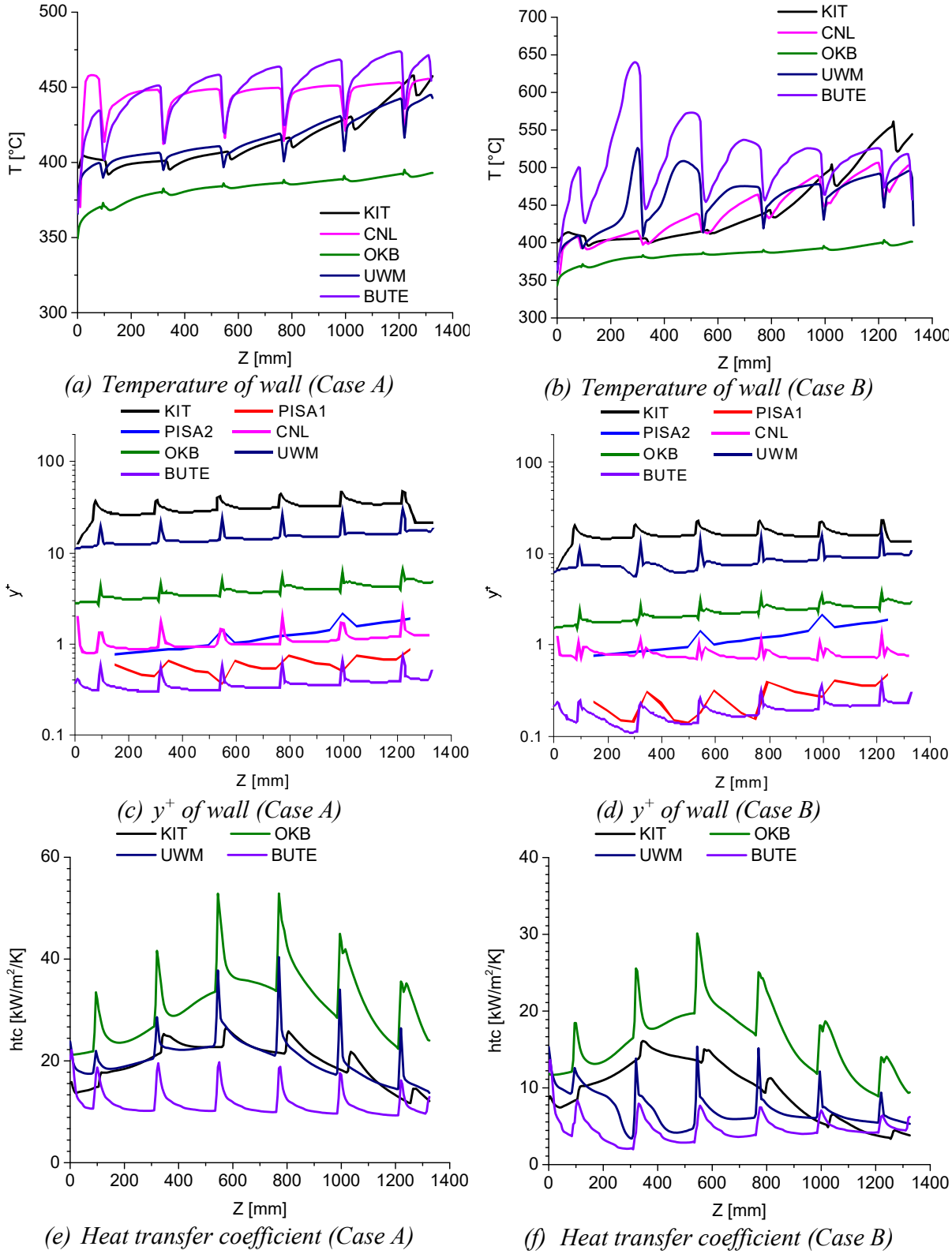

(a) Temperature of wall (Case A)

(b) Temperature of wall (Case B)

(c) y^+ of wall (Case A)

(d) y^+ of wall (Case B)

(e) Heat transfer coefficient (Case A)

(f) Heat transfer coefficient (Case B)

Fig. 12.26. Axial profiles.

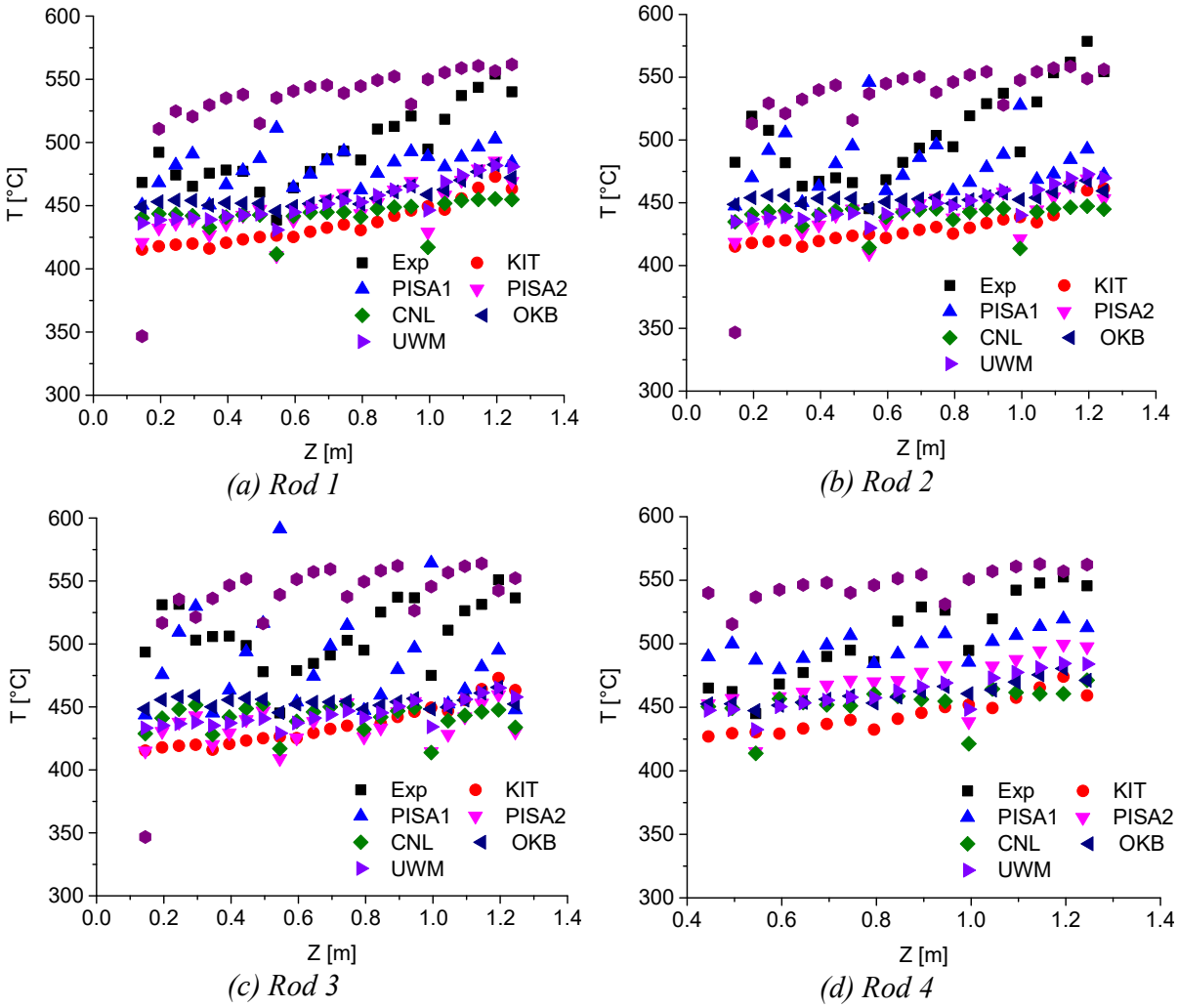

(a) Rod 1 *(b) Rod 2*

(c) Rod 3 *(d) Rod 4*

Fig. 12.27. Comparison of predicted and measured wall temperatures for Case A.

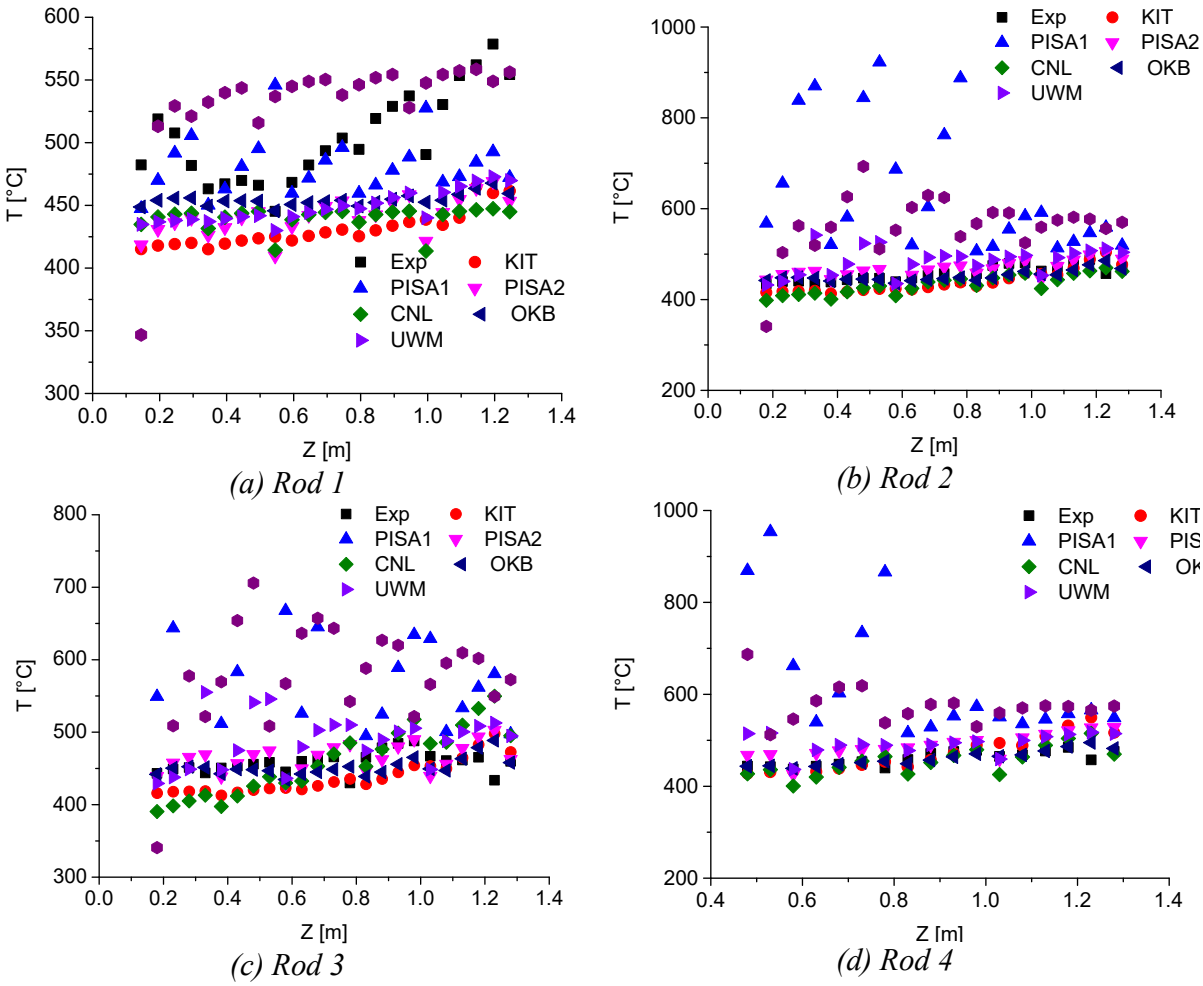

Fig. 12.28. Comparison of predicted and measured wall temperatures for Case B.

12.2.3. SUBCHANNEL CODE BENCHMARK

For the subchannel model description, the information shown below was collected from each participant (see Table 12.11):

- Code;
- Models (turbulence mixing, pressure drop, etc.)
- Model settings (steady state or transient simulation, numerical schemes, subchannel geometry, axial mesh size, etc.);
- Properties of coolant;
- Properties of solid;
- Applied boundary conditions;
- Result convergence.

TABLE 12.11. SUBCHANNEL MODEL DESCRIPTION

Participants	For short	Code	Property	Heat transfer model	Turbulent mixing	Pressure drop model
Karlsruhe Institute of Technology	KIT	MATRA	NIST database	D-B	Equal mass exchange	f=0.184 $Re^{-0.2}$
Shanghai Jiao Tong University	SJTU	COBRA-SC	NIST database	Swenson	Equal mass exchage Beta=0.05	f=0.18027 $Re^{-0.18}$
Bhabha Atomic Research Centre	BARC	COBRA-IV	NIST database	Swenson, Yao et al.	Single phase correlation	f=0.316 $Re^{-0.25}$

The following calculated results were contributed by the participants:

- Average and maximum wall temperatures on the heater rod with the peak-temperature location;
- Axial profiles (along the heated section) of:
  - Absolute pressure of each subchannel;
  - Coolant bulk temperature/enthalpy of each subchannel;
  - Coolant velocity of each subchannel;
  - Mass flux of the coolant at each subchannel;
  - Heat transfer coefficient of each rod; and
  - Outer surface cladding temperature of the heating rod.
- Predicted temperature at the locations of thermocouples (23 TCs).

All compiled results are shown in Table 12.12 and Fig. 12.29 to Fig. 12.32.

TABLE 12.12. GENERAL RESULTS

	Case A	
	SJTU	KIT
$T_{average}$ (°C):	450.439	410.8
T_{max} (°C):	487.79	417.9
Axial position (z) of T_{max} (mm):	1185 - 1200 (at Rod 2 – Subchannel 5)	465
	Case B	
	SJTU	KIT
$T_{average}$ (°C):	490.975	414.9
T_{max} (°C):	558.83	424
Axial position (z) of T_{max} (mm):	1050 - 1065 (at Rod 1 - Subchannel 1)	385

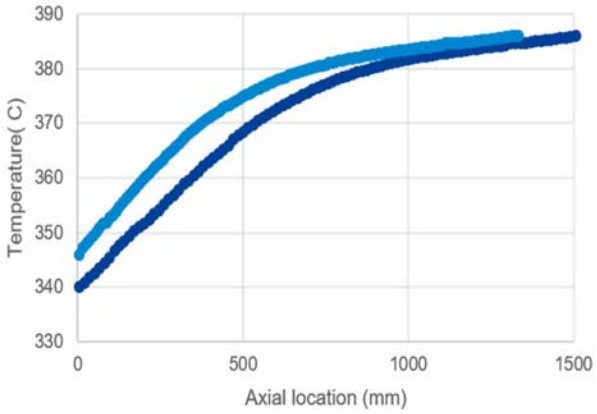

(a) Coolant temperature in SC 1 (Case A)

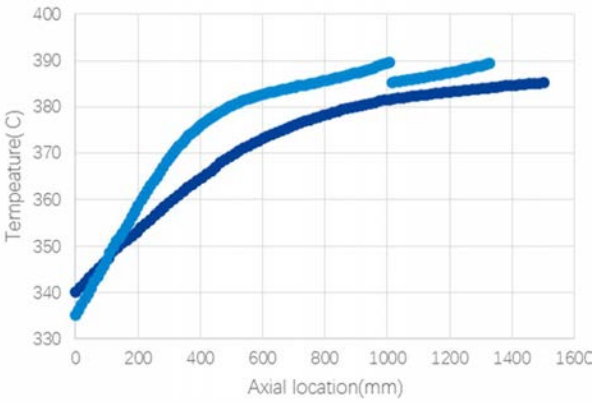

(b) Coolant temperature in SC 1(Case B)

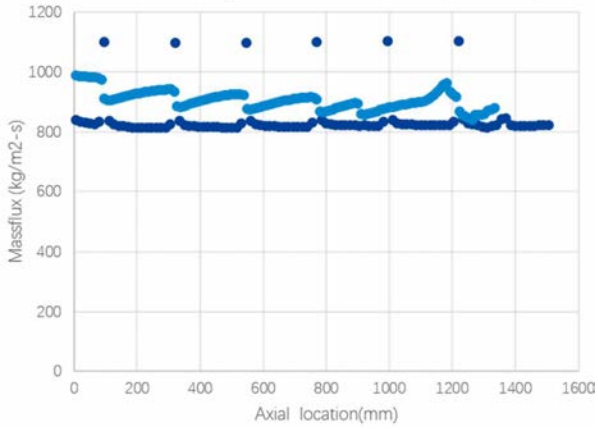

(c) Mass flux in SC 1 (Case A)

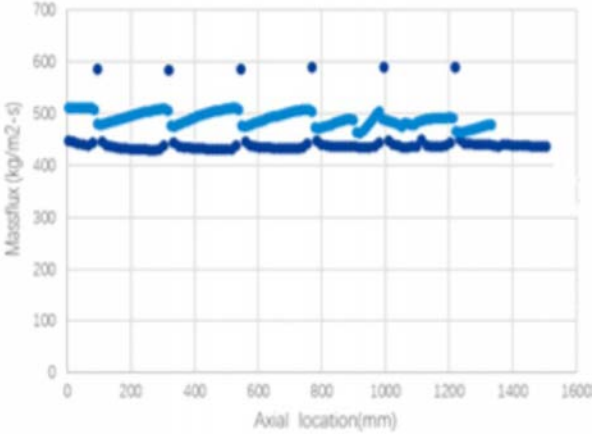

(d) Mass flux in SC 1(Case B)

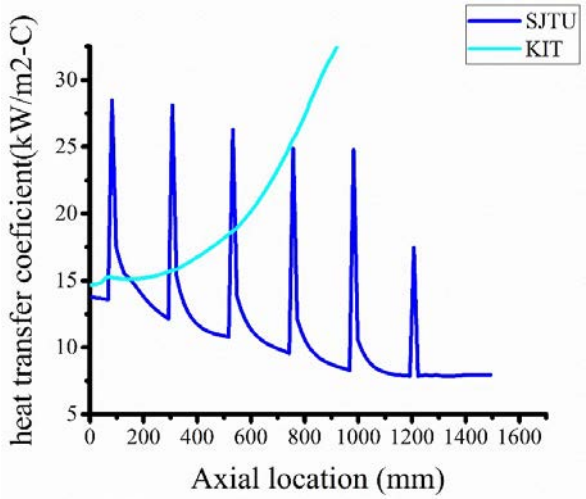

(e) Heat transfer coefficient at Rod1(Case A)

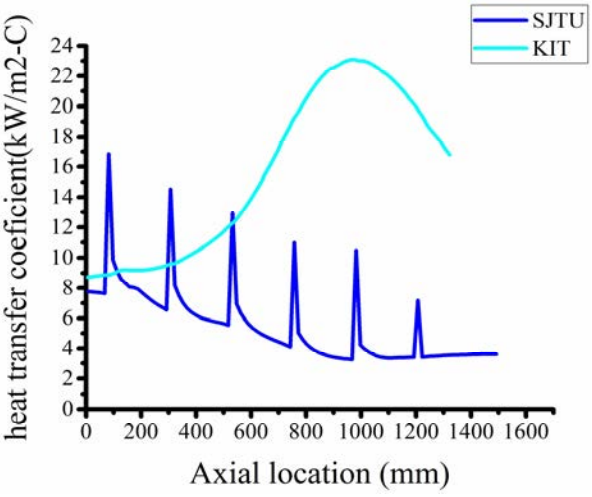

(f) Heat transfer coefficient at Rod1(Case B)

Fig. 12.29. Axial profiles.

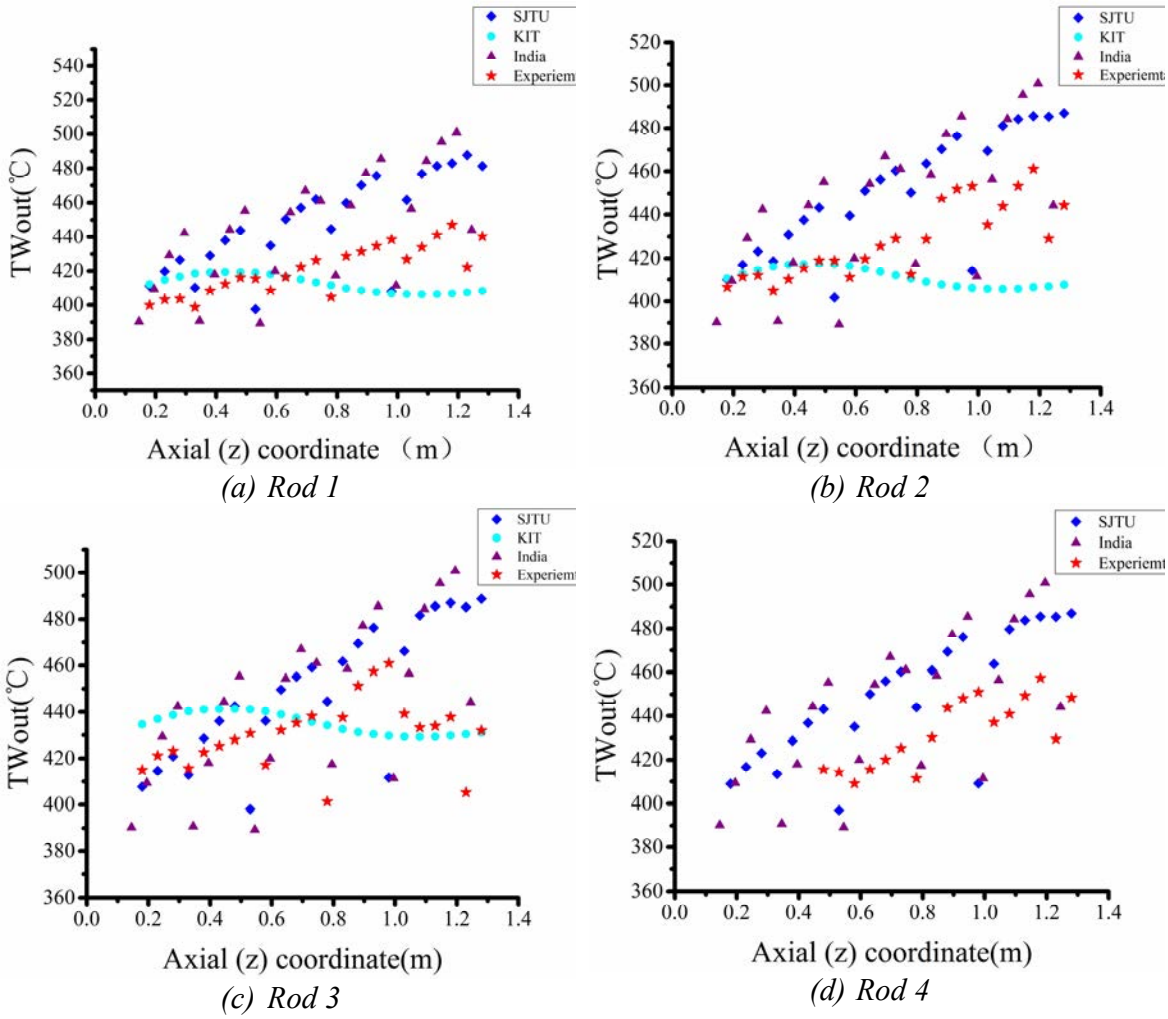

Fig. 12.30. Comparison of predicted and measured wall temperatures for Case A.

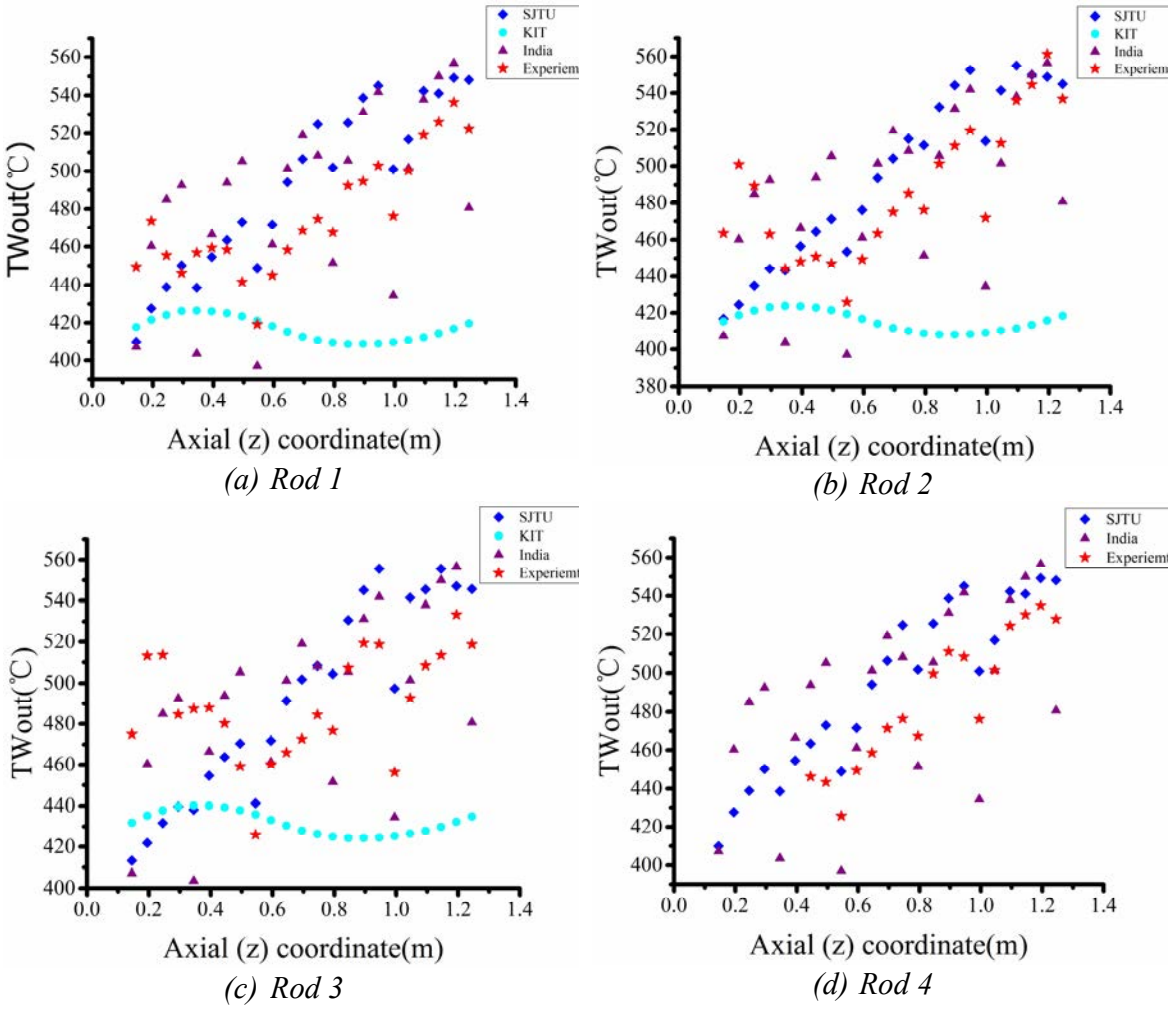

Fig. 12.31. Comparison of predicted and measured wall temperatures for Case B.

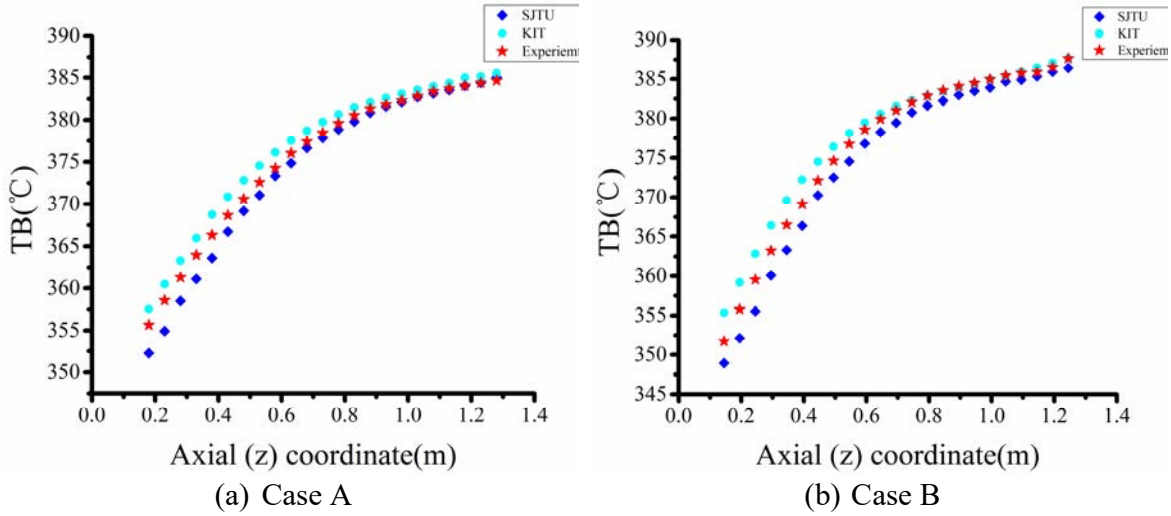

Fig. 12.32. Average yemperature of bulk fluid.

12.3. BENCHMARKING AGAINST NTUU NON-BUNDLE AND BUNDLE TESTS

Two CRP participants (UoP and BME) took part in CFD benchmark and one participant (CNL) carried out subchannel numerical analysis of non-bundle and bundle tests based on the experimental data submitted by NTUU. The aspects of the CFD model (selection of computational domain, turbulence modeling, wall treatment, near wall mesh, etc.) and settings (numerical schemes, etc.) were at the discretion of the participants.

12.3.1. SPECIFICATIONS FOR THE BENCHMARK EXERCISE BASED ON NTUU NON-BUNDLE EXPERIMENT

NTUU has performed experiments in smooth vertical 600 mm heated-length tubes A of 8.11/6.28 mm OD/ID and B of 12.28/9.50 mm OD/ID (Fig. 12.33).

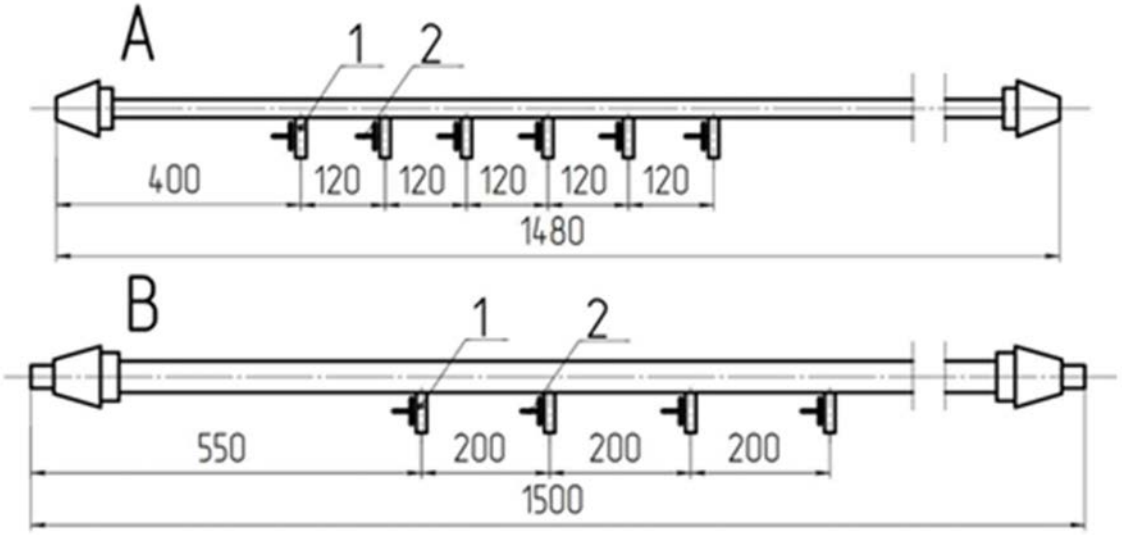

Fig. 12.33 Tube test sections A (ID = 6.28 mm) and B (ID = 9.50 mm).

The tubes were made of stainless steel 12Kh18N10T (Kh – Cr; N – Ni; T – Ti). Wall temperatures in the test sections were measured with 16 and 10 thermocouples in Tube A and Tube B, respectively, placed at the distances from the entrance in the heated sections as shown in Table 12.13.

TABLE 12.13. LOCATIONS (IN MM) OF THERMOCOUPLES ALONG HEATED SECTIONS OF TUBE A AND TUBE B.

TC	1	2	3	4	5	6	7	8	9	10	11	12	13	14	15	16
Tube A	0	40	80	120	160	200	240	280	320	360	400	440	480	520	560	600
Tube B	0	67	134	200	267	334	400	467	534	600	-	-	-	-	-	-

The operating conditions for the NTUU experiments with water are listed in Table 12.14.

TABLE 12.14. OPERATING CONDITIONS FOR THE NTUU TUBE EXPERIMENTS.

Tube (T)	A		B	
Case	1	2	1	2
Pressure (MPa)	23.5			
Heat flux at the internal surface of the tube (MW/m^2)	1.34	0.802	0.104	0.51
Mass flux (kg/(m^2·s))	2193	509	248	248
Inlet water temperature (°C)	394	367	377	300
Vertical flow direction	up	down	up	down

12.3.2. SPECIFICATIONS FOR THE BENCHMARK EXERCISE AGAINST NTUU BUNDLE EXPERIMENTS

NTUU performed experiments with vertical 3 and 7-rod bundle simulators in water flow. The rod was constructed with a tube of 5.2 mm OD, 4.5 mm ID and 485 mm heated length. Four helical ribs of 0.6 mm height and 1 mm width were wound over the tube in a 400 mm pitch. Rods in the bundle were positioned in a triangular array and were separated from each other by a 1 mm gap, which were maintained with the ribs (see Fig. 12.34). In addition, a shaped dielectric displacer was installed with calibrated stainless-steel fins of 0.1 mm thickness welded to the cylindrical surface of the rods at seven axial locations (i.e., 125, 185, 245, 305, 365, 425, and 485 mm) from the start of the heated length.

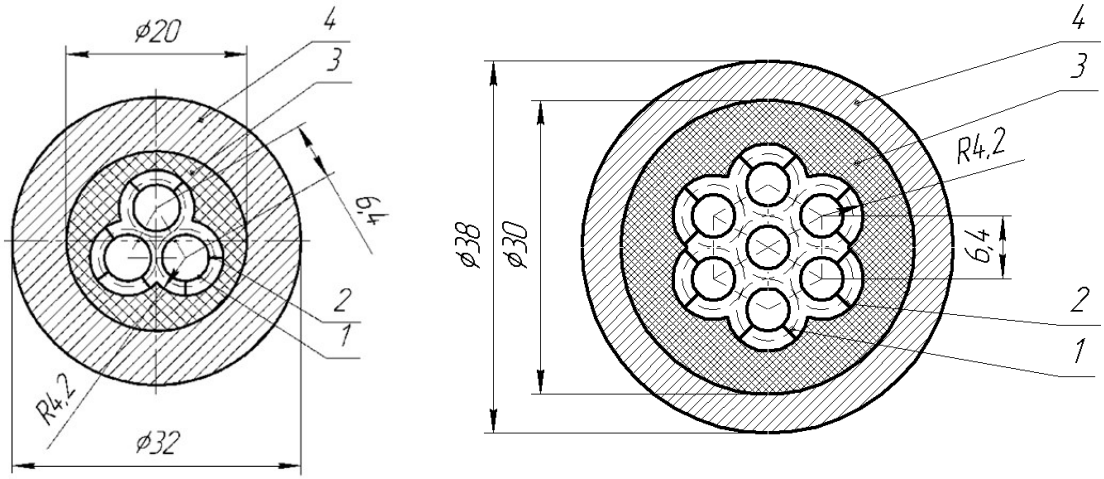

Fig. 12.34 Cross section of bundle test sections (1 – heated rod (rod); 2 – distancing rib; 3 – shaped dielectric displacer; 4- pressure tube).

Main geometric parameters of the 3-rod and 7-rod bundles are listed in Table 12.15. The displacer was inserted inside the pressure tube (see Fig. 12.34 for dimensions). Wall temperatures in the test section were measured with eight thermocouples placed inside the central rod at locations of 95, 195, 255, 315, 375, 412, 425 and 475 mm from the start of the heated length.

TABLE 12.15. MAIN GEOMETRIC PARAMETERS OF 3-rod AND 7-rod BUNDLES.

Test section	S (mm^2)	F (mm^2)	D_{hydr} (mm)	D_h (mm)	S/F	Π_{wetted} (mm)
3-rod	74.16	30855	2.65	5.19	$2.46 \cdot 10^{-3}$	111.8
7-rod	140.09	71995	2.56	3.78	$1.95 \cdot 10^{-3}$	218.46

Characteristics of the regimes for 3R and 7R tests are given in Table 12.16 and Table 12.17.

TABLE 12.16. OPERATING CONDITIONS FOR THE 3-rod (3R) BUNDLE TEST WITH UPWARD WATER FLOW.

Case	***P* (MPa)**	***G* (kg/(m^{2}s))**	***T*$_{in}$ (°C)**	***q* (MW/m^2)**
3R_1	24.5	1500	168	2.180
3R_2	24.5	2700	260	2.874
3R_3	27.5	1500	212	2.143

TABLE 12.17. OPERATING CONDITIONS FOR THE 7-rod (7R) BUNDLE TEST WITH UPWARD WATER FLOW.

Case	***P* (MPa)**	***G* (kg/(m^{2}s))**	***T*$_{in}$ (°C)**	***q* (MW/m^2)**
7R_1	22.6	1000	180	1.288
7R_2	24.5	800	185	1.067
7R_3	24.5	800	245	0.960
7R_4	27.5	800	210	1.180

12.3.3. CFD MODELS USED IN THE BENCHMARK AND ITS RESULTS

The CFD models applied by the participants are described in Table 12.18.

TABLE 12.18. CFD MODEL DESCRIPTION.

Participants	**For short**	**Code**	***T***	**3R**	**7R**
Budapest University of Technology and Economics	BME	Subchannel	+	-	-
National Technical University of Ukraine	NTUU	FLUENT(T), ANSYS CFX (3R, 7R)	FLUENT (RNG)	CFX (SST, RNG)	CFX (SST)
University of Pisa	UoP	STAR-CCM+	-	SST	-
Canadian Nuclear Laboratories	CNL	Subchannel (ASSERT-PV)	-	-	(Jackson and Bishop correlations, Turbulent mixing: Rogers and Tahir)

12.3.3.1.PRESSURE DROP RESULTS FOR TUBE EXPERIMENTS

Fig. 12.35 and Fig. 12.36 compare predictions of BME and NTUU against the experimental results obtained with water in tubes. NTUU applied the Fluent CFD tool in axisymmetric formulation to analyze the supercritical flow in the channels using an average value of y^+~ 0.1. The model took into account the area of initial hydrodynamic stabilization of 0.55 and 0.4 m, respectively. Thermophysical properties were evaluated with libraries based on user define functions, and the data arrays were generated using the WaterSteamPro code. Implemented libraries were supported by parallel computations.

Fig. 12.35 shows good agreement between predicted and experimental wall temperature and pressure distributions in upward water flow by both BME and NTUU for Case 1 of Tube A (i.e., T_A1), which corresponds to normal heat transfer with developed turbulence of gas-like flow (q/G = 0.61 kJ/kg). However, both BME and NTUU overpredicted the experimental distributions in downward water flow for Case 2 of Tube A (i.e., T_A2 with q/G = 1.58 kJ/kg and $Gr/Re^2 <$ 0.05), especially the predicted wall temperature distribution of BME.

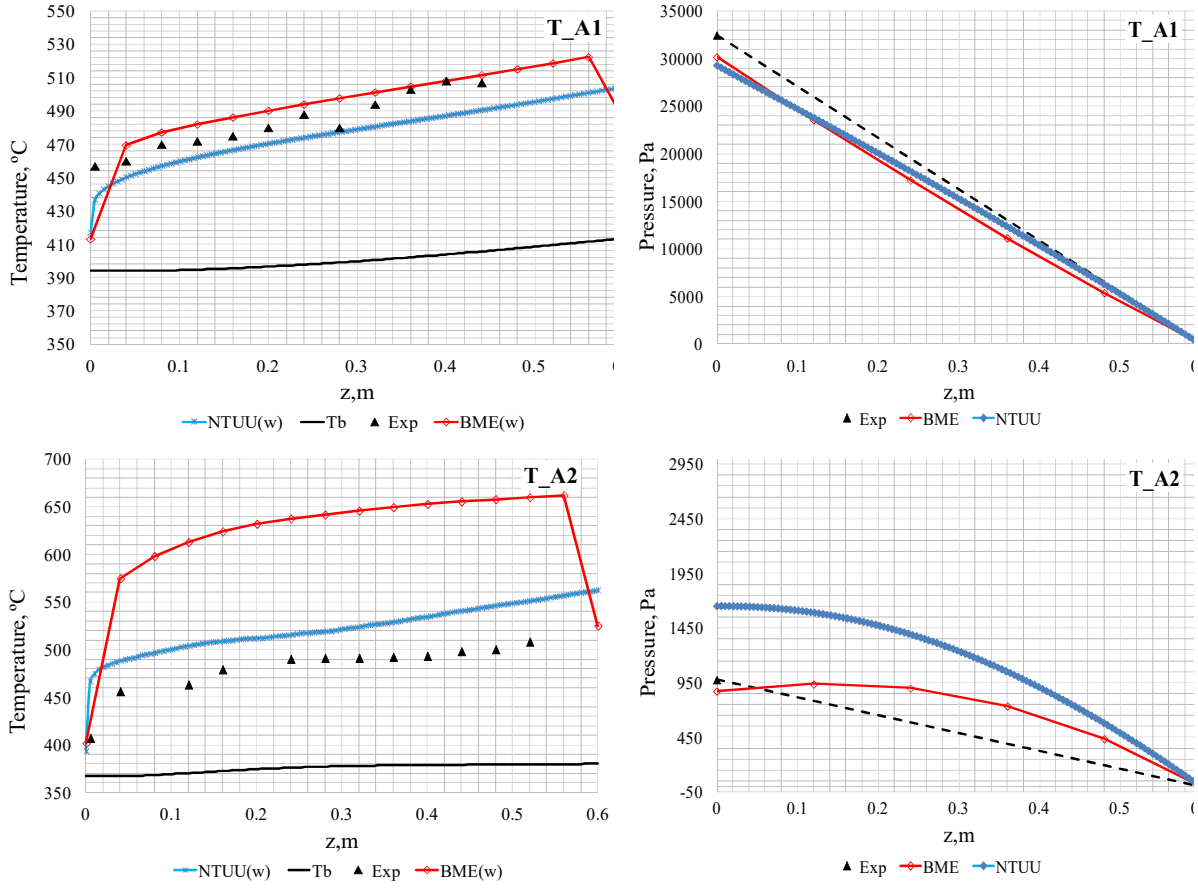

Fig. 12.35 Comparison of predicted and experimental axial temperature and pressure profiles in tube A.

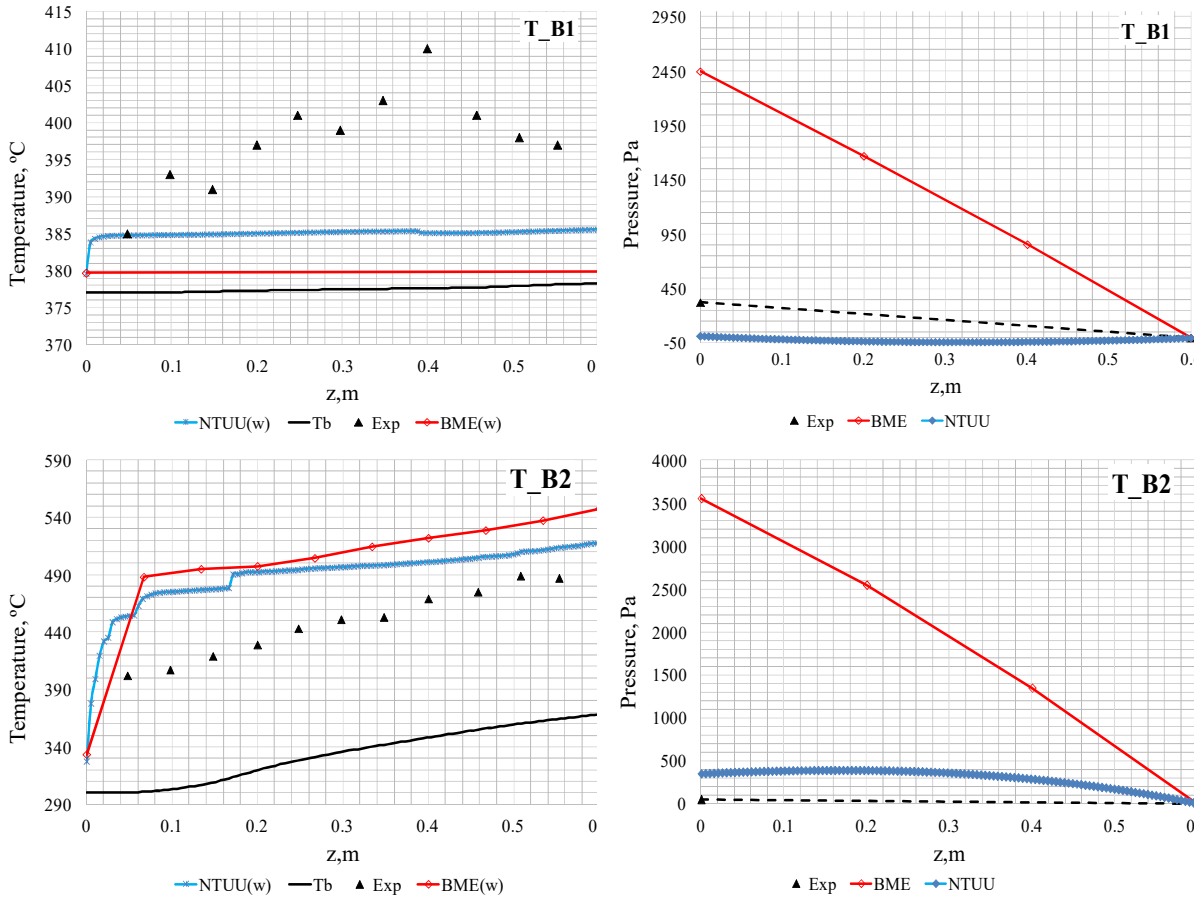

Fig. 12.36 Comparison of predicted and experimental axial temperature and pressure profiles in tube B.

Fig. 12.36 shows underpredictions of the wall temperature distributions in upward water flow by both BME and NTUU for Case 1 of Tube B (i.e., T_B1 with q/G = 0.42 kJ/kg and $Gr/Re^2 > 0.17$), where DHT was encountered in the experiment. The pressure distribution was overpredicted in quite a large margin by BME but underpredicted by NTUU. On the other hand, both BME and NTUU overpredicted the wall temperature and pressure distributions in downward water flow for Case 2 of Tube B (i.e., T_B2 with q/G = 2.06 kJ/kg and $Gr/Re^2 > 0.6$). As for Case 1, BME overpredicted the pressure distribution by a large margin.

12.3.3.2.HEAT TRANSFER IN ROD BUNDLES

NTUU and UoP tested 3R modes using CFD [12.19], [12.20] and [12.21]. NTUU tested RNG and SST turbulence models using the Scalable Wall Function. Thermophysical properties were generated in table form based on the library IAPWS IF-97. The axial wall temperature distribution was obtained by averaging over heating perimeter of the rods, and flow temperature was averaged by mass flow through the passage area. The results of benchmark are plotted in Fig. 12.37.

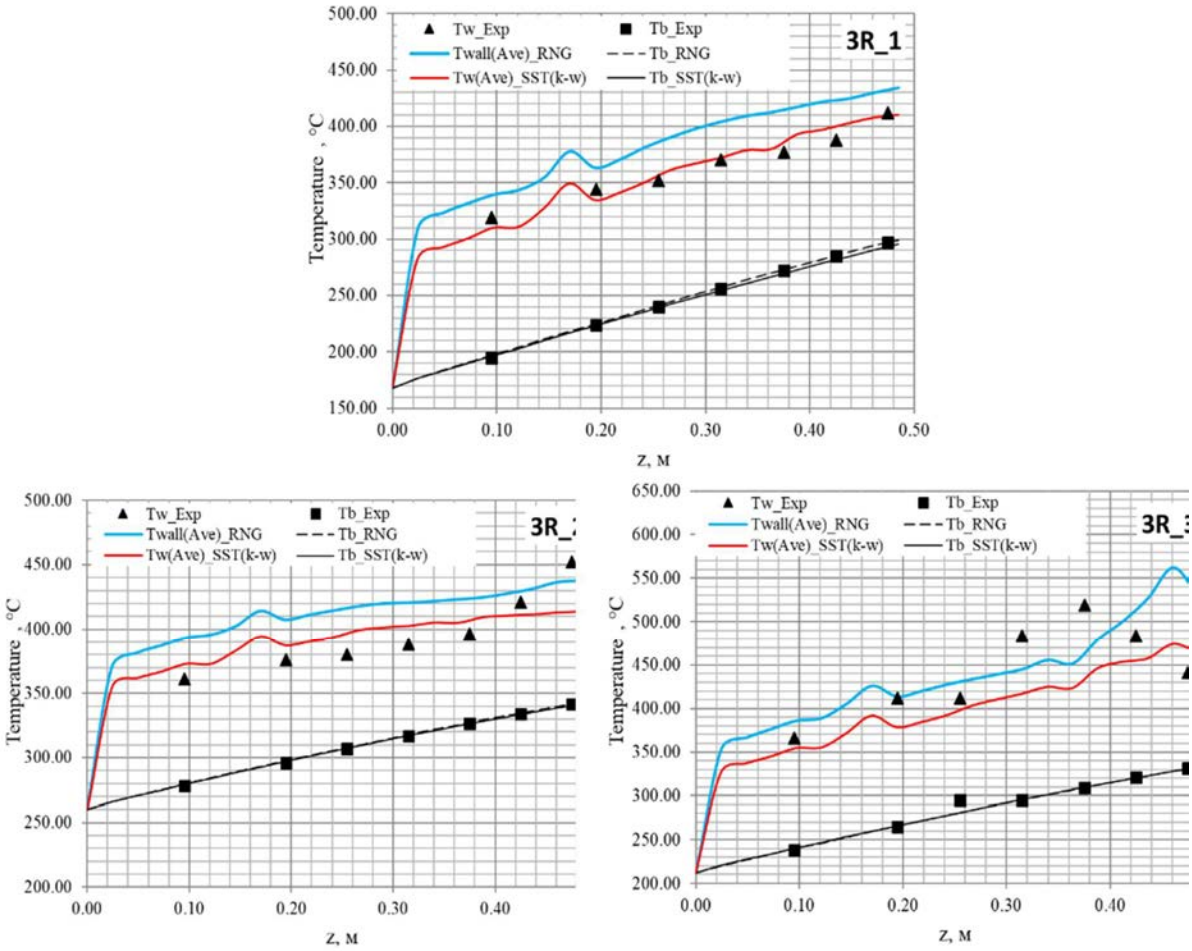

Fig. 12.37 NTUU 3R bundle axial profiles.

University of Pisa carried out complex tests using CD-Adapco STARCCM+ code (version 10.06.10). The fluid properties were obtained via the REFRPROP 7 tool and implemented in the form of cubic spline polynomials, only as a function of temperature, being the maximum calculated pressure drop in the range of 0.2 bar. Many turbulence models have been tested (SST, Standard k-ε and the Realizable k–ε, Wilcox k–ω and the Reynolds Stress Transport turbulence models). As different nodalizations were adopted in the present work, the next figures often report in the legend the number of boundary layer (BL) nodes used for the mesh of the corresponding simulation; the shortened form ‘‘BL preceded by a number indicates how many nodes were actually used for the corresponding calculation in the boundary (or prism) layer. Depending on the boundary layer discretization , low *Re* effects were taken into account.

Additionally, an analysis of turbulent Prandtl number variation was made, as well as the different implementation of heat source in the model (Imposed Heat Flux or Volumetric Heat Source). The most representative results are shown in Fig. 12.38. Comparison of the total pressure drop by RNG and SST is presented in Table 12.19.

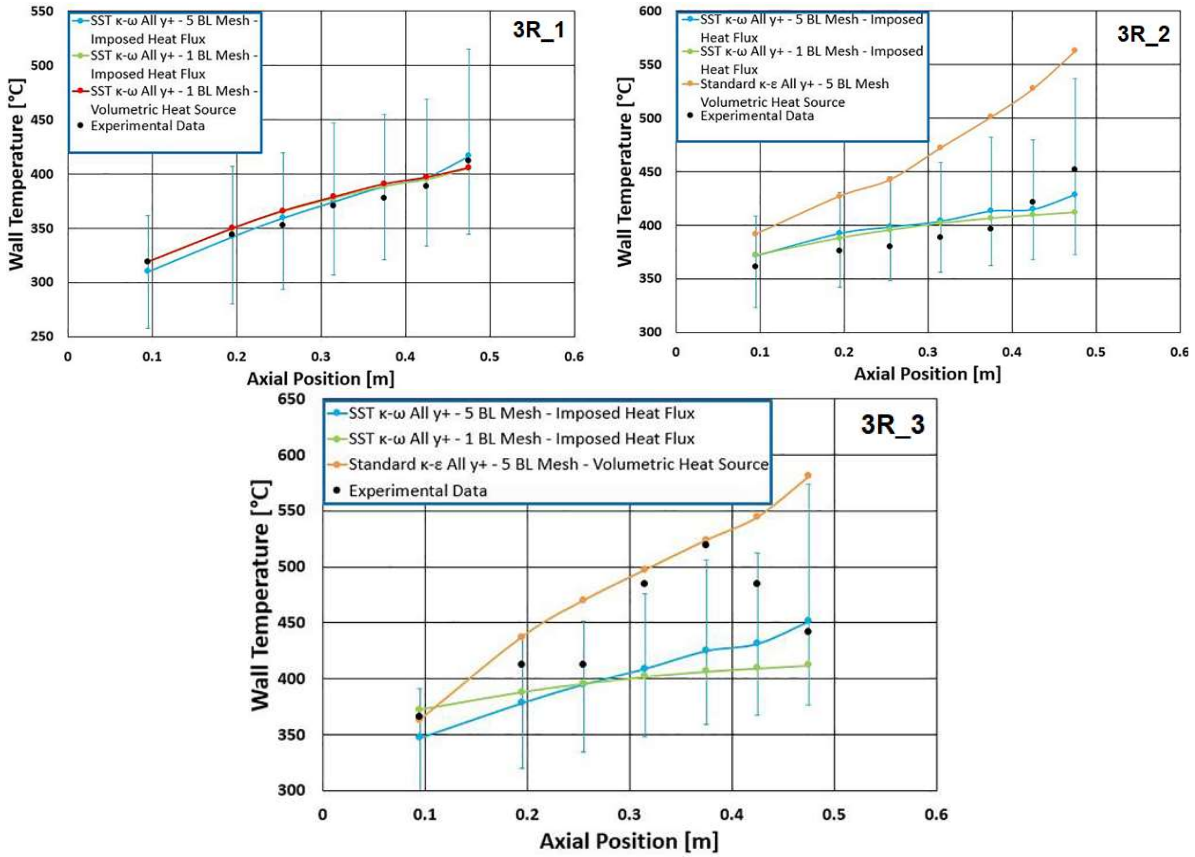

Fig. 12.38 UoP 3R bundle axial profiles.

TABLE 12.19. 3R BUNDLE INTEGRAL PRESSURE LOSS.

Case	Experiment, (Pa)	NTUU, (Pa)		Pisa, (Pa)
		RNG	SST	
3R_1	6260	5690	6360	-
3R_2	20840	17600	18800	-
3R_3	6420	5820	6710	-

NTUU tested 7R modes using CFD. SST with Scalable Wall Function was used as the final turbulence model. Thermophysical properties were generated in table form based on the library IAPWS IF-97. Testing was carried out on different boundary-layer discretizations. The axial wall temperature distribution was obtained by averaging over heating perimeter of the rods, and flow temperature was averaged by mass flow through the passage area. The most representative results obtained on mesh with using near-wall functions are shown in Fig. 12.39. Canadian Nuclear Laboratories carried out subchannel analysis based on the Pressure-Velocity numerical method (code ASSERT-PV). Heat transfer rate was estimated according to Jackson and Bishop correlations for supercritical flows. Wire wrap modeled using increased wetted and heated perimeter. Results are shown in Fig. 12.39. Integral pressure loss comparison is shown in Table 12.20.

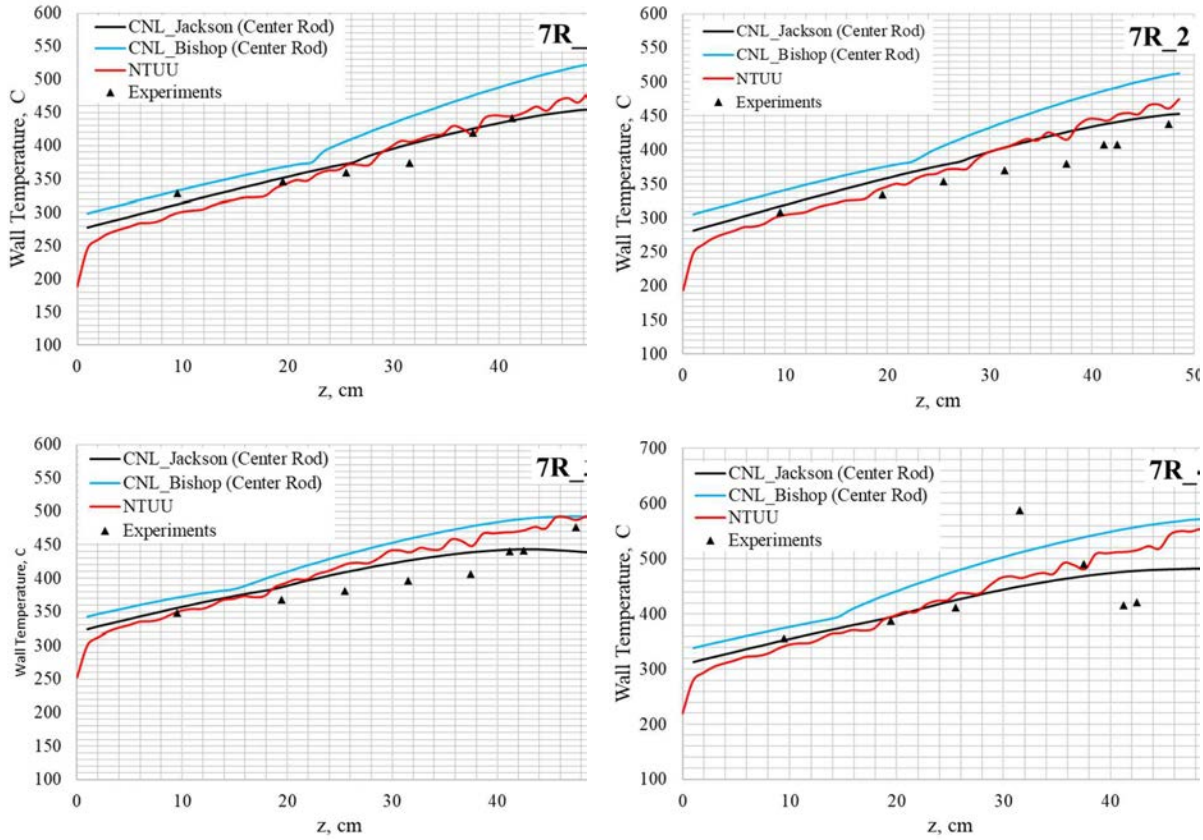

Fig. 12.39 7R axial profiles.

TABLE 12.20. 7R INTEGRAL PRESSURE LOSS.

Case	Experiment (Pa)	NTUU (Pa)	CNL (Pa)
7R_1	4290	3180	7180
7R_2	3190	2110	6070
7R_3	3700	2100	5930
7R_4	3360	2080	6050

Nomenclature and Acronyms

D	diameter (mm)
F	Heat transferring surface (m^2)
G	mass flux ($kg/(m^2s)$)
g	gravitational acceleration (m/s^2)
htc	Heat transfer coefficient ($W/(m^2 \cdot K)$)
L	length (m)
P	Pitch (m)
p	absolute pressure (MPa)
q	heat flux (W/m^2)
S	Area of flow cross section (m^2)

T	temperature (°C)
y	distance from the wall
z	axial position (mm)

Greek Letters

α	Heat transfer coefficient (W/(m^2·K))
β	volumetric thermal expansion coefficient (1/K)
Δ	difference
δ	Gap size (m)
λ	thermal conductivity (W/(m·K))
μ	dynamic viscosity, Pa s
ν	kinematic viscosity, kg/m s
Π	Perimeter (mm)

Non-Dimensional Numbers

Gr	Grashof number; ($g \beta \Delta T D^3/\nu^2$)
Nu	Nusselt number; ($\alpha D/\lambda$)
Re	Reynold number; ($G D/\mu$)

Subscripts or Superscripts

ave	average
h	heated
hydr	Hydraulic equivalent
i	inner
in	inlet
max	maximum
o	outer
out	outlet
pc	pseudocritical
ref	reference
w	wall
+	Non-dimensional

Acronyms and abbreviations

2D	two dimensional
3D	three dimensional
AHFM	Algebraic Heat Flux Model
ANSYS CFX	commercial CFD code developed by ANSYS Inc.
BARC	Bhabha Atomic Research Center
BCSS	boundary condition sensitivity study
BL	Boundary layer
BME, BUTE	Budapest University of Technology and Economics
BoHL	beginning of heated length
BSL-RSM	BSL Reynolds Stress (turbulence) Model
CFD	Computational Fluid Dynamics
CHT	Conjugate Heat Transfer

CIAE	China Institute of Atomic Energy
CRP	Coordinated Research Project
CNL	Canadian Nuclear Laboratories
DHT	deteriorated heat transfer or deterioration of heat transfer
EHT	enhanced heat transfer
F1/F2/F4	factor-1/factor-2/factor-4, the number indicates the size of the numerical grid
GIDROPRESS	OKB GIDROPRESS
IAEA	International Atomic Energy Agency
IAPWS-95	formulation of material properties created in 1995 by the International Association for the Properties of Water and Steam
IAPWS-IF97	industrial formulation of material properties created in 1997 by the International Association for the Properties of Water and Steam
ID	Inner diameter
k-ε	notation of k-ε turbulence model
k-ω	notation of k- ω turbulence model
KIT	Karlsruher Institut für Technologie
M	million
MFR	mass flow rate
MSS	mesh sensitivity study
NAFA	Numerical Analysis of Flows in Axi-symmetric geometries (on-house CFD code name developed by BARC)
NHT	normal heat transfer
NIST	National Institute of Standards and Technology
NTUU	National Technical University of Ukraine
OD	Outer diameter
OKB	OKB GIDROPRESS
REFRPROP	NIST Reference Fluid Thermodynamic and Transport Properties Database
RANS	Reynolds Averaged Navier Stokes
RSM	Reynolds Stress Model
SCW	Super-Critical Water
SCWR	Super-Critical Water-cooled Reactor
SJTU	Shanghai Jiao Tong University
SS	Stainless Steel
SST	Shear Stress Transport
STAR-CCM+	commercial CFD code developed by SIEMENS Gmbh.
TC	thermocouples
TMSS	turbulence model sensitivity study
UOIT	University of Ontario Institute of Technology
UPisa, UoP	University of Pisa
UW, UWM	University of Wisconsin-Madison

REFERENCES TO SECTION 12

[12.1] PIORO, I.L., DUFFEY, R.B., Heat Transfer and Hydraulic Resistance at Supercritical Pressures in Power Engineering Applications, ASME Press, (2007).

[12.2] KISS, A., BALASKÓ, M., HORVÁTH, L., KIS, Z., ASZÓDI, A., Experimental Investigation of the Thermal Hydraulics of Supercritical Water under Natural Circulation in a Closed Loop, Annals of Nuclear Energy, **100, 2**, (2017), 178-203..
[12.3] KISS, A., ASZÓDI, A., Summary for Three Different Validation Cases of Coolant Flow in Supercritical Water Test Sections with the CFD Code ANSYS CFX 11.0, Nuclear Technology, **170, 1**, (2010), 40, 53.
[12.4] ROHDE, M., PEETERS, J.W.R., PUCCIARELLI, A., KISS, A., RAO, Y.F., ONDER, E.N., MUEHLBAUER, P., BATTA, A., HARTIG, M., CHATOORGOON, V., THIELE, R., CHANG, D., TAVOULARIS, S., NOVOG, D., MCCLURE, D., GRADECKA, M., TAKASE, K., A Blind, Numerical Benchmark Study on Supercritical Water Heat Transfer Experiments in a 7-Rod Bundle, ASME Journal of Nuclear Engineering and Radiation Science, **2, 2**, (2016), 021012-24.
[12.5] KISS, A., ASZÓDI, Numerical Investigation on the Physical Background of Deteriorated Heat Transfer Mode in Supercritical Pressure Water, Proc. 6th International Symposium on Supercritical Water-Cooled Reactors (ISSCWR-6), Shenzhen, 2013.
[12.6] YAMAGATA K., NISHIKAWA K., HASEGAWA S., FUJI T., YOSHIDA S., Forced Convective Heat Transfer to Supercritical Water Flowing in Tubes, J Heat Mass Transfer, **15, 12**, (1972), 2575, 2593.
[12.7] JACKSON, J.D., Fluid Flow and Convective Heat Transfer to Fluids at Supercritical Pressure, Nuclear Engineering and Design, **264**, (2013), 24-40.
[12.8] JACKSON, J.D., Models of Heat Transfer to Fluids at Supercritical Pressure with Influences of Buoyancy and Acceleration, Applied Thermal Engineering, **124**, (2017), 1481-1491.
[12.9] PIORO, I.L., KHARTABIL, H.F., DUFFEY, R.B., Heat Transfer to Supercritical Fluids Flowing in Channels - Empirical Correlations (Survey), Nuclear Engineering and Design, 230, (2004), 69–91.
[12.10] KISS, A., LAURIEN, E., ASZÓDI, A., YU, Z., Numerical Simulation on a HPLWR Fuel Assembly Flow with One Revolution of Wrapped Wire Spacers, Kerntechnik, **4**, (2010), 148–157.
[12.11] KISS, A., VÁGÓ, T., ASZÓDI, A., Numerical Analysis on Inlet and Outlet Sections of a Test Fuel Assembly for a Supercritical Water Reactor, Nuclear Engineering and Design, **295**, (2015), 415 – 428.
[12.12] KISS, A. et al., Summary on the results of two computational fluid dynamic benchmarks of tube and different channel geometries, J. Nucl. Eng. Rad. Sci. 4 (2018).
[12.13] CHEN, Y., ZHAO, M., YANG, C., BI, K., DU, K., An Experiment on Flow and Heat Transfer Characteristics in Natural Circulation of Supercritical Water, Proc. 3rd China–Canada Joint Workshop on Supercritical-Water-Cooled Reactors (CCSC-2012), Xi'an, 2012.
[12.14] LICHT, J., ANDERSON, M., CORRADINI, M., Heat Transfer and Fluid Flow Characteristics in Supercritical Pressure Water, Journal of Heat Transfer, **131**, (2009), 1-14.
[12.15] LICHT, J., ANDERSON, M., CORRADINI, M., Heat Transfer to Water at Supercritical Pressures in A Circular and Square Annular Flow Geometry, International Journal of Heat and Fluid Flow, **29**, (2008), 156–166.
[12.16] PAVITHRA, E., SENTHIL KUMAR, V.S., Microstructural Evolution of Hydroformed Inconel 625 Bellows, Journal of Alloys and Compounds, **669, 5**, (2016), 199-204.

[12.17] MENTER, F., HEMSTROM, B., KARLSSON, R., LATROBE, A., MARTIN, A., MUHLBAUER, P., SCHEUERER, M., SMITH, B., TAKACS, T., WILLEMSEN, S., CFD Best Practise Guidelines for CFD Code Validation for Reactor-Safety Applications, ECORA project, FIKS-CT-2001-00154, Brussels, 2002.
[12.18] KISS, A., ASZÓD, A., Sensitivity Studies on CFD analysis for Heat Transfer of Supercritical Water Flowing in Vertical Tubes, Proc. CFD4NRS-4, Daejeon, 2012.
[12.19] BROGNA, C., CFD Modelling of Heated Rod Bundles with Water at Supercritical Pressure, Tesi di laurea magistrale in ingegneria energetica, Università Di Pisa, 2017.
[12.20] BROGNA, C., PUCCIARELLI, A., AMBROSINI, W. et al., Capability of High y^+ Wall Approaches in Predicting Heat Transfer to Supercritical Fluids in Rod Bundle Geometries, Annals of Nuclear Energy, **120**, (2018), 272-278.
[12.21] FILONOV, V.V., FILONOVA, YU.S,, RAZUMOVSKIY, V.G., PIS'MENNYI E.N., On Experimental and Computational Investigation of Heat Transfer Deterioration and Hydraulic Resistance in Annular Channel and SCWR 3-Rod Bundle, Proc. 26th International Conference on Nuclear Engineering (ICONE-26), London, 2018.

13. SUMMARY AND CONCLUDING REMARKS

In closing, the present publication discusses the advancements achieved during the Coordinated Research Project *Understanding and Prediction of Thermal–hydraulics Phenomena Relevant to SCWRs*. A few considerations on the relevance and the perspectives of the material collected so far are in order.

As mentioned in the Introduction, information presented in this TECDOC has been compiled from the second CRP of the IAEA on the issues involved in the design of Generation IV SCWRs, which was initiated to further the results achieved from the first CRP. In fact, it happened that the technical problems addressed in the first CRP were found so intriguing and interesting, and the activities springing from the resulting international cooperation were felt so promising that a second CRP was considered a strict need, in the aim to harvest the knowledge and the wealth of experimental data being produced.

The period in between these two CRPs and the one during the second project witnessed a very fruitful cooperation among the invoved institutions, leading to remarkable contributions in the field. Fluid-to-fluid similarity theories, a better understanding of deteriorated heat transfer phenomena, new data on CHF, flow stability, critical flow, heat transfer in geometries representative of fuel bundles added new material to what already available from previous studies. It should also be considered as a very useful outcome of the new CRP the cohesion established among the cooperating institutions and the expansion of the group of scientists and investigators collected around the problems encountered in the design of the SCWRs. In addition to experts in classical research approaches, as experimentalists and theoreticists aiming at setting up new engineering correlations and models, the group now includes also experts in the techniques of computational fluid-dynamics (CFD) capable to report fundamental data even from direct numerical simulation (DNS) that can shed new light on the tough problems to be tackled, with a level of resolution that cannot be attained with experiments.

The technical developments and the new experiments, going on in particular in Canada, China, India, Ukraine and USA, were certainly worth of this new step, which provided new data on complex geometries as the ones of fuel bundles with different kinds of spacers, bringing the studies from their first steps in relatively simple geometries to a new level of complexity, much closer to the real plant configurations. These new data have been deposited to the central server of the Nuclear Energy Agency for future use. In addition to the current TECDOC, a number of joint conference and journal publications have been (and will be) published to disseminate the technical information, advance the technology and expedite the SCWR development.

Indeed, the wealth of new data and observations achieved during this CRP represents a mine where exploitation would extend beyond the time frame of a CRP. In this regard, future effort is required to draw adequate conclusions from this material, refine prediction tools on the basis of the new information and design new experiments to reveal the subtleties of the intriguing physical phenomena related to the use of fluids at supercritical pressures as coolants and moderators in SCWRs.

This CRP is successful in affirming that the material supports further studies, possibly made in the frame of IAEA. At the end of the previous CRP, the scientists involved in it felt clearly that the investigation on supercritical pressure fluids was just at the beginning of a systematic approach. Now the same group, enlarged with other specialists, feels that we are now in the middle of the path to a complete understanding, fully aware that the new information is starting to tell our minds the reasons of the complex and somehow puzzling behaviour observed with these peculiar fluids.

In this regard, it is necessary to consider that whether a new CRP would be considered feasible for continuing a process of understanding that can be reasonably terminated only when sufficient knowledge will be available to proceed to the design of a prototype, it has to be also suggested that the new pattern of cooperation should allow for better interactions and creative thinking among the participating scientists. The Research Coordination Meetings in the future could leave much more time to free discussions on the technical and scientific issues, taking better use of the time spent together. The greatest added value to research provided by IAEA is in fact achieved in joining for a few days researchers who generally read of each others' work in peer reviewed journal, thus creating intense 'think tanks' focused on the important problems to be solved: apparently too complex problems may turn out into occasions for real breakthroughs achieved by a common effort.

It is with this grateful acknowledgement of the role of IAEA in favouring mutual exchanges in view of problem solving that the group of scientist who contributed to this report presents to the scientific community the fruit of this further step in their path towards a fuller understanding of the fascinating phenomena characterising fluids at supercritical pressures.

Appendix I. COMPARISON OF THERMOPHYSICAL PROPERTIES OF REACTOR COOLANTS

This Appendix is mainly based on or directly reproduced from [I.1] and published with permission from the American Society of Mechanical Engineers (ASME).

Current fleet of nuclear-power reactors uses the following reactor coolants (see Table I.1):

- Light water (H_2O) at subcritical pressures and temperatures[10] - in PWRs (single phase cooling, i.e., liquid cooling); BWRs (two phase cooling, i.e., with flow boiling, outlet reactor steam quality is usually about 10%) and LGRs (two phase cooling, i.e., with flow boiling, outlet fuel-channel steam quality is usually about 14% (maximum – 20%));
- Heavy water (D_2O) at subcritical pressures and temperatures[11] - in PHWRs (single phase cooling, however, there is a possibility for boiling within some subchannels at the fuel-channel outlet, steam quality usually does not exceed 5%);
- Carbon dioxide (CO_2) at subcritical pressures, but at supercritical temperatures[12] – in an GCR and AGRs; and
- Liquid sodium (Na)[13] – in an SFR.

Power cycles of Generation III and III$^+$ NPPs are shown in Dragunov et al.[I.2]].

[10] Water: Critical pressure - 22.064 MPa and critical temperature – 373.95°C.

[11] Heavy water: Critical pressure - 21.671 MPa and critical temperature – 370.7°C.

[12] Carbon dioxide: Critical pressure - 7.3773 MPa and critical temperature – 30.978°C.

[13] Sodium: Melting temperature – 97.7°C and boiling temperature – 882.8°C.

TABLE I.1. TYPICAL RANGES OF THERMAL EFFICIENCIES (GROSS[14]) OF SELECTED MODERN NUCLEAR POWER PLANTS (NPPS SHOWN ACCORDING TO THE DECREASING VALUES OF THERMAL EFFICIENCY) [I.3], [I.4].

No	Nuclear Power Plant	Gross Efficiency
1	AGR NPP (Generation-III); thermal-neutron spectrum; moderator – graphite; reactor coolant - carbon dioxide: P=4 MPa, T_{in}=290°C & T_{out}=650°C; indirect cycle (double loop, i.e., carbon dioxide – water/superheated steam); Rankine power cycle with single steam reheat – primary steam (turbine inlet): P_{in}=17 MPa (T_{sat}=352°C) & T_{in}=560°C; secondary steam: P_{in}≈4.1 MPa (T_{sat}=252°C) & T_{in}=560°C (T_{cr}=374°C)	Up to 42%
2	SFR (based on Russian BN-600 reactor) NPP (Generation-IV); fast-neutron spectrum; no moderator; reactor coolant - sodium: P≈0.1 MPa & T_{in}=380°C & T_{out}=550°C; indirect cycle (triple loop, i.e., sodium-sodium-water/superheated steam); Rankine power cycle with single steam reheat – primary steam (turbine inlet): P_{in}=14.2 MPa (T_{sat}=338°C) & T_{in}=505°C; secondary steam: P_{in}=2.45 MPa (T_{sat}=223°C) & T_{in}=505°C (T_{cr}=374°C)	Up to 40%
3	PWR NPP (Generation-III+ (reactors: EPR, VVER, APR-1400, AP-1000, etc. [I.5]), already put into operation within last years); thermal-neutron spectrum; moderator & reactor coolant - light water: P=15.5 MPa (T_{sat}=345°C) & T_{out}=327°C; indirect cycle (double loop, i.e., water – water/saturated steam); Rankine power cycle with single steam reheat – primary steam (turbine inlet): P_{in}=7.8 MPa & $T_{in/sat}$=293°C	Up to 38%
4	PWR NPP (Generation-III); thermal-neutron spectrum; moderator & reactor coolant - light water: P=15.7 MPa (T_{sat}=346°C) & T_{out}=322°C; indirect cycle (double loop, i.e., water – water/saturated steam); Rankine power cycle with single steam reheat – primary steam (turbine inlet): P_{in}=5.9 MPa & $T_{in/sat}$=274°C; secondary steam: P_{in}=1.15 MPa (T_{sat}=186°C) & T_{in}=250°C	Up to 36%
5	ABWR NPP (first Generation-III$^+$ reactor put into operation in 1996 in Japan); thermal-neutron spectrum; direct cycle (single loop); moderator / reactor coolant / working fluid in Rankine power cycle with single steam reheat – light water; primary steam (turbine inlet): P_{in}=6.97 MPa & $T_{in/sat}$=286°C; secondary steam: P_{in}=1.7 MPa (T_{sat}=204°C) & T_{in}=259°C	Up to 34%
6	LGR (based on Russian RBMK - pressure-channel boiling reactor) NPP (Generation-III); thermal-neutron spectrum; moderator graphite; direct cycle (double loop with steam separator in between); reactor coolant / working fluid in Rankine power cycle with single steam reheat – light water; primary steam (turbine inlet): P_{in}=6.46 MPa & $T_{in/sat}$=280°C; secondary steam: P_{in}=0.29 MPa (T_{sat}=132°C) & T_{in}=263°C	Up to 32%
7	PHWR NPP (Generation-III); thermal-neutron spectrum; moderator - heavy water: P=0.1 MPa & T≈70°C; reactor coolant – heavy water: P_{in}=9.95 MPa (T_{sat}=310°C) & T_{in}=249°C; P_{out}=8.65 MPa (T_{sat}=300°C) & T_{out}=293°C; indirect cycle (double loop, i.e., heavy water – light water/saturated steam); Rankine power cycle with single steam reheat – primary steam (turbine inlet): P_{in}=4.7 MPa & $T_{in/sat}$=260°C; secondary steam: P_{in}=≈1 MPa (T_{sat}=180°C) & T_{in}≈230°C	Up to 32%

[14] Gross thermal efficiency of a unit during a given period of time is the ratio of the gross electrical energy generated by a unit to the thermal energy of a fuel consumed during the same period by the same unit. The difference between gross and net thermal efficiencies includes internal needs for electrical energy of a power plant, which might be not so small (5% or even more).

I.1. GENERATIONS IV REACTORS' COOLANTS

Generation-IV nuclear-reactor concepts will use the following reactor coolants [I.3] (see also, Table I.2):

- Light water (H_2O) at supercritical pressures and temperatures[3] - in SCWRs (single phase cooling, because at supercritical pressures fluids are considered single phase substances);
- Helium (He) at supercritical pressures and temperatures[15] – in GCRs and VHTRs;
- Liquid sodium (Na)[6] – in SFRs;
- Liquid lead (Pb)[16] – in LFRs;
- Liquid Lead-Bismuth Eutectic (LBE) (Pb (44.5%) and Bi (55.5%))[17] - in Liquid Metal-cooled Reactors (LMRs), for example, in Russian SVBRs; and
- Molten fluoride salts (for example, FLiNaK)[18]– in MSRs.

For better understanding of thermodynamics terms such as subcritical/supercritical pressures, supercritical fluid, superheated / saturated steam, etc., thermodynamcis diagrams for light water, carbon dioxide and helium are shown in Fig. I.1–Fig. I.3 (partially based on figures in [I.6]).

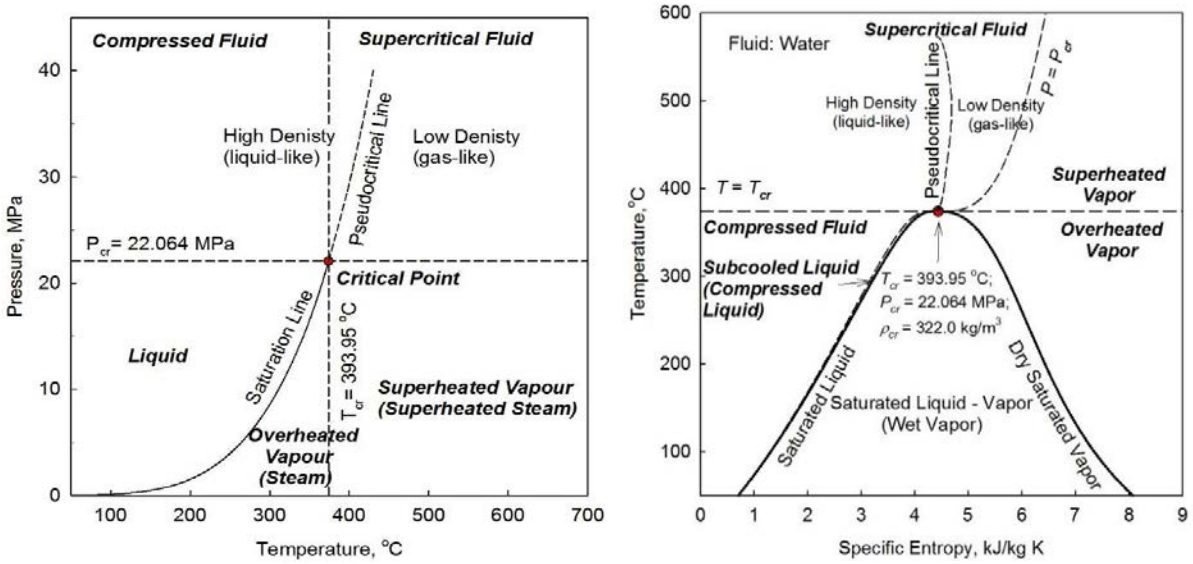

Fig. I.1. Thermodynamics diagrams for light water: (a) Pressure–Temperature diagram; and (b) Temperature–Specific-Entropy diagram.

[15] Helium: Critical pressure - 0.2276 MPa and critical temperature – -267.95°C.

[16] Lead: Melting temperature – 327.5°C and boiling temperature – 1750°C.

[17] LBE: Melting temperature – 123.5°C and boiling temperature – 1670°C.

[18] FLiNaK (LiF-NaF-KF): Melting temperature – 454°C and boiling temperature – 1570°C.

TABLE I.2. ESTIMATED RANGES OF THERMAL EFFICIENCIES (GROSS) OF GENERATION IV NPP CONCEPTS (NPP CONCEPTS SHOWN ACCORDING TO THE DECREASING VALUES OF THERMAL EFFICIENCY) [I.3], [I.4].

No	Nuclear Power Plant	Gross Efficiency
1	VHTR NPP; thermal-neutron spectrum; moderator graphite; reactor coolant – helium: P=7 MPa and T_{in}=640°C & T_{out}=1000°C; primary power cycle – direct Brayton gas-turbine cycle; possible back-up – indirect Rankine steam cycle	≥55%
2	GFR or HTR NPP; fast-neutron spectrum; no moderator; reactor coolant – helium: P=9 MPa and T_{in}=490°C & T_{out}=850°C; primary power cycle – direct Brayton gas-turbine cycle; possible back-up – indirect Rankine steam cycle	≥50%
3	SCWR NPP (one of Canadian concepts, i.e., pressure-channel reactor); thermal-neutron spectrum; moderator – heavy water; reactor coolant – light water: P=25 MPa (P_{cr}=22.064 MPa) and T_{in}=350°C & T_{out}=625°C (T_{cr}=374°C); direct cycle, i.e., single loop; supercritical-pressure Rankine power cycle with single steam reheat – primary steam (turbine inlet): P_{in}=25 MPa (P_{cr}=22.064 MPa) & T_{in}=625°C (T_{cr}=374°C); secondary steam: P_{in}=5.7 MPa (T_{sat}=252°C) & T_{in}=625°C; possible back-up - indirect supercritical-pressure Rankine steam cycle with single steam reheat (superheat)	45-50%
4	MSR NPP; thermal-neutron spectrum (moderator – graphite) or fast-neutron spectrum (no moderator); reactor coolant – sodium-fluoride salt with dissolved uranium fuel: P≈0.1 MPa and T_{out}≈800°C; primary power cycle – indirect supercritical-pressure carbon dioxide Brayton gas-turbine cycle; possible back-up – indirect Rankine steam cycle	~50%
5	LFR NPP (based on Russian design Brest-300 reactor); fast-neutron spectrum; no moderator; reactor coolant – liquid lead: P≈0.1 MPa and T_{in}=420°C & T_{out}=540°C; primary power cycle – indirect supercritical-pressure Rankine steam cycle: P_{in}≈24.5 MPa (P_{cr}=22.064 MPa) and T_{in}=340°C & T_{out}=520°C (T_{cr}=374°C) or subcritical-pressure Rankine steam cycle with superheated steam; single steam reheat; possible back-up in some other countries – indirect supercritical-pressure carbon dioxide Brayton gas-turbine cycle	~43%
6	SFR (based on Russian BN-600 reactor) NPP (Generation-IV); fast-neutron spectrum; no moderator; reactor coolant - sodium: P≈0.1 MPa & T_{in}=380°C & T_{out}=550°C; indirect cycle (triple loop, i.e., sodium-sodium-water/superheated steam); Rankine power cycle with single steam reheat – primary steam (turbine inlet): P=14.2 MPa (T_{sat}=338°C) & T_{in}=505°C (T_{cr}=374°C); secondary steam: P=2.45 MPa (T_{sat}=223°C) & T_{in}=505°C; possible back-up in some other countries - indirect supercritical-pressure carbon dioxide Brayton gas-turbine cycle	~40%

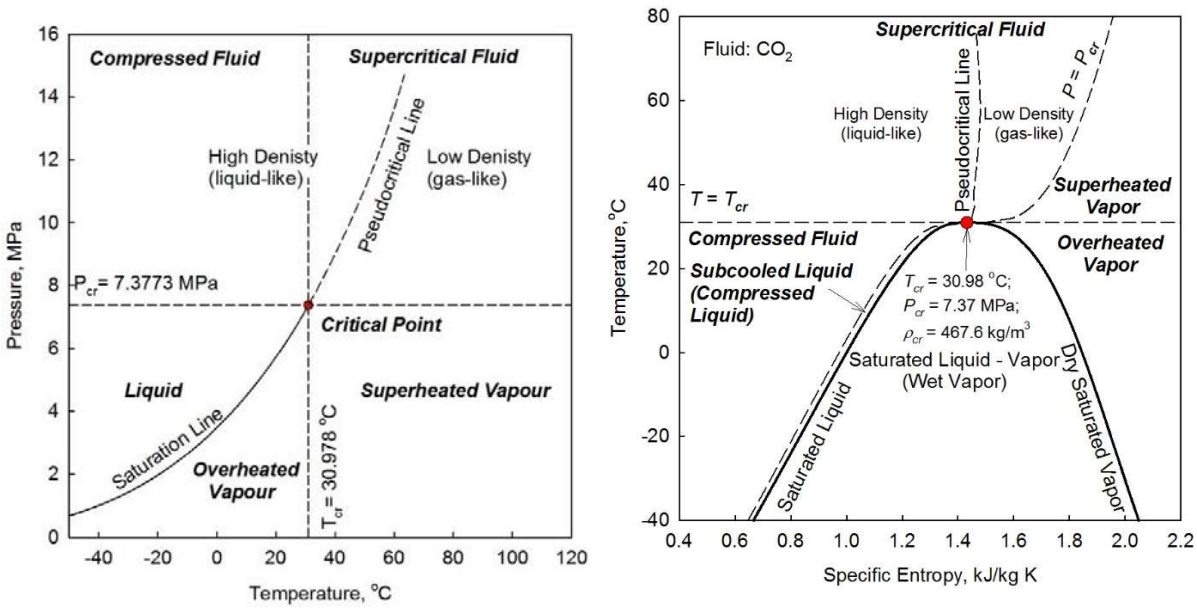

(a) **(b)**

Fig. I.2. Thermodynamics diagrams for carbon dioxide: (a) Pressure–Temperature diagram; and (b) Temperature–Specific-Entropy diagram.

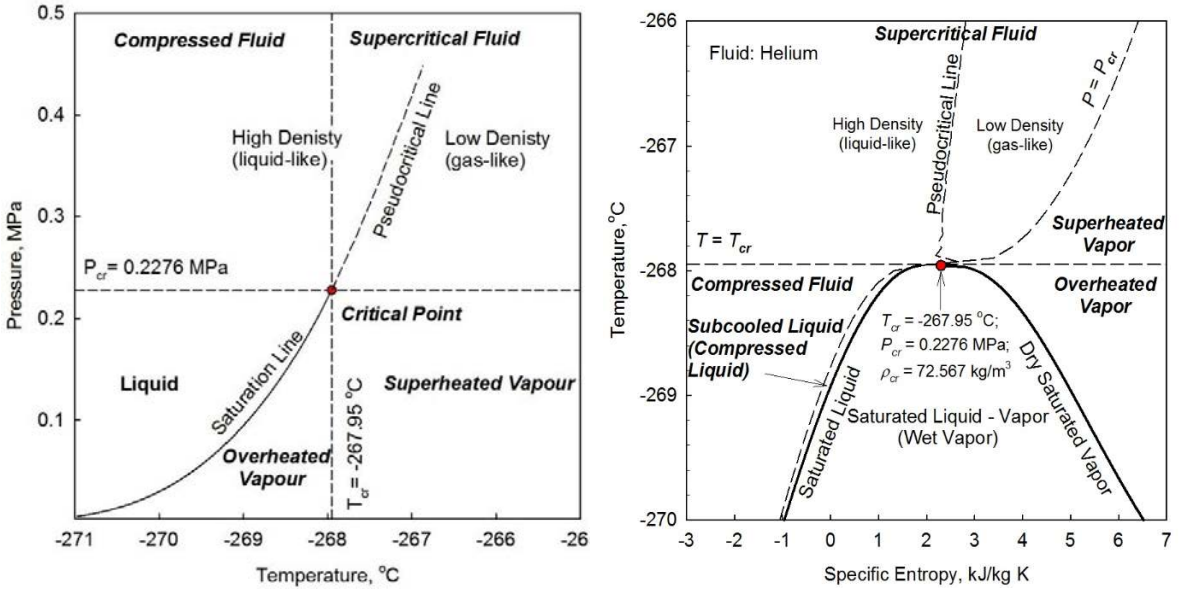

(a) **(b)**

Fig. I.3. Thermodynamics diagrams for helium: (a) Pressure–Temperature diagram; and (b) Temperature–Specific-Entropy diagram.

Glossary of the terms used in Fig. I.1–Fig. I.3 and further in the text are listed below:

— ***Compressed fluid*** is a fluid at a pressure above the critical pressure, but at a temperature below the critical temperature.

— ***Critical point*** (also called a critical state) is a point in which the distinction between the liquid and gas (vapor) phases disappears, i.e., both phases have the same temperature, pressure and specific volume or density. The critical point is characterized with the phase-state parameters T_{cr}, P_{cr} and v_{cr} (or ρ_{cr}), which have unique values for each pure substance.
— ***Pseudocritical line*** is a line, which consists of pseudocritical points.
— ***Pseudocritical point*** (characterized with P_{pc} and T_{pc}) is a point at a pressure above the critical pressure and at a temperature ($T_{pc} > T_{cr}$) corresponding to the maximum value of the specific heat at this particular pressure.
— ***Pseudocritical region*** is actually a narrow region around a pseudocritical point, where all thermophysical properties of a pure fluid exhibit rapid variations. For light water it is about ±25°C from pseudocritical temperature.
— ***Supercritical fluid*** is a fluid at pressures and temperatures that are higher than the critical pressure and critical temperature. However, quite often in various publications, a term supercritical fluid includes both terms – supercritical fluid and compressed fluid.
— ***Overheated vapor*** is a dry vapor at a pressure and temperature below the critical pressure and temperature, respectively, but above the corresponding parameters of dry saturated vapor.
— ***Supercritical 'steam'*** is actually supercritical water, because at supercritical pressures fluid is considered as a single phase substance. However, this term is widely (and incorrectly) used in the literature in relation to supercritical 'steam' generators and turbines.
— ***Superheated vapor*** is a vapor at pressures below the critical pressure, but at temperatures above the critical temperature.

I.2. REACTOR COOLANTS BY TYPE

I.2.1. FLUID COOLANTS

Subcritical-pressure light water is a very well-known and the mostly used reactor coolant, due to that it will be used in the subsequent comparisons as a reference case. In general, heavy water by many thermophysical properties and their behavior is quite close to those of light water (for details, see Table I.3). However, heavy water has significantly lower neutron capture compared to that of light water, which allows more thorough moderation. Therefore, only heat-transfer characteristics of subcritical-pressure heavy water will be compared with those of other coolants.

One of the advantages of light / heavy water is high heat transfer coefficients at forced convection and at flow boiling. However, there is a limit for efficient heat transfer, called critical heat flux, which usually cannot be exceeded during nuclear-reactor operation.

TABLE I.3. COMPARISON OF SELECTED THERMOPHYSICAL PROPERTIES OF HEAVY WATER AND LIGHT WATER [I.2].
(a) at subcooled conditions: P=11 MPa and T=260°C (approximately CANDU-reactor fuel-channel inlet conditions)

Coolant	ρ	c_p	k	μ	Pr
	kg/m^3	J/kg K	W/m K	μPa s	-
D_2O	875.4	4657.1	0.536	114.7	0.997
H_2O	791.5	4887.5	0.618	103.7	0.820
Δ, %	9.6	-5.0	-15.3	9.6	17.7

(b) at saturated conditions: P=10 MPa and T_{sat}=310°C for heavy water (approximately CANDU-reactor fuel-channel outlet conditions) and T_{sat}=311°C (Δ=0.3%) for light water

Coolant	$\frac{\boldsymbol{\rho_f}}{\boldsymbol{\rho_v}}$	$\frac{\boldsymbol{c_{pf}}}{\boldsymbol{c_{pv}}}$	$\frac{\boldsymbol{k_f}}{\boldsymbol{k_v}}$	$\frac{\boldsymbol{\mu_f}}{\boldsymbol{\mu_v}}$	$\frac{\mathbf{Pr_f}}{\mathbf{Pr_v}}$	h_{fg}
	kg/m^3	J/kg K	W/m K	μPa s	-	kJ/kg
D_2O	$\frac{760.0}{62.5}$	$\frac{5823.6}{6730.7}$	$\frac{457.7}{82.0}$	$\frac{89.2}{20.2}$	$\frac{1.13}{1.66}$	1178.8
H_2O	$\frac{688.4}{55.5}$	$\frac{6123.7}{7140.8}$	$\frac{526.8}{76.6}$	$\frac{81.7}{20.2}$	$\frac{0.95}{1.88}$	1317.4
Δ, %	$\frac{9.4}{11.2}$	$\frac{-5.2}{-6.1}$	$\frac{-15.1}{6.6}$	$\frac{8.4}{0}$	$\frac{16.3}{-13.5}$	-11.8

$$\Delta = \frac{Property_{D2O} - Property_{H2O}}{Property_{D2O}} \times 100\%$$

SCW is a coolant in an SCWR concept with an operating pressure of about 25 MPa, and reactor inlet and outlet temperatures of about 350°C and 625°C (max), respectively. Specifics of SCW thermophysical properties and heat transfer are discussed in following publications [I.3], [I.7], [I.8], [I.9], [I.10], [I.11], [I.2], [I.12].

Main disadvantage of water as a reactor coolant is, that to reach higher thermal efficiencies of NPP higher temperatures are needed, which in turn requires high or even supercritical pressures.

I.2.2. GAS COOLANTS

For comparison purposes in this paper, it was also decided to consider subcritical-pressure carbon dioxide. Carbon dioxide at subcritical pressures is currently being used in the most efficient nuclear-power reactors – AGRs. In general, carbon dioxide is not a strong absorber of thermal neutrons and does not become extremely radioactive. Other advantages of carbon dioxide are its chemical stability within the operating range of temperatures (292–650°C). In addition, carbon dioxide does not react with either the moderator or fuel.

Helium as a reactor coolant at high outlet temperatures of 850°C and 1,000°C (in GFR and VHTR, respectively) makes it possible to achieve very high thermal efficiencies of the plant close to those of modern advanced thermal power plants. Major advantages of helium are: 1) relatively high

thermal conductivity compared to that of other gases (exception is hydrogen), which is close to that of liquids; and 2) its behavior as nobble or inert gas.

In general, advantages of gaseous reactor coolants compared to those of water are a possibility to achieve high or even very temperatures at the reactor outlet at significantly lower pressures and there is no critical heat flux phenomena at gas cooling, which limits heat transfer in fluid cooling. However, heat transfer coefficients at gas forced-convection cooling are usually significantly lower than those at water cooling.

I.2.3. LIQUID-METAL COOLANTS

Liquid sodium is currently used in the Russian BN-600 and BN-800 – the only ones operating SFR so far in the world and is proposed to be used in Generation-IV SFRs. Sodium is a well-known low-melting-point (97.7°C) alkali metal, main advantages of which are high thermal conductivity and low neutron-absorption cross section. Also, relatively high boiling point (882.8°C) of sodium allows a reactor to operate at pressures close to ~0.1 MPa. In addition, very high heat transfer coefficients can be achieved at sodium cooling.

However, sodium is very chemically-reactive substance, which requires special precautions to be taken when it used as a reactor coolant. Therefore, for improved reactor safety a secondary sodium loop is utilized, which acts as a buffer between the radioactive sodium – reactor coolant in the primary loop and the water / steam in the third loop – a steam Rankine power cycle.

Lead is proposed for use in an LFR at pressures close to ~0.1 MPa. Lead has higher melting point (327.5°C) and significantly higher boiling point (1,750°C) compared to that of sodium, which significantly impacts the way of a reactor operation. Also, it is more inert liquid metal than sodium, due to that LFR has only two loops: 1) primary with lead as a reactor coolant and 2) secondary with water / steam as a steam Rankine power cycle.

LBE is an eutectic alloy of lead (44.5%) and bismuth (55.5%) being considered as an option for the LFR instead of lead. One of the main advantages of LBE is its melting point of 123.5°C, which is significantly lower than that of lead and quite close to that of sodium. Neither lead nor LBE react readily with water or air, in contrast to sodium, which allows for elimination of the intermediate-coolant loop used in SFRs. Moreover, LBE is not a new technology – it has been proven by years of reliable experience as a coolant in nuclear-powered submarines operated by the Soviet Union since the 1970's.

Major advantage of liquid-metal reactor coolants is low operating pressures inside a reactor (close to atmospheric one) with a possibility to achieve high temperatures. Also, all current liquid-metal reactors are of fast-neutron spectrum, which allow to have more efficient fuel cycles.

More information on liquid-metal reactor coolants cab found in the following publications [I.13], [I.14], [I.15], [I.16].

I.2.4. MOLTEN SALT COOLANTS

Molten salt fluorides, which are proposed as coolants for MSR, have promising thermophysical and thermal hydraulic properties. Molten salts similar to liquid metals have low vapor pressure even at high temperatures, which is quite attractive compared to water and gaseous coolants. Also, salts are less chemically reactive than sodium. In addition, salts can provide moderation due to light elements like FLiBe.

In the next section, a comparison of the main thermophysical properties for all the coolants mentioned above will be conducted. The investigated range of temperatures covers the operating ranges of the corresponding reactors (see Table I.1 and Table I.2, and Fig. A2.4). Basic averaged parameters for each of the reactors in which these coolants are utilized are listed in Table I.4.

I.3. THERMOPHYSICAL PROPERTIES OF PROPOSED GENERATION II, III, III+ AND IV REACTOR COOLANTS

In this section, a comparison of main thermophysical properties of various coolants of Generation-IV reactor systems is presented. It is important to note that basic properties are shown within a wide range of temperatures (from 250°C to 1,000°C), which covers the range of operating ranges of current and Generation-IV reactors (see Fig. I.4 and Table I.1 and Table I.2).

Properties of subcritical and supercritical water, carbon dioxide, and helium-4 were obtained from NIST REFPROP software [I.2]. Properties of sodium were taken from [I.17]. Properties of other coolants were calculated either using original correlations presented in [I.18] or using correlations recommended by authors of this book.

Before comparing thermophysical properties of the coolants (see Fig. I.5–Fig. I.11), it is reasonable to have general overview of the desired characteristics of a generic reactor coolant. Nuclear reactors have certain specific requirements for coolants, such as:

- high specific heat, thermal conductivity and low viscosity;
- low corrosive and low erosive effects on all the reactor materials;
- high boiling point and low melting point (not related to gaseous coolants);
- high thermal resistance and radiation resistance;
- low neutron absorption cross section;
- explosion-proof, non-combustible, non-toxic;
- widely available (not rare); and
- low activation.

TABLE I.4. BASIC REFERENCE PARAMETERS OF SELECTED GENERATIONS II, III, III+ AND IV NUCLEAR-POWER REACTORS/CONCEPTS.

Reactor	**Neutron spectrum**	**Core design**		**Reactor coolant**	**Moderator**	**Reactor cycle**	**No of circuits**	***P***	***T***
								MPa	°C
PWR	Thermal	Heterogeneous	PV	Water		Indirect	2	~15.5	292–329
AGR	Thermal	Heterogeneous	PV*	CO_2	Graphite	Indirect	2	4	292–650
SFR	Fast	Heterogeneous	PV	Sodium	–	Indirect	3	~0.1	370–550
GFR	Fast	Heterogeneous	PV	Helium	–	Direct	1	9	490–850
						Indirect	2		
VHTR	Thermal	Heterogeneous	PV	Helium	Graphite	Direct	1	7	490–1000
						Indirect	2		
LFR	Fast	Heterogeneous	PV	Lead (LBE)	–	Indirect	2	~0.1	550–800 (420–540)
MSR	Epithermal	Homogeneous	PV	Sodium fluoride with dissolve uranium	Graphite	Indirect	3	~0.1	T_{out}=700–800
MSFR	Fast	Homogeneous	PV	Sodium fluoride with dissolve uranium	–	Indirect	3	~0.1	T_{out}=700–800
SCWR	Thermal	Heterogeneous	PV	Water	Water	Direct	1	~25	300–625
			PCh (PT)		Heavy water	Indirect	2		
	Fast		PV	Water	–	Direct	1		300 – 625
			PCh (PT)			Indirect	2		

* Though coolant flows through individual channels inside graphite moderator, the actual pressure boundary is the vessel surrounding the moderator.

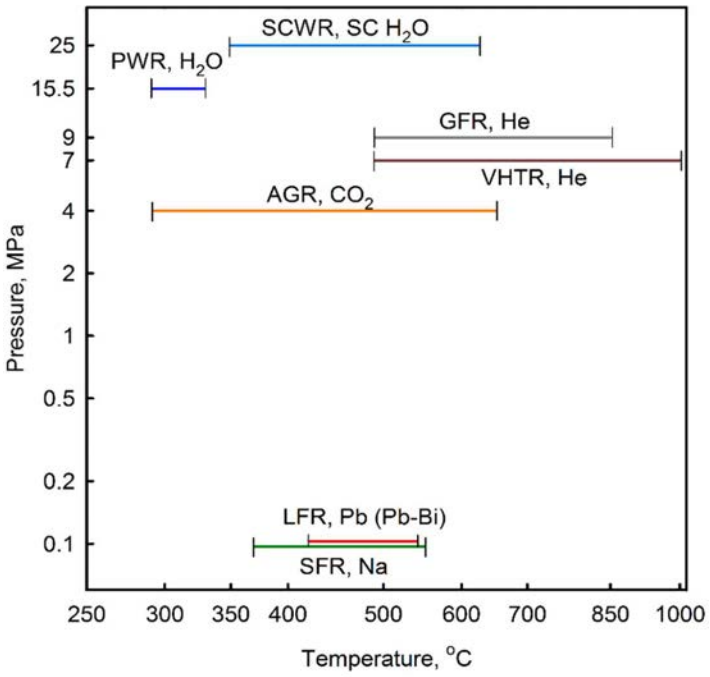

Fig. I.4. Pressure–temperature diagram for PWR, AGR, SFR and proposed Generation IV reactor concepts (pressure drop is not considered).

Fig. I.5 shows densities profiles of reactor coolants vs. temperature. As it is expected molten lead and lead-bismuth alloy have the highest densities following by molten salt and sodium. Actually, at ~250°C densities of molten sodium, subcritical pressure water and SCW are quite close. However, with temperature increase densities of water and SCW steadily decline. Within the pseudocritical range SCW density drops quite significantly due to the transition from 'liquid-like' fluid to 'gas-like' fluid. The lowest densities have gases, especially, helium. The density of carbon dioxide quite significantly higher than that of helium.

In general, densities of reactor coolants with exception of SCW decline almost linearly with temperature increasing (see Fig. I.5). Densities of gases (helium and carbon dioxide) decrease about 1.6 times, but the density change for liquid metals is insignificant. For SCW the density drops almost 8 times within the pseudocritical region.

As one would expect, the thermal conductivity of liquid metals is significantly higher than that of gases (50 – 3,000 times, see Fig. I.6). The thermal conductivity of Na drops slightly, while that for Pb, LBE, He, and CO_2 increases linearly with the temperature. The thermal conductivity behavior of SCW is special. The thermal conductivity decreases linearly for temperature between 250 – 350°C, then goes through a small peak in the pseudocritical point, before decreasing smoothly from about 0.4 to 0.1 W/m·K. As the temperature increases above 500°C the thermal conductivity increase linearly to values higher than those of CO_2, but lower than those of He.

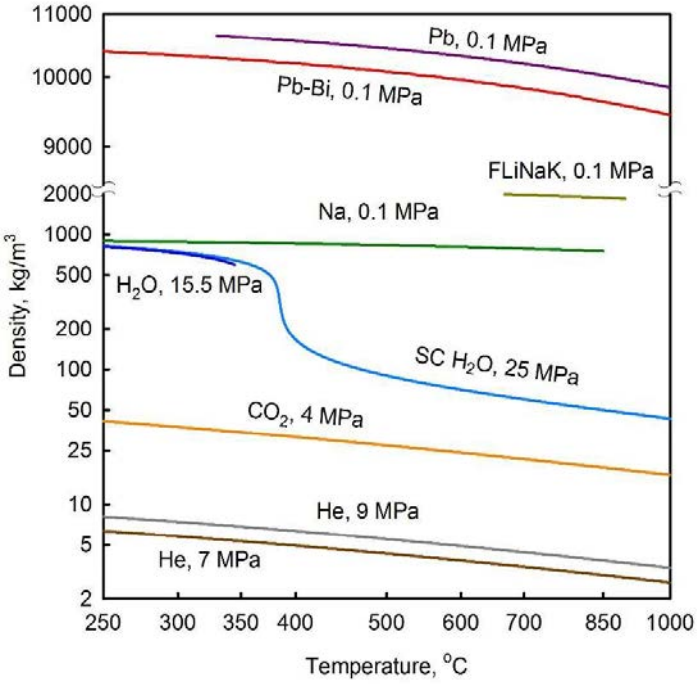

Fig. I.5. Density vs. temperature.

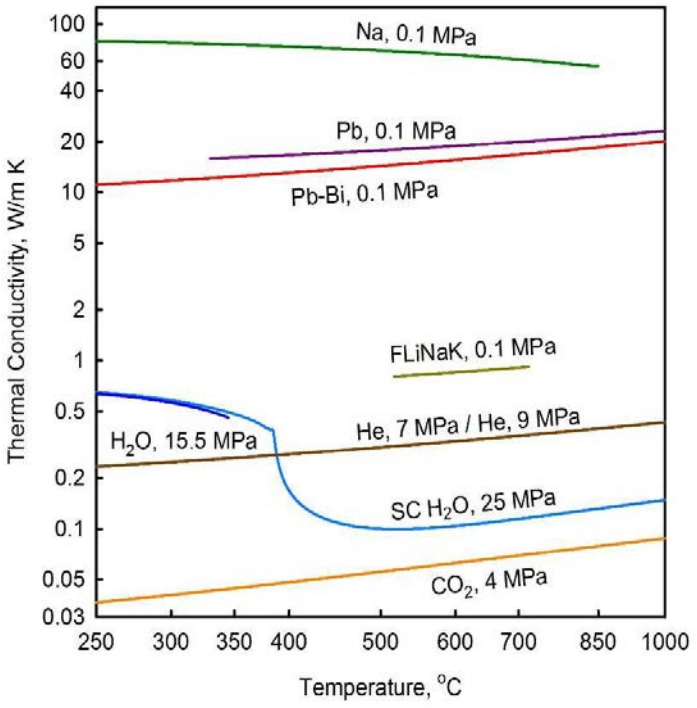

Fig. I.6. Thermal conductivity vs. temperature.

The majority of the thermal properties[20] of FLiNaK molten salt have intermediate values between those of liquid metals and fluids. However, viscosity of FLiNaK appears to be significantly higher than that of the rest of the coolant. This also causes the Prandtl number to be very high.

The temperature dependence of the viscosity of liquid metals is quite the opposite behavior to that of gases (Fig. I.7). The viscosity of Na and Pb drop linearly over the whole range of temperature, while the viscosity of Pb-Bi has a slower linear drop up to 600°C. The viscosity increases for temperatures between 600 and 1,000°C, attaining a value close to that measured at 250°C. Viscosities of gases increase linearly with temperature, and viscosity of SCW at temperatures beyond the pseudocritical range behave in a fashion similar to that of gases. In general, the shape of viscosity–temperature curve for SCW is similar to that of thermal conductivity. However, viscosity does not exhibit a peak in the pseudocritical point.

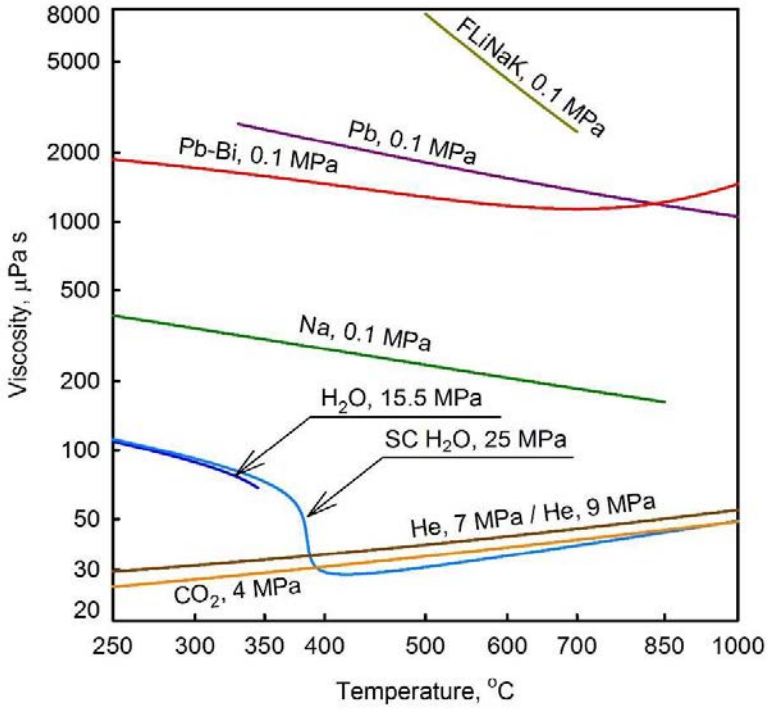

Fig. I.7. Viscosity vs. temperature.

The specific heat of He, Na, Pb, and Pb-Bi (Fig. I.8) is nearly constant over the whole range of operational parameters. In the case of CO_2, the specific heat increases linearly and reaches the same value as Na at around 750°C. The specific heat of water goes through a peak (where its value increases almost 8 times) within the pseudocritical region. The specific heats of Pb and LBE are nearly identical and 10 times less than those of Na and CO_2, and almost 40 times less than that of He. At temperatures higher than 450°C, the specific heat of He is higher than that of SCW.

[20] Thermal properties of FLiNaK were calculated from [I.19], [I.20], [I.21], [I.22].

Fig. I.9 shows enthalpy increase vs. temperature for all reactor coolants. Enthalpy increase is straight-forward related with the behavior of specific heat. Therefore, the highest increase in enthalpy is in SCW, especially, within the pseudocritical range in which specific heat has a peak. Eventually, SCW, water and helium show quite close trends in enthalpy increase. Enthalpy increase for sodium and carbon dioxide are located within the medium range. The lowest enthalpy increase are shown by lead-bismuth alloy, and, especially, by lead itself. And enthalpy rise for molten salt is very sharp starting from relatively low values (below that for lead and lead-bismuth alloy) and almost reaching values for carbon dioxide and sodium at higher temperatures.

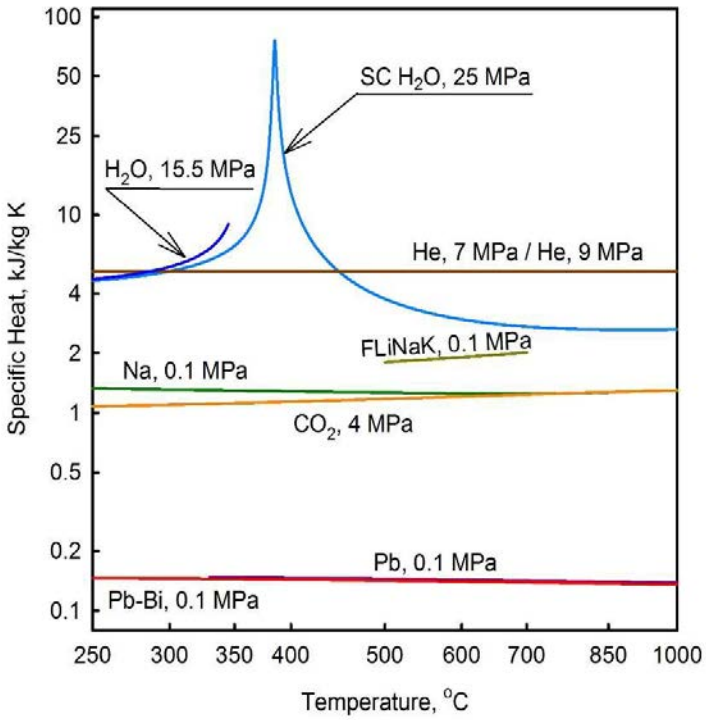

Fig. I.8. Specific heat vs. temperature.

The dependence of the Prandtl number (which is defined as a ratio of product of viscosity and specific heat to thermal conductivity) on temperature for different coolants is shown in Fig. I.10. As follows from the definition, the shape of ***Pr*** is governed by the more significantly changing property of the coolant. We have established that the specific heat is nearly constant for all of the Generation-IV reactors' coolants, except that of SCW. Therefore, for the rest of the coolants ratio of viscosity to thermal conductivity will affect the shape of the ***Pr***/temperature curve.

As we see from Fig. I.6, the changes in viscosity and thermal conductivity of gases are such that they compensate each other, and ***Pr*** of gases is virtually constant over most of the 750°C temperature span. However, for the liquid metals the viscosity drops more significantly than the thermal conductivity increases. As a result, the ***Pr*** of liquid metals drops almost linearly with temperature. Due to an increase in viscosity of LBE at high temperatures, the corresponding value of Prandtl number of Pb-Bi also increases. Since the specific heat of SCW goes through the most

rapid changes compared with its other thermophysical properties, the ***Pr*** of SCW behaves similar to the specific heat. At high temperatures (>500°C), the ***Pr*** of SCW behaves similar to that of gases.

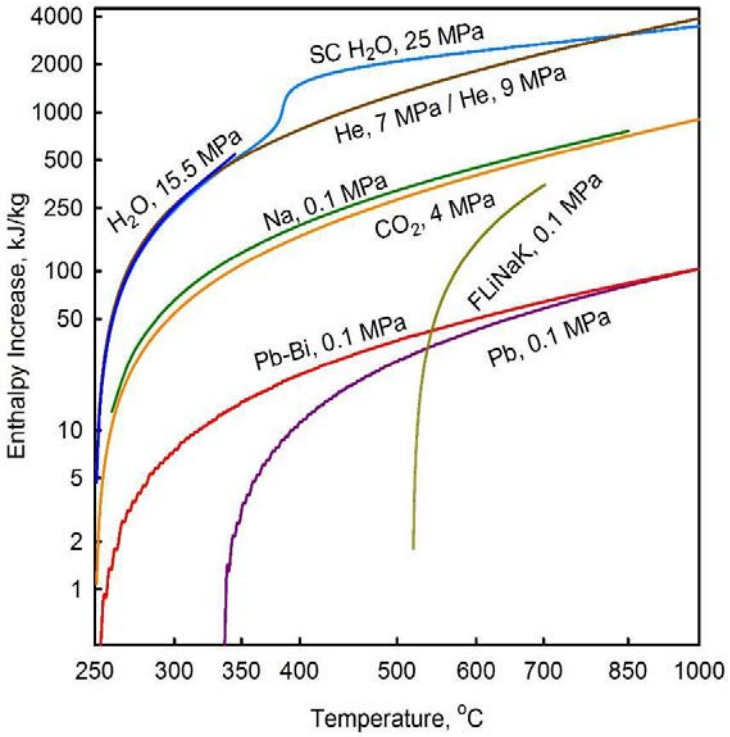

Fig. I.9. Enthalpy vs. temperature.

Volumetric expansivity of liquid metals is much smaller than that of the remaining coolants, and stays almost constant (see Fig. I.11). The volumetric expansivity of gases drops almost twice in a linear fashion, from 250 to 1,000°C. Remarkably, values of volumetric expansivity for SCW at temperatures below the pseudocritical point are close to those for gases. Near the pseudocritical point, the volumetric expansivity of SCW peaks. At higher temperatures, the volumetric expansivity of SCW gradually reaches values corresponding to those of gases.

To summarize the above, the thermophysical properties of liquid metals and gases experience only minor linear changes with increasing temperature. However, all the properties of water at pseudocritical conditions go through very rapid changes. Basic properties of helium, carbon dioxide and water are summarized in Table I.5. Basic properties of lead, molten salt (FLiNaK), and sodium are summarized in Table I.6.

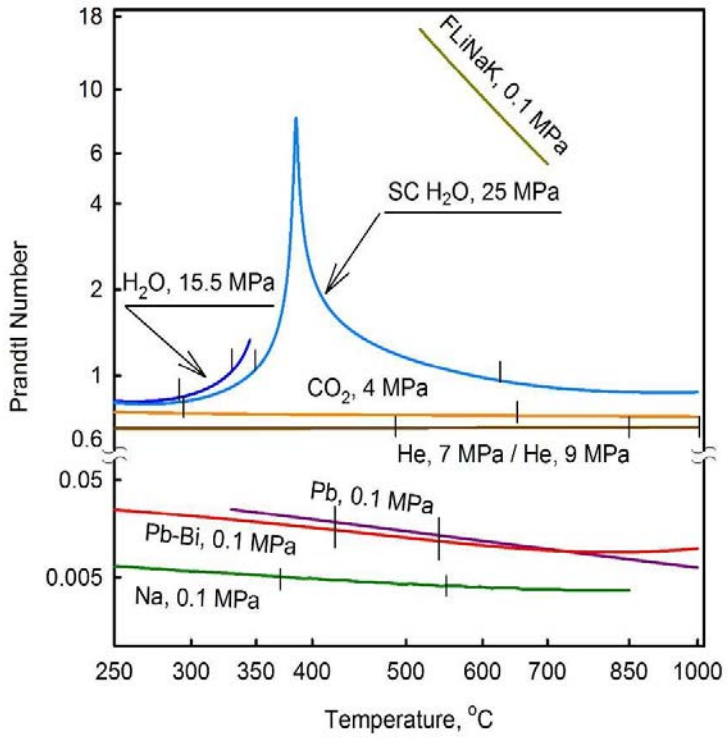

Fig. I.10. Prandtl number vs. temperature.

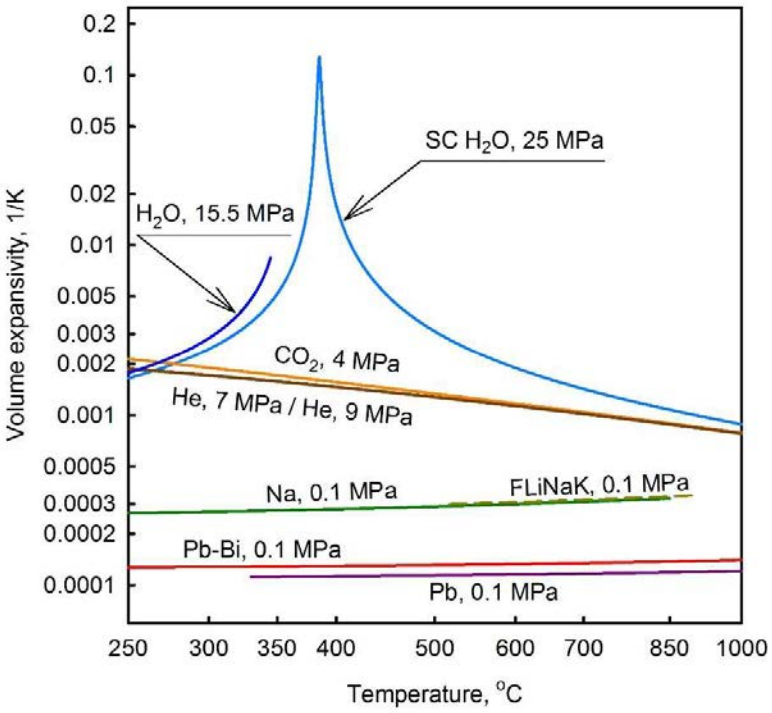

Fig. I.11. Volume expansivity vs. temperature.

TABLE I.5. BASIC PROPERTIES OF HELIUM, CARBON DIOXIDE AND WATER [I.2].

No	Properties	Fluids		
		Helium	**Carbon Dioxide**	**Water**
1	**Chemical formula**	**He**	**CO_2**	**H_2O**
2	**Molar mass, kg/kmol**	4.0026	44.01	18.015
3	**Triple point,°C**	-270.97	-56.558	0.01
4	**Normal boiling-point temperature,°C**	-268.93	-78.464	99.974
5	**Critical point temperature,°C**	-267.95	30.978	373.95
6	**Critical point pressure, MPa**	0.2276	7.3773	22.064
7	**Critical point density, kg/m^3**	72.567	467.6	322.0
8	**Flammability**	-	-	-
9	**Explosion hazard**	-	-	-
10	**Chemical reactivity**	Inert gas	?	?
11	**Toxicity**	-	-	-
12	**Corrosiveness**	Inert gas	?	?

TABLE I.6. BASIC PROPERTIES OF LEAD, LEAD-BISMUTH, MOLTEN SALT AND SODIUM.

No	Properties	Fluids			
		Lead	**Lead-Bismuth**	**Fluoride Salt** [I.21]	**Sodium**
1	**Chemical formula**	**Pb**	**44.5 Pb-55.5 Bi**	**FLiNaK**	**Na**
2	**Molar mass, kg/kmol**	207.2	~208	41.3	23
3	**Density at 20°C, kg/m^3**	11,340	10,500	–	968
4	**Melting-point temperature,°C**	327.5	123.5	454	97.8
5	**Boiling-point temperature,°C**	1749	1670	1570	883
6	**Heat of fusion, kJ/mol (kJ/kg)**	4.77 (23.0)	8.08 (38.8)	–	2.60 (113.0)

7	**Heat of vaporization, kJ/mol (kJ/kg)**	179.5 (866.3)	178.1 (856.3)	–	97.42 (4,236)
8	**Flammability**	Highly purified lead fine powder can ignite in air	?	–	Spontaneously ignites when heated above 115°C in air, which has even modest moisture content; Generates flammable H_2 and caustic sodium hydroxide upon contact with water
9	**Explosion hazard**	?	?	–	Sodium powder is highly explosive in water and may spontaneously explode in the presence of oxygen
10	**Chemical reactivity**	Reactive (oxidized in air)	Corrosive	–	Highly reactive
11	**Toxicity**	Highly poisonous	?	–	Can be poisonous
12	**Corrosiveness**	?	?	Intrinsically non-corrosive	High

I.4. HEAT TRANSFER COEFFICIENTS IN NUCLEAR-POWER RECTORS

Typical heat transfer coefficient ranges for various reactor coolants are listed in Table I.7. It shows that sodium has the highest heat transfer coefficient among all the proposed coolants, making it more competitive.

Fig. I.12 shows calculated heat transfer coefficients at conditions corresponding to those of the operating reactors. The calculated values fall very close to those presented in Table I.7. Among the coolants considered, sodium in conditions close to SFR, has the highest heat transfer coefficient of all the proposed (70 – 80 kW/m^2K). Conditions achieved in a generic CANDU reactor (added for comparison purposes) allow heat transfer coefficients above 60 kW/m^2K. Calculations also showed that in PWR, the heat transfer coefficients are about 45 kW/m^2K. Lead, as expected, has heat transfer coefficients around 25 kW/m^2K, which is lower than that of another liquid-metal – sodium. Heat transfer coefficients of SCW (5 – 15 kW/m^2K) and CO_2 (1.8 – 2.5 kW/m^2K) also lie within the typical ranges of values.

TABLE I.7. TYPICAL RANGES OF HEAT TRANSFER COEFFICIENTS, HEAT FLUXES AND SHEATH TEMPERATURES FOR REACTORS' COOLANTS (PARTIALLY BASED ON [I.23] AND DATA PROVIDED BY [I.17]).

Typical ranges of heat transfer coefficients for reactors' coolants		
Coolant	**Heat transfer coefficient, kW/m^{2}K**	
Na (forced convection) (~SFR conditions)	50–80	
Boiling water (flow boiling) (~BWR conditions)	~40	
CANDU reactor	~50	
Water (single phase forced convection)	~30	
SCW (~SCWR conditions)	7-10	
Pb (forced convection) (~LFR conditions)	25–35	
Pb-Bi (forced convection) (~SVBR conditions)	20–30	
He (rough surface)	10	
CO_2 (high pressure) (~AGR conditions)	2–5	
Typical ranges of heat fluxes for reactors' coolants		
Coolant	**Heat Flux, kW/m^2**	**T_{sheath}-$T_{coolant}$, ^{o}C**
Na (forced convection) SFR	2000 (1800-2400)	25-30
Water (single phase forced convection)	1500	50
Boiling water (flow boiling) BWR	1000	15
CANDU reactor	625	15
Boiling water in a kettle	150	15
Reactor Type	**Sheath Temperature, ^{o}C**	
AGR	750	
SFR	700	
GCR (MAGNOX)	450	
PWR	390	
BWR	300	

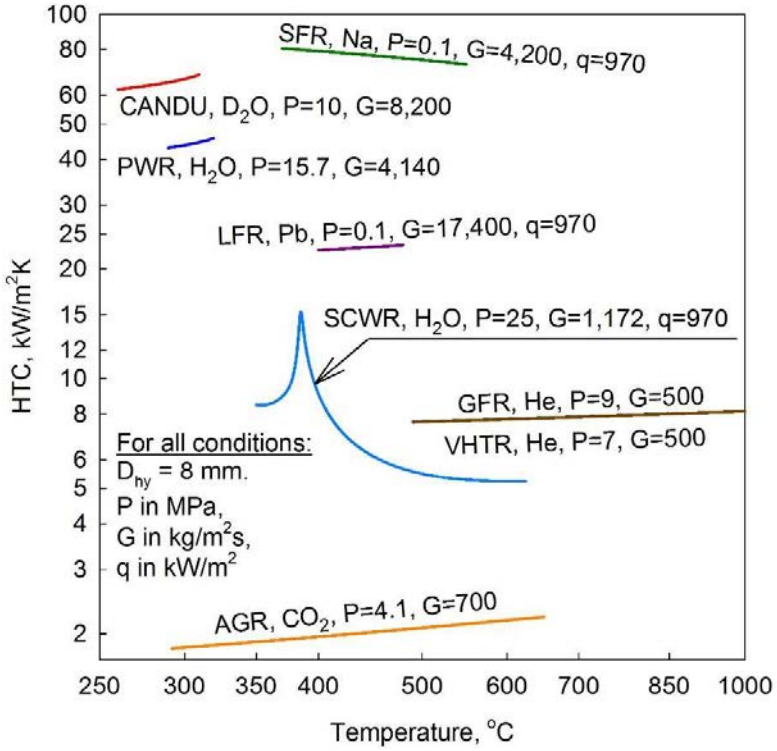

Fig. I.12. Heat transfer coefficients calculated for a flow of coolants of Generation-IV, AGR and PWR reactors in a bare tube at nominal operating pressures and at mass fluxes close to actual mass fluxes in the reactors.

For calculations of subcritical H_2O, D_2O, CO_2 and He the value of heat flux was not taken into account, while for SC H_2O, Pb and Na value of heat flux was assumed to be 970 kW/m^2. Hydraulic equivalent diameter of 8 mm was used in calculations for all the coolants.

Fig. I.13 shows heat transfer coefficients calculated for all coolants (including FLiNaK) at generic conditions: G = 1000 kg/m^{2}s, q = 970 kW/m^{2}K, and D_{hy} = 8 mm.

It can be seen that at the chosen generic conditions, sodium coolant has the highest heat transfer coefficients, ranging from 58 – 96 kW/m^{2}K, while CO_2 and FLiNaK have the lowest heat transfer coefficients, ranging from 1 – 4 kW/m^{2}K. The heat transfer coefficient of SCW starts at ~5 kW/m^{2}K, then goes through a peak within the pseudocritical region, where its value increases by almost 2 times, and after that drops close 4 kW/m^{2}K at temperatures above 450°C. Heat transfer coefficients of the gases, water, heavy water, and lead increase slightly with temperature. Heat transfer coefficients of molten salt increase quite significantly with temperature. The heat transfer coefficient of sodium drops linearly with temperature increase.

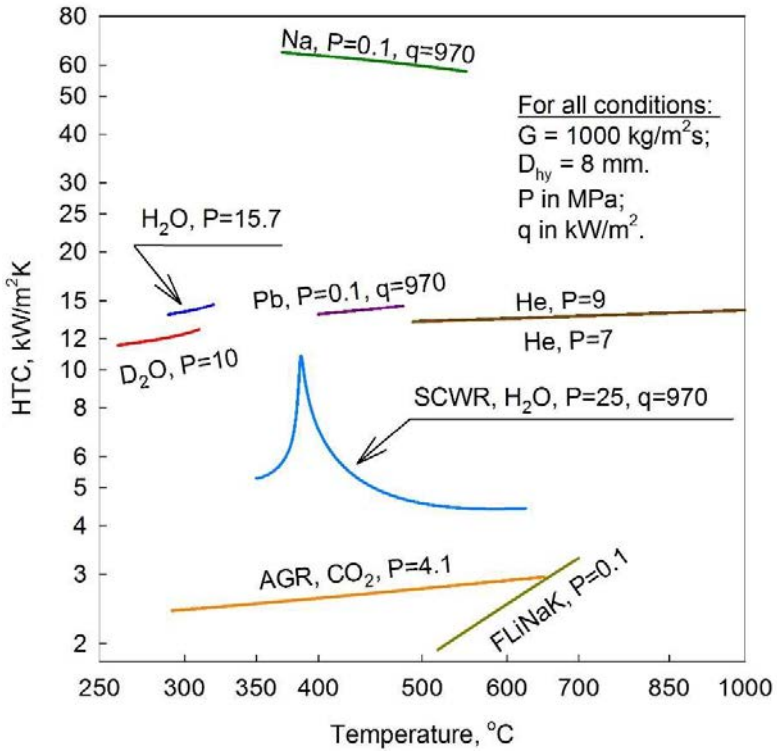

Fig. I.13. Heat transfer coefficients calculated for a flow of coolants of Generation-IV, AGR and PWR reactors in a bare tube at generic operating conditions.

Nomenclature and Acronyms

a	power removed/required circulation power ratio
c_p	specific heat at constant pressure, J/kg·K
D_{hy}	hydraulic-equivalent diameter, m
G	mass flux, kg/m^{2}s
HTC	heat transfer coefficient, W/m^{2}K
h_{fg}	Latent heat of vaporization, J/kg
k	thermal conductivity, W/m K
$\dot{m}$	mass flow rate, kg/s
P	pressure, Pa
$\dot{Q}$	heat-transfer rate, W
q	heat flux, W/m^{2}K
T	temperature,°C
v	specific volume, m^3/kg
W	circulation power, W

Greek symbols

Δ	difference
μ	dynamic viscosity, Pa·s

ρ density, kg/m^3

Non-Dimensional Numbers

Nu Nusselt number $\left(\frac{HTC \cdot D_{hy}}{k}\right)$

Pr Prandtl number $\left(\frac{\mu \cdot c_p}{k}\right)$

Re Reynolds number $\left(\frac{G \cdot D_{hy}}{\mu_b}\right)$

Subscipts

cr	critical
el	electrical
f	fluid
fg	fluid-gas
hy	hydraulic-equivalent
in	inlet
max	maximum
out	outlet
sat	saturation
scw	supercritical water
v	vapor

Acronyms

HTC	Heat Transfer Coefficient
LBE	Lead-Bismuth Eutectic
PCh	Pressure Channel
PT	Pressure Tube
PV	Pressure Vessel
REFPROP	REFerence PROPerties
SC	SuperCritical
TECDOC	TEChnical DOCument

REFERENCES TO APPENDIX I

[I.1] DRAGUNOV, A., SALTANOV, EU., PIORO, I., IKEDA, B., MILETIC, M., ZVORYKINA, A., Investigation of Thermophysical and Nuclear Properties of Prospective Coolants for Generation-IV Nuclear Reactors, Proc. 21st International Conference on Nuclear Engineering (ICONE-21), Chengdu, 2013.

[I.2] DRAGUNOV, A., SALTANOV, EU., PIORO, I., KIRILLOV, P., DUFFEY, R., Power cycles of Generation III and III+ nuclear power plants, ASME Journal of Nuclear Engineering and Radiation Science 1 (2015)

[I.3] Handbook of Generation IV Nuclear Reactors, Editor: I.L. Pioro, Elsevier – Woodhead Publishing, Duxford, (2016).

[I.4] PIORO, I.L., DUFFEY, R.B., Nuclear Power as a Basis for Future Electricity Generation, ASME Journal of Nuclear Engineering and Radiation Science, **1, 1**, (2015).

[I.5] PIORO, I., DUFFEY, R.B., KIRILLOV, P.L., PIORO, R., ZVORYKIN, A., MACHRAFI, R., Current Status and Future Developments in Nuclear-Power Industry of the World, ASME Journal of Nuclear Engineering and Radiation Science, **5, 2**, (2019).
[I.6] MANN, D., PIORO, I., Study on Specifics of Thermophysical Properties of Supercritical Fluids in Power Engineering Applications, Proc. 23rd International Conference on Nuclear Engineering (ICONE-23), Chiba, 2015.
[I.7] INTERNATIONAL ATOMIC ENERGY AGENCY, Heat Transfer Behaviour and Thermohydraulics Code Testing for Supercritical Water Cooled Reactors (SCWRs), IAEATECDOC-1746, IAEA, Vienna (2014).
[I.8] GUPTA, S., SALTANOV, EU., MOKRY, S.J., PIORO, I., TREVANI, L., MCGILLIVRAY, D., Developing Empirical Heat-Transfer Correlations for Supercritical CO_2 Flowing in Vertical Bare Tubes, Nuclear Engineering and Design, **261**, (2013), 116-131.
[I.9] PIORO, I., The Potential Use of Supercritical Water-Cooling in Nuclear Reactors, Nuclear Energy Encyclopedia: Science, Technology, and Applications, Editors: S.B. Krivit, J.H. Lehr and Th.B. Kingery, J. Wiley & Sons, Hoboken, NJ, USA, (2011), 309–347.
[I.10] PIORO, I., MOKRY, S., DRAPER, SH., Specifics of Thermophysical Properties and Forced-Convective Heat Transfer at Critical and Supercritical Pressures, Reviews in Chemical Engineering, **27, 3-4**, (2011), 191-214.
[I.11] PIORO, I., MOKRY, S., Thermophysical Properties at Critical and Supercritical Conditions, Heat Transfer. Theoretical Analysis, Experimental Investigations and Industrial Systems, Editor: A. Belmiloudi, INTECH, Rijeka, Croatia, (2011), 573-592.
[I.12] PIORO, I.L., DUFFEY, R.B., Heat Transfer and Hydraulic Resistance at Supercritical Pressures in Power Engineering Applications, ASME Press, (2007).
[I.13] BEZNOSOV, A.V., DRAGUNOV, YU.G., RACHKOV, V.I., Heavy-Liquid Metal Coolants in Nuclear Engineering, IzdAt Publishing House, Moscow, Russia, 2007, (in Russian).
[I.14] TODREAS, N.E., MACDONALD, P.E., HEIZLAR P., BUONGIORNO, J., LOEWEN, E., Medium-Power Lead-Alloy Reactors: Missions for this Reactor Technology, Nuclear Technology, **147, 3**, (2004), 305.
[I.15] DEMENTYEV, B.D., Nuclear Power Reactors, Energoatomizdat Publishing House, Moscow, Russia, 1990 (In Russian).
[I.16] WALTAR, A.E., REYNOLDS A.B., Fast Breeder Reactors, Pergamon Press, USA, 1981.
[I.17] KIRILLOV, P.L., TERENTIEVA, M.I., DENISKINA, N.B., Thermophsical Properties of Materials for Nuclear Engineering, 2nd ed., IzdAT Publishing House, Moscow, Russia, 2007.
[I.18] Nuclear Energy Agency, Handbook on Lead-bismuth Eutectic Alloy and Lead Properties, Materials Compatibility, Thermal–hydraulics and Technologies, Organisation for Economic Co-operation and Development (OECD), 2007.
[I.19] SOHAL, M., EBNER, M., SABHARWALL, P., SHARPE, PH., Engineering Database of Liquid Salt Thermophysical and Thermochemical Properties, INL/EXT-10-18297 report, 2010.

[I.20] KHOKHLOV, V., IGNATIEV, V., AFONICHKIN, V., Evaluating Physical Properties of Molten Salt Reactor Fluoride Mixtures, Journal of Fluorine Chemistry, **130**, (2009), 30–37.
[I.21] WILLIAMS, D.F., TOTH, L.M., CLARNO, K.T., Assessment of Candidate Molten Salt Coolants for the Advanced High-Temperature Reactor (AHTR), Oak Ridge National Lab. Report ORNL-TM-12, 2006.
[I.22] CHRENKOVA, M., DANEK, V., VASILJEV, R., SILNY, A., KREMENETSKY, V., POLYAKOV, E., Density and Viscosity of the $(LiF\text{-}NaF\text{-}KF)_{eut}$–$KBF_4$–$B_2O_3$ Melts, Journal of Molecular Liquids, **102, 1**, (2003), 213–226.
[I.23] HEWITT, G.F., COLLIER, J.G, Introduction to Nuclear Power, 2nd edition, Taylor and Francis Publishing Office, USA, 2000.

Appendix II. HEAT TRANSFER AND PRESSURE DROP IN FORCED CONVECTION TO FLUIDS AT SUPERCRITICAL PRESSURES

This Appendix is mainly based on Ref [II.1]

The first works devoted to the problem of heat transfer at supercritical pressures started as early as the 1930s [II.1] PIORO, I., MOKRY, S., 2011. "Heat transfer to fluids at supercritical pressures", Heat Transfer. Theoretical Analysis, Experimental Investigations and Industrial Systems (BELMILOUDI, A., Ed.), INTECH (2011) Ch. 19.
[II.2]. investigated free-convection heat transfer of fluids at the near critical point with the application to a new effective cooling system for turbine blades in jet engines. They found that the free-convection heat transfer coefficient at the near critical state was quite high, and decided to use this advantage in single phase thermosyphons with an intermediate working fluid at the near critical point.

In the 1950s, the idea of using supercritical water appeared to be rather attractive for steam generators/turbines in the thermal-power industry. The objective was to increase the total thermal efficiency of coal-fired thermal power plants. At supercritical pressures there is no liquid-vapour phase transition; therefore, there is no such phenomenon as Critical Heat Flux (CHF) or dryout. It is only within a certain range of parameters that deteriorated heat transfer may occur. Work in this area was mainly performed in the former USSR and in the USA in the 1950s – 1980s. At the end of the 1950s and the beginning of the 1960s, early studies were conducted to investigate a possibility of using supercritical water in nuclear reactors. Several concepts of nuclear reactors using supercritical water were developed in Great Britain, France, the USA, and the former USSR. However, this idea was abandoned for almost 30 years with the emergence of Light Water Reactors (LWRs), but regained interest in the 1990s following LWRs' maturation [II.1], [II.3], [II.4], [II.5], [II.6], [II.7].

The most widely used supercritical fluids are water and after that carbon dioxide, helium and refrigerants. Quite often, carbon dioxide and refrigerants are considered as modeling fluids and used instead of water due to significantly lower critical pressures and temperatures, which decreases the complexity and costs of thermalhydraulic experiments.

II.1. DEFINITIONS OF TERMS AND EXPRESSIONS RELATED TO SUPERCRITICAL-PRESSURE HEAT TRANSFER

Prior to a general discussion on specifics of forced-convective heat transfer at critical and supercritical pressures, it is important to define special terms and expressions used at these conditions. For a better understanding of these terms and expressions their definitions are listed below together with complementary Fig. II.1.

- ***Deteriorated Heat Transfer (DHT)*** is characterized with lower values of the heat transfer coefficient compared to those for normal heat transfer; and hence, has higher values of wall temperature within some part of a test section or within the entire test section.
- ***Improved Heat Transfer (IHT)*** is characterized with higher values of the heat transfer coefficient compared to those for normal heat transfer; and hence, lower values of wall

temperature within some part of a test section or within the entire test section. In our opinion, the improved heat-transfer regime or mode includes peaks or 'humps' in the heat transfer coefficient near the critical or pseudocritical points.

— ***Normal Heat Transfer (NHT)*** can be characterized in general with heat transfer coefficients similar to those of subcritical convective heat transfer far from the critical or pseudocritical regions, when they are calculated according to the conventional single phase Dittus–Boelter type correlations: $\mathbf{Nu} = 0.0243\ \mathbf{Re}^{0.8}\mathbf{Pr}^{0.4}$.

— ***Pseudo-boiling*** is a physical phenomenon similar to subcritical-pressure nucleate boiling, which may appear at supercritical pressures. Due to heating of a supercritical fluid with a bulk fluid temperature below the pseudocritical temperature (high-density fluid, i.e., 'liquid'), some layers near the heating surface may attain temperatures above the pseudocritical temperature (low-density fluid, i.e., 'gas'). This low-density 'gas' leaves the heating surface in a form of variable density (bubble) volumes. During the pseudo-boiling, the heat transfer coefficient usually increases (improved heat-transfer regime).

— ***Pseudo-film boiling*** is a physical phenomenon similar to subcritical-pressure film boiling, which may appear at supercritical pressures. At pseudo-film boiling, a low-density fluid (a fluid at temperatures above the pseudocritical temperature, i.e., 'gas') prevents a high-density fluid (a fluid at temperatures below the pseudocritical temperature, i.e., 'liquid') from contacting ('rewetting') a heated surface. Pseudo-film boiling leads to the deteriorated heat-transfer regime.

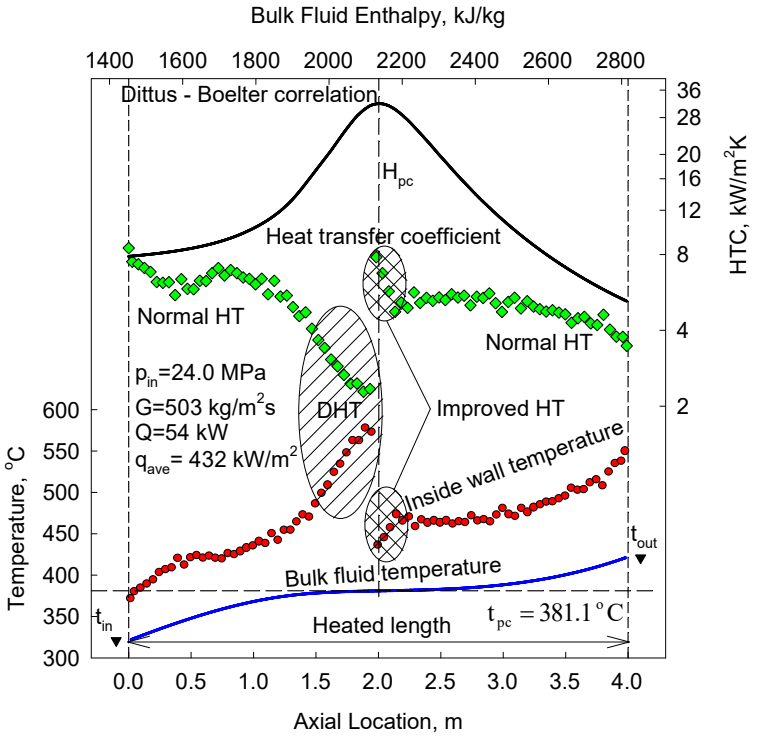

Fig. II.1. Temperature and Heat-Transfer-Coefficient (HTC) profiles along heated length of vertical circular tube (data by [II.8]): Water, D = 10 mm and L_h = 4 m.

II.2. SPECIFICS OF FORCED CONVECTION HEAT TRANSFER AT SUPERCRITICAL PRESSURES

Water is the most widely used coolant or working fluid at supercritical pressures. The largest application of supercritical water is in supercritical 'steam' generators and turbines, which are widely used in the thermal-power industry worldwide. Currently, upper limits of pressures and temperatures used in the thermal-power industry are about 30 – 38 MPa and 600 – 625ºC, respectively. A new direction in supercritical-water application in the power industry has been the development of SCWR concepts, as part of the Generation-IV International Forum (GIF) initiative [II.1], [II.3], [II.4], [II.5], [II.6], [II.7] (for details, see proceedings of the International Symposiums on SCWRs (ISSCWR); the ISSCWR-7 was in 2015 and ISSCWR-8 was in 2017, and selected augmented and revised papers have been published in the ASME Journal of Nuclear Engineering and Radiation Science in 2016, Vol. 2, No. 1 and in 2018, Vol. 4, No. 1). However, other areas of using supercritical water exist [II.7].

Experiments at supercritical pressures are very expensive and require sophisticated equipment and measuring techniques. Therefore, some of these studies (for example, heat transfer in fuel bundles) are proprietary and, hence, are not published in open literature.

The majority of studies deal with heat transfer and hydraulic resistance of working fluids, mainly water, carbon dioxide and helium, in circular bare tubes [II.7]. A limited number of studies were devoted to heat transfer and pressure drop in annuli, rectangular-shaped channels and bundles [II.3], [II.7], [II.9], [II.10].

Accounting that supercritical water and carbon dioxide are the most widely used fluids and that the majority of experiments were performed in circular tubes, specifics of heat transfer and pressure drop, including generalized correlations, will be discussed in this paper based on these conditions. Specifics of heat transfer and pressure drop at other conditions and/or for other fluids are discussed in [II.7].

II.2.1. BASICS OF SUPERCRITICAL HEAT TRANSFER

All primary sources (i.e., all sources found by the authors from a total of 650 references dated mainly from 1950 till beginning of 2006) of heat-transfer experimental data for water and carbon dioxide flowing inside circular tubes at supercritical pressures are listed in [II.7].

In general, three major heat transfer regimes (for their definitions, see the beginning of the paper) can be noticed at critical and supercritical pressures (for details, see Fig. II.1):

- Normal heat transfer;
- Improved heat transfer; and
- Deteriorated heat transfer.

Also, two special phenomena (for their definitions, see the beginning of this Section) may appear along a heated surface: 1) pseudo boiling; and 2) pseudo film boiling.

These heat transfer regimes and special phenomena appear to be due to significant variations of thermophysical properties near the critical and pseudocritical points and due to operating conditions.

Therefore, the following conditions can be distinguished at critical and supercritical pressures (partially shown in Fig. II.1 and Fig. II.2):

- Wall and bulk fluid temperatures are below a pseudocritical temperature within a part of or for the entire heated channel;
- Wall temperature is above, and bulk fluid temperature is below a pseudocritical temperature within a part of or for the entire heated channel;
- Wall temperature and bulk fluid temperature is above a pseudocritical temperature within a part of or for the entire heated channel;
- High heat fluxes;
- Entrance region;
- Upward and downward flows;
- Horizontal flows; and
- Effect of gravitational forces at lower mass fluxes; etc.

All these conditions can affect supercritical heat transfer.

Fig. II.3 shows temperature and thermophysical-properties profiles along heated length of vertical circular tube (operating conditions in this figure correspond to those in Fig. II.2).

Some researchers have suggested that variations in thermophysical properties near critical and pseudocritical points result in the maximum value of HTC. Thus, [II.11] found that for water flowing in vertical and horizontal tubes, the HTC increases significantly within the pseudocritical region (Fig. II.4). The magnitude of the peak in HTC decreases with increasing heat flux and pressure. The maximum HTC values correspond to a bulk fluid enthalpy, which is slightly less than the pseudocritical bulk fluid enthalpy.

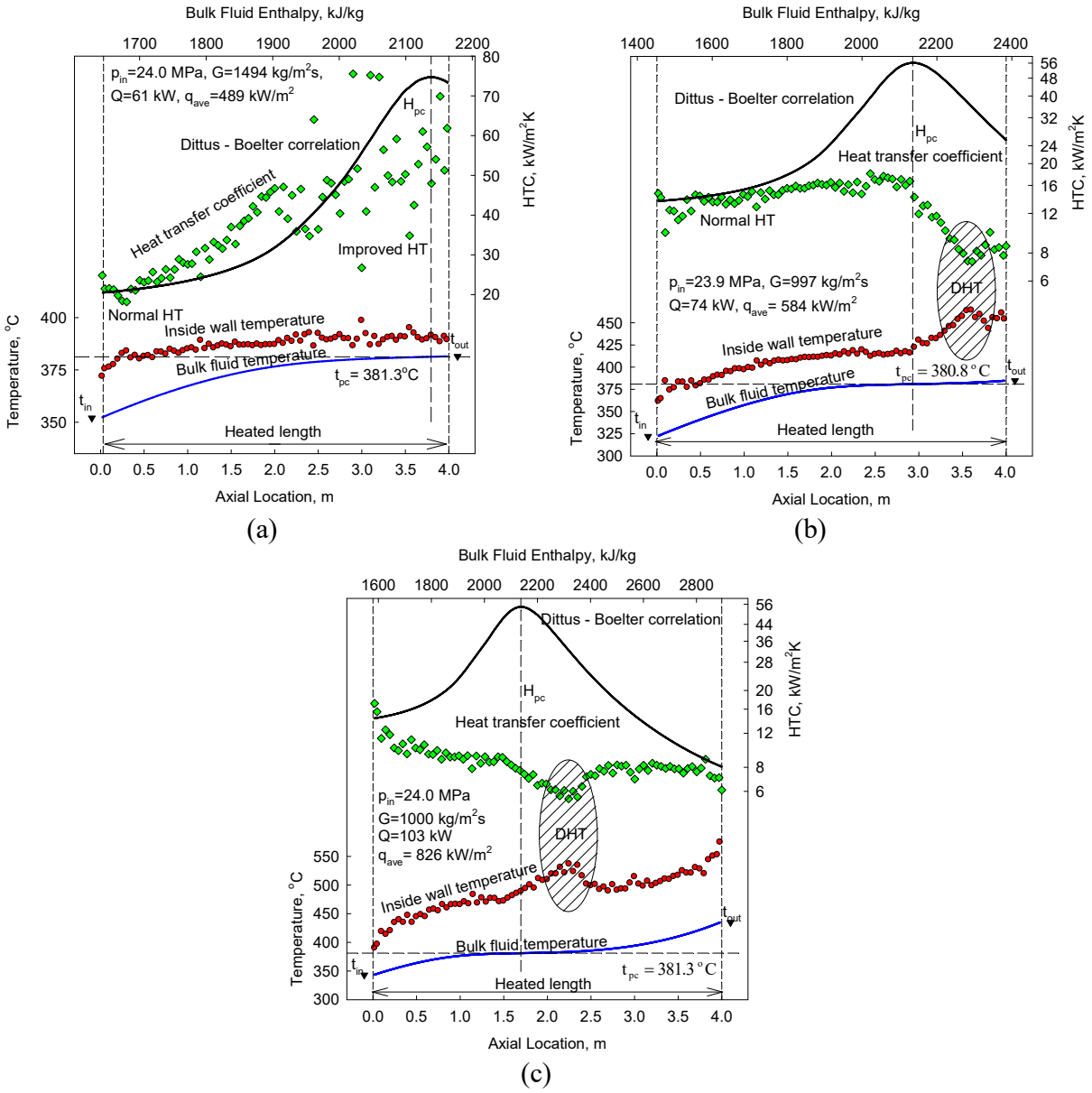

Fig. II.2. Temperature and heat-transfer-coefficient profiles along heated length of vertical circular tube (data by [II.8]): Water, D = 10 mm and L_h = 4 m; (a) Bulk fluid temperature ranges from below to the pseudocritical temperature; (b) Bulk fluid temperature ranges from below to slightly above the pseudocritical temperature; and (c) Bulk fluid temperature ranges from below to above the pseudocritical temperature.

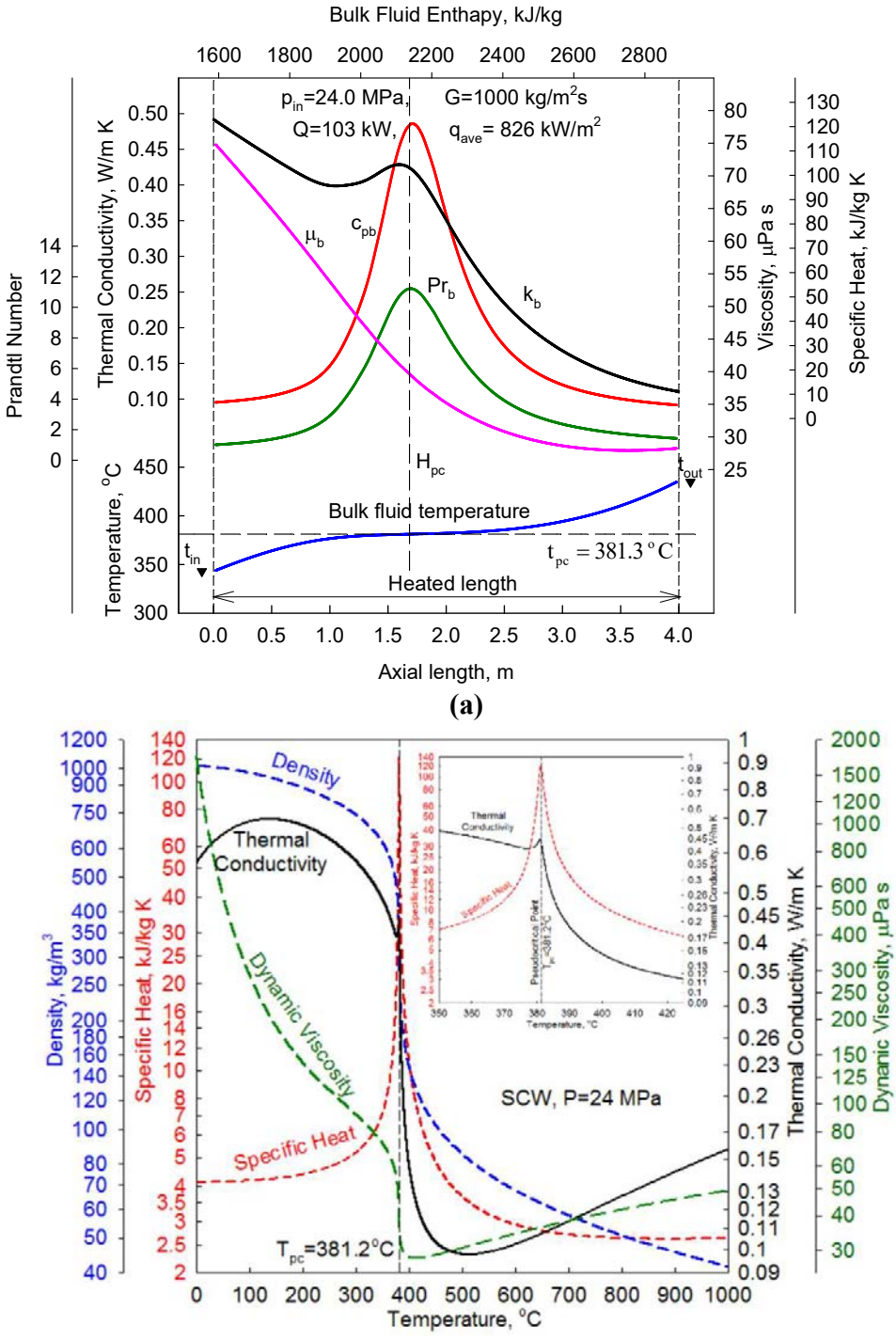

Fig. II.3. Thermophysical-properties profiles of SCW at P=24 MPa: (a) along heated length of vertical circular tube (operating conditions in this figure correspond to those in Fig. II.2c): D = 10 mm and L_h = 4 m; thermophysical properties based on bulk fluid temperature (T_b); and (b) vs. temperature.

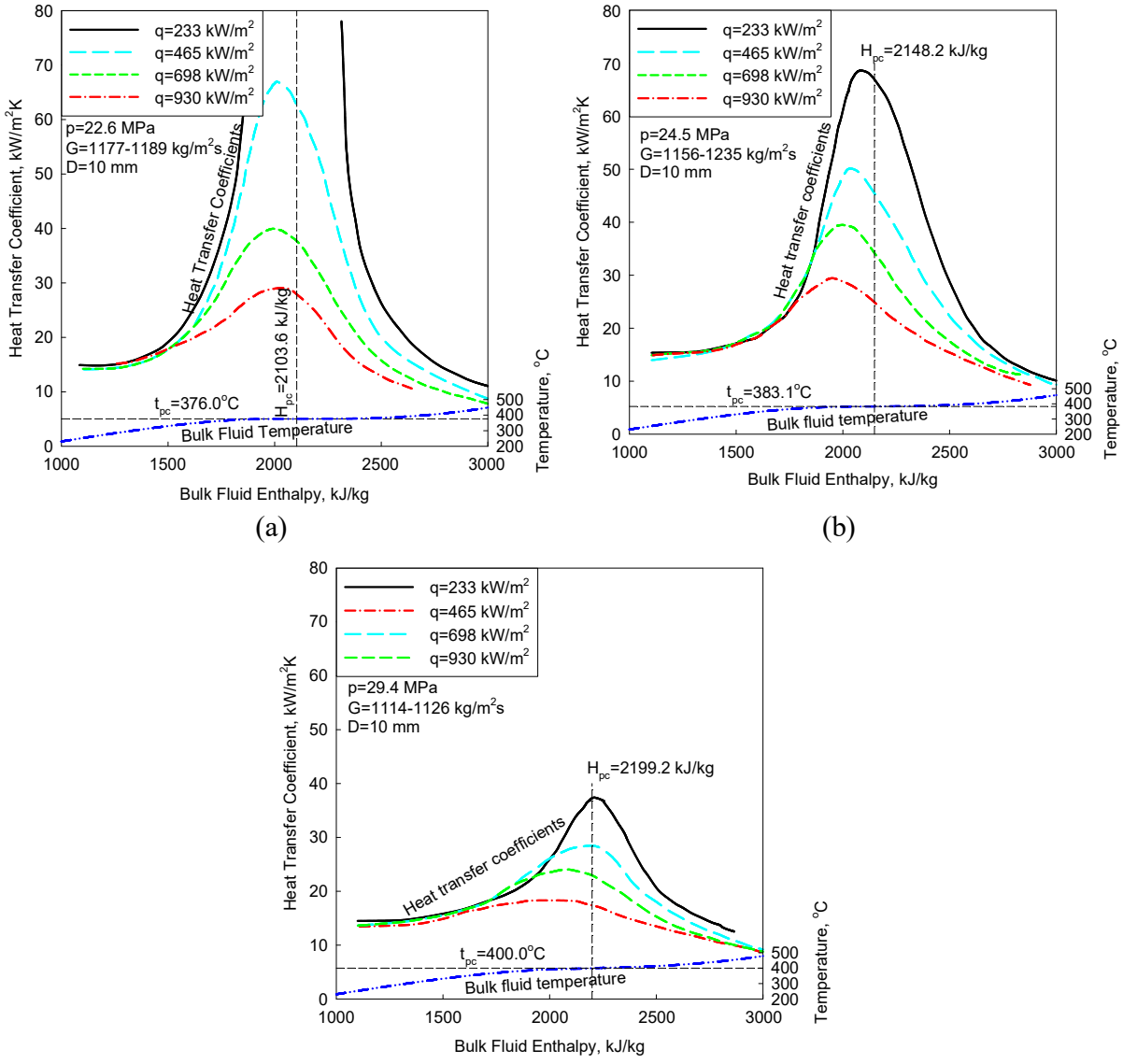

Fig. II.4. Heat transfer coefficient vs. bulk fluid enthalpy in vertical tube with upward flow at various pressures (data from [II.11]): Water: (a) p = 22.6 MPa; (b) p = 24.5 MPa; and (c) p = 29.4 MPa.

Results of [II.12] are shown in Fig. II.5. Improved and deteriorated heat-transfer regimes, as well as a peak ('hump') in HTC near the pseudocritical point, are clearly shown in this figure. The deteriorated heat-transfer regime appears within the middle part of the test section at a heat flux of about 640 kW/m^2, and it may exist together with the improved heat-transfer regime at certain conditions. With the further heat flux increase, the improved heat-transfer regime is eventually replaced with that of deteriorated heat transfer.

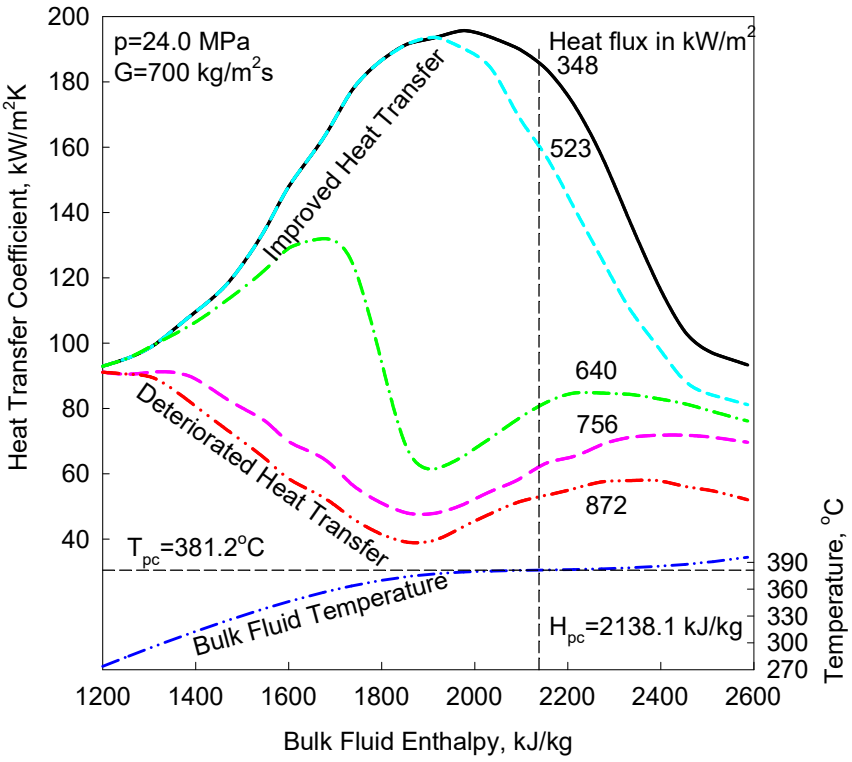

Fig. II.5. Variations in heat-transfer-coefficient values of water flowing in tube (data from [II.12]).

[II.13], [II.14] found that at a mass flux of 495 kg/m^{2}s, two types of deteriorated heat transfer existed (Fig. II.6): 1) The first type appeared within the entrance region of the tube $L / D < 40 – 60$; and 2) The second type appeared at any section of the tube, but only within a certain enthalpy range. In general, the deteriorated heat transfer occurred at high heat fluxes.

The first type of deteriorated heat transfer observed was due to the flow structure within the entrance region of the tube. However, this type of deteriorated heat transfer occurred mainly at low mass fluxes and at high heat fluxes (Fig. II.6a,b) and eventually disappeared at high mass fluxes (Fig. II.6c,d).

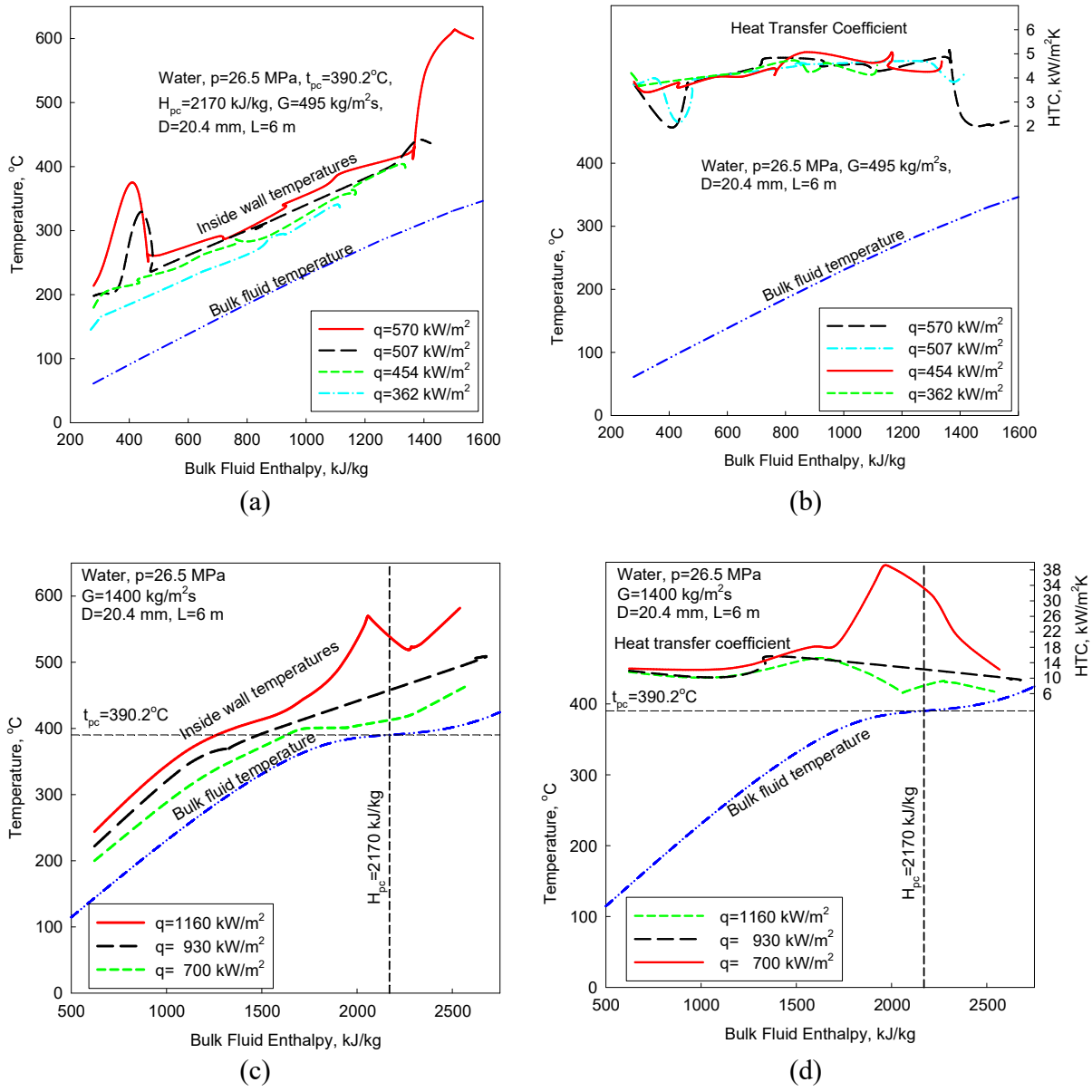

Fig. II.6. Temperature profiles (a) and (c) and heat-transfer-coefficient values (b) and (d) along heated length of a vertical tube (data by [II.13], [II.14]): Heat-transfer-coefficient values were calculated by the author of the current appendix using the data from the corresponding figure; several test series were combined in each curve in figures (c) and (d).

The second type of deteriorated heat transfer occurred when the wall temperature exceeded the pseudocritical temperature (Fig. II.6). According to [II.13], the deteriorated heat transfer appeared when q / G > 0.4 kJ/kg (where q is in kW/m^2 and G is in kg/m^{2}s). This value is close to that suggested by [II.12] (q / G > 0.49 kJ/kg). However, the above-mentioned definitions of two types of deteriorated heat transfer are not enough for their clear identification.

II.2.2. PSEUDO BOILING AND PSEUDO FILM BOILING PHENOMENA

[II.15] investigated heat transfer to water at supercritical pressures flowing in smooth vertical tubes, with and without internal ribs, within a wide range of pressures, mass fluxes, heat fluxes and diameters. He found that the pseudo-boiling phenomenon could occur at supercritical pressures. The pseudo-boiling phenomenon is thought to be due to large differences in fluid density below the pseudocritical point (high-density fluid, i.e., 'liquid') and beyond (low-density fluid, i.e., 'gas'). This heat-transfer phenomenon was affected by pressure, bulk fluid temperature, mass flux, heat flux and tube diameter.

The process of pseudo-film boiling (i.e., low-density fluid prevents high-density fluid from 'rewetting' a heated surface) is similar to film boiling, which occurs at subcritical pressures. Pseudo-film boiling leads to deteriorated heat transfer. However, the pseudo-film boiling phenomenon may not be the only reason for deteriorated heat transfer. [II.15] noted that unpredictable heat-transfer performance was sometimes observed when the pseudocritical temperature of the fluid was between the bulk fluid temperature and the heated surface temperature.

[II.16], [II.17], while analyzing data of various fluids (water, ethyl and methyl alcohols, heptane, etc.), suggested a mechanism for 'pseudo-boiling that accompanies heat transfer to liquids flowing in small-diameter tubes at supercritical pressures. The onset of pseudo-boiling was assumed to be associated with the breakdown of a low-density wall layer that was present at an above-pseudocritical temperature, and with the entrainment of individual volumes of the low-density fluid into the cooler (below pseudocritical temperature) core of the high-density flow, where these low-density volumes collapse with the generation of pressure pulses. At certain conditions, the frequency of these pulses can coincide with the frequency of the fluid column in the tube, resulting in resonance and in a rapid rise in the amplitude of pressure fluctuations. This theory was supported with experimental results.

II.2.3. HORIZONTAL FLOWS

All primary sources (i.e., all sources found by the authors from a total of 650 references dated mainly from 1950 till beginning of 2006) of experimental data for heat transfer to water and carbon dioxide flowing in horizontal test sections are listed in [II.7].

[II.18] found that in a horizontal tube, in addition to the effects of non-isothermal flow that is relevant to a vertical tube, the effect of gravitational forces is important. The latter effect leads to the appearance of temperature differences between the lower and upper parts of the tube. These temperature differences depend on flow enthalpy, mass flux and heat flux. A temperature difference in a tube cross section was found at $G = 300 – 1000$ kg/m^{2}s and within the investigated range of enthalpies ($H_b = 840 – 2520$ kJ/kg). The temperature difference was directly proportional to increases in heat flux values. The effect of mass flux on the temperature difference is the opposite, i.e., with increase in mass flux the temperature difference decreases. Deteriorated heat transfer was also observed in a horizontal tube. However, the temperature profile for a horizontal tube at locations of deteriorated heat transfer differs from that for a vertical tube, being smoother for a horizontal tube compared to that of a vertical tube with a higher temperature increase on the upper part of the tube than on the lower part.

II.2.4. HEAT TRANSFER ENHANCEMENT

Similar to subcritical pressures, turbulization of flow usually leads to heat-transfer enhancement at supercritical pressures [II.7].

[II.19] determined both theoretically (for supercritical water) and experimentally (for supercritical carbon dioxide) the limits for safe operation, in terms of the maximum heat flux for a particular mass flux. Their experiments with a twisted tape inserted inside a test section showed that heat transfer was enhanced by this method. Also, they found that at high heat fluxes, deteriorated heat transfer occurred when the bulk fluid temperature was below and the wall temperature was above the pseudocritical temperature.

[II.20] found heat flux and tube diameter to be the important parameters affecting the minimum mass-flux limits to prevent pseudo-film boiling. Multi-lead ribbed tubes were found to be effective in preventing pseudo-film boiling.

II.3. PRACTICAL PREDICTION METHODS FOR FORCED-CONVECTION HEAT TRANSFER AT SUPERCRITICAL PRESSURES

Unfortunately, satisfactory analytical methods for practical prediction of forced-convection heat transfer at supercritical pressures have not yet been developed due to the difficulty in dealing with steep property variations, especially in turbulent flows and at high heat fluxes. Therefore, generalized correlations based on experimental data are used for HTC calculations at supercritical pressures.

There are numerous correlations for convective heat transfer in circular tubes at supercritical pressures (for details, see in [II.7]). However, an analysis of these correlations has shown that they are more or less accurate only within the particular dataset, which was used to derive the correlation, but show a significant deviation in predicting other experimental data. Therefore, only selected correlations are listed below.

In general, many of these correlations are based on the conventional Dittus–Boelter type correlation (see Eq. (II.1)) in which the regular specific heat is replaced with the cross sectional averaged specific heat within the range of (T_w – T_b); $\left(\frac{H_w - H_b}{T_w - T_b}\right)$, J/kg K (see Fig. II.7). Also, additional terms, such as: $\left(\frac{k_b}{k_w}\right)^k$; $\left(\frac{\mu_b}{\mu_w}\right)^m$; $\left(\frac{\rho_b}{\rho_w}\right)^n$; etc., can be added into correlations to account for significant variations in thermophysical properties within a cross section due to a non-uniform temperature profile, i.e., due to heat flux.

It should be noted that usually generalized correlations, which contain fluid properties at the wall temperature, require iterations to be solved, because there are two unknowns: 1) HTC and 2) the corresponding wall temperature. Therefore, the initial wall temperature value at which fluid properties will be estimated should be ‘guessed’ to start iterations.

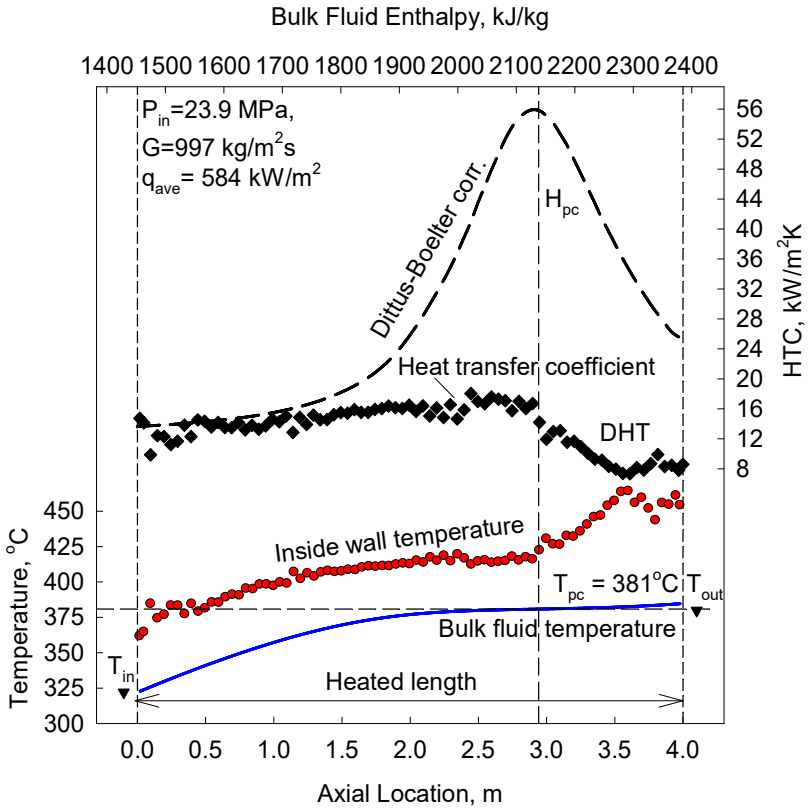

Fig. II.7. Temperature and heat-transfer-coefficient (experimental and calculated values) profiles along heated length of bare vertical tube (data from [II.24]): G = 1500 kg/m²s and q = 884 kW/m².

The most widely used heat-transfer correlation at subcritical pressures for forced convection is the Dittus–Boelter correlation [II.21]. In 1942, [II.22] proposed to use the Dittus–Boelter correlation in the following form, for forced-convective heat transfer in turbulent flows at subcritical pressures:

$$Nu_b = 0.0243\ Re_b^{0.8} Pr_b^{0.4} \tag{II.1}$$

However, it was noted that Eq. (II.1) might produce unrealistic results within some flow conditions (see Fig. II.1, Fig. II.2 and Fig. II.7), especially, near the critical and pseudocritical points, because it is very sensitive to properties variations.

In general, experimental heat-transfer-coefficient values show just a moderate increase within the pseudocritical region. This increase depends on flow conditions and heat flux: higher heat flux – less increase. Thus, the bulk fluid temperature might not be the best characteristic temperature at which all thermophysical properties should be evaluated. Therefore, the cross sectional averaged Prandtl number (see Fig. II.8), which accounts for thermophysical properties variations within a cross section due to heat flux, was proposed to be used in many supercritical heat-transfer correlations instead of the regular Prandtl number. Nevertheless, this classical correlation (Eq. (II.1)) was used extensively as a basis for various supercritical heat-transfer correlations [II.7].

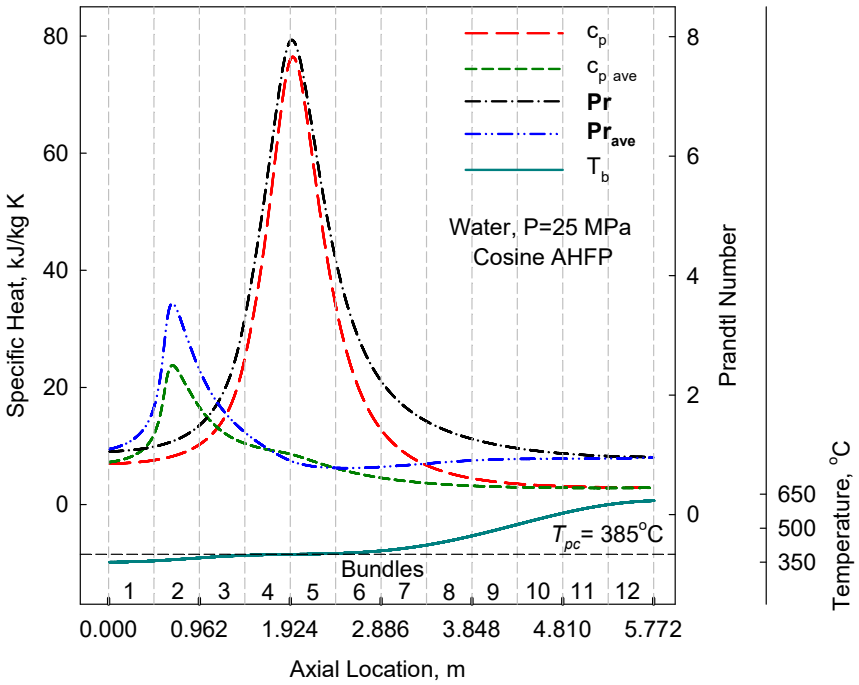

Fig. II.8. Regular and averaged Prandtl number and specific-heat profiles for water along heated length of fuel channel (data from [II.23]): AHFP – Axial Heat Flux Profile.

The majority of empirical correlations were proposed in the 1960s – 1970s [II.7], when experimental techniques were not at the same level (i.e., advanced level) as they are today. Also, thermophysical properties of water have been updated since that time (for example, a peak in thermal conductivity in critical and pseudocritical points within a range of pressures from 22.1 to 25 MPa for water was not officially recognized until the 1990s). Therefore, new correlations within the SCWRs operating range, were developed and evaluated by I. Pioro with his students (mainly, by S. Mokry et al. [II.25], [II.26] (bulk fluid temperature approach) and S. Gupta et al. [II.27], [II.28] (wall temperature approach)) using the best SCW dataset by P.L. Kirillov and his co-workers and adding smaller datasets by other researchers:

— Pioro-Mokry correlation (bulk fluid-temperature approach) [II.25], [II.26]:

$$Nu_b = 0.0061 \quad Re_b^{0.904} \overline{Pr}_b^{0.684} \left(\frac{\rho_w}{\rho_b}\right)^{0.564} \tag{II.2}$$

Fig. II.9 shows scatter plots of experimental HTC values versus calculated HTC values according to Eq. (II.2), and calculated and experimental values for wall temperatures. Both plots lie along a 45-degree straight line with an experimental data spread of ±25% for the HTC values and ±15% for the wall temperatures. The Pioro-Mokry correlation was verified within the following operating conditions (only for NHT and IHT regimes, but not for DHT regime): Water, upward flow, vertical bare tubes with inside diameters of 3 – 38 mm, pressure – 22.8 – 29.4 MPa, mass flux – 200 – 3000 kg/m^{2}s, and heat flux – 70 – 1250 kW/m^2. All thermophysical properties of SCW were

calculated according to NIST REFPROP software [II.29]. This correlation can be also used for supercritical carbon dioxide and other fluids. However, its accuracy will be less in these cases.

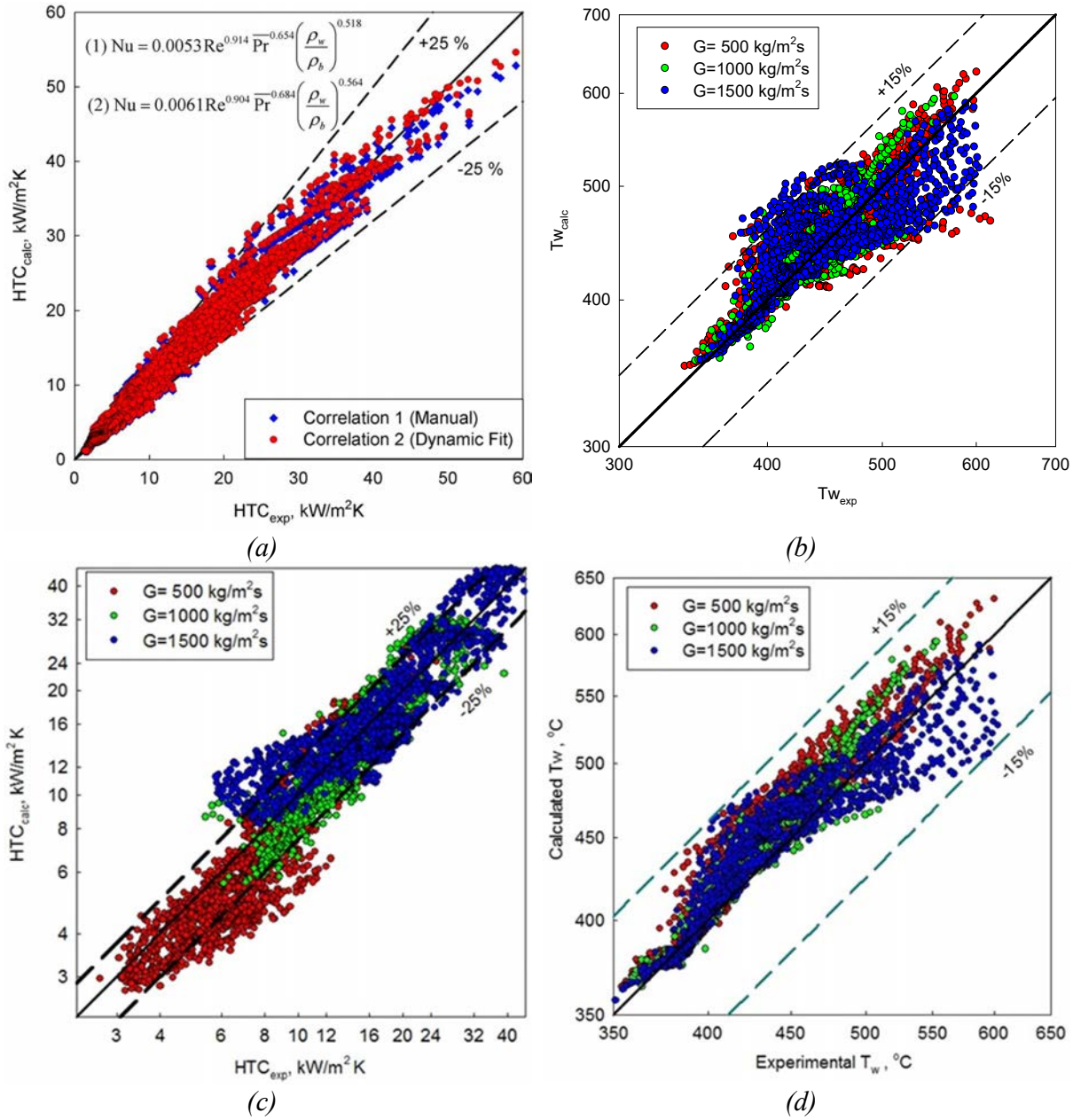

Fig. II.9. Comparison of data fit with experimental data by [II.8]: 1) Pioro-Mokry correlation (bulk fluid-temperature approach; Eq. (II.2) [II.26]: (a) for HTC and (b) for wall temperature; and 2) Pioro-Gupta correlation (wall temperature approach; Eq. (II.3)) [II.27]: (c) for HTC and (d) for wall temperature.

— Pioro-Gupta correlation (wall temperature approach) [II.27]:

$$\boldsymbol{Nu_w} = 0.0033\, \boldsymbol{Re_w^{0.941}}\, \overline{\boldsymbol{Pr_w}}^{0.764} \left(\frac{\mu_w}{\mu_b}\right)^{0.398} \left(\frac{\rho_w}{\rho_b}\right)^{0.156} \tag{II.3}$$

Equation (II.3) has an uncertainty about ±25% for HTC values and about ±15% for calculated wall temperatures within the same ranges as those for Eq. (II.2). Also, it was decided to add an entrance effect to make this correlation even more accurate. This entrance effect was modeled by an exponentially-decreasing term as shown below:

$$\boldsymbol{Nu_w} = \boldsymbol{Nu}_w \left[1 + exp\left(-\frac{x}{24\, D}\right)\right]^{0.3} \tag{II.4}$$

where, $\mathbf{Nu}_w$ is calculated using Eq. (II.3). Fig. II.10 – Fig. II.11 show that the latest correlation (Eq. (II.2)) closely represents experimental data and follows trends closely even within the pseudocritical range. It should be noted that all heat-transfer correlations presented in this paper are intended only for the normal and improved heat-transfer regimes. The following empirical correlation was proposed by I. Pioro and S. Mokry for calculating the minimum heat flux at which the deteriorated heat-transfer regime appears.

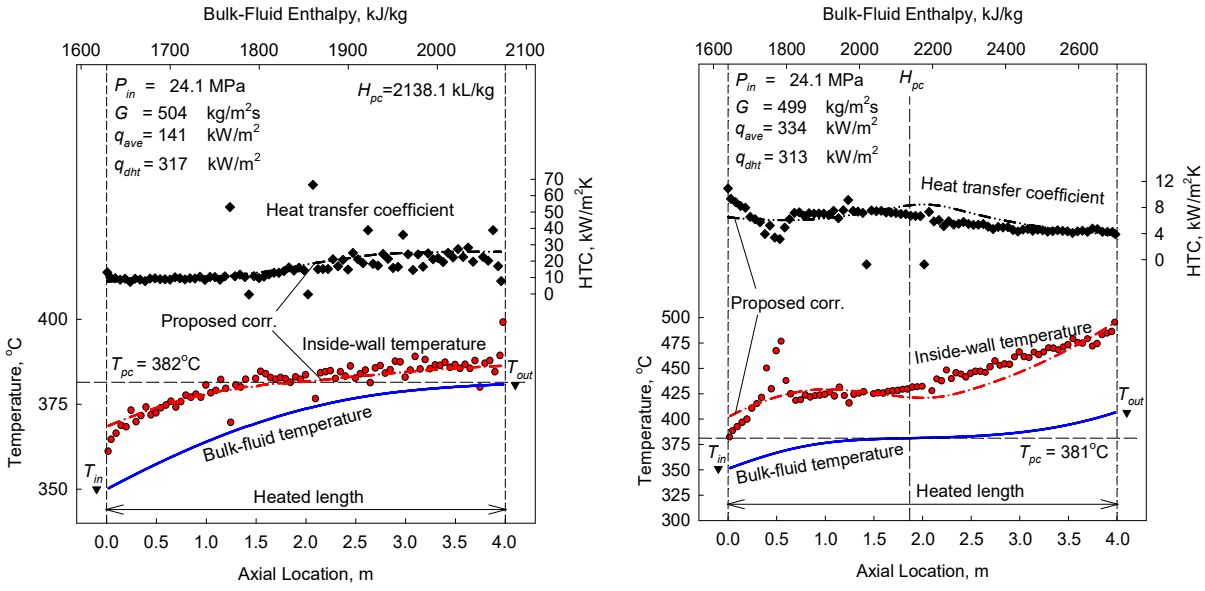

Fig. II.10. Temperature and heat-transfer-coefficient profiles at various heat fluxes along 4-m circular tube (D = 10 mm) (data by [II.8]): P_{in} ≈ 24 MPa and G ≈ 500 kg/m²s; proposed correlation – Eq. (II.2): **(a)** $\mathbf{q}_{ave}$ ≈ *140 W/m² and (b)* $\mathbf{q}_{ave}$ ≈ *330.*

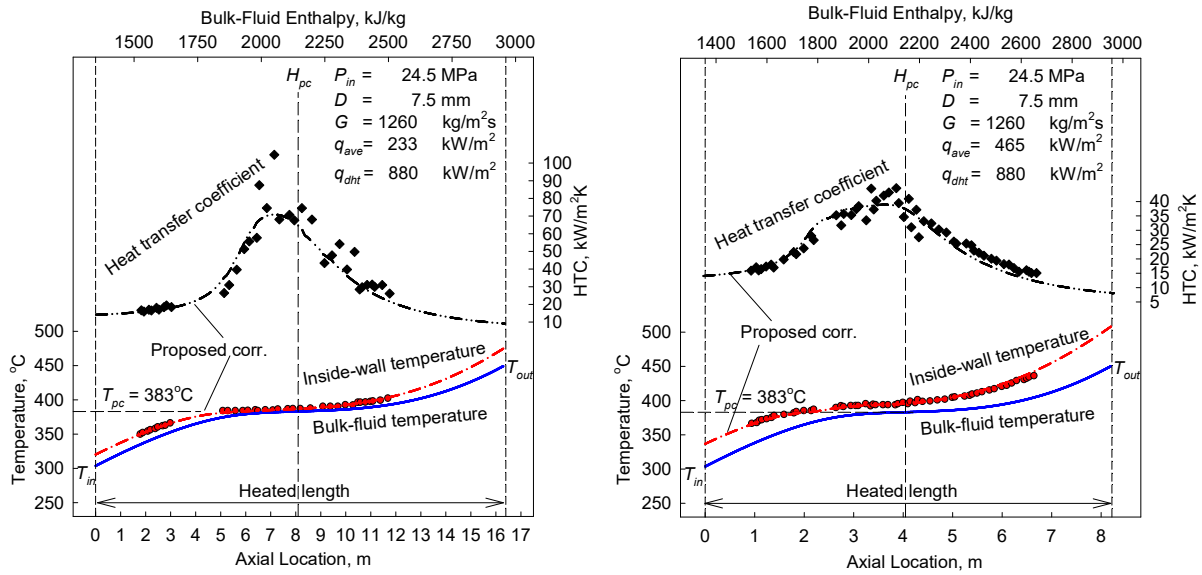

Fig. II.11. Temperature and heat-transfer-coefficient profiles along circular tube at various heat fluxes: Nominal operating conditions – P_{in} = 24.5 MPa, G = 1260 kg/m^{2}s and D = 7.5 mm (data by [II.11]); proposed correlation – Eq. (II.2): (a) $\mathbf{q}_{ave}$ = 233 W/m^2 and (b) $\mathbf{q}_{ave}$ = 465 W/m^2.

— Pioro-Mokry correlation for q_{dht} [II.26]:

$$q_{dht} = -58.97 + 0.745 \cdot G,\ kW/m^2 \tag{II.5}$$

Correlation (Eq. (II.5)) is valid within the following range of experimental parameters: SCW, upward flow, vertical bare tube with inside diameter 10 mm, pressure 24 MPa, mass flux 200 – 1500 kg/m^{2}s, and bulk fluid inlet temperature 320 – 350°C: Uncertainty ±15% for the DHT heat flux.

[II.30] have evaluated 15 q_{dht} correlations for SCW, and they have concluded that Pioro-Mokry correlation (Eq. (II.5)) "may be used for preliminary estimations". A recent study was conducted by [II.31], [II.32] in order to develop a heat-transfer look-up table for the critical/supercritical pressures. An extensive literature review was conducted, which included 28 datasets and 6663 trans-critical heat-transfer data. TABLE II.1–Table Ii.3 list results from this study in the form of the overall-weighted average and Root-Mean-Square (RMS) errors: (a) Within three supercritical sub-regions; and (b) For subcritical liquid and superheated steam. Many of the correlations listed in these tables can be found in [II.7]. In their conclusions, [II.31], [II.32] determined that within the supercritical region, the latest correlation by Pioro-Kirillov [II.26] (Eq. (II.2)) showed the best prediction for the data within all three sub-regions investigated (based on RMS error) (see TABLE II.1). Also, the Pioro-Kirillov correlation showed quite good predictions for subcritical-pressure water and superheated steam compared to other several correlations (see TABLE II.3).

TABLE II.1. OVERALL WEIGHTED AVERAGE AND RMS ERRORS WITHIN THREE SUPERCRITICAL SUB-REGIONS (CORRELATIONS ARE LISTED ACCORDING TO THE YEAR OF PUBLICATION, I.E., FROM EARLY ONES TO THE LATEST ONES) (CORRELATIONS ARE SHOWN IN TABLE II.2) [II.31], [II.32].

No	**Correlation**	**Regions**					
		Liquid-like		**Gas-like**		**Critical or pseudocritical**	
		Errors, %					
		Ave.	**RMS**	**Ave.**	**RMS**	**Ave.**	**RMS**
1	Dittus–Boelter [II.21]	24	44	90	127	-	-
2	Sieder & Tate [II.33]	46	65	97	132	-	-
3	Bishop et al. [II.34]	5	28	5	20	23	31
4	Swenson et al. [II.35]	**1**	31	-16	21	4	23
5	Krasnoshchekov et al. [II.36]	18	40	-30	32	24	65
6	Hadaller & Banerjee [II.37]	34	53	14	24	-	-
7	Gnielinski [II.38]	10	36	99	139	-	-
8	Watts & Chou [II.39], NHT	6	30	-6	21	11	28
9	Watts & Chou [II.39], DHT	2	**26**	9	24	17	30
10	Griem [II.40]	2	28	11	28	9	35
11	Koshizuka & Oka [II.41]	26	47	27	54	39	83
12	Jackson [II.42]	15	36	15	32	30	49
13	Mokry et al. [II.25], [II.26]	-5	**26**	-9	**18**	**-1**	**17**
14	Kuang et al. [II.43]	-6	27	10	24	-3	26
15	Cheng et al. [II.44]	4	30	**2**	28	21	85
16	Gupta et al. [II.27]	-26	33	-12	20	**-1**	18

In bold – minimum values.

TABLE II.2. LIST OF SUPERCRITICAL-PRESSURE HEAT-TRANSFER CORRELATIONS (CORRELATIONS ARE LISTED ACCORDING TO THE YEAR OF PUBLICATIONS, I.E., FROM EARLY ONES TO THE LATEST ONES) [II.32].

No.	Reference	Prediction method
1	Dittus–Boelter [II.21] (Eq. (II.1))	$Nu_b = 0.0243\, Re_b^{0.8}\, Pr_b^{0.4}$
2	Sieder and Tate [II.33]	$Nu_b = 0.027\, Re_b^{0.8}\, Pr_b^{1/3} (\mu/\mu_w)^{0.14}$
3	Bishop et al. [II.34]	$\mathrm{NU}_b = 0.0069\, Re_b^{0.9}\, \overline{Pr_b^{0.66} \frac{\rho_w}{\rho_b}^{0.43} \frac{D}{L}}$
4	Swenson et al. [II.35]	$\mathrm{Nu}_w = 0.00459 \mathrm{Re}_w^{0.923} \overline{\mathrm{Pr}}_w^{0.613} (\rho_w/\rho_b)^{0.231}$
5	Krasnoscheckov et al. [II.36]	$\mathrm{NU}_b = \mathrm{NU}_0 (\rho_w/\rho_b)^{0.3} (C_p/C_{pb})^n$, $\mathrm{Nu}_0 = \frac{(\xi/8)\mathrm{Re}_b \overline{\mathrm{Pr}}}{12.7(\xi/8)^{0.5}(\overline{\mathrm{Pr}}^{2/3} - -1) + 1.07}$ and $\xi = 1/(1.82 Log_{10}\, Re_b - 1.64)^2$, $n = 0.4$ for $(T_w/T_{pc}) \leq 1$ or $(T_b/T_{pc}) \geq 1.2$, $n = n_1 = 0.22 + 0.18(T_w/T_{pc})$ for $1 \leq (T_w/T_{pc}) < 2.5$ and $n = n_1 + (5n_1\text{-}2)\,(1\text{-}(T_b/T_{pc}))$ for $1 \leq (T_b/T_{pc}) \leq 1.2$, T in K
6	Hadaller and Banerjee [II.37]	$\mathrm{Nu_f} = 0.0101 \mathrm{Re}_f^{0.8774}\, \mathrm{Pr}_f^{0.6112} (L/D)^{0.0328}$
7	Yamagata et al. [II.11]	$Nu_b = 0.0135\, Re_b^{0.85}\, Pr_b^{0.8} F_c$, $F_c = 1$ for $E > 1$, $Fc = 0.67 \overline{Pr_{pc}^{(-0.05)} \overline{Cp}_b^{n1} E}$ and $Fc = (\overline{Cp}/Cp_b)^{n2}$ for $E < 0$, $E = (T_{pc} - -T_b)/(T_w - -T_b)$ $n_1 = 0.77(1 + 1/\mathrm{Pr_{pc}}) + 1.49$ and $n_2 = 1.44(1 + 1/\mathrm{Pr_{pc}}) - 0.53$
8	Gnielinski [II.38]	$\mathrm{Nu} = \frac{(f/8)(\mathrm{Re}_b - 1000)\mathrm{Pr}_b}{1 + 12.7(f/8)^{1/2}(\mathrm{Pr}^{2/3} - 1)} \left(\frac{\mathrm{Pr}_b}{\mathrm{Pr}_w}\right)^{0.11} (1 + (D/L)^{2/3})$ where $f = 1/(1.82\, log_{10}(\mathrm{Re}) - 1.64)^2$ $(T_b/T_w)^{0.45}$ replaces $(\mathrm{Pr}_b/\mathrm{Pr}_w)^{0.11}$ when $T_b > T_{pc}$
9	Watts and Chou [II.39]	$\mathrm{Nu}_b = 0.021 \mathrm{Re}_b^{0.8} \mathrm{Pr}_b^{0.55} \left(\frac{\rho_w}{\rho_b}\right)^{0.35} f\left(\frac{\mathrm{Gr}_b}{\mathrm{Re}_b^{2.7}\mathrm{Pr}_b^{0.5}}\right)$, for Normal Heat Transfer (NHT): $f\left(\frac{\mathrm{Gr}_b}{\mathrm{Re}_b^{2.7}\mathrm{Pr}_b^{-0.5}}\right) = \left(1 - 3000 \frac{\mathrm{Gr}_b}{\mathrm{Re}_b^{2.7}\mathrm{Pr}_b^{0.5}}\right)^{0.295}$ if $\frac{\mathrm{Gr}_b}{\mathrm{Re}_b^{2.7}\mathrm{Pr}_b^{0.5}} \leq 10^{-4}$, or $f\left(\frac{\mathrm{Gr}_b}{\mathrm{Re}_b^{2.7}\mathrm{Pr}_b^{-0.5}}\right) = \left(7000 \frac{\mathrm{Gr}_b}{\mathrm{Re}_b^{2.7}\mathrm{Pr}_b^{0.5}}\right)^{0.295}$ if $\frac{\mathrm{Gr}_b}{\mathrm{Re}_b^{2.7}\mathrm{Pr}_b^{0.5}} > 10^{-4}$ where $\mathrm{Gr}_b = (\rho_b - \rho_{\mathrm{avg}}) D_{hy}{}^3 \mathrm{g}/\rho_b \nu_b{}^2$
10	Griem [II.40]	$\mathrm{Nu}_b = 0.0169 \mathrm{Re}_b^{0.8356} \mathrm{Pr}_{\mathrm{sel}}^{0.432} \omega$, $\overline{k} = 0.5(k_b + k_w)$, $\mu = \mu_b$, $\mathrm{Pr_{sel}} = Cp_{sel}\, \mu_b/\overline{k}$ and $\omega = min(1.0, max(0.82; 0.82 + 9.7 \times 10^{-7}(H_b - 1.54 \times 10^6))$, H_b in kJ/kg

No.	Reference	Prediction method
11	Koshizuka and Oka [II.41]	$\mathrm{Nu}_b = 0.015\mathrm{Re}_b{}^{0.85}\mathrm{Pr}_b{}^{(0.69-81000/CHF+1000f_cq)}, q(\mathrm{W/m^2}), fc = 2.9\times10^{-8}+0.11/CHF$,for $H < 1.5\mathrm{MJ/kg}$ $fc = -8.7\times10^{-8}-0.65/CHF$,for $1.5 \le H \le 3.3$ MJ/kg and $fc = -9.7\times10^{-7}+1.3/CHF$,for $3.3 < H \le 4$ MJ/kg, $CHF = 200G^{1.2}$
12	Jackson [II.42]	$\mathrm{Nu}_b = 0.0183\mathrm{Re}_b^{0.82}\mathrm{Pr}_b^{0.5}(\frac{\rho_w}{\rho_b})^{0.3}(\frac{\bar{Cp}}{Cp_b})^n$
13	Kuang et al. [II.43]	$\mathrm{Nu} = 0.0239\mathrm{Re}_b^{0.759}\bar{\mathrm{Pr}}^{0.833}(\frac{k_w}{k_b})^{0.0863}(\frac{\mu_w}{\mu_b})^{0.832}(\frac{\rho_w}{\rho_b})^{0.31}(\overset{*}{\mathrm{Gr}})^{0.014}(\overset{+}{q})^{-0.021}$ This correlation is valid for: P = 22.75–31.03 MPa, G = 380–3600 kg/m^{2}s, q = 233–3474 kW/m^2, D = 7.5–26 mm; and P = 22.75–31.03 MPa, G = 380–3600 kg/m^{2}s, q = 233–3474 kW/m^2, D = 7.5–26 mm
14	Mokry et al. [II.26], [II.25] (Eq. (II.2))	$\mathrm{Nu} = 0.0061\mathrm{Re}_b^{0.904}\bar{\mathrm{Pr}}_b^{0.684}(\frac{\rho_w}{\rho_b})^{0.564}$
15	Cheng et al. [II.44]	$F = \mathrm{Nu}/\mathrm{Nu}_0 = \mathrm{Nu}/0.023\mathrm{Re}_b{}^{0.8}\mathrm{Pr}_b{}^{1/3} = min(F_1, F_2),\ F_1 = 0.85+0.776(\pi_A\times10^3)^{2.4}$and $F_2 = 0.48/(\pi_{A,pc}\times10^3)^{1.55}+1.21(1-\pi_A/\pi_{A,pc})$
16	Gupta et al. [II.27] (Eq. (II.3))	$\mathrm{Nu}_w = 0.0033\mathrm{Re}_w^{0.941}\mathrm{Pr}_{\mathrm{avg,w}}^{0.764}(\frac{\rho_w}{\rho_b})^{0.156}(\frac{\mu_w}{\mu_b})^{0.398}$;$\mathrm{Nu}_{\mathrm{w,entrance}} = \mathrm{Nu}_w(1+exp(-\frac{L}{24D}))^{0.3}$

TABLE II.3. OVERALL AVERAGE AND RMS ERROR WITHIN SUBCRITICAL REGION (CORRELATIONS ARE LISTED ACCORDING TO THE YEAR OF PUBLICATION, I.E., FROM EARLY ONES TO THE LATEST ONES) (CORRELATIONS ARE SHOWN IN TABLE II.2) [II.31], [II.32].

No.	Correlation	Subcritical liquid		Superheated steam	
		Error, %			
		Ave.	RMS	Ave.	RMS
1	Dittus & Boelter [II.21] (TABLE II.2, Eq. (1))	10	23	75	127
2	Sieder & Tate [II.33] (TABLE II.2, Eq. (2))	28	37	84	138
3	Hadaller & Banerjee [II.37] (TABLE II.2, Eq. (6))	27	36	19	34
4	Gnielinski [II.38] (TABLE II.2, Eq. (8))	-4	**18**	80	130
5	Mokry et al. [II.25], [II.26] (Eq. (4.2) or TABLE II.2, Eq. (14))	**-1**	19	**-5**	**20**

In bold – minimum values.

[II.45] has also concluded that the Pioro-Mokry correlation for SCW HT "performs best" compared to other 14 correlations.

II.4. HYDRAULIC RESISTANCE

In general, the total pressure drop for forced convection flow inside a test section, installed in a closed-loop system, can be calculated according to the following expression [II.7], [II.46]:

$$\Delta p = \sum \Delta p_{fr} + \sum \Delta p_{\ell} + \sum \Delta p_{ac} + \sum \Delta p_{g} \tag{II.6}$$

where Δp is the total pressure drop, in Pa.

The pressure drop due to frictional resistance, Δp_{fr} (Pa), is defined as

$$\Delta p_{fr} = \left(\xi_{fr} \frac{L}{D} \frac{\rho u^2}{2}\right) = \left(\xi_{fr} \frac{L}{D} \frac{G^2}{2 \rho}\right) \tag{II.7}$$

where ξ_{fr} is the frictional coefficient, which can be obtained from appropriate correlations for different flow geometries. For smooth circular tubes, ξ_{fr} is given by [II.47]

$$\xi_{fr} = \left(\frac{1}{(1.82 \ log_{10} Re_b - 1.64)^2}\right)$$

(II.8)

Equation (II.8) is valid within a range of **Re** = $4 \cdot 10^3 - 10^{12}$.

Usually, thermophysical properties and the Reynolds number in Eqs. (II.7) and (II.8), respectively, are based on arithmetic average of inlet and outlet values. The pressure drop due to local flow obstruction, Δp_ℓ is (Pa), is defined as

$$\Delta\, p_\ell = \left(\xi_\ell\ \frac{\rho\ u^2}{2}\right) = \left(\xi_\ell\ \frac{G^2}{2\ \rho}\right) \tag{II.9}$$

where ξ_ℓ is the local resistance coefficient, which can be obtained from appropriate correlations for different flow obstructions. The pressure drop due to acceleration of flow, Δp_{ac} (Pa), is defined as

$$\Delta\, p_{ac} = (\rho_{out}\ u_{out}^2 - \rho_{in}\ u_{in}^2) = G^2\ \left(\frac{1}{\rho_{out}} - \frac{1}{\rho_{in}}\right) \tag{II.10}$$

The pressure drop due to gravity, Δp_g (Pa), is defined as

$$\Delta\, p_g = \pm g\ \left(\frac{\rho_{out} + \rho_{in}}{2}\right)\ L\ \ sin\ \ \theta \tag{II.11}$$

where θ is the test section inclination angle to the horizontal plane, sign '+' is for the upward flow and sign '–' is for the downward flow. The arithmetic-average value of densities can be used only for short sections in the case of strongly nonlinear dependency of the density versus temperature. Therefore, in long test sections at high heat fluxes and within the critical and pseudocritical regions, the integral value of densities should be used (see Eq. (II.12)).

[II.48] and [II.49] proposed that Δp_g at supercritical pressures can be obtained by

$$\Delta\, p_g = \pm g\ \ \left(\frac{H_{out}\ \rho_{out} + H_{in}\ \rho_{in}}{H_{out} + H_{in}}\right)\ L\ \ sin\,\theta \tag{II.12}$$

Equation (II.6) is applicable for subcritical and supercritical pressures. However, adjustment of this expression to conditions of supercritical pressures, with single phase dense gas and significant variations in thermophysical properties near the critical and pseudocritical points, was the major task for the researchers and scientists. In general, two major approaches to solve this problem were taken: an analytical approach (including numerical approach) and an experimental (empirical) approach.

For reference purposes, selected results obtained at Chalk River Laboratories [II.7] are shown in Fig. II.12. In these experiments, the local pressure drop due to obstructions along the heated length was 0, because of a smooth test section. Therefore, the measured pressure drop consists only of three components:

$$\Delta\ p_{meas} = \Delta\ p_{fr} + \Delta\ p_{ac} + \Delta\ p_g \tag{II.13}$$

Additional details of pressure drop at supercritical pressures are listed in [II.7]. An important issue at supercritical and subcritical pressures is uncertainties of measured and calculated parameters. Appendix IV in [II.7] is dedicated to this important issue.

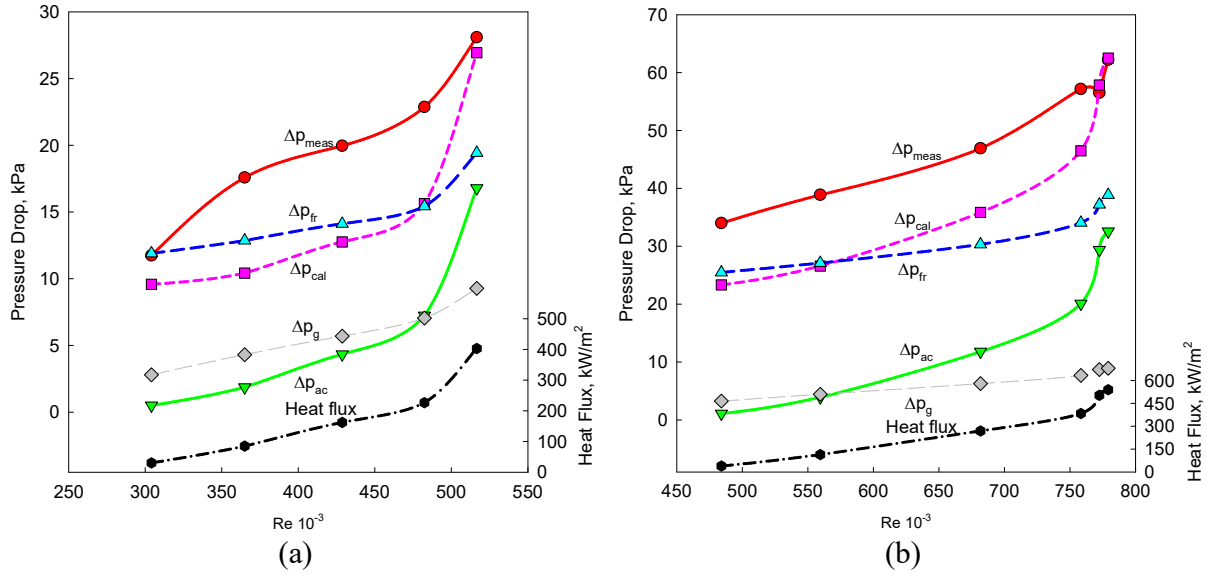

Fig. II.12. Effect of Reynolds number on total pressure drop (measured and calculated) and its components (calculated values) in supercritical carbon dioxide flowing in vertical circular tube: p_{out} = 8.8 MPa; (a) G = 2040 kg/m^{2}s and t_{in} = 32°C; and (b) G = 3040 kg/m^{2}s and t_{in} = 31°C.

Nomenclature and Acronyms

A	area, m^2
c_p	specific heat at constant pressure, J/kg K
$\overline{c}_p$, $c_{p\ ave}$	averaged specific heat within the range of ($t_w - t_b$); $\left(\frac{H_w - H_b}{T_w - T_b}\right)$, J/kg K
D	inside diameter, m
G	mass flux, kg/m^{2}s; $\left(\frac{m}{A_{fl}}\right)$
g	gravitational acceleration, m/s^2
H	specific enthalpy, J/kg
h	heat transfer coefficient, W/m^{2}K
k	thermal conductivity, W/m K
L	heated length, m
m	mass flow rate, kg/s; $(\rho\ \cdot V)$
P, p	pressure, Pa
Q	heat-transfer rate, W

q	heat flux, W/m^2; $\left(\frac{Q}{A_h}\right)$
T, t	temperature, ºC
u	axial velocity, m/s
V	volume-flow rate, m^3/s

Greek Letters

α	thermal diffusivity, m^2/s; $\left(\frac{k}{c_p \cdot \rho}\right)$
Δ	difference
θ	test section inclination angle, degree
μ	dynamic viscosity, Pa·s
ξ	friction coefficient
ρ	density, kg/m^3
υ	kinematic viscosity, m^2/s; $\left(\frac{\mu}{\rho}\right)$

Non-dimensional Numbers

Nu	Nusselt number; $\left(\frac{h \cdot D}{k}\right)$
Pr	Prandtl number; $\left(\frac{\mu \cdot c_p}{k}\right) = \left(\frac{\upsilon}{\alpha}\right)$
$\overline{\text{Pr}}$	cross sectional average Prandtl number within the range of $(t_w - t_b)$; $\left(\frac{\mu \quad \cdot \overline{c}_p}{k}\right)$
Re	Reynolds number; $\left(\frac{G \cdot D}{\mu}\right)$

Subscripts or superscripts

ac	acceleration
ave	average
b	bulk
calc	calculated
dht	deteriorated heat transfer
exp	experimental
fl	flow
fr	friction
g	gravitational
h	heated
in	inlet
ℓ	local
meas	measured
out	outlet or outside
pc	pseudocritical
w	wall

Abbreviations and acronyms widely used in the text and list of references

AECL	Atomic Energy of Canada Limited

AHFP	Axial Heat Flux Profile
ASME	American Society of Mechanical Engineers
Ave.	Average
corr.	correlation
DHT	Deteriorated Heat Transfer
HT	Heat Transfer
HTC	Heat Transfer Coefficient
IHT	Improved Heat Transfer
LWR	Light Water Reactor
NHT	Normal Heat Transfer
RMS	Root-Mean Square (error)
SCW	SuperCritical Water
SCWR	SuperCritical Water-cooled Reactor
USA	United States of America
USSR	Union of Soviet Socialist Republics

REFERENCES TO APPENDIX II

[II.1] PIORO, I., MOKRY, S., 2011. "Heat transfer to fluids at supercritical pressures", Heat Transfer. Theoretical Analysis, Experimental Investigations and Industrial Systems (BELMILOUDI, A., Ed.), INTECH (2011) Ch. 19.

[II.2] SCHMIDT, E., ECKERT, E., AND GRIGULL, V., Heat Transfer by Liquids near the Critical State, AFF Translation, No. 527, Air Materials Command, Wright Field, Dayton, OH, USA, April, 1946.

[II.3] INTERNATIONAL ATOMIC ENERGY AGENCY, Heat Transfer Behaviour and Thermohydraulics Code Testing for Supercritical Water Cooled Reactors (SCWRs), IAEATECDOC-1746, IAEA, Vienna (2014).

[II.4] SCHULENBERG, T., STARFLINGER, J., High Performance Light Water Reactor - Design and Analyses, KIT Scientific Publishing, Karlsruhe (2012)..

[II.5] PIORO, I., The Potential Use of Supercritical Water-Cooling in Nuclear Reactors, Nuclear Energy Encyclopedia: Science, Technology, and Applications, Editors: S.B. Krivit, J.H. Lehr and Th.B. Kingery, J. Wiley & Sons, Hoboken, NJ, USA, (2011), 309–347.

[II.6] OKA, Y, KOSHIZUKA, S., ISHIWATARI, Y., YAMAJI, A., Super Light Water Reactors and Super Fast Reactors, Springer, New York, NY, USA, 2010.

[II.7] PIORO, I.L., DUFFEY, R.B., Heat Transfer and Hydraulic Resistance at Supercritical Pressures in Power Engineering Applications, ASME Press, (2007).

[II.8] KIRILLOV, P.L., LOZHKIN, V.V., SMIRNOV, A.M., Investigation of Borders of Deteriorated Regimes of a Channel at Supercritical Pressures, State Scientific Center of Russian Federation, Institute of Physics and Power Engineering by the name of A.I. Leypunskiy, FEI-2988, Obninsk, Russia, 2003, (In Russian).

[II.9] RAZUMOVSKIY, V.G., PIS'MENNYI, EU.N., SIDAWI, K., PIORO, I.L., KOLOSKOV, A.EU., Experimental Heat Transfer in an Annular Channel and 3-Rod Bundle Cooled with Upward Flow of Supercritical Water, ASME Journal of Nuclear Engineering and Radiation Science, **2, 1**, (2016).

[II.10] RICHARDS, G., HARVEL, G.D., PIORO, I.L., SHELEGOV, A.S., KIRILLOV, P.L., Heat Transfer Profiles of A Vertical, Bare, 7-Element Bundle Cooled with Supercritical Freon R-12, Nucl. Eng. Des., **264**, (2013), 246-256.

[II.11] YAMAGATA K., NISHIKAWA K., HASEGAWA S., FUJI T., YOSHIDA S., Forced Convective Heat Transfer to Supercritical Water Flowing in Tubes, J Heat Mass Transfer, **15, 12**, (1972), 2575, 2593.

[II.12] STYRIKOVICH, M.A., MARGULOVA, T.KH., MIROPOL'SKII, Z.L., Problems in the Development of Designs of Supercritical Boilers, Thermal Engineering (Теплоэнергетика, стр. 4–7), **14, 6**, (1967), 5–9.

[II.13] VIKHREV, YU.V., BARULIN, YU.D., KON'KOV, A.S., A Study of Heat Transfer in Vertical Tubes at Supercritical Pressures, Thermal Engineering (Теплоэнергетика, стр. 80–82), **14, 9**, (1967), 116–119.

[II.14] VIKHREV, YU.V., KON'KOV, A.S., LOKSHIN, V.A. et al., Temperature Regime of Steam Generating Tubes at Supercritical Pressure, Transactions of the IVth All-Union Conference on Heat Transfer and Hydraulics at Movement of Two-Phase Flow inside Elements of Power Engineering Machines and Apparatuses, Leningrad, Russia, (1971), 21–40, (In Russian).

[II.15] ACKERMAN, J.W., Pseudo-Boiling Heat Transfer to Supercritical Pressure Water in Smooth and Ribbed Tubes, J Heat Transfer, Trans. ASME, **92, 3**, (1970), 1, 8.

[II.16] KAFENGAUS, N.L., About Some Peculiarities in Fluid Behaviour at Supercritical Pressure in Conditions of Intensive Heat Transfer, Applied Thermal Sciences, (Промышленная Теплотехника, стр. 6–10), **8, 5**, (1986), 26–28.

[II.17] KAFENGAUS, N.L., The Mechanism of Pseudoboiling, Heat Transfer-Soviet Research, 7, 4, (1975), 94–100.

[II.18] KRASYAKOVA, L.YU., RAYKIN, YA.M., BELYAKOV, I.I., et al.,. Investigation of Temperature Regime of Heated Tubes at Supercritical Pressure, Soviet Energy Technology (Энергомашиностроение), **1**, (1967), 1–4, (In Russian).

[II.19] SHIRALKAR, B.S., GRIFFITH P., The Effect of Swirl, Inlet Conditions, Flow Direction, and Tube Diameter on the Heat Transfer to Fluids at Supercritical Pressure, J Heat Transfer, Transactions of the ASME, **92, 3**, (1970), 465, 474.

[II.20] LEE, R.A., HALLER, K.H., Supercritical Water Heat Transfer Developments and Applications, Proc. 5th Int. Heat Transfer Conference (IHTC-5), Tokyo, (1974), 335–339.

[II.21] DITTUS, F.W., BOELTER, L.M.K., Heat Transfer in Automobile Radiators of the Tubular Type, University of California, Berkeley, Publications on Engineering, **2, 13**, (1930), 443-461.

[II.22] MCADAMS, W.H., Heat Transmission, 2nd edition, McGraw-Hill, New York, (1942).

[II.23] MOKRY, S., NAIDIN, M., BAIG, F., GOSPODINOV, YE., ZIRN, U., BAKAN, K., PIORO, I., NATERER, G., Conceptual Thermal-Design Options for Pressure-Tube SCWRs with Thermochemical Co-Generation of Hydrogen, Proc. 16th Int. Conf. On Nuclear Engineering (ICONE-16), Orlando, 2008.

[II.24] PIORO, I.L, KIRILLOV, P.L., MOKRY, S.J., GOSPODINOV, Y.K., Supercritical Water Heat Transfer in a Vertical Bare Tube: Normal, Improved and Deteriorated Regimes, Proc. 2008 International Congress on Advances in Nuclear Power Plants (ICAPP'08), Anaheim, 2008.

[II.25] MOKRY, S., GOSPODINOV, YE., PIORO, I., KIRILLOV, P., Supercritical Water Heat-Transfer Correlation for Vertical Bare Tubes, Proc. 17th Int. Conf. On Nuclear Engineering ICONE-17, Brussels, 2009.
[II.26] MOKRY, S., PIORO, I.L., FARAH, A., KING, K., GUPTA, S., PEIMAN, W., KIRILLOV, P.L., Development of Supercritical Water Heat-Transfer Correlation for Vertical Bare Tubes, Nuclear Engineering and Design, 241, (2011), 1126-1136.
[II.27] GUPTA, S., MOKRY, S., PIORO, I., Developing a Heat-Transfer Correlation for Supercritical-Water Flowing in Vertical Tubes and Its Application in SCWR, Proc. 19th Int. Conf. On Nuclear Engineering (ICONE-19), Makuhari, 2011.
[II.28] GUPTA, S., SALTANOV, EU., MOKRY, S.J., PIORO, I., TREVANI, L., MCGILLIVRAY, D., Developing Empirical Heat-Transfer Correlations for Supercritical CO_2 Flowing in Vertical Bare Tubes, Nuclear Engineering and Design, **261**, (2013), 116-131.
[II.29] NATIONAL INSTITUTE OF STANDARDS AND TECHNOLOGY, NIST Reference Fluid Thermodynamic and Transport Properties - REFPROP, Standard Reference Database 23, Ver. 9.1, Department of Commerce, Boulder, CO, USA, 2013.
[II.30] WANG, H., LEUNG, L.K.H., WANG, W., BI, Q., A Review on Recent Heat Transfer Studies to Supercritical Pressure Water in Channels, Applied Thermal Engineering, **142**, (2018), 573-596.
[II.31] ZAHLAN, H., GROENEVELD, D., TAVOULARIS, S., Look-Up Table for Trans-Critical Heat Transfer, Proc. 2nd Canada-China Joint Workshop on Supercritical Water-Cooled Reactors (CCSC-2010), Toronto, 2010.
[II.32] ZAHLAN, H., GROENEVELD, D.C., TAVOULARIS, S., MOKRY, S., PIORO, I., Assessment of Supercritical Heat Transfer Prediction Methods, Proc. 5th Int. Symp. on SCWR (ISSCWR-5), Vancouver, 2011.
[II.33] SIEDER, N.M., TATE, G.E., Heat Transfer and Pressure Drop of Liquids in Tubes, Ind. Eng. Chem., **28, 12**, (1936), 1429–1435.
[II.34] BISHOP, A.A., SANDBERG, R.O., AND TONG, L.S., Forced Convection Heat Transfer to Water at Near-Critical Temperatures and Supercritical Pressures, A.I.Ch.E.-I. Chem. E. Symposium Series, **2**, (1965), 77−85.
[II.35] SWENSON, H.S., CARVER, J.R., KAKARALA, C.R., Heat transfer to Supercritical Water in Smooth-Bore Tubes, J Heat Transfer, **87**, **4**, (1965), 477-484.
[II.36] KRASNOSHCHEKOV, E.A., PROTOPOPOV, V.S., VAN, F., KURAEVA, I.V., Experimental Investigation of Heat Transfer for Carbon Dioxide in the Supercritical Region, Gazley, Jr., C., Hartnett, J.P., Ecker, E.R.C. (Eds.), Proc. 2nd All-Soviet Union Conference on Heat and Mass Transfer, Minsk, 1964 (Published as Rand Report R-451-PR, **1**, (1967), 26–35).
[II.37] HADALLER, G., BANERJEE, S., Heat Transfer to Superheated Steam in Round Tubes, AECL Report, 1969.
[II.38] GNIELINSKI, V., New Equation for Heat and Mass Transfer in Turbulent Pipe and Channel Flow, International Journal of Chemical Engineering, **16, 2**, (1976), 359–368.
[II.39] WATTS, M.J., CHOU, C.T., Mixed Convection Heat Transfer to Supercritical Pressure Water, Proc. 7th Int. Heat Transfer Conference (IHTC-7), Munich, (1982), 495–500.
[II.40] GRIEM, H. A New Procedure for the Prediction of Forced Convection Heat Transfer at Near- and Super-Critical Pressure, Heat Mass Transf., **31**, (1996), 301–305.

[II.41] KOSHIZUKA, S., OKA, Y., Computational Analysis of Deterioration Phenomena and Thermal-hydraulic Design of SCR, Proc. 1st Int. Symp. on Supercritical Water-Cooled Reactor Design and Technology (SCR-2000), Tokyo, 2000.
[II.42] JACKSON, J.D., Consideration of the Heat Transfer Properties of Supercritical Pressure Water in Connection with the Cooling of Advanced Nuclear Reactors, Proc. 13th Pacific Basin Nuclear Conference, Shenzhen, 2002.
[II.43] KUANG, B., ZHANG, Y., CHENG, X., A New, Wide-Ranged Heat Transfer Correlation of Water at Supercritical Pressures in Vertical Upward Ducts, Proc. 7th International Topical Meeting on Nuclear Reactor Thermal Hydraulics, Operation and Safety (NUTHOS-7), Seoul, 2008.
[II.44] CHENG, X., YANG, Y.H., HUANG, S.F., A Simple Heat Transfer Correlation for SC Fluid Flow in Circular Tubes, Proc. 13th Int. Topical Meeting on Nuclear thermal–hydraulics (NURETH-13), Kanazawa City, 2009.
[II.45] CHEN, W., FANG, X., XU, YU., SU, X., An Assessment of Correlations of Forced Convection Heat Transfer to Water at Supercritical Pressure, Annals of Nuclear Energy, **76**, (2015), 451-460.
[II.46] PIORO, I., DUFFEY, R., DUMOUCHEL, T., Hydraulic Resistance of Fluids Flowing in Channels at Supercritical Pressures (Survey), Nuclear Engineering and Design, **231, 2**, (2004), 187–197.
[II.47] FILONENKO, G.K., Hydraulic Resistance of Pipelines, Thermal Engineering (Tyeploenergyetika), **4**, (1954), 40-44 (In Russian).
[II.48] ORNATSKIY, A.P., DASHKIEV, YU.G., PERKOV, V.G., Supercritical Steam Generators, VyshchaShkola Publishing House, Kiev, Ukraine, 1980, (In Russian).
[II.49] RAZUMOVSKIY, V.G., Private Communications, National Technical University “KPI”, Kiev, Ukraine, 2003.

Appendix III. SAMPLE OF UNCERTAINTY ANALYSIS

This Appendix is mainly based on or directly reproduced from Ref [III.1] and published with permission from the American Society of Mechanical Engineers (ASME).

The proposed uncertainty analysis[1] is based on our current experience with heat-transfer and pressure-drop experiments in supercritical water [III.1], [III.2] and carbon dioxide [III.3] and on our long-term experience in conducting heat-transfer experiments at subcritical pressures [III.4], [III.5], [III.6], [III.7], [III.9], [III.10], [III.11], [III.12]. Also, basic principles of the theory of thermophysical experiments and their uncertainties were applied [III.13], [III.14], [III.15], [III.16], [III.17], [III.18], [III.19]. More details on experimental setups, procedures and data reduction at supercritical pressures, and some experimental features of various supercritical-pressure installations are fully described in [III.20].

In general, an uncertainty analysis is quite complicated process in which some uncertainties[2] (for example, uncertainties of thermophysical properties [III.21], uncertainties of constants, etc.) may not be known or may not be exactly calculated. Therefore, applying the engineering judgement is the only choice in some uncertainty calculations.

This section summarizes instrument calibrations and uncertainty calculations for the measured parameters such as temperature, pressure, pressure drop, mass flow rate, power, tube dimensions, etc. and for the calculated parameters such as mass flux, heat flux, etc. in supercritical heat-transfer and pressure-drop tests. Uncertainties for these parameters are based on the RMS of component uncertainties. All uncertainty values are at the 2σ level, unless otherwise specified.

Calibration of the instruments used in the tests was performed either *in situ*, e.g., power measurements, test section thermocouples, etc., or at an instrumentation shop, e.g., pressure transducers and bulk fluid temperature thermocouples. In general, instruments were tested against a corresponding calibration standard.

When the same calibration standard is used for serial instruments, the calibration standard uncertainty is treated as a systematic uncertainty. In general, high accuracy calibrators were used, hence systematic errors for calibrated instruments are considered to be negligible. All other uncertainties are assumed to be random. Also, errors correspond to the normal distribution. Usually, the uncertainties have to be evaluated for three values of the corresponding parameter: minimum, mean and maximum value within the investigated range.

Uncertainties are presented below for instruments, which are commonly used in heat-transfer and pressure-drop experiments. It is important to know the exact schematics for sensor signal

---

[1] The authors of the current appendix express their appreciation to D. Bullock and Y. Lachance (CRL AECL) for their help in preparation of this uncertainty analysis.

[2] Uncertainty refers to the accuracy of measurement standards and equals the sum of the errors that are at work to make the measured value different from the true value. The accuracy of an instrument is the closeness with which its reading approaches the true value of the variable being measured. Accuracy is commonly expressed as a percentage of a measurement span, measurement value or full-span value. Span is the difference between the full-scale and the zero scale value [III.22].

processing. Some commonly used cases, which are mainly based on a DAS recording, are shown in Fig. III.1 for thermocouples and in Fig. III.2 for RTDs, pressure cells and differential pressure cells.

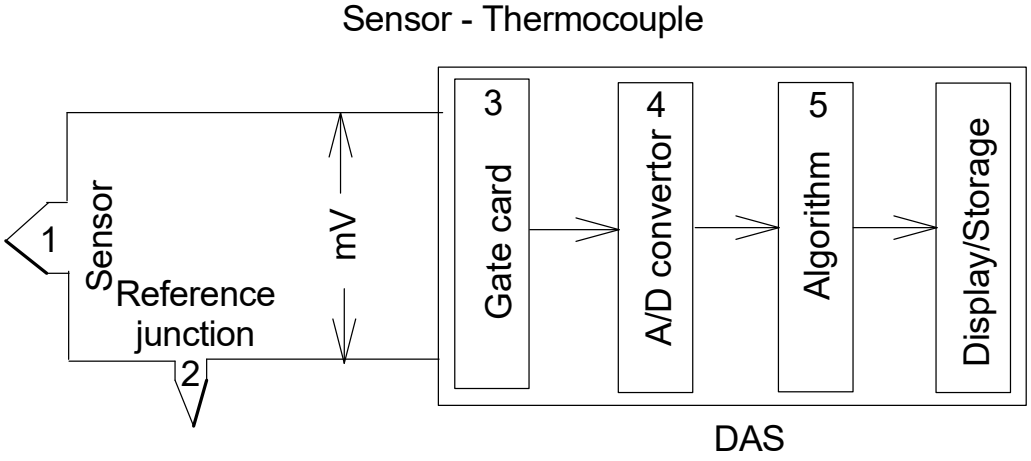

Fig. III.1. Schematic of signal processing for temperature (based on thermocouple) measurements. Numbers in figure identify uncertainty of particular device in measuring circuit: 1 – sensor uncertainty, 2 – reference junction uncertainty, 3 – Analog Input (A/I) uncertainty, 4 – Analog-to-Digital (A/D) conversion uncertainty, and 5 – DAS algorithm uncertainty.

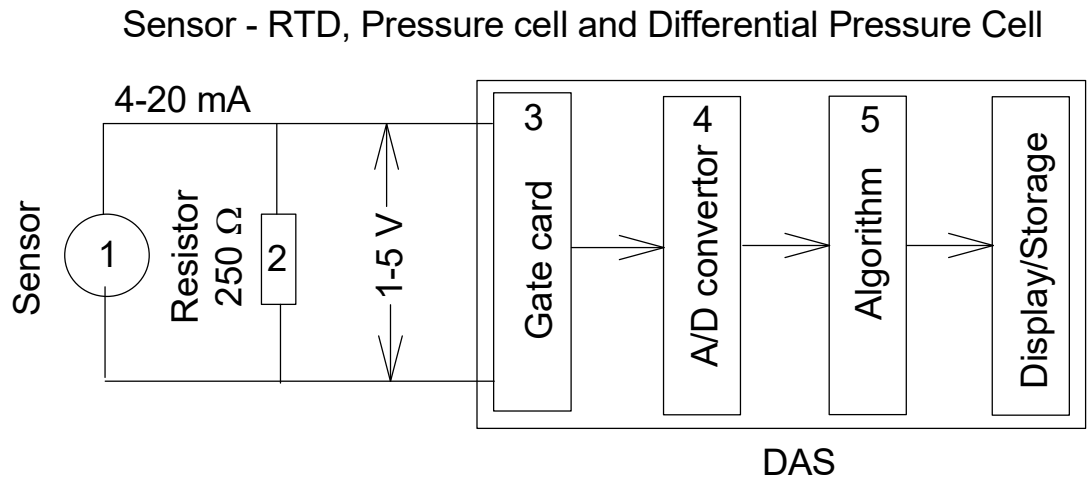

Fig. III.2. Schematic of signal processing for temperature (based on RTD), absolute pressure and differential pressure. Numbers in figure identify uncertainty of particular device in measuring circuit: 1 – sensor uncertainty, 2 – uncertainty due to temperature effect, 3 – A/I uncertainty, 4 – A/D conversion uncertainty, and 5 – DAS algorithm uncertainty; for RTD and both types pressure cells – DAS algorithm uncertainty is usually 0 due to linear fit.

Also, absolute and relative errors for commonly used functions are listed in TABLE III.1 for reference purposes.

TABLE III.1. ABSOLUTE AND RELATIVE ERRORS FOR COMMONLY USED FUNCTIONS [III.18].

Function	Absolute error	Relative error
$Y = X_1 + X_2 + \ldots + X_n$	$\pm\sqrt{\Delta X_1^2 + \Delta X_2^2 + \ldots + \Delta X_n^2}$	$\pm\frac{\sqrt{\Delta X_1^2 + \Delta X_2^2 + \ldots + \Delta X_n^2}}{X_1 + X_2 + \ldots + X_n}$
$Y = \frac{X_1 + X_2 + \ldots + X_n}{n}$	$\pm\frac{\sqrt{\Delta X_1^2 + \Delta X_2^2 + \ldots + \Delta X_n^2}}{\sqrt{n}}$	$\pm\frac{\sqrt{n}\cdot\sqrt{\Delta X_1^2 + \Delta X_2^2 + \ldots + \Delta X_n^2}}{X_1 + X_2 + \ldots + X_n}$
$Y = X_1 - X_2$	$\pm\sqrt{\Delta X_1^2 + \Delta X_2^2}$	$\pm\frac{\sqrt{\Delta X_1^2 + \Delta X_2^2}}{X_1 - X_2}$
$Y = X_1 \cdot X_2$	$\pm\sqrt{(X_1 \cdot \Delta X_2)^2 + (X_2 \cdot \Delta X_1)^2}$	$\pm\sqrt{\left(\frac{\Delta X_1}{X_1}\right)^2 + \left(\frac{\Delta X_2}{X_2}\right)^2}$
$Y = a \cdot X$	$\pm a \cdot \Delta X$	$\pm\frac{\Delta X}{X}$
$Y = X^n$	$\pm n \cdot X^{n-1}\Delta X$	$\pm\frac{n \cdot \Delta X}{X}$
$Y = sin\, X$	$\pm\, cos\, X \cdot \Delta X$	$\pm\mathrm{ctg}X \cdot \Delta X$
$Y = cos\, X$	$\pm\, sin\, X \cdot \Delta X$	$\pm\mathrm{tg}X \cdot \Delta X$
$Y = \mathrm{tg}X$	$\pm\frac{\Delta X}{cos^2 X}$	$\pm\frac{2 \cdot \Delta X}{sin(2 \cdot X)}$
$Y = \mathrm{ctg}X$	$\pm\frac{\Delta X}{sin^2 X}$	$\pm\frac{2 \cdot \Delta X}{sin(2 \cdot X)}$

III.1. TEMPERATURE

For the calibrated thermocouples, the following linear characteristics were found:

$$V_{act} = a \cdot V_{meas} + b \tag{III.1}$$

where V_{act} is the 'actual value'[3] of the given parameter, V_{meas} is the value measured by the given instrument, and a and b are the calibration coefficients.

[3] The value obtained from the calibration standard.

III.1.1. MEASURED BULK FLUID TEMPERATURE

The test section (see Figures 10.5 and 10.6) has three thermocouples to measure the inlet and outlet bulk fluid temperatures. Also, the temperature at the flowmeter is monitored by thermocouple for fluid density calculations.

The test section inlet and outlet bulk fluid temperatures were measured with sheathed K type thermocouples (for thermocouple signal processing, see Fig. III.1). These thermocouples were calibrated against the temperature standard RTD over the temperature range from 0 to 100ºC. For the reference RTD, the maximum error was ±0.3ºC. The maximum uncertainty of a data fit for inlet and outlet bulk fluid temperature measurements is listed in TABLE III.2. The inlet and outlet bulk fluid measurement uncertainties are listed in TABLE III.3.

TABLE III.2. LINEAR COEFFICIENTS FOR INLET AND OUTLET TEMPERATURE THERMOCOUPLES (FROM INSTRUMENT CALIBRATION RECORDS).

TC	**Coefficient**		**Uncertainty, ºC**	**Number of points**
–	***a***	***b***	**Maximum (2σ)**	**–**
TE-1	1.000	–0.1798	0.12	5
TE-2	0.9980	0.1502	0.12	5
TE-3	0.9985	0.0980	0.12	5

TABLE III.3. THE INLET AND OUTLET BULK FLUID MEASUREMENT UNCERTAINTIES.

Calibration system uncertainty	±0.3ºC
Thermocouple sensor accuracy after linear fit	±0.12ºC
A/I accuracy	±0.06°C, i.e., ±0.025% of f.s.; $\left(= \pm \frac{0.00025 \cdot 10 \text{ mV}}{0.045 \frac{\text{mV}}{^\circ C}}\right)$; where f.s. is the full scale
A/D resolution accuracy (minimum 1 bit)	±0.03°C $\left(= \pm \frac{10 \text{ mV (f.s.)}}{8192 \text{ counts} \cdot 0.045 \frac{\text{mV}}{^\circ C}}\right)$, where 0.045 mV/ºC is the conversion rate, i.e., 4.509 mV for 100ºC (The Temperature Handbook 2000)
Reference junction accuracy	±0.4ºC

For a given test section inlet or outlet temperature t, the uncertainty Δt is given by

$$\frac{\Delta t}{t} = \sqrt{\left(\frac{0.3}{t}\right)^2 + \left(\frac{0.12}{t}\right)^2 + \left(\frac{0.03}{t}\right)^2} \tag{III.2}$$

The first term is the maximum error of the calibration system (±0.3ºC). The second term is the maximum error for the sheathed thermocouple (≤100ºC), obtained from the calibration. The third term is the uncertainty introduced by the DAS, i.e., the A/D resolution uncertainty (±0.03ºC). Note that since the calibration was done *in situ* using the DAS as the measuring system for the RTD and for the calibrated thermocouples, the uncertainty introduced by the reference junction and the A/I accuracy was included in calibration curves.

All bulk fluid temperature thermocouples were calibrated *in situ*, only within the range of 0 – 100ºC. Therefore, individual correction factors were implemented for each thermocouple within the range of 0 – 100ºC (see TABLE III.2). For this range of temperatures, the uncertainty Δt is

— for T_{min} = 20ºC ΔT = ±0.32ºC (or ±1.62%), and

— for T = 100ºC ΔT = ±0.32ºC (or ±0.32%).

Beyond this range, thermocouple uncertainties were taken as per The Temperature Handbook (2000), i.e., ±2.2°C.

Thermocouple installed near the flowmeter was calibrated using another calibrating system and procedure. All inputs below are from instrument calibration record and device manuals unless otherwise specified.

Calibration system uncertainty: ±0.5°C, i.e., $\left(= \pm\sqrt{0.06^2 + 0.5^2 + 0.041^2}\right)$, where the first term is the accuracy of standard RTD, the second term is the accuracy of thermocouple signal measuring device and the third term is the accuracy of RTD signal measuring device (all uncertainties are in ºC).

TABLE III.4. CALIBRATION SYSTEM UNCERTAINTY.

TC maximum calibration accuracy[4] (>2σ) within 0.0 – 45.0ºC	±0.53°C
A/I accuracy	±0.06°C, i.e., ±0.025% of f.s. $\left(= \pm\frac{0.00025 \cdot 10\ \text{mV}}{0.045\ \frac{\text{mV}}{°C}}\right)$
A/D resolution accuracy (minimum 1 bit)	±0.03°C $\left(= \pm\frac{10\ \text{mV (f.s.)}}{8192\ \text{counts} \cdot 0.045\ \frac{\text{mV}}{°C}}\right)$, where 0.045 mV/ºC is the conversion rate, i.e., 4.509 mV for 100ºC (The Temperature Handbook 2000)
Reference junction accuracy	±0.02°C

For a given flowmeter bulk fluid temperature t_{fm}, the uncertainty Δt_{fm} is given by

[4] The TC calibration accuracy is the maximum difference in °C between what the calibration standard measured and what TC indicated.

$$\left(\frac{\Delta\ t_{fm}}{t_{fm}}\right)_{TC} = \left(\pm\sqrt{\left(\frac{0.5}{t_{fm}}\right)^2 + \left(\frac{0.53}{t_{fm}}\right)^2 + \left(\frac{0.06}{t_{out}}\right)^2 + \left(\frac{0.03}{t_{out}}\right)^2 + \left(\frac{0.02}{t_{out}}\right)^2}\right)_{TC} \quad \text{(III.3)}$$

Therefore, the flowmeter bulk fluid temperature uncertainty is:

— for $t_{fm\ min}$ = 19ºC Δt_{fm} = ±0.74ºC (or ±3.9%), and
— for $t_{fm\ max}$ = 35ºC Δt_{fm} = ±0.74ºC (or ±2.1%).

Additional uncertainties due to thermocouple installation and possible electrical pickup have been minimized by using good engineering practices.

If a bulk fluid temperature is measured with an RTD, then the following will apply.

The bulk fluid temperature measurement uncertainties at the 2σ level are characterized with the following for an RTD (for RTD signal processing, see Fig. III.2):

Calibration system uncertainty in ºC (from the instrument calibration record): $\text{Cal. Sys. Unc.} = \pm\sqrt{\left[\left(0.01\%\ \text{of Reading}\ \frac{16\ \text{mA}}{100°C} + 0.015\%\ \text{of f.s.}\right)\frac{100°C}{16\ \text{mA}}\right]^2 + (0.05°C)^2} \approx 0.06°C$, where the first term is the accuracy of calibrator in which reading is in ºC and f.s. is 30 mA and a conversion rate is 16 mA for 100ºC; and the second term is the accuracy of standard RTD.

The RTD accuracy after linear fit, i.e., maximum deviation (from the instrument calibration record), is about ±0.08°C;

A/I accuracy (from the device manual):

±0.032°C (±0.025% of f.s.), i.e., $\left(= \pm\frac{0.00025 \cdot 5.12\ \text{V (f.s.)}}{0.04\ \frac{V}{°C}}\right)$.

A/D conversion accuracy (minimum 1 bit accuracy) (from the device manual):

±0.016°C, i.e., $\left(= \pm\frac{5.12\ V\ \text{(f.s.)}}{8192\ \text{counts} \cdot 0.04\ \frac{V}{°C}}\right)$, where 0.04 V/ºC is the conversion rate, i.e., 4 V for 100ºC (from the instrument calibration record). DAS algorithm uncertainty is 0 due to a linear fit. Therefore, for a given test section inlet temperature, its uncertainty (Δt) is given by

$$\frac{\Delta t}{t} = \pm\sqrt{\left(\frac{Cal.\ Sys.\ Unc.}{t}\right)^2 + \left(\frac{0.08}{t}\right)^2 + \left(\frac{0.032}{t}\right)^2 + \left(\frac{0.016}{t}\right)^2} \quad \text{(III.4)}$$

The resulting uncertainties in the bulk fluid temperature are

— For t = 10°C Δt = ±0.10°C (or ±1.2%); and
— For t = 50°C Δt = ±0.11°C (or ±0.2%).

If the bulk fluid temperature is measured with several devices installed in a one cross section (for example, two RTDs and one thermocouple), the following equation may apply:

$$\frac{\Delta \bar{t}}{\bar{t}} \cong \pm \frac{\sqrt{(\Delta t_{RT} \quad)^2 + (\Delta t_{RTD2})^2 + (\Delta t_{TC})^2}}{\sqrt{3}\ \bar{t}} \tag{III.5}$$

In this case, the resulting uncertainty will be close to the larger uncertainty, i.e., the thermocouple uncertainty. Therefore, if several devices have to be used for measuring a non-uniform temperature or any other parameter, they have to be with a similar accuracy.

III.1.2. EXTERNAL WALL TEMPERATURE

Temperatures for the test section external surface were measured using fast-response K type thermocouples (Fig. III.3). In general, thermocouple uncertainties for K type thermocouples are ±2.2°C within a range of 0–277ºC [III.23]. However, all fast response thermocouples were calibrated *in situ* within a range of 0–100ºC prior to use (for details, see below). Therefore, individual correction factors were implemented for each thermocouple within the range of 0–100ºC. Beyond this range, thermocouple uncertainties were taken as per [III.23], i.e., ±2.2°C.

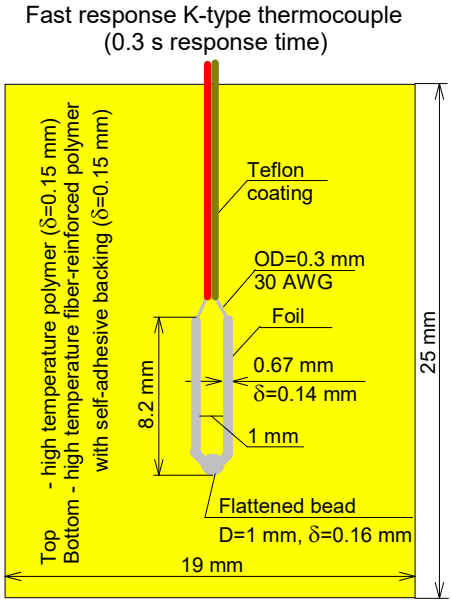

Fig. III.3. Sketch drawing of fast response K type thermocouple.

All K type thermocouples were calibrated against the temperature calibration standard (i.e., the reference RTD) over the temperature range from 0 to 100ºC. These thermocouple assemblies were immersed in a liquid bath thermostat together with the RTD. For the reference RTD, the maximum uncertainty is ±0.3ºC. The combined uncertainty[5] for wall temperature measurements is as follows:

TABLE III.5. THE COMBINED UNCERTAINTY FOR WALL TEMPERATURE MEASUREMENTS.

Calibration system accuracy	±0.3ºC
Thermocouple sensor accuracy after linear fit	±0.16ºC max at values ≤100°C
A/I accuracy	±0.06°C, i.e., ±0.025% of f.s. $\left(=\pm\frac{0.00025\cdot 10\ \text{mV}}{0.045\ \frac{\text{mV}}{^\circ C}}\right)$
A/D resolution accuracy (minimum 1 bit)	±0.03°C $\left(=\pm\frac{10\ \text{mV (f.s.)}}{8192\ \text{counts}\cdot 0.045\ \frac{\text{mV}}{^\circ C}}\right)$, where 0.045 mV/ºC is the conversion rate, i.e., 4.509 mV for 100ºC (The Temperature Handbook 2000)

For a given test section wall temperature t, the uncertainty Δt is given by

$$\frac{\Delta t}{t}=\sqrt{\left(\frac{0.3}{t}\right)^2+\left(\frac{0.16}{t}\right)^2+\left(\frac{0.03}{t}\right)^2} \tag{III.6}$$

The first term is the maximum error of the calibration system (±0.3ºC). The second term is the maximum error of the sheathed thermocouple (≤100ºC), obtained from the calibration. The third term is the uncertainty introduced by the DAS, i.e., the A/D resolution uncertainty (±0.03ºC). Note that since the calibration was done *in situ* using the DAS as the measuring system for the RTD and the calibrated thermocouples, the uncertainty introduced by the reference junction and the A/I accuracy was included in calibration curves. Within the calibrated range of measured temperatures, i.e., from 0 to 100ºC, the uncertainty Δt is

— for t_{min} = 25ºC Δt = ±0.34ºC (or ±1.36%), and

— for t = 100ºC Δt = ±0.34ºC (or ±0.34%).

Also, the external wall temperatures measured with fast-response thermocouples were compared to the inlet and outlet bulk fluid temperatures measured with sheathed thermocouples, at 0 power and 0 mass flux through the test section (see Fig. III.4). The comparison showed that, in general, all measured temperatures were within ±0.3ºC.

[5] All inputs are from instrument calibration records and device manuals unless otherwise specified.

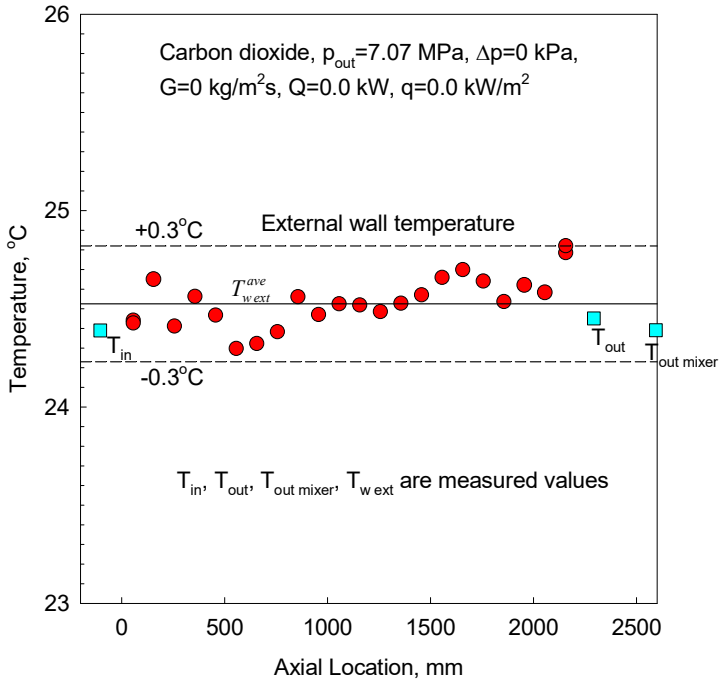

Fig. III.4. Temperature profile along test section at 0 power and 0 mass flux values.

III.2. ABSOLUTE PRESSURE

A high-accuracy gauge pressure cell with a range of 0–10,000 kPa (0–10 MPa) was used for the outlet-pressure measurements (for pressure signal processing, see Fig. III.2). A small correction (77.2 kPa) is applied in the DAS program for the elevation difference between the pressure tap and transmitter. The combined uncertainty for absolute pressure measurements is as follows.

Accuracy of gauge pressure cell (from the calibration record) is ±0.1% of calibrated span (10,000 kPa), and this accuracy was verified during the calibration check.

Calibration system uncertainty in kPa (from the instrument calibration record): Cal. Sys. Unc. $= \pm\sqrt{\left[\left(0.015\%\text{ of Reading }\frac{16\text{ mA}}{10000\text{ kPa}} + 0.015\%\text{ of f.s.}\right)\frac{10000\text{ kPa}}{16\text{ mA}}\right]^2 + (0.1\%\text{ of Reading })^2}$, where the first term is the accuracy of calibrator in which reading is in kPa and f.s. is 30 mA and conversion rate is 16 mA for 10000 kPa; and the second term is the accuracy of tester.

Uncertainty due to temperature effect in 250-Ω resistor: ±0.1%.

A/I accuracy (from the device manual):

±3.2 kPa, i.e., ±0.025% of f.s., i.e., 5.12 V $\left(= \pm\frac{0.00025\cdot 5.12\ V}{0.0004\ \frac{V}{\text{kPa}}}\right)$.

A/D conversion accuracy (minimum 1 bit accuracy) (from the device manual):

±1.56 kPa $\left(= \pm \frac{5.12\ V\ \text{(f.s.)}}{8192\ \text{counts} \cdot 0.0004\ \frac{V}{\text{kPa}}}\right)$, where 0.0004 V/kPa is the conversion rate, i.e., 4 V for 10,000 kPa (from the instrument calibration record).

For a given test section outlet pressure p, the uncertainty Δp is given by

$$\frac{\Delta\ p}{p} = \pm\sqrt{\left(\frac{0.001 \cdot 10000}{p}\right)^2 + \left(\frac{0.1}{100}\right)^2 + \left(\frac{A/I}{p}\right)^2 + \left(\frac{A/D}{p}\right)^2} \tag{III.7}$$

For the range of p from 7.6 to 8.8 MPa, the uncertainty Δp is given by

— for p_{min} = 7600 kPa Δp = ±13.1 kPa (or ±0.17%),
— for p = 8400 kPa Δp = ±13.5 kPa (or ±0.16%).
— for p_{max} = 8800 kPa Δp = ±13.8 kPa (or ±0.16%).

III.3. DIFFERENTIAL PRESSURE CELLS

Five differential-pressure transducers for measuring test section pressure drops (for differential-pressure signal processing, see Fig. III.2) were connected to the corresponding pressure taps installed as shown in Figure 10.6. They were used for measuring the test section axial pressure gradient and the overall pressure drop. Also, one differential-pressure transducer was used to measure a pressure drop across the flowmeter (see Figure 10.5). All these pressure drops were measured using pressure transmitters.

A calibrator and a pressure module were used for the calibration check of the differential-pressure transducers. Basic characteristics of the test section and flowmeter differential-pressure cells are listed in TABLE III.6.

TABLE III.6. BASIC CHARACTERISTICS OF DIFFERENTIAL-PRESSURE CELLS.

Instrument Name	Description	Output	Output kPa	Span kPa	Accuracy ±% of span
PDT-1	Total test section pressure drop	10–50 mV	0–300	300	0.5
PDT-2	Test section pressure drop	1–5 V	0–50	50	0.5
PDT-3	Test section pressure drop	1–5 V	0–50	50	0.5
PDT-4	Test section pressure drop	1–5 V	0–50	50	0.5
PDT-5	Test section pressure drop	1–5 V	0–50	50	0.5
PDT-FM-1	Orifice-plate pressure drop	10–50 mV	0–37	37	0.5

Accuracy, includes combined effects of linearity, hysteresis and repeatability in % of a calibrated span are listed in TABLE III.6.

Calibration system uncertainty in kPa (from instrument calibration records): $\text{Cal. Sys. Unc.} = \pm\sqrt{\left[\left(0.015\%\text{ of Reading }\frac{16\text{ mA}}{\text{Span kPa}} + 0.015\%\text{ of f.s.}\right)\frac{\text{Span kPa}}{16\text{ mA}}\right]^2 + (0.05\%\text{ of f.s. })^2}$, where the first term is the accuracy of process calibrator in which reading is in kPa, f.s. is 30 mA and conversion rate is 16 mA for span in kPa; and the second term is the accuracy of calibrator in which f.s. is 690 kPa (100 psig).

Uncertainty due to temperature effect in 250-Ω resistor: ±0.1%.

A/I accuracy (from a device manual):

±0.025% of f.s., i.e., $\left(= \pm\frac{0.00025\cdot 5.12\ V}{\frac{4\ V}{\text{Span kPa}}}\right)$.

A/D conversion accuracy (minimum 1 bit accuracy) (from a device manual):

$\left(= \pm\frac{5.12\ V\text{ (f.s.)}}{8192\text{ counts}\cdot\frac{4\ V}{\text{Span kPa}}}\right)$.

For a given pressure drop (Δp) for PDT-1, PDT-2 to PDT-5 and PDT-FM-1, the uncertainty $\Delta(\Delta p)$ is given by

$$\frac{\Delta\ (\Delta\ p)}{\Delta\ p} = \pm\sqrt{\left(\frac{\%\ of\ span\ in\ kPa}{\Delta\ p}\right)^2 + \left(\frac{0.1}{100}\right)^2 + \left(\frac{A/I}{\Delta\ p}\right)^2 + \left(\frac{A/D}{\Delta\ p}\right)^2} \tag{III.8}$$

For the range of the total Δp from 5 to 70 kPa, the uncertainty $\Delta(\Delta p)$ for PDT-1 is given by

— for Δp_{min} = 5 kPa $\Delta(\Delta p)$ = ±1.50 kPa (or ±30.1%), and
— for Δp_{max} = 70 kPa $\Delta(\Delta p)$ = ±1.51 kPa (or ± 2.2%).

For the range of the local Δp from 5 to 30 kPa, the uncertainty $\Delta(\Delta p)$ for PDT-2 – PDT-5 is given by

— for Δp_{min} = 5 kPa $\Delta(\Delta p)$ = ±0.25 kPa (or ±5.0%), and
— for Δp_{max} = 30 kPa $\Delta(\Delta p)$ = ±0.25 kPa (or ±0.84%).

For the local Δp equals to 37 kPa, the uncertainty $\Delta(\Delta p)$ for PDT-FM-1 is given by

— for Δp_{min} = 1.5 kPa $\Delta(\Delta p)$ = ±0.19 kPa (or ±12.5%), and
— for Δp_{max} = 16.9 kPa $\Delta(\Delta p)$ = ±0.19 kPa (or ± 1.1%).

III.4. MASS FLOW RATE

The loop mass flow rate FM-1 (see Figure 10.5) is measured by a small orifice plate[6] with an orifice diameter of 0.308", and monitored by a differential-pressure cell with the range of 0–37 kPa. This cell has a square root output, with an accuracy of ±0.5% of full scale. The square root output is converted in the program to obtain kPa for use in the following flow equation, for a mass flow rate of 0–0.24 kg/s (see Fig. III.4):

$$m = C_{fl}\sqrt{\rho\ \Delta\ p} \tag{III.9}$$

where $C_{fl} = 0.00130$ is the constant (White 1994), ρ is the density at the orifice plate in kg/m^3, and Δp is the pressure drop across the orifice plate in kPa. It is known that orifice-plate flowmeters usually have a working range within (0.3 and 1)·m_{max}, i.e., 0.08–0.24 kg/s [III.24].

In general, the constant C_{flow} is a function of Reynolds number (see Fig. III.5). However, this effect is minor within the investigated range of Reynolds numbers (**Re** = 57,000–1,130,000). We attempted to calibrate the flowmeter FM-1 with water using the direct weighting method [III.14] within the supercritical CO_2 investigated Reynolds numbers range. Due to significantly different values of water dynamic viscosity compared to those of supercritical carbon dioxide and restrictions applied to the maximum water flow and its temperature, the flowmeter was calibrated (see Fig. III.6) within a lower range of Reynolds numbers (***Re*** = 2,700–27, 000) compared to those of supercritical carbon dioxide (***Re*** = 57,000–1,130,000).

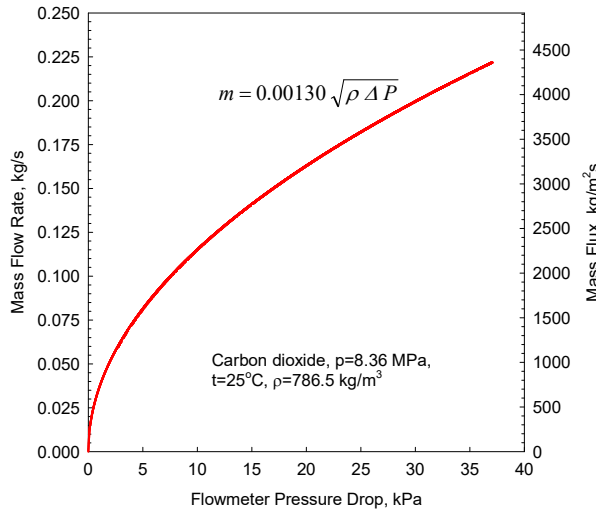

Fig. III.5. Flow measurement curve.

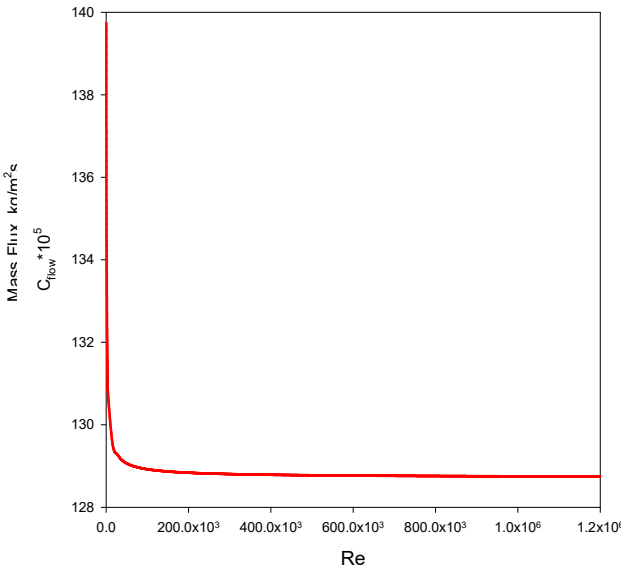

Fig. III.6. Effect of Reynolds number on flow constant.

[6] This small diameter orifice plate is a non-standard orifice plate, because International Standard ISO 5167-2:2003(E), "Measurement of fluid flow by means of pressure differential devices inserted in circular-cross section conduits running full – Part 2: Orifice Plates", applies only to orifice plates with a diameter not less than 12.5 mm.

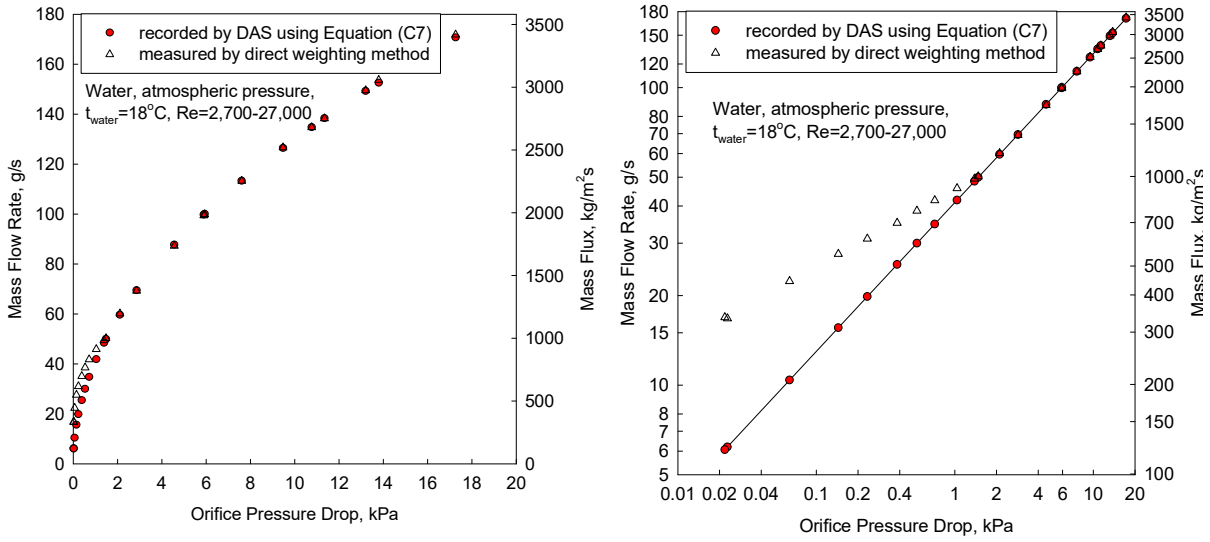

Fig. III.7. Calibration results for FM-1 orifice-plate flowmeter: (a) linear scale, and (b) logarithmic scale.

However, the calibration results showed that Equation (III.9) is reasonably accurate (a mean error is –0.15% and an RMS error is 0.5%) for flows that are not less than 0.045 kg/s. This finding is consistent with heat-balance error data obtained in supercritical CO_2. However, the heat-balance error data for m < 0.045 kg/s show the opposite trend, i.e., steeper slope than that shown in Fig. III.6b. Mass flow rates lower than 0.045 kg/s were calculated using

$$m = \frac{POW}{H_{out} - H_{in}} \tag{III.10}$$

In general, flow rate measurement uncertainty within the range of m = 0.045–0.24 kg/s is given by

$$\frac{\Delta\, m}{m} = \sqrt{\left(\frac{\Delta\, C_1}{C_1}\right)^2 + \left(\frac{0.5\ \Delta\ \rho}{\rho}\right)^2 + \left(\frac{0.5\ \Delta\ (\Delta\ p)}{\Delta\ p}\right)^2} \tag{III.11}$$

The estimated uncertainty in the constant C_1 is ±0.08% as a result of the minor effect of Reynolds number on the constant within the investigated range [III.25].

Temperature, pressure (see Figure 10.5) and NIST software [III.21] were used for the CO_2 density calculation. At pressures up to 30 MPa and temperatures up to 249.9ºC (523 K), the estimated uncertainty in density [III.21] varies up to 0.05%. Also, additional uncertainty in density arises from variations in density within the measured temperature uncertainty of ±1.1ºC. This additional uncertainty is about ±1.1% at p = 8.36 MPa and t = 19ºC, and ±5.0% at p = 8.8 MPa and t = 35ºC. Therefore, the total uncertainty in density is

$$\frac{\Delta \rho}{\rho} = \sqrt{\left(\frac{0.05}{100}\right)^2 + \left(\frac{1.1}{100}\right)^2} = 0.011 \; at\; p = 8.36\; MPa\; and\; t = 19ºC \tag{III.12}$$

and

$$\frac{\Delta \rho}{\rho} = \sqrt{\left(\frac{0.05}{100}\right)^2 + \left(\frac{5.0}{100}\right)^2} = 0.05 \; at\; p = 8.8\; MPa\; and\; t = 35ºC \tag{III.13}$$

However, the vast majority of the experimental data were obtained at pressure of 8.36 MPa. Therefore, the uncertainty value of 0.011 was used below.

Pressure-drop measurement uncertainties for PDT-FT-1/1 are according to Section III.3.

Hence,

— for m_{min} = 46 g/s Δm = ±5.7 g/s (or ±12.5%) at t = 19ºC and p = 8.36 MPa, and
— for m_{max} = 155 g/s Δm = ±2.4 g/s (or ± 1.6%) at t = 19ºC and p = 8.36 MPa.

III.5. MASS FLUX

Mass flux, G, is based on mass flow rate measurements. The uncertainty, ΔG, includes an error in the estimation of the cross sectional flow area, A_{fl} = 5.1 10^{-5} m^2. The test section is a tube of 8.058 mm ID and 10 mm OD, made of Inconel 600, with tolerances of ±0.02 mm. The uncertainties are as follows:

For ID ΔD = ±0.02 mm (or ±0.25%),

For OD ΔD_{ext} = ±0.02 mm (or ±0.20%), and

For A_{flow} $\Delta A_{fl} = \frac{\pi\, D\, \Delta\, D}{2}$ = ±0.253 mm^2 (or ±0.50%).

The uncertainty, ΔG, is obtained from the following equation:

$$\frac{\Delta\, G}{G} = \sqrt{\left(\frac{\Delta\, m}{A_{fl}\, G}\right)^2 + \left(\frac{m\, \Delta\, A_{fl}}{A_{fl}^2\, G}\right)^2} = \sqrt{\left(\frac{\Delta\, m}{m}\right)^2 + \left(\frac{\Delta\, A_{fl}}{A_{fl}}\right)^2} \tag{III.14}$$

For the range of interest, the uncertainties, ΔG, are

for G_{min} = 902 kg/m^2·s (m_{min} = 46 g/s) ΔG = ±112.8 kg/m^2·s (or ±12.5%), and

for G_{max} = 3039 kg/m^2·s (m_{max} = 155 g/s) ΔG = ± 49.8 kg/m^2·s (or ± 1.6%).

III.6. ELECTRICAL RESISTIVITY

Electrical resistivity is a calculated value (for details, see Equation (III.2)) that is based on measured values of electrical resistance, heated length and tube diameters. The accuracy of the micro-ohmmeter used in test section electrical resistance measurements is ±0.04% of the reading (its readings are in milliohms). The uncertainties in ID and OD are $\Delta D = \Delta D_{ext} = \pm 0.02$ mm, and in L it is $\Delta L = \pm 0.5$ mm.

For a given electrical resistivity, the uncertainty $\Delta\rho$ is given by

$$\frac{\Delta \rho_{el}}{\rho_{el}} = \sqrt{\left(\frac{0.04}{100}\right)^2 + \left(\frac{\Delta D_{ext}}{D_{ext}}\right)^2 + \left(\frac{\Delta D}{D}\right)^2 + \left(\frac{\Delta L}{L}\right)^2} \tag{III.15}$$

The uncertainty in $\Delta\rho_{el}$ ($\rho_{el} = 104.3 \cdot 10^{-8}$ Ohm·m) is

— for $L = 2461$ mm $\Delta\rho_{el} = \pm 0.212 \cdot 10^{-8}$ Ohm·m (or ±0.20%).

III.7. TOTAL TEST SECTION POWER

The total test section power is obtained by measuring the current through a 2000 A/100 mV current shunt and the voltage across the test section. These signals are fed into a Power–Measuring Unit (PMU), where the test section voltage is scaled down to a 1 V level. Both the voltage and current signals are fed into isolation amplifiers and then into instrumentation amplifiers with outputs of 0–10 V. The amplifier outputs are fed to the computer analog inputs and represent a full-scale voltage of 175 V and a full-scale current of 2000 A. These signals are multiplied in the computer program to represent a 0–350 kW power level.

Calibration of the power measurement unit was performed *in situ*. Test section voltage and current inputs were removed from the PMU. Simulated inputs were used to check the calibration of the unit. A comparison between the computer readings and the calibrated simulated inputs was used to create a curve fit for the DAS to correct for the differences. The voltage input from 0–110 V DC was simulated with a DC power supply and verified with a multimeter. The current shunt input was simulated with a calibrator for inputs from 10 to 100 mV, which represents 200–2000 A range:

TABLE III.7. PARAMETERS OF CURRENT SHUNT.

Accuracy of current shunt	±0.25% of reading
Error due to current shunt resistance change	±0.02%
A/D accuracy	±0.025% of f.s., 10.00 V

The uncertainty, ΔPOW_{TS}, in power measurements (the power is a product of U and I) is given by

$$\frac{\Delta\ POW_{TS}}{POW_{TS}} = \sqrt{\left(\frac{0.25}{100}\right)^2 + \left(\frac{0.02}{100}\right)^2 + \left(\frac{0.1}{100}\right)^2 + \left(\frac{0.09}{100}\right)^2 + \left(\frac{\Delta\ I_1}{I}\right)^2 + \left(\frac{\Delta\ U_1}{U}\right)} \quad \text{(III.16)}$$

The first term is the accuracy of the current shunt, the second term is the effect of a temperature change on the current shunt, the third term is the error in the test section voltage drop from the PMU output of ΔU = +0.1% (0.10 V) up to 100 V, the fourth term is the error in the test section current from the PMU output with a maximum offset of ΔI = +0.09% (0.75 A) at 800 A, and the fifth and sixth terms are the ±0.025% uncertainties introduced by the AC/DC conversion process for reading the current (ΔI_1 = ±0.5 A) and (ΔU_1 = ± 0.04 V) for reading the voltage, respectively.

For the power range, POW_{TS}, from 3.0 to 35.0 kW, and for L = 2.208 m, the corresponding values of voltage drop and current are

— $POW_{TS\,min}$ = 3000 W U = 16.0 V, I = 188 A, and

— $POW_{TS\,max}$ = 35,000 W U = 54.6 V, I = 641 A.

The uncertainty in ΔPOW_{TS} is as follows:

— For $POW_{TS\,min}$ = 3000 W ΔPOW_{TS} = ± 13.9 W (or ±0.46%), and

— For $POW_{TS\,max}$ = 35,000 W ΔPOW_{TS} = ±106.4 W (or ±0.30%).

III.8. AVERAGE HEAT FLUX

The uncertainty in heat flux, Δq_{ave}, involves the uncertainties in the total test section power (see Section III.7) and in the heated area measurements, ΔA_h, where $A_h = \pi D L$. The uncertainty in ID is ΔD = ±0.02 mm, and in L it is ΔL = ±0.5 mm. Thus, ΔA_h can be calculated from

$$\frac{\Delta A_h}{A_h} = \sqrt{\left(\frac{\Delta D}{D}\right)^2 + \left(\frac{\Delta L}{L}\right)^2} \quad \text{(III.17)}$$

The uncertainty in A_h (A_h = 55,895.4 mm^2) is

— for L = 2208 mm and D = 8.058 mm ΔA_h = ±78.3 mm^2 (or ±0.14%).

Then, the uncertainty in q_{ave} can be computed from

$$\frac{\Delta\ q_{ave}}{q_{ave}} = \sqrt{\left(\frac{\Delta\ POW_{\ TS}}{POW_{\ TS}}\right)^2 + \left(\frac{\Delta\ A_h}{A_h}\right)^2} \quad \text{(III.18)}$$

which, for the given power values, results in

— $q_{ave\ min}$ = 53.7 kW (POW_{TS} = 3.0 kW) Δq = ± 0.28 kW/m^2 (or ±0.53%), and

— $q_{ave\ max}$ = 626.2 kW (POW_{TS} = 35.0 kW) Δq = ± 2.46 kW/m^2 (or ±0.39%).

However, Equation (D18) does not account for the uncertainties related to the heat loss, which are subtracted from the applied heat flux (for details, see Section 10.3.8), because the heat loss was negligible, i.e., less than 0.5%.

III.9. UNCERTAINTIES IN HEAT-TRANSFER COEFFICIENT

Local HTC is as follows:

$$HTC = \frac{q}{t_w^{int_b}} \tag{III.19}$$

Uncertainty in the temperature difference is

$$\frac{\Delta(t_w^{int_b}}{t_w^{int_b} = \pm \frac{\sqrt{(\Delta t_w^{int}()^2(\Delta t_b)^2)}}{t_w^{in\ _b}}} \tag{III.20}$$

where uncertainty in t_w^{int} is taken as uncertainty in t_w^{ext} and uncertainty in t_b is taken as uncertainty in t_{out}.

And uncertainty ΔHTC is

$$\frac{\Delta\ HTC}{HTC} = \sqrt{\left(\frac{\Delta\ q}{q}\right)^2 + \left(\frac{\Delta(\ t_w^{\text{int}} - t_b\ )}{t_w^{\text{int}} - t_b}\right)^2} \tag{III.21}$$

III.10. UNCERTAINTIES IN THERMOPHYSICAL PROPERTIES NEAR PSEUDOCRITICAL POINT

Uncertainties in thermophysical properties [III.21] near the pseudocritical point within the uncertainty range of the measured value of bulk fluid temperature (Δt = ±0.4ºC) are as follows (for example, at p = 8.38 MPa (t_{pc} = 36.7ºC)):

$\Delta\rho$ = ±7%; ΔH = ±2.5%; Δc_p = 4.5%; Δk = ±2%, and $\Delta\mu$ = ±7%.

III.11. HEAT LOSS TESTS

Heat loss is an important component of the total heat-balance analysis. Heat loss from the test section, HL_{TS}, to the surrounding area was measured at various wall temperatures, with electrical power applied to the test section (the loop was previously evacuated to minimise heat removal through the coolant). This test provided (*i*) an indication of the difference between the measured external wall temperatures and ambient temperature, and (*ii*) data (voltage and current applied to the test section) to calculate the heat loss from the test section.

To perform the heat loss power test, a small power supply was used. The temperature difference between the external wall temperatures and ambient temperature at zero power was found to be ±0.2ºC (i.e., within the accuracy range for the thermocouples); with an increase in power to the test section, the difference ($\Delta t = t_w^{ave} - t_{amb}$) increases. This temperature difference permits the evaluation of the heat loss from the test section to the surrounding area as follows:

$$HL_{TS} = POW_{TS} = f(\Delta t) \tag{III.22}$$

or, as calculated,

$$HL_{TS} = POW_{TS} = U \; I \tag{III.23}$$

where U is the voltage drop over the test section, and I is the current through the test section wall. This heat loss test, compared to the usual zero-power test, eliminates uncertainties that are related to the estimation of the thermophysical properties of CO_2. This test also eliminates flow-measurement uncertainties and uncertainties that are incurred when measuring very small temperature differences (0.5–1ºC) between the inlet and outlet bulk fluid temperatures.

The heat loss power test was performed with the insulated reference test section (heated length of 2.208 m). The heat loss assessed from these tests, as a function of the wall-ambient temperature difference, ($t_w^{ave} - t_{amb}$), is shown in Fig. III.7, and can be approximated by the following equation:

$$HL_{TS} = 0.47(t_w^{ave} - t_{amb}) \text{ [W]} \tag{III.24}$$

There were some nonuniformities in the temperature distribution along the heated length. These non-uniformities were caused by the power clamps and structural support elements for the test section, which acted as heat sinks. Therefore, a conservative approach (maximum possible heat loss and therefore, minimum HTC value) was taken, i.e., only two external wall thermocouples (TEC01 and TEC24), which are located in the same cross sections as TEC02 and TEC23, respectively, but 180º apart, were not taken into account (see Figure 10.6). For local heated lengths, the following formula would apply:

$$HL_{TS}\big|_{L_\ell} = HL_{TS}\big|_{L=2.208m}\frac{L_\ell}{2.208}\ [kW] \tag{III.25}$$

where L_ℓ is in metres. In general, heat loss was negligible, i.e., less than 0.5%.

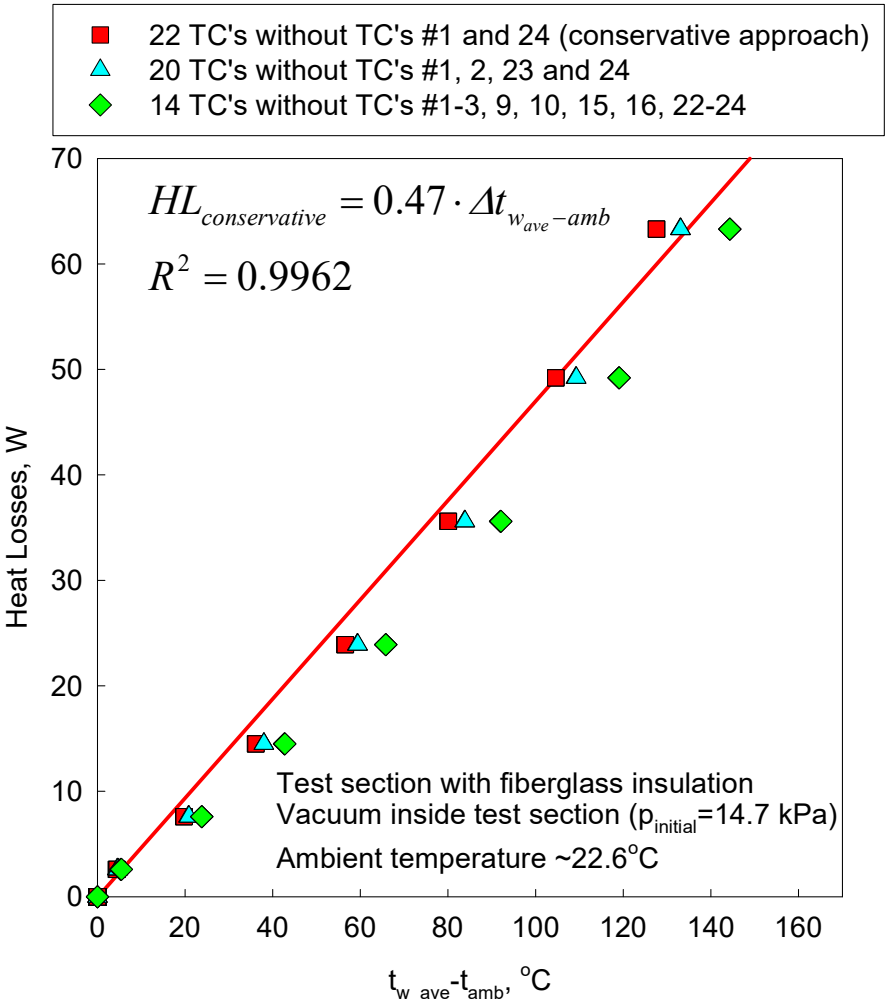

Fig. III.8. Heat loss from test section: Direct electrical heating of test section, heated length of 2.208 m, and loop vacuumed.

III.12. HEAT BALANCE EVALUATION NEAR PSEUDOCRITICAL REGION

For each run, an error in the heat balance was calculated using the following expression:

$$\Delta_{HB} = \frac{POW - HL - m\ (H_{out} - H_{in})}{POW} \cdot 100\% \tag{III.26}$$

In general, an analysis of errors in the heat-balance data shows that, at mass-flux values equal to or higher than 900 kg/m^{2}s, at medium and high values of power ($POW \geq 5$ kW) and at the inlet and outlet bulk fluid temperatures below or beyond the pseudocritical region (i.e., t_{in} and $t_{out} < t_{pc} - 2$ºC or t_{in} and $t_{out} > t_{pc} + 2$ºC), these errors are within ±4%.

Increased values of heat-balance error (i.e., more than ±4%) at lower values of power ($POW < 5$ kW) and at inlet or outlet bulk fluid temperatures within the pseudocritical region (i.e., $t_{pc} - 2$ºC $< t_{in} < t_{pc} + 2$ºC or $t_{pc} - 2$ºC $< t_{out} < t_{pc} + 2$ºC) can be explained with the following (see TABLE III.8 and Fig. III.8).

At lower values of power, the increase in bulk fluid enthalpy is relatively small. However, uncertainties in bulk fluid enthalpy within the pseudocritical region are larger for the same uncertainty range in bulk fluid temperature, compared to the enthalpy values' uncertainties that correspond to temperatures far from the pseudocritical region.

TABLE III.8. MAXIMUM UNCERTAINTIES IN ΔH CALCULATIONS NEAR PSEUDOCRITICAL POINT (p_{out}=8.36 MPa, t_{pc}=36.7ºC, t_{in}=21ºC, m=0.1 kg/s, and G=2000 kg/m^{2}s).

t_b	H_b	Uncertainty in H_b at Δt_b=+0.4ºC	Uncertainty in H_b at Δt_b=–0.4ºC	$\Delta H_b = H_{out} - H_{in}$	Max uncertainty in ΔH_b
ºC	kJ/kg	kJ/kg	kJ/kg	kJ/kg	%
21	248.94	1.18	–1.19	–	–
35	313.72	4.29	–5.04	64.78	14.4
37	349.26	8.51	–7.82	100.32	16.3
41	395.75	2.56	–2.4	144.41	3.4

Also, an additional error in the heat balance appears at mass-flux values below 900 kg/m^{2}s (see Fig. III.6), where the flow measuring curve is steep. Therefore, lower values of mass flux should be measured with a smaller diameter orifice flowmeter[7] or other type flowmeters.

Fig. III.8 shows an example of the heat-balance evaluation near the pseudocritical region. This graph shows that, at lower power values ($POW < 5$ kW) and at the outlet bulk fluid temperature within the pseudocritical region, variations in bulk fluid enthalpy difference can be up to 11.5% within the nominal uncertainty range for bulk fluid temperatures (i.e., ±0.4ºC).

[7] However, orifice-plate flowmeters with a diameter of the orifice less than 12.5 mm is considered a non-standard type.

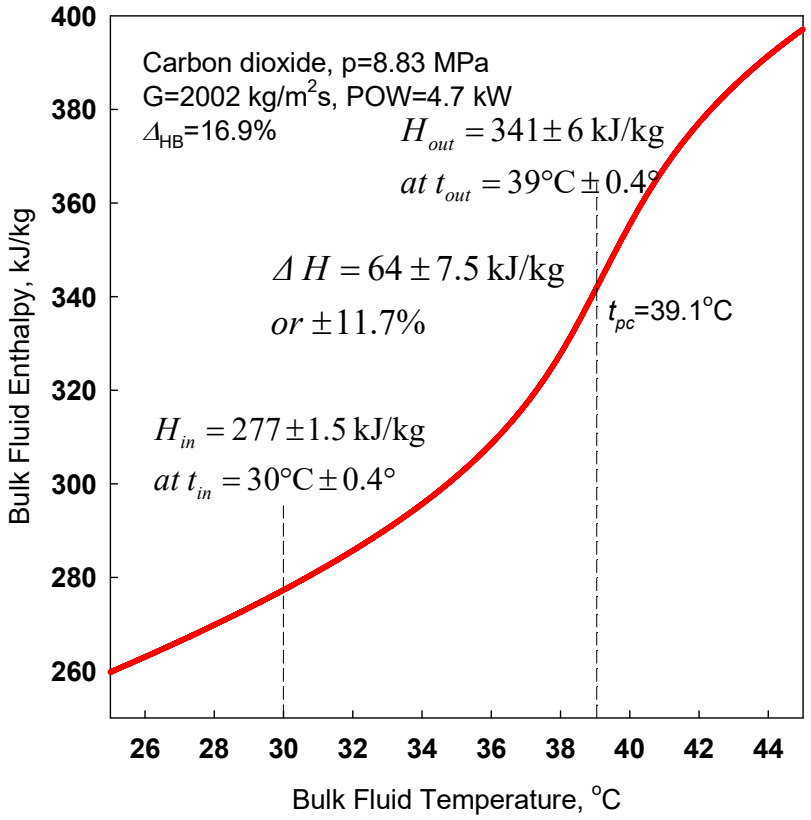

Fig. III.9. Heat balance evaluation near pseudocritical region.

III.13. SELECTED PRACTICAL RECOMMENDATIONS FOR PERFORMING EXPERIMENTS

More detailed recommendations can be found in [III.20].

NIST REFPROP software (Ver. 10) [III.21] is recommended for property calculations of various fluids (liquids, gases, cryogenic and supercritical fluids) and their mixtures. Version 10.0 includes 147 pure fluids, 5 pseudo-pure fluids (such as air), and mixtures with up to 20 components. Many thermodynamic, thermophysical and other properties are provided within a wide range of pressures and temperatures starting from melting / freezing point and up to supercritical pressures. Source codes are also provided, which allow to connect users calculating programs with the NIST REFPROP software for fluid properties.

DC power supply is more preferable for direct-heating applications compared to that of alternative current (AC), especially, for thin-wall test sections[8]. However, test section surface temperature

[8] It was found that critical heat flux (CHF) values at boiling obtained in or on a test section with DC direct heating can differ from those obtained in or on a test section with AC direct heating. This difference is larger for thin-walled test sections. At supercritical pressures, there is a similar phenomenon, which is called pseudo-boiling.

measurements with a DC power supply will be more complicated, because they require insulating the thermocouple measuring tip from the electrically heated surface. With an AC power supply, a thermocouple-measuring tip may be in contact with an electrically heated surface as there is no average voltage offset across the probe junction. Nevertheless, special precautions should be taken to avoid spurious electromagnetic induction (emf), for example, in a thermocouple wiring, which can be generated by the pulsating electromagnetic field around a test section.

To minimize thermal inertia and pressure drop of a preheater, a directly heated tube or tubes can be used with an additional power supply.

Material for a directly heated test section should be chosen with a relatively high value of the specific electrical resistivity, which in turn should ideally be invariant or nearly independent of wall temperature. In this case, there is a wider range for changing the test section wall thickness and heated length. Also, the local heat flux will be more uniform along the test section in spite of variable wall temperature, if a test section diameter and wall thickness are constant along the heated length. Therefore, Inconel 600 or Inconel 718 will be the best choice for material of the test section (Fig. III.9). Additional characteristics of the test section, such as the chemical content, precise measurements of the inside/outside tube diameters, the tube burst pressure, tube electrical resistance, and the electrical resistivity and thermal conductivity of the tube material are also essential for the complete performance and safety analysis.

For a uniform temperature profile in a cross section of a test section at the inlet and for accurate bulk fluid temperature measurements, mixing chambers should be used together with sheathed thermocouples installed just downstream of them. It is especially important for supercritical pressures applications. Also, between the inlet mixing chamber and the test section the flow stabilization part should be installed with the same diameter as that of the test section, acting as a settling length. In general, the length of this part should be about (20–50)$\cdot D$. The outlet mixing chamber should be installed just downstream of the test section outlet to reduce uncertainties in the outlet bulk fluid temperature measurement, and, hence, in the loop heat balance. Effect of mixing chambers are shown in Fig. III.10: t_{out} is lower than $t_{\text{out mixer}}$, which indicates that t_{out} is the temperature of a cooler core; and after mixing, $t_{\text{out mixer}}$ represents uniform cross sectional temperature, i.e., a bulk fluid temperature.

Calibration of various measuring instruments *in situ* is the best way to minimize measurement uncertainties compared to other calibration techniques (calibration at instrument shop, calibration check, etc.), because a calibration curve will take care of uncertainties of measuring, signal transmitting, signal converting devices, etc. (see Subsection D1).

For bulk fluid temperature measurements, Resistance Temperature Detectors (RTDs) are more preferable to use compared to thermocouples because they are usually more accurate. However, it is a good practice to use thermocouples in addition to RTDs as the backup temperature devices.

Therefore, the above-mentioned findings may apply to the supercritical case.

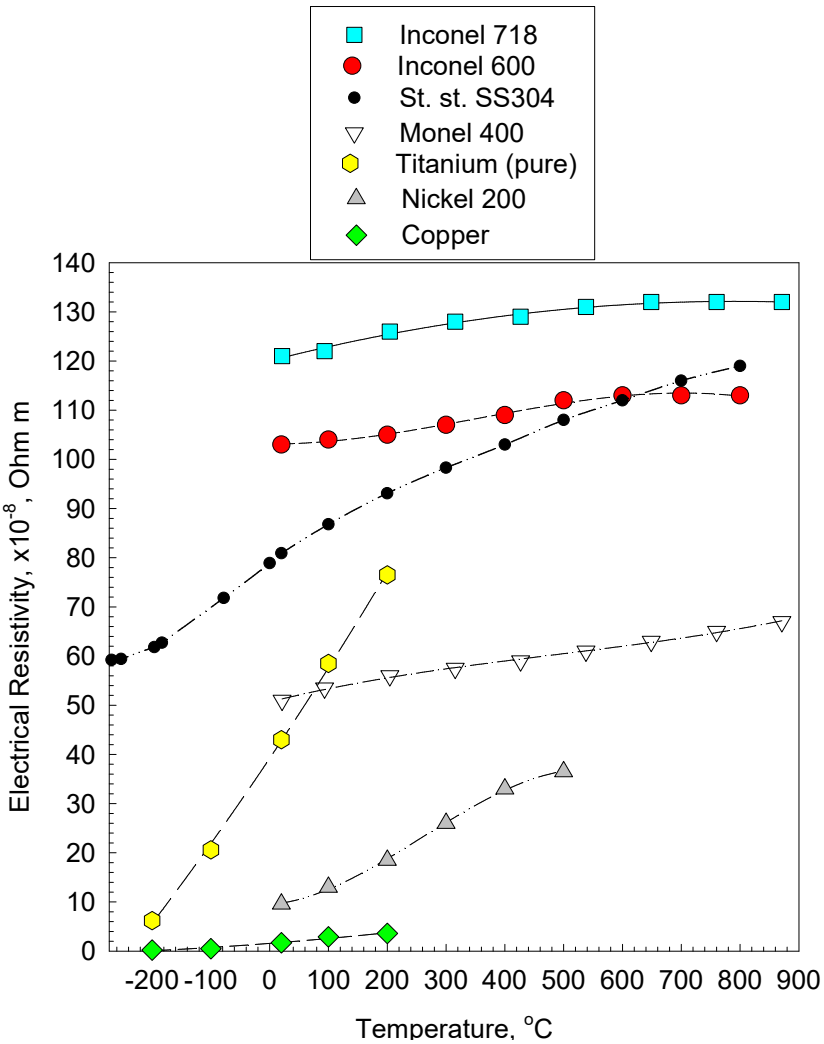

Fig. III.10. Effect of temperature on electrical resistivity of alloys and pure metals.

For relatively low wall temperature measurements, i.e., up to 260°C, fast response thermocouples (see Fig. III.3) are the easiest way to go. However, beyond this range sheathed ungrounded thermocouples should be used welded to the surface and calibrated *in situ*. This recommendation applies to flow geometry cooled from inside (circular tubes, etc.).

Do not rely solely on a DAS and other electronic measuring devices, but also use, in parallel, simple devices for measuring or just for indication of the most important/safety/limiting parameters: for example, high-accuracy mechanical gauges (for pressure), arrow type voltmeters and ammeters, plus use remote video cameras for monitoring heated parts of a test section, etc.

Always use multiple trips setup in DAS for safe and reliable test rig operation.

Fig. III.11 shows supercritical dioxide experimental data with uncertainty bars on each point; and Fig. III.12 shows the experimental data repeatability check.

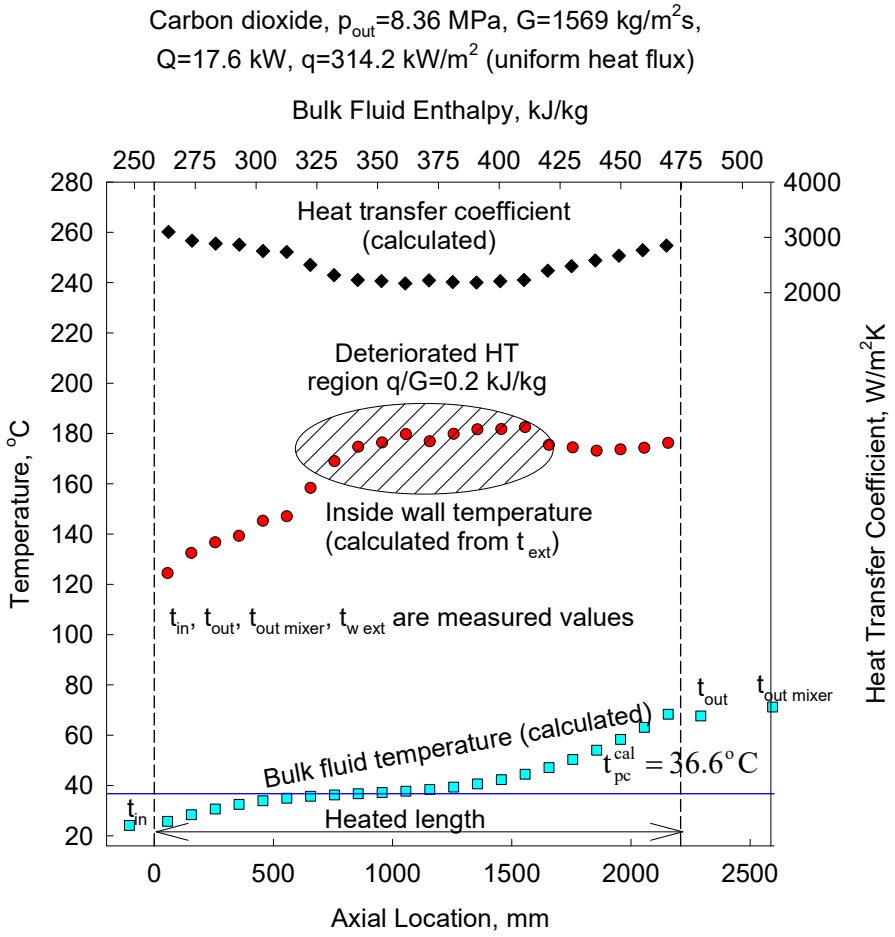

Fig. III.11. Temperatures and HTC profiles along vertical circular tube with supercritical CO_2. Flow conditions (nominal values): p_{out}=8.4 MPa, G=1570 kg/m²s, q=315 kW/m² and t_{in}=25°C.

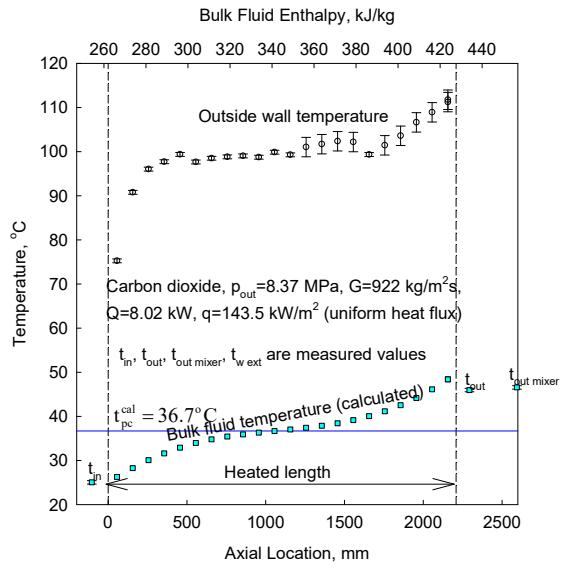

Fig. III.12. Temperature and their uncertainties along vertical circular tube with supercritical CO_2. Flow conditions (nominal values): p_{out}=8.36 MPa, G=900 kg/m²s, t_{in}=25ºC, and q=145 kW/m².

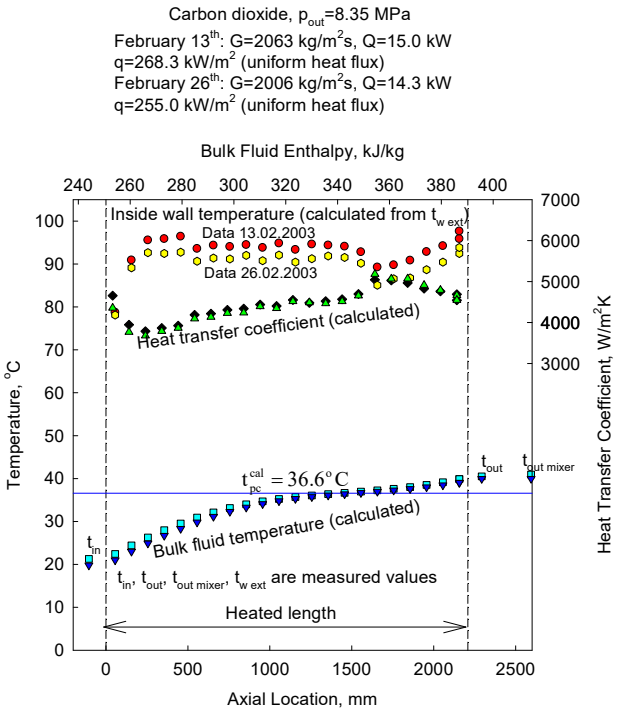

Fig. III.13. Temperatures and HTC profiles along vertical circular tube with supercritical CO_2 (check for data repeatability). Flow conditions (nominal values): p_{out}=8.36 MPa, G=2000 kg/m²s, t_{in}=20ºC, and q=265 kW/m².

Nomenclature and Abbreviations

A	area, m^2
A_{fl}	flow area, m^2
c_p	specific heat at constant pressure, J/kg K
D	inside diameter, m
G	mass flux, kg/m^{2}s; $\left(\frac{m}{A_{fl}}\right)$
H	specific enthalpy, J/kg
HTC	heat transfer coefficient, W/m^{2}K
HL	heat loss, W
I	current, A
k	thermal conductivity, W/m K
L	heated length, m
m	mass flow rate, kg/s; $(\rho\ V)$
p, P	pressure, Pa
POW	power, W
Q	heat-transfer rate, W

q	heat flux, W/m^2; $\left(\frac{Q}{A_h}\right)$
t	temperature, ºC
U	voltage, V
V	volume, m^3 or volumetric flow rate, m^3/s

Greek Letters

Δ	difference
Δ_{HB}	error in heat balance, %
μ	dynamic viscosity, Pa s
ρ	density, kg/m^3
σ	dispersion

Non-dimensional Numbers

Re	Reynolds number; $\left(\frac{G\ D}{\mu}\right)$

Subscripts or superscripts

amb	ambient
ave	average
b	bulk
ext	external
fl	flow
fm	flowmeter
h	heated
HB	Heat Balance
in	inlet
int	internal
ℓ	liquid or local
max	maximum
meas	measured
min	minimum
out	outlet or outside
pc	pseudocritical
RTD	Resistance Temperature Detector
TC	ThermoCouple
w	wall

Abbreviations and acronyms widely used in the text and list of references

AC	Alternating Current
A/D	Analog-to-Digital (conversion)
A/I	Analog Input
AECL	Atomic Energy of Canada Limited (Canada)
CRL	Chalk River Laboratories, AECL (Canada)
DAS	Data Acquisition System
DC	Direct Current
FM	FlowMeter

f.s.	full scale
FT	Flow Transducer
HTC	Heat Transfer Coefficient
ID	Inside Diameter
NIST	National Institute of Standards and Technology (USA)
OD	Outside Diameter
PDT	Pressure Differential Transducer
PMU	Power-Measuring Unit
RMS	Root-Mean-Square (error or surface roughness)
RTD	Resistance Temperature Detector
TC	ThermoCouple
TE	TEmperature
TEC	TEmperature of CO_2

REFERENCES TO APPENDIX III

[III.1] PIORO, I.L. AND DUFFEY, R.B., Heat Transfer and Hydraulic Resistance at Supercritical Pressures in Power Engineering Applications, ASME Press, New York, (2007).

[III.2] PIS'MENNYI, E.N., RAZUMOVSKIY, V.G., MAEVSKIY, E.M. et al., Experimental Study on Temperature Regimes to Supercritical Water Flowing in Vertical Tubes at Low Mass Fluxes, Proc. International Conference GLOBAL-2005, Tsukuba, 2005.

[III.3] PIORO, I.L., KHARTABIL, H.F., Experimental Study on Heat Transfer to Supercritical Carbon Dioxide Flowing Upward in a Vertical Tube, Proc. 13th International Conference on Nuclear Engineering (ICONE-13), Beijing, 2005.

[III.4] GUO, Y., BULLOCK, D.E., PIORO, I.L. AND MARTIN, J., Measurements of Sheath Temperature Profiles in LVRF Bundles under Post-Dryout Heat Transfer Conditions in Freon, Proc. 14th International Conference on Nuclear Engineering (ICONE-14), Miami, 2006.

[III.5] LEUNG, L.K.H., PIORO, I.L., BULLOCK, D.E., Post-Dryout Surface-Temperature Distributions in a Vertical Freon-Cooled 37-Element Bundle, Proc. 10th International Topical Meeting on Nuclear Reactor Thermal Hydraulics (NURETH-10), Seoul, 2003.

[III.6] PIORO, I.L., Maximum Heat-Transferring Capacity of Two-Phase Thermosiphons with Separate Vapor and Condensate Streams, Heat Transfer Research, **24, 4**, (1992), 535–542.

[III.7] PIORO I.L., Experimental Evaluation of Constants for the Rohsenow Pool Boiling Correlation, International Journal of Heat and Mass Transfer, **42**, (1999), 2003–2013.

[III.8] PIORO, I.L., CHENG, S.C., VASIĆ, A., FELISARI, R., Some Problems for Bundle CHF Prediction based on CHF Measurements in Simple Flow Geometries, Nuclear Engineering and Design, **201, 2–3**, (2000), 189–207.

[III.9] PIORO, I.L., GROENEVELD, D.C., LEUNG, L.K.H. et al., Comparison of CHF Measurements in Horizontal and Vertical Tubes Cooled with R-134a, International Journal of Heat and Mass Transfer, **45, 22**, (2002), 4435–4450.

[III.10] PIORO, I.L., GROENEVELD, D.C., DOERFFER, S.S. et al., Effects of Flow Obstacles on the Critical Heat Flux in a Vertical Tube Cooled with Upward Flow of R-134a, International Journal of Heat and Mass Transfer, **45, 22**, (2002), 4417–4433.

[III.11] PIORO, I.L., GROENEVELD, D., CHENG, S.C. et al., Comparison of CHF Measurements in R-134a Cooled Tubes and the Water CHF Look-Up Table, International Journal of Heat and Mass Transfer, **44, 1**, (2001), 73–88.
[III.12] KICHIGIN, A.M., PIORO, I.L., Analysis of Methods for Detecting Dryout and Burnout Fluxes, Heat Transfer Research, **24, 7**, (1992), 957–964.
[III.13] COLEMAN, H.W., STEELE, W.G., Experimentation and Uncertainty Analysis for Engineers, 2nd edition, J. Wiley & Sons, Inc., New York, USA, 1999.
[III.14] HARDY, J.E., HYLTON, J.O., MCKNIGHT, T.E. et al., Flow Measurement Methods and Applications. J. Wiley & Sons, Inc., New York, NY, USA, (1999), 207–208.
[III.15] Guide to the Expression of Uncertainty in Measurement, Corrected and Reprinted, International Bureau of Weights and Measures and other International Organizations, 1995.
[III.16] HOLMAN, J.P., Experimental Methods for Engineers, 6th edition, McGraw-Hill, Inc., New York, NY, USA, 1994.
[III.17] MOFFAT, R.J., Describing the Uncertainties in Experimental Results, Experimental Thermal and Fluid Science, **1**, (1988), 3–17.
[III.18] GORTYSHOV, YU.F., DRESVYANNIKOV, F.N., IDIATULLIN, N.S. et al., Theory and Technique of Thermophysical Experiment, Textbook for Technical Universities, Editor V.K. Shchukin, Energoatomizdat Publishing House, Moscow, Russia, 1985, (In Russian).
[III.19] TOPPING, J., Errors of Observation and Their Treatment, 3rd edition, Chapman and Hall Ltd., London, UK, 1971.
[III.20] PIORO, I.L., DUFFEY, R.B., Heat Transfer and Hydraulic Resistance at Supercritical Pressures in Power Engineering Applications, ASME Press, (2007).
[III.21] NATIONAL INSTITUTE OF STANDARDS AND TECHNOLOGY, NIST Reference Fluid Thermodynamic and Transport Properties - REFPROP, Standard Reference Database 23, Ver. 9.1, Department of Commerce, Boulder, CO, USA, 2013.
[III.22] Mark's Standard Handbook for Mechanical Engineers, Editors: Eu.A. Avallone and Th. Baumeister III, McGraw-Hill, New York, NY, USA, (1996), 16-20.
[III.23] The Temperature Handbook, OMEGA Engineering, Inc., 21st Century Edition, Vol. MM, 2000.
[III.24] The Flow and Level Handbook, OMEGA Engineering, Inc., 21st Century Edition, Vol. MM, (Transactions, Vol. 4, p. 22), 2000.
[III.25] White, F., Fluid Mechanics, McGraw-Hill Education, 8th ed., New York, NY, USA, 2016.

Appendix IV. ASSESSMENT OF CORRELATIONS FOR NATURAL CIRCULATION HEAT TRANSFER

TABLE IV.1. DESCRIPTIONS OF HEAT TRANSFER CORRELATION.

No.	Reference	Correlation	Fluid / Geometry /Validity
1.	Dittus and Boelter [IV.1]	$Nu_b = 0.023\, Re_b^{0.8}\, Pr_b^{0.4}$	P: 0.6 – 160 Re: > 10000 L/D > 10
2.	McAdams [IV.2]	$Nu_b = 0.0243\, Re_b^{0.8}\, Pr_b^{0.4}$	P: High q: Low
3.	Bringer and Smith [IV.3]	$Nu_x = C\, Re_x^{0.77}\, Pr_w^{0.55}$ Nu_x and Re_x are evaluated at T_x; C = 0.0266 for water; C = 0.0375 for CO_2 $T_x = T_b, if \left(\frac{T_{pc} - T_b}{T_w - T_b}\right) < 0$ $T_x = T_{pc}, if 0 \le \left(\frac{T_{pc} - T_b}{T_w - T_b}\right) \le 1.0$ $T_x = T_w, if \left(\frac{T_{pc} - T_b}{T_w - T_b}\right) > 1.0$	For SC–H_2O and SC–CO_2 P: up to 34.5 MPa (For SC–H_2O) Away from critical and pseudo-critical region
4.	Shitsman [IV.4]	$Nu_b = 0.023\ Re_b^{0.8}\, Pr_{min}^{0.8}\, Pr_{(Pr_{@t_b}, Pr_{@t_w})min}$	SC–H_2O D: 7.8 mm, 8.2 mm Applied for Pr ~1.
5.	Petukhov and Kirillov [IV.5]	$Nu_b = \frac{\left(\frac{\xi}{8}\right) Re_b\, Pr_b}{12.7\sqrt{\left(\frac{\xi}{8}\right)}\left(Pr_b^{\frac{2}{3}} - 1\right) + 1.07}$; $\xi = \frac{1}{(1.82\, log_{10}(Re_b) - 1.64)^2}$	Tube geometry
6.	Petukhov et al. [IV.6]	$Nu = Nu_0 \left(\frac{\mu_b}{\mu_w}\right)^{0.11} \left(\frac{k_b}{k_w}\right)^{-0.33} \left(\frac{\overline{Cp}}{Cp_b}\right)^{0.35}$	For SC–H_2O and SC–CO_2 P: 22.3 – 32 MPa

		where, $Nu_0 = \frac{(\xi/8)\, Re_b\, \overline{Pr}}{12.7\sqrt{(\xi/8)}\left(\overline{Pr^{2/3}}\right)}$; $\xi = \frac{1}{(1.82\, log_{10}(Re_b) - 1.64)^2}$	(SC–H_2O) P: 8.3 MPa (SC–CO_2) $2\times10^4 < Re_b < 8.6\times10^5$ $0.85 < \overline{Pr}_b < 65$ $0.9 < \frac{\mu_b}{\mu_w} < 3.6$ $1.0 < \frac{k_b}{k_w} < 6.0$ $0.07 < \frac{\overline{Cp}}{Cp_b} < 4.50$
7.	Domin [IV.7]	$Nu_b = 0.1\, Re_b^{0.66}\, Pr_b^{1.2}$; for $t_w \geq 350^oC$ $Nu_b = 0.036\, Re_b^{0.8}\, Pr_b^{0.4}\left(\frac{\mu_w}{\mu_b}\right)$; for $250 \leq t_w < 350^oC$	SC–H_2O, Horizontal tubes D, L: 2 mm & 1.075 m ; & : 4 mm & 1.233 m P:23.3 – 26.3 MPa q: 0.58 – 4.65 MW/m^2
8.	Bishop et al. [IV.8]	$Nu_x = 0.0069\, Re_x^{0.9}\, \overline{Pr_x^{0.66}} \left(\frac{\rho_w}{\rho_b}\right)_x^{0.43} \left(1 + 2.4\frac{D}{x}\right)$ where x = axial location along the heated length	SC–H_2O, upward flow, tubes & annuli P: 22.8 – 27.6 MPa T_b: 282 – 527 ^oC G: 651 – 3662 kg/m^{2}s q: 0.31 – 3.46 MW/m^2
9.	Swenson et al. [IV.9]	$Nu_w = 0.00459\, Re_w^{0.923}\, \overline{Pr_w^{0.613}} \left(\frac{\rho_w}{\rho_b}\right)^{0.231}$	SC–H_2O, tubes P: 22.8 – 41.4 MPa G: 542 – 2150 kg/m^2.s t_w: 93 – 649 ^oC t_b: 75 – 576 ^oC Re = 7.5 x 10^4 – 3.16 x 10^6
10.	Krasnoshchekov et al. [IV.10]	$Nu = Nu_0 \left(\frac{\rho_w}{\rho_b}\right)^{0.3} \left(\frac{\overline{Cp}}{Cp_b}\right)^n$; Nu_0 is same as defined earlier. $n = 0.4$; for $\left(\frac{T_w}{T_{pc}}\right) \leq 1$ or $\left(\frac{T_b}{T_{pc}}\right) \geq 1.2$	SC–CO_2 P: 7.85 and 9.81 MPa Re_b: 8 x 10^4 – 5 x 10^5 $\overline{Pr}_b$: 0.85 – 65 $\frac{T_w}{T_{pc}}$: 0.09 – 2.5

		$n = n1 = 0.22 + 0.18\left(\frac{T_w}{T_{pc}}\right)$; at $1 \le \left(\frac{T_w}{T_{pc}}\right) \le 2.5$ $n = n1 + (5n1 - 2)\left(1 - \left(\frac{T_b}{T_{pc}}\right)\right)$; at $1 \le \left(\frac{T_b}{T_{pc}}\right) \le 1.2$; All 'T' are in K.	q: 4.6×10^4 – 2.6×10^6 W/m^2 $\frac{x}{D} \ge 15$
11.	Ornatsky et al. [IV.11]	$Nu_b = 0.023\, Re_b^{0.8}\, Pr_{min}^{0.8} \left(\frac{\rho_w}{\rho_b}\right)^{0.3}$; $Pr_{(Pr_{@t_b}, Pr_{@t_w})min}$	Parallel tube flow
12.	Grass et al. [IV.12]	$Nu_b = \frac{(\xi/8)\, Re_b\, Pr_b}{1.07 + 12.7\sqrt{(\xi/8)}\left(Pr_G^{2/3}\frac{Cp_b}{Cp_w} - 1\right)}$; ξ is same as defined earlier. $Pr_G = \begin{Bmatrix} Pr_b \; ; \; Pr_b < 0.5\, Pr_w \\ Pr_w \; ; \; Pr_b > 0.5\, Pr_w \end{Bmatrix}$	
13.	Yamagata et al. [IV.13]	$Nu_b = 0.0135\, Re_b^{0.85}\, Pr_b^{0.8}\, F_C$ $F_C = 1$; for $E > 1$ $= 0.67\, Pr_{pc}^{-0.05}\left(\frac{\overline{Cp}}{Cp_b}\right)^{n1}$; for $0 \le E \le 1$ $= \left(\frac{\overline{Cp}}{Cp_b}\right)^{n2}$; for $E < 0$; $E = \frac{T_{pc} - T_b}{T_w - T_b}$ $n1 = -0.77\left(1 + \frac{1}{Pr_{pc}}\right) + 1.49$; $n2 = -1.44\left(1 + \frac{1}{Pr_{pc}}\right) - 0.53$	SC–H_2O, tube P: 22.6 – 29.4 MPa G: 310 – 1830 kg/m^2.s q: 116 – 930 kW/m^2 t_b: 230 – 540 °C D: 7.5, 10 mm
14.	Jackson and Fewster [IV.14]	$Nu = 0.0183\, Re_b^{0.82}\, \overline{Pr^{0.5}} \left(\frac{\rho_w}{\rho_b}\right)^{0.3}$	
15.	Gnielinski [IV.15]	$Nu_b = \frac{\frac{\xi}{8}(Re_b - 1000)\, Pr_b}{1.07 + 12.7\sqrt{\frac{\xi}{8}}\left(Pr_b^{2/3} - 1\right)}$	SC–CO_2 Pr_b: 0.5 – 2000 Re_b: 3 x 10^3 – 5 x 10^6
16.	Jackson and Hall [IV.16]	$Nu = 0.023\, Re_b^{0.82}\, \overline{Pr_b^{0.5} \left(\frac{\rho_w}{\rho_b}\right)^{0.231}}$	SC–CO_2 P: 7.85 – 9.81 MPa G: 0.35 Mg/m^2.s D: 4.08 mm

17.	Jackson and Hall [IV.17]	$$Nu = 0.0183\, Re_b^{0.82}\, Pr_b^{0.5} \left(\frac{\rho_w}{\rho_b}\right)^{0.3} \left(\frac{\overline{C_p}}{C_{p,b}}\right)^{n}$$ $$where,$$ $$n = 0.4\,;\, if\, \frac{T_w}{T_{pc}} < 1 \text{ or } \frac{T_b}{T_{pc}} \geq 1.2$$ $$n = 0.4 + 0.2\left(\frac{T_w}{T_{pc}} - 1\right)\,;\, for\, \frac{T_b}{T_{pc}} < 1 \text{ and } \frac{T_w}{T_{pc}} > 1$$ $$n = 0.4 + 0.2\left(\frac{T_w}{T_{pc}} - 1\right)\left[1 - 5\left(\frac{T_b}{T_{pc}} - 1\right)\right]\,;\, for\, \frac{T_b}{T_{pc}} < 1.2$$ All 'T' are in K.	
18.	Watts and Chou [IV.18]	$$Nu_b = 0.021\, Re_b^{0.8}\, Pr_b^{0.55} \overline{\left(\frac{\rho_w}{\rho_b}\right)^{0.35} (Bu^*)}$$ $$where,$$ $$f(Bu^*) = \begin{cases} 1\,;\, \text{for } Bu^* \leq 10^{-5} \\ (1 - 3000Bu^*)^{0.295}\,;\, \text{for } 10^{-5} < Bu^* < 10^{-4} \\ (7000Bu^*)^{0.295}\,;\, \text{for } Bu^* \geq 10^{-4} \end{cases} \text{For Normal Heat Tran}$$ $$f(Bu^*) = \begin{cases} (1.27 - 19500Bu^*)^{0.7}\,;\, \text{for } Bu^* \leq 4.5 \times 10^{-5} \\ (2600Bu^*)^{0.305}\,;\, \text{for } Bu^* > 4.5 \times 10^{-5} \end{cases} \text{For Minimum in Nu}$$	SC–H_2O P: 25.0 MPa G: 130 – 1000 kg/m^2.s q: 170 – 450 kW/m^2 $\overline{\text{Pr}}_b$: 0.85 – 2.30 Re_b: 6.5 x 10^3 – 3 x 10^5
19.	Petukhov et al. [IV.19]	$$Nu_b = \frac{(\xi'/8)\,\text{Re}_b\,\overline{\text{Pr}}_b}{1 + \frac{900}{\text{Re}_b} + 12.7\sqrt{(\xi'/8)}\left(\overline{\text{Pr}}_b^{2/3} - 1\right)} \quad where, \xi' = \xi\left(\frac{\rho_w}{\rho_b}\right)^{0.4}\left(\frac{\mu_w}{\mu_b}\right)^{0.2}$$	
20.	Razumovskiy et al. [IV.20]	$$Nu_b = \frac{(\xi_r/8)\, Re_b\, \overline{Pr_b}}{1.07 + 12.7\sqrt{(\xi_r/8)}\left(\overline{Pr_b^{2/3}}\right)\left(\frac{\overline{Cp}}{Cp_b}\right)^{0.65}}$$	

		$where, \xi_r = \xi \left(\frac{\rho_w}{\rho_b}\right)^{0.18} \left(\frac{\mu_w}{\mu_b}\right)^{0.18}$	
21.	Gorban et al. [IV.21]	$Nu_b = 0.0059\, Re_b^{0.90}\, Pr_b^{-0.12}$; For Water $Nu_b = 0.0094\, Re_b^{0.86}\, Pr_b^{-0.15}$; For R-12	Flow inside tubes at temperature higher than the critical temperature
22.	Griem [IV.22]	$Nu_b = 0.0169\, Re_b^{0.8356}\, Pr_b^{0.432}$	Tube
23.	Kitoh et al. [IV.23]	$Nu_b = 0.015\, Re_b^{0.85}\, Pr_b^{m}$ $where,$ $m = 0.69 - \frac{81000}{200G^{1.2}} + f_c q$ $f_c = 2.9 \times 10^{-8} + \frac{0.11}{200G^{1.2}}$; for $0 \le h_b \le 1500$ kJ/kg $= -8.7 \times 10^{-8} - \frac{0.65}{200G^{1.2}}$; for $1500 < h_b < 3300$ kJ/kg $= -9.7 \times 10^{-7} + \frac{1.3}{200G^{1.2}}$; for $3300 \le h_b \le 4000$ kJ/kg	SC–H_2O t_b = 20 – 550 °C G: 100 – 1750 kg/m^2.s q: 0 – 1.8 MW/m^2
24.	Jackson [IV.24]	$Nu = 0.0183\, Re_b^{0.82}\, Pr_b^{0.5} \left(\frac{\rho_w}{\rho_b}\right)^{0.3} \left(\frac{\overline{Cp}}{Cp_b}\right)^{n}$ $where,$ $n = 0.4$; for $T_b < T_w < T_{pc}$ or $1.2T_{pc} < T_b < T_w$ $n = 0.4 + 0.2\left(\frac{T_w}{T_{pc}} - 1\right)$; $for\ T_b < T_{pc} < T_w$ $n = 0.4 + 0.2\left(\frac{T_w}{T_{pc}} - 1\right)\left[1 - 5\left(\frac{T_b}{T_{pc}} - 1\right)\right]$; $for\ T_{pc} < T_b < 1.2T_{pc}$ or $T_b < T_w$ All 'T' are in K.	SC–H_2O P:23.4 – 29.3 MPa G: 700 – 3600 kg/m^2.s q: 46 – 2600 kW/m^2 Re_b: 8 x 10^4 – 5 x 10^5 D: 1.6 – 20 mm
25.	Liao and Zhao [IV.25]	$Nu_b = 0.124\, Re_b^{0.8}\, Pr_b^{0.4} \left(\frac{Gr}{Re_b^2}\right)^{0.203} \left(\frac{\rho_w}{\rho_b}\right)^{0.842} \left(\frac{\overline{Cp}}{Cp_b}\right)^{0.384}$; For horizontal fl	SC–CO_2 P: 74 – 120 bar tb: 20 – 110 °C D: 0.7, 1.4 and 2.16 mm m = 0.02 – 0.2 kg/min

		$Nu_b = 0.354\, Re_b^{0.8}\, Pr_b^{0.4} \left(\frac{\overline{Gr}}{Re_b^{2.7}}\right)^{0.157} \left(\frac{\rho_w}{\rho_b}\right)^{1.297} \left(\frac{\overline{Cp}}{Cp_b}\right)^{0.296}$; For upward flo $Nu_b = 0.643\, Re_b^{0.8}\, Pr_b^{0.4} \left(\frac{\overline{Gr}}{Re_b^{2.7}}\right)^{0.186} \left(\frac{\rho_w}{\rho_b}\right)^{2.154} \left(\frac{\overline{Cp}}{Cp_b}\right)^{0.751}$; For downward	Re_b: 10^4 – 2 x 10^5 Pr: 0.9 – 10
26.	Feng et al. [IV.26]	$Nu_b = 0.02269\, Re_b^{0.8079}\, Pr_b^{0.9213} \left(\frac{\rho_w}{\rho_b}\right)^{0.6638} \left(\frac{\mu_w}{\mu_b}\right)^{0.8687}$	
27.	Bo et al. [IV.27]	$Nu_b = 0.0239\, Re_b^{0.759}\, Pr_b^{0.833} \left(\frac{k_w}{k_b}\right)^{0.0863} \left(\frac{\rho_w}{\rho_b}\right)^{0.31} \left(\frac{\mu_w}{\mu_b}\right)^{0.832} (Gr^*)^{0.014} (q^*)^{-0.021}$	
28.	Kuang et al. [IV.28]	$Nu_b = \overline{0.0239\, Re_b^{0.759}\, Pr_b^{0.833} \left(\frac{\rho_w}{\rho_b}\right)^{0.31} \left(\frac{k_w}{k_b}\right)^{0.0863} \left(\frac{\mu_w}{\mu_b}\right)^{0.832} (Gr^*)^{0.014} (q^*)^{-0.021}}$	SC–H_2O P: 22.8 – 31.0 MPa G:380 – 3.600kg/m^2.s q = 233 – 3474 kW/m^2
29.	Zhu et al. [IV.29]	$Nu_b = 0.0068\, Re_b^{0.9}\, Pr_b^{0.63} \overline{\left(\frac{\rho_w}{\rho_b}\right)^{0.17} \left(\frac{k_w}{k_b}\right)^{0.29}}$	SC–H_2O P: 22.0 – 30.0 MPa G: 600 – 1200 kg/m^2.s q: 200 – 600 kW/m^2 D: 26.0 mm
30.	Yu et al. [IV.30]	$Nu_b = 0.01378\, Re_b^{0.9078}\, Pr_b^{0.6171} \overline{\left(\frac{\rho_w}{\rho_b}\right)^{0.4356} (Gr^*)^{-0.012} (q^*)^{0.0605}}$	SC–H_2O P: 22.6 – 41.0 MPA G: 90 – 2441 kg/m^2.s q: 90 – 1800 kW/m^2 D: 1.5 – 38.1 mm
31.	Bae and Kim [IV.31]	$Nu = Nu_0 \left(\frac{\rho_w}{\rho_b}\right)^{0.3} \left(\frac{\overline{Cp}}{Cp_b}\right)^n F$ Nu_0 and n are same as defined earlier for Krasnoshchekov et al. [IV.10]	SC–CO_2 G: 400 – 1200 kg/m^2.s

		$F = \begin{Bmatrix} (1 + 1.0 \times 10^8 Bu)^{-0.032} \text{ ; for } 5.0 \times 10^{-8} < Bu < 7.0 \times 10^{-7} \\ 0.0185 Bu^{-0.4365} \text{ ; for } 7.0 \times 10^{-7} < Bu < 1.0 \times 10^{-6} \\ 0.75 \text{ ; for } 1.0 \times 10^{-6} < Bu < 1.0 \times 10^{-5} \\ 0.0119 Bu^{-0.36} \text{ ; for } 1.0 \times 10^{-5} < Bu < 3.0 \times 10^{-5} \\ 32.4 \text{Bu}^{0.40} \text{ ; for } 3.0 \times 10^{-5} < Bu < 1.0 \times 10^{-4} \end{Bmatrix}$	
32.	Cheng et al. [IV.32]	$Nu_b = 0.023\, Re_b^{0.8}\, \overline{Pr_b^{1/3}}$ $where, F = min(F1, F2)$; $F1 = 0.85 + 0.776(1000 q_b^*)^{2.4}$; $F2 = \frac{0.48}{(1000 q_{pc}^*)^{1.55}} + 1.21\left(1 - \frac{q_b^*}{q_{pc}^*}\right)$	SC–H_2O P: 22.5 – 25.0 MPa G: 700 – 3500 kg/m^2.s q: 300 – 2000 kW/m^2 t_b: 300 – 450 °C D: 10 and 20 mm
33.	Gupta et al. [IV.33]	$Nu_w = 0.004\, Re_w^{0.923}\, \overline{Pr_w^{0.773} \left(\frac{\rho_w}{\rho_b}\right)^{0.186} \left(\frac{\mu_w}{\mu_b}\right)^{0.366}}$	SC–H_2O P: 24.0 MPa G: 200 – 1500 kg/m^2.s q: 0 – 1250 kW/m^2 D: 10 mm
34.	Bae et al. [IV.34]	$Nu = Nu_0 \left(\frac{\rho_w}{\rho_b}\right)^{0.3} \left(\frac{\overline{Cp}}{Cp_b}\right)^n F$ Nu_0 and n are same as defined earlier for Krasnoshchekov et al (1967)	SC–CO_2 D: 6.32 mm

		$F = \begin{cases} \left.\begin{cases} 1.0 \text{ ; for } \frac{\overline{\mathrm{Gr}}_b}{\mathrm{Re}_b^{2.7}} < 2.0\times10^{-7} \\ 0.043\left(\frac{\overline{\mathrm{Gr}}_b}{\mathrm{Re}_b^{2.7}}\right)^{-0.2} \text{ ; for } 2.0\times10^{-7} < \frac{\overline{\mathrm{Gr}}_b}{\mathrm{Re}_b^{2.7}} < 6.0\times10^{-6} \\ 1120\left(\frac{\overline{\mathrm{Gr}}_b}{\mathrm{Re}_b^{2.7}}\right)^{0.64} \text{ ; for } 6.0\times10^{-6} < \frac{\overline{\mathrm{Gr}}_b}{\mathrm{Re}_b^{2.7}} < 1.5\times10^{-5} \\ 3.6\times10^{-8}\left(\frac{\overline{\mathrm{Gr}}_b}{\mathrm{Re}_b^{2.7}}\right)^{-1.53} \text{ ; for } 1.5\times10^{-5} < \frac{\overline{\mathrm{Gr}}_b}{\mathrm{Re}_b^{2.7}} < 4.0\times10^{-5} \\ 200\mathrm{Bu}^{0.68} \text{ ; for } 4.0\times10^{-5} < Bu < 2.0\times10^{-4} \end{cases} \right\} \text{Deter} \\ \left.\begin{cases} \left(1+3\times10^{5}\frac{\overline{\mathrm{Gr}}_b}{\mathrm{Re}_b^{2.7}}\right)^{0.35} \text{ ; for } \frac{\overline{\mathrm{Gr}}_b}{\mathrm{Re}_b^{2.7}} < 2.0\times10^{-6} \\ 0.48\left(\frac{\overline{\mathrm{Gr}}_b}{\mathrm{Re}_b^{2.7}}\right)^{-0.07} \text{ ; for } \frac{\overline{\mathrm{Gr}}_b}{\mathrm{Re}_b^{2.7}} > 2.0\times10^{-6} \end{cases} \right\} \text{Normal HT} \end{cases}$	
35.	Kim and Kim [IV.35]	$Nu_b = 0.226\, Re_b^{1.174}\, Pr_b^{1.057} \left(\frac{\rho_w}{\rho_b}\right)^{0.571} \left(\frac{Cp}{Cp_b}\right)^{1.032} Ac^{0.489} Bu^{+0.0021}$ Where, $Ac = \frac{q_b^*}{Re_b^{0.625}} \left(\frac{\rho_b}{\rho_w}\right)^{0.5} \left(\frac{\mu_w}{\mu_b}\right)$; $Bu^+ = \frac{Gr^*}{Re_b^{3.245}\, Pr_b^{0.8}} \left(\frac{\rho_b}{\rho_w}\right)^{0.5} \left(\frac{\mu_w}{\mu_b}\right)$	
36.	Kim and Kim [IV.36]	$Nu_b = 2.0514\, Re_b^{0.928}\, Pr_b^{0.742} \left(\frac{\rho_w}{\rho_b}\right)^{1.305} \left(\frac{\mu_w}{\mu_b}\right)^{-0.669} \left(\frac{\overline{Cp}}{Cp_b}\right)^{0.888} (q*)^{0.792}$	$SC–CO_2$; Upward and downward flow in tube P: 74.6 – 102.6 bar q: 38 – 234 kW/m^2 G: 208 – 874 kg/m^2.s t_b: 29 – 115 °C D: 4.5 mm

37.	Mokry and Pioro [IV.38]	$Nu_b = 0.0121\, Re_b^{0.86}\, \overline{Pr_b^{0.23}\left(\frac{\rho_w}{\rho_b}\right)^{0.59}}$	SC–CO_2 P: 7.6, 8.4 and 8.8 MPa G: 840 – 3000 kg/m^2.s q: up to 600 kW/m^2 t_b-inlet: 20 – 40 °C
38.	Mokry et al. [IV.37]	$Nu_b = 0.0061\, Re_b^{0.904}\, \overline{Pr_b^{0.684}\left(\frac{\rho_w}{\rho_b}\right)^{0.564}}$	SC–H_2O, Vertical tube P: 24 MPa t_b-inlet: 320 – 350 °C G: 200 – 1500 kg/m^2.s q: up to 1250 kW/m^2
39.	Gupta et al. [IV.39]	$Nu_w = 0.0033\, Re_w^{0.941}\, \overline{Pr_w^{0.764}\left(\frac{\mu_w}{\mu_b}\right)^{0.398}\left(\frac{\rho_w}{\rho_b}\right)^{0.156}}$	SC–H_2O; Upward flow P: 24.0 – 25.0 MPa G: 200 – 1500 kg/m^2.s q = 70 – 1250 kW/m^2 D: 10 mm t_b-inlet: 320 – 350 °C
40.	Bae [IV.40]	$Nu_w = 0.021\, Re_b^{0.8}\, \overline{Pr_b^{0.55}\left(\frac{\rho_w}{\rho_b}\right)^{0.35}}$ $where,$ $F = \begin{cases} \left(1 - 8000\frac{\overline{\mathrm{Gr}}_b}{\mathrm{Re}_b^{2.7}}\right)^{0.5} & ;\text{for } \frac{\overline{\mathrm{Gr}}_b}{\mathrm{Re}_b^{2.7}} < 1.0\times10^{-4} \\ 15\left(\frac{\overline{\mathrm{Gr}}_b}{\mathrm{Re}_b^{2.7}}\right)^{0.38} & ;\text{for } \frac{\overline{\mathrm{Gr}}_b}{\mathrm{Re}_b^{2.7}} > 1.0\times10^{-4} \end{cases}$	SC–CO_2; Upward flow D: 4.57 mm t_w: up to 190 °C
41.	Preda et al. [IV.41]	$Nu_b = 0.0015\, Re_w^{1.03}\, Pr_w^{0.76}\left(\frac{\mu_w}{\mu_b}\right)^{0.53}\left(\frac{\rho_w}{\rho_b}\right)^{0.46}\left(\frac{k_w}{k_b}\right)^{0.43}$	SC–CO_2; Horizontal and vertical tubes
42.	Liu and Kuang [IV.42]	$Nu_b = 0.01\, Re_b^{0.889}\, \overline{Pr_b^{0.73}\left(\frac{\rho_w}{\rho_b}\right)^{0.401}\left(\frac{k_w}{k_b}\right)^{0.24}\left(\frac{\mu_w}{\mu_b}\right)^{0.153}\left(\frac{\overline{Cp}}{Cp_b}\right)^{0.014}}\,(Gr^*)^{0.007}($	SC–H_2O P:22.40 – 31.0 MPa G: 200 – 3500 kg/m^2.s q: 37 – 2000 kW/m^2 D:6 – 38 mm

43.	Gupta et al. [IV.43] – Based on bulk fluid temperature	$\overline{Nu_b = 0.01\, Re_b^{0.89}\, Pr_b^{-0.14} \left(\frac{\rho_w}{\rho_b}\right)^{0.93} \left(\frac{k_w}{k_b}\right)^{0.22} \left(\frac{\mu_w}{\mu_b}\right)^{-1.13}}$	$SC–CO_2$; vertical bare tube D, L: 1.8 mm and 2.208 m P: 7.4 – 8.8 MPa G: 900 – 3000 kg/m^2.s q: 15 – 615 kW/m^2 t_b-inlet: 20 – 40 °C
44.	Gupta et al. [IV.43] – Based on film temperature	$Nu_f = 0.0043\, Re_f^{0.94} \left(\frac{\rho_w}{\rho_b}\right)^{0.57} \left(\frac{k_w}{k_b}\right)^{-0.52}$	
45.	Gupta et al. [IV.43] – Based on wall temperature	$\overline{Nu_w = 0.0038\, Re_w^{0.96}\, Pr_w^{-0.14} \left(\frac{\rho_w}{\rho_b}\right)^{0.84} \left(\frac{k_w}{k_b}\right)^{-0.75} \left(\frac{\mu_w}{\mu_b}\right)^{-0.22}}$	
46.	Wang and Li [IV.44]	$\overline{Nu_b = 0.00684\, Re_b^{0.89765}\, Pr_b^{0.68625} \left(\frac{\rho_w}{\rho_b}\right)^{0.31142} \left(\frac{k_w}{k_b}\right)^{0.832}}$	
47.	Chen and Fang [IV.45]	$Nu_b = 0.46\, Re_b^{0.16} \left(\frac{Pr_w}{Pr_b}\right)^{0.1} \left(\frac{\nu_w}{\nu_b}\right)^{-0.55} \left(\frac{\overline{Cp}}{Cp_b}\right)^{0.88} \left(\frac{Gr\,*}{Gr}\right)^{0.831}$	$SC–H_2O$, Vertical tubes P: 22.0 – 34.3 MPa G: 201 – 2500 kg/m^2.s q: 129 – 1735 kW/m^2 D:6 – 26 mm H_b: 278 – 3169 kJ/kg
48.	Zhao et al. [IV.46]	$Nu_b = 0.023\, Re_b^{0.8}\, Pr_b^{1/3}\, F$ $where, F = min(F1, F2)$; $F1 = 0.62 + 0.06 \times ln(\pi_B)$; $F2 = 11.46 \times (ln\, \pi_B)^{-1.74}$	$SC–H_2O$, downward flow in tube P: 23.0 – 26.0 MPa G: 450 – 1500 kg/m^2.s q: 170 – 1400 kW/m^2 t_b: 280 – 410 °C D: 7.6 mm
49.	Saltanov et al. [IV.48]	$Nu_b = 0.0164\, Re_b^{0.823}\, Pr_b^{0.195} \left(\frac{\rho_w}{\rho_b}\right)^{0.374}$	
50.	Saltanov et al. [IV.47] – Based on bulk fluid temperature	$\overline{Nu_b = 0.0052\, Re_b^{0.937}\, Pr_b^{-0.242} \left(\frac{\rho_w}{\rho_b}\right)^{0.854} \left(\frac{\mu_w}{\mu_b}\right)^{-1.37} \left(\frac{k_w}{k_b}\right)^{0.426}}$	$SC–CO_2$, Upward flow in bare tube P: 7.58 – 8.91 MPa G: 885 – 3048 kg/m^2.s q: 26 – 616 kW/m^2 t_b: 20 – 142 °C
51.	Saltanov et al. [IV.47] – Based on	$\overline{Nu_w = 0.0052\, Re_w^{0.937}\, Pr_w^{-0.242} \left(\frac{\rho_w}{\rho_b}\right)^{0.854} \left(\frac{\mu_w}{\mu_b}\right)^{-0.195} \left(\frac{k_w}{k_b}\right)^{-0.816}}$	

	wall temperature		t_w: 32 – 231 °C D: 8.1 mm
52.	Saltanov et al. [IV.47] – Based on film temperature	$\overline{Nu_f = 0.0034\, Re_f^{0.957}\, Pr_f^{-0.143} \left(\frac{\rho_f}{\rho_b}\right)^{1.08} \left(\frac{\mu_f}{\mu_b}\right)^{-0.313} \left(\frac{k_f}{k_b}\right)^{-0.839}}$	
53.	Liu et al. [IV.49]	$\overline{Nu_w = 0.0022\, Re_b^{1.03}\, Pr_b^{0.58} \left(\frac{\rho_w}{\rho_b}\right)^{0.57^{0.026}}}$	SC–CO_2 P: 7.44 – 8.86 MPa G: 285 – 3059 kg/m^2.s q: 29.3 – 537.2 kW/m^2 D: 4.4 – 10 mm Re_b: 1.8x10^4 – 1.17x10^6 $\overline{Pr}_b$: 0.77 – 10.30 SC–H_2O P: 22.5 – 24.9 MPa G: 204 – 1503 kg/m^2.s q: 88 – 1308 kW/m^2 D: 4 – 10.4 mm Re_b: 3.9x10^3 – 5.4x10^5 $\overline{Pr}_b$: 0.52 – 9.27

TABLE IV.2. ASSESSMENT RESULTS FOR NATURAL CIRCULATION HEAT TRANSFER IN A HORIZONTAL TUBE.

Sr. No.	Reference	Mean Relative Error (%)	Mean of Abs. Relative Error (%)	RMS Relative Error (%)	Standard Deviation (%)
1	Dittus and Boelter [IV.1]	24.47	26.68	30.38	18.21
2	McAdams [IV.2]	31.51	32.53	36.80	19.24
3	Bringer and Smith [IV.3]	28.48	28.48	30.10	9.86
4	Shitsman [IV.4]	16.44	16.91	21.28	13.67
5	Petukhov and Kirillov [IV.5]	27.24	28.11	33.31	19.40
6	Petukhov et al. [IV.6]	4.05	11.01	13.13	12.63
7	Domin [IV.7]	66.22	66.62	83.72	51.82
8	Bishop et al. [IV.8]	10.99	13.57	16.68	12.69
9	Swenson et al. [IV.9]	0.06	6.90	9.74	9.85
10	Krasnoshchekov et al. [IV.10]	-8.58	14.98	16.63	14.41
11	Ornatsky et al. [IV.11]	1.07	11.13	14.08	14.20
12	Grass et al. [IV.12]	18.68	18.95	20.29	8.01
13	Yamagata et al. [IV.13]	217.29	217.29	312.23	226.82
14	Jackson and Fewster [IV.14]	5.20	7.13	7.76	5.83
15	Gnielinski [IV.15]	26.58	27.60	32.80	19.44
16	Jackson and Hall [IV.16]	36.69	36.69	37.48	7.73
17	Jackson and Hall [IV.17]	6.42	7.80	8.64	5.85
18	Watts and Chou [IV.18]	-5.65	6.81	8.35	6.22
19	Petukhov et al. [IV.19]	-3.07	4.63	6.53	5.83
20	Razumovskiy et al. [IV.20]	-7.72	15.57	18.16	16.63
21	Gorban et al. [IV.21]	-16.85	25.55	31.01	26.34
22	Griem [IV.22]	43.78	44.04	48.68	21.52
23	Kitoh et al. [IV.23]	56.96	57.00	61.20	22.64
24	Jackson [IV.24]	6.42	7.80	8.64	5.85
25	Liao and Zhao [IV.25]	104.57	104.57	105.50	14.14
26	Feng et al. [IV.26]	14.96	16.72	19.87	13.24
27	Bo et al. [IV.27]	27.62	27.88	32.39	17.11
28	Kuang et al. [IV.28]	10.42	12.44	15.06	10.99
29	Zhu et al. [IV.29]	11.76	12.66	14.41	8.42
30	Yu et al. [IV.30]	6.29	8.73	9.62	7.36
31	Bae and Kim [IV.31]	-1.31	41.26	47.81	48.34
32	Cheng et al. [IV.32]	-17.44	20.21	23.78	16.34
33	Gupta et al. [IV.33]	-10.78	11.45	13.34	7.94
34	Bae et al. [IV.34]	4.04	12.02	16.19	15.86
35	Kim and Kim [IV.35]	-18.91	18.91	22.35	12.06
36	Kim and Kim [IV.36]	4.45	14.65	18.14	17.79
37	Mokry and Pioro [IV.38]	-11.13	14.00	16.40	12.18
38	Mokry et al. [IV.37]	-6.83	12.09	13.90	12.25
39	Gupta et al. [IV.39]	-7.59	8.83	10.91	7.92
40	Bae [IV.40]	-16.73	23.52	26.24	20.45
41	Preda et al. [IV.41]	4.75	14.61	21.17	20.87

42	Liu and Kuang [IV.42]	18.06	18.13	20.28	9.33
43	Gupta et al. [IV.43] – Based on bulk fluid temperature	-10.35	11.05	13.68	9.05
44	Gupta et al. [IV.43] – Based on film temperature	-17.00	17.00	20.55	11.68
45	Gupta et al. [IV.43] – Based on wall temperature	-15.92	15.92	18.30	9.14
46	Wang and Li [IV.44]	-2.17	12.43	14.84	14.85
47	Chen and Fang [IV.45]	9.40	9.75	11.41	6.55
48	Zhao et al. [IV.46]	-29.97	29.97	30.77	7.06
49	Saltanov et al. [IV.48]	-12.57	15.52	19.74	15.40
50	Saltanov et al. [IV.47] – Based on bulk fluid temperature	-16.55	16.55	20.16	11.65
51	Saltanov et al. [IV.47] – Based on wall temperature	-16.50	16.50	20.09	11.60
52	Saltanov et al. [IV.47] – Based on film temperature	-21.47	21.47	25.38	13.70
53	Liu et al. [IV.49]	-5.26	18.79	21.11	20.68

TABLE IV.3. ASSESSMENT RESULTS FOR NATURAL CIRCULATION HEAT TRANSFER IN A VERTICAL TUBE.

Sr. No.	Reference	Mean Relative Error (%)	Mean of Abs. Relative Error (%)	RMS Relative Error (%)	Standard Deviation (%)
1	Dittus and Boelter [IV.1]	47.44	47.86	55.53	28.95
2	McAdams [IV.2]	55.77	56.01	63.56	30.59
3	Bringer and Smith [IV.3]	46.85	46.85	50.99	20.19
4	Shitsman [IV.4]	27.97	28.82	33.53	18.56
5	Petukhov and Kirillov [IV.5]	51.93	52.02	62.31	34.53
6	Petukhov et al. [IV.6]	15.30	20.12	25.68	20.68
7	Domin [IV.7]	87.28	89.20	110.64	68.21
8	Bishop et al. [IV.8]	17.27	20.27	24.21	17.01
9	Swenson et al. [IV.9]	6.37	12.53	15.72	14.42
10	Krasnoshchekov et al. [IV.10]	-1.48	17.52	21.36	21.37
11	Ornatsky et al. [IV.11]	7.40	13.49	19.57	18.17
12	Grass et al. [IV.12]	33.77	33.99	36.81	14.69
13	Yamagata et al. [IV.13]	502.75	502.75	1044.40	918.25
14	Jackson and Fewster [IV.14]	15.97	17.35	19.40	11.05
15	Gnielinski [IV.15]	50.75	50.88	61.29	34.46
16	Jackson and Hall [IV.16]	51.84	51.84	53.78	14.34
17	Jackson and Hall [IV.17]	17.67	18.78	20.75	10.91
18	Watts and Chou [IV.18]	3.64	9.22	11.69	11.14
19	Petukhov et al. [IV.19]	5.39	9.73	11.52	10.21
20	Razumovskiy et al. [IV.20]	0.16	20.68	26.22	26.30
21	Gorban et al. [IV.21]	-9.57	27.31	31.38	29.97
22	Griem [IV.22]	68.61	68.64	76.86	34.73
23	Kitoh et al. [IV.23]	66.50	66.86	74.13	32.87
24	Jackson [IV.24]	17.67	18.78	20.75	10.91
25	Liao and Zhao [IV.25]	61.64	61.64	70.05	33.40
26	Feng et al. [IV.26]	29.67	33.12	44.62	33.43
27	Bo et al. [IV.27]	49.56	50.54	62.04	37.43
28	Kuang et al. [IV.28]	20.51	21.89	26.83	17.35
29	Zhu et al. [IV.29]	19.79	20.76	23.93	13.49
30	Yu et al. [IV.30]	13.56	15.90	17.65	11.34
31	Bae and Kim [IV.31]	-33.40	33.42	36.04	13.58
32	Cheng et al. [IV.32]	-10.33	20.63	24.75	22.56
33	Gupta et al. [IV.33]	-5.57	10.27	13.22	12.02
34	Bae et al. [IV.34]	5.07	17.19	21.03	20.48
35	Kim and Kim [IV.35]	-5.58	10.91	13.93	12.81
36	Kim and Kim [IV.36]	14.62	17.77	18.91	12.04
37	Mokry and Pioro [IV.38]	-6.84	14.66	17.47	16.13
38	Mokry et al. [IV.37]	-3.03	13.13	16.06	15.81
39	Gupta et al. [IV.39]	-2.65	9.78	12.38	12.13
40	Bae [IV.40]	-14.94	28.22	32.49	28.94
41	Preda et al. [IV.41]	0.03	17.37	24.06	24.13
42	Liu and Kuang [IV.42]	24.37	24.66	28.33	14.50

43	Gupta et al. [IV.43] – Based on bulk fluid temperature	-8.26	11.42	15.72	13.42
44	Gupta et al. [IV.43] – Based on film temperature	-14.39	15.72	19.25	12.82
45	Gupta et al. [IV.43] – Based on wall temperature	-15.60	16.34	20.06	12.65
46	Wang and Li [IV.44]	1.56	17.44	21.37	21.38
47	Chen and Fang [IV.45]	11.54	11.72	13.58	7.18
48	Zhao et al. [IV.46]	-14.94	15.28	18.72	11.31
49	Saltanov et al. [IV.48]	-3.49	17.63	20.02	19.77
50	Saltanov et al. [IV.47] – Based on bulk fluid temperature	-15.70	16.96	21.31	14.46
51	Saltanov et al. [IV.47] – Based on wall temperature	-15.64	16.90	21.24	14.42
52	Saltanov et al. [IV.47] – Based on film temperature	-19.77	20.40	24.63	14.74
53	Liu et al. [IV.49]	-6.25	24.17	28.44	27.83

REFERENCES TO APPENDIX IV

[IV.1] DITTUS, F.W., BOELTER, L.M.K., Heat Transfer in Automobile Radiators of the Tubular Type, University of California, Berkeley, Publications on Engineering, **2, 13**, (1930), 443-461.

[IV.2] MCADAMS, W.H., Heat Transmission, 2nd edition, McGraw-Hill, New York, (1942).

[IV.3] BRINGER, R.P., SMITH, J.M., Heat Transfer in the Critical Region, AIChE J., **3, 1**, (1957), 49–55.

[IV.4] SHITSMAN, M.W., Heat Transfer to Supercritical Helium, Carbon-Dioxide, and Water: Analysis of Thermodynamic and Transport Properties and Experimental Data, Cryogenics, **14, 2**, (1974), 77–83.

[IV.5] PETUKHOV, B.S., KIRILLOV, P.L., About Heat Transfer at Turbulent Fluid Flow in Tubes, Thermal Eng. (TenjioaHepreriiKa), **4**, (1958), 63–68, (In Russian).

[IV.6] PETUKHOV, B.S., KRASNOSHCHEKOV, E.A., PROTOPOPOV, V.S., An Investigation of Heat Transfer to Fluids Flowing in Pipes under Supercritical Conditions, Proc. 1961 International Heat Transfer Conference, Boulder, (1961), 569–578.

[IV.7] DOMIN, G., Wärmeübergang in kritischen und überkritischen Bereichen von Wasser in Rohren, Brennstoff-Warme-Fraft (BWK), **15, 11**, (1963), 527–532.

[IV.8] BISHOP, A.A., SANDBERG, L.O., TONG, L.S., Forced Convection Heat Transfer to Water at Near-Critical Temperature and Supercritical Pressures, Westinghouse Electric Corporation Report (WCAP-2056), Pittsburg, 1964.

[IV.9] SWENSON, H.S., CARVER, J.R., KAKARALA, C.R., Heat transfer to Supercritical Water in Smooth-Bore Tubes, J Heat Transfer, **87**, **4**, (1965), 477-484.

[IV.10] KRASNOSHCHEKOV, E.A., PROTOPOPOV, V.S., FEN VAN, KURAEVA, I.V., Experimental Investigation of Heat Transfer for Carbon Dioxide in the Supercritical Region, Gazley, Jr., C., Hartnett, J.P., Ecker, E.R.C. (Eds.), Proc. 2nd All-Soviet Union Conference on Heat and Mass Transfer, Minsk, 1964 (Published as Rand Report R-451-PR, **1**, (1967), 26–35).

[IV.11] ORNATSKY, A.P., GLUSHCHENKO, L.P., SIOMIN, E.T., KALACHYOV, S.I., The Research of Temperature Conditions of Small Diameter Parallel Tubes Cooled by Water under Supercritical Pressures, Proc. 4th International Heat Transfer Conference, Paris-Versailles, 1970.

[IV.12] GRASS, G., HERKENRATH, H., HUFSCHMIDT, W., Anwendung des Prandtlschen Grenzschichtmodells auf den Waermeuebergang an Fluessigkeiten mitstark temperaturabhaengigen Stoffeigenschaften bei erzwungener Stroemung, Waerme-und Stoffuebertragung, **4**, (1971), 113–119 (In German).

[IV.13] YAMAGATA K., NISHIKAWA K., HASEGAWA S., FUJI T., YOSHIDA S., Forced Convective Heat Transfer to Supercritical Water Flowing in Tubes, J Heat Mass Transfer, **15, 12**, (1972), 2575, 2593.

[IV.14] JACKSON, J.D., FEWSTER, J., Forced Convection Data for Supercritical Pressure Fluids, HTFS 1975, Paper No. 21540, (1975).

[IV.15] GNIELINSKI, V., New Equation for Heat and Mass Transfer in Turbulent Pipe and Channel Flow, International Journal of Chemical Engineering, **16, 2**, (1976), 359–368.

[IV.16] JACKSON, J.D., HALL, W.B., Influence of Buoyancy on Heat Transfer to Fluids Flowing in Vertical Tubes under Turbulent Conditions, Hemisphere Publishing Company, Turbulent Forced Convection in Channels and Bundles, **2**, (1979), 613, 640.

[IV.17] JACKSON, J.D., HALL, W.B., Forced Convection Heat Transfer to Fluids at Supercritical Pressure, Turbulent Forced Convection in Channels and Bundles, Editors: S. Kakaç and D.B. Spalding, Hemisphere Publishing Corp., New York, **2**, (1979), 563–612.
[IV.18] WATTS, M.J., CHOU, C.T., Mixed Convection Heat Transfer to Supercritical Pressure Water, Proc. 7th Int. Heat Transfer Conference (IHTC-7), Munich, (1982), 495–500.
[IV.19] PETUKHOV, B.S., KURGANOV, V.A., ANKUDINOV, V.B., Heat Transfer and Flow Resistance in the Turbulent Pipe Flow of a Fluid with Near-Critical State Parameters, High Temp. Sci., **21**, (1983), 81–89.
[IV.20] RAZUMOVSKIY, V.G., ORNATSKIY, A.P., MAYEVSKIY, Y.M., Local Heat Transfer and Hydraulic Behavior in Turbulent Channel Flow of Water at Supercritical Pressure, Heat Transfer-Soviet Res., **22, 1**, (1990), 91–102.
[IV.21] GORBAN', L.M., POMET'KO, R.S., KHRYASCHEV, O.A., Modeling of Water Heat Transfer with Freon of Supercritical Pressure, FEI-1766, Institute of Physics and Power Engineering, Obninsk, Russia, 1990 (in Russian).
[IV.22] GRIEM, H. A New Procedure for the Prediction of Forced Convection Heat Transfer at Near- and Super-Critical Pressure, Heat Mass Transf., **31**, (1996), 301–305.
[IV.23] KITOH, K., KOSHIZUKA, S., OKA, Y., Refinement of Transient Criteria and Safety Analysis for a High Temperature Reactor Cooled by Supercritical Water, Proc. 7th International Conference on Nuclear Engineering (ICONE-7), Tokyo, 1999.
[IV.24] JACKSON, J.D., Consideration of the Heat Transfer Properties of Supercritical Pressure Water in Connection with the Cooling of Advanced Nuclear Reactors, Proc. 13th Pacific Basin Nuclear Conference, Shenzhen, 2002.
[IV.25] LIAO, S.M., ZHAO, T.S., An Experimental Investigation of Convection Heat Transfer to Supercritical Carbon Dioxide in Miniature Tubes, International Journal of Heat and Mass Transfer, **45**, (2002), 5025–5034.
[IV.26] X. FENG, G. LIEJIN, M. YUFEI, J. XIAN'EN, Experimental Investigation to the Heat Transfer Characteristics of Water in Vertical Pipes under Supercritical Pressure, J Xi'an Jiaotong University, 2005.
[IV.27] KUANG, B., ZHANG, Y., CHENG, X., A Wide-Ranged Heat Transfer Correlation of Water at Supercritical Pressures in Vertical Upward Ducts, Proc. 2008 China-Canada Joint Workshop on SCWR (CCSC-2008), Shanghai, 2008.
[IV.28] KUANG, B., ZHANG, Y., CHENG, X., A New, Wide-Ranged Heat Transfer Correlation of Water at Supercritical Pressures in Vertical Upward Ducts, Proc. 7th International Topical Meeting on Nuclear Reactor Thermal Hydraulics, Operation and Safety (NUTHOS-7), Seoul, 2008.
[IV.29] ZHU, X., BI, Q., YANG, D., CHEN, T., An Investigation on Heat Transfer Characteristics of Different Pressure Steam-Water in Vertical Upward Tube, Nucl. Eng. Des., **239**, (2009), 381–388.
[IV.30] YU, J., JIA, B., WU, D., WANG, D., Optimization of Heat Transfer Coefficient Correlation at Supercritical Pressure Using Genetic Algorithms, Heat Mass Transfer, **45**, (2009), 757–766.
[IV.31] BAE, Y.Y., KIM, H.Y., Convective Heat Transfer to CO_2 at a Supercritical Pressure Flowing Vertically in Tubes and an Annular Channel, Experimental Thermal and Fluid Science, **33**, (2009), 329–339.
[IV.32] CHENG, X., YANG, Y.H., HUANG, S.F., A Simplified Method for Heat Transfer Prediction of Supercritical Fluids in Circular Tubes, Ann. Nucl. Energy, **36**, 1120–1128.

[IV.33] GUPTA, S., FARAH, A., KING, K., MOKRY, S., PIORO, I., Developing New Heat-Transfer Correlation for Supercritical-Water Flow in Vertical Bare Tubes, Proc. 18th International Conference on Nuclear Engineering (ICONE–18), Xi'an, 2009.
[IV.34] BAE, Y.Y., KIM, H.Y., KANG, D.J., Forced and Mixed Convection Heat Transfer to Supercritical CO_2 Vertically Flowing in a Uniformly-Heated Circular Tube, Experimental Thermal and Fluid Science, **34**, (2010), 1295–1308.
[IV.35] KIM, D.E., KIM, M.H., Experimental Study of the Effects of Flow Acceleration and Buoyancy on Heat Transfer in a Supercritical Fluid Flow in a Circular Tube, Nucl. Eng. Des., **240**, (2010), 3336–3349.
[IV.36] KIM, D.E., KIM, M.H., Experimental Investigation of Heat Transfer in Vertical Upward and Downward Supercritical CO_2 Flow in a Circular Tube, International Journal of Heat and Fluid Flow, **32**, (2011), 176–191.
[IV.37] MOKRY, S., PIORO, I.L., FARAH, A., KING, K., GUPTA, S., PEIMAN, W., KIRILLOV, P.L., Development of Supercritical Water Heat-Transfer Correlation for Vertical Bare Tubes, Nuclear Engineering and Design, 241, (2011), 1126-1136.
[IV.38] MOKRY, S., PIORO, I., Heat Transfer Correlation for Supercritical Carbon Dioxide Flowing Upward in a Vertical Bare Tube, Proc. Supercritical CO_2 Power Cycle Symposium, Boulder, 2011.
[IV.39] GUPTA, S., MOKRY, S., PIORO, I., Developing a Heat-Transfer Correlation for Supercritical-Water Flowing in Vertical Tubes and Its Application in SCWR, Proc. 19th Int. Conf. On Nuclear Engineering (ICONE-19), Makuhari, 2011.
[IV.40] BAE, Y.Y., Mixed Convection Heat Transfer to Carbon Dioxide Flowing Upward and Downward in a Vertical Tube and an Annular Channel, Nuclear Engineering and Design, **241**, (2011), 3164–3177.
[IV.41] PREDA, T., SALTANOV, EU., PIORO, I., GABRIEL, K., Development of a Heat Transfer Correlation for Supercritical CO_2 based on Multiple Data Sets, Proc. 20th International Conference On Nuclear Engineering (ICONE-20), Anaheim, (2012), 211-217.
[IV.42] LIU, X., KUANG, B., Wide-Ranged Heat Transfer Correlations of Supercritical Water in Vertical Upward Channels, Nucl. Sci. Eng., **32**, (2012), 344–354 (in Chinese).
[IV.43] GUPTA, S., SALTANOV, E., MOKRY, S.J., PIORO, I., TREVANI, L., MCGILLIVRAY, D., Developing Empirical Heat-Transfer Correlations for Supercritical CO_2 Flowing in Vertical Bare Tubes, Nuclear Engineering and Design, **261**, (2013), 116– 131.
[IV.44] WANG, C., LI, H., Evaluation of the Heat Transfer Correlations for Supercritical Pressure Water in Vertical Tubes, Heat Transfer Eng., **35, 6–8**, (2014), 685–692.
[IV.45] CHEN, W., FANG, X., A New Heat Transfer Correlation for Supercritical Water Flowing in Vertical Tube, International Journal of Heat and Mass Transfer, **78**, (2014), 156–160.
[IV.46] ZHAO, M., GU, H.Y., CHENG, X., Experimental Study on Heat Transfer of Supercritical Water Flowing Downward in Circular Tubes, Annals of Nuclear Energy, **63**, (2014), 339–349.
[IV.47] SALTANOV, E., Specifics of Forced Convective Heat Transfer to Supercritical CO_2 Flowing Upward in Vertical Bare Tubes, Ph.D. Thesis, University of Ontario Institute of Technology, 2015.
[IV.48] SALTANOV, E., PIORO, I., MANN, D., GUPTA, S., MOKRY, S., HARVEL, G., Study on Specifics of Forced-Convective Heat Transfer in Supercritical Carbon Dioxide, J. Nucl. Eng. Radiat. Sci., **1**, (2015), 1–8.

[IV.49] LIU, G., HUANG, Y., WANG J., LEUNG, L.H.K., Heat Transfer of Supercritical Carbon Dioxide Flowing in a Rectangular Circulation Loop, Applied Thermal Engineering, **98**, (2016), 39–48.

Appendix V. HEAT TRANSFER CORRELATIONS FOR SUPERCRITICAL FLUIDS IMPLEMENTED IN NOLSTA CODE

The Bringer-Smith correlation [V.1]

$$Nu_x = C\ Re_x^{0.77}\ Pr_w^{0.55}$$

where $C = 0.0266$ for water, $C = 0.0375$ for carbon dioxide. Nu_x and Re_x are evaluated at T_x and temperatures T_{pc}, T_b and T_w are in °C.

$$T_x = \begin{pmatrix} T_b, & if[(T_{pc}-T_b)/(T_w-T_b)] < 0 \\ T_{pc}, & if[(T_{pc}-T_b)/(T_w-T_b)] \leq 1.0 \\ T_w, & if[(T_{pc}-T_b)/(T_w-T_b)] > 1.0 \end{pmatrix}$$

The Jackson correlation [V.2]

$$Nu_b = 0.0183\ Re_b^{0.82}\ \ Pr_b^{0.5}\ \left(\frac{\rho_w}{\rho_b}\right)^{0.3}\ \left(\frac{h_w - h_b}{T_w - T_b}\frac{1}{C_{pb}}\right)^n$$

where exponent n is defined as

$$n = \begin{pmatrix} 0.4, & if\ T_b < T_w < T_{pc}\ and\ 1.2\,T_{pc} < T_b < T_w \\ 0.4 + 0.2\left(\frac{T_w}{T_{pc}} - 1\right), & if\ T_b < T_{pc} < T_w \\ 0.4 + 0.2\left(\frac{T_w}{T_{pc}} - 1\right)\left[1 - 5\left(\frac{T_b}{T_{pc}} - 1\right)\right], & if\ T_{pc} < T_b < 1.2\,T_{pc}\ and\ T_b < T_w \end{pmatrix}$$

and temperatures T_{pc}, T_b and T_w are in Kelvin (K).

The correlation of Bishop et al. [V.3]

$$Nu_x = 0.0069\ (Re_x)^{0.9}\ (Pr'_x)^{0.66}\ \left(\frac{\rho_w}{\rho_b}\right)_x^{0.43}\left(1 + 2.4\frac{D_h}{x}\right)$$

The Shitsman correlation [V.4]

$$Nu_b = 0.023\, Re_b^{0.8}\, Pr_{min}^{0.8}$$

where Pr_{min} = *Minimum of* (Pr_b, Pr_w)

The McAdams correlation [V.5]

$$Nu_b = 0.023\, Re_b^{0.8}\, Pr_b^{0.4}$$

Correlation of Swenson et al. [V.6]

$$Nu_w = 0.00459\ \left(\frac{GD_h}{\mu_w}\right)^{0.923}\ \ \left(\frac{h_w - h_b}{T_w - T_b}\frac{\mu_w}{k_w}\right)^{0.613}\ \left(\frac{\rho_w}{\rho_b}\right)$$

The Jackson-Fewster correlation [V.7]

$$Nu = 0.0183\ \mathrm{Re}_b^{0.82}\ \mathrm{Pr'}^{\ 0.5}\left(\frac{\rho_w}{\rho_b}\right)^{0.3}$$

REFERENCES TO APPENDIX V

[V.1] BRINGER, R.P., SMITH, J.M., Heat Transfer in the Critical Region, AIChE J., **3, 1**, (1957), 49–55.

[V.2] JACKSON, J.D., Consideration of the Heat Transfer Properties of Supercritical Pressure Water in Connection with the Cooling of Advanced Nuclear Reactors, Proc. 13th Pacific Basin Nuclear Conference, Shenzhen, 2002.

[V.3] BISHOP, A.A., SANDBERG, L.O., TONG, L.S., Forced Convection Heat Transfer to Water at Near-Critical Temperature and Supercritical Pressures, Westinghouse Electric Corporation Report (WCAP-2056), Pittsburg, 1964.

[V.4] SHITSMAN, M.W., Heat Transfer to Supercritical Helium, Carbon-Dioxide, and Water: Analysis of Thermodynamic and Transport Properties and Experimental Data, Cryogenics, **14, 2**, (1974), 77–83.

[V.5] MCADAMS, W.H., Heat Transmission, 2nd edition, McGraw-Hill, New York, (1942).

[V.6] SWENSON, H.S., CARVER, J.R., KAKARALA, C.R., Heat transfer to Supercritical Water in Smooth-Bore Tubes, J Heat Transfer, **87**, **4**, (1965), 477-484.

[V.7] JACKSON, J.D., FEWSTER, J., Forced Convection Data for Supercritical Pressure Fluids, HTFS 1975, Paper No. 21540, (1975).

CONTRIBUTORS TO DRAFTING AND REVIEW

Ambrosini, W.	University of Pisa, Italy
Amin, M. M.	Sheffield University, United Kingdom
Anderson, M.	University of Wisconsin, USA
Bodkha, K.	Bhaba Atomic Research Institute (BARC), India
Borgohain, A.	Bhaba Atomic Research Institute (BARC), India
Chen, Y.	China Institute of Atomic Energy (CIAE), China
Cheng, X.	Karlsruhe Institute of Technology (KIT), Germany
Churkin, A.	Gidropress, Russian Federation
Feuerstein, F.	Karlsruhe Institute of Technology (KIT), Germany
Gupta, S.	Bhaba Atomic Research Institute (BARC), India
He, S.	Sheffield University, United Kingdom
Jana, S. S.	Bhaba Atomic Research Institute (BARC), India
Jevremovic, T.	International Atomic Energy Agency (IAEA), Vienna, Austria
Kiss, A.	Budapest University of Technology & Economics, Hungary
Koeckert, L.	Karlsruhe Institute of Technology (KIT), Germany
Kuzmichev, A.	Gidropress, Russian Federation
Leung, L.	Canadian Nuclear Laboratories, Canada
Liu, X.	Shanghai Jiao Tong University (SJTU), China
Lv, L.	China Institute of Atomic Energy (CIAE), China

Pilkhwal, D.S.	Bhaba Atomic Research Institute (BARC), India
Pioro, I.	University of Ontario Institute of Technology (UOIT), Canada
Pucciarelli, A.	University of Pisa, Italy
Razumovskiy, V.	National Technical University of Ukraine Kiev Polytechnic Institute, Ukraine
Saenz, B.	International Atomic Energy Agency (IAEA), Vienna, Austria
Sharma, M.	Bhaba Atomic Research Institute (BARC), India
Vaidya, A. M.	Bhaba Atomic Research Institute (BARC), India
Vijaya, P. K.	Bhaba Atomic Research Institute (BARC), India
Xiong, J.	Shanghai Jiao Tong University (SJTU), China
Yamada, K.	International Atomic Energy Agency (IAEA), Vienna, Austria
Zang, J.	Nuclear Power Institute of China (NPIC), China

RESEARCH COORDINATION MEETINGS

1st RCM: Vienna, Austria, 28–31 October 2014

2nd RCM: Mumbai, India, 23–27 November 2015

3rd RCM: Madison, WI, USA, 26–29 June 2017

4th RCM: Vienna, Austria, 28–31 January 2019

IAEA
International Atomic Energy Agency

No. 26

ORDERING LOCALLY

IAEA priced publications may be purchased from the sources listed below or from major local booksellers.

Orders for unpriced publications should be made directly to the IAEA. The contact details are given at the end of this list.

NORTH AMERICA

Bernan / Rowman & Littlefield
15250 NBN Way, Blue Ridge Summit, PA 17214, USA
Telephone: +1 800 462 6420 • Fax: +1 800 338 4550
Email: orders@rowman.com • Web site: www.rowman.com/bernan

Renouf Publishing Co. Ltd
22-1010 Polytek Street, Ottawa, ON K1J 9J1, CANADA
Telephone: +1 613 745 2665 • Fax: +1 613 745 7660
Email: orders@renoufbooks.com • Web site: www.renoufbooks.com

REST OF WORLD

Please contact your preferred local supplier, or our lead distributor:

Eurospan Group
Gray's Inn House
127 Clerkenwell Road
London EC1R 5DB
United Kingdom

Trade orders and enquiries:
Telephone: +44 (0)176 760 4972 • Fax: +44 (0)176 760 1640
Email: eurospan@turpin-distribution.com

Individual orders:
www.eurospanbookstore.com/iaea

For further information:
Telephone: +44 (0)207 240 0856 • Fax: +44 (0)207 379 0609
Email: info@eurospangroup.com • Web site: www.eurospangroup.com

Orders for both priced and unpriced publications may be addressed directly to:

Marketing and Sales Unit
International Atomic Energy Agency
Vienna International Centre, PO Box 100, 1400 Vienna, Austria
Telephone: +43 1 2600 22529 or 22530 • Fax: +43 1 26007 22529
Email: sales.publications@iaea.org • Web site: www.iaea.org/publications

International Atomic Energy Agency
Vienna
ISBN 978–92–0–102320–9
ISSN 1011–4289